# AIR POLLUTION REMOTE SENSING AND THE SUBSEQUENT INTERACTIONS WITH ECOLOGY ON REGIONAL SCALES

EDITED BY: Honglei Wang, Lijuan Shen, Xiaobin Guan, Xinyao Xie and Junke Zhang

PUBLISHED IN: Frontiers in Environmental Science

frontiers Research Topics

ISSN 1664-8714
ISBN 978-2-83250-249-5
DOI 10.3389/978-2-83250-249-5

## About Frontiers

Frontiers is more than just an open-access publisher of scholarly articles: it is a pioneering approach to the world of academia, radically improving the way scholarly research is managed. The grand vision of Frontiers is a world where all people have an equal opportunity to seek, share and generate knowledge. Frontiers provides immediate and permanent online open access to all its publications, but this alone is not enough to realize our grand goals.

## Frontiers Journal Series

The Frontiers Journal Series is a multi-tier and interdisciplinary set of open-access, online journals, promising a paradigm shift from the current review, selection and dissemination processes in academic publishing. All Frontiers journals are driven by researchers for researchers; therefore, they constitute a service to the scholarly community. At the same time, the Frontiers Journal Series operates on a revolutionary invention, the tiered publishing system, initially addressing specific communities of scholars, and gradually climbing up to broader public understanding, thus serving the interests of the lay society, too.

## Dedication to Quality

Each Frontiers article is a landmark of the highest quality, thanks to genuinely collaborative interactions between authors and review editors, who include some of the world's best academicians. Research must be certified by peers before entering a stream of knowledge that may eventually reach the public - and shape society; therefore, Frontiers only applies the most rigorous and unbiased reviews.
Frontiers revolutionizes research publishing by freely delivering the most outstanding research, evaluated with no bias from both the academic and social point of view. By applying the most advanced information technologies, Frontiers is catapulting scholarly publishing into a new generation.

## What are Frontiers Research Topics?

Frontiers Research Topics are very popular trademarks of the Frontiers Journals Series: they are collections of at least ten articles, all centered on a particular subject. With their unique mix of varied contributions from Original Research to Review Articles, Frontiers Research Topics unify the most influential researchers, the latest key findings and historical advances in a hot research area! Find out more on how to host your own Frontiers Research Topic or contribute to one as an author by contacting the Frontiers Editorial Office: frontiersin.org/about/contact

# AIR POLLUTION REMOTE SENSING AND THE SUBSEQUENT INTERACTIONS WITH ECOLOGY ON REGIONAL SCALES

Topic Editors:
**Honglei Wang,** Nanjing University of Information Science and Technology, China
**Lijuan Shen,** University of Toronto, Canada
**Xiaobin Guan,** Wuhan University, China
**Xinyao Xie,** Institute of Mountain Hazards and Environment, Chinese Academy of Sciences (CAS), China
**Junke Zhang,** Southwest Jiaotong University, China

**Citation:** Wang, H., Shen, L., Guan, X., Xie, X., Zhang, J., eds. (2022). Air Pollution Remote Sensing and the Subsequent Interactions With Ecology on Regional Scales. Lausanne: Frontiers Media SA. doi: 10.3389/978-2-83250-249-5

# Table of Contents

frontiers | Frontiers in Environmental Science

TYPE Editorial
PUBLISHED 06 September 2022
DOI 10.3389/fenvs.2022.1014003



OPEN ACCESS

EDITED AND REVIEWED BY
Martin Siegert,
Imperial College London,
United Kingdom

*CORRESPONDENCE
Xinyao Xie,
xinyaoxie@imde.ac.cn

SPECIALTY SECTION
This article was submitted to Atmosphere and Climate, a section of the journal Frontiers in Environmental Science

RECEIVED 08 August 2022
ACCEPTED 15 August 2022
PUBLISHED 06 September 2022

CITATION
Wang H, Shen L, Zhang J, Xie X and Guan X (2022), Editorial: Air pollution remote sensing and the subsequent interactions with ecology on regional scales.
*Front. Environ. Sci.* 10:1014003.
doi: 10.3389/fenvs.2022.1014003



# Editorial: Air pollution remote sensing and the subsequent interactions with ecology on regional scales

Honglei Wang[1], Lijuan Shen[2], Junke Zhang[3], Xinyao Xie[4]* and Xiaobin Guan[5]

[1]Collaborative Innovation Center on Forecast and Evaluation of Meteorological Disasters(CIC-FEMD), Key Laboratory for Aerosol-Cloud-Precipitation of China Meteorological Administration, Nanjing University of Information Science &Technology, Nanjing, China, [2]Department of Geography and Planning, University of Toronto, Toronto, ON, Canada, [3]Faculty of Geosciences and Environmental Engineering, Southwest Jiaotong University, Chengdu, China, [4]Research Center for Digital Mountain and Remote Sensing Application, Institute of Mountain Hazards and Environment, Chinese Academy of Sciences, Chengdu, China, [5]School of Resource and Environmental Sciences, Wuhan University, Wuhan, China

KEYWORDS

**air pollution, remote sensing, haze, ozone, meteorology, ecology interactions**

Editorial on the Research Topic
Air pollution remote sensing and the subsequent interactions with ecology on regional scales

With the rapid increase of global population and urbanization, the impact of human activities on the earth's ecological environment has become increasingly serious. Human beings are currently facing unprecedented atmospheric environmental challenges, such as the polar ozone ($O_3$) hole, global warming, haze and photochemical pollution, etc. Air pollution, defined as the release of pollutants into the atmosphere, has been regarded as one of the greatest environmental problems that closely related to our lives due to its significant impacts on the environment and human health. Fortunately, in recent decades, we have deeply realized the harm of air pollution, and the related detection technology and treatment methods have also been greatly improved. In particular, the development of remote sensing, such as radar and satellite, has greatly enhanced our understanding of the spatiotemporal, transmission mechanism, and formation mechanism of air pollution.

Air pollution events near the ground, such as sandstorms, acid rain, haze and $O_3$ pollution, etc., can cause great harm to buildings, vegetation, and human health. Generally, the occurrence of these air pollutions has an extensive spatial range and a very random timing. Previous site-based studies can only represent very local information, and there are few long-term continuous observations. As an important approach of monitoring the large-scale atmospheric condition, remote sensing plays a significant role in characterizing the temporal and spatial distributions of air pollution, as well as its multiple feed-back effects on the ecosystem. The continually improved spatial

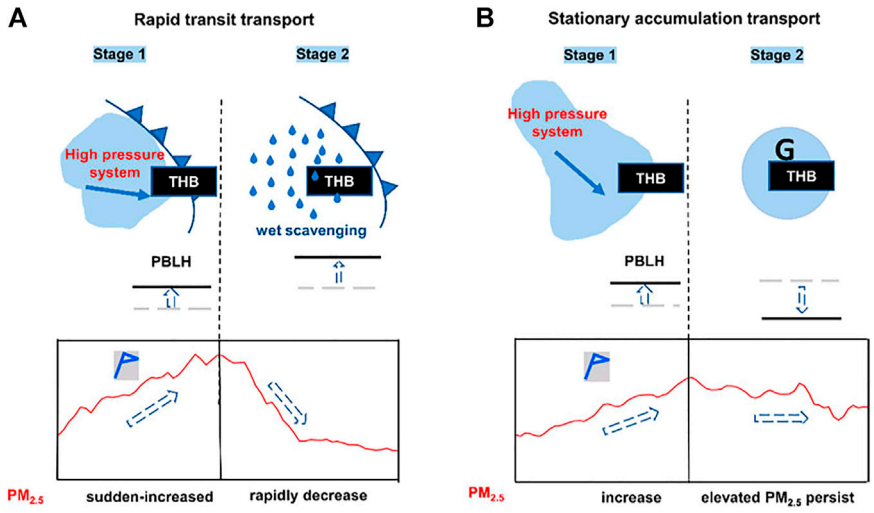


FIGURE 1
Diagram of meteorological mechanism on regional $PM_{2.5}$ transport with the typical patterns of **(A)** rapid transit transport (RTT) and **(B)** stationary accumulation transport (SAT) driving the $PM_{2.5}$ concentration changes (bottom line graphs) for heavy air pollution over the Twain-Hu Basin (THB) revealed in this study. Adapted from Wang et al.

resolution of sensors acts as a key component to satisfy the description of the pollution-ecology interactions at a regional or the global scale. In turn, the changes in ecosystem and atmospheric environment also influence the budget and chemistry of air pollutants and remote sensing monitoring. Numerous studies have confirmed that air pollution can affect the vertical structure of the atmosphere, the optical properties of the aerosol, the acidity and alkalinity of water and soil, precipitation and solar radiation, etc., which affects the accuracy of remote sensing observations and the ecological environment.

In general, an adequate understanding and an improved representation of these complex interactions are crucial for air pollution control, climate change mitigation, and ecosystem restoration. To fully understand these interaction mechanisms requires a large amount of monitoring data (ground, aircraft, and satellite) and various models (box, regional, and global models). This Research Topic aims to cover all theoretical, observational, experimental, and modeling studies that present new knowledge of air pollution, remote sensing, and pollution-ecology interactions at the regional scale, such as the study of air pollution in central China (Figure 1).

This Research Topic collected a total of 29 papers, which can be mainly divided into the following five areas. ①Regional air pollution, a total of 9 papers, covering $O_3$ pollution, $PM_{2.5}$ pollution, aerosol chemical composition and particle size distribution, etc.②Remote sensing observations and model simulations of meteorological conditions, a total of five papers, including precipitation, urban heat islands, typhoons, aerosol radiative effects, etc.③Aircraft observations, a total of three papers, mainly associated with aircraft remote sensing measurement technology in precipitation and cloud microphysical structure. ④Lightning remote sensing and model simulations, a total of seven papers, mainly related to lightning discharge mechanism, spatiotemporal distribution, and the interaction between lightning and aerosol, meteorological elements and ecological environment, etc. ⑤ Remote sensing and pollution-ecology interactions at the regional scale, a total of five papers, mostly correlated with the application of remote sensing technology in the ecological environment and the interaction between air pollution and the ecological environment, etc.

## Regional air pollution

In cities, air pollution is mainly dominated by particulate matter and $O_3$ pollution. The most typical cases are the Great Smog of London event and the Los Angeles photochemical smog event. In recent years, more and more regions have suffered from air pollution, such as the Yangtze River Delta (YRD) and the Pearl River Delta (PRD) in China. Xie et al. investigated the spatiotemporal variability of air stagnation in summer as well as its relation to summer $O_3$ over YRD region of China. They found that air stagnation days (ASDs) in the YRD during the summers from 2001 to 2017 range from 9 to 54 days (9.2–58.4% of the entire summer days). According to the empirical orthogonal function (EOF) analysis, they also assessed the dominant weather systems affecting air stagnation in the YRD. Based on the observation data of environmental and meteorological stations

in the nine cities of PRD in 2019, Yu et al. investigated the variations of secondary $PM_{2.5}$ ($PM_{2.5}$-sec) in the PRD under different photochemical reactivity backgrounds. Results showed that the average maximum concentration of each pollutant appeared higher for polluted stations than for clean ones, indicating that the atmospheric oxidation background was conducive to the formation of $PM_{2.5}$-sec. Using the gaseous pollutants, the 9 sizes of segregated particles, and water-soluble inorganic ions (WSII) data, Wu et al. investigated the size distribution of WSII during the rain period (Meiyu) in the East Asian summer monsoon season. They suggested that the WSII mass concentration peaks at a particle size of 1.1–2.1 μm for fine particles, while at 5.8–9.0 μm (before the Meiyu onset) and 9.0–10.0 μm (during the Meiyu period) for coarse particles, respectively. Mamtimin et al. analyzed the impacts of winter and summer COVID-19 lockdowns on urban air quality in Urumqi, Northwest China. Based on ground and satellite observations, they assessed the impacts of these lockdowns on the air quality in Urumqi and the seasonal differences between them. Liu et al. studied the uncertainty of premature death estimation under various open $PM_{2.5}$ datasets.

Wang et al.analyzed the temporal and spatial patterns of air pollution and the heterogeneity of its influencing factors in central Inner Mongolia from 2016 to 2018. As Inner Mongolia is one of the primary sources of dust in North China, they used multiple auxiliary variables and the geographically weighted regression to estimate the spatial distribution of $PM_{2.5}$ concentration, and further characterized the socioeconomic determinants of $PM_{2.5}$ concentration by geographic detectors. There are also three papers that provide an in-depth analysis of haze pollution in central and eastern China. Yu et al. studied a unique case of joint occurrence of heavy $PM_{2.5}$ pollution episodes and persistent foggy days in central east China. Based on hourly data of ground level meteorological parameters, $PM_{2.5}$ data and CALIPSO-based (the Cloud-Aerosol Lidar and Infrared Pathfinder Satellite Observation) aerosol data, combined with ECMWF (European Centre for Medium-Range Weather Forecasts) reanalysis data and radiosonde temperature profile, they revealed the meteorological reasons for the evolution of the episode at horizontal and vertical scales. Liu et al. and Wang et al. made great efforts to establish conceptual models for typical fog-haze processes. Liu et al. adopted the characteristics of atmospheric circulations and boundary layer dynamic conditions to develop a movable boundary layer conceptual model for the Jianghuai area in the winter half of the year. This conceptual model was validated to well explain the causes of air quality change and frequent fog-haze episodes. Results also suggested that variations of the intensity and range of the cold and warm fronts in the winter half of the year lead to form a movable boundary in the Jianghuai area. Wang et al.identified two distinct patterns of regional transport named rapid transit transport (RTT) and stationary accumulation transport (SAT), both of which induced severe $PM_{2.5}$ pollution episodes in central China from 2015 to 2020. Using influencing meteorological factors, they summarized the differences and similarities between the two regional transport patterns of air pollution.

## Remote sensing observations and model simulations of meteorological conditions

Besides the emission sources, meteorological conditions are the most important influencing factors of regional air pollution. With the development of remote sensing technology and numerical models, it is now possible to carry out detailed and in-depth research on the spatial and temporal distribution, influence area, influence degree and formation mechanism of regional meteorological conditions. Using remote sensing and geodetector, Xiong et al. analyzed long time-series urban heat island (UHI) monitoring and driving factors from 2000 to 2018. Their study mainly focused on the impact of land cover type and landscape metric factors on surface temperature. Urban et al. used google street view photographs to assess the long-term outdoor thermal perception and thermal comfort in the urban environment during heatwaves. In this study, they proposed an approach to the assessment of long-term thermal perception that combines features of currently used methods (i.e., rating scales of thermal perception, surveys, and photographs representing places) and they provided some preliminary validation of this approach. Based on hourly gridded precipitation data (0.1°) calculated by the China Meteorological Administration (CMA), ECMWF data, and microwave measurements, Zhu et al.investigated the extreme precipitation induced by the Typhoon Maysak in Northeast China (September 2020). Their study focused on Changbai Mountain topography and the extreme precipitation in Jilin Province. Hao et al. studied impacts on meteorological parameters and pollutants by aerosol direct radiative effect over Tianjin, China. Sun et al. studied the effects of relative humidity on the diurnal variation of raindrop size distribution in southwest China.

## Aircraft observations

The aircraft observation platform could provide detailed three-dimensional (3D) information of ecosystem and atmospheric environment within a few km of the ground. Aircraft observations can directly obtain 3D atmospheric physics and atmospheric chemistry information, and can also verify remote sensing observations and numerical model results. In China, numerous studies of aircraft observation experiments have been carried out for precipitation, cloud physical chemistry and air pollution. Three papers looked closely at the aircraft measurement. Huang et al. studied the vertical structure of a snowfall event based on observations from the aircraft and mountain station in Beijing. In this study, an aircraft platform,

ground-based dendrometers, cloud radar, radiometer, and automatic station were combined to study a snowfall case on the Yangqing Mountains in Beijing. Dong et al.showed the aircraft observation of a two-layer cloud and the analysis of cold cloud seeding effect. King-air 350 meteorological aircraft was designated to acquire the microphysical characteristics of this cloud. Yang et al. investigated the response of mixed-phase cloud microphysical properties to cloud-seeding near cloud top over Hebei, China. Their findings suggested that the cloud microphysical properties showed obvious responses to the artificial introduction of silver iodide, which was important for human weather modification.

## Lightning remote sensing and model simulations

Lightning is a natural phenomenon of strong discharge, and its high-temperature and high-brightness discharge characteristics can affect atmospheric chemical processes, such as producing a large amount of LNOx, which affects the concentration of $O_3$ in the atmosphere. In addition, the lightning also causes wildfires, and the strong discharge cause harm to human and animals. Lightning is often accompanied by strong convection processes. Severe convection and lightning often occur in the world, and the lightning activities may cause great economic losses and social impact. Jin et al.studied lightning disaster risk zoning in Jiangsu province of China based on the analytic hierarchy process and entropy weight method. They investigated the risk of hazard factors, the sensitivity of hazard-pregnant environment, and the frangibility of a hazard-bearing body in Jiangsu Province. Zhao et al. discussed the potential relationship between aerosols and positive cloud-to-ground lightning (CGL) during the warm season in Sichuan, southwest China. They discussed the influence of aerosols on the relative frequency of CGL and its dependence on thermodynamic and cloud-related factors in Sichuan during the warm season from 2005 to 2017. Liu et al.investigated the spatiotemporal distribution of CGL activities on the Yungui Platea by using a 5-years dataset (2016–2020) from the ground-based National Lightning Detection Network (CNLDN). They also analyzed the correlations between the lightning activities and different meteorological factors. Based on the lightning location data from 2009 to 2019, Li et al. studied the distribution characteristics and formula revision of lightning current amplitude and cumulative probability in Zhejiang province. Guo et al. developed a three-dimensional (3D) numerical model for the diffusion of positive corona charges based on a 2D model with a uniform grid to explore the characteristics of corona discharge at a building tip during a thunderstorm in the presence of wind. The proposed model has advantages in terms of the acquisition of the parameters of corona charges and the spatial distribution of the electric field (E-field) in the environment. Liu et al.performed to analyze the effects of both soil water content and porosity, two of the influencing factors of the finite conductivity, on the propagation of lightning electromagnetic fields (LEMFs) and lightning-induced voltages (LIVs) on overhead lines. A two-dimensional finite difference time domain (FDTD) model together with an improved Archie's soil model is adopted for the field calculation at close distances from the lightning channel. Wang et al. studied characteristics of regular pulse bursts generated from lightning discharges. They studied the waveforms of all lightning discharges from about 15 min.

## Remote sensing and pollution-ecology interactions at the regional scale

Net primary productivity (NPP) is a critical component in terrestrial carbon cycles. Quantitatively estimating and monitoring the dynamics of NPP have become key aspects for exploring the carbon cycle of terrestrial ecosystems. Wu et al. explored the spatiotemporal variation of NPP from 2001 to 2012 and its corresponding relationship with urbanization, taking the Hubei Province in China as a case study area. Based on trend analysis, partial correlation analysis, and Mann-Kendall test, Tian et al. analyzed the spatiotemporal variations of NPP in the Yellow River Basin and their responses to meteorological factors during 1981–2020. Their results revealed that NPP had high values in the mid-south part but low values in the northwestern part of the Yellow River Basin. Wu et al. evaluated the cumulative drought effect on global vegetation photosynthesis using numerous gross primary production (GPP) products. Their findings highlighted the importance of characterizing moisture conditions across vegetation types in generating GPP datasets and the necessity of select multiple GPP dataset to reduce uncertainties in assessing the drought effect on photosynthesis. Ding et al. estimated the contribution of Land-Use and Land-Cover Change (LUCC) to $PM_{2.5}$ pollution levels in the Changsha-Zhuzhou-Xiangtan (CZT) urban agglomeration in the central south China, especially cleared the implications for sustainable land and environment management. Their results suggested that it is necessary to further strengthen the goal of sustainable development rather than following the traditional way of "governance after development". An et al. assessed the vegetation phenological extractions derived from three satellite-derived vegetation indices based on different extraction algorithms over the Tibetan Plateau. In this study, three satellite-derived vegetation indices (enhanced vegetation index, EVI; normalized difference vegetation index, NDVI; and normalized difference phenology index, NDPI; calculated using surface reflectance data from MOD09A1) and two algorithms were used to detect the start and end of growing season (SOS and EOS, respectively) in the Tibetan Plateau (TP).

The 29 papers in this Research Topic use field observations, remote sensing, and numerical models, have conducted in-depth

and detailed discussions on the air pollution, remote sensing and the subsequent interactions with ecology on regional scales from five aspects of regional air pollution processes, remote sensing observations and model simulations of meteorological conditions, aircraft observations, lightning remote sensing and model simulations, and remote sensing and pollution-ecology interactions at the regional scale, the air pollution, remote sensing and the subsequent interactions with ecology on regional scales were discussed in detail, and obtained very interesting and meaningful results.

We thank the authors and reviewers who contributed to this Research Topic. Together these papers provide valuable insight into the air pollution, remote sensing and the subsequent interactions with ecology on regional scales in the future, and open up exciting avenues for future research.

## Author contributions

All authors listed have made a substantial, direct, and intellectual contribution to the work and approved it for publication.

## Funding

This work was supported by the National Natural Science Foundation of China (41830965 and 41805096) and the Postdoctoral Science Foundation of China (Grant No. 2021M700139).

## Conflict of interest

The authors declare that the research was conducted in the absence of any commercial or financial relationships that could be construed as a potential conflict of interest.

## Publisher's note

frontiers in Environmental Science

ORIGINAL RESEARCH
published: 08 November 2021
doi: 10.3389/fenvs.2021.783524

# Spatiotemporal Variability of Air Stagnation and its Relation to Summertime Ozone in the Yangtze River Delta of China

*Min Xie[1]*, Chenchao Zhan[1], Yangzhihao Zhan[1], Jie Shi[1], Yi Luo[1], Ming Zhang[2,3], Qian Liu[4] and Fanhui Shen[3]*

[1]School of Atmospheric Sciences, Nanjing University, Nanjing, China, [2]School of the Environment, Nanjing University, Nanjing, China, [3]State Environmental Protection Key Laboratory of Atmospheric Physical Modeling and Pollution Control, Nanjing, China, [4]Jiangsu Provincial Academy of Environmental Science, Nanjing, China

This paper investigates the spatiotemporal variability of air stagnation in summer as well as its relation to summer ozone ($O_3$) over the Yangtze River Delta (YRD) region of China. Air stagnation days (ASDs) in the YRD during the summers from 2001 to 2017 range from 9 to 54 days (9.2–58.4% of the entire summer days). With the empirical orthogonal function (EOF) analysis, the dominant weather systems affecting air stagnation in the YRD are illustrated. The first three EOFs explain 68.8, 11.3, and 7.1% of the total variance of ASDs, respectively. The first EOF represents the same phase of the entire YRD, which is attributed to the East Asian summer monsoon and mainly depends on the area and the intensity of the South China Sea subtropical high. The second EOF shows significant maritime-continental contrasts, which is related to stronger near-surface winds on sea. As for the third EOF, the air stagnation in the north and the south of the YRD has the opposite phase, with a dividing line along approximately 31°N. This spatial pattern depends on the area and the intensity of the northern hemisphere polar vortex that affects the meridional circulation. $O_3$ is the typical air pollutant in hot seasons in the YRD. It is generally at a high pollution level in summer, and has a positive trend from 2013 to 2017. Air stagnation can affect $O_3$ pollution levels in the YRD. In ASDs, there are usually weak wind, less precipitation, low relative humidity, high temperature, strong solar radiation and high surface pressure, which are favorable to the formation of $O_3$. More $O_3$ pollution episodes in 2013 than 2015 can be partly attributed to more ASDs in 2013. These results show that stagnant meteorological state can lead to the hazardous air quality, and provide valuable insight into the effect of air stagnation on the changes in surface $O_3$ during hot months.

**Keywords: air quality, ozone, air stagnation, the Yangtze River Delta region, pollution meteorological characteristics**

OPEN ACCESS

***Edited by:***
*Lijuan Shen,*
*University of Toronto, Canada*

***Reviewed by:***
*Junjun Deng,*
*Tianjin University, China*
*Yongwei Wang,*
*Nanjing University of Information Science and Technology, China*
*Xianyu Yang,*
*Chengdu University of Information Technology, China*

****Correspondence:***
*Min Xie*
*minxie@nju.edu.cn*

***Specialty section:***
*This article was submitted to Atmosphere and Climate, a section of the journal Frontiers in Environmental Science*

***Received:*** *26 September 2021*
***Accepted:*** *21 October 2021*
***Published:*** *08 November 2021*

***Citation:***
*Xie M, Zhan C, Zhan Y, Shi J, Luo Y, Zhang M, Liu Q and Shen F (2021) Spatiotemporal Variability of Air Stagnation and its Relation to Summertime Ozone in the Yangtze River Delta of China. Front. Environ. Sci. 9:783524. doi: 10.3389/fenvs.2021.783524*

## INTRODUCTION

Air stagnation is usually described as the stable weather condition with less rainfalls and weak winds in the lower to mid troposphere (Garrido-Perez et al., 2018; Li et al., 2019). Weak winds indicate a stable atmospheric stratification with reduced advection and dispersion. Less precipitation means that the wet scavenging process is minimal. It has been revealed that this kind of stagnant weather condition can elevate $O_3$ or $PM_{2.5}$ concentrations, and thereby deteriorate air quality on daily to

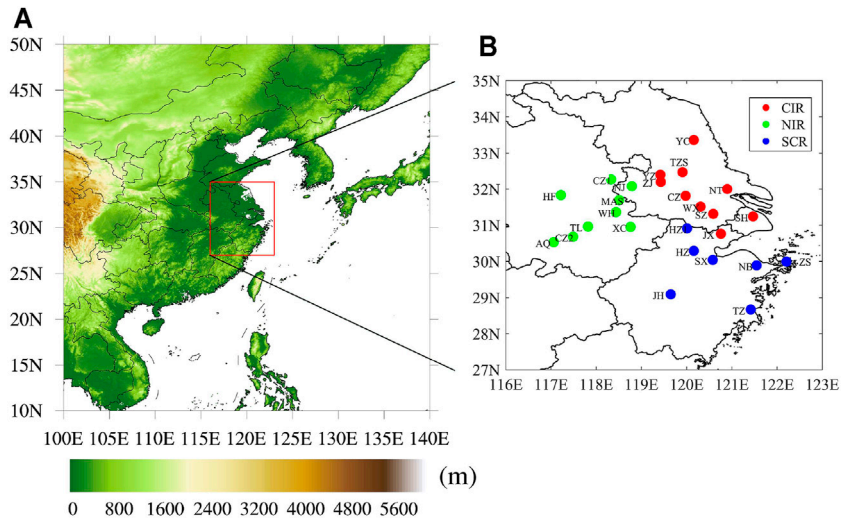


**FIGURE 1 |** The geographic information of the YRD region, including **(A)** its location in China with terrain elevation data and **(B)** the 26 typical YRD cities. In **(B)**, the cities include Nanjing (NJ), Wuxi (WX), Changzhou (CZ), Suzhou (SZ), Nantong (NT), Yancheng (YC), Yangzhou (YZ), Zhenjiang (ZJ), Taizhoushi (TZS), Hangzhou (HZ), Ningbo (NB), Jiaxing (JX), Huzhou (HZ1), Shaoxing (SX), Jinhua (JH), Zhoushan (ZS), Taizhou (TZ), Hefei (HF), Wuhu (WH), Maanshan (MAS), Tongling (TL), Anqing (AQ), Chuzhou (CZ1), Chizhou (CZ2), Xuancheng (XC) and Shanghai (SH). CIR, NIR and SCR respectively represent the cities in the Central Inland, the Northwest Inland and the Southeast Coastal Region, which are discussed in *Spatiotemporal Distribution of $O_3$* Section in details.

inter-annual timescales (Wang and Angell, 1999; Jacob and Winner 2009; Horton et al., 2012, Horton et al., 2014; Schnell and Prather, 2017; Garrido-Perez et al., 2018, 2019). Consequently, air stagnation has significant environmental and health effects (Kerr and Waugh, 2018).

As is well known, China is facing serious air quality deterioration along with the fast economic growth and rapid urban expansion (Chan and Yao, 2008; Ma et al., 2012; Xie et al., 2014; Wang et al., 2017; Zhu, 2017; Wu et al., 2020; Hu et al., 2021). In and around the megacities, poor air quality is usually caused by high emissions and adverse meteorological conditions characterized by light wind and less precipitation (Chan and Yao, 2008; Ma et al., 2012; Li et al., 2017; Wang et al., 2017; Xie et al., 2017; Xu et al., 2018; Shen et al., 2021; Wang et al., 2021). In recent years, under the very strict emission control strategies implemented by the Chinese government, the effects of meteorological conditions on air pollution have attracted more attention and interest from researchers, especially in the Beijing-Tianjin-Hebei (BTH) region (Xu et al., 2011; Zhang et al., 2016), the Yangtze River Delta (YRD) region (Shu et al., 2016, 2017; Xie et al., 2016a, 2016b; Gao et al., 2020, 2021; Zhan et al., 2020, 2021), the Pearl River Delta (PRD) region (Xie et al., 2016c; Zhu et al., 2017) and the Sichuan Basin (Zhan et al., 2019; Yang et al., 2020, 2021). Previous investigations have found that air quality can be worse under stagnant weather conditions. Moreover, Huang et al. (2017) revealed that there was a nationwide increasing trend of air stagnation occurrence in China from 1985 to 2014. Li et al. (2019) also reported that urbanization contributed to air stagnation in Shenzhen (a metropolitan city of the PRD). Therefore, how and to what extent air quality deterioration relates to air stagnation need to be further investigated in the city cluster areas of China.

The YRD region is one of the most developed city clusters in the world. It is located in the eastern coast areas of China (**Figure 1A**). $O_3$ pollution is the typical atmospheric environment problem in this region, with a positive trend in $O_3$ concentration in recent years (Li et al., 2011; Ding et al., 2016; Xu et al., 2018). In previous studies, it was found that high $O_3$ events generally occur in hot and dry seasons, and are usually related to strong photochemical reactions and high air temperature (Chan and Yao, 2008; Li et al., 2011; Ma et al., 2012; Ding et al., 2013, 2016; Xie et al., 2016b; Hu et al., 2016; Pu et al., 2017; Wang et al., 2017; Gao et al., 2021; Zhan et al., 2021). The subtropical high also have significant impacts on $O_3$ concentrations (Shu et al., 2016; Gao et al., 2020; Zhan et al., 2020). Numerous current projections also suggested that $O_3$ pollution in the YRD is likely to worsen in the future due to the changes in weather conditions, such as the increase of air temperature and the decrease in precipitation (Wang et al., 2013; Xie et al., 2017), which can increase air stagnation as well. Therefore, it is necessary to study air stagnation and its impacts on summertime $O_3$ in the YRD. Though some researchers found that air stagnation should not directly used as an index to assess meteorological or climatic effects on air quality without proper assessments, they still pointed out that $O_3$ pollution and air stagnation can co-occur with greater correlations in some areas (Kerr and Waugh, 2018; Garrido-Perez et al., 2019). Consequently, to study this issue in the YRD can help to evaluate the role of air stagnation in this high polluted region.

The main purpose of this study is to investigate the regional characteristic of air stagnation and its influence on summertime $O_3$ in the YRD, including 1) the inter-annual variation of air stagnation in summer over the YRD, 2) the dominant weather

systems and the corresponding meteorological factors related to air stagnation, 3) the spatiotemporal distribution of summertime $O_3$ in the YRD and the relations to air stagnation, and 4) the meteorological mechanism of air stagnation impacting $O_3$ pollution. In the following, the data and the detailed analytical methods used in this study are presented in *Data and Methods* Section. *Results and Discussions* Section gives the main findings. A brief summary is shown in *Conclusion* Section.

# DATA AND METHODS

## Meteorological Data

Air stagnation in the YRD are calculated based on meteorological data from 2001 to 2017. The data include precipitation, 500 hPa winds, 10 m winds, 2 m temperature, relative humidity, surface pressure and solar radiation. As for precipitation, the TRMM 3B42 data (https://pmm.nasa.gov/data-access/downloads/trmm) are used. TRMM 3B42 products are an estimate of precipitation rate based on the combined instrument rain calibration algorithm, with a temporal resolution of 3 h and a spatial resolution of 0.25° (Huffman et al., 2001; Mao and Wu, 2012). These data have been widely used in China in the field of meteorology, hydrology and water resources management (Sun et al., 2012; Zhang et al., 2013). For solar radiation, the monthly data from 2000 to 2017 over China provided by Feng and Wang (2021) are adopted. This dataset has the spatial resolution of 0.1°. It was generated by the geographically weighted regression method to merge the sunshine-duration-derived solar radiation data with the satellite-derived cloud fraction data (MODAL2 M CLD) and aerosol optical depth data (CERES SYN AOD). The data for other meteorological factors are obtained from the daily ERA datasets provided by European Center for Medium-Range Weather Forecasts (ECMWF) (Dee et al., 2011). The datasets have the spatial resolution of 0.25°. They are widely used and have a good application in China as well (Bao and Zhang, 2013; Wang et al., 2015).

## Ozone Observation Data

To illustrate the overview of summertime $O_3$ in the YRD, the air quality monitoring data in the typical YRD cities from 2013 to 2017 are used. The data are acquired from the national air quality real-time publishing platform (http://106.37.208.233:20035), which provides hourly concentrations of six air pollutants ($PM_{2.5}$, $PM_{10}$, $SO_2$, $NO_2$, $O_3$, and CO) over China. These data are strictly in accordance with the national monitoring regulations. The hourly values for each city are calculated by averaging the concentrations at all national monitoring sites in that city. Identification and handling of invalid and lacking data are also manually performed during data processing, following the methods adopted in some previous studies (Xie et al., 2016b; Shu et al., 2016; Gao et al., 2020, 2021; Zhan et al., 2020, 2021). The YRD region consists of 26 typical cities. As shown in **Figure 1B**, the cities include Shanghai (SH); Nanjing (NJ), Wuxi (WX), Changzhou (CZ), Suzhou (SZ), Nantong (NT), Yancheng (YC), Yangzhou (YZ), Zhenjiang (ZJ), Taizhoushi (TZS) in Jiangsu province; Hangzhou (HZ), Ningbo (NB), Jiaxing (JX), Huzhou (HZ1), Shaoxing (SX), Jinhua (JH), Zhoushan (ZS), Taizhou (TZ) in Zhejiang province; and Hefei (HF), Wuhu (WH), Maanshan (MAS), Tongling (TL), Anqing (AQ), Chuzhou (CZ1), Chizhou (CZ2) and Xuancheng (XC) in Anhui province.

## Air Stagnation Day, ASDs, and $S_n$

Air stagnation is usually identified by using predefined thresholds of daily upper level winds, near-surface winds and precipitation (Wang and Angell, 1999; Horton et al., 2012; Horton et al., 2014; Huang et al., 2017; Garrido-Perez et al., 2018, 2019). In this study, based on the previous researches, the used meteorological variables include wind speed at 500 hPa (as upper level wind), 10 m wind speed (as near-surface wind) and precipitation. Thus, a given day can be considered as an air stagnant day when the daily mean 500 hPa wind speed is weaker than 13 m $s^{-1}$, the daily mean 10 m wind speed is weaker than 3.2 m $s^{-1}$, and the daily precipitation is less than 1 mm (Wang and Angell, 1999; Horton et al., 2014; Huang et al., 2017). We use ASDs to represent the total number of air stagnation days throughout the summer (June–August).

To study the relation between $O_3$ pollution and air stagnation (*Ozone Pollution and its Relation to Air Stagnation* Section), $S_n$ is further defined to indicate the air stagnant intensity in a day, given by:

$$S_n = \sum_{i=1}^{3} \frac{A_i - B_i}{A_i} \quad (1)$$

where $A_i$ denotes the threshold of the $i$th meteorological variable and $B_i$ is the exact daily value of the $i$th variable. In this study, the value of $A_1$ for wind speed at 500 hPa is set as 13 m $s^{-1}$, $A_2$ for 10 m wind speed is 3.2 m $s^{-1}$, and $A_3$ for precipitation is 1 mm. The used meteorological data are described in *Meteorological Data* Section. Large $S_n$ represents strong air stagnant intensity. Because the spatial resolutions of the data are 0.25°, the values of ASDs and $S_n$ are calculated at each 0.25° grid over the YRD (116–123°E, 27–35°N).

## Empirical Orthogonal Function Analysis

The empirical orthogonal function (EOF) analysis has been widely used to split the temporal variance of spatially distributed data into orthogonal spatial patterns called EOFs (Gianelli et al., 2007; Hannachi et al., 2007; Fu et al., 2015). Each EOF has a corresponding eigenvalue, which determines the relative variance contribution to the total variance in the field. Furthermore, the eigenvector, which describes the spatial pattern of the EOFs, is associated with a time series that represents the temporal evolution of that spatial pattern. Most of the variance contribution can be contained into the first few EOFs, which can convey enough information to understand the underlying process. In this study, the NCAR Command Language (NCL) EOF coding package is used. For detailed calculation formulas of EOF as well as the manuals can refer to official website of NCL (https://www.ncl.ucar.edu/Applications/eof.shtml).

To investigate the reasons for the variations of ASDs, the EOFs of ASDs are calculated. Since the time series represent the

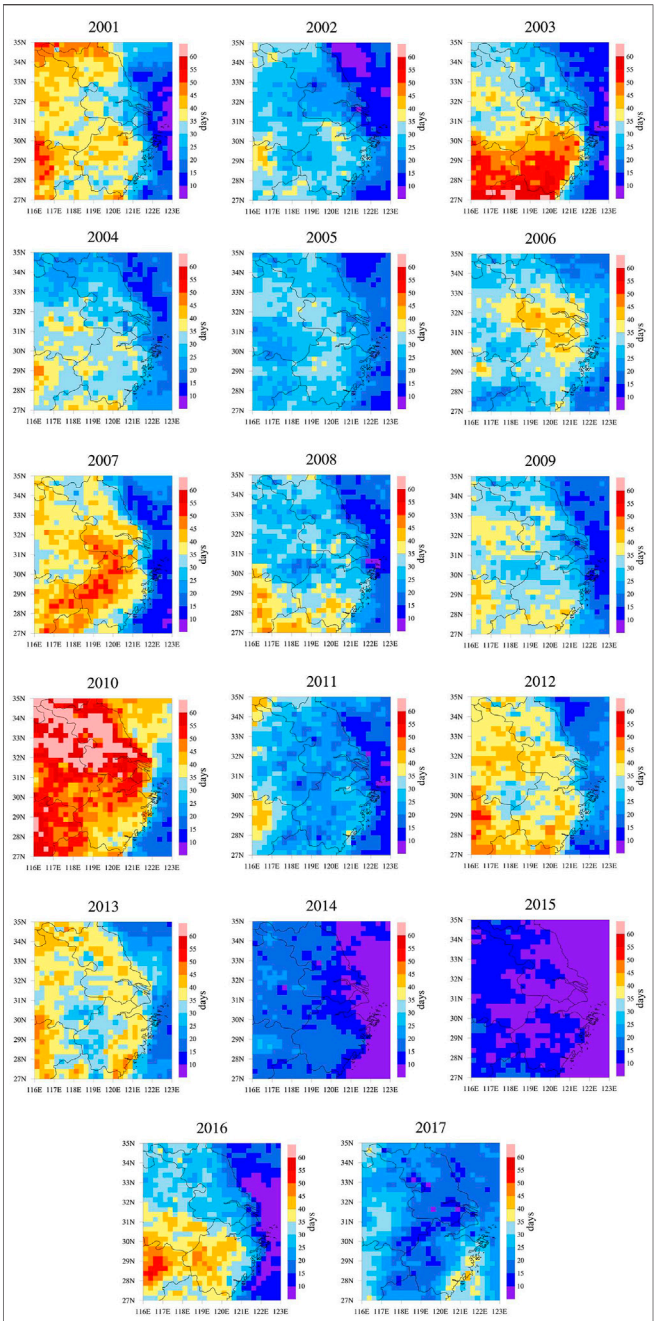


**FIGURE 2 |** The spatiotemporal distribution of summertime air stagnation days over the YRD from 2001 to 2017.

temporal evolution of its associated spatial pattern, we can effectively obtain the dominant weather systems that affects the spatial pattern by establishing the connection between time series and existing atmospheric circulation indexes (Hannachi et al., 2007; Fu et al., 2015). The atmospheric circulation indexes used in this paper come from 130 climate system monitoring indexes (http://cmdp.ncc-cma.net/Monitoring/cn_index_130.php) issued by the National Climate Center of China. Based on the meteorological reanalysis data, these historical indexes were calculated and provided monthly. Furthermore, we calculate the linear regression coefficients between the time series and the meteorological variables (500 hPa wind speed, 10 m wind speed and precipitation) defined ASD to investigate the specific mechanism. The regression coefficients are equal to the increment of the variables when the time series change by unit 1.

# RESULTS AND DISCUSSIONS

## Spatiotemporal Variability of Air Stagnation in Summer Over the YRD

**Figure 2** gives the spatiotemporal distribution of ASDs in summer over the YRD from 2001 to 2017. The regional average value of summertime ASDs is about 30 days (32.3% of the entire summer days), similarly as found by Huang et al. (2017). There are significant spatial and temporal variations for ASDs. For the inter-annual variation, the regional average value of ASDs ranges from 9 to 54 days (9.2–58.4% of the entire summer days), with the maximum ASDs value in 2010 and the minimum value in 2015. This may be associated with the anomaly of the intensity and position of the western Pacific subtropical high system (discussed in *Meteorological Dynamic Mechanism for Air Stagnation Days in Summer of the YRD* Section in detail). For the spatial distribution, the values of ASDs on the ocean are usually smaller than those on land for a particular year. In the YRD, ASDs generally show a considerable regional heterogeneity, which is similar with the finding reported by Garrido-Perez et al. (2018) for Europe and Huang et al. (2017) for China.

## Meteorological Dynamic Mechanism for Air Stagnation Days in Summer of the YRD

EOF analysis of ASDs is carried out to investigate the above spatiotemporal variations. The first three EOFs explain 68.6, 11.3, and 7.1% of the total variations in ASDs, respectively. **Figure 3** shows the results for the first EOF (EOF1). As shown in **Figure 3A**, the spatial pattern of EOF1 is characterized by the same phase over the entire YRD. **Figure 3B** further illustrates the atmospheric circulation condition causing this consistency. The time series of EOF1 is correlated with the South China Sea subtropical high area index and the South China Sea subtropical high intensity index, with the correlation coefficients of 0.40 and 0.42, respectively (statistically significant at the 90% confidence level), implying that the consistency over the YRD may depend on the area and the intensity of the South China Sea subtropical high. When the South China Sea subtropical high is large and strong, this spatial pattern is usually typical, which means it is likely to appear air stagnation in the YRD. As the main component of the East Asian summer monsoon, the subtropical high acts on the monsoon anomaly through its location, area and intensity, which can directly affect the summertime precipitation, rain belt distribution, and drought/flood anomalies in eastern China (Ding and Chan, 2005). **Figures 3C–E** illustrate the regression

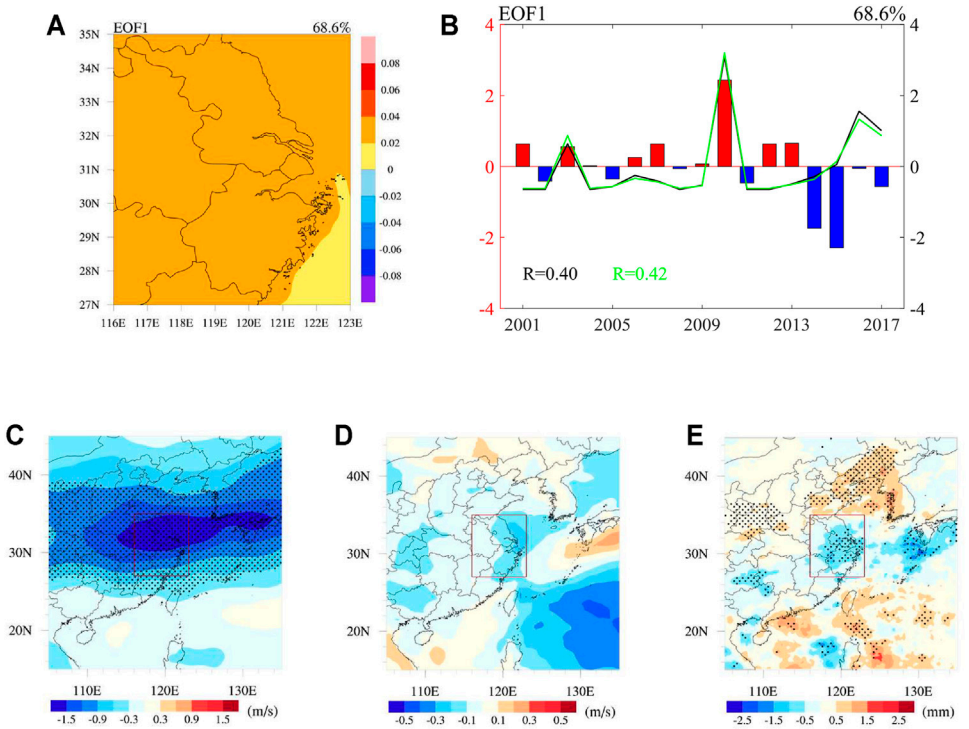


**FIGURE 3 |** The results for the first EOF (EOF1), including **(A)** the spatial pattern of EOF1, **(B)** the time series of EOF1 (histogram), the South China Sea subtropical high area index (black solid line) and the South China Sea subtropical high intensity index (green solid line), and the regression coefficients between time series of EOF1 and **(C)** 500 hPa wind speed, **(D)** 10 m wind speed, and **(E)** precipitation. In **(B)**, the indexes are normalized. In **(C)** to **(E)**, the spotted area passes 90% of the significance test, and the red rectangular region indicates the YRD.

coefficients between the time series of EOF1 and the three meteorological variables used to define ASD. The role of each meteorological variable is different in EOF1. Wind speed at 500 hPa (**Figure 3C**) and precipitation (**Figure 3E**) are the main affecting factors. Generally, with the north jump of the subtropical high, its intensity increases and it controls wide areas of eastern China. In this case, the YRD region is dominated by the subtropical high. The weather is usually stable, and the upper and lower wind fields are generally weak (**Figures 3C,D**). In addition, once the subtropical high is northward, the rain belt generated by the cold and the warm air also moves to north, which can result in less precipitation in midsummer of the YRD as well (**Figure 3E**). Both weak wind and little precipitation in EOF1 are favorable to cause more air stagnation days.

**Figure 4** illustrates the results for the second EOF (EOF2). As shown in **Figure 4A**, the spatial pattern of EOF2 shows significant maritime-continental contrasts, suggesting opposite changes between ocean and land, which can be explained by the fact that the surface wind is usually stronger on sea than on land (**Figure 4D**). **Figure 4B** presents that the time series of EOF2 cannot be linked to existing atmospheric circulation indexes. However, as shown in **Figure 4C**, it can be found that the north of the YRD is affected by the subtropical jet while the south is affected by the easterlies, corresponding to high wind speeds in the north and low in the south of the YRD at the 500 hPa layer. This may be the factor leading to the spatial pattern of EOF2 on land.

**Figure 5** presents the results for the third EOF (EOF3). With regard to the spatial pattern, the ASDs in the north and the south of the YRD has the opposite phase, with a dividing line of approximately 31°N (**Figure 5A**). **Figure 5B** shows that the time series of EOF3 has a good relation to the northern hemisphere polar vortex (the tropospheric polar vortex) area index and the northern hemisphere polar vortex intensity index, with the correlation coefficients of −0.42 and −0.42, respectively (statistically significant at the 90% confidence level). When the northern hemisphere polar vortex is small and weak, the north part of the YRD has high ASDs values while the south has low ones. The specific physical process is probably as follows: with the small and weak tropospheric polar vortex, an abnormal high-pressure center is prone to occur above the mid-high latitudes of Asia, which is conductive to the weakening of the westerly wind at 500 hPa (**Figure 5C**). The atmospheric circulation shows a meridional distribution and the position of the upper-level jet stream is southward. Thus, the cold air can move southward easily, which can form precipitation in the south of the YRD with the warm and wet flow conveyed by the subtropical high (**Figure 5E**). For another, the subtropical high is usually strong while the tropospheric polar vortex is weak. The near-surface wind speed is low in the areas dominated by the subtropical high (**Figure 5B**). The tropospheric polar vortex

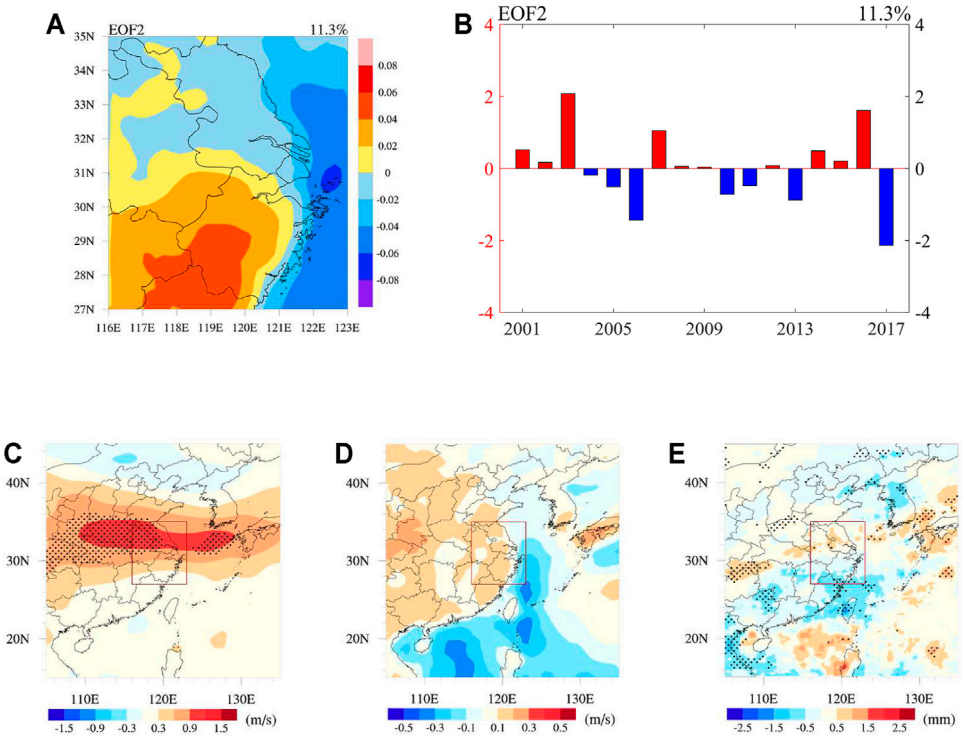


**FIGURE 4 |** The results for the second EOF (EOF2), including **(A)** the spatial pattern of EOF2, **(B)** the time series of EOF2 (histogram), and the regression coefficients between time series of EOF2 and **(C)** 500 hPa wind speed, **(D)** 10 m wind speed, and **(E)** precipitation. In **(B)**, the indexes are normalized. In **(C)** to **(E)**, the spotted area passes 90% of the significance test, and the red rectangular region indicates the YRD.

controls the semi-permanent atmospheric center of action, which has important effects on atmospheric circulation at high latitudes. These effects are usually continuous more than seasonal scales. Furthermore, these effects are commonly expressed by significant atmospheric oscillations in climatology, such as the Northern Atlantic Oscillation, the Arctic Oscillation and the East Atlantic-West Russia Pattern (Waugh et al., 2017), which provides a way to link the variances of air stagnation to climate anomalies.

## Summertime Ozone in the YRD and its Relation to Air Stagnation

### Spatiotemporal Distribution of $O_3$

**Figure 6** presents the spatiotemporal distribution of MDA8 $O_3$ during the summers from 2013 to 2017 over the YRD. The summer mean values of MDA8 $O_3$ in many cities are over 120 μg $m^{-3}$. According to the geographical locations and the summer mean MDA8 $O_3$ concentrations, the 26 typical cities in the YRD can be classified into three categories, which are the cities in the Central Inland Region (CIR), the Northwest Inland Region (NIR) and the Southeast Coastal Region (SCR) (**Figure 1B**). The cities in the CIR include SH, WX, CZ, SZ, NT, YC, YZ, ZJ, TZS, and JX. These cities have the highest $O_3$ concentrations, with the average summer MDA8 $O_3$ of 134.4 μg $m^{-3}$ in 2017. The cities in the NIR include NJ, HF, WH, MAS, TL, AQ, CZ1, CZ2, and XC. These cities usually have relatively high $O_3$ concentrations, with the average summer MDA8 $O_3$ of 121.3 μg $m^{-3}$ in 2017. The cities in the SCR include HZ, NB, HZ1, SX, JH, ZS, and TZ. These cities have relatively low $O_3$ concentrations, but still have the average summer MDA8 $O_3$ of 112.0 μg $m^{-3}$ in 2017. The increasing rates of $O_3$ concentrations in these three regions are also different. Among them, the MDA8 $O_3$ of the cities in the NIR increases the most rapidly, with an average increment of 22.6 μg $m^{-3}$ $a^{-1}$ from 2015 to 2017. The cities in the CIR have the second highest increase rate of MDA8 $O_3$, with an average increment of 2.5 μg $m^{-3}$ $a^{-1}$. As for those cities in the SCR, the MDA8 $O_3$ almost remains the same, with a small average increment of 0.9 μg $m^{-3}$ $a^{-1}$. The YRD is located in a typical monsoon affected region. The summer monsoon can play an important role in the transport and the dilution processes of $O_3$ in the YRD. The strong solar radiation and the high air temperature that are related with subtropical high are the main causes of the high $O_3$ concentration, especially before and after the monsoon rain belt (He et al., 2008; Wang et al., 2011; Zhou et al., 2013; Yin et al., 2019; Jiang et al., 2021). For the low concentration of $O_3$ in the SCR, it associates with clean maritime airflows from the Pacific Ocean driven by the monsoon (Xie et al., 2016b; Shu et al., 2016).

### Ozone Pollution and its Relation to Air Stagnation

To reveal whether air stagnation affects summertime $O_3$ pollution, **Figure 7** illustrates the relationship between air

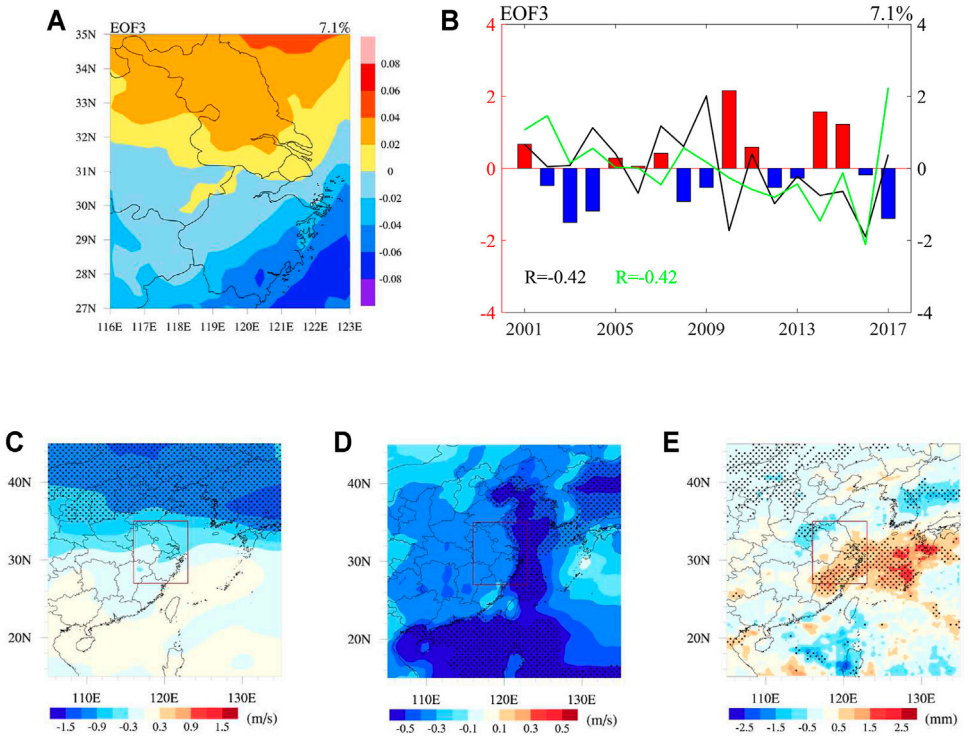


**FIGURE 5 |** The results for the third EOF (EOF3), including **(A)** the spatial pattern of EOF3, **(B)** the time series of EOF3 (histogram), the northern hemisphere polar vortex (the tropospheric polar vortex) area index (back solid line) and the northern hemisphere polar vortex intensity index (green solid line), and the regression coefficients between time series of EOF3 and **(C)** 500 hPa wind speed, **(D)** 10 m wind speed, and **(E)** precipitation. In **(B)**, the indexes are normalized. In **(C)** to **(E)**, the spotted area passes 90% of the significance test, and the red rectangular region indicates the YRD.

stagnation state and $O_3$ pollution level in the CIR, the NIR, the SCR, and the whole YRD region. The MDA8 $O_3$ concentrations are divided into three pollution levels from low to high, which are 0–100 μg $m^{-3}$ (level I), 100–160 μg $m^{-3}$ (level II) and higher than 160 μg $m^{-3}$ (level III). 100 and 160 μg $m^{-3}$ are the class 1 and 2 criterion for MDA8 $O_3$ in the National Ambient Air Quality Standard of China, respectively. Moreover, $S_n$ defined in *Air Stagnation Day, ASDs, and $S_n$* Section are used to reflect the stagnant intensity.

As shown in **Figure 7A**, when the $O_3$ pollution becomes worse, the percentage of $S_n$ greater than 0 (tendency to form air stagnation) increases while the percentage of $S_n$ less than 0 (tendency to cause the atmosphere unstable) decreases. For the distribution of percentages of the MDA8 $O_3$ concentrations for a given $S_n$ value range, as presented in **Figure 7B**, the percentage of high $O_3$ concentration increases with the increasing of $S_n$ value, which means more $O_3$ pollution events occur when the atmosphere is more stable. These findings reveal that the air stagnant status does have an influence on $O_3$ pollution. It is worth mentioning that the positive relation between $O_3$ pollution and air stagnation not only occurs in special areas in the YRD (the CIR, the NIR and the SCR) but also is the common phenomena throughout the YRD.

Since the calculation of $S_n$ does not cover all meteorological factors that affect $O_3$ concentrations, it is necessary to discuss the performance of other meteorological factors in air stagnation days. **Figure 7C** gives the distribution of meteorological factors for a given $S_n$ value range. The meteorological factors include relative humidity (RH), 2 m air temperature (Temp) and surface air pressure (SP). As illustrated in **Figure 7C**, the days with $S_n$ greater than 0 (tendency to form air stagnation) usually have lower relative humidity, higher 2 m temperature and higher surface pressure than days with $S_n$ less than 0 (tendency to cause the atmosphere unstable) in the YRD. Low relative humidity and high temperature, as well as less precipitation that results in more solar radiation to penetrate the atmosphere, are all favorable to form $O_3$ pollution episodes (Ding et al., 2013, 2016; Pu et al., 2017). Particularly, the 2 m temperature increases with the $S_n$ value, which explains that the high $O_3$ pollution level tends to occur when $S_n$ is greater than 1 (the atmosphere is more stagnant).

## Mechanism for the Effect of Air Stagnation on $O_3$ Pollution in the Summer of 2013 and 2015

Previous studies, as well as the result of *Spatiotemporal Distribution of $O_3$* Section, show a positive trend of $O_3$ concentrations in the YRD during 2013–2017 (Lu et al., 2020; Wang et al., 2020; Zhan et al., 2021). However, the $O_3$ pollution

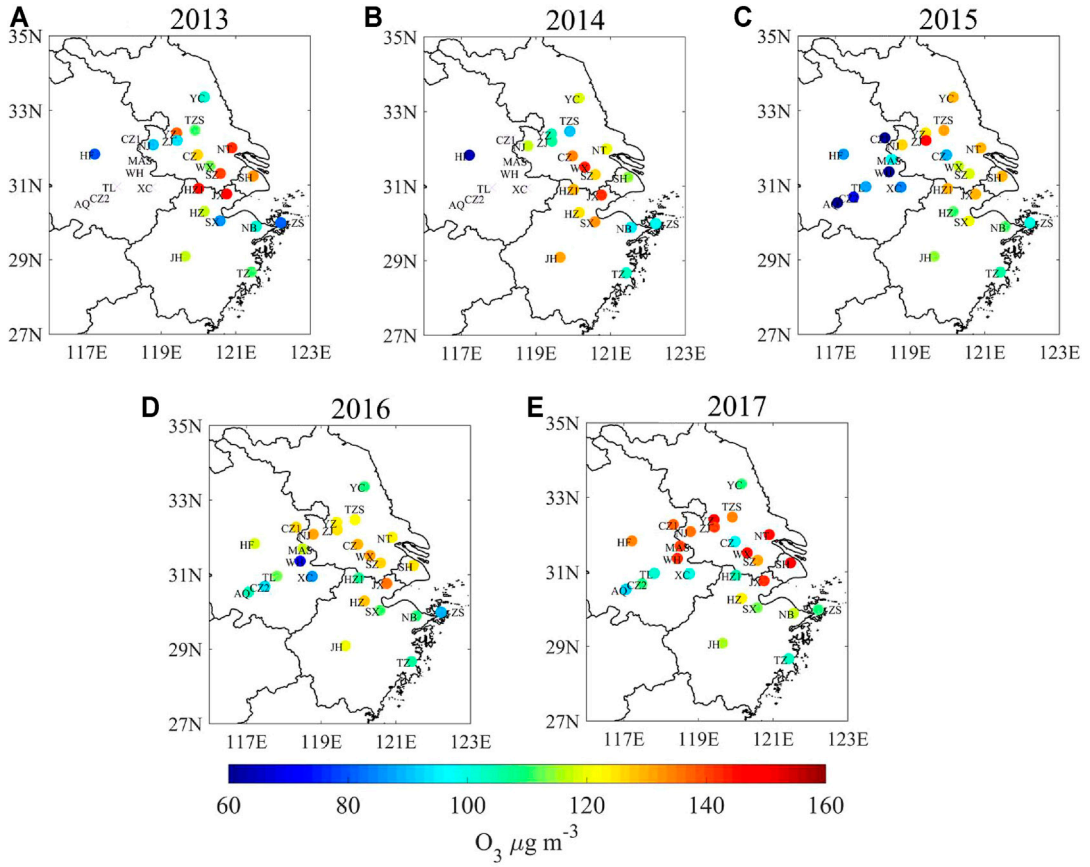


**FIGURE 6 |** The spatial distribution of summer average MDA8 $O_3$ in the YRD, including **(A)** 2013, **(B)** 2014, **(C)** 2015, **(D)** 2016, and **(E)** 2017. The purple x symbols in **(A)** and **(B)** indicate that there are no data.

days account for 17.0, 16.1, 14.7, 15.3, and 20.2% (from 2013 to 2017 respectively) of the summer days of the YRD. It seems that $O_3$ pollution episodes are more likely to occur in the summer of 2013 than 2015. Additionally, **Figure 2** shows that there are more air stagnant days in 2013 than 2015. **Figures 3–5** also illustrate that the time series of all three EOFs show opposite phase in 2013 and 2015. Therefore, comparing the meteorological fields between 2013 and 2015 may reveal how air stagnation affects $O_3$ pollution in the YRD from the perspective of meteorological conditions.

**Figure 8** shows the summertime averages and the differences between 2013 and 2015 for the three meteorological variables identifying air stagnation day. In the 500 hPa weather map of 2013 (**Figure 8A**), the tropospheric polar vortex is large and strong. The flat isopleths indicate that there is a small geopotential height gradient, which can result in weak wind in the YRD. However, in 2015, the tropospheric polar vortex is small and weak. There are obvious troughs and ridges in the upper reaches of the YRD (**Figure 8B**), and thereby the cold air can move southward. These differences are visually shown in **Figure 8C**. Compared to 2015, there is a significant positive potential height perturbation in 2013, which can lead to easterly wind component over the YRD and result in a smaller wind speed at 500 hPa atmospheric layer. Furthermore, the westerly component appearing at 45°N confirms the fact that the westerly jet lies more to the north. For 10 m wind speed, it is higher on the ocean than on the land in both 2013 (**Figure 8D**) and 2015 (**Figure 8E**), which partly explains the reason why the ocean usually has a smaller ASDs. **Figure 8F** shows that the 10 m wind speed has a southwest component in 2013 (compared with 2015), which can block the prevailing southeasterly wind.

As for precipitation, there is a significant difference in the spatial distribution between 2013 and 2015. In the summer of 2013, there are more rainfalls in the south of China, and there is less precipitation in the YRD and the north part of China (**Figure 8G**). In the summer of 2015, however, more rains fall in the YRD, especially in the south of Anhui province (**Figure 8H**). The difference of precipitation between 2013 and 2015 (precipitation in the summer of 2013 minus that in 2015) are shown in **Figure 8I**. Obviously, the precipitation over the YRD is much higher in 2015, implying that the processes of the dilution and the removal of air pollutants are more intensive in 2015. Less precipitation in 2013 also means there are more intensive solar radiation reaching the

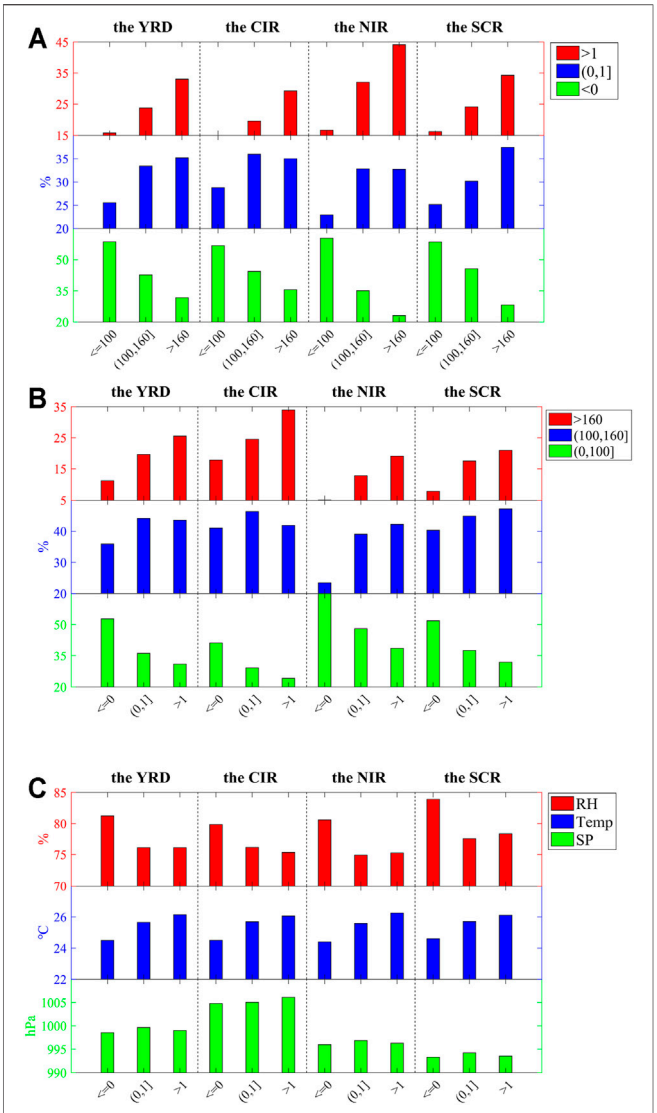


**FIGURE 7 |** The relations between $O_3$ pollution levels and air stagnation intensity in the YRD, including **(A)** the distribution of percentages of $S_n$ values under different $O_3$ pollution levels, **(B)** the distribution of percentages of the $O_3$ pollution levels for a given $S_n$ value range, and **(C)** the distribution of relative humidity (RH), 2 m air temperature (Temp) and surface air pressure (SP) for a given $S_n$ value range.

ground and higher air temperature near the surface over the YRD, as shown in **Figure 9**.

In summary, larger and stronger of the tropospheric polar vortex and the subtropical high result in more air stagnation days over the YRD in the summer of 2013. Under this circumstance, the upper- and lower-level winds are weak, and more air pollutants including $O_3$ and its precursors are trapped near surface over the YRD. Moreover, less precipitation, higher air temperature and stronger solar radiation that are associated with air stagnation facilitate the photochemical reactions of $O_3$ formation. Then, more $O_3$ pollution days occur in the summer of 2013. The weather systems and the changes in relevant meteorological factors related to air stagnation can affect the physical and chemical processes of $O_3$ formation, and thereby severe $O_3$ pollution tends to form under air stagnant conditions.

## CONCLUSION

Stagnant meteorological state can lead to hazardous air quality. $O_3$ is the typical air pollutant in hot seasons of the YRD. In this study, air stagnation and its impact on summertime $O_3$ in the YRD are investigated. The summertime air stagnation days over the YRD have significant spatiotemporal variations from 2001 to 2017. The regional average value is about 30 days (32.3% of the entire summer days) in the YRD. The values range from 9 days (9.2%) in 2015 to 54 days (58.4%) in 2010. The values on the ocean are usually smaller than those on land. Based on EOF analysis, the first three EOFs explain 68.8, 11.3, and 7.1% of the variations of air stagnation days in the YRD, respectively. The spatial pattern of the first EOF is related to the East Asian summer monsoon, and mainly depends on the area and the intensity of the South China Sea subtropical high. When the South China Sea subtropical high is large and strong, air stagnation is likely to appear in the YRD. The second EOF shows significant maritime-continental contrasts, which is due to stronger surface wind on sea than that on land. As for the third EOF, the north and the south of the YRD has the opposite phase, with a dividing line along approximately 31°N. This spatial pattern is related to the area and the intensity of the northern hemisphere polar vortex that can affect the meridional circulation. When the northern hemisphere polar vortex is small and weak, the north part of the YRD has more air stagnation days. $O_3$ concentration is high in summer and shows an increase from 2013 to 2017 over the YRD. The 26 typical YRD cities can be classified into three categories (CIR, NIR, and SCR) based on their $O_3$ characteristics and geographical locations. The cities in the CIR have the highest concentrations of MDA8 $O_3$. The cities in the NIR have the most rapid increasing of MDA8 $O_3$. Air stagnation can affect $O_3$ pollution levels in the YRD. The percentage of high $O_3$ pollution level increases with air stagnant intensity both in special areas and all over the YRD. Weak wind, less precipitation, low relative humidity, high temperature, strong solar radiation and high surface pressure under stagnant days are favorable to form severe $O_3$ pollution. More stagnant weather condition in 2013 can explain more $O_3$ pollution episodes in that year than in 2015. Larger and stronger of the tropospheric polar vortex and the subtropical high result in more air stagnation days over the YRD in the summer of 2013. Under this circumstance, there are weaker upper- and lower-level winds, less precipitation, higher air temperature and stronger solar radiation over the YRD in 2013 than 2015. The weather systems and the changes in relevant meteorological factors can affect the physical and chemical processes of $O_3$ formation, and thereby severe $O_3$ pollution tends to form.

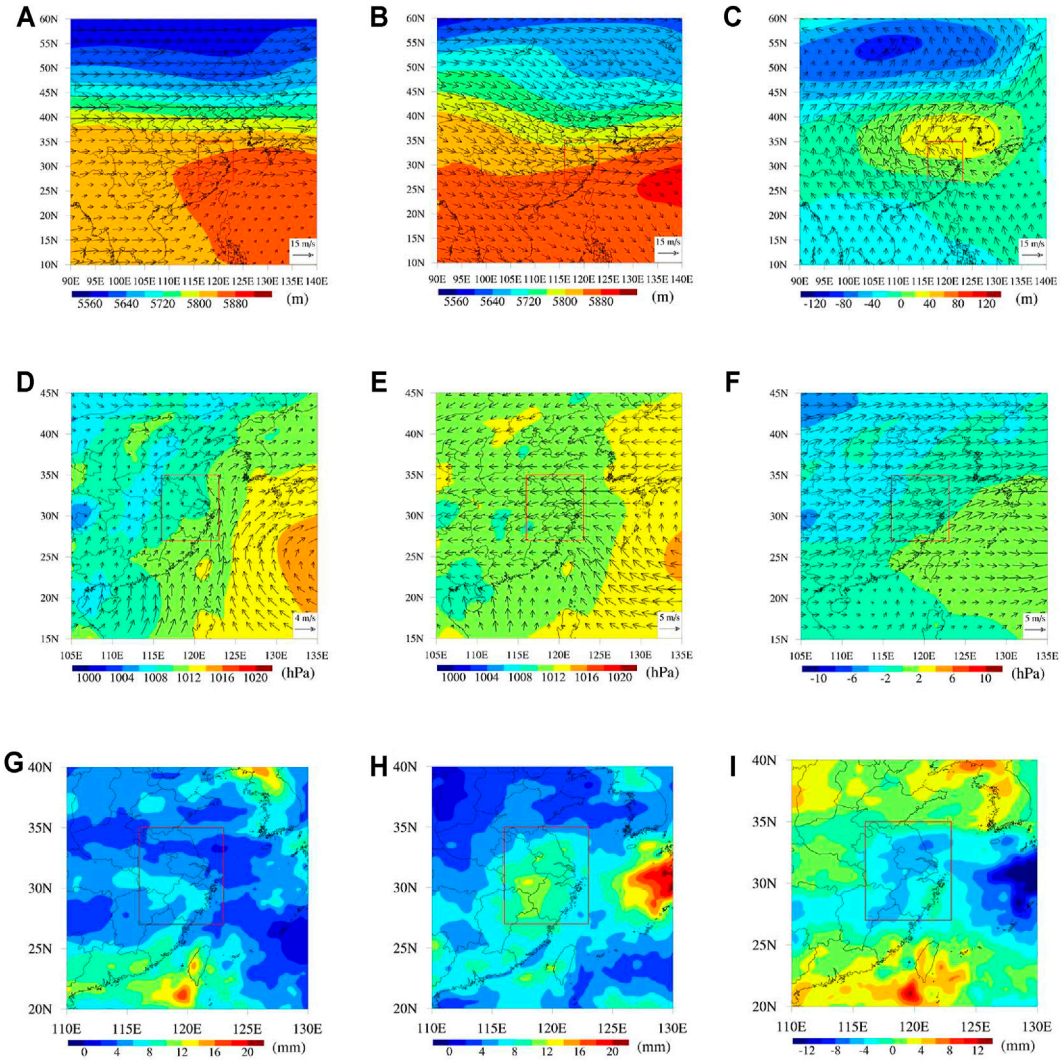


**FIGURE 8 |** The summertime averages for the three meteorological variables identifying an air stagnation day, including the fields of geopotential height and wind at 500 hPa atmospheric layer **(A–C)**, the sea level pressure field and 10 m wind field **(D–F)**, and the precipitation **(G–I)**. **(A)**, **(D)**, and **(G)** show the results in 2013. **(B)**, **(E)** and **(H)** show the results in 2015. **(C)**, **(F)**, and **(I)** show the differences between 2013 and 2015. In **(A–I)**, the red rectangular region indicates the YRD.

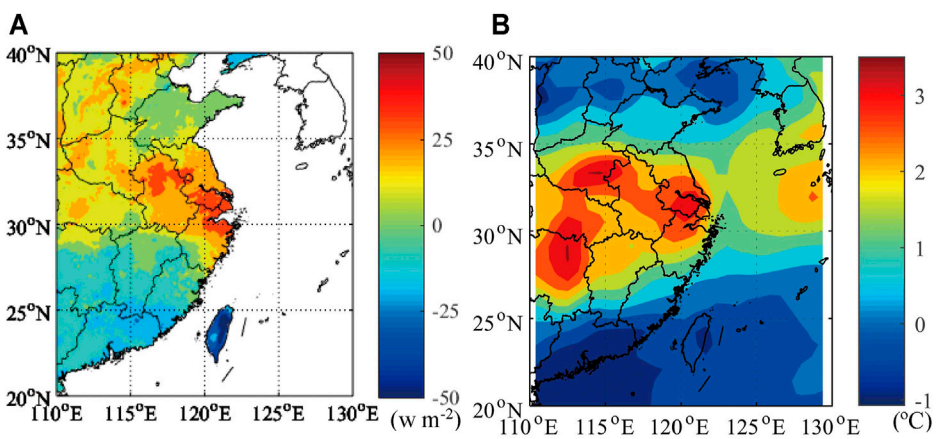


**FIGURE 9 |** The differences of solar radiation **(A)** and 2 m air temperature **(B)** over the YRD between the summer in 2013 and 2015.

This work provides an overview of air stagnation and its behaviors over the YRD, and discusses its effects on the summertime $O_3$ pollution over this region in recent years. The above findings provide valuable insight into the formation of $O_3$ pollution in the YRD, and help to understand the effect of air stagnant state on the changes in surface $O_3$ concentration in hot seasons.

## DATA AVAILABILITY STATEMENT

The original contributions presented in the study are included in the article/supplementary material, further inquiries can be directed to the corresponding author.

## AUTHOR CONTRIBUTIONS

MX had the original ideas, designed the research, collected the data, prepared the original draft, and acquired financial support for the project leading to this publication. CZ carried out the data analysis and helped to prepare the original draft. YZ, JS, and YL help to collect the data and prepare the original draft. MZ, QL, and FS reviewed the initial draft and checked the English of the original manuscript.

## FUNDING

This work was supported by the Natural Science Foundation of Jiangsu Province (BK20211158), the National Natural Science Foundation of China (41475122, 40805059) and the National Key Basic Research Program of China (2006CB403701).

## ACKNOWLEDGMENTS

We are grateful to NEMC for the air quality monitoring data and to ECMWF for the meteorological reanalysis data.

## REFERENCES

Bao, X., and Zhang, F. (2013). Evaluation of NCEP-CFSR, NCEP-NCAR, ERA-Interim, and ERA-40 Reanalysis Datasets against Independent Sounding Observations over the Tibetan Plateau. *J. Clim.* 261, 206–214. doi:10.1175/Jcli-D-12-0005610.1175/jcli-d-12-00056.1

Chan, C. K., and Yao, X. (2008). Air Pollution in Mega Cities in China. *Atmos. Environ.* 42, 1–42. doi:10.1016/j.atmosenv.2007.09.003

Dee, D. P., Uppala, S. M., Simmons, A. J., Berrisford, P., Poli, P., Kobayashi, S., et al. (2011). The ERA-Interim Reanalysis: Configuration and Performance of the Data Assimilation System. *Q.J.R. Meteorol. Soc.* 137, 553–597. doi:10.1002/qj.828

Ding, A. J., Fu, C. B., Yang, X. Q., Sun, J. N., Zheng, L. F., Xie, Y. N., et al. (2013). Ozone and fine Particle in the Western Yangtze River Delta: an Overview of 1 Yr Data at the SORPES Station. *Atmos. Chem. Phys.* 13, 5813–5830. doi:10.5194/acp-13-5813-2013

Ding, A. J., Nie, W., Huang, X., Chi, X., Sun, J., Kerminen, V.-M., et al. (2016). Long-Term Observation of Air Pollution-Weather/climate Interactions at the SORPES Station: a Review and Outlook. *Front. Environ. Sci. Eng.* 10 (5), 15. doi:10.1007/s11783-016-0877-3

Ding, Y. H., and Chan, J. C. L. (2005). The East Asian Summer Monsoon: an Overview. *Meteorol. Atmos. Phys.* 89, 117–142. doi:10.1007/s00703-005-0125-z

Feng, F., and Wang, K. (2021). Merging Ground-Based sunshine Duration with Satellite Cloud and Aerosol Data to Produce High Resolution Long-Term Surface Solar Radiation over China. *Earth Syst. Sci. Data* 13 (3), 907–922. doi:10.5194/essd-13-907-2021

Fu, T.-M., Zheng, Y., Paulot, F., Mao, J., and Yantosca, R. M. (2015). Positive but Variable Sensitivity of August Surface Ozone to Large-Scale Warming in the Southeast United States. *Nat. Clim Change* 5, 454–458. doi:10.1038/Nclimate2567

Gao, D., Xie, M., Chen, X., Wang, T., Liu, J., Xu, Q., et al. (2020). Systematic Classification of Circulation Patterns and Integrated Analysis of Their Effects on Different Ozone Pollution Levels in the Yangtze River Delta Region, China. *Atmos. Environ.* 242, 117760. doi:10.1016/j.atmosenv.2020.117760

Gao, D., Xie, M., Liu, J., Wang, T., Ma, C., Bai, H., et al. (2021). Ozone Variability Induced by Synoptic Weather Patterns in Warm Seasons of 2014-2018 over the Yangtze River Delta Region, China. *Atmos. Chem. Phys.* 21, 5847–5864. doi:10.5194/acp-21-5847-2021

Garrido-Perez, J. M., Ordóñez, C., García-Herrera, R., and Barriopedro, D. (2018). Air Stagnation in Europe: Spatiotemporal Variability and Impact on Air Quality. *Sci. Total Environ.* 645, 1238–1252. doi:10.1016/j.scitotenv.2018.07.238

Garrido-Perez, J. M., Ordóñez, C., García-Herrera, R., and Schnell, J. L. (2019). The Differing Impact of Air Stagnation on Summer Ozone across Europe. *Atmos. Environ.* 219, 117062. doi:10.1016/j.atmosenv.2019.117062

Gianelli, S. M., Carlson, B. E., and Lacis, A. A. (2007). Using EOF Analysis to Qualitatively Analyze, and Identify Inhomogeneities in, Data from Ground-Based Aerosol Monitoring Instruments. *J. Geophys. Res.* 112. D20210. doi:10.1029/2006jd008300

Hannachi, A., Jolliffe, I. T., and Stephenson, D. B. (2007). Empirical Orthogonal Functions and Related Techniques in Atmospheric Science: A Review. *Int. J. Climatol.* 27, 1119–1152. doi:10.1002/joc.1499

He, Y. J., Uno, I., Wang, Z. F., Pochanart, P., Li, J., and Akimoto, H. (2008). Significant Impact of the East Asia Monsoon on Ozone Seasonal Behavior in the Boundary Layer of Eastern China and the West Pacific Region. *Atmos. Chem. Phys.* 8, 7543–7555. doi:10.5194/acp-8-7543-2008

Horton, D. E., Harshvardhanand Diffenbaugh, N. S. (2012). Response of Air Stagnation Frequency to Anthropogenically Enhanced Radiative Forcing. *Environ. Res. Lett.* 7, 044034. doi:10.1088/1748-9326/7/4/044034

Horton, D. E., Skinner, C. B., Singh, D., and Diffenbaugh, N. S. (2014). Occurrence and Persistence of Future Atmospheric Stagnation Events. *Nat. Clim Change* 4, 698–703. doi:10.1038/Nclimate2272

Hu, J., Chen, J., Ying, Q., and Zhang, H. (2016). One-year Simulation of Ozone and Particulate Matter in China Using WRF/CMAQ Modeling System. *Atmos. Chem. Phys.* 16, 10333–10350. doi:10.5194/acp-16-10333-2016

Hu, C., Kang, P., Jaffe, D. A., Li, C., Zhang, X., Wu, K., et al. (2021). Understanding the Impact of Meteorology on Ozone in 334 Cities of China. *Atmos. Environ.* 248, 118221. doi:10.1016/j.atmosenv.2021.118221

Huang, Q., Cai, X., Song, Y., and Zhu, T. (2017). Air Stagnation in China (1985-2014): Climatological Mean Features and Trends. *Atmos. Chem. Phys.* 17, 7793–7805. doi:10.5194/acp-17-7793-2017

Huffman, G. J., Adler, R. F., Morrissey, M. M., Bolvin, D. T., Curtis, S., Joyce, R., et al. (2001). Global Precipitation at One-Degree Daily Resolution from Multisatellite Observations. *J. Hydrometeor* 2, 36–50. doi:10.1175/1525-7541(2001)002<0036:gpaodd>2.0.co;2

Jacob, D. J., and Winner, D. A. (2009). Effect of Climate Change on Air Quality. *Atmos. Environ.* 43, 51–63. doi:10.1016/j.atmosenv.2008.09.051

Jiang, Z., Li, J., Lu, X., Gong, C., Zhang, L., and Liao, H. (2021). Impact of Western Pacific Subtropical High on Ozone Pollution over Eastern China. *Atmos. Chem. Phys.* 21, 2601–2613. doi:10.5194/acp-21-2601-2021

Kerr, G. H., and Waugh, D. W. (2018). Connections between Summer Air Pollution and Stagnation. *Environ. Res. Lett.* 13, 084001. doi:10.1088/1748-9326/Aad2e2

Li, L., Chen, C. H., Fu, J. S., Huang, C., Streets, D. G., Huang, H. Y., et al. (2011). Air Quality and Emissions in the Yangtze River Delta, China. *Atmos. Chem. Phys.* 11, 1621–1639. doi:10.5194/acp-11-1621-2011

Li, Z., Guo, J., Ding, A., Liao, H., Liu, J., Sun, Y., et al. (2017). Aerosol and Boundary-Layer Interactions and Impact on Air Quality. *Natl. Sci. Rev.* 4, 810–833. doi:10.1093/nsr/nwx117

Li, Z., Zhou, Y., Wan, B., Chen, Q., Huang, B., Cui, Y., et al. (2019). The Impact of Urbanization on Air Stagnation: Shenzhen as Case Study. *Sci. Total Environ.* 664, 347–362. doi:10.1016/j.scitotenv.2019.01.232

Lu, X., Zhang, L., Wang, X., Gao, M., Li, K., Zhang, Y., et al. (2020). Rapid Increases in Warm-Season Surface Ozone and Resulting Health Impact in China since 2013. *Environ. Sci. Technol. Lett.* 7, 240–247. doi:10.1021/acs.estlett.0c00171

Ma, J., Xu, X., Zhao, C., and Yan, P. (2012). A Review of Atmospheric Chemistry Research in China: Photochemical Smog, Haze Pollution, and Gas-Aerosol Interactions. *Adv. Atmos. Sci.* 29, 1006–1026. doi:10.1007/s00376-012-1188-7

Mao, J., and Wu, G. (2012). Diurnal Variations of Summer Precipitation over the Asian Monsoon Region as Revealed by TRMM Satellite Data. *Sci. China Earth Sci.* 55, 554–566. doi:10.1007/s11430-011-4315-x

Pu, X., Wang, T. J., Huang, X., Melas, D., Zanis, P., Papanastasiou, D. K., et al. (2017). Enhanced Surface Ozone during the Heat Wave of 2013 in Yangtze River Delta Region, China. *Sci. Total Environ.* 603, 807–816. doi:10.1016/j.scitotenv.2017.03.056

Schnell, J. L., and Prather, M. J. (2017). Co-occurrence of Extremes in Surface Ozone, Particulate Matter, and Temperature over Eastern North America. *Proc. Natl. Acad. Sci. USA* 114, 2854–2859. doi:10.1073/pnas.1614453114

Shen, L., Wang, H., Zhu, B., Zhao, T., Liu, A., Lu, W., et al. (2021). Impact of Urbanization on Air Quality in the Yangtze River Delta during the COVID-19 Lockdown in China. *J. Clean. Prod.* 296, 126561. doi:10.1016/j.jclepro.2021.126561

Shu, L., Xie, M., Wang, T., Gao, D., Chen, P., Han, Y., et al. (2016). Integrated Studies of a Regional Ozone Pollution Synthetically Affected by Subtropical High and Typhoon System in the Yangtze River Delta Region, China. *Atmos. Chem. Phys.* 16, 15801–15819. doi:10.5194/acp-16-15801-2016

Shu, L., Xie, M., Gao, D., Wang, T., Fang, D., Liu, Q., et al. (2017). Regional Severe Particle Pollution and its Association with Synoptic Weather Patterns in the Yangtze River Delta Region, China. *Atmos. Chem. Phys.* 17, 12871–12891. doi:10.5194/acp-17-12871-2017

Sun, Z., Chang, N.-B., Huang, Q., and Opp, C. (2012). Precipitation Patterns and Associated Hydrological Extremes in the Yangtze River basin, China, Using TRMM/PR Data and EOF Analysis. *Hydrological Sci. J.* 57, 1315–1324. doi:10.1080/02626667.2012.716905

Wang, J. X. L., and Angell, J. K. (1999). *Air Stagnation Climatology for the United States(1948-1998)*. USA: NOAA/Air Resources Laboratory ATLAS, Silver Spring.

Wang, Y., Zhang, Y., Hao, J., and Luo, M. (2011). Seasonal and Spatial Variability of Surface Ozone over China: Contributions from Background and Domestic Pollution. *Atmos. Chem. Phys.* 11, 3511–3525. doi:10.5194/acp-11-3511-2011

Wang, Y., Shen, L., Wu, S., Mickley, L., He, J., and Hao, J. (2013). Sensitivity of Surface Ozone over China to 2000-2050 Global Changes of Climate and Emissions. *Atmos. Environ.* 75, 374–382. doi:10.1016/j.atmosenv.2013.04.045

Wang, S., Zhang, M., Sun, M., Wang, B., Huang, X., Wang, Q., et al. (2015). Comparison of Surface Air Temperature Derived from NCEP/DOE R2, ERA-Interim, and Observations in the Arid Northwestern China: a Consideration of Altitude Errors. *Theor. Appl. Climatol* 119, 99–111. doi:10.1007/s00704-014-1107-1

Wang, T., Xue, L., Brimblecombe, P., Lam, Y. F., Li, L., and Zhang, L. (2017). Ozone Pollution in China: A Review of Concentrations, Meteorological Influences, Chemical Precursors, and Effects. *Sci. Total Environ.* 575, 1582–1596. doi:10.1016/j.scitotenv.2016.10.081

Wang, Y., Gao, W., Wang, S., Song, T., Gong, Z., Ji, D., et al. (2020). Contrasting Trends of PM2.5 and Surface-Ozone Concentrations in China from 2013 to 2017. *Natl. Sci. Rev.* 7, 1331–1339. doi:10.1093/nsr/nwaa032

Wang, H. L., Pei, Y., Yin, Y., Shen, L. J., Chen, K., Shi, Z., et al. (2021). Observational Evidence of Lightning-generated Ultrafine Aerosols. *Geophys. Res. Lett.* 48, e2021GL093771. doi:10.1029/2021gl093771

Waugh, D. W., Sobel, A. H., and Polvani, L. M. (2017). What Is the Polar Vortex and How Does it Influence Weather? *B Am. Meteorol. Soc.* 98 (1), 37–44. doi:10.1175/bams-d-15-00212.1

Wu, K., Yang, X., Chen, D., Gu, S., Lu, Y., Jiang, Q., et al. (2020). Estimation of Biogenic VOC Emissions and Their Corresponding Impact on Ozone and Secondary Organic Aerosol Formation in China. *Atmos. Res.* 231, 104656. doi:10.1016/j.atmosres.2019.104656

Xie, M., Zhu, K., Wang, T., Yang, H., Zhuang, B., Li, S., et al. (2014). Application of Photochemical Indicators to Evaluate Ozone Nonlinear Chemistry and Pollution Control Countermeasure in China. *Atmos. Environ.* 99, 466–473. doi:10.1016/j.atmosenv.2014.10.013

Xie, M., Liao, J., Wang, T., Zhu, K., Zhuang, B., Han, Y., et al. (2016a). Modeling of the Anthropogenic Heat Flux and its Effect on Regional Meteorology and Air Quality over the Yangtze River Delta Region, China. *Atmos. Chem. Phys.* 16, 6071–6089. doi:10.5194/acp-16-6071-2016

Xie, M., Zhu, K., Wang, T., Chen, P., Han, Y., Li, S., et al. (2016b). Temporal Characterization and Regional Contribution to O3 and NOx at an Urban and a Suburban Site in Nanjing, China. *Sci. Total Environ.* 551, 533–545. doi:10.1016/j.scitotenv.2016.02.047

Xie, M., Zhu, K., Wang, T., Feng, W., Gao, D., Li, M., et al. (2016c). Changes in Regional Meteorology Induced by Anthropogenic Heat and Their Impacts on Air Quality in South China. *Atmos. Chem. Phys.* 16, 15011–15031. doi:10.5194/acp-16-15011-2016

Xie, M., Shu, L., Wang, T.-j., Liu, Q., Gao, D., Li, S., et al. (2017). Natural Emissions under Future Climate Condition and Their Effects on Surface Ozone in the Yangtze River Delta Region, China. *Atmos. Environ.* 150, 162–180. doi:10.1016/j.atmosenv.2016.11.053

Xu, W. Y., Zhao, C. S., Ran, L., Deng, Z. Z., Liu, P. F., Ma, N., et al. (2011). Characteristics of Pollutants and Their Correlation to Meteorological Conditions at a Suburban Site in the North China Plain. *Atmos. Chem. Phys.* 11, 4353–4369. doi:10.5194/acp-11-4353-2011

Xu, W., Xu, X., Lin, M., Lin, W., Tarasick, D., Tang, J., et al. (2018). Long-term Trends of Surface Ozone and its Influencing Factors at the Mt Waliguan GAW Station, China - Part 2: The Roles of Anthropogenic Emissions and Climate Variability. *Atmos. Chem. Phys.* 18, 773–798. doi:10.5194/acp-18-773-2018

Yang, X., Wu, K., Wang, H., Liu, Y., Gu, S., Lu, Y., et al. (2020). Summertime Ozone Pollution in Sichuan Basin, China: Meteorological Conditions, Sources and Process Analysis. *Atmos. Environ.* 226, 117392. doi:10.1016/j.atmosenv.2020.117392

Yang, X., Wu, K., Lu, Y., Wang, S., Qiao, Y., Zhang, X., et al. (2021). Origin of Regional Springtime Ozone Episodes in the Sichuan Basin, China: Role of Synoptic Forcing and Regional Transport. *Environ. Pollut.* 278, 116845. doi:10.1016/J.Envpol.2021.116845

Yin, C. Q., Solmon, F., Deng, X. J., Zou, Y., Deng, T., Wang, N., et al. (2019). Geographical Distribution of Ozone Seasonality over China. *Sci. Total Environ.* 689, 625–633. doi:10.1016/j.scitotenv.2019.06.460

Zhan, C., Xie, M., Fang, D.-X., Wang, T.-J., Wu, Z., Lu, H., et al. (2019). Synoptic Weather Patterns and Their Impacts on Regional Particle Pollution in the City Cluster of the Sichuan Basin, China. *Atmos. Environ.* 208, 34–47. doi:10.1016/j.atmosenv.2019.03.033

Zhan, C., Xie, M., Huang, C., Liu, J., Wang, T., Xu, M., et al. (2020). Ozone Affected by a Succession of Four Landfall Typhoons in the Yangtze River Delta, China: Major Processes and Health Impacts. *Atmos. Chem. Phys.* 20, 13781–13799. doi:10.5194/acp-20-13781-2020

Zhan, C., Xie, M., Liu, J., Wang, T., Xu, M., Chen, B., et al. (2021). Surface Ozone in the Yangtze River Delta, China: A Synthesis of Basic Features, Meteorological Driving Factors, and Health Impacts. *Geophys. Res. Atmos.* 126, e2020JD033600. doi:10.1029/2020jd033600

Zhang, M., Chen, S., Qi, Y. C., and Yang, Y. (2013). Evaluation of TRMM Summer Precipitation Over Huai-River Basin in China. *Amr* 726-731, 3401–3406. doi:10.4028/www.scientific.net/amr.726-731.3401

Zhang, Z., Zhang, X., Gong, D., Kim, S.-J., Mao, R., and Zhao, X. (2016). Possible Influence of Atmospheric Circulations on winter Haze Pollution in the Beijing-Tianjin-Hebei Region, Northern China. *Atmos. Chem. Phys.* 16, 561–571. doi:10.5194/acp-16-561-2016

Zhou, D., Ding, A., Mao, H., Fu, C., Wang, T., Chan, L. Y., et al. (2013). Impacts of the East Asian Monsoon on Lower Tropospheric Ozone over Coastal South China. *Environ. Res. Lett.* 8, 044011. doi:10.1088/1748-9326/8/4/044011

Zhu, K., Xie, M., Wang, T., Cai, J., Li, S., and Feng, W. (2017). A Modeling Study on the Effect of Urban Land Surface Forcing to Regional Meteorology and Air Quality over South China. *Atmos. Environ.* 152, 389–404. doi:10.1016/j.atmosenv.2016.12.053

Zhu, T. (2017). Air Pollution in China: Scientific Challenges and Policy Implications. *Natl. Sci. Rev.* 4, 800. doi:10.1093/nsr/nwx151

**Conflict of Interest:** The authors declare that the research was conducted in the absence of any commercial or financial relationships that could be construed as a potential conflict of interest.

**Publisher's Note:** All claims expressed in this article are solely those of the authors and do not necessarily represent those of their affiliated organizations, or those of the publisher, the editors and the reviewers. Any product that may be evaluated in this article, or claim that may be made by its manufacturer, is not guaranteed or endorsed by the publisher.

frontiers in Environmental Science

ORIGINAL RESEARCH
published: 30 November 2021
doi: 10.3389/fenvs.2021.802316

# A Movable Fog-Haze Boundary Layer Conceptual Model Over Jianghuai Area, China

*Duanyang Liu[1,2,3]*, Wenlian Yan[1,4]*, Junlong Qian[1,5], Mei Liu[1,4], Zida Wang[6], Muning Cheng[3] and Huaqing Peng[5]*

*[1]Key Laboratory of Transportation Meteorology, China Meteorological Administration (CMA), Nanjing, China, [2]Nanjing Joint Institute for Atmospheric Sciences, Nanjing, China, [3]Collaborative Innovation Center of Atmospheric Environment and Equipment Technology, Jiangsu Key Laboratory of Atmospheric Environment Monitoring and Pollution Control (AEMPC), Nanjing University of Information Science & Technology, Nanjing, China, [4]Meteorological Observatory of Jiangsu Province, Nanjing, China, [5]Wuxi Meteorological Observatory of Jiangsu Province, Wuxi, China, [6]Department of Integrated Traffic Information and Control Engineering, School of Transportation Engineering, Tongji University, Shanghai, China*

The Jianghuai area is an "important" region not only for its local pollutant accumulation but the belt for pollutant transportation between North China and the Yangtze River Delta during the winter half of the year (often from October to next February). In this study, a movable boundary layer conceptual model for the Jianghuai area in the winter half of the year is established based on the analyses of characteristics of atmospheric circulations and boundary layer dynamic conditions. This conceptual model can well explain the causes of air quality change and frequent fog-haze episodes. Variations of the intensity and range of the cold and warm fronts in the Jianghuai area in the winter half of the year lead to form a movable boundary in this area. When the southerly wind is strong, or affected by strong cold air mass, the air quality in the Jianghuai area may be excellent with a low air pollution index; Two atmospheric circulations provide favorable conditions for the fog-haze formation and maintenance in Jianghuai area: 1) When the shallow weak cold air mass is below the deep moist warm air mass, a stable temperature inversion occurs. The pollutants are transported to the Jianghuai area by the weak cold air mass, and local emissions also accumulate. As a result, a severe air pollution episode appears. 2) When the northerly cold air mass is as intense as the southerly moist warm air mass, the pollutants transported from North China as well as local emissions will continuously accumulate in the study area, which may lead to more severe air pollution. This conceptual model can help us analyze atmospheric diffusion capacity, and benefit the forecast and early warning of airflow stagnation area and fog-haze episode.

**Keywords: heavy air pollution, atmospheric circulation, atmospheric boundary layer, movable boundary layer conceptual model, jianghuai area, China**

OPEN ACCESS

***Edited by:***
*Lijuan Shen,*
*University of Toronto, Canada*

***Reviewed by:***
*Mengmeng Li,*
*Nanjing University, China*
*Gui Hai Lin,*
*China Meteorological Administration, China*

****Correspondence:***
*Duanyang Liu*
*liuduanyang@cma.gov.cn*
*Wenlian Yan*
*yike-112@163.com*

***Specialty section:***
*This article was submitted to Atmosphere and Climate, a section of the journal Frontiers in Environmental Science*

***Received:*** *26 October 2021*
***Accepted:*** *16 November 2021*
***Published:*** *30 November 2021*

***Citation:***
*Liu D, Yan W, Qian J, Liu M, Wang Z, Cheng M and Peng H (2021) A Movable Fog-Haze Boundary Layer Conceptual Model Over Jianghuai Area, China. Front. Environ. Sci. 9:802316. doi: 10.3389/fenvs.2021.802316*

## INTRODUCTION

Regional air quality is a rising concern in East China in recent years, many severe air pollutions were recorded in East China (Dai et al., 2020; Gu et al., 2020; Shi et al., 2020; Sun et al., 2020; Wang et al., 2021), Beijing-Tianjin-Hebei region (Liu et al., 2019a; Li et al., 2019, 2020; Lv et al., 2020) and the Pearl River Delta (Wu et al., 2013; Li et al., 2018; Dai et al., 2019), due to rapid developments of

economy and urbanization in these regions. The rapid and varied industrial development, the use of coal for power generation, and the increasing number of vehicles on the roads have increased the emission of pollutants in the region, especially particulate matter (PM) and its precursors. Stable circulation, stable atmospheric stratification, and high humidity are all important factors for the formation and aggravation of haze pollution (Ding and Liu, 2014; Mu and Zhang, 2014; Liu et al., 2019b). Zhang et al. (2014) reported that meteorological factors could explain more than 2/3 of the variance of fog-haze diurnal variation.

East China is a region with frequent fog and haze (Chen et al., 2021; Wang et al., 2020; Zhang et al., 2018; Zong et al., 2020). Local emissions, pollutants transported from the North China Plain, and boundary layer change can all affect the intensity and duration of the fog-haze episode (Liang et al., 2017; Wang et al., 2016; Yu et al., 2016). The atmosphere boundary layer conditions in the Jianghuai area, which covers Jiangsu and Anhui provinces in this article, can affect not only local pollutant concentration but also pollutant transportation between North China and the Yangtze River Delta (Dai et al., 2020; Gu et al., 2020; Liu et al., 2018a; Liu et al., 2018b; Peng et al., 2016; Shen et al., 2021a; Shen et al., 2021b; Xie et al., 2021; Zhou et al., 2021).

Conceptual models for different types of weather will help us analyze the synoptic situations and boundary layer features, and improve forecasting and early warning and understanding the weather processes (Pal, 2016; Wojtal, et al., 2011). Over the past decade, different researchers have developed conceptual models about different weather phenomena (Lohou et al., 2020; Toledo et al., 2021), for example, Toledo et al. (2021) presents a new conceptual model for adiabatic fog, Lohou et al. (2020) build a conceptual model of diurnal cycle of low-level stratiform clouds over southern West Africa.

Fog-haze weather researches are all aspects, the research on conceptual models of weather is very systematic, which contributes to a comprehensive understanding of different types of weather (Ding et al., 2017; Wu et al., 2017). Wu et al. (2017) give a conceptual diagram for the formation mechanism of persistent haze pollution events in North China. When a severe persistent haze event occurs, North China is dominated by zonal westerly airflow or by northwesterly airflow in the mid-upper troposphere.

The purpose of this study is to analysis the relationship between synoptic weather patterns and the boundaries layers in the Jianghuai area, China and in comparison with the North China Plain (Xu et al., 2012; Jiang et al., 2015; Li et al., 2015; Ding et al., 2017; Meng et al., 2017) and the Pearl River Delta, China (Fan et al., 2005, Fan et al., 2006). To explore air quality change and frequent fog-haze episodes in the Jianghuai area, China during the winter half of the year, characteristics of atmospheric circulation and BL dynamic and thermal conditions are analyzed. A movable boundaries layers conceptual model approach using synoptic analysis methods is proposed here to investigate the good air quality synoptic situations, and the heavy air pollution weather synoptic background.

The remainder of this paper is organized as follows: The study area, data, and methods are described in **Section 2**. In **Section 3** we summarize the atmospheric circulation and boundary layers' dynamic conditions on fog-haze days. A movable BL conceptual model is established in **Section 4**. Finally, summary and conclusions are presented in **Section 5**.

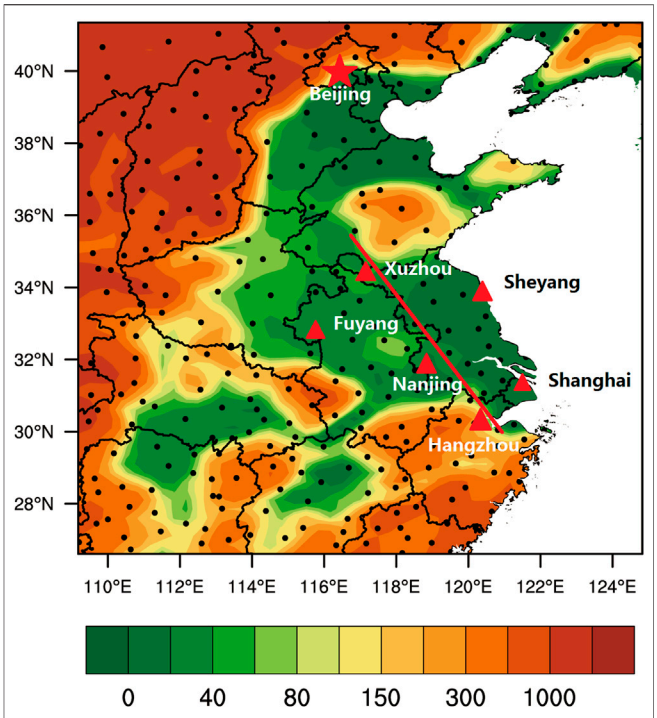


**FIGURE 1 |** The geographical environment of the Jianghuai area (where the red triangles region), referring to as Jiangsu and Anhui provinces in this article. The red triangles represent the primary meteorological stations (Xuzhou (XZ), Sheyang (SY), Fuyang (FY), Nanjing (NJ), Shanghai (SH), Hangzhou (HZ)) in the Jianghuai area, the red line is used to analyze the wind field and the conceptual model, and the black dots are the other stations of CMA. The color is the altitude.

## THE STUDY AREA, DATA, AND METHOD

### Study Area

The geographical environment of the Jianghuai area referring to as Jiangsu and Anhui provinces in this article (**Figure 1**). In terms of physical geography, the Jianghuai area located in the transitional area from the subtropics to the warm temperate zone belongs to the East Asian monsoon region. The Huai River divides the Jianghuai area into two parts. The north part belongs to the warm temperate zone and is of humid and semi-humid monsoon climatic region. The south part is of subtropical humid monsoon climate. With the Yellow Sea to the east, the Jianghuai area is significantly impacted by the ocean. The solar radiation, atmospheric circulation, specific geographical location, and landform characteristics jointly make the area a place with a mild climate, distinct seasons, and significant monsoons. In terms of economic geography, the Jianghuai area is the transition area for the Yangtze River Delta economic belt and north China economic Belt. Therefore, the Jianghuai area is an "important" region not only for its local pollutant accumulation but the belt for pollutant

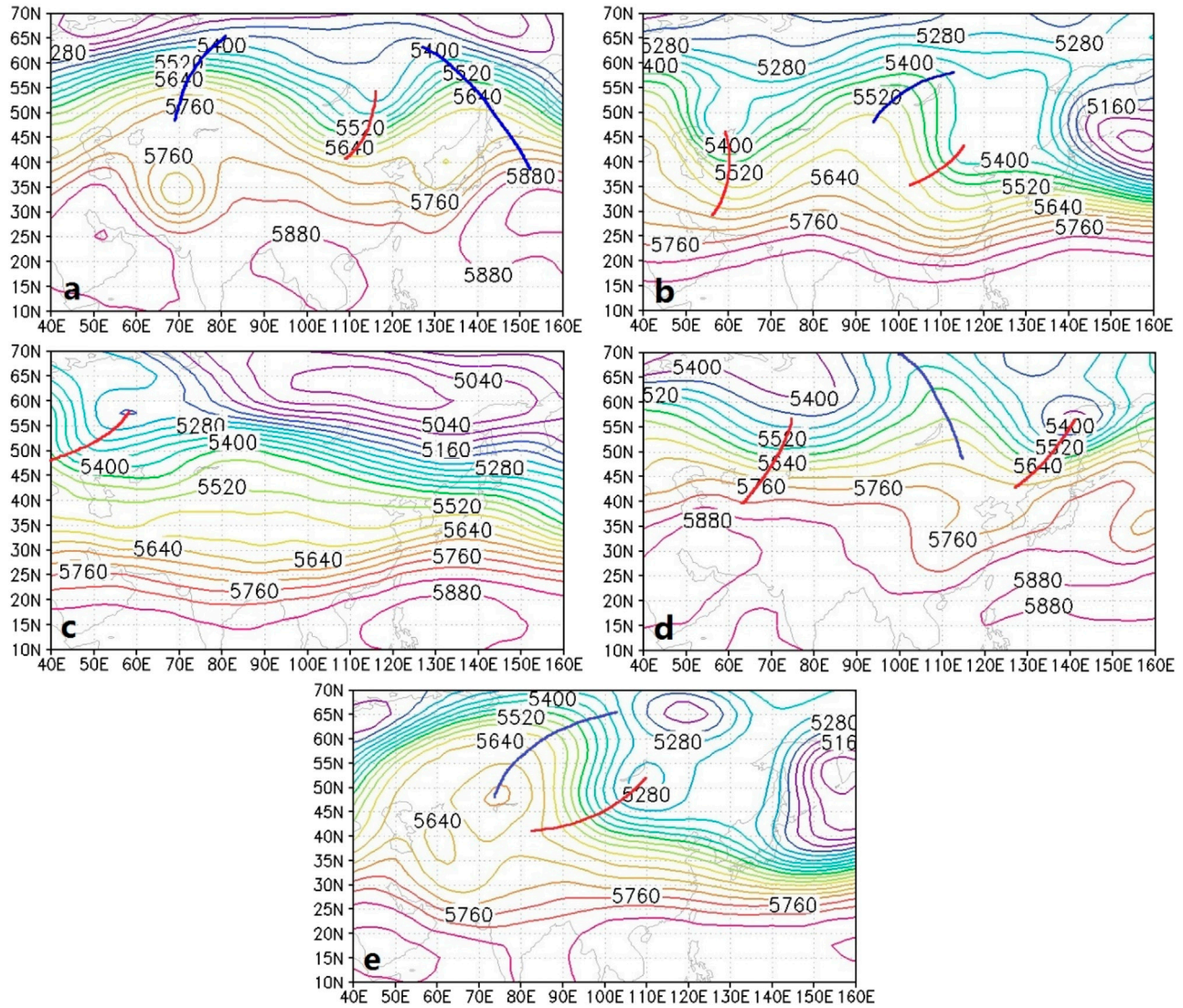


**FIGURE 2 |** Five 500-hPa circulation patterns favoring hazes in the Jianghuai area, China. They are **(A)** zonal circulation pattern, **(B)** two troughs and one ridge pattern, **(C)** one trough and one ridge pattern, **(D)** two ridges and one trough pattern, and **(E)** uniform dynamic geopotential height pattern.

transportation between North China and the Yangtze River Delta during the winter half of the year (often from October to next February).

Four primary meteorological stations (Xuzhou (XZ), Sheyang (SY), Fuyang (FY), Nanjing (NJ)) in Jianghuai Area and two (Shanghai (SH), Hangzhou (HZ)) in the Yangtze River Delta are selected for analysis. The red line (**Figure 1**) is used to analyze the wind field.

## Data and Method

The sounding data from stations XZ, SY, FY, NJ, HZ, and SH are used in this study, with temperature profiles as the main variable. The sea-level pressure data from 709 stations of the China Meteorological Administration during the same period are also used (**Figure 1**). The Final Operational Global Analysis (FNL) data from the National Centers for Environmental Prediction (NCEP) of the U.S. are used for cross-section wind and boundary layer height. The FNL data have a spatial resolution 1°×1°.

# ATMOSPHERIC CIRCULATION AND BOUNDARY LAYERS

## Circulation Characteristics

### Circulations on 500 hPa

According to the synoptic conditions in the Jianghuai area over the past 30 years, the 500-hPa circulations on haze days can be classified into five patterns (**Figure 2**). They are zonal circulation patterns, two troughs, and one ridge patterns, one trough and one ridge patterns, two ridges and one trough patterns, and uniform geopotential height patterns.

**TABLE 1 |** 10 heavy haze episodes in the past few years.

| | Date | | Date |
|---|---|---|---|
| 1 | Jan. 1–10, 2013 | 6 | Dec. 14–16, 2016 |
| 2 | Dec. 1–10, 2013 | 7 | Dec. 18–20, 2016 |
| 3 | Dec. 27–31, 2014 | 8 | Dec. 22–24, 2016 |
| 4 | Jan. 3–4, 2015 | 9 | Dec. 21–24, 2017 |
| 5 | Jan. 7–11, 2015 | 10 | Nov. 24–30, 2018 |

The zonal circulation pattern is featured in **Figure 2A**. The high levels (700–500 hPa) of the Jianghuai area are controlled by the westerly. Occasionally, weak cold air mass from the polar vortex moves eastward along the westerly airflow, with its main part located to the north of 35°N. Thus, the cold air mass has little impact on the Jianghuai area. When the cold air mass is in North China, the surface of the Jianghuai area is on the south of the weak cold high-pressure system and under weak high-pressure control, with a stable atmospheric stratification.

The two troughs and one ridge patterns are featured in **Figure 2B**. Sometimes, a small trough or ridge in front of a big ridge or trough invades North China and East China. When the cold air mass leaves, the surface pressure quickly weakens and the atmosphere becomes stable, which facilitates the accumulation of air pollutants. When the pollutants reach a certain level, haze may form, usually before the arrival of the next cold air mass. If the cold air mass cannot reach the south of 35°N, the haze in the Jianghuai area will aggravate, and a persistent haze is likely to appear. If the cold air mass can reach 30°N, the haze will dissipate. The duration of this kind of haze episode is related to the southernmost location the cold air mass can reach.

The one trough and one ridge patterns is featured shown in **Figure 2C**. The Jianghuai area is under the westerly in front of an inclined trough. For the surface pressure field, the main cold air mass is to the north of Xinjiang and the west of Lake Baikal. Occasionally, the weak cold air mass is detached from the main part and moves eastward along the westerly, affecting East China. Similar to the two troughs and one ridge pattern, the haze always appears in the latter half of the intermission between two cold air masses. The haze will dissipate when the new cold air mass arrives. For this pattern, the interval between the two cold air masses is relatively long.

The two ridges and one trough pattern is featured in **Figure 2D**. In most cases of this pattern, the study region is under a large but weak high-pressure system, extending across the Hetao region of Inner Mongolia to the Guanzhong District of Shaanxi Province and the west of it. The Jianghuai area is located under the weak pressure system, on the east of the high-pressure system. So, the atmosphere is stable, and the haze episode usually lasts for about 2 days. In the above four patterns on 500 hPa, if the northern trough is located further north and the southern trough is located further south, the mid-and high-latitude circulations would become zonal and haze could last for a longer time.

The uniform geopotential height pattern is featured in **Figure 2E**. The Jianghuai area is located north of the southern trough, and under the uniform geopotential height field in front of the northern trough. The Jianghuai area is under the weak pressure zone of a high-pressure system, with a stable atmospheric stratification; the situation can remain for a longer time.

We analyzed 10 heavy haze episodes in the past few years, there were westerly or northwesterly airflows on 500 hPa (**Table 1**), and the wind direction turned to northwesterly in 6–12 h before the haze dissipated. For example, on Dec. 28, 2014, a westerly was maintained on 500 hPa and turned into the northwesterly at 2:00 on Dec. 29. Eight hours later, the heavy haze in Jiangsu Province was reduced to light/moderate haze. At 14:00 on Dec. 30, the westerly prevailed on 500 hPa over the Jianghuai area, and the circulation in the mid-latitude area was relatively zonal. The cold air mass was weak, and an equalized pressure field was likely formed. The static wind was conducive to the maintenance of heavy haze. However, at 2:00 on Dec. 31, the northwesterly appeared on 500 hPa. Visibility started to improve at 10:00 on Dec. 31, and the haze was finally mitigated. As the wind on 500 hPa turned northwesterly, the downward transport of momentum could intensify the turbulence in the BL. The wind near the surface was then strengthened. Clearly, the 500-hPa wind direction change can indicate the mitigation of heavy haze, about 6–12 h in advance. Therefore, an analysis of high-level circulation on heavy haze days should help predict the evolution characteristics of the high levels 12 h before heavy haze.

During the large-area, persistent haze episode over the Jianghuai area in January 2013, the 500-hPa circulation in the mid and high latitudes of Eurasia (**Figure 2A**) was zonal. There was a flat and weak trough over Jiangsu Province, while the main trough was over North China. The trough gradually moved eastward, and its south part moved more slowly. The southern branch of the trough over the Bay of Bengal was relatively shallow, and the frontal zone was to the south of 28°N. The corresponding west-southwesterly wind was south of the Lower Reach of the Yangtze River. Such a weak weather system could not bring precipitation for the wet deposition of pollutants.

During the first 10 days of Dec. 2013, large-size fog and haze existed in the Jianghuai area. In this period, the area was controlled by the zonal circulation on 500 hPa, so the meridional wind was weak. The configuration of the upper- and lower-level circulations facilitated the accumulation of pollutants in the BL, which was a typical synoptic condition for a persistent fog-haze episode.

## Synoptic Conditions Near the Surface

Surface synoptic conditions on heavy haze days include equalized pressure (EQP), advancing edge of a cold front (ACF), base of high pressure (BOH), backside of high pressure (BAH), inverted trough (INT), and others. The EQP is featured in **Figure 3A**: the cold air mass is blocked in the north, and the Jianghuai area is controlled by an EQP field. The ACF is featured in **Figure 3B**: the cold air mass from the north strongly advances southward, and the Jianghuai area is controlled by the advancing edge of the cold front. The BOH is featured in **Figure 3C**: with the continental high moving southward slowly, the Jianghuai area is located at the base of the high. The BAH is featured in **Figure 3D**: as the continental high moves eastward, the Jianghuai area is on the

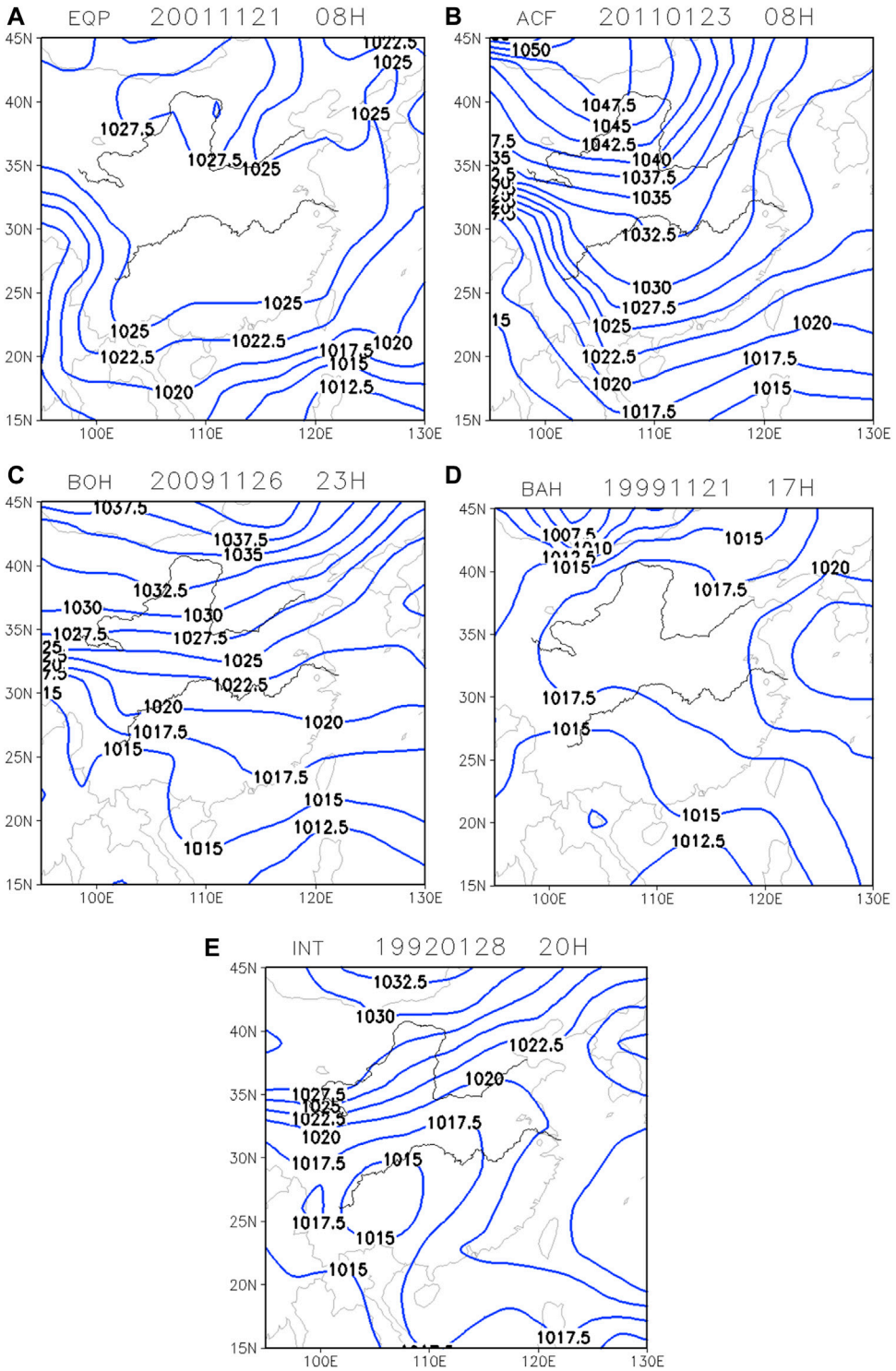


**FIGURE 3 |** Surface conditions on heavy haze days. They are **(A)** equalized pressure field (EQP), **(B)** advancing edge of a cold front (ACF), **(C)** base of high pressure (BOH), **(D)** backside of high pressure (BAH), and **(E)** inverted trough (INT).

backside of the high that is over the sea. The INT is featured in **Figure 3E**: the Jianghuai area is affected by the weak high-pressure system over the ocean in the early stage. Then, the weak high-pressure system recedes, and an inverted trough develops. The Jianghuai area is below the top of the inverted trough. In a persistent haze episode in our study area, the surface

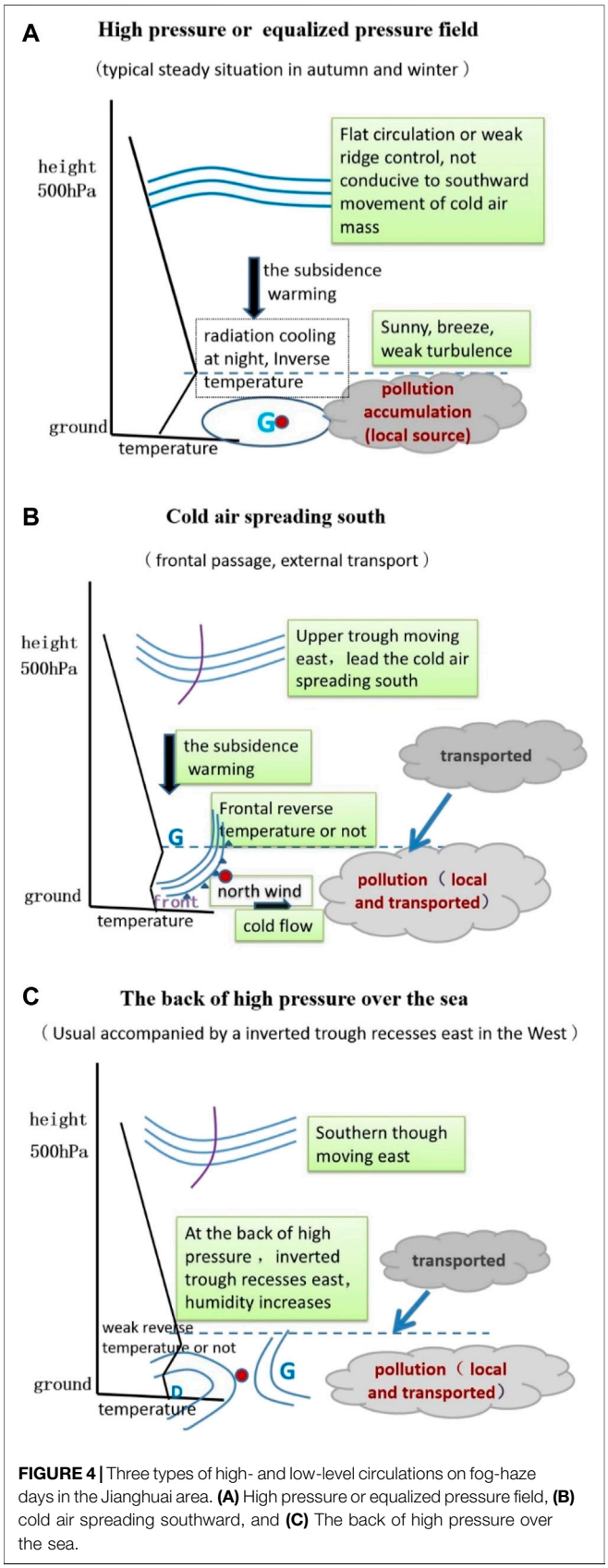


**FIGURE 4 |** Three types of high- and low-level circulations on fog-haze days in the Jianghuai area. **(A)** High pressure or equalized pressure field, **(B)** cold air spreading southward, and **(C)** The back of high pressure over the sea.

condition is among the five surface types mentioned above (Peng et al., 2016).

During the large-size, persistent haze episode over the Jianghuai area in January 2013, the surface cold high ridge was in North and Northeast China. Jiangsu Province was under the equalized pressure at the front of the cold high-pressure system, and an easterly prevailed in the lower levels. According to the change in the surface pressure field in January 2013, Jiangsu Province experienced two surface synoptic situations successively: the equalized pressure field at the front of the cold high-pressure system and the equalized pressure field at the back of the high-pressure system. Both were favorable for the fog-haze episode in Jiangsu Province.

Another example is the fog-haze episode in the Jianghuai area during the first 10 days of December 2013. The central and eastern parts of the surface pressure field were controlled by the equalized pressure. The pressure gradient was weak, so was the horizontal wind speed. The configuration of the upper- and lower-circulations was beneficial for the accumulation of pollutants in the BL, which was a typical synoptic situation for a persistent fog-haze episode.

## Configuration of Upper- and Lower-Level Circulations

Based on the above analyses, several circulation patterns favoring hazes are summarized, including the equalized high-pressure field, the cold air mass southward diffusion, and the backside of a high-pressure system over the ocean (**Figure 4**).

The high or equalized pressure pattern is shown in **Figure 4A**. The study area is under a high or equalized pressure system, the circulation at high levels is zonal, and the stratification is stable. It is sunny with strong radiative cooling at night. So, an inversion near the surface is likely to form. The surface wind speed is less than 3 m/s. The air pollutants mainly come from local accumulation. The diurnal variation of pollution is significant. The heavy pollution mainly occurs at night and in the morning and, the air quality will improve in the afternoon.

The cold air mass southward diffusion pattern is given in **Figure 4B**. The high-level trough guides the cold air mass to advance southward. The weather gradually turns to be overcast or rainy, the cloud cover increases, and precipitation may occur (mainly as light rain). The wind gradually turns to be northerly and becomes stronger. The local pollutants from previous days and the external pollutants transported from the north jointly cause heavy pollution. Its duration is related to the cold air's intensity and its southward speed. The affected area is closely related to the intensity of the cold air mass, and the relatively strong cold air mass can affect northern Zhejiang Province. Large-scale heavy pollution episodes often occur under this circulation pattern.

The backside of a high-pressure system over the ocean is the pattern featured in **Figure 4C**. On the west of the backside of the high-pressure system over the ocean, there is usually an inverted trough extending eastward. As the high-level trough moves eastward, the weather gradually turns to be overcast or rainy, and precipitation occurs. It is mainly light rain during the pollution days. The Jianghuai area is dominated by gradually strengthening southerly wind. The high relative humidity is

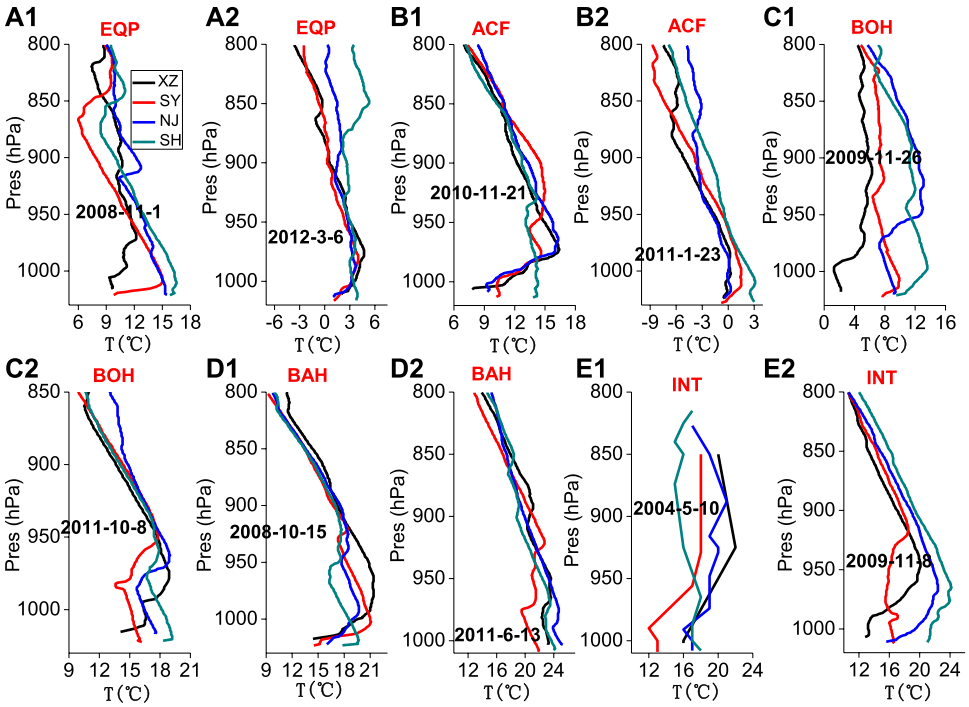


**FIGURE 5 |** Typical temperature profiles of regional heavy hazes at XZ, SY, NJ, and SH: **(A)** EQP, **(B)** ACF, **(C)** BOH, **(D)** BAH, and **(E)** INT. The *x*-axis is the temperature, and the *y*-axis is the pressure. After Peng et al. (2016).

conducive to the growth of pollutant particles, reduction of visibility, and aggravation of pollution. The heavy pollution is mainly due to local pollutants, though there is a certain amount of transported pollutants (mostly in southern Jiangsu and northern Zhejiang). With the further strengthening of the wind, the pollution is reduced.

## Boundary Layer Conditions in Jianghuai Area

### Boundary Layer Structures During the Heavy Haze

BL condition is an important factor for the formation and maintenance of haze. According to the patterns of the surface synoptic conditions introduced in previous sections, the BL structures of different patterns are compared and analyzed. The heavy haze in EQP is characterized by an inversion or isothermal layer near the surface, and the inversion is mainly in a single layer or double layers (**Figure 5A**). The BL structure in ACF shows that the height of the inversion layer varies in different haze processes. The height of the inversion is very low, and the inversion mainly appears in a single layer. But the isothermal layer often appears at high levels (**Figure 5B**). In BOH, there is a relatively large difference in the heights of the inversion layers among the stations, but the inversion appears below the height of 950 hPa at all these stations, and multi-layer inversions are also found (**Figure 5C**). In BAH, the inversion or the isothermal layer mainly appears near the surface, and most of the cases exhibit multi-layer inversion structures (**Figure 5D**). On hazy days, the BL in INT is typically characterized by a thick inversion layer and a high bottom of the inversion (**Figure 5E**) (Peng et al., 2016).

### Dynamic Conditions in the Boundary Layer

Under the long-lasting inversion near the surface, the atmosphere is relatively stable. Taking the spatiotemporal profiles of wind at stations Fuyang, Nanjing, Xuzhou, and Sheyang on Dec. 1–9, 2013 as an example (**Figure 6**), there were mainly southwesterly or southeasterly airflows below 500 m (inside the inversion layer) in Jiangsu Province and its surrounding areas. The wind was weaker than 3 m/s, with an average wind speed of 1–2 m/s. When the fog appeared, the wind speed was between 0.5 and 1.5 m/s. Therefore, the low wind speed was the dynamic condition for this fog-haze event, and a poor dynamic condition was not conducive to the vertical diffusion of air pollutants and water vapor. As a result, the fog-haze event was maintained for a long time.

To investigate the spatial variation characteristics of the BL in the Jianghuai area (line in **Figure 1**), we analyze the south-north cross-section of the wind field in the area using the NCEP reanalysis and observation data. **Figure 7** displays the results of two typical cases that occurred at 0,800 on Dec. 19, 2016, and at 2000 on Dec. 23, 2016. When the wind was strong (**Figure 7A**), the wind speed near the surface was relatively uniform, without local recirculation. When the wind became weak (**Figure 7B**), local recirculation appeared in the Jianghuai area, that the wind directions in the layers 0–2 km were northerly wind, and the layer 2–5 km was southerly wind, which was greatly affected by other many factors, such as landform, urban heat island, the differences of underlying surfaces, and so on.

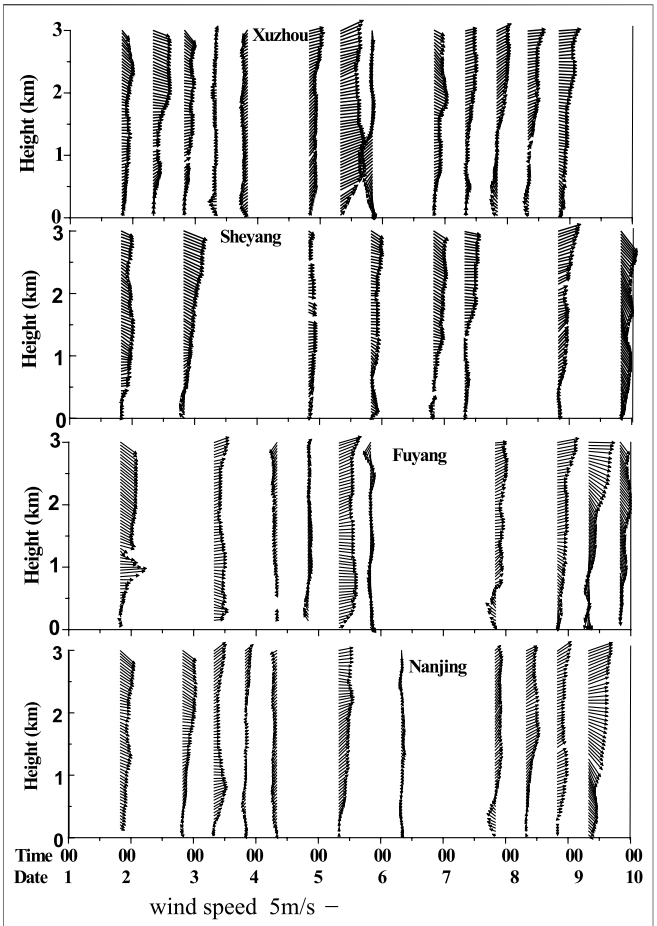


**FIGURE 6 |** Spatiotemporal cross-sections of the wind field at Xuzhou, Sheyang, Fuyang, and Nanjing during Dec. 1 and Dec. 9, 2013.

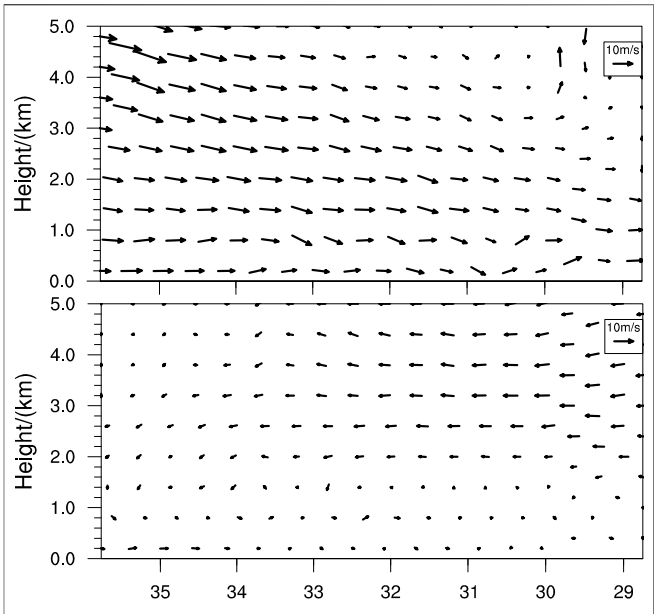


**FIGURE 7 |** The north-south cross-section (along with the red line in **Figure 1**) of the wind field in the Jianghuai area (top) 0,800 19–12-2016 (bottom) 2000 23–12- 2016.

# ATMOSPHERIC BOUNDARY LAYER CONCEPTUAL MODEL AND ITS APPLICATIONS IN JIANGHUAI AREA

## The Fixed Boundaries Over the North China Plain and the Pearl River Delta, China

On the west of the Beijing-Tianjin-Hebei region (the North China Plain), there is the north-south-oriented Taihang Mountain. To the north of this region is the east-west-oriented Yanshan Mountain. When the stratification is stable or the southeasterly wind prevails, local pollutants and the pollutants transported from other places accumulate here, which can easily lead to heavy haze (**Figure 8A**). Unique landform and weather conditions play certain roles in the formation of haze in the Beijing-Tianjin-Hebei region (Ding et al., 2017). The blocking of the westerly by the Taihang Mountain is an important factor in the aggravation of air pollution in the central and southern parts of Hebei. When the prevailing wind is southerly, the wind will recirculate locally or climb over the Yanshan Mountain, which leads to decreased wind speed near the surface. It is unfavorable for the diffusion of pollutants, and the air pollutions are aggravated in the cities in the central and southern Beijing-Tianjin-Hebei region (Jiang et al., 2015). There is a high-value band of pollutants from northeast to southwest in North China, with the highest center concentrated in front of the Taihang Mountain and the Yanshan Mountain, affecting Tangshan, Beijing, Tianjin, Langfang, Baoding, Shijiazhuang, Xingtai, and Handan (Meng et al., 2017). Li et al. (2015) also found that the remote transport rates of $PM_{2.5}$ in Beijing, Tianjin, and Shijiazhuang were 58, 54, and 39%, respectively. During a heavy pollution event of Oct. 6–12, 2014 in the Beijing-Tianjin-Heibei region, the pollutants were transported from south to north, and the interregional transport greatly affected $PM_{2.5}$ concentration in various regions (Li et al., 2015). Influenced by the southerly, the region along the Taihang Mountain and the Shandong Peninsula-Bohai Bay area made great contributions to the summer air pollution. Especially, the high concentrations of $O_3$ and $PM_{2.5}$ in the summer over the Beijing-Tianjin-Hebei region had important impacts on the overall pollutant concentration increase in the background air pollution of North China (Xu et al., 2012).

Similar to the Beijing-Tianjin-Hebei region (the North China Plain), to the north of the Pearl River Delta (South China) is the south-east-oriented Nanling Mountains. When the stratification is stable or the southerly prevails, the pollutants are accumulated, and the accumulation may easily lead to heavy haze or air pollution (**Figure 8B**). Fan et al. (2006) reported that the unique geographical environment of the Pearl River Delta, which is surrounded by mountains on three sides, went against the transport and diffusion of air pollutants. The air pollutants from different cities and sources in the Pearl River Delta all have sizeable impacts on the air quality of the whole Pearl River Delta.

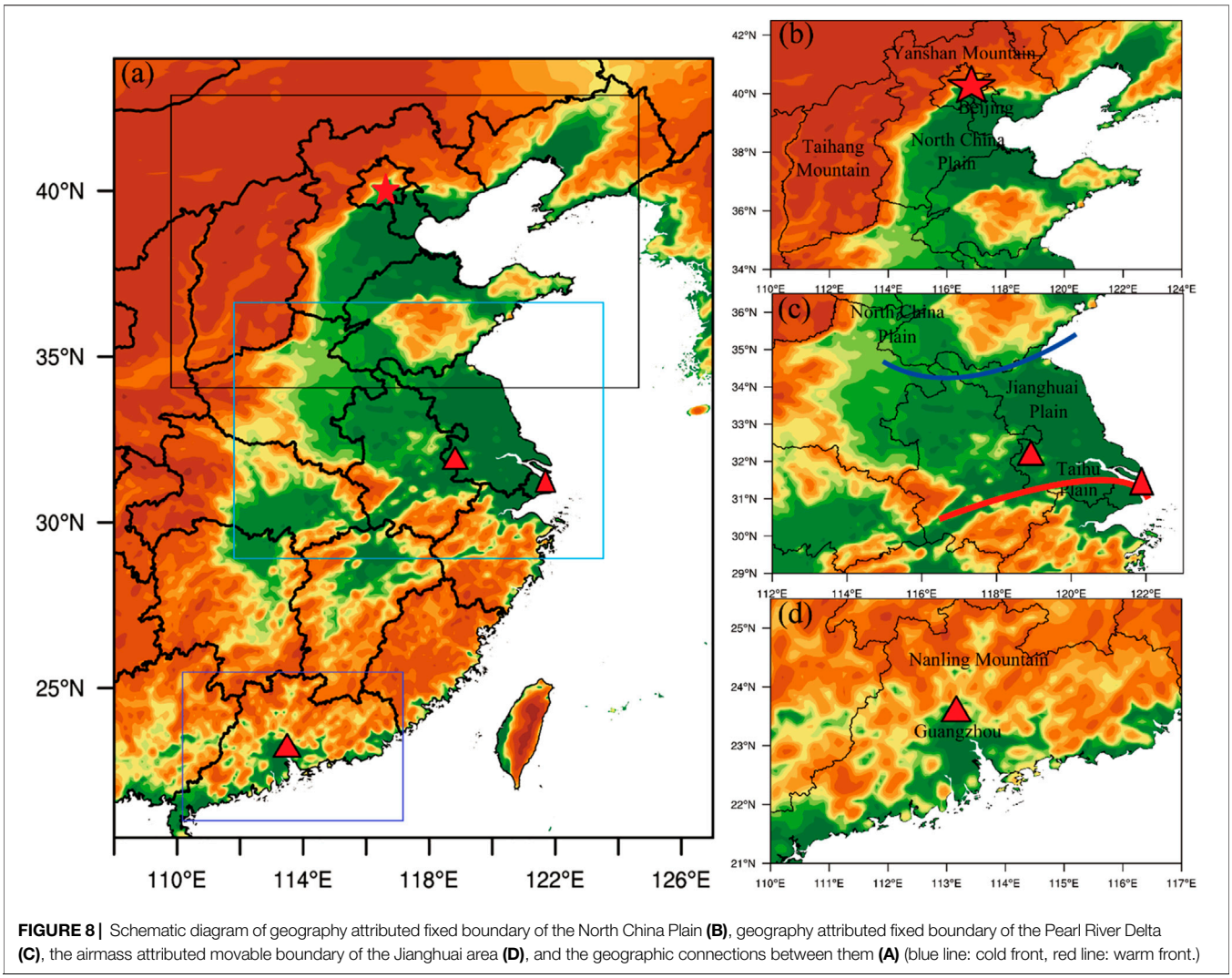


**FIGURE 8 |** Schematic diagram of geography attributed fixed boundary of the North China Plain **(B)**, geography attributed fixed boundary of the Pearl River Delta **(C)**, the airmass attributed movable boundary of the Jianghuai area **(D)**, and the geographic connections between them **(A)** (blue line: cold front, red line: warm front.)

## The Movable Boundaries of the Jianghuai Area

The landform and terrain of the Jianghuai area are rather different from those of the Beijing-Tianjin-Hebei region or the Pearl River Delta. There are no significant mountains around the area. From the south of the North China Plain to the Jianghuai Plain and the Taihu Plain, the terrain is relatively flat with a dense river network and better moisture conditions. The Yangtze River Delta in the south has a prosperous economy. Although there is no significant boundary, haze occurs more frequently from October to the following February (winter half of the year). As mentioned in **Section 3.1**, in the winter half of the year the cold dry northerly and the warm moist southeasterly influence this area alternately. The changes in the intensity and range of the cold and warm fronts can influence the changes in the range and boundary of a haze episode. Thus, a unique movable boundary forms as the changes of the cold and warm fronts in the Jianghuai area. We establish a movable boundary conceptual model in this study (**Figure 8C**).

## A Conceptual Model for Fog-Haze Episodes in the Winter Half of the Year

### Transport From Jianghuai Area to North China

In the winter half of the year, when the Jianghuai area is affected by strong southerly or by significant precipitation, the air quality is good (**Figure 9A** shows the reasons). With a strong and long-lasting southerly, the pollutants can be transported to North China by the southerly, instead of accumulating in the Jianghuai area. Thus, the air quality in the study area can be excellent. Besides, significant precipitation can improve the air quality by wet scavenging.

### Strong Cold Air Mass Sweeping Over North China and East China

In the winter half of the year when the Jianghuai area is influenced by strong cold air mass, the air quality may remain good in the Yangtze River Delta. **Figure 9A** explains the reasons. As long as the cold air mass is strong enough and the duration is long enough, the pollutants can be transported

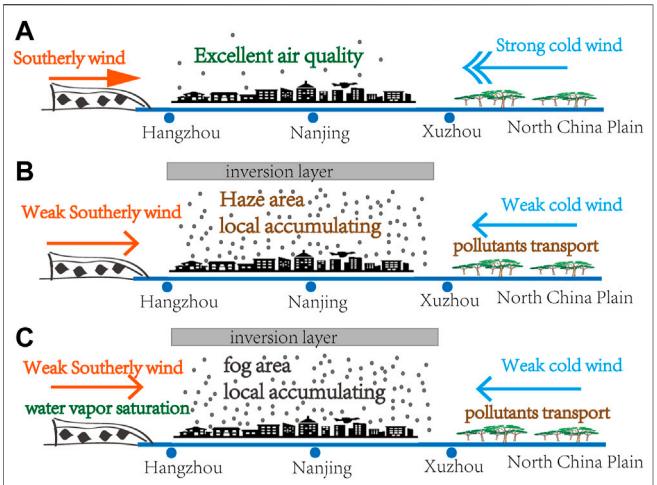


**FIGURE 9 |** Atmospheric BL conceptual model for the Jianghuai area. **(A)** Excellent air quality due to the southerly wind or the strong cold air; **(B)** haze and heavy pollution due to both the weak cold air and southerly wind; and **(C)** fog and heavy air pollution due to both the weak cold air and southerly wind (the scale with the city name represents the distance between the cities on the red line in **Figure 1**).

to the south of the Jianghuai area by the northerly, instead of accumulating in the Jianghuai area. The air quality may be excellent. The cold air affecting the Jianghuai area mainly has three paths: the easterly path, the westerly path, and the middle path. According to previous analyses, the influence of the easterly-path cold air mass on the Jianghuai area is greater than that of the westerly-path cold air mass; and the influence of the middle-path cold air mass is the weakest. When the strong wind sweeps over North China and East China, it can blow away pollutants and improve air quality in these regions (Gu et al., 2020).

### Local Accumulation and Pollutant Transportation From North China

In the Jianghuai area, fog, haze, poor air quality, and high air pollution index often appear in the days with poor air diffusion capacities, such as calm wind and significant inversion (Liu et al., 2014a, Liu et al., 2014b). **Figures 9B,C** reveal that two situations may cause poor air quality and high air pollution in this area. First, when the cold air mass from the north is relatively weak, the thin cold air mass is pushed from north to south but sits under the deep warm moist air mass, forming a stable inversion in the BL. In this situation, the wind speed is relatively low; thus, the pollutants are transported by the weak cold air mass from North China to the Jianghuai area. Meanwhile, the local pollutants accumulate rapidly. Then, such conditions lead to the formation of the heavy air pollution. Second, when the intensity of the cold northerly is equal to that of the warm moist southerly, the wind speed in the BL is so low that it is difficult for horizontal diffusion of pollutants. The inversion layer is like a large-cap that prevents the pollutants from spreading upwards. Therefore, the pollutants keep accumulating in the Jianghuai area. This can lead to severe air pollution. In the above two situations, the front edge of the cold or warm air mass is the horizontal boundary when the wind speed is less than 3 m/s. The upper boundary and horizontal boundary are the inversion layer and downward flow or are the wind shear zone between the southerly and northerly. The heavy pollution episodes are caused by both pollutant transportation and local emissions. These two situations often appear in the winter half of the year. Once there is a high humidity condition, it is easy to form dense fog over a large area, which will cause more serious problems for both traffic and public health.

## CONCLUSION

Based on the analyses of atmospheric circulation characteristics and BL conditions in the Jianghuai area, a movable boundary conceptual model is established. The model can explain the causes of frequent haze and the change in the environmental air quality in the study area.

The changes in the intensity and range of the cold and warm fronts in the winter half of the year lead to unique movable (fluid) boundary characteristics in the Jianghuai area, which affect the range and boundary of the haze in this area. Based on these characteristics, the movable boundary conceptual model in the Jianghuai area is established. The main features of the conceptual model are as follows:

1) With a strong southerly, the pollutants can be spread to North China. Thus, the air quality in the Jianghuai area can be excellent, and significant precipitation can also improve the air quality by wet scavenging.
2) Under the influence of strong cold air mass, the air quality of the Jianghuai area is excellent. The influence of the easterly-path cold air mass on this area is greater than that of the westerly-path cold air mass, and the influence of the middle-path cold air mass is the weakest.
3) The thin cold air mass sits under the deep warm moist air mass, and a stable inversion is thus formed. The pollutants from both local accumulation and remote transportation can jointly cause heavy air pollution in the study area.
4) When the intensity of the cold northerly is equal to that of the warm moist southerly, the pollutants from local emissions and from North China can keep on accumulating in the Jianghuai area, which may lead to more severe air pollution.

Under the situations of (3) and (4), the front edge of cold/warm air mass (wind speed less than 3 m/s) is the horizontal boundary. The upper boundaries are the inversion layer or downward flow, or the wind shear zone between the southerly and northerly. The heavy pollution episodes are caused by both pollutant transportation and local emissions. Combined with the results of the numerical weather forecast, this model has been applied to guiding the air quality weather forecasting and all of the air pollutant processes can be accurately predicted. Although this conceptual model needs to be tested and verified by more cases, it will help analyze the atmospheric diffusion

capacity in the Jianghuai area. It can provide the forecast and early warning of airflow stagnation area or fog-haze.

## DATA AVAILABILITY STATEMENT

The original contributions presented in the study are included in the article/Supplementary Material, further inquiries can be directed to the corresponding authors.

## AUTHOR CONTRIBUTIONS

Conceptualization, DL; methodology, WY and ML; software, JQ and ZW; validation, DL and WY; formal analysis, HP; investigation, MC; resources, DL; data curation, WY; writing—original draft preparation, DL and WY; writing—review and editing, DL; visualization, JQ and HP; supervision, DL and WY; project administration, DL; funding acquisition, DL. All authors have read and agreed to the published version of the manuscript.

## FUNDING

This work was jointly supported by the National Natural Science Foundation of China (42075063), Open fund by Jiangsu Key Laboratory of Atmospheric Environment Monitoring and Pollution Control (KHK2005), and the Jiangsu Meteorological Bureau General project (KZ201902).

## ACKNOWLEDGMENTS

Thanks to the Chinese Ministry of Environmental Protection for providing the environmental monitoring data.

## REFERENCES

Chen, S., Liu, D., Kang, Z., Shi, Y., and Liu, M. (2021). Anomalous Atmospheric Circulation Associated with the Extremely Persistent Dense Fog Events over Eastern China in the Late Autumn of 2018. *Atmosphere* 12 (1), 111. doi:10.3390/atmos12010111

Dai, J., Wang, X., Dai, W., and Chang, M. (2019). The Impact of Inhomogeneous Urban Canopy Parameters on Meteorological Conditions and Implication for Air Quality in the Pearl River Delta Region. *Urban Clim.* 29, 100494. doi:10.1016/j.uclim.2019.100494

Dai, Z., Liu, D., Yu, K., Cao, L., and Jiang, Y. (2020). Meteorological Variables and Synoptic Patterns Associated with Air Pollutions in Eastern China during 2013-2018. *Int. J. Environ. Res. Public Health* 17 (7), 2528. doi:10.3390/ijerph17072528

Ding, Y., and Liu, Y. (2014). Analysis of Long-Term Variations of Fog and Haze in China in Recent 50 Years and Their Relations with Atmospheric Humidity. *Sci. China Earth Sci.* 57, 36–46. doi:10.1007/s11430-013-4792-1

Ding, Y., Wu, P., Liu, Y., and Song, Y. (2017). Environmental and Dynamic Conditions for the Occurrence of Persistent Haze Events in North China. *Engineering* 3, 266–271. doi:10.1016/j.eng.2017.01.009

Fan, S., Wang, A., Fan, Q., Liu, J., and Wang, B. (2005). Atmospheric Boundary Layer Conceptual Model of the Pearl River Delta and its Application. *J. Trop. Meteorology* 21, 286–292.

Fan, S., Wang, A., Fan, Q., Liu, J., and Wang, B. (2006). Atmospheric Boundary Layer Features of Pearl River Delta and its Conception Model. *China Environ. Sci.* 26, 4–6.

Gu, P., Qian, J., Liu, D., Wang, K., Dai, Z., Peng, X., et al. (2020). Cold Fronts Transport Features of North China Pollutant over Jiangsu Province, China. *Atmos. Pollut. Res.* 11 (10), 1785–1796. doi:10.1016/j.apr.2020.07.015

Jiang, Y., Zhu, R., Zhu, K., and Li, Z. (2015). Numerical Simulation on the Air Pollution Potential in the Severe Air Pollution Episodes in the Beijing-Tianjin-Hebei Region. *Acta Scientiae Circumstantiae* 35, 2681–2692.

Li, S., Cheng, N., Xu, J., Nie, L., Meng, F., Pan, T., et al. (2015). Spatial and Temporal Distributions and Source Simulation of $PM_{2.5}$ in the Beijing-Tianjin-Hebei Region in 2014. *China Environ. Sci.* 35, 2908–2916.

Li, W., Liu, X., Zhang, Y., Sun, K., Wu, Y., Xue, R., et al. (2018). Characteristics and Formation Mechanism of Regional Haze Episodes in the Pearl River Delta of China. *J. Environ. Sci.* 63, 236–249. doi:10.1016/j.jes.2017.03.018

Li, M., Wang, T., Xie, M., Li, S., Zhuang, B., Huang, X., et al. (2019). Formation and Evolution Mechanisms for Two Extreme Haze Episodes in the Yangtze River Delta Region of China during winter 2016. *J. Geophys. Res. Atmos.* 124, 3607–3623. doi:10.1029/2019jd030535

Li, M., Wang, L., Liu, J., Gao, W., Song, T., Sun, Y., et al. (2020). Exploring the Regional Pollution Characteristics and Meteorological Formation Mechanism of PM2.5 in North China during 2013-2017. *Environ. Int.* 134, 105283. doi:10.1016/j.envint.2019.105283

Liang, D., Wang, H., Zhou, L., An, J., Tang, L., Lu, C., et al. (2017). Regional and Local New Particle Formation Events Observed in the Yangtze River Delta Region, China. *J. Geophys. Res. Atmos.* 122 (4), 2016JD026030. doi:10.1002/2016JD026030

Liu, D., Zhang, J., Wu, X., Yan, W., Zhou, B., and Xie, Z. (2014a). Characteristics and Sources of Atmospheric Pollutants during a Fog-Haze Process in Huai'an. *Trans. Atmos. Sci.* 37, 484–492. doi:10.13878/j.cnki.dqkxxb.20121007001

Liu, D., Pu, M., Yan, W., and Xie, Z. (2014b). Study on the Formation and the Cause of the Fog-Haze Transformation in the Lower Reaches of Huaihe River. *China Environ. Sci.* 34, 1622–1632.

Liu, D., Yan, W., Kang, Z., Liu, A., and Zhu, Y. (2018a). Boundary-layer Features and Regional Transport Process of an Extreme Haze Pollution Event in Nanjing, China. *Atmos. Pollut. Res.* 9 (6), 1088–1099. doi:10.1016/j.apr.2018.04.009

Liu, D., Su, Y., Peng, H., Yan, W., Li, Y., Liu, X., et al. (2018b). Size Distributions of Water-Soluble Inorganic Ions in Atmospheric Aerosols during the Meiyu Period on the North Shore of Taihu Lake, China. *Aerosol. Air Qual. Res.* 18 (12), 2997–3008. doi:10.4209/aaqr.2018.04.0123

Liu, C., Hua, C., Zhang, H., Zhang, B., Wang, G., Zhu, W., et al. (2019a). A Severe Fog-Haze Episode in Beijing-Tianjin-Hebei Region: Characteristics, Sources and Impacts of Boundary Layer Structure. *Atmos. Pollut. Res.* 10 (4), 1190–1202. doi:10.1016/j.apr.2019.02.002

Liu, C., Wang, T. J., Chen, P. L., Li, M. M., Zhao, M., Zhao, K., et al. (2019b). Effects of Aerosols on the Precipitation of Convective Clouds: A Case Study in the Yangtze River Delta of China. *J. Geophys. Res. Atmos.* 124 (14), 7868–7885. doi:10.1029/2018jd029924

Lohou, F., Kalthoff, N., Adler, B., Babić, K., Dione, C., Lothon, M., et al. (2020). Conceptual Model of Diurnal Cycle of Low-Level Stratiform Clouds over Southern West Africa. *Atmos. Chem. Phys.* 20 (4), 2263–2275. doi:10.5194/acp-20-2263-2020

Lv, Z., Wei, W., Cheng, S., Han, X., and Wang, X. (2020). Meteorological Characteristics within Boundary Layer and its Influence on PM2.5 Pollution in Six Cities of North China Based on WRF-Chem. *Atmos. Environ.* 228, 117417. doi:10.1016/j.atmosenv.2020.117417

Meng, K., Cheng, X., Xu, X., Qu, X., Ma, C., Zhao, Y., et al. (2017). Spatial-temporal Variations of Pollutant Emission Sources Inversed by Adaptive Nudging Scheme over Beijing-Tianjin-Hebei Region Based on the CMAQ Model. *Acta Scientiae Circumstantiae* 37, 52–60.

Mu, M., and Zhang, R. (2014). Addressing the Issue of Fog and Haze: A Promising Perspective from Meteorological Science and Technology. *Sci. China Earth Sci.* 57, 1–2. doi:10.1007/s11430-013-4791-2

Pal, S. (2016). On the Factors Governing Water Vapor Turbulence Mixing in the Convective Boundary Layer over Land: Concept and Data Analysis Technique Using Ground-Based Lidar Measurements. *Sci. Total Environ.* 554-555, 17–25. doi:10.1016/j.scitotenv.2016.02.147

Peng, H., Liu, D., Zhou, B., Su, Y., Wu, J., Shen, H., et al. (2016). Boundary-Layer Characteristics of Persistent Regional Haze Events and Heavy Haze Days in Eastern China. *Adv. Meteorol.* 2016, 1–23. doi:10.1155/2016/6950154

Shen, L., Wang, H., Kong, X., Zhang, C., Shi, S., and Zhu, B. (2021a). Characterization of Black Carbon Aerosol in the Yangtze River Delta, China: Seasonal Variation and Source Apportionment. *Atmos. Pollut. Res.* 12 (1), 195–209. doi:10.1016/j.apr.2020.08.035

Shen, L., Wang, H., Cheng, M., Ji, D., Liu, Z., Wang, L., et al. (2021b). Chemical Composition, Water Content and Size Distribution of Aerosols during Different Development Stages of Regional Haze Episodes over the North China Plain. *Atmos. Environ.* 245, 118020. doi:10.1016/j.atmosenv.2020.118020

Shi, C., Nduka, I. C., Yang, Y., Huang, Y., Yao, R., Zhang, H., et al. (2020). Characteristics and Meteorological Mechanisms of Transboundary Air Pollution in a Persistent Heavy PM2.5 Pollution Episode in Central-East China. *Atmos. Environ.* 223, 117239. doi:10.1016/j.atmosenv.2019.117239

Sun, X., Zhao, T., Liu, D., Gong, S., Xu, J., and Ma, X. (2020). Quantifying the Influences of PM2.5 and Relative Humidity on Change of Atmospheric Visibility over Recent Winters in an Urban Area of East China. *Atmosphere* 11, 461. doi:10.3390/atmos11050461

Toledo, F., Haeffelin, M., Wærsted, E., and Dupont, J.-C. (2021). A New Conceptual Model for Adiabatic Fog. *Atmos. Chem. Phys.* 21 (17), 13099–13117. doi:10.5194/acp-21-13099-2021

Wang, H., Zhu, B., Shen, L., Xu, H., An, J., Pan, C., et al. (2016). Regional Characteristics of Air Pollutants during Heavy Haze Events in the Yangtze River Delta, China. *Aerosol Air Qual. Res.* 16 (9), 2159–2171. doi:10.4209/aaqr.2015.09.0551

Wang, H., Zhang, Z., Liu, D., Zhu, Y., Zhang, X., and Yuan, C. (2020). Study on a Large-Scale Persistent Strong Dense Fog Event in Central and Eastern China. *Adv. Meteorol.* 2020, 8872334. doi:10.1155/2020/8872334

Wang, H., Pei, Y., Yin, Y., Shen, L., Chen, K., Shi, Z., et al. (2021). Observational Evidence of Lightning-Generated Ultrafine Aerosols. *Geophys. Res. Lett.* 48 (14), e2021GL093771. doi:10.1029/2021gl093771

Wojtal, P., Halla, J. D., and McLaren, R. (2011). Pseudo Steady States of HONO Measured in the Nocturnal marine Boundary Layer: a Conceptual Model for HONO Formation on Aqueous Surfaces. *Atmos. Chem. Phys.* 11 (7), 3243–3261. doi:10.5194/acp-11-3243-2011

Wu, M., Wu, D., Fan, Q., Wang, B. M., Li, H. W., and Fan, S. J. (2013). Observational Studies of the Meteorological Characteristics Associated with Poor Air Quality over the Pearl River Delta in China. *Atmos. Chem. Phys.* 13 (21), 10755–10766. doi:10.5194/acp-13-10755-2013

Wu, P., Ding, Y., and Liu, Y. (2017). Atmospheric Circulation and Dynamic Mechanism for Persistent Haze Events in the Beijing-Tianjin-Hebei Region. *Adv. Atmos. Sci.* 34 (4), 429–440. doi:10.1007/s00376-016-6158-z

Xie, M., Zhan, C., Zhan, Y., Shi, J., Luo, Y., Zhang, M., et al. (2021). Spatiotemporal Variability of Air Stagnation and its Relation to Summertime Ozone in the Yangtze River Delta of China. *Front. Environ. Sci.* 9, 517. doi:10.3389/fenvs.2021.783524

Xu, X., Liu, Z., Gao, W., Wang, Y., and Xin, J. (2012). Changes in Atmospheric Background Pollution during Summer in the Beijing-Tianjin-Hebei Region after the 2008 Olympic Games in China. *Res. Environ. Sci.* 9, 959–967.

Yu, X., Ma, J., An, J., Yuan, L., Zhu, B., Liu, D., et al. (2016). Impacts of Meteorological Condition and Aerosol Chemical Compositions on Visibility Impairment in Nanjing, China. *J. Clean. Prod.* 131, 112–120. doi:10.1016/j.jclepro.2016.05.067

Zhang, R., Qiang, L., and Zhang, R. (2014). Meteorological Conditions for the Persistent Severe Fog and Haze Event over Eastern China in January 2013. *Sci. China Earth Sci.* 57, 26–35. doi:10.1007/s11430-013-4774-3

Zhang, L., Zhao, T., Gong, S., Kong, S., Tang, L., Liu, D., et al. (2018). Updated Emission Inventories of Power Plants in Simulating Air Quality during Haze Periods over East China. *Atmos. Chem. Phys.* 18 (3), 2065–2079. doi:10.5194/acp-18-2065-2018

Zhou, B., Liu, D., and Yan, W. (2021). A Simple New Method for Calculating Precipitation Scavenging Effect on Particulate Matter: Based on Five-Year Data in Eastern China. *Atmosphere* 12 (6), 759. doi:10.3390/atmos12060759

Zong, P., Zhu, Y., Wang, H., and Liu, D. (2020). WRF-chem Simulation of Winter Visibility in Jiangsu, China, and the Application of a Neural Network Algorithm. *Atmosphere* 11 (5), 520. doi:10.3390/atmos11050520

**Conflict of Interest:** The authors declare that the research was conducted in the absence of any commercial or financial relationships that could be construed as a potential conflict of interest.

**Publisher's Note:** All claims expressed in this article are solely those of the authors and do not necessarily represent those of their affiliated organizations, or those of the publisher, the editors and the reviewers. Any product that may be evaluated in this article, or claim that may be made by its manufacturer, is not guaranteed or endorsed by the publisher.

frontiers in Environmental Science

ORIGINAL RESEARCH
published: 06 December 2021
doi: 10.3389/fenvs.2021.799115

# Characteristics of Regular Pulse Bursts Generated From Lightning Discharges

*Wang Yanhui*[1,2*†], *Fan Xiangpeng*[2,3], *Wang Tuo*[1], *Min Yingchang*[1], *Liu Yali*[1] *and Zhao Guo*[3]

[1]Key Laboratory for Aerosol-Cloud-Precipition of China Meteorological Administration, Collaborative Innovation Center on Forecast and Evaluation of Meteorological Disaster, Nanjing University of Information Science and Technology, Nanjing, China, [2]State Key Laboratory of Severe Weather, Chinese Academy of Meteorological Sciences, Beijing, China, [3]Pingliang Land Surface Process and Severe Weather Research Station, Gansu Land Surface Process and Severe Weather Observation and Research Station, Chinese Academy of Sciences, Lanzhou, China

In this work, we studied the waveforms of all lightning discharges from about 15 min. Eighty-three percent of all lightning discharges contain particular waveforms called regular pulse bursts (RPBs), which have regular microsecond-scale electric or magnetic field pulses. Maximum proportion of RPBs occur in middle or rear of lightning discharges. Prior to or after RPBs, there is always a chaotic pulse period. The analysis indicated that RPBs are caused by a secondary discharge in the fractured old breakdown channel, likeness to dart-stepped leader occuring in negative cloud-to-ground discharge (-CG). Four types of RPBs, namely, category of normal RPBs, category of back RPBs, category of symmetric RPBs, and category of reversal RPBs, were sorted in the light of the evolution of the pulse amplitude, interval between neighboring pulses and pulse polarity. In addition, the difference between normal RPBs and back RPBs was considered to be caused by the distance between neighboring charge pockets and the magnitude of the charge in every charge pocket. The symmetric RPBs were considered to be caused by a discharge channel with a large central charge area. Reversal RPBs were considered to be caused by a bending channel or superposition of two or more RPBs. We located some RPBs in a typical intra-cloud flash (IC) in three-dimensional. The analysis showed that the developing velocity of RPBs ranged from approximately 1.2 × 106 m/s to 3.0 × 106 m/s, which slower less than both of the dart leader or dart-stepped leader process from previous studies. And we found it is several meters to dozens of meters that the lengths range of discharge step which between two adjacent pulses.

**Keywords: regular pulse burst, lightning discharge, lightning location, dart-stepped leader, VHF radiation**

## HIGHLIGHTS

- Most lightning discharges have regular pulse bursts.
- The physical mechanisms of different types of RPBs are discussed.
- RPBs are located with high spatial and temporal resolution.

OPEN ACCESS

***Edited by:***
*Lijuan Shen,*
*University of Toronto, Canada*

***Reviewed by:***
*Xiufeng Guo,*
*Wuxi University, China*
*Pengguo Zhao,*
*Chengdu University of Information Technology, China*
*Kun Liu,*
*Chengdu University of Information Technology, China*
*Caixia Wang,*
*Beijing Information Science and Technology University, China*

****Correspondence:***
*Wang Yanhui*
*wangyanh@nuist.edu.cn*

***†Present address:***
*Wang Yanhui,*
*Key Laboratory for Aerosol-Cloud-Precipition of China Meteorological Administration, Collaborative Innovation Center on Forecast and Evaluation of Meteorological Disaster, Nanjing University of Information Science and Technology, Nanjing, China*

***Specialty section:***
*This article was submitted to Atmosphere and Climate, a section of the journal Frontiers in Environmental Science*

***Received:*** *21 October 2021*
***Accepted:*** *11 November 2021*
***Published:*** *06 December 2021*

***Citation:***
*Yanhui W, Xiangpeng F, Tuo W, Yingchang M, Yali L and Guo Z (2021) Characteristics of Regular Pulse Bursts Generated From Lightning Discharges. Front. Environ. Sci. 9:799115. doi: 10.3389/fenvs.2021.799115*

## 1 INTRODUCTION

Researchers have performed excellent work using high-speed cameras or coaxial shunts (Wang, D. H. et al., 2014; Jiang, R. B. et al., 2015; Tran and Rakov, 2017). However, compared with lightning discharges close to the ground (e.g., return strokes and step leaders), the discharge portion of a lightning discharges in the cloud cannot be observed directly by instruments (e.g., high-speed cameras, coaxial shunts, etc.) under certain conditions. Studies rely on radio waveforms detected by ground-based instruments [Rison et al., 1999; Qie et al., 2009; Zhang et al., 2010; Liu et al., 2013; Wang et al., 2021]. Generally, the pulse trains in waveforms generated by lightning discharges can be classified into chaotic pulse trains and regular pulse trains. Chaotic pulse trains were first studied by Wiedman (1982), who pointed out that the subsequent strokes were preceded by 'chaotic leaders'. Moreover, further studies have been performed on chaotic pulse trains (Bailey et al., 1988; Rakov and Uman, 1990; Willett et al., 1989). Chaotic pulse train events in negative cloud-to-ground (CG) flashes were imaged by three-dimensional very high-frequency (VHF) broadband digital interferometers by Liu et al., 2013, who found that the breakdown process associated with a chaotic pulse train is negative and similar to an attempt leader or dart leader; moreover, they suggested that some chaotic pulse trains may be a part of dart or dart-stepped leaders. Regular pulse trains include stepped leaders or dart-stepped leaders (Beasley et al., 1983; Cooray and Lundquist, 1985; Krider et al., 1977; Weidman and Krider, 1978) in cloud-to-ground and RPBs (Krider et al., 1975; Muller-Hillebrand D., 1962; Rakov et al., 1996; Kolmasová and Santolík, 2013; Ismail et al., 2017) associated with K-changes and M-components. RPBs have high rate of fluctuation of lightning discharges and may play an important role in lightning discharges (Füllekrug Martin, 2011; Kolmasová and Santolík, 2013), and they were earliest studied in detail by Krider et al., 1975, they observed microsecond-scale RPBs in a large part of the waveforms generated by long-distance lightning discharges in Florida and Arizona. These RPBs are basically unipolar pulses. Based on their observations, the RPBs exhibited two principal characteristics, first is a typical duration of 100–400 μs and second is mean time intervals of several microseconds between adjacent pulses. Generally, a pulse lasts for 1–2 μs and the rising edge is about 0.75 μs and followed by a weak overshoot waveform. RPBs usually begin with the largest pulses, and the pulse amplitudes decrease with time. Krider et al., 1975 suggested that the RPBs are related to "an intra-cloud (IC) dart-stepped leader process" and possibly associated with K streamers (Ogawa and Brook, 1964) that developed in the previously formed channels. Muller-Hillebrand (1962) and Krider et al., 1975 suggested that interference or upset can occur in sensitive electronic systems. Rakov et al., 1996 analyzed RPBs in both CG and IC lightning discharges and found that large proportion of RPBs occurred in falling edge of K-changes in both IC and CG. However, Krider et al., 1975 stated that pulse amplitudes often decrease during bursts, and they observed that pulse amplitudes often increase first and then decrease with time and that the interval between adjacent pulses

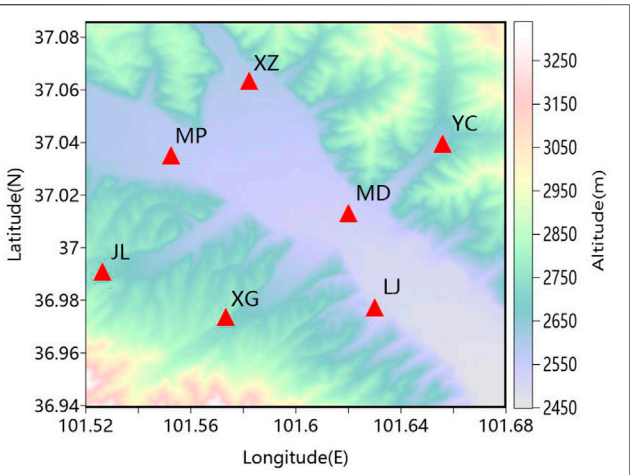


**FIGURE 1 |** Layout of the detectors (unit = meter; longitude and latitude of the central stations = E101.6,200,592 and N37.0133,483, respectively).

tends to increase toward the end of RPBs (Rakov et al., 1996). According to these observations, Rakov et al., 1996 suggested that an adequate definition of the standard lightning environment needed to develop after considering more experimental data in aircraft-measured lightning currents and in lightning electromagnetic radiation.

Using a multi-point measurement of the time derivative of the electric field with five stations, Davis et al., 1999 estimated the three-demensional locations and develop speeds of the leaders. The average intervals between two pulses of RPBs were 2.8 μs in dart-stepped leaders, 7.6 μs in leaders preceding new ground termination, and 5.1 μs in intra-cloud (IC) discharges respectively. They found that the polarity of 66% pulses was consistent with the current flowing direction in discharge channel. The polarity reversal may be caused by change of channel develop direction and may be caused by development of branches. Kolmasová and Santolík (2013) pointed out that the distances changed between adjacent charge pockets and increase of leader propagation speed could probably also explain the different sort of the trains of the pulses. Ismail et al., 2017 analyzed chaotic pulse bursts and pointed out that RPBs are probably caused by dart-stepped leaders or K-changes in cloud; moreover, they suggested that superposition of electric fields of two and more pulses trains which propagating simultaneously formed chaotic pulse trains. This hypothesis is supported by the observation fact that regular pulse trains tend to ocurred at beginning, middle or later stages of RPBs.

In this work, the RPBs in lightning discharges were analyzed with high time resolution in the inland plateau in China using a lightning mapping system working in VHF and VLF/LF frequency bands (Qie et al., 2009; Zhang et al., 2010; Wang et al., 2010). We analyzed four typical RPBs and mapped some RPBs. A comparative analysis of RPBs parameters in a positive cloud-to-ground discharge (+CG), a negative cloud-to-ground discharge (–CG), and an intra-cloud discharge (IC) are presented. Some location results of RPBs are analyzed and discussed in this work.

## 2 OBSERVATION AND CLASSIFICATION OF RPBS

In this work, the data was observed by a lightning mapping system (Zhang et al., 2010). The study area was the northeastern edge of the Qinghai-Tibet Plateau (center station: Mingde (MD); 37.01°N, 101.62°E; other station: Yaocao (YC), Liangjiao (LJ), Xiegou (XG), Jile (JL), Miaopu (MP), Xinzhuang (XZ)), and data were collected from 2009 to 2011. The stations were evenly spaced approximately 10 km around the center station, as shown in **Figure 1**. Each station was arranged with a lightning mapping system detector working at VHF and VLF/LF passband (Qie et al., 2009; Zhang et al., 2010), the bandwidth of VHF detector is about 267–273 MHz and the bandwidth of VLF/LF detector is approximately 200 kHz to 10 MHz. This lightning mapping system can mapped radiation sources which indicate spatial and temporal development of lightning discharges similar to a lightning mapping array (LMA) (Rison et al., 1999). In addition, a high-precision GPS clock (±25 ns) was equipped to synchronize all equipment at each station. Data collection was controlled either by the central station via a broadband wireless network system or operated freely. The arrival time of radiation pulses were caught by all seven stations, and then a set of nonlinear equations was used to get solution of equation each station as follows:

$t_i = t + \sqrt{(x_i - x)^2 + (y_i - y)^2 + (z_i - z)^2}/c$, where $c$ is the speed of light in a vacuum; $t$ is start time of break from source location $(x, y, z)$; and $t_i$ is the arrival time at station $i$ $(x_i, y_i, z_i)$. The typical horizontal error and altitude error was less than 100 and 300 m respectively on a network plane in the range of about 100 km and this two system error was increasing with distance.

We checked all data during a period of 00:00:00–00:15:00 on August 15, 2011 (GMT+8). The results showed that 430 RPBs occurred in 67 cases of all 81 lightning discharges in this period. The rest of the lightning discharges that did not contain RPBs were considered to have lost some detailed sections in their waveforms and occurred far from the observation site in this work. A statistical analysis of all these 430 RPBs shows that the typical width of pulses in RPBs was 1.0 μs, the typical interval between pulses of RPBs was approximately 5.0 μs and the typical duration of RPBs was several hundred μs. Obviously, the ranges of typical intervals and durations of RPBs were greater than those observed by Krider et al., 1975 and Rakov et al., 1996 with the application of broad electric change (EFC) receivers in this paper. A chaotic pulse period always occurred prior to or after an RPB. Maximum proportion of RPBs occur in middle or rear of lightning discharges, which is similar to the observations of Krider et al., 1975 and Rakov et al., 1996. Moreover, most RPBs were associated with VHF radiation. Generally, RPBs were associated with K-changes or M process. RPBs were considered widely distributed events in lightning discharges in this work. We found that the initial part of a normal RPBs is a periodic vibration similar to that observed by Rakov et al., 1996. In addition, some other RPBs did not show regular pulses similarities with those observed by (Rakov et al., 1996; Kolmasová and Santolík, 2013; Ismail et al., 2017). To further understand the RPBs, the waveforms of RPBs are sorted into four categories as follows.

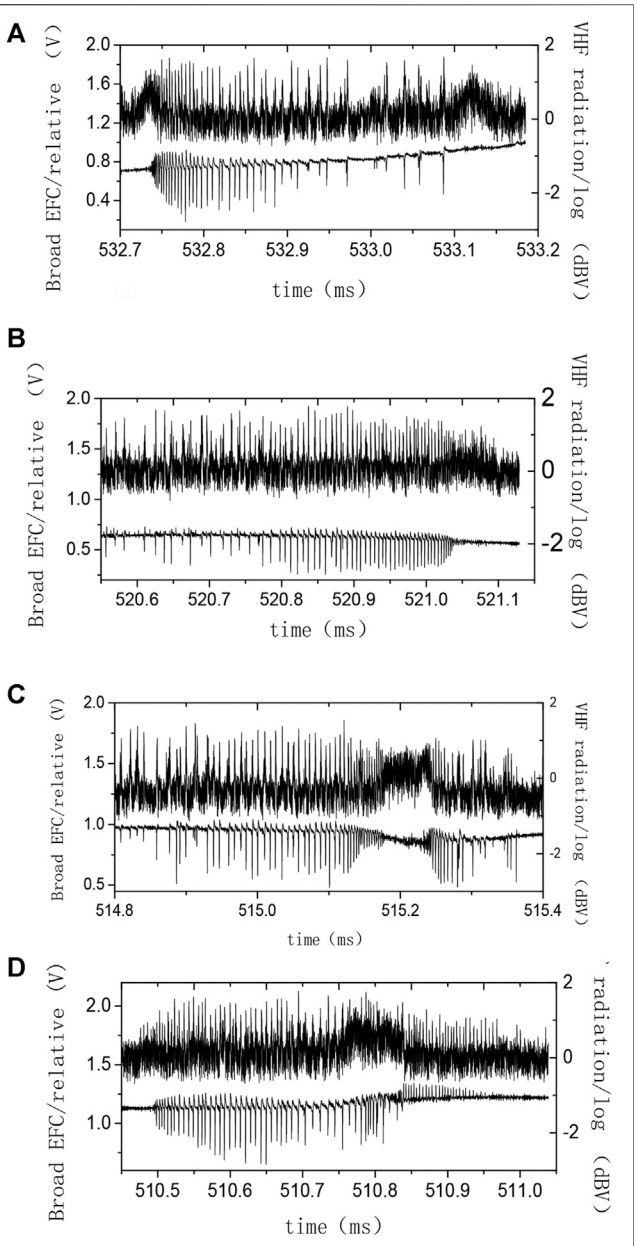


**FIGURE 2 |** Categories of RPBs. Here (and same below), the upper part is the relative change in VHF radiation and the lower part is the relative change in the VLF/LF radiation in picture. **(A)** Normal RPBs, **(B)** back RPBs, **(C)** symmetric RPBs, and **(D)** reversal RPBs.

### 2.1 Normal RPBs

The category of normal RPBs tend to occur in the latter part of a ramp-like [ Rakov et al., 1996] field change (see **Figure 2A**). The initial part of RPBs waveform has a chaotic wave shape and changes to a periodic vibration. RPBs gradually develop into intensive pulses as the pulse amplitude increases. Then, the pulse amplitude decreases and the interval between two pulses

gradually increases with time. It is intense that the VHF radiation synchronized with RPBs. The VHF pulses and EFC pulses are one-to-one correspondence. The amplitude of RPBs pulse in VHF band does not decrease obviously with time for logarithmic amplification. More RPBs belong to normal RPBs, which is similar to the findings of Rakov et al., 1996 and Kolmasová and Santolík (2013). Kolmasová and Santolík (2013) explained that the distances between adjacent charge pockets in thundercloud is nearly constant and they imaged a periodic charge structure which spatial scales is about order of 10 m. The speed of RPBs development decreases with time; therefore, the wave shape shows that the interval between two pulses increases with time. These authors pointed out that the amplitude of the pulses decreases with time, which could be explained reasonably based on the opinion of Uman and McLain (1970), who suggested that the radiated magnetic field is related to the develop speed of leader. However, we can see that the amplitude of pulses increases with time in VLF/LF band of radiation in the initial part of RPBs in **Figure 2** in our work. The amplitude of pulses is stable in the VHF band and dissimilar to that in VLF/LF. Almost all normal RPBs have this characteristic in wave shape. In general, the wavelength of radiation in air gap discharge depends on the discharge gap and discharge velocity. We consider that the discharge is weaker in the initial stage than in the later stage; therefore, the discharge step size is shorter than that in the later stage. Because its radiation spectrum focuses on an even higher VHF band, the quantity of radiant energy in the VLF/LF band is less than that in the VHF band in the initial stage. Furthermore, we think the distribution of charge pockets is not regular absolute in detail; thus, small charge pockets that are uniformly distributed in the vicinity of a large charge pocket was named the charge group, although the distance between the neighboring charge groups in the thundercloud on the macro level is nearly constant, which is similar to the finding of Kolmasová and Santolík (2013). The small charge pockets uniformly distributed in the vicinity of large charge pockets may represent cessation sites of the leader step in the initial stage of RPBs for lower discharge energy. Therefore, the discharge gaps in the initial stage of RPBs are shorter than those in the later stage.

## 2.2 Back RPBs

The category of back RPBs represent a recoil version of the normal type in the time series (see **Figure 2B**). The pulses in the initial portion of RPBs are sparse, and the amplitude of pulses is lower in the beginning period. Over time, the time interval decreases gradually, the pulse amplitude increases, the pulse amplitude decreases and the interval between two pulses decreases so that the wave shape reaches a chaotic waveshape at all times. The VHF radiation is intense, and the VHF pulses and EFC pulses are one-to-one correspondence similar to normal RPBs. The proportion of this type of RPBs is less than that of normal RPBs in lightning discharges. Based on the hypothetical periodic charge structure of Kolmasová and Santolík (2013), the distances changed between adjacent charge pockets and increase of leader propagation speed could probably also explain the different sort of the trains of the pulses. We suggest that the speed increase of the leader propagation provides a better explanation of the discharge process of the back RPBs.

## 2.3 Symmetric RPBs

In this study, some RPBs developed symmetrically in the time series (see **Figure 2C**), and these pairs consisted of one normal RPBs and one back RPBs, with the latter followed by the former. The distances between neighboring pulses are large, and the amplitude of pulses is lower in the initial portion. Over time, the time interval decreases gradually, the pulse amplitude increases, the pulse amplitude decreases and the interval between neighboring pulses decreases and then changes to a chaotic periodic vibration wave shape. After a period of intensive and chaotic wave shape, the wave shape reached periodic vibration again and developed into pulses that burst gradually as the pulse amplitude increased. Then, the pulse amplitude decreased and the interval between two pulses increased with time. The VHF radiation also is intense, and the VHF pulses and EFC pulses are one-to-one correspondence, which is similar to normal RPBs. Ismail et al., 2017 suggested possible mechanisms it is that superposition of electric fields of two and more pulses trains which propagating simultaneously formed chaotic pulse trains, which could explain chaotic pulse trains of symmetric RPBs. However, the detailed evolution of pulse amplitude and time intervals cannot be explained reasonably by the opinion of Ismail et al., 2017. We consider that there is a neighboring large charge area at the discharge channel, with back RPBs occurring before this charge area and normal RPBs occurring after this charge area.

## 2.4 Reversal RPBs

In reversal RPBs, the pulse polarity of the RPBs inverts one or more times in the develop process (see **Figure 2D**). The reverse develop process is always associated with more intense VHF radiation. Some RPBs of this type could be explained by the mechanism suggested by Ismail et al., 2017, which is the superposition of electric fields caused by two RPBs with different polar pulses simultaneously. It is conceivable that the proportional wave shapes of RPBs belong to the type that is superposed by two RPBs with different or the same polar pulses. Of course, not all reverse RPBs present this mechanism, as suggested by Ismail et al., 2017, and we have obtained direct evidence proving this supposition (see '4. Three-dimensional map and characterization of RPBs').

# 3 STATISTICAL DATA ON THE PRBS UNDER VARIOUS LIGHTNING DISCHARGES

A statistical analysis of all 430 RPBs over a period of 15 min indicates that the width of the pulses in RPBs is approximately 0.5–2.0 μs, with a typical width value of 1.0 μs; the interval of neighboring pulses of RPBs is approximately 2.0–10.0 μs, with a typical interval value of approximately 5.0 μs; and the duration of RPBs is approximately 20.0–2000.0 μs, with a typical duration value of several hundred μs. A total of 224 normal RPBs

**TABLE 1 |** Statistical comparison of data from CG. Rows one to three are statistical data given by Rokav et al., 1996; rows five to six are statistical data of–CG from Qinghai; and rows seven to eight are statistical data of +CG from Qinghai.

| Flash id (from first to third refers to Rakov et al., 1996) | RS number | Polarity of RPBs | | Type of RPBs | | | | Parameter of RPBs | | | |
|---|---|---|---|---|---|---|---|---|---|---|---|
| | | Posi-tive | Nega-tive | No-rmal | Ba-ck | Sym-metry | Rever-sal | Average duration | Pulse number | Average interval | Polari-ty |
| 9,122,246.18: 41:17 | 7 | 15 | 20 | / | / | / | / | 173 | 30 | 6.1 | / |
| 91,231,107.14: 40:44 | 9 | 21 | 12 | / | / | / | / | 192 | 28 | 7.3 | / |
| 91,231,111.14: 44:53 | 3 | 10 | 10 | / | / | / | / | 235 | 39 | 6.1 | / |
| 20,110,815.00: 02:28 | 4 | 2 | 3 | 1 | 1 | 1 | 2 | 185 | 41 | 4.5 | - |
| 20,110,815.00: 04:26 | 15 | 1 | 2 | 3 | 0 | 0 | 0 | 564 | 89 | 6.3 | - |
| 20,110,815.00: 03:27 | 1 | 7 | 3 | 5 | 2 | 2 | 1 | 277 | 50 | 5.5 | + |
| 20,110,815.00: 05:24 | 2 | 2 | 4 | 4 | 2 | 0 | 0 | 224 | 42 | 5.5 | + |

**TABLE 2 |** Statistical comparison of data from IC. Rows one to three are statistical data from Rokav et al., 1996; and rows five to six are statistical data of IC from Qinghai.

| Flash id (from first to third refers to Rakov et al., 1996) | Polarity of RPBs | | | Type of RPBs | | | Parameter of RPBs | | |
|---|---|---|---|---|---|---|---|---|---|
| | Posi-tive | Nega-tive | Nor-mal | Ba-ck | Sym-metry | Rever-sal | Average duration | Pulse number | Average interval |
| 91,225,297.19:58:49 | 11 | 16 | / | / | / | / | 161 | 18 | 6.8 |
| 9,123,164.13:59:42 | 3 | 5 | / | / | / | / | 133 | 24 | 6.4 |
| 912,366.15:19:46 | 31 | 6 | / | / | / | / | 117 | 20 | 7.2 |
| 20,110,815.00:01:57 | 3 | 5 | 2 | 4 | 1 | 1 | 203 | 40 | 5 |
| 20,110,815.00:02:49 | 1 | 6 | 4 | 1 | 0 | 2 | 217 | 37 | 5.9 |

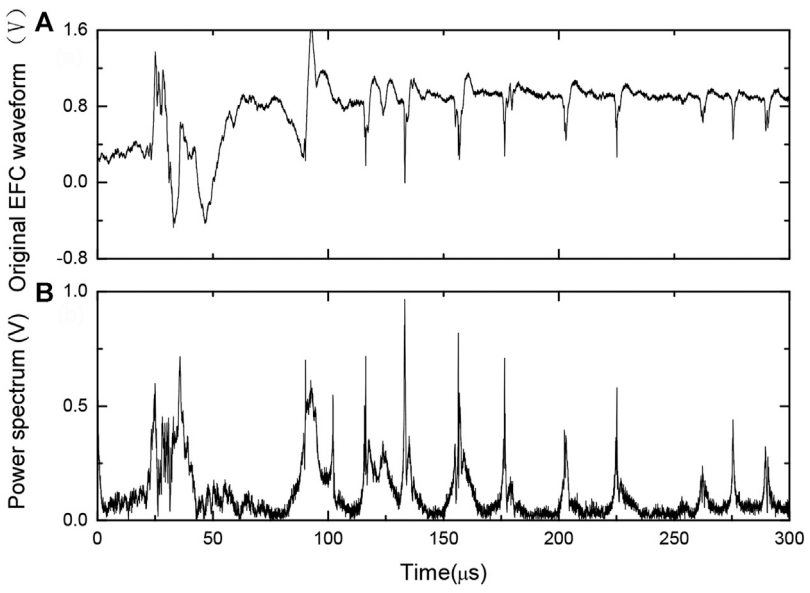


**FIGURE 3 | (A)** Original VLF/LF radiation waveform. **(B)** Power waveform.

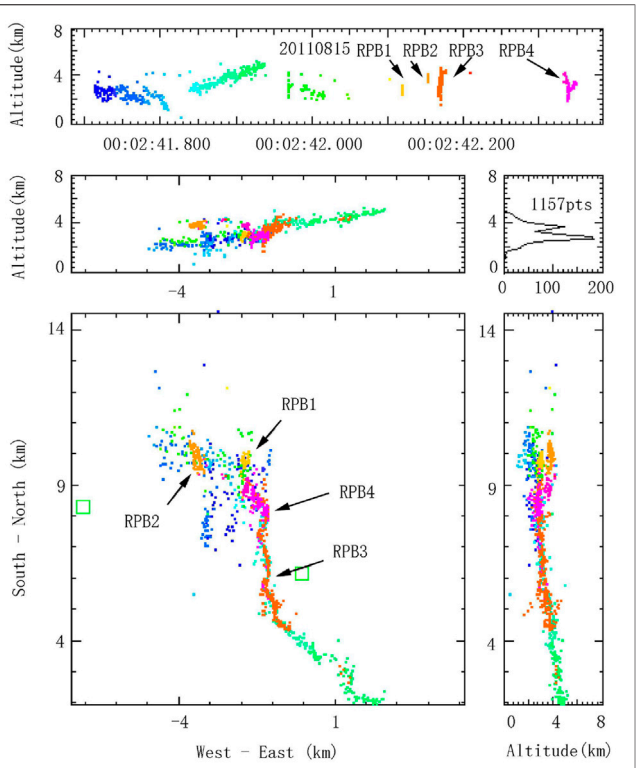


**FIGURE 4 |** Typical intra-cloud lightning discharges includes four RPBs (In this work, the time-variant of radiation sources marked by different colors from blue, green, yellow to red. The green square denotes the LMS station. The height versus time plot (the units of time are hour:minute:second: microsecond) exhibited in top panel; the north-south vertical projection exhibited in mid-left panel; the height distribution of number of radiation events exhibited in mid-right panel shows; the plan view exhibited in bottom-left panel; and the east-west vertical projections exhibited in bottom-right panel).

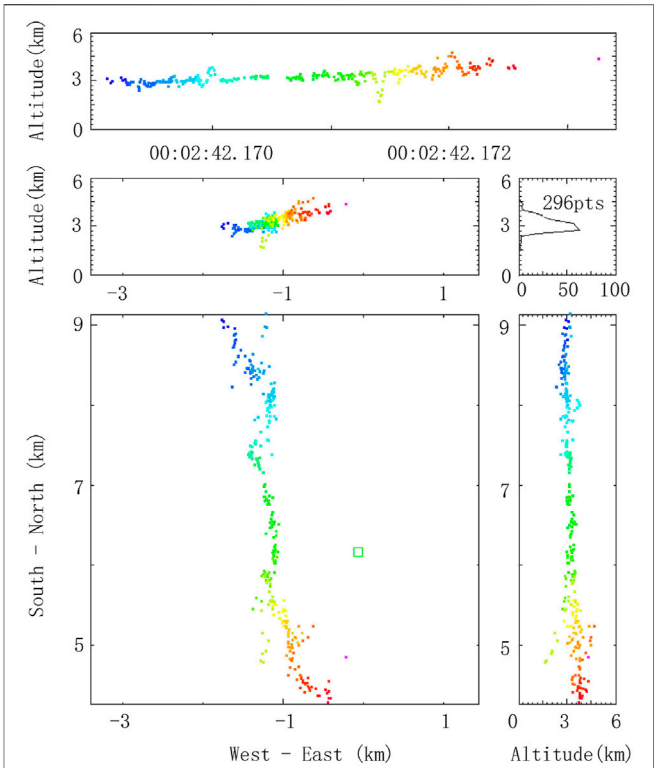


**FIGURE 5 |** Third RPBs in **Figure 4**.

accounted for approximately 52% of all RPBs, 73 back RPBs accounted for approximately 17% of all RPBs, 89 symmetric RPBs accounted for approximately 21% of all RPBs, and 44 reverse RPBs accounted for approximately 10% of all RPBs.

Six typical lightning discharges, including two + CG, two -CG and two IC lightning discharges, are analyzed in detail in this work. **Table 1** and **Table 2** show comparisons between the statistical parameters presented by Rakov et al., 1996 and those from our observations. All parameters in our work are similar to the RPBs observed by Rakov et al., 1996. Moreover, the average duration and pulse number from our observation are slightly greater than those from Rakov et al., 1996. The number of RPBs was five in the-CG (00:02:28), three in the-CG (00:04:26), 10 in the + CG (00:03:27), six in the +CG (00:05:24), eight in the IC (00:01:57), and seven in the IC (00:02:49).

In this study, we only considered regular RPBs with atypical characteristics. The sign '/' indicates absence for this data. The average interval between adjacent pulses of RPBs in lightning discharges observed in Qinghai was slightly lower than that of Rakov et al., 1996. The number of normal-type RPBs shown in **Table 1** is greater than that of the other RPBs, which indicates that most RPBs originate from the hypothetical periodic charge structure which spatial scales is about order of 10 m, as suggested by Kolmasová and Santolík (2013).

RPBs tend to occur at the end of discharge, where many K-changes often occur. More RPBs discharge always occurs in the latter part of a ramp-like field change characteristic of a K-changes. Many RPBs were found to be related with hook-shaped field change M-components (Rakov et al., 1996). In this work, the RPBs can be synchronously detected by broad EFC and VHF detectors. Krider et al., 1975 and Rakov et al., 1996 considered that maximum proportion of RPBs occur in middle or rear of lightning discharges. However, some weak RPBs occurred in the initial stage of lightning discharge in this work. These RPBs were due to "an intra-cloud dart-stepped leader process", as suggested by Krider et al., 1975. Therefore, we think that many secondary breakdowns similar to dart leaders occurred for–CG in the initial stage of lightning discharges.

## 4 THREE-DIMENSIONAL MAP AND CHARACTERIZATION OF RPBS

The lightning mapping system (LMS) takes advantage of 1.2 s uninterrupted waveforms after the detector was triggered, so we can analyze every fragments of lightning discharge with high time resolution (time resolution is 50 ns). The power waveform was converted from a VLF/LF waveforms using the Hilbert transform (see **Figure 3**), which is similar to the work of Shao et al., 2005. Accordingly, we developed a algorithm which could

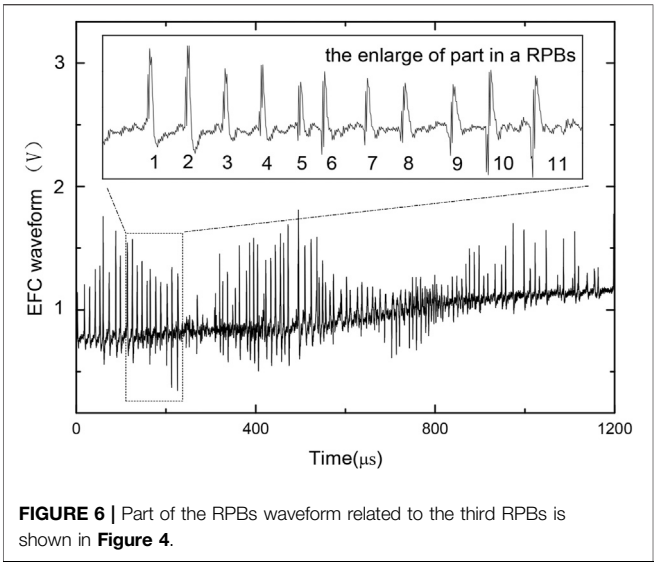


**FIGURE 6 |** Part of the RPBs waveform related to the third RPBs is shown in **Figure 4**.

automatically match pulses from seven stations based sevral intervals between pulses of RPBs (see **Figure 3**). This algorithm improved the efficiency of locating RPBs in three dimensions in a high time resolution although limited by different amplitudes of pulses in different stations. We initially located 11 RPBs in three dimensions and one regular pulse train associated with a dart-stepped leader.

**Figure 4** shows a VHF map of a typical IC which including four process of RPBs. In addition, **Figure 5** shows a three-deimensional picture of a typical RPBs in **Figure 4**. The analysis shows that the ranges of RPBs developing velocity is about from approximately 1.2 × 106 m/s to 3.0 × 106 m/s, which is slightly less than that of the dart-stepped leader process or dart leader (Biagi et al., 2010), and the lengths range of break step which marked by pulses is about from approximately several meters to dozens of meters. The developmental span of RPBs reaches 5 km in this work. The developed channel of RPBs always along the original channel which formed in earlier discharges, which indicates RPBs are re-breakdown processes in IC and similar to dart-stepped leader processes in CG. Many VHF three-dimensional pictures of RPBs show clusters in position of earlier formed channels, and their developing diameters are less than 1 km. Generally, the developmental scan of RPBs cannot reach the ends of old channels.

Multi-polarity inversions of these RPBs are shown in **Figure 6**. The enlarged wave shape of part of the RPBs indicates that the initial half of wave of pulse one is entirely positive. Then, the polarity starts to reverse in the second pulse, with a slightly negative change in the wave shape in the initial half of the wave. Then, the negative change wave shape increases with each pulse until the ninth pulse, which forms an obvious negative half wave pulse, and in the eleventh pulse, the amplitude of the negative half wave is greater than that of the positive half wave and polarity reversal is completed. This phenomenon could not be explained by Ismail et al., 2017. We think that the formation of reverse RPBs may be caused by bending of the lightning discharges channel. The entire RPBs process has multiple reversals and generally

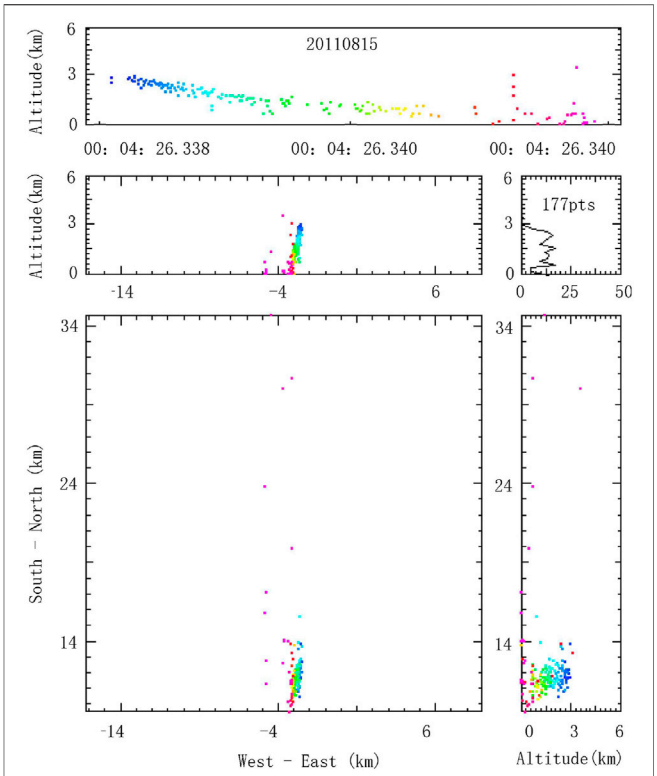


**FIGURE 7 |** RPBs (dart-stepped leader) in a -CG.

develops with snaking discharge channels from the three-dimensional picture in **Figure 5**, although the details are indistinguishable in detail. In addition, a dart-stepped leader was located in three-dimensional in this work (**Figure 7**). The developed velocity of the dart-stepped leader is approximately 1.2 × 106 m/s (**Figure 7**).

## 5 SUMMARY AND DISCUSSION

In this work, we studied the waveforms of lightning discharges from about 15 min.In addition, some typical RPBs were loacted in three dimensions and analyzed in detail. Several conclusions are presented below.

1) The typical width of pulses in RPBs is approximately 1 μs, and the typical interval between pulses of RPBs is approximately 5 μs. According to the interpulse interval and pulse polarity, category of normal RPBs, back RPBs, symmetric RPBs, and reversal RPBs are sorted. Moreover, these four types were related to the different discharge processes and structures of the discharge channels.
2) A total of 83% of all lightning discharges include one or more RPB. RPBs are similar in both broad EFC and VHF radiation waveforms. Generally, RPBs are associated with K-changes, M processes or dart-stepped leaders. Maximum proportion of RPBs occur in middle or rear of lightning discharges.

However, some RPBs was found to occur at the preliminary stage of lightning discharges.

3) The lasting time of RPBs is about from 20 to 2000 μs which larger than that in earlier literature (Krider et al., 1975; Rakov et al., 1996).
4) The RPBs developing velocity ranges from approximately 1.2 × 106 m/s to 3.0 × 106 m/s, which is slightly less than the dart-stepped leader process. The developmental span of RPBs could reach 5 km in this work.

Compared with the primary discharge channel of lightning discharges, such as the preliminary breakdown process and step leader, the secondary breakdown activity is more difficult to be caught by the instrument due to its short time duration and speed of development. Obviously, RPBs are a typical secondary discharge. The dart-stepped leader in CG is similar to this phenomenon. The development of high-speed acquisition technology has allowed detailed observations of the secondary discharge, which can even be mapped in three dimensions.

RPBs are typical waveshapes in the process of lightning discharges. Four types, i.e., normal RPBs, back RPBs, symmetric RPBs, and reversal RPBs, were sorted according to the interpulse interval and pulse polarity. More RPBs belong to normal RPBs. The classification in this paper can enable a more thorough analysis of the different RPBs. Kolmasová and Santolík (2013) investigated the evolution of the pulse amplitude and interval in normal RPBs and suggested that the observed time interval between the adjacent pulses increases with time based on a hypothesis that the equal distance between the neighboring charge pockets and speed of the movement of the RPBs decrease with time. The back RPBs represent a recoil version of the normal type in the time series, which could be explained by the suggestions of Kolmasová and Santolík (2013). In the observation data, we also found some interesting examples, such as symmetric RPBs and reversal RPBs. Symmetric RPBs present normal RPBs followed by back RPBs. A chaotic process occurs between normal RPBs and back RPBs. The superposition of electric fields of two and more pulses trains which propagating simultaneously formed chaotic pulse trains suggusted by (Ismail et al., 2017); however, this explanation cannot easily be applied to symmetric RPBs because these RPBs included a whole back RPBs followed by a whole normal RPBs in the waveform. Thus, the evolution of the amplitude of pulses and the interval between neighboring pulses cannot be well explained by Ismail et al., 2017. We consider that there is a neighboring large charge area at the discharge channel, with back RPBs observed before this charge area and normal RPBs observed after this charge area. For the reversal RPBs, the pulse polarity of RPBs inverts one time or more in their life cycle. (see **Figure 2 4**) and **Figure 6**). Some RPBs of this type could be explained by the mechanism suggested by Ismail et al., 2017, which is the simultaneous superposition of electric fields caused by two RPBs with different polar pulses. However, some cases, including chaotic waveshapes, could not be explained by Ismail et al., 2017. Inverse processes can be observed in the EFC waveform in **Figure 6**, and they are associated with a part of the RPBs channel in **Figure 5**. From the waveform, we can see that the inverse process is frequent and gradually changes in the enlarged waveform in **Figure 6**. We considered that some inverse pulse polarity in RPBs originates from bending of the discharge channel in RPBs.(Wang et al., 2014).

## DATA AVAILABILITY STATEMENT

The original contributions presented in the study are included in the article/Supplementary Material further inquiries can be directed to the corresponding author.

## AUTHOR CONTRIBUTIONS

Data acquisition, WY; methodology, FX and WT; software, MY and LY; validation, WT, MY, and LY; investigation, FX and WY; writing—original draft preparation, WY; writing—review and editing, WY, FX, and WT All authors have read and agreed to the published version of the manuscript.

## FUNDING

This work was supported by the National Key R and D Program of China (2017YFC1501502), Second Tibetan Plateau Scientific Expedition and Research (STEP) program (2019QZKK0104), National Natural Science Foundation of China (41675006, 41875002), Open Research Program of the State Key Laboratory of Severe Weather (2019LASW-B11) and Startup Foundation for Introducing Talent of NUIST (2017r013#).

## ACKNOWLEDGMENTS

The authors are indebted to all members of the Qinghai lightning observation experiment (especially professor Zhang Guangshu) and Qinghai Province. For further details, please contact WY (wangyanh@nuist.edu.cn).

## REFERENCES

Bailey, J., Willett, J., Krider, E., and Leteinturier, C. (1988), Submicrosecond Structure of the Radiation fields from Multiple Events in Lightning Flashes, Proceedings of the paper presented at International Conference on Atmospheric Electricity, 8 th, Uppsala, Sweden.

Beasley, W. H., Uman, M. A., Jordan, D. M., and Ganesh, C. (1983). Simultaneous Pulses in Light and Electric Field from Stepped Leaders Near Ground Level. *J. Geophys. Res.* 88 (C13), 8617–8619. doi:10.1029/jc088ic13p08617

Biagi, C. J., Uman, M. A., Hill, J. D., Jordan, D. M., Rakov, V. A., and Dwyer, J. (2010). Observations of Stepping Mechanisms in a Rocket-And-Wire Triggered Lightning Flash. *J. Geophys. Res. Atmospheres* 115 (D23). doi:10.1029/2010jd014616

Cooray, V., and Lundquist, S. (1985). Characteristics of the Radiation fields from Lightning in Sri Lanka in the Tropics. *J. Geophys. Res.* 90 (D4), 6099–6109. doi:10.1029/jd090id04p06099

Davis, S. (1999). Properties of Lightning Discharges from Multiple Station Wideband Measurements, Dissertation. *Grad. Sch. Univ. Fla.* UMI Microform 9945961.

Füllekrug Martin, F.-S. A. C. (2011). The Earth's Electromagnetic Environment. *Geophys. Res. Lett.* 38 (21). doi:10.1029/2011gl049572

Ismail, M. M., Rahman, M., Cooray, V., Fernando, M., Hettiarachchi, P., and Johari, D. (2017). On the Possible Origin of Chaotic Pulse Trains in Lightning Flashes. *Atmosphere* 8 (2), 29. doi:10.3390/atmos8020029

Jiang, R., Qie, X., Wang, Z., Zhang, H., Lu, G., Sun, Z., et al. (2015). Characteristics of Lightning Leader Propagation and Ground Attachment. *J. Geophys. Res. Atmos.* 120, 11988–12002. doi:10.1002/2015jd023519

Kolmasová, I., and Santolík, O. (2013). Properties of Unipolar Magnetic Field Pulse Trains Generated by Lightning Discharges. *Geophys. Res. Lett.* 40 (8), 1637–1641.

Krider, E. P., Radda, G. J., and Noggle, R. C. (1975). Regular Radiation Field Pulses Produced by Intracloud Lightning Discharges. *J. Geophys. Res.* 80 (27), 3801–3804. doi:10.1029/jc080i027p03801

Krider, E. P., Weidman, C. D., and Noggle, R. C. (1977). The Electric fields Produced by Lightning Stepped Leaders. *J. Geophys. Res.* 82 (6), 951–960. doi:10.1029/jc082i006p00951

Liu, H. Y., Dong, W. S., Zhang, Y. J., Zheng, D., Yan, B. W., Shi, Y. H., et al. (2013). Three-Dimensional Observation of Chaotic Pulse Train Event in Negative Cloud-To-Ground Lightning Using VHF Broadband Digital Interferometer. *Plateau Meteorology* 32 (4), 1186–1194.

Muller-Hillebrand, D. (1962), The Magnetic Field of the Lightning Discharge, in *Gas Discharge and the Electricity Supply Industry*, edited, pp. 89–111. London, England.

Ogawa, T., and Brook, M. (1964). The Mechanism of the Intracloud Lightning Discharge. *J. Geophys. Res.* 69 (24), 5141–5150. doi:10.1029/jz069i024p05141

Qie, X., Yang, Z., Zhang, Q., Jing, Y., Feng, G., Kong, X., et al. (2009). Characteristics of Triggered Lightning during Shandong Artificial Triggering Lightning experiment (SHATLE). *Atmos. Res.* 91 (2), 310–315. doi:10.1016/j.atmosres.2008.08.007

Rakov, V. A., Uman, M. A., Hoffman, G. R., and Brook, M. W. M. (1996). Burst of Pulses in Lightning Electromagnetic Radiation: Observations and Implications for Lightning Test Standards. *IEEE Trans. Electromagn. Compat.* 38 (2), 156–164. doi:10.1109/15.494618

Rakov, V. A., and Uman, M. A. (1990). Waveforms of First and Subsequent Leaders in Negative Lightning Flashes. *J. Geophys. Res.* 95 (D10), 16561–16577. doi:10.1029/jd095id10p16561

Rison, W., Thomas, R. J., Krehbiel, P. R., Hamlin, T., and Harlin, J. (1999). A GPS-Based Three-Dimensional Lightning Mapping System: Initial Observations in central New Mexico. *Geophys. Res. Lett.* 26 (23), 3573–3576. doi:10.1029/1999gl010856

Shao, X. M., Jacobson, A. R., and Fitzgerald, T. J. (2005). Radio Frequency Radiation Beam Pattern of Lightning Return Strokes: Inferred from FORTE Satellite Observations. *J. Geophys. Res. Atmospheres* 110 (D24). doi:10.1029/2005jd006010

Tran, M. D., and Rakov, V. A. (2017). A Study of the Ground-Attachment Process in Natural Lightning with Emphasis on its Breakthrough Phase. *Sci. Rep.* 7 (1), 15761. doi:10.1038/s41598-017-14842-7

Uman, M. A., and Mclain, D. K. (1970). Radiation Field and Current of the Lightning Stepped Leader. *J. Geophys. Res.* 75 (6), 1058–1066. doi:10.1029/jc075i006p01058

Wang, D., Gamerota, W. R., Uman, M. A., Takagi, N., Hill, J. D., Pilkey, J., et al. (2014). Lightning Attachment Processes of an "Anomalous" Triggered Lightning Discharge. *J. Geophys. Res. Atmos.* 119, 1524–1533. doi:10.1002/2013JD020787

Wang, H., Pei, Y., Yin, Y., Shen, L., Chen, K., Shi, Z., et al. (2021). Observational Evidence of Lightning-Generated Ultrafine Aerosols. *Geophys. Res. Lett.* 48, e2021GL093771–14. doi:10.1029/2021gl093771

Wang, Y., Zhang, G., Tong, Z., Li, Y., Zhao, Y., Zhang, T., et al. (2010). The Regular Pulses Bursts in Electromagnetic Radiation from Lightning, Asia-Pacific International Symposium on Electromagnetic Compatibility, Beijing, China, December 4, 2010, IEEE.

Wang, Y., Zhang, G., Li, Y., Tong, Z., and Rong, Z. (2014). Regular Pulses Bursts Observation Using a Time of Arrival Lightning Mapping System with Dual Channels, Intemational Conference of Lighbling Protection, IEEE, 11 Oct. 2014, Shanghai, China

Weidman, C. D., and Krider, E. P. (1978). The Fine Structure of Lightning Return Stroke Wave Forms. *J. Geophys. Res.* 83 (C12), 6239–6247. doi:10.1029/jc083ic12p06239

Weidman, C. D. (1982). The Submicrosecond Structure of Lightning Radiation Fields. Thesis. Arizona, US: The univesity of Arizona.

Willett, J. C., Bailey, J. C., and Krider, E. P. (1989). A Class of Unusual Lightning Electric Field Waveforms with Very strong High-Frequency Radiation. *J. Geophys. Res.* 94 (D13), 16255–16267. doi:10.1029/jd094id13p16255

Zhang, G., Wang, Y., Qie, X., Zhao, T. Y., Li, Y., and Cao, D. (2010). Using Lightning Locating System Based on Time-Of-Arrival Technique to Study Three-Dimensional Lightning Discharge Processes. *Sci. China Earth Sci.* 53 (4), 591–602. doi:10.1007/s11430-009-0116-x

**Conflict of Interest:** The authors declare that the research was conducted in the absence of any commercial or financial relationships that could be construed as a potential conflict of interest.

**Publisher's Note:** All claims expressed in this article are solely those of the authors and do not necessarily represent those of their affiliated organizations, or those of the publisher, the editors and the reviewers. Any product that may be evaluated in this article, or claim that may be made by its manufacturer, is not guaranteed or endorsed by the publisher.

frontiers in Environmental Science

ORIGINAL RESEARCH
published: 06 December 2021
doi: 10.3389/fenvs.2021.794189

# Assessment of Vegetation Phenological Extractions Derived From Three Satellite-Derived Vegetation Indices Based on Different Extraction Algorithms Over the Tibetan Plateau

*Chunchun An[1], Zhi Dong[1], Hongli Li[1]*, Wentai Zhao[2] and Hailiang Chen[1]*

*[1]College of Forestry, Mountain Tai Forest Ecosystem Research Station of State Forestry Administration, Shandong Agricultural University, Tai'an, China, [2]Shandong Forestry Protection and Development Service Center, Jinan, China*

OPEN ACCESS

**Edited by:**
*Xiaobin Guan,*
*Wuhan University, China*

**Reviewed by:**
*Yu Yipeng,*
*Chinese Academy of Forestry, China*
*Shenxin Li,*
*Central South University, China*

***Correspondence:**
*Hongli Li*
*nmglihl@163.com*

**Specialty section:**
*This article was submitted to Atmosphere and Climate, a section of the journal Frontiers in Environmental Science*

**Received:** *13 October 2021*
**Accepted:** *05 November 2021*
**Published:** *06 December 2021*

**Citation:**
*An C, Dong Z, Li H, Zhao W and Chen H (2021) Assessment of Vegetation Phenological Extractions Derived From Three Satellite-Derived Vegetation Indices Based on Different Extraction Algorithms Over the Tibetan Plateau. Front. Environ. Sci. 9:794189. doi: 10.3389/fenvs.2021.794189*

Remote sensing phenology retrieval can remedy the deficiencies in field investigations and has the advantage of catching the continuous characteristics of phenology on a large scale. However, there are some discrepancies in the results of remote sensing phenological metrics derived from different vegetation indices based on different extraction algorithms, and there are few studies that evaluate the impact of different vegetation indices on phenological metrics extraction. In this study, three satellite-derived vegetation indices (enhanced vegetation index, EVI; normalized difference vegetation index, NDVI; and normalized difference phenology index, NDPI; calculated using surface reflectance data from MOD09A1) and two algorithms were used to detect the start and end of growing season (SOS and EOS, respectively) in the Tibetan Plateau (TP). Then, the retrieved SOS and EOS were evaluated from different aspects. Results showed that the missing rates of both SOS and EOS based on the Seasonal Trend Decomposition by LOESS (STL) trendline crossing method were higher than those based on the seasonal amplitude method (SA), and the missing rate varied using different vegetation indices among different vegetation types. Also, the temporal and spatial stabilities of phenological metrics based on SA using EVI or NDPI were more stable than those from others. The accuracy assessment based on ground observations showed that phenological metrics based on SA had better agreements with ground observations than those based on STL, and EVI or NDVI may be more appropriate for monitoring SOS than NDPI in the TP, while EOS from NDPI had better agreements with ground-observed EOS. Besides, the phenological metrics over the complex terrain also presented worse performances than those over the flat terrain. Our findings suggest that previous results of inter-annual variability of phenology from a single data or method should be treated with caution.

**Keywords: remote sensing, satellite-derived vegetation index datasets, vegetation phenology, seasonal amplitude method, STL trendline crossing method, Tibetan Plateau**

## 1 INTRODUCTION

Vegetation phenology can reflect the response of terrestrial ecosystem to climate change and is critical for understanding the effects of these changes on the carbon cycle (Zhang et al., 2004; Xie and Li, 2020a), water cycle (Yu et al., 2018), and energy exchange (Shen et al., 2014b) of terrestrial ecosystems. Remote sensing data have been widely used to monitor vegetation phenology at large scales (Liang et al., 2011; Shen et al., 2013; Shen et al., 2014a; Wang et al., 2020), because satellite-derived vegetation indices (VIs) can measure vegetation canopy greenness and have the advantages of wide coverage, high revisiting frequency, and relatively low cost (Jin et al., 2013; Shen et al., 2015; Liu et al., 2017). The normalized difference vegetation index (NDVI) is one of the most commonly used vegetation indices for monitoring vegetation phenology.

The Moderate Resolution Imaging Spectroradiometer (MODIS) remote sensing data provide the possibility to monitor vegetation phenology and have been increasingly used for monitoring vegetation phenology (Zhang et al., 2004; Wang et al., 2015b; Shang et al., 2018). MODIS sensors aboard Terra and Aqua satellites have been in operation since 1999 and 2002, respectively, and can provide long-term remote sensing NDVI and enhanced vegetation index (EVI) records of >10 years (Wang et al., 2021; Zhu et al., 2021). Generally, the NDVI tends to lose sensitivity over dense canopies because of saturation (Liu et al., 2017; Wu et al., 2017), while the EVI has a larger dynamic range and is more resistant to atmospheric and soil background effects compared with the NDVI (Zhang G. et al., 2013; Cao et al., 2015). Many studies have explored other VIs to indicate the growing season transitions, such as normalized difference phenology index (NDPI), which is designed to best distinguish vegetation from the background (i.e., soil and snow) as well as to minimize the difference among the backgrounds (Wang et al., 2017a). These parameters provide more precise information on the phenological changes of vegetation and have been widely used because of the convenient acquisition of multiple remote sensing data and its indicative function of physical and biological processes related to vegetation dynamics at global and regional scales (Xie et al., 2021b).

Besides, a lot of methods have been proposed and applied to monitor vegetation phenological parameters using long-term satellite data, such as threshold based, curve fitting, curve derivative, delayed moving average, phenological cumulative frequency, etc. These methods determine vegetation phenology based on a predefined or relative reference value, autoregressive moving average model, fitted function, etc. (Wang et al., 2017c; Shang et al., 2018; Wu et al., 2018). The threshold-based method considers the growing season begins when the vegetation index reached a predefined or relative reference value (Shang et al., 2018; Wu et al., 2018). The curve derivative method defines the growing season starts when the second derivative value of the time series curve reaches a maximum (Wang et al., 2017c).

The differences between NDVI and EVI have been evaluated in some previous studies (Yang et al., 2006; Duveiller et al., 2011; Wang et al., 2012; Gamon et al., 2013). However, few studies have conducted a comparative analysis of the performance of EVI, NDVI, and NDPI in monitoring vegetation phenology. Given that MODIS data has been extensively used for monitoring vegetation phenology (Araya et al., 2016; Zeng et al., 2016; Massey et al., 2017), it is necessary to analyze the difference between vegetation phenology derived from different VIs and consequently investigate the uncertainty in monitoring vegetation phenology due to methods. Since the Terra data is more affected by the sensor degradation than Aqua data (Han and Xu, 2013; Tang et al., 2018), this study focused on the Terra MODIS VI and surface reflectance (SR) products.

Three different vegetation indices based on two methods were adopted to identify the start and end of growing season (SOS and EOS) of the vegetation on the Tibetan Plateau (TP). Then, a comparative analysis of vegetation phenology derived from the six combined products was conducted for each phenological extraction. Meanwhile, the performances of vegetation phenology derived in capturing ground-observed phenology

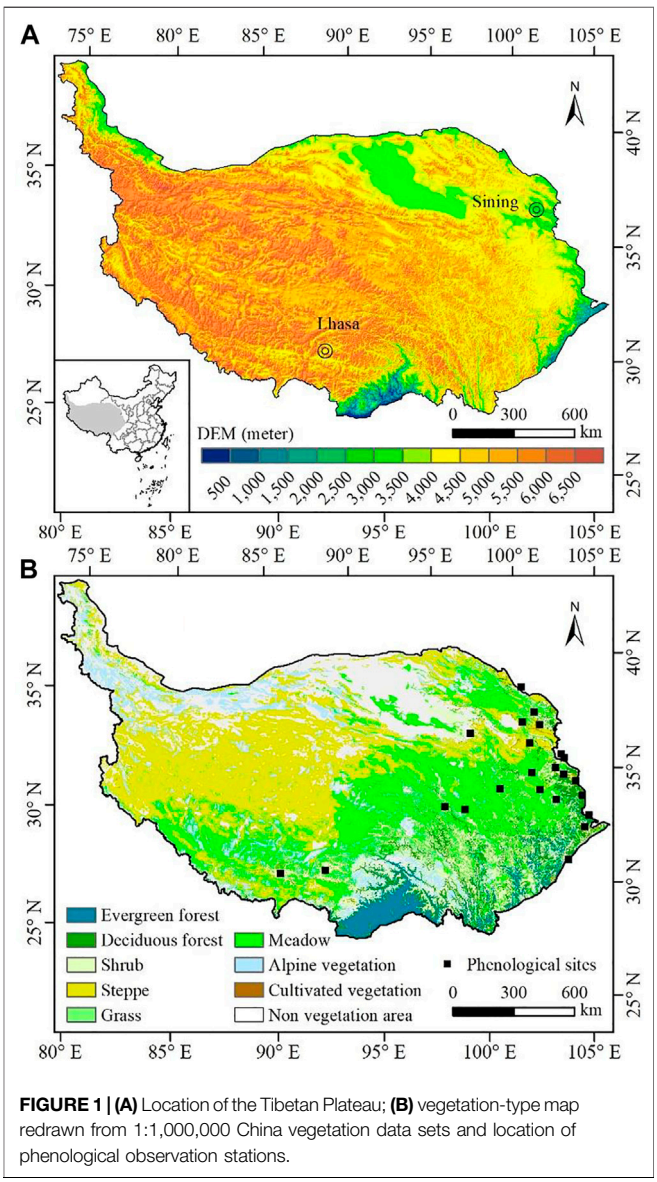


**FIGURE 1 | (A)** Location of the Tibetan Plateau; **(B)** vegetation-type map redrawn from 1:1,000,000 China vegetation data sets and location of phenological observation stations.

were also evaluated. In addition, the performances of phenological metrics from the six products at different degrees of terrain complexity were compared.

This paper aims to assess the differences in phenological metrics extracted using the EVI, NDVI, and NDPI time series based on seasonal amplitude (SA) and Seasonal Trend Decomposition by LOESS (STL) methods and to determine whether either of them performs well for all vegetation types over a large scale. To achieve this objective, the missing rates of SOS and EOS from the six products were counted and compared firstly. Then, the temporal and spatial stabilities of phenological metrics from each product were calculated and analyzed in different vegetation types in the TP. Finally, the differences between ground observations and satellite-derived phenological metrics from the three satellite-derived VIs based on different extraction algorithms are evaluated. Our work lays the foundation for uniting multisource data and for improving remote sensing phenological products in the future.

# 2 DATA AND METHODS

## 2.1 Study Area

The TP (**Figure 1A**) is located in western and southwestern China, covering an area of approximately 2.6 million $km^2$ (26.5–40.0°N, 73.5–105.8°E), accounting for about one quarter of China's total land territory. Recognized as the "roof of the world" and the Third Pole of the Earth, elevation on the TP increases rapidly from about 2,000 m in the east to more than 8,000 m in the west with an average altitude higher than 4,000 m above sea level. As the highest and most extensive region in the world, climate in the TP exhibits a thermal/moisture gradient varying from warm and humid in the southeast to cold and arid in the northwest as influenced by high elevation, Indian monsoon in the summer, and westerlies in the winter. Affected by the mountain plateau climate, a variety of vegetation species is distributed widely on the TP generally following the moisture and temperature gradient. Vegetation in the plateau includes evergreen forests (EF), deciduous forests (DF), shrubs, steppes, grass, meadows, alpine vegetation (AV), and cultivated vegetation (CV). Besides, sparse and no vegetation are mainly distributed in the cold and arid northwestern area (**Figure 1B**).

## 2.2 Data

### 2.2.1 Satellite-Derived Vegetation Index Datasets

The time series NDVI, EVI, and NDPI data were used to extract the phenological metrics in this paper. The 16-day interval vegetation index datasets containing NDVI and EVI with a spatial resolution of 500 m from 2001 to 2017 were derived from the MODIS/Terra MOD13A1 Version 6 product, which can be obtained from the Land Processes Distributed Active Archive Center (LP DAAC) of the National Aeronautics and Space Administration's (NASA) Earth Observing System Data and Information System (EOSDIS) (https://lpdaac.usgs.gov/). A series of the sophisticated algorithm (constrained view angle-maximum value composite algorithm, etc.) and strict quality control (low clouds, low view angle, and the highest NDVI/EVI value) were performed in the process of data production to reduce the effect of clouds, solar zenith angles, stratospheric aerosol, etc.

The time series of SR data from MOD09A1 Version 6 product were used to calculate the NDPI, as shown in **Eqs. 1**, **2**, **3**. The MOD09A1 product provided an estimate of the surface spectral reflectance of Terra MODIS bands 1 through 7 systematically corrected for atmospheric conditions such as gasses, aerosols, and Rayleigh scattering. The temporal resolution of MOD09A1 is 8 days, and the spatial resolution is 500 m. These data are also freely distributed through the LP DAAC. In this study, surface reflectance in the red (band 1, 620–670 nm), near-infrared (NIR: 841–876 nm, band 2), and short-wave infrared band (SWIR: 1,628–1,652 nm, band 6) during 2001 and 2017 necessary to calculate NDPI were extracted.

$$NDPI = \frac{\rho_{NIR} - \rho_{red}^{SWIR}}{\rho_{NIR} + \rho_{red}^{SWIR}} \tag{1}$$

$$\rho_{red}^{SWIR} = \alpha \times \rho_{red} + (1 - \alpha) \times \rho_{SWIR} \tag{2}$$

$$\begin{aligned} NDPI &= \frac{\rho_{NIR} - \left(\alpha \times \rho_{red} + (1 - \alpha) \times \rho_{SWIR}\right)}{\rho_{NIR} + \left(\alpha \times \rho_{red} + (1 - \alpha) \times \rho_{SWIR}\right)} \\ &= \frac{\rho_{NIR} - \left(0.74 \times \rho_{red} + 0.26 \times \rho_{SWIR}\right)}{\rho_{NIR} + \left(0.74 \times \rho_{red} + 0.26 \times \rho_{SWIR}\right)} \end{aligned} \tag{3}$$

### 2.2.2 Vegetation-Type Data

Information of the vegetation distribution in the plateau was derived from the digitized vegetation datasets of China with a scale of 1:1,000,000, published by the Institute of Geography Science and Natural Sources Research, Chinese Academy of Sciences in 2001 (http://www.geodata.cn/Portal/), which was used to identify the vegetation coverage over pixels, as shown in **Figure 1B**. Due to the lack of seasonality in vegetation index signal, EF mostly in the southeast is not included in our study. We assumed that there were no changes in the vegetation types and distributions on the plateau during the study period as previous studies had done.

### 2.2.3 Ground-Observed Phenological Data

The ground phenological observations provided by the China Meteorological Administration (CMA, http://cdc.cma.gov.cn) were taken as the true values to validate the accuracy of the phenological products. However, the ground-based phenology was observed in a number of individual plants, while the remote sensing phenology represented the integrated phenological characteristics of a plant community in one pixel. Ground validation of remote sensing measurements with coarse resolution entails considerable difficulties. To improve the reliability of the statistical analysis based on ground observations, ground phenological observations meeting the following requirements (Wang et al., 2017c) were selected: 1) Data integrity—the selected ground sites should have phenological phase continuity and few missing records. 2) Spatial representation—the vegetation type of dominant species at one site must be the same with remote sensing data. The ground phenological observations were selected according to

**TABLE 1 |** Summary of ground phenological observation sites in TP.

| Station name | Code | Latitude | Longitude |
|---|---|---|---|
| Minle | 52656 | 38.45 | 100.82 |
| Menyuan | 52765 | 37.38 | 101.61 |
| Dulan | 52836 | 36.30 | 98.10 |
| Haiyan | 52853 | 36.92 | 100.98 |
| Huzhu | 52863 | 36.82 | 101.95 |
| Guide | 52868 | 36.03 | 101.43 |
| Linxia | 52984 | 35.58 | 103.18 |
| Hezheng | 52985 | 35.43 | 103.35 |
| Rikaze | 55578 | 29.25 | 88.88 |
| Lasa | 55591 | 29.67 | 91.13 |
| Yushu | 56029 | 33.02 | 97.02 |
| Shiqu | 56038 | 32.98 | 98.10 |
| Gande | 56045 | 33.97 | 99.90 |
| Henan | 56065 | 34.73 | 101.60 |
| Maqu | 56074 | 34.00 | 102.08 |
| Ruoergai | 56079 | 33.58 | 102.97 |
| Hezuo | 56080 | 35.00 | 102.90 |
| Lintan | 56081 | 34.70 | 103.35 |
| Minxian | 56093 | 34.43 | 104.01 |
| Zhouqu | 56094 | 33.78 | 104.37 |
| Guanxian | 56188 | 30.98 | 103.66 |
| Wenxian | 56192 | 32.93 | 104.75 |
| Pingwu | 56193 | 32.42 | 104.52 |

the above requirements, and the information and spatial distribution of phenological sites are shown in **Figure 1** and **Table 1**.

### 2.2.4 Topographic Data

The Shuttle Radar Topography Mission (SRTM) digital elevation model (DEM) data with a spatial resolution of 90 m distributed free of charge was acquired from the Consortium for Spatial Information of the Consultative Group for International Agricultural Research (CGIAR-CSI, http://www.cgiar-csi.org). In this work, the SRTM DEM was used to describe the terrain characteristics. The elevation of each ground phenological site was obtained from the center pixel based on the geolocation information of the ground sites. Furthermore, the relief amplitude and mean slope were extracted from the $3.0 \times 3.0$-pixel area centered on the phenological sites.

## 2.3 Data Pre-Processing

Although the effects of satellite orbit shift; solar zenith angles; and atmospheric contaminations of clouds, aerosols, etc. had been systematically corrected from the vegetation index datasets, the time series VI curves still remained jagged because of the residual contamination (Ding et al., 2016; Cong et al., 2017; Chu et al., 2021). The abnormally high and low values existed in the VI trajectories may result in errors and confound retrievals of vegetation phenology (Wang et al., 2015b; Chang et al., 2016). Therefore, the adaptive Savitzky–Golay (S-G) filtering procedure was performed to reduce residual noises in the time series VI datasets by smoothing the VI time series curve, and high-quality NDVI time series datasets were reconstructed (Chang et al., 2016). The adaptive S-G filtering method has been proven to be effective in rebuilding time series from which vegetation phenological metrics can be extracted. The related noise reduction parameters were selected empirically as described in previous studies, which were as follows: spike method = 1, iteration time = 3, adaption strength = 5, and smoothing window = 3, respectively (Borges et al., 2014).

In order to focus on the areas with vegetation and seasonality and to further reduce the impacts of soil variations in bare and sparsely vegetated areas on vegetation, pixels simultaneously satisfying the following criteria were selected: 1) The multiyear average NDVI during growing season (from April to October) should be greater than 0.1. 2) The annual maximum NDVI should be higher than 0.15 and occur between July and September (Piao et al., 2011; Jin et al., 2013; Shen et al., 2014b; Wang et al., 2018). Pixels with lower NDVI value were often considered photosynthetically inactive in land surface phenology, and they could not reveal regular growth cycles along the trajectories and were usually regarded as bare soil or sparsely vegetated lands (Wang et al., 2015a; Wang et al., 2015b). These pixels were masked in the vegetation index datasets and excluded in the following analysis. Besides, evergreen forests were removed from this study due to the lack of seasonality in vegetation index signal relative to those of the other vegetation types (Zhang et al., 2004; Piao et al., 2011; Zheng and Zhu, 2017).

## 2.4 Phenology Retrieval Algorithms

In this paper, vegetation phenological metrics were retrieved from each of the three vegetation indices (EVI, NDVI, and NDPI) by adopting each of the two methods, respectively, including SA method and STL trendline crossing method. In general, those methods determine the vegetation SOS (EOS) around the time when VI begins to increase (decrease) in spring or early summer (autumn or early winter). Details of those two methods are given as follows.

### 2.4.1 Seasonal Amplitude Method

In the SA method, SOS is defined as the date (Julian day of the year, DOY) when the left part of the fitted curve has reached a certain ratio of the seasonal amplitude during the VI rising stage, counted from the base level; EOS is defined similarly, as the DOY for which the right side of the fitted curve has decreased to a certain fraction of the seasonal amplitude during the VI decline stage (Jamali et al., 2015; Jönsson and Eklundh, 2004). The seasonal amplitude is defined as difference between the maximum VI value and the base level for each individual season (Eklundh and Jönsson, 2016; Eklundh and Jönsson, 2017). The VI ratio is defined as follows:

$$VI_{ratio} = \frac{VI_t - VI_{base}}{VI_{max} - VI_{base}} \tag{4}$$

$$VI_{base} = 0.5 \times \left(VI_{minimum\ left} + VI_{minimum\ right}\right) \tag{5}$$

where $VI_t$ is the VI value at time $t$, $VI_{max}$ is the annual maximum VI value, and $VI_{base}$ is given as the average of the left and right minimum values. In this study, we selected a VI ratio threshold of

0.2 to indicate the SOS and a drop of the VI ratio below 0.6 to show the EOS, as determined by Yu et al. (2010).

Among the various retrieval algorithms, the SA method is relatively less affected by surface snow cover, can effectively avoid the mutual interference caused by different hydrothermal conditions, and has been widely used in the extraction of vegetation phenology.

### 2.4.2 STL Trendline Crossing Method

The seasonal-trend decomposition algorithm based on locally weighted regression (LOESS), widely known as "STL," is a filtering procedure for decomposing seasonal time series into three additive components of variation: non-linear trend line, seasonal component of time series, and remainder (B Cleveland et al., 1990; Rojo et al., 2017; Sanchez-Vazquez et al., 2012). The trend component ($T_t$) is considered as the low-frequency variation in the data together with non-stationary, long-term changes in the levels over the time horizon; the seasonal component ($S_t$) is the variation in the data at or near the seasonal frequency, which is the repetitive pattern over time; the remainder component ($R_t$) is defined as the irregular remaining variation in the data after the seasonal and trend components have been removed (Aguilera et al., 2015; Cristina et al., 2016).

The STL method is straightforward to use, and advantages of the STL decomposition include simplicity and speed of computation, responsiveness to non-linear trends, flexibility in identifying a seasonal component that changes over time, and robustness of results that are not distorted by transient outliers (Sanchez-Vazquez et al., 2012; Cristina et al., 2016; Rojo et al., 2017). The STL technique has been widely and successfully applied in many fields, especially in natural sciences, such as ecology, environmental science, hydrology, and water resources science, and more details about the STL method can be found in the literature (Aguilera et al., 2015; B Cleveland et al., 1990; Cristina et al., 2016; Jamali et al., 2015; Lafare et al., 2015; Verbesselt et al., 2010).

In this method, the SOS/EOS occurs when the VI time series curve intersect with the STL trend line.

Based on combination of the above two methods and the three vegetation indices, six products were generated, and they were as follows: EVI-based phenological product using SA (E-SA, $SOS_{E\text{-}SA}$, and $EOS_{E\text{-}SA}$), EVI-based phenological product using STL (E-STL, $SOS_{E\text{-}STL}$, and $EOS_{E\text{-}STL}$), NDVI-based phenological product using SA (N-SA, $SOS_{N\text{-}SA}$, and $EOS_{N\text{-}SA}$), NDVI-based phenological product using STL (N-STL, $SOS_{N\text{-}STL}$, and $EOS_{N\text{-}STL}$), NDPI-based phenological product using SA (P-SA, $SOS_{P\text{-}SA}$, and $EOS_{P\text{-}SA}$), and NDPI-based phenological product using STL (P-STL, $SOS_{P\text{-}STL}$, and $EOS_{P\text{-}STL}$).

## 2.5 Classification of Terrain Complexity

According to the definition of mountainous regions from the United Nations Environment World Conservation Monitoring Centre (UNEP-WCMC) (Kapos, 2000) and relative studies in the literature (Zhang W. et al., 2013; Xie et al., 2019), the degree of terrain complexity was defined using the altitude, relief amplitude, and slope. Then, the topographic conditions were classified into complex terrain if one of the following three criteria was satisfied: 1) when the altitude was lower than 500 m and the relief amplitude exceeds 100 m, 2) when the altitude ranged from 500 to 2,500 m and the relief amplitude exceeds 300 m or slope exceeds 5°, and 3) when the altitude was higher than 2,500 m and the relief amplitude exceeds 500 m or slope exceeds 10°. Otherwise, the topographic conditions were classified into flat terrain.

## 2.6 Methods for Evaluating the Phenological Products

The difference of the six products was compared comprehensively over the same spatial extent and temporal span: first, at validity containing the missing rate and temporal and spatial stabilities and second at accuracy validation of the retrievals.

The average phenological metrics for each pixel of each product were calculated as the spatial pattern of the TP, and missing rate was calculated as the ratio of all missing pixel counts to the total pixel counts that should be retrieved (Wang et al., 2017b; Wang et al., 2017c; Shang et al., 2018).

Temporal stability means that the inter-annual growth characteristics of vegetation in the same location are similar to some extent as the climatic factors that affect the growth of vegetation (such as temperature, precipitation, etc.) do not change dramatically in the same area (Wang et al., 2017b). Here, the coefficient of variance (CV) (**Eq 6**) of phenological metric was used as an indicator to describe the temporal stability of each product. The lower the CV was, the more stable the product was at time scale.

$$CV = \frac{\sigma}{\mu} \tag{6}$$

where σ is the standard deviation of phenological metric within 2001 and 2017, and $\mu$ is the average value of phenological metric within 17 years.

Spatial stability means that the phenological characteristics of the same vegetation type growing in the same region in 1 year are supposed to be more similar because the meteorological conditions are nearly the same, which means the growth of vegetation should be synchronous in a small window (Tobler, 1970; Wang et al., 2017b; Shang et al., 2018). Here, we use the CV (**Eq 6**) of phenological metric within a window (3 × 3) to indicate the spatial stability of each product. The greater the CV was, the lower the stability of the product.

$$CV = \frac{\sigma}{\mu} \tag{7}$$

where σ is the standard deviation of phenological metric within the window, and $\mu$ is the average value of phenological metric within the window.

In addition, the phenological metrics of products through retrieval algorithms using three satellite-derived VI datasets were validated against ground-observed phenology, respectively (Zheng and Zhu, 2017). The average value of a 3 × 3 window centered at each ground site was extracted as the final result for comparison with the ground-observed phenology. The mean absolute error (MAE) and root mean square error (RMSE) between remote sensing phenological estimations and ground

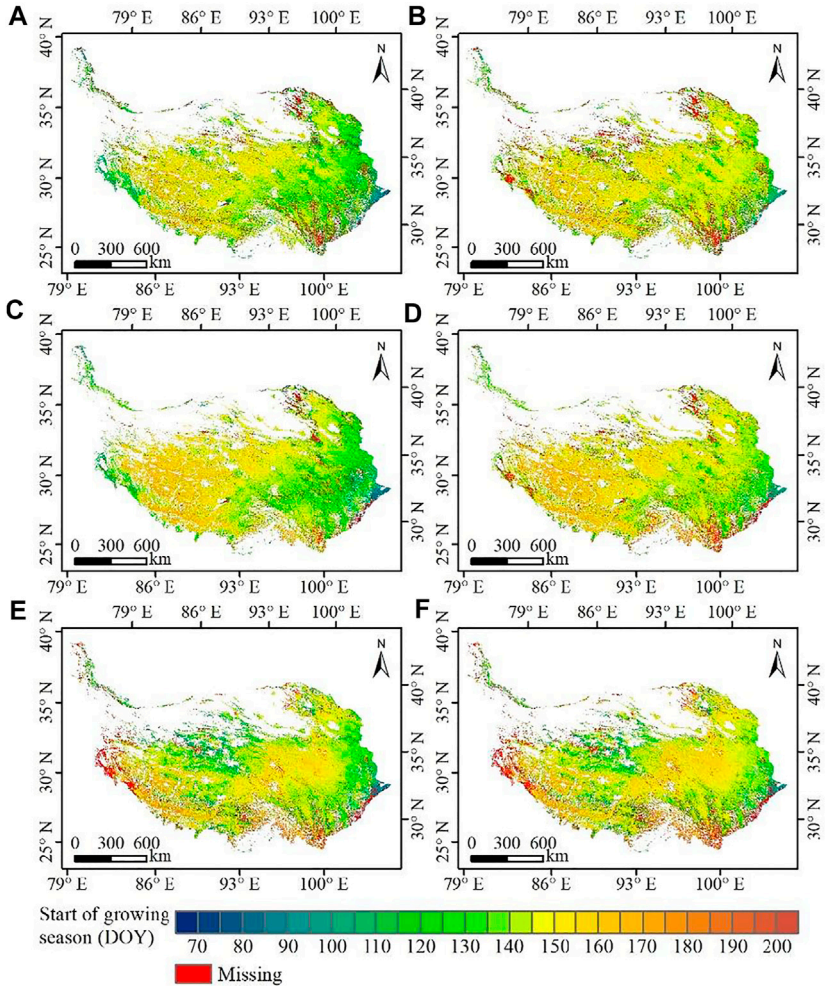


**FIGURE 2 |** Spatial pattern of mean start of season (SOS) between **(A)** E-SA, **(B)** E-STL, **(C)** N-SA, **(D)** N-STL, **(E)** P-SA, and **(F)** P-STL.

observations were adopted as validation indicators (Wang et al., 2017c; Liu et al., 2017; Guan et al., 2021), as shown in **Eqs 8** and **9**.

$$MAE = \frac{\sum_{i=1}^{n} \left(\left|P(rs)_i - P(site)_i\right|\right)}{n} \tag{8}$$

$$RMSE = \sqrt{\frac{\sum_{i=1}^{n} \left(P(rs)_i - P(site)_i\right)^2}{n}} \tag{9}$$

where $P(rs)_i$ is the satellite-derived phenological date at year $i$, $P(site)_i$ is the ground observation at year $i$, and $n$ is the number of years.

# 3 RESULTS AND ANALYSIS

## 3.1 Comparison of Phenological Products at Regional Scales

**Figure 2** presents the mean SOS for the TP during 2001–2017 derived from the six products. In general, inconsistencies of SOS derived from different VI datasets using different methods existed and varied in different areas. The SOS derived from the same VI using different algorithms had consistent patterns in the west, but inconsistent patterns were exhibited in the east. The SOS based on SA (**Figure 2A, C, E**) in the east was 5–15 days earlier than that based on STL (**Figure 2B, D, F**) from the same VI dataset. The SOS derived from different VI using the same method have consistent patterns in the east, but inconsistent patterns were exhibited in the middle and northwest. The SOS from NDVI (**Figure 2C, D**) in the middle was 5–10 days earlier than that from EVI (**Figure 2A, B**), while the SOS from NDPI (**Figure 2E, F**) in the northwest was 10–20 days earlier than that from EVI.

For each product, various degrees of differences among the multi-year average EOS for the TP from 2001 to 2017 are found in **Supplementary Figure S1**. The EOS derived using STL (**Supplementary Figure S1B, D, F**) had the same spatial pattern as those using SA (**Supplementary Figure S1A, C, E**) with the same VI, but was 15–30 days later than that using SA with the same VI in the same area. Also, inconsistencies of EOS derived from different VI using the same method existed and varied in different regions. The EOS from NDVI (**Supplementary**

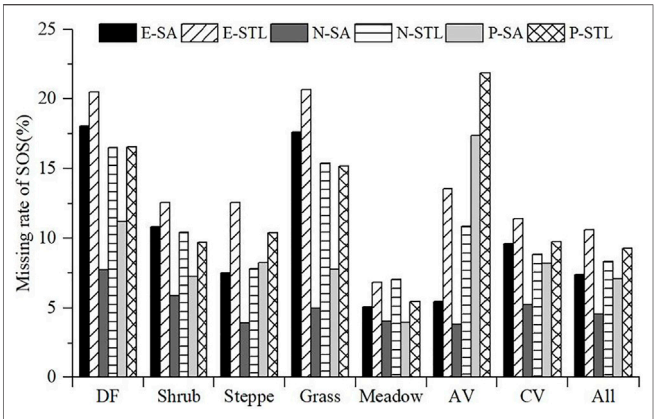


**FIGURE 3 |** Missing rates of SOS over different vegetation types.

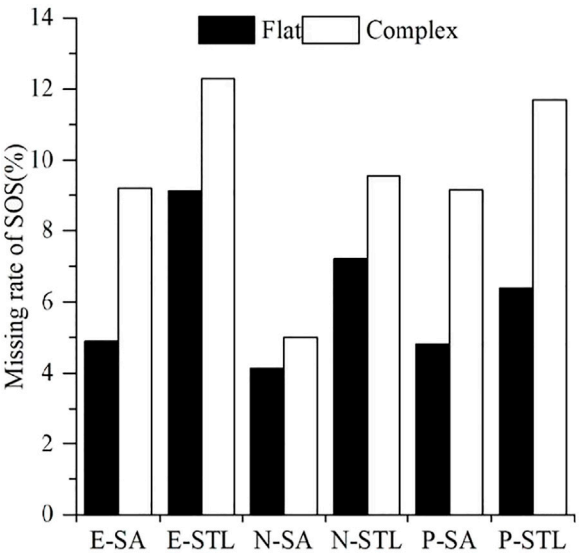


**FIGURE 4 |** Comparison of missing rates of SOS over the flat terrain and the complex terrain.

**Figure S1C, D**) was 10–30 days later than that from EVI (**Supplementary Figure S1A, B**) in the south, respectively, while the EOS from NDPI (**Supplementary Figure S1E, F**) was 5–10 days earlier in the south.

### 3.1.1 Missing Rate

For the six phenological products, the missing data existed inevitably and varied in different regions. In general, the missing rates of SOS in E-SA, E-STL, N-SA, N-STL, P-SA, and P-STL were 7.38%, 10.6%, 4.58%, 8.3%, 7.11%, and 9.25%, respectively, as shown in and **Figures 2** and **3**. For the same VI source, the missing rate of SOS based on STL was higher than that based on SA; for the same retrieval algorithm, the missing rate of SOS derived from NDVI was the lowest, then the NDPI, and the missing rate of SOS derived from EVI was the highest (**Figure 3**). **Figure 3** presents the missing rates of the six products in different vegetation types. For SOS (**Figure 3**), the missing rate was the lowest or relatively lower in the meadow (E-SA: 5.06%, E-STL: 6.83%, N-SA: 4.08%, N-STL: 7.04%, P-SA: 3.99%, and P-STL: 5.46%), but the relatively higher or the highest missing rates of the six products existed in different vegetation types; for SOS from EVI and NDVI, the missing rate was relatively higher in DF (E-SA: 18.03%, E-STL: 20.49%, N-SA: 7.72%, and N-STL: 16.49%); for SOS from NDPI, the missing rate was the highest in AV (P-SA: 17.34% and P-STL: 21.84%).

As displayed in **Supplementary Figures S1 and S2**, the overall missing rates of EOS in E-SA, E-STL, N-SA, N-STL, P-SA, and P-STL were 7.82%, 17.53%, 6%, 18.51%, 12.96%, and 29.21%, respectively. For the same VI source, the missing rate of EOS based on STL was twice more than that based on SA; for the same retrieval algorithm, the missing rate of EOS derived from NDVI was still the lowest, different from SOS; EOS with the highest missing rate was derived from EVI. Similar to SOS, EOS of the six products (**Supplementary Figure S2**) in meadow had the lowest missing rate (E-SA: 4.73%, E-STL: 6.83%, N-SA: 4.59%, N-STL: 13.43%, P-SA: 6.92%, and P-STL: 20.13%), and the highest missing rate was in DF from NDVI or EVI (E-SA: 18.54%, E-STL: 29.59%, N-SA: 13.41%, and N-STL: 37.20%) and in AV from NDPI (P-SA: 19.49% and P-STL: 45.46%).

In addition, the missing rates of phenological metrics from the six products at different degrees of terrain complexity were compared. As shown in **Figure 4**, the missing rates of SOS from the six products at the complex terrain were larger than those at the flat terrain. Over the flat terrain, the missing rates of SOS in E-SA, E-STL, N-SA, N-STL, P-SA, and P-STL were 4.89%, 9.14%, 4.13%, 7.20%, 4.82%, and 6.39%, respectively; over the complex terrain, the missing rates of SOS in E-SA, E-STL, N-SA, N-STL, P-SA, and P-STL were 9.21%, 12.29%, 5.01%, 9.57%, 9.17%, and 11.70%, respectively. In addition, EOS at the complex terrain also showed higher missing rates than the flat terrain (**Supplementary Figure S3**). The missing rates of EOS in E-SA, E-STL, N-SA, N-STL, P-SA, and P-STL over the flat terrain were 5.31%, 15.20%, 4.48%, 14.20%, 11.61%, and 27.23%, respectively, and the missing rates of EOS in E-SA, E-STL, N-SA, N-STL, P-SA, and P-STL over the complex terrain were 9.99%, 20.83%, 7.53%, 23.14%, 14.62%, and 31.44%, respectively.

The high spatial variations in geographic configurations caused by obvious topographic conditions over the complex terrain may affect the quality of input VI data for phenological extractions and then lead to higher missing rates of phenological metrics compared with the flat terrain.

### 3.1.2 Temporal Stability

**Table 2** shows the temporal stabilities of SOS from 2001 to 2017 using CV as indicator. In general, the SOS derived from EVI or NDVI had higher temporal stabilities than those from NDPI for each method, and SOS based on the SA method were a little more stable than those based on the STL method for each vegetation index. Specifically, the SOS from E-SA, E-STL, N-SA, and N-STL product had lower CVs (the means and standard deviations were $0.147 \pm 0.112$, $0.148 \pm 0.103$, $0.137 \pm 0.098$, and $0.141 \pm 0.092$, respectively) than those from P-SA and P-STL product (the means and standard deviations were $0.191 \pm 0.146$,

**TABLE 2 |** The means and standard deviations of SOS CV for different vegetation types from 2001 to 2017.

| Methods/vegetation type | E-SA | E-STL | N-SA | N-STL | P-SA | P-STL |
|---|---|---|---|---|---|---|
| DF | 0.160 ± 0.124 | 0.162 ± 0.105 | 0.177 ± 0.120 | 0.186 ± 0.104 | 0.188 ± 0.121 | 0.192 ± 0.132 |
| Shrub | 0.130 ± 0.104 | 0.138 ± 0.092 | 0.142 ± 0.102 | 0.150 ± 0.088 | 0.158 ± 0.128 | 0.163 ± 0.134 |
| Steppe | 0.164 ± 0.113 | 0.160 ± 0.109 | 0.133 ± 0.091 | 0.131 ± 0.095 | 0.235 ± 0.142 | 0.231 ± 0.139 |
| Grass | 0.190 ± 0.117 | 0.190 ± 0.106 | 0.219 ± 0.121 | 0.220 ± 0.100 | 0.228 ± 0.108 | 0.236 ± 0.115 |
| Meadow | 0.127 ± 0.103 | 0.134 ± 0.095 | 0.122 ± 0.091 | 0.130 ± 0.084 | 0.155 ± 0.136 | 0.157 ± 0.141 |
| AV | 0.187 ± 0.110 | 0.213 ± 0.123 | 0.170 ± 0.094 | 0.194 ± 0.104 | 0.285 ± 0.192 | 0.293 ± 0.192 |
| CV | 0.111 ± 0.087 | 0.124 ± 0.081 | 0.130 ± 0.102 | 0.148 ± 0.100 | 0.143 ± 0.124 | 0.140 ± 0.124 |
| All | 0.147 ± 0.112 | 0.148 ± 0.103 | 0.137 ± 0.098 | 0.141 ± 0.092 | 0.191 ± 0.146 | 0.192 ± 0.149 |

**TABLE 3 |** The means and standard deviations of SOS CV for different terrains from 2001 to 2017.

| Methods/terrain | E-SA | E-STL | N-SA | N-STL | P-SA | P-STL |
|---|---|---|---|---|---|---|
| Flat | 0.146 ± 0.111 | 0.147 ± 0.100 | 0.127 ± 0.092 | 0.132 ± 0.092 | 0.188 ± 0.153 | 0.192 ± 0.139 |
| Complex | 0.148 ± 0.113 | 0.150 ± 0.106 | 0.146 ± 0.103 | 0.148 ± 0.092 | 0.195 ± 0.138 | 0.199 ± 0.156 |

0.192 ± 0.149, respectively). Besides, the temporal stabilities of SOS varied among different vegetation types, as shown in **Table 2**. For DF, shrub, and CV types, the SOS from E-SA were superior to those from others in the aspect of temporal stability, with the lowest CVs of 0.160 ± 0.124, 0.130 ± 0.104, and 0.111 ± 0.087, respectively, followed by the SOS from E-STL, with CVs of 0.162 ± 0.105, 0.138 ± 0.092, and 0.124 ± 0.081, respectively. For steppes, $SOS_{N\text{-}SA}$ and $SOS_{N\text{-}STL}$ had better temporal stabilities compared with others, with CVs of 0.133 ± 0.091 and 0.131 ± 0.095, respectively. However, for grass, $SOS_{E\text{-}SA}$ and $SOS_{E\text{-}STL}$ were relatively more stable, with CVs of 0.190 ± 0.117 and 0.190 ± 0.106, respectively. For meadows, $SOS_{N\text{-}SA}$ was the most stable, followed by $SOS_{E\text{-}SA}$ and $SOS_{N\text{-}STL}$, with CVs of 0.122 ± 0.091, 0.127 ± 0.103, and 0.130 ± 0.084, respectively. For AVs, the CV of $SOS_{N\text{-}SA}$ was the lowest, with CV of 0.170 ± 0.094, followed by $SOS_{E\text{-}SA}$ and $SOS_{N\text{-}STL}$, with CVs of 0.187 ± 0.110 and 0.194 ± 0.104, respectively.

**Supplementary Table S1** presents the temporal stabilities of EOS from 2001 to 2017 using CV as an indicator. In general, the temporal stabilities of EOS were slightly different from SOS. Differences existed between EOS based on the SA method and the STL method for each vegetation index in the aspect of temporal stability; EOS based on STL ($EOS_{E\text{-}STL}$: 0.070 ± 0.042, $EOS_{N\text{-}STL}$: 0.044 ± 0.023, and $EOS_{P\text{-}STL}$: 0.051 ± 0.032) had higher CVs than those based on SA ($EOS_{E\text{-}SA}$: 0.037 ± 0.018, $EOS_{N\text{-}SA}$: 0.037 ± 0.018, and $EOS_{P\text{-}SA}$: 0.046 ± 0.028). Besides, the temporal stabilities of EOS varied among different vegetation types, as shown in **Supplementary Table S1**. For DF, shrub, grass, and CV types, $EOS_{E\text{-}SA}$, $EOS_{N\text{-}SA}$, and $EOS_{P\text{-}SA}$ had higher temporal stabilities than others, as their CVs were lower than others. For steppe, meadow, and AV types, $EOS_{E\text{-}SA}$ and $EOS_{N\text{-}SA}$ were more stable than others, with lower CVs.

**Table 3** shows temporal stability comparisons of satellite-derived SOS over the flat terrain and the complex terrain. The SOS over complex the terrain showed lower stabilities than those over the flat terrain. Over the flat terrain, the CV values of SOS from E-SA, E-STL, N-SA, N-STL, P-SA, and P-STL were 0.146 ± 0.111, 0.147 ± 0.100, 0.127 ± 0.092, 0.132 ± 0.092, 0.188 ± 0.153, and 0.192 ± 0.139, respectively. Over the complex terrain, the CV values of SOS from E-SA, E-STL, N-SA, N-STL, P-SA, and P-STL were 0.148 ± 0.113, 0.150 ± 0.106, 0.146 ± 0.103, 0.148 ± 0.092, 0.195 ± 0.138, and 0.199 ± 0.156, respectively. Similar to SOS, the CV values of satellite-derived EOS over the complex terrain were much higher than those over the flat terrain, as shown in **Supplementary Table S2**. Over the flat terrain, the CV values of SOS from E-SA, E-STL, N-SA, N-STL, P-SA, and P-STL were 0.036 ± 0.017, 0.067 ± 0.040, 0.035 ± 0.016, 0.040 ± 0.019, 0.042 ± 0.026, and 0.051 ± 0.032, respectively. Over the complex terrain, the CV values of EOS from E-SA, E-STL, N-SA, N-STL, P-SA, and P-STL were 0.038 ± 0.019, 0.072 ± 0.043, 0.039 ± 0.019, 0.048 ± 0.026, 0.050 ± 0.029, and 0.056 ± 0.032, respectively.

The CV differences of phenological metrics over different terrains on time scale revealed the fact that the complexity of topography could affect the temporal stabilities of retrieved phenological results; the temporal stabilities of retrieved phenological metrics over the flat terrain were more stable than those over the complex terrain.

### 3.1.3 Spatial Stability

To analyze the spatial stability of each product, a 3 × 3 sliding window was used to search the phenological metrics in the study area, and the CV value of the central point in the window and the same vegetation type in the sliding window was calculated.

The spatial stabilities of SOS are displayed in **Table 4**. In general, the SOS derived from NDVI had relatively higher spatial stabilities than those from EVI or NDPI for each method, with CVs of 0.040 ± 0.033 and 0.040 ± 0.040, respectively, and the differences of spatial stability were small between SOS based on the SA method and the STL method for each vegetation index. In

**TABLE 4 |** The means and standard deviations of SOS spatial CV for different vegetation types.

| Methods/vegetation type | E-SA | E-STL | N-SA | N-STL | P-SA | P-STL |
|---|---|---|---|---|---|---|
| DF | 0.068 ± 0.067 | 0.058 ± 0.064 | 0.053 ± 0.050 | 0.058 ± 0.067 | 0.067 ± 0.072 | 0.069 ± 0.078 |
| Shrub | 0.050 ± 0.053 | 0.042 ± 0.050 | 0.039 ± 0.037 | 0.039 ± 0.046 | 0.057 ± 0.075 | 0.057 ± 0.077 |
| Steppe | 0.050 ± 0.051 | 0.051 ± 0.052 | 0.033 ± 0.034 | 0.035 ± 0.036 | 0.064 ± 0.075 | 0.061 ± 0.075 |
| Grass | 0.093 ± 0.093 | 0.077 ± 0.081 | 0.065 ± 0.064 | 0.074 ± 0.081 | 0.089 ± 0.086 | 0.093 ± 0.090 |
| Meadow | 0.039 ± 0.040 | 0.037 ± 0.042 | 0.031 ± 0.027 | 0.031 ± 0.033 | 0.051 ± 0.069 | 0.051 ± 0.070 |
| AV | 0.042 ± 0.049 | 0.049 ± 0.056 | 0.032 ± 0.033 | 0.038 ± 0.041 | 0.095 ± 0.180 | 0.098 ± 0.119 |
| CV | 0.041 ± 0.049 | 0.032 ± 0.044 | 0.035 ± 0.038 | 0.033 ± 0.044 | 0.040 ± 0.053 | 0.038 ± 0.055 |
| All | 0.053 ± 0.049 | 0.050 ± 0.048 | 0.040 ± 0.033 | 0.040 ± 0.040 | 0.068 ± 0.077 | 0.067 ± 0.079 |

**TABLE 5 |** The means and standard deviations of SOS spatial CV for different terrains.

| Methods/terrain | E-SA | E-STL | N-SA | N-STL | P-SA | P-STL |
|---|---|---|---|---|---|---|
| Flat | 0.032 ± 0.039 | 0.032 ± 0.042 | 0.024 ± 0.029 | 0.025 ± 0.032 | 0.039 ± 0.053 | 0.037 ± 0.054 |
| Complex | 0.050 ± 0.054 | 0.046 ± 0.053 | 0.037 ± 0.036 | 0.038 ± 0.045 | 0.067 ± 0.088 | 0.067 ± 0.090 |

addition, N-SA and N-STL also performed better in the extraction of SOS for each vegetation type than others, as the CV values of $SOS_{N\text{-}SA}$ and $SOS_{N\text{-}STL}$ for each vegetation type were a little lower than those of others. Among the vegetation types, the spatial stabilities of SOS in meadows, AVs, and CVs were better than other vegetation types, with lower CV values, and the greatest CV values occurred in grass. Following behind grass, the CV values in DFs were relatively larger.

**Supplementary Table S3** presents the spatial stabilities of EOS. Similar to SOS, for all vegetation types, the EOS derived from NDVI had relatively better spatial stabilities than those from EVI or NDPI for each method, with CVs of $0.012 \pm 0.009$ and $0.013 \pm 0.012$, respectively, and the differences of spatial stability were small between SOS based on the SA method and the STL method for each vegetation index. Besides, EOS from N-SA and N-STL were relatively stable than those from others for each vegetation type, as the CV values of $EOS_{N\text{-}SA}$ and $EOS_{N\text{-}STL}$ for each vegetation type were a little lower than those of others. Among the vegetation types, the EOS in meadows and CVs were a little more stable than other vegetation types, with lower CV values, and the CV values in grass and DFs were relatively larger.

**Table 5** presents spatial stability comparisons of satellite-derived SOS over the flat terrain and the complex terrain. The SOS over the complex terrain showed lower stabilities than those over the flat terrain. Over the flat terrain, the CV values of SOS from E-SA, E-STL, N-SA, N-STL, P-SA, and P-STL were $0.032 \pm 0.039$, $0.032 \pm 0.042$, $0.024 \pm 0.029$, $0.025 \pm 0.032$, $0.039 \pm 0.053$, and $0.037 \pm 0.054$, respectively. Over the complex terrain, the CV values of SOS from E-SA, E-STL, N-SA, N-STL, P-SA, and P-STL were $0.050 \pm 0.054$, $0.046 \pm 0.053$, $0.037 \pm 0.036$, $0.038 \pm 0.045$, $0.067 \pm 0.088$, and $0.067 \pm 0.090$, respectively. Similarly, the CV values of satellite-derived EOS over the complex terrain were much higher than those over the flat terrain, as presented in **Supplementary Table S4**. Over the flat terrain, the CV values of $EOS_{E\text{-}SA}$, $EOS_{E\text{-}STL}$, $EOS_{N\text{-}SA}$, $EOS_{N\text{-}STL}$, $EOS_{P\text{-}SA}$, and $EOS_{P\text{-}STL}$ were $0.009 \pm 0.010$, $0.009 \pm 0.010$, $0.007 \pm 0.007$, $0.009 \pm 0.009$, $0.010 \pm 0.013$, and $0.012 \pm 0.013$, respectively. Over the complex terrain, the CV values of $EOS_{E\text{-}SA}$, $EOS_{E\text{-}STL}$, $EOS_{N\text{-}SA}$, $EOS_{N\text{-}STL}$, $EOS_{P\text{-}SA}$, and $EOS_{P\text{-}STL}$ were $0.015 \pm 0.016$, $0.013 \pm 0.011$, $0.011 \pm 0.010$, $0.012 \pm 0.013$, $0.016 \pm 0.020$, and $0.017 \pm 0.021$, respectively.

The CV differences of phenological metrics over the different terrains on spatial scale revealed the fact that the complexity of topography could affect the spatial stabilities of extracted phenological results, and the spatial stabilities of extracted phenological metrics over the complex terrain were less stable than those over the flat terrain.

## 3.2 Accuracy Assessment of Satellite-Derived Phenologies Based on Ground Observations

The difference between ground-observed SOS and satellite-derived SOS from the three satellite-derived VIs based on different extraction algorithms is shown in **Figure 5**. For all vegetation types, the SA-extracted SOS from EVI and NDVI ($SOS_{E\text{-}SA}$ and $SOS_{N\text{-}SA}$) had better agreements with ground observations than others, with MAEs of 18.95 and 19.60 days $year^{-1}$, respectively. The differences were smaller for SOS based on the SA method and larger for that based on the STL method; the MAEs of $SOS_{E\text{-}STL}$, $SOS_{N\text{-}STL}$, and $SOS_{P\text{-}STL}$ were 4 days higher than those of $SOS_{E\text{-}SA}$, $SOS_{N\text{-}SA}$, and $SOS_{P\text{-}SA}$, respectively. For steppes, the SA-extracted SOS from NDVI and EVI ($SOS_{N\text{-}SA}$ and $SOS_{E\text{-}SA}$) matched better with ground-observed SOS than others, with MAEs of 23.05 and 25.01 days $year^{-1}$, respectively. The SA method can extract information of SOS with higher accuracy than the STL method, and the MAEs of $SOS_{E\text{-}STL}$, $SOS_{N\text{-}STL}$, and $SOS_{P\text{-}STL}$ were more than 6 days higher than those of $SOS_{E\text{-}SA}$, $SOS_{N\text{-}SA}$, and $SOS_{P\text{-}SA}$, respectively. Of all the vegetation types, the SOS in meadows were closer to the 1:1 line than in other vegetation types, with the lowest MAEs and RMSEs. The correlations between

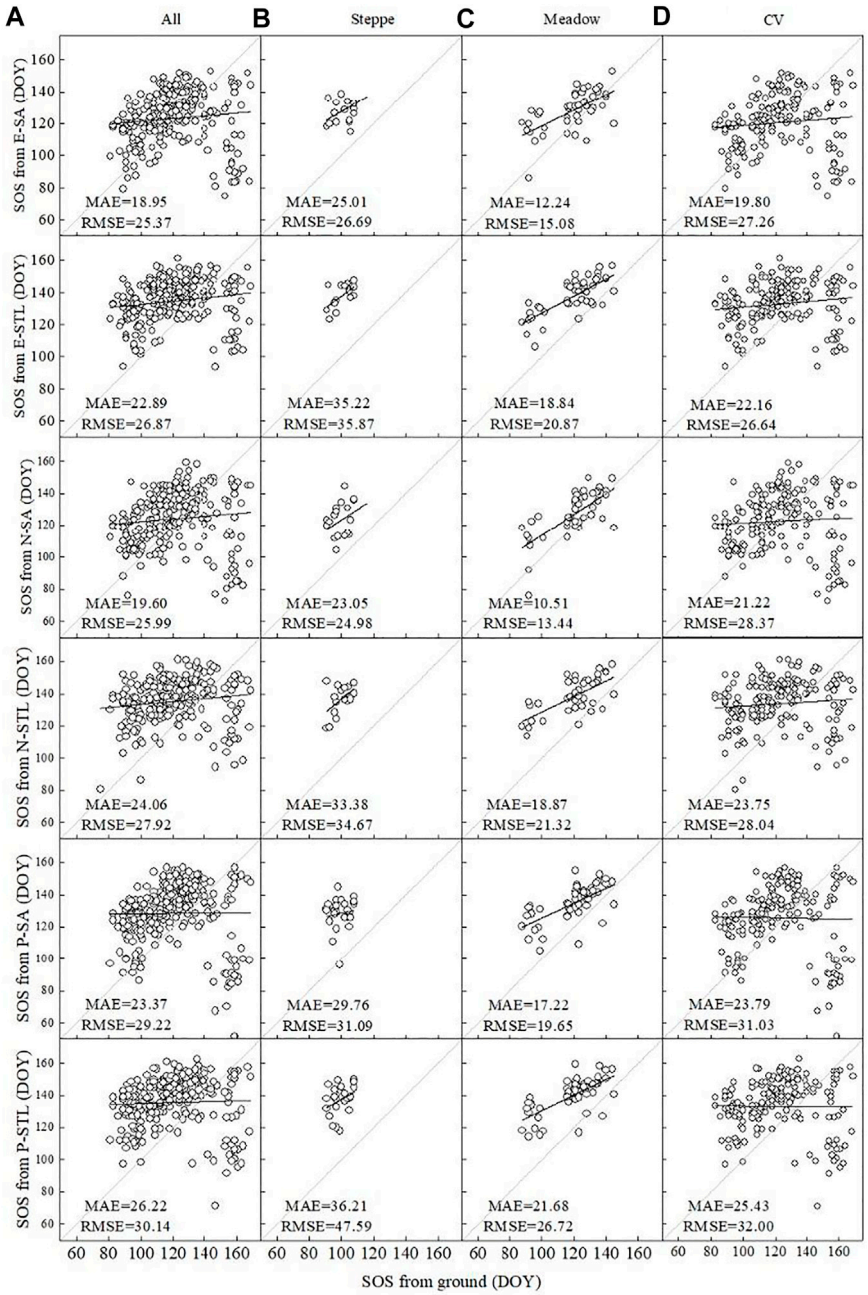


**FIGURE 5 |** Comparison between SOS from E-SA, E-STL, N-SA, N-STL, P-SA, and P-STL for different vegetation types based on the ground observations. **(A)** All, **(B)** steppe, **(C)** meadow, and **(D)** cultivated vegetation (CV). Gray lines are the 1:1 line, and black lines are the best linear regression line.

SA-extracted SOS from NDVI and EVI ($SOS_{N\text{-}SA}$ and $SOS_{E\text{-}SA}$) and ground observations were stronger than others, with MAEs of 10.51 and 12.24 days $year^{-1}$, respectively. Differences still existed between SOS based on the SA method and the STL method and were similar to those in steppes. At CV sites, SOS based on the SA method matched relatively better with ground-observed SOS than those based on the STL method, but the differences of extraction accuracies between SA and STL were relatively smaller compared with those in other vegetation types.

**Supplementary Figure S4** shows comparisons between EOS from E-SA, E-STL, N-SA, N-STL, P-SA, and P-STL for different vegetation types based on the ground observations. In general, the SA method performed much better than the STL method, either for all vegetation types together or only one of them, as the MAEs of EOS based on STL were about twice and even much more than MAEs of EOS based on SA. Besides, the accuracies of EOS from EVI, NDVI, and NDPI were different for different vegetation types. For all vegetation types, the SA-extracted SOS from NDPI

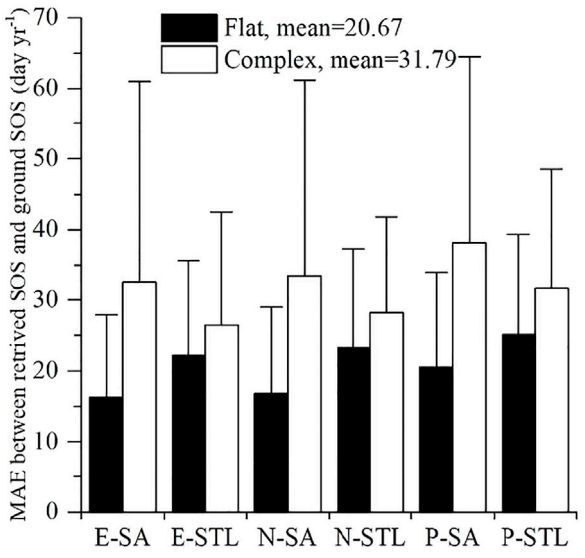


**FIGURE 6 |** Comparison of mean absolute error (MAE) values of SOS over the flat terrain and the complex terrain.

and EVI had better agreements with ground-observed EOS than that from NDVI, and the MAEs of $EOS_{P\text{-}SA}$ and $EOS_{E\text{-}SA}$ were 22.84 and 25.60 days year$^{-1}$, respectively, while it was 33.72 days year$^{-1}$ for $EOS_{N\text{-}SA}$. Of all the vegetation types, the accuracy of EOS in steppes was the highest compared to other vegetation types, with the lowest MAEs and RMSEs, and the accuracies of $EOS_{P\text{-}SA}$, $EOS_{N\text{-}SA}$, and $EOS_{E\text{-}SA}$ had little difference in steppes than in others, with MAEs of 8.46, 10.84, and 13.07 days year$^{-1}$, respectively. For meadows, EOS from P-SA matched best with ground observations (with MAE of 18.41 days year$^{-1}$), followed by EOS from E-SA (with MAE of 24.24 days year$^{-1}$), and the accuracy of $EOS_{N\text{-}SA}$ was the lowest among EOS based on the SA method (with MAE of 27.20 days year$^{-1}$). At CV sites, the correlations between $EOS_{P\text{-}SA}$, $EOS_{E\text{-}SA}$, and ground-observed EOS were stronger than $EOS_{N\text{-}SA}$, with MAEs of 27.16, 27.99, and 36.38 days year$^{-1}$, respectively.

**Figure 6** presents accuracy comparisons of satellite-derived SOS over the flat terrain and complex terrain. The complex terrain showed lower accuracy of satellite-derived SOS (MAE = 31.79 days year$^{-1}$) than the flat terrain (MAE = 20.67 days year$^{-1}$). Over the flat terrain, the MAE values between SOS from E-SA, E-STL, N-SA, N-STL, P-SA, and P-STL and ground-observed SOS were 16.23 ± 11.65 days year$^{-1}$, 22.17 ± 13.52 days year$^{-1}$, 16.8 ± 12.19 days year$^{-1}$, 23.21 ± 14.13 days year$^{-1}$, 20.5 ± 13.49 days year$^{-1}$, and 25.13 ± 14.22 days year$^{-1}$, respectively. Over the complex terrain, the MAE values between SOS from E-SA, E-STL, N-SA, N-STL, P-SA, and P-STL and ground-observed SOS were 32.63 ± 28.42 days year$^{-1}$, 26.48 ± 16.07 days year$^{-1}$, 33.48 ± 27.65 days year$^{-1}$, 28.21 ± 13.61 days year$^{-1}$, 38.14 ± 26.32 days year$^{-1}$, and 31.80 ± 16.72 days year$^{-1}$, respectively. Similarly, the MAE values between satellite-derived EOS and ground EOS over the complex terrain (mean = 49.97 days year$^{-1}$) were much higher than those over the flat terrain (mean = 39.08 days year$^{-1}$), as presented in **Supplementary Figure S5**. Over the flat terrain, the MAE values between EOS from E-SA, E-STL, N-SA, N-STL, P-SA, and P-STL and ground-observed EOS were 24.68 ± 21.09 days year$^{-1}$, 52.38 ± 22.94 days year$^{-1}$, 28.44 ± 22.87 days year$^{-1}$, 59.65 ± 24.32 days year$^{-1}$, 20.11 ± 20.02 days year$^{-1}$, and 49.22 ± 24.85 days year$^{-1}$, respectively. Over the complex terrain, the MAE values between EOS from E-SA, E-STL, N-SA, N-STL, P-SA, and P-STL and ground-observed EOS were 28.79 ± 16.01 days year$^{-1}$, 60.91 ± 19.57 days year$^{-1}$, 42.94 ± 15.97 days year$^{-1}$, 72.30 ± 21.13 days year$^{-1}$, 32.24 ± 14.29 days year$^{-1}$, and 62.61 ± 20.27 days year$^{-1}$, respectively.

The larger MAE values between phenological metrics and ground observations over the complex terrain revealed the fact that the extraction of phenological metrics over the complex terrain had larger disagreements with ground observations than those over the flat terrain, and it can be concluded that the complex terrain had a larger influence on extraction accuracy than the flat terrain.

# 4 DISCUSSION

## 4.1 Comparison of Different Methods Using Different VI Datasets in Phenological Metric Extractions

The time series of satellite-derived VI datasets have made it possible to study the vegetation phenology and its interactions with surrounding environment conditions for a long time at large scale (An et al., 2018; Wang and Wu, 2019). The time series VI datasets, together with phenological retrieval algorithms, could affect the vegetation phenological metrics, but few evaluations are performed. In this study, we employed two methods using three VI datasets to retrieve the vegetation phenological metrics in the TP, and the effectiveness of each result was evaluated.

It is shown that the missing rates of phenological metrics (**Figure 3**; **Supplementary Figure S2**) based on SA for each VI were lower than those based on STL; as the vegetation index value was relatively lower in the TP, the seasonal trend line may not cross with part of the vegetation index time series curve and then lead to missing of phenological metrics. Besides, phenological metrics derived from NDVI had lower missing rates than other VIs. However, the missing rates of EOS were higher than those of SOS, which were mainly because the DOY of EOS were more likely to be larger than 365 in the process of retrieval and thus treated as an invalid value.

In general, the phenological metrics based on SA for each VI were a little more stable than those based on STL in the aspect of temporal stability, and the phenological metrics derived from NDVI had higher temporal stabilities than those from EVI or NDPI (**Table 2**; **Supplementary Table S1**). However, for the DFs, shrubs, grass, and CVs, SOS derived from EVI were superior to those from others. In addition, EOS based on STL were much more unstable than those based on SA, and SOS derived from NDVI or EVI had higher temporal stabilities than those from

NDPI. The higher CV values of SOS for each vegetation type than those of EOS meant that the SOS varied greater than EOS during the study period and was more sensitive to environmental factors, which was almost consistent with the study of Wang et al. (2019).

As for the spatial stability (**Table 4**; **Supplementary Table S3**), phenological metrics derived from NDVI had relatively better spatial stabilities than those from EVI or NDPI for each method, and the differences of spatial stability were relatively small between phenological metrics based on the SA method and the STL method for each vegetation index. The higher spatial CV values of SOS than EOS indicated that the differences of SOS in different regions for each vegetation type were larger than those of EOS.

The accuracy assessment based on ground observations (**Figure 5**; **Supplementary Figure S4**) in this paper shows that phenological metrics based on SA had better agreements with ground observations than those based on STL for each VI, as MAEs between phenological metrics based on SA and ground observations were much lower than those between phenological metrics based on STL and ground observations, implying that the SA method was more suitable to monitor phenology on the TP. The same conclusion was also found in previous studies (Yu et al., 2010; Zheng and Zhu, 2017). Moreover, smaller MAEs and RMSEs were found between $SOS_{E\text{-}SA}$, as well as $SOS_{N\text{-}SA}$, and ground-observed SOS, indicating that NDVI or EVI might be more consistent than NDPI with the ground-observed SOS. EVI or NDVI may be more appropriate for monitoring SOS than NDPI in the TP. However, regarding EOS, smaller MAEs and RMSEs between $EOS_{P\text{-}SA}$ and ground-observed EOS were found for all the vegetation types. However, more ground-observed phenological records are needed to confirm it due to only fewer available sites mainly in the east of the TP in our study. When compared with SOS, EOS is much difficult to be monitored (Liu et al., 2016; Jeong et al., 2017; Wu et al., 2017; Zheng and Zhu, 2017) as the MAEs were larger between derived EOS and ground-observed EOS than those between derived SOS and ground-observed SOS. However, it was opposite for the steppes, which was probably due to the relatively lower vegetation coverage in these areas, and it was difficult to capture the greenness change of vegetation as it was likely to be affected by the background of soil.

## 4.2 The Topographic Effect on Phenological Estimations

As the complex terrain usually present high spatial heterogeneity, the satellite-derived phenology results in complex areas displayed more uncertainties than those in flat areas. In this study, we have checked the topographic influence on retrieved phenological metrics. The results showed that phenological metrics over the complex terrain had higher missing rates than those over the flat terrain (**Figures 2** and **4**; **Supplementary Figures S1 and S3**). In addition, the phenological results over the complex terrain were more unstable at the temporal and spatial scale than those over the flat terrain (**Tables 3** and **5**; **Supplementary Tables S2 and S4**). Besides, the phenological metrics over the complex terrain also had larger disagreements with ground observations than those over the flat terrain (**Figure 6**; **Supplementary Figure S5**). The high spatial variations in geographic configurations caused by obvious topographic conditions may cause sustainable and complex uncertainties in the surface reflectance data, then may affect the quality of input VI data for phenological extractions, and then lead to higher uncertainties of phenological metrics compared with the flat terrain (Jin et al., 2017; Xie and Li, 2020b). As terrain gradients usually result in frequent changes of local climate, the surface reflectance data over the complex terrain is more susceptible to external environmental conditions. The surface reflectance data over the complex terrain is more likely to be contaminated by clouds, aerosols, snow, etc. (Xie et al., 2019). The increasing angular variations between the sun and satellite over the complex terrain may lead to more complicated solar irradiances than those over the flat terrain (Yan et al., 2018; Xie et al., 2021a).

Nevertheless, the topographical effects tend to be ignored (Jin et al., 2017) by most of the current retrieval methods for phenological extractions and then lead to more uncertainties into the phenological metrics. In this work, the lower missing rates, better stabilities on the temporal and spatial scale, and higher accuracies in phenological metrics were found over the flat terrain than the complex terrain; thus, the retrieval work of phenological metrics over the complex terrain is more challenging than that over the flat terrain (Xie et al., 2018).

## 4.3 Deficiencies in Ground Observations

Accuracy assessment using ground observations is always an important concern in any remote sensing-based monitoring and analysis, especially at a large scale (Wang et al., 2017c; Shen et al., 2021). However, the limitations of ground-observed validation data in the TP and the inconsistency and scale effect between remote sensing results and observations at ground sites make it difficult to validate large-scale remote sensing monitoring results by using ground-observed data (Wang et al., 2017b). Due to the limitations of ground-observed validation data in the TP, the accuracy assessment of this study only considers the vegetation types of steppe, CV, and meadow mainly in the east. In the future research, it is necessary to continue to expand the area and consider more vegetation types to conduct a more comprehensive precision evaluation of phenological products. It is worth noting that retrieved phenological metrics were derived from 500-m, 16-day composite NDVI/EVI or 8-day composite NDPI data, while ground observations are daily point-based observations. The remote sensing phenological metrics are based upon greenness of a pixel, while ground observations rely on the morphological changes of individual plants; thus, inconsistencies exist between them as different species at the same stage could exhibit different greenness because of differences in the characteristic area of individual leaves (Shen et al., 2015; Wang et al., 2017c). Although the studied sites are the best representation for each station and the surrounding area, a great number of species that exhibit diverse phenological stages coexist within a pixel, and the scale effect of incomplete match between ground site and remote sensing pixel at the temporal and spatial scales is unavoidable (Wang et al., 2017c). All these might lead to disagreements between retrieved phenological metrics and ground observations.

## 5 CONCLUSION

In this study, vegetation phenological metrics in the TP were derived based on different extraction algorithms using three satellite-derived vegetation indices, and comparative analyses of the results were conducted in different aspects. We found that the SA method performed better than STL in the extraction of phenological metrics, as phenological metrics based on SA had lower missing rate, better stability on the temporal and spatial scales, and better agreements with ground observations. Meanwhile, the EVI, NDVI, and NDPI had advantages in different aspects. Different retrieving approaches may produce significantly different estimates of SOS and EOS, with VI differences also accounting for differences. Besides, the results also showed that the complex terrain had larger influence on extraction accuracy than the flat terrain, and extraction of phenological metrics over the complex terrain was more challenging than that over the flat terrain. Furthermore, given present approaches and datasets, substantial room for improvement exists for using remote sensing applications to predict ecosystem phenology at broad spatial scales. It should be considered that uniting multisource data is an effective way to improve the accuracy and validity of remote sensing phenological products. Different combinations of datasets and retrieval methods may need to be applied for different plant functional types, and in particular, identifying the specific best settings to each ecosystem type will be a future research challenge. These findings are of great value for improving the spatial resolution of remote sensing phenological products to promote their application and development in the future.

## DATA AVAILABILITY STATEMENT

The original contributions presented in the study are included in the article/**Supplementary Material**; further inquiries can be directed to the corresponding author.

## AUTHOR CONTRIBUTIONS

All authors listed have made a substantial, direct, and intellectual contribution to the work and approved it for publication.

## FUNDING

This work was sponsored by the National Natural Science Foundation of China (Grant No. 31870708 and 51879155).

## SUPPLEMENTARY MATERIAL

The Supplementary Material for this article can be found online at: https://www.frontiersin.org/articles/10.3389/fenvs.2021.794189/full#supplementary-material

## REFERENCES

Aguilera, F., Orlandi, F., Ruiz-Valenzuela, L., Msallem, M., and Fornaciari, M. (2015). Analysis and Interpretation of Long Temporal Trends in Cumulative Temperatures and Olive Reproductive Features Using a Seasonal Trend Decomposition Procedure. *Agric. For. Meteorol.* 203, 208–216. doi:10.1016/j.agrformet.2014.11.019

An, S., Zhu, X., Shen, M., Wang, Y., Cao, R., Chen, X., et al. (2018). Mismatch in Elevational Shifts between Satellite Observed Vegetation Greenness and Temperature Isolines during 2000-2016 on the Tibetan Plateau. *Glob. Change Biol.* 24, 5411–5425. doi:10.1111/gcb.14432

Araya, S., Lyle, G., Lewis, M., and Ostendorf, B. (2016). Phenologic Metrics Derived from MODIS NDVI as Indicators for Plant Available Water-Holding Capacity. *Ecol. Indic.* 60, 1263–1272. doi:10.1016/j.ecolind.2015.09.012

B Cleveland, R., Cleveland, S. W., E McRae, J., and Terpenning, I. (1990). STL: A Seasonal-Trend Decomposition Procedure Based on Loess. *J. Official Stat.* 6, 3–33.

Borges, E. F., Sano, E. E., and Medrado, E. (2014). Radiometric Quality and Performance of TIMESAT for Smoothing Moderate Resolution Imaging Spectroradiometer Enhanced Vegetation index Time Series from Western Bahia State, Brazil. *J. Appl. Remote Sens.* 8, 083580. doi:10.1117/1.jrs.8.083580

Cao, R., Chen, J., Shen, M., and Tang, Y. (2015). An Improved Logistic Method for Detecting spring Vegetation Phenology in Grasslands from MODIS EVI Time-Series Data. *Agric. For. Meteorol.* 200, 9–20. doi:10.1016/j.agrformet.2014.09.009

Chang, Q., Zhang, J., Jiao, W., Yao, F., and Wang, S. (2016). Spatiotemporal Dynamics of the Climatic Impacts on greenup Date in the Tibetan Plateau. *Environ. Earth Sci.* 75, 1343. doi:10.1007/s12665-016-6148-6

Chu, D., Shen, H., Guan, X., Chen, J. M., Li, X., Li, J., et al. (2021). Long Time-Series NDVI Reconstruction in Cloud-Prone Regions via Spatio-Temporal Tensor Completion. *Remote Sens. Environ.* 264, 112632. doi:10.1016/j.rse.2021.112632

Cong, N., Shen, M., Piao, S., Chen, X., An, S., Yang, W., et al. (2017). Little Change in Heat Requirement for Vegetation green-up on the Tibetan Plateau over the Warming Period of 1998-2012. *Agric. For. Meteorol.* 232, 650–658. doi:10.1016/j.agrformet.2016.10.021

Cristina, S., Cordeiro, C., Lavender, S., Costa Goela, P., Icely, J., and Newton, A. (2016). MERIS Phytoplankton Time Series Products from the SW Iberian Peninsula (Sagres) Using Seasonal-Trend Decomposition Based on Loess. *Remote Sens.* 8, 449. doi:10.3390/rs8060449

Ding, M., Chen, Q., Li, L., Zhang, Y., Wang, Z., Liu, L., et al. (2016). Temperature Dependence of Variations in the End of the Growing Season from 1982 to 2012 on the Qinghai-Tibetan Plateau. *GIScience Remote Sens.* 53, 147–163. doi:10.1080/15481603.2015.1120371

Duveiller, G., Weiss, M., Baret, F., and Defourny, P. (2011). Retrieving Wheat Green Area Index during the Growing Season from Optical Time Series Measurements Based on Neural Network Radiative Transfer Inversion. *Remote Sens. Environ.* 115, 887–896. doi:10.1016/j.rse.2010.11.016

Eklundh, L., and Jönsson, P. (2016). "TIMESAT for Processing Time-Series Data from Satellite Sensors for Land Surface Monitoring," in *Multitemporal Remote Sensing: Methods and Applications*. Editor Y. Ban (Cham: Springer International Publishing), 177–194. doi:10.1007/978-3-319-47037-5_9

Eklundh, L., and Jönsson, P. (2017). *TIMESAT 3.3 with Seasonal Trend Decomposition and Parallel Processing Software Manual*. Sweden: Lund University.

Gamon, J. A., Huemmrich, K. F., Stone, R. S., and Tweedie, C. E. (2013). Spatial and Temporal Variation in Primary Productivity (NDVI) of Coastal Alaskan Tundra: Decreased Vegetation Growth Following Earlier Snowmelt. *Remote Sens. Environ.* 129, 144–153. doi:10.1016/j.rse.2012.10.030

Guan, X., Chen, J. M., Shen, H., and Xie, X. (2021). A Modified Two-Leaf Light Use Efficiency Model for Improving the Simulation of GPP Using a Radiation Scalar. *Agric. For. Meteorol.* 307, 108546. doi:10.1016/j.agrformet.2021.108546

Han, G., and Xu, J. (2013). Land Surface Phenology and Land Surface Temperature Changes along an Urban-Rural Gradient in Yangtze River Delta, China. *Environ. Manage.* 52, 234–249. doi:10.1007/s00267-013-0097-6

Jamali, S., Jönsson, P., Eklundh, L., Ardö, J., and Seaquist, J. (2015). Detecting Changes in Vegetation Trends Using Time Series Segmentation. *Remote Sens. Environ.* 156, 182–195. doi:10.1016/j.rse.2014.09.010

Jeong, S.-J., Schimel, D., Frankenberg, C., Drewry, D. T., Fisher, J. B., Verma, M., et al. (2017). Application of Satellite Solar-Induced Chlorophyll Fluorescence to Understanding Large-Scale Variations in Vegetation Phenology and Function over Northern High Latitude Forests. *Remote Sens. Environ.* 190, 178–187. doi:10.1016/j.rse.2016.11.021

Jin, Z., Zhuang, Q., He, J.-S., Luo, T., and Shi, Y. (2013). Phenology Shift from 1989 to 2008 on the Tibetan Plateau: an Analysis with a Process-Based Soil Physical Model and Remote Sensing Data. *Climatic Change* 119, 435–449. doi:10.1007/s10584-013-0722-7

Jin, H., Li, A., Bian, J., Nan, X., Zhao, W., Zhang, Z., et al. (2017). Intercomparison and Validation of MODIS and GLASS Leaf Area index (LAI) Products over Mountain Areas: A Case Study in Southwestern China. *Int. J. Appl. Earth Observ. Geoinf.* 55, 52–67. doi:10.1016/j.jag.2016.10.008

Jönsson, P., and Eklundh, L. (2004). TIMESAT-a Program for Analyzing Time-Series of Satellite Sensor Data. *Comput. Geosci.* 30, 833–845. doi:10.1016/j.cageo.2004.05.006

Kapos, V. (2000). UNEP-WCMC Web Site: Mountains and Mountain Forests. *Mountain Res. Dev.* 20, 378. doi:10.1659/0276-4741(2000)020[0378:uwwsma]2.0.co;2

Lafare, A. E. A., Peach, D. W., and Hughes, A. G. (2015). Use of Seasonal Trend Decomposition to Understand Groundwater Behaviour in the Permo-Triassic Sandstone Aquifer, Eden Valley, UK. *Hydrogeol J.* 24, 141–158. doi:10.1007/s10040-015-1309-3

Liang, L., Schwartz, M. D., and Fei, S. (2011). Validating Satellite Phenology through Intensive Ground Observation and Landscape Scaling in a Mixed Seasonal forest. *Remote Sens. Environ.* 115, 143–157. doi:10.1016/j.rse.2010.08.013

Liu, Y., Wu, C., Peng, D., Xu, S., Gonsamo, A., Jassal, R. S., et al. (2016). Improved Modeling of Land Surface Phenology Using MODIS Land Surface Reflectance and Temperature at evergreen Needleleaf Forests of central North America. *Remote Sens. Environ.* 176, 152–162. doi:10.1016/j.rse.2016.01.021

Liu, Z., Wu, C., Liu, Y., Wang, X., Fang, B., Yuan, W., et al. (2017). Spring green-up Date Derived from GIMMS3g and SPOT-VGT NDVI of winter Wheat Cropland in the North China Plain. *ISPRS J. Photogramm. Remote Sens.* 130, 81–91. doi:10.1016/j.isprsjprs.2017.05.015

Massey, R., Sankey, T. T., Congalton, R. G., Yadav, K., Thenkabail, P. S., Ozdogan, M., et al. (2017). MODIS Phenology-Derived, Multi-Year Distribution of Conterminous U.S. Crop Types. *Remote Sens. Environ.* 198, 490–503. doi:10.1016/j.rse.2017.06.033

Piao, S., Cui, M., Chen, A., Wang, X., Ciais, P., Liu, J., et al. (2011). Altitude and Temperature Dependence of Change in the spring Vegetation green-up Date from 1982 to 2006 in the Qinghai-Xizang Plateau. *Agric. For. Meteorol.* 151, 1599–1608. doi:10.1016/j.agrformet.2011.06.016

Rojo, J., Rivero, R., Romero-Morte, J., Fernández-González, F., and Pérez-Badia, R. (2017). Modeling Pollen Time Series Using Seasonal-Trend Decomposition Procedure Based on LOESS Smoothing. *Int. J. Biometeorol.* 61, 335–348. doi:10.1007/s00484-016-1215-y

Sanchez-Vazquez, M. J., Nielen, M., Gunn, G. J., and Lewis, F. I. (2012). Using Seasonal-Trend Decomposition Based on Loess (STL) to Explore Temporal Patterns of Pneumonic Lesions in Finishing Pigs Slaughtered in England, 2005-2011. *Prev. Vet. Med.* 104, 65–73. doi:10.1016/j.prevetmed.2011.11.003

Shang, R., Liu, R., Xu, M., Liu, Y., Dash, J., and Ge, Q. (2018). Determining the Start of the Growing Season from MODIS Data in the Indian Monsoon Region: Identifying Available Data in the Rainy Season and Modeling the Varied Vegetation Growth Trajectories. *Remote Sensing* 10, 122. doi:10.3390/rs10010122

Shen, M., Sun, Z., Wang, S., Zhang, G., Kong, W., Chen, A., et al. (2013). No Evidence of Continuously Advanced green-up Dates in the Tibetan Plateau over the Last Decade. *Proc. Natl. Acad. Sci.* 110, E2329. doi:10.1073/pnas.1304625110

Shen, M., Tang, Y., Chen, J., Yang, X., Wang, C., Cui, X., et al. (2014a). Earlier-season Vegetation Has Greater Temperature Sensitivity of spring Phenology in Northern Hemisphere. *PLoS One* 9, e88178. doi:10.1371/journal.pone.0088178

Shen, M., Zhang, G., Cong, N., Wang, S., Kong, W., and Piao, S. (2014b). Increasing Altitudinal Gradient of spring Vegetation Phenology during the Last Decade on the Qinghai-Tibetan Plateau. *Agric. For. Meteorol.* 189-190, 71–80. doi:10.1016/j.agrformet.2014.01.003

Shen, M., Piao, S., Dorji, T., Liu, Q., Cong, N., Chen, X., et al. (2015). Plant Phenological Responses to Climate Change on the Tibetan Plateau: Research Status and Challenges. *Natl. Sci. Rev.* 2, 454–467. doi:10.1093/nsr/nwv058

Shen, L., Wang, H., Kong, X., Zhang, C., Shi, S., and Zhu, B. (2021). Characterization of Black Carbon Aerosol in the Yangtze River Delta, China: Seasonal Variation and Source Apportionment. *Atmos. Pollut. Res.* 12, 195–209. doi:10.1016/j.apr.2020.08.035

Tang, K., Zhu, W., Zhan, P., and Ding, S. (2018). An Identification Method for Spring Maize in Northeast China Based on Spectral and Phenological Features. *Remote Sens.* 10, 193. doi:10.3390/rs10020193

Tobler, W. R. (1970). A Computer Movie Simulating Urban Growth in the Detroit Region. *Econ. Geogr.* 46, 234–240. doi:10.2307/143141

Verbesselt, J., Hyndman, R., Newnham, G., and Culvenor, D. (2010). Detecting Trend and Seasonal Changes in Satellite Image Time Series. *Remote Sensing Environ.* 114, 106–115. doi:10.1016/j.rse.2009.08.014

Wang, X., and Wu, C. (2019). Estimating the Peak of Growing Season (POS) of China's Terrestrial Ecosystems. *Agric. For. Meteorol.* 278, 107639. doi:10.1016/j.agrformet.2019.107639

Wang, D., Morton, D., Masek, J., Wu, A., Nagol, J., Xiong, X., et al. (2012). Impact of Sensor Degradation on the MODIS NDVI Time Series. *Remote Sens. Environ.* 119, 55–61. doi:10.1016/j.rse.2011.12.001

Wang, C., Guo, H., Zhang, L., Liu, S., Qiu, Y., and Sun, Z. (2015a). Assessing Phenological Change and Climatic Control of alpine Grasslands in the Tibetan Plateau with MODIS Time Series. *Int. J. Biometeorol.* 59, 11–23. doi:10.1007/s00484-014-0817-5

Wang, C., Guo, H., Zhang, L., Qiu, Y., Sun, Z., Liao, J., et al. (2015b). Improved alpine Grassland Mapping in the Tibetan Plateau with MODIS Time Series: a Phenology Perspective. *Int. J. Digital Earth* 8, 133–152. doi:10.1080/17538947.2013.860198

Wang, C., Chen, J., Wu, J., Tang, Y., Shi, P., Black, T. A., et al. (2017a). A Snow-free Vegetation index for Improved Monitoring of Vegetation spring green-up Date in Deciduous Ecosystems. *Remote Sens. Environ.* 196, 1–12. doi:10.1016/j.rse.2017.04.031

Wang, C., Li, J., Liu, Q., Bai, J., Xu, B., Zhao, J., et al. (2017b). Validation and Analysis of Remote Sensing Phenology Products in the Heihe River Basin. *J. Remote Sens.* 21, 442–457. doi:10.11834/jrs.20176184

Wang, C., Li, J., Liu, Q., Zhong, B., Wu, S., and Xia, C. (2017c). Analysis of Differences in Phenology Extracted from the Enhanced Vegetation Index and the Leaf Area Index. *Sensors (Basel)* 17, 1982. doi:10.3390/s17091982

Wang, X., Wu, C., Peng, D., Gonsamo, A., and Liu, Z. (2018). Snow Cover Phenology Affects alpine Vegetation Growth Dynamics on the Tibetan Plateau: Satellite Observed Evidence, Impacts of Different Biomes, and Climate Drivers. *Agric. For. Meteorol.* 256-257, 61–74. doi:10.1016/j.agrformet.2018.03.004

Wang, X., Xiao, J., Li, X., Cheng, G., Ma, M., Zhu, G., et al. (2019). No Trends in spring and Autumn Phenology during the Global Warming Hiatus. *Nat. Commun.* 10, 2389. doi:10.1038/s41467-019-10235-8

Wang, H., Miao, Q., Shen, L., Yang, Q., Wu, Y., and Wei, H. (2020). Air Pollutant Variations in Suzhou during the 2019 Novel Coronavirus (COVID-19) Lockdown of 2020: High Time-Resolution Measurements of Aerosol Chemical Compositions and Source Apportionment. *Environ. Pollut.* 271, 116298. doi:10.1016/j.envpol.2020.116298

Wang, X., Li, Y., Wang, X., Li, Y., Lian, J., and Gong, X. (2021). Temporal and Spatial Variations in NDVI and Analysis of the Driving Factors in the Desertified Areas of Northern China from 1998 to 2015. *Front. Environ. Sci.* 9, 633020. doi:10.3389/fenvs.2021.633020

Wu, C., Peng, D., Soudani, K., Siebicke, L., Gough, C. M., Arain, M. A., et al. (2017). Land Surface Phenology Derived from Normalized Difference Vegetation index (NDVI) at Global FLUXNET Sites. *Agric. For. Meteorol.* 233, 171–182. doi:10.1016/j.agrformet.2016.11.193

Wu, C., Wang, X., Wang, H., Ciais, P., Peñuelas, J., Myneni, R. B., et al. (2018). Contrasting Responses of Autumn-Leaf Senescence to Daytime and Night-Time Warming. *Nat. Clim Change* 8, 1092–1096. doi:10.1038/s41558-018-0346-z

Xie, X., and Li, A. (2020a). An Adjusted Two-Leaf Light Use Efficiency Model for Improving GPP Simulations over Mountainous Areas. *J. Geophys. Res. Atmos.* 125, e2019JD031702. doi:10.1029/2019jd031702

Xie, X., and Li, A. (2020b). Development of a Topographic-Corrected Temperature and Greenness Model (TG) for Improving GPP Estimation over Mountainous Areas. *Agric. For. Meteorol.* 295, 108193. doi:10.1016/j.agrformet.2020.108193

Xie, X., Li, A., Jin, H., Yin, G., and Bian, J. (2018). Spatial Downscaling of Gross Primary Productivity Using Topographic and Vegetation Heterogeneity Information: A Case Study in the Gongga Mountain Region of China. *Remote Sens.* 10, 647. doi:10.3390/rs10040647

Xie, X., Li, A., Jin, H., Tan, J., Wang, C., Lei, G., et al. (2019). Assessment of Five Satellite-Derived LAI Datasets for GPP Estimations through Ecosystem Models. *Sci. Total Environ.* 690, 1120–1130. doi:10.1016/j.scitotenv.2019.06.516

Xie, X., Chen, J., Gong, P., and Li, A. (2021a). Spatial Scaling of Gross Primary Productivity over Sixteen Mountainous Watersheds Using Vegetation Heterogeneity and Surface Topography. *J. Geophys. Res. Biogeosci.* 126, e2020JG005848. doi:10.1029/2020jg005848

Xie, X., Li, A., Guan, X., Tan, J., Jin, H., and Bian, J. (2021b). A Practical Topographic Correction Method for Improving Moderate Resolution Imaging Spectroradiometer Gross Primary Productivity Estimation over Mountainous Areas. *Int. J. Appl. Earth Observ. Geoinf.* 103, 102522. doi:10.1016/j.jag.2021.102522

Yan, G., Tong, Y., Yan, K., Mu, X., Chu, Q., Zhou, Y., et al. (2018). Temporal Extrapolation of Daily Downward Shortwave Radiation over Cloud-free Rugged Terrains. Part 1: Analysis of Topographic Effects. *IEEE Trans. Geosci. Remote Sens.* 56, 6375–6394. doi:10.1109/tgrs.2018.2838143

Yang, X., Zhang, Y., Zhang, W., Yan, Y., Wang, Z., Ding, M., et al. (2006). Climate Change in Mt. Qomolangma Region since 1971. *J. Geogr. Sci.* 16, 326–336. doi:10.1007/s11442-006-0308-7

Yu, H., Luedeling, E., and Xu, J. (2010). Winter and spring Warming Result in Delayed spring Phenology on the Tibetan Plateau. *Proc. Natl. Acad. Sci.* 107, 22151–22156. doi:10.1073/pnas.1012490107

Yu, S., Xia, J., Yan, Z., and Yang, K. (2018). Changing spring Phenology Dates in the Three-Rivers Headwater Region of the Tibetan Plateau during 1960-2013. *Adv. Atmos. Sci.* 35, 116–126. doi:10.1007/s00376-017-6296-y

Zeng, L., Wardlow, B. D., Wang, R., Shan, J., Tadesse, T., Hayes, M. J., et al. (2016). A Hybrid Approach for Detecting Corn and Soybean Phenology with Time-Series MODIS Data. *Remote Sens. Environ.* 181, 237–250. doi:10.1016/j.rse.2016.03.039

Zhang, X., Friedl, M. A., Schaaf, C. B., and Strahler, A. H. (2004). Climate Controls on Vegetation Phenological Patterns in Northern Mid- and High Latitudes Inferred from MODIS Data. *Glob. Change Biol.* 10, 1133–1145. doi:10.1111/j.1529-8817.2003.00784.x

Zhang, G., Dong, J., Zhang, Y., and Xiao, X. (2013a). Reply to Shen et al.: No evidence to show nongrowing season NDVI affects spring phenology trend in the Tibetan Plateau over the last decade. *Proc. Natl. Acad. Sci.* 110, E2330–E2331. doi:10.1073/pnas.1305593110

Zhang, W., Ai-Nong, L. I., and Jiang, X. B. (2013b). Study on Computing the Area of Mountain Regions in China Based on DEM. *Geogr. Geo-Inf. Sci.* 29(05), 58–63. doi:10.7702/dlydlxxkx20130513

Zheng, Z., and Zhu, W. (2017). Uncertainty of Remote Sensing Data in Monitoring Vegetation Phenology: A Comparison of MODIS C5 and C6 Vegetation Index Products on the Tibetan Plateau. *Remote Sens.* 9, 1288. doi:10.3390/rs9121288

Zhu, M., Zhang, J., and Zhu, L. (2021). Article Title Variations in Growing Season NDVI and its Sensitivity to Climate Change Responses to Green Development in Mountainous Areas. *Front. Environ. Sci.* 9, 678450. doi:10.3389/fenvs.2021.678450

**Conflict of Interest:** The authors declare that the research was conducted in the absence of any commercial or financial relationships that could be construed as a potential conflict of interest.

**Publisher's Note:** All claims expressed in this article are solely those of the authors and do not necessarily represent those of their affiliated organizations, or those of the publisher, the editors, and the reviewers. Any product that may be evaluated in this article, or claim that may be made by its manufacturer, is not guaranteed or endorsed by the publisher.

frontiers in Environmental Science

ORIGINAL RESEARCH
published: 14 December 2021
doi: 10.3389/fenvs.2021.788115

# Size Distributions of Water-Soluble Inorganic Ions in Atmospheric Aerosols During the Meiyu Period in the Yangtze River Delta, China

*Zhaoye Wu*[1,2], *Duanyang Liu*[2,3,4]*, *Tianliang Zhao*[1], *Yan Su*[5] *and Bin Zhou*[5]

[1]Key Laboratory for Aerosol-Cloud-Precipitation of China Meteorological Administration, Nanjing University of Information Science and Technology, Nanjing, China, [2]Key Laboratory of Transportation Meteorology, CMA, Nanjing, China, [3]Nanjing Joint Institute for Atmospheric Sciences, Nanjing, China, [4]Collaborative Innovation Center of Atmospheric Environment and Equipment Technology, Jiangsu Key Laboratory of Atmospheric Environment Monitoring and Pollution Control (AEMPC), Nanjing University of Information Science and Technology, Nanjing, China, [5]Wuxi Meteorological Observatory of Jiangsu Province, Wuxi, China

In order to investigate the chemical composition distributions and pollution characteristics of Total water-soluble inorganic ions (TWSII) in the rain period (Meiyu) in the East Asian summer monsoon season, including the impact of Meiyu on air pollution in the Yangtze River Delta, East China, the gaseous pollutant concentrations, the 9 sizes segregated particles, and water-soluble inorganic ions of aerosols were measured on the north shore of Taihu Lake from June 4 to July 5, 2016. Results show that the mass concentrations of atmospheric particulate matters ($PM_{2.5}$ and $PM_{10}$) and main gaseous pollutants ($SO_2$, $NO_2$, CO, and $O_3$) decrease during the Meiyu period, with the largest decline in $PM_{10}$ and the smallest in CO. TWSII in atmospheric particles are mainly concentrated in fine particles during the Meiyu period. The values of ρ (TWSII) for $PM_{1.1}$, $PM_{1.1–2.1}$, and $PM_{2.1–10}$ before the Meiyu onset are generally greater than those during the Meiyu period. During the first pollution process, the ρ(TWSII) for $PM_{1.1}$ and $PM_{1.1–2.1}$ first increase to the peak values, and then decrease during the moderate rainfall period, when the ρ(TWSII) in $PM_{2.1–10}$ increase to its maximum before the Meiyu onset. The mass concentrations for anions, cations, and total ions at different particle-size sections all exhibit bimodal distributions before and after the Meiyu onset. The mass concentration peaks at a particle size of 1.1–2.1 μm for fine particles, while at 5.8–9.0 μm (before the Meiyu onset) and 9.0–10.0 μm (during the Meiyu period) for coarse particles, respectively. The peak particle size for mass concentration of coarse particles moves toward larger sizes during the Meiyu period. The mass concentrations of $SO_4^{2-}$ at different particle-size sections show a bimodal distribution before the Meiyu onset and a multi-modal distribution during the Meiyu period. The mass concentrations of $NO_3^-$ at different particle-size sections show a bimodal distribution before the Meiyu onset and a unimodal distribution during the Meiyu period. The mass concentrations of $NH_4^+$ at different particle-size sections present a bimodal distribution before and after the Meiyu onset, with the particle-size for peak concentrations distributing in 1.1–2.1 and 5.8–9.0 μm before the Meiyu onset, and 9.0–10.0 μm during the Meiyu period. The mean value of nitrogen oxidation ratio (NOR) is higher before the Meiyu onset than after, indicating that the

OPEN ACCESS

**Edited by:**
*Lijuan Shen,*
*University of Toronto, Canada*

**Reviewed by:**
*Yi Li,*
*Intel, United States*
*Chao Liu,*
*China Meteorological Administration, China*
*Jinhui Gao,*
*Chengdu University of Information Technology, China*

***Correspondence:**
*Duanyang Liu*
*liuduanyang2001@126.com*

**Specialty section:**
*This article was submitted to Atmosphere and Climate, a section of the journal Frontiers in Environmental Science*

**Received:** *01 October 2021*
**Accepted:** *21 October 2021*
**Published:** *14 December 2021*

**Citation:**
*Wu Z, Liu D, Zhao T, Su Y and Zhou B (2021) Size Distributions of Water-Soluble Inorganic Ions in Atmospheric Aerosols During the Meiyu Period in the Yangtze River Delta, China. Front. Environ. Sci. 9:788115. doi: 10.3389/fenvs.2021.788115*

secondary conversion of $NO_2$ before the Meiyu onset is enhanced. The sulfur oxidation ratio (SOR) values are greater than NOR values, but the concentrations of $NO_2$ in the same period during the Meiyu period are higher than those of $SO_2$, which indicates that the secondary conversion of $SO_2$ during the Meiyu period on the north bank of Taihu Lake is stronger than that of $NO_2$. During the whole observation, the contribution of stationary sources mainly contributed to the atmospheric particulate matters during the Meiyu period. The contributions of vehicle exhaust and coal combustion to fine particles are more obviously affected by the changes in meteorological conditions during the Meiyu period, and the vehicle emissions contribute more to $PM_{1.1–2.1}$ than to $PM_{1.1}$.

**Keywords: fine particles, meiyu, size distribution, taihu lake, water-soluble inorganic ions, the Yangtze River Delta**

## INTRODUCTION

In recent years, the negative impact of particulate matter on air quality, climate, and human health in China has attracted more and more public attention (Huang et al., 2018; Zhou et al., 2018; Liu et al., 2019; Zhang et al., 2019; Gu et al., 2020; Gui et al., 2020; Zhang et al., 2020; Wang et al., 2021). Atmospheric particulate matter includes primary particulate matter and secondary particulate matter (Dai et al., 2013; Wang S. et al., 2019). Primary particulate matter is usually produced by direct emissions of pollutant sources, such as soil dust from the ground, roads, and construction sites, biomass burning, and sea salt particles transported from the ocean. The secondary particulate matter is generally formed by the oxidation reaction of $SO_2$ (sulfur dioxide), $NO_X$ (nitrogen dioxide), $NH_3$(ammonia), and other gases (Yao et al., 2020).

Long-term exposure to fine particulate matter ($PM_{2.5}$) is one of the risk factors for excess deaths in China, with heavy smog significantly increasing the risk of acute death among residents (Wang et al., 2015, 2020). Previous studies have found that WSII accounts for 30–80% of urban particulate matter (Shen, et al., 2009; Tan, et al., 2009; Wang et al., 2015). It can be seen that WSII is an important component of particulate matter, and the study of characteristic changes of WSII helps us to have a deeper understanding of the physical and chemical properties, sources, and formation mechanism of particulate matter (Guo et al., 2020; Wang et al., 2019 b). Some studies have found that there are significant seasonal differences in WSII concentration (Qiao et al., 2015). Gao, et al. (2016) found that $NO_3^-$, $SO_4^{2-}$, and $NH_4^+$ (SNA) in WSII were characteristic ions of secondary pollution. The proportion of SNA mass concentration in $PM_{2.5}$ ranges from 20 to 70%, and even exceeds 70% (He et al., 2017). Guo et al. (2010) and Zhang et al. (2018) studied that the ion mass concentration spectrum can be used to investigate the formation mechanism of WSII. Some studies have found that the concentration of $NO_3^-$ and $SO_4^{2-}$ in droplet modes increases significantly in the process of pollution, and their peak particle sizes move towards larger particle sizes (Sun et al., 2013; Tian et al., 2016).

Located on the north bank of Taihu Lake, Wuxi is one of the central cities in the Yangtze River Delta region with a dense population, large industrial volume, and a high level of urbanization. With the rapid development of the regional economy, a large amount of energy consumption and the continuous growth of motor vehicle ownership, the air quality of Wuxi presents complex air pollution dominated by $PM_{2.5}$, $PM_{10}$, $O_3$, and $NO_2$ (Guo et al., 2013). Meiyu in Jianghuai Region is an important weather phenomenon in eastern China, and the meiyu rainy season precipitation is a product of interactions between the East Asian summer monsoon system and the Eurasian mid-high-latitude circulation (Xia et al., 2021). Due to the prevailing wind direction and precipitation in the monsoon climate, the air quality in Wuxi is relatively clean in summer compared with winter. However, in the summer harvest and planting stage in June, the particulate matter emitted from straw burning will lead to haze pollution events in Wuxi (Guo et al., 2013; Wang et al., 2021).

In this study, we collected size-segregated aerosol samples in Wuxi during an intensive sampling campaign from June to July 2016. The primary motivation of this study is to determine the chemical composition distributions and pollution characteristics of the TWSII species in the nine size segregated particles in the season changing period, including evolution in the components and particle size changes in the pollution process. Furthermore, the correlation of sulfur and nitrogen oxidation rates with the meteorological conditions were investigated to clarify the dominant meteorological factors affecting the secondary formation of sulfate and nitrate in different size fractions. The results would improve our understanding of the secondary formation of haze pollutions in the economically developed area during the Meiyu period and can also provide insight for the investigation of the human health effects of urban particulate matter in different sizes.

First, the instruments, experiments, data, and analysis methods are described in *Experiments and Data*. We analyze the meteorological conditions pollutions features, spectral distribution, and ionic species of aerosol in *Results and discussion*. Concluding is made in *Conclusion*.

## EXPERIMENTS AND DATA

### Observation Stations and Experiment Descriptions

Wuxi is located in the middle of the Yangtze River Delta, on the northern shore of Taihu Lake. In this study, we selected Wuxi

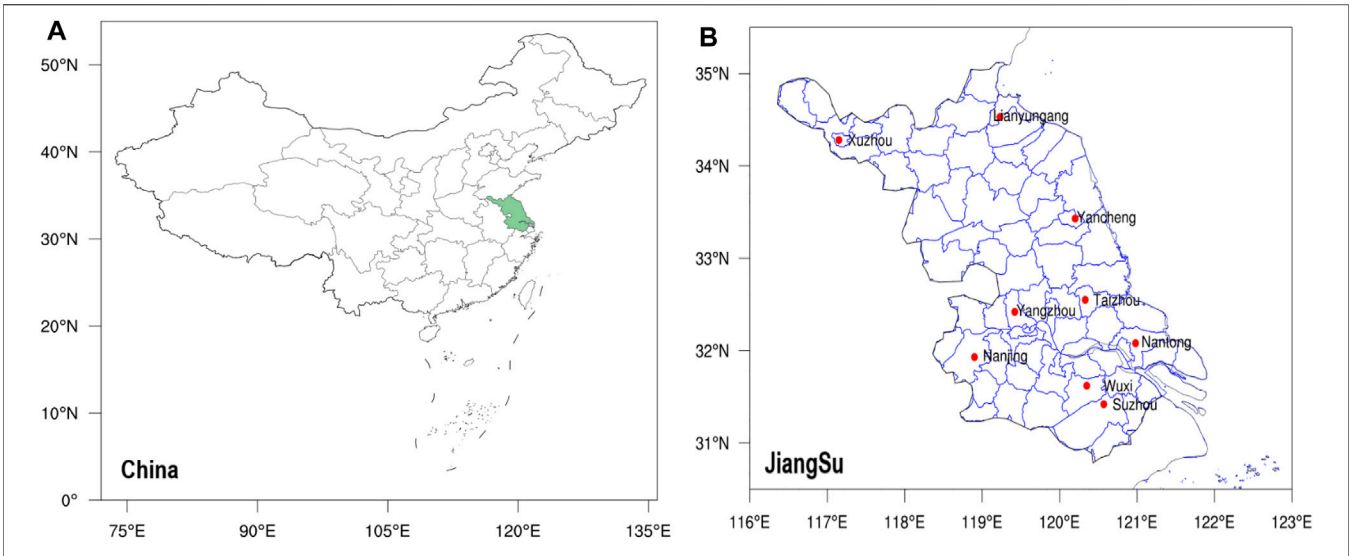


**FIGURE 1 |** Locations of the observation sites in Jiangsu province, China.

meteorological observational station (WMOS, 31.6127°N, 120.3544°E, altitude: 3.2 m) as the sampling site (**Figure 1**). All the measurements were conducted on June 4 to July 5, 2016 (Guo et al., 2013; Liu et al., 2018). The monitoring site is surrounded by farms and is located on the ground. Thus, the observations at this site could help further understand the atmospheric pollution condition in the Yangtze River Delta Cities Group Area (YRDCGA) and the influences from the inland or upwind polluted areas and the Taihu Lake in a regional air quality perspective.

## Water-Soluble Inorganic Ions

The observation of aerosol particles was conducted by using a 9-stage Anderson-type aerosol sampler (Anderson 2000 Inc., United States). 31 batches of aerosol samples were gathered across the Meiyu period in Wuxi. The sampling was conducted on the Meteorological observation field. 24 h size-fractioned PM samples were taken continuously for 1 month (begin at 8:00 am the first day and end at 08:00 the next day) at the flow rate of 28.3 L/min. The particle size range of the nine stages are <0.43, 0.43–0.65, 0.65–1.1, 1.1–2.1, 2.1–3.3, 3.3–4.7,4.7–5.8, 5.8–9.0, and 9.0–10.0 μm for water-soluble ionic components.

The sampling instrument was using the 80 mm Teflon filter (Whatman, Clifton, England) for water-soluble inorganic ionic components, and the membranes were weighted by Mettler Toledo MX-5 microbalance after constant temperature (25°C) and humidity (50%) treatment for 48 h before and after sampling, the microbalance was calibrated using standard weight. The weight difference before and after sampling is particle weight (Wang et al., 2015; Liu et al., 2018).

The 850 professional Ion Chromatography (IC) (Metrohm, Switzerland) was used to analyze the water-soluble inorganic ions, $NO_3^-$, $SO_4^{2-}$, $NH_4^+$, $Ca^{2+}$, $Mg^{2+}$, $Na^+$, $K^+$, $Cl^-$, $F^-$, and $NO_2^-$ were measured. Chromatography includes a conductivity detector, column oven, with an 858 auto-injector, and MagIC Net chromatography workstation (Metrohm, Switzerland); Detailed information can be referred to Wang et al. (2015).

## Meteorological and Pollutant Data

In this study, monitoring instruments (Thermo-Fisher Scientific, United States) were selected to analyze gaseous pollutants, including CO (48i), $NO_2$ (42i), $O_3$ (49i), and $SO_2$ (43i), and the particulate matters, including $PM_{10}$ and $PM_{2.5}$ during the sampling times. The meteorological parameters, including relative humidity (RH), pressure, vapor pressure, precipitation, dew point temperature (Td), temperature (T), visibility, wind direction (WD), and wind speed (WS). All the data were obtained hourly from the Wuxi meteorological observational station (MOS) worked synchronously on the observation site.

## Meiyu in 2016

Meiyu (rainy period of East Asian monsoon season) is a weather phenomenon with regional and temporal characteristics in the middle and lower reaches of the Yangtze River in China (Xiang et al., 2016). It is the product of the transition season of east Asian atmospheric circulation from spring to summer. There is always a persistent precipitation stage of Meiyu from June to July every year, which is called Meiyu period for the middle and lower reaches of the Yangtze River. During the Meiyu periods, precipitation shows obvious interannual variabilities (Xia et al., 2021).

Based on the observation of the Meiyu period lasting from June 19, 2016, to July 11 on the north bank of Taihu Lake, the periods from June 4, 2016, to June 18, 2016, and from June 19, 2016, to July 5, 2016, are defined respectively before and after the onset of Meiyu in this study. The total precipitation during the Meiyu period is 404.5 mm, which is much greater than that (105.4 mm) before the Meiyu onset.

**TABLE 1 |** Statistic of meteorological conditions during sampling time.

| | Before the meiyu period | | | During the meiyu period | | | The observation period | | |
|---|---|---|---|---|---|---|---|---|---|
| | Min | Max | Mean | Min | Max | Mean | Min | Max | Mean |
| T (°C) | 19.9 | 32.8 | 24.6 | 19.5 | 33.0 | 25.7 | 18.7 | 33.0 | 25.2 |
| $T_d$ (°C) | 17.0 | 24.8 | 21.2 | 17.5 | 28.2 | 23.9 | 16.4 | 28.2 | 22.7 |
| Surface pressure (hPa) | 998.7 | 1010.7 | 1006.3 | 999.4 | 1012.4 | 1006.3 | 998.7 | 38.2 | 1006.3 |
| Surface vapor pressure (hPa) | 19.4 | 31.4 | 25.3 | 20.0 | 38.2 | 29.8 | 18.6 | 1012.4 | 27.7 |
| RH (%) | 45.0 | 100.0 | 82.9 | 51.0 | 100.0 | 90.7 | 45.0 | 100.0 | 87.2 |
| Wind speed (m/s) | 0.2 | 6.1 | 2.1 | 0.0 | 6.0 | 1.0 | 0.0 | 6.1 | 2.0 |
| Total precipitation (mm) | | 105.4 | | | 404.5 | | | 509.9 | |

# RESULTS AND DISCUSSION

## Pollutant Concentrations and Meteorological Conditions During the Meiyu Period

### Meteorological Conditions

The changes of meteorological conditions on the north bank of Taihu Lake during the observation period are shown in **Table 1** and **Figure 2**. The surface pressure, wind speed, and temperature change little around the onset of Meiyu. During the observation period, the average wind speed maintains about 2.0 m $s^{-1}$, while the air temperature keeps in the range of 19.0°C–33.0°C with an average of 25.2°C. The frequency and amount of precipitation increase significantly after the Meiyu onset, with the precipitation increasing from 105.4 mm (from June 4 to June 18) to 404.5 mm (from June 19 to July 11). The precipitation increase leads to significant increases in surface water-vapor pressure, relative humidity, and dew-point temperature. Specifically, the average surface water-vapor pressure is 25.3 hPa before the Meiyu onset, which is significantly lower than that (29.8 hPa) during the Meiyu period. The average dew-point temperatures (relative humidity) before and after the onset of Meiyu are 21.2 and 23.9°C (82.9 and 90.7%), respectively. Comparatively, the relative humidity after the onset of Meiyu is closer to saturation than before. Moreover, the wind direction changes obviously and frequently during the Meiyu period on the north bank of Taihu Lake.

### Concentration Variations of $PM_{2.5}$, $PM_{10}$, and Gaseous Pollutants

**Table 2** shows the daily mean concentrations of $PM_{2.5}$, $PM_{10}$, and main gaseous pollutants before and after the onset of Meiyu. The mass concentrations of five main air pollutants after the onset of Meiyu significantly decrease due to the rainfall influence. Specifically, the mass concentrations of $PM_{10}$ and $PM_{2.5}$ are 65.36 and 50.20 μg $m^{-3}$ before the onset of Meiyu, which respectively drop to 38.27 and 29.05 μg $m^{-3}$ after the Meiyu onset. For gaseous pollutants, the mass concentrations of $SO_2$, $NO_2$, and $O_3$ decrease from 12.10, 51.77, and 77.83 μg $m^{-3}$ to 7.91, 41.51, and 51.89 μg $m^{-3}$, respectively.

Before the Meiyu onset, the north bank of Taihu Lake experienced two pollution processes. The first process lasted from 0800 Beijing Time (BJT) on June 6 to 2000 BJT on June 9, and the second process lasted from 2000 BJT on June 12 to 2000 BJT on June 18. The mass concentrations of $PM_{2.5}$ and $PM_{10}$ peaked at 112 and 172 μg $m^{-3}$ in the first process, and peaked at 103 and 148 μg $m^{-3}$ during the second process (**Figures 2D,E**). Although the pollution process during the Meiyu period is not as long as that before the Meiyu onset, the mass concentrations of air pollutants during this period also experienced short fluctuations, where the mass concentrations of $PM_{2.5}$ reached 106 and 120 μg $m^{-3}$ at 2000 BJT on June 21 and 2300 BJT on June 23, respectively (**Figures 2D,E**). According to the hourly precipitation (**Figure 2**) in the Meiyu period, these two fluctuations occurred during the intermittent period of precipitation. While the mass concentrations of air pollutants were significantly lower during other periods, which maintained below 30 μg $m^{-3}$ for $PM_{2.5}$. The precipitation increase and changeable wind direction could be the reasons for the decline of air pollutants.

## Changes of Water-Soluble Inorganic Ions in Atmospheric Aerosols

### Differences of Water-Soluble Inorganic Ions Before and After the Onset of Meiyu

**Table 3** depicts the differences between the concentrations of water-soluble inorganic ions before and after the onset of Meiyu. The average concentration of total water-soluble inorganic ions (ρ(TWSII)) in $PM_{10}$ is (28.59 ± 7.27) μg $m^{-3}$, while the average ρ(TWSII) in $PM_{1.1}$, $PM_{1.1-2.1}$ and $PM_{2.1-10}$ are (11.22 ± 3.90) μg $m^{-3}$ (5.18 ± 2.77) μg $m^{-3}$ and (12.19 ± 2.89) μg $m^{-3}$, respectively. Before the onset of Meiyu, the average ρ(TWSII) in $PM_{1.1}$, $PM_{1.1-2.1}$ and $PM_{2.1-10}$ are 13.36 ± 4.84, 6.55 ± 3.46, and 12.3 ± 3.46 μg $m^{-3}$, and they are 9.34 ± 3.72, 3.98 ± 2.19, and 12.10 ± 5.3 μg $m^{-3}$ after the onset of Meiyu, with the ρ(TWSII) decreasing by 30, 39 and 2%, respectively. The values of ρ (TWSII) in fine and coarse particles before the Meiyu onset are higher than those during the Meiyu period.

As shown in **Figure 3A**, the total proportions of four major water-soluble inorganic ions ($NH_4^+$, $Ca^{2+}$, $SO_4^{2-}$ and $NO_3^-$) in $PM_{1.1}$ and $PM_{1.1-2.1}$ are 82 and 87%, respectively. The major water-soluble inorganic ions for $PM_{2.1-10}$ are$Ca^{2+}$, $NH_4^+$, $SO_4^{2-}$ and $Na^+$, accounting for 72% of the total. The anion with the largest proportion in $PM_{1.1}$, $PM_{1.1-2.1}$, and $PM_{2.1-10}$ is $SO_4^{2-}$. Besides, the cation with the largest proportion in $PM_{1.1}$ and $PM_{1.1-2.1}$ is $NH_4^+$, but it is $Ca^{2+}$ in $PM_{2.1-10}$. It indicates that $NH_4^+$ mainly exists in fine particles, while $Ca^{2+}$ mainly in coarse

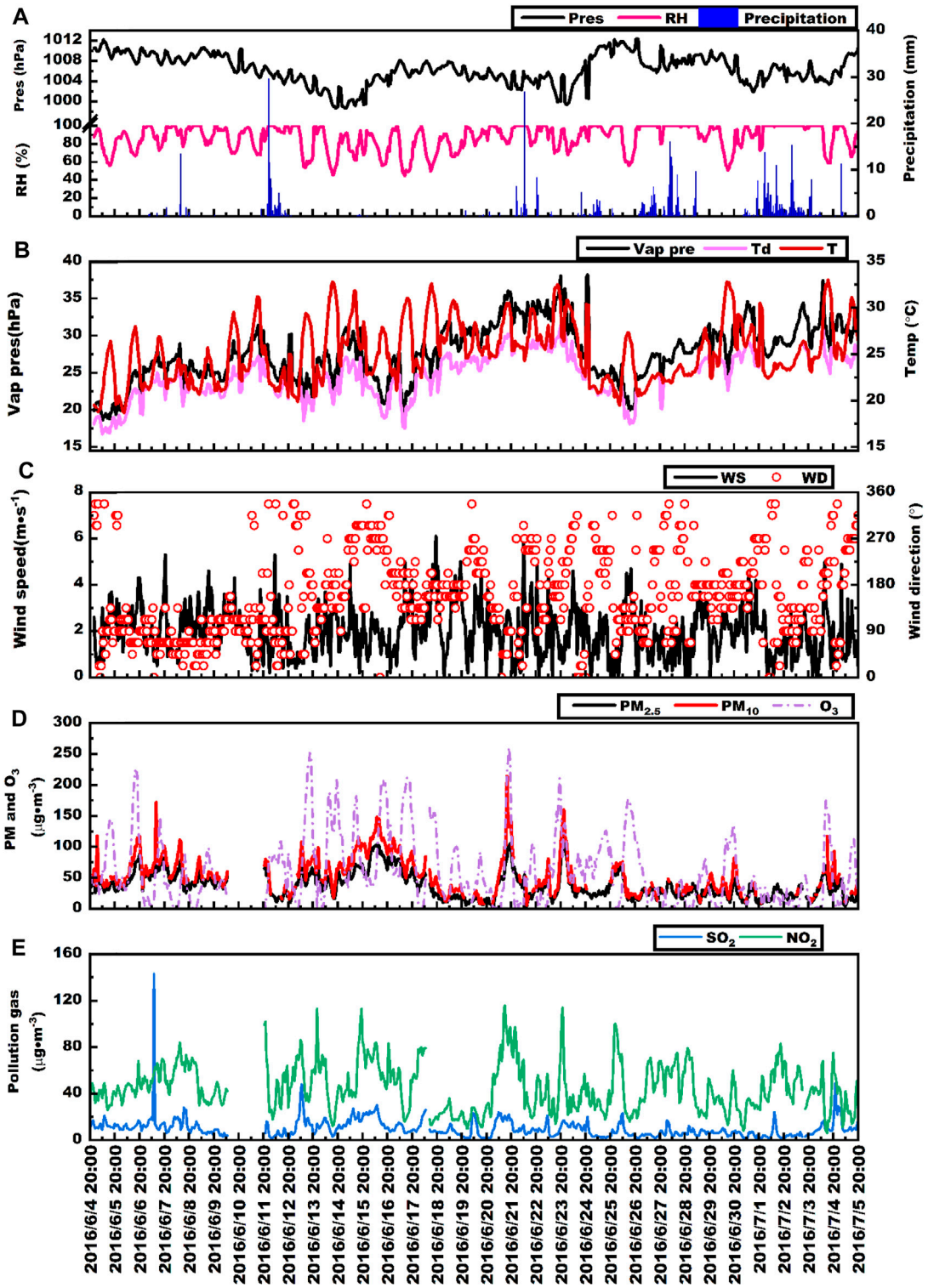


**FIGURE 2 |** Changes of meteorology, gaseous pollutants records, $PM_{2.5}$ and $PM_{10}$ concentrations in sampling periods.

particles. Furthermore, the concentration of $NH_4^+$ decreases with the increase of particle size before and after the onset of Meiyu (**Figure 3B**).

The concentrations of $NH_4^+$, $Ca^{2+}$, $SO_4^{2-}$ and $NO_3^-$ rank top four in submicron particles, fine particles, or coarse particles before the Meiyu onset (**Table 3** and **Figure 3**). The average

**TABLE 2 |** The daily average concentration of $PM_{2.5}$, $PM_{10}$, and gaseous pollutants before and during the Meiyu period.

| | Before the meiyu period | | | During the meiyu period | | |
|---|---|---|---|---|---|---|
| | Min | Max | Mean | Min | Max | Mean |
| $PM_{2.5}$ (μg/m$^3$) | 23.79 | 84.67 | 50.20 | 12.21 | 52.88 | 29.05 |
| $PM_{10}$ (μg/m$^3$) | 30.13 | 111.71 | 65.36 | 16.17 | 81.10 | 38.27 |
| $SO_2$ (μg/m$^3$) | 4.90 | 18.46 | 12.10 | 3.67 | 15.71 | 7.91 |
| $NO_2$ (μg/m$^3$) | 37.75 | 90.33 | 51.77 | 20.58 | 73.38 | 41.51 |
| $O_3$ (μg/m$^3$) | 12.33 | 133.67 | 77.83 | 15.14 | 101.87 | 51.89 |

concentrations of ten kinds of ions in $PM_{1.1}$ are in decreasing order of $NH_4^+>SO_4^{2-}>Ca^{2+}>NO_3^->Na^+>K^+>Mg^{2+}>Cl^->F^->NO_2^-$, while those in $PM_{1.1-2.1}$ follow the order of $NH_4^+>SO_4^{2-}>NO_3^->Ca^{2+}>Na^+>K^+>Mg^{2+}>Cl^->F^->NO_2^-$. For $PM_{2.1-10}$, the average concentrations are in order of $Ca^{2+}>NH_4^+>SO_4^{2-}>Na^+>NO_3^->Mg^{2+}>K^+>Cl^->F^->NO_2^-$.

The concentrations of $NH_4^+$, $Ca^{2+}$, $SO_4^{2-}$and $NO_3^-$ are still the highest four after the Meiyu onset, with slight changes in the concentrations of different ions. The concentration of $Ca^{2+}$ increases after the Meiyu onset, which is related to the road construction around the observation site (Wang et al., 2021). The concentrations of $NH_4^+$, $SO_4^{2-}$ and $NO_3^-$ decrease significantly, while the concentrations of $Na^+$, $K^+$, $Mg^{2+}$, $Cl^-$, $F^-$ and $NO_2^-$ change little. During the Meiyu period, the average concentrations of ten kinds of ions follow the order of $NH_4^+>Ca^{2+}>SO_4^{2-}>NO_3^->Na^+>K^+>Mg^{2+}>Cl^->F^->NO_2^-$ in $PM_{1.1}$, the order of $NH_4^+>Ca^{2+}>NO_3^->SO_4^{2-}>Na^+>K^+>Mg^{2+}>Cl^->F^->NO_2^-$ in $PM_{1.1-2.1}$, and the order of $Ca^{2+}>NH_4^+>SO_4^{2-}>Na^+>NO_3^->Mg^{2+}>K^+>Cl^->F^->NO_2^-$ in $PM_{2.1-10}$.

## Compositions of Water-Soluble Inorganic Ions in $PM_{1.1}$, $PM_{1.1-2.1}$ and $PM_{2.1-10}$

The changes of the mass concentrations of water-soluble inorganic ions in $PM_{1.1}$, $PM_{1.1-2.1}$, and $PM_{2.1-10}$ with time during the Meiyu period on the north bank of Taihu Lake are depicted in **Figure 4**. The ρ(TWSII) in $PM_{1.1}$, $PM_{1.1-2.1}$, and $PM_{2.1-10}$ before the Meiyu onset are generally greater than those during the Meiyu period, but there are some differences in the concentration changes. The ρ(TWSII) in $PM_{1.1-2.1}$ changes most obviously before and after the Meiyu onset, followed by $PM_{1.1}$, while the ρ(TWSII) changes little in $PM_{2.1-10}$. This indicates the effect of frequent precipitation during the Meiyu period on the removal of $PM_{1.1}$, $PM_{1.1-2.1}$, and $PM_{2.1-10}$, especially for $PM_{1.1-2.1}$.

**Figure 4** also shows that the changes of ρ(TWSII) in $PM_{1.1}$, $PM_{1.1-2.1}$, and $PM_{2.1-10}$ with time are generally consistent, but there are some differences in some periods. During June 18–20, 2016, the ρ(TWSII) in $PM_{1.1}$ decreased first and then increased, while the change of ρ(TWSII) in $PM_{2.1-10}$ was opposite, and the ρ(TWSII) in $PM_{1.1-2.1}$ presented a consistent increase. Besides, the concentrations varied little in fine particles but changes drastically for coarse particles. This changing trend may be related to the compositions and formation mechanisms of water-soluble inorganic ions of different sizes.

Corresponding to the pollution processes mentioned in *Concentration variations of PM2.5, PM10, and gaseous pollutants*, the ρ(TWSII) in $PM_{1.1}$ and $PM_{1.1-2.1}$ increased obviously from June 5 to June 7 before the Meiyu onset, and the ρ(TWSII) in $PM_{1.1}$ and $PM_{1.1-2.1}$ decreased from June 7 to June 8, while the ρ(TWSII) in $PM_{2.1-10}$ increased to a maximum value before the Meiyu onset. From June 14 to June 16, the ρ(TWSII) in $PM_{1.1}$ and $PM_{1.1-2.1}$ increased to their maximums of 21.34 and 12.05 μg m$^{-3}$ during the observation period, respectively. Meanwhile, the ρ (TWSII) of $PM_{2.1-10}$ decreased from June 14 to June 15 and increased from June 15 to June 16.

During the first process of air pollution (from 0800 BJT on June 6 to 2000 BJT on June 9) before the Meiyu onset, the mass concentrations of $NH_4^+$, $SO_4^{2-}$ and $NO_3^-$ in $PM_{1.1}$, $PM_{1.1-2.1}$ and $PM_{2.1-10}$ increased, especially the concentrations of $NH_4^+$ in $PM_{1.1}$ and $PM_{1.1-2.1}$. During the second process (from 2000 BJT on June 12 to 2000 BJT on June 18), the concentrations of $NH_4^+$, $SO_4^{2-}$ and $NO_3^-$ in $PM_{1.1}$ and $PM_{1.1-2.1}$ increased, while the concentrations of these ions in $PM_{2.1-10}$ had no change, which is different from those in the first process. What is the reason for this?

Moreover, the two short fluctuations at 2000 BJT on June 21 and 2300 BJT on June 23 are only reflected as the increases in the concentrations of $NH_4^+$, $SO_4^{2-}$ and $NO_3^-$ in $PM_{1.1}$ and $PM_{1.1-2.1}$. The above four fluctuations may be related to the change of $SO_2$ concentration before and after the Meiyu onset. On the one hand,

**TABLE 3 |** The average concentrations (μg/m$^3$) of WSII in particulate matters before and during the Meiyu period.

| | Berfore the meiyu period | | | During the meiyu period | | |
|---|---|---|---|---|---|---|
| | $PM_{1.1}$ | $PM_{1.1-2.1}$ | $PM_{2.1-10}$ | $PM_{1.1}$ | $PM_{1.1-2.1}$ | $PM_{2.1-10}$ |
| $NH_4^+$ | 5.74 ± 2.64 | 3.30 ± 2.13 | 1.86 ± 2.13 | 3.16 ± 1.79 | 1.72 ± 1.29 | 1.59 ± 0.63 |
| $Ca^{2+}$ | 1.79 ± 0.37 | 0.58 ± 0.09 | 3.05 ± 0.09 | 2.03 ± 0.49 | 0.65 ± 0.14 | 4.77 ± 2.93 |
| $SO_4^{2-}$ | 2.10 ± 0.67 | 0.99 ± 0.50 | 2.08 ± 0.50 | 1.26 ± 0.41 | 0.46 ± 0.21 | 1.33 ± 0.41 |
| $NO_3^-$ | 1.56 ± 0.67 | 0.92 ± 0.54 | 1.82 ± 0.54 | 0.93 ± 0.53 | 0.51 ± 0.37 | 0.88 ± 0.30 |
| $Na^+$ | 0.85 ± 0.19 | 0.30 ± 0.09 | 1.36 ± 0.09 | 0.71 ± 0.20 | 0.22 ± 0.08 | 1.43 ± 0.51 |
| $K^+$ | 0.47 ± 0.12 | 0.15 ± 0.03 | 0.64 ± 0.03 | 0.50 ± 0.12 | 0.16 ± 0.03 | 0.66 ± 0.08 |
| $Mg^{2+}$ | 0.46 ± 0.05 | 0.15 ± 0.02 | 0.78 ± 0.02 | 0.45 ± 0.07 | 0.14 ± 0.02 | 0.92 ± 0.26 |
| $Cl^-$ | 0.23 ± 0.10 | 0.12 ± 0.06 | 0.43 ± 0.06 | 0.17 ± 0.09 | 0.07 ± 0.04 | 0.30 ± 0.16 |
| $F^-$ | 0.11 ± 0.02 | 0.04 ± 0.00 | 0.20 ± 0.00 | 0.11 ± 0.01 | 0.04 ± 0.01 | 0.18 ± 0.01 |
| $NO_2^-$ | 0.03 ± 0.01 | 0.01 ± 0.00 | 0.08 ± 0.00 | 0.03 ± 0.01 | 0.01 ± 0.00 | 0.04 ± 0.01 |
| TWSII | 13.36 ± 4.84 | 6.55 ± 3.46 | 12.30 ± 3.46 | 9.34 ± 3.72 | 3.98 ± 2.19 | 12.10 ± 5.30 |

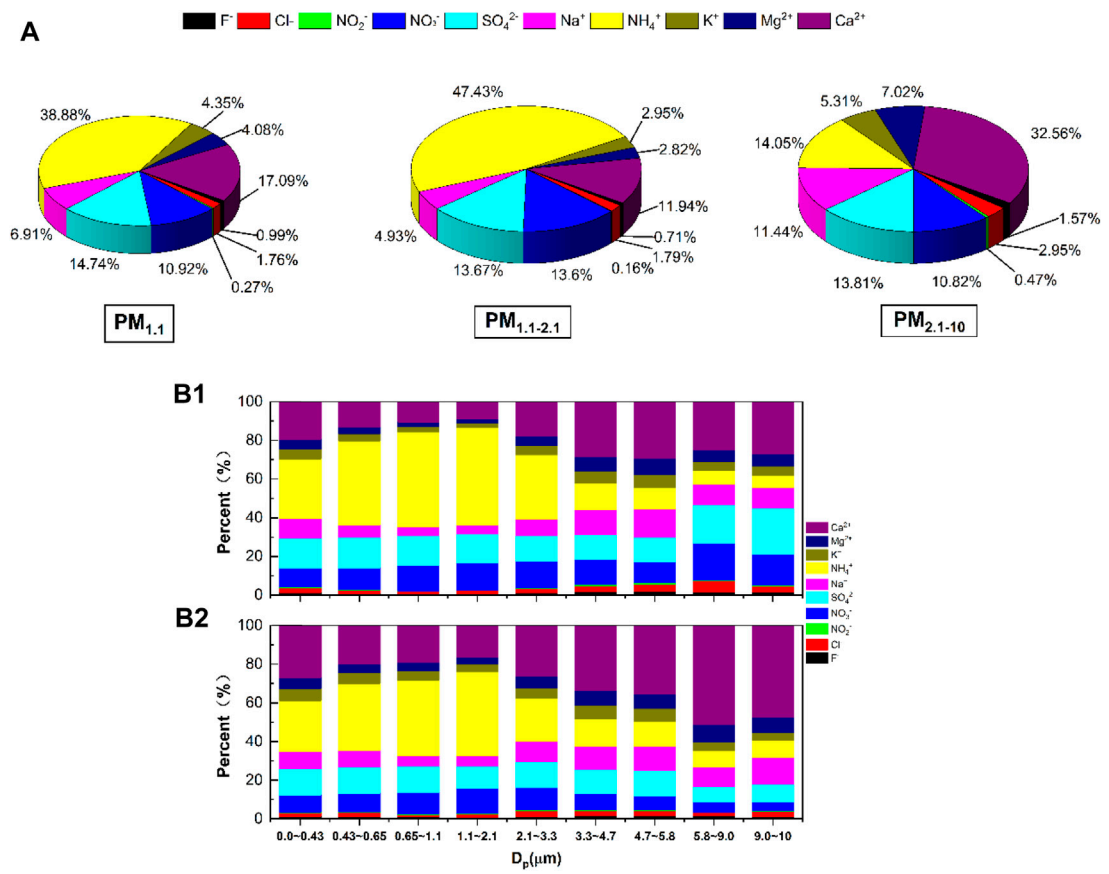


**FIGURE 3 |** Mass percentage of **(A)** major ions in the $PM_{1.1}$, $PM_{1.1\text{-}2.1}$ and $PM_{2.1\text{-}10}$, and rations distribution of WSII mass concentration in different size distribution and period (b1: before the Meiyu period, b2: during the Meiyu period).

the increase of $SO_4^{2-}$ concentration in $PM_{1.1-2.1}$ during the Meiyu period is due to the gas-to-particle conversion of smaller particles; on the other hand, the $SO_4^{2-}$ converts to larger-size particles.

## Spectrum Distribution of Mass Concentrations of TWSII

The particle-size distribution of water-soluble ions can characterize the source and formation mechanism of ions (Zhang et al., 2018). **Figure 5A** indicates that the mass concentration spectrums of total anions, total cations, and total ions within different particle-size sections present bimodal distributions before and after the Meiyu onset. The mass concentrations of fine particles peak at the particle-size of 1.1–2.1 μm, while the mass concentrations of coarse particles respectively peak at particle-size of 5.8–9.0 and 9.0–10.0 μm before and after the Meiyu onset, indicating that the particle-size corresponding to peak concentrations in coarse particles moves toward the larger particle sizes after the Meiyu onset. The variation characteristics for mass concentrations of anions, cations, and total ions are similar during the observation period, with the ions mainly concentrating in the section of fine particles. The peak concentration of ions in fine particles before the Meiyu onset is higher than that during the Meiyu period. While in coarse particles, the peak concentration of anions before the Meiyu onset is higher. Meanwhile, the peak concentrations of total cations and total ions before the Meiyu onset are lower than those during the Meiyu period.

**Figure 6** displays the variations of the particle-size distributions of total anions, total cations, and total ions in water-soluble inorganic ions overtime during the observation. Before June 19, 2016, the total anions, total cations, and total ions in fine particles grew rapidly and reached their peak concentrations. During June 8–15 before the Meiyu onset, the concentration of total anions with the particle sizes of 4.5– and 0.65–1.1 μm in coarse particles increased more rapidly than those in other particle sizes (**Figure 6A**). The particle sizes for the peak of mass concentrations of total ions in coarse particles moved toward larger particle sizes after the Meiyu onset. The period with an increasing concentration for total anions with the particle size of 9–10 μm in coarse particles accounted for 47% of the total Meiyu period, while the concentration of the total anions at the particle size of 5.8–9.0 μm decreased during the same period. Meanwhile, the environmental relative humidity was greater than 90% (**Figure 2C**), indicating an obvious effect of the hygroscopic growth of the total anions in coarse particles. As shown in

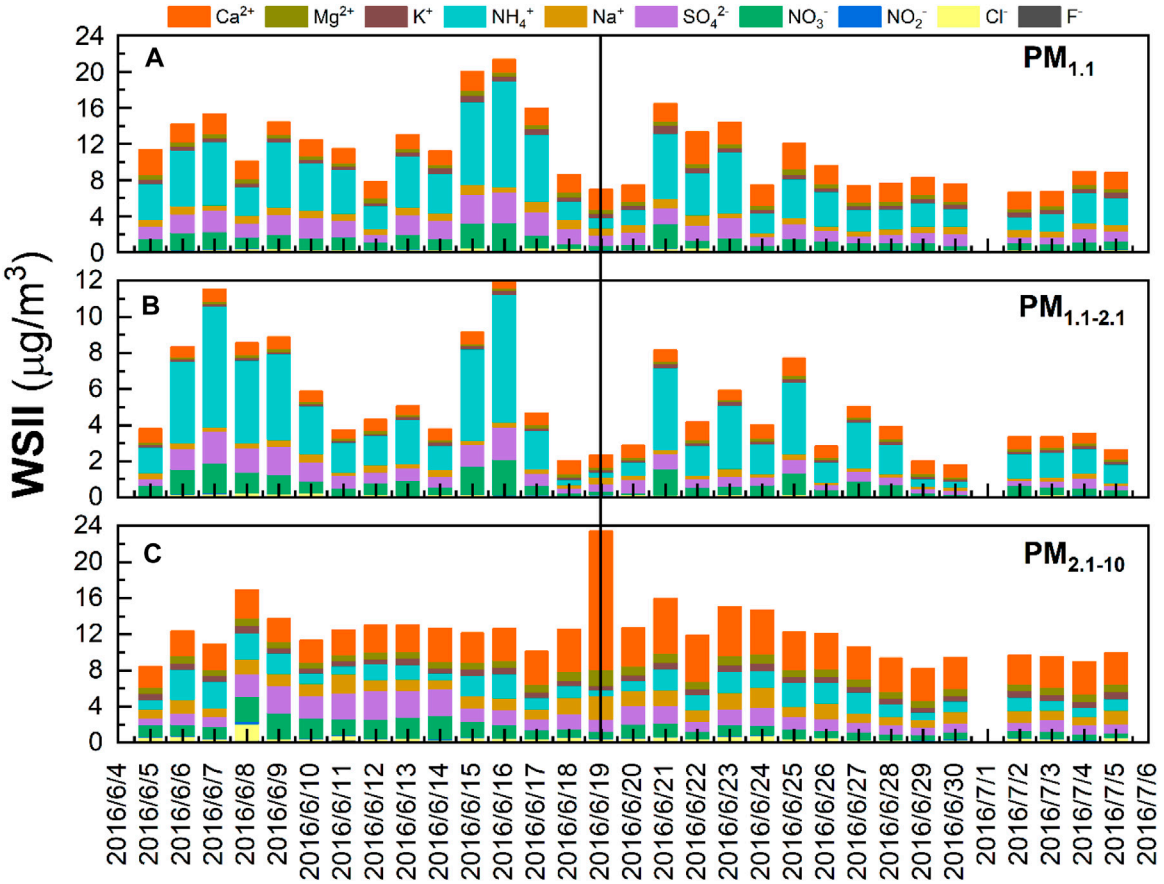


**FIGURE 4 |** Time series of major inorganic ions in **(A)** $PM_{1.1}$, **(B)** $PM_{1.1\text{-}2.1}$, **(C)** $PM_{2.1\text{-}10}$ during the sampling period.

**Figure 6B**, the concentrations of total cations and total ions in coarse particles during the Meiyu period were higher than those before the Meiyu onset, with the maximum concentrations of total cations and total ions in coarse particles being 0.81 (0.95) and 3.28 μg $m^{-3}$ (10.56 μg $m^{-3}$) before (after) the Meiyu onset, respectively. The maximum concentration during the Meiyu period was 3.2 times that before the Meiyu onset. The main reason for the sharp increase in the peak concentration during the Meiyu period was that the concentrations of the cations at 5.8–9.0 and 9.0–10.0 μm increased sharply on June 19, and the changes of total cation concentrations in coarse particles were roughly the same on both June 18 and June 19, indicating the same source for the total cations on June 18 and 19. **Figure 2** shows that the winds on June 18 and 19 were both southerly, and the daily means of temperature, relative humidity, and surface wind speed were 27.6°C (28.4°C), 75.6% (77.9%), and 3.0 m $s^{-1}$ (2.6 m $s^{-1}$) on June 18 (June 19), indicating no significant changes in meteorological elements. While the local anthropogenic emissions near the observation site have a more obvious effect on the concentration of total cations than meteorological factors do. During the observation period, the particle size of total ions has a more consistent distribution with that of total cations than total anions. It indicates that the cations in water-soluble inorganic ions in atmospheric particulate matters on the north bank of Taihu Lake played an important role in the chemical composition of ions during the Meiyu period in 2016 (Wang et al., 2021).

The particle-size distribution characteristics of different ions and their sources are further analyzed, with the size distributions of each ion before and after the Meiyu onset shown in **Figure 7**, and the time series for different particle-size distributions shown in **Figure 5B**. The particle size of $SO_4^{2-}$ shows a bimodal distribution before the Meiyu onset and a multi-modal distribution during the Meiyu period. Before the Meiyu onset, the mass concentration of $SO_4^{2-}$ peaks at a particle size of 1.1–2.1 μm in fine particles, while at 5.8–9.0 μm in coarse particles. After the Meiyu onset, the mass concentration of $SO_4^{2-}$ presents a bimodal distribution with its peaks at particle-size of 0.43–0.65 μm and 1.1–2.1 μm in fine particles, and particle-size of 4.7–5.8 and 9.0–10.0 μm in coarse particles. As indicated in the sequence variation (**Figure 7**), before the Meiyu onset, the mass concentration of $SO_4^{2-}$ in fine particles peaks at particle-size of 0.43–2.1 μm and the proportions for the frequencies in three different particle-size sections are 36, 21, and 43%, respectively. During the Meiyu period, the mass concentration of $SO_4^{2-}$ in fine particles peaks at particle-size of 0–2.1 μm, and the proportions for the frequencies in different particle sizes are 19, 25, 6, and 40%, respectively. It indicates that

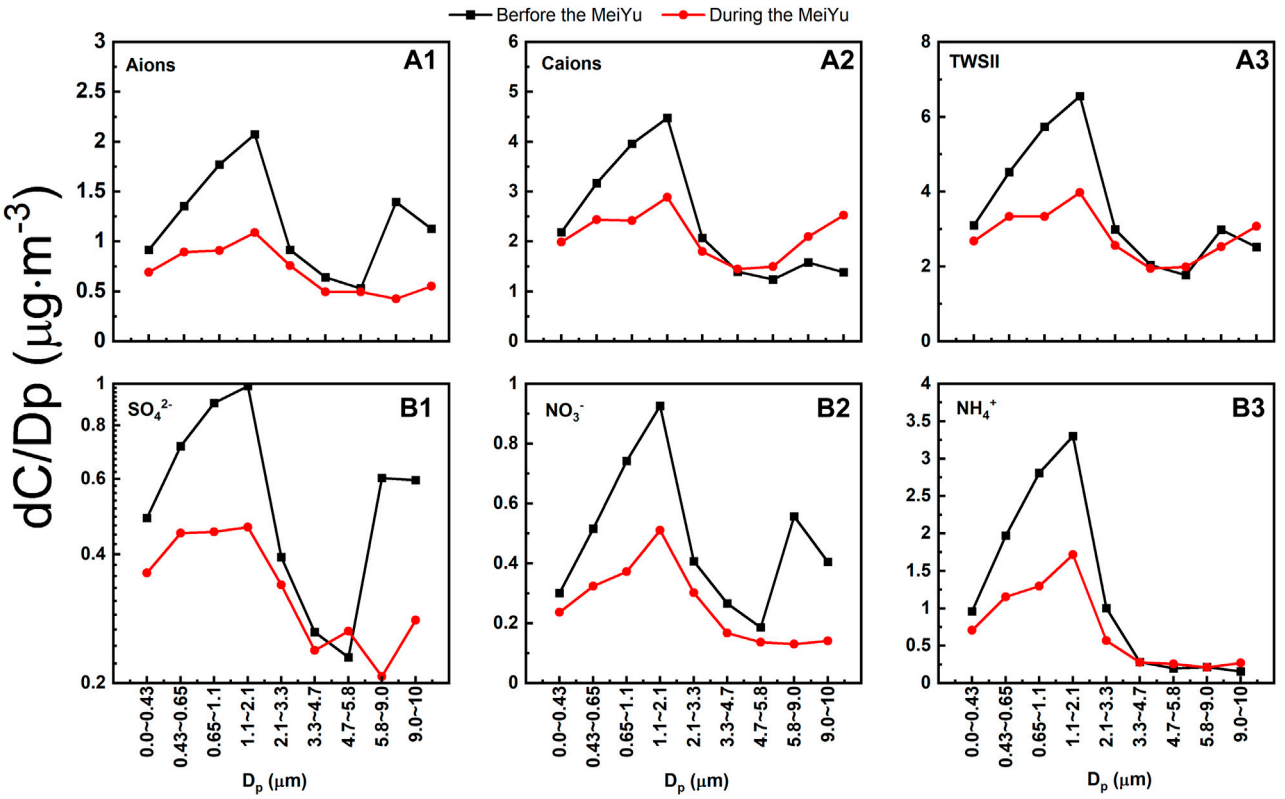


**FIGURE 5 |** Spectral distributions of water-soluble inorganic (a1) Aions (a2) caions (a3) ionic (b1) $SO_4^{2-}$ (b2) $NO_3^-$, and (b3) $NH_4^+$ at different periods.

$SO_4^{2-}$ in fine particles is mainly generated by the reactions in the cloud and the gas-phase reaction. While the two reactions during the Meiyu period are weaker than those before the Meiyu onset. The particle size for the peak concentration of $SO_4^{2-}$ in coarse particles moves toward larger particle sizes during the Meiyu period. This may be related to higher environmental humidity during the Meiyu period, resulting in the hygroscopic growth of sulfates in coarse particles.

The mass concentration of $NO_3^-$ at different particle-size sections shows a bimodal distribution before the Meiyu onset, and a unimodal distribution after the Meiyu onset. The mass concentration of $NO_3^-$ in fine particles peaks at particle-size of 1.1–2.1 μm, while at 5.8–9.0 μm in coarse particles. **Figure 5B** shows that before the Meiyu onset, the mass concentration of $NO_3^-$ in fine particles peaks at particle-size of 0.43–2.1 μm, with the proportions of frequencies for particle-size in four particle-size sections accounting for 13, 25, 6, and 56%, respectively. The effect of gas-phase conversion (liquid-phase reaction) during Meiyu is stronger (weaker) than that before Meiyu. Before the Meiyu onset, the mass concentration of $NO_3^-$ in coarse particles peaks at particle-size of 2.1–3.3 and 5.8–10.0 μm, and the proportions of frequencies for particle-size within the three particle-size sections account for 36, 57, and 7%, respectively. The peak particle-size of $NO_3^-$ distributes in all five particle-size sections of 2.1–10 μm after the Meiyu onset, with the proportions of frequencies accounting for 50, 6, 6, 13, and 25%, respectively. It can be concluded that the sources of $NO_3^-$ in coarse particles after the Meiyu onset are more complex than before. The proportion for $NO_3^-$ having particle-size within 5.8–9.0 μm decreases significantly, which may be attributed to the removal effect of increasing rainfall during the Meiyu period. The concentration of $NH_4^+$ at different particle-size sections presents a bimodal distribution before and unimodal distribution during the Meiyu, with the particle-size of peak concentration distributing in 1.1–2.1 and 5.8–9.0 μm (before the Meiyu), and 9.0–10.0 μm (during the Meiyu). $NH_4^+$ is mainly found in fine particles, with the mass fraction accounting for 79.2% (**Figure 5B**).

## Changes of Secondary Aerosols

The sulfur oxidation ratio (SOR) and nitrogen oxidation ratio (NOR) are often used to characterize the conversion degree of $SO_2$ and $NO_2$ to $SO_4^{2-}$ and $NO_3^-$, respectively (SOR = $[SO_4^{2-}]/([SO_4^{2-}]+[SO_2])$,NOR = $[NO_3^-]/([NO_3^-]+[NO_2])$, where the $[SO_4^{2-}]$, $[SO_2]$, $[NO_3^-]$, and $[NO_2]$ are the molar concentrations (μmol $m^{-3}$) in the particulate matters and gas phase.) (Guo et al., 2020). Higher SOR or NOR values indicate that more secondary aerosol particulates are converted from $SO_2$ and $NO_2$ (Liu et al., 2016; Wang et al., 2019a,b). It has been found that when the SOR and NOR values are greater than 0.1, the photochemical reaction occurs in the atmosphere (Ohta and Okita 1990). **Figure 8** shows the time series for the NOR, SOR, and concentrations of $SO_2$, $NO_2$, $SO_4^{2-}$ and $NO_3^-$

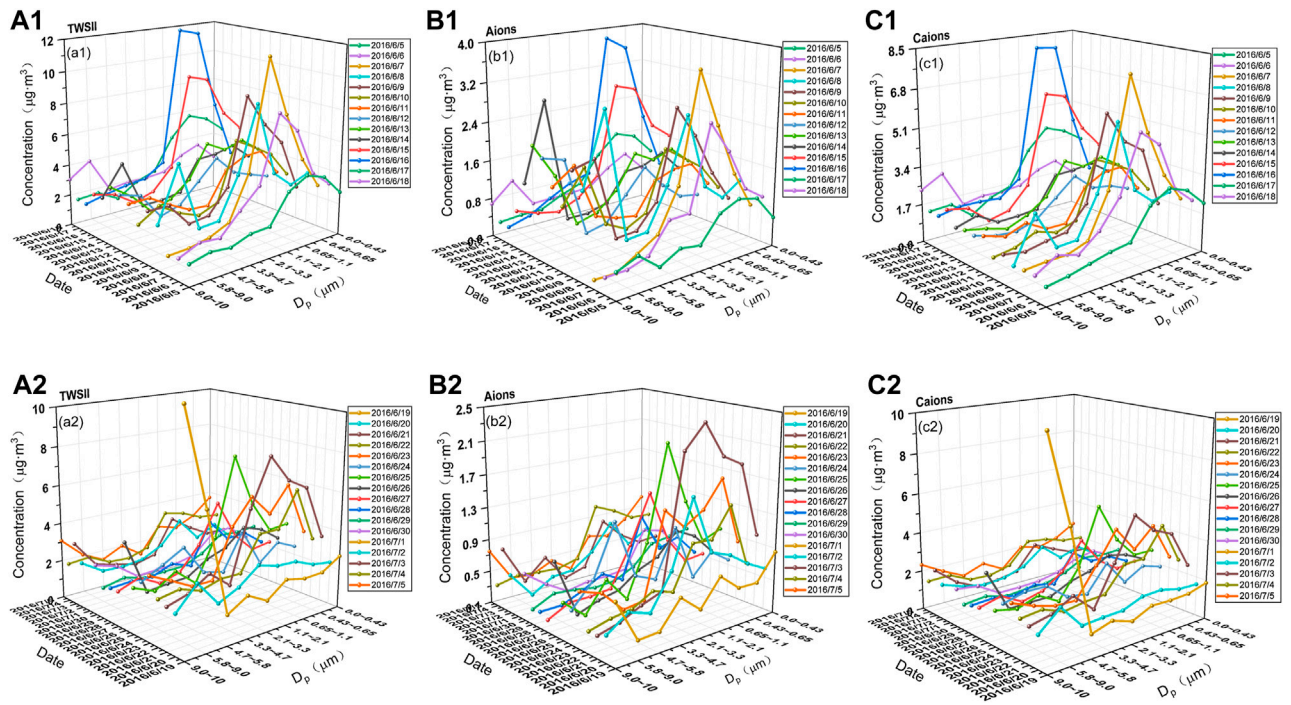


**FIGURE 6 |** Daily variations in spectral distribution of water-soluble inorganic (a1, a2) ionic (b1, b2) aions and (c1, c2) caions at different period ((a1, b1, c1) before the Meiyu period and (a2, b2, c2) during the Meiyu period).

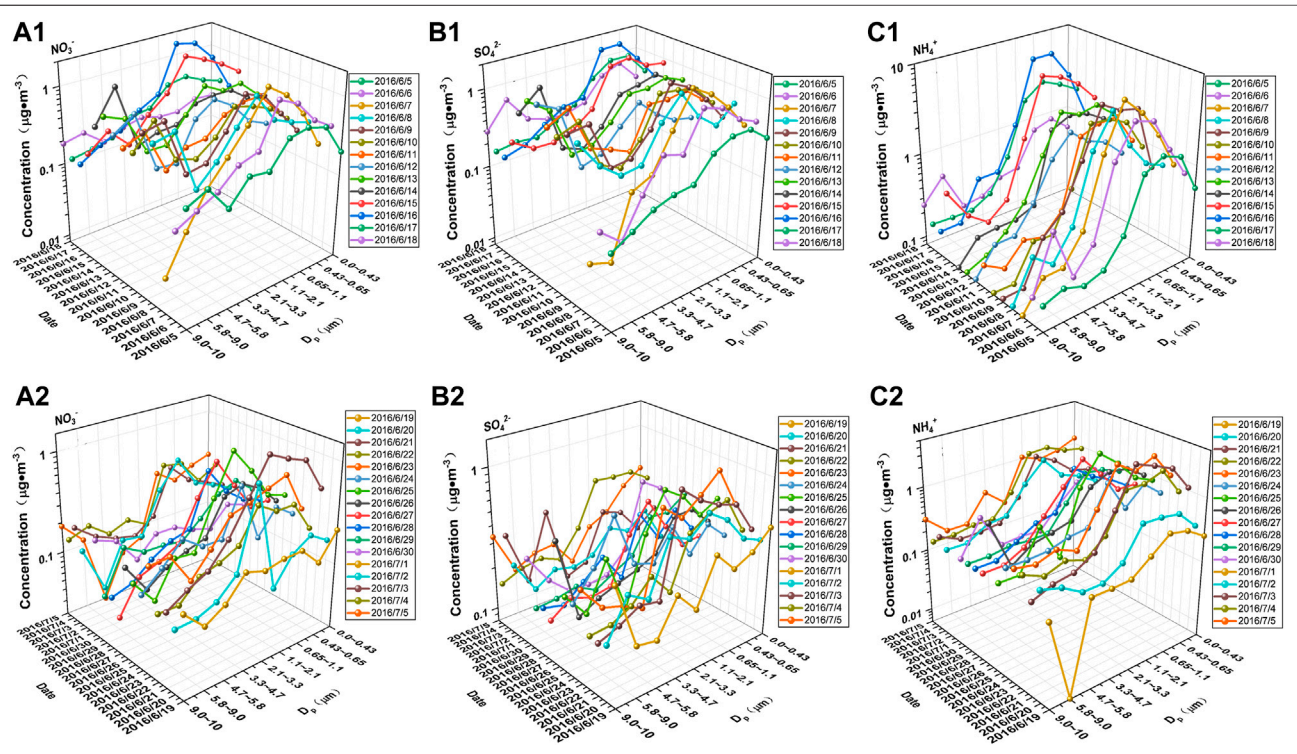


**FIGURE 7 |** Daily variations in spectral distribution of water-soluble inorganic (a1, a2) $NO_3^-$ (b1, b2) $SO_4^{2-}$and (c1, c2) $NH_4^+$ at different period.

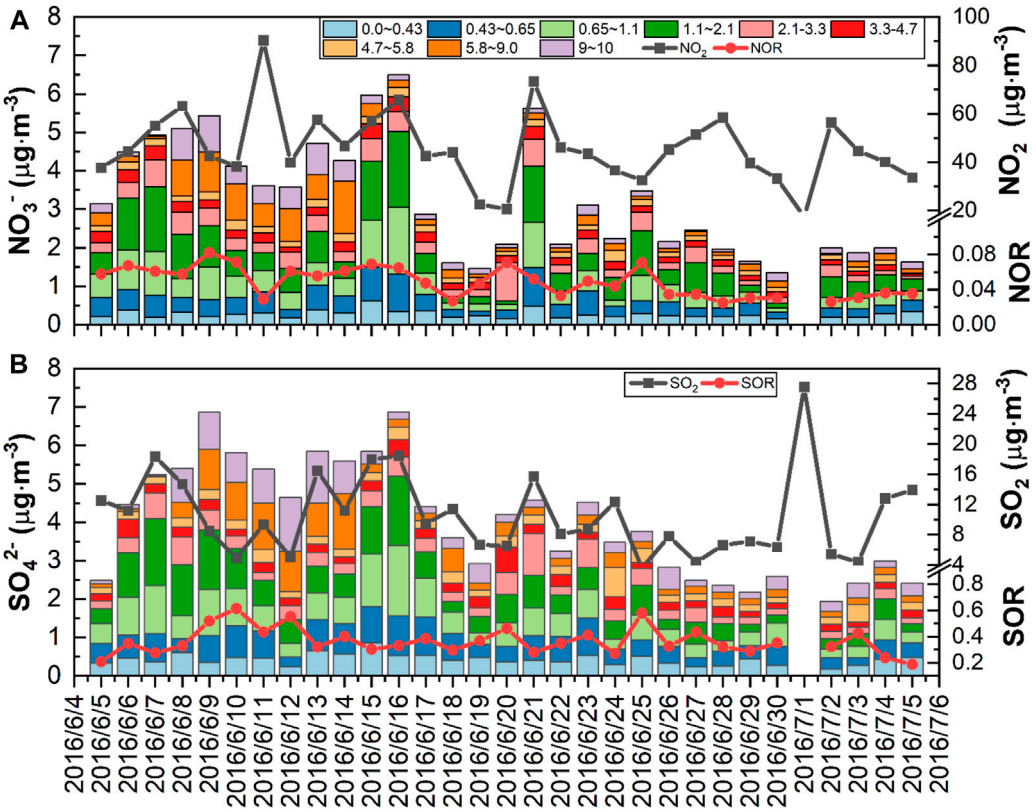


**FIGURE 8 |** Time series of **(A)** size distribution of $NO_3^-$, $NO_2$ concentration and NOR, and **(B)** size distribution of $SO_4^{2-}$, $SO_2$ concentration and SOR during the sampling period.

**TABLE 4 |** Correlation coefficient of NOR and SOR between $O_3$ concentrations, Temperature, Relative humidity and Precipitation in particulate matters.

| | $O_3$ | T | RH | Precipitation |
|---|---|---|---|---|
| $SOR_{PM_{1.1}}$ | 0.12 | −0.13 | 0.01 | −0.11 |
| $SOR_{PM_{1.1-2.1}}$ | −0.07 | −0.51[a] | 0.33 | 0.07 |
| $SOR_{PM_{2.1-10}}$ | −0.19 | −0.28 | 0.35 | 0.28 |
| $NOR_{PM_{1.1}}$ | 0.58[a] | −0.11 | −0.33 | −0.49[a] |
| $NOR_{PM_{1.1-2.1}}$ | 0.34 | −0.44[b] | 0.05 | −0.13 |
| $NOR_{PM_{2.1-10}}$ | 0.15 | −0.14 | −0.10 | −0.25 |

[a]*Correlation is significant at the 0.01 level.*
[b]*Correlation is significant at the 0.05 level.*

during the Meiyu period on the north bank of Taihu Lake. It can be found that the NOR values during the observation are below 0.1, and the average NOR value before the Meiyu onset is higher, indicating that the secondary conversion of $NO_2$ before the Meiyu onset is greater than after.

**Table 4** shows the correlation coefficients of the SOR and NOR with $O_3$, temperature, relative humidity, and daily precipitation in different particle-size sections. It can be seen that the NOR in $PM_{1.1}$ is positively correlated with the $O_3$ concentration ($R_2$ = 0.58) and negatively correlated with the daily precipitation ($R_2$ = −0.49), indicating that the $O_3$ concentration has a more obvious impact on the NOR in $PM_{1.1}$. The NOR in $PM_{1.1-2.1}$ is negatively correlated with the temperature, where high-temperature results in disassociation of and volatilization of $NH_4NO_3$ to form gaseous $HNO_3$ (Zhao et al., 2018). As the average temperature during the Meiyu period is higher than that before the Meiyu onset, the NOR decreases during the Meiyu period.

During the Meiyu period, the SOR values in $PM_{2.1-10}$ are all above 0.1, the SOR values in $PM_{1.1}$ are generally above 0.1 in most periods, while the SOR values in $PM_{1.1-2.1}$ are the smallest among the three particle-size sections. For $PM_{1.1}$, $PM_{1.1-2.1}$ and $PM_{2.1-10}$, the SOR values are greater than the NOR values, but the concentration of $NO_2$ in the same period during the Meiyu period is higher than that of $SO_2$, indicating that the secondary conversion of $SO_2$ during the Meiyu period on the north bank of Taihu Lake is stronger than that of $NO_2$.

The mass ratio of $NO_3^-/SO_4^{2-}$ can be used to qualitatively analyze the relative importance of mobile sources (vehicle exhaust) and stationary sources (coal combustion) to particle matters of sulfur and nitrogen in the atmosphere. A higher ratio indicates the predominance of mobile sources over stationary sources of pollutants (Chang et al., 2015). **Figure 9** shows that the mass ratios of $NO_3^-/SO_4^{2-}$ in $PM_{1.1}$, $PM_{1.1-2.1}$ and $PM_{2.1-10}$ before the Meiyu onset range in 0.13–0.38 (the mean ratio is 0.29), 0.22–0.55 (the mean ratio is 0.36) and 0.21–0.67 (the mean ratio is 0.36), respectively. While during the Meiyu period, the

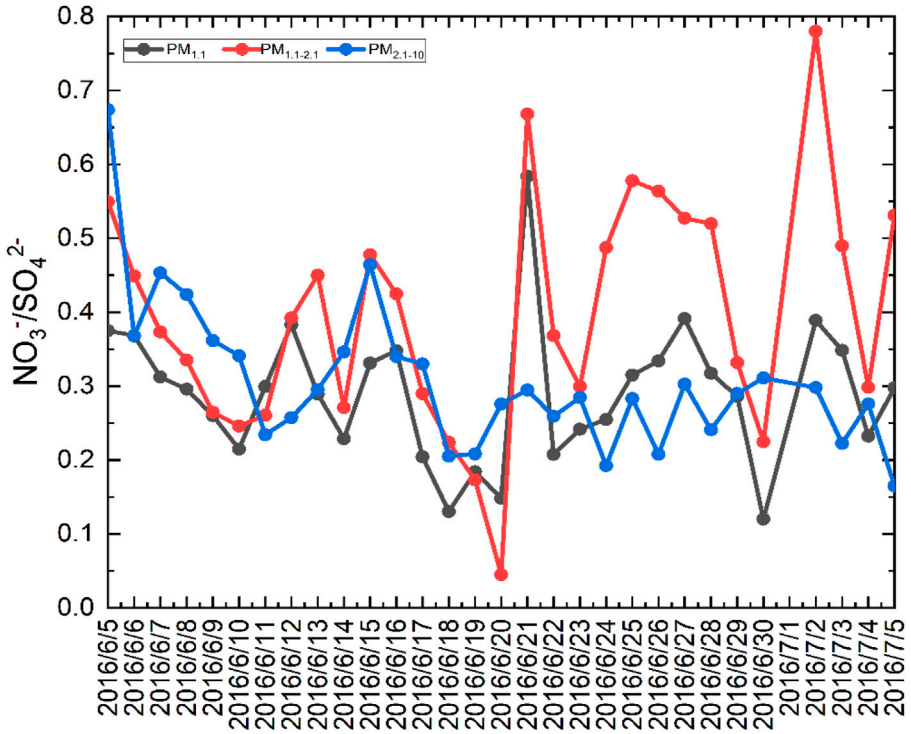


**FIGURE 9 |** Time series of $NO_3^-/SO_4^{2-}$ in $PM_{1.1}$, $PM_{1.1\text{-}2.1}$, $PM_{2.1\text{-}10}$ during the sampling time.

mass ratios of $NO_3^-/SO_4^{2-}$ in $PM_{1.1}$, $PM_{1.1-2.1}$ and $PM_{2.1-10}$ range in 0.12–0.58 (the mean ratio is 0.29), 0.05–0.78 (the mean ratio is 0.43) and 0.17–0.31 (the mean ratio is 0.26), respectively. The mass ratios of $NO_3^-/SO_4^{2-}$ during the whole observation period are less than 0.80, indicating that compared with mobile sources, the stationary sources contribute more to the relative contribution of atmospheric particulate matter on the north bank of Taihu Lake.

The variation ranges for the mass ratio of $NO_3^-/SO_4^{2-}$ before the Meiyu onset are smaller than those during the Meiyu period in $PM_{1.1}$ and $PM_{1.1-2.1}$, while the situation is quite the reverse in $PM_{2.1-10}$. It indicates that the contributions of vehicle exhaust and coal combustion to fine particles are more obviously affected by the changes in meteorological conditions during the Meiyu period. **Figure 9** reveals that the mean ratio of $NO_3^-/SO_4^{2-}$ in $PM_{1.1-2.1}$ before Meiyu onset is smaller than that during the Meiyu period, and it is higher than that in $PM_{1.1}$, indicating that the vehicle emissions contribute more to $PM_{1.1-2.1}$ than to $PM_{1.1}$. Moreover, the contribution of vehicle exhaust increases during the Meiyu period, which is the same as the result from a case study in Wuxi in 2014 (Liu et al., 2018).

## CONCLUSION

In order to investigate the chemical composition distributions and the impact of Meiyu on air pollution in the Yangtze River Delta, East China, the gaseous pollutant concentrations, the nine sizes segregated particles, and water-soluble inorganic ions of aerosols were measured on the north shore of Taihu Lake from June 4 to July 5, 2016. This observational study is concluded as follows:

The mass concentrations of atmospheric particulate matters ($PM_{2.5}$ and $PM_{10}$) and main gaseous pollutants ($SO_2$, $NO_2$, CO, and $O_3$) decrease during the Meiyu period, with the largest decline in $PM_{10}$ and the smallest in CO, which could be regulated by meteorological changes before and after Meiyu onset. Water-soluble inorganic ions in atmospheric particles are mainly concentrated in fine particles during the Meiyu period on the north bank of Taihu Lake. The values of ρ(TWSII) for $PM_{1.1}$, $PM_{1.1-2.1}$, and $PM_{2.1-10}$ before the Meiyu onset are generally greater than those during the Meiyu period. During the first pollution process, the ρ(TWSII) for $PM_{1.1}$ and $PM_{1.1-2.1}$ first increase to the peak values, and then decrease during the moderate rainfall period, when the ρ(TWSII) in $PM_{2.1-10}$ increase to its maximum before the Meiyu onset.

The mass concentrations for anions, cations, and total ions at different particle-size sections all exhibit bimodal distributions before and after the Meiyu onset. The mass concentration peaks at a particle size of 1.1–2.1 μm for fine particles, while at 5.8–9.0 μm (before the Meiyu onset) and 9.0–10.0 μm (during the Meiyu period) for coarse particles, respectively. The peak particle size for mass concentration of coarse particles moves toward larger particle sizes during the Meiyu period. The mass concentrations of $SO_4^{2-}$ at different particle-size sections show a bimodal distribution before the Meiyu onset and a multi-modal distribution during the Meiyu period. The mass concentrations of

$NO_3^-$ at different particle-size sections show a bimodal distribution before the Meiyu onset and a unimodal distribution during the Meiyu period. The mass concentrations of $NH_4^+$ at different particle-size sections present a bimodal distribution before and after the Meiyu onset, with the particle-size for peak concentrations distributing in 1.1–2.1 and 5.8–9.0 μm before the Meiyu onset, and 9.0–10.0 μm during the Meiyu period.

The mean value of NOR is higher before the Meiyu onset than after, indicating that the secondary conversion of $NO_2$ before the Meiyu onset is greater. The SOR values are greater than NOR values, but the concentrations of $NO_2$ in the same period during the Meiyu period are higher than those of $SO_2$, which indicates that the secondary conversion of $SO_2$ during the Meiyu period on the north bank of Taihu Lake is stronger than that of $NO_2$. During the whole observation, the relative contribution of stationary sources to atmospheric particulate matter on the north bank of Taihu Lake is more than the relative contribution of mobile sources. The contributions of vehicle exhaust and coal combustion to fine particles are more obviously affected by the changes in meteorological conditions during the Meiyu period, and the vehicle emissions contribute more to $PM_{1.1-2.1}$ than to $PM_{1.1}$.

As the crop residue burning ban was issued in 2015, the air quality before and after the Meiyu has improved a lot, further studies are needed to determine the effect of meiyu on the removal of air pollutants.

## DATA AVAILABILITY STATEMENT

The raw data supporting the conclusions of this article will be made available by the authors, without undue reservation.

## AUTHOR CONTRIBUTIONS

Author Contributions: Conceptualization, DL; methodology, TZ; software, ZW and BZ; validation, DL; formal analysis, ZW; investigation, ZW and YS; resources, DL, and YS; data curation, ZW and BZ; writing—original draft preparation, DL and ZW; writing—review and editing, DL and TZ; visualization, ZW and BZ; supervision, DL and ZW; project administration, DL; funding acquisition, DL.

## FUNDING

This work was jointly supported by the National Key Research and Development Program of China (No. 2019YFC0214604), the Postgraduate Research and Practice Innovation Program of Jiangsu Province (Grant Nos. KYCX21_0972), the National Natural Science Foundation of China (42075063), Open fund by Jiangsu Key Laboratory of Atmospheric Environment Monitoring and Pollution Control (KHK 2005), and the Jiangsu Meteorological Bureau General project (KZ201902).

## REFERENCES

Chang, Q., Yang, F., Li, X., Cao, Y., Wang, H., and Tian, M. (2015). Characteristics of Mass and Chemical Species Size Distributions of Particulate Matter during Haze Pollution in the winter in Beijing. *Acta Scientiae Circumstantiae* 35, 363–370. (In Chinese).

Dai, W., Gao, J., Cao, G., and Ouyang, F. (2013). Chemical Composition and Source Identification of PM2.5 in the Suburb of Shenzhen, China. *Atmos. Res.* 122, 391–400. doi:10.1016/j.atmosres.2012.12.004

Gao, J., Peng, X., Chen, G., Xu, J., Shi, G.-L., Zhang, Y.-C., et al. (2016). Insights into the Chemical Characterization and Sources of PM2.5 in Beijing at a 1-h Time Resolution. *Sci. Total Environ.* 542, 162–171. doi:10.1016/j.scitotenv.2015.10.082

Gu, P., Qian, J., Liu, D., Wang, K., Dai, Z., Peng, X., et al. (2020). Cold Fronts Transport Features of North China Pollutant over Jiangsu Province, China. *Atmos. Pollut. Res.* 11 (10), 1785–1796. doi:10.1016/j.apr.2020.07.015

Gui, K., Che, H., Zeng, Z., Wang, Y., Zhai, S., Wang, Z., et al. (2020). Construction of a Virtual PM2.5 Observation Network in China Based on High-Density Surface Meteorological Observations Using the Extreme Gradient Boosting Model. *Environ. Int.* 141. 105801. doi:10.1016/j.envint.2020.105801

Guo, H., Simpson, I. J., Ding, A. J., Wang, T., Saunders, S. M., Wang, T. J., et al. (2010). Carbonyl Sulfide, Dimethyl Sulfide and Carbon Disulfide in the Pearl River Delta of Southern China: Impact of Anthropogenic and Biogenic Sources. *Atmos. Environ.* 44 (31), 3805–3813. doi:10.1016/j.atmosenv.2010.06.040

Guo, W., Zhang, Z., Zheng, N., Luo, L., Xiao, H., and Xiao, H. (2020). Chemical Characterization and Source Analysis of Water-Soluble Inorganic Ions in $PM_{2.5}$ from a Plateau City of Kunming at Different Seasons. *Atmos. Res.* 234. 104687. doi:10.1016/j.atmosres.2019.104687

Guo, Y. F., Liu, D. Y., Zhou, B., Xia, J., Wu, Y., and Hu, Y. H. (2013). Study on Haze Characteristics in Wuxi and its Impact Factors. *Meteorol. Monthly* 39, 1314–1324. (in Chinese).

He, J., Gong, S., Yu, Y., Yu, L., Wu, L., Mao, H., et al. (2017). Air Pollution Characteristics and Their Relation to Meteorological Conditions during 2014-2015 in Major Chinese Cities. *Environ. Pollut.* 223, 484–496. doi:10.1016/j.envpol.2017.01.050

Huang, X., Wang, Z., and Ding, A. (2018). Impact of Aerosol-PBL Interaction on Haze Pollution: Multiyear Observational Evidences in North China. *Geophys. Res. Lett.* 45 (16), 8596–8603. doi:10.1029/2018gl079239

Liu, C., Hua, C., Zhang, H., Zhang, B., Wang, G., Zhu, W., et al. (2019). A Severe Fog-Haze Episode in Beijing-Tianjin-Hebei Region: Characteristics, Sources and Impacts of Boundary Layer Structure. *Atmos. Pollut. Res.* 10 (4), 1190–1202. doi:10.1016/j.apr.2019.02.002

Liu, D., Su, Y., Peng, H., Yan, W., Li, Y., Liu, X., et al. (2018). Size Distributions of Water-Soluble Inorganic Ions in Atmospheric Aerosols during the Meiyu Period on the North Shore of Taihu Lake, China. *Aerosol Air Qual. Res.* 18, 2997–3008. doi:10.4209/aaqr.2018.04.0123

Liu, Z., Hu, B., Zhang, J., Yu, Y., and Wang, Y. (2016). Characteristics of Aerosol Size Distributions and Chemical Compositions during Wintertime Pollution Episodes in Beijing. *Atmos. Res.* 168, 1–12. doi:10.1016/j.atmosres.2015.08.013

Ohta, S., and Okita, T. (1990). A Chemical Characterization of Atmospheric Aerosol in Sapporo. *Atmos. Environ. A. Gen. Top.* 24, 815–822. doi:10.1016/0960-1686(90)90282-r

Qiao, T., Zhao, M., Xiu, G., and Yu, J. (2015). Seasonal Variations of Water Soluble Composition (WSOC, Hulis and WSIIs) in PM1 and its Implications on Haze Pollution in Urban Shanghai, China. *Atmos. Environ.* 123, 306–314. doi:10.1016/j.atmosenv.2015.03.010

Shen, Z., Cao, J., Arimoto, R., Han, Z., Zhang, R., Han, Y., et al. (2009). Ionic Composition of TSP and PM2.5 during Dust Storms and Air Pollution Episodes at Xi'an, China. *Atmos. Environ.* 43 (18), 2911–2918. doi:10.1016/j.atmosenv.2009.03.005

Sun, Y., Wang, Z., Fu, P., Jiang, Q., Yang, T., Li, J., et al. (2013). The Impact of Relative Humidity on Aerosol Composition and Evolution Processes during Wintertime in Beijing, China. *Atmos. Environ.* 77, 927–934. doi:10.1016/j.atmosenv.2013.06.019

Tan, J.-H., Duan, J.-C., Chen, D.-H., Wang, X.-H., Guo, S.-J., Bi, X.-H., et al. (2009). Chemical Characteristics of Haze during Summer and winter in Guangzhou. *Atmos. Res.* 94 (2), 238–245. doi:10.1016/j.atmosres.2009.05.016

Tian, S. L., Pan, Y. P., and Wang, Y. S. (2016). Size-resolved Source Apportionment of Particulate Matter in Urban Beijing during Haze and Non-haze Episodes. *Atmos. Chem. Phys.* 16 (1), 1–19. doi:10.5194/acp-16-1-2016

Wang, B., Luo, X., Liu*, D., Su, Y., and Wu, Z. (2021). The Effect of Construction Dust and Agricultural Fertilization on the Precipitation Chemical Composition during Summer in the Yangtze River Delta Area, China. *Atmos. Pollut. Res.* 12 (7). 101121. doi:10.1016/j.apr.2021.101121

Wang, H., Zhu, B., Shen, L., Xu, H., An, J., Xue, G., et al. (2015). Water-soluble Ions in Atmospheric Aerosols Measured in Five Sites in the Yangtze River Delta, China: Size-Fractionated, Seasonal Variations and Sources. *Atmos. Environ.* 123, 370–379. Part B. doi:10.1016/j.atmosenv.2015.05.070

Wang, S., Yin, S., Zhang, R., Yang, L., Zhao, Q., Zhang, L., et al. (2019a). Insight into the Formation of Secondary Inorganic Aerosol Based on High-Time-Resolution Data during Haze Episodes and Snowfall Periods in Zhengzhou, China. *Sci. Total Environ.* 660, 47–56. doi:10.1016/j.scitotenv.2018.12.465

Wang, X., Wei, W., Cheng, S., Yao, S., Zhang, H., and Zhang, C. (2019b). Characteristics of PM2.5 and SNA Components and Meteorological Factors Impact on Air Pollution through 2013-2017 in Beijing, China. *Atmos. Pollut. Res.* 10, 1976–1984. doi:10.1016/j.apr.2019.09.004

Wang, Y., Wild, O., Chen, H., Gao, M., Wu, Q., Qi, Y., et al. (2020). Acute and Chronic Health Impacts of $PM_{2.5}$ in China and the Influence of Interannual Meteorological Variability. *Atmos. Environ.* 229. 117397. doi:10.1016/j.atmosenv.2020.117397

Xia, Y., Qian, H., Yao, S., and Sun, T. (2021). Multiscale Causes of Persistent Heavy Rainfall in the Meiyu Period over the Middle and Lower Reaches of the Yangtze River. *Front. Earth Sci.* 9. 700878. doi:10.3389/feart.2021.700878

Xiang, Y., Lu, P., Cheng, T., Xie, Z., and Wang, W. (2016). Evolution Characteristics of the Jiangsu Plum Rain in Recent 54 Years and its Monitoring Analysis in 2014. *J. Meteorol. Sci.* 36 (5), 681–688. (In Chinese).

Yao, Q., Liu, Z., Han, S., Cai, Z., Liu, J., Hao, T., et al. (2020). Seasonal Variation and Secondary Formation of Size-Segregated Aerosol Water-Soluble Inorganic Ions in a Coast Megacity of North China Plain. *Environ. Sci. Pollut. Res. Int.* 27 (21), 26750–26762. doi:10.1007/s11356-020-09052-0

Zhang, J., Tong, L., Huang, Z., Zhang, H., He, M., Dai, X., et al. (2018). Seasonal Variation and Size Distributions of Water-Soluble Inorganic Ions and Carbonaceous Aerosols at a Coastal Site in Ningbo, China. *Sci. Total Environ.* 639, 793–803. doi:10.1016/j.scitotenv.2018.05.183

Zhang, L., Guo, X., Zhao, T., Gong, S., Xu, X., Li, Y., et al. (2019). A Modelling Study of the Terrain Effects on Haze Pollution in the Sichuan Basin. *Atmos. Environ.* 196, 77–85. doi:10.1016/j.atmosenv.2018.10.007

Zhang, W., Wang, H., Zhang, X., Peng, Y., Zhong, J., Wang, Y., et al. (2020). Evaluating the Contributions of Changed Meteorological Conditions and Emission to Substantial Reductions of PM2.5 Concentration from winter 2016 to 2017 in Central and Eastern China. *Sci. Total Environ.* 716. 136892. doi:10.1016/j.scitotenv.2020.136892

Zhao, Q. Y., Jiang, N., Yan, Q. S., Wang, S. B., Han, S. J., Yang, L. M., et al. (2018). Size Distribution Characteristics of Water-Soluble Inorganic Ions during Summer and Autumn in Zhengzhou. *Huan Jing Ke Xue* 39, 4866–4875. (In Chinese). doi:10.13227/j.hjkx.201803102

Zhou, D., Ding, K., Huang, X., Liu, L., Liu, Q., Xu, Z., et al. (2018). Transport, Mixing and Feedback of Dust, Biomass Burning and Anthropogenic Pollutants in Eastern Asia: a Case Study. *Atmos. Chem. Phys.* 18 (22), 16345–16361. doi:10.5194/acp-18-16345-2018

**Conflict of Interest:** The authors declare that the research was conducted in the absence of any commercial or financial relationships that could be construed as a potential conflict of interest.

**Publisher's Note:** All claims expressed in this article are solely those of the authors and do not necessarily represent those of their affiliated organizations, or those of the publisher, the editors and the reviewers. Any product that may be evaluated in this article, or claim that may be made by its manufacturer, is not guaranteed or endorsed by the publisher.

frontiers in Environmental Science

ORIGINAL RESEARCH
published: 10 January 2022
doi: 10.3389/fenvs.2021.808401

# Long-Term Spatiotemporal Variation of Net Primary Productivity and Its Correlation With the Urbanization: A Case Study in Hubei Province, China

*Ke Wu*[1]*, *Chengfeng Zhou*[2], *Yuxiang Zhang*[1] and *Ying Xu*[3,4]

[1]Institute of Geophysics and Geomatics, China University of Geosciences, Wuhan, China, [2]Bureau of Geology and Mineral Exploration of Anhui Provincial, Hefei, China, [3]National Satellite Ocean Application Service, Ministry of Natural Resources, Beijing, China, [4]Key Laboratory of Space Ocean Remote Sensing and Application, Ministry of Natural Resources, Beijing, China

OPEN ACCESS

**Edited by:**
Xinyao Xie,
Institute of Mountain Hazards and Environment (CAS), China

**Reviewed by:**
Jianbo Tan,
Changsha University of Science and Technology, China
Weiwei Sun,
Ningbo University, China

***Correspondence:**
Ke Wu
kewu@cug.edu.cn

**Specialty section:**
This article was submitted to Atmosphere and Climate, a section of the journal Frontiers in Environmental Science

**Received:** 03 November 2021
**Accepted:** 02 December 2021
**Published:** 10 January 2022

**Citation:**
Wu K, Zhou C, Zhang Y and Xu Y (2022) Long-Term Spatiotemporal Variation of Net Primary Productivity and Its Correlation With the Urbanization: A Case Study in Hubei Province, China. Front. Environ. Sci. 9:808401. doi: 10.3389/fenvs.2021.808401

Net primary productivity (NPP) is a critical component in terrestrial ecosystem carbon cycles. Thus, quantitatively estimating and monitoring the dynamics of NPP have become key aspects for exploring the carbon cycle of terrestrial ecosystems. Anthropogenic activity, such as urbanization, has significant effects on NPP and increases pressure on the natural resources of a specific region. However, to date, although many studies have focused on the relationship between NPP variation and urbanization, they usually ignored any differences at a long-term spatiotemporal variation of urbanization factors, which led to the insufficient understanding of the urbanization-induced impacts on NPP. As a result, this study effectively explored the spatiotemporal variation of NPP from 2001 to 2012 and its corresponding relationship with urbanization, taking the Hubei Province in China as a case study area. To clarify the degree of urbanization, the spatial distribution and temporal variation of population and gross domestic product (GDP) were simulated based on the elevation-adjusted human settlement index and nighttime lights data. The major results showed that high NPP areas were located in those highlands with widespread woodland, in which the NPP value continued to grow during the period. The low NPP areas were mainly distributed in urban areas, and the NPP value had a continued and visible loss. The population and GDP both had a strong correlation with NPP. The significant negative correlation was concentrated in the center of Hubei, with a dense population and developed economy. In order to further realize their complex relationship, the correlation coefficients between the annual NPP and the two factors from 2001 to 2012 were calculated, and the changing trends were investigated. Overall, the findings of this study may provide a reference for studies on the interaction between ecological environment and socioeconomic processes under the background of global rapid urbanization.

**Keywords: NPP, CASA, spatiotemporal dynamics, urbanization, Hubei province**

## INTRODUCTION

As one of the most important components of terrestrial ecosystems, vegetation can mitigate the trend of increasing atmospheric greenhouse gases, maintain the global climate, and adjust the global carbon balance (Piao and Fang, 2003; Peng et al., 2015). Net primary productivity (NPP), which refers to the net accumulation of organic matter by plants over a period of time, is an important evaluation indicator of vegetation growth (Buyantuyev and Wu, 2009; Shang et al., 2018; Yan et al., 2018). Moreover, as a critical component of the terrestrial ecosystem carbon cycle, NPP is a sensitive indicator of ecosystem's health at both the local and global scale (Fang et al., 2000; Gao et al., 2003; Xu et al., 2011). Therefore, quantitative estimates of vegetation NPP are critical for monitoring regional carbon exchanges, thus understanding ecosystem functions and further developing regional carbon management plans (Yu et al., 2009; Zhang et al., 2016).

A series of models have been established to estimate the net primary productivity, which can be mainly grouped into three aspects: statistical models, process-based models, and light-use efficiency (LUE) models (Potter et al., 1993; Wang et al., 2009; Chu et al., 2021). The Carnegie–Ames–Stanford approach (CASA) model, which is a typical LUE model, has been widely used to perform carbon cycling parameter estimations because of its applicability at both local and continental scales (Wang et al., 2017; He et al., 2018). Based on the CASA model, lots of researchers have investigated the long-term variation of NPP in different regions, and many different conclusions have been reached. For example, Gao et al. estimated the grassland net primary productivity in northern Tibet using remote sensing and meteorological data for the period from 1981–2004 (Gao et al., 2009). Potter et al. estimated the carbon flux of the ecosystem of Yellowstone National Park using MODIS data based on the CASA model (Potter et al., 2011). Tan et al. calculated NPP of Xuzhou, China, and the results showed that the average NPP showed a decreasing trend from 2001 to 2010 (Tan et al., 2015). Zhu et al. estimated NPP based on the CASA model in the Greater Khingan Mountain region and analyzed the temporal-spatial variability characteristics of net primary productivity during the period from 1982 to 2013 (Xie et al., 2021).

As we knew, the distribution patterns of NPP and their changes are both driven by natural and anthropogenic factors (Luo et al., 2018). Natural factors, such as temperature and precipitation, have significant influences on vegetative photosynthesis. In addition, the high amount of anthropogenic activities has increased the demand for resources and energy, which can strongly affect the carbon cycle of terrestrial ecosystems. Urban expansion converts vegetation into impervious surfaces, which leads to a significant decrease in vegetation productivity and carbon sequestration capacity (Solecki et al., 2013). It means that the formation of NPP is a typical natural ecosystem function and can effectively indicate the ecological response of urbanization. In general, the urbanization level is very closely related to economic and demographic factors. There is a significant positive correlation between urbanization level and economic growth, and the higher the level of economic development, the higher the level of urbanization. The level of economic development can be quantified through the gross domestic product (GDP), which can be regarded as the typical characteristics of urbanization that can explain the emergence and development of cities (Jiang and Zeng, 2019; Li, 2019). Meanwhile, the increasing intensity of the population makes the impact of anthropogenic activities on the terrestrial ecosystem more and more complex (Shen et al., 2021). Urbanization is a process in which the population of a country or region shifts from rural to urban areas, the rural areas gradually evolve into urban areas, and the urban population keeps growing. Cities that are less populated tend to have a more compact land-scape structure and more vegetation in the city center. Therefore, the study of NPP changes during urbanization and their ecological impacts have become an important topic for clarifying the interactions between GDP and population. The previous studies have assessed the effect of anthropogenic activities on vegetation NPP dynamics by quantifying the population and GDP. For example, Li and Cheng found that there was a stable long-term equilibrium relationship between China's urbanization development and economic growth from 1978 to 2004 (Li and Cheng, 2006). Lu et al. concluded that population and GDP had a significant negative correlation with NPP in Southeast China in a specific year (Lu et al., 2010). Zhao et al. chose NPP and GDP as proxy evaluators to explore the interaction between economic development and environmental change in China (Zhao et al., 2011). Li et al. analyzed the impact of urbanization on vegetation degradation in the Yangtze River Delta of China, and the results showed that the rise of population growth rate and GDP growth has significantly deepened vegetation degradation (Li, 2019). However, these studies only focused on either the spatial or temporal growth of population and GDP. They often ignore any differences at a long-term spatiotemporal variation of urbanization and lack a comprehensive measure associated with NPP relating to population urbanization and economic urbanization.

To overcome this issue, in this article, a long-term spatiotemporal variation of NPP and associated influence of urbanization in Hubei Province from 2001–2012 were monitored and analyzed. As a significant component of the Yangtze River economic zone development strategy, Hubei Province represents a typical region for studying the long-term impact of population and GDP on NPP and should receive considerable attention (Chai et al., 2019). According to the Hubei Statistical Yearbook, the proportion of the urban population increased from 40.8 to 53.5% during the period from 2001 to 2012, and the GDP value grew from 388,000 million CNY to 1,963,200 million CNY. With the rapid growth of the population and the acceleration of urbanization, the ecosystem of Hubei changed significantly, and it is facing severe challenges caused by the pursuit of development. Therefore, understanding the impact of urbanization on NPP in this region has important practical significance. The main objectives of this article are: 1) to analyze the spatiotemporal variations and change trend of NPP in Hubei Province; 2) to estimate the distribution of the population and GDP density and explain their variation trends; and 3) to discuss the correlation

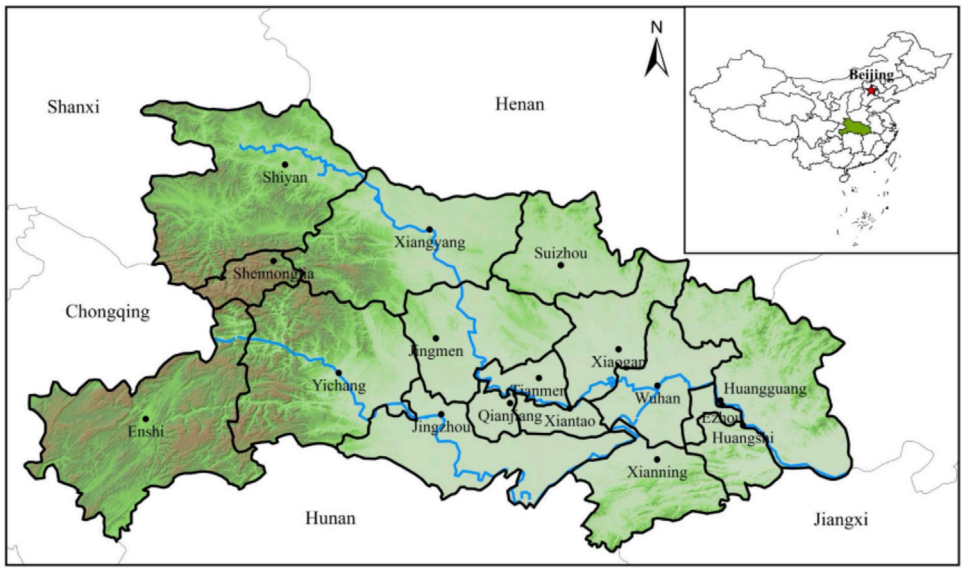


**FIGURE 1 |** Study area location.

relationship between the population and GDP with NPP from both time and space. The results of this study are of great theoretical and practical significance for the effective coordination of nature, economy, and society as well as for sustainable development in Hubei Province.

The remainder of this article is organized as follows: In the *Data Description* section, the materials and methods are described, including the study area, dataset, data processing, and methods. In the *Results and Discussion* section, the results and analysis are presented. The discussion is provided, and it includes information on the spatiotemporal variations of NPP, effects of urbanization on NPP dynamics, limitations, and future research recommendations. In the *Conclusion* section, the conclusions are drawn.

# DATA DESCRIPTION

## Study Area

Hubei Province is located in Central China (between 29°01′ and 33°06′ north latitude and between 108°21′ and 116°07′ east longitude), and it has an area of approximately 185,900 km$^2$ (**Figure 1**) (Wang et al., 2014; Chen et al., 2018). The terrain of Hubei is higher in the west and lower in the middle and includes various and complicated geomorphic types, such as mountains, hills, and plains, among which mountains account for approximately 55%, hills account for 24.5%, and plains account only for 20% of the total area. The province has a humid subtropical climate, with average temperatures of 15–17°C and rainfall of 1100–1300 mm (Lin et al., 2016). The dominant land cover types in Hubei are forests, cropland, wetland, grassland, water bodies, and urban building. There are various vegetation types, including subtropical evergreen broad-leaved forest and subtropical mixed evergreen broad-leaved/deciduous broad-leaved forest (Tao et al., 2017). In 2001, Hubei Province's population was 59.56 million, and its GDP was RMB 0.39 trillion, which rose to 61.65 million and RMB 2.25 trillion in 2012. With the rapid growth of population and urbanization, environmental protection in Hubei Province is facing severe challenges caused by the pursuit of development.

## Data Preprocessing

### MODIS13Q1 Data

The 16-day composition MODIS NDVI product (MOD13Q1) with a spatial resolution of 250 m between January 2001 and December 2012 was acquired from the National Aeronautics and Space Administration (NASA, http://edcimswww.cr.usgs.gov/pub/imswelcome/). The MOD13Q1 dataset is a MODIS Level-3 data product, which has been preprocessed with radiance calibration and atmospheric correction. The MODIS NDVI dataset was transformed to the Universal Transverse Mercator (UTM) with a World Geodetic System (WGS-84) datum using the MODIS Reprojection Tool (MRT), and monthly NDVI datasets were generated using the maximum value composite (MVC) method.

### Nighttime Light Data

Global inter-calibrated nighttime lights (NTLs) (1992–2012), which were provided by Zhang et al. (2016), were downloaded from the website of Yale University (https://urban.yale.edu/data). NTLs were generated from the stable nighttime light annual composite product (version 4) acquired from the National Oceanic and Atmospheric Administration's National Geophysical Data Center (NGDC) using a novel "ridgeline sampling and regression" method. The DMSP/OLS stable nighttime light annual composite product cannot be used directly due to the lack of continuity and comparability. The "ridgeline sampling and regression" method can create a

consistent NTL time series that can be applied globally. The NTL data need to be re-scaled by multiplying pixel values with a scaling factor of 0.01 and reprojected to a value equivalent to NDVI data. The bilinear algorithm was used to resample the NTL data to a pixel size of 250 m × 250 m to match the spatial resolution of the MODIS NDVI dataset.

### Meteorological Data

The meteorological data included the monthly mean temperature, monthly cumulated precipitation, and the monthly total solar radiation from 2001–2012, and these data were acquired from the monthly datasets of the terrestrial climate data and the monthly datasets of the radiation data published on the China Meteorological Data Sharing Service System (http://data.cma.cn/). There were 32 stations of temperature and precipitation and 11 stations of solar radiation. Meteorological data were interpolated to the same spatial resolution as NDVI data using the kriging spatial interpolation method.

### Other Ancillary Data

Ancillary data used in this study include digital elevation model (DEM) data, land use/land cover data, the MODIS NPP products (MOD17A3), and the GDP and population data at the county level. DEM data with a spatial resolution of 90 m were obtained from the geospatial data cloud (http://www.gscloud.cn/), and land use/land cover data were acquired from the MODIS Level-3 land cover type product (MCD12Q1). Land cover types were divided into evergreen needleleaf forest (ENF), evergreen broadleaf forest (EBF), deciduous broadleaf forest (DBF), mixed forest (MF), grassland, wetland, cropland, urban, and water bodies. The MODIS NPP products (MOD17A3) covering the period from 2001 to 2012 were selected to validate the simulated NPP results. Datasets with a spatial resolution of 1 km and a temporal resolution of 1 year were acquired from the Land Processes Distributed Active Archive Center (https://lpdaac.usgs.gov). All the above data were resampled to match the 250 m spatial resolution of MODIS NDVI data using the Resample tool of ArcGIS. The GDP and population data from 2001–2012 at the county level for Hubei Province (81 counties in total) were obtained from the Hubei Provincial Bureau of Statistics (Hubei Statistical Yearbook and Hubei Rural Statistical Yearbook).

## Methods

### NPP Estimation

The CASA model is based on light-use efficiency (LUE) theory, and it simulates net primary productivity by estimating optimal metabolic rates of carbon fixation under the limiting effect of temperature and water stress scales (Potter et al., 2003). In the original CASA model, the maximum light energy utilization rate of all vegetation in the world was set to 0.389 g C $MJ^{-1}$. However, different vegetation types should correspond to different maximum light energy utilization rates. The researchers simulated the maximum light energy utilization rate of all vegetation types according to the actual vegetation distribution in China (Guan et al., 2021). Therefore, the improved NPP estimation model developed was applied in this study to simulate NPP over Hubei Province from 2001 to 2012. NPP can be calculated based on the following equation:

$$\mathrm{NPP}(x,t) = \mathrm{APAR}(x,t) \times \varepsilon(x,t), \tag{1}$$

where x represents the spatial location, t represents time, APAR represents absorbed photosynthetically active radiation, and ε represents light-use efficiency.

$$\mathrm{APAR}(x,t) = \mathrm{SQL}(x,t) \times \mathrm{FPAR}(x,t) \times 0.5; \tag{2}$$

$$\varepsilon(x,t) = T_1 1(x,t) \times T_2(x,t) \times W(x,t) \times \varepsilon *, \tag{3}$$

where SQL represents the total solar radiation per unit time, FPAR represents the fraction of photosynthetically active radiation, T1 and T2 represent the effect of temperature on light-use efficiency, and W represents the effect of soil moisture on light-use efficiency.

### Population Density Mapping

It has been proved that the night light data are an effective tool for the spatialization of population and GDP density at national and province levels (Yue et al., 2014; Song et al., 2015; Wang et al., 2018). The global inter-calibrated nighttime light (NTL) data were introduced in our study to spatialize the population and GDP density. Moreover, the human settlement index (HSI) is an index for mapping spatial population distribution by incorporating vegetation information into the nighttime light data. This index was proposed by Lu et al. (2008) and based on the rationale that impervious surfaces are closely and inversely correlated with vegetation abundance. Many studies have shown that elevation has a profound impact on the human population distribution because most human settlements occur at lower elevations in China (Yue et al., 2003; Yang et al., 2013). If the influence of altitude is not taken into account, then large errors will be introduced into the population simulation results for high-altitude areas. In our study, the average population density and average altitude of 81 counties in Hubei Province were analyzed by exponential function regression. The coefficient of determination ($R^2$) was greater than 0.7 (the coefficient of the exponential equation was -0.002), which indicated that there was a strong negative correlation between altitude and population density. Therefore, an elevation-adjusted human settlement index (EAHSI) was used to estimate the population density in Hubei Province. The data include DEM, standard MODIS NDVI products (23 images per year), and nighttime light data from 2001 to 2012. The EAHSI is defined as follows:

$$\mathrm{EAHSI} = \frac{(1 - \mathrm{NDVI_{max}}) + \mathrm{NTL_{nor}}}{(1 - \mathrm{NTL_{nor}}) + \mathrm{NDVI_{max}} + \mathrm{NTL_{nor}} \times \mathrm{NDVI_{max}}} \times e^{-0.002\mathrm{DEM}}; \tag{4}$$

$$NDVI_{\max} = \mathrm{MAX}(NDVI_1, NDVI_2, ...., NDVI_{23}); \tag{5}$$

$$NTL_{nor} = \frac{(\mathrm{NTL} - \mathrm{NTL_{min}})}{(\mathrm{NTL_{max}} - \mathrm{NTL_{min}})}, \tag{6}$$

where $\mathrm{NDVI_{max}}$ is the maximum image of 23 MODIS NDVI composite images, $\mathrm{NTL_{nor}}$ is the normalized value (0–1) of the nighttime light image, and $\mathrm{NTL_{max}}$ and $\mathrm{NTL_{min}}$ are the maximum and minimum values of the image, respectively.

A total of 41 cities were randomly selected from Hubei Province as experimental areas and the remaining 40 counties as verification areas. A population density model was then built by inputting the cumulative DN of EAHSI at the county level and the corresponding population of the 41 experimental counties into the regression. The model creates a spatial population density map, and the performance of the modeled population density results is calculated by the relative error (RE) and mean relative error (MRE) (Yang et al., 2013; Yue et al., 2014; Sun et al., 2017). The RE and MRE are calculated as follows:

$$RE = \frac{POP_m - POP_a}{POP_a} \times 100\%; \quad (7)$$

$$MRE = \frac{\sum_{=1}^{ni} |(RE_i)|}{n}, \quad (8)$$

where $POP_m$ and $POP_a$ represent the simulated population and the actual statistical population, respectively, and n represents the number of counties.

### GDP Density Mapping

Night light data have the strongest correlation with the sum of the GDP of secondary and tertiary industries; however, these data are not well suited for estimating GDP in rural areas. Therefore, the spatialization process of non-agricultural GDP (the GDP of secondary and tertiary industries) is similar to that of population, while that for agricultural GDP (the GDP of the primary industry) uses land cover data. In this study, MCD12Q1 land cover data were used to model the agricultural GDP, and the EAHSI images were used to model the non-agricultural GDP.

To conduct the spatial simulation of agricultural GDP, the land cover types related to agricultural activities in MCD12Q1 were combined into farmland, forestland, grassland, and water, which corresponded to the gross production values of agriculture, forest, animal husbandry, and fishery, respectively. The EAHSI image was used to model the non-agricultural GDP. When the non-agricultural GDP is spatialized, the minimum value of the NTL image ($NTL_{min}$) was determined. The agricultural and non-agricultural regions were divided by a threshold value. First, the mean NDVI value of artificial surfaces in land cover data was calculated for Hubei Province. Second, the regions with non-artificial surfaces larger than the average NDVI value and NTL DN values >0 were divided. The DN threshold value of the image was determined by the mean NTL DN value in this region.

### Trend Analysis

Ordinary least square estimations were performed for each pixel to quantify the linear trends of NPP in Hubei Province from 2001 to 2012. The equation was calculated as follows:

$$Slope = \frac{n \times \sum_{=1}^{ni} i \times \theta_i - \sum_{=1}^{ni} i \sum_{=1}^{ni} \theta_i}{n \sum_{=1}^{ni} i^2 - \left(\sum_{=1}^{ni} i\right)^2}, \quad (9)$$

where i represents the ordinal year, 1, 2, . . . , 12; n = 12 (the time series is from 2001 to 2012); $\theta_i$ is the annual NPP, in the year i; and Slope is the slope of the linear fitting equation. Slope >0 indicates an increasing trend, and the converse denotes a decreasing trend. The F-test is generally used to determine the significance of the change trends. The equation for this test is as follows:

$$F = U \times \frac{n-2}{Q}, \quad (10)$$

where U is the error sum of squares, and Q is the regression sum of squares, n = 12. Based on the results of the F-test and the trend analysis, the trends were classified according to four ranks: significant decrease (Slope <0 and $p \leq 0.05$), insignificant decrease (Slope <0 and $p > 0.05$), significant increase (Slope ≥0 and $p \leq 0.05$), and insignificant increase (Slope ≥0 and $p > 0.05$).

### Analysis of the Impacts of Urbanization on NPP

In this study, a correlation analysis, which is a common method of analyzing the relations between the net primary productivity and associated influencing factors, was performed to quantify the impact of population and GDP on NPP at the pixel scale, and Pearson's correlation coefficient, which can show the strength of the relationship between urbanization indicators and NPP, was calculated. The T-test was used to determine the significance of the correlation analysis. A value of $p < 0.05$ was considered significant. The equation of the correlation coefficient is expressed as follows:

$$r = \frac{\sum_{i=1}^{n}\left[\left(x_i - \bar{x}\right) \times \left(y_i - \bar{y}\right)\right]}{\sqrt{\sum_{i=1}^{n}\left[\left(x_i - \bar{x}\right)^2 \times \left(y_i - \bar{y}\right)^2\right]}}, \quad (11)$$

where $x_i$ is the NPP of the ith year, $y_i$ is the corresponding population or GDP density of the ith year, $\bar{x}$ and $\bar{y}$ are the means of x and y, respectively, and r is the correlation coefficient of the two variables x and y.

### Study Process

The study process includes the following steps.

1) The NPP values in Hubei Province from 2001 to 2012 were calculated based on the modified CASA model. After that, the spatial patterns, temporal variations, and the spatiotemporal variation trends of NPP were acquired.
2) The MODIS NDVI data, SRTM DEM data, land cover map, NTL data, and other ancillary data were all effectively coupled. Then, the population and GDP density were spatialized under the specified scale.
3) The correlation relationship between the population and GDP density with NPP was calculated. Finally, the variation trend of NPP with population and GDP density was analyzed. The flow chart of this study is shown in **Figure 2**.

## RESULTS AND DISCUSSION

## Validation of the Estimated Results

### Validation of the NPP Calculations

The MOD17A3 NPP products were used to assess the accuracy. First, the MOD17A3 NPP products were resampled to a 250-m

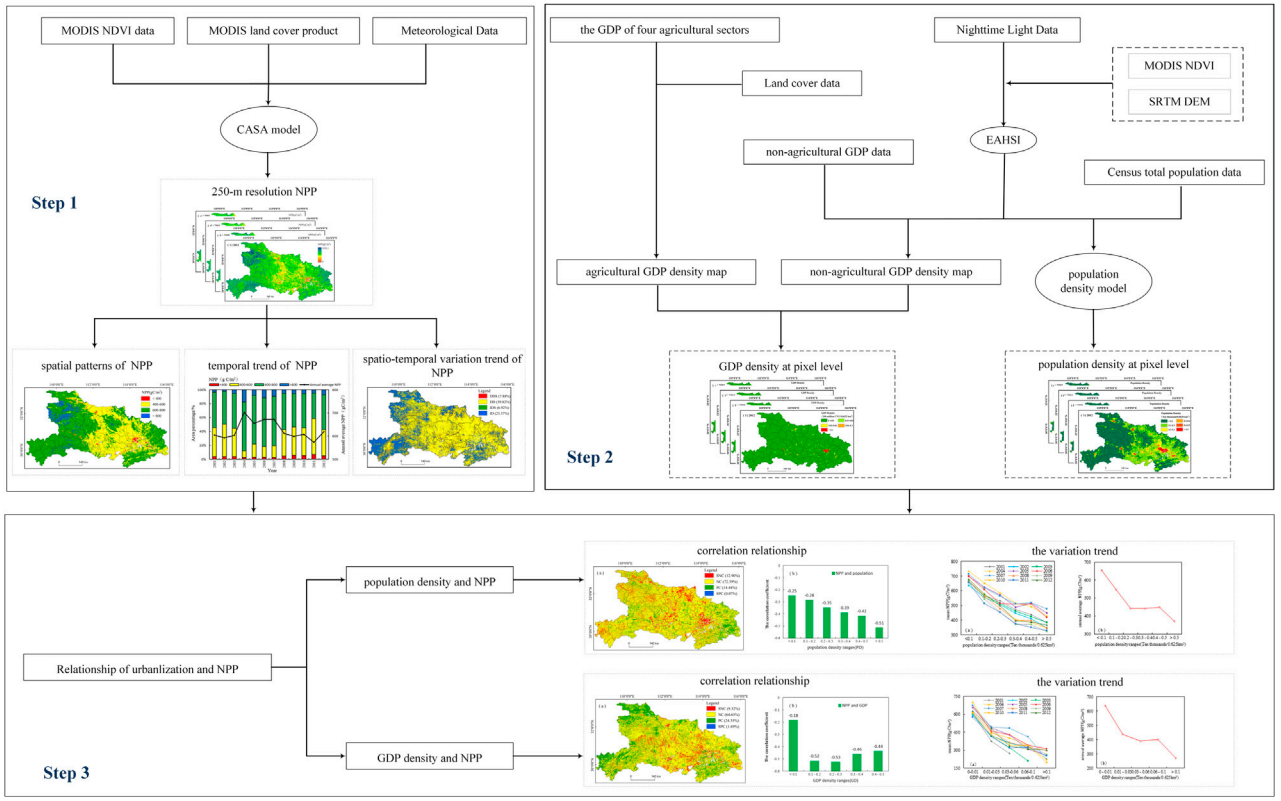


**FIGURE 2 |** Methodological framework of this study.

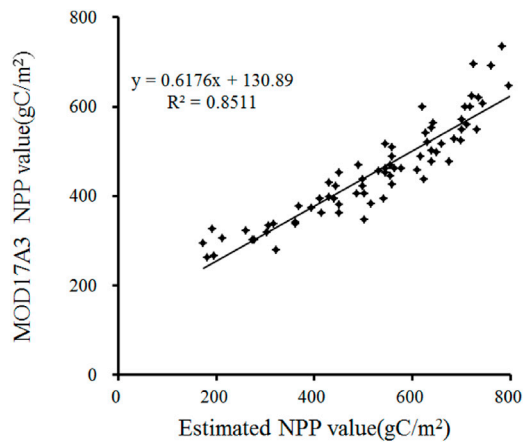


**FIGURE 3 |** Correlation between the estimated NPP values and MOD17A3 NPP values.

spatial resolution. After that, the average NPP values estimated by the CASA model for different land cover types were calculated and compared with the MOD17A3 NPP. The linear regression analysis results between the NPP estimates based on the CASA model and MOD17A3 NPP products are shown in **Figure 3**. A strong correlation was observed between them; the average relative error was 19.52%, and the correlation coefficient was 0.85. The results calculated in this article are similar to those of the MOD17A3 NPP products. Additionally, the estimated results of specific cities in Hubei Province can also be compared with those observed in previous studies. For example, the average inter-annual NPP of the evergreen needleleaf forest in Wuhan in our study was 578.06 g C/m$^2$, which is similar to the value of 582.4 g C/m$^2$ based on historical data as estimated in Zhang et al, (2011). Therefore, the CASA model in our study is practical and applicable for calculating NPP in Hubei Province.

## Error Analysis of the Population Density Map

The NTL, NDVI, DEM, and census population data at the county level were used to generate the spatial population density maps of Hubei Province with a resolution of 250 m from 2001 to 2012 based on the population spatial model mentioned in the *Population Density Mapping* section. The cumulative DN values of the EAHSI at the county level were input into the regression with the corresponding population of 41 counties selected randomly in Hubei Province. Then, the overall accuracies of the regression model were evaluated by calculating the MRE in the remaining 40 counties. **Table 1** presents the regression model among the cumulative EAHSI, population statistical data, and the results of accuracy assessment from 2001 to 2012. In the table, the $R^2$ represents the fitting degree of the regression equation of the population spatial model,

**TABLE 1 |** Population spatial model from 2001 to 2012 (ρ and β are the population density and Ln values of EAHSI, respectively).

| Year | Regression model | $R^2$ | MRE (%) |
|---|---|---|---|
| 2001 | ρ = 0.649×β-0.869 | 0.790 | 27.28 |
| 2002 | ρ = 0.658×β-0.943 | 0.793 | 28.06 |
| 2003 | ρ = 0.663×β-0.962 | 0.839 | 27.95 |
| 2004 | ρ = 0.678×β-1.072 | 0.820 | 26.73 |
| 2005 | ρ = 0.664×β-1.259 | 0.654 | 28.86 |
| 2006 | ρ = 0.695×β-1.291 | 0.867 | 25.82 |
| 2007 | ρ = 0.663×β-0.982 | 0.877 | 26.93 |
| 2008 | ρ = 0.653×β-1.097 | 0.891 | 27.81 |
| 2009 | ρ = 0.664×β-1.144 | 0.898 | 26.84 |
| 2010 | ρ = 0.645×β-1.002 | 0.913 | 26.35 |
| 2011 | ρ = 0.651×β-1.093 | 0.899 | 26.77 |
| 2012 | ρ = 0.649×β-1.049 | 0.901 | 26.11 |

**TABLE 2 |** Non-agricultural GDP spatial model from 2001 to 2012 (ρ and β are the GDP density and Ln values of EAHSI, respectively).

| Year | Regression model | $R^2$ | MRE (%) |
|---|---|---|---|
| 2001 | ρ = 0.6622×β+0.0344 | 0.858 | 26.58 |
| 2002 | ρ = 0.6664×β+0.0031 | 0.851 | 26.98 |
| 2003 | ρ = 0.6558×β+0.1145 | 0.819 | 27.44 |
| 2004 | ρ = 0.6699×β+0.4443 | 0.808 | 28.65 |
| 2005 | ρ = 0.6546×β+0.4419 | 0.828 | 28.40 |
| 2006 | ρ = 0.6631×β+0.5498 | 0.811 | 27.74 |
| 2007 | ρ = 0.6502×β+0.511 | 0.826 | 28.87 |
| 2008 | ρ = 0.6421×β+0.6246 | 0.830 | 27.53 |
| 2009 | ρ = 0.6377×β+0.8756 | 0.842 | 25.54 |
| 2010 | ρ = 0.6688×β+0.9583 | 0.843 | 26.40 |
| 2011 | ρ = 0.6658×β+1.0782 | 0.808 | 29.01 |
| 2012 | ρ = 0.6622×β+0.0344 | 0.834 | 26.48 |

and the values were all relatively large over the 12 study years. Their values were all above 0.79, and the highest value occurred in 2012. The excellent fitting effect of the model indicates that the night light data can well reflect the spatial distribution of the population. For the accuracy of the model, all the MRE values were less than 30%, indicating that the overall simulation error is small during the period from 2001–2012. In addition, the error in 2006 was the smallest whereas the error in 2005 was the largest, with MRE values of 25.82 and 28.86%, respectively.

### Error Analysis of the GDP Density Map

The spatialization process and error analysis of non-agricultural GDP density were similar to those of the population density. **Table 2** presents the regression model between the cumulative EAHSI and GDP statistical data and the results of the accuracy assessment from 2001 to 2012. The table shows that the determination coefficients were all relatively large with values above 0.80 during the period from 2001 to 2012. The excellent fitting effect of the model indicates that the night light data can well reflect the spatial distribution of non-agricultural GDP. For the accuracy of the model, all the values of MRE were less than 30%, indicating that the overall simulation error was small from 2001 to 2012.

## Spatiotemporal Variation of NPP

In this section, the long-term characteristics of NPP in Hubei Province were evaluated from three aspects: spatial patterns, temporal variations, and the variation trend of NPP.

### Spatial Patterns of Mean Annual NPP

In order to conveniently describe the distribution of NPP, the degree of NPP can be divided into four different grades with red, yellow, blue, and green, which mean very lower (NPP <400 g C/$m^2$), lower (400 < NPP < 600 g C/$m^2$), middle (600 < NPP < 800 g C/$m^2$), and higher (NPP >800 g C/$m^2$), respectively. According to the land cover type product MCD12Q1 in Hubei Province, the main land cover types are ENF, EBF, DBF, MF, grassland, wetland, cropland, urban, and water, respectively. Except for water, all of the land cover types had the influence on NPP. The spatial pattern of the mean annual NPP from 2001–2012 in Hubei Province is shown in **Figure 4A**, and the land cover types and mean NPP are shown in **Figure 4B**. As shown, the western part of Hubei has a high altitude, and the main land cover types are woodland (ENF, EBF, DBF, and MF) and grassland, which can be seen as the higher NPP grade areas. Woodland and grassland accounted for 63.78% of the study area, and the mean annual NPP value was more than 500 g C/$m^2$. Among them, the mean annual NPP values of EBF and DBF were both more than 800 g C/$m^2$, which were mainly distributed in the northwest of Hubei. East Hubei was the middle NPP area. There are three main land cover types, including cropland, little woodland, and grassland. Due to the hilly region, the mean annual NPP value was general lower than that of west Hubei. Central Hubei, especially in the south central region, is the Middle-Lower Yangtze Plain. It presents a flat terrain and concentrated population. The main land cover types are cropland, wetland, and urban. The mean annual NPP values of wetland and urban land were both lower than 500 g C/$m^2$. Therefore, the very lower and lower grade NPP values were both distributed in this region. In addition, the different land cover types had a different combination of four NPP grades. **Figure 4C** explains the percentage of four NPP grades according to each land cover type. In the higher grade, EBF and DBF showed higher NPP percentages with 83.9 and 63.8%, respectively. In the middle grade, MF and grassland were the mainly distributed land cover types with 83.9 and 81.7%. In the lower grade, the proportions of wetland, cropland, ENF, and urban were higher than those of others, which were both more than 50%. In the very lower grade, urban and wetland were accounted for 37.7 and 25.9%, respectively.

### Temporal Variations of NPP

The temporal variations of the annual average NPP of Hubei Province from 2001 to 2012 are shown in **Figure 5**. Generally, the annual NPP varied from 573.51 g C/$m^2$ to 701.85 g C/$m^2$ over the past 12 years, with the highest in 2004 and the lowest in 2011. The change in NPP can be divided into two sub-periods throughout the period. NPP showed an increasing trend from 2001 to 2004 (32.34 g C/$m^2$ yr), followed by a wavelike decrease from 2004 to 2012 (11.30 g C/$m^2$ yr). **Table 3** lists the different changes for the four grades. In the very lower NPP areas (NPP <400 g C/$m^2$),

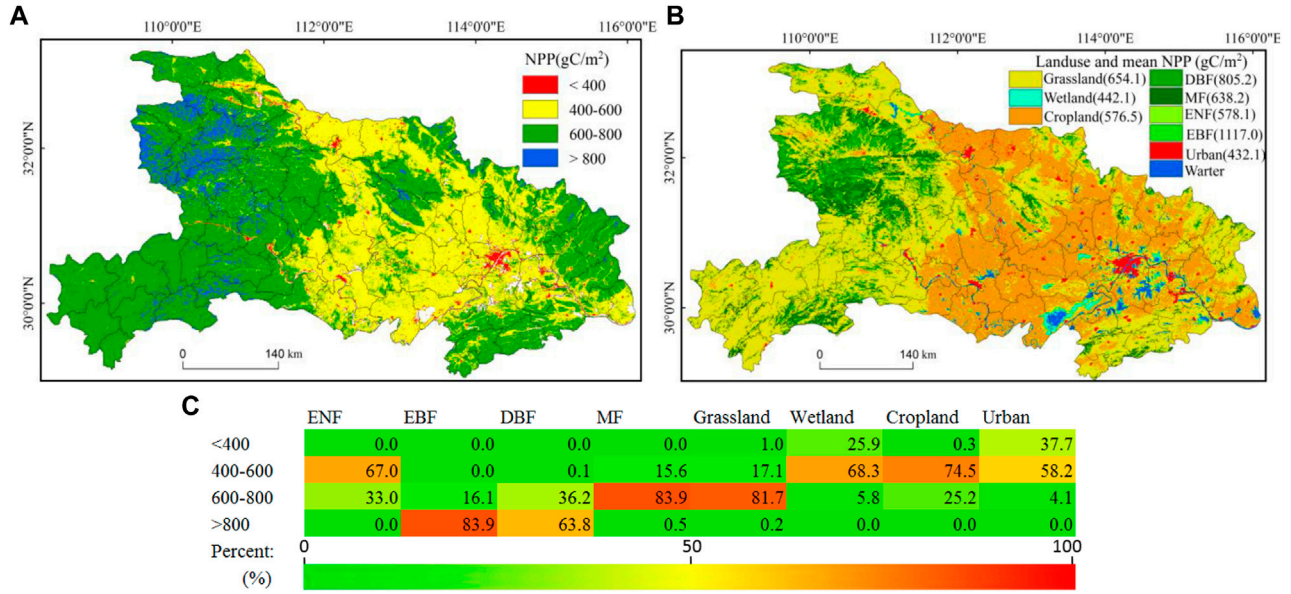


**FIGURE 4 | (A)** Spatial distribution of the mean annual NPP; **(B)** land cover types of Hubei Province and mean NPP; and **(C)** percentage of four NPP grades for eight land cover types.

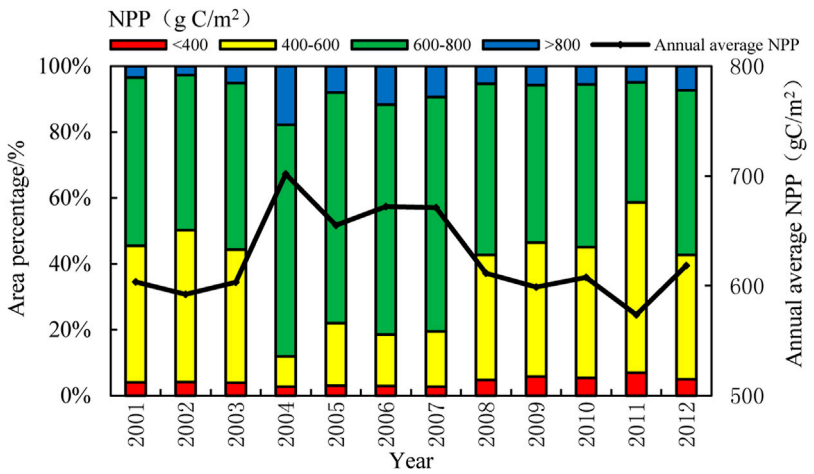


**FIGURE 5 |** Temporal variations of the annual average NPP.

**TABLE 3 |** Change of NPP for the four grades.

| NPP grade (g C/m$^2$) | Change of NPP (g C/m$^2$) | Main land cover type | Percentage of area in 2001 (%) | Percentage of area in 2012 (%) |
|---|---|---|---|---|
| <400 | −18.58 | Urban | 32.62 | 37.87 |
| 400–600 | 10.60 | Cropland | 55.67 | 58.42 |
| 600–800 | 5.44 | Grassland | 74.67 | 68.69 |
| | | Cropland | 31.33 | 34.93 |
| >800 | 13.86 | DBF | 91.72 | 82.70 |
| | | Grassland | 8.09 | 17.00 |

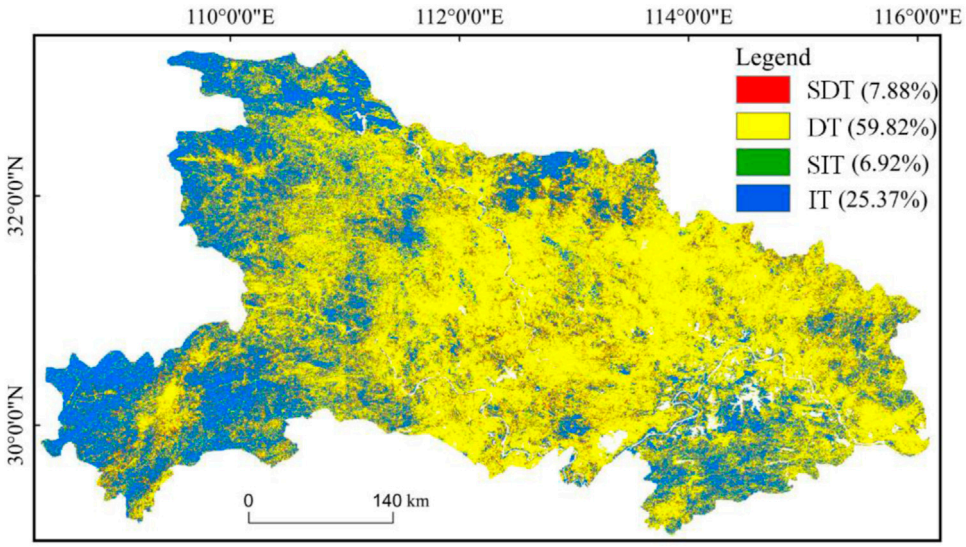


**FIGURE 6 |** Change trends in annual NPP within Hubei Province between 2001 and 2012.

there was a negative change with a value of −18.58 g C/m$^2$ from 2001 to 2012. The main reason for the decline was that more and more cropland and grassland are converted into urban land with the development of the economy and the acceleration of urbanization. The percentage of urban area was increased by 5.25% during the period, and approximately 90.36% of the total urban area has negative change rates on NPP, which led to a significant NPP loss in time and space. In contrast, the different positive changes occurred when the NPP value exceeded 400 g C/m$^2$. In the lower NPP areas (400 g C/m$^2$ < NPP < 600 g C/m$^2$), there was a positive change with 10.60 g C/m$^2$. The main land cover type is the cropland, and the percentage area increased from 55.67 to 58.42% from 2001 to 2012. In the middle NPP areas (600 g C/m$^2$ < NPP < 800 g C/m$^2$), the NPP value has increased by 5.44 g C/m$^2$. The grassland is the main land cover type. Although the area of grassland has been reduced little from 74.67 to 68.69%, the percentage of cropland area increased from 31.33 to 34.93%, which still kept the NPP in an increased state. In the higher NPP areas (NPP > 800 g C/m$^2$), the NPP values have increased by 13.86 g C/m$^2$. The main land cover type is DBF decreased from 91.72 to 82.70% from 2001 to 2012. But, the percentage of grassland area increased from 8.09 to 17.00% from 2001 to 2012. The high increase rate was maintained due to the significant NPP correlation of the DBF and grassland.

## The Variation Trend of NPP

The slope of the equation obtained by linear least-square fitting of long-term NPP series can show the development trend of NPP over 12 years. As shown in **Figure 6**, there are four different colors (red, yellow, green, and blue) representing the variation trends, including the significant decreasing trend (SDT, $p$ >0.05), decreasing trend (DT, $p$ <0.05), significant increasing trend (SIT, $p$ >0.05), and increasing trend (IT, $p$ <0.05). The area with DT of annual NPP accounted for 59.82% of Hubei Province and was distributed roughly in the central area of the study region. The area with an IT of annual NPP was mainly distributed in west Hubei and accounted for 25.37%. Only 7.88 and 6.92% of the study area showed SDT and SIT, respectively. Therefore, the number of pixels of the two variation trends is too small to find in the figure.

**TABLE 4 |** Rate of NPP change for each land cover type.

| Land cover type | NPP change rate(g C/m$^2$ y r) | DT (%) | SDT (%) | IT (%) | SIT (%) |
|---|---|---|---|---|---|
| ENF | −9.51 | 75.36 | 3.08 | 18.70 | 2.87 |
| EBF | 37.38 | 4.11 | 1.58 | 90.19 | 4.11 |
| DBF | 4.03 | 31.62 | 7.13 | 54.24 | 7.02 |
| MF | −2.64 | 58.78 | 7.86 | 25.89 | 7.48 |
| Grassland | −1.73 | 54.02 | 8.55 | 29.51 | 7.91 |
| Wetland | −9.95 | 81.44 | 3.90 | 11.59 | 3.07 |
| Cropland | −3.52 | 73.66 | 7.71 | 12.78 | 5.85 |
| Urban | −10.63 | 87.28 | 3.08 | 7.20 | 2.44 |

Different land cover types had different responses to NPP, which was the major reason for the variation trend. The rate of NPP change for each land cover type is listed in **Table 4**. It is found that there were only two land cover types with positive change rates, EBF (37.38 g C/m$^2$ yr) and DBF (4.03 g C/m$^2$ yr). The rest of land cover types all had negative change rates. The order of the decreasing rate from high to low was as follows: urban (-10.63 g C/m$^2$ yr), wetland (−9.95 g C/m$^2$ yr), ENF (−9.51 g C/m$^2$ yr), cropland (−3.52 g C/m$^2$ yr), MF (−2.64 g C/m$^2$ yr), and grassland (−1.73 g C/m$^2$ yr). Among all land cover types, grassland showed the most significant SIT with 7.91% and the most significant SDT with 8.55%. Moreover, the largest percentage of DT and IT occurred in urban areas with 87.28% and EBF with 90.19%. The main land cover types are cropland, grassland, and MF in the area with DT of annual NPP. They all had the negative change rates, and the percentages of DT were both more than 50% in these

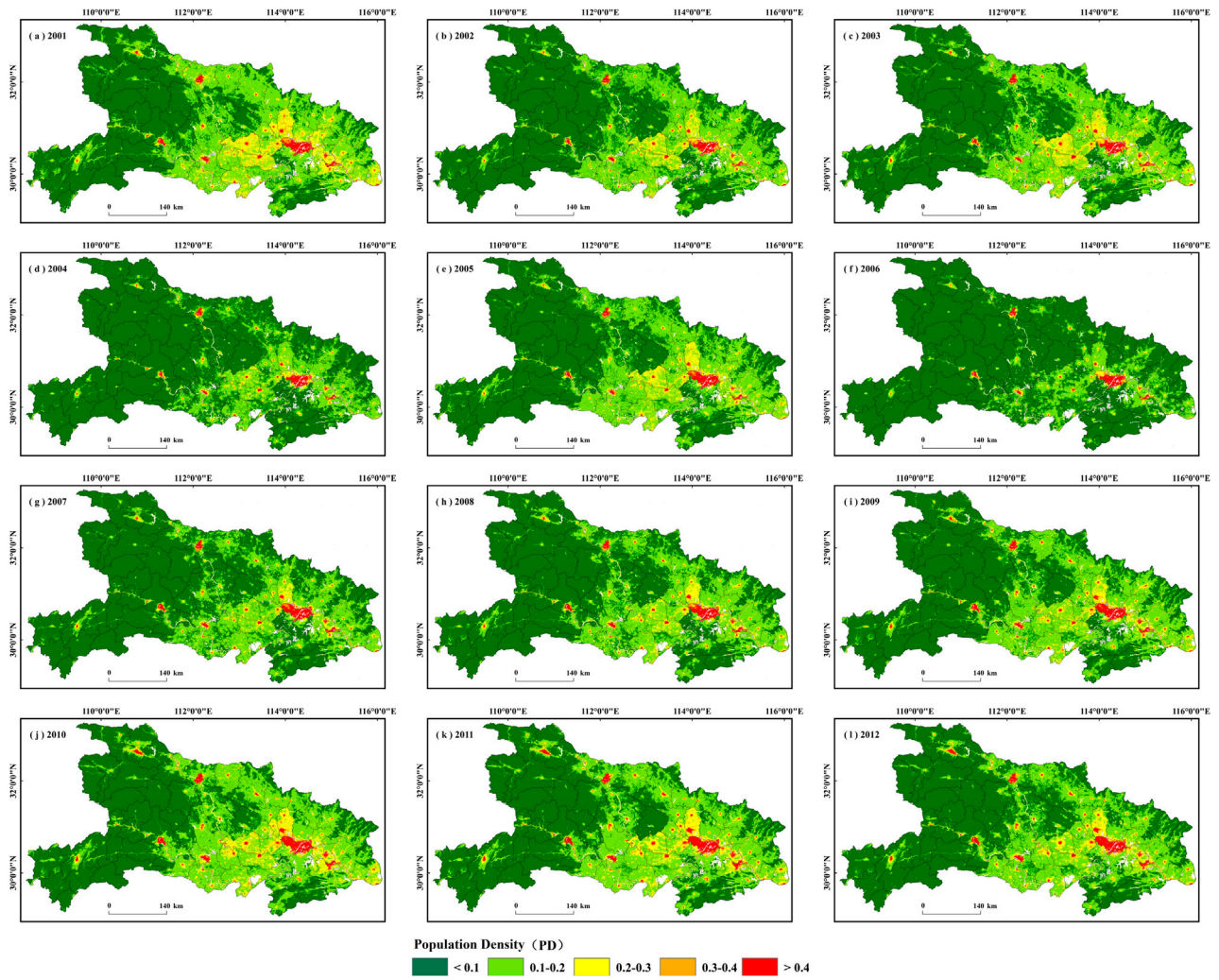


**FIGURE 7 |** Population density maps with a 250 m × 250 m grid **(A)**–**(L)** the different maps from 2001 to 2012.

areas, which caused the decreasing trend. In the area with IT of annual NPP, the main land cover types are EBF, DBF, and grassland. There were higher positive change rates in EBF and DBF, which caused the increasing trend on the whole.

## Correlation Between Urbanization and NPP

The urbanization process has an important impact on NPP variation. Population growth and economic development, a representation of the agglomeration effects, are highly correlated with urbanization. In this section, the relationships between NPP and the two urbanization indicators were described.

### Population Density Map

The spatial distributions of the population density for Hubei Province from 2001 to 2012 are presented in **Figure 7**. The unit of population density is defined as PD = 10,000/0.0625 $km^2$ because the resolution of the population density map is 250 m (0.25 km). The sparsely populated areas (population density less than 0.1 PD) were mainly distributed in the western areas of Hubei Province, such as Shiyan, Enshi, and Shennongjia Forestry District, while densely populated areas (population density more than 0.4 PD) were mainly in the highly urbanized regions, such as Wuhan City, Xiangyang City, Yichang City, and Jingzhou City. The population of sparsely populated areas increased from 22.87 to 47.87% from 2001 to 2004 and continued to decline after 2004, accounting for only 28.37% in 2012. The population in the densely populated areas decreased from 2001 to 2004 and increased steadily after 2004, accounting for 10.97% in 2012. In general, from 2001 to 2012, the proportions of the population in sparsely populated areas were large but showed a decreasing trend, whereas the population in densely populated areas increased steadily.

### Correlation Between Population and NPP

With the change in population density, the NPP values would change. **Figure 8A** shows the change in NPP in different population density ranges from 2001 to 2012. Even though the

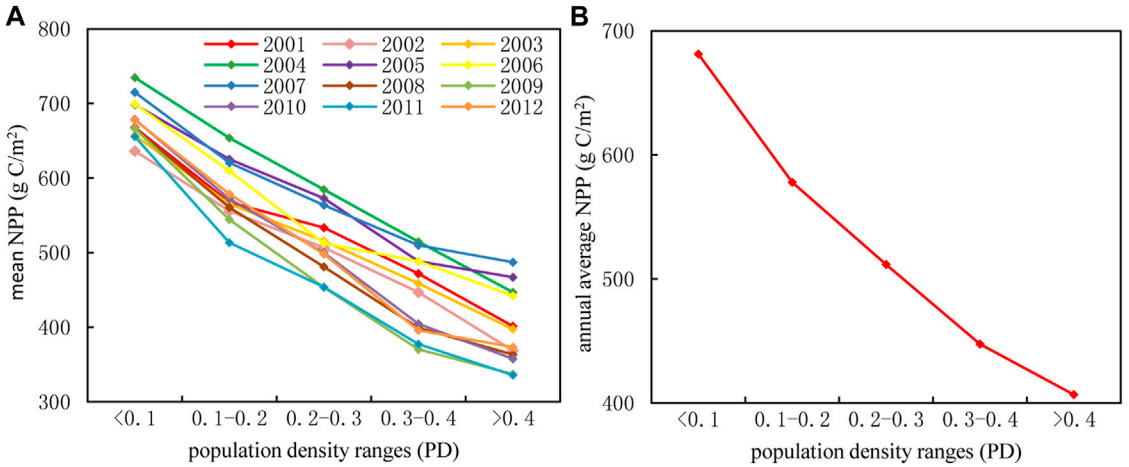


**FIGURE 8 | (A)** NPP change in different population density ranges from 2001 to 2012 and **(B)** annual average NPP change in different population density ranges.

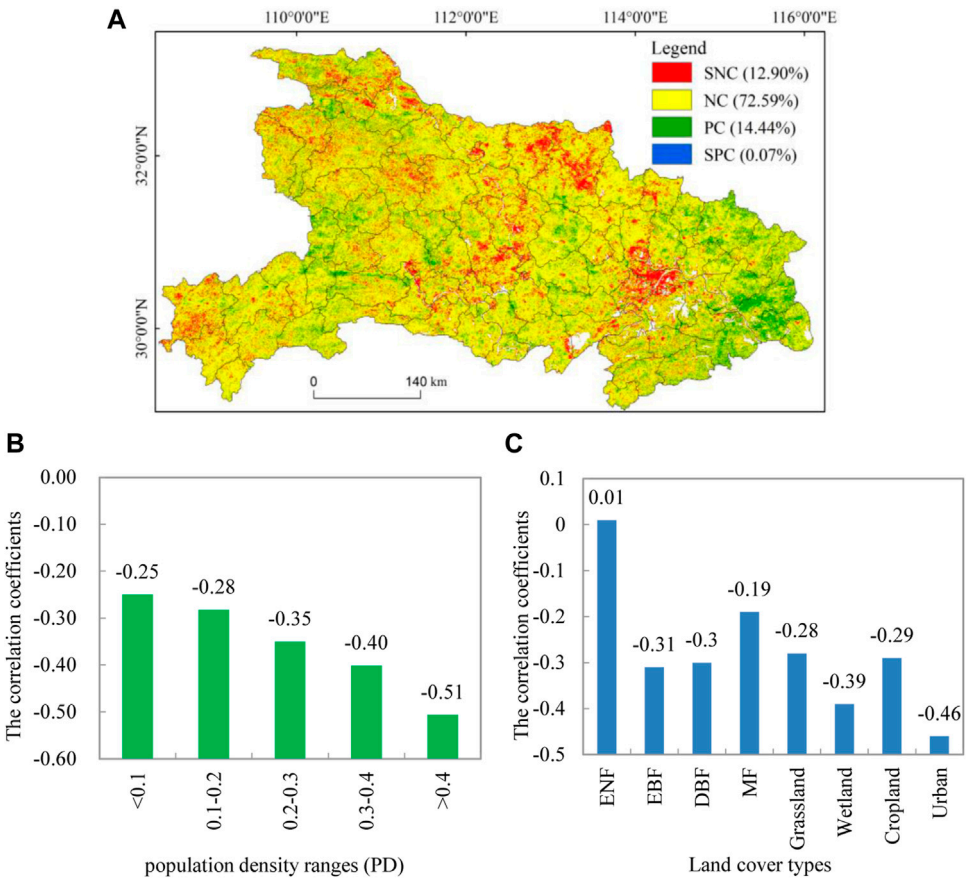


**FIGURE 9 | (A)** Spatial distribution of the correlations between population and annual NPP; **(B)** correlation coefficients between population and annual NPP for the different population density ranges; and **(C)** correlation coefficients between NPP and population for different land cover types.

population densities of 12 years were quite different, the trends in NPP were the same. With an increase in population density, the average NPP value decreased. **Figure 8B** shows the annual average NPP changes during the period. It is found that the average NPP value was the minimum when the population density was more than 0.4 PD.

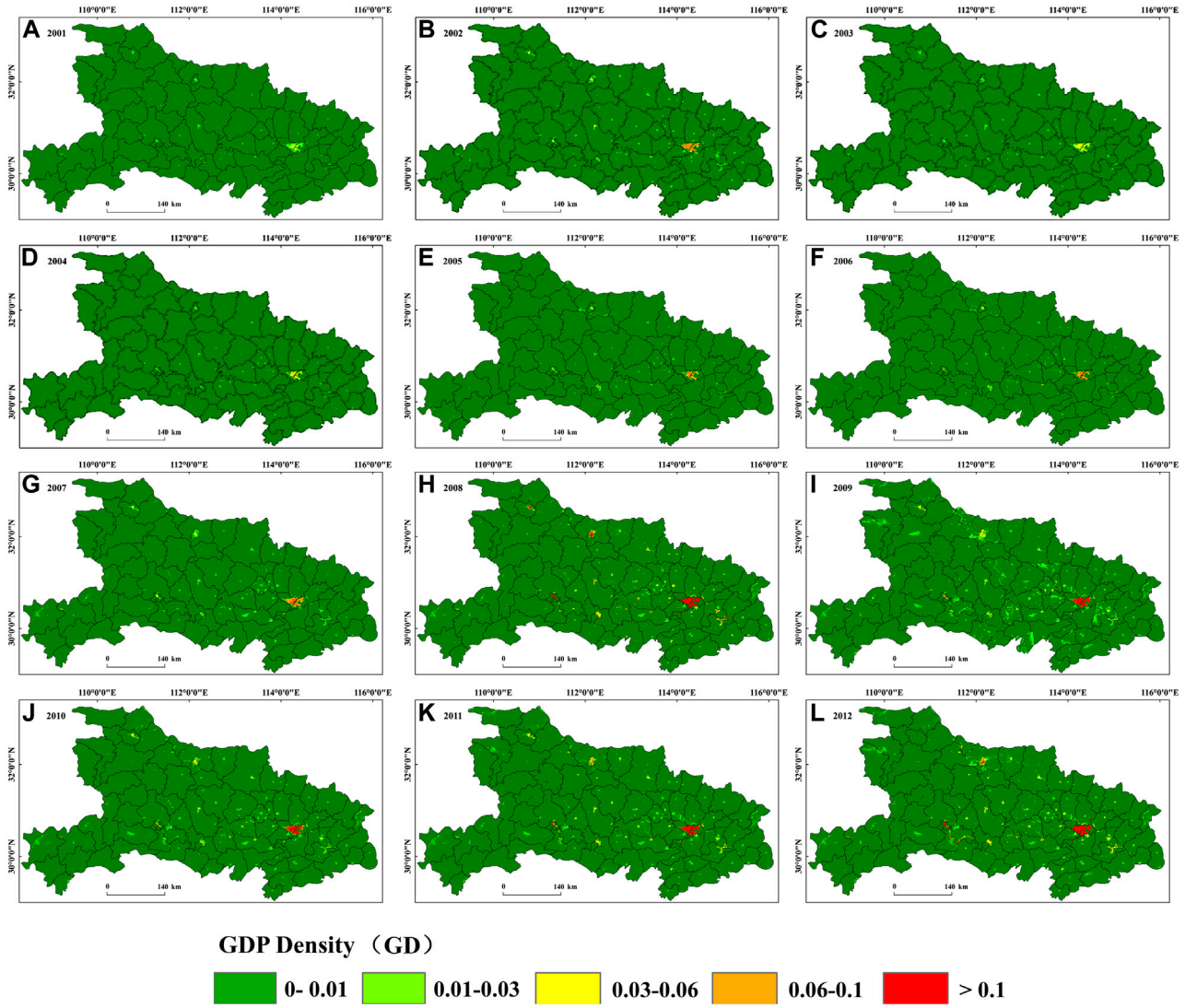


**FIGURE 10 |** GDP density maps with a 250 m × 250 m grid. **(A)**–**(L)** the different maps from 2001 to 2012.

To further investigate the correlation between NPP and population density, the correlation coefficient is calculated and analyzed from two aspects. First, the spatial pattern of the correlation coefficient is shown in **Figure 9A**. The negative correlation (NC) is labeled as yellow, significant negative correlation (SNC; $p$ <0.05) is labeled as red, positive correlation is labeled as green, and significant positive correlation (SPC; $p$ <0.05) is labeled as blue. The area with NC between NPP and population accounted for almost 85.49% of Hubei Province, of which approximately 15.08% showed SNC. The significant negative relationship was concentrated in the center of Hubei, which was mainly covered by cropland and urban areas. With the increase of population density, the negative correlation coefficients become more significant. The tendency and process of the mass population gathering toward big cities that leads to land-use/cover change. It is found that more and more cropland and woodland (including EBF, DBF, and MF) are converted into urban land during the period. This is probably the main reason for the decrease in NPP caused by population growth. Moreover, areas with PC accounted for almost 14.51% of the study region, and approximately 0.48% showed SPC. These areas were mainly distributed in the western Hubei mountains and eastern Hubei Province. Second, the main considerations and affecting factors of the correlation coefficient were provided. **Figure 9B** describes that the correlation coefficient is different when the population density ranges. The coefficients were all negative that shows NC and SNC were dominant in the five population densities. The negative correlations become larger and larger with increased population density. When the population density was more than 0.4 PD, the negative correlation coefficient with the population was the maximum. Besides, correlation coefficients were different for different land cover types, which could be seen as indirect impacts. As shown in **Figure 9C**, the negative correlation

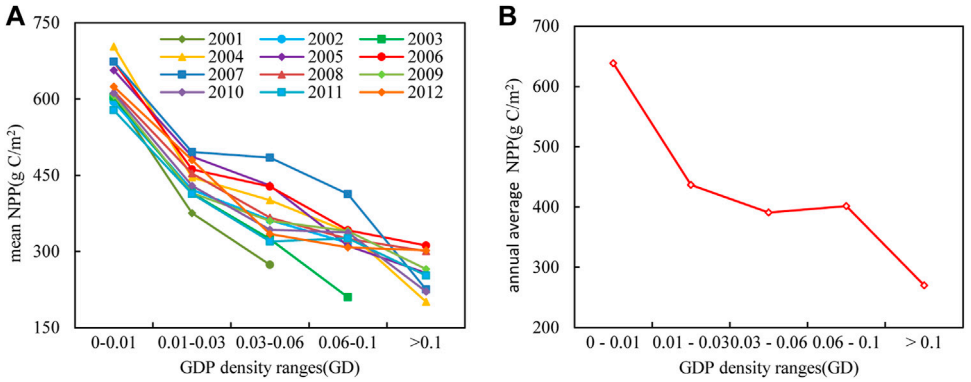


**FIGURE 11 | (A)** NPP and GDP density from 2001 to 2012 and **(B)** annual average NPP and its regression slope with GDP density.

coefficient between NPP and population was the largest in urban, with the mean value of −0.46. The negative correlation coefficients of other land-use types were smaller. The order from high to low was mainly as follows: wetland (−0.39), EBF (−0.31), DBF (−0.30), cropland (−0.29), grassland (−0.28), and MF (−0.19). Although there was a positive correlation in ENF with a mean value of 0.01, it had little influence on NPP. Therefore, urban had more importance in influencing NPP than other land cover types.

## GDP Density Map

The spatial distributions of the GDP density for Hubei Province from 2001 to 2012 are presented in **Figure 10**. The unit of GDP density is defined as GD = 100 million CNY/0.0625 $km^2$. As shown in the figure, most of the GDP contributions were from regions with a concentrated population and a high level of economic development, especially from Wuhan City, which had a high level of urbanization. Areas with a GDP density greater than 0.1 GD mainly occurred in Wuhan City. In addition, the GDP density in most areas of Hubei Province was in the range of 0–0.01 D. GDP density ranging from 0 to 0.01 GD accounted for 95.31% of the study region in 2001, while in 2012 it only accounted for 76.94%. Since 2004, the GDP density had exceeded 0.1 GD. The proportions of GDP density greater than 0.1 GD increased from 0.06% in 2001 to 2.70% in 2012.

## Correlation Between Population and GDP With NPP

Similarly, the correlation between NPP and GDP is described as follows: **Figure 11A** shows the variation trend of the annual average NPP with GDP density. With the increase of GDP density, the average NPP value decreased. Therefore, the higher the GDP density, the greater the reduction rate of NPP. **Figure 11B** shows the annual average NPP changes during the period. The average NPP value was the minimum when the population density was more than 0.1 GD.

The correlation coefficient was calculated and analyzed from two aspects. First, the spatial pattern of the correlation coefficient between GDP and NPP is shown in **Figure 12A**. The areas with negative correlation (NC) between NPP and GDP accounted for almost 73.97% of Hubei Province, of which approximately 12.6% showed a significant negative correlation (SNC; $p$ <0.05). The areas with a positive correlation (PC) between NPP and GDP accounted for almost 36.03% of the study region, and approximately 6.48% showed a significant positive correlation (SPC; $p$ <0.05). Areas with a negative correlation between NPP and GDP were mainly located in central Hubei Province, while the areas with positive correlations were mainly distributed in northwest, southwest, and southeast Hubei Province. Second, the affecting factors of the correlation coefficient are analyzed, including the GDP density and land cover types. The correlation coefficients for the different GDP density ranges are described in **Figure 12B**. The trend of the negative correlation was not the same as the one between NPP and population. In the beginning, it increased with the continuous increase of GDP density. When the GDP density was 0.2–0.3 GD, the negative correlation coefficient reached the maximum. After that, the negative correlation between NPP and GDP was not significant, which means that the growth of GDP might lead to the increase of NPP in some regions under a certain threshold. For example, the economic growth can further improve management capacity with good policies. Artificial management, such as irrigation and planting, resulted in improved vegetation coverage and increased NPP. Similar to NPP and population, correlations between NPP and GDP were also different for different land cover types. Urban had more importance in influencing the relationship between NPP and GDP than other land cover types. In **Figure 12C**, the cropland, wetland, ENF, and MF were all greater than −0.3. There was a positive correlation in EBF with a mean value of 0.26. But, its area was so small that it was almost negligible.

## Limitations and Future Research

Due to urbanization being a complex process, the interaction between terrestrial ecosystems and socioeconomic processes is also relatively complicated. The process of population urbanization is different in different stages of urbanization, so is economic urbanization. The relationship of NPP and urbanization needs to be studied over a longer period of time. Some researchers have indicated that the negative impacts of urbanization on vegetation gradually weaken with the continuous

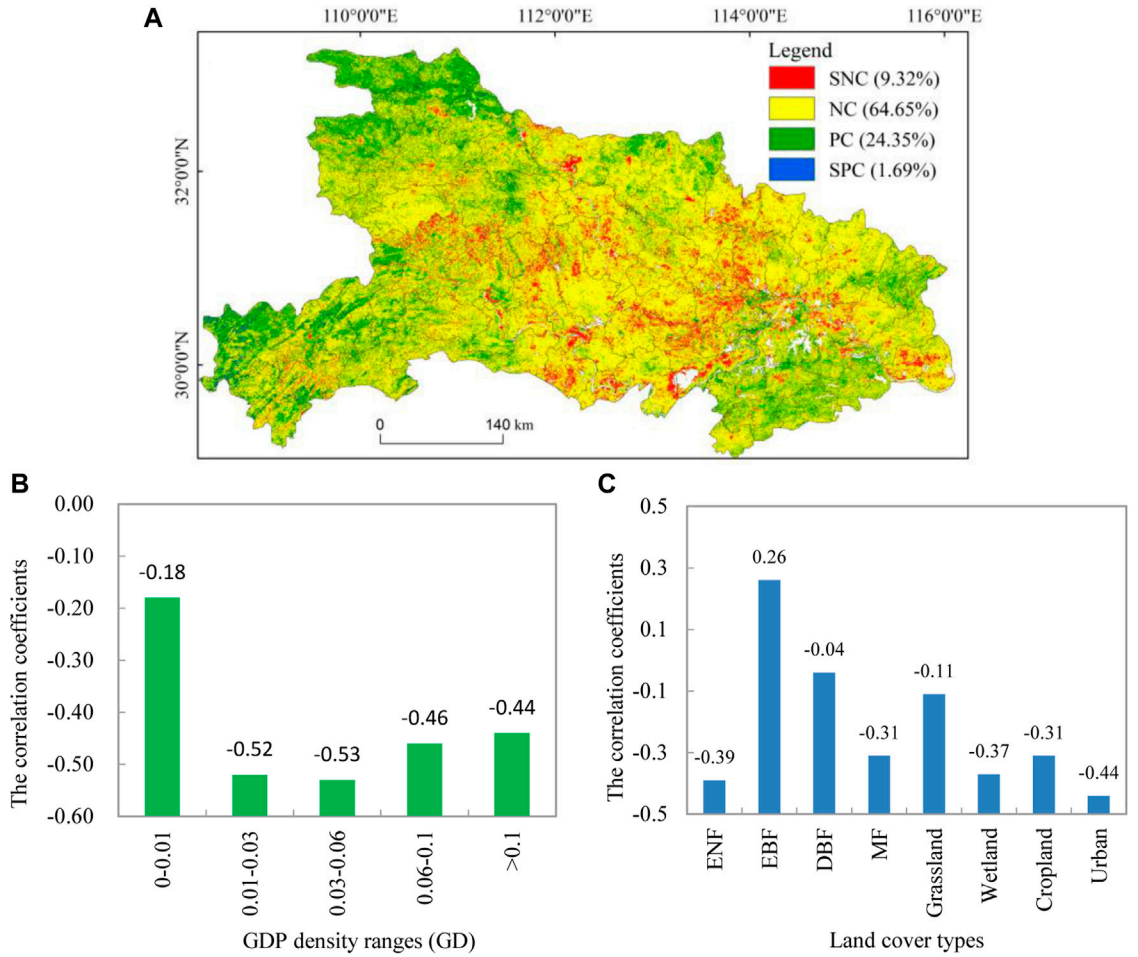


**FIGURE 12 | (A)** Spatial distribution of the correlations between GDP and annual NPP; **(B)** correlation coefficients between GDP and annual NPP for the different GDP density range; and **(C)** correlation coefficients between NPP and GDP for different land cover types.

improvement of urbanization levels, and the positive impacts of urbanization on vegetation will be increasingly obvious. It is because that some anthropogenic activities have led to an increase of vegetation cover in urban areas, such as irrigation and tree transplantation. This means that urbanization unavoidably leads to the degradation of vegetation and the decrease of vegetation productivity. However, cities may further strengthen ecological management capacity as the economy grows. These measures can make a great contribution to the vegetation in urban areas. In addition, the population is gathering toward the city with the expansion of the city size. Population migration can improve the vegetation conditions in rural areas with the increase of urbanization levels. Although 12 years were analyzed to determine the impacts of urbanization on vegetation, the different stages of urbanization cannot be fully described. Therefore, in future studies, vegetation NPP should be estimated and monitored over a longer study period to explore the effects of population and GDP on NPP in different stages of urbanization.

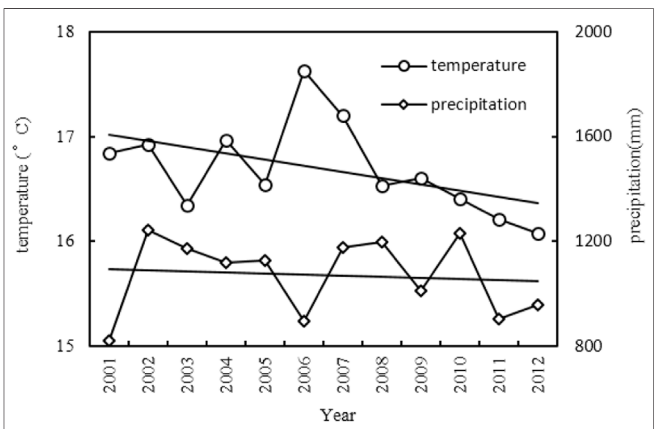


**FIGURE 13 |** Inter-annual variations of temperature and precipitation of Hubei Province from 2001 to 2012.

Moreover, climate change is also a major controlling factor in the response of NPP. Research shows that the temperature had a significant decreasing trend during the period from 2001–2012, which was similar to the trends of the annual NPP (**Figure 13**). Precipitation also tended to decrease but was not significant. The decreasing trend in temperature and precipitation changes the environmental conditions of vegetation growth, which further affects the vegetation distribution and vegetation net primary productivity. The two factors need to be further investigated.

## CONCLUSION

In this study, the NPP in Hubei Province during the period from 2001 to 2012 was calculated, and the spatiotemporal dynamics of NPP and its relationships with the urbanization indicators (population and GDP) were investigated. The main conclusions can be summarized as follows: 1) The distribution pattern of NPP is as follows: northwest Hubei has a high altitude, and the main land cover type is woodland with high vegetation coverage and little human activities. Therefore, there were higher NPP values in northwest Hubei. The urban areas, which have an extensive distribution of urban and built areas, showed the lowest NPP values. In addition, the land cover type had significant influences on the spatial distribution of NPP. 2) During the study period, the average NPP value increased in high NPP areas. Because the inter-annual variation of NPP in DBF, the main land cover type in this region, was positive. On the contrary, the average NPP value decreased in low NPP areas. The urban areas continued to expand, but the inter-annual variation of NPP was negative in urban areas. From 2001 to 2012, NPP decreased by 18.58 g C/$m^2$ in low NPP areas. The losses of NPP in urban areas are continuing and evident. 3) Population and GDP density are the typical indicators of anthropogenic activities, which can play an important role in the distribution and dynamics of NPP. During the study period, there was a negative correlation between NPP, population, and GDP. On the whole, the highest values of negative correlation coefficients were found in urban areas and the lowest in woodlands. The expansion of the built-up land in the middle and east can decrease the size of green areas and reduce the productivity of vegetation. Meanwhile, the remaining woodlands are mostly distributed in the west. The estimated NPP values were likely to remain unchanged with the urbanization developments. In addition, the impact of human activity on NPP was different depending on the intensity of human activity. With the increase of population density, the negative correlation coefficients between population and annual NPP become larger. But, the correlations between NPP and GDP were not the same as the correlation between NPP and population. The negative correlation coefficients between GDP and NPP increased first and then decreased with the continuous increase of GDP density. This indicates that the impact of urbanization on NPP is not completely negative when GDP reaches a certain threshold.

## DATA AVAILABILITY STATEMENT

The original contributions presented in the study are included in the article/supplementary material; further inquiries can be directed to the corresponding author.

## AUTHOR CONTRIBUTIONS

KW and CZ contributed to conceptualization; KW and CZ contributed to methodology; CZ contributed to writing—original draft preparation; and KW, CZ, YZ, and YX contributed to writing—review and editing. All authors have read and agreed to the published version of the manuscript.

## FUNDING

The research was supported by the Global Change and Air-Sea Interaction II under Grant GASI-01-DLYG-WIND01 and in part by the National Defense Pre-Research Foundation of China during the 13th Five-Year Plan Period: the High Spectral Resolution Infrared Space-Based Camera and the Applied Technology under Grant D040104. this work was also supported in part by the National Natural Science Foundation of China under Grant 62071438.

## REFERENCES

Buyantuyev, A., and Wu, J. (2009). Urbanization Alters Spatiotemporal Patterns of Ecosystem Primary Production: A Case Study of the Phoenix Metropolitan Region, USA. *J. Arid Environ.* 73, 512–520. doi:10.1016/j.jaridenv.2008.12.015

Chai, J., Wang, Z., Yang, J., and Zhang, L. (2019). Analysis for Spatial-Temporal Changes of Grain Production and farmland Resource: Evidence from Hubei Province, central China. *J. Clean. Prod.* 207, 474–482. doi:10.1016/j.jclepro.2018.10.008

Chen, W., Huang, C., Wang, L., and Li, D. (2018). Climate Extremes and Their Impacts on Interannual Vegetation Variabilities: a Case Study in Hubei Province of Central China. *Remote Sens.* 10, 477. doi:10.3390/rs10030477

Chu, D., Shen, H., Guan, X., Chen, J. M., Li, X., Li, J., et al. (2021). Long Time-Series NDVI Reconstruction in Cloud-Prone Regions via Spatio-Temporal Tensor Completion. *Remote Sens. Environ.* 264, 112632. doi:10.1016/j.rse.2021.112632

Fang, Y., Tang, H., and Lin, D. (2000). *Global Ecology: Climate Change and Ecological Responses*, 18. Beijing and Heidelberg: China Higher Education Press and Springer-Verlag Press, 113–121.

Gao, Q., Li, X., and Yang, X. (2003). Responses of Vegetation and Primary Production in north-south Transect of Eastern China in Global Change under Land Use Constraint. *Acta Botan. Sin.* 45, 1274–1284.

Gao, Q., Li, Y., Wan, Y., Qin, X., Jiangcun, W., and Liu, Y. (2009). Dynamics of alpine Grassland NPP and its Response to Climate Change in Northern Tibet. *Clim. Change* 97, 515–528. doi:10.1007/s10584-009-9617-z

Guan, X., Chen, J., Shen, H., and Xie, X. (2021). A Modified Twoleaf Light Use Efficiency Model for Improving the Simulation of GPP Using a Radiation Scalar. *Agric. Meteorol.* 307, 108546. doi:10.1016/j.agrformet.2021.108546

He, J., Zhang, P., Jing, W., and Yan, Y. (2018). Spatial Responses of Net Ecosystem Productivity of the Yellow River Basin under Diurnal Asymmetric Warming. *Sustainability* 10, 3646. doi:10.3390/su10103646

Jiang, W., and Zeng, Y. (2019). Relationship between Urbanization and Economic Growth in Hubei Province. *Econ. Res. Guide* 7, 45–46+63.

Li, J.-c., and Cheng, K.-m. (2006). An Analysis of Dynamic Econometric Relationship between Urbanization and Economic Growth in China [J]. *J. Finance Econ.* 9, 19–30.

Li, H. (2019). Empirical Analysis on the Effect of Population Concentration and Urban Agglomeration on Economic Growth -- a Case Study of Chi- Na's Ten Largest Urban Agglomeration. *J. Henan Univ. (Soc. Sci.)* 59, 43–52.

Lin, A., Zhu, H., Wang, L., Gong, W., and Zou, L. (2016). Characteristics of Long-Term Climate Change and the Ecological Responses in central China. *Earth Interact.* 20, 1–24. doi:10.1175/ei-d-15-0004.1

Lu, D., Tian, H., Zhou, G., and Ge, H. (2008). Regional Mapping of Human Settlements in southeastern China with Multisensor Remotely Sensed Data. *Remote Sens. Environ.* 112, 3668–3679. doi:10.1016/j.rse.2008.05.009

Lu, D., Xu, X., Tian, H., Moran, E., Zhao, M., and Running, S. (2010). The Effects of Urbanization on Net Primary Productivity in southeastern China. *Environ. Manage.* 46, 404–410. doi:10.1007/s00267-010-9542-y

Luo, Z., Wu, W., Yu, X., Song, Q., Yang, J., Wu, J., et al. (2018). Variation of Net Primary Production and its Correlation with Climate Change and Anthropogenic Activities over the Tibetan Plateau. *Remote Sens.* 10, 1352. doi:10.3390/rs10091352

Peng, J., Li, Y., Tian, L., Liu, Y., and Wang, Y. (2015). Vegetation Dynamics and Associated Driving Forces in Eastern China during 1999-2008. *Remote Sens.* 7, 13641–13663. doi:10.3390/rs71013641

Piao, S., and Fang, J. (2003). Seasonal Changes in Vegetation Activity in Response to Climate Changes in China between 1982 and 1999. *Acta Geogr. Sin.* 1. doi:10.1007/BF02948883

Potter, C. S., Randerson, J. T., Field, C. B., Matson, P. A., Vitousek, P. M., Mooney, H. A., et al. (1993). Terrestrial Ecosystem Production: a Process Model Based on Global Satellite and Surface Data. *Glob. Biogeochem. Cycles* 7, 811–841. doi:10.1029/93gb02725

Potter, C., Klooster, S., Myneni, R., Genovese, V., Tan, P.-N., and Kumar, V. (2003). Continental-scale Comparisons of Terrestrial Carbon Sinks Estimated from Satellite Data and Ecosystem Modeling 1982-1998. *Glob. Planet. Change* 39, 201–213. doi:10.1016/j.gloplacha.2003.07.001

Potter, C., Klooster, S., Crabtree, R., Huang, S., Gross, P., and Genovese, V. (2011). Carbon Fluxes in Ecosystems of Yellowstone National Park Predicted from Remote Sensing Data and Simulation Modeling. *Carbon Balance Manage* 6, 3. doi:10.1186/1750-0680-6-3

Shang, E., Xu, E., Zhang, H., and Liu, F. (2018). Analysis of Spatiotemporal Dynamics of the Chinese Vegetation Net Primary Productivity from the 1960s to the 2000s. *Remote Sens.* 10, 860. doi:10.3390/rs10060860

Shen, L., Wang, H., Zhu, B., Zhao, T., Liu, A., Lu, W., et al. (2021). Impact of Urbanization on Air Quality in the Yangtze River Delta during the COVID-19 Lockdown in China. *J. Clean. Prod.* 296, 126561. doi:10.1016/j.jclepro.2021.126561

Solecki, W., Seto, K. C., and Marcotullio, P. J. (2013). It's Time for an Urbanization Science. *Environ. Sci. Pol. Sustain. Dev.* 55, 12–17. doi:10.1080/00139157.2013.748387

Song, G., Yu, M., Liu, S., and Zhang, S. (2015). A Dynamic Model for Population Mapping: a Methodology Integrating a Monte Carlo Simulation with Vegetation-Adjusted Night-Time Light Images. *Int. J. Remote Sens.* 36, 4054–4068. doi:10.1080/01431161.2015.1073862

Sun, W., Zhang, X., Wang, N., and Cen, Y. (2017). Estimating Population Density Using DMSP-OLS Night-Time Imagery and Land Cover Data. *IEEE J. Sel. Top. Appl. Earth Observ. Remote Sens.* 10, 2674–2684. doi:10.1109/jstars.2017.2703878

Tan, K., Zhou, S., Li, E., and Du, P. (2015). Assessing the Impact of Urbanization on Net Primary Productivity Using Multi-Scale Remote Sensing Data: a Case Study of Xuzhou, China. *Front. Earth Sci.* 9, 319–329. doi:10.1007/s11707-014-0454-7

Tao, J., Wu, W., and Liu, W. (2017). Spatial-Temporal Dynamics of Cropping Frequency in Hubei Province over 2001-2015. *Sensors* 17, 2622. doi:10.3390/s17112622

Wang, H., Li, X., Long, H., Gai, Y., and Wei, D. (2009). Monitoring the Effects of Land Use and Cover Changes on Net Primary Production: A Case Study in China's Yongding River basin. *For. Ecol. Manag.* 258, 2654–2665. doi:10.1016/j.foreco.2009.09.028

Wang, L., Gong, W., Ma, Y., Hu, B., and Zhang, M. (2014). Photosynthetically Active Radiation and its Relationship with Global Solar Radiation in Central China. *Int. J. Biometeorol.* 58, 1265–1277. doi:10.1007/s00484-013-0690-7

Wang, X., Tan, K., Chen, B., and Du, P. (2017). Assessing the Spatiotemporal Variation and Impact Factors of Net Primary Productivity in China. *Sci. Rep.* 7, 44415. doi:10.1038/srep44415

Wang, L., Wang, S., Zhou, Y., Liu, W., Hou, Y., Zhu, J., et al. (2018). Mapping Population Density in China between 1990 and 2010 Using Remote Sensing. *Remote Sens. Environ.* 210, 269–281. doi:10.1016/j.rse.2018.03.007

Xie, X., Li, A., Guan, X., Tan, J., Jin, H., and Bian, J. (2021). A Practical Topographic Correction Method for Improving Moderate Resolution Imaging Spectroradiometer Gross Primary Productivity Estimation over Mountainous Areas. *Int. J. Appl. Earth Observ. Geoinform.* 103, 102522. doi:10.1016/j.jag.2021.102522

Xu, X., Tan, Y., Yang, G., Li, H., and Su, W. (2011). Impacts of China's Three Gorges Dam Project on Net Primary Productivity in the Reservoir Area. *Sci. Total Environ.* 409, 4656–4662. doi:10.1016/j.scitotenv.2011.08.004

Yan, Y., Liu, X., Wang, F., Li, X., Ou, J., Wen, Y., et al. (2018). Assessing the Impacts of Urban Sprawl on Net Primary Productivity Using Fusion of Landsat and MODIS Data. *Sci. Total Environ.* 613-614, 1417–1429. doi:10.1016/j.scitotenv.2017.09.139

Yang, X., Yue, W., and Gao, D. (2013). Spatial Improvement of Human Population Distribution Based on Multi-Sensor Remote-Sensing Data: an Input for Exposure Assessment. *Int. J. Remote Sens.* 34, 5569–5583. doi:10.1080/01431161.2013.792970

Yu, D., Shi, P., Shao, H., Zhu, W., and Pan, Y. (2009). Modelling Net Primary Productivity of Terrestrial Ecosystems in East Asia Based on an Improved CASA Ecosystem Model. *Int. J. Remote Sens.* 30, 4851–4866. doi:10.1080/01431160802680552

Yue, T. X., Wang, Y. A., Chen, S. P., Liu, J. Y., Qiu, D. S., Deng, X. Z., et al. (2003). Numerical Simulation of Population Distribution in China. *Popul. Environ.* 25, 141–163. doi:10.1023/b:poen.0000015562.88915.01

Yue, W., Gao, J., and Yang, X. (2014). Estimation of Gross Domestic Product Using Multi-Sensor Remote Sensing Data: A Case Study in Zhejiang Province, East China. *Remote Sensing* 6, 7260–7275. doi:10.3390/rs6087260

Zhang, N., Mao, F., and Gong, W. (2011). Estimation of Net Primary Productivity of Wuhan in 2009[J]. *Geomatics Inf. Sci. Wuhan Univ.* 36, 1447–1450.

Zhang, Y., Zhang, C., Wang, Z., Chen, Y., Gang, C., An, R., et al. (2016). Vegetation Dynamics and its Driving Forces from Climate Change and Human Activities in the Three-River Source Region, China from 1982 to 2012. *Sci. Total Environ.* 563-564, 210–220. doi:10.1016/j.scitotenv.2016.03.223

Zhao, N., Currit, N., and Samson, E. (2011). Net Primary Production and Gross Domestic Product in China Derived from Satellite Imagery. *Ecol. Econ.* 70, 921–928. doi:10.1016/j.ecolecon.2010.12.023

**Conflict of Interest:** The authors declare that the research was conducted in the absence of any commercial or financial relationships that could be construed as a potential conflict of interest.

## GLOSSARY

**APAR** Absorbed photosynthetically active radiation
**CASA** Carnegie–Ames–Stanford Approach
**DEM** Digital elevation model
**DBF** Deciduous broadleaf forest
**DT** Decreasing trend
**EAHSI** Elevation-adjusted human settlement index
**ENF** Evergreen needleleaf forest
**EBF** Evergreen broadleaf forest
**FPAR** Fraction of photosynthetically active radiation
**GLO-PEM** Global production efficiency model
**GDP** Gross domestic product
**HIS** Human settlement index
**IT** Increased trend
**LUE** Light-use efficiency
**MRT** MODIS Reprojection Tool
**MVC** Maximum value composite
**MF** Mixed forest
**MRE** Mean relative error
**NGDC** National Geophysical Data Center
**NDVI** Normalized difference vegetation index
**NTLs** Nighttime lights
**NPP** Net primary productivity
**NC** Negative correlation
**PC** Positive correlation
**RE** Relative error
**$R^2$** Determination coefficient
**SDT** Significant decreasing trend
**SIT** Significant increasing trend
**SNC** Significant negative correlation
**SPC** Significant positive correlation
**UTM** Universal Transverse Mercator

frontiers in Environmental Science

ORIGINAL RESEARCH
published: 17 January 2022
doi: 10.3389/fenvs.2021.818402

# Impacts of Changbai Mountain Topography on the Extreme Precipitation From Super Typhoon Maysak

*Dan Zhu*[1,2], *Xiefei Zhi*[1]*, *Ning Wang*[3], *Changsheng Chen*[4], *Xiao Tian*[5] *and Yueming Yu*[2]

[1]Collaborative Innovation Centre on Forecast and Evaluation of Meteorological Disasters, Key Laboratory of Meteorological Disasters of Ministry of Education/Joint International Research Laboratory of Climate and Environment Change, Nanjing University of Information Science and Technology, Nanjing, China, [2]Changchun Meteorological Bureau, Changchun, China, [3]Jilin Meteorological Observatory, Changchun, China, [4]Jilin Key Laboratory of Changbai Mountain Meteorology and Climate Change/Laboratory of Research for Middle-High Latitude Circulation Systems and East Asian Monsoon, Jilin Institute of Meteorological Sciences, Changchun, China, [5]Tianjin Meteorological Observatory, Tianjin, China

Based on hourly gridded precipitation data (0.1°) calculated by the China Meteorological Administration (CMA), the European Centre Medium-Range Weather Forecasts (ECMWF) reanalysis data, and microwave measurements, this paper investigated the extreme precipitation induced by the Typhoon Maysak in Northeast China (September 2020), using the Advanced Research dynamic core of the Weather Research and Forecasting Model (WRF-ARW). The study focused on Changbai Mountain topography and the extreme precipitation in Jilin Province. The results show that two extreme precipitation centers corresponded well to the local terrain height in Jilin Province. The Changbai Mountain range, which mainly lies in southeastern Jilin Province, affected the typhoon in three aspects: blocking drag, forcing uplift, and promoting moisture convergence. Because of the blocking drag of the mountain topography, the duration of severe precipitation was prolonged. The overlap of the area affected by the peripheral cloud band of the typhoon and the direction of the typhoon was largely responsible for the extreme rainfall. The dynamic lifting by the mountainous terrain and the reinforced moisture convergence also considerably increased precipitation. Microwave measurements show that water vapor density profile increased rapidly at the peak (14 g/m3), and the high moisture density was retained for at least 15 h in the lower layer. The prolonged, continuous, and abundant moisture transport offered a sufficient water vapor supply for this severe precipitation event. According to the estimation of precipitation rate, the increment of torrential rainfall on Changbai Mountain during the severe precipitation period reached 6.8 mm/h, about 41% of the total rainfall in this period. Finally, the topographic sensitivity test indicated that when the terrain of Changbai Mountain was lower, the convergent ascending motion, precipitable water, and storm-relative helicity were weaker, and the rainfall distribution markedly changed. This finding further verifies the importance of the Changbai orography in the extreme precipitation event induced by Typhoon Maysak.

**Keywords: typhoon Maysak, extreme precipitation, Changbai mountain, topography, numerical simulation**

OPEN ACCESS

***Edited by:***
*Lijuan Shen,*
*University of Toronto, Canada*

***Reviewed by:***
*Jinqing Zuo,*
*National Climate Center, China*
*Jin Chenxi,*
*Beijing Meteorological Bureau, China*

***Correspondence:**
*Xiefei Zhi*
*zhi@nuist.edu.cn*

***Specialty section:***
*This article was submitted to Atmosphere and Climate, a section of the journal Frontiers in Environmental Science*

***Received:*** *19 November 2021*
***Accepted:*** *08 December 2021*
***Published:*** *17 January 2022*

***Citation:***
*Zhu D, Zhi X, Wang N, Chen C, Tian X and Yu Y (2022) Impacts of Changbai Mountain Topography on the Extreme Precipitation From Super Typhoon Maysak. Front. Environ. Sci. 9:818402. doi: 10.3389/fenvs.2021.818402*

## INTRODUCTION

Typhoons are one of the most disastrous weather systems, causing extreme weather, including gales, rainstorms, and storm surge (Needham et al., 2015). Much research has been conducted on their structure and dynamics, e.g., through machine learning (Pan et al., 2013; Chen et al., 2020) and dynamic real-time predicting (Lin and Jhong, 2015). The region of Northeast China, located at mid-to-high latitudes, is affected by typhoons far less frequently than the southeast coastal areas, but we note that more than half (56%) of the tropical cyclones annually travel the mid-to-high latitudes (Sun et al., 2010), bringing widespread strong winds and heavy rain. The ability to prepare for and cope with typhoons in Northeast China is inferior to that of the southeast coast, and once a typhoon moves northward, it can readily cause meteorological disasters. There are fewer studies on typhoon rainstorms and torrential rains in Northeast China, and the understanding and prediction of typhoons need to be further improved (Wang et al., 2007). Continuing to develop high-resolution numerical models and improving the forecasting skills of tropical cyclone tracks are still the most important means to save human life and reduce economic losses (Roy and Kovordányi, 2012).

Several studies have shown that large-scale circulation background, mesoscale systems, water vapor conditions, local topography, stratification stability, boundary layer convergence, and high-level outflow are among the variables closely related to the intensity of typhoons (Chen and Meng, 2001). When studying the influence of circulation in detail, Hogsett and Zhang, 2010 found that the MJO (Madden-Julian Oscillation) may provide convergence and energy for the low-level disturbance of typhoons, together with an eastward-developing Kelvin wave. Other scientists have studied the formation mechanisms of typhoon rainstorms and the extreme characteristics of typhoon precipitation from the aspects of monsoon circulation, water vapor helicity, and wet potential vorticity, including simulation and evaluation studies with numerical prediction models (Hsiao et al., 2010; Van Nguyen and Chen, 2011; Wang and Wang, 2014; Rendfrey et al., 2021).

In addition to the impact of weather systems, topography effects on heavy precipitation are particularly important. The thermodynamic effect of topography can induce localized severe rainfall. Many scientists have promoted the necessity of analyzing the impact of terrain (Weissmann et al., 2011), especially the relationship between the orographic-forced uplifting areas and short-time heavy precipitation (Maussion et al., 2011; Zhao, 2012). The higher the terrain, the greater the increase in localized torrential rainfalls. Apart from the lifting effect of terrain, the vertical water vapor flux (Flesch and Reuter, 2012), turbulent flux, and the variations of surface variables (Kilpela¨ Inen et al., 2011) influence areas affected by torrential rains. Undulate mountainous terrain can also enhance the drag effect of the ground on the atmosphere, which makes the typhoon circulation remain in place, resulting in continuous heavy rain (Chen and Luo, 2004). In Northeast China, the topographic blocking function of Greater Khingan Mountain and Changbai Mountain facilitates the southerly airflow in summer to the windward slopes of the two mountain ranges, which creates an ascending motion and local moisture increases (HE et al., 2020). Agyakwaha and Lin (2021) have revised and tested the topographic precipitation index to better predict the typhoon precipitation caused by topography.

With the rapid development of computers, numerical models are widely used (Bai et al., 2021; Wang H. et al., 2021). Several researchers have pointed out that the simulation results of the mesoscale Weather Research and Forecast Model (WRF) are robust (Jianfeng et al., 2005; Raju et al., 2011; Islam et al., 2015; Kim et al., 2015; Zhu et al., 2021), but better simulations can be achieved by adjusting the microphysical parameterization scheme and the planetary boundary layer (Tao et al., 2011). Pillay and Fitchett (2021) proposed that terrain height is of great significance in the occurrence and intensification of tropical cyclones in the Southern Hemisphere. In a topographic sensitivity test of WRF, the characteristics of extreme precipitation changed and the amount of rainfall decreased significantly with lower terrain height (Wang K. et al., 2021). The uncertainty of the topographic effect on the initial field of numerical simulations of typhoon circulation has increased the challenges of quantitative precipitation prediction (Fang et al., 2011). Heavy precipitation frequencies generally decrease with topographic height whereas light precipitation frequency increases in a nonlinear manner (Song and Zhang, 2020). Another study pointed out there are small-scale topographic vortices generated after a typhoon encounters a mountain range, adding further complexities to modeling efforts (Tang and Chan, 2015).

From 26 August to September 8, 2020, Northeast China was hit by three typhoons, causing heavy rainfall that has rarely been seen before in history, to which Typhoon Maysak contributed the most. This paper conducted an in-depth analysis of the extreme precipitation using observational analysis and numerical simulations, and we focused on the key role of Changbai Mountain's topography on the increase in heavy rainfall. The European Centre for Medium Range Weather Forecasts (ECMWF) ERA5 reanalysis data were used to revisit the features of physical parameters, the precipitation fusion data of automatic weather stations and CMORPH (Climate Prediction Centre Morphing Technique) were adopted to describe the characteristics of the precipitation, and the topographic role of Changbai Mountain during the typhoon was tested by numerical simulations. Three roles of topography on extreme precipitation are discussed. We believe that the results of this study will help elucidate the topographic effect during extreme precipitation events to improve the predictability of typhoon precipitation patterns.

## MATERIALS AND METHODS

### Study Area

Changbai Mountain is a dormant volcano located in the eastern part of Jilin Province, China. The topographic map of Jilin

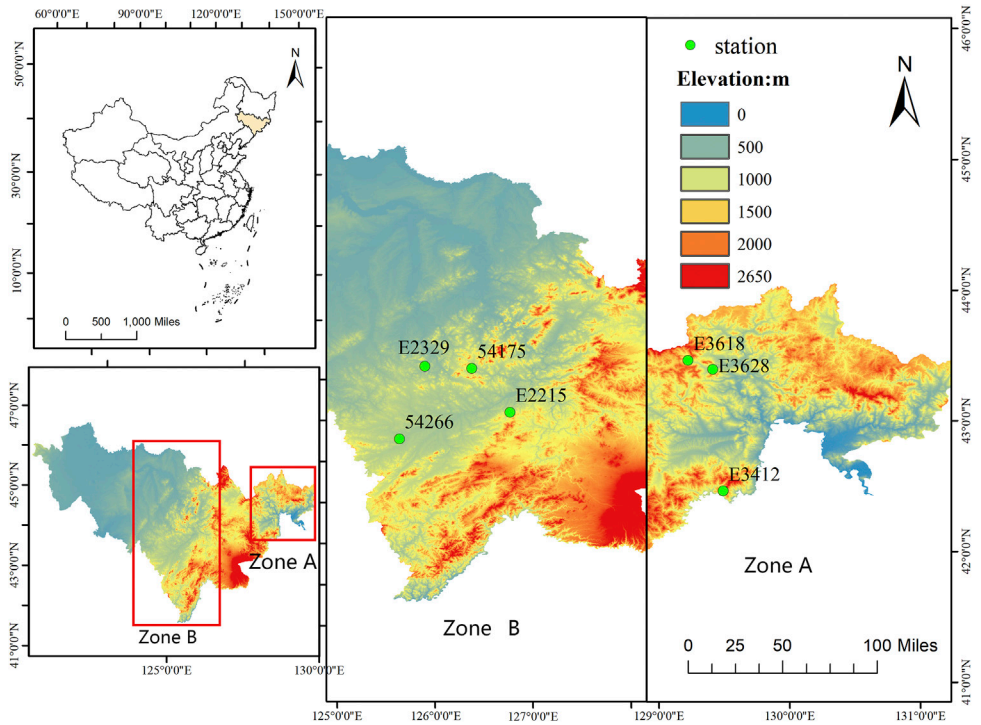


**FIGURE 1 |** Location of seven selected meteorological stations on a topographic map of Jilin province (red: higher elevation; blue: lower elevation, 0–2,650 m a.s.l), and Zone A and Zone B indicate two alpine areas of the mountain region.

**TABLE 1 |** Main features of the analyzed meteorological stations and rainfall ranking in Jilin Province.

| Ranking | Rainfall/mm | Meteorological station | Station no | Latitude | Longitude | Altitude/m | Terrain | Location |
|---|---|---|---|---|---|---|---|---|
| 1 | 221.7 | Panshi Jiefang Nantun | E2329 | 125.89 | 43.27 | 375.0 | Foothills | ZONE B |
| 2 | 198.4 | Longjing Pingding Cun | E3412 | 129.49 | 42.46 | 773.0 | Mountain | ZONE A |
| 3 | 157.7 | Wangqing Dongyang Cun | E3628 | 129.41 | 43.39 | 330.0 | Foothills | ZONE A |
| 4 | 157.4 | Meihekou | 54,266 | 125.63 | 42.53 | 341.3 | Foothills | ZONE B |
| 5 | 145.4 | Huadian Xiaowudaogou Cun | E2215 | 126.76 | 42.8 | 375.0 | Foothills | ZONE B |
| 6 | 142.8 | Beidahu | 54,175 | 126.37 | 43.25 | 537.0 | Mountain | ZONE B |
| 7 | 138.4 | Wangqing Dashi Cun | E3618 | 129.22 | 43.46 | 451.0 | Mountain | ZONE A |

Province (**Figure 1**) shows that Baiyun Peak, the highest peak of Changbai Mountain, is 2,693 m above sea level (a.s.l.), and the lower sections of Changbai Mountain are all above 1,000 m a.s.l. Jilin Province elevation inclines from the northwest to southeast with Daheishan Mountain in the middle. The region can be divided into two major geomorphic regions: the eastern mountain region and the central-western plain. The eastern mountain region is made up of lower mountains and foothills. Jilin Province is the geographical and economic center of Northeast Asia with a population of 27 million and an area of 187,400 ha. It is one of the most important agriculture producing areas in China. To evaluate spatial and temporal variability in rainfall characteristics, all meteorological stations located in the Jinlin Province were used, and we exhibit the top seven stations with the most precipitation in **Figure 1**. The main features of the selected seven stations are given in **Table 1**.

## Data Collection

The data adopted in this paper are as follows:

(1) The typhoon optimal path dataset was provided by the Tropical Cyclone Data Centre of the China Meteorological Administration (CMA)[1] (Ying et al., 2014; Lu et al., 2021);
(2) The European Centre for Medium Range Weather Forecasts (ECMWF) ERA5 reanalysis dataset (Hersbach et al., 2020), which has a horizontal resolution of 0.25° × 0.25°;
(3) GTOPO30 topographical height data provided by the US Geological Survey (USGS)[2] with a resolution of 30 s (about 1 km);

[1]http://tcdata.typhoon.org.cn.
[2]https://www.usgs.gov.

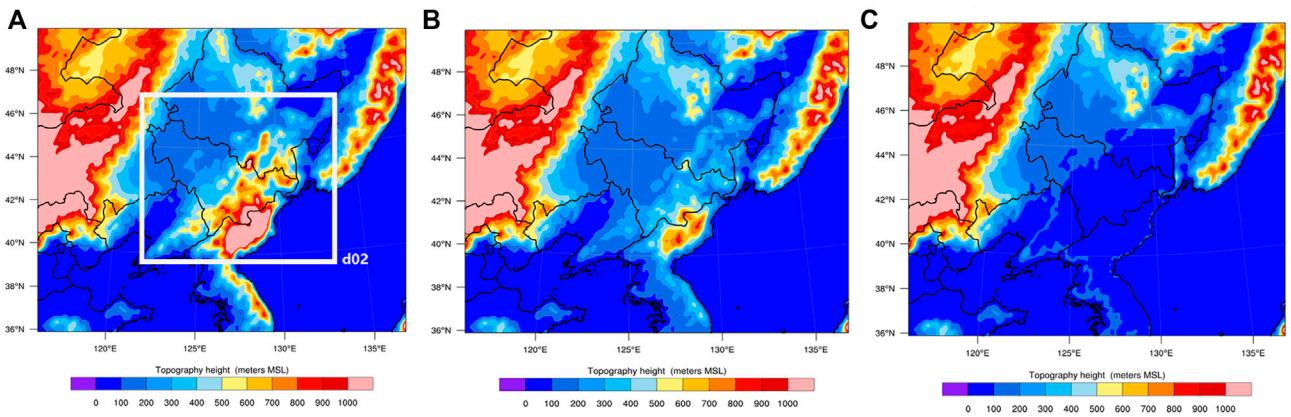


**FIGURE 2 |** Model domain and Control experiment 1, original terrain height of model **(A)**; Sensitivity experiment 2, half of the original terrain height **(B)**, and Sensitivity experiment 3, with the terrain height 0 m **(C)** in the control area (126.5°E-131°E, 41°N-45°N).

(4) Microwave measurements (MWP967KV) located in Jinlin City (in Jilin Province) and Changchun City (the capital of Jilin Province) were used for analyzing the characteristics of water vapor during the typhoon event. Ground-based microwave measurements are a detection approach, which can conduct the multi-channel continuous detection of the atmospheric microwave radiation moisture, and can automatically invert the atmospheric parameters, such as real-time water vapor (Chan and Hon, 2011);

(5) The hourly precipitation grid dataset (0.1°) over China was provided by the National Meteorological Information Centre of China Meteorological Administration (NMIC-CMA).[3] The gridded data were produced by a two-step data fusion algorithm of the probability density function and optimal interpolation (PDF + OI) using the hourly precipitation observations at 30,000–40,000 automatic weather stations (AWSs) and the CMORPH (Climate Prediction Centre Morphing Technique) dataset (Joyce et al., 2004). These coupled datasets effectively utilize the respective advantages of ground-based observations and satellite inversion of rainfall, with high spatial correlation and high accuracy (Shen et al., 2010; Xie and Xiong, 2011; Shen et al., 2014). It is applied to improve our understanding of precipitation variation over Jilin Province.

## Model Configuration and Design

To further study the topographic effect of Changbai Mountain on the extreme precipitation induced by Typhoon Maysak in 2020, this study used the WRF model version WRF3.3.1 with the Advanced Research WRF (ARW) dynamic core (Skamarock et al., 2008) to carry out the control simulation experiment and the topographic sensitivity experiment. The initial field data for the model was the global reanalysis data from the National Centres for Environmental Prediction/National Centre for Atmospheric Research (NCEP/NCAR) with a resolution of 1° × 1° at intervals of 6 h (Kalnay et al., 1996). The following parameterizations were used: the two-stream correlated-k distribution Rapid Radiative Transfer Model (Iacono et al., 2008) for the radiation schemes, the cloud microphysics of the WRF Single-Moment 5-class scheme (Hong et al., 2004), the Thermal Diffusion scheme boundary layer parameterization scheme (Hong et al., 2006), the revised Monin–Obukhov surface layer (Jiménez et al., 2012), the unified Noah land surface model (Chen and Dudhia, 2001), and the cumulus parameterization based on the Grell 3D scheme (Grell and Dévényi, 2002).

A double nested grid scheme was adopted in the simulation, with the grid spacing of the first layer 9 km and the second layer 3 km. The simulation domain is shown in **Figure 2A**. The vertical resolution is 34 non-uniform layers with 50 hPa at the top of the atmospheric columns. The simulation center was at the point (43°N, 127°E), the initial time was 08:00 BT 02 September 2020, and the integral was 48 h. Scheme I was the control simulation experiment, that is, the original terrain height was used for numerical simulation; Scheme II and Scheme III were topographic sensitivity experiments. In Scheme II the terrain altitude of the WRF model was replaced by 1/2 of the original terrain height within 126.5°E-131°E and 41°N-45°N (see **Figure 2B**), and in Scheme III the terrain altitude was set as 0 m in the same domain as in Scheme II (see **Figure 2C**).

## Algorithm of Topographic Precipitation Rate

When the wind blows along a mountain slope, it produces a vertical component, the so-called topographical vertical velocity. According to **Eq. 1**, the greater the slope of a mountain, the greater the wind speed on the ground surface, the more perpendicular the wind direction to the mountain direction, and the stronger the atmospheric vertical motion on the ground surface. To calculate the distribution of terrain ascending motion with height, the $\omega$ equation is introduced. Without considering the vorticity advection, temperature

[3]http://data.cma.cn/.

advection, and diabatic heating, the geostrophic approximation can be used to obtain **Formula 2** and **Formula 3** [see reference (Zhu et al., 2000) for details]:

$$\omega_{s0} = -\rho_0 g \vec{V}_0 \cdot \nabla h \tag{1}$$

$$\omega_s = \Gamma(p)\omega_{s0} \tag{2}$$

$$\Gamma(p) = \frac{sh\left(\sqrt{2}\frac{2\pi}{L}\sqrt{\frac{\sigma}{f^2}}\cdot P\right)}{sh\left(\sqrt{2}\frac{2\pi}{L}\sqrt{\frac{\sigma}{f^2}}\cdot p_0\right)} \tag{3}$$

where $\omega_{s0}$ represents the topographic ascending velocity of the ground surface, h refers to the topographic height, $\vec{V}_0$ and $P_0$ are the surface wind vector and air pressure, respectively, $\Gamma(p)$ denotes the attenuation coefficient of topographic vertical velocity with height, L stands for the wavelength of the periodic function of the surface, and $\sigma = g/K$ is a constant. It can be seen that the vertical velocity increases exponentially with an increase of $p$. That is, with a decrease of the height index, the smaller the topographic scale, and the faster the topographic vertical motion decays with height. The precipitation rate $I = -\int_0^\infty \rho \frac{dq_s}{dt} dz$ is placed into the static force equation and the relation expression $\frac{dq_s}{dt} = \frac{dq_s}{dp}\frac{dp}{dt} = \omega\frac{dq_s}{dp}$, and the following expression can be obtained:

$$I = \frac{1}{g}\int_{q_{s0}}^{0} \omega_s dq_s = -\frac{1}{g}\bar{\omega} q_{s0} \tag{4}$$

where $\bar{\omega}$ is the average vertical velocity of the whole atmospheric layer and $q_{s0}$ is the surface saturation specific humidity. It is assumed that the entire atmosphere is saturated during precipitation and the temperature declines according to the moist-adiabatic lapse rate. The humidity of the entire layer becomes a function of the surface saturation specific humidity, so the ground saturation specific humidity is used to represent the specific humidity of the entire layer. Suppose the non-divergent layer is $p_0/2$ and $\omega$ is distributed sinusoidally with height, then:

$$\bar{\omega} = \frac{1}{p_0}\int_0^{p_0} \omega_s dp \tag{5}$$

Then considering **Formulas (2, 3, 4)**, and neglecting negligible terms:

$$\bar{\omega} = \frac{\omega_{s0}}{p_0}\int_0^{p_0} \Gamma(p)\, dp \cong \frac{\omega_{s0}}{A/p_0}, \; -A = \sqrt{2}\,\frac{2\pi}{L}\sqrt{\frac{\sigma}{f^2}} \tag{6}$$

## Typhoon Maysak and its Precipitation Characteristics

The No. 9 Typhoon Maysak in 2020 was generated in the northwest Pacific Ocean surface at 08:00 BT (Beijing Time, 8 h later than UTC), August 28, 2020, on the ocean surface of the Northwest Pacific Ocean. Then it traveled toward the northwest steadily with its force strengthening. It intensified into a super typhoon at 05:00 BT, 1 September, and landed on the coast of Busan, South Gyeongsang Province, South Korea around 1:30 BT on 3 September. At the time of landfall, its maximum wind force near the center was CAT-14 (42 m/s), and the lowest pressure was 950 hPa in the center. After landing, Maysak shifted to the northwest direction, and at 14:00 BT on 3 September the center moved into Helong of Yanbian Prefecture, Jilin Province, China. Maysak remained at a super typhoon level for 18 h, with a minimum atmospheric pressure of 940 hPa and a maximum wind speed of 52 m/s in its center. After landing, it stayed in Northeast China for 27 h, and direct effects lasted as long as 45 h. The typhoon path is shown in **Figure 3A**.

Typhoon Maysak gave rise to intense precipitation, with some local rainfalls exceeding historical records. Generally, the typhoon precipitation could be divided into four stages: the first rainfall stage was affected by the typhoon from a long distance, the second stage was dominated by the spiral cloud belt in the typhoon periphery, the third stage was the extreme rainstorm near the typhoon center after it made landfall, and the last was the stage influenced by the extratropical cyclone which was developed from the weakening of this typhoon. The intense precipitation was mainly concentrated in the period from 08:00 BT, 3 September, to 08:00 BT, 4 September, peaking from 14:00 BT in the third typhoon stage to 02:00 BT in the 4th stage. In 48 h (20:00 BT in the 2nd stage to 20:00 BT in the 4th stage), the average rainfall in the whole region of Northeast China was ~54 mm, and that in Jilin Province reached up to 72.5 mm. The daily rainfall at 49 national stations in Northeast China exceeded the historical extremes (since 1961) for every September, and two stations broke historical records since the establishment of the stations (since 1961).

A group of 201 meteorological stations received >100 mm of accumulated precipitation in Jilin Province. From 20:00 BT, 3 September, to 20:00 BT, 4 September, the two extreme rainfall centers were in Zone A, where Yanji city and Longjing city are located, and Zone B at the junction of the plains and mountains in the south-central parts of Jilin Province (**Figures 3B,C**). The peak amount of accumulated precipitation was 221.7 mm, found at the Jiefang Nantun Station of Panshi City, in Zone B with topographic lifting after Maysak's landfall; it had the maximum rainfall intensity of 57 mm/h. Combined with the topography of Jilin Province, it can be seen that there was clear correspondence between the extreme rainfall center and the terrain height (**Table 1**). In addition, those stations with rainfall of more than 100 mm at a single station are all in the two zones with high rainfall values, and the terrain heights of these stations are all ~300 m a.s.l. (**Table 1**). **Table 1** compares the distribution of rainfall extremes with altitude, revealing that the two extreme rainfall regions corresponded to the windward slopes and inclining areas of the mountains. So, we can see the topography of Changbai Mountain played a significant role in the extreme precipitation process caused by the super typhoon.

# RESULTS

## Influence of Terrain

Northeast China is an important grain-producing region in China, and the abnormal precipitation of typhoons directly

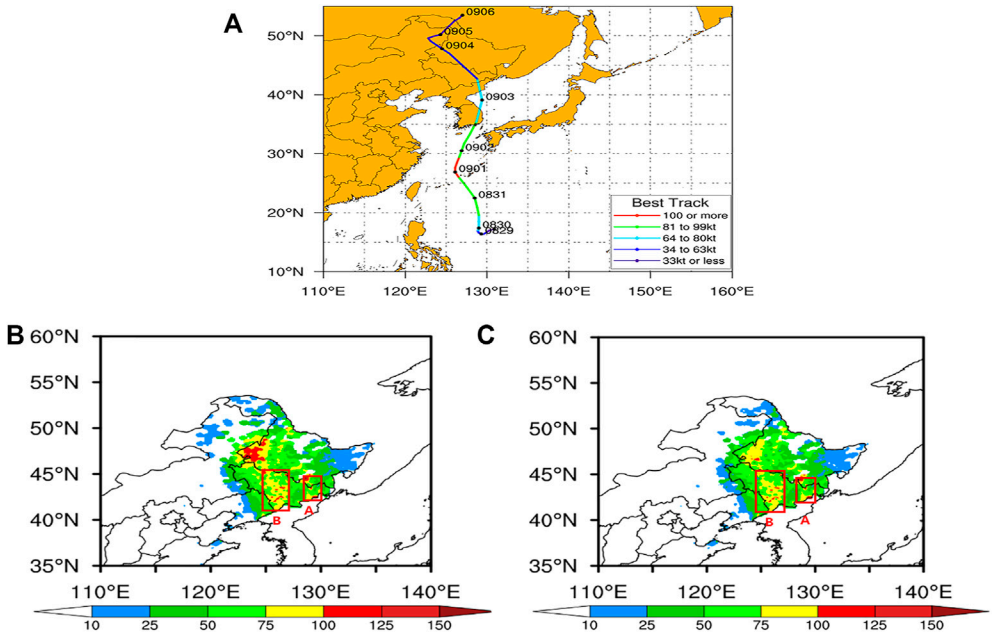


**FIGURE 3 |** Track of super typhoon Maysak **(A)**; accumulated rainfall (shaded, unit: mm) in Northeast China from 20:00 BT 2 to 20:00 BT 4 **(B)**, and from 08:00 BT 3 to 08:00 BT 4 **(C)** September 2020.

affects the grain harvest. When a typhoon moves northward, in addition to the transition of the underlying surface from ocean to land, the interaction with weather systems at middle and high latitudes is important. Likewise, as one of the major landforms in Northeast China, the Changbai Mountain range has critical impacts on the summer rainfall in this region.

## The Drag Effect of Terrain

After a typhoon makes landfall, because of the frictional drag of the underlying surface, its strength will be weakened and speed slowed. Typhoon Maysak weakened soon after making landfall in Busan, South Gyeongsang Province, South Korea, and then continued to lose its strength as it made a second landing in Helong of Yanbian Prefecture, Jilin Province, China. Specifically, on the open sea surface, Maysak moved at a speed of 40–50 m/s. When Maysak landed for the second time, the friction and obstruction effects of the Changbai Mountain terrain slowed it down to 18 m/s. In **Figure 1** and **Table 1**, it can be seen that the deceleration period of the typhoon corresponded to the period of heavy precipitation in Zone A. Thus, the blocking effect of the Changbai Mountain terrain lengthened the period of accumulating precipitation in the eastern part of Jilin Province. The combination of the typhoon peripheral cloud belt and the typhoon traveling direction maintained severe precipitation in certain areas.

## Orographic Forced Uplift

Topography promotes the formation of precipitation and affects its distribution, both driven by the blocking terrain which forces air to rise. The Changbai Mountain range comprises a series of parallel and folded fault mountains, basins, and valleys oriented in a northeast-southwest direction, with three main ridges extending to the southwest, northeast, and southeast. The temporal and spatial evolutions of vorticity, divergence, and horizontal wind speed in the high rainfall areas (42°–45°N, 124°–131°E; **Figures 4A,B**) indicate that the positive vorticity circulation was maintained throughout the troposphere from 20:00 BT, 2 September, to 20 00 BT, 4 September. After Maysak's landfall, the positive vorticity reached its maximum at 20:00 BT 3 September, with the maximum in the center emerging at 850 hPa and areas extended from the center were over 200 hPa. From the perspective of spatiotemporal variation of the divergence field, before 20:00 BT 3 September, all the areas below 400 hPa were dominated by mid-low level convergence zones, and the mid-high level between 400 hPa and 100 hPa were under the control of divergence zones. Near the typhoon center during 08:00–20:00 BT 3 September, there was a strong convergence center from 925 hPa to the ground, with the center value greater than $15 \times 10^{-5}$ $s^{-1}$. After the typhoon changed direction at 20:00 BT 3 September, the convergence intensity in the lower layer faded with increasing height and shifted to a divergence area near the ground.

To further study the influence of mountain topography on the distribution of vorticity and divergence, the lifting areas on the east and west sides of Changbai Mountain ridge (Zone A and Zone B in **Figure 1**) were selected for comparative analysis of temporal vertical profiles. As shown in **Figures 4C,D**, the two selected areas corresponding to the typhoon-affected phases are both lifting areas, and both are close to the typhoon center. During the influence phase of the peripheral spiral cloud belt of the typhoon, Zone A was the area on the windward slope. From 08:00 to 20:00 BT on 3 September, the intensity of the positive

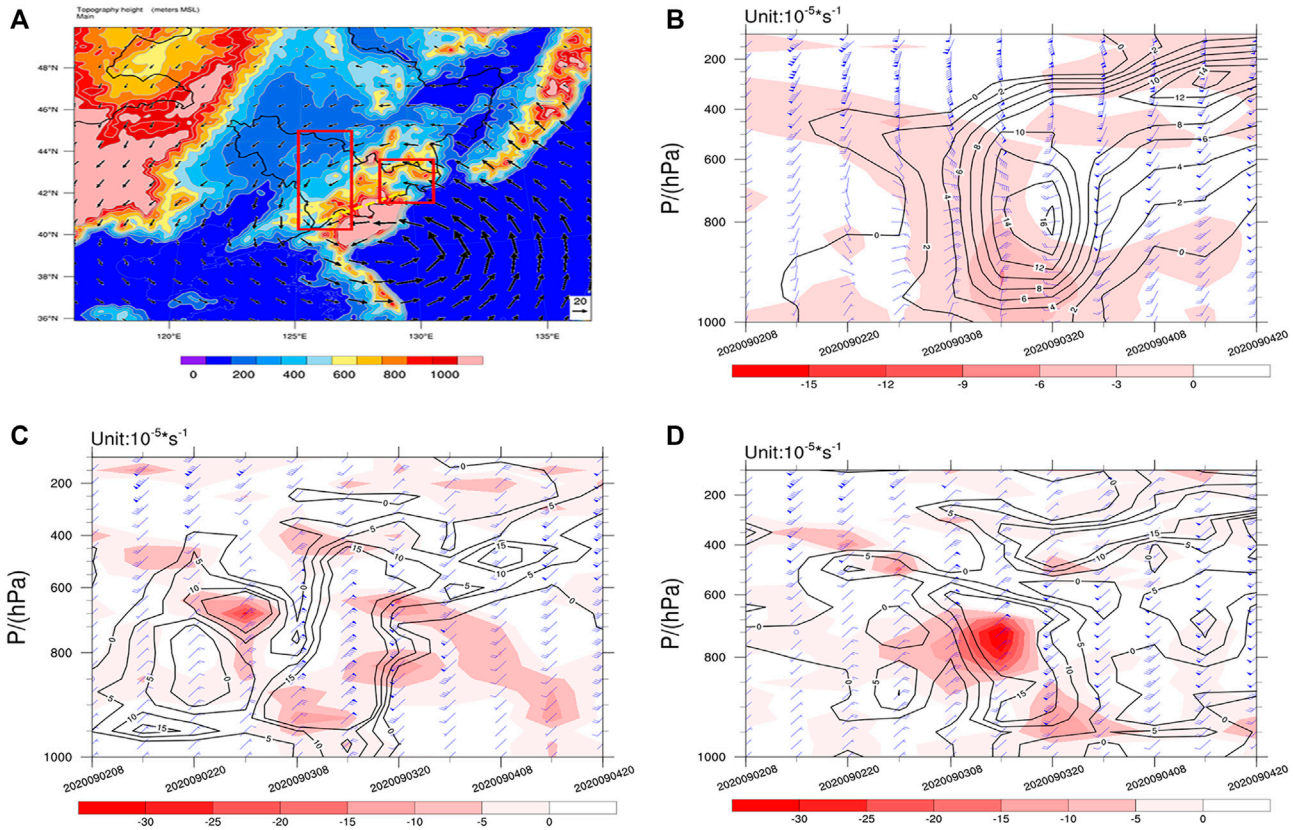


**FIGURE 4 | (A)** Terrain height of Jilin Province (shaded, unit: m) and 850 hPa wind at 08:00 BT 3 September (black arrow, unit: m/s). The yellow solid line is the mountain ridge of Changbai Mountain. Red dotted boxes are the high rainfall areas in Jilin Province; **(B)** Time-vertical profile of the averaged vorticity (black solid line, unit: $10^{-5}$ $s^{-1}$), divergence (red shaded area, unit: $10^{-5}$ $s^{-1}$), and horizontal wind speed (blue wind barb, unit: m/s) in the red dotted area from 08:00 BT, 2 September, to 20:00 BT 4, September 2020. The time-vertical profile of vorticity, divergence, and horizontal wind speed on **(C)** the windward slope (42.8°N, 129.4°E; Zone A) and **(D)** leeward slope (42.9°N, 126.5°E; Zone B) are also shown.

vorticity area was much larger than the regional average, in which the center intensity of vorticity in Zone A of the windward slope reached its maximum at 850 hPa, and the upward extending area developed to around 300 hPa. During the typhoon-weakening period from 08:00 to 20:00 BT on 4 September, Zone A on the windward slope had negative vorticity below 700 hPa in the lower layer and a positive vorticity center near 300 hPa in the upper layer. The vorticity variation before and after the typhoon center passed was more symmetrical.

As shown in the distribution of the divergence field, there was an obvious convergence center in the lower layer of Zone A on the windward slope from 08:00 BT, 3 September, to 08:00 BT, 4 September. Especially at 14:00 BT on 3 September, the convergence in the lower layer was significantly enhanced, whereas the divergence in the upper layer at this time was also the greatest. The strong convergence center at the lower level of the windward slope appeared in the northeast wind in front of the typhoon center, and after the typhoon center passed, it turned toward the south and the convergence decreased. When the typhoon center passed through Zone B, the terrain altitude increased, strengthening the convergent lifting, and the strong convergence center was in the southwest wind behind the typhoon center. At 20:00 BT on 3 September, the middle layer became a compact area of convergence, the upper layer was a divergent field, and the vertical wind shear gradient was large. At this time, the maximum hourly rainfall intensity was in Panshi of Jinlin Province. Hence, the dynamic conditions of precipitation in Jilin Province are largely strengthened by the cooperation of terrain lifting and convergence.

Ascending motion is one of the conditions related to torrential rain, and vertical velocity can well reflect the strength of ascending motion. Combined with the terrain height of Jilin Province, the vertical velocity profile was developed (**Figure 5**) along a 43°N latitude line, and it shows that at 02:00 BT on 3 September, the typhoon was still in the area to the east of 127.5°E, corresponding with a strong vertical up-rising area above it. At this time, a relatively small vertical rising center emerged on the east side of the Changbai Mountain range. As the typhoon gradually moved westward, the vertical velocity center above the typhoon center kept tilting forward, and merged with the center in front of the mountain, strengthening, and with the velocity center value reaching 15 m/s. This strong center before the mountain remained until the typhoon landed again in Jilin Province. After the typhoon landed, the southwest wind area in

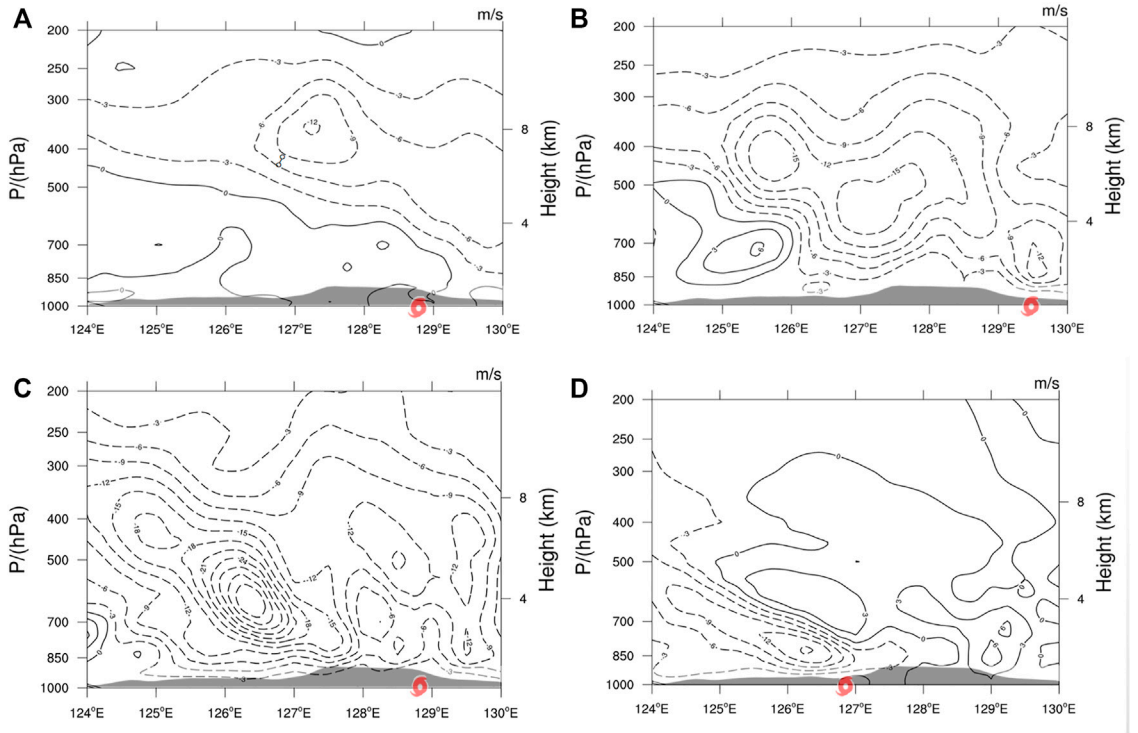


**FIGURE 5 |** Longitudinal cross-section of vertical velocity (contour, unit: m/s) and terrain height (shaded, unit: m) along 43°N at **(A)** 02:00, **(B)** 08:00, **(C)** 14:00, **(D)** 20:00 BT 3 September 2020. The typhoon mark indicates the longitude location of typhoon Maysak.

the fourth quadrant of the typhoon center was once again lifted by the terrain behind the mountain, and the velocity center value reached 33 m/s, thus forming favorable conditions for heavy precipitation in Panshi City. After the typhoon crossed the mountain, the vertical velocity area was weakened. We can see that topographic lifting has a dynamic strengthening effect on the two severe precipitation phases.

## Moisture Convergence

In addition to the dynamic effect, moisture condensation due to the cooling of airflow passing over the mountain also increased significantly. At 02:00 BT 3 September, Maysak made landfall on the coast of Busan, South Gyeongsang Province, South Korea, and at this moment the moisture in the periphery of the typhoon began to affect eastern Jilin Province. Obstructed by the topography of Changbai Mountain, the convergence center of water vapor flux above $-90 \times 10^{-5}$ s$^{-1}$ was observed on the eastern side of the mountain range (**Figure 6**). With the typhoon approaching, the convergence of piedmont water vapor flux was continuously strengthened, gradually expanding to the west of Jilin Province. At 10:00 BT on 3 September, the convergence center reached its maximum value of $-120 \times 10^{-5}$ s$^{-1}$, far higher than the typhoon near-center circulation. Before and after the typhoon landed, Jilin Province was located in the strong convergence zone of water vapor flux, whose central extreme value was maintained at $-120 \times 10^{-5}$ s$^{-1}$. There were two extreme centers in the strong convergence zone, one was the east side of Changbai Mountain before the typhoon landed, and the other was the terrain lifting area in the fourth quadrant on the southwest side of the typhoon center after the typhoon landed, which corresponded to the two precipitation extremum centers Zone A and Zone B. In addition, it was found from the two microwave measurements in Changchun City and Jilin City that the water vapor density profile and integrated water vapor at 0–3 km increase significantly with the precipitation process. In the stage of heavy precipitation, water vapor density profile increased rapidly, with a peak of 14 g/m$^3$. The high value of the water vapor density profile lasted from 01:00 BT, 3 September to 16:00 BT, 3 September (**Figure 7**). With the weakening of precipitation, the water vapor density profile and integrated water vapor began to decrease at the same time. As a result, the sustained and abundant water vapor transport provided a sufficient moisture supply for this precipitation. The convergent lifting of the Changbai Mountain topography promoted the provision of very favorable water vapor conditions for the occurrence of a heavy rainstorm.

## Rate Calculation of Topographic Precipitation in Changbai Mountain

It can be seen from the analysis of the actual field of physical parameters that the topography of Changbai Mountain produced a critical convergent lifting effect on the extreme precipitation brought by the typhoon, which was mainly manifested as dynamic lifting and water vapor convergence. The effect of terrain on the increased precipitation can be estimated by parameters such as wind direction and wind force during a typhoon.

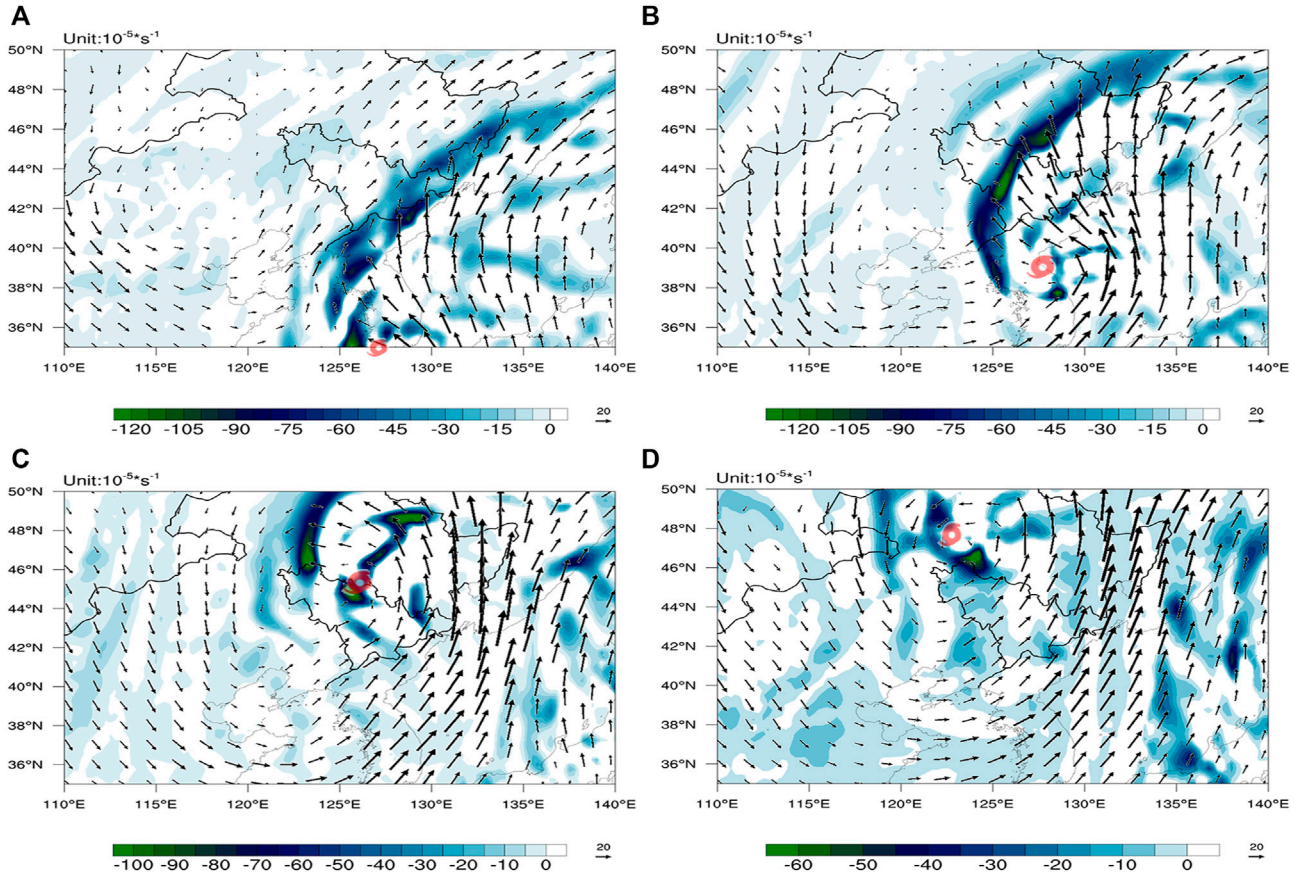


**FIGURE 6 |** The 850 hPa water-vapor flux divergence (shaded, unit: $10^{-5}$ $s^{-1}$) and horizontal wind speed (black arrow, unit: m/s) at **(A)** 20:00 BT 2, **(B)** 08:00 BT 3, **(C)** 20:00 BT 3, and **(D)** 08:00 BT 4 September 2020. The typhoon mark represents the position of Maysak.

The direction of the strongest wind at the Longjing Pingdingshan station on the windward slope of Changbai Mountain was dramatically affected by topography, and precipitation was closely related to wind shear. Under the influence of the surrounding terrain, there were only two wind directions, northerly and southerly, at the Longjing Pingdingshan station during the lifecycle of the typhoon. When the northeast wind in the periphery of the typhoon encountered the Changbai Mountain, it was blocked and forced to turn to the south, and the precipitation at the Longjing Pingdingshan station occurred mainly when the southerly wind was blowing. With the increasing southerly wind, precipitation was intensified. This was because the southerly wind can behave actively on the southwest side of the mountain range only after it was over the mountain, thus most precipitation occurred before the wind passed over the mountain.

Take the latitude of the Longjing Pingdingshan station at 42.5°N, $f = 9.8 \times 10^{-5}$ $s^{-1}$, $P_0 = 906$ hPa, $K = 5.2 \times 102$ $hPa^2$ $m^{-1}$, $L$ is 100 km, and then $\overline{\omega} \cong \omega_{s0}/118$ can be obtained.

Set α is the terrain slope, β is the angle between wind direction and terrain, then **Eq. 1** can be rewritten as:

$$\omega_{s0} = -\frac{p_0 g}{RT_0} V_0 \cos\beta \tan\alpha \tag{7}$$

where $p_0$ and $T_0$ represent surface pressure and temperature, respectively, and $V_0 \cos\beta$ indicates the wind component perpendicular to the terrain. For a certain time, the calculation formula for the rate of topographic precipitation in Changbai Mountain can be simplified as:

$$I = \frac{1}{118} \frac{p_0 q_{s0}}{RT_0} \cdot V_0 \cos\beta \tan\alpha \tag{8}$$

The hourly average values of the Longjing Pingdingshan station during the heaviest precipitation (from 01:00 BT to 13:00 BT on 3 September) are taken for each parameter. At the Longjing Pingdingshan station, the average surface pressure was 906 hPa, the average surface temperature was 16.9°C, the average specific humidity was 10 g/kg, the terrain slope was about 11.1°, and the velocity perpendicular to the terrain was about 8 m/s. Then, the precipitation increment caused by terrain lifting can be estimated to be about 6.8 mm/h, and the 12-h accumulated rainfall increased by nearly 82 mm, accounting for 41% of the observed rainfall during the

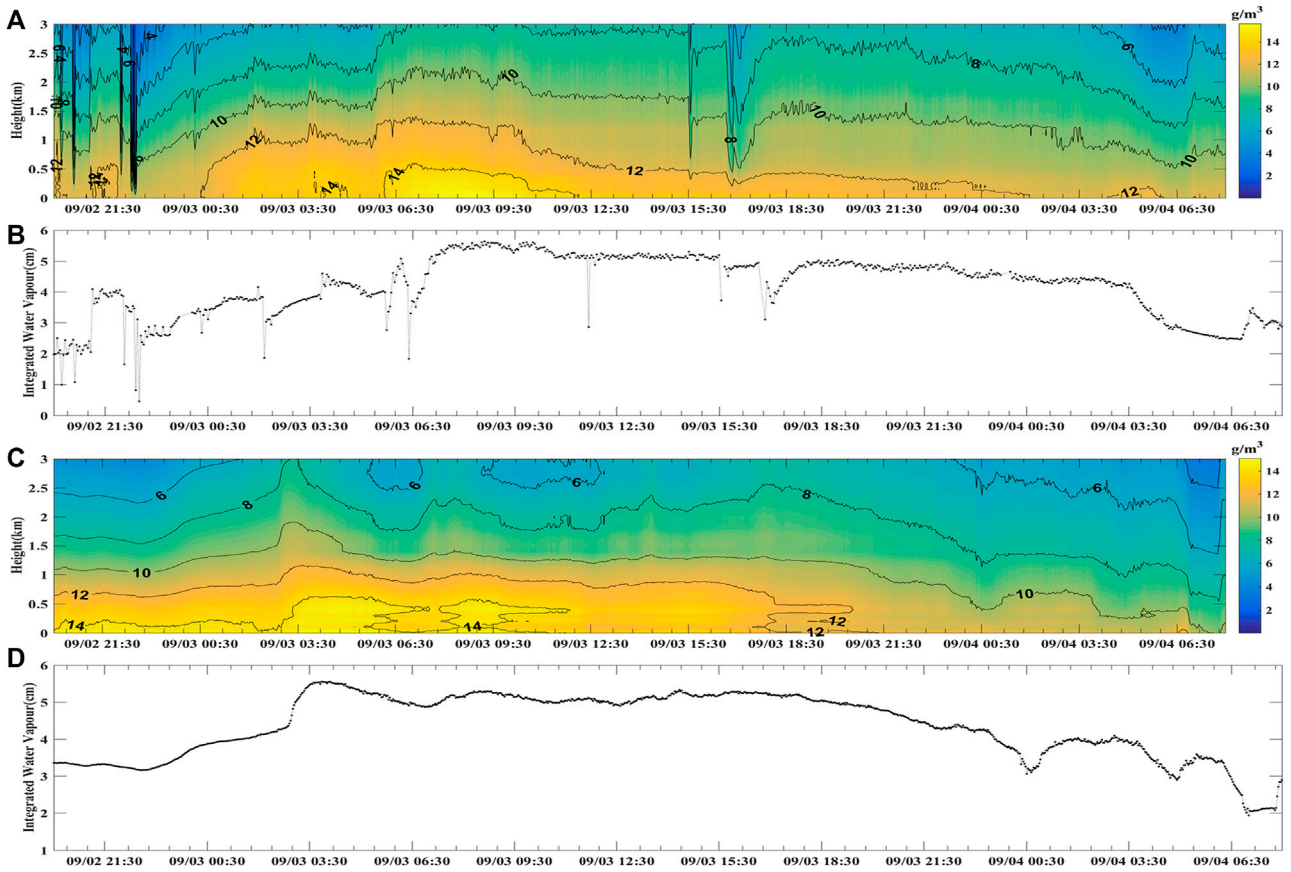


**FIGURE 7 |** The water vapor density profile (unit: g/m$^3$) and integrated water vapor (unit: kg/m$^2$) of microwave measurements at Changchun city **(A,B)** and Jilin city **(C,D)** from 20:00 BT 2 to 08:00 BT 4 September 2020.

period. Therefore, we can see that much of the precipitation was caused by the uplift of the terrain.

## Numerical Simulation Experiment

### Comparison of Model Simulation and Observation

Comparing the model simulation of Typhoon Maysak with the observed data (**Figure 8D**), the mesoscale numerical model WRF-ARW can well simulate the track of the typhoon before its landing, and especially the simulated and observed landfall locations in Jilin Province. But after its landing, it degenerates into an extratropical cyclone and the simulated track is slightly to the north until it leaves Jilin Province (**Figures 8A–C**). According to the precipitation distribution from 20:00 BT, 2 September, to 08:00 BT, September 4, 2020, the precipitation distribution pattern in Jilin Province simulated by the WRF numerical model is consistent with empirical observations and, in particular, the two extreme rainfall centers are consistent (as is shown in **Figure 8B**). There is an obvious asymmetric structure near the typhoon center, with extreme precipitation concentrated in the first quadrant and the third quadrant of its center.

The comparison of the precipitation distributions in the control simulation experiment and topographic sensitivity experiment indicates that the path and intensity of the typhoon did not change significantly at lower terrains, with the overall precipitation trend in most parts of Jilin Province consistent with that in the control experiment (**Figure 8C**). To better analyze the impact of topography on this extreme rainfall, we conducted three sets of numerical modal experiments, which were Scheme I, Scheme II, and Scheme III (for details see the section Model Configuration and Design). The precipitation of the control experiment Scheme I is used to standardize that of Scheme II and Scheme III, and **Figures 8E,F** show the anomalies of precipitation difference of Scheme I minus Scheme II and Scheme I minus Scheme III during the three simulation experiments. After the terrain altitude was changed to half of the original terrain height (or 0 m), the anomalies of precipitation in rainfall amount between the two schemes gradually increases at the border of North Korea and the eastern part of Jilin Province, and the maximum difference exceeds 40 mm, which can further indicate the effect of mountain topography on the precipitation. It is worth mentioning that the negative anomalies' precipitation difference reaches 20 mm over the eastern part of central Jilin Province in the fourth quadrant of the typhoon center. We will further analyze in the next section.

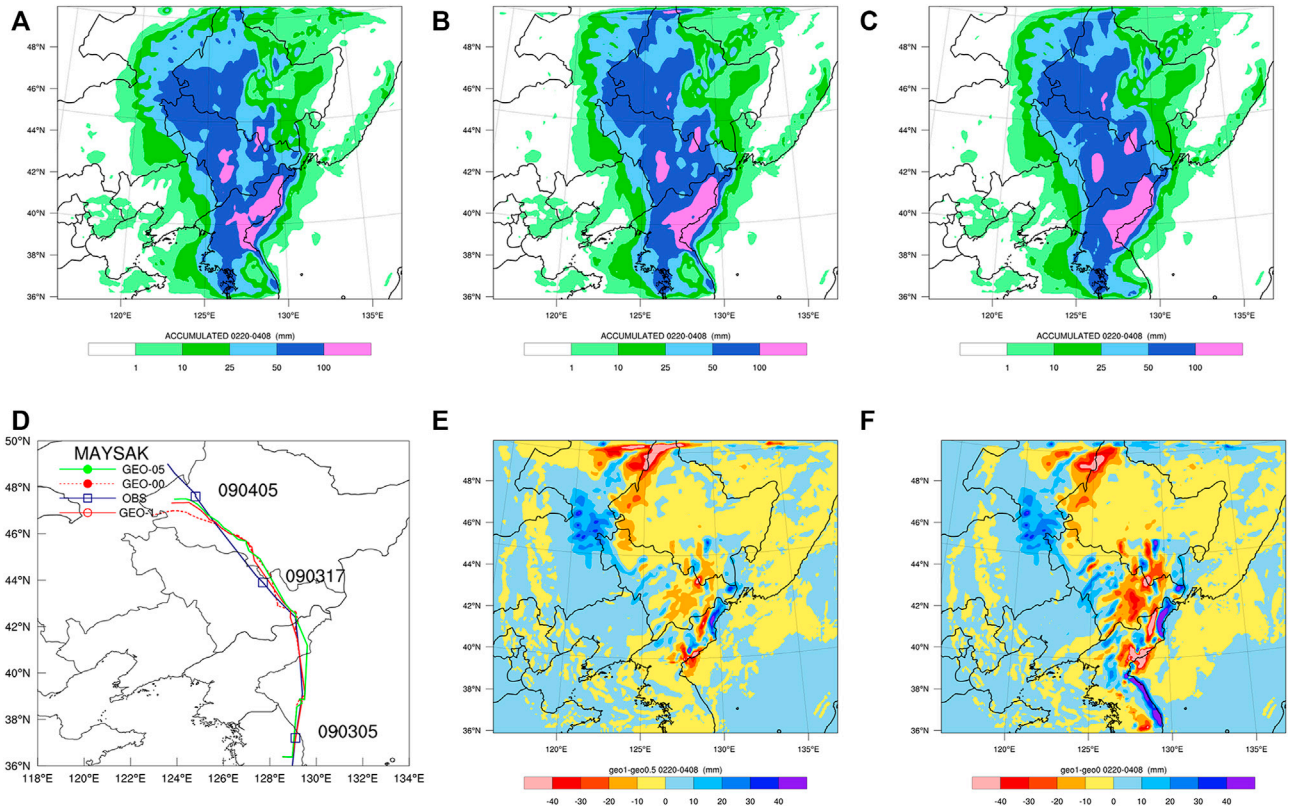


**FIGURE 8 |** The simulated precipitation of Scheme I, Scheme II, and Scheme III **(A–C)**, the simulated and observed tracks of Maysak (blue solid line is for the observed typhoon track, red solid line for the track simulated by Scheme I, green solid line for the track simulated by Scheme II and red dotted line for the track simulated by Scheme III) **(D)**; The anomalies of precipitation difference of Scheme I minus Scheme II **(E)**, and Scheme I minus Scheme III **(F)** from 20:00 BT 2 to 08:00 BT 4 September 2020 (shaded, unit: mm).

### Analysis of Simulation Parameters

The storm-relative helicity was a parameter used to measure the strength of storm inflow and the magnitude of the vorticity component along the inflow direction. It can reveal the relative inflow strength of a storm and the rotation degree of the ambient wind field, thus reflecting the potential of rotation development (Lilly, 1986). The distribution comparison (**Figures 9A–C**) of storm-relative helicity at 06: 00 BT, 3 September, shows that when the terrain height is lower, the storm-relative helicity near the eastern border of Jilin Province declines distinctly. At 08:00 BT on 3 September, because of the lifting effect of terrain, the high-value center of storm-relative helicity in the control experiment Scheme I is located in the eastern part of Jilin Province (**Figures 9B,C**), matching the extreme area of precipitation. When the terrain height is lower, the storm-relative helicity in the east of Jilin Province decreases, and the potential for the development of storm rotation is weakened. After the terrain height drops to 0 m, the rainstorm gradually moves to the central part of Jilin Province, and the rainfall in Dunhua and Jiaohe of Jilin Province in the first quadrant of the typhoon center is enhanced.

Comparing the whole layer of atmospheric precipitable water distributions (**Figures 10A,C,E**) of the topographic sensitivity experiment, we found that after removing the obstruction of mountains, the high-value area of atmospheric precipitable water in Jilin Province became even wider, and the moisture transport is even more apparent (**Figures 10B,D,F**), so the precipitation in the eastern part of central Jilin Province and the southern part of Heilongjiang Province was intensified instead. Even when Zone B (including Panshi city) lies in the third quadrant after typhoon landfall, the extreme precipitation center still fails to appear because there is no topographic lifting. This finding can further verify the critical significance of the Changbai Mountain topography for extreme precipitation.

## DISCUSSION

The September 2020 extreme precipitation resulting from Typhoon Maysak in Northeast China was analyzed based on the hourly gridded precipitation data, ECMWF ERA5 reanalysis data, and microwave measurements. The control simulation experiment and topographic sensitivity experiment were carried out in combination with the mesoscale numerical model WRF-ARW, and then the simulation results from the reduced and the altered terrain heights were compared. During the influencing period of Maysak, two extreme precipitation centers existed in Jilin Province, both of which were found in

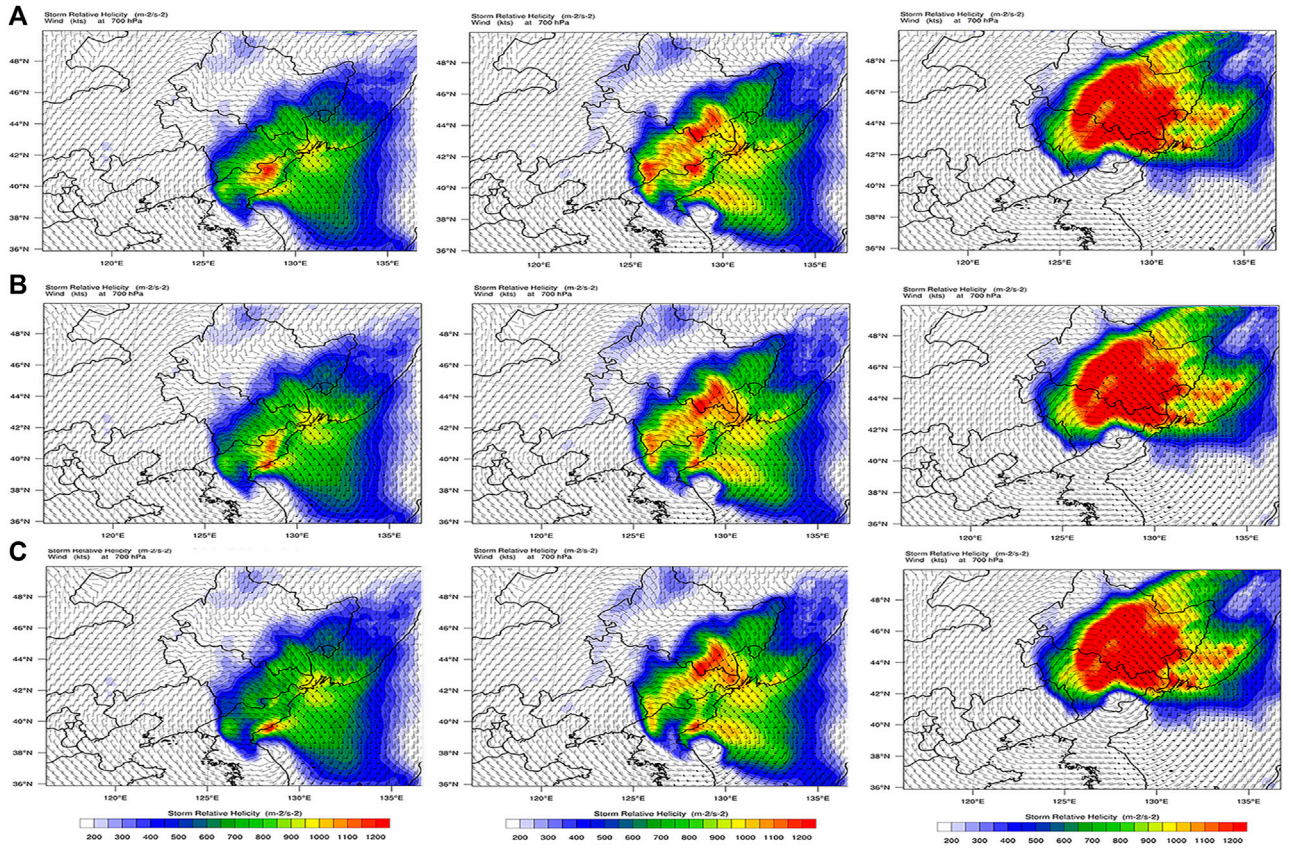


**FIGURE 9 |** Storm relative helicity (shaded, unit: $m^{-2}$ $s^{-2}$) and 700 hPa horizontal wind speed (barb, unit: m/s) in the simulated precipitation of Scheme I **(A)**, Scheme II **(B)**, and Scheme III **(C)** at 06:00, 08:00, and 14:00 BT, September 3, 2020.

the upslope areas of the Changbai Mountain range, corresponding well to the terrain height. The overlap of the typhoon-affected region and the typhoon-moving direction also contributed significantly to the persistence of the extremely severe rainfall, during which the topography of Changbai Mountain had a critical promoting function.

In summation, the topographic impacts of the Changbai Mountain on the extreme typhoon rainfall are reflected in three aspects:

(1) Blocking and dragging. During the heavy precipitation period after the typhoon made landfall, the topography of the mountain slowed down the typhoon, helping prolong the rainfall duration, which facilitated the occurrence of severe precipitation;
(2) Forced lifting. The mountainous terrain made the high-value area of positive vorticity extend to 200 hPa through the remarkable dynamic lifting in front of the mountain, accelerating the vertical upward motion. The strong low-level convergence and high-level divergence strengthened the dynamic action;
(3) The corresponding moisture convergence intensified. The microwave measurements show the higher water vapor density profile was in lower layer. The high-water vapor density profile lasting for 15 h coupled with the strong convergence of water vapor flux supplied sufficient water vapor and transported it, supporting the extreme precipitation. The dense moisture area corresponded to the terrain height with increasing precipitation.

According to the estimated precipitation rate, the positive effect of Changbai Mountain on the torrential rains reached 6.8 mm/h, which nears 41% of the total rainfall of this period. After the terrain height is lowered in the topographic sensitivity experiment, the convergence and ascending motion in the eastern part of Jilin Province weakens, and the rainfall is significantly diminished. The calculated difference between the topographic sensitivity experiment and control experiment denotes that the terrain obstruction also affects the distribution of storm-relative helicity and atmospheric precipitable water, which further indicates that the topography of Changbai Mountain is one of the significant causes for this extreme precipitation event.

In short, the topography of Changbai Mountain played a very important role in the extreme precipitation caused by the super typhoon Maysak. In this paper, we have analyzed how Changbai Mountain influenced the extreme heavy rainfall in the respect of dynamics and moisture transport, but in terms of the thermodynamic effect, it is worthy of further research. The trace of typhoon will be influenced by the subtropical high

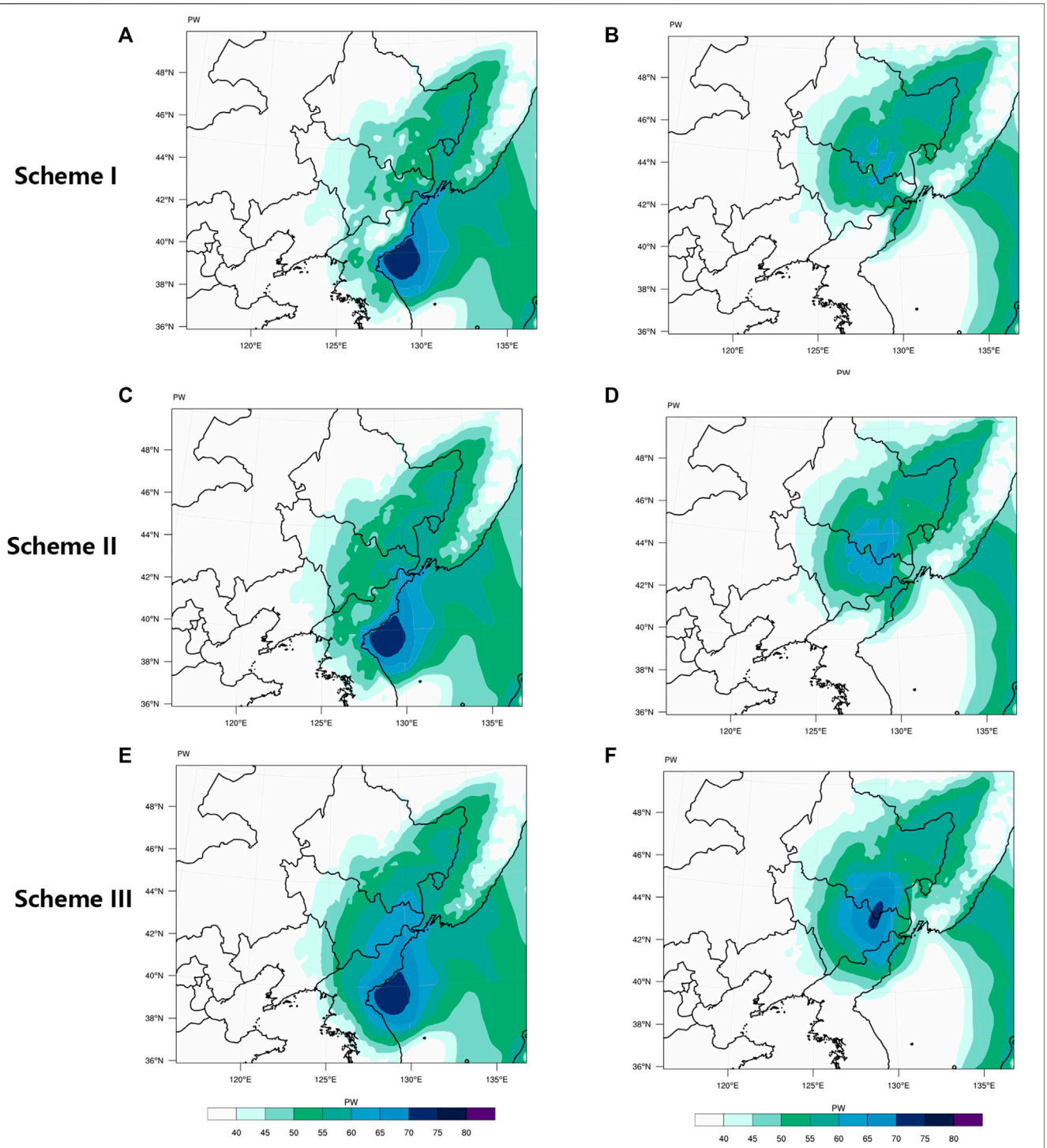


**FIGURE 10 |** Atmospheric precipitable water (shaded, unit: mm) in Scheme I **(A,B)**, Scheme II **(C,D)**, and Scheme III **(E,F)** at 09:00 and 14:00 BT, September 3, 2020.

pressure, westerly trough ridge, and typhoon internal force, among which the most decisive is the subtropical high pressure. In July 2020, the intensity of the subtropical high pressure was significantly stronger with its abnormal ridge line. The radial circulation composed of subtropical high pressure and northeastern cold vortex maintained a relatively stable state, guiding all three typhoons to move north along the "straight" similar path as the longitude line, and combined with the western belt system, bringing continuous strong wind and rain weather to Northeast China. With global warming, the warming ocean surface may drive and generate the necessary convections to sustain tropical cyclones (Sobel et al., 2016; Velden

et al., 2017). Thus, whether the physical mechanism of typhoons affecting the middle and high latitudes follows the historical statistical laws or not needs to be further deeply studied and discussed in the light of high-resolution data, numerical simulation, and analysis techniques.

## DATA AVAILABILITY STATEMENT

The raw data supporting the conclusions of this article will be made available by the authors, without undue reservation.

## AUTHOR CONTRIBUTIONS

XZ and DZ conceived the study. DZ, YY, and NW performed the data analysis. DZ, CC, and XT. revised and edited the manuscript. All authors contributed to the article and approved the submitted version.

## FUNDING

This research is funded by the National Key R&D Program of China (No. 2017YFC1502000) and Mesoscale Numerical Model Application Innovation Team of Changchun Meteorological Bureau (NO.202001).

## ACKNOWLEDGMENTS

The critical and useful comments of the reviewers greatly improved this work. The authors would like to acknowledge Prof. Hua Liu for her advice and English language polishing.

## REFERENCES

Agyakwah, W., and Lin, Y. L. (2021). Generation and Enhancement Mechanisms for Extreme Orographic Rainfall Associated with Typhoon Morakot (2009) Over the Central Mountain Range of Taiwan. *Atmos. Res.* 247, 105160. doi:10.1016/j.atmosres.2020.105160

Bai, Y.-Q., Wang, Y., Kong, S.-F., Zhao, T.-L., Zhi, X.-F., Zheng, H., et al. (2021). Modelling the Effect of Local and Regional Emissions on PM2.5 Concentrations in Wuhan, China during the COVID-19 Lockdown. *Adv. Clim. Change Res* 12, 871–880. doi:10.1016/j.accre.2021.09.013

Chan, P. W., and Hon, K. K. (2011). Application of Ground-Based, Multi-Channel Microwave Radiometer in the Nowcasting of Intense Convective Weather through Instability Indices of the Atmosphere. *Metz* 20 (4), 431–440. doi:10.1127/0941-2948/2011/0276

Chen, F., and Dudhia, J. (2001). Coupling an Advanced Land Surface-Hydrology Model with the Penn State-NCAR MM5 Modeling System. Part I: Model Implementation and Sensitivity. *Mon. Wea. Rev.* 129 (4), 569–585. doi:10.1175/1520-0493(2001)129<0569:caalsh>2.0.co;2

Chen, L., and Luo, Z. (2004). A Study of the Effect of Topography on the Merging of Vortices. *Adv. Atmos. Sci.* 21 (1), 13–22. doi:10.1007/BF02915676

Chen, L. S., and Meng, Z. Y. (2001). An Overview on Tropical Cyclone Research Progress in China during the Past Ten Years. *Chin. J. Atmos. Sci.* 25, 420–432. doi:10.3878/j.issn.1006-9895.2001.03.11

Chen, R., Zhang, W., and Wang, X. (2020). Machine Learning in Tropical Cyclone Forecast Modeling: A Review. *Atmosphere* 11 (7), 676. doi:10.3390/atmos11070676

Fang, X., Kuo, Y.-H., and Wang, A. (2011). The Impacts of Taiwan Topography on the Predictability of Typhoon Morakot's Record-Breaking Rainfall: A High-Resolution Ensemble Simulation. *Wea. Forecast.* 26 (5), 613–633. doi:10.1175/WAF-D-10-05020.1

Flesch, T. K., and Reuter, G. W. (2012). WRF Model Simulation of Two Alberta Flooding Events and the Impact of Topography. *J. Hydromet.* 13 (2), 695–708. doi:10.1175/JHM-D-11-035.1

Grell, G. A., and Dévényi, D. (2002). A Generalized Approach to Parameterizing Convection Combining Ensemble and Data Assimilation Techniques. *Geophys. Res. Lett.* 29 (14), 38-1–38-34. doi:10.1029/2002GL015311

He, B., Sun, J., Yu, E., Wang, H., Zhang, M., and Hua, W. (2020). Simulation Study on the Influence of the Great Khingan Strip and Changbai Mountain on Summer Rainfall in Northeast China. *Clim. Environ. Res.* 25 (3), 268–280. doi:10.3878/j.issn.1006-9585.2020.19189

Hersbach, H., Bell, B., Berrisford, P., Hirahara, S., Horányi, A., Muñoz-Sabater, J., et al. (2020). The ERA5 Global Reanalysis. *Q.J.R. Meteorol. Soc.* 146 (730), 1999–2049. doi:10.1002/qj.3803

Hogsett, W., and Zhang, D.-L. (2010). Genesis of Typhoon Chanchu (2006) from a Westerly Wind Burst Associated with the MJO. Part I: Evolution of a Vertically Tilted Precursor Vortex. *J. Atmos.* 67 (12), 3774–3792. doi:10.1175/2010jas3446.1

Hong, S.-Y., Dudhia, J., and Chen, S.-H. (2004). A Revised Approach to Ice Microphysical Processes for the Bulk Parameterization of Clouds and Precipitation. *Mon. Wea. Rev.* 132 (1), 103–120. doi:10.1175/1520-0493(2004)132<0103:aratim>2.0.co;2

Hong, S.-Y., Noh, Y., and Dudhia, J. (2006). A New Vertical Diffusion Package with an Explicit Treatment of Entrainment Processes. *Mon. Wea. Rev.* 134 (9), 2318–2341. doi:10.1175/MWR3199.1

Hsiao, L.-F., Liou, C.-S., Yeh, T.-C., Guo, Y.-R., Chen, D.-S., Huang, K.-N., et al. (2010). A Vortex Relocation Scheme for Tropical Cyclone Initialization in Advanced Research WRF. *Mon. Wea. Rev.* 138 (8), 3298–3315. doi:10.1175/2010MWR3275.1

Iacono, M. J., Delamere, J. S., Mlawer, E. J., Shephard, M. W., Clough, S. A., and Collins, W. D. (2008). Radiative Forcing by Long-Lived Greenhouse Gases: Calculations with the AER Radiative Transfer Models. *J. Geophys. Res.* 113 (D13), 1–8. doi:10.1029/2008jd009944

Islam, T., Srivastava, P. K., Rico-Ramirez, M. A., Dai, Q., Gupta, M., and Singh, S. K. (2015). Tracking a Tropical Cyclone through WRF-ARW Simulation and Sensitivity of Model Physics. *Nat. Hazards* 76 (3), 1473–1495. doi:10.1007/s11069-014-1494-8

Jianfeng, G., Xiao, Q., Kuo, Y.-H., Barker, D. M., Jishan, X., and Xiaoxing, M. (2005). Assimilation and Simulation of Typhoon Rusa (2002) Using the WRF System. *Adv. Atmos. Sci.* 22 (3), 415–427. doi:10.1007/BF02918755

Jiménez, P. A., Dudhia, J., González-Rouco, J. F., Navarro, J., Montávez, J. P., and García-Bustamante, E. (2012). A Revised Scheme for the WRF Surface Layer Formulation. *Mon. Wea. Rev.* 140 (3), 898–918. doi:10.1175/MWR-D-11-00056.1

Joyce, R. J., Janowiak, J. E., Arkin, P. A., and Xie, P. (2004). CMORPH: A Method that Produces Global Precipitation Estimates from Passive Microwave and Infrared Data at High Spatial and Temporal Resolution. *J. Hydrometeor.* 5 (3), 487–503. doi:10.1175/1525-7541(2004)005<0487:camtpg>2.0.co;2

Kalnay, E., Kanamitsu, M., Kistler, R., Collins, W., Deaven, D., Gandin, L., et al. (1996). The NCEP/NCAR 40-year Reanalysis Project. *Bull. Amer. Meteorol. Soc.* 77 (3), 437–471. doi:10.1175/1520-0477(1996)077<0437:tnyrp>2.0.co;2

Kilpela¨Inen, T., Vihma, T., Lafsson, H. O., and Karlsson, P. E. (2011). Modelling of Spatial Variability and Topographic Effects over Arctic Fjords in Svalbard. *Tellus A: Dynamic Meteorol. Oceanogr.* 63 (2), 223–237. doi:10.1111/j.1600-0870.2010.00481.x

Kim, D., Jin, C.-S., Ho, C.-H., Kim, J., and Kim, J.-H. (2015). Climatological Features of WRF-Simulated Tropical Cyclones over the Western North Pacific. *Clim. Dyn.* 44 (11-12), 3223–3235. doi:10.1007/s00382-014-2410-3

Lilly, D. K. (1986). The Structure, Energetics and Propagation of Rotating Convective Storms. Part II: Helicity and Storm Stabilization. *J. Atmos. Sci.* 43 (2), 126–140. doi:10.1175/1520-0469(1986)043<0126:tseapo>2.0.co;2

Lin, G.-F., and Jhong, B.-C. (2015). A Real-Time Forecasting Model for the Spatial Distribution of Typhoon Rainfall. *J. Hydrol.* 521, 302–313. doi:10.1016/j.jhydrol.2014.12.009

Lu, X., Yu, H., Ying, M., Zhao, B., Zhang, S., Lin, L., et al. (2021). Western north pacific Tropical Cyclone Database Created by the china Meteorological Administration. *Adv. Atmos. Sci.* 38 (4), 690–699. doi:10.1007/s00376-020-0211-7

Maussion, F., Scherer, D., Finkelnburg, R., Richters, J., Yang, W., and Yao, T. (2011). WRF Simulation of a Precipitation Event over the Tibetan Plateau, China - an Assessment Using Remote Sensing and Ground Observations. *Hydrol. Earth Syst. Sci.* 15 (6), 1795–1817. doi:10.5194/hess-15-1795-2011

Needham, H. F., Keim, B. D., and Sathiaraj, D. (2015). A Review of Tropical Cyclone-Generated Storm Surges: Global Data Sources, Observations, and Impacts. *Rev. Geophys.* 53 (2), 545–591. doi:10.1002/2014RG000477

Pan, T.-Y., Yang, Y.-T., Kuo, H.-C., Tan, Y.-C., Lai, J.-S., Chang, T.-J., et al. (2013). Improvement of Watershed Flood Forecasting by Typhoon Rainfall Climate Model with an ANN-Based Southwest Monsoon Rainfall Enhancement. *J. Hydrol.* 506, 90–100. doi:10.1016/j.jhydrol.2013.08.018

Pillay, M. T., and Fitchett, J. M. (2021). On the Conditions of Formation of Southern Hemisphere Tropical Cyclones. *Weather Clim. Extremes* 34, 100376. doi:10.1016/j.wace.2021.100376

Raju, P. V. S., Potty, J., and Mohanty, U. C. (2011). Sensitivity of Physical Parameterizations on Prediction of Tropical Cyclone Nargis over the Bay of Bengal Using WRF Model. *Meteorol. Atmos. Phys.* 113 (3), 125–137. doi:10.1007/s00703-011-0151-y

Rendfrey, T. S., Bukovsky, M. S., McCrary, R. R., and Fuentes-Franco, R. (2021). An Assessment of Tropical Cyclones in North American CORDEX WRF Simulations. *Weather Clim. Extremes* 34, 100382. doi:10.1016/j.wace.2021.100382

Roy, C., and Kovordányi, R. (2012). Tropical Cyclone Track Forecasting Techniques — A Review. *Atmos. Res.* 104-105, 40–69. doi:10.1016/j.atmosres.2011.09.012

Shen, Y., Xiong, A., Wang, Y., and Xie, P. (2010). Performance of High-Resolution Satellite Precipitation Products over China. *J. Geophys. Res.* 115 (D2), 1–17. doi:10.1029/2009JD012097

Shen, Y., Zhao, P., Pan, Y., and Yu, J. (2014). A High Spatiotemporal Gauge-Satellite Merged Precipitation Analysis over China. *J. Geophys. Res. Atmos.* 119 (6), 3063–3075. doi:10.1002/2013jd020686

Skamarock, W. C., Klemp, J. B., Dudhia, J., Gill, D. O., Barker, D. M., Duda, M. G., et al. (2008). *A Description of the Advanced Research WRF Version 3*. NCAR Technical Note. Boulder, CO, USA: National Center for Atmospheric Research.

Sobel, A. H., Camargo, S. J., Hall, T. M., Lee, C.-Y., Tippett, M. K., and Wing, A. A. (2016). Human Influence on Tropical Cyclone Intensity. *Science* 353 (6296), 242–246. doi:10.1126/science.aaf6574

Song, Z., and Zhang, J. (2020). Diurnal Variations of Summer Precipitation Linking to the Topographical Conditions over the Beijing-Tianjin-Hebei Region. *Sci. Rep.* 10 (1), 1–9. doi:10.1038/s41598-020-65743-1

Sun, L., Sui, B., Wang, X., and Liu, S. (2010). Climatic Characteristics of the Summer Hard Rain in the Northeastern Part of China. *Clim. Environ. Res.* 15, 778–786. doi:10.3878/j.issn.1006-9585.2010.06.07

Tang, C. K., and Chan, J. C. L. (2015). Idealized Simulations of the Effect of Local and Remote Topographies on Tropical Cyclone Tracks. *Q.J.R. Meteorol. Soc.* 141 (691), 2045–2056. doi:10.1002/qj.2498

Tao, W. K., Shi, J., Lin, P. L., Chen, J. Y., Lang, S., and Chang, M. Y. (2011). High-resolution Numerical Simulation of the Extreme Rainfall Associated with Typhoon Morakot. Part I: Comparing the Impact of Microphysics and PBL Parameterizations with Observations. *Terr. Atmos. Ocean. Sci.* 22 (6), 6. doi:10.3319/tao.2011.08.26.01(tm)

Van Nguyen, H., and Chen, Y.-L. (2011). High-resolution Initialization and Simulations of Typhoon Morakot (2009). *Mon. Wea. Rev.* 139 (5), 1463–1491. doi:10.1175/2011MWR3505.1

Velden, C., Olander, T., Herndon, D., and Kossin, J. P. (2017). Reprocessing the Most Intense Historical Tropical Cyclones in the Satellite Era Using the Advanced Dvorak Technique. *Mon. Wea. Rev.* 145 (3), 971–983. doi:10.1175/MWR-D-16-0312.1

Wang, H., and Wang, Y. (2014). A Numerical Study of Typhoon Megi (2010). Part I: Rapid Intensification. *Mon. Wea. Rev.* 142 (1), 29–48. doi:10.1175/MWR-D-13-00070.1

Wang, D.-h., Zhong, S.-x., Liu, Y., Li, J., Hu, K.-x., and Yang, S. (2007). Advances in the Study of Rainstorm in Northeast China. *Adv. Earth Sci.* 22 (6), 549–560. doi:10.1002/jrs.1570

Wang, H., Miao, Q., Shen, L., Yang, Q., Wu, Y., and Wei, H. (2021). Air Pollutant Variations in Suzhou during the 2019 Novel Coronavirus (COVID-19) Lockdown of 2020: High Time-Resolution Measurements of Aerosol Chemical Compositions and Source Apportionment. *Environ. Pollut.* 271, 116298. doi:10.1016/j.envpol.2020.116298

Wang, K., Qi, D., Gao, L., and Weng, Z. M. (2021). Analysis of the Effects of the Topography of Eastern Zhejiang on the Extreme Precipitation of Typhoon Lekima. *J. Meteorol. Sci.* 41, 162–171. doi:10.12306/2019jms.0071

Weissmann, M., Harnisch, F., Wu, C.-C., Lin, P.-H., Ohta, Y., Yamashita, K., et al. (2011). The Influence of Assimilating Dropsonde Data on Typhoon Track and Midlatitude Forecasts. *Mon. Wea. Rev.* 139 (3), 908–920. doi:10.1175/2010MWR3377.1

Xie, P., and Xiong, A.-Y. (2011). A Conceptual Model for Constructing High-Resolution Gauge-Satellite Merged Precipitation Analyses. *J. Geophys. Res.* 116 (D21), 1–14. doi:10.1029/2011JD016118

Ying, M., Zhang, W., Yu, H., Lu, X., Feng, J., Fan, Y., et al. (2014). An Overview of the China Meteorological Administration Tropical Cyclone Database. *J. Atmos. Oceanic Technol.* 31 (2), 287–301. doi:10.1175/JTECH-D-12-00119.1

Zhao, Y. (2012). Numerical Investigation of a Localized Extremely Heavy Rainfall Event in Complex Topographic Area during Midsummer. *Atmos. Res.* 113, 22–39. doi:10.1016/j.atmosres.2012.04.018

Zhu, Q., Lin, J., Shou, S., and Tang, D. (2000). *Principles and Methods of Weather*. Beijing: China Meteorological Press.

Zhu, Y., Qiao, F., Liu, Y., Liang, X.-Z., Liu, Q., Wang, R., et al. (2022). The Impacts of Multi-Physics Parameterization on Forecasting Heavy Rainfall Induced by Weak Landfalling Typhoon Rumbia (2018). *Atmos. Res.* 265, 105883. doi:10.1016/j.atmosres.2021.105883

**Conflict of Interest:** The authors declare that the research was conducted in the absence of any commercial or financial relationships that could be construed as a potential conflict of interest.

**Publisher's Note:** All claims expressed in this article are solely those of the authors and do not necessarily represent those of their affiliated organizations, or those of the publisher, the editors and the reviewers. Any product that may be evaluated in this article, or claim that may be made by its manufacturer, is not guaranteed or endorsed by the publisher.

frontiers in Environmental Science

ORIGINAL RESEARCH
published: 19 January 2022
doi: 10.3389/fenvs.2021.821648

# Joint Occurrence of Heavy $PM_{2.5}$ Pollution Episodes and Persistent Foggy Days in Central East China

*Caixia Yu*[1,2,3,4], *Yuanjian Yang*[5] *and Dong Liu*[2]*

[1]Key Laboratory of Atmospheric Optics, Anhui Institute of Optics and Fine Mechanics Chinese Academy of Sciences, Hefei Institutes of Physical Science, Chinese Academy of Sciences, Hefei, China, [2]Science Island Branch, Graduate School of USTC, Hefei, China, [3]Anhui Province Key Laboratory of Atmospheric Sciences and Satellite Remote Sensing, Anhui Institute of Meteorological Sciences, Hefei, China, [4]Shouxian National Climate Observatory, Typical Farmland Eco-Meteorology Field Scientific Test Base of China Meteorological Administration in Huaihe River Basin, Shouxian, China, [5]School of Remote Sensing and Geomatics Engineering, Nanjing University of Information Science and Technology, Nanjing, China

Although many severe pollution events in Central and East China have been analyzed in recent years, the heavy $PM_{2.5}$ pollution episode happened on persistent foggy days from January 13 to 18, 2018 was unique, characterized by explosive increase and sharp decrease in $PM_{2.5}$ (particles with kinetic equivalent diameter less than or equal to 2.5 microns) concentration. Based on hourly data of ground level meteorological parameters, $PM_{2.5}$ data and CALIPSO-based (the Cloud-Aerosol Lidar and Infrared Pathfinder Satellite Observation) aerosol data, combined with ECMWF (European Centre for Medium-Range Weather Forecasts) reanalysis data and radiosonde temperature profile, a comprehensive analysis was conducted to reveal the meteorological reasons for the evolution of the episode at horizontal and vertical scales. The $PM_{2.5}$ concentration experienced four stages: a slow-increase phase, rapid-increase phase, rapid-decrease phase, and rebound phase. Results show that because Central and East China (CEC) were located at the back of a high-pressure system, humid southerly winds and near surface inversion (NSI) were responsible for the slow accumulation of pollutants. The rapid-increase phase was attributed to pollution transport at both ground level and in the lower troposphere because of weak cold air invasion. The significant subsidence at 500 hPa and 700 hPa intensified the NSI and led to dense fog. In that case, corresponding to the supersaturated atmosphere, the particles entered the fog droplets and were scavenged partly by deposition at night and were resuspended on the next day when the atmosphere was unsaturated. Our findings provide convincing evidence that surface $PM_{2.5}$ rapid-decrease phase and the rebound phase were closely associated with dense fog process.

**Keywords: $PM_{2.5}$ pollution episodes, fog process, wet deposition, subsidence motions, rebound**

OPEN ACCESS

***Edited by:***
*Junke Zhang,*
*Southwest Jiaotong University, China*

***Reviewed by:***
*Lei Shu,*
*Southern University of Science and Technology, China*
*Yefu Gu,*
*the Chinese University of Hong Kong, China*

***Correspondence:**
*Dong Liu*
*dliu@aiofm.cas.cn*

***Specialty section:***
*This article was submitted to Atmosphere and Climate, a section of the journal Frontiers in Environmental Science*

***Received:*** *24 November 2021*
***Accepted:*** *20 December 2021*
***Published:*** *19 January 2022*

***Citation:***
*Yu C, Yang Y and Liu D (2022) Joint Occurrence of Heavy $PM_{2.5}$ Pollution Episodes and Persistent Foggy Days in Central East China. Front. Environ. Sci. 9:821648. doi: 10.3389/fenvs.2021.821648*

## INTRODUCTION

In recent years, severe air pollution events have received media and public coverage as common phenomena in China (Guo et al., 2011; Ding and Liu, 2014; Wang et al., 2019). High particulate matter levels are usually closely associated with high levels of precursor emissions (Markovicl et al., 2014; Holt et al., 2015). Therefore, the government took strong measures to improve those enterprises with high energy consumption, such as coal, to reduce pollution emissions (Liu

et al., 2015; Guo et al., 2016; Gao et al., 2020). However, according to the statistics, humans still suffer from air pollution during most of the wintertime in some Chinese cities (Chen et al., 2013; Yang et al., 2020). Especially in the Beijing-Tianjin-Hebei region (BTH) and Yangtze River Delta region (YRD), large amounts of data indicate that air pollution has been very serious as a consequence of the phenomenal economic growth (Zhang et al., 2012; Wang et al., 2015; Zhang et al., 2015; Zheng et al., 2018). Fine particles suspended in the air contain high concentration of heavy metals, which enter the blood circulation through the respiratory system and then result in disease (Peters et al., 1996; Delfino et al., 2005; Pope and Dockery, 2006; Wei et al., 2017; Gu et al., 2020), which vitally affects social activities.

The formation mechanisms of typical $PM_{2.5}$ pollution episodes over China have been extensively studied to provide references for local governments to take air pollution control measures (Gao et al., 2012; Zhou et al., 2015; Jin et al., 2017; Wu et al., 2020; Wang, et al., 2021a; Wang, et al., 2021b). Normally, meteorological factors play a significant role in the generation, development and end of pollution events through a complex combination of processes, including pollutant transitions, secondary particle production, particle hygroscopic growth and wet removal processes, and are principally responsible for heavy pollution episodes (Pasch et al., 2011; Wang and ChenSun, 2014; Wang et al., 2015; Miao et al., 2017; Yang et al., 2018). Many studies have been carried out to understand the correlation between climate and pollution episodes in China (Zhu et al., 2012; Li et al., 2016; Yang et al., 2018). It is generally believed that the weakening East Asia winter monsoons result in reductions in the number of strong cold outburst events and increases in stagnant weather conditions, both of which further lead to more heavy pollution events (Lin et al., 2018). In addition, studies have shown that pollutant accumulations are directly influenced by local adverse meteorological parameters (Chen et al., 2008; Deng et al., 2012; Ji et al., 2014). It has been indicated that reduced rainfall amounts, gentle winds and high relative humidity are key factors in the formation of heavy pollution (Sun et al., 2013; Shi et al., 2018; Chen et al., 2020).

Meanwhile, wet deposition of particulate matter caused by precipitation and fog are also important process to purified air and maintain the source-sink balance of suspended particles in the atmosphere. Previous studies reported that the air quality deteriorated during haze but improved in fog (Wang and ChenSun, 2014; Xu et al., 2017). Especially in the late stage of extremely dense fog episodes, particulate mass concentration reached the lowest value because of the progressive accumulated effect of wet deposition of large fog droplets (Yang et al., 2012). The observations showed also that in a core city of BTH region, the concentrations of $PM_{2.5}$ and SO2 obviously decreased during the heavy fog period (Han et al., 2018). Compared with dry deposition, the wet deposition by fog formation led to pollutant lifetimes on the order of 6–12 h, while pollutant removal by ventilation of valley air required at least 5 days (Waldman and Hoffmann, 1987).

CEC lies in the north and south climate intermediate belts with time-varying weather conditions, and both increase the difficulty of studying pollution episodes. The formation and evolution of heavy $PM_{2.5}$ pollution episodes are characterized by distinctive regional features. Even though studies have analyzed the characteristics and mechanisms of heavy $PM_{2.5}$ pollution episode in CEC, few studies have reported the joint occurrence of persistent $PM_{2.5}$ pollution episodes and foggy days. In this paper, the heavy air pollution episode accompanied by dense fog in CEC was taken as an example to comprehensively analyze the driving meteorological conditions for slow-increase, rapid-increase and short-term dissipation of $PM_{2.5}$ pollution by using meteorological data (including high-resolution sounding data, surface observation data, and reanalysis data); real-time pollutant concentration monitoring data; and vertical aerosol extinction coefficient data that were monitored by CALIPSO.

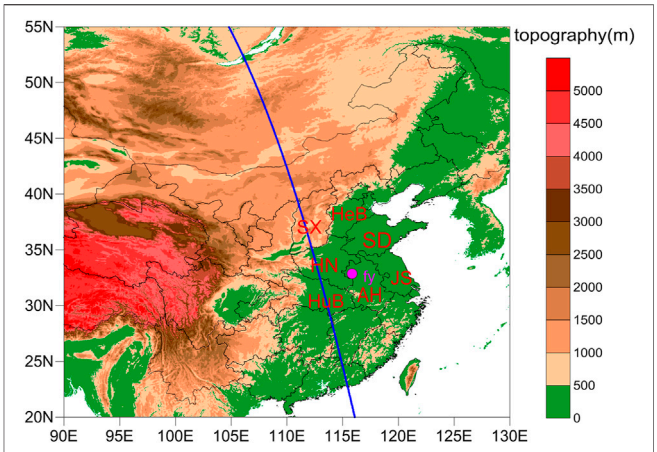


**FIGURE 1 |** The topography of Central East China, locations of representative cities and the CALIPSO satellite orbit used in this paper. The red letters indicate provinces (e.g., SX: Shanxi, HeB: Hebei, SD: Shandong, HN: Henan, HuB: Hubei, AH: Anhui, and JS: Jiangsu). The pink spot indicates a city (fy: Fuyang). The blue spots indicate the CALIPSO satellite orbit that passed over CEC on January 16.

# DATA AND METHODS

## Region and Site

Severe $PM_{2.5}$ pollution episodes occurred in central and eastern China (mainly in Shanxi, Hebei, Shandong, Henan and Anhui provinces) during January 13–18, 2018. In addition, Fuyang was selected as the representative city in this paper. Fuyang (115.82°E, 32.92°N, 39 m above sea level) is located in northwestern Anhui Province and has a seasonal temperate semi humid monsoon climate (Deng et al., 2019). The monsoon climate is clearly defined with concentrated rainy summers and cold winters. Northerly winds rule in winter, while southerly winds prevail in summer. Fuyang station possesses a modern observation system that can conduct surface meteorological observations and sounding measurements and provides abundant and reliable observational data for relevant research.

## Air Quality Data

All the data and results in this study were presented at Beijing Standard Time (BST). The $PM_{2.5}$ hourly concentration data were downloaded from the website of the Ministry of Environmental Protection of China. Based on the $PM_{2.5}$ concentration, heavy air pollution was found to occur in central and eastern China on January 13–18 and accompanied by large-scale dense fog. During this episode, the areas with $PM_{2.5}$ concentration greater than 150 μg/m$^3$ expanded and moved southward. In addition, the characteristics of the pollutant concentration at different stages and their relationships with the meteorological parameters were analyzed, which included slow increases, rapid increases and sharp decreases in $PM_{2.5}$ concentration. **Figure 1** shows the topography of CEC and the surrounding areas and the location of the representative city, Fuyang, which experienced violent swings in the $PM_{2.5}$ concentration during January 13–18.

## Meteorological Data

The circulation patterns and vertical motions of the middle-lower troposphere are closely related to the surface meteorological conditions. The sea level pressure (SLP) and vertical velocity data with a resolution of 0.25°* 0.25° obtained from the ECMWF were obtained from the European Centre for Medium-Range Weather Forecasts were used to analyze the influence of the weather systems during the severe pollution episode.

To understand the effects of surface meteorological parameters on pollutant concentration, hourly ground meteorological observation data and sounding data from Fuyang station were obtained from the Anhui Information Center of Meteorology, where data quality control had been carried out and were utilized in the study. The surface meteorological variables included hourly ground level temperature, dew point temperature, wind speed, wind direction, relative humidity and visibility. The high-resolution (1.2 s) sounding data that were obtained at 07:00 and 19:00 at the Fuyang sounding station were used to determine the temperature inversions and vertical wind distributions. The accuracies of the radiosonde temperature data are within 0.1 K and have been broadly used to characterize the boundary layer structures in China (Guo et al., 2019). These observations are conducted by specially trained personnel and use the procedures established by the World Meteorological Organization (WMO).

## CALIPSO Data

During the study period, CALIPSO passed over the contaminated area. The CALIOP instrument was launched in 2006 and has provided nearly continuous global measurements of aerosols and clouds with high vertical and spatial resolutions (David et al., 2009), which are important for studies of radiative forcing (Satheesh, 2002) and air quality (Al-Saadi et al., 2005). The level 2 products are reported both as layer products and as profile products. In this paper, the version 3.01 level 2 aerosol layer product was used to obtain the altitude-height distributions of the aerosol extinction coefficients and further investigate the vertical distributions of the aerosols. The product has a horizontal resolution of 333 m and vertical resolution of 30 m below 8 km.

# THE POLLUTION PROCESS AND DENSE FOG EVENT

## Spatiotemporal Variations in $PM_{2.5}$ Concentration

**Figure 2** depicts the $PM_{2.5}$ concentration distributions at 06:00 for each day during January 13–18, 2018. We observed that a heavy pollution zone ($PM_{2.5}$ > 150 μg/m$^3$) began in Shanxi Province on January 13 and worsened the next day. On January 15, the heavily contaminated area moved eastward to the BTH region and expanded southward to the border with Shandong and Hebei Provinces. On the morning of January 16, we found that the pollution zone moved southward and that the center of heavy pollution was located at the region where Henan, Shandong and Hubei Provinces intersect. On January 17, the heavily polluted area moved further southward and the air quality in eastern Hebei Province was improved, while the $PM_{2.5}$ concentration for most parts of Henan rose to above 250 μg/m$^3$. Meanwhile, it should be noted that $PM_{2.5}$ concentration in northwest Anhui, where the Fuyang sounding station is located, sharply decreased to below 100 μg/m$^3$ at 06:00 January 17. The air quality exhibited large differences between southeastern Henan and northwestern Anhui.

Previous studies have shown that cold air intrusion and precipitation are the main removal mechanisms of large-scale severe pollution (Kang et al., 2019), especially in winter. However, improvements in air quality occurred in limited areas with no precipitation at 06:00 January 17, while the pollution in the surrounding areas remained, which indicated that local meteorological parameters played a role during the episode. On January 18, the pollutants again remained in the atmosphere above Henan, Shandong and their border with Anhui and Jiangsu Provinces.

The whole pollution process led to average $PM_{2.5}$ concentration reach 120 μg/m$^3$ from 04:00 January 13 to 04:00 January 18 in Fuyang city. Time series plots of the $PM_{2.5}$ concentration are shown in **Figure 3**. We found that the $PM_{2.5}$ mass concentration evolution trend in Fuyang could be divided into four phases (**Table 1**): 1) a slow-increase phase from 04:00 January 13 to 08:00 January 16, 2) rapid-increase phase from 08:00 January 16 to 20:00 January 16, 3) rapid-decrease phase from 20:00 January 16 to 07:00 January 17, and 4) rebound phase from 07:00 January 17 to 04:00 January 18. In the first stage, the $PM_{2.5}$ mass concentration increased slowly to 139 μg/m$^3$ from 43 μg/m$^3$. The most severe $PM_{2.5}$ pollution levels occurred in the second stage, with a peak value of 285 μg/m$^3$ at 20:00 January 16. Thereafter, the $PM_{2.5}$ mass concentration decreased sharply to 31 μg/m$^3$ within 11 h. However, after short-term dissipation, the $PM_{2.5}$ mass concentration rebounded to 166 μg/m$^3$ in 1 day. This means that although the air quality improved quickly during the evening of January 16, the pollutants were not cleaned up.

The $PM_{2.5}/PM_{10}$ ratios of the mass concentration exhibited obvious differences at different stages. The ratios were always between 0.63 and 0.86 with no obvious trends during the slow-increase stage, and the ratios increased overall to 0.79–0.95 in the rapid-increase stage, which suggested that fine particles accounted for a large proportion of the particle mass.

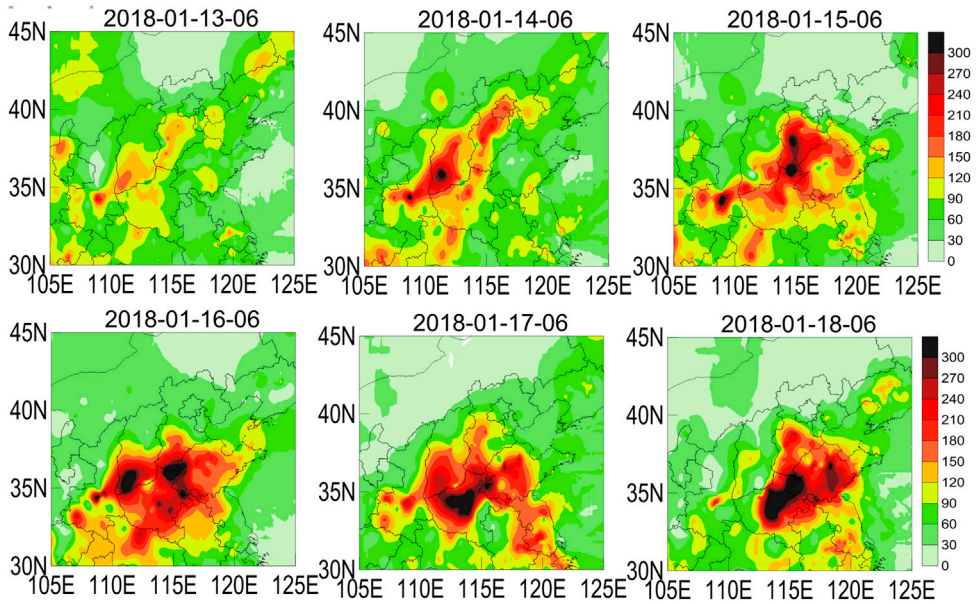


**FIGURE 2 |** Distributions of $PM_{2.5}$ (unit: μg/m$^3$) concentration at 06:00 in Central-East China on 13–18 **(A–F)** January 2018.

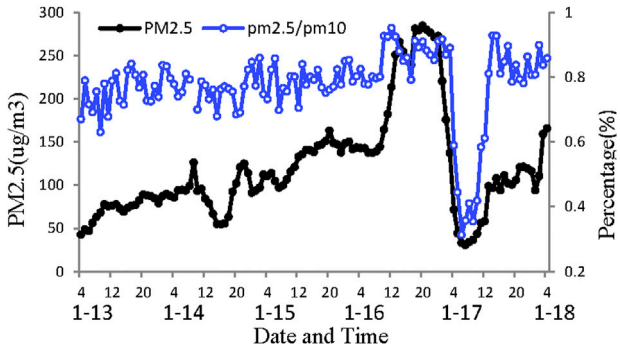


**FIGURE 3 |** Variations in the hourly $PM_{2.5}$ concentration and proportions of $PM_{2.5}$ to $PM_{10}$ in Fuyang.

Thereafter, the particles exhibited irregular fluctuations, the $PM_{2.5}/PM_{10}$ ratios dropped to 0.31, and $PM_{10}$ became the main pollutant in the rapid-decrease stage. Corresponding to the rebound in pollutant concentration in the daytime on January 17, the ratios rose to 0.93 and remained above 0.78 on January 18.

## Fog Weather Process During the Episode

Fog is a weather phenomenon, which occurs when the atmospheric relative humidity in the boundary layer is greater than 90% and the horizontal visibility is less than 1 km. The visibility within 1–10 km is called light fog. It is worth noting that large-scale foggy weather was observed on the mornings of January 16–18 and affected more than 20 provinces in China. **Figure 4** depicts the dense fog areas with visibility below 1 km and the relative humidity exceeds 90%. On the morning of January 17, dense fog occurred in most parts of Anhui and Jiangsu Provinces and their border with Hebei and Shandong Provinces. Especially in northern Anhui Province, the visibility was less than 0.4 km.

# THE DRIVING METEOROLOGICAL CONDITIONS FOR SLOW-INCREASE, RAPID-INCREASE AND SHORT-TERM DISSIPATION OF $PM_{2.5}$ POLLUTION

## Large Scale Synoptic Patterns

**Figure 5** shows that evolution of the sea level pressure fields during the heavy pollution episode. The results show that CEC

**TABLE 1 |** Summary of the different air pollution stages in Fuyang during the study period.

| Stage | Date | Duration (h) | Initial $PM_{2.5}$ concentration (μg/m$^3$) | End $PM_{2.5}$ concentration (μg/m$^3$) | $PM_{2.5}$ difference (μg/m$^3$) |
|---|---|---|---|---|---|
| Slow increase | 04:00 January13-08:00 January16 | 76 | 43 | 139 | 96 |
| Rapid increase | 08:00 January16-20:00 January16 | 12 | 139 | 285 | 146 |
| Rapid decrease | 20:00 January16-07:00 January17 | 11 | 285 | 31 | -254 |
| Rebound | 07:00 January17-04:00 January18 | 21 | 31 | 166 | 135 |

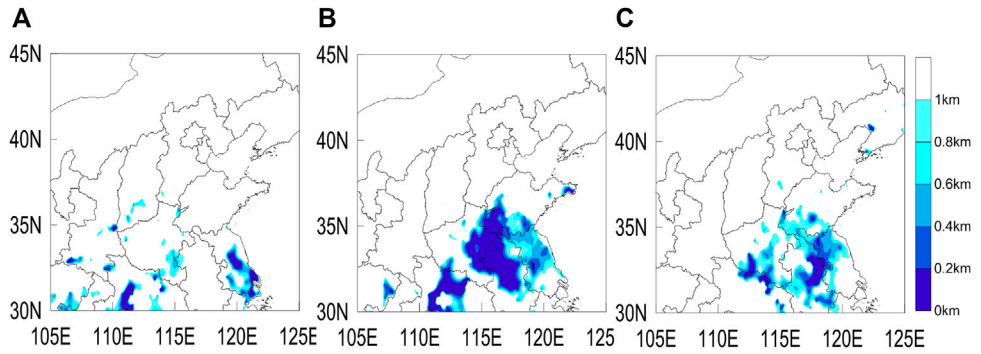


**FIGURE 4 |** Distributions of the daily visibility at 06:00 in Central-East China on 16–18 **(A–C)** January 2018.

experienced sustained south winds due to its location near the rear of the high-pressure system that was caused by the East Asian trough on January 13 (**Figure 5A**). In addition to the East Asian trough moving east on January 14, the atmospheric circulation adjusted, as is demonstrated by the continuous high-pressure systems, and was separated from the Mongolia-Siberian High Pressure (**Figure 5B**). A separate high-pressure system centered at the Bohai Gulf area moved rapidly east on January 15 (**Figure 5C**). After that, a slightly stronger high-pressure system was separated again on the morning of January 16 and affected a wider area, while weak north winds prevailed in Anhui (**Figure 5D**). However, the high pressure system was not strong enough and gradually diminished by the night of January 16. Meanwhile, the southerly airstream strengthened and moved northward, which meant that convergence lines formed at night on January 16 in CEC when the enhanced southerly winds met the original northerly winds. By the morning of January 17, CEC was entirely dominated by southerly winds.

The changes in SLP in Anhui, along with the surface winds, demonstrate that heavy pollution episodes occurred during the atmospheric circulation adjustment period, with several weak colds fronts intruding into the North China Plain and Northeast Plain. Most of the time, the SLP were uniformly distributed, with southerly wind speeds that were low in CEC.

## Inversion of Boundary Layer Temperature

The wind and temperature profiles at the Fuyang sounding station that were obtained at 07:00 and 19:00 on each day during the episode were used to reveal the vertical structures of the atmospheric layer (**Figure 6**). On January 13–14, all of the middle and lower troposphere was controlled by southwesterly winds. In particular, the southwesterly warm moisture flow was stronger between 500 m and 1,500 m (**Figure 6A**), which led to the temperature of the lower atmosphere being higher than that at the surface. Therefore, an NSI was observed in the morning and night of January 13–14 (**Figures 6B,C**). The top of the NSI was below 500 m, and its intensity was approximately 1–2.4°C/100 m. These results indicate that a persistent temperature inversion decreased the thickness of the mixing layer and hindered the upward transport of pollutants and was favorable for the gradual air pollution accumulation on the ground at the early stage of the pollution episode.

The prevailing wind direction within 1 km of the ground shifted to northeast on the evening of January 15 (**Figure 6A**). At 07:00 on January 16, northerly winds further strengthened and dominated from ground level to 3 km or higher, which indicated that the warm air mass had weakened and retreated southward when the cold air mass was enhanced and the CEC area was controlled. The northerly wind broke the NSI and an inversion layer appeared between 1,400 and 1,500 m, which was higher in the daytime on January 16 (**Figure 6E**).

Although the vertical diffusion conditions improved, the ground pollution levels were pushed upward (**Figure 3**). Therefore, we further investigated the effect of pollutant transport in the daytime of January 16. **Figure 7** shows the height-latitude cross section of aerosol extinction along the orbit displayed in **Figure 1** on 13:00 January 16. After removing the influence of clouds, the high extinction coefficients were attributed to high aerosol concentration. Large amounts of aerosols were distributed from the ground up to 1.5 km between 31.5°N and 35°N. As mentioned in **Figures 5D**, **6A**, not only the surface but also the lower atmosphere were controlled by north winds in Anhui and Henan Provinces as a result of the development of the high-pressure system. It can be deduced that in addition to pollution transport on the ground, the north winds in the lower atmosphere were also conducive to the transport of particulate matter from North China to CEC during the episode.

On the morning of January 17 (07:00), corresponding to the northerly winds at ground level up to 1.5 km and southwesterly winds above 2 km, the ground temperature dropped to 0°C, but the temperature at 1,500 m rose from −3°C to 3°C and formed a deep, strong SBI in the boundary layer with the inversion top located at approximately 200 m and the top of the isothermal layer at approximately 2 km. The SBI at 07:00 January 17 decreased the thickness of the mixing layer and was favorable for the accumulation of air pollution on the ground. However, under unfavorable conditions, the $PM_{2.5}$ mass concentration at Fuyang decreased sharply and decreased by 254 μg/m$^3$ within 11 h (**Table 1**). We further investigate the reasons for the sharp reduction in $PM_{2.5}$ concentration in *Analysis of the Reasons for the Dramatic Drop and Rebound in $PM_{2.5}$ Concentration*. At the night of January 17 (**Figure 6F**), the surface temperature rose from 0°C to about 4°C, but the NSI was not broke. The top of the isothermal layer located at approximately 2 km.

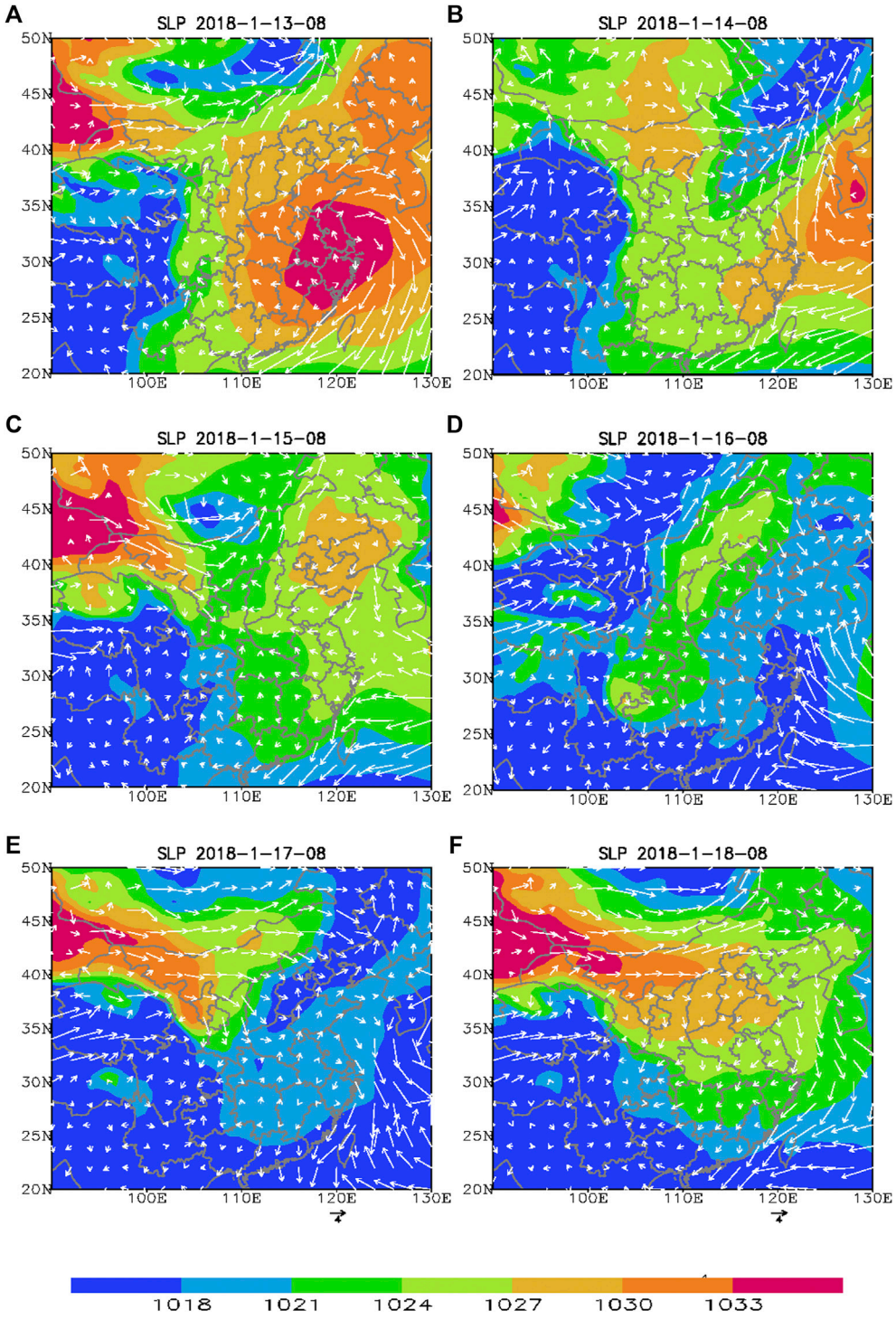


**FIGURE 5 |** Distributions of the sea level pressure (unit: hPa) and 10 m winds (unit: m/s) at 08:00 on January 13–18, 2018. The arrow length represents wind speed with 4 m/s. Wind speed 4 m/s.

## Surface Meteorological Factors

To further understand the formation, maintenance and short-term dissipation of the episode, especially the two increasing phases and one sharp reduction phase, extensive analyses were conducted to understand the driving meteorological conditions. Hence, the hourly near-surface meteorological conditions (e.g., wind speed, wind direction, temperature, dew point temperature, relative humidity, and visibility) and important weather events

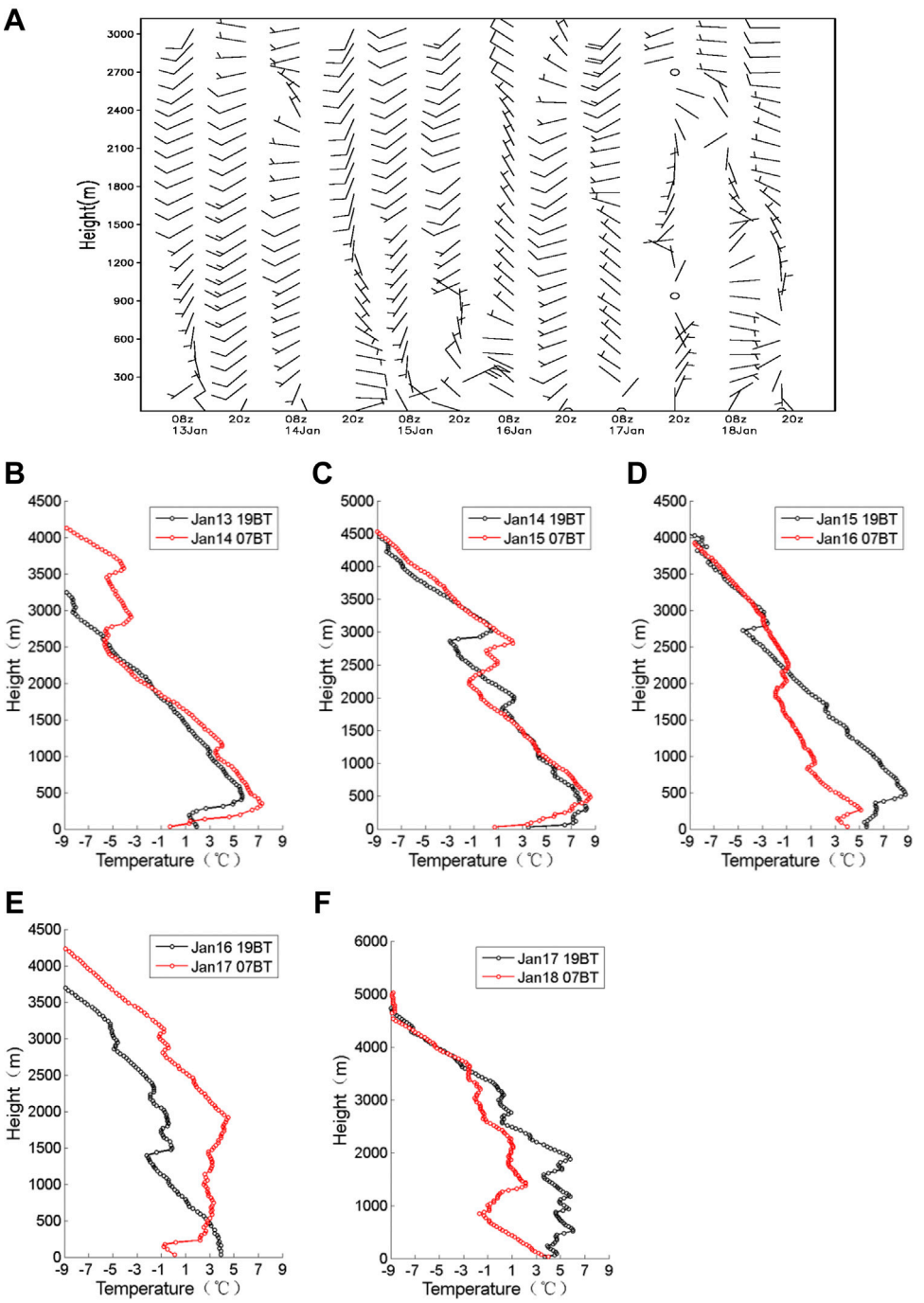


**FIGURE 6 |** Vertical distributions of wind vector **(A)** and temperature **(B–F)** at the Fuyang sounding station, which are shown in **Figure 1**, from January 13 to January 18, 2018.

from January 13 to January 18, 2018 in Fuyang are shown in **Figure 8**.

In the early period of the slow-increase stage (January 13–14), the prevailing wind direction was mainly southeast on January 13–14 with wind speeds of approximately 2–3 m/s. The ground relative humidity correspondingly showed fluctuating growth and reached 90% at 00:00 on January 15 (**Figure 8B**). In combination with **Figures 6**, **8A**, it can be deduced that the existence of the NSI led to pollutants being confined to the shallow mixing layer, and the sustained southerly winds increased the moisture content of the atmosphere and particle hygroscopic growth occurred, which were both conducive to an increase in the $PM_{2.5}$ mass concentration. In the

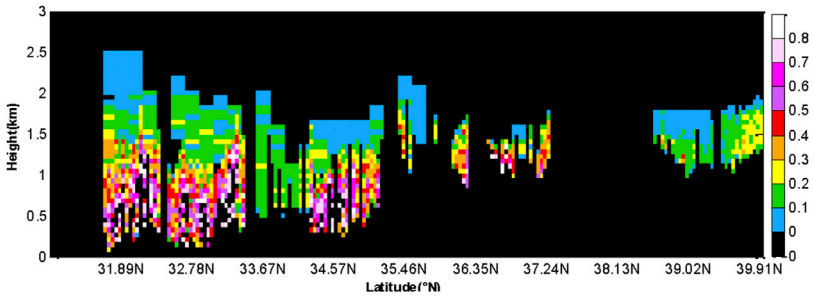


**FIGURE 7 |** Vertical distribution of the aerosol extinction coefficients along the CALIPSO orbit at 13:00 January 16.

later period of the slow-increase stage (January 15), the prevailing wind speeds were light, and the directions changed frequently from southeast to northeast due to a weak high-pressure system that originated in Mongolia (**Figure 8C**). This meant that the enhanced northerly winds met the southerly winds and the wind fields converged near Fuyang, which led to the pollutants and vapor that had been transported in the earlier stage remaining for a longer period and were not conducive to the diffusion of pollutants.

On January 16, due to the development of the high-pressure system shown in **Figure 5D**, weak cold air invaded southward, and north winds prevailed on the ground with velocities below 2 m/s in Fuyang (**Figure 8A**). It is worth noting that the center of highest pollution was located in the region north of Fuyang, so it transported pollutants from Henan and Shandong. However, the cold air was so weak that the pollutants in CEC could not be carried away and continued to accumulate. Meanwhile, along with a sharp increase in the $PM_{2.5}$ mass concentration, the visibility further decreased to less than 1 km by 17:00 January 16.

It could not be neglected that the value of relative humidity increased gradually from January 13 to 15 (**Figure 8B**). At the night

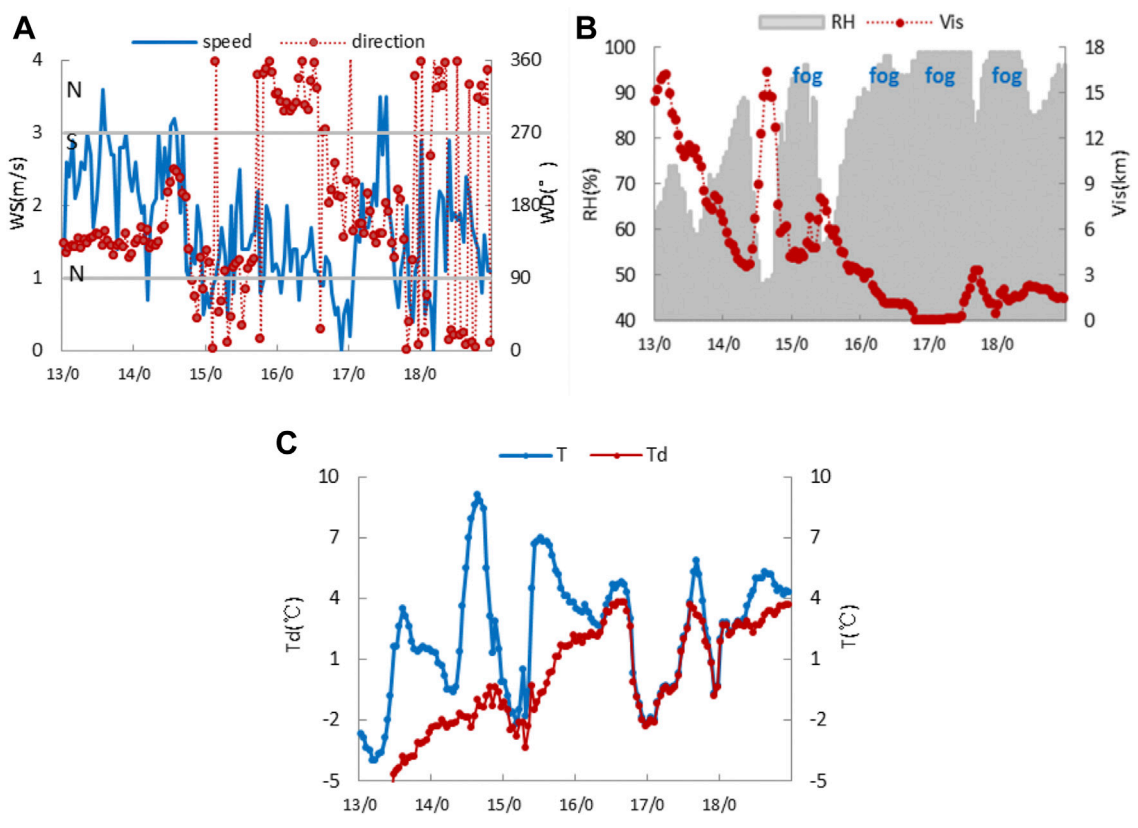


**FIGURE 8 |** Hourly surface meteorological conditions from January 13 to January 23, 2018 at Fuyang station including **(A)** wind speeds (WS), wind directions (WD), **(B)** relative humidity (RH) and visibility (Vis), **(C)** temperature (T) and dew point temperature (Td).

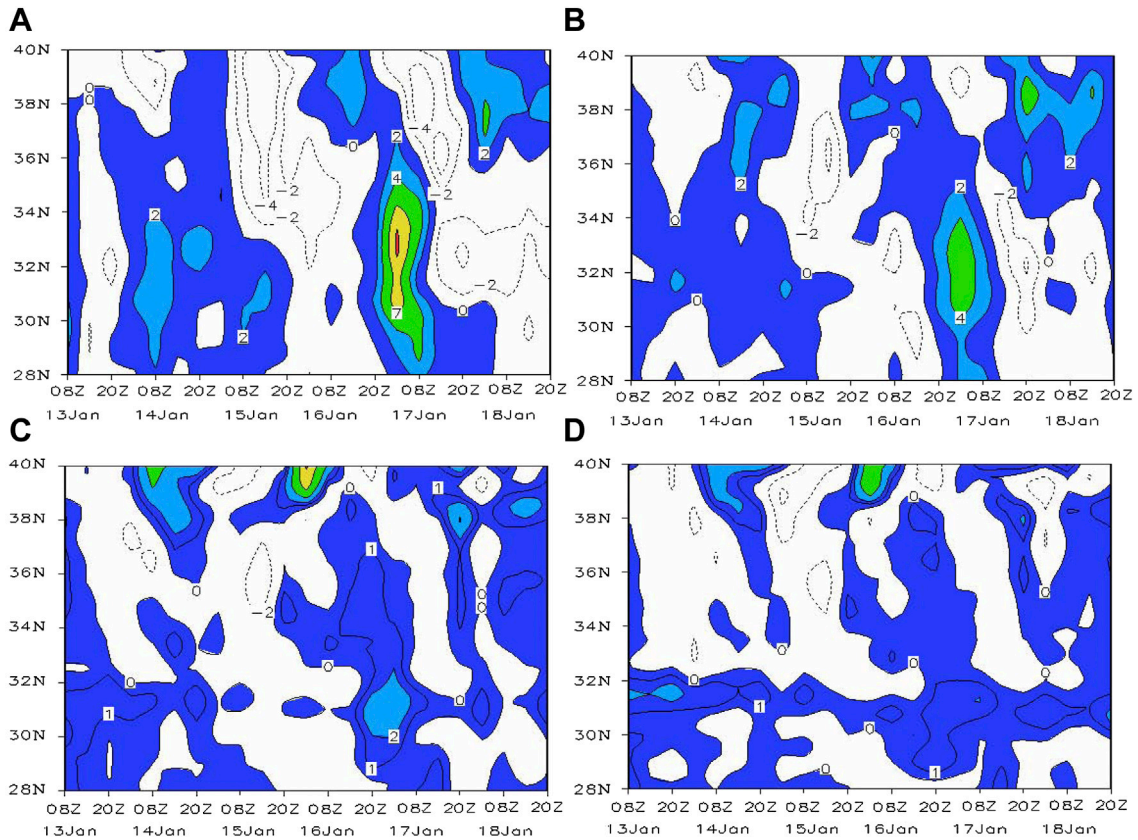


**FIGURE 9 |** Vertical velocity distributions at 115.75E **(A)** 500 hPa; **(B)** 700 hPa; **(C)** 850 hPa; **(D)** 925 hPa; unit: 0.1 Pa/s.

of January 14, the relative humidity exceeded 90% and haze turned into light fog. However the fog days just sustained for about 7 h and then dissipated as the sun rose. At the afternoon of January 16, because of the weakening of the high-pressure system, the surface winds changed to the south in Fuyang which brought warm, moist air, which resulted in relative humidity greater than 95% by the evening of January 16 and maintained at a high level over the next few days. From 08:00 January 16 to 14:00 January 17, the dew point temperature was nearly equal to the temperature, and the air was totally saturated (**Figure 8C**). Therefore, psersistant fog days were observed in Fuyang and surrounding areas during January 16–18, as shown in **Figure 4B**. Especially at the night of January 16, the visibility was below 300 m, which meant dense fog formed. It should be noted that it was during that time that the $PM_{2.5}$ mass concentration dropped to 31 μg/m$^3$ from 285 μg/m$^3$. Therefore, it can be deduced that the dense fog played an important role in the sharp decline in $PM_{2.5}$ concentration during the pollution episode.

## Analysis of the Reasons for the Dramatic Drop and Rebound in $PM_{2.5}$ Concentration

As mentioned above (**Figures 6**, **7**), the meteorological characteristics in Fuyang from 20:00 January 16 to 07:00 January 17 can be summarized as a strong NSI, high humidity, and ground breeze, none of which were conducive to pollution dissipation (He et al., 2017). Therefore, we further investigated the reason for the sudden pollution decrease on the night of January 16.

**Figure 9**, shows the time-latitude cross sections of the vertical velocities at 500, 700, 850, and 925 hPa along 115.75°E (Fuyang Station 115.82°E, 32.92°N). The results show that significant subsidence occurred from the evening of January 16 to the morning of January 17 in the mid-low troposphere and that the center was located at 33°N. The greatest subsidence speed at 500 hPa was approximately 1.0 Pa/s, which decreased to 0.4 Pa/s at 700 hPa and was weaker and not obvious at 850 and 925 hPa. The local subsidence motions at 500 and 700 hPa led to a temperature increase in the lower atmosphere, and a strong NSI occurred. This is consistent with previous research results. Gramsch et al. (2014), Shi et al. (2019) suggested that subsidence movements in the middle and upper layers cause warming in the lower troposphere, and an inversion layer then forms. As a result, the strong NSI confined the vapor water to the shallow mixing layer, and large-scale fog occurred.

In **Figure 10**, the colored areas show the dense fog regions with surface visibility below 500 m at 06:00 January 17. The heavier the fog, the lower the visibility. The region of dense fog was located in the region of the intersection of Shandong, Hebei and Anhui. In Fuyang, the visibility was lower than 100 m. The colored spots depict the $PM_{2.5}$ concentration differences between 20:00 January 16 and 07:00 January 17. Negative

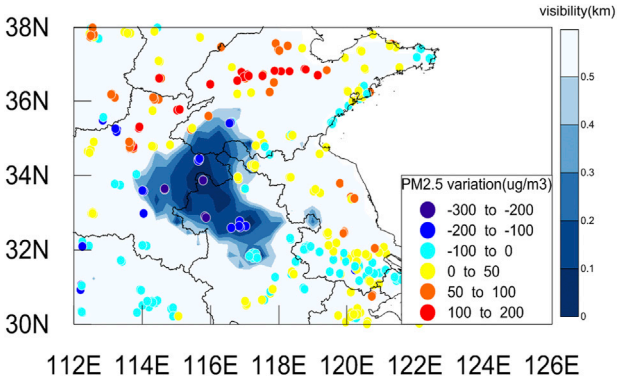


**FIGURE 10 |** Surface visibility distributions at 07:00 January 17 (colored areas) and $PM_{2.5}$ concentration difference from 20:00 January 16 to 07:00 January 17 (colored spots) in CEC.

values indicate decreases in the $PM_{2.5}$ concentration. The $PM_{2.5}$ concentration in the region of the intersection of Shandong, Hebei and Anhui experienced the largest drop with a concentration decrease that exceeded 100 μg/m$^3$ within 11 h. Especially in Fuyang city, Bozhou city of Anhui Province and Zhoukou city of Henan Province, the $PM_{2.5}$ concentration fell by more than 200 μg/m$^3$, which meant that sharp reductions occurred in the areas where dense fog appeared. It can be deduced that the scavenging of particles was caused by fog droplet deposition.

Previous research has shown that large fractions of the pollutants scavenged in fog could be removed from the atmosphere so that the occurrence of fog could diminish or limit the accumulation of particulate matter in stagnant air masses (Jacob et al., 1984). Studies have revealed that many air pollutants are deposited *via* fog droplets, and the nitrogen deposition rate *via* fog water is of the same magnitude as that *via* rainwater (Igawa et al., 1998). Moreover, a simple formula for cleaning a polluted atmosphere by fog (haze) events was deduced for fog that lasts more than 4 h (Podzimek, 1998). As mentioned above (**Figure 8**), the atmosphere was supersaturated and condensed from fog droplets on the evening of January 16. The particles entered the fog droplets and were scavenged partly by the deposition of large droplets on the surface.

On the morning of January 17, the air quality was good with $PM_{2.5}$ concentration sustained in the range of 31–58 μg/m3. At 14:00 of January 17, the relative humidity decreased to about 80% and the atmosphere was unsaturated (**Figure 8B**), the droplets dehydrated, and the aerosol particles resuspended again in the atmosphere. It resulted in a rebound in the mass concentration with the $PM_{2.5}$ concentration jumped to about 100 μg/m$^3$ at 14:00 of January 17 (**Figure 3**). Thereafter the air quality continued to deteriorate and started another pollution process under the unfavorable meteorological conditions.

## CONCLUSION

Based on multisource observations, the characteristics and mechanisms of the heavy $PM_{2.5}$ pollution episode that was accompanied by dense fog that occurred in CEC from January 13 to 18, 2018 were comprehensively investigated. The results showed that the episode occurred during an atmospheric circulation adjustment and that the surface $PM_{2.5}$ concentration slowly increased in Fuyang city in four stages: 1) the slow-increasing phase, 2) the rapid-increasing phase, 3) the rapid-decreasing phase, and 4) the rebound phase. The slow-increase phase was due to high humidity, ground breeze and a surface-based inversion, whereas the rapid-increase phase was due to pollution transport. In particular, the CALIPSO satellite monitoring suggested that pollution transport occurred not only at ground level but also in the lower troposphere.

The rapid-decrease phase and rebound phase were closely associated with the dense fog process. A rapid decrease in $PM_{2.5}$ concentration occurred in the region of the intersection of Shandong, Hebei and Anhui, where dense fog was observed. The analysis showed that the significant subsidence at 500 and 700 hPa led to a strong NSI, which confined the vapor water to the shallow mixing layer, and the atmosphere was supersaturated. Under these conditions, the particles entered the fog droplets and were scavenged partly by deposition of the large droplets on the surface. However, the aerosol particles were resuspended when the atmosphere was unsaturated Kang et al., 2019, Ni et al., 2018, Su et al., 2020, Wang et al., 2017, Wang et al., 2021c, Wang et al., 2014, Wang et al., 2016, Xu and Zhu, 2017, Xu et al., 2015, Zheng et al., 2019.

## DATA AVAILABILITY STATEMENT

The original contributions presented in the study are included in the article/Supplementary Material, further inquiries can be directed to the corresponding author.

## AUTHOR CONTRIBUTIONS

CY wrote the first draft of the manuscript, YY contributed to manuscript revision, DL contributed to conception and design of

the study. All authors contributed to manuscript revision approved the submitted version.

## FUNDING

This study was jointly supported by the National Nature Science Foundation of China (No. 42061134009 and 42175098); ANSO Joint Research Special Project (No. ANSO-CR-KP-2020-09); Key Research and Development Projects in Anhui, China (No. 202004b11020012). The following are websites from which the data were obtained: The air quality data were downloaded from: http://106.37.208.233:20035/, the routine meteorological data were downloaded from: http://www.nmic.cn/, the ECMWF reanalysis data were downloaded from: http://apps.ecmwf.int/datasets/data/interimfull-daily/levtype=sfc/, the CALIPSO data were downloaded from: https://www-calipso.larc.nasa.gov/.

## REFERENCES

Al-Saadi, J., Szykman, J., Pierce, R. B., Kittaka, C., Neil, D., Chu, D. A., et al. (2005). Improving National Air Quality Forecasts with Satellite Aerosol Observations. *Bull. Amer. Meteorol. Soc.* 86, 1249–1262. doi:10.1175/bams-86-9-1249

Chen, R., Peng, R. D., Meng, X., Zhou, Z., Chen, B., and Kan, H. (2013). Seasonal Variation in the Acute Effect of Particulate Air Pollution on Mortality in the China Air Pollution and Health Effects Study (CAPES). *Sci. Total Environ.* 450-451, 259–265. doi:10.1016/j.scitotenv.2013.02.040

Chen, Z., Chen, D., Zhao, C., Kwan, M.-p., Cai, J., Zhuang, Y., et al. (2020). Influence of Meteorological Conditions on $PM_{2.5}$ Concentrations across China: A Review of Methodology and Mechanism. *Environ. Int.* 139, 105558. doi:10.1016/j.envint.2020.105558

Chen, Z. H., Cheng, S. Y., Li, J. B., Guo, X. R., Wang, W. H., and Chen, D. S. (2008). Relationship between Atmospheric Pollution Processes and Synoptic Pressure Patterns in Northern China. *Atmos. Environ.* 42, 6078–6087. doi:10.1016/j.atmosenv.2008.03.043

Delfino, R. J., Sioutas, C., and Malik, S. (2005). Potential Role of Ultrafine Particles in Associations between Airborne Particle Mass and Cardiovascular Health. *Environ. Health Perspect.* 113, 934–946. doi:10.1289/ehp.7938

Deng, X., Cao, W., Huo, Y., Yang, G., Yu, C., He, D., et al. (2019). Meteorological Conditions during a Severe, Prolonged Regional Heavy Air Pollution Episode in Eastern China from December 2016 to January 2017. *Theor. Appl. Climatol.* 135, 1105–1122. doi:10.1007/s00704-018-2426-4

Deng, X., Shi, C., Wu, B., Chen, Z., Nie, S., He, D., et al. (2012). Analysis of Aerosol Characteristics and Their Relationships with Meteorological Parameters over Anhui Province in China. *Atmos. Res.* 109-110, 52–63. doi:10.1016/j.atmosres.2012.02.011

Ding, Y., and Liu, Y. (2014). Analysis of Long-Term Variations of Fog and Haze in China in Recent 50 Years and Their Relations with Atmospheric Humidity. *Sci. China Earth Sci.* 57, 36–46. doi:10.1007/s11430-013-4792-1

Gao, B., Guo, H., Wang, X.-M., Zhao, X.-Y., Ling, Z.-H., Zhang, Z., et al. (2012). Polycyclic Aromatic Hydrocarbons in $PM_{2.5}$ in Guangzhou, Southern China: Spatiotemporal Patterns and Emission Sources. *J. Hazard. Mater.* 239-240, 78–87. doi:10.1016/j.jhazmat.2012.07.068

Gao, M., Liu, Z., Zheng, B., Ji, D., Sherman, P., Song, S., et al. (2020). China's Emission Control Strategies Have Suppressed Unfavorable Influences of Climate on Wintertime $PM_{2.5}$ Concentrations in Beijing since 2002. *Atmos. Chem. Phys.* 20, 1497–1505. doi:10.5194/acp-20-1497-2020

Gramsch, E., Cáceres, D., Oyola, P., Reyes, F., Vásquez, Y., Rubio, M. A., et al. (2014). Influence of Surface and Subsidence thermal Inversion on $PM_{2.5}$ and Black Carbon Concentration. *Atmos. Environ.* 98, 290–298. doi:10.1016/j.atmosenv.2014.08.066

Gu, Y., Zhang, W., Yang, Y., Wang, C., Streets, D. G., and Yim, S. H. L. (2020). Assessing Outdoor Air Quality and Public Health Impact Attributable to Residential Black Carbon Emissions in Rural China. *Resour. Conservation Recycling* 159, 104812. doi:10.1016/j.resconrec.2020.104812

Guo, J.-P., Zhang, X.-Y., Wu, Y.-R., Zhaxi, Y., Che, H.-Z., La, B., et al. (2011). Spatio-temporal Variation Trends of Satellite-Based Aerosol Optical Depth in China during 1980-2008. *Atmos. Environ.* 45, 6802–6811. doi:10.1016/j.atmosenv.2011.03.068

Guo, J., He, J., Liu, H., Miao, Y., Liu, H., and Zhai, P. (2016). Impact of Various Emission Control Schemes on Air Quality Using WRF-Chem during APEC China 2014. *Atmos. Environ.* 140, 311–319. doi:10.1016/j.atmosenv.2016.05.046

Guo, J., Li, Y., Cohen, J. B., Li, J., Chen, D., Xu, H., et al. (2019). Shift in the Temporal Trend of Boundary Layer Height in China Using Long-Term (1979-2016) Radiosonde Data. *Geophys. Res. Lett.* 46, 6080–6089. doi:10.1029/2019GL082666

Han, S., Liu, J., Hao, T., Zhang, Y., Li, P., Yang, J., et al. (2018). Boundary Layer Structure and Scavenging Effect during a Typical winter Haze-Fog Episode in a Core City of BTH Region, China. *Atmos. Environ.* 179, 187–200. doi:10.1016/j.atmosenv.2018.02.023

He, J., Gong, S., Yu, Y., Yu, L., Wu, L., Mao, H., et al. (2017). Air Pollution Characteristics and Their Relation to Meteorological Conditions during 2014-2015 in Major Chinese Cities. *Environ. Pollut.* 223, 484–496. doi:10.1016/j.envpol.2017.01.050

Holt, J., Selin, N. E., and Solomon, S. (2015). Changes in Inorganic Fine Particulate Matter Sensitivities to Precursors Due to Large-Scale US Emissions Reductions. *Environ. Sci. Technol.* 49, 4834–4841. doi:10.1021/acs.est.5b00008

Igawa, M., Tsutsumi, Y., Mori, T., and Okochi, H. (1998). Fogwater Chemistry at a Mountainside Forest and the Estimation of the Air Pollutant Deposition via Fog Droplets Based on the Atmospheric Quality at the Mountain Base. *Environ. Sci. Technol.* 32, 1566–1572. doi:10.1021/es970213x

Jacob, D. J., Waldman, J. M., Munger, J. W., and Hoffmann, M. R. (1984). A Field Investigation of Physical and Chemical Mechanisms Affecting Pollutant Concentrations in Fog Droplets. *Tellus B: Chem. Phys. Meteorology* 36, 272–285. doi:10.3402/tellusb.v36i4.14909

Ji, D., Li, L., Wang, Y., Zhang, J., Cheng, M., Sun, Y., et al. (2014). The Heaviest Particulate Air-Pollution Episodes Occurred in Northern china in January, 2013: Insights Gained from Observation. *Atmos. Environ.* 92, 546–556. doi:10.1016/j.atmosenv.2014.04.048

Jin, Q., Fang, X., Wen, B., and Shan, A. (2017). Spatio-temporal Variations of $PM_{2.5}$ Emission in China from 2005 to 2014. *Chemosphere* 183, 429–436. doi:10.1016/j.chemosphere.2017.05.133

Kang, H. Q., BZhuGao, J., He, Y., Wang, H., and Su, J. (2018). Cold Fronts -- a Potential Air Quality Threat over the Yangtze River Delta, China. *Atmos. Chem. Phys.*, 1–17. doi:10.5194/acp-2018-588-AC2

Kang, H., Zhu, B., Gao, J., He, Y., Wang, H., Su, J., et al. (2019). Potential Impacts of Cold Frontal Passage on Air Quality over the Yangtze River Delta, China. *Atmos. Chem. Phys.* 19, 3673–3685. doi:10.5194/acp-19-3673-2019-supplement

Li, Z., Lau, W. K. M., Ramanathan, V., Wu, G., Ding, Y., Manoj, M. G., et al. (2016). Aerosol and Monsoon Climate Interactions over Asia. *Rev. Geophys.* 54, 866–929. doi:10.1002/2015RG000500

Liu, F., Zhang, Q., Tong, D., Zheng, B., Li, M., Huo, H., et al. (2015). High-Resolution Inventory of Technologies, Activities, and Emissions of Coal-Fired Power Plants in China from 1990 to 2010. *Atmos. Chem. Phys.* 15, 18787. doi:10.5194/acp-15-13299-2015

Markovic, M. Z., VandenBoer, T. C., Baker, K. R., Kelly, J. T., and Murphy, J. G. (2014). Measurements and Modeling of the Inorganic Chemical Composition of fine Particulate Matter and Associated Precursor Gases in California's San Joaquin Valley during CalNex 2010. *J. Geophys. Res. Atmos.* 119, 6853–6866. doi:10.1002/2013jd021408

Miao, Y., Guo, J., Liu, S., Liu, H., Li, Z., Zhang, W., et al. (2017). Classification of Summertime Synoptic Patterns in Beijing and Their Associations with

Boundary Layer Structure Affecting Aerosol Pollution. *Atmos. Chem. Phys.* 17, 3097–3110. doi:10.5194/acp-17-3097-2017

Ni, Z.-z., Luo, K., Zhang, J.-x., Feng, R., Zheng, H.-x., Zhu, H.-r., et al. (2018). Assessment of winter Air Pollution Episodes Using Long-Range Transport Modeling in Hangzhou, China, during World Internet Conference, 2015. *Environ. Pollut.* 236, 550–561. doi:10.1016/j.envpol.2018.01.069

Pasch, A. N., Macdonald, C. P., Gilliam, R. C., Knoderer, C. A., and Roberts, P. T. (2011). Meteorological Characteristics Associated with $PM_{2.5}$ Air Pollution in Cleveland, Ohio, during the 2009-2010 Cleveland Multiple Air Pollutants Study. *Atmos. Environ.* 45, 7026–7035. doi:10.1016/j.atmosenv.2011.09.065

Pei, L., Yan, Z., Sun, Z., Miao, S., and Yao, Y. (2018). Increasing Persistent Hazes in Beijing: Potential Impacts of Weakening East Asian Winter Monsoons Associated with Northwestern Pacific SST Trend since 1900. *Atmos. Chem. Phys.* 18, 3173–3183. doi:10.5194/acp-2017-757

Peters, A., Goldstein, I. F., Beyer, U., Franke, K., Heinrich, J., Dockery, D. W., et al. (1996). Acute Health Effects of Exposure to High Levels of Air Pollution in Eastern Europe. *Am. J. Epidemiol.* 144, 570–581. doi:10.1093/oxfordjournals.aje.a008967

Podzimek, J. (1998). Aerosol Particle Scavenging by Fog and Haze Droplets. *Stud. Geophys. Geod.* 42, 540–560. doi:10.1023/A:1023305423337

Pope, C. A., and Dockery, D. W. (2006). Health Effects of Fine Particulate Air Pollution: Lines that Connect. *J. Air Waste Manag. Assoc.* 56, 709–742. doi:10.1080/10473289.2006.10464485

Satheesh, S. K. (2002). Radiative Forcing by Aerosols over Bay of Bengal Region. *Geophys. Res. Lett.* 29, 40–41. doi:10.1029/2002GL015334

Shi, C. E., Nduka, I. C., Yang, Y., Huang, Y., Yao, R., Zhang, H., et al. (2019). Characteristics and Meteorological Mechanisms of Transboundary Air Pollution in a Persistent Heavy $PM_{2.5}$ Pollution Episode in Central-East China. *Atmos. Environ.* 223, 117239. doi:10.1016/j.atmosenv.2019.117239

Shi, C., Yuan, R., Wu, B., Meng, Y., Zhang, H., Zhang, H., et al. (2018). Meteorological Conditions Conducive to $PM_{2.5}$ Pollution in winter 2016/2017 in the Western Yangtze River Delta, China. *Sci. Total Environ.* 642, 1221–1232. doi:10.1016/j.scitotenv.2018.06.137

Su, T., Li, Z., Li, C., Li, J., Han, W., Shen, C., et al. (2020). The Significant Impact of Aerosol Vertical Structure on Lower Atmosphere Stability and its Critical Role in Aerosol-Planetary Boundary Layer (PBL) Interactions. *Atmos. Chem. Phys.* 20, 3713–3724. doi:10.5194/acp-20-3713-2020

Sun, Y., Wang, Z., Fu, P., Jiang, Q., Yang, T., Li, J., et al. (2013). The Impact of Relative Humidity on Aerosol Composition and Evolution Processes during Wintertime in Beijing, China. *Atmos. Environ.* 77, 927–934. doi:10.1016/j.atmosenv.2013.06.019

Waldman, J. M., and Hoffmann, M. R. (1987). *Depositional Aspects of Pollutant Behavior in Fog and Intercepted Clouds [M].* ISBN: 9780841209831.

Wang, H., Miao, Q., Shen, L., Yang, Q., Wu, Y., and Wei, H. (2021a). Air Pollutant Variations in Suzhou during the 2019 Novel Coronavirus (COVID-19) Lockdown of 2020: High Time-Resolution Measurements of Aerosol Chemical Compositions and Source Apportionment. *Environ. Pollut.* 271, 116298. doi:10.1016/j.envpol.2020.116298

Wang, H., Pei, Y., Yin, Y., Shen, L., Chen, K., Shi, Z., et al. (2021c). Observational Evidence of Lightning-Generated Ultrafine Aerosols. *Geophys. Res. Lett.* 48, e2021GL093771. doi:10.1029/2021gl093771

Wang, H., Tan, Y., Zhang, L., Shen, L., Zhao, T., Dai, Q., et al. (2021b). Characteristics of Air Quality in Different Climatic Zones of China during the COVID-19 Lockdown. *Atmos. Pollut. Res.* 12, 101247. doi:10.1016/j.apr.2021.101247

Wang, J., Zhang, M., Bai, X., Tan, H., Li, S., Liu, J., et al. (2017). Large-scale Transport of $PM_{2.5}$ in the Lower Troposphere during winter Cold Surges in China. *Sci. Rep.* 7, 13238. doi:10.1038/s41598-017-13217-2

Wang, L., Zhang, N., Liu, Z., Sun, Y., Ji, D., and Wang, Y. (2014). The Influence of Climate Factors, Meteorological Conditions, and Boundary-Layer Structure on Severe Haze Pollution in the Beijing-Tianjin-Hebei Region during January 2013. *Adv. Meteorology* 2014, 1–14. doi:10.1155/2014/685971

Wang, M., Cao, C., Li, G., and Singh, R. P. (2015). Analysis of a Severe Prolonged Regional Haze Episode in the Yangtze River delta, China. *Atmos. Environ.* 102, 112–121. doi:10.1016/j.atmosenv.2014.11.038

Wang, M. Y., Yim, S. H. L., Dong, G. H., Ho, K. F., and Wong, D. C. (2020). Mapping Ozone Source-Receptor Relationship and Apportioning the Health Impact in the Pearl River Delta Region Using Adjoint Sensitivity Analysis. *Atmos. Environ.* 222, 117026. doi:10.1016/j.atmosenv.2019.117026

Wang, X., Chen, J., Sun, J., Li, W., Yang, L., Wen, L., et al. (2014). Severe Haze Episodes and Seriously Polluted Fog Water in Ji'nan, China. *Sci. Total Environ.* 493 (15), 133–137. doi:10.1016/j.scitotenv.2014.05.135

Wang, Z., Liu, X., Xie, X., and Xie, X. M. (2016). Effects of Strong East Asian Cold Surges on Improving the Air Quality over Mainland China. *Atmosphere* 7, 38. doi:10.3390/atmos7030038

Wei, Y., Cao, X. N., Tang, X. L., Shen, L. J., Lin, T., He, D. W., et al. (2017). Urban fine Particulate Matter ($PM_{2.5}$) Exposure Destroys Blood-Testis Barrier (BTB) Integrity through Excessive ROS-Mediated Autophagy. *Toxicol. Mech. Methods* 28, 302–319. doi:10.1080/15376516.2017.1410743

Winker, D. M., Vaughan, M. A., Omar, A., Hu, Y., Powell, K. A., Liu, Z., et al. (2009). Overview of the CALIPSO Mission and CALIOP Data Processing Algorithms. *J. Atmos. Ocean. Tech.* 26, 2310–2323. doi:10.1175/2009JTECHA1281.1

Wu, X., Chen, B., Wen, T., Habib, A., and Shi, G. (2020). Concentrations and Chemical Compositions of $PM_{10}$ during Hazy and Non-hazy Days in Beijing. *J. Environ. Sci.* 87, 1–9. doi:10.1016/j.jes.2019.03.021

Xu, J., Chang, L., Yan, F., and He, J. (2017). Role of Climate Anomalies on Decadal Variation in the Occurrence of Wintertime Haze in the Yangtze River Delta, China. *Sci. Total Environ.* 599-600, 918–925. doi:10.1016/j.scitotenv.2017.05.015

Xu, J., Yan, F., Xie, Y., Wang, F., Wu, J., and Fu, Q. (2015). Impact of Meteorological Conditions on a Nine-Day Particulate Matter Pollution Event Observed in December 2013, Shanghai, China. *Particuology* 20, 69–79. doi:10.1016/j.partic.2014.09.001

Xu, Y., and Zhu, X. (2017). Recognizing Dew as an Indicator and an Improver of Near-Surface Air Quality. *Adv. Meteorology* 2017, 1–9. doi:10.1155/2017/3514743

Yang, J., Xie, Y.-J., Shi, C.-E., Liu, D.-Y., Niu, S.-J., and Li, Z.-H. (2012). Ion Composition of Fog Water and its Relation to Air Pollutants during Winter Fog Events in Nanjing, China. *Pure Appl. Geophys.* 169, 1037–1052. doi:10.1007/s00024-011-0342-y

Yang, Y., Zheng, X., Gao, Z., Wang, H., Wang, T., Li, Y., et al. (2018). Long-Term Trends of Persistent Synoptic Circulation Event`s in Planetary Boundary Layer and Their Relationships with Haze Pollution in Winter Half Year over Eastern China. *J. Geophys. Res. Atmos.* 123, 10991–11007. doi:10.1029/2018JD028982

Yang, Y., Zheng, Z., Yim, S. Y. L., Roth, M., Ren, G., Gao, Z., et al. (2020). $PM_{2.5}$ Pollution Modulates Wintertime Urban Heat Island Intensity in the Beijing-Tianjin-Hebei Megalopolis, China. *Geophys. Res. Lett.* 47, e2019GL084288. doi:10.1029/2019gl084288

Zhang, J. P., Zhu, T., Zhang, Q. H., Li, C. C., Shu, H. L., Ying, Y., et al. (2012). The Impact of Circulation Patterns on Regional Transport Pathways and Air Quality over Beijing and its Surroundings. *Atmos. Chem. Phys.* 12, 5031–5053. doi:10.5194/acp-12-5031-2012

Zhang, Q., Quan, J., Tie, X., Li, X., Liu, Q., Gao, Y., et al. (2015). Effects of Meteorology and Secondary Particle Formation on Visibility during Heavy Haze Events in Beijing, China. *Sci. Total Environ.* 502, 578–584. doi:10.1016/j.scitotenv.2014.09.079

Zheng, Z., Li, Y., Wang, H., Ding, H., Li, Y., Gao, Z., et al. (2019). Re-evaluating the Variation in Trend of Haze Days in the Urban Areas of Beijing during a Recent 36-year Period. *Atmos. Sci. Lett.* 20, e878. doi:10.1002/asl.878

Zheng, Z., Ren, G., Wang, H., Dou, J., Gao, Z., Duan, C., et al. (2018). Relationship between Fine-Particle Pollution and the Urban Heat Island in Beijing, China: Observational Evidence. *Boundary-layer Meteorol.* 169, 93–113. doi:10.1007/s10546-018-0362-6

Zhou, W., Tie, X., Zhou, G., and Liang, P. (2015). Possible Effects of Climate Change of Wind on Aerosol Variation during winter in Shanghai, China. *Particuology* 20, 80–88. doi:10.1016/j.partic.2014.08.008

Zhu, J., Liao, H., and Li, J. (2012). Increases in Aerosol Concentrations over Eastern China Due to the Decadal-Scale Weakening of the East Asian Summer Monsoon. *Geophys. Res. Lett.* 39, a–n. doi:10.1029/2012GL051428

**Conflict of Interest:** The authors declare that the research was conducted in the absence of any commercial or financial relationships that could be construed as a potential conflict of interest.

**Publisher's Note:** All claims expressed in this article are solely those of the authors and do not necessarily represent those of their affiliated organizations, or those of the publisher, the editors and the reviewers. Any product that may be evaluated in this article, or claim that may be made by its manufacturer, is not guaranteed or endorsed by the publisher.

frontiers in Environmental Science

ORIGINAL RESEARCH
published: 20 January 2022
doi: 10.3389/fenvs.2022.825732

# Contribution Isolation of LUCC Impact on Regional $PM_{2.5}$ Air Pollution: Implications for Sustainable Land and Environment Management

*Ying Ding*[1], *Huihui Feng*[1,2]*, *Bin Zou*[1,2] *and Shuchao Ye*[1]

[1]School of Geosciences and Info-Physics, Central South University, Changsha, China, [2]Key Laboratory of Metallogenic Prediction of Nonferrous Metals and Geological Environment Monitoring of Chinese Ministry of Education, Central South University, Changsha, China

Understanding of the contribution of LUCC to air pollution is the basis for land management and air pollution control. This study aimed to estimate the contribution of LUCC to $PM_{2.5}$ pollution levels in the Changsha-Zhuzhou-Xiangtan (CZT) urban agglomeration in the central south China. Methodologically, residual analysis was adopted to isolate the LUCC contribution with the aid of multiple datasets from satellite observations and reanalysis products. The results revealed that the $PM_{2.5}$ concentration increased significantly from 2001 to 2008 and then decreased. LUCC tended to enhance both the increasing and decreasing trends, while the magnitudes varied under different climate conditions. During 2001–2008, LUCC exerted more important influence on the air pollution, which contributed 40.59% of the total increase. During 2008–2014, the changing climate enhanced air pollution removal. During this time, the government of the CZT proposed the "Two Oriented Society" policy for sustainable urban development. Under this condition, the LUCC accounted for only 25.66% of the total $PM_{2.5}$ decrease. This result suggested that it is necessary to further strengthen the goal of sustainable development rather than following the traditional way of "governance after development".

**Keywords: fine particulate matter, land use and cover change, multiple linear regression model, changsha-zhuzhou-xiangtan urban agglomeration, remote sensing**

OPEN ACCESS

***Edited by:***
*Xinyao Xie,*
*Institute of Mountain Hazards and Environment (CAS), China*

***Reviewed by:***
*Guicai Ning,*
*Hong Kong Polytechnic University, Hong Kong SAR, China*
*Kaixu Bai,*
*East China Normal University, China*

***Correspondence:**
*Huihui Feng*
*hhfeng@csu.edu.cn*

***Specialty section:***
*This article was submitted to Atmosphere and Climate, a section of the journal Frontiers in Environmental Science*

***Received:*** *30 November 2021*
***Accepted:*** *03 January 2022*
***Published:*** *20 January 2022*

***Citation:***
*Ding Y, Feng H, Zou B and Ye S (2022) Contribution Isolation of LUCC Impact on Regional $PM_{2.5}$ Air Pollution: Implications for Sustainable Land and Environment Management. Front. Environ. Sci. 10:825732. doi: 10.3389/fenvs.2022.825732*

## INTRODUCTION

The global urban area has expanded by ~ 130% in recent decades (He et al., 2019), which exerts significant impacts on the environment through changes in surface energy and the hydrologic cycle, i.e., air pollution, global and regional climate change and biodiversity reduction (Foley et al., 2005). Among them, air pollution poses a severe threat to human health (Zou et al., 2019; Zou et al., 2020), climate change (Feng and Zou 2019; Feng et al., 2019), atmospheric visibility (Wang et al., 2019) and economic development (Chen et al., 2019), which has attracted increasing attention from researchers and governments.

It is crucial to clarify the land use and cover change (LUCC) impact on air pollution for land planning and environmental management during urban growth. Physically, LUCC affects air pollution in direct and indirect ways (Feng et al., 2017). First, LUCC can directly affect the spatial distribution of emission sources (Heald and Spracklen, 2015). Second, different land

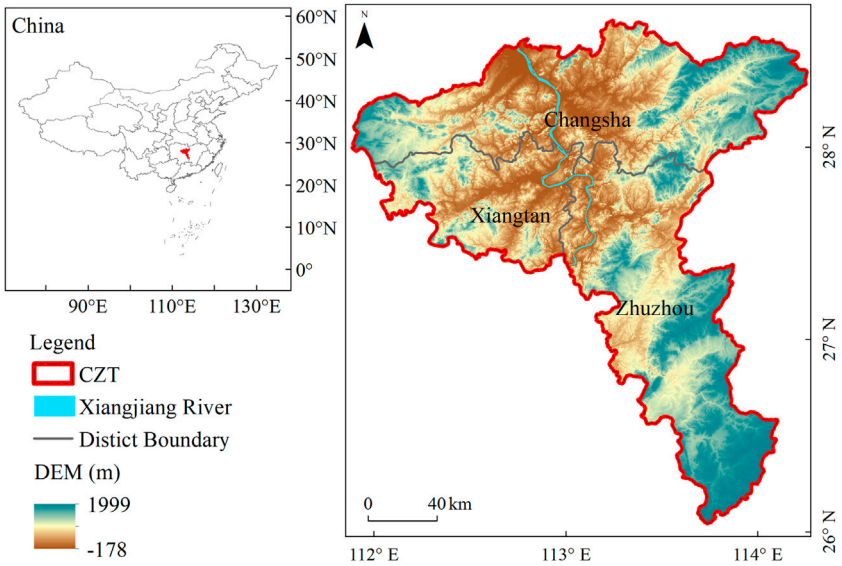


**FIGURE 1 |** Study area.

types exert various influences on dry deposition (Dzierzanowski et al., 2011). In addition, LUCC helps alter the dispersion and transportation of air pollution by changing the local or regional climate conditions (Bai et al., 2017). On the other hand, air pollution is also strongly affected by natural factors and anthropogenic emissions (Yang et al., 2018; Zheng et al., 2018). For example, precipitation controls wet deposition, which acts as one of the main removal methods of atmospheric pollutants (Ouyang et al., 2015). Wind has a direct influence on the variation in the air pollution concentration by enhancing its dispersion (Janhall 2015). Temperature and relative humidity play crucial roles in the formation of secondary aerosols by affecting the gas-to-particle process (Raes et al., 2000). Natural and anthropogenic factors affect air pollution through complex interactions, making it difficult to isolate individual effects.

Researchers have adopted several air quality models to isolate the LUCC impact by measuring the difference in air pollution with and without the influence of LUCC (i.e., WRF-Chem and GEOS-Chem) (Avise et al., 2009; Wu et al., 2012; Martin et al., 2015). However, the results are controversial due to the unavoidable uncertainty originating from the initial input, model error and prediction scenarios in different models (Bonan and Doney, 2018). For example, the modeled LUCC contribution to ozone variation ranges from −5 ppb to +5 ppb in different published works (Ganzeveld and Lelieveld, 2004; Chen et al., 2009; Squire et al., 2014). Considering these uncertainties, it has been suggested that direct observations (satellite and *in situ*) are required for accurately performing an air pollution evaluation and determining the corresponding driving factors (Bellouin et al., 2005; Seinfeld et al., 2016).

Focusing on the driving factors of air pollution, this study attempted to estimate the effect of LUCC using a statistical method with the aid of multisource satellite observations and reanalysis products. The Changsha-Zhuzhou-Xiangtan (CZT) urban agglomeration in central China, which suffers from serious air pollution of fine particulate matter ($PM_{2.5}$), was selected as the study area. First, the spatial-temporal variations in the annual $PM_{2.5}$ concentration were analyzed during the last decade (2001–2014). Then, residual analysis of the MLR model was performed to isolate the influence of LUCC on $PM_{2.5}$. The results of this study will help capture the characteristics of air pollution evolution and provide valuable information for improving urban air quality by optimizing land management strategies.

# METHODS

## Study Area

The Changsha-Zhuzhou-Xiangtan (CZT) urban agglomeration, which spans 111°53′E to 114°15′E longitude and 23°2′N to 28°39′N latitude, was selected as the study area for this investigation. The study area is located in northeast Hunan Province, China, and includes the cities of Changsha, Zhuzhou and Xiangtan (**Figure 1**). The climate of the CZT is characterized by the subtropical humid monsoon with abundant precipitation and warm temperatures. The center of the CZT is at a low altitude and is surrounded by mountains, resulting in unfavorable diffusion conditions. As one of the regions with the fastest economic development and urbanization in midwest China, the study area has experienced severe atmospheric environmental problems. Considering the serious air pollution in the CZT, this area was designated one of the thirteen priority areas for air pollution control according to the National Plan on Air Pollution Control by the Chinese government during the 12th Five-Year Plan (2011–2015) (Chen et al., 2013).

## Data Sources and Preprocessing

According to our previous study (Feng and Zou, 2020), the variation in air pollution is controlled by natural and anthropogenic factors. Natural factors mainly refer to meteorological or natural surface parameters, including precipitation, surface and air temperatures, surface wind speed, relative humidity and terrain. Anthropogenic factors are strongly represented by human activities, such as anthropogenic emissions and land use and cover change (LUCC) (Feng and Zou, 2019). These datasets were also adopted to carry out the investigation in this study. Multi-source data sets have different spatial and temporal scales, which must be uniform before the investigation. Thus, All the datasets were resampled to the same spatial resolution (0.01°) through the NEAREST interpolation method and temporal scale (annual).

1) **$PM_{2.5}$ concentration.** The annual surface $PM_{2.5}$ concentration, at a resolution of 0.01°, was collected from the Atmospheric Composition Analysis Group (http://fizz.phys.dal.ca/~atmos/martin/). The data were estimated by combining aerosol optical depth (AOD) retrievals from MODIS, MISR, and SeaWIFS with the GEOS-Chen chemical transport model. The annual mean $PM_{2.5}$ estimate from this dataset was highly consistent with global ground observations ($R^2$ = 0.81; slope = 0.90). This study used the China regional datasets of V4.CH.03 from 2001 to 2014, which are widely used in national- and regional-scale research (van Donkelaar et al., 2019; Shi et al., 2020; Yue et al., 2020).
2) **Natural parameter datasets.** Natural parameter data were used to investigate the natural factors of air pollution, including precipitation, surface and air temperatures, wind speed, relative humidity and terrain. Integrated Multi-Satellite Retrievals for Global Precipitation Mission (IMERG) monthly precipitation data at a resolution of 0.1° were downloaded from the NASA Goddard Earth Sciences Data and Information Services Center (GES DISC) (https://disc.gsfc.nasa.gov/datasets/GPM_3IMERGM_V06/summary). The data showed the best expression of precipitation, with a correlation of 0.79 (Yu et al., 2020). The land surface temperature of MODIS/Terra Land Surface Temperature/Emissivity Monthly L3 Global 0.05Deg CMG (MOD11C3) (https://lpdaac.usgs.gov/products/mod11c3v006/) at a resolution of 0.05° was selected over the time period of 2001–2014. The annually averaged air temperature and wind speed data from the China Meteorological Forcing Dataset (CMFD) were downloaded from the National Tibetan Plateau Data Center (http://data.tpdc.ac.cn/zh-hans/data/8028b944-daaa-4511-8769-965612652c49/), which were produced by merging a variety of data sources (He et al., 2020a). The relative humidity data at a resolution of 0.1° were collected from the Copernicus Climate Change Service (C3S) Climate Data Store (https://cds.climate.copernicus.eu/cdsapp#!/dataset/reanalysis-era5-land-monthly-means?tab = overview). In addition to the atmospheric data, terrain DEM data were adopted; these data were available from the ASTER GDEM at a resolution of 30 m collected from the Geospatial Data Cloud (http://www.gscloud.cn).
3) **Anthropogenic factors datasets.** In addition to the natural parameter data, land use and cover data and anthropogenic emissions inventories were used to investigate the anthropogenic drivers of air pollution. Specifically, land use data at a 1 km resolution in 2000, 2005, 2010, and 2015 from the Resource and Environment Science and Data Center, Chinese Academy of Science (http://www.resdc.cn), were reclassified into classes of built-up, forest, grassland, water, agricultural land, and bare soil. The land use data were generated by artificial visual interpretation from Landsat TM/ETM remote sensing images, and the overall accuracy was above 91.20% (Liu et al., 2014). Anthropogenic emissions inventories of $PM_{2.5}$ with a spatial resolution of 0.1° were obtained from the Peking University website (http://inventory.pku.edu.cn/).

## Methodology

Considering the unavoidable uncertainty of the model, this study used the statistical method of residual analysis to estimate the LUCC impact. The method has been applied in several studies and has shown great potential for identifying and clarifying the driving factors of environmental change (Tai et al., 2010; Che et al., 2019; Li et al., 2019; He et al., 2020b). Methodologically, the trend of observed $PM_{2.5}$ was used to present the actual change in air pollution. Then, the theoretical $PM_{2.5}$ concentration without LUCC impact was simulated by a stepwise MLR model. Finally, the residual trend between the observed and theoretical $PM_{2.5}$ trends was adopted to represent the LUCC influence.

For each grid, the theoretical $PM_{2.5}$ concentration estimated by the MLR model can be written as:

$$\boldsymbol{P_{mod}} = \boldsymbol{f}(\boldsymbol{P}, \boldsymbol{T_a}, \boldsymbol{T_s}, \boldsymbol{WS}, \boldsymbol{RH}, \boldsymbol{DEM}, \boldsymbol{EMI}) \quad (1)$$

where $P_{mod}$ is the $PM_{2.5}$ concentration under the control of factors other than land use, *P*, *Ta*, *Ts*, *WS*, *RH, DEM* and *EMI* represent the explanatory variables of precipitation, air temperature, land surface temperature, wind speed, relative humidity, terrain and anthropogenic emissions, respectively.

Because the MLR model does not consider the LUCC impact, a residual exists between the observed and MLR-simulated $PM_{2.5}$ concentrations, which reflects the land use influence. The residual is calculated by the following equation:

$$\boldsymbol{residual} = \boldsymbol{P_{obs}} - \boldsymbol{P_{mod}} \quad (2)$$

where *residual* is the residual of the MLR model, $P_{obs}$ represents the observed $PM_{2.5}$ concentration, and $P_{mod}$ is the MLR simulated $PM_{2.5}$ concentration.

The trends of the observed $PM_{2.5}$ concentration and the residual represent the actual variation and the LUCC impact of the $PM_{2.5}$ concentration. We then estimate the relative contribution of LUCC as:

$$\boldsymbol{C} = \frac{\boldsymbol{T_{res}}}{\boldsymbol{T_{obs}}} \times 100\% \quad (3)$$

where *C* is the relative contribution of LUCC to the $PM_{2.5}$ concentration variation, $T_{res}$ represents the trend of the residual, and $T_{obs}$ is the trend of the observed $PM_{2.5}$ concentration.

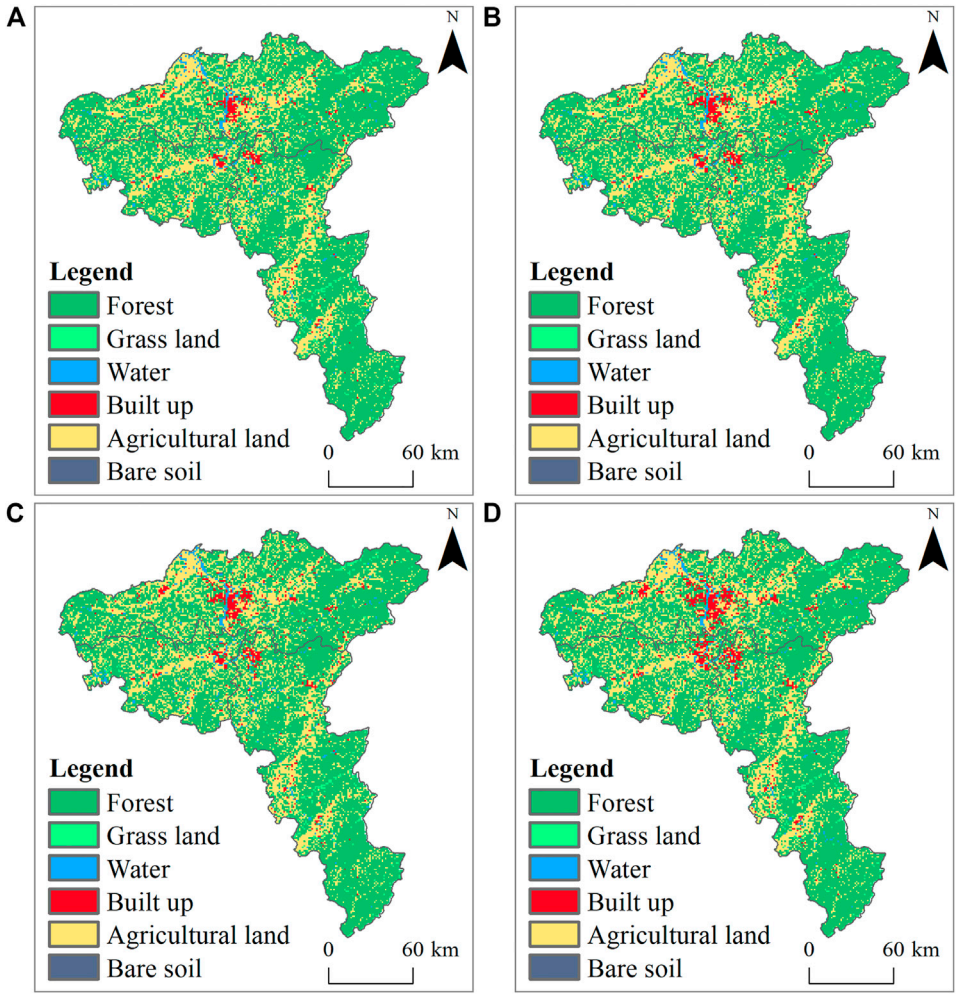


**FIGURE 2 |** Spatial distribution of land use in **(A)** 2000, **(B)** 2005, **(C)** 2010, and **(D)** 2015 in the CZT.

**TABLE 1 |** Area percentage statistics of land use types.

| Land use type | 2000 (%) | 2005 (%) | 2010 (%) | 2015 (%) |
|---|---|---|---|---|
| Agricultural land | 30.59 | 30.31 | 30.13 | 29.41 |
| Forest | 63.80 | 63.56 | 63.43 | 63.03 |
| Grass land | 1.46 | 1.45 | 1.45 | 1.43 |
| Water | 1.87 | 1.89 | 1.91 | 1.96 |
| Built-up | 2.27 | 2.78 | 3.07 | 4.16 |
| Bare soil | 0.01 | 0.01 | 0.01 | 0.01 |

# RESULTS AND DISCUSSION

## Spatial Pattern and Temporal Trend of LUCC, Meteorological Conditions and Anthropogenic Emissions in the CZT

It is necessary to first capture the spatial and temporal trends of LUCC, climate and anthropogenic emissions to understand the mechanism of air pollution in the CZT. The distributions of land use in 2000, 2005, 2010, and 2015 are presented in **Figure 2** and **Table 1**. Generally, forest (63.46%) is the dominant land use type in the CZT, followed by agricultural land (30.11%) and built-up land (3.07%). Spatially, forests are mainly distributed in the west, east and south of the urban agglomeration at a high altitude. urban are located mainly along the Xiangjiang River, and agricultural land is distributed around the built-up areas. Since China implemented the reform and opening up policy in 1978, urban sprawl and industrial development in the CZT have been increasingly occupying forest and farmland. The proportion of built-up areas increased from 637.57 $km^2$ in 2000 to 1168.42 $km^2$ in 2015. The expansion of built-up areas is mainly from the conversion of agricultural land and forest, whose areas were reduced to 331.43 and 216.27 $km^2$, respectively. The water area increased slightly (from 1.87 to 1.96%). In addition, grassland decreased from 1.46 to 1.43%.

**Figures 3**, **4** present the spatial patterns of the temporal trends of the meteorological factors and anthropogenic emission. The relative humidity decreased in the central CZT and slightly increased in southern Zhuzhou. The rising trend of

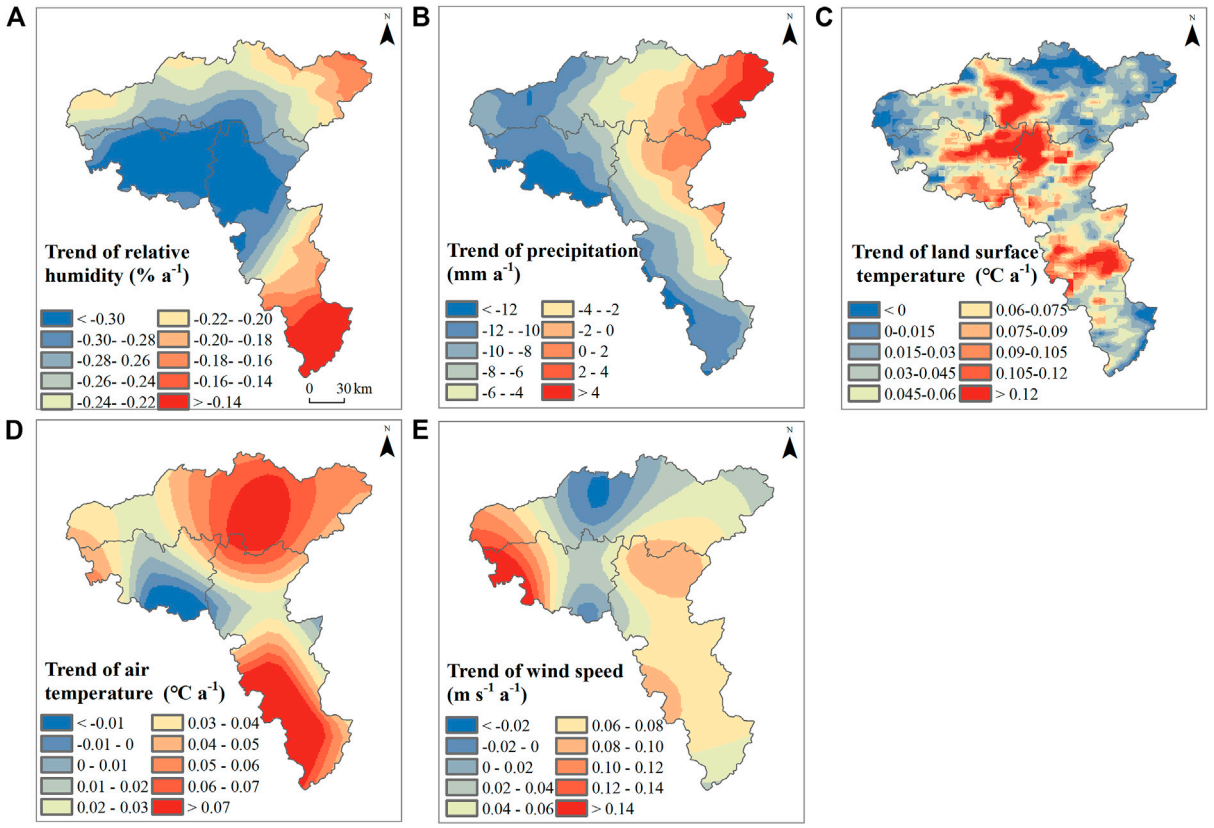


**FIGURE 3 |** Spatial patterns of the trends in **(A)** relative humidity, **(B)** precipitation, **(C)** land surface temperature, **(D)** air temperature and **(E)** wind speed from 2001 to 2014.

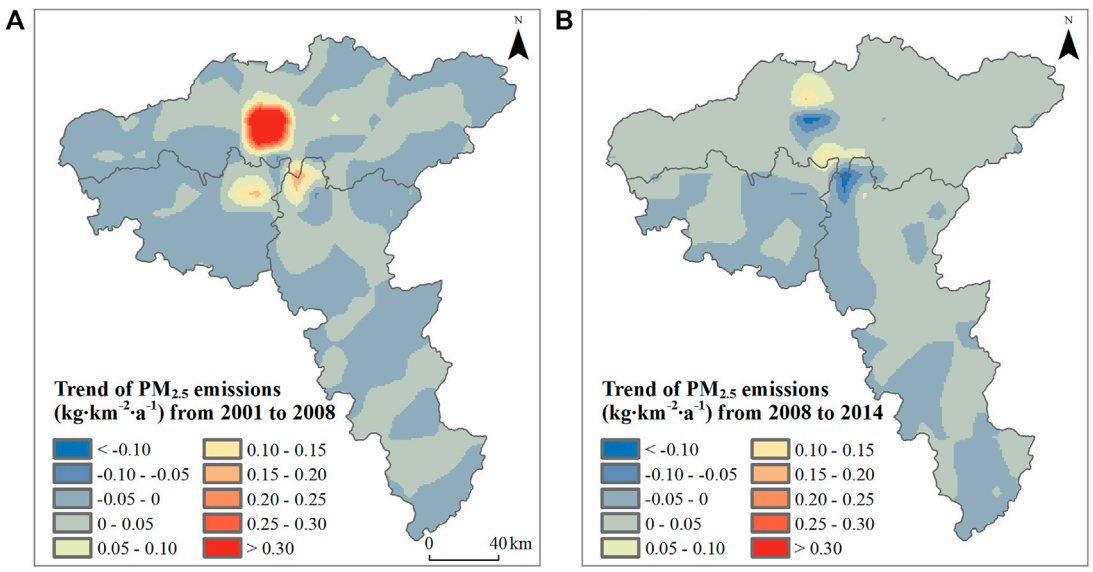


**FIGURE 4 |** Spatial pattern of the trends in anthropogenic $PM_{2.5}$ emissions during **(A)** 2001–2008 and **(B)** 2008–2014.

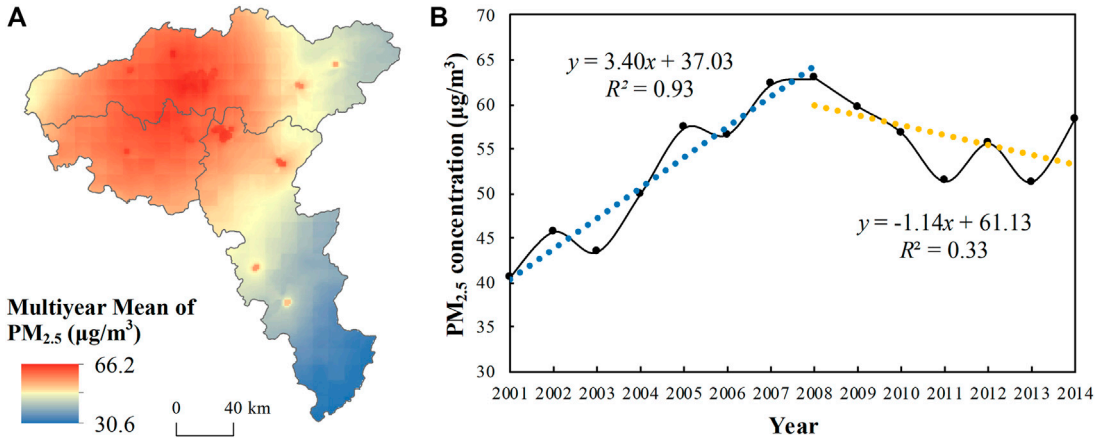


**FIGURE 5 | (A)** Multiyear mean of the $PM_{2.5}$ concentration and **(B)** the annually averaged $PM_{2.5}$ concentration variations from 2001 to 2014.

precipitation gradually weakened from east to west and showed a decreasing trend in the west. Because of the urban heat island effect, the land surface temperature increased in both urban and suburban areas. Air temperature dropped in the western CZT, while it increased in eastern Changsha and southern Zhuzhou. Wind speed presented a significantly increasing trend in the entire CZT, with the greatest increase occurring in the western region. Some studies also found the recovery of surface wind speed from stilling (Kim and Paik 2015; Li et al., 2018; Zeng et al., 2019). During the 2001–2008 period, anthropogenic emissions increased significantly in urban areas of the central CZT. From 2008 to 2014, emissions in Changsha and Zhuzhou urban areas decreased, while other areas changed slightly.

## Spatial-Temporal Characteristics of $PM_{2.5}$ Concentrations

Under the background of regional LUCC, air pollution was characterized by significant spatial and temporal variations in the CZT (**Figure 5**). Generally, the multiyear mean of the $PM_{2.5}$ concentrations was 53.71 $\mu g/m^3$, with the spatial distribution mainly characterized as high in the west and north and low in the east and south (**Figure 5A**). At the scale of land use types, the $PM_{2.5}$ concentrations are high in urban areas and relatively low in rural and suburban areas, which is consistent with most of the previous studies (Zou et al., 2016; Liu et al., 2020). Specifically, the most polluted districts were central Changsha, northeastern Xiangtan and northwestern Zhuzhou, while the areas with the best air quality were eastern Changsha and southern Zhuzhou. **Figure 5B** shows the temporal changes in the $PM_{2.5}$ concentrations, which present a significant peak pattern. During the 2001–2008 period, the $PM_{2.5}$ concentrations increased significantly by 3.40 $\mu g\, m^{-3} \cdot a^{-1}$ ($R^2$ = 0.93, $p < 0.05$). During the period 2008–2014, however, the $PM_{2.5}$ concentrations decreased by −1.14 $\mu g\, m^{-3} \cdot a^{-1}$ ($R^2$ = 0.33, $p$ = 0.18). The decreasing trend of the $PM_{2.5}$ concentration starting from 2008 resulted because the CZT became one of the areas that implemented the "Two Oriented Society" policy in 2007. To build a resource-saving and environmentally friendly society, local governments have adopted a series of policies of land management and air pollution mitigation, including encouraging high-tech industries with clean production to replace traditional industries, afforesting waste hills or unclaimed lands, and building greenbelts along streets. Moreover, the original disordered productive land use has gradually been replaced by science parks (Zou et al., 2016).

**Figure 6** further shows the spatial distribution of the $PM_{2.5}$ concentration trends during the periods 2001–2008 and 2008–2014. From 2001 to 2008, the $PM_{2.5}$ concentrations increased over the entire CZT. The worsening air pollution was mainly found in northern Zhuzhou, where the $PM_{2.5}$ concentration was relatively low. With respect to the period 2008–2014, the $PM_{2.5}$ concentration showed a significant reduction over the entire study area. The largest decreasing trend occurred in the central regions, where $PM_{2.5}$ pollution was relatively severe. Despite great improvement, the study area still faced serious air pollution in 2014, with 96.62% of the area still greatly exceeding the Chinese National Ambient Air Quality Standards (CNAAQS, i.e., Level-2, 35 $\mu g/m^3$). Strict controlling policies need to be continued in the future.

## Impact of LUCC on $PM_{2.5}$ Evolution

This study next explores the LUCC impact on $PM_{2.5}$ for land and environmental management. **Figure 7** shows the annually averaged $PM_{2.5}$ concentrations for five land use types in 2000, 2005, 2010, and 2015. From 2000 to 2005, the annual mean $PM_{2.5}$ concentrations for all land use types greatly increased. The magnitude of the increase was highest in built-up areas. This increase may be because urban land concentrates high anthropogenic emissions, such as automobile exhaust and industrial activities. Notably, the $PM_{2.5}$ concentrations in the water body and farmland use types were also relatively high. The water body land use type is mainly distributed in urban and suburban areas. Thus, particles from the built-up area are transmitted to water areas with low altitudes through

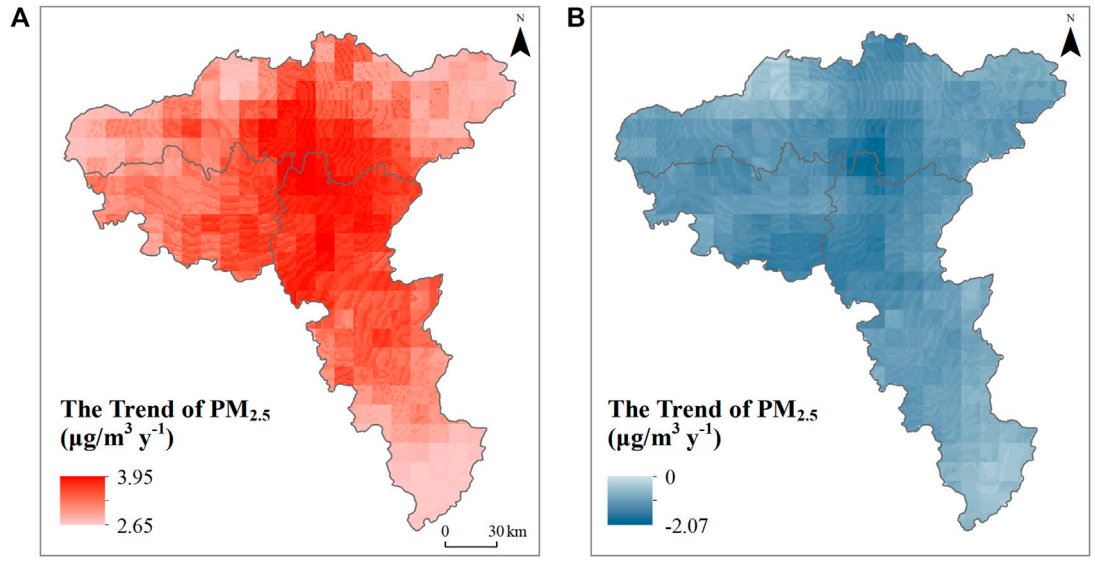


**FIGURE 6 |** Spatial distribution of the $PM_{2.5}$ concentration trends during **(A)** 2001–2008 and **(B)** 2008–2014.

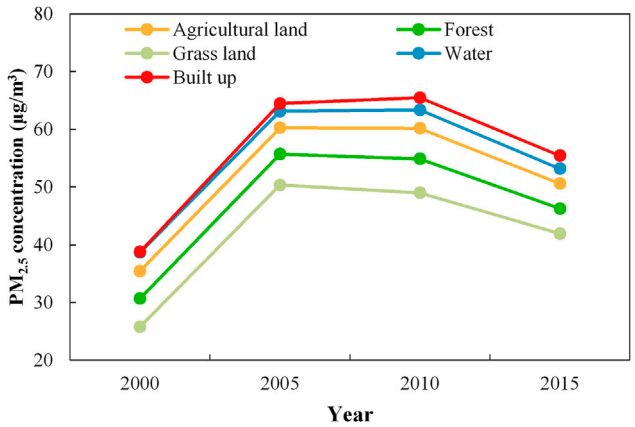


**FIGURE 7 |** Annually averaged $PM_{2.5}$ concentrations for different land uses.

diffusion, resulting in a higher $PM_{2.5}$ concentration. Agricultural waste burning and clearing, including open field burning and burning as household fuel, are significant emission sources of $PM_{2.5}$ (Zhang et al., 2017). In contrast, the $PM_{2.5}$ concentrations in forests and grasslands were relatively low, indicating that these land types could promote a decrease in the $PM_{2.5}$ concentration through the deposition effect and stomatal absorption from the vegetation blade surface (Nowak et al., 2013; Reddington et al., 2015). Correlations between air pollution and natural factors were also evaluated (see **Supplementary Figure S1**). Specifically, the $PM_{2.5}$ concentration showed negative correlations with relative humidity, precipitation and wind speed. Conversely, both air temperature and land surface temperature showed positive correlations with the $PM_{2.5}$ concentration.

To quantify the LUCC influence, the MLR model was used to simulate the $PM_{2.5}$ concentrations under the control of other factors (factors except for land use). **Figure 8** shows the trends of the MLR-simulated $PM_{2.5}$ concentrations and the residual during the periods 2001–2008 and 2008–2014, which present similar trends with the observed $PM_{2.5}$. Specifically, the simulated $PM_{2.5}$ concentration and the residual increased by 2.02 $\mu g\, m^{-3}{\cdot}a^{-1}$ ($R^2 = 0.96$, $p < 0.05$) and 1.37 $\mu g\, m^{-3}{\cdot}a^{-1}$ ($R^2 = 0.76$, $p < 0.05$) during 2001–2008. As a result, the relative contributions of the LUCC and other factors were 40.59 and 59.41%, indicating the predominant factors of emissions and meteorological conditions for the worsening air quality. During 2008–2014, the observed $PM_{2.5}$ concentration decreased by $-1.13\ \mu g\, m^{-3}{\cdot}a^{-1}$, while the simulated $PM_{2.5}$ concentration and residual decreased by $-0.85\ \mu g\, m^{-3}{\cdot}a^{-1}$ ($R^2 = 0.46$, $p = 0.09$) and $-0.29\ \mu g\, m^{-3}{\cdot}a^{-1}$ ($R^2 = 0.13$, $p = 0.43$). The relative contributions of land use and other factors were therefore 25.66 and 74.34%, suggesting the increasing influences of climate factors and anthropogenic emission. The main reason might be attributed to the strengthening influence of the climate conditions. As shown in **Supplementary Figure S3**, the meteorological conditions changed significantly after 2008, characterized by increased humidity, precipitation, and wind speed and decreased land surface temperature. Under these conditions, the climate tends to mitigate air pollution effectively. Our results are similar to Zhang et al. (2020), which implemented sensitivity experiments based on atmospheric chemistry model and demonstrated that contribution of more favorable meteorological conditions on decrease in $PM_{2.5}$ were higher than emission in Beijing. In conclusion, the signs of the LUCC impact remain positive, suggesting that land activities promote air pollution evolution. On the other hand, the magnitude is much greater in the process of the

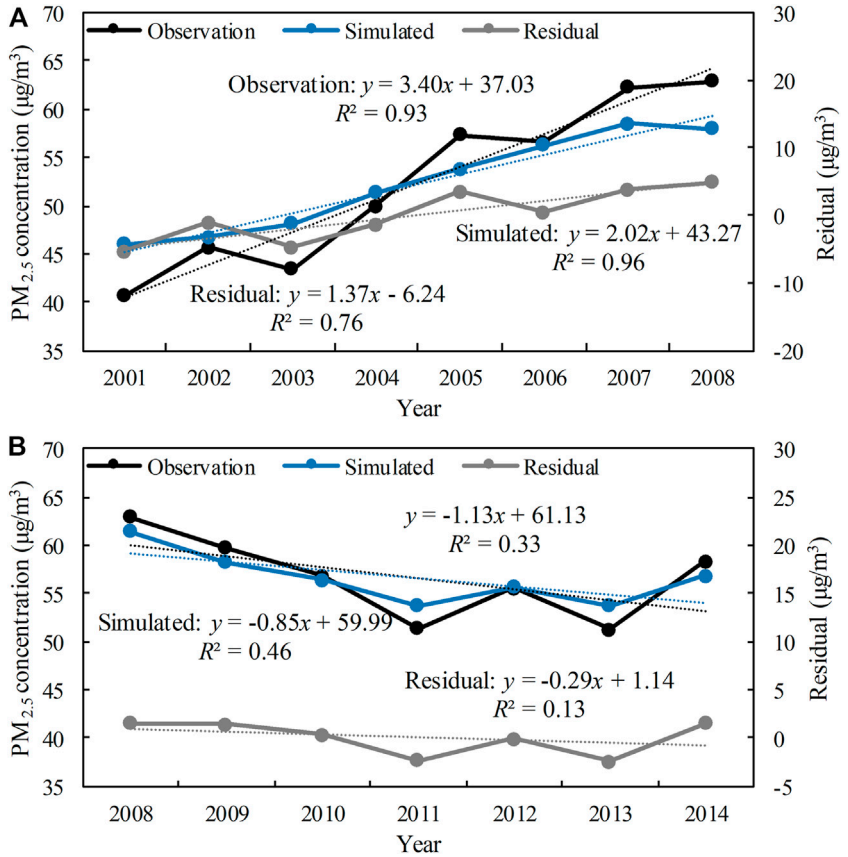


**FIGURE 8 |** Temporal trends of the observed, MLR simulated, and residual $PM_{2.5}$ concentrations during the periods **(A)** 2001–2008 and **(B)** 2008–2014.

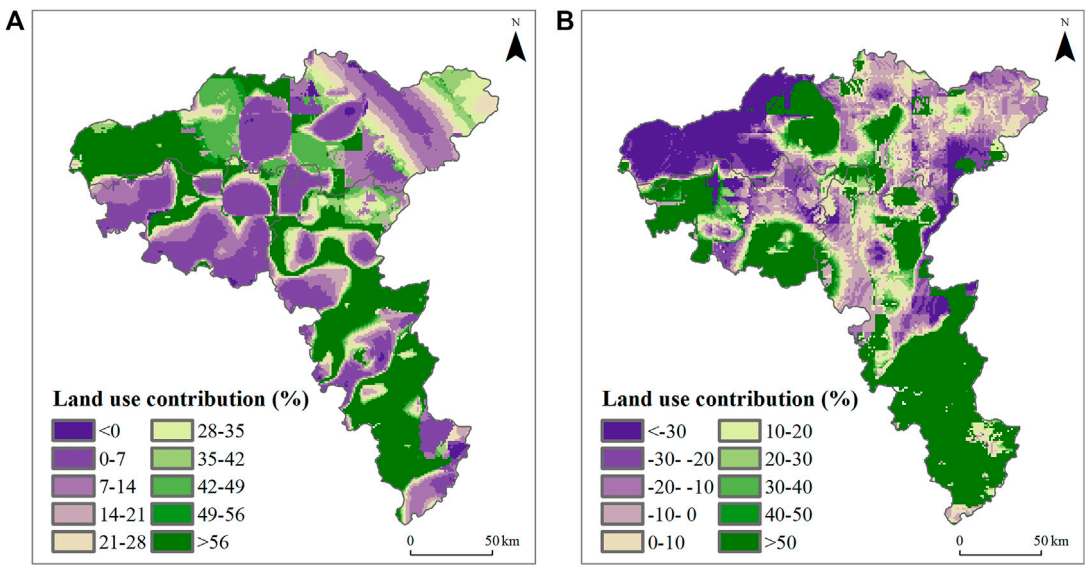


**FIGURE 9 |** Pixelwise contributions of LUCC impact during the period **(A)** 2001–2008 and **(B)** 2008–2014.

increase in $PM_{2.5}$, suggesting that the costs of unreasonable land activities are much higher than the benefits of rational land policy. Therefore, strengthening sustainable land management rather than following the traditional way of "governance after development" is required.

**Figure 9** further shows the pixelwise contributions of the LUCC impact. From 2001 to 2008, the influences of natural factors and emissions were relatively large in urban areas. In contrast, land use acted as the primary contributor in western Changsha and southern Zhuzhou. During 2008–2014, the decreasing trend of the $PM_{2.5}$ concentration was also mainly controlled by natural factors and anthropogenic emissions, with most of the LUCC contributions less than 50%. The land use-dominant areas were located in southern Xiangtan, the urban area of Changsha and southern Zhuzhou. Additionally, LUCC weakened the decreasing trend in the suburbs located in western Changsha, which might be attributed to the increase of built-up areas and the decrease of vegetation coverage during the rapid urbanization after 2008 (**Figure 2** and **Supplementary Figure S4**).

## CONCLUSION

This study aimed to explore the impact of LUCC on $PM_{2.5}$ pollution levels in the CZT from 2000 to 2014. Residual analysis of the MLR model was adopted with the aid of multiple source datasets (including satellites and reanalysis). The main conclusions are as follows:

Because of the implementation of the Two-Orientated Society policy since 2007, there was a turning point of air pollution evolution after 2008 in the CZT. Specifically, the $PM_{2.5}$ concentration increased significantly by 3.40 $\mu g\,m^{-3}{\cdot}a^{-1}$ ($R^2$ = 0.93, $p < 0.05$) from 2001 to 2008 and then decreased by -1.14 $\mu g\,m^{-3}{\cdot}a^{-1}$ ($R^2$ = 0.33, $p$ = 0.18) after 2008. However, the study area still suffered from serious air pollution, which requires sustained efforts from environmental management.

LUCC exhibited a strong influence on air pollution. The statistical results show that the $PM_{2.5}$ concentrations were high in built-up, water body and farmland land use types, while they were relatively low in forest and grassland land use types. The correlations between air pollution and climate were relatively complex. The $PM_{2.5}$ concentration had negative correlations with relative humidity, precipitation and wind speed and positive correlations with air temperature and land surface temperature. However, the weak correlation ($p > 0.05$) between the $PM_{2.5}$ concentration and individual meteorological parameters suggests that it is difficult for individual factors to explain the $PM_{2.5}$ concentration variation.

With the MLR model, the LUCC influence was finally estimated. From 2001 to 2008, LUCC accounted for 40.59% of the increase. During 2008–2014, the meteorological conditions changed, significantly enhancing the air pollution cleaning ability, which was characterized by increased humidity, precipitation and wind speed and decreased land surface temperature. Under this condition, the natural and emissions contributions (74.34%) were much greater than the contribution of LUCC (25.66%). This result suggested that the negative impact of unreasonable land management was much stronger than the positive impact of sustainable land development. Therefore, it is necessary to further strengthen the goal of sustainable development in regional land and environment management rather than following the traditional way of "governance after development". Furthermore, the LUCC impact presented significant spatial variabilities. From 2001 to 2008, LUCC significantly worsened the air quality in western Changsha and southern Zhuzhou. During 2008–2014, the $PM_{2.5}$ concentration variation was mainly controlled by natural factors and emissions, and land use-dominant areas were only located in southern Xiangtan, the urban area of Changsha and southern Zhuzhou.

This study clarified the impact of LUCC on air pollution, which could help capture the driving factors of air pollution and support sustainable land planning. Several issues should be addressed in future research. First, the physical mechanism of the LUCC impact should be fully investigated to understand its influences. Furthermore, natural factors and anthropogenic factors exert significant interactions under the complex system of Earth, which will require further evaluation to capture the sign and magnitude of the LUCC impacts.

## DATA AVAILABILITY STATEMENT

The original contributions presented in the study are included in the article/**Supplementary Material**, further inquiries can be directed to the corresponding author.

## AUTHOR CONTRIBUTIONS

YD: Data curation, Software, Visualization, Writing-Original draft preparation. HF: Conceptualization, Methodology, Supervision, Editing. BZ: Investigation and Reviewing. SY: Editing.

## FUNDING

This work was supported in part by the National Natural Science Foundation of China (Grant No. 42071378) and the Natural Science Foundation of Hunan Province (No. 2020JJ3045).

## SUPPLEMENTARY MATERIAL

The Supplementary Material for this article can be found online at: https://www.frontiersin.org/articles/10.3389/fenvs.2022.825732/full#supplementary-material

## REFERENCES


Avise, J., Chen, J., Lamb, B., Wiedinmyer, C., Guenther, A., Salathé, E., et al. (2009). Attribution of Projected Changes in Summertime US Ozone and PM2.5 Concentrations to Global Changes. *Atmos. Chem. Phys.* 9 (4), 1111–1124. doi:10.5194/acp-9-1111-2009

Bai, X., McPhearson, T., Cleugh, H., Nagendra, H., Tong, X., Zhu, T., et al. (2017). Linking Urbanization and the Environment: Conceptual and Empirical Advances. *Annu. Rev. Environ. Resour.* 42, 215–240. doi:10.1146/annurev-environ-102016-061128

Bellouin, N., Boucher, O., Haywood, J., and Reddy, M. S. (2005). Global Estimate of Aerosol Direct Radiative Forcing from Satellite Measurements. *Nature* 438 (7071), 1138–1141. doi:10.1038/nature04348

Bonan, G. B., and Doney, S. C. (2018). Climate, Ecosystems, and Planetary Futures: The challenge to Predict Life in Earth System Models. *Science* 359, eaam8328. doi:10.1126/science.aam8328

Che, H., Gui, K., Xia, X., Wang, Y., Holben, B. N., Goloub, P., et al. (2019). Large Contribution of Meteorological Factors to Inter-Decadal Changes in Regional Aerosol Optical Depth. *Atmos. Chem. Phys.* 19 (16), 10497–10523. doi:10.5194/acp-19-10497-2019

Chen, J., Avise, J., Guenther, A., Wiedinmyer, C., Salathe, E., Jackson, R. B., et al. (2009). Future Land Use and Land Cover Influences on Regional Biogenic Emissions and Air Quality in the United States. *Atmos. Environ.* 43 (36), 5771–5780. doi:10.1016/j.atmosenv.2009.08.015

Chen, J., Chen, K., Wang, G., Chen, R., Liu, X., and Wei, G. (2019). Indirect Economic Impact Incurred by Haze Pollution: an Econometric and Input-Output Joint Model. *Int. J. Environ. Res. Public Health* 16 (13), 2328. doi:10.3390/ijerph16132328

Chen, Z., Wang, J.-N., Ma, G.-X., and Zhang, Y.-S. (2013). China Tackles the Health Effects of Air Pollution. *Lancet* 382 (9909), 1959–1960. doi:10.1016/s0140-6736(13)62064-4

Dzierżanowski, K., Popek, R., Gawrońska, H., Sæbø, A., and Gawroński, S. W. (2011). Deposition of Particulate Matter of Different Size Fractions on Leaf Surfaces and in Waxes of Urban forest Species. *Int. J. Phytoremediation* 13 (10), 1037–1046. doi:10.1080/15226514.2011.552929

Feng, H., Zou, B., and Ding, Y. (2019). Satellite Detection of Aerosol-Produced Temperature Change. *Remote Sensing Lett.* 10 (9), 854–863. doi:10.1080/2150704x.2019.1629707

Feng, H., and Zou, B. (2019). Satellite-Based Estimation of the Aerosol Forcing Contribution to the Global Land Surface Temperature in the Recent Decade. *Remote Sensing Environ.* 232, 111299. doi:10.1016/j.rse.2019.111299

Feng, H., and Zou, B. (2020). Satellite-Based Separation of Climatic and Surface Influences on Global Aerosol Change. *Int. J. Remote Sensing* 41 (14), 5443–5456. doi:10.1080/01431161.2020.1731934

Feng, H., Zou, B., and Tang, Y. (2017). Scale- and Region-Dependence in Landscape-PM2.5 Correlation: Implications for Urban Planning. *Remote Sensing* 9 (9), 918. doi:10.3390/rs9090918

Foley, J. A., DeFries, R., Asner, G. P., Barford, C., Bonan, G., Carpenter, S. R., et al. (2005). Global Consequences of Land Use. *Science* 309 (5734), 570–574. doi:10.1126/science.1111772

Ganzeveld, L., and Lelieveld, J. (2004). Impact of Amazonian Deforestation on Atmospheric Chemistry. *Geophys. Res. Lett.* 31 (6), L06105. doi:10.1029/2003gl019205

He, C., Liu, Z., Gou, S., Zhang, Q., Zhang, J., and Xu, L. (2019). Detecting Global Urban Expansion over the Last Three Decades Using a Fully Convolutional Network. *Environ. Res. Lett.* 14 (3), 034008. doi:10.1088/1748-9326/aaf936

He, J., Yang, K., Tang, W., Lu, H., Qin, J., Chen, Y., et al. (2020a). The First High-Resolution Meteorological Forcing Dataset for Land Process Studies over China. *Sci. Data* 7 (1), 25. doi:10.1038/s41597-020-0369-y

He, L., Wang, L., Huang, B., Wei, J., Zhou, Z., and Zhong, Y. (2020b). Anthropogenic and Meteorological Drivers of 1980-2016 Trend in Aerosol Optical and Radiative Properties over the Yangtze River Basin. *Atmos. Environ.* 223, 117188. doi:10.1016/j.atmosenv.2019.117188

Heald, C. L., and Spracklen, D. V. (2015). Land Use Change Impacts on Air Quality and Climate. *Chem. Rev.* 115 (10), 4476–4496. doi:10.1021/cr500446g

Janhäll, S. (2015). Review on Urban Vegetation and Particle Air Pollution - Deposition and Dispersion. *Atmos. Environ.* 105, 130–137. doi:10.1016/j.atmosenv.2015.01.052

Kim, J., and Paik, K. (2015). Recent Recovery of Surface Wind Speed after Decadal Decrease: A Focus on South Korea. *Clim. Dyn.* 45 (5-6), 1699–1712. doi:10.1007/s00382-015-2546-9

Li, K., Jacob, D. J., Liao, H., Shen, L., Zhang, Q., and Bates, K. H. (2019). Anthropogenic Drivers of 2013-2017 Trends in Summer Surface Ozone in China. *Proc. Natl. Acad. Sci. USA* 116 (2), 422–427. doi:10.1073/pnas.1812168116

Li, Y., Chen, Y., Li, Z., and Fang, G. (2018). Recent Recovery of Surface Wind Speed in Northwest China. *Int. J. Climatol* 38 (12), 4445–4458. doi:10.1002/joc.5679

Liu, J., Ding, J., Li, L., Li, X., Zhang, Z., Ran, S., et al. (2020). Characteristics of Aerosol Optical Depth over Land Types in central Asia. *Sci. Total Environ.* 727, 138676. doi:10.1016/j.scitotenv.2020.138676

Liu, J., Kuang, W., Zhang, Z., Xu, X., Qin, Y., Ning, J., et al. (2014). Spatiotemporal Characteristics, Patterns, and Causes of Land-Use Changes in China since the Late 1980s. *J. Geogr. Sci.* 24 (2), 195–210. doi:10.1007/s11442-014-1082-6

Martin, M. V., Heald, C. L., Lamarque, J.-F., Tilmes, S., Emmons, L. K., and Schichtel, B. A. (2015). How Emissions, Climate, and Land Use Change Will Impact Mid-century Air Quality over the United States: a Focus on Effects at National parks. *Atmos. Chem. Phys.* 15 (5), 2805–2823. doi:10.5194/acp-15-2805-2015

Nowak, D. J., Hirabayashi, S., Bodine, A., and Hoehn, R. (2013). Modeled PM2.5 Removal by Trees in Ten U.S. Cities and Associated Health Effects. *Environ. Pollut.* 178, 395–402. doi:10.1016/j.envpol.2013.03.050

Ouyang, W., Guo, B., Cai, G., Li, Q., Han, S., Liu, B., et al. (2015). The Washing Effect of Precipitation on Particulate Matter and the Pollution Dynamics of Rainwater in Downtown Beijing. *Sci. Total Environ.* 505, 306–314. doi:10.1016/j.scitotenv.2014.09.062

Raes, F., Dingenen, R. V., Vignati, E., Wilson, J., Putaud, J.-P., Seinfeld, J. H., et al. (2000). Formation and Cycling of Aerosols in the Global Troposphere. *Atmos. Environ.* 34 (25), 4215–4240. doi:10.1016/s1352-2310(00)00239-9

Reddington, C. L., Butt, E. W., Ridley, D. A., Artaxo, P., Morgan, W. T., Coe, H., et al. (2015). Air Quality and Human Health Improvements from Reductions in Deforestation-Related Fire in Brazil. *Nat. Geosci* 8 (10), 768–771. doi:10.1038/ngeo2535

Seinfeld, J. H., Bretherton, C., Carslaw, K. S., Coe, H., DeMott, P. J., Dunlea, E. J., et al. (2016). Improving Our Fundamental Understanding of the Role of Aerosol–Cloud Interactions in the Climate System. *Proc. Natl. Acad. Sci. USA* 113 (21), 5781–5790. doi:10.1073/pnas.1514043113

Shi, T., Hu, Y., Liu, M., Li, C., Zhang, C., and Liu, C. (2020). How Do Economic Growth, Urbanization, and Industrialization Affect Fine Particulate Matter Concentrations? an Assessment in Liaoning Province, China. *Int. J. Environ. Res. Public Health* 17 (15), 5441. doi:10.3390/ijerph17155441

Squire, O. J., Archibald, A. T., Abraham, N. L., Beerling, D. J., Hewitt, C. N., Lathière, J., et al. (2014). Influence of Future Climate and Cropland Expansion on Isoprene Emissions and Tropospheric Ozone. *Atmos. Chem. Phys.* 14 (2), 1011–1024. doi:10.5194/acp-14-1011-2014

Tai, A. P. K., Mickley, L. J., and Jacob, D. J. (2010). Correlations between fine Particulate Matter (PM2.5) and Meteorological Variables in the United States: Implications for the Sensitivity of PM2.5 to Climate Change. *Atmos. Environ.* 44 (32), 3976–3984. doi:10.1016/j.atmosenv.2010.06.060

van Donkelaar, A., Martin, R., Li, C., and Burnett, R. T. (2019). Regional Estimates of Chemical Composition of Fine Particulate Matter Using a Combined Geoscience-Statistical Method with Information from Satellites, Models, and Monitors. *Environ. Sci. Technol.* 53 (5), 2595–2611. doi:10.1021/acs.est.8b06392

Wang, X., Zhang, R., and Yu, W. (2019). The Effects of PM 2.5 Concentrations and Relative Humidity on Atmospheric Visibility in Beijing. *J. Geophys. Res. Atmos.* 124 (4), 2235–2259. doi:10.1029/2018jd029269

Wu, S., Mickley, L. J., Kaplan, J. O., and Jacob, D. J. (2012). Impacts of Changes in Land Use and Land Cover on Atmospheric Chemistry and Air Quality over the 21st Century. *Atmos. Chem. Phys.* 12 (3), 1597–1609. doi:10.5194/acp-12-1597-2012

Yang, Y., Zheng, X., Gao, Z., Wang, H., Wang, T., Li, Y., et al. (2018). Long-term Trends of Persistent Synoptic Circulation Events in Planetary Boundary Layer and Their Relationships with Haze Pollution in winter Half Year over Eastern

China. *J. Geophys. Res. Atmos.* 123 (19), 10991–11007. doi:10.1029/2018JD028982

Yu, C., Hu, D., Liu, M., Wang, S., and Di, Y. (2020). Spatio-Temporal Accuracy Evaluation of Three High-Resolution Satellite Precipitation Products in China Area. *Atmos. Res.* 241, 104952. doi:10.1016/j.atmosres.2020.104952

Yue, H., He, C., Huang, Q., Yin, D., and Bryan, B. A. (2020). Stronger Policy Required to Substantially Reduce Deaths from PM2.5 Pollution in China. *Nat. Commun.* 11, 1462. doi:10.1038/s41467-020-15319-4

Zeng, Z., Ziegler, A. D., Searchinger, T., Yang, L., Chen, A., Ju, K., et al. (2019). A Reversal in Global Terrestrial Stilling and its Implications for Wind Energy Production. *Nat. Clim. Chang.* 9 (12), 979–985. doi:10.1038/s41558-019-0622-6

Zhang, H., Hu, J., Qi, Y., Li, C., Chen, J., Wang, X., et al. (2017). Emission Characterization, Environmental Impact, and Control Measure of PM2.5 Emitted from Agricultural Crop Residue Burning in China. *J. Clean. Prod.* 149, 629–635. doi:10.1016/j.jclepro.2017.02.092

Zhang, W., Wang, H., Zhang, X., Peng, Y., Zhong, J., Wang, Y., et al. (2020). Evaluating the Contributions of Changed Meteorological Conditions and Emission to Substantial Reductions of PM2.5 Concentration from winter 2016 to 2017 in Central and Eastern China. *Sci. Total Environ.* 716, 136892. doi:10.1016/j.scitotenv.2020.136892

Zheng, Z., Ren, G., Wang, H., Dou, J., Gao, Z., Duan, C., et al. (2018). Relationship between Fine-Particle Pollution and the Urban Heat Island in Beijing, China: Observational Evidence. *Boundary-layer Meteorol.* 169 (1), 93–113. doi:10.1007/s10546-018-0362-6

Zou, B., Li, S., Lin, Y., Wang, B., Cao, S., Zhao, X., et al. (2020). Efforts in Reducing Air Pollution Exposure Risk in China: State versus Individuals. *Environ. Int.* 137, 105504. doi:10.1016/j.envint.2020.105504

Zou, B., Xu, S., Sternberg, T., and Fang, X. (2016). Effect of Land Use and Cover Change on Air Quality in Urban Sprawl. *Sustainability* 8, 677. doi:10.3390/su8070677

Zou, B., You, J., Lin, Y., Duan, X., Zhao, X., Fang, X., et al. (2019). Air Pollution Intervention and Life-Saving Effect in China. *Environ. Int.* 125, 529–541. doi:10.1016/j.envint.2018.10.045

**Conflict of Interest:** The authors declare that the research was conducted in the absence of any commercial or financial relationships that could be construed as a potential conflict of interest.

**Publisher's Note:** All claims expressed in this article are solely those of the authors and do not necessarily represent those of their affiliated organizations, or those of the publisher, the editors and the reviewers. Any product that may be evaluated in this article, orclaim that may be made by its manufacturer, is not guaranteed or endorsed by the publisher.

frontiers in Environmental Science

ORIGINAL RESEARCH
published: 21 January 2022
doi: 10.3389/fenvs.2022.837158

# Characteristics of Secondary $PM_{2.5}$ Under Different Photochemical Reactivity Backgrounds in the Pearl River Delta Region

*Xinyang Yu[1], Yin Zhang[2], Ningwei Liu[3]* and Suying Yang[4]*

*[1]Zhongshan Meteorological Service, Zhongshan, China, [2]Bureau of Hydrology and Water Resources, Pearl River Water Resources Commission of Ministry of Water Resources, Guangzhou, China, [3]Institute of Atmospheric Environment, China Meteorological Administration, Shenyang, China, [4]Key Laboratory for Aerosol-Cloud-Precipitation of China Meteorological Administration, Nanjing University of Information Science Technology, Nanjing, China*

With the increasing control of air pollution, the levels of atmospheric particulates in the Pearl River Delta (PRD) region are gradually decreasing. However, ozone pollution has become more and more serious, and the problem of secondary aerosol pollution caused by photochemical reactions cannot be ignored. Based on the observation data of environmental and meteorological stations in the nine cities of the PRD during 2019, we investigated the variations of secondary $PM_{2.5}$ ($PM_{2.5\text{-sec}}$) in the PRD under different photochemical reactivity backgrounds. It was shown that the photochemical reactivities appeared more significant in the central and western areas than those in the eastern areas of the PRD and appeared more significant in inland areas than those in coastal areas. The days of moderate and high photochemical reactivities mainly appeared from August to November. $PM_{2.5\text{-sec}}$ concentrations were the highest in autumn, during which the regional discrepancies appeared most significantly with the highest levels in the southern areas. With the enhancement of the photochemical reactivity background, the $PM_{2.5\text{-sec}}$ level at each station increased significantly, which appeared significantly higher in coastal areas than in inland areas. Both $PM_{2.5\text{-sec}}$ and ozone concentrations showed single-peak variations, which appeared higher in the daytime than at night with the peak occurring at about 15:00. For each pollutant, the average maximum concentration appeared higher for polluted stations than for clean ones, indicating that the atmospheric oxidation background was conducive to the formation of $PM_{2.5\text{-sec}}$.

**Keywords: secondary $PM_{2.5}$, ozone, photochemical reactivity, oxidation background, coordinated increase**

OPEN ACCESS

***Edited by:***
*Junke Zhang,*
*Southwest Jiaotong University, China*

***Reviewed by:***
*Jinhui Gao,*
*Chengdu University of Information Technology, China*
*Junli Jin,*
*China Meteorological Administration, China*

****Correspondence:***
*Ningwei Liu*
*liunw@iaesy.cn*

***Specialty section:***
*This article was submitted to Atmosphere and Climate, a section of the journal Frontiers in Environmental Science*

***Received:*** *16 December 2021*
***Accepted:*** *03 January 2022*
***Published:*** *21 January 2022*

***Citation:***
*Yu X, Zhang Y, Liu N and Yang S (2022) Characteristics of Secondary $PM_{2.5}$ Under Different Photochemical Reactivity Backgrounds in the Pearl River Delta Region. Front. Environ. Sci. 10:837158. doi: 10.3389/fenvs.2022.837158*

## INTRODUCTION

With the strengthening of environmental governance, air pollution in some cities of China has been gradually transforming from single to complex pollution as a result of the increase in ozone and aerosol levels (Zhang et al., 2019; Wang et al., 2021a; Wang et al., 2021b; Wang et al., 2021c). Ozone and aerosols significantly influence human health, crop yield, and global climate change (Mills et al., 2009; Stoker et al., 2013; Zhang et al., 2017; Fleming et al., 2018), meaning that their coordinated control is very urgent. Therefore, many scholars have carried out relevant studies and found that their coordinated variations are fulfilled through the influence of aerosols on the levels of atmospheric radiation and hydroxyl radicals and

the influence of ozone on atmospheric photochemical reactivities (Yuan et al., 2012; Liu et al., 2021; Wang et al., 2021a; Wang et al., 2021b; Wang et al., 2021c). It is worth noting that the strengthening of atmospheric photochemical reactivities and the following significant growth of secondary aerosols resulting from ozone enhancement have become the common causes of complex pollution in China. However, because of the influence of weather background, emission source structure, and geographical factors, the characteristics of complex pollution are different (Liu et al., 2019; Zhao et al., 2021). Some scholars found that with the increase of $PM_{2.5}$ levels, the maximum values and change rates of ozone concentrations with different backgrounds in Guangzhou increase gradually, indicating the coordinated increase between $PM_{2.5}$ and ozone (Yao et al., 2021). Some scholars found that in Handan, the fourth largest city of Hebei Province, ozone increased with the enhancement of $PM_{2.5}$ during summer in the case of its concentration being below the standard values, whereas high-level $PM_{2.5}$ had an inhibitory effect on ozone formation in winter (Zhao et al., 2021).

The common precursors of aerosols and ozone (i.e., $VOC_S$ and $NO_x$) can be transformed into secondary aerosols and inorganic salts through gas–particulate matter interactions (Xing et al., 2017), contributing to the formation of $PM_{2.5}$. Li (Li et al., 2020) evaluated the coordinated increase of ozone and secondary aerosols in Beijing, Shanghai, and Guangzhou and found that the formation of secondary aerosols in Shanghai and Guangzhou increased by multiples with the enhancement of photochemical reactivities, whereas that in Beijing was scarcely varied. Previous studies were mainly based on a single city or station and rarely focused on regional ozone and secondary aerosol variations (Wu et al., 2021).

The Pearl River Delta (PRD) region is located south of the Tropic of Cancer, bordering the South China Sea, with good thermal conditions. The regional economy is developed, the manufacturing industry is prosperous, and the population is dense. The precursors produced by a large number of industrial sources and man-made sources are conducive to the generation of ozone photochemical reactions. In recent years, the ozone levels in the PRD have gradually increased (Zhan, 2018; Yin and Wang, 2020), with complex pollution of ozone and secondary aerosols occurring frequently (Lai et al., 2018). In this article, we analyze the various characteristics of $PM_{2.5\text{-sec}}$ concentration in the PRD under different photochemical reactivity backgrounds, based on the observed data from environmental and meteorological stations in nine cities of the PRD in 2019; the correlation between ozone pollution and secondary $PM_{2.5}$ were revealed; and the possible mechanisms of formation of $PM_{2.5\text{-sec}}$ under different ozone levels were analyzed, which provide scientific support for the coordinated control of PM2.5 and ozone in the PRD.

# DATA AND METHODS

## Data Sources

This article selects the PRD as the research area including nine cities of Guangdong Province, i.e., Zhaoqing, Guangzhou, Foshan, Zhuhai, Jiangmen, Zhongshan, Huizhou, Shenzhen, and Dongguan. The data come from the national control station of the Department of Ecology and Environment of Guangdong Province (Station No. 1345A-1400A, **Figure 1**). Season classification criteria are as follows: spring (March, April, and May), summer (June, July, and August), autumn (September, October, and November), and winter (December, January, and February). The validities of atmospheric pollutant concentration data meet the requirements of the Environmental Air Quality Standard (GB3095-2012) and the Technical Specification for Environmental Air Quality Assessment (TRIAL) (HJ633-2013). The meteorological data come from the national basic meteorological observation stations of the respective cities, and the accuracy of all meteorological data was over 98% after quality control. Data on the 10 m mean wind and accumulated rainfall in the PRD in 2019 were obtained from the EC ERA5 monthly reanalysis data.

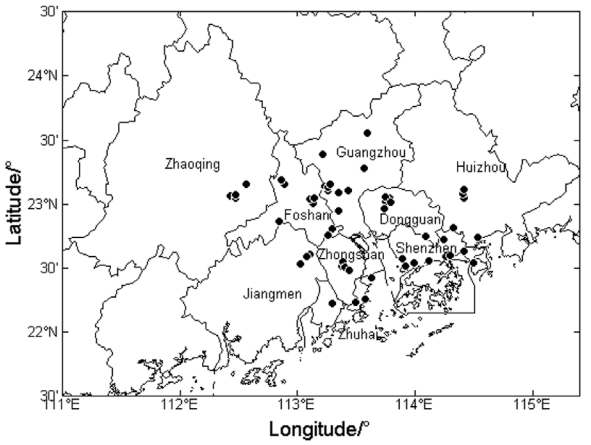


**FIGURE 1 |** Distribution of national control stations in the Pearl River Delta.

## Research Methods

Li et al. (2020) used the following research methods to analyze the coordinated increase of ozone and secondary aerosols in typical Chinese cities: First, the daily maximum 1 h average concentration of ozone ($O_3$-max) was used to classify the atmospheric photochemical reactivity level. $O_3$-max < 100 μg/$m^3$ was defined as a low level of photochemical reactivity ($O_{3L}$), and 100 μg/$m^3$ ≤ $O_3$-max < 160 μg/$m^3$ was defined as a light level of photochemical reactivity ($O_{3LH}$). 160 μg/$m^3$ ≤ $O_3$-max < 200 μg/$m^3$ was defined as a moderate level of photochemical reactivity ($O_{3M}$), and $O_3$-max ≥ 200 μg/$m^3$ was defined as a high level of photochemical reactivity ($O_{3H}$). Then, CO was used as a tracer of the primary emission source, assuming that the structure of the emission source is basically stable; the larger the ratio of $PM_{2.5}$/CO mass concentration is, the larger the proportion of secondary components in $PM_{2.5}$ is (Chang and Lee, 2007; Zhang et al., 2015). Specific equations are as follows:

$$(PM_{2.5})_{p,LH,t} = CO_{LH,t} \times (PM_{2.5}/CO)_{p,L}, \quad (1)$$

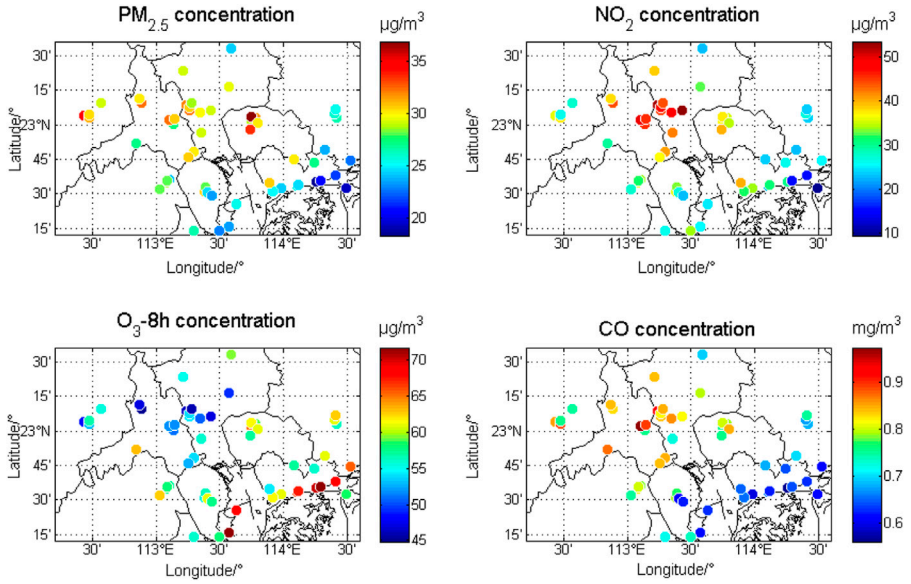


**FIGURE 2 |** Mean concentrations of $PM_{2.5}$, $NO_2$, $O_{3-8h}$, and CO at various stations.

$$(PM_{2.5})_{p,M,t} = CO_{M,t} \times (PM_{2.5}/CO)_{p,L}, \quad (2)$$

$$(PM_{2.5})_{p,H,t} = CO_{H,t} \times (PM_{2.5}/CO)_{p,L}, \quad (3)$$

$$(PM_{2.5})_{sec,LH,t} = (PM_{2.5})_{obs,LH,t} - (PM_{2.5})_{p,LH,t}, \quad (4)$$

$$(PM_{2.5})_{sec,M,t} = (PM_{2.5})_{obs,M,t} - (PM_{2.5})_{p,M,t}, \quad (5)$$

$$(PM_{2.5})_{sec,H,t} = (PM_{2.5})_{obs,H,t} - (PM_{2.5})_{p,H,t}, \quad (6)$$

where p is the primary pollutant, sec is a secondary pollutant, and obs is observed $PM_{2.5}$ concentration. t is the specific time of the day. L, LH, M, and H represent $O_{3L}$, $O_{3LH}$, $O_{3M}$, and $O_{3H}$, respectively. $CO_{LH,t} \times (PM_{2.5}/CO)_{p,L}$ is 25% of the hourly $PM_{2.5}$/CO in $O_{3H}$. It is the reference value of the primary aerosol for the calculation of different levels of photochemical reactivities. Finally, since ozone concentrations in eastern China generally peak between 14:00 and 16:00, the phenomenon of $PM_{2.5}$ and ozone concentration increasing simultaneously and continuously for no less than 2 h from 11:00 to 19:00 is defined as the coordinated increase of $PM_{2.5}$ and ozone. In this article, the aforementioned methods are used to estimate the hourly concentration of $PM_{2.5\text{-}sec}$ under different photochemical reactivities and to calculate the time for the coordinated increase of $PM_{2.5\text{-}sec}$ and ozone. More details can be found in Li et al. (2020).

# DISTRIBUTION CHARACTERISTICS OF AIR POLLUTANT CONCENTRATION IN THE PEARL RIVER DELTA

## Annual Average Variations

**Figure 2** shows the mean concentrations of $PM_{2.5}$, $NO_2$, $O_{3-8h}$, and CO at various stations in the PRD in 2019. The air pollutants have obvious spatial variation characteristics. Concentrations of $PM_{2.5}$, $NO_2$, and CO are higher in the central and northern parts of the PRD (e.g., Guangzhou, Foshan, and Dongguan), whereas they are lower in coastal areas. The maximum annual mean concentrations of $PM_{2.5}$, $NO_2$, and CO appear in Dongguan (37 μg/m$^3$), Guangzhou (54 μg/m$^3$), and Foshan (980 μg/m$^3$), respectively. The average ozone concentrations in coastal areas (e.g., Zhuhai, Shenzhen, and Huizhou) are higher than those in other areas, and the maximum appears in Shenzhen with a value of 72 μg/m$^3$.

## Seasonal Variations

**Table 1** shows the seasonal variations of air pollutants in the PRD in 2019. The average concentrations of $PM_{2.5}$, CO, and $NO_2$ in the PRD appear the highest in winter and the lowest in summer, whereas the concentrations of $O_{3-8h}$ appear the highest in autumn and the lowest in winter. The concentrations of $PM_{2.5}$, $NO_2$, and CO in the northern part of the PRD are higher than those in the southern part, whereas the distributions of $O_{3-8h}$ appear vice versa. **Figure 3** shows the variations of $PM_{2.5}$ and ozone with temperature and humidity during autumn and winter in the PRD. The high-level $PM_{2.5}$ in autumn mainly occurs in the environment with humidity over 80%, but there is no similar distribution in winter. High ozone concentrations in autumn and winter appear under high-temperature and low-humidity conditions. According to the 10 m average wind field and cumulative rainfall distribution in the PRD (**Figure 4**), the prevailing wind directions in spring and summer are southeast and southwest, which bring clean marine air mass. Meanwhile, abundant precipitation is also conducive to pollutant removal. In autumn and winter, the prevailing wind changes to the northeastern direction, leading to inland polluted air masses influencing the air quality of the PRD, and the precipitation decreasing significantly compared with that in

**TABLE 1 |** Seasonal variations of air pollutants in the PRD.

| City | Pollutant[a] | Spring | Summer | Autumn | Winter | Average | City | Pollutant | Spring | Summer | Autumn | Winter | Average |
|---|---|---|---|---|---|---|---|---|---|---|---|---|---|
| Dongguan | $PM_{2.5}$ | 26.6 | 18.7 | 40.7 | 42.8 | 32.2 | Foshan | $PM_{2.5}$ | 25.6 | 17.6 | 37.8 | 39.1 | 30 |
| | $NO_2$ | 35.9 | 28.4 | 39.5 | 43.3 | 36.8 | | $NO_2$ | 41.9 | 28.5 | 44.3 | 49.9 | 41.2 |
| | $O_{3-8\ h}$ | 49.4 | 60.6 | 89.1 | 44.9 | 61.0 | | $O_{3-8\ h}$ | 38.2 | 53.1 | 82.8 | 34.7 | 52.2 |
| | CO | 0.767 | 0.689 | 0.781 | 0.92 | 0.789 | | CO | 0.837 | 0.733 | 0.813 | 1.043 | 0.857 |
| Guangzhou | $PM_{2.5}$ | 24 | 18.1 | 37 | 38.8 | 29.5 | Huizhou | $PM_{2.5}$ | 20.5 | 14.4 | 31.3 | 33.8 | 25 |
| | $NO_2$ | 44 | 32 | 45 | 50.1 | 42.8 | | $NO_2$ | 22.7 | 19.9 | 26.5 | 29.1 | 24.6 |
| | $O_{3-8\ h}$ | 39.4 | 51.9 | 79 | 37.4 | 51.9 | | $O_{3-8\ h}$ | 60.9 | 50.9 | 84 | 50.6 | 61.6 |
| | CO | 0.794 | 0.664 | 0.795 | 1.013 | 0.817 | | CO | 0.636 | 0.563 | 0.672 | 0.855 | 0.682 |
| Jiangmen | $PM_{2.5}$ | 22.8 | 15.4 | 34.6 | 36 | 27.2 | Shenzhen | $PM_{2.5}$ | 19.7 | 13.2 | 31.7 | 32.3 | 24.2 |
| | $NO_2$ | 28.6 | 17.4 | 36.7 | 46.5 | 32.3 | | $NO_2$ | 22.9 | 20.1 | 26.5 | 32.4 | 25.5 |
| | $O_{3-8\ h}$ | 43.6 | 53.6 | 98.2 | 41.4 | 59.2 | | $O_{3-8\ h}$ | 60.5 | 49.7 | 90.7 | 51.6 | 63.1 |
| | CO | 0.744 | 0.6 | 0.781 | 1.033 | 0.79 | | CO | 0.599 | 0.545 | 0.625 | 0.743 | 0.628 |
| Zhuhai | $PM_{2.5}$ | 19.2 | 11.9 | 31.6 | 35.4 | 24.5 | Zhaoqing | $PM_{2.5}$ | 29.8 | 19 | 35.6 | 41.3 | 31.4 |
| | $NO_2$ | 27.6 | 15.4 | 25.1 | 42 | 27.5 | | $NO_2$ | 32.5 | 21.2 | 34.2 | 39 | 31.7 |
| | $O_{3-8\ h}$ | 55.5 | 52 | 96 | 51.3 | 63.7 | | $O_{3-8\ h}$ | 38.6 | 53.1 | 83 | 40 | 53.7 |
| | CO | 0.67 | 0.541 | 0.617 | 0.86 | 0.672 | | CO | 0.829 | 0.66 | 0.8 | 0.963 | 0.813 |
| Zhongshan | $PM_{2.5}$ | 20.5 | 12.9 | 34.3 | 38.6 | 26.6 | Average | $PM_{2.5}$ | 23.2 | 15.7 | 35 | 37.6 | 27.9 |
| | $NO_2$ | 23.8 | 14.1 | 34.4 | 46.4 | 29.7 | | $NO_2$ | 31.1 | 21.9 | 34.7 | 42.1 | 32.4 |
| | $O_{3-8\ h}$ | 46.5 | 55.4 | 91.9 | 38.1 | 58 | | $O_{3-8\ h}$ | 48.1 | 53.4 | 88.3 | 43.3 | 58.3 |
| | CO | 0.656 | 0.558 | 0.681 | 0.895 | 0.698 | | CO | 0.726 | 0.617 | 0.729 | 0.925 | 0.749 |

[a]*Concentration of air pollutants: ① $PM_{2.5}$, μg/m$^3$, ② $NO_2$, μg/m$^3$, ③ ozone-8h, μg/m$^3$, and ④ CO, mg/m$^3$.*

spring and summer, thus forming high levels of $PM_{2.5}$, $NO_2$, and CO in autumn and winter. In addition, concentrated human activities in the central PRD (e.g., Guangzhou, Foshan, and Dongguan) cause the local levels of primary air pollutants to be higher than those in the coastal areas. For the secondary pollutants (e.g., ozone), the northeast wind in autumn brings polluted air masses from the upwind direction in the PRD (Dongguan, Foshan, and Guangzhou), and the air masses mix with the local pollution, forming ozone enhancement in the southern and coastal areas. In summer, under the conditions of high temperature and strong radiation, a large number of local photochemical reactions cause ozone concentrations to be slightly higher than those in spring and winter.

# PHOTOCHEMICAL REACTIVITY BACKGROUND AND COORDINATED INCREASE CHARACTERISTICS IN THE PEARL RIVER DELTA REGION

## Regional Distribution Characteristics of Photochemical Reactivities

A previous study showed that air pollutants in the PRD have significant temporal and spatial variation characteristics. To explore the differences of photochemical reactivities in various cities, the day distributions of different photochemical reactivities at each station are presented in **Figure 5**. In 2019, the PRD mainly experienced $O_{3L}$ and $O_{3LH}$ for an average of 151 and 115 days, respectively, totally accounting for 74.9% of the year, whereas it experienced 46 days of $O_{3M}$ and 43 days of $O_{3H}$. Most stations in Shenzhen, Zhuhai, Huizhou, and Zhaoqing experience more days of low- and light-photochemical reactivities than the median in the PRD (264 days). **Figure 6** shows the cumulative time of the coordinated increase between $PM_{2.5}$ and ozone and the mean values of $PM_{2.5}$/CO in the PRD. The cumulative time of the coordinated increase is 511–1,048 h, in accordance with the results of Li et al. (2020) in Guangzhou from April to October 2017 (580 h). The high values of cumulative time are mainly concentrated in Jiangmen, Zhongshan, and Dongguan. The ratio of $PM_{2.5}$/CO is between 0.030 and 0.045, which is lower than that in Beijing and Shanghai in 2017 and comparable to that of Guangzhou in 2017 (Li et al., 2020). The high values are concentrated in Dongguan and Shenzhen.

## Seasonal Variation of the Coordinated Increase of $PM_{2.5}$ and Ozone

**Figure 7** shows the monthly averaged days of different photochemical reactivities and average hours of the coordinated increase in 2019. $O_{3M}$ and $O_{3H}$ mainly concentrate from August to November, among which the maximum $O_{3M}$ days appear in November (10.1 days), whereas the maximum $O_{3H}$ days appear in September (11.7 days). What is more, the trend of coordinated increase time is basically opposite to that of $O_{3L}$ days. Therefore, a coordinated increase of $PM_{2.5}$ and ozone mainly occurs under more significant oxidation backgrounds.

In general, photochemical reactivities in the PRD have obvious spatial and temporal variation differences. In terms of spatial variations, photochemical reactivities appear high in central and western regions but low in eastern regions and high in inland regions but low in coastal regions. In terms of seasonal variations, moderate and high levels of photochemical reactivities mainly

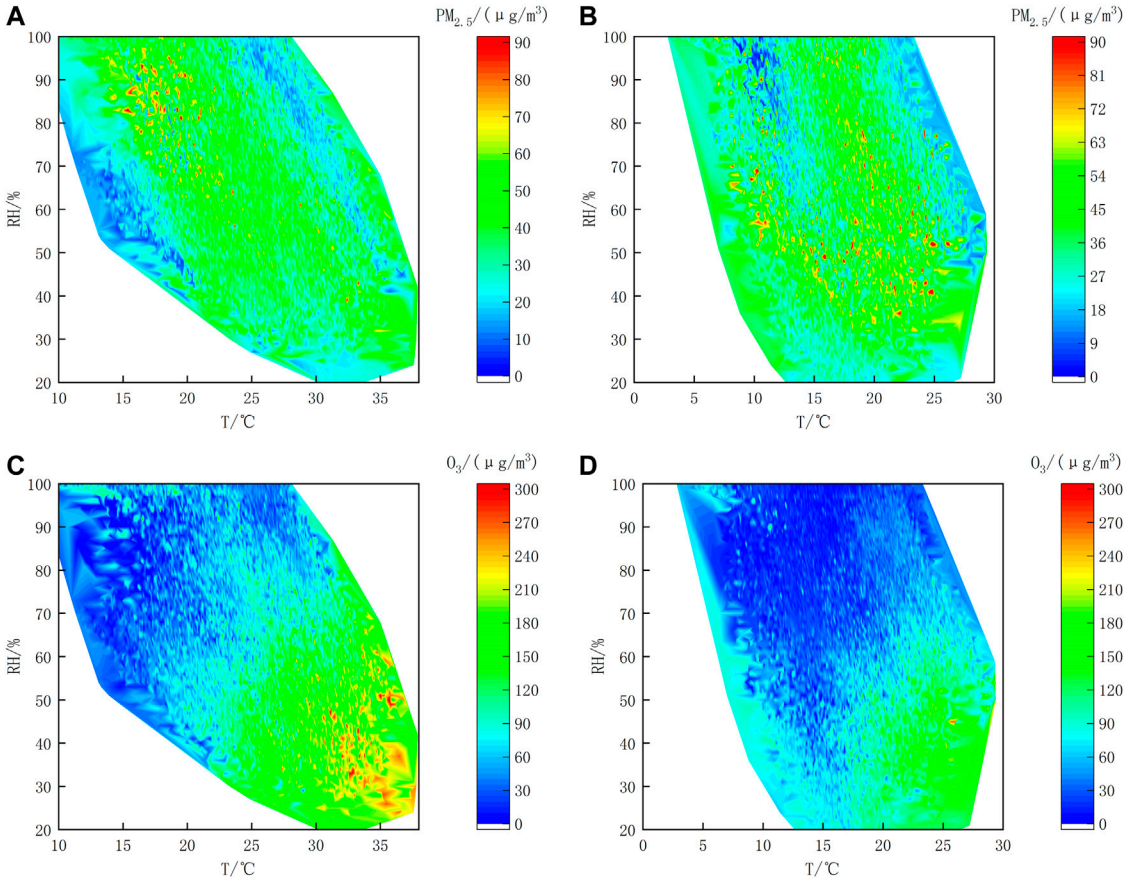


**FIGURE 3 |** Variations of $PM_{2.5}$ and ozone with temperature and humidity in autumn and winter. **(A)**. $PM_{2.5}$ in autumn, **(B)**. $PM_{2.5}$ in winter, **(C)**. ozone in autumn, and **(D)**. ozone in winter.

appear in autumn. In general, higher levels of photochemical reactivities are more conducive to the coordinated increase of $PM_{2.5}$ and ozone, and the proportions of secondary aerosols in $PM_{2.5}$ are also higher. However, some coastal stations in Shenzhen and Zhuhai have a long-term coordinated increase or a high $PM_{2.5}$/CO value, which requires further research.

## DISTRIBUTION CHARACTERISTICS OF $PM_{2.5\text{-}SEC}$ UNDER DIFFERENT PHOTOCHEMICAL REACTIVITY BACKGROUNDS

### Temporal and Spatial Variation Characteristics of $PM_{2.5\text{-}sec}$

**Figure 8** shows the seasonal variation of the average $PM_{2.5\text{-}sec}$ concentration at each station. The concentration in autumn is significantly higher than that in other seasons, and the concentration varies from 6 μg/m$^3$ to 13 μg/m$^3$, with the maximum appearing at Jida station in Zhuhai. $PM_{2.5\text{-}sec}$ concentrations are the highest in autumn, during which the regional discrepancies appear the most significantly with the highest levels in the southern areas. High concentrations of $PM_{2.5\text{-}sec}$ and ozone occur in the southern areas in autumn, indicating that the atmospheric oxidation background promotes the formation of $PM_{2.5\text{-}sec}$.

### Variation Characteristics of $PM_{2.5\text{-}sec}$ Under Different Photochemical Backgrounds

In addition to seasonal differences, there are also differences in $PM_{2.5\text{-}sec}$ concentrations and the proportions of $PM_{2.5\text{-}sec}$ in $PM_{2.5}$ under different photochemical reactivity backgrounds. **Figure 9** shows the regional variations of $PM_{2.5\text{-}sec}$ under different photochemical reactivities. With the enhancement of photochemical reactivities, $PM_{2.5\text{-}sec}$ levels increase significantly. Under the background of $O_{3H}$, the annual average $PM_{2.5\text{-}sec}$ concentrations at the coastal stations are generally above 13 μg/m$^3$ with a maximum of 20 μg/m$^3$ at some stations, whereas under the background of $O_{3M}$, the concentrations at the coastal stations are basically around 10 μg/m$^3$. Moreover, under the same photochemical reactivity background, $PM_{2.5\text{-}sec}$ concentrations in coastal areas are significantly higher than those in inland areas. **Figure 10** shows that the proportions of $PM_{2.5\text{-}sec}$

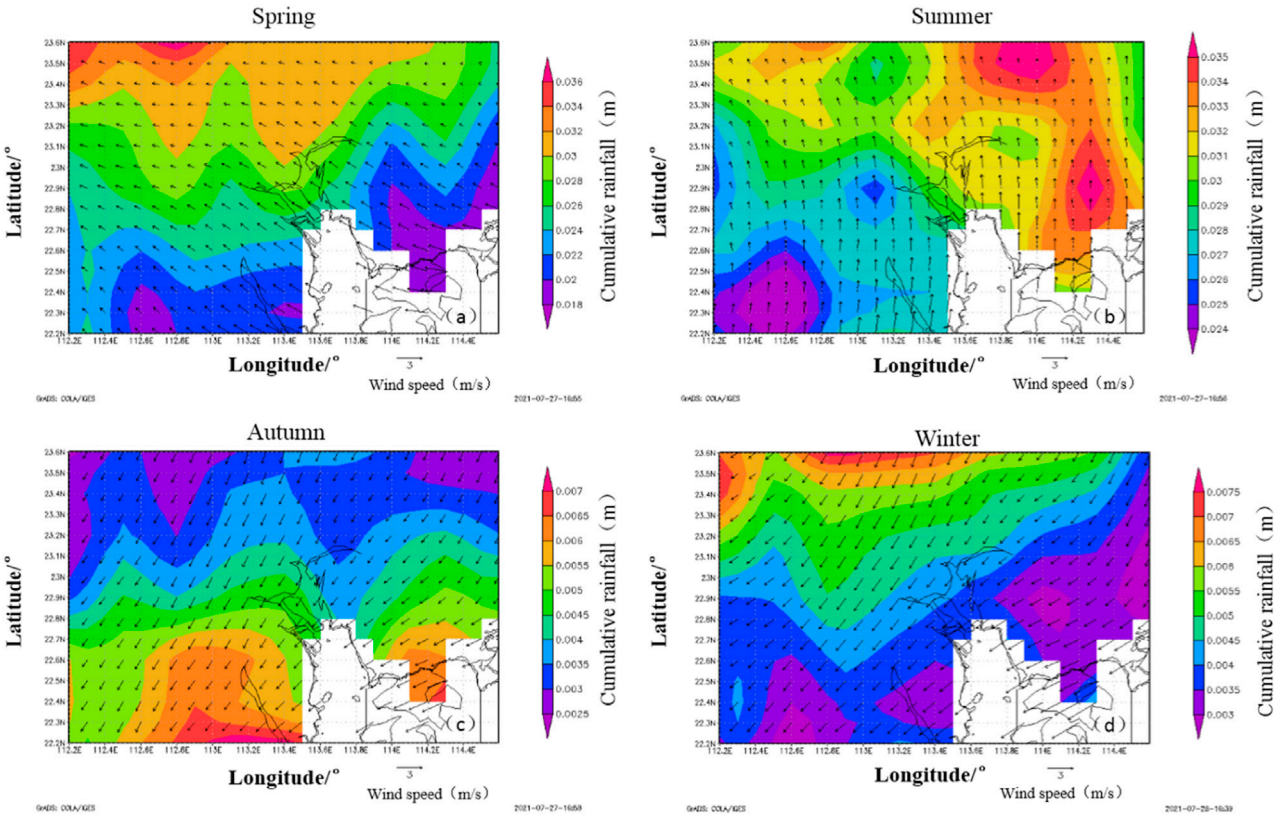


**FIGURE 4 |** 10 m wind field and accumulated rainfall in the PRD.

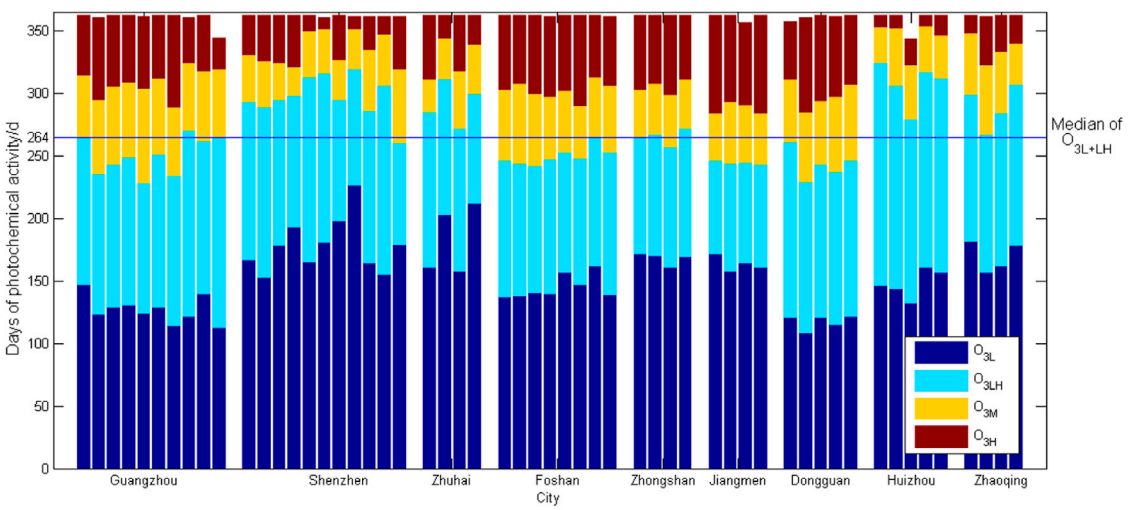


**FIGURE 5 |** Daily distribution of photochemical activities in the PRD.

in $PM_{2.5}$ have similar characteristics under different photochemical reactivity backgrounds. The ratios are about 10% in $O_{3L}$, 20%–30% in $O_{3M}$, and 20–50% in $O_{3H}$. Meanwhile, under the same photochemical background, the ratios of $PM_{2.5\text{-}sec}/PM_{2.5}$ in coastal areas are significantly higher than those in inland areas.

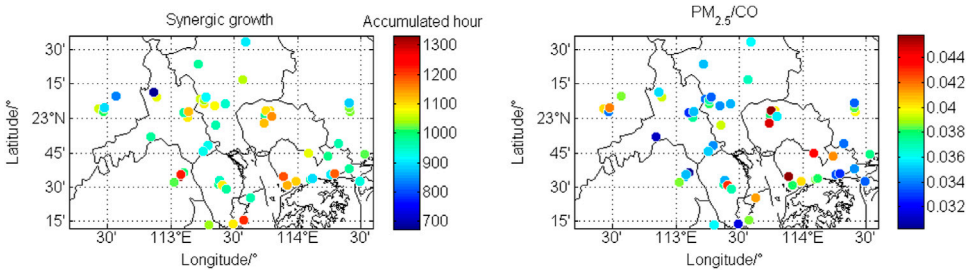


**FIGURE 6 |** Coordinated increase time and $PM_{2.5}$/CO distribution in the PRD.

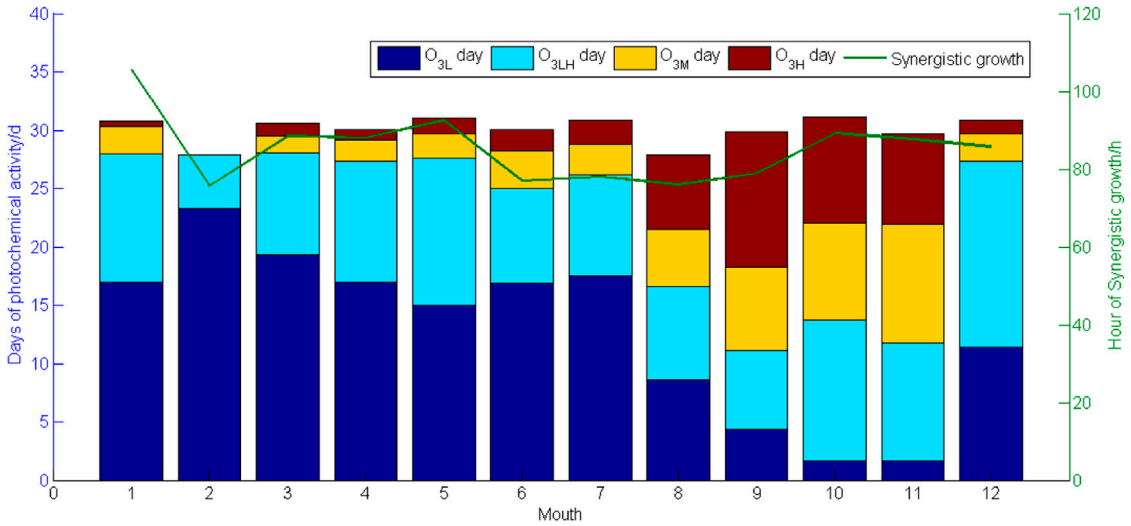


**FIGURE 7 |** Monthly averaged days of different photochemical reactivities and the average hours of coordinated increase.

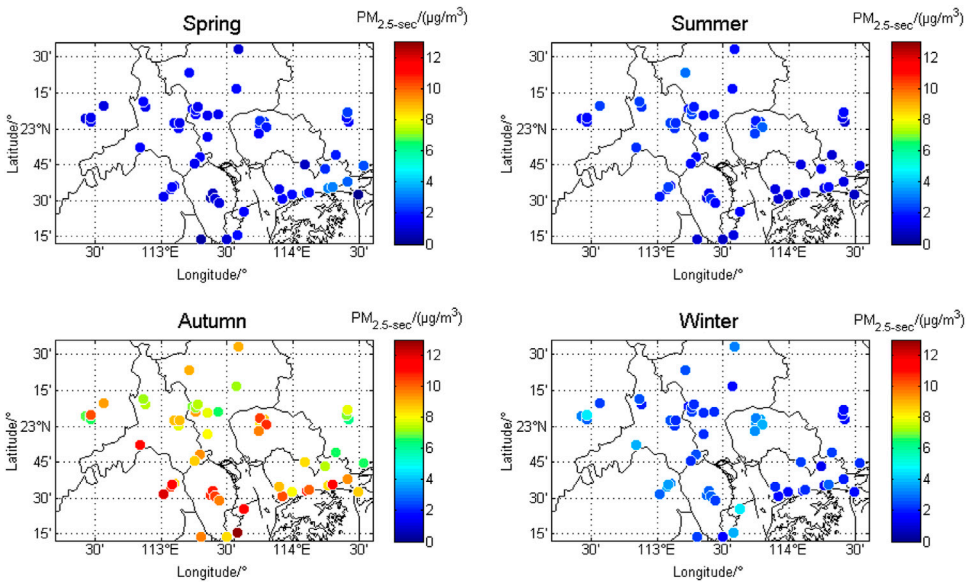


**FIGURE 8 |** Seasonal variations of $PM_{2.5\text{-}sec}$ in the PRD.

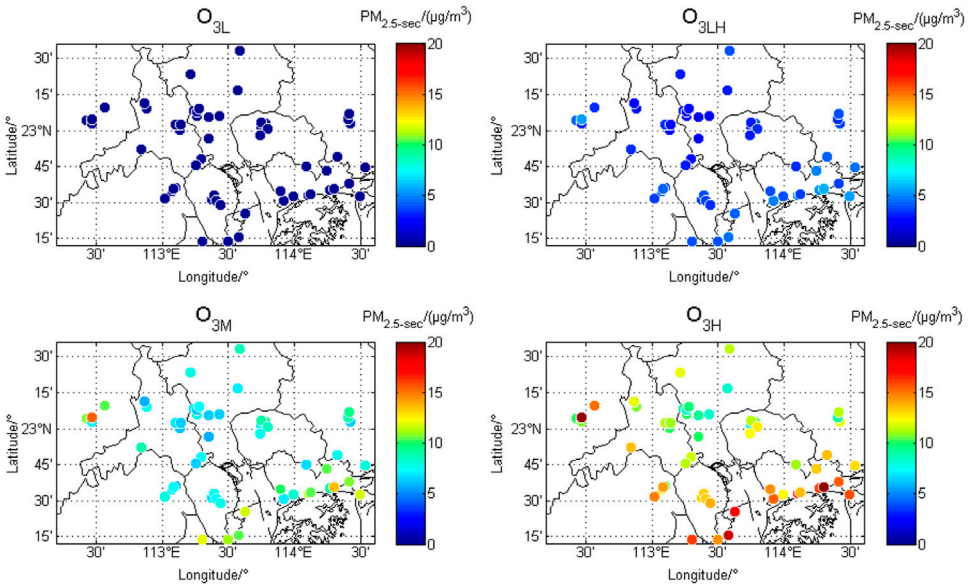


**FIGURE 9 |** $PM_{2.5\text{-}sec}$ variations under different photochemical backgrounds.

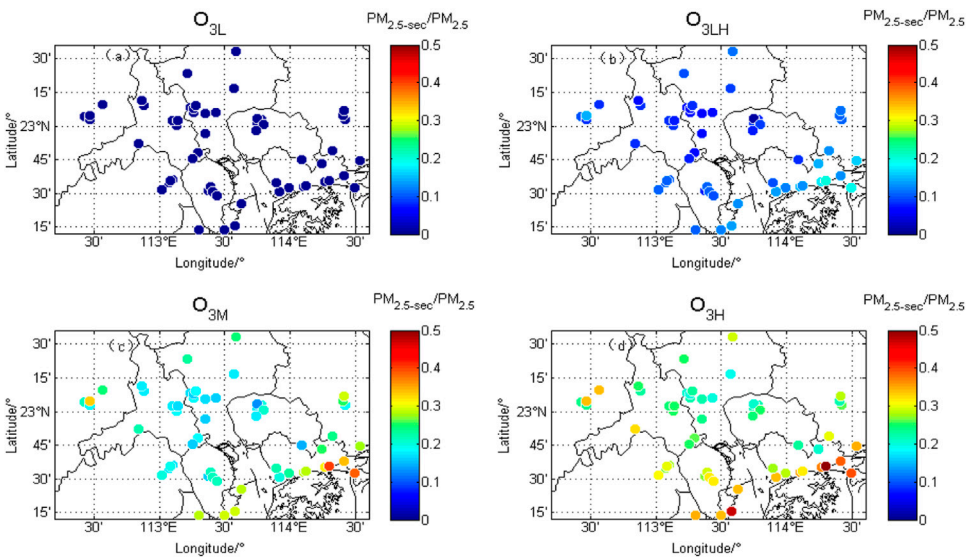


**FIGURE 10 |** Variations of the ratios in $PM_{2.5\text{-}sec}/PM_{2.5}$ under different photochemical backgrounds.

## Diurnal Variation Characteristics

Because the stations in the PRD are widespread with significant background discrepancies, we refer to the standard of ozone pollution in the Ambient Air Quality Standard (GB3095-2012) and take MDA8-$O_3$ (daily maximum 8 h average value of $O_3$) ≥ 160 μg/$m^3$ as the classification standard. Then, the three stations with the most days exceeding the standard (located in Guangzhou, Foshan, and Dongguan) are identified as polluted stations, whereas the three stations with the least number (located in Zhuhai, Shenzhen, and Huizhou) are defined as clean stations. Finally, diurnal variations and standard deviations of $PM_{2.5\text{-}sec}$ and ozone are presented (**Figure 11**, the error bars depict the standard deviation). The concentrations of the two pollutants are higher in the daytime than at night, and their maximum concentrations for both appear at about 15:00. As for ozone, the variation at polluted stations is larger than that at clean stations because the maximum concentration of ozone at polluted stations (91 μg/$m^3$) is higher than that at clean stations (60 μg/$m^3$) due to the photochemical reactions of a large number of precursors in the daytime, whereas the minimum concentration

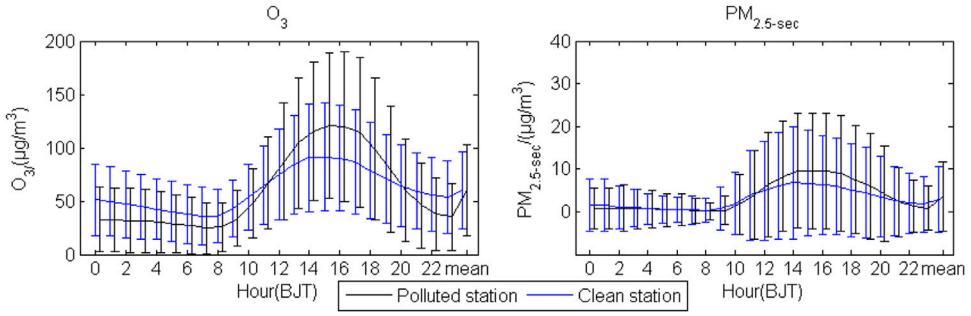


**FIGURE 11 |** Diurnal variations of ozone and $PM_{2.5\text{-sec}}$ under different photochemical backgrounds.

of ozone in polluted stations is lower than that in clean stations due to the consumption of a large number of NO in polluted stations at night. Under the background of high-photochemical reactivities, the concentration of $PM_{2.5\text{-sec}}$ at polluted stations is higher than that at clean stations from 12:00 to 20:00, which further reflects the promoting effect of the atmospheric oxidation background on $PM_{2.5\text{-sec}}$ formation.

Both $PM_{2.5\text{-sec}}$ and ozone concentrations show single-peak variations, which appear higher in the daytime than at night with the peak occurring at about 15:00. As for each pollutant, the average maximum concentration appears higher for polluted stations than for clean ones, indicating that the atmospheric oxidation background is conducive to the formation of $PM_{2.5\text{-sec}}$.

## CONCLUSION

Based on the observation data of environmental and meteorological stations in the nine cities of the PRD during 2019, the variations of $PM_{2.5\text{-sec}}$ and the coordinated increase of $PM_{2.5\text{-sec}}$ and ozone under different photochemical reactivity backgrounds in the PRD are revealed.

The trend of coordinated increase time is basically opposite to that of $O_{3L}$ days, meaning that the coordinated increase of $PM_{2.5}$ and ozone mainly occurs under more significant oxidation backgrounds. The photochemical reactivities appear more significant in the central and western areas than in the eastern areas of the PRD and appear more significant in inland areas than in coastal areas. The days of moderate- and high-photochemical reactivities mainly appear from August to November.

The $PM_{2.5\text{-sec}}$ concentrations are the highest in autumn, during which the regional discrepancies appear the most significantly with the highest levels in the southern areas. With the enhancement of the photochemical reactivity background, the $PM_{2.5\text{-sec}}$ level at each station increases significantly, which appears significantly higher in coastal areas than that in inland areas. The ratios of $PM_{2.5\text{-sec}}/PM_{2.5}$ are as high as 30–50% under the high-photochemical reactivity background.

## DATA AVAILABILITY STATEMENT

The original contributions presented in the study are included in the article/Supplementary Material; further inquiries can be directed to the corresponding author.

## AUTHOR CONTRIBUTIONS

XY contributed to data processing, mapping, analysis, and writing; YZ contributed to software and mapping; NL contributed to conceptualization and check on; and SY contributed to writing and editing.

## FUNDING

This research was funded by the Basic Research Funds of Central Public Welfare Research Institutes, under grant number 2020SYIAEZD1, the Science and Technology Project of Liaoning Province, under grant number 2019JH8/10300095, and the Key Program of Science Foundation of Liaoning Meteorological Office, under grant number D202101.

## REFERENCES

Chang, S.-C., and Lee, C.-T. (2007). Secondary Aerosol Formation through Photochemical Reactions Estimated by Using Air Quality Monitoring Data in Taipei City from 1994 to 2003. *Atmos. Environ.* 41, 4002–4017. doi:10.1016/j.atmosenv.2007.01.040

Fleming, Z., Doherty, R., Schneidemesser, E., Malley, C., Cooper, O., Pinto, J., et al. (2018). Tropospheric Ozone Assessment Report: Present-Day Ozone Distribution and Trends Relevant to Human Health. *Elementa: Sci. Anthropocene* 6, 12. doi:10.1525/elementa.273

Lai, A., Cheng, X., Liu, Y., Jiang, M., Liu, Y., Wang, X., et al. (2018). Characteristics of Complex Pollution with High Concentrations of PM2.5 and Ozone over the Pearl River Delta, China. *Acta Scientiarum Naturalium Universitatis Sunyatseni* 57, 30–36.

Li, H., Wang, Y., Huang, L., Liu, Z., Wang, W., Feng, J., et al. (2020). Analysis of Coordinated Increase Effects between Ozone and Secondary Aerosol in Typical Cities in China. *Acta Scientiae Circumstantiae* 40, 157–168.

Liu, N., Li, X., Ren, W., Li, L., Su, C., and Wang, C. (2021). Concentration Characteristics and Photochemical Reactivities of VOCs in Shenyang, China. *Atmosphere* 12, 1240. doi:10.3390/atmos12101240

Liu, N., Lin, W., Ma, J., Xu, W., and Xu, X. (2019). Seasonal Variation in Surface Ozone and its Regional Characteristics at Global Atmosphere Watch Stations in China. *J. Environ. Sci.* 77, 291–302. doi:10.1016/j.jes.2018.08.009

Mills, G., Hayes, F., Wilkinson, S., and Davies, W. J. (2009). Chronic Exposure to Increasing Background Ozone Impairs Stomatal Functioning in Grassland Species. *Glob. Change Biol.* 15, 1522–1533. doi:10.1111/j.1365-2486.2008.01798.x

Stoker, T., Qin, D., Plattner, G., Tignor, M., Allen, S., Boschung, J., et al. (2013). *Climate Change 2013: The Physical Science Basis. Contribution of Working Group I to the Fifth Assessment Report of the Intergovernmental Panel on Climate Change*. Cambridge, United Kingdom and New York, NY, USA: Cambridge University Press.

Wang, H., Miao, Q., Shen, L., Yang, Q., Wu, Y., and Wei, H. (2021a). Air Pollutant Variations in Suzhou during the 2019 Novel Coronavirus (COVID-19) Lockdown of 2020: High Time-Resolution Measurements of Aerosol Chemical Compositions and Source Apportionment. *Environ. Pollut.* 271, 116298. doi:10.1016/j.envpol.2020.116298

Wang, H., Pei, Y., Yin, Y., Shen, L., Chen, K., Shi, Z., et al. (2021b). Observational Evidence of Lightning-Generated Ultrafine Aerosols. *Geophys. Res. Lett.* 48. doi:10.1029/2021gl093771

Wang, H., Tan, Y., Zhang, L., Shen, L., Zhao, T., Dai, Q., et al. (2021c). Characteristics of Air Quality in Different Climatic Zones of China during the COVID-19 Lockdown. *Atmos. Pollut. Res.* 12, 101247. doi:10.1016/j.apr.2021.101247

Wu, Y., Chen, W., Yan, F., Mao, J., Yuan, B., Wang, W., et al. (2021). *Nonlinear Response Relationship between Ozone and Precursor Emissions in the Pearl River Delta Region under Different Transmission Channels*. Springer.

Xing, J., Wang, J., Mathur, R., Wang, S., Sarwar, G., Pleim, J., et al. (2017). Impacts of Aerosol Direct Effects on Tropospheric Ozone through Changes in Atmospheric Dynamics and Photolysis Rates. *Atmos. Chem. Phys.* 17, 9869–9883. doi:10.5194/acp-17-9869-2017

Yao, Y., Wang, M., Zeng, C., Fan, L., and Ye, D. (2021). Pollution Characteristics and Interaction between PM2.5 and Ozone at Different Types of Stations in Guangzhou. *China Environ. Sci.* 41, 4495–4506.

Yin, Z., and Wang, X. (2020). Analysis of the Spatial and Temporal Variation Characteristics of Ozone Concentration in the Pearl River Delta Urban Agglomerations. *J. Fudan Univ. (Natural Science)* 59, 748–760.

Yuan, T., Remer, L., Bian, H., Jerald, R., Albrecht, R., Pickering, K., et al. (2012). Aerosol Indirect Effect on Tropospheric Ozone via Lightning. *J. Geophys. Res. Atmospheres* 117. doi:10.1029/2012jd017723

Zhan, S. (2018). *Research on Trend and Influencing Factors of Conventional Air Pollutants in Guangdong-Hong Kong-Macao Greater Bay Area*. Guangzhou: The University of Chinese Academy of Sciences.

Zhang, H., Wang, Y., Hu, J., Ying, Q., and Hu, X.-M. (2015). Relationships between Meteorological Parameters and Criteria Air Pollutants in Three Megacities in China. *Environ. Res.* 140, 242–254. doi:10.1016/j.envres.2015.04.004

Zhang, L., Fan, F., Jiang, W., Chao, T., Zhang, W., and Liu, J. (2017). Concentrations and Health Risk Assessment of Heavy Metals in Atmospheric PM_(2.5) in the Pearl River Delta Region. *Acta Scientiae Circumstantiae* 37, 370–380.

Zhang, Y., Zhao, T., Ying, C., Wang, Z., Ge, B., Liu, D., et al. (2019). Seasonal Variation of the Relationship between Surface PM2.5 and Ozone Concentrations in Xuzhou. *China Environ. Sci.* 39, 2267–2272.

Zhao, S., Wang, L., Qi, M., Lu, X., Wang, Y., Liu, Z., et al. (2021). Study on the Characteristics and Mutual Influence of PM2.5-ozone Complex Pollution in Handan. *Acta Scientiae Circumstantiae* 41, 2250–2261.

**Conflict of Interest:** The authors declare that the research was conducted in the absence of any commercial or financial relationships that could be construed as a potential conflict of interest.

**Publisher's Note:** All claims expressed in this article are solely those of the authors and do not necessarily represent those of their affiliated organizations, or those of the publisher, the editors, and the reviewers. Any product that may be evaluated in this article, or claim that may be made by its manufacturer, is not guaranteed or endorsed by the publisher.

frontiers in Environmental Science

ORIGINAL RESEARCH
published: 10 February 2022
doi: 10.3389/fenvs.2021.828230

# Long Time-Series Urban Heat Island Monitoring and Driving Factors Analysis Using Remote Sensing and Geodetector

*Liwei Xiong*[1,2], *Shenxin Li*[2,3]*, *Bin Zou*[2,3], *Fen Peng*[4], *Xin Fang*[1] *and Yun Xue*[1]

[1]School of Municipal and Surveying Engineering, Hunan City University, Yiyang, China, [2]Key Laboratory of Nonferrous Metal Metallogenic Prediction and Geological Environment Monitoring, Ministry of Education, School of Geosciences and Info-physics, Central South University, Changsha, China, [3]School of Geosciences and Info-physics, Central South University, Changsha, China, [4]School of Architecture, Changsha University of Science and Technology, Changsha, China

Urban heat island (UHI) effect decribes significant change due to rapid urbanization development. This study focused on the long time series analysis of UHI during the period 2000-2018, and analyzed the impact of land cover type and landscape metric factors on surface temperature. The results revealed that the UHI had a continuously decreasing trend in 2005–2010, and an increasing trend in 2000–2005 and 2010–2018. Cropland, built-up land, patch density (PD), Shannon Diversity Index (SHDI), and Landscape Shape Index (LSI) had a positive relationship with UHI, whereas forestland, open water, and CONTAG had a negative correlation with the UHI effect. The Geodetector analysis further revealed that PD, SHDI, and LSI had the greatest influences on LST as the three factors had the largest q values (0.287, 0.286, and 0.278). Forestland, cropland, and built-up land had greater impacts on the UHI than other land cover type factors. The explanatory power reached a maximum value of 0.408 when built-up land and cropland variables interacted. The findings of this study provide new understandings of the relationship between urban landscape and UHI, as well as important insights for urban planners to mitigate the UHI effect for the sustainable development of future urban agglomeration.

**Keywords: urban heat island, long time series analysis, urban landscape, correlation analysis, sustainable development**

OPEN ACCESS

***Edited by:***
*Xinyao Xie,*
*Institute of Mountain Hazards and Environment (CAS), China*

***Reviewed by:***
*Taixia Wu,*
*Hohai University, China*
*Limin Jiao,*
*Wuhan University, China*

***Correspondence:**
*Shenxin Li*
*shenxin823@csu.edu.cn*

***Specialty section:***
*This article was submitted to Atmosphere and Climate, a section of the journal Frontiers in Environmental Science*

***Received:*** *03 December 2021*
***Accepted:*** *30 December 2021*
***Published:*** *10 February 2022*

***Citation:***
*Xiong L, Li S, Zou B, Peng F, Fang X and Xue Y (2022) Long Time-Series Urban Heat Island Monitoring and Driving Factors Analysis Using Remote Sensing and Geodetector. Front. Environ. Sci. 9:828230. doi: 10.3389/fenvs.2021.828230*

## 1 INTRODUCTION

Rapid urban social and economic development can lead to substantial urban ecological environment issues including environmental pollution, Urban Heat Island (UHI), traffic congestion, and so on. Among them, UHI is one of the most serious environmental problems related to urban landscape changes (Howard, 1833). In the "Guidelines for the Medium- and Long-Term National Science and Technology Development Program (2006–2020)", the formation mechanism of the UHI effect and artificial control technology was brought forward in China as the key contents of urban studies.

Land use/cover changes deeply depend on urbanization. A study on the quantitative relationships between land use/cover type and the UHI effects is an important step for understanding the mechanism of UHI (Hou and Wen, 2020). Traditional UHI studies using the observed temperature data from fixed or mobile monitoring stations may lead to a potential bias that cannot represent the

holistic urban thermal environment. Remote sensing, with the advantages of low cost and large coverage, have been widely applied to environmental monitoring that can be used to estimate the UHI effect. It also can greatly improve the identification of temporal-spatial patterns of temperature for studying climatological processes on regional and global scales (Chen et al., 2006; Flores R. et al., 2016). At the same time, remote sensing techniques have been extensively used in recent years to monitor changes in land use/cover patterns and map up-to-date landscape structures (Xian and Crane, 2006; Wu et al., 2014). Few studies have focused on the relationships between land use/cover type and the UHI effect (Du et al., 2020; Elliot et al., 2020) in depth. Analysis of the influenced mechanisms of the regional urban landscape on the urban thermal environment is still unclear (Nimish et al., 2020; Xie et al., 2020; Yao et al., 2020). Meanwhile, although the correlation analysis and regression equations used in previous studies can simply describe the degree of closeness in a relationship between factors of urban landscape and UHI, they are incapable of describing the explanatory power of interactions among multiple factors for the UHI effect (Estoque et al., 2017; Peng et al., 2018). Fortunately, a newly-developed method, the Geodetector method, can be introduced to analyze the influencing factors of the UHI effect, since the novel method contributes to developing interaction effects among multi-factors (Wang et al., 2010; Zou et al., 2017). Q-statistic in Geodetector has already been applied in many fields of natural and social sciences that can be used to measure spatial stratified heterogeneity, detect explanatory factors and analyze the interactive relationship between variables. Duan and Tan used Geodetector to identify the key factors that influence urban forest spatial differences within China (Duan and Tan, 2020). Many studies also widely applied the Geodetector method to quantify the spatial heterogeneity influences of factors and factor interactions on air pollution (Zou et al., 2017; Bai et al., 2019). To date, few studies have used Geodetector to analyze the interaction effects of factors of land cover and landscape metrics to the UHI effect.

Previous studies have revealed that urban areas can influence the local UHI circulation (Wang et al., 2020). Considering that the conclusions from studies of a single city might be limited by local conditions, few studies have attempted to investigate the UHI effect in multiple cities. For instance, Zhou et al. focused on the SUHI in 32 major Chinese cities and found the spatial pattern of the UHI effect had high spatial heterogeneities (Zhou et al., 2015). Even though spatial patterns of the UHI effect have been discussed in detail, the long-term trends of the UHI effect and associated factors are still unclear in current multi-city investigations. Therefore, a long temporal trend of the UHI effect in the urban agglomeration of the Xiangjiang river valley covering multiple cities, needs to be undertaken, because the currently reported UHI studies of Xiangjiang river valley mainly concentrate on individual cities (e.g., Changsha (Ye et al., 2017), Chang-Zhu-Tan urban agglomeration (Tang, 2018; Yuan et al., 2018; Xiong et al., 2019)).

Hence, we attempted to fill the above-mentioned gaps in this study. Overall, this study selects the urban agglomeration of the Xiangjiang river valley as the study area and collected remote sensing land surface temperature (LST) products from 2000 to 2018 to disclose the long time series characteristics of the UHI effect. The study applies the correlation analysis method to analyze the correlation coefficients between UHI and land cover types and urban landscape metric factors and further employs the Geodetector method to find the main contributors to the UHI effect. The results from this study could enhance understanding of UHI intensities with changing land cover and urban landscape patterns. In addition, important insights can be provided to urban planners and natural resource managers on how to mitigate the impact of urbanization on UHI through urban design and vegetation management for sustainable development.

# 2 DATA AND METHODS

## 2.1 Study Area and Data

This study examines an area of urban agglomeration in the Xiangjiang river valley, including the core area as well as the regions with the most prominent ecological and environmental problems in Hunan province. The area has a dense population and rapid economic development with a complex and diverse urban landscape. According to the "overall plan for the scientific development of Xiangjiang river basin" on the website of the People's Government of Hunan Province in 2016, the study area covers nine cities (Changsha, Zhuzhou, Xiangtan, Yueyang, Yongzhou, Shaoyang, Hengyang, Loudi, and Chenzhou), which include 68 counties or districts (**Figure 1**). The Xiangjiang river valley belongs to the Pacific monsoon humid climate, with rich light and hot water resources. Generally, the weather is wet and cold in winter, and humid, rainy, and hot in summer. In the context of global warming, the annual average air temperature in Xiangjiang river valley is between 16°C and 18°C. The changing urban temperature will bring effects to the spatial and temporal patterns of water resources in the Xiangjiang river valley.

This study employs Moderate Resolution Imaging Spectroradiometer (MODIS)/Terra LST and Emissivity 8-Day L3 Global 1 km Grid SIN V006 (MOD11A2) from 2000 to 2018 for analyzing the trend of LST with a spatial resolution of 1 × 1 km and temporal resolution of 8-days, the data were collected from the website of NASA (https://ladsweb.modaps.eosdis.nasa.gov). ArcGIS 10.3 was used to convert the geographic coordinate system (Asia_Lambert_Conformal_Conic) to the appropriate projection system and tiff format for further analysis. To prepare the LST map of the study area, the mask tool in ArcGIS was used to extract the study area from the collected MOD11A2 LST data based on the vector boundary data. The mean LST of the season in the study period was calculated by the ratio of the sum of the mean daily LST to days, which indicates the number of season days. The mean LSTs of the spring season (March-May), summer season (June-August), the autumn season (September-November), and winter season (December-February) in the selected years (2000, 2005, 2010, 2015, and 2018) and for 18 years (2000–2018) were further obtained. Then,

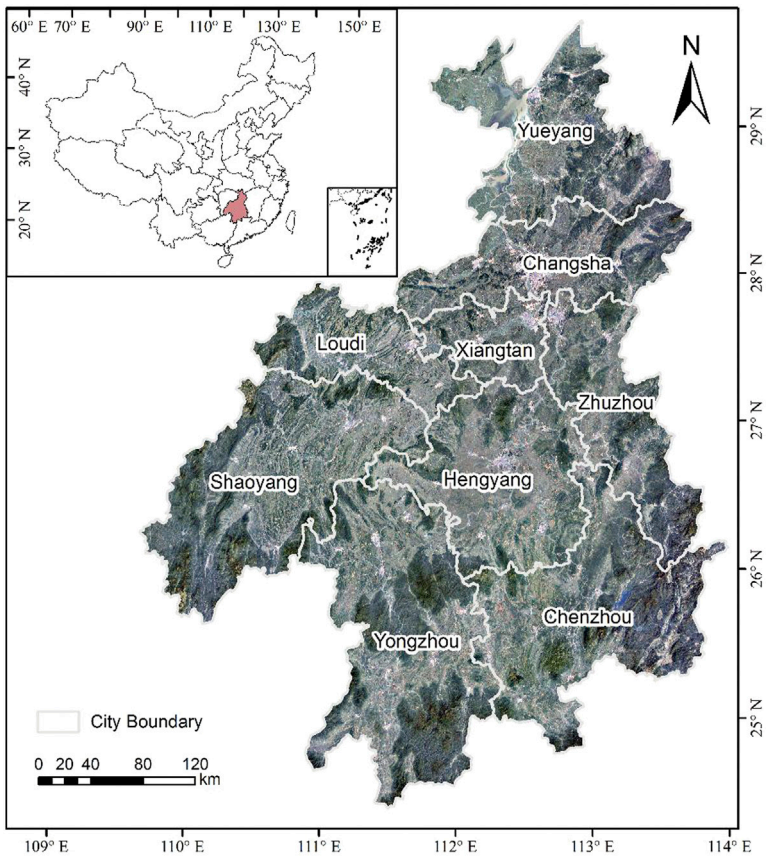


**FIGURE 1 |** Study area: Urban agglomeration of Xiangjiang river valley.

the annual average LST can be calculated based on the mean LST of the season.

## 2.2 Methods

To visually illustrate the process used in this study, a general technical flowchart describing the preprocessing of the spatial pattern of UHI classification, land cover/use type, landscape metrics, and factor analysis influencing UHI is shown in **Figure 2**.

### 2.2.1 Classification of UHI

The annual or seasonal mean LST, which was calculated using the raster calculator in ArcGIS, was inaccurate because of the existence of nodata value in the collected MOD11A2 LST data. It was therefore calculated using Matlab software by selecting the pixel with MOD11A2 LST value excluding the pixel with nodata value in the study period (2000–2018). MODIS LST data with 1 km spatial resolution was calibrated to obtain the temperature in degrees Celsius (°C) based on (**Eq. (1)**) (Li and Zeng, 2015).

$$\text{Temperature } (^{\circ}\text{C}) = (\text{Digital Number} * 0.02) - 273.15 \quad (1)$$

Most previous studies are focused on the spatial distribution or temporal changes by calculating the temperature difference between urban and rural areas or equally segmenting the urban surface temperatures from thermal remote sensing images. However, these methods are not suitable when weather stations in rural areas or threshold values are selected arbitrarily, and the results may not well represent the high-temperature area (Hawkins et al., 2004). In this study, a standard deviation segmenting method was thus proposed to calculate the UHI effect from the LST image for seeking a more suitable threshold value (Chen and Wang, 2009). The specific implementation was as follows. Firstly, the mean surface temperatures (μ) for the study area and their standard deviation (std) were calculated. The mean surface temperature ±0.5 times standard deviation can be determined as the background value for urban LST, and can thus be recognized as the threshold value for extracting the UHI area (strongest UHI, strong UHI, and medium UHI) and non-UHI area (strong urban cool island (UCI) and strongest UCI). The threshold of (μ+0.5*std) was used to extract the outlines of the hot island and then determine the strong UHI area by calculating the total number of pixels that the temperature is higher than (μ+0.5*std) (Wong et al., 2016). The LST classification could reflect the spatial extent and the seriousness of UHI and could be used to quantify the UHI effect. The UHI and non-UHI classifications of the study area are listed in **Table 1**.

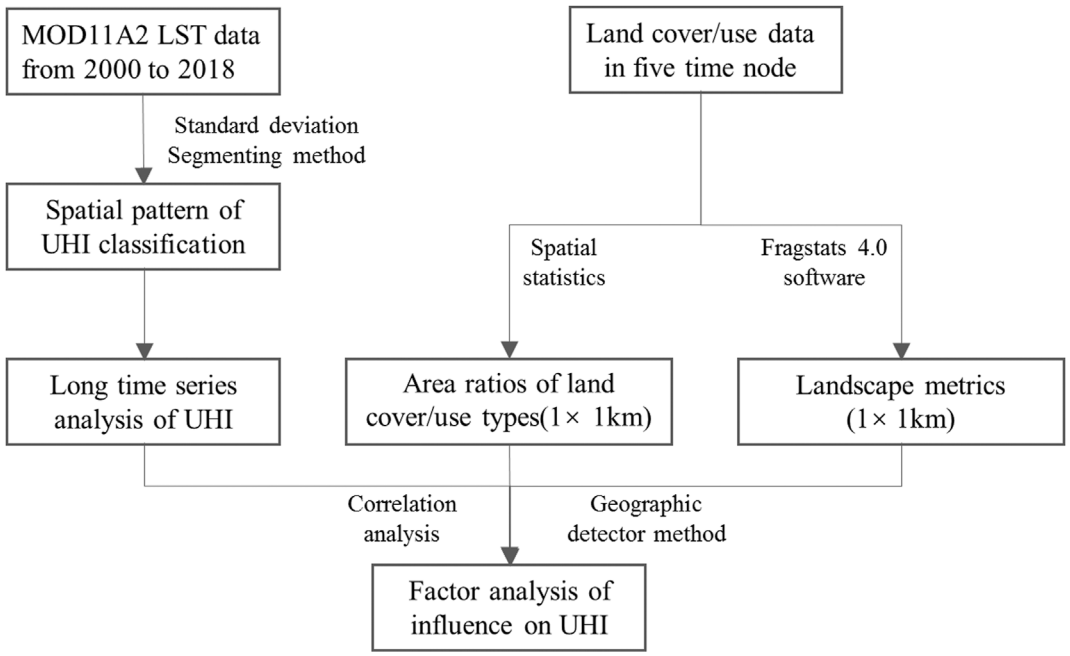


**FIGURE 2 |** The flowchart of the study.

**TABLE 1 |** The classification of UHI and non-UHI effects.

| UHI classification | Class |
|---|---|
| Strongest UHI | Temperature > u + std |
| Strong UHI | u+0.5std < Temperature ≤ *u* + std |
| Medium UHI | u-0.5std ≤ Temperature ≤ *u*+0.5std |
| Strong UCI | u-std ≤ Temperature < u-0.5std |
| Strongest UCI | Temperature < u-std |

### 2.2.2 Landscape Metrics

The land cover data were used to observe the dominant causative factors influencing the UHI in this study. The land cover/use data in the years 2000, 2005, 2010. 2013 and 2017 were collected from the Geographical Information Monitoring Cloud Platform (http://www.dsac.cn/). Given the insignificant change of land cover type during one or 2 years, the land cover data in 2013 and 2017 were used to develop factor analysis instead of the land cover data in 2015 and 2018. The landscape metrics were calculated based on classification maps including six land-cover types: cropland, forestland, grassland, open water, built-up land, and unused land. The accuracy of the classification result was evaluated by the overall Kappa index as 0.85, which was acceptable for the urban scale. The landscape metrics are demonstrated in many studies to measure the composition and configuration of land cover features (Wu et al., 2010; Xu, 2015). Landscape metrics (i.e. contagion index (CONTAG), patch density (PD), Shannon Diversity Index (SHDI), and landscape shape index (LSI)) were calculated at the landscape level using Fragstats 4.0 (McGarigal et al., 2002) for describing landscape size, shape, diversity, aggregation and fragmentation.

Considering the spatial units of LST data, all the statistical variables were entered into the database of 1 km × 1 km grid cells for further processing analysis of the factor interaction detector (**Figure 3A**). For the spatial land cover data of 30 m × 30 m grid cells, the area percentage of each land cover type in each 1 km × 1 km grid cell was calculated. In addition, the use of land cover data for the latest year was more beneficial in providing guidance for future planning. The results of land cover data and landscape metric values in 2017 were therefore described with the classification method of natural breaks (**Figures 3F–K**). The landscape metric values for each grid were calculated in every 1 km × 1 km grid (**Figures 3B–E**). The spatial patterns of land cover data and landscape metric values in 2000, 2005, 2010, 2013, and 2017 were derived.

CONTAG describes the aggregation degree and extension degree of different patch types. A smaller value indicates a higher degree of plaque dispersion. PD is the degree of fragmentation of the landscape, which reveals the complexity between landscape spatial structures. SHDI depicts the diversity of landscape types, and the higher value indicates the richer the land use type. LSI represents the size of the landscape shape. As the shape becomes more and more irregular, the LSI becomes larger, indicating that the landscape is less disturbed.

### 2.2.3 Geodetector

The effects of spatial configuration on LST distribution were examined by using landscape metrics. (Weng et al., 2008; Zhou et al., 2011). Geodetector represents a new spatial statistics method that is used to detect spatial heterogeneity and identify driving factors based on risk, factors, ecology, and interaction (Wang and Geodetector, 2017). The advantage of

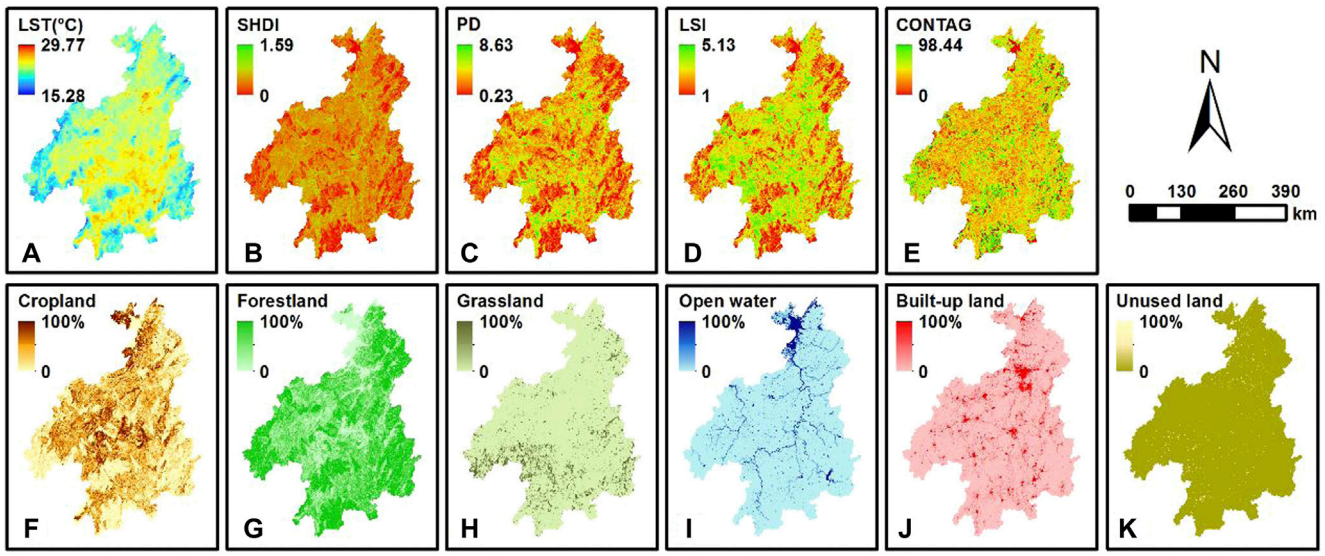


**FIGURE 3 |** Spatial patterns of land cover types and landscape metrics in 2017. **(A)** LST, **(B)** SHDI, **(C)** PD, **(D)** LSI, **(E)** CONTAG, **(F)** Cropland, **(G)** Forestland, **(H)** Grassland, **(I)** Open water, **(J)** Built-up land, **(K)** Unused land.

the Geodetector method is that it can examine the interactions of two driving factors affecting the dependent variable and it reveals whether the interactions of two factors are linear or nonlinear. The Geodetector method is therefore employed to find the main contributors to the UHI effect. Land cover and urban landscape factors were divided into different spatial types or subzones. A significance test for the differences of mean values of land cover and urban landscape factors was conducted to detect the relative importance of land cover and urban landscape factors. The calculation model of the explanatory power of each land cover and urban landscape factor is as **Eq. 2**:

$$q = 1 - \frac{\sum_{i=1}^{m} N_i \sigma_i^2}{N\sigma^2} \quad (2)$$

where $q$ is the explanatory power of land cover and urban landscape factors on LST, $i = 1, \ldots, m$ are the stratification of $y$ or factor $x$, that is, classification or partition. $N_i$ and $m$ are the number of units in $i$ and the whole region, respectively. $N$ and $\sigma^2$ are the total number of samples and the variance of $y$ value in the whole region. $\sigma_i^2$ is the variance of units $i$. The range of $q$ value is between 0 and 1. Note that one value means that one of the land cover and urban landscape factors completely controls the spatial distribution of LST, whereas 0 value implies a completely random spatial occurrence of LST.

Interaction detection is used to identify the interaction between land cover and urban landscape factors to evaluate the accountability of the combined effect (enhancing or weakening) and respective effect on the LST. The q values of two factors with respect to LST were calculated as follows (the symbol "∩" denotes the intersection between $X_1$ and $X_2$):

Enhance: $q(X_1 \cap X_2) > q(X_1)$ or $q(X_2)$
Enhance, bilinear: $q(X_1 \cap X_2) > q(X_1)$ and $q(X_2)$
Enhance, nonlinear: $q(X_1 \cap X_2) > q(X_1) + q(X_2)$
Weaken: $q(X_1 \cap X_2) < q(X_1) + q(X_2)$
Weaken, unique: $q(X_1 \cap X_2) < q(X_1)$ or $q(X_2)$
Weaken, nonlinear: $q(X_1 \cap X_2) < q(X_1)$ and $q(X_2)$
Independent: $q(X_1 \cap X_2) = q(X_1) + q(X_2)$

# 3 RESULTS

## 3.1 Spatial Pattern of UHI Intensity

### 3.1.1 Annual UHI Intensity

The spatial pattern of the annual mean UHI effect at the city level were depicted in **Figure 4**. Most areas of the Xiangjiang river valley are concentrated at the medium UHI level. The strong and strongest UHI effect were located in the southern and southwestern study areas. The strong and strongest UCI area was concentrated in the western, northeastern, and southeastern study areas. The spatial pattern and area ratio of the 18-years mean UHI effect at the city level in **Figure 4G** shows that the medium UHI level had a larger coverage than the other levels in the six cities of Yueyang, Changsha, Xiangtan, Zhuzhou, Loudi, and Shaoyang. Thus, the total area ratios of the strong and strongest UHI effect in Yueyang, Changsha, Xiangtan, Loudi, and Shaoyang were only 1.62, 15.76, 14.60, 10.47, and 13.85% respectively, while that of the strongest UCI effect were respectively up to 23.07, 10.67, 0.47, 19.19, and 32.42%. It demonstrated that the UHI effect was insignificant in the five cities, especially in Yueyang and Shaoyang. Changsha as the provincial capital of Hunan, China has the largest administrative area. The UHI effect in Changsha was weaker than that in Hengyang, Chenzhou, Yongzhou, and Zhuzhou because Changsha had a slow urbanization increase in the earlier year. The total area ratio of the strong and strongest

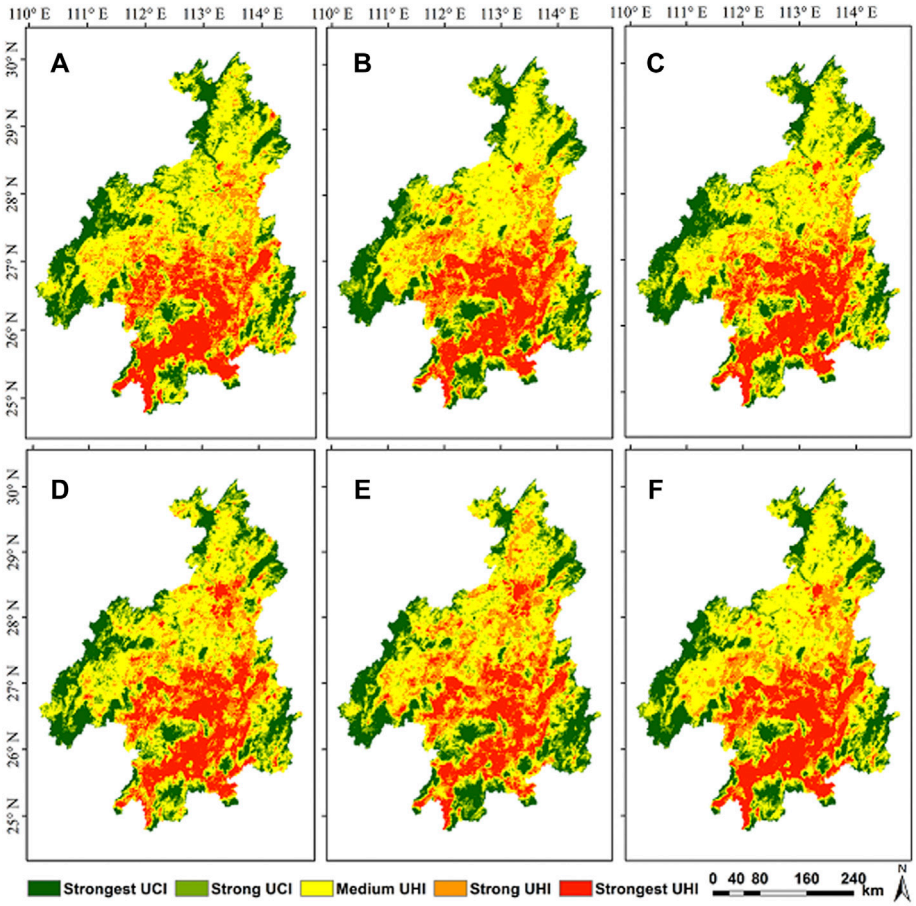


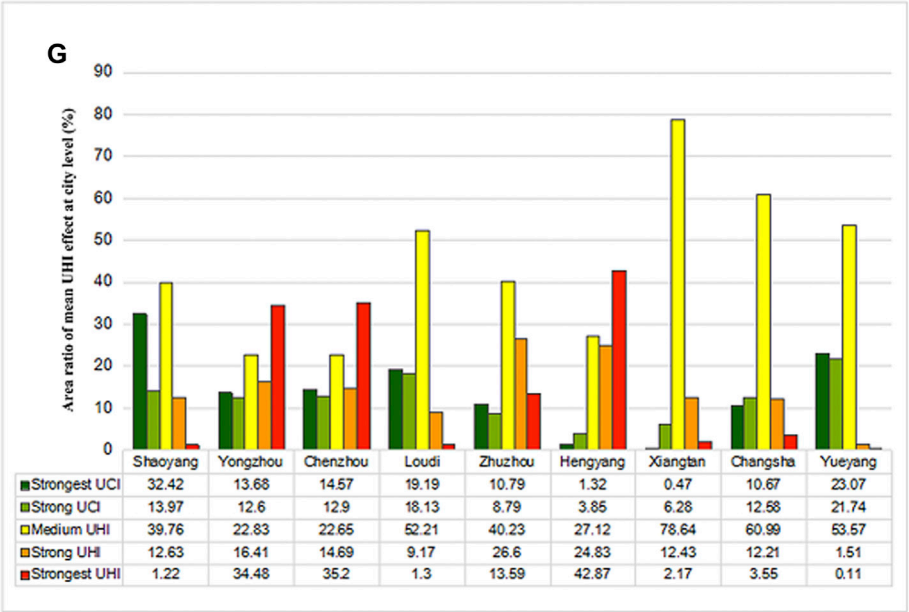


| | Shaoyang | Yongzhou | Chenzhou | Loudi | Zhuzhou | Hengyang | Xiangtan | Changsha | Yueyang |
|---|---|---|---|---|---|---|---|---|---|
| Strongest UCI | 32.42 | 13.68 | 14.57 | 19.19 | 10.79 | 1.32 | 0.47 | 10.67 | 23.07 |
| Strong UCI | 13.97 | 12.6 | 12.9 | 18.13 | 8.79 | 3.85 | 6.28 | 12.58 | 21.74 |
| Medium UHI | 39.76 | 22.83 | 22.65 | 52.21 | 40.23 | 27.12 | 78.64 | 60.99 | 53.57 |
| Strong UHI | 12.63 | 16.41 | 14.69 | 9.17 | 26.6 | 24.83 | 12.43 | 12.21 | 1.51 |
| Strongest UHI | 1.22 | 34.48 | 35.2 | 1.3 | 13.59 | 42.87 | 2.17 | 3.55 | 0.11 |

**FIGURE 4 |** Spatial pattern of the UHI effect in **(A)** 2000, **(B)** 2005, **(C)** 2010, **(D)** 2015, **(E)** 2018, **(F)** 18-year (2000–2018), and **(G)** area ratio of the 18-year mean UHI effect at the city level.

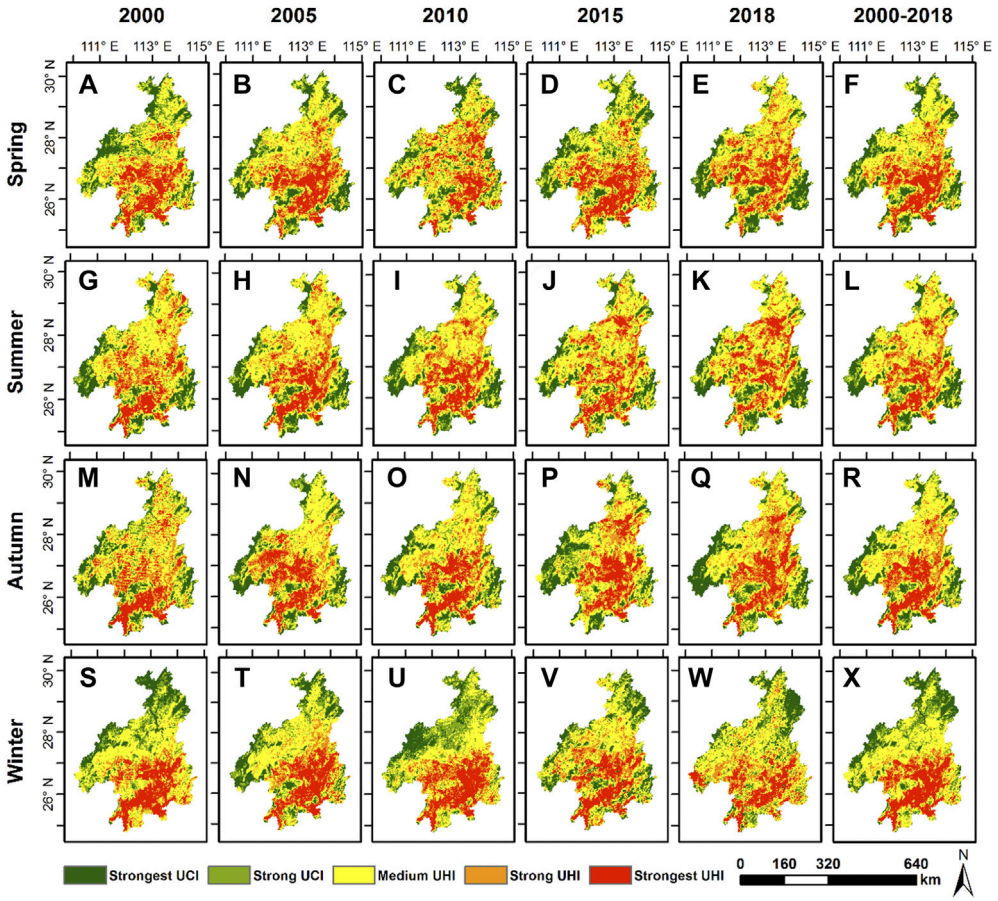


**FIGURE 5 |** Spatial distribution map of UHI effect for the **(A–F)** spring, **(G–L)** summer, **(M–R)** autumn, and **(S–X)** winter seasons during the period 2000–2018.

UHI in Zhuzhou was 40.19%, which was identified as the significant UHI effect in this city. The area ratios of the strongest UHI level in Hengyang city, Chenzhou city, and Yongzhou city were respectively 42.87, 35.20, and 34.48%, which had a higher proportion than the area of the other levels. Therefore, the three cities of Hengyang, Chenzhou, and Yongzhou experienced a significant UHI effect during the period 2000–2018. The UHI effect of Hengyang was strongest in the Xiangjiang river valley.

### 3.1.2 Seasonal UHI Intensity

The seasonal mean UHI effect between 2000–2018 was calculated to describe the spatial pattern of the seasonal mean UHI (seen in **Figure 5**). In total, the areas of the central and southern study area had strong and strongest UHI during all the seasons. In contrast, the western areas were with UCI in different seasons. The northern areas were with medium UHI in spring (**Figures 5A–F**), summer (**Figures 5G–L**), and autumn (**Figures 5M–R**), and were with strong and strong UHI in winter (**Figures 5S–X**). The UHI the south western area was significant in winter, but in the other three seasons, it showed UCI or medium UHI in these regions. Strong UHI also happened in the north-central areas in spring, and relieved to medium UHI in summer and autumn, then changed to UCI in winter.

## 3.2 Long-Time Series Analysis of UHI Intensity

### 3.2.1 Annual UHI Variations

The magnitude of 18-year UHI has significantly changed over time. The statistical results of five classes representing UHI and non-UHI effects in the study area based on **Figure 4** are listed in **Table 2**. The area ratio of the different levels of the UHI effect was calculated by the ratio of the area of the different levels to the total area of the Xiangjiang river valley. The area ratio of 39.80% of medium UHI in 2000 was larger than the strong UHI (14.48%) and the strongest UHI (16.34%). The total area ratio of the strong and strongest UHI in 2005 was 33.19%, which was larger than 30.82% in 2000. There was a significant increasing trend from 2000 to 2005. The total area ratio (30.66%) of the strong and strongest UHI in 2010 compared to 2005, which had a small decrease, while the area ratio of the strongest UHI increased from 16.99 to 17.76%. The total area ratio of the strong and strongest UHI had a significant decreasing trend since 2010, then

**TABLE 2 |** Area ratios of five levels of the UHI effect during the period 2000-2018 (unit: %).

| Year | Non-UHI | | | — | Non-UHI | | |
|---|---|---|---|---|---|---|---|
| | Strongest UCI | Strong UCI | Total | MediumUHI | Strong UHI | Strongest UHI | Total |
| 2000 | 15.51 | 13.87 | 29.38 | 39.80 | 14.48 | 16.34 | 30.82 |
| 2005 | 16.44 | 12.45 | 28.89 | 37.92 | 16.20 | 16.99 | 33.19 |
| 2010 | 15.51 | 13.85 | 29.36 | 39.98 | 12.90 | 17.76 | 30.66 |
| 2015 | 15.66 | 13.73 | 29.39 | 38.16 | 15.26 | 17.18 | 32.44 |
| 2018 | 17.05 | 12.52 | 29.57 | 36.47 | 18.43 | 15.54 | 33.97 |
| 2000-2018 | 15.74 | 12.61 | 28.35 | 38.47 | 14.77 | 18.41 | 71.65 |

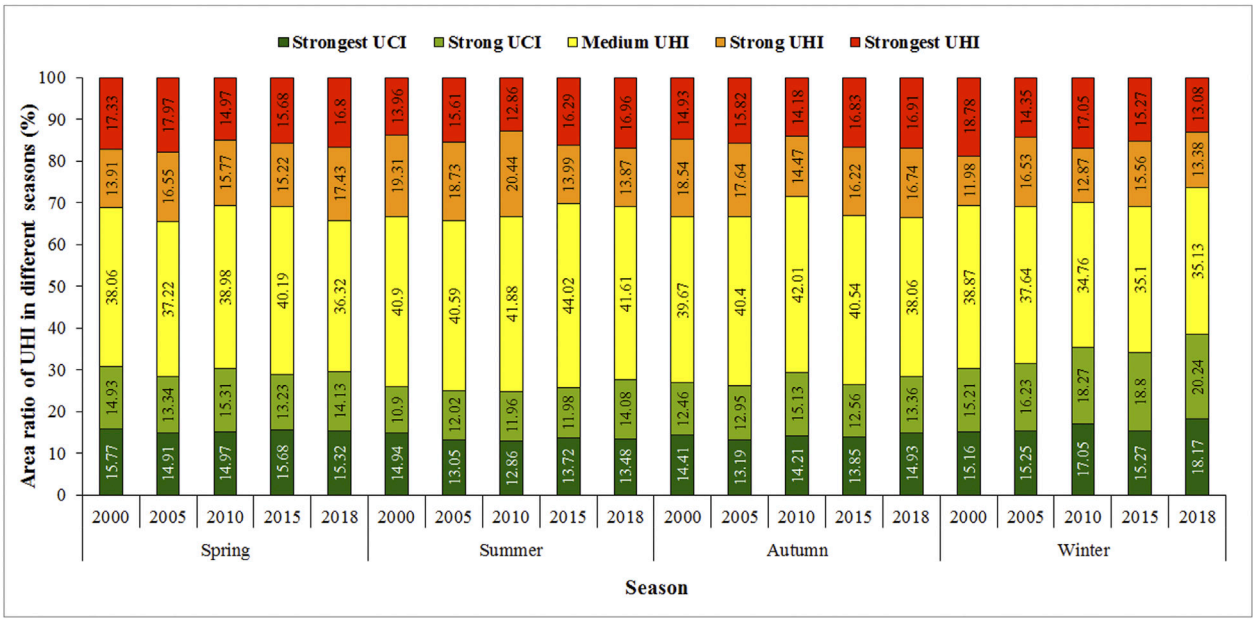


**FIGURE 6 |** Area ratio of the UHI effect for the spring, summer, autumn, and winter seasons during the period 2000–2018.

increasing until 2018, was respectively 32.44% in 2015 and 33.97% in 2018. The total area ratio of the non-UHI experienced a decreasing trend from 29.38% in 2000 to 28.89% in 2005, then increased slowly from 29.36% in 2010 to 29.57% in 2018. The area ratio of the strongest UHI was more than that of the strongest UCI, with a difference of 2.67% in 2000–2018. The total area ratio of the medium, strong, and strongest UHI was 71.65%, which demonstrated the significant UHI effect in the Xiangjiang river valley.

### 3.2.2 Seasonal UHI Variations

The area ratio of the UHI effect for the spring, summer, autumn, and winter seasons during the period 2000–2018 are depicted in **Figure 6** according to **Figure 5**. The area ratio of medium UHI for the spring season is noticed in the range of 36.32–40.19%. The area ratios of the strongest UHI were 17.33, 17.97, 14.97, 15.68, and 16.80% for the year 2000, 2005, 2010, 2015, and 2018, respectively. The total area ratios of the strong and strongest UHI were 31.24, 34.52, 30.74, 30.90, and 34.23% for the years 2000, 2005, 2010, 2015, and 2018, respectively. It can be concluded that the UHI effect experienced an increasing trend during the period 2000–2005 and 2010–2018, whereas had a decreasing trend during the period 2005–2010.

The area ratio of medium UHI for the summer season ranged from 40.59 to 44.02%, which was the high proportion level. The area ratios of the strongest UHI were noticed as 13.96, 15.61, 12.86, 16.29, and 16.96% for the years 2000, 2005, 2010, 2015, and 2018, respectively. The total area ratios of the strong and strongest UHI were observed as 33.27, 34.34, 33.3, 30.28, and 30.83% for the years 2000, 2005, 2010, 2015, and 2018, respectively. The same changing tendency of the strongest UHI effect during the period 2000–2018 for the summer season compared to the spring season was found. However, it can be observed according to the total area ratio that there was an increasing trend during the period 2000–2005 and 2015–2018, and a decreasing trend during the 2005–2015 period.

The area ratio of medium UHI level of the high proportion for the autumn season was in the range of 38.06–42.01%. The area ratios of the strongest UHI were noticed as 14.93, 15.82, 14.18,

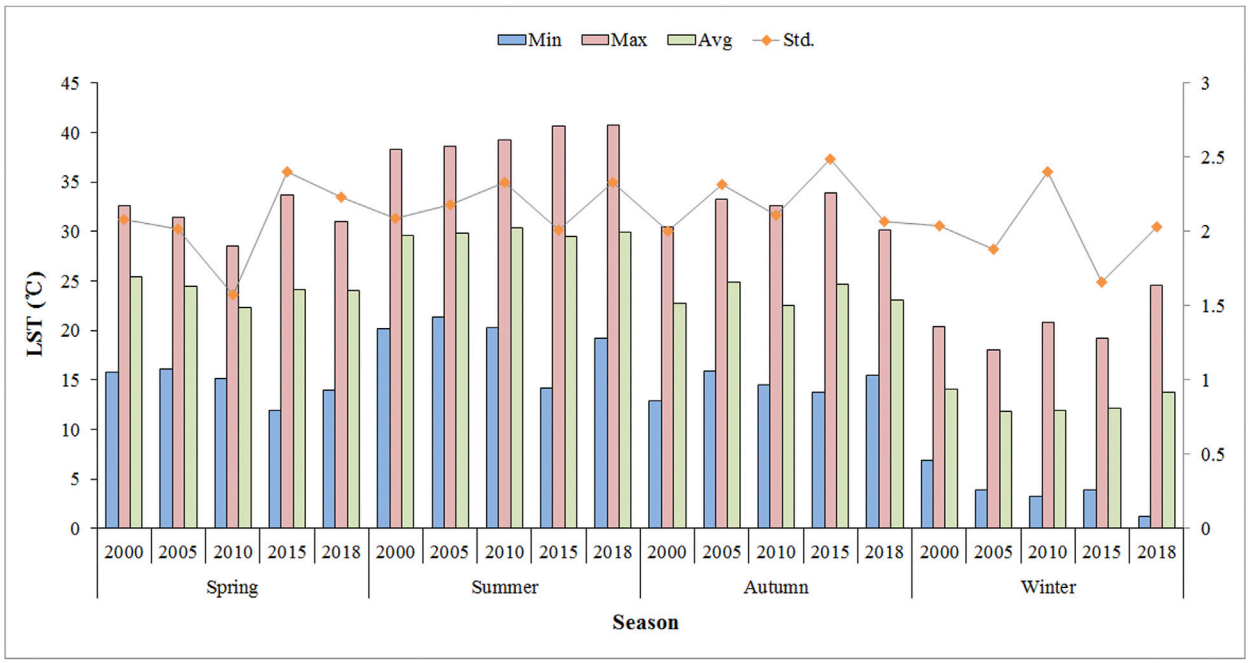


**FIGURE 7 |** Histogram of seasonal LST during the period 2000–2018 to evaluate the temperature change in each season.

16.83, and 16.91% for the years 2000, 2005, 2010, 2015, and 2018, respectively. The total area ratios of the strong and strongest UHI were observed as 33.47, 33.46, 28.65, 33.05, and 33.65% for the years 2000, 2005, 2010, 2015, and 2018, respectively. It can be observed that the UHI effect experienced an increasing trend during the period 2000–2005 and 2010–2018, whereas it had a decreasing trend during the period 2005–2010. The changing tendency of the UHI effect during the period 2000–2018 for the autumn season was consistent with the summer season.

The area ratio of medium UHI level for the winter season was in the range of 34.76–38.87%, which was larger than the area ratio for the spring, summer, and autumn seasons. The area ratios of the strongest UHI were noticed as 18.78, 14.35, 17.05, 15.27, and 13.08% for the years 2000, 2005, 2010, 2015, and 2018, respectively. The total area ratios of the strong and strongest UHI were observed as 30.76, 30.88, 29.92, 30.83, and 26.46% for the years 2000, 2005, 2010, 2015, and 2018, respectively. The strongest UHI effect experienced a decreasing trend during the period 2000–2005 and 2010–2018, whereas it had an increasing trend during the period 2005–2010. The change trend of the strongest UHI effect for the winter season has the opposite result with the trend for the spring, summer, and autumn seasons. According to the total area ratio, there was an increasing trend during the period 2000–2005 and 2010–2015, and a decreasing trend during the period of 2005–2010 and 2015–2018.

The area ratio of medium UHI level of the high proportion of the 18-years UHI effect was in the range of 37.31–39.28%. The maximum total area ratio of the strong and strongest UHI was observed as 33.33% in spring, the minimum was 29.52% in winter. The total area ratio of the strong and strongest UCI level of 32.19% for the winter season compared to the spring, summer, and autumn seasons was at the highest proportion level, while the minimum of the total area ratio was 27.66% occurring in summer. Therefore, the UHI effect was the strongest for the spring season and weakest for the winter by analyzing the seasonal variation of the 18-years UHI effect.

The UHI in the Xiangjiang river valley was different and clearly show the effect of ecological context on seasonal UHI amplitudes during the period 2000–2018 (**Figure 7**). The high LST in a year is distributed mainly in summer, and the maximum was 40.73°C occurring in 2018 among all these years, while the low LST in a year focused on the winter season and the minimum was 1.22°C occurring similarly in 2018 among all these years. The maximum seasonal mean temperature during the period 2000–2018 was 30.36°C occurring in summer 2010. The maximum difference between the maximum and minimum temperatures was 26.52°C in summer 2015, the minimum was 13.33°C in spring 2010. The standard deviation was used to evaluate the temperature change in a season, the higher value indicated the larger temperature difference. **Figure 7** shows that all standard deviations in spring, summer, autumn, and winter 2018 were greater than 2.0, which illustrated the significant temperature difference in a season. The maximum standard deviation was 2.49 in autumn 2015, while the minimum was 1.57 in winter 2010.

## 3.3 Factor Analysis Influencing UHI

### 3.3.1 Correlation Analysis

The correlation analysis between UHI and 10 influencing factors is obtained and summarized in **Table 3**. The Pearson correlation

**TABLE 3 |** Pearson correlation coefficients between UHI intensity and land cover features and landscape metrics.

| Factor | | 2000 | 2005 | 2010 | 2015 | 2018 |
|---|---|---|---|---|---|---|
| Land cover/use data | Cropland | 0.365** | 0.394** | 0.352** | 0.440** | 0.498** |
| | Forestland | –0.264** | –0.277** | –0.264** | –0.365** | –0.449** |
| | Grassland | –0.011** | –0.088** | –0.057** | –0.082** | –0.104** |
| | Open water | –0.195** | –0.172** | –0.161** | –0.151** | –0.125** |
| | Built-up land | 0.126** | 0.150** | 0.163** | 0.233** | 0.273** |
| | Unused land | –0.076** | –0.069** | –0.072** | –0.067** | –0.007** |
| Landscape metric | CONTAG | –0.130** | –0.146** | –0.104** | –0.135** | –0.164** |
| | LSI | 0.429** | 0.437** | 0.376** | 0.441** | 0.498** |
| | PD | 0.397** | 0.425** | 0.380** | 0.450** | 0.501** |
| | SHDI | 0.388** | 0.406** | 0.349** | 0.433** | 0.494** |

***Presents the Pearson correlation coefficient is significant at the 0.01 level (p < 0.01).*

**TABLE 4 |** Results of factor and interaction detector for LST.

| | Cropland | Forestland | Grassland | Open water | Built-up land | Unused land | CONTAG | LSI | PD | SHDI |
|---|---|---|---|---|---|---|---|---|---|---|
| Cropland | 0.322** | — | — | — | — | — | — | — | — | — |
| Forestland | 0.347 (EB) | 0.273** | — | — | — | — | — | — | — | — |
| Grassland | 0.337 (EB) | 0.356 (EN) | 0.016 | — | — | — | — | — | — | — |
| Open water | 0.344 (EB) | 0.332 (EN) | 0.052 (EN) | 0.034 | — | — | — | — | — | — |
| Built-up land | 0.408 (EB) | 0.314 (EB) | 0.159 (EB) | 0.175 (EB) | 0.146** | — | — | — | — | — |
| Unused land | 0.324 (IN) | 0.277 (EN) | 0.019 (EN) | 0.039 (EN) | 0.148 (IN) | 0.002 | — | — | — | — |
| CONTAG | 0.355 (EB) | 0.319 (EB) | 0.250 (EN) | 0.227 (EB) | 0.294 (EB) | 0.210 (IN) | 0.208** | — | — | — |
| LSI | 0.382 (EB) | 0.359 (EB) | 0.333 (EN) | 0.298 (EB) | 0.352 (EB) | 0.288 (IN) | 0.296 (EB) | 0.286** | — | — |
| PD | 0.396 (EB) | 0.360 (EB) | 0.320 (EN) | 0.300 (EB) | 0.338 (EB) | 0.288 (EB) | 0.306 (EB) | 0.312 (EB) | 0.287** | — |
| SHDI | 0.388 (EB) | 0.341 (EB) | 0.354 (EN) | 0.302 (EB) | 0.331 (EB) | 0.280 (IN) | 0.290 (EB) | 0.303 (EB) | 0.319 (EB) | 0.278** |

*Abbreviations (EN) denotes the nonlinear enhancement of two variables (EB) denotes the binary enhancing of two variables (IN) denotes the variables are independent in leading to the LST, change. **Donates that q value is significant at the 0.01 level (p < 0.01).*

coefficients between UHI and cropland range from 0.365 to 0.498 during the 2000–2018 period, indicating increased correlated levels from 2000 to 2018. A positive Pearson correlation coefficient for an independent variable indicates that the variable has a positive effect on UHI intensity, or that UHI intensity increases with the increase of the value of that variable; whereas a negative coefficient indicates UHI intensity decreases with the increase of the value of that variable. In this study, both coefficients of percent cover of cropland and built-up land were positive, suggesting that an increase in the percent of the cover of cropland and built-up land would increase UHI intensity. In contrast, the negative coefficients of percent cover of forestland, grassland, open water, and unused land indicated that UHI intensity would decrease with the increase of relative abundances of vegetation and water. The correlation analysis also shows that several landscape metrics are significantly related to the UHI effect, as shown in **Table 3**. LSI, PD, and SHDI have a positive relationship with UHI, whereas CONTAG has a negative correlation with the UHI effect. These indicate that the higher the degree of plaque dispersion, the richer the land use type, and a more irregular the size of the landscape shape will lead to higher UHI intensity.

### 3.3.2 Geodetector Analysis

Although the correlation analysis can measure how close the influencing factors are to the UHI intensity, it is unable to disclose the spatial stratification heterogeneity of the UHI effect and cannot determine the interactive influences of factors. To overcome these shortcomings, this subsection presents the analysis results of the Geodetector. In addition, the use of land cover data for the latest year was more beneficial for providing guidance for future planning.

The impact (q values) of the 10 influencing factors on the LST are obtained by means of the factor detector, the results of which are reported in **Table 4**. As shown in **Table 4**, of the 10 influencing factors, seven factors are statistically significant. The q values of these seven factors are, in descending order: Cropland (0.322) > PD (0.287) > LSI (0.286) > SHDI (0.278) > Forestland (0.273) > CONTAG (0.208) > Built-up land (0.146). Among the landscape metric factors, PD and LSI have the greatest influence on the LST as the two factors have the largest q values. Among the land cover factors, cropland, forestland, and built-up land have greater impacts on the LST than other factors. However, grassland, open water, and unused land layers among all factors have no significant influences on the LST, a possible reason being that these factors from land cover are not good proxy indicators for accurately depicting the spatial configuration of urban sprawl and growth because of the development of urbanization.

Among the 10 factors, a total of 45 pairs of interaction effects were obtained by means of the interaction factor, as summarized in **Table 4**. According to **Table 4**, each pair of factors is shown to

be larger than the q values of each factor, and smaller than the sum of the two factors' q values. Hence, the interactions between cropland and the other land cover types, excluding unused land or landscape metrics, exhibited binary enhancement in this analysis. If each pair of factors is shown to be equal to the sum of the two factors' q values, two factors leading to the LST change are independent. Therefore, the relationships between unused land and cropland, built-up land, CONTAG, LSI, SHDI are independent in influencing the LST. Furthermore, the interaction effects of a few factors on the LST represent nonlinear enhancements (represented as EN), whereas most of the factors have bivariate enhanced interaction effects. The interactions between landscape metrics including CONTAG, LSI, PD, and SHDI, and land cover types excluding the unused land and grassland types revealed binary enhancement, while the interaction with grassland type exhibited nonlinear enhancement. More specifically, perspective values for forestland and grassland were 0.273 and 0.016 but their interactive q-statistic reached as high as 0.356, which is larger than the sum of the two factors' q values. Furthermore, calculations show that when built-up land and cropland variables interacted, explanatory power reached a maximum value of 0.408. Data also show that landscape metrics can enhance the explanatory power of the land cover types. For example, perspective values for cropland and PD were 0.322 and 0.287 but their interactive q-statistic reached as high as 0.396. The q-statistic values for forestland and LSI were 0.273 and 0.286 but their interactive q-statistic reached as high as 0.359, which was higher than the q-statistic value of a single factor of the forest type. The interactive q-statistic values for forestland and land cover types including cropland, grassland, built-up land, and open water, as well as landscape metrics including LSI, PD, and SHDI, were more than 0.300, which was higher than the q-statistic value of 0.273 of the single factor. The study also tried to explore the temporal variations of single and interactive contortions of different factors. The results showed that the contribution of each factor has little temporal heterogeneity. These indicate that the interaction relationships of pair factors of cropland, forestland, grassland, built-up land, and landscape metrics were significant in influencing the LST. The conclusion may be drawn that the interaction of two factors plays a more important role in influencing the urban thermal environment than each factor separately.

## 4 DISCUSSION

The ground surface in urbanized areas is a key factor influencing the spatial structure and formation of UHI. This study investigated the long term series variations of the surface temperature in nine cities in the Xiangjiang river valley in Hunan province, China. The UHI effect was the strongest for the spring season and weakest for the winter by analyzing the seasonal variation of the 18-years UHI effect. The increases in vegetation in spring exhibit a low temperature, it was therefore observed that the UHI is more intense during the spring season due to the significant thermal changes between vegetation and built-up land. As the vegetation decreased during the winter, resulting in less temperature difference, the UHI of Xiangjiang river valley is lower in the winter than in other seasons. In terms of spatial distribution, the strong and strongest heat island areas are distributed mainly in the southern and southwestern study area and expanded gradually north, for the cities of Hengyang city, Chenzhou city, Yongzhou city, and Zhuzhou. The weakest heat island areas focused on the northeastern, western, and southeastern study areas. The reason is that the study areas having a good proportion of vegetation mostly on these parts of the study area shows lower temperature as compared to the densely built-up areas in the southern and southwestern parts of the study area.

This study also presents the results of an investigation of the relationships between spatial variations of the surface temperature and the land surface attributes. Our results indicated that both the composition and configuration of land cover features significantly affect the magnitude of LST. By explicitly describing the quantitative relationships of LST with the composition and configuration of land cover features, this research expands our scientific understanding of the effects of land cover pattern on LST in urban landscapes. Our results showed that the increasing vegetation cover or surface water could significantly decrease LST, and thus help to mitigate excess heat in urban areas; whereas the increase of buildings would significantly increase LST, exacerbating the UHI phenomena. However, our results are inconsistent with those from previous research that shows an increase in the percent cover of cropland would increase UHI intensity. This is because the LST of cropland is affected by the status and type of crops, and changes with time to a certain extent. The vegetation cover on this arable land may be attributed to the intensification of agricultural activities (almost 30% of the study areas are covered by cultivated plants), such as artificial fertilizer use and irrigation (surface or groundwater). If there are no cultivated plants or agricultural activities on this arable land, the cropland is equivalent to bare land, which may lead to increased UHI intensity. In this study, the total areas of forestland and cropland are more than 90%, the insignificant cooling effect of cropland compared to forestland leads to the positive correlation between the UHI intensity and the percent cover of cropland. Cropland neighboring buildings can mitigate UHI intensity. By developing correlation analysis to cropland neighboring buildings and forestland in 2018, our study found that the correlation coefficient between the cropland neighboring building and the UHI intensity is -0.316, and the cropland neighboring forestland and the UHI intensity is 0.530. Therefore, a large area of cropland in the suburban area contributes to the mitigation of UHI intensity in this study area.

These results have important theoretical and management implications. Urban planners and natural resource managers attempting to mitigate the impact of urban development on UHI can gain insights on the importance of balancing the relative amount of various types of land cover features and optimizing their spatial distributions, especially forest conservation and crop planting for food security.

The analysis of the impact of land cover type and landscape metrics factors and their interactions on surface temperature was implemented by means of a novel spatial stratified heterogeneity analysis method, the Geodetector method. This method has a few advantages compared with classical linear regression and spatial overlay analysis. Empirical results verified that the Geodetector could not only identify the main contribution of land cover type and landscape metric factors on LST, but they could also better uncover the interaction of two factors on LST in the urban agglomeration of Xiangjiang river valley. For example, the q-statistic values were calculated using the geographic detector method and reveal that the major variables influencing LST are cropland, forestland, and built-up land. This result is similar to previously reported findings (Kumari et al., 2019; Xiong et al., 2019).

Data also show that grassland, open water, and unused land exerted no significant influence on LST. If these variables are integrated with the other variables, they act to greatly enhance the explanatory power of other variables. PD and LSI have the greatest influence on the LST among landscape metric factors. In addition, the Pearson correlation coefficient between UHI intensity and PD and LSI indicates that a high degree of fragmentation in the landscape could exert a significant influence on increased UHI intensity.

The interaction q values of cropland with landscape metrics had the greatest influence on LST in this study. The use of the Geodetector method provides a new perspective for interactive analysis of multi-factors influencing LST. The new findings obtained from the novel method indicate that only using land cover type to analyze the formation of the UHI is not comprehensive. Landscape metrics need to be further emphasized for quantitatively exploring the influence of the spatial configuration of the urban landscape on the UHI.

This study has limitations. The research was conducted for one region, using only the daytime thermal image to obtain LST. Previous studies have shown that there are diurnal and seasonal variations in the relationships between LST and land cover features (Yuan and Bauer, 2007; Buyantuyev and Wu, 2010). For example, vegetation abundance, measured by NDVI, had a strong relationship with daytime LST but was only very weakly related to nighttime LST (Wang and Geodetector, 2017). Therefore, the diurnal thermal image needs to be used to study the phenomenon of UHI and the impact factors of UHI. In addition, the difference of spatial scales based on the urban size in different climate conditions could be compared to its influence on the formation of UHI. The application of the local climate scale has to be taken into account for developing the factor analysis of the UHI effect. The reasons for this are that the percent cover of cropland near the building has a negative correlation with the UHI intensity, while the percent cover of cropland near the forestland has a positive correlation with the UHI intensity. This is also a possible reason for the local UHI intensity of built-up area at the small spatial scale surrounded by open water, cropland, or forestland would be found to be decreased from the urban landscape perspective, especially in a large study area. The magnitude of local LST differences is driven by various environmental or anthropogenic factors. It is important to investigate the effect of human activities and other impact factors on decreasing the contributions of UHI under the context of global warming.

## 5 CONCLUSION

In this study, an analysis based on multi-temporal remote sensing data was carried out to study not only the long term variations of UHI over the period 2000–2018 but the impact factors of UHI. Throughout the analyzed period, the UHI effect experienced an increasing trend during the period 2000–2005 and 2010–2018, whereas it had a decreasing trend during the period 2005–2010. The UHI effect was the strongest for the spring season and weakest for the winter by analyzing the seasonal variation of the 18-year UHI effect. The UHI effect was the strongest in spring 2005 and 2018, in autumn 2000 and 2015, and summer 2010. In terms of spatial distribution, the strong and strongest heat island areas were distributed mainly in the southern and southwestern study areas and expanded gradually north.

The correlation analysis between UHI and 10 influencing factors found that the increase in the percent cover of cropland and built-up land would aggravate UHI intensity. In contrast, the negative coefficients of percent cover of forestland, grassland, open water, and unused land indicated that UHI intensity would decrease with the increase of relative abundances of vegetation and water. However, factor interaction detector analysis revealed that grassland, open water, and unused land layers among all factors have no significant influences on the LST. PD, LSI, and SHDI are determined to have the greatest influences on the LST as the three factors have the largest q values, which are consistent with the results of correlation analysis. LSI, PD, and SHDI have a positive relationship with UHI, whereas CONTAG has a negative correlation with the UHI effect. These indicate that the higher the degree of plaque dispersion, the richer the land use type, and a more irregular the size of landscape shape will lead to a higher UHI intensity. Landscape metrics can enhance the explanatory power of land cover types. Therefore, for UHI mitigation, a prerequisite for multifactor analysis must be taken into consideration during the implementation of cropland and built-up land to alleviate urban thermal stress and thus promote urban ecological sustainability. Our findings are a good theoretical supplement for current UHI research, providing urban administrators with useful information for achieving optimized urban agglomeration development.

## DATA AVAILABILITY STATEMENT

The original contributions presented in the study are included in the article/**Supplementary Material**,further inquiries can be directed to the corresponding author.

## AUTHOR CONTRIBUTIONS

All authors participated in the field survey and data collection. LX drafted the manuscript. LX and FP analyzed the data. SL and BZ designed the study. XF and YX revised the manuscript. All authors participated in the field survey and data collection, critically revised the manuscript, and gave final approval to the version submitted for publication.

## FUNDING

This research was funded by the Natural Science Foundation of Hunan Province (Project NOs. 2019JJ50640, 2021JJ40022, 2021JJ50155), the Scientific Research Project of Education Department of Hunan province (Project N0. 19C0060), the Scientific Research Project of Education Department of Hunan province (Project N0. 19B107), and the Key Laboratory Open Fund Project of the Ministry of Education (Project N0. 2017ysjs07).

## ACKNOWLEDGMENTS

The authors would like to thank the journal reviewers for providing insightful comments which improved the quality of the manuscript.

## SUPPLEMENTARY MATERIAL

The Supplementary Material for this article can be found online at: https://www.frontiersin.org/articles/10.3389/fenvs.2021.828230/full#supplementary-material

## REFERENCES

Bai, L., Jiang, L., Yang, D.-y., and Liu, Y.-b. (2019). Quantifying the Spatial Heterogeneity Influences of Natural and Socioeconomic Factors and Their Interactions on Air Pollution Using the Geographical Detector Method: A Case Study of the Yangtze River Economic Belt, China. *J. Clean. Prod.* 232, 692–704. doi:10.1016/j.jclepro.2019.05.342

Buyantuyev, A., and Wu, J. (2010). Urban Heat Islands and Landscape Heterogeneity: Linking Spatiotemporal Variations in Surface Temperatures to Land-Cover and Socioeconomic Patterns. *Landscape Ecol.* 25 (1), 17–33. doi:10.1007/s10980-009-9402-4

Chen, S., and Wang, T. (2009). Comparison Analyses of Equal Interval Method and Mean-Standard Deviation Method Used to Delimitate Urban Heat Island. *Geo-information Sci.* 11 (2), 145–150. doi:10.3724/sp.j.1047.2009.00145

Chen, X.-L., Zhao, H.-M., Li, P.-X., and Yin, Z.-Y. (2006). Remote Sensing Image-Based Analysis of the Relationship between Urban Heat Island and Land Use/cover Changes. *Remote Sensing Environ.* 104, 2133–2146. doi:10.1016/j.rse.2005.11.016

Du, H., Zhou, F., Li, C., Cai, W., Jiang, H., and Cai, Y. (2020). Analysis of the Impact of Land Use on Spatiotemporal Patterns of Surface Urban Heat Island in Rapid Urbanization, a Case Study of Shanghai, China. *Sustainability* 12 (3), 1171. doi:10.3390/su12031171

Duan, Q., and Tan, M. (2020). Using a Geographical Detector to Identify the Key Factors that Influence Urban forest Spatial Differences within China. *Urban For. Urban Green.* 49, 126623. doi:10.1016/j.ufug.2020.126623

Elliot, T., Babí Almenar, J., and Rugani, B. (2020). Modelling the Relationships between Urban Land Cover Change and Local Climate Regulation to Estimate Urban Heat Island Effect. *Urban For. Urban Green.* 50, 126650. doi:10.1016/j.ufug.2020.126650

Estoque, R. C., Murayama, Y., and Myint, S. W. (2017). Effects of Landscape Composition and Pattern on Land Surface Temperature: An Urban Heat Island Study in the Megacities of Southeast Asia. *Sci. Total Environ.* 577, 349–359. doi:10.1016/j.scitotenv.2016.10.195

Flores R., J. L., Pereira Filho, A. J., and Karam, H. A. (2016). Estimation of Long Term Low Resolution Surface Urban Heat Island Intensities for Tropical Cities Using MODIS Remote Sensing Data. *Urban Clim.* 17, 32–66. doi:10.1016/j.uclim.2016.04.002

Hawkins, T. W., Brazel, A. J., Stefanov, W. L., Bigler, W., and Saffell, E. M. (2004). The Role of Rural Variability in Urban Heat Island Determination for Phoenix, Arizona. *J. Appl. Meteorol.* 43 (3), 476–486. doi:10.1175/1520-0450(2004)043<0476:Trorvi>2.0.Co;2

Hou, K., and Wen, J. (2020). Quantitative Analysis of the Relationship between Land Use and Urbanization Development in Typical Arid Areas. *Environ. Sci. Pollut. Res.* 27, 38758–38768. doi:10.1007/s11356-020-08577-8

Howard, L. (1833). *Climate of London Deduced from Metrological Observations*. 3th ed London: Harvey and Dorton Press.

Kumari, M., Sarma, K., and Sharma, R. (2019). Using Moran's I and GIS to Study the Spatial Pattern of Land Surface Temperature in Relation to Land Use/cover Around a thermal Power Plant in Singrauli District, Madhya Pradesh, India. *Remote Sensing Appl. Soc. Environ.* 15, 100239. doi:10.1016/j.rsase.2019.100239

Li, X., and Zeng, S. (2015). Comparisive Research on Characteristics of Urban Heat Island Effects between Chengdu and Chongqing. *Meteorol. Sci. Technol.* 43 (5), 888–897.

McGarigal, K., Cushman, S., Neel, M. C., and Ene, E. (2002). FRAGSTATS: Spatial Pattern Analysis Program for Categorical Maps. Availabe online: http://www.umass.edu/landeco/research/fragstats/fragstats.html.

Nimish, G., Bharath, H. A., and Lalitha, A. (2020). Exploring Temperature Indices by Deriving Relationship between Land Surface Temperature and Urban Landscape. *Remote Sensing Appl. Soc. Environ.* 18, 100299. doi:10.1016/j.rsase.2020.100299

Peng, J., Jia, J., Liu, Y., Li, H., and Wu, J. (2018). Seasonal Contrast of the Dominant Factors for Spatial Distribution of Land Surface Temperature in Urban Areas. *Remote Sensing Environ.* 215, 255–267. doi:10.1016/j.rse.2018.06.010

Tang, Y. (2018). Effect Analysis of Land-Use Pattern with Landscape Metrics on an Urban Heat Island. *J. Appl. Rem. Sens.* 12 (2), 1. doi:10.1117/1.Jrs.12.026004

Wang, J. F., and Geodetector, C. D. X. (2017). Principle and Prospective. *Acta Geogr. Sin.* 72 (1), 116–134.

Wang, J. F., Li, X. H., Christakos, G., Liao, Y., Zhang, T., Gu, X., et al. (2010). Geographical Detectors-Based Health Risk Assessment and its Application in the Neural Tube Defects Study of the Heshun Region, China. *Int. J. Geogr. Inf. Sci.* 24 (1-2), 107–127. doi:10.1080/13658810802443457

Wang, Q., Zhang, C., Ren, C., Hang, J., and Li, Y. (2020). Urban Heat Island Circulations over the Beijing-Tianjin Region under Calm and Fair Conditions. *Building Environ.* 180, 107063. doi:10.1016/j.buildenv.2020.107063

Weng, Q., Liu, H., Liang, B., and Lu, D. (2008). The Spatial Variations of Urban Land Surface Temperatures: Pertinent Factors, Zoning Effect, and Seasonal Variability. *IEEE J. Sel. Top. Appl. Earth Observations Remote Sensing* 1 (2), 154–166. doi:10.1109/JSTARS.2008.917869

Wong, M., Peng, F., Zou, B., Shi, W., and Wilson, G. (2016). Spatially Analyzing the Inequity of the Hong Kong Urban Heat Island by Socio-Demographic Characteristics. *Ijerph* 13 (3), 317. doi:10.3390/ijerph13030317

Wu, H., Wang, W., Wang, W., Qin, J., and Bai, X. (2010). Research on the Characteristics of Landscape Pattern and Change in Changsha-Zhuzhou-Xiangtan Metropolitan Region. *Geo-information Sci.* 12 (1), 133–142. doi:10.3724/sp.j.1047.2010.00133

Wu, H., Ye, L.-P., Shi, W.-Z., and Clarke, K. C. (2014). Assessing the Effects of Land Use Spatial Structure on Urban Heat Islands Using HJ-1B Remote Sensing Imagery in Wuhan, China. *Int. J. Appl. Earth Observation Geoinformation* 32, 67–78. doi:10.1016/j.jag.2014.03.019

Xian, G., and Crane, M. (2006). An Analysis of Urban thermal Characteristics and Associated Land Cover in Tampa Bay and Las Vegas Using Landsat Satellite Data. *Remote Sensing Environ.* 104 (2), 147–156. doi:10.1016/j.rse.2005.09.023

Xie, M., Chen, J., Zhang, Q., Li, H., Fu, M., and Breuste, J. (2020). Dominant Landscape Indicators and Their Dominant Areas Influencing Urban thermal Environment Based on Structural Equation Model. *Ecol. Indicators* 111, 105992. doi:10.1016/j.ecolind.2019.105992

Xiong, Y., Peng, F., and Zou, B. (2019). Spatiotemporal Influences of Land Use/cover Changes on the Heat Island Effect in Rapid Urbanization Area. *Front. Earth Sci.* 13 (3), 614–627. doi:10.1007/s11707-018-0747-3

Xu, S. (2015). Impact Analysis of Land Use/Cover on Air Pollution. *J. Geo-inf. Sci.* 17 (3), 290–299.

Yao, L., Li, T., Xu, M., and Xu, Y. (2020). How the Landscape Features of Urban green Space Impact Seasonal Land Surface Temperatures at a City-Block-Scale: An Urban Heat Island Study in Beijing, China. *Urban For. Urban Green.* 52, 126704. doi:10.1016/j.ufug.2020.126704

Ye, Y., Qin, J., and Hu, S. (2017). Spatial-temporal Evolution of Urban Heat Island Effects in Changsha City. *J. Geo-inf. Sci.* 19 (4), 518–527.

Yuan, F., and Bauer, M. E. (2007). Comparison of Impervious Surface Area and Normalized Difference Vegetation Index as Indicators of Surface Urban Heat Island Effects in Landsat Imagery. *Remote Sensing Environ.* 106 (3), 375–386. doi:10.1016/j.rse.2006.09.003

Yuan, J., Li, J., Ye, S., Han, X., and Hu, Y. (2018). The Urban Heat Island Analysis of Changsha-Zhuzhou-Xiangtan Urban Agglomeration Aased on Modis Data. *E3s Web Conf.* 53, 03045. doi:10.1051/e3sconf/20185303045

Zhou, D., Zhao, S., Zhang, L., Sun, G., and Liu, Y. (2015). The Footprint of Urban Heat Island Effect in China. *Sci. Rep.* 5, 11160. doi:10.1038/srep11160

Zhou, W., Huang, G., and Cadenasso, M. L. (2011). Does Spatial Configuration Matter? Understanding the Effects of Land Cover Pattern on Land Surface Temperature in Urban Landscapes. *Landscape Urban Plann.* 102, 54–63. doi:10.1016/j.landurbplan.2011.03.009

Zou, B., Xu, S., and Zhang, J. (2017). Spatial Variation Analysis of Urban Air Pollution Using GIS: A Land Use Perspective. *Wuhan Univ. J. Inf. Sci.* 42 (2), 216–222.

**Conflict of Interest:** The authors declare that the research was conducted in the absence of any commercial or financial relationships that could be construed as a potential conflict of interest.

**Publisher's Note:** All claims expressed in this article are solely those of the authors and do not necessarily represent those of their affiliated organizations, or those of the publisher, the editors and the reviewers. Any product that may be evaluated in this article, or claim that may be made by its manufacturer, is not guaranteed or endorsed by the publisher.

frontiers in Environmental Science

ORIGINAL RESEARCH
published: 12 November 2021
doi: 10.3389/fenvs.2021.783356

# Vertical Structure of a Snowfall Event Based on Observations From the Aircraft and Mountain Station in Beijing

*Yu Huang*[1,2,3], *Delong Zhao*[1,2,3]*, *Yuanmou Du*[1,2,3]*, *Yichen Chen*[1], *Lei Zhang*[1], *Xia Li*[1] and *Yingying Jing*[1]

[1]Beijing Weather Modification Center, Beijing, China, [2]Key Laboratory of Cloud, Precipitation and Atmospheric Water Resources, Beijing Meteorological Service, Beijing, China, [3]Field Experiment Base of Cloud and Precipitation Research in North China, China Meteorological Administration, Beijing, China

OPEN ACCESS

**Edited by:**
Junke Zhang,
Southwest Jiaotong University, China

**Reviewed by:**
Dawei Hu,
The University of Manchester, United Kingdom
Zixia Liu,
King's College London, United Kingdom
Cenlin He,
National Center for Atmospheric Research (UCAR), United States

***Correspondence:**
Delong Zhao
zhaodelong@bj.cma.gov.cn
Yuanmou Du
yuanmoudu24@163.com

**Specialty section:**
This article was submitted to Atmosphere and Climate, a section of the journal Frontiers in Environmental Science

**Received:** 26 September 2021
**Accepted:** 15 October 2021
**Published:** 12 November 2021

**Citation:**
Huang Y, Zhao D, Du Y, Chen Y, Zhang L, Li X and Jing Y (2021) Vertical Structure of a Snowfall Event Based on Observations From the Aircraft and Mountain Station in Beijing. Front. Environ. Sci. 9:783356. doi: 10.3389/fenvs.2021.783356

An aircraft platform, ground-based disdrometer, cloud radar, radiometer, and automatic station were combined to study a snowfall case (16:30–21:00 observed by ground cloud radar) on the Yangqing Mountains in Beijing. Comparing the variation of ice habit and number concentration at aircraft altitude (2.9–3.2 km) and ground, we discussed the ice growth mechanisms in the Beijing Mountains. Results indicated that the snowfall was steady but not strong with reflectivity less than 20dBZ, and cloud top altitude less than 4.5 km. The number concentrations for both liquid and ice crystals at aircraft altitude and ground were very similar, both dominated by small particles at diameters of 0.1–1.2 mm, and the proportion of mean number concentrations at small diameters both in the aircraft and on the ground was large, peaking at 44 $L^{-1}$ $mm^{-1}$ and 8826 $L^{-1}$ $mm^{-1}$ respectively, and decreased rapidly as the diameter increased. There was no mixed phase in clouds with little liquid water. Particles were relatively regular, and were transparent with dendritic and disk-hexagonal shapes. The ice crystals and snowflakes were mainly grown by the deposition and aggregation, rarely by the riming process, and no secondary ice formation was observed.

**Keywords: Beijing mountains snowfall, ground-based disdrometer, aircraft platform, vertical structure, cComprehensive observation**

## INTRODUCTION

The microphysical characteristics of snowfall are affected by pollution (Shen et al., 2021; Zheng and Chen, 2021) and other factors, and the microphysical characteristics of snowflakes are important for microphysical parameterizations in numerical models and remote sensing retrieval (Hobbs et al., 1973; Cotton et al., 1982; Lin et al., 1983; Thompson et al., 2004; Cifelli et al., 2011; Morrison and Milbrandt, 2015; Guan et al., 2021; Chu et al., 2021). Most precipitation in mid and high latitudes is initiated by ice aggregation. Enhanced reflectivity near 0 °C in many precipitation clouds is due to large snowflakes and/or water-coated ice particles. Woods et al. (2008) demonstrated that more realistic empirical mass-diameter relationships and velocity-diameter relationships can change the mesoscale model simulation results significantly. Gang (2007) found that ice crystal habits and their representations are very important for calculations of radar backscattering cross sections.

Many scholars focused on the snow size distributions, which can reflect the details of snowfall microphysical processes. Alessandro and Elke (2010) used a single two-dimensional disdrometer (2-

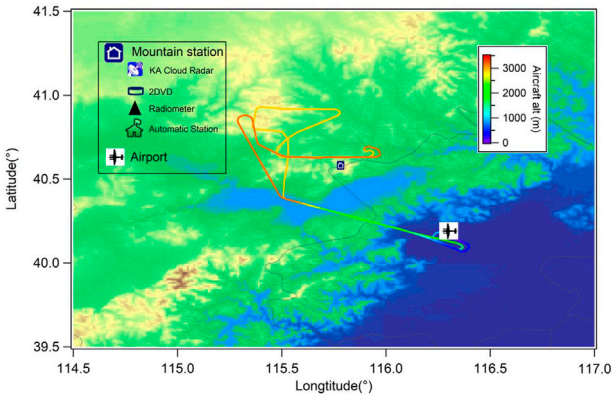


**FIGURE 1 |** Terrain of observational region, tracks of aircraft (colored lines).

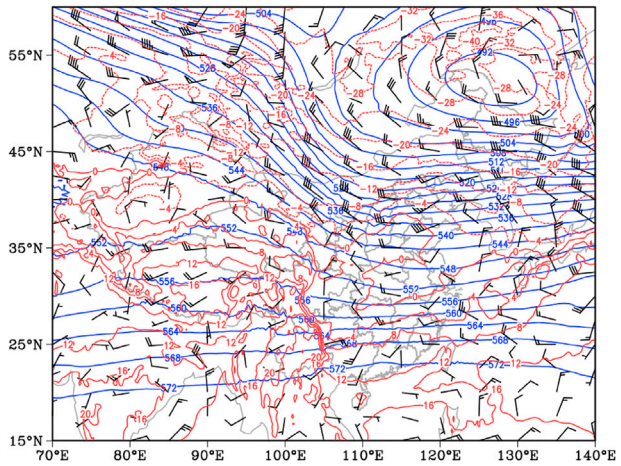


**FIGURE 2 |** 0800 BJT (Beijing time) Jan 27, 2021 850 hpa synoptic situation.

DVD) consisting of two PARSIVEL disdrometers to assess the snowflakes fall speed. They found that, unlike raindrop size distributions, snowflake size distributions were much more complex and harder to be parameterized. Brandes et al. (2007) fitted the relationship between the snow density and the particle median volume diameter, and revised the snow particle size distributions fitting Gamma parameters. Newman et al. (2009a, 2009b) used a Snowflake Video Imager-based PSD parameterization combined with the profiler of the snowflake perimeter to investigate the aggregation at different temperatures, levels of humidity, and wind conditions.

Much of the research on snow size distributions were based on measurements from ground-based or airborne probes. Yuter et al. (2006) observed the particle distribution and velocity by the PARSIVEL to identify the snow phase. Masaaki et al. (2013) identified the types of solid hydrometeors according to the measurements of its size and fall speed data. Airborne probes can detect ice particles at high altitudes directly, which is beneficial for the study of snowfall microphysical characteristics. Through well-designed spectra flight plans, Lo and Passarelli (1982) made it possible to study the ice particle spectra in detail. Woods et al. (2007) analyzed the snow size spectra collected by aircrafts and improved correlations between the size spectrum parameters and temperatures. Based on aircraft observations, Lawson et al. (2017) found that the drop-freezing secondary ice production mechanism was operating in cumulus updraft cores. Geerts et al. (2015) observed 16 snowfall cases in Wyoming by the aircraft and analyzed the snowfall growth, transmission, and deposition processes. They summarized the dynamic processes of the three types of airflows over the mountains and analyzed the characteristics of each type. They also summarized the three conceptual models of each flow regime. Saleeby et al. (2011) analyzed the *in-situ* observation data and concluded that the cloud microphysical parameters in cold clouds were related to raindrop number concentrations and ice crystal number concentrations, as well as the final falling velocities of raindrops. Chang et al. (2019) reported the cloud microphysical properties over the Tibetan Plateau based on aircraft data, and summarized the size distributions of cloud drops and ice microphysics characteristics. The above studies are only based on ground or aircraft observations, and cannot obtain the complete vertical snowfall microphysics characteristics.

Beijing is surrounded by mountains on three sides and the southeast plain, and has its own unique climatic characteristics. The Yanqing Mountains are located in the northern mountainous area of Beijing, with an altitude of 2199 m. The snowfall cloud there has typical winter terrain cloud characteristics. In this paper, we combined ground-based and onboard instruments to observe the formation and development of snowflakes in a snowfall case that occurred in the Beijing Yanqing Mountains, compared the variations of ice habit as well as size distributions from high altitudes with those from ground station, and discussed the snowfall mechanisms in the Beijing Mountains. This is the first study to combine high-altitude aircraft and ground measurements of snow ice crystals in the Beijing area, and will help better understanding of snow structure characteristics, improving our knowledge of the characteristics of snowfall in Beijing's mountainous areas and providing basic theories for artificial snow enhancement, which will increase the amount of snowfall in mountainous areas, restore the ecology, and increase the water storage capacity of inland rivers.

## INSTRUMENTATION AND METHODS

The aircraft measurements were conducted from 15:46 to 17:30 on Jan 27, 2021, when a light snowfall case took place in Beijing. The flight track of the scientific aircraft King Air 350 ER and observational region terrain are shown in **Figure 1**. The aircraft flew over the Beijing Yanqing mountain and close to the Yanjiaping station, with an

**TABLE 1 |** Instrument parameters.

| **Ground station** | | |
|---|---|---|
| Name | Elements | Data frequence |
| KA Cloud radar | Reflectivity factor, Depolarization factor | 0.5–8.8 s |
| OTT Disdrometer | 0.06–24.5 mm Size distribution | 1 min |
| 2DVD | 0.1–10 mm Average size distribution, Size image | 1 min |
| Radiometer | Liquid water contents (LWC), Liquid water paths (LWP) | 2 min |
| Automatic station | Precipitation, Temperature, Pressure, Wind, Relative Humidity (RH) | 1 min |
| Aircraft | | |
| Name | Elements | Data frequence |
| CPI | 7μm-3 mm Cloud drops image | 1 s |
| FCDP | 1.5–50μ m Cloud drop Size distribution | 1 s |
| HVPS | 150μm-19.2 mm Raindrops image, Size distribution | 1 s |
| 2DS | 10μm-6.4 mm Cloud drops image, Size distribution | 1 s |
| AIMMS-PMS | Temperature, RH, Pressure, Wind, GPS | 1 s |

altitude of 2900–3200 m at 16:30–17:05 (tracks of the aircraft are shown with the orange segment of the colored line).

The instrument (including ground station and aircraft) information used in this article is listed in **Table 1**. The King Air 350 ER aircraft with cloud microphysical probes was used to conduct measurements. It can detect meteorological conditions and the macro and micro characteristics of clouds and precipitation. Aircraft Integrated Meteorological Measurement System (AIMMS- PMS) can obtain correct ambient temperature, humidity, pressure, horizontal wind speed and direction, vertical wind speed, and other information. Through the GPS module, it can also get the aircraft's geographic location and flight altitude information. The Fast Cloud Droplet Probe (FCDP) measures particle size distributions and concentrations (Lawson et al., 2017). The instrument can sample cloud particles from 1–50 μm with a resolution of about 3 μm. It is capable of sizing particles with velocities from 10–200 m/ s. The liquid water content (LWC) (unit: g $m^{-3}$) is derived by

$$\mathrm{LWC} = 10^{-9} \times \frac{\pi}{6} \sum c_i d_i^3$$

where $c_i$ is the number concentration in channel $i$, and $d_i$ is the size of particles in channel $i$ of size distributions.

The Three-View Cloud Particle Imager (3V-CPI) measures the size, shape, and concentration of water drops and ice particles in clouds (Lawson et al., 2001). The probe is a combination of three imaging instruments. Two of them comprise a 2D-S (Two-Dimensional Stereo hydrometeor spectrometer), in which two high-resolution (about 9 μm resolutions) 2D probes image particles as they pass through laser beams that are orthogonal to each other (Lawson et al., 2017). If particles also lie in the intersection of the sensitive areas of two beams, they are seen by both 2D probes. In that case, the third instrument, a Cloud Particle Imager (CPI), is triggered to take a high-resolution picture, via a briefly illuminated high-resolution imaging array (Lawson et al., 2001; Lawson et al., 2015). The probe is particularly suited for imaging such crystals, but also provides good detection of other hydrometeors including large cloud droplets, drizzle and small rain drops, as well as other precipitation particles. The High Volume Precipitation Spectrometer (HVPS) measures the size, shape, and concentration of water droplets and ice crystals (Woods et al., 2018). The HVPS consists of a source laser that produces a sheet of light that is roughly 19.2 mm × 162 mm in size and passes between two windows located on the inboard sides of the optical arms. Particle fragmentation is the biggest error source of cloud particle spectrum probes in aircraft observation, and it has great influence on measured particle number concentration and particle size distribution. The IAT (interarrival time) algorithm is usually used to correct cloud particle spectrum probe data (Field et al., 2003; Field et al., 2006; Korolev and Field, 2015). This is because broken particles tend to appear in groups, and the arrival interval between them is often much smaller than that of intact particles, resulting in the bimodal distribution of IAT. In this research, the threshold of IAT was set to eliminate the errors of FCDP, 2DS, and HVPS data caused by particle fragmentation. The method of the identification about the ice and liquid phase particles from 2DS and HVPS is as below:

The raw images from optical array probe (2DS,HVPS) are analyzed by circularity of particles(C) to discriminate liquid and ice particles. The definition of circularity(C) is based on the perimeter around the edge of the particle (P) and the total area of the particle(A), in which the perfect circle has a circularity of 1, and the other shapes have larger circularities (Crosier et al., 2010). In the practical observations, the circularity of measured particles may be less than 1 due to the discretization of images into pixels and only a small number of pixels being contained in the image.

$$\mathrm{C} = \frac{P^2}{4\pi A}$$

In this research, particles with an area smaller than 20 pixels are classified as small particles, and those with an area greater than 20 pixels are classified as round ($0.9 \leq \mathrm{C} < 1.2$) and irregular ($\mathrm{C} \geq 1.2$) shapes according to the value of circularity(C). The small particles and round particles are usually liquid particles, and the irregular particles are ice particles.

The mountain station (Yanjiaping station) (115.73°N, 40.52°E; 1344 m asl) is in the Yanqing mountains, which are located in the northwest of Beijing. The instruments in the mountain station include an automatic station, a cloud radar, a radiometer, an OTT

**TABLE 2 |** Cloud radar performances parameters

| RADAR TYPE | Ka cloud radar |
|---|---|
| Sampling frequency | 33.44GHz ± 65MHz |
| Wavelength /mm | 8 |
| Sampling period /s | 0.5-8.8 |
| Elements | Reflectivity factor, Radial velocity, Spectral width, linear depolarization ratio |
| Bin length /m | 15/30/60 (adjustable) |
| Detection height /m | 150–15000 |
| Radar system | Single-emission and dual-back polarization |

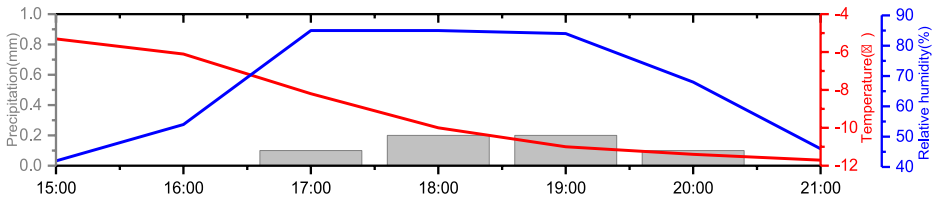


**FIGURE 3 |** Meteorological elements at Yanjiaping station from 1500 BJT to 2100 BJT Jan 27, 2021 [gray column: precipitation (units: mm); red line: temperature (units: ˚C); blue line: relative humidity (units: %)]

Particle Size Velocity (Parsivel$^2$; P$^2$) disdrometer, and a two-dimensional video disdrometer (2DVD) (**Table 1**).

The millimeter wave cloud radar is in Ka band with a velocity resolution of 0.1 m/s and reflectivity factor accuracy < 1dB. It can effectively penetrate the cloud layer and obtain the echo information and movement status inside the cloud in real time, including parameters such as reflectivity factor, velocity, spectral width, linear depolarization ratio, and power spectrum (Zhong. et al., 2011). In this paper, the cloud radar was operated in zenith mode for continuous observation, and sampled every 0.6s to observe cloud structures and phase change information. The specifics of the cloud radar are shown in **Table 2**.

Radiometer data were sampled by a Radiometrics 12-channel (TP WVP-3000) microwave radiometer. It observes the water vapor band from 22 to 30 GHz and the oxygen band from 51 to 59 GHz, and can obtain 58 layers' vertical profile of temperature, water vapor, relative humidity, and liquid water from the ground to 10 km altitude with a time resolution of 2 min (Hewison, 2007). In this article, it was used to provide the vertical distribution of water vapor conditions at Yanjiaping station.

The disdrometer data used in this paper were collected from an OTT Particle Size Velocity (PARSIVEL$^2$) disdrometer. The laser system is used to observe the variation of particle number concentrations, particle velocities, and spectrum. The sampling interval is 1min and measurement area is 180 × 30 mm with particle diameter range 0.2–5 mm for liquid precipitation, and 0.2–25 mm for solid precipitation with particle velocity range 0.2–20 m/ s (Tokay. et al., 2014). It has 32 diameter levels and 32 velocity levels. In this paper, data were corrected with the method of Battaglia.et al. (2010). The quality control also includes: (1) for particles with a diameter <0.3 mm, the first and second diameters were deleted; (2) When the particles were in ice phase, the particle density correction formula was used: $\rho_s = 0.17D^{-1}$ (Where $\rho_s$ is particle density and D is the particle diameter).

# RESULTS

## Background

The snowfall cloud system moved from the west to the east, and the main influenced system was the Yellow River cyclone. Guided by vorticity advection in front of the high-altitude trough and warm and cold advection, a near-surface cyclone gradually strengthened and moved eastward and northward seen from **Figure 2**. The snow clouds were located in the front of the cyclone. Warm-humid airflow from the southwest in front of the trough was the main source of water vapor in this snow case.

The snowfall period was about 15:00–21:00 BJT on 27 January. Snowfall was relatively weak and mainly occurred in Beijing's northwest mountains. **Figure 3** shows the observations from the automatic weather station at the Yanjiaping Station. As shown in **Figure 3A**, when the snowfall continued in 16:00–20:00 BJT on 27 January, the cumulative snowfall reached the light snow level (0.4 mm), and the maximum snowfall time was 17:00–19:00, with an hourly average snowfall of 0.2 mm/ h. With the beginning of the snowfall, the ground temperature dropped from -5˚C to -12˚C, while the relative humidity (RH) rose from 40 to 85%. When the RH decreased, the snowfall gradually stopped.

**Figure 4** shows radar reflectivity observed by the Ka cloud radar at Yanjiapin station. The snowfall reflectivity factor was relatively weak. The cloud top was low overall (<4.5 km) and passed the station from west to east. As can be seen from **Figure 4**, the snow grounded the station at 16:30 27 Jan and the reflectivity factor above the station was weak with the maximum <15dBZ.

Wind barbs were observed by the wind profiler radar at Yanjiapin station (**Figure 5**). **Figure 5** showed that the wind

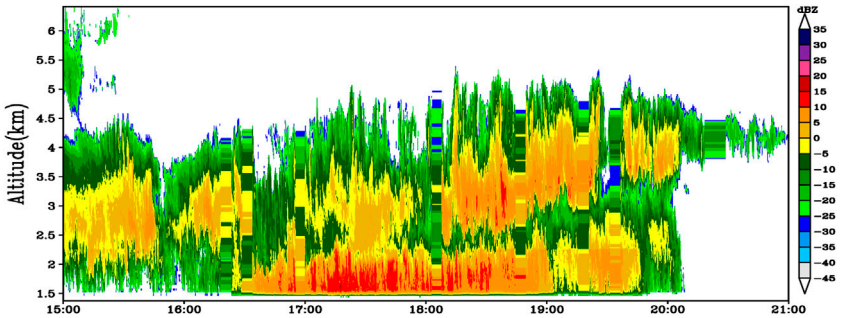


**FIGURE 4 |** Evolution of reflectivity factor (units: dBZ) observed by cloud radar from 1500 BJT to 2100 BJT Jan 27, 2021.

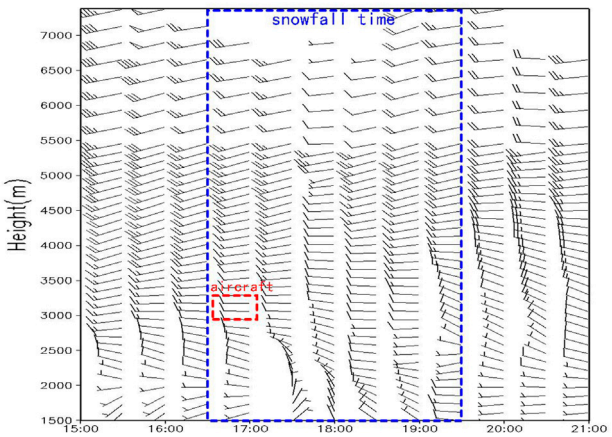


**FIGURE 5 |** Wind barbs observed by the wind profiler radar from 1500 BJT to 2100 BJT on Jan 27, 2021 (blue box: snowfall time, red box: aircraft close to Yanjiaping time at aircraft altitude).

was mainly westerly above 3 km, and wind direction rotated with heights below 3 km during the snowfall period (blue box). When the wind direction turned westerly, the snowfall was over.

When an airplane flew over the Beijing Yanqing Mountains, located within 10 km from the west to east of Yanjiaping station (16:30–17:05), the aircraft altitude was 2900–3200 m (red box in **Figure 5**) with westerly wind.

The radiometer (**Figure 6**) observed that the liquid water content (LWC) increased during the entire snowfall process (16:30–19:30, black box in **Figure 6**), and there were two peaks which appeared at the beginning of the snowfall and at the end of snowfall, respectively. But the LWC was very low with the maximum value only 0.018 g $m^{-3}$ that occurred at 19:15 at an altitude of 3–4 km. The liquid water integral path (LWP) showed the same evolution trend of LWC. The maximum was 0.05 mm at 19:15. Water vapor was also increased during the entire snowfall process. At the beginning of the snowfall, the water vapor increased rapidly below 2km, with the maximum (2.4 g $m^{-3}$ at 1.9 km) occurring at 17:05, corresponding to the first peak of LWC. The max value (0.49 cm) of precipitable water vapor (PWV) also appeared at this moment. With snowfall going on, the water vapor consumed and gradually decreased. The water vapor dropped to 0.3 cm at the second peak of LWC (19:08), and continued to decrease less than 0.2 cm after snowfall ended.

When the airplane was near Yanjiaping station (16:30–17:05), LWC (observed by Radiometer) at aircraft altitude (2900–3200 m, red box in **Figure 6**) was 0.005–0.015 g $m^{-3}$, and water vapor was 0.8–1.8 g $m^{-3}$. The observations above show that in this case, the whole cloud was extremely dry, and contained very little liquid water.

## Cloud Physics Characteristic

**Figure 7A**; **Figure 7B** showed the reflectivity factor and linear depolarization ratio (LDR) observed by the Ka cloud radar at Yanjiaping station during the airplane flight over the Yanqing mountain area located within 10 km from the west to east of the Yanjiaping station (16:30–17:05 on 27 Jan). As can be seen in **Figure 7A**, the snowfall at Yanjiaping station started at 16:30, the cloud top gradually rose up (from 2.5 to 4 km), and the strong reflectivity factor (close to 15 dBZ) appeared in the altitude<2 km. However, the snow development was relatively weak. The maximum reflectivity factor was about 20dBZ with the cloud top (defined as reflectivity factor > −15 dbz and span more than 3 bin (1bin = 50 m)) < 4 km. The reflectivity factor was about 0-10dBZ at the aircraft flight altitude (2.9–3.2 km).

The LDR observed by the cloud radar can reflect the non-spherical particle scattering power differences between the parallel polarization component and the vertical polarization component in the backscattering (Neiman et al., 2014; Matthew et al., 2014). The LDR reflects the difference determined by the particle shape, size, spatial orientation, and particle phase. For example, the larger the diameter of snowflakes with the same spatial orientation (horizontal orientation) in radar sampling volume, the larger the LDR value is. If there exists mixed phase in cloud, the LDR value will reflect a jump increase (>10dB) (Chen et al., 2018). In **Figure 7B**, the LDR value during the flight period was steady in the range of -22 to -10dB, without a jump increase. The previous observation results showed that the low LWC indicates that there was no mixed phase in snowfall at this stage, and there may present many solid crystals in the cloud (Neiman et al., 2014).

**Figure 7C** showed the LWC and temperature observed by the onboard FCDP when the airplane flew over the Yanqing mountain area (16:30–17:05). From 16:30–16:50, the airplane

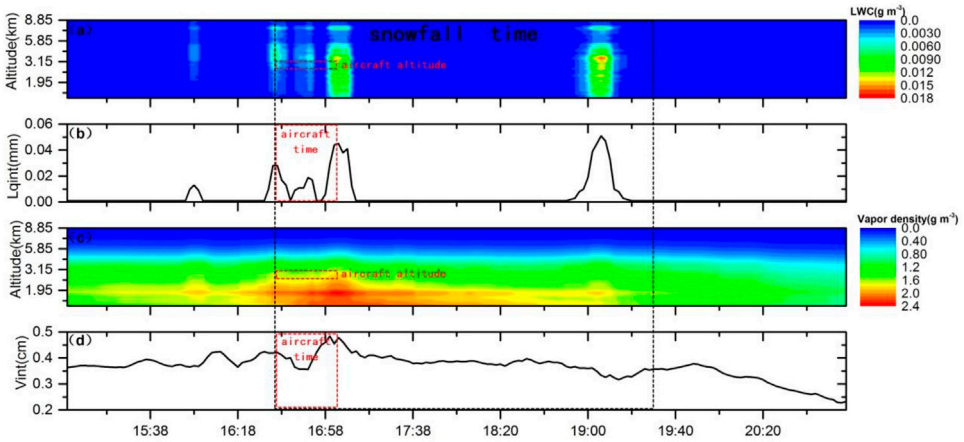


**FIGURE 6 | (A)** LWC (g $m^{-3}$), **(B)** LWP (mm), **(C)** Vapor density (g $m^{-3}$), and **(D)** PWV (cm) observed by Radiometer from 1500 BJT to 2100 BJT Jan 27, 2021 (black box: snowfall time, red box: aircraft close to Yanjiaping time at aircraft altitude).

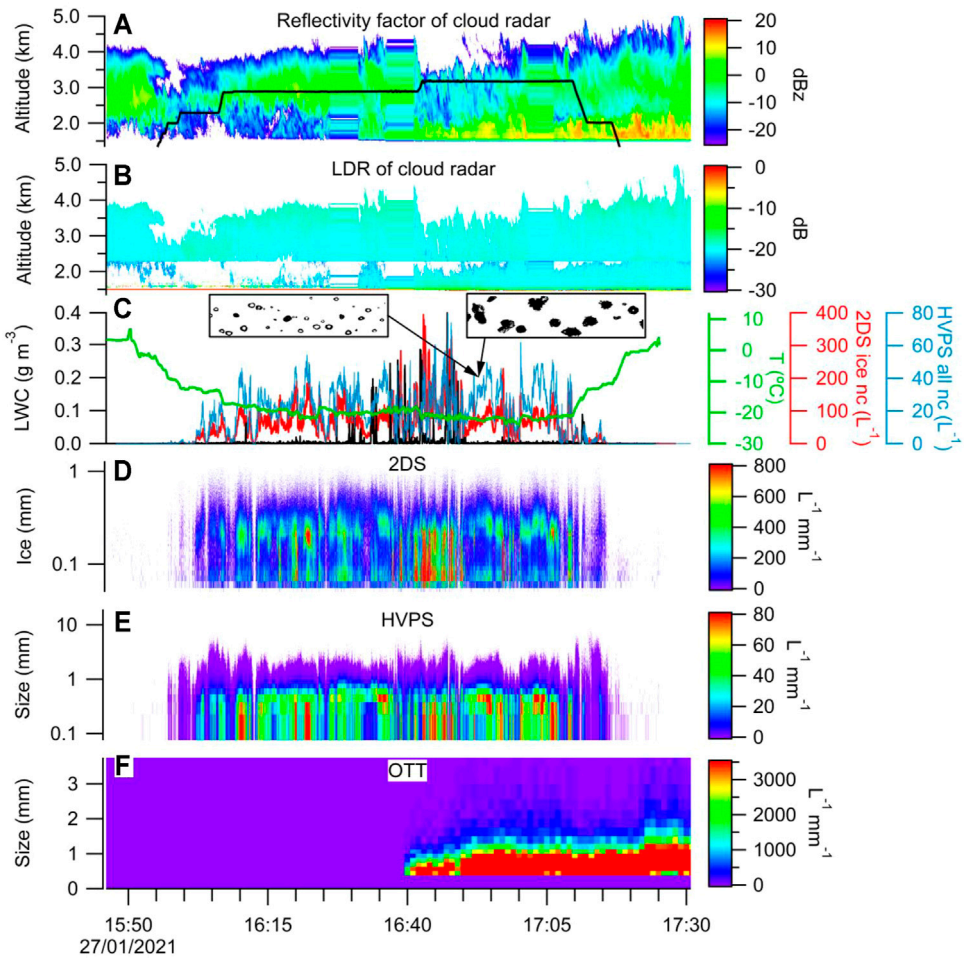


**FIGURE 7 | (A)** Reflectivity factor (dBZ) (the black line is aircraft altitude), **(B)** LDR (dB) observed by Ka cloud radar, **(C)** LWC (g $m^{-3}$) (black line) and Temperature (°C) (green line) by FCDP, Ice number concentration ($L^{-1}$) (red lines) by 2DS, all particle number concentration ($L^{-1}$) (blue lines) by HVPS, 2DS images (Bar graph above c) **(D)** Ice size distribution ($L^{-1}mm^{-1}$) by 2DS, **(E)**Particle size distribution ($L^{-1}mm^{-1}$) by HVPS, **(F)** Particle size distribution ($L^{-1}mm^{-1}$) by OTT from 1630 BJT to 1705 BJT Jan 27, 2021.

carried out round-trip detection over Yanjiaping station. LWC average value from Radiometer and from FCDP was at the same order of magnitude. The average value from Radiometer at aircraft altitude (2.9–3.2 km) during 16:30–17:05 was 0.01437 g $m^{-3}$and LWC average value from FCDP was 0.01357 g $m^{-3}$at the same period. Snowfall on the ground at Yanjiaping started at this moment (16:30). The temperature was-18°C ~ -23°C. The LWC increased (basically closed to zero at other times), but the value was low (~0.01–0.18 g $m^{-3}$). The maximum LWC was about 0.4 g $m^{-3}$, which coincided with that observed by the radiometer (0.005–0.015 g $m^{-3}$) at aircraft altitude (2900–3200 m), demonstrating that the cloud was dry and cold at the airplane altitude (2.9–3.2 km).

The ice size distribution observed by the onboard 2DS probe (**Figure 7D**) showed that at the airplane altitude (2.9–3.2 km, −18°C ~ −23°C) the diameter of ice particles was mainly concentrated at the range of 0.1–0.8 mm. The max value of the ice number concentration (INC) was 800 $L^{-1}mm^{-1}$ with the diameter at 0.08–0.6 mm. The max value of the INC appeared at 16:40–16:50 when the airplane was over Yanjiapin, which corresponded to the moment when the LWC increased. This shows that the ice content in clouds above Yanjiaping was higher than clouds at other regions.

It can be seen from **Figure 7E** that the particle (including ice crystals, snowflakes, and raindrops) size distribution observed by the HVPS on the aircraft at 2.9–3.2 km (−18°C ~ -23°C) during this period was dominated by small particles. There were almost no particles with a diameter larger than 3 mm. Most particle diameters were 0.1–1 mm with the number concentration 30–70 $L^{-1}mm^{-1}$. Correspondingly, the max number concentration value (80 $L^{-1}mm^{-1}$) were also in the period of 16:40–16:50 with a smaller diameter range (about 0.1–0.9 mm). At 16:40–16:50 when the LWC increased, the concentration of ice and large particles showed a significant increase, which verified that the LWC had a greater impact on the growth of ice crystals, and the rimming process was the main reason for the growth of the ice crystals. But the LWC over Yanjiapin was low overall, which resulted in the number concentration of large particles being lower than expected, and the particle growth rate being slow. The growth mechanism of ice crystals over Yanjiaping was relatively simple, mainly by collision-coalescence and deposition.

At the same stage, the particles' size distribution on the ground (−8°C) observed by OTT (**Figure 7F**) showed that the particles were also mainly small, with the largest particle diameter <3 mm. The max number concentration of particles was 3500 $L^{-1}$ $mm^{-1}$ with the diameter <1 mm. The high number concentration appeared after 16:40, with snowfall appearing on the ground, and the snowfall start time corresponded well with the moment when LWC and INC increased by aircraft observation. The number concentration and size of the particles observed on the ground were not large at high altitudes, particle growth was not dramatic, and, due to the lack of the LWC, the particles grew only by deposition and aggregation.

All the above results indicated that when the airplane carried out round-trip detection over Yanjiaping station (16:30–16:50), the snowfall was beginning. The LWC increased, and the particles' number concentration at high altitude (2.9–3.2 km) and on the ground both increased. The LWC occupies an important position in the formation and growth of snow. However, because the LWC was insufficient in this case, riming or secondary ice forming process influence was small, ice grew by deposition and aggregation mainly, and the main phase was dry snow (Geerts et al., 2015)

## DISCUSSIONS

**Figure 8** showed the average number concentration measured by the aircraft and on the ground in this period (16:30–17:05). Normalization process was made to display their respective proportions. The right images are particle images.

The average number concentration (observed by HVPS in aircraft) from the *in-situ* observation (**Figure 8A**) showed that the particles were mainly concentrated in the diameter range of 0.15–0.9 mm, which accounted for 96% in total (**Figure 8C**). The maximum value of the number concentration was 44 $L^{-1}$ $mm^{-1}$ at 0.3 mm, which accounted for 26%. With the increasing of the diameter, the number concentration decreased rapidly. The number concentration of particles larger than 1 mm was 2.7 $L^{-1}$ $mm^{-1}$ (accounted for 1.6%), and the particle number concentration of 2 mm diameter was only 0.08 $L^{-1}$ $mm^{-1}$ (accounted for 0.05%). The particle number concentration of diameter>3 mm decreased close to zero. Compared with other snowfall research results (Woods et al., 2008), the spectra were narrow, and the ratio of number concentration decreased when the diameter was large, with only one peak in small size (about at 0.2–0.3 mm); the particle size was small overall, and basically had no large snowflakes (2.5–10 mm). The number concentration of large-size ice crystals was relatively low, indicating that the formation and growth mechanism of ice crystals was relatively single, and the growth rate was slow.

The images from CPI (**Figure 8C** right) showed that there were mainly relatively regular particles, and the shapes of ice particles were plate-like and star features at 2.9–3.2 km (-18°C ~ −23°C). This is consistent with the results of previous studies (Taylor et al., 2016; Hou et al., 2014). As we know, the shape of ice crystals is affected by environmental temperature, humidity or supersaturation. Temperature is the main factor controlling the basic shape of ice crystals; although supersaturation cannot change the basic shape of ice crystals, it will greatly affect its growth rate and secondary characteristics developing (Taylor et al., 2016). Transparent, regular crystals with dendritic and disk-hexagonal forming ice shape indicated the cloud in that altitude was relatively dry, and there was basically no rimming process (Hou et al., 2014; Chang et al., 2019).

The average number concentration (observed by OTT) on the ground (**Figure 8B**) illustrated that the main particles were concentrated in the diameter range of 0.3–1.2mm, which accounted for 97% in total (**Figure 8D**), with the maximum value of 8826 $L^{-1}mm^{-1}$ in 0.45 mm which accounted for 25%. The particle number concentration also decreased rapidly with the diameter increasing. But the rate of decrease was slightly

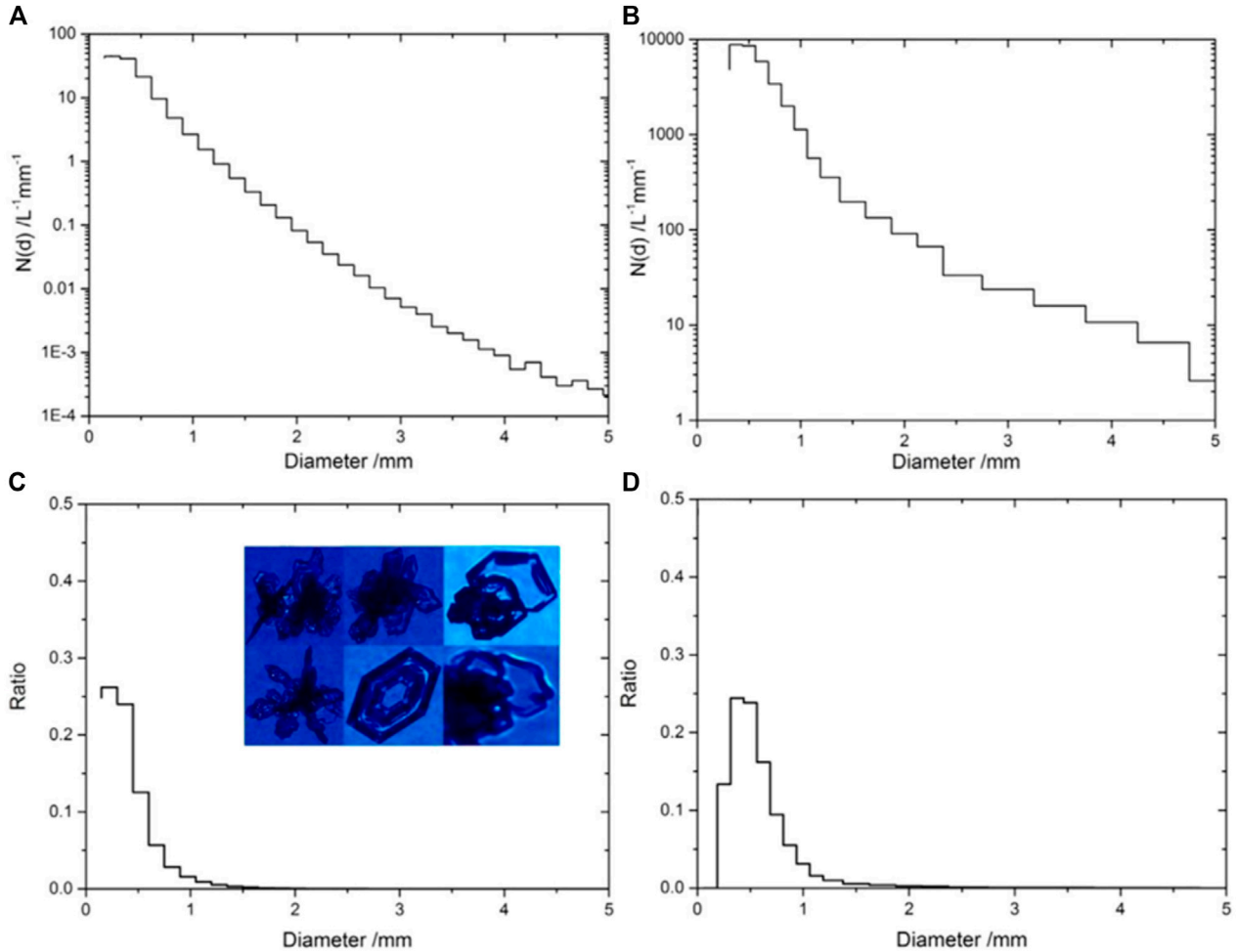


**FIGURE 8 |** Average number concentration observed by **(A)** aircraft, **(B)** OTT disdrometer; Normalization size spectra observed by **(C)** aircraft (right are particle images by CPI), **(D)** OTT disdrometer from 1630 BJT to 1705 BJT 27 Jan 2021.

different from that observed by the aircraft. When the diameter was 1.0mm, the number concentration was 1130 $L^{-1}$ $mm^{-1}$ (accounted for 3.1%); the number concentration in 2 mm was 91 $L^{-1}$ $mm^{-1}$ (accounted for 0.2%), the number concentration in 3 mm was 23 $L^{-1}$ $mm^{-1}$ (accounted for 0.06%), and the number of particles with a diameter> 4 mm was decreased close to zero. The spectra on the ground were also narrow, with only one peak at small scale, but the peak was located at 0.5 mm, and the average number concentration decreased when the scale increased, which was slower than that in high altitude. All the above results demonstrated that, in the range of <1 mm, the scale of particles in high altitude was smaller (<0.3 mm) than that on ground (mainly concentrated around 0.5 mm). The particle size increase shown in the ground spectra was attributed to the aggregation process in falling down, but the scale increase was not obvious, and the number concentration was not high.

Comparing the observation from the aircraft and on the ground, it can be seen that the trend of number concentrations and size distributions was basically the same, and both in Gamma distribution. The number concentration decreased rapidly when size increased, but the number concentration from the *in-situ* observation at small sizes was much lower than that on the ground. The proportion of small particles from the *in-situ* observation was higher than that on the ground, and lower for the large side. The proportion of number concentration with diameter <0.5 mm was 75% for the *in-situ* observation, and was 62% on the ground. The proportion of number concentration with diameter 0.5–1 mm was 21% from the *in-situ* observation and was 34% on the ground. The proportion of number concentration with diameter >1 mm was 3.8% from the *in-situ* observation and was 7.3% on the ground. The ice fell down and grew by deposition and aggregation, so the diameter became larger and the number concentration increased. However, the LWC were insufficient, riming growing was rare, and there was basically no agglutination or clustering process in this case. Moreover, the increase ratio of particles' number concentrations on the ground was slower than expected, and the particle shape was regular, indicating that there was no secondary ice forming process. As a result,

particles on the ground were not enlarged significantly. The conclusion above was based on the combined reasonable analysis of the ground and the aircraft observation. Whether it is the real snowfall formation mechanism is still uncertain, and needs further verification, and the causes of ice crystals' characteristics also need to be further studied.

## CONCLUSION

In this paper, we used onboard probes, ground-based disdrometer combined with the cloud radar, a radiometer, and an automatic station together to study a snowfall case in the Beijing Yanqing mountains from 16:30 to 17:05 on Jan 27, 2021. We demonstrated the microphysical characteristics and compared the variations in the particle size distribution at 2.9–3.2 km and ground level. The results showed that:

1) This case was a slight snowfall. The cumulative snowfall was 0.4 mm, and the max reflectivity factor was lower than 20dBZ. The cloud top was lower than 4.5 km. The wind direction was changed from southerly to westerly below 2.5 km, and dominated by westerly at aircraft altitude.
2) Airborne probes combined with the ground observation can obtain the detailed microphysical characteristics of snowfall. The number concentration of HVPS at the aircraft altitude and ground level was similar and increased at the same time after snow began. The snowfall was dominated by small particles with diameters of 0.15–1.2 mm at both aircraft altitude and ground level. The proportion of number concentrations of these small particles was very high, with the max number concentration 44 $L^{-1}$ $mm^{-1}$ and 8826 $L^{-1}$ $mm^{-1}$ respectively. But the number concentration of particles decreased rapidly with diameter increasing. It is notable that the number concentration of small particles at aircraft altitude was much lower than that on the ground.
3) Both onboard and ground-based observations showed that there was no mixed phase in clouds, and the LWC was very low in this snowfall case. Many particles were relatively regular, and were transparent with dendritic and disk-hexagonal form. The ice crystals and snowflakes mainly grew up by the deposition and aggregation, seldom by the riming process, and there was rarely the secondary ice forming process.
4) The results in this paper can offer a better understanding of the snowfall mechanism in the Beijing Mountains, and provide a reference for the choice of physical schemes in numerical simulations. This article only analyzes one snowfall process. As the next plan, we will analyze more snowfall cases to obtain typical structures and characteristics of snowfall in this region.

## DATA AVAILABILITY STATEMENT

The raw data supporting the conclusions of this article will be made available by the authors, without undue reservation.

## AUTHOR CONTRIBUTIONS

YH and DZ contributed to conception and design of the study. YH organized the database. YD performed the aircraft analysis. YH wrote the first draft of the manuscript. YH wrote sections of the manuscript. All authors contributed to manuscript revision, read, and approved the submitted version.

## FUNDING

This work was supported by the National Key R and D Program of China (2016YFA0601704) and National Natural Science Foundation of China(Grants 41805112, 42075084).

## REFERENCES

Alessandro, B., and Elke, R. (2010). PARSIVEL Snow Observations: a Critical Assessment. *J. Atmos. Oceanic Technol.* 27, 333–344. doi:10.1175/2009JTECHA1332.1

Battaglia, A., Rustemeier, E., Tokay, A., Blahak, U., and Simmer, C. (2010). PARSIVEL Snow Observations: A Critical Assessment. *J. Atmos. Oceanic Technol.* 27 (2), 333–344. doi:10.1175/2009jtecha1332.1

Brandes, E. A., Ikeda, K., Zhang, G., Schönhuber, M., and Rasmussen, R. M. (2007). A Statistical and Physical Description of Hydrometeor Distributions in Colorado Snowstorms Using a Video Disdrometer. *J.Appl.Meteor.Climatol* 46, 634–650. doi:10.1175/jam2489.1

Chang, Y., Guo, X., Tang, J., and Lu, G. Aircraft Measurement Campaign on Summer Cloud Microphysical Properties over the Tibetan Plateau. *Sci. Rep.* 2019, 9:4912. doi:10.1038/s41598-019-41514-5

Chen, Y. C., Jin, Y. L., and Ding, D. P. (2018). Preliminary Analysis on the Application of Millimeter Wave Cloud Radar in Snow Observation. *Chin. J. Atmos. Sci.* 42 (1), 134–149. doi:10.3878/j.issn.1006-9895.1705.17121

Chu, D., Shen, H. F., and Guan, X. B. (2021). Long Time-Series NDVI Reconstruction in Cloud-Prone Regions via Spatio-Temporal Tensor Completion. *Remote Sensing Environ.*, 264. doi:10.1016/j.rse.2021.112632

Cifelli, R., Chandrasekar, V., Lim, S., Kennedy, P. C., Wang, Y., and Rutledge, S. A. (2011). A New Dual-Polarization Radar Rainfall Algorithm: Application in Colorado Precipitation Events. *J. Atmos. Oceanic Technol.* 28, 352–364. doi:10.1175/2010jtecha1488.1

Cotton, W. R., Stephens, M. A., and Nehrkorn, T. (1982). The Colorado State University Three-Dimensional Cloud/mesoscale Model. Part II: An Ice Phase Parameterization. *J.Rech. Atmos.* 16, 295–319.

Crosier, J., Bower, K. N., and Choularton, T. W. (2010). Observations of Ice Multiplication in a Weakly Convective Cell Embedded in Supercooled Mid-level Stratus. *Atmos. Chem. Phys.* 11 (1), 257–273. doi:10.5194/acp-11-257-2011

Field, P. R., Wood, R., and Brown, P. R. A. (2003). Ice Particle Interarrival Times Measured with a Fast FSSP. *J. Atmos. Oceanic Techn.* 20 (20), 249–261. doi:10.1175/1520-0426(2003)020<0249:ipitmw>2.0.co;2

Field, P. R., Heymsfield, A. J., and Bansemer, A. (2006). Shattering and Particle Interarrival Times Measured by Optical Array Probes in Ice Clouds. *J. Atmos. Oceanic Techn.* 23 (10), 1357–1371. doi:10.1175/jtech1922.1

Fraser, A. B., Easter, R. C., and Hobbs, P. V. (1973). A Theoretical Study of the Flow of Air and Fallout of Solid Precipitation over Mountainous Terrain: Part I. Airflow Model. *J. Atmos. Sci.* 30, 801–812. doi:10.1175/1520-0469(1973)030<0801:atsotf>2.0.co;2

Hobbs, P. V., Easter, R. C., and Fraser, A. B. (1973). A Theoretical Study of the Flow of Air and Fallout of Solid Precipitation Over Mountainous Terrain: Part I. Airflow Model. *Journal of the Atmospheric Sciences* 30 (5), 813–823.

Geerts, B., Yang, Y., and Rasmussen, R. (2015). Snow Growth and Transport Patterns in Orographic Storms as Estimated from Airborne Vertical-Plane Dual-Doppler Radar Data. *Monthly Weather Review* 143 (2), 644–655. doi:10.1175/mwr-d-14-00199.1

Guan, X. B., Chen, J. M*, and Shen, H. F. (2021). A Modified Two-Leaf Light Use Efficiency Model for Improving the Simulation of GPP Using a Radiation Scalar. *Agric. For. Meteorology*, 307. doi:10.1016/j.agrformet.2021.108546

Hewison, T. J. (2007). 1D-VAR Retrieval of Temperature and Humidity Profiles from a Ground-Based Microwave Radiometer. *IEEE Trans. Geosci. Remote Sensing* 45 (7), 2163–2168. doi:10.1109/tgrs.2007.898091

Hou, T., Lei, H., Hu, Z., and Zhou, J. (2014). Aircraft Observations of Ice Particle Properties in Stratiform Precipitating Clouds. *Adv. Meteorology* 2014, 1–12. doi:10.1155/2014/206352

Korolev, A., and Field, P. R. (2015). Assessment of the Performance of the Inter-arrival Time Algorithm to Identify Ice Shattering Artifacts in Cloud Particle Probe Measurements. *Atmos. Meas. Tech.* 8 (2), 761–777. doi:10.5194/amt-8-761-2015

Lawson, P., Gurganus, C., Woods, S., and Bruintjes, R. (2017). Aircraft Observations of Cumulus Microphysics Ranging from the Tropics to Midlatitudes: Implications for a "New" Secondary Ice Process. *J. Atmos. Sci.* 74 (9), 2899–2920. doi:10.1175/jas-d-17-0033.1

Lawson, R. P., Baker, B. A., and Schmitt, C. G. (2001). An Overview of Microphysical Properties of Arctic Stratus Clouds Observed during FIRE. *ACE. J. Geophys. Res.* 106 (D1414), 989–1015. doi:10.1029/2000jd900789

Lawson, R. P., Woods, S., and Morrison, H. (2015). The Microphysics of Ice and Precipitation Development in Tropical Cumulus Clouds. *Journal of the Atmospheric Sciences* 72 (6), 150310071420004.

Lin, Y.-L., Farley, R. D., and Orville, H. D. (1983). Bulk Parameterization of the Snow Field in a Cloud Model. *J. Clim. Appl. Meteorol.* 22, 1065–1092. doi:10.1175/1520-0450(1983)022<1065:bpotsf>2.0.co;2

Lo, K. K., and Passarelli, R. E. (1982). The Growth of Snow in Winter Storms:. An Airborne Observational Study. *J. Atmos. Sci.* 39 (4), 697–706. doi:10.1175/1520-0469(1982)039<0697:tgosiw>2.0.co;2

Masaaki, I., Hiroki, M., and Sento, N. (2013). A New Method for Identifying the Main Type of Solid Hydrometeors Contributing to Snowfall from Measured Size Fall Speed Relationship. *J. Meteorol. Soc. Jpn.* 91 (3), 747–762. doi:10.2151/jmsj.2013-602

Matthew, R., Steven, A., and Roy, M. (2014). High-Resolution Polarimetric Radar Observations of Snow-Generating Cells. *J.Appl.Meteor.Climatol.* 53, 1636–1658. doi:10.1175/JAMC-D-13-0312.1

Morrison, H., and Milbrandt, J. A. (2015). Parameterization of Cloud Microphysics Based on the Prediction of Bulk Ice Particle Properties. Part I: Scheme Description and Idealized Tests. *J.Atmos. Sci.* 72, 287–311. doi:10.1175/jas-d-14-0065.1

Neiman, P. J., Gottas, D. J., White, A. B., Schick, L. J., and Ralph, F. M. (2014). The Use of Snow-Level Observations Derived from Vertically Profiling Radars to Assess Hydrometeorological Characteristics and Forecasts over Washington's Green River Basin. *J. Hydrometeorology* 15, 2522–2541. doi:10.1175/jhm-d-14-0019.1

Newman, A. J., Kucera, P. A., and Bliven, L. F. (2009a). Presenting the Snowflake Video Imager (SVI)flake Video Imager (SVI). *J. Atmos. Oceanic Technol.* 26, 167–179. doi:10.1175/2008jtecha1148.1

Newman, A. J., Kucera, P. A., Williams, C. R., and Bliven, L. F. (2009b). Snowflake Size Spectra Retrieved from a UHF Vertical Profiler. *J. Atmos. Oceanic Technol.* 26, 180–199. doi:10.1175/2008jtecha1105.1

Saleeby, S. M., Cotton, W. R., and Fuller, J. D. (2011). The Cumulative Impact of Cloud Droplet Nucleating Aerosols on Orographic Snowfall in Colorado. *J.Appl.Meteor.Climatol* 50, 604–625. doi:10.1175/2010jamc2594.1

Shen, L. J., Honglei, W., and Bin, Z. (2021). Impact of Urbanization on Air Quality in the Yangtze River Delta during the COVID-19 Lockdown in China. *J. Clean. Prod.* 296 (2021), 126561. doi:10.1016/j.jclepro.2021.126561

Taylor, J. W., Choularton, T. W., Blyth, A. M., Liu, Z., Bower, K. N., Crosier, J., et al. (2016). Observations of Cloud Microphysics and Ice Formation during COPE. *Atmos. Chem. Phys.* 16, 799–826. doi:10.5194/acp-16-799-2016

Thompson, G., Rasmueesn, R. M., and Manning, K. (2004). Explicit Forecasts of winter Precipitation Using an Improved Bulk Microphysics Scheme. Part I: Description and Sensitivity Analysis. *Mon. Wea. Rev.* 132, 519–542. doi:10.1175/2008MWR2387.1

Tokay, A., Wolff, D. B., and Petersen, W. A. (2014). Evaluation of the New Version of the Laser-Optical Disdrometer, OTT Parsivel2. *J. Atmos. Oceanic Techn.* 31 (6), 1276–1288. doi:10.1175/jtech-d-13-00174.1

Woods, C. P., Stoelinga, M. T., and Locatelli, J. D. (2008). Size Spectra of Snow Particles Measured in Wintertime Precipitation in the Pacific Northwest. *J.Atmos. Sci.* 65, 189–205. doi:10.1175/2007jas2243.1

Woods, C. P., Stoelinga, M. T., and Locatelli, J. D. (2007). The IMPROVE-1 Storm of 1-2 February 2001. Part III: Sensitivity of a Mesoscale Model Simulation to the Representation of Snow Particle Types and Testing of a Bulk Microphysical Scheme with Snow Habit Prediction. *J.Atmos. Sci.* 64, 3927–3948. doi:10.1175/2007jas2239.1

Woods, S., Lawson, R. P., Jensen, E., Bui, T. P., Thornberry, T., Rollins, A., et al. (2018). Microphysical Properties of Tropical Tropopause Layer Cirrus. *J. Geophys. Res. Atmos.* 123, 6053–6069. doi:10.1029/2017JD028068

Yuter, S. E., Kingsmill, D. E., Nance, L. B., and Löffler-Mang, M. (2006). Observations of Precipitation Size and Fall Speed Characteristics within Coexisting Rain and Wet Snow. *J.Appl.Meteor. Climatol.* 45, 1450–1464. doi:10.1175/jam2406.1

Zheng, S., and Chen, J. H. (2021). Observational Evidence of Lightning-Generated Ultrafine Aerosols. *Geophys. Res. Lett.* 48–14. e2021GL093771. doi:10.1029/2020gl091881

Zhong, L., Liu, L., Feng, S., Ge, R., and Zhang, Z. (2011). A 35-GHz Polarimetrie Doppler Radar and its Application for Observing Clouds Associated with Typhoon Nuri. *Adv. Atmos. Sci.* 28 (4), 945–956. doi:10.1007/s00376-010-0073-5

**Conflict of Interest:** The authors declare that the research was conducted in the absence of any commercial or financial relationships that could be construed as a potential conflict of interest.

frontiers in Environmental Science

CORRECTION
published: 01 March 2022
doi: 10.3389/fenvs.2022.850113

# Corrigendum: Vertical Structure of a Snowfall Event Based on Observations From the Aircraft and Mountain Station in Beijing

*Yu Huang*[1,2,3], *Delong Zhao*[1,2,3]*, *Yuanmou Du*[1,2,3]*, *Yichen Chen*[1], *Lei Zhang*[1], *Xia Li*[1] and *Yingying Jing*[1]

[1]Beijing Weather Modification Center, Beijing, China, [2]Key Laboratory of Cloud, Precipitation and Atmospheric Water Resources, Beijing Meteorological Service, Beijing, China, [3]Field Experiment Base of Cloud and Precipitation Research in North China, China Meteorological Administration, Beijing, China

**Keywords: Beijing mountains snowfall, ground-based disdrometer, aircraft platform, vertical structure, comprehensive observation**

OPEN ACCESS

***Edited by:***
*Junke Zhang,*
*Southwest Jiaotong University, China*

***Reviewed by:***
*Zixia Liu,*
*King's College London, United Kingdom*
*Dawei Hu,*
*The University of Manchester, United Kingdom*

****Correspondence:***
*Delong Zhao*
*zhaodelong@bj.cma.gov.cn*
*Yuanmou Du*
*yuanmoudu24@163.com*

***Specialty section:***
*This article was submitted to Atmosphere and Climate, a section of the journal Frontiers in Environmental Science*

***Received:*** *07 January 2022*
***Accepted:*** *08 February 2022*
***Published:*** *01 March 2022*

***Citation:***
*Huang Y, Zhao D, Du Y, Chen Y, Zhang L, Li X and Jing Y (2022) Corrigendum: Vertical Structure of a Snowfall Event Based on Observations From the Aircraft and Mountain Station in Beijing. Front. Environ. Sci. 10:850113. doi: 10.3389/fenvs.2022.850113*

## A Corrigendum on

**Vertical Structure of a Snowfall Event Based on Observations From the Aircraft and Mountain Station in Beijing**

*by Huang, Y., Zhao, D., and Du, Y. (2021). Front. Environ. Sci. 9:783356. doi: 10.3389/fenvs.2021.783356*

In the original article, there was a mistake in **Figure 8** as published.

In the original article, there was a mistake in the legend for **Figure 8** as published. Due to the error in **Figure 8D**, reference to the particle image should be removed.

The original legend is:

"Average number concentration observed by **(A)** aircraft, **(B)** OTT disdrometer; Normalization size spectra observed by **(C)** aircraft (right are particle images by CPI), **(D)** OTT disdrometer (right are particle images by microscope) from 1630 BJT to 1705 BJT 27 Jan 2021."

The corrected legend appears below.

"Average number concentration observed by **(A)** aircraft, **(B)** OTT disdrometer; Normalization size spectra observed by **(C)** aircraft (right are particle images by CPI), **(D)** OTT disdrometer from 1630 BJT to 1705 BJT 27 Jan 2021."

In the original article, there was an error in **Discussions**, paragraph five. Due to the error in **Figure 8D**, the original paragraph five should be removed. The original paragraph to be removed appears below:

"The ground (about −9°C) images (**Figure 8D** right, observed by microscope) showed that the snowflakes were also transparent and regular, revealing that the water vapor was scarce in lower altitudes. The snowflake shape showed mainly hexagonal plates, and had little rimed dendrites, which was also consistent with previous observations (Hou et al., 2014; Chang et al., 2019). It is reflected that snowflake growth mechanism was relatively simple in lower altitudes; most snowflakes increased by aggregation process, and there was basically no agglutination or clustering process in snowflake growth (Taylor et al., 2016)."

The authors apologize for this error and state that this does not change the scientific conclusions of the article in any way. The original article has been updated.

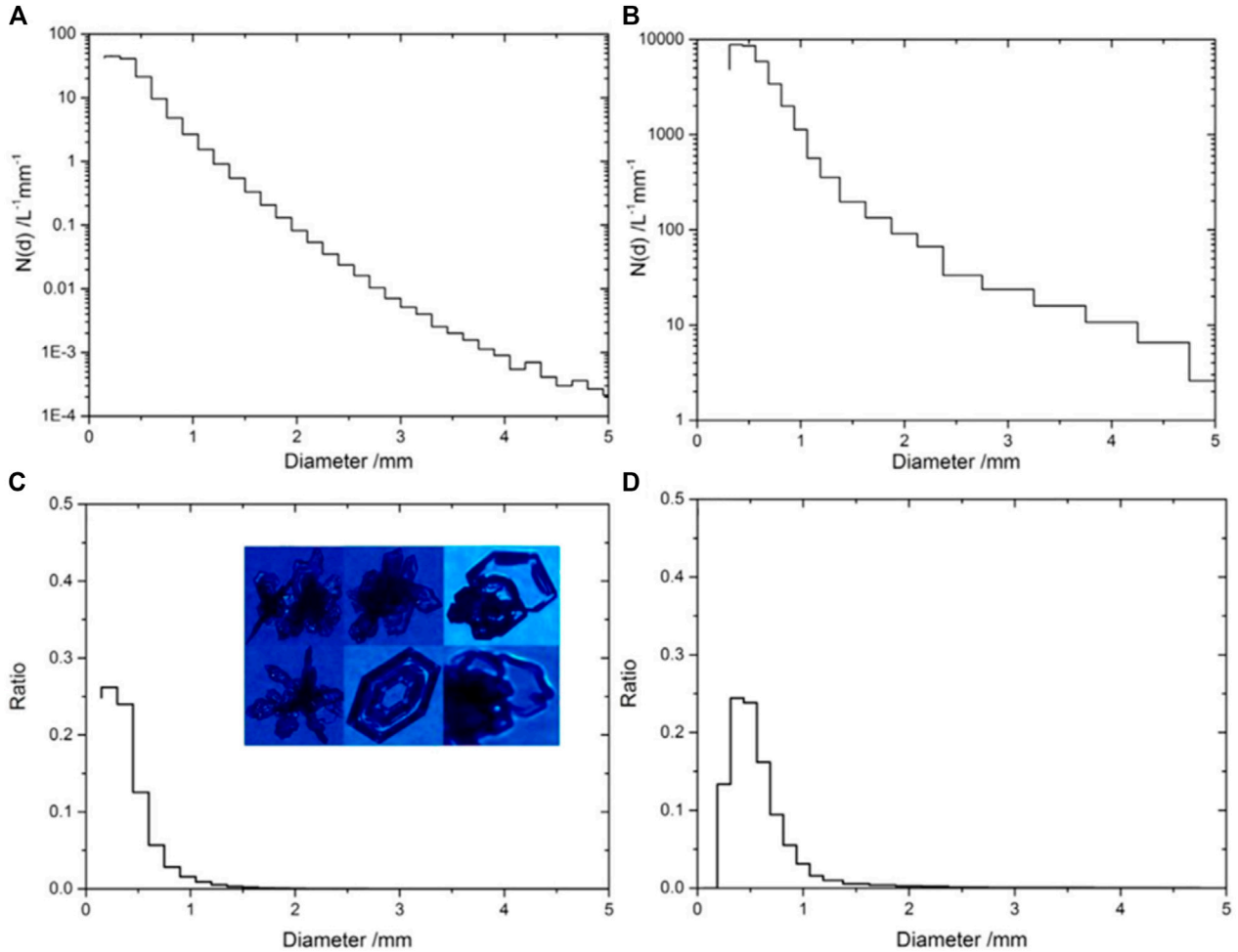


**FIGURE 8 |** Average number concentration observed by **(A)** aircraft, **(B)** OTT disdrometer; Normalization size spectra observed by **(C)** aircraft (right are particle images by CPI), **(D)** OTT disdrometer from 1630 BJT to 1705 BJT 27 Jan 2021.

frontiers in Environmental Science

ORIGINAL RESEARCH
published: 24 March 2022
doi: 10.3389/fenvs.2022.865966

# Response of Mixed-Phase Cloud Microphysical Properties to Cloud-Seeding Near Cloud Top Over Hebei, China

*Yang Yang*[1,2], *Chuanfeng Zhao*[1,3]*, *Jiao Fu*[2], *Yi Cui*[2], *Xiaobo Dong*[2], *Rong Mai*[2] *and Feng Xu*[2]

[1]Key Laboratory of Meteorology and Ecological Environment of Hebei Province, Shijiazhuang, China, [2]Weather Modification Office of Hebei Province, Shijiazhuang, China, [3]College of Global Change and Earth System Science, Beijing Normal University, Beijing, China

On November 29, 2019, an aircraft observation during the period of cloud-seeding was carried out for a mixed-phase cloud over Xingtai, Hebei Province, China. This study investigates the response of mixed-phase cloud microphysical properties to cloud-seeding near cloud top. Before cloud seeding, the cloud droplet concentration from fast cloud droplet probe ($N_{C\_FCDP}$) presented a multi-peak vertical distribution structure, with a maximum concentration of 192 $cm^{-3}$ at a height of 3,322 m; the maximum concentration of ice crystals from cloud imaging probe ($N_{C\_CIP}$) was 10 $L^{-1}$, which appeared at 4,500 m in the upper part of cloud; and the peak value of liquid water content (LWC) in the cloud also appeared at 4,500 m, with a value of 0.15 $g/m^3$. The coexistence of supercooled liquid water and ice crystals implies that they are particularly suitable for cloud seeding at the height of 4,550 m. About 7–8 min later after cloud seeding at this height, the average $N_{C\_FCDP}$ decreased from 160.3 to 129 $cm^{-3}$, and the average $N_{C\_CIP}$ increased from 7.1 to 10 $L^{-1}$. Moreover, after cloud seeding, high $N_{C\_CIP}$ as well as larger and more ice crystals appeared almost in the same areas within the cloud, and LWC presented an obvious decreasing trend. In contrast, the concentration of small cloud droplets and LWC decreased obviously after seeding. The findings suggest that the cloud microphysical properties showed obvious responses to the artificial introduction of silver iodide, which is important for human weather modification.

**Keywords: mixed-phase, cloud-seeding, microphysical properties, respond, cloud top**

OPEN ACCESS

***Edited by:***
*Honglei Wang,*
*Nanjing University of Information Science and Technology, China*

***Reviewed by:***
*Shaofeng Hu,*
*China Meteorological Administration, China*
*Jiefan Yang,*
*Institute of Atmospheric Physics (CAS), China*

***Correspondence:**
*Chuanfeng Zhao*
*czhao@bnu.edu.cn*

***Specialty section:***
*This article was submitted to Atmosphere and Climate, a section of the journal Frontiers in Environmental Science*

***Received:*** *30 January 2022*
***Accepted:*** *14 February 2022*
***Published:*** *24 March 2022*

***Citation:***
*Yang Y, Zhao C, Fu J, Cui Y, Dong X, Mai R and Xu F (2022) Response of Mixed-Phase Cloud Microphysical Properties to Cloud-Seeding Near Cloud Top Over Hebei, China. Front. Environ. Sci. 10:865966. doi: 10.3389/fenvs.2022.865966*

## INTRODUCTION

Clouds play an important role on both Earth's weather and climate (Ramanathan et al., 1989; Norris, 2005; Zhao and Garrett, 2015; Yang et al., 2016a; Yang et al., 2016b; Chuanfeng Zhao et al., 2020). Moreover, anthropogenic activities, by changing cloud properties, have contributed to increased extreme weather and climate events (Lohmann and Feichter, 2005; Andreae and Rosenfeld, 2008; Tao et al., 2012; Li et al., 2016; Yang et al., 2018; Zhao et al., 2018; Sun et al., 2019; Xin Zhao et al., 2020), and extreme weather generally has great impact on human life. The changes of latent heat release, precipitation, and radiation during cloud development, which are essential parts in Earth's energy budget and hydrological cycle, are all affected by the microphysical processes in the cloud (Pruppacher and Klett, 2010).

The cloud microphysical properties could be further influenced by human activities. In 1946, American scientists proposed that the number of ice crystals in cold clouds could be increased by artificially introducing silver iodide (AgI) into the cloud, thus achieving the effect of rain enhancement (Schaefer, 1946; Vonnegut, 1947). Weather modification has gradually become an important application field of cloud and precipitation physics. At present, the theory of weather modification has been able to explain how the catalyst works in the cloud—that is, under appropriate meteorological conditions, seeding silver iodide into clouds containing supercooled water droplets can cause the liquid water droplets to transform into ice crystals, and then the newly formed ice crystals grow larger through the Bergeron process (Bergeron, 1935). After decades of experiments, the catalysis of winter orographic clouds on the windward slope has achieved a high success rate (Pokharel and Geerts, 2016; Pokharel et al., 2017; Tessendorf et al., 2020). Seeding in supercooled water clouds with a thickness less than 1 km can leave a very obvious cloud groove (Dong et al., 2021). These studies provide a solid foundation for the feasibility of artificial cloud seeding. While various experiments have been carried out, sufficient evidences of seeding effects are still needed under different conditions—for example, there are relatively few experiments on artificial catalysis and studies about the changes of microphysical properties in deep layered clouds. Particularly, many existing studies evaluate the performance of cloud seeding only by investigating the changes of macroscopic properties, such as the changes of reflectivity from ground-based radars or by directly using statistical verification. These methods are usually not intuitionistic and intelligible enough to reflect how AgI works within the cloud, leading to the effect of cloud seeding still in insufficient credibility.

The response of cloud microphysical properties to seeding can be observed by airborne instruments with high temporal resolution, which provides us a good opportunity with reliable basis to understand the mechanism of artificial precipitation enhancement. In this study, through a well-designed aircraft seeding experiment of a winter snowfall deep cloud system, we investigate the changes in phase and size distribution of cloud particles due to seeding. We first analyze the weather background before cloud seeding and then the structure of the cloud system. Finally, the response of the cloud microphysical properties was examined based on the changes between before and after cloud seeding.

# METHODOLOGY

## Instruments

In this experiment, a snow cloud system was selected on November 29, 2019 for research about the response of mixed-phase cloud microphysical properties to cloud seeding, and aircraft detection and cloud seeding were carried out over Xingtai, Hebei Province. The King Air-350 aircraft operated by Hebei Weather Modification Office was used for the observation of clouds with an airborne detection system on board, including cloud particle detection system, meteorological measurement system, Nevzorov hot wire liquid water content (LWC), total water content (TWC) probe, and global positioning system. The cloud particle detection system in this study consists of fast cloud droplet probe (FCDP), cloud imaging probe (CIP), and cloud particle imager (CPI). The FCDP probe can obtain the concentration of cloud droplets in the size range of 2–50 μm in radius, with uncertainty of approximately 20% (Faber et al., 2018; Lance et al., 2010). CIP can detect large cloud particles in the size range of 25–1,550 μm, and the CPI probe is able to obtain high-resolution images of cloud particles. The LWC and the TWC were obtained by the Nevzorov hot wire LWC/TWC probe, and the uncertainty was about 15% (Emery et al., 2004; Korolev et al., 2013). CPI uses a CCD camera to capture a high-resolution image of cloud particles, which can distinguish water drops from ice particles. Vertical profiles of temperature and humidity were obtained using the meteorology monitoring system called Aircraft-Integrated Meteorological Measurement System. **Table 1** shows these main detection equipment used in this study, along with their detected cloud variables and measurable ranges. Cloud seeding and the detection of cloud microphysical properties were performed by the same aircraft. Also noted is that the silver iodide flames used in this study contain AgI of 1.8 g per stick.

## Data Processing

The cloud particle size spectra observed in this study were obtained by FCDP and CIP probes. Considering that most of the ice crystal particles in stratiform clouds are larger than 100 μm in diameter, we assume that cloud particles larger than 100 μm are ice crystals, which can be obtained by CIP probe of 100–1,550 μm, and that the particles smaller than 100 μm are cloud droplets, which can be obtained by FCDP (Korolev and Field, 2015). Considering the higher supersaturation condition of the ice surface than the liquid droplet surface in the mixed-phase cloud, ice crystals larger than 25 μm can grow rapidly in 1 min. Thus, our assumption in general that the FCDP observed particles are all droplets in the cloud examined here should be reasonable. In order to obtain the changes of cloud particle spectra between before and after catalysis in a more detailed manner, the sampling frequency of all instruments used in this study is 1 Hz. Before using the data, we performed quality control on the observed data based on the instrument operating status and true air speed values.

The cloud microphysical parameters used in this study, including the effective radius of cloud particles $r_e$, number concentration of cloud particles $N_{ci}$, and ice water content (IWC) of clouds measured by Nevzorov-LWC/TWC $IWC_{Nevzorov}$ are calculated as follows:

$$r_e = \frac{\int r^3 n(r) dr}{\int r^2 n(r) dr} = \frac{\sum N_{ci} r_i^3}{\sum N_{ci} r_i^2} \quad (1)$$

$$N_d = \int n(r) dr = \sum N_{ci} \quad (2)$$

$$IWC_{Nevzorov} = TWC_{Nevozrov} - LWC_{Nevzorov} \quad (3)$$

where $n(r)$ is the droplet size distribution with number concentration of $n$ at size $r$, and $N_{ci}$ and $r_i$ are the droplet

**TABLE 1 |** The cloud microphysical detection instruments, the main parameters observed in this study, and the measureable range of each variable by the instrument, along with the reference for instrument details.

| Instrument | Detection variable | Measurable range | References |
|---|---|---|---|
| FCDP | Cloud droplets | 2–50 μm | www.specinc.com |
| CIP | Ice crystal particles | 25–1,550 μm | Baumgardner et al. (2001) |
| CPI | Cloud particle images | 2–3,000 μm | Lawson et al. (2001) |
| Nevzorov—LWC/TWC | TWC/LWC | 0.005–3 g/m$^3$ | Korolev et al. (1998) |

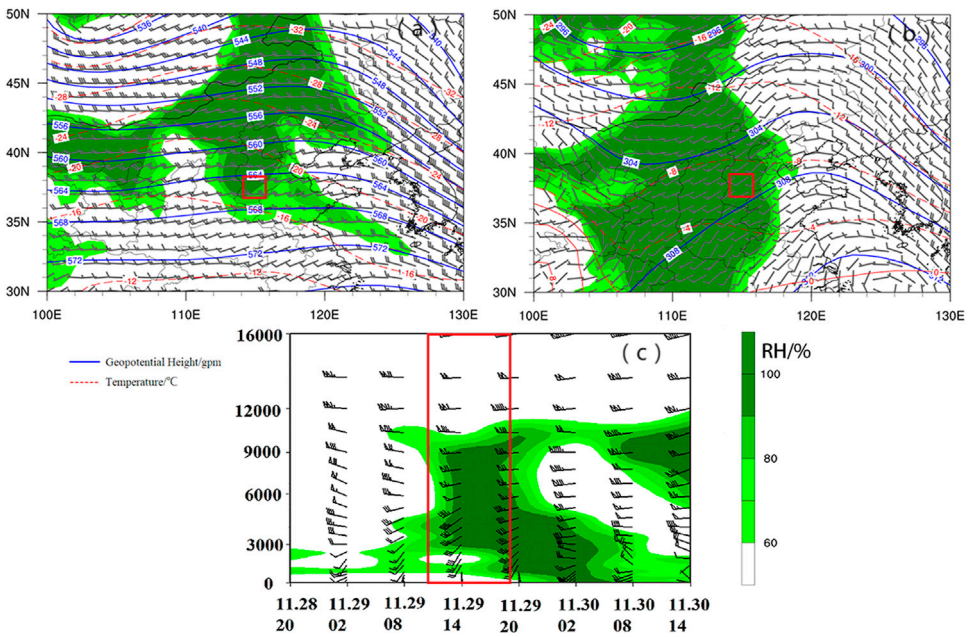


**FIGURE 1 |** The weather pattern at 14:00 LT on November 29, 2019 at **(A)** 500 hPa and **(B)** 700 hPa. The blue line represents the geopotential height field, while the red dotted line represents the temperature field. **(C)** Relative humidity (filled with green-colored contours) and wind field from NCEP reanalysis data above Xingtai site over the observation area in time series. The Xingtai site area was marked by a rectangle in **(A**,**B)**.

number concentration and the particle size radius of the *i*-th bin of the instrument, respectively. Nevzorov hot wire LWC/TWC probe can only obtain liquid and total water content, and $IWC_{Nevzorov}$ is calculated by subtracting $LWC_{Nevzorov}$ from $TWC_{Nevzorov}$. Due to the potential uncertainty of each instrument, the first and last bins of FCDP and the first three bins of CIP were discarded and not used, which was similar to our previous studies (Yang et al., 2019; Zhao et al., 2019; Dong et al., 2020). The whole size range of cloud particles at 3–1,550 μm was obtained by combining the observations of FCDP and CIP. The time used in this study were all converted to local time (UTC + 8).

# RESULTS AND DISCUSSION

## Weather Background and Flight Plan

Weather background was analyzed using 1° × 1° NCEP/NCAR reanalysis data at 14:00 LT on November 29, 2019, and the flight seeding and observation areas were marked in **Figure 1**. There was a zonal circulation with two troughs and a ridge at 500 hPa (**Figure 1A**) at mid-high latitudes over Asia. There was also an obvious westerly trough near Hetao, and the detection area was dominated by a southwest airflow in front of the trough. The trough line at 700 hPa (**Figure 1B**) was located from the Mongolian Plateau to the Hetao area. The flight observation area was under the control of a southwest airflow in the south of the trough with obvious warm moisture advection, making the relative humidity close to saturation. The warm–humid air from the southwest and the cold air from the north converged, causing the formation of a large cloud system at the east of Hetao and the north of Shanxi. The cloud system gradually affected Hebei during its eastward movement. In this process, the atmosphere over the observation area was relatively stable, and the cloud system was dominated by stratus clouds. On the day of November 29, 2019, the relative humidity above the Xingtai site (**Figure 1C**) that lies within the observation area was relatively low at below 3,000 m, and the wet layer was mainly concentrated in 3,000–5,000 m, which was consistent with the detection results of the aircraft.

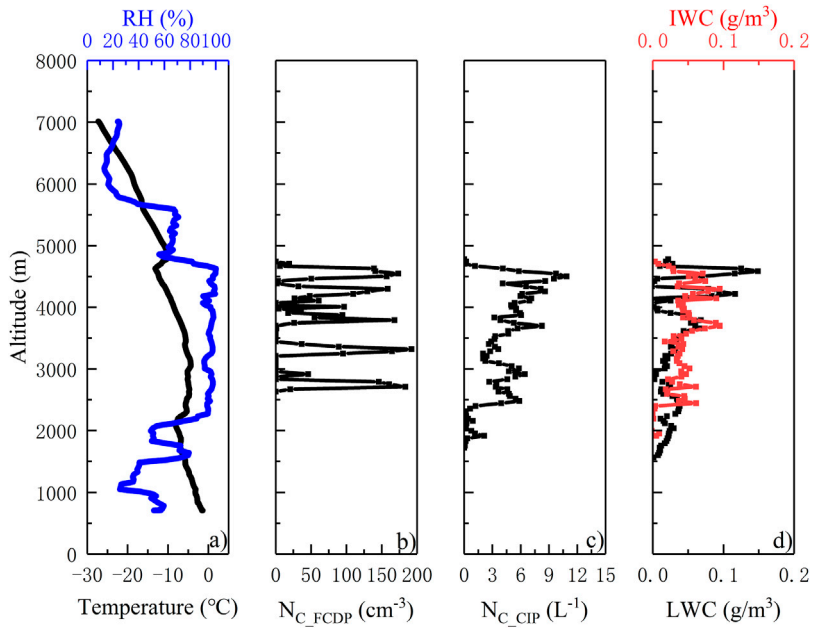


**FIGURE 2 | (A)** Temperature and relative humidity profiles, **(B)** cloud droplet number concentration observed by fast cloud droplet probe, **(C)** ice crystal number concentration observed by cloud imaging probe, and **(D)** liquid water content and ice water content over Xingtai on November 29, 2019.

The aircraft took off from Zhengding Airport at 14:50 LT, lifted to 2,100 m, and then leveled over Xingtai, which was located in south-central Hebei Province. After arriving at the detection area, the aircraft first descended to a height of 600 m and then conducted vertical detection of the macro- and micro-properties of cloud by flying from the bottom to the top during the period 15:52–16:18 LT, with an altitude range of 600–7,000 m and a hovering radius of 10 km. After knowing the vertical structure of cloud properties, the aircraft was lowered from a height of 7,000–4,550 m from 16:19 to 16:34 LT. Then, cloud seeding was carried out over Xingtai along the same circular trajectory at 16:37 LT at an altitude of 4,550 m, where the supercooled liquid water content was relatively abundant, and a total of 14 AgI bars were lighted. After cloud seeding, the flight continued to detect the cloud macro- and micro-physical properties in order to know the effect of cloud seeding.

## Vertical Structure of Cloud Properties

**Figure 2** shows the vertical distribution of stratus cloud microphysical properties along with the temperature and relative humidity profiles. It can be seen from **Figure 2A** that good humidity conditions existed above the height of 2,500 m, which was consistent with the results at around 16:00, as shown in **Figure 1C**. The corresponding heights of 500 and 700 hpa are about 5,600 and 3,000 m, respectively, and the temperature values in **Figure 2A** are approximately the same as those in **Figure 1A** and **Figure 1B**. As shown in **Figure 2A**, the vertical detection area of the aircraft was all above the height of 0°C layer, and the temperature decreased with the increase of altitude. However, there were two thin temperature inversion layers near the cloud base and the cloud top, respectively. The temperature at the lower inversion layer varied from -8.2 to −5.4°C with heights from 2,100 m to 2,355 m, and the temperature at the upper inversion layer varied from -13.5 to −10.2°C with heights from 4,600 to 4,800 m. Unlike temperature, relative humidity gradually increased with height, reached saturation in the cloud region, and gradually decreased with height above the cloud top.

It was generally believed that when the number concentration obtained by FCDP ($N_{C\_FCDP}$) was greater than 10 $cm^{-3}$ and LWC ≥ 0.01 $g{\cdot}m^{-3}$ at the same time, the corresponding location of the aircraft was determined to be in the cloud (Hobbs, 1991). The dramatic changes of $N_{C\_FCDP}$ with height, as shown in **Figure 2B**, indicated that the vertical distribution of stratus cloud properties varied greatly. The maximum $N_{C\_FCDP}$ appeared in lower clouds at heights of about 3,220 m, with the peak value of 192 $cm^{-3}$. The number concentration of ice crystals ($N_{C\_CIP}$) showed a growing trend with height within clouds and reached the maximum value of 10 $L^{-1}$ at the top of the cloud, as shown in **Figure 2C**. The maximum LWC of 0.15 $g/m^3$ appeared near the top of the cloud (**Figure 2D**), which was similar to the results found by Zhao and Lei (2014). IWC was on the same order of magnitude as LWC, with peak values of up to 0.1 $g/m^3$ at heights of around 4,000 m. **Figure 2** shows that both liquid droplets and ice crystals were detected at altitudes from 3,500 to 4,700 m, indicating the mixed-phase status at this height range, which was also the optimal part for cloud seeding due to the existence of supercooled liquid droplets.

## Horizontal Distribution of Cloud Properties

After knowing the vertical properties of the cloud system, the flight leveled at the height of 4,550 m, which was rich of supercooled liquid water, to obtain the horizontal

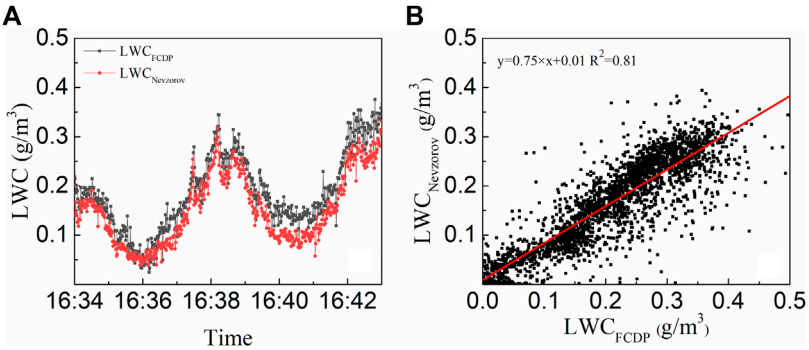


**FIGURE 3 |** For a cloud layer at height 4,550 m: **(A)** temporal variation of $LWC_{FCDP}$ and $LWC_{NEVZOROV}$, **(B)** scattered plots between $LWC_{FCDP}$ and $LWC_{NEVZOROV}$.

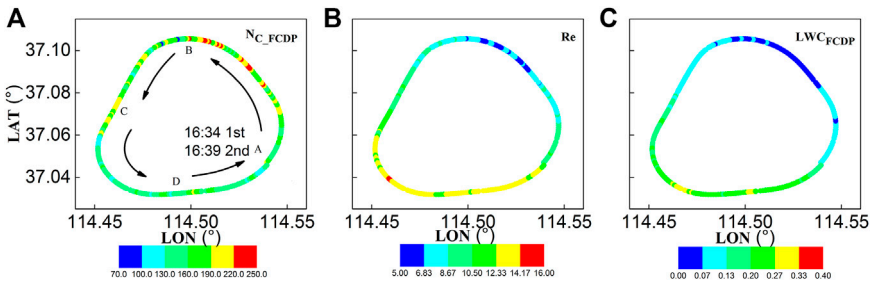


**FIGURE 4 |** For a cloud layer at height 4,550 m: **(A)** concentration of cloud droplets ($N_{C\_FCDP}$) with unit $cm^{-3}$, **(B)** effective radius ($r_e$) with unit μm, and **(C)** $LWC_{FCDP}$ with unit g $m^{-3}$ along the first flight observation trap.

microphysical properties of the cloud. The corresponding flight time was 16:34-16:43 LT, and two laps were flown along the same trajectory due to the wind speed in the detection area being less than 5 m/s. We believe that the cloud properties do not change much in a short time. To make sure that the LWC obtained during this experiment was reliable, **Figure 3** shows a comparison of LWC in the cloud obtained by two different instruments of FCDP and Nevzorov hot wire, which were denoted as $LWC_{FCDP}$ and $LWC_{NEVZOROV}$, respectively. $LWC_{FCDP}$ and $LWC_{NEVZOROV}$ had a good consistency on time series (**Figure 3A**), and the correlation coefficient between them reached 0.81 (**Figure 3B**), indicating that the LWC detection results had high reliability and accuracy. Note that the LWC from Nevzorov hot wire is slightly smaller than that from FCDP, which might be associated with the potential ice crystals with sizes smaller than 100 μm. $LWC_{FCDP}$ was used in the following sections to represent the liquid water content during the aircraft observation period.

**Figure 4** presents the cloud droplet number concentration ($N_{C\_FCDP}$; **Figure 4A**), the cloud droplet effective radius ($r_e$) measured by FCDP (**Figure 4B**), and the liquid water content ($LWC_{FCDP}$, **Figure 4C**) during the level flight process at a height of 4,550 m. The flight observation started in a counter-clockwise direction from point A. **Figure 4** presents the observation results from 16:34 LT (the observation started from point A) to 16:39 LT (the flight returned to point A for the second time after one lap). The cloud seeding and detection were carried along the same circular trajectory. Even though the AgI flame bars were lighted at 16:37 LT, the aircraft still detected the unseeded area before the end of the lap. Differently from the general expectation that cloud microphysical properties vary weakly at a horizontal layer for stratus clouds (Wang et al., 2013), $N_{C\_FCDP}$, $r_e$, and $LWC_{FCDP}$ varied a lot horizontally. The $N_{C\_FCDP}$ ranged from 70 to 248.4 $cm^{-3}$, corresponding to which the cloud droplet $r_e$ ranged from 43.71 to 10.2 μm. In addition, the large amount of small cloud droplets implied that condensation, rather than collision, was likely the main way of droplet growth. By comparing the horizontal distribution of $N_{C\_FCDP}$, $r_e$ and $LWC_{FCDP}$ along the flight track, it was clear that high $N_{C\_FCDP}$ corresponded to low $r_e$ and $LWC_{FCDP}$ and high $LWC_{FCDP}$ corresponded to high $r_e$. This suggested that while small droplets had a great contribution to number concentration, LWC in clouds was mainly contributed by large droplets.

Not only cloud microphysical properties but also the cloud particle phase varied greatly along the flight track at the selected cloud layer. From 16:34 to 16:37 LT (A-B-C in **Figure 4A**), the concentration of cloud droplets was relatively high, while $r_e$ and LWC in the cloud were relatively small. The cloud particle images obtained by CPI during this period are shown in **Figure 5A**. In this period, the particles are mostly spherical droplets with a small amount of ice crystals. The effective radius of the particles is relatively small, so the concentration of $LWC_{FCDP}$ was low, although $N_{C\_FCDP}$ was at a high level. From 16:37-16:39 LT

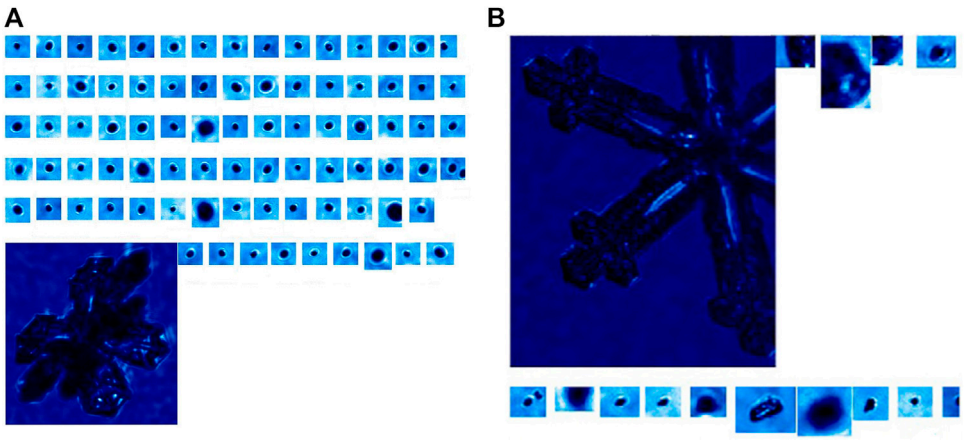


**FIGURE 5 |** Cloud particle images at the height of 4,550 m in the cloud: **(A)** A-B-C and **(B)** C-D-A.

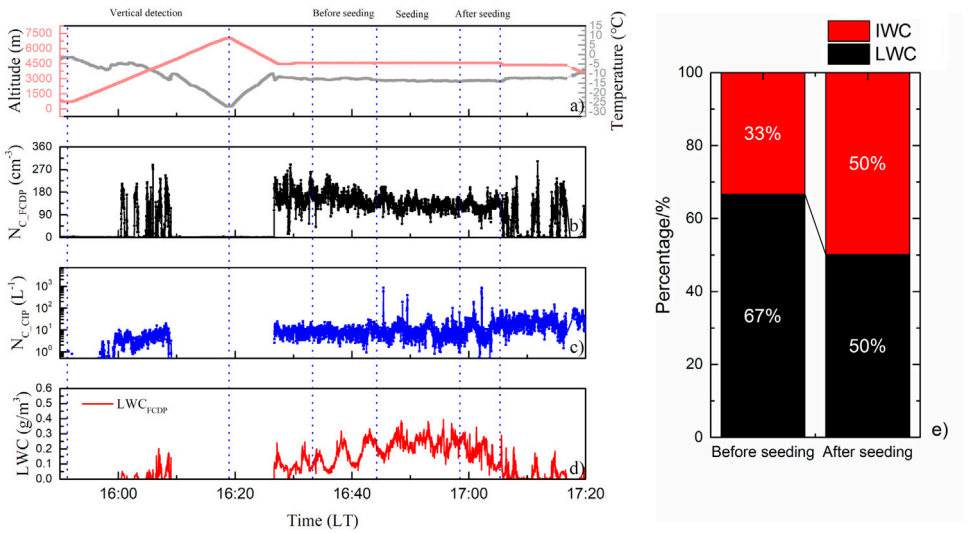


**FIGURE 6 |** Changes of microphysical properties in the cloud during the observation and the seeding periods: **(A)** temperature and height, **(B)** $N_{C\_FCDP}$, **(C)** $N_{C\_CIP}$, **(D)** $LWC_{FCDP}$, and **(E)** percentage of liquid water content and ice water content relative to the total water content.

(C-D-A in **Figure 4A**), the number concentration of cloud droplets was relatively low, with an average of 152.24 cm$^{-3}$. The cloud particle image (**Figure 5B**) showed that, at this time, cloud particles were mostly in ice phase. Large ice crystals coexist with small ice crystals in irregular shapes, which might come from the shattering of large crystals. The differences of microphysical properties in the clouds at different horizontal locations were clear, which reflect the serious heterogeneity of stratus cloud properties when they were in a mixed phase.

## Microphysical Properties After Cloud Seeding

**Figure 6** shows the temporal variation of cloud microphysical properties along with the flight height and environmental temperature. Note that the time periods shown in **Figure 6** include those before and after cloud seeding. The flight made the observations of vertical profiles during the period from 15:52 to 16:18 LT at heights of 600–7,000 m. Then, the altitude of 4,550 m near cloud top, where LWC (supercooled droplets) was relatively abundant, was chosen for cloud seeding at 16:37 LT, with a total of 14 AgI bars lighted. The cloud seeding and detection were carried along the same circular trajectory. Even though the AgI flame bars were lighted at 16:37 LT, the aircraft still detected the unseeded area before the end of the lap. The aircraft returned to the position where the cloud seeding started at 16:43 LT, and the AgI flame bars got extinguished at 16:58 LT. Then, the aircraft started the observation of cloud microphysical properties after seeding along the same trajectory until 17:05 LT. The concentration of $N_{C\_CIP}$ and $N_{C\_FCDP}$ were 7.1 L$^{-1}$ and

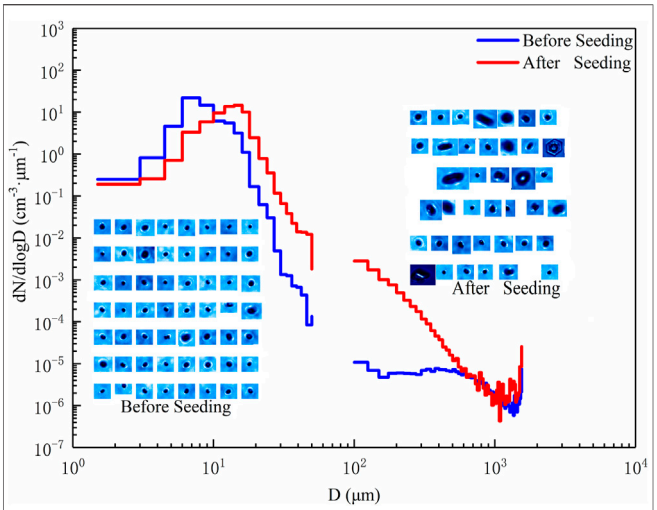


**FIGURE 7 |** Size distribution and phase state of particles in the cloud with abundant liquid water content before and after seeding.

160.3 cm$^{-3}$, on average, after two circles of detection in horizontal flight, which showed no significant difference from that in the vertical detection stage. As presented from the particle images, the cloud droplets and ice crystals coexisted before cloud seeding (**Figure 5A** and **Figure 5B**). The concentration of $N_{C\_FCDP}$ (**Figure 6B**) decreased from 160.3 to 129 cm$^{-3}$, on average, in about 7 to 8 min after seeding. When the plane arrived at the initial seeding position after a circle of flat flight, the concentration of $N_{C\_FCDP}$ reduced obviously to 88.94 cm$^{-3}$ in minimum, and the horizontal spatial distribution became more uniform. LWC showed obvious regional differences before seeding, and these differences were no longer evident during the seeding process. After seeding (16: 58–17:05 LT), LWC presented a significant decreasing trend, which indicated that the silver iodide ice nuclei were introduced into the clouds, and the supercooled water in the cloud was consumed through the Bergeron process. It can be seen from **Figure 6C** that the concentration of ice crystals at 4,550 m was distributed relatively uniformly before seeding, and the concentration fluctuates after seeding. The concentration of $N_{C\_CIP}$ increased slightly after seeding, and several peaks appeared (for example, $N_{C\_CIP}$ reached 52.2 L$^{-1}$ at 16:53:59 LT and 149.3 L$^{-1}$ at 17:00:52 LT). The concentration of ice crystals increased from 7.1 to 10 L$^{-1}$ on average. The maximum $N_{C\_CIP}$ reached 785.5 L$^{-1}$ especially in some specific regions. In other studies in central and southern Hebei Province, it was also found that the concentration of ice crystals in some areas increased to hundreds after seeding. Compared with the results of this study, the concentrations of ice crystals are of a similar magnitude (Dong et al., 2020; Dong et al., 2021). Moreover, **Figure 6E** shows that the proportion of LWC decreased significantly from 67 to 50% after seeding, indicating that part of the LWC was consumed. As a result, the temperature decreased to a certain extent, instead of increasing, due to latent heat released by condensation as we usually thought.

**Figure 7** shows the cloud particle size distribution measured by FCDP and CIP in the region with abundant LWC before (16: 34–16:43 LT) and after seeding (16:58–17:05 LT). Before seeding, the cloud showed a bimodal particle size distribution. The concentration of cloud particles showed a peak value of about 44.10 cm$^{-3}$ in the size range of 4.5–6 μm (droplets) and another peak value of 0.195 cm$^{-3}$ in the size range of 350–375 μm (ice particles). After seeding, the cloud showed a unimodal particle size distribution. The spectrum of small cloud particles measured by FCDP shifted to the right, and the peak value appeared in the range of 12–14 μm. Compared with cloud particle size distribution before seeding, the peak concentration was slightly decreased, which was about 29.28 cm$^{-3}$. The concentration of small cloud particles (1.5–4.5 μm) on the left side of the peak decreased by about 1 order of magnitude after seeding, but the concentration on the right side of the peak (6–50 μm) increased by about 1 order of magnitude. The changes of particle size distribution of the ice crystals measured by CIP were more obvious. The peak value of ice crystal number concentration at 350–375 μm disappeared after seeding, and the concentration of ice crystals at 100–675 μm increased significantly by about 1–2 orders of magnitude. Particularly, the ice crystal concentration at 100–125 μm increased from $2.73 \times 10^{-4}$ to $7.08 \times 10^{-2}$ cm$^{-3}$. Moreover, cloud particle images showed that flaky or columnar ice crystals appeared after seeding. From the analysis above, it can be concluded that the aircraft cloud seeding in this study presented a remarkable effect on mixed-phase cloud microphysical properties.

## SUMMARY

Based on the aircraft observations for a mixed-phase cloud over Xingtai, Hebei Province, China, on November 29, 2019, this study investigates the response of mixed-phase cloud microphysical properties to cloud seeding near cloud top. Several valuable findings have been found.

Through the weather background analysis before cloud seeding, the suitable dynamic and humidity conditions between 700 and 500 hPa led to the abundance of supercooled water in the cloud, which was consistent with the aircraft detection results, and had a certain guiding significance for the early identification about the existence of supercooled water.

The aircraft observations showed that the vertical distribution of cloud properties was not uniform. The vertical distribution of $N_{C\_FCDP}$ presented a multi-peak structure, with the maximum value that appeared at 3,322 m. In contrast, the maximum value of $N_{C\_CIP}$ appeared at 4,550 m in the upper part of the cloud. The height with peak LWC in the cloud was consistent with $N_{C\_CIP}$, which was also 4,550 m. Liquid water and ice water coexisted at the altitude range from 3,500 to 4,700 m. Therefore, the middle and upper parts of this cloud were considered as mixed phase with the coexistence of supercooled liquid water and ice crystals, illustrating the suitable cloud seeding condition at the height of 4,550 m.

Cloud microphysical properties had distinct responses to cloud seeding. After seeding, the concentration of ice crystals increased on average, and the size of ice crystals increased obviously at the same time. The horizontal variation of LWC in the cloud was no longer obvious, and LWC showed an obvious decreasing trend after seeding, which indicated that the silver iodide ice nuclei were introduced into the clouds through aircraft seeding and the supercooled water in the cloud was consumed. Similarly, the cloud particle size response to cloud seeding was also obvious with increased ice crystal sizes. In short, the phase state, size distribution, and LWC in the cloud all had an obvious response to the artificial introduction of silver iodide, indicating that cloud seeding played a significant effect in this study. The results of this study are helpful to understand the response mechanism of cloud microphysical properties to cloud seeding and provide an effective basis for the artificial precipitation enhancement effect.

## DATA AVAILABILITY STATEMENT

The original contributions presented in the study are included in the article/Supplementary Material, further inquiries can be directed to the corresponding author.

## AUTHOR CONTRIBUTIONS

CZ provided theoretical guidance. XD and RM carried out the flight observation mission. YC, FX, and JF helped with data analysis.

## FUNDING

This work was supported by the National Key Research and Development Program of China (Grant 2019YFC1510301), the Hebei province Key Research and Development project (Grants 20375402D and 19275420D), the National Natural Science Foundation of China (Grant 41925022), and the Key Laboratory of Meteorology and Ecological Environment of Hebei Province Project (Grant Z202002H).

## ACKNOWLEDGMENTS

Special appreciation is extended to the project participants for aircraft data acquisition. The NCEP/NCAR reanalysis data used for weather background analysis can be downloaded from https://psl.noaa.gov/data/gridded/data.ncep.reanalysis.pressure.html. The aircraft datasets and data description for this research can be downloaded publicly online from https://pan.bnu.edu.cn/l/KnHC01.

## REFERENCES

Andreae, M. O., and Rosenfeld, D. (2008). Aerosol-cloud-precipitation Interactions. Part 1. The Nature and Sources of Cloud-Active Aerosols. *Earth Sci. Rev.* 89 (1-2), 13–41. doi:10.1016/j.earscirev.2008.03.001

Baumgardner, D., Jonsson, H., Dawson, W., O'Connor, D., and Newton, R. (2001). The Cloud, Aerosol and Precipitation Spectrometer: a New Instrument for Cloud Investigations. *Atmos. Res.* 59-60, 251–264. doi:10.1016/S0169-8095(01)00119-3

Bergeron, T. (1935). On the physics of cloud and precipitation. Proc 5th Assembly of IUGG, Lisbon, 156–178.

Dong, X., Zhao, C., Yang, Y., Wang, Y., Sun, Y., and Fan, R. (2020). Distinct Change of Supercooled Liquid Cloud Properties by Aerosols from an Aircraft-Based Seeding experiment. *Earth Space Sci.* 7 (8), e2020EA001196. doi:10.1029/2020EA001196

Dong, X., Zhao, C., Huang, Z., Mai, R., Lv, F., Xue, X., et al. (2021). Increase of Precipitation by Cloud Seeding Observed from a Case Study in November 2020 over Shijiazhuang, China. *Atmos. Res.* 262 (5), 105766. doi:10.1016/j.atmosres.2021.105766

Emery, E., Miller, D., Plaskon, S., Strapp, W., and Lillie, L. (2004). "Ice Particle Impact on Cloud Water Content Instrumentation," in 42nd AIAA Aerospace Sciences Meeting and Exhibit, Reno, Nevada, January 5–8, 2004. doi:10.2514/6.2004-731

Faber, S., French, J. R., and Jackson, R. (2018). Laboratory and In-Flight Evaluation of Measurement Uncertainties from a Commercial Cloud Droplet Probe (CDP). *Atmos. Meas. Tech.* 11 (6), 3645–3659. doi:10.5194/amt-11-3645-2018

Hobbs, P. V. (1991). Twenty Years of Airborne Research at the University of Washington. *Bull. Amer. Meteorol. Soc.* 72 (11), 1707–1716. doi:10.1175/1520-0477(1991)072<1707:tyoara>2.0.co;2

Korolev, A., and Field, P. R. (2015). Assessment of the Performance of the Inter-arrival Time Algorithm to Identify Ice Shattering Artifacts in Cloud Particle Probe Measurements. *Atmos. Meas. Tech.* 8 (2), 761–777. doi:10.5194/amt-8-761-2015

Korolev, A. V., Strapp, J. W., Isaac, G. A., and Nevzorov, A. N. (1998). The Nevzorov Airborne Hot-Wire LWC-TWC Probe: Principle of Operation and Performance Characteristics. *J. Atmos. Ocean. Technol.* 15 (6), 1495–1510. doi:10.1175/1520-0426(1998)015<1495:tnahwl>2.0.co;2

Korolev, A., Strapp, J. W., Isaac, G. A., and Emery, E. (2013). Improved Airborne Hot-Wire Measurements of Ice Water Content in Clouds. *J. Atmos. Ocean. Techn.* 30 (9), 2121–2131. doi:10.1175/JTECH-D-13-00007.1

Lance, S., Brock, C. A., Rogers, D., and Gordon, J. A. (2010). Water droplet calibration of the Cloud Droplet Probe (CDP) and in-flight performance in liquid, ice and mixed-phase clouds during ARCPAC. *Atmos. Meas. Tech.* 3 (6), 1683–1706. doi:10.5194/amt-3-1683-2010

Lawson, R. P., Baker, B. A., Schmitt, C. G., and Jensen, T. L. (2001). An Overview of Microphysical Properties of Arctic Clouds Observed in May and July 1998 during FIRE ACE. *J. Geophys. Res.* 106 (D14), 14989–15014. doi:10.1029/2000JD900789

Li, Z., Lau, W. K. M., Ramanathan, V., Wu, G., Ding, Y., Manoj, M. G., et al. (2016). Aerosol and Monsoon Climate Interactions over Asia. *Rev. Geophys.* 54 (4), 866–929. doi:10.1002/2015RG000500

Lohmann, U., and Feichter, J. (2005). Global Indirect Aerosol Effects: a Review. *Atmos. Chem. Phys.* 5 (3), 715–737. doi:10.5194/acp-5-715-2005

Norris, J. R. (2005). Multidecadal Changes in Near-Global Cloud Cover and Estimated Cloud Cover Radiative Forcing. *J. Geophys. Res. Atmos.* 110. doi:10.1029/2004JD005600

Pokharel, B., and Geerts, B. (2016). A Multi-Sensor Study of the Impact of Ground-Based Glaciogenic Seeding on Clouds and Precipitation over Mountains in Wyoming. Part I: Project Description. *Atmos. Res.* 182, 269–281. doi:10.1016/j.atmosres.2016.08.008

Pokharel, B., Geerts, B., Jing, X., Friedrich, K., Ikeda, K., and Rasmussen, R. (2017). A Multi-Sensor Study of the Impact of Ground-Based Glaciogenic Seeding on Clouds and Precipitation over Mountains in Wyoming. Part II: Seeding Impact Analysis. *Atmos. Res.* 183, 42–57. doi:10.1016/j.atmosres.2016.08.018

Pruppacher, H. R., and Klett, J. D. (2010). "Microstructure of Atmospheric Clouds and Precipitation," in *Microphysics of Clouds and Precipitation* (Dordrecht: Springer), Vol. 18, 10–73. Atmospheric and Oceanographic Sciences Library. doi:10.1007/978-0-306-48100-0_2

Ramanathan, V., Cess, R. D., Harrison, E. F., Minnis, P., Barkstrom, B. R., Ahmad, E., et al. (1989). Cloud-radiative Forcing and Climate: Results from the Earth

Radiation Budget experiment. *Science* 243 (4887), 57–63. doi:10.1126/science.243.4887.57

Schaefer, V. J. (1946). The Production of Ice Crystals in a Cloud of Supercooled Water Droplets. *Science* 104 (2707), 457–459. doi:10.1126/science.104.2707.457

Sun, Y., Zhao, C., Su, Y., Ma, Z., Li, J., Letu, H., et al. (2019). Distinct Impacts of Light and Heavy Precipitation on PM 2.5 Mass Concentration in Beijing. *Earth Space Sci.* 6 (10), 1915–1925. doi:10.1029/2019EA000717

Tao, W., Chen, J., Li, Z., Wang, C., and Zhang, C. (2012). Impact of Aerosols on Convective Clouds and Precipitation. *Rev. Geophys.* 50. doi:10.1029/2011RG000369

Tessendorf, S. A., Ikeda, K., Weeks, C., Rasmussen, R., Wolff, J., and Xue, L. (2020). An Assessment of Winter Orographic Precipitation and Cloud-Seeding Potential in Wyoming. *J. Appl. Meteorol. Climatol.* 59 (7), 1217–1238. doi:10.1175/JAMC-D-19-0219.1

Vonnegut, B. (1947). The Nucleation of Ice Formation by Silver Iodide. *J. Appl. Phys.* 18, 593–595. doi:10.1063/1.1697813

Wang, L., Yin, Y., Lunge, L. I., Wang, X., and Fugang, L. I. (2013). Analyses on Typical Autumn Multi-Layer Stratiform Clouds over the Sanjiangyuan National Nature Reserve with Airborne Observations. *Chin. J. Atmos. Sci.* 37 (28), 1038–1058. doi:10.1016/j.atmosenv.2009.04.022

Yang, X., Zhao, C., Guo, J., and Wang, Y. (2016a). Intensification of Aerosol Pollution Associated with its Feedback with Surface Solar Radiation and Winds in Beijing. *J. Geophys. Res. Atmos.* 121 (8), 4093–4099. doi:10.1002/2015JD024645

Yang, X., Zhao, C., Zhou, L., Wang, Y., and Liu, X. (2016b). Distinct Impact of Different Types of Aerosols on Surface Solar Radiation in China. *J. Geophys. Res. Atmos.* 121 (11), 6459–6471. doi:10.1002/2016JD024938

Yang, X., Zhou, L., Zhao, C., and Yang, J. (2018). Impact of Aerosols on Tropical Cyclone-Induced Precipitation over the mainland of China. *Climatic Change* 148, 173–185. doi:10.1007/s10584-018-2175-5

Yang, Y., Zhao, C., Dong, X., Fan, G., Zhou, Y., Wang, Y., et al. (2019). Toward Understanding the Process-Level Impacts of Aerosols on Microphysical Properties of Shallow Cumulus Cloud Using Aircraft Observations. *Atmos. Res.* 221, 27–33. doi:10.1016/j.atmosres.2019.01.027

Zhao, C., Yang, Y., Fan, H., Huang, J., Fu, Y., Zhang, X., et al. (2020). Aerosol Characteristics and Impacts on Weather and Climate over the Tibetan Plateau. *Natl. Sci. Rev.* 7 (3), 492–495. doi:10.1093/nsr/nwz184

Zhao, C., and Garrett, T. J. (2015). Effects of Arctic Haze on Surface Cloud Radiative Forcing. *Geophys. Res. Lett.* 42 (2), 557–564. doi:10.1002/2014GL062015

Zhao, X., Sun, Y., Zhao, C., and Jiang, H. (2020). Impact of Precipitation with Different Intensity on PM 2.5 over Typical Regions of China. *Atmosphere* 11 (9), 906. doi:10.3390/atmos11090906

Zhao, Z., and Lei, H. (2014). Aircraft Observations of Liquid and Ice in Midlatitude Mixed-phase Clouds. *Adv. Atmos. Sci.* 31, 604–610. doi:10.1007/s00376-013-3083-2

Zhao, C., Lin, Y., Wu, F., Wang, Y., Li, Z., Rosenfeld, D., et al. (2018). Enlarging Rainfall Area of Tropical Cyclones by Atmospheric Aerosols. *Geophys. Res. Lett.* 45 (16), 8604–8611. doi:10.1029/2018GL079427

Zhao, C., Zhao, L., and Dong, X. (2019). A Case Study of Stratus Cloud Properties Using In Situ Aircraft Observations over Huanghua, China. *Atmosphere* 10 (1), 19. doi:10.3390/atmos10010019

**Conflict of Interest:** The authors declare that the research was conducted in the absence of any commercial or financial relationships that could be construed as a potential conflict of interest.

**Publisher's Note:** All claims expressed in this article are solely those of the authors and do not necessarily represent those of their affiliated organizations or those of the publisher, the editors, and the reviewers. Any product that may be evaluated in this article or claim that may be made by its manufacturer is not guaranteed or endorsed by the publisher.

frontiers | Frontiers in Environmental Science

ORIGINAL RESEARCH
published: 01 April 2022
doi: 10.3389/fenvs.2022.855813

# Aircraft Observation of a Two-Layer Cloud and the Analysis of Cold Cloud Seeding Effect

*Xiaobo Dong[1,2], Xiaoshen Sun[2], Fei Yan[2]*, Jiannan Zhang[2], Shuyi Wang[2], Min Peng[2] and Haipeng Zhu[2]*

[1]Key Laboratory of Meteorology and Ecological Environment of Hebei Province, Shijiazhuang, China, [2]Hebei Weather Modification Center, Shijiazhuang, China

A two-layer stratus cloud was developed under the weather of an upper-level trough and return flow in North China. King-air 350 meteorological aircraft was designated to acquire the microphysical characteristics of this cloud. Within the lower-level warm cloud, the width of cloud particle size distribution (PSD) grew larger from the cloud top to the base. The particles in the warm cloud were developed mostly through collision–coalescence process. Supercooled liquid water (SLW) was detected abundantly in the upper layer cold cloud, which was developed under the westerly trough. In this study, the cold cloud in the upper level was targeted for AgI seeding. After seeding, the PSD of both cloud droplets and ice crystals were broadened as SLW was consumed and developed into ice crystals.

**Keywords: supercooled liquid water, aircraft observation, cloud seeding, stratus cloud, precipitation**

OPEN ACCESS

***Edited by:***
*Honglei Wang,*
*Nanjing University of Information Science and Technology, China*

***Reviewed by:***
*Liang Yuan,*
*Chengdu University of Information Technology, China*
*Jing Duan,*
*China Meteorological Administration (CMA), China*

****Correspondence:***
*Fei Yan*
*yanfei_11@126.com*

***Specialty section:***
*This article was submitted to Atmosphere and Climate, a section of the journal Frontiers in Environmental Science*

***Received:*** *16 January 2022*
***Accepted:*** *15 February 2022*
***Published:*** *01 April 2022*

***Citation:***
*Dong X, Sun X, Yan F, Zhang J, Wang S, Peng M and Zhu H (2022) Aircraft Observation of a Two-Layer Cloud and the Analysis of Cold Cloud Seeding Effect. Front. Environ. Sci. 10:855813. doi: 10.3389/fenvs.2022.855813*

## INTRODUCTION

Water depletion has been an arising problem in North China and put negative effects on climate, agriculture, and air pollution (Kendy et al., 2004; Fan et al., 2012; Chen et al., 2013; Yuan and Shen, 2013). For the past decades, the Hebei Weather Modification Office has implemented abundant cloud seeding experiments to increase rainfall and snowfall, preferably into reliable ground water resources. Based on field experiments, stratiform clouds were the main rainfall sources during the spring and autumn seasons. These precipitation clouds were always connected with large-scale weather systems and consisted of several cloud (rain) bands (Zhou, 2004). Stratiform clouds have been the most targeted clouds in North China for artificial rainfall enhancement (Zhao and Lei, 2008; Guo et al., 2015).

Stratus clouds are normally categorized as warm and cold clouds. A detailed microphysical mechanism for both warm and cold clouds can be found in Flossmann *et al.* (2019). Warm clouds were packed with water droplets that can grow into falling precipitation particles mainly through collision–coagulation, especially when large cloud droplets already existed (Kenneth and Harry, 1993). Hu *et al.* (1983) investigated the precipitation mechanism of warm clouds by a one-dimension time-dependent numerical model. They pointed out that raindrop growth through randomly gravitational collision required the vertical depth of cloud to be thicker than 1 km. For cold clouds that vertically develop above the freezing level, the Wegener–Bergeron–Findeisen (WBF) process was applied, and it explained cloud particle transformation (Wegener, 1911; Bergeron, 1935; Findeisen, 1938). Precipitation can be generated through water vapor diffusion as well as the collision–coalescence and riming of ice crystals (Flossmann et al., 2019). The "seeder–feeder" mechanism was first brought up by Bergeron to explain orographic cloud seeding (Bergeron, 1960) but also laid the theoretical foundation for stratus cloud seeding. Gu (1980) proposed a conceptual model for precipitation particle formation within stratus clouds. The vertical structure of a stratiform

cloud was layered into ice-phase layer, mixed layer with both ice and liquid water, and liquid water layer. In addition to the "seeder–feeder" structure, You *et al.* (2002) discovered a dry layer between the two-layer clouds in North China. Yang *et al.* (2010) simulated a stratiform precipitation in Jilin Province by a single-dimension cloud classification model. Within the frontal stratus cloud, the ice crystal layer acted as a "seeder" layer to provide ice crystals for the lower mixed layer. In their findings, ice crystals thinner than 300 μm were the most active particles, and water droplets larger than 100 μm and partially melting ice crystals were both fueled into the mixed layer. Large particles were proven to be the most competent for collision and collection of surrounding small cloud particles in the warm layer (Yang et al., 2010).

According to the WBF process (Wegener, 1911; Bergeron, 1935; Findeisen, 1938), in the mixed layer, the temperature was below zero, and ice crystals and water vapor coexisted. When saturated vapor pressure was between the value of ice and water, vapor condensed over ice crystals because the equilibrium vapor saturation pressure was lower over the icy surface than the water surface (Rauber et al., 2019). Therefore, water drops continuously evaporated until completely absent. These formed ice crystals would "compete" to capture the water drops and consume water content. Consequently, catalysts like solid carbon dioxide and silver iodide (AgI) were released into cold clouds that can either increase the concentration of aerosol particles (INP) or freeze SLW (Flossmann et al., 2019). The mass of ice increased to compensate for available water vapor and SLW, finally enhancing the precipitation probability. Researchers worldwide have put efforts into the exploration of stratus clouds by high spatial and temporal resolution airborne particle measurement system (PMS), satellite, and radar for comprehensive observations of stratified cloud structures. Geerts *et al.* (2010) adopted an airborne Doppler radar to detect the change of wintertime orographic clouds after AgI seeding. Intensified radar echo near the ground was observed as strong evidence for increased ground precipitation. Cai *et al.* (2013) compared the number of concentration variations of cloud particles and ice crystals before and after seeding along the flight trajectory. They concluded that clouds with higher SLW content were confirmed to be more affected by the seeding. AgI acted as ice-nucleating agents for glaciogenic seeding, and heterogeneous ice nucleation was mainly though immersion freezing, condensation freezing, and contact freezing (Marcolli et al., 2016). AgI agents were released into the SLW layer to accelerate these water droplets to participate in ice nucleation and ice crystal growth. As ice crystals were falling, they continually grew into large precipitation particles through the process of riming (Dong et al., 2021), aggregation (Breed et al., 2014), or collision–coalesce (Dong et al., 2020).

Cloud seeding projects have been carried out for mountainous snowfall like Wyoming Weather Modification Pilot Project (WWMPP, Breed et al., 2014) and Seeded and Natural Orographic Wintertime Clouds: The Idaho Experiment (SNOWIE, French et al., 2018). When evaluating and quantifying cloud seeding, ground radar was one of the most obvious approaches to evaluate and confirm airborne AgI seeding (Rauber et al., 2019; Friedrich et al., 2020; Wang et al., 2021). Recent attempts on evaluating the cloud seeding included coherent Doppler wind lidar (Yuan et al., 2021), satellite, weather radar, and disdrometer (Wang et al., 2021) and Weather Research and Forecasting model (Liu et al., 2021). Similar to orographic cloud seeding, stratus cloud seeding shall also follow the hypothesis from Rauber *et al.* (2019). The timing and the location to release artificial INP were the key to perform an effective cloud seeding. However, synoptic weather background shall not be neglected when performing the cloud seeding. Even though the aircraft was mobile and would easily locate the optimal microphysical condition inside the cloud, airborne AgI seeding still required verification from abundant field experiments.

In this study, we conducted a cloud seeding experiment together with cloud detection to a two-layer stratus cloud. The vertical structure of both warm and cold cloud was explored, and the microphysical response of cloud seeding was analyzed.

Data and process methods are described in "Data and Methods", followed by synoptic weather in "Synoptic Weather Analysis". The sections "Analysis and Results" and "Conclusion" show the details of the result analysis and conclusion.

# DATA AND METHODS

## Seeding Experiment

We carried out an airborne seeding experiment after the vertical detection to the clouds on May 15, 2021 over Shijiazhuang, Hebei Province (**Figure 1**). Airborne AgI was released into the cloud for potential rainfall enhancement. Theoretically, a single seeding agent contains 27 g AgI. The mean size of AgI is 0.1 μm (Flossmann et al., 2019). The same approach can be found in previous studies (Dong et al., 2020; Dong et al., 2021). The cloud seeding experiment lasted from 12:02 to 14:32 UTC (20:02–22:32 in local time, UTC time as follows) over Luancheng District of Shijiazhuang.

The terrain altitude and aircraft trajectory above the seeding targeted region is shown in **Figure 1**. The research plane took off from Zhengding Airport at 12:09 and flew southward at 2,400 m towards the target location. In the experiment zone, the aircraft first spiraled upwards from 900 to 6,000 m with a radius of 5 km to acquire the vertical profile of the stratiform cloud. SLW was detected at the height of 5,200 m, and afterwards seeding agents were released into the clouds at this altitude. The flight flew elliptically with a longitudinal and latitudinal trajectory of 6 and 15 km. In total, 18 AgI agents were released during the experiment, and each 6-AgI agent was ignited at 13:23, 13:29, and 13:36. After seeding, the plane continued circling throughout the clouds at 5,200 m for further detection of catalyzed physical response.

## Instrumentation

The "King Air" 350 research aircraft, belonging to the Hebei Weather Modification Center, was outfitted for cloud detection and cloud seeding. Details on airborne instruments and related parameters are listed in **Table 1**. The PMS was mounted on this research aircraft as well as aircraft integrated meteorological measurement system (AIMMS-20) with 20-Hz detection frequency, remote temperature probe, Nevzorov hotwire probe,

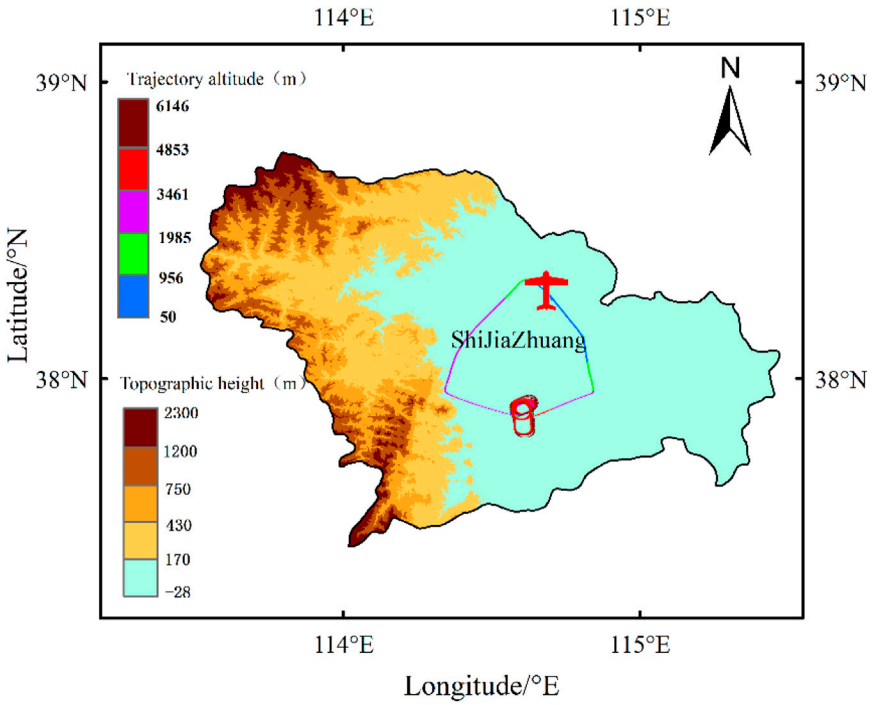


**FIGURE 1 |** The altitudinal terrain and flight trajectory in the experiment zone on May 15, 2021.

**TABLE 1 |** Detailed instruments and related parameters during the seeding experiment.

| Instrument | Detection parameters | Detection range | Manufacturer |
|---|---|---|---|
| FCDP | Droplet size distribution | 2–50 μm | Stratton Park Engineering Company (SPEC) |
| AIMMS-20 | Meteorology (temperature, humidity, wind) | – | Advanced Airborne Measurement Solutions |
| CIP | Particle shadow image at 25-μm pixel resolution | 25–1,550 μm | Droplet Measurement Technologies (DMT) |
| HVPS | Precipitation particle size distribution | 150–19,200 μm | SPEC |
| Remote Total Temperature | Ambient air temperature | -54–71°C | GOODRICH |
| Nevzorov Hotwire | Liquid water content and total water content | 1.5–3 g/m$^3$ | SkyPhysTech, Inc |
| CPI | Cloud particle image | 2–3,000 μm | SPEC |

and global positioning system. The PMS consists of three particle size detectors, including a fast cloud droplet probe (FCDP), cloud imager probe (CIP), cloud particle imager (CPI), and high-volume precipitation spectrometer (HVPS). FCDP can measure cloud particles ranging from 2 to 50 μm in diameter with an uncertainty of 20% (Lance et al., 2010; Faber et al., 2018). The CIP detects both cloud droplets and ice crystals from 25 to 1,500 μm (Lawson, 2011). The HVPS probe can detect even larger ice crystals and raindrops, covering the range of 150–19,200 μm. The CPI imager can capture images of cloud particles, water droplets, and ice crystals. Nevzorov hotwire can provide both liquid water content (LWC) and total water content (TWC) data with 15% inaccuracy (King et al., 1978). All probes were checked and calibrated before cloud detection and cloud seeding.

## Data Processing Method

As recommended by previous studies (Yang et al., 2019; Zhao et al., 2019), the last size bin of FCDP and the first three bins of CIP are all excluded due to large uncertainties. PSD was retrieved from original FCDP data from 2 to 50 μm. For large particles, the size bins were chosen between 100 and 1,500 μm for the CIP probe, where small cloud particles were excluded. The particle diameter range within 150–19,200 μm was set for the HVPS probe. We followed with a previous method to differ ice crystals and cloud droplets (Dong et al., 2020; Dong et al., 2021). A 100-μm threshold is introduced such that particles in cold clouds larger than 100 will be defined as ice crystals; otherwise, they are cloud droplets. The time interval for each airborne prober data is 1 s.

The effective radius $r_e$ and number concentration $N_d$ of cloud particles are calculated based on the cloud PSD as follows:

$$r_e = \frac{\int r^3 n(r) dr}{\int r^2 n(r) dr} = \frac{\sum N_{ci} r_i^3}{\sum N_{ci} r_i^2}$$

$$N_d = \int n(r) dr = \sum N_{ci}$$

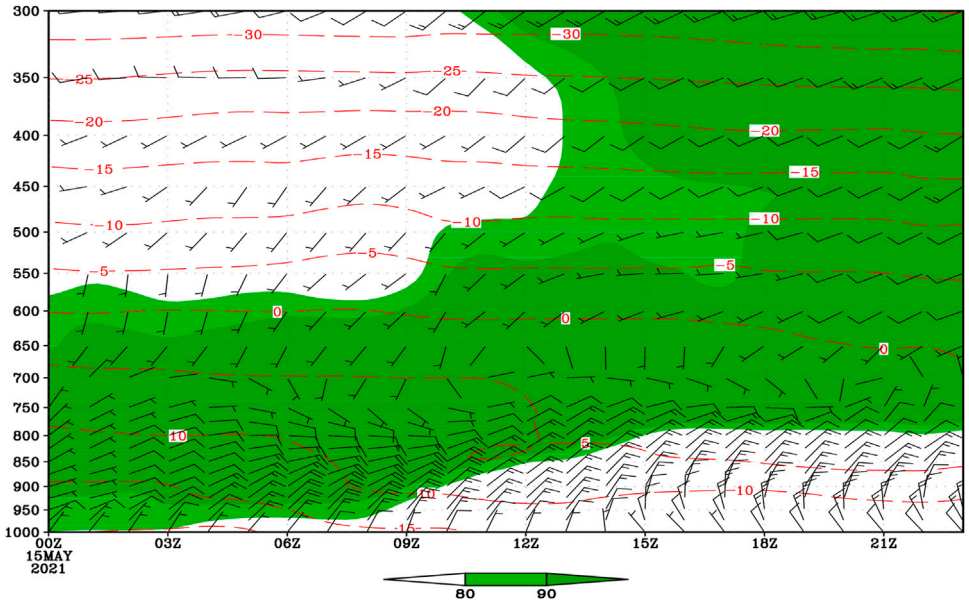


**FIGURE 2 |** The temporal variation of relative humidity (contour), temperature (dotted line), and wind on May 15, 2021 in Luancheng District of Shijiazhuang.

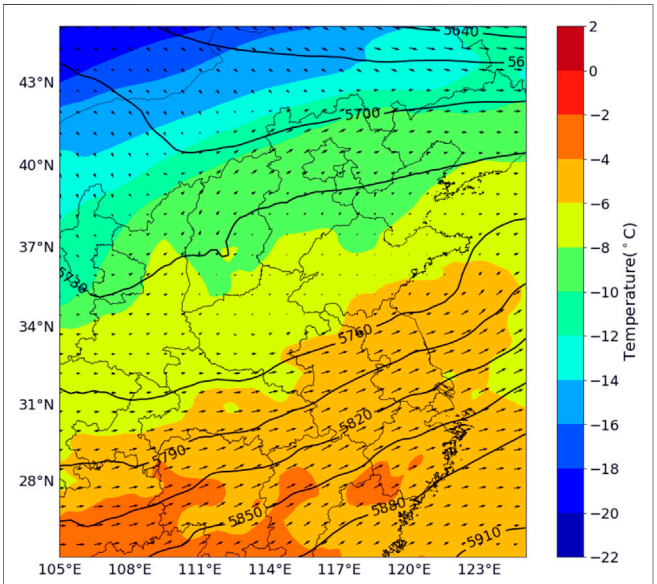


**FIGURE 3 |** Geopotential height (black contour line, units: pm), temperature (shaded, unit: °C), and wind field (arrows) at 500 hPa 12:00 on May 15, 2021.

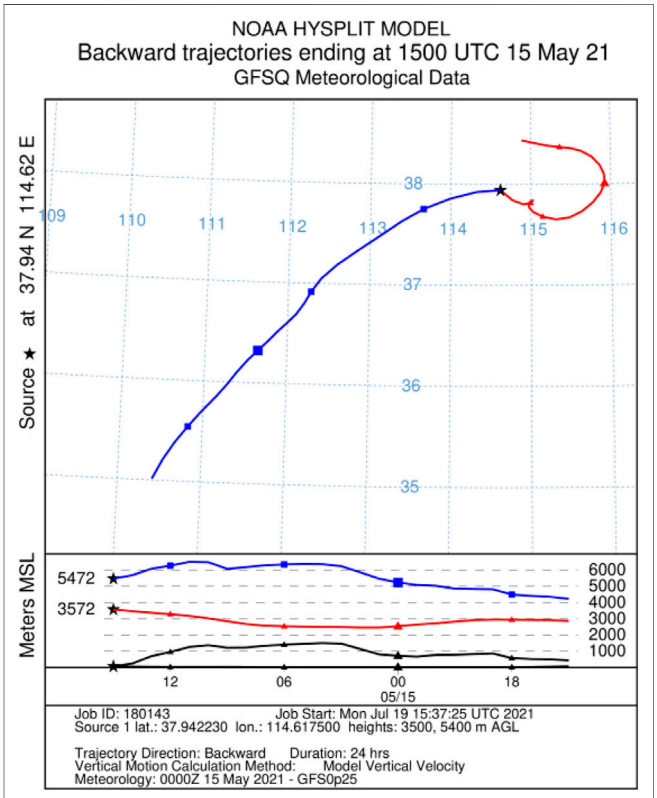


**FIGURE 4 |** The 24-h backward trajectory of cloud mass in the experiment zone simulated from the HYSPLIT model starting from 15:00 May 15, 2021 (black star). The red and the blue lines represent the trajectory of warm and cold cloud mass at 3,572 and 5,472 m, respectively.

where $n(r)$ denotes the cloud PSD, and $N_{ci}$ and $r_i$ correspondingly represent the number concentration and mean diameter of cloud droplets at the $i$-th size bin. The merged cloud particle spectrum is therefore derived from FCDP, CIP, and HVPS prober data, covering the whole size range of both droplets and ice crystals.

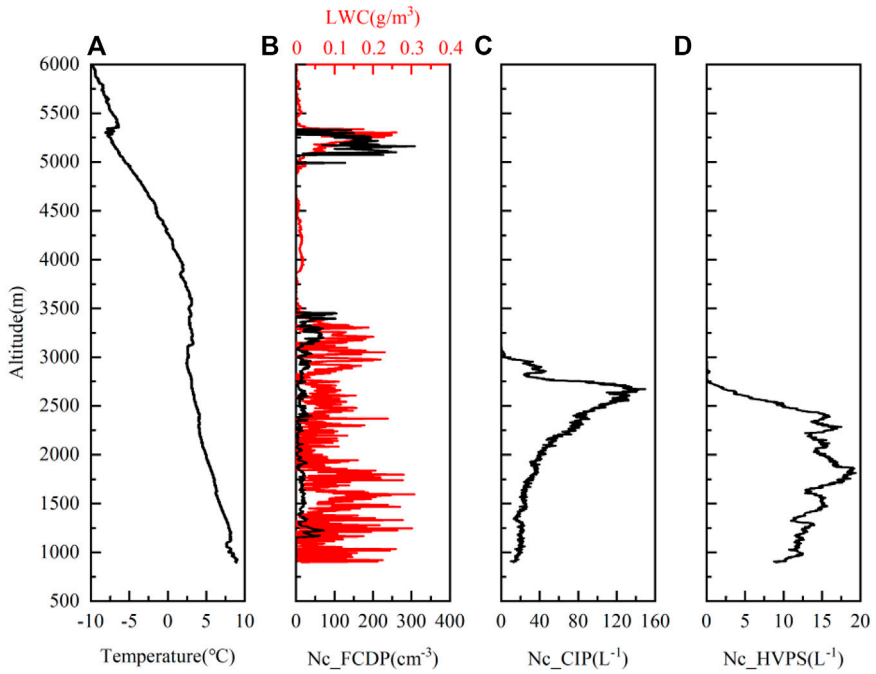


**FIGURE 5 |** The vertical distribution of **(A)** atmosphere temperature, **(B)** cloud particle number concentration measured by fast cloud droplet probe and liquid water content measured by Nevzorov, **(C)** cloud particles larger than 100 μm number concentration measured by cloud imager probe, and **(D)** cloud particle number concentration measured by a high-volume precipitation spectrometer.

## SYNOPTIC WEATHER ANALYSIS

According to daytime weather analysis and observations (**Figure 2**), wide-range, stable, low clouds were developed in the southern part of Hebei Province. The low clouds were below 4 km and consecutively brought warm cloud precipitation under the influence of east wind and warm shear at 700 hPa. Meanwhile, no high cloud was observed over the experiment area due to the influence of a weak ridge. Near dawn, the aircraft observed clouds around 500 hPa under the influence of an upper trough (**Figure 3**).

HYSPLIT model was employed to calculate the estimated trajectory of cloud air mass 24 h prior to the experiment zone on May 15, 2021 (**Figure 4**). A return flow was notable at 3,572 m, and at 5472 m an air mass approached from the southwest. Aircraft detection was in the beginning period of a high-level trough and the last stage of a return flow. Under the interactive impact of two cloud masses, the stratus cloud was layered with low-level warm clouds and high-level cold clouds.

## ANALYSIS AND RESULTS

### Vertical Structure of "Two-Layer" Clouds

The vertical profiles of temperature (temperature probe), liquid water content (Nevzorov), and cloud particle number concentration (FCDP, CIP, and HVPS) are shown in **Figure 5**. The research aircraft spiraled upwards from 900 to 6,000 m, with a cycling radius of 5 km. During the climbing, the temperature dropped from 9°C (900 m) to −9.7°C (6,000 m), and 0°C was recorded at 4,262 m. Entirely 3 thermal inversion layers were detected, including 1,100–1,200 m, 3,100–3,500 m, and near 5,400 m.

To define cloud boundaries, we required the FCDP number concentration to be greater than 10 $cm^{-3}$ to be considered "in-cloud". From the FCDP probe, the vertical distribution of cloud particle number concentration was notably divided into two layers, roughly representing the two-layer cloud. The lower layer was defined as the warm cloud, spread from 1,100 to 3,500 m. In this layer, the cloud particle number concentration reached a maximum of 105.9 $cm^{-3}$ according to the FCDP probe (small cloud particles), while the temperature varied from 2.9 to 8.2°C. The other layer was a cold cloud located at an altitude of 5,100–5,300 m, and the largest cloud particle number concentration was 309.3 $cm^{-3}$, with temperature ranging from −6 to −7.5°C. The highest liquid water content in the warm and cold layer was 0.308 and 0.26 $g/m^3$ at 1,596 and 5,250 m, respectively. Supercooled water droplets existed in the upper-level cold cloud. Particles larger than 100 μm are captured by the CIP probe, and the highest number concentration is 149.86 $L^{-1}$ at 2,671 m in the warm layer but only 0.2 $L^{-1}$ in the cold layer. For even larger particles, within the warm clouds, the number concentration measured by the HVPS probe is 19.4 $L^{-1}$ at 1,811 m but less than 0.2 $L^{-1}$ in the cold layer. From these observations, cloud droplets and raindrops were mostly found in low-level warm layers, while supercooled water droplets were in high-level cold clouds. However, in the high-level cloud, ice crystals were scarce, and cloud seeding was logically favorable.

Near the top of warm cloud (around 3,500 m), cloud particles were only detected by the FCDP probe, and the highest

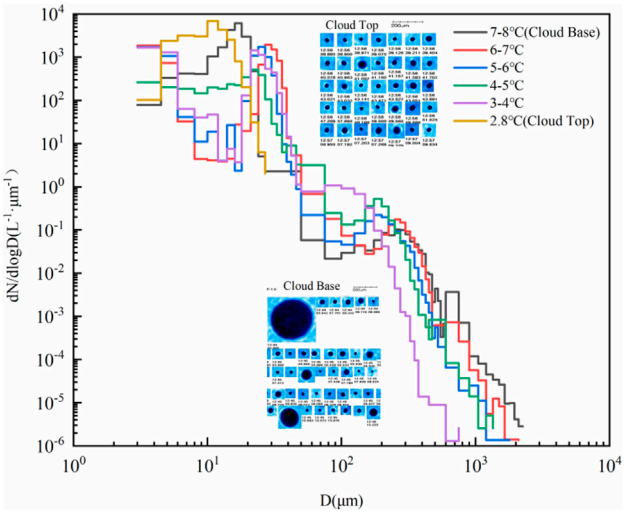


**FIGURE 6 |** Cloud particle size distribution and cloud particle images in the warm layer from 1,158 to 3,456 m. The colored lines represent cloud particle distribution under different temperatures.

concentration of cloud particle was 100 $cm^{-3}$, while both CIP and HVPS detected almost nothing. At the top of warm cloud, only cloud droplets smaller than 50 μm existed according to the FCDP probe. The LWC content was also less than 0.1 $g/m^3$. Below 3,000 m, the cloud particle number concentration was reduced for the FCDP probe but increased for both the CIP and HVPS probes. The CIP and HVPS probes can both detect cloud particles larger than 100 μm, and the highest number concentration reached was at 2,700 and 1,800 m, respectively. Meanwhile, the LWC content increased. This indicated the growth of small cloud droplets into large droplets through collision–coalescence. Near the warm cloud base, the small cloud droplets detected by FCDP increased, and the large cloud droplets or raindrop number concentration detected by CIP and HVPS appeared to follow a decreasing trend due to the break-up and evaporation of large droplets. Afterwards the large droplets grew into raindrops, which would fall outside the cloud. The decrease of the number concentration of CIP and HVPS was also possibly from the larger velocity of raindrops.

The cloud PSD in the lower warm cloud was retrieved from the FCDP, CIP, and HVPS probes (**Figure 6**). The PSD combined with temperatures and CPI images is shown in **Figure 6**. The cloud top reached up to 3,456 m, with a temperature of 2.8°C. The particle spectrum was narrow, and the particle size ranged from 3 to 27 μm, where the peak size was 10 μm. Near the cloud top, only cloud droplets were observed. In order from the cloud top towards the base, the diameters of the cloud droplets at the highest number concentration with corresponding temperature are listed as follows: 21 μm (temperature 3–5°C), 24 μm (5–6°C), 27 μm (6–7°C), and 16 μm (1,158 m at cloud base, 8.2°C). The maximum diameters for raindrops with corresponding temperature were 1,050 μm (temperature 3–4°C), 1,350 μm (4–5°C), 2,100 μm (5–7°C), and 2,250 μm (cloud base, 8.2°C).

In the warm cloud, the cloud particle spectrum spanned wider from the cloud top to the base as the temperature rose higher. While falling, these cloud droplets enlarged through collision–coalescence. The CPI probe captured both small and large cloud droplets near the cloud base. As shown in **Figure 6**, raindrops larger than 200 μm only existed in the cloud base, while in the top cloud the droplets were less than 100 μm. The broadening of the large-particle spectrum indicated the growth of large droplets into raindrops. This could explain why the HVPS concentration gradually dropped near the cloud base. Subject to entrainment and evaporation (Yamaguchi and Randall, 2008), the diameter of cloud droplets was comparatively smaller near the cloud top than the cloud base.

## Microphysical Response for Cold Cloud Seeding

At an altitude of 5,200 m, the aircraft flew several loops for cloud seeding experiments and *in situ* cloud microphysical detection. The elliptical flight trajectory was 15-km south–north long and 6-km east–west wide. A single whole circuit took approximately 5 min. **Figure 7** demonstrates the real-time track of a research aircraft during seeding, overlaid with cloud particle concentration detected by FCDP. At this altitude, the horizontal wind speed and the wind direction were 4.8 m/s and 210° as the average temperature was −6.9°C. As shown in **Figure 7**, the cloud particle concentration that was less than 10 $cm^{-3}$ (black dots) indicated that the aircraft was outside of the cloud. The airborne seeding was counter-clockwise from A to B.

**Figure 8** illustrates the temporal variation of cloud particle number concentration, LWC, and TWC before and after the cloud seeding. In total, 18 AgI seeding agents were activated at 13: 23, 13:29, and 13:36, with 6 agents at each time. Each AgI agent was estimated for a life of 5 min. During the airborne seeding, from 13:23 to 13:27, no change was detected, and the number concentration of cloud particles remained unchanged. This is because the seeding agent was just released into the cloud, and the cloud droplets were not responsive yet. The average number concentration and LWC content were 167 $cm^{-3}$ and 0.124 $g/m^3$, and the maximum values were 274.79 $cm^{-3}$ and 0.211 $g/m^3$. The change of LWC content was

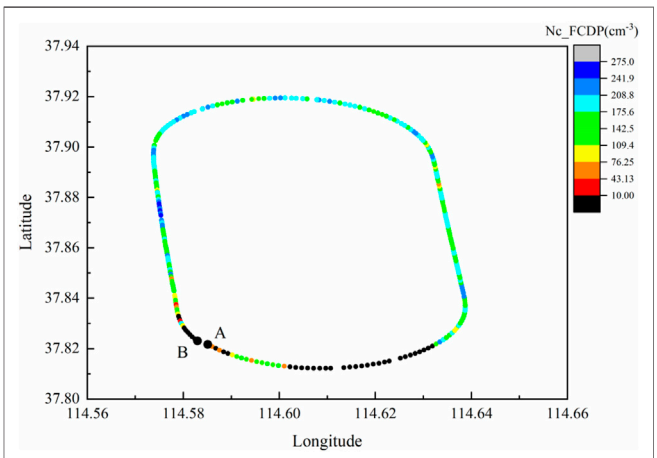


**FIGURE 7 |** The flight trajectory at 5,200 m for the cloud seeding with cloud particle number concentration retrieved from fast cloud droplet probe. Black marks denote that the aircraft was outside the cloud.

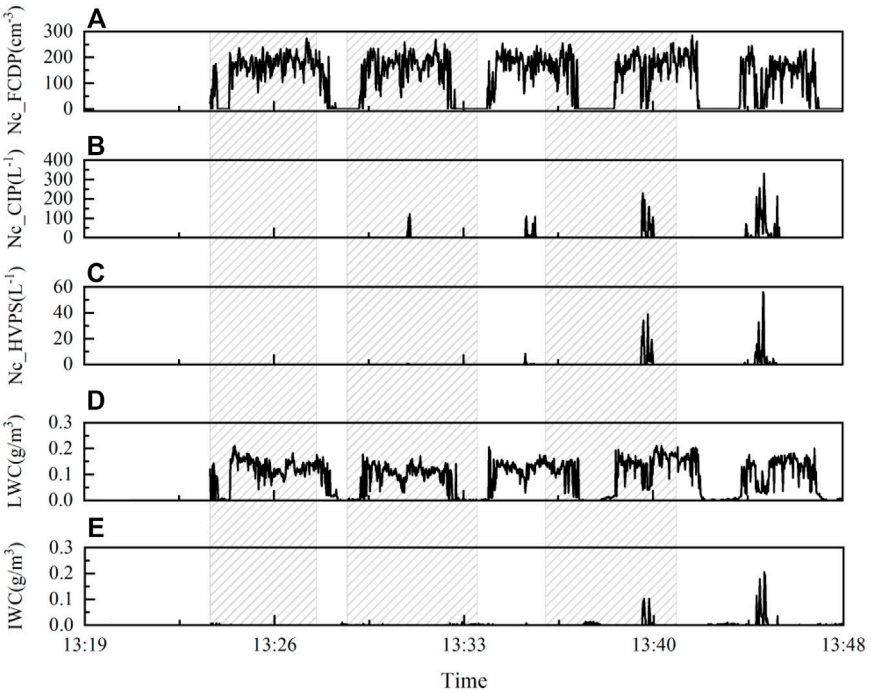


**FIGURE 8 |** The temporal change of cloud particle number concentration measured by fast cloud droplet probe, cloud imager probe, and high-volume precipitation spectrometer as well as liquid water content and ice water content measured by Nevzrov hotwire, where the seeding periods were marked as shaded areas.

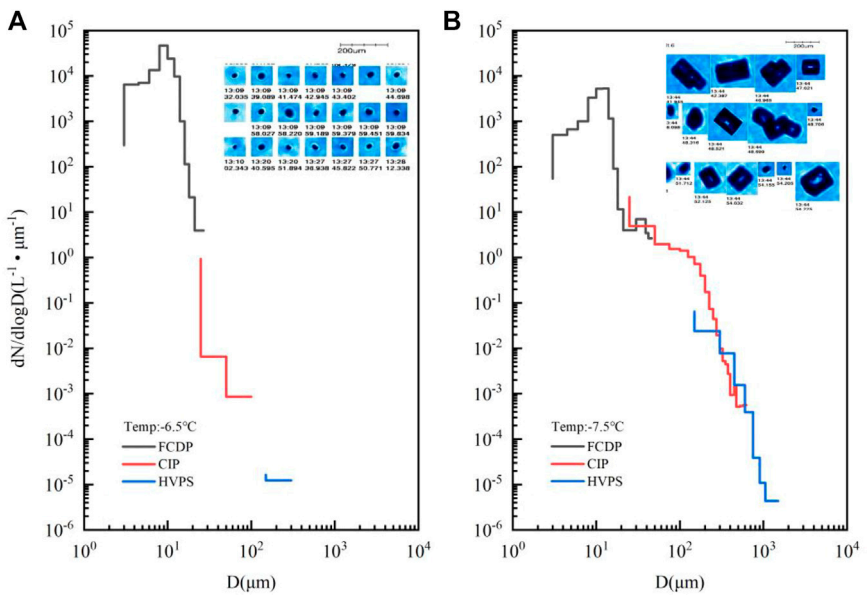


**FIGURE 9 |** The cloud particle spectrum and particle images before [**(A)**, 13:09] and after seeding [**(B)**, 13:44]. The black line denotes cloud particle measured by fast cloud droplet probe, the red line denotes ice crystals measured by cloud imager probe, and the blue line denotes ice crystals measured by HVPS. The particle images captured by the cloud particle imager are shown on the upper right side of the figure.

almost consistent with the FCDP concentration. The zero value of FCDP concentration and LWC content indicated that the aircraft was outside the cloud. After seeding, the number concentration of cloud droplets dropped dramatically at times 13:31, 13:36, 13:40, and 13:45. Meanwhile, ice crystals measured by CIP and HVPS both increased notably from 0 $L^{-1}$ before the seeding into 332.53 $L^{-1}$ (13:45:01) and

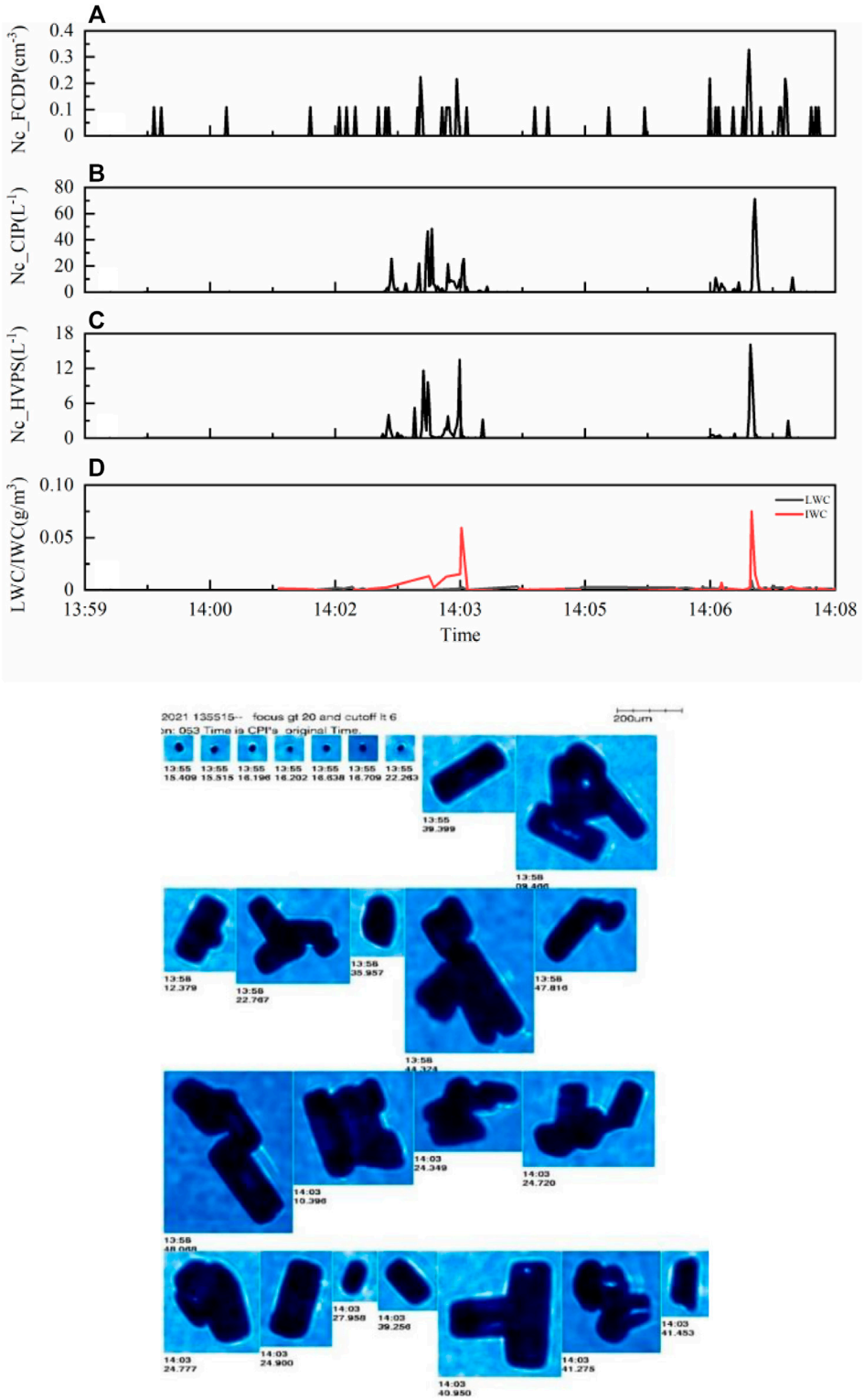


**FIGURE 10 |** The temporal change of cloud particle number concentration measured by fast cloud droplet probe **(A)**, cloud imager probe **(B)**, high-volume precipitation spectrometer **(C)**, and liquid water content and ice water content **(D)** measured by Nevzorov hotwire and particle images (below) at 4,700 m.

56.25 $L^{-1}$ (13:44:59) after seeding. The increase of both CIP and HVPS concentration was evident when the FCDP concentration was depleted. At the same time, the amount of liquid water was reduced, while the ice water content was augmented with the highest value of 0.21 $g/m^3$. This proved that the seeding was activated inside the cloud.

**Figure 9** shows the cloud PSD and particle images before (13:09) and after (13:44) the seeding experiment within the seeded plume. The CPI probe captured spherical drops before the seeding, indicating the existence of SLW. After seeding, the column shape and the aggregates of ice crystals were photographed. As mentioned, FCDP measured small cloud particles (droplets), while CIP and HVPS detected ice crystals (**Figure 8**). The cloud particle spectrum width from FCDP enlarged from 27 to 46 μm after seeding. The cloud PSD exhibited a single peak distribution both before and after seeding. The number concentration peaked at 10 and 14 μm before and after seeding, respectively. After seeding, the cloud particle number concentration decreased in the areas affected by the seeding material. Remarkably, more ice crystals (>100 μm) were detected within the stratus cloud. The spectrum of ice crystals widened as the maximum diameter measured by the CIP probe increased from 100 to 625 μm. The same results were concluded from HVPS; the maximum diameter was enlarged from 300 to 1,500 μm.

For detection of falling ice crystals after seeding, the plane flew at 4,700 m (−4.2°C) during 14:00–14:08 following the same longitude and latitude trajectory as at 5,200 m. Consistent with the previous vertical profile, the number concentration of cloud particles measured by the FCDP probe was lower than 0.4 $cm^{-3}$, indicating that the plane was in a dry sub-cloud middle layer (**Figure 10**). However, CIP and HVPS both recorded ice crystals larger than 100 μm, with a maximum value of 71.04 and 13.47 $L^{-1}$ correspondingly. The LWC content was less than 0.01 $g/m^3$, while the highest IWC content was merely 0.075 $g/m^3$. This was largely resulting from the change of cloud particles. The particle images showed that most ice crystals were aggregated ice crystals.

At around 14:11, the plane descended at 4,500 m with no detection of cloud particles and ice crystals. A dry layer was therefore defined between the lower warm cloud and upper cold cloud. Due to the dry layer that was too thick, the ice crystals detected above 4,500 m sublimated before reaching the lower cloud. Therefore, the seeding experiment targeting the upper layer with abundant SLW was not effective as the aggregated ice crystals were not able to fall into the lower warm cloud.

## CONCLUSION

A two-layer stratus cloud was developed under the weather of an upper-level trough and return flow on May 15, 2021. The vertical characteristics of the cloud was well investigated with airborne observation equipment. A cloud seeding experiment targeting the SLW within the upper-layer cold cloud was carried out. Both before and after seeding, the microphysical characteristics of the two-layer cloud were analyzed, and the related microphysical response of cloud seeding was concluded as follows:

1) A two-layer cloud structure was formed under the influence of an upper-level trough and return flow, where warm clouds were in the low level and cold clouds were above. Within the low-level warm clouds, the particle spectrum expanded wider from the cloud top to the base. The upper cold cloud was detected with abundant SLW but with few ice crystals.
2) In the warm cloud, the cloud particles were relatively smaller near the cloud top due to entrainment and evaporation. The small cloud particles grew into large droplets and further into raindrops through collision–coalescence during falling. Near the warm cloud base, the small cloud droplets increased, and the concentration of CIP and HVPS appeared to follow a decreasing trend due to the break-up and evaporation.
3) Artificial nuclei (AgI agents) were released into cold clouds with SLW, and liquid droplets were vastly consumed and formed into large ice crystals. The CPI imager captured pristine columns and aggregated ice crystals. The spectrum of both cloud particles and ice crystals broadened, therefore proving the evidence for the microphysical response of cloud seeding.

## DATA AVAILABILITY STATEMENT

The raw data supporting the conclusions of this article will be made available by the authors without undue reservation.

## AUTHOR CONTRIBUTIONS

XD was the main contributor. XS contributed to writing and translation. FY contributed to data analysis and description. JZ contributed to weather analysis. SW contributed to data analysis. MP and HZ were in charge of the graphics.

## FUNDING

This work was supported by the S & T Program of Hebei (20375042D) and Hebei Meteorological Service Scientific Research and Development Project (20ky28).

## REFERENCES

Bergeron, T. (1935). "On the Physics of Cloud and Precipitation," in Proceedings of Fifth Assembly UGGI (Lisbon, Portugal: Union Géodésique et Géophysique Internationale), 156–178.

Bergeron, T. (1960). "Problems and Methods of Rainfall Investigation, Address of the Honorary Chairman of the Conference," in *Physics of Precipitation* (Massachusetts, United States: American Geophysical Union), 5, 152–157. Geophysical Monogram.

Breed, D., Rasmussen, R., Weeks, C., Boe, B., and Deshler, T. (2014). Evaluating winter Orographic Cloud Seeding: Design of the Wyoming Weather Modification Pilot Project (WWMPP). *J. Appl. Meteorol. Climatol.* 53 (2), 282–299. doi:10.1175/JAMC-D-13-0128.1

Cai, Z. X., Zhou, Y. Q., and Cai, M. (2013). Analysis on Comprehensive Observation of Artificial Precipitation Enhancement Operation for a

Convective-Stratiform Mixed Cloud. *Plateau Meteorol.* 32 (5), 1460–1469. (In Chinese). doi:10.7522/j.issn.1000-0534.2012.00115

Chen, C., Baethgen, W. E., and Robertson, A. (2013). Contributions of Individual Variation in Temperature, Solar Radiation and Precipitation to Crop Yield in the North China Plain, 1961–2003. *Climatic Change* 116 (3), 767–788. doi:10.1007/s10584-012-0509-2

Dong, X. B., Zhao, C. F., Yang, Y., Wang, Y., Sun, Y., and Fan, R. (2020). Distinct Change of Supercooled Liquid Cloud Properties by Aerosols from an Aircraft-Based Seeding experiment. *Earth Space Sci.* 7 (8), e2020EA001196. doi:10.1029/2020EA001196

Dong, X. B., Zhao, C. F., Huang, Z. C., Mai, R., Lv, F., Xue, X. W., et al. (2021). Increase of Precipitation by Cloud Seeding Observed from a Case Study in November 2020 over Shijiazhuang, China. *Atmos. Res.* 262 (5), 105766. doi:10.1016/j.atmosres.2021.105766

Faber, S., French, J. R., and Jackson, R. (2018). Laboratory and In-Flight Evaluation of Measurement Uncertainties from a Commercial Cloud Droplet Probe (CDP). *Atmos. Meas. Tech.* 11 (6), 3645–3659. doi:10.5194/amt-11-3645-2018

Fan, L., Lu, C., Yang, B., and Chen, Z. (2012). Long-term Trends of Precipitation in the North China Plain. *J. Geogr. Sci.* 22 (6), 989–1001. doi:10.1007/s11442-012-0978-2

Findeisen, W. (1938). Die kolloidmeteorologischen Vorgänge bei der Niederschlagsbildung (Colloidal meteorological processes in the formation of precipitation). *Meteorol. Z.* 55, 121–133. doi:10.1127/metz/2015/0675

Flossmann, A. I., Manton, M., Abshaev, A., Bruintjes, R., Murakami, M., Prabhakaran, T., et al. (2019). Review of Advances in Precipitation Enhancement Research. *Bull. Am. Meteorol. Soc.* 100 (8), 1465–1480. doi:10.1175/BAMS-D-18-0160.1

French, J. R., Friedrich, K., Tessendorf, S. A., Rauber, R. M., Geerts, B., Rasmussen, R. M., et al. (2018). Precipitation Formation from Orographic Cloud Seeding. *Proc. Natl. Acad. Sci. USA* 115 (6), 1168–1173. doi:10.1073/pnas.1716995115

Friedrich, K., Ikeda, K., Tessendorf, S. A., French, J. R., Rauber, R. M., Geerts, B., et al. (2020). Quantifying Snowfall from Orographic Cloud Seeding. *Proc. Natl. Acad. Sci. USA* 117 (10), 5190–5195. doi:10.1073/pnas.1917204117

Geerts, B., Miao, Q., Yang, Y., Rasmussen, R., and Breed, D. (2010). An Airborne Profiling Radar Study of the Impact of Glaciogenic Cloud Seeding on Snowfall from winter Orographic Clouds. *J. Atmos. Sci.* 67 (10), 3286–3302. doi:10.1175/2010JAS3496.1

Gu, Z. C. (1980). *Base of Cloud and Mist Precipitation Physics*. Beijing: Science Press, 173–179. (In Chinese).

Guo, X. L., Fu, D. H., Li, X. Y., Hu, Z. X., Lei, H. C., Xiao, H., et al. (2015). Advances in Cloud Physics and Weather Modification in China. *Adv. Atmos. Sci.* 32, 230–249. doi:10.1007/s00376-014-0006-9

Hu, Z. J., Qin, Y., and Wang, Y. B. (1983). An Numerical Model of the Cold Stratified Clouds. *Acta Meteorol. Sin.* 41 (2), 194–202. (In Chinese). doi:10.11676/qxxb1983.021

Kendy, E., Zhang, Y., Liu, C., Wang, J., and Steenhuis, T. (2004). Groundwater Recharge from Irrigated Cropland in the North China Plain: Case Study of Luancheng County, Hebei Province, 1949-2000. *Hydrol. Process.* 18 (12), 2289–2302. doi:10.1002/hyp.5529

Kenneth, V. B., and Harry, T. O. (1993). Warm-Rain Initiation: An Overview of Microphysical Mechanisms. *J. Appl. Meteorol.* 32 (4), 608–625. doi:10.1175/1520-0450(1993)032<0608:WRIAOO>2.0.CO;2

King, W. D., Parkin, D. A., and Handsworth, R. J. (1978). A Hot-Wire Liquid Water Device Having Fully Calculable Response Characteristics. *J. Appl. Meteorol.* 17 (12), 1809–1813. doi:10.1175/1520-0450(1978)017<1809:ahwlwd>2.0.co;2

Lance, S., Brock, C. A., Rogers, D., and Gordon, J. A. (2010). Water Droplet Calibration of the Cloud Droplet Probe (CDP) and In-Flight Performance in Liquid, Ice and Mixed-phase Clouds during ARCPAC. *Atmos. Meas. Tech.* 3 (6), 1683–1706. doi:10.5194/amt-3-1683-2010

Lawson, R. P. (2011). Effects of Ice Particles Shattering on the 2D-S Probe. *Atmos. Meas. Tech.* 4 (7), 1361–1381. doi:10.5194/amt-4-1361-2011

Liu, W. G., Tao, Y., Zhou, Y. Q., Dang, J., Tan, C., and Gao, Y. (2021). Simulation of Stratiform Cloud Seeding, its Rainfall Enhancement Effect and Mechanism Study Based on a Real Trajectory of Aircraft. *Acta Meteorol. Sin.* 79 (2), 340–358. (In Chinese). doi:10.11676/qxxb2021.011

Marcolli, C., Nagare, B., Welti, A., and Lohmann, U. (2016). Ice Nucleation Efficiency of AgI: Review and New Insights. *Atmos. Chem. Phys.* 16 (14), 8915–8937. doi:10.5194/acp-16-8915-2016

Rauber, R. M., Geerts, B., Xue, L., French, J., Friedrich, K., Rasmussen, R. M., et al. (2019). Wintertime Orographic Cloud Seeding-A Review. *J. Appl. Meteorol. Climatol.* 58 (10), 2117–2140. doi:10.1175/JAMC-D-18-0341.1

Wang, J., Yue, Z., Rosenfeld, D., Zhang, L., Zhu, Y., Dai, J., et al. (2021). The Evolution of an AgI Cloud-Seeding Track in Central China as Seen by a Combination of Radar, Satellite, and Disdrometer Observations. *J. Geophys. Res. Atmos.* 126 (11), e2020JD033914. doi:10.1029/2020JD033914

Wegener, A. (1911). *Thermodynamik der Atmosphäre (Thermodynamics of the Atmosphere)*. Leipzig: J. A. Barth, 331.

Yamaguchi, T., and Randall, D. A. (2008). Large-eddy Simulation of Evaporatively Driven Entrainment in Cloud-Topped Mixed Layers. *J. Atmos. Sci.* 65 (5), 1481–1504. doi:10.1175/2007JAS2438.1

Yang, J. F., Lei, H. C., and Hu, Z. X. (2010). Simulation of the Stratiform Cloud Precipitation Microphysical Mechanism with the Numerical Model. *Chin. J. Atmos. Sci.* 34 (2), 275–289. (In Chinese). doi:10.3878/j.issn.1006-9895.2010.02.04

Yang, Y., Zhao, C. F., Dong, X. B., Fan, G. C., Zhou, Y. Q., Wang, Y., et al. (2019). Toward Understanding the Process-Level Impacts of Aerosols on Microphysical Properties of Shallow Cumulus Cloud Using Aircraft Observations. *Atmos. Res.* 221, 27–33. doi:10.1016/j.atmosres.2019.01.027

You, L. G., Ma, P. M., and Hu, Z. J. (2002). Researches on Precipitation Enhancement of Strati Form Cloud in Northern China. *Sci. Meteorol. Sin.* 30, 19–56. (In Chinese).

Yuan, Z., and Shen, Y. (2013). Estimation of Agricultural Water Consumption from Meteorological and Yield Data: a Case Study of Hebei, North China. *PloS one* 8 (3), e58685. doi:10.1371/journal.pone.0058685

Yuan, J., Wu, K., Wei, T., Wang, L., Shu, Z., Yang, Y., et al. (2021). Cloud Seeding Evidenced by Coherent Doppler Wind Lidar. *Remote Sensing* 13 (19), 3815. doi:10.3390/rs13193815

Zhao, Z., and Lei, H. C. (2008). A Numerical Simulation of Cloud Physical Structure and Microphysical Processes Associated with Stratiform Precipitation in Northwest China. *Chin. J. Atmos. Sci.* 32 (2), 323. (In Chinese). doi:10.3878/j.issn.1006-9895.2008.02.11

Zhao, C. F., Zhao, L. J., and Dong, X. B. (2019). A Case Study of Stratus Cloud Properties Using *In Situ* Aircraft Observations over Huanghua, China. *Atmosphere* 10 (1), 19. doi:10.3390/atmos10010019

Zhou, Y. Q. (2004). *Study on the Stratiform Cloud Multi-Scale Structures and Artificial Rainfall Increase in Henan Province*. Dissertation, (In Chinese). Nanjing, China: School of Atmospheric Sciences of Nanjing University of Information Science & Technology.

**Conflict of Interest:** The authors declare that the research was conducted in the absence of any commercial or financial relationships that could be construed as a potential conflict of interest.

**Publisher's Note:** All claims expressed in this article are solely those of the authors and do not necessarily represent those of their affiliated organizations or those of the publisher, the editors, and the reviewers. Any product that may be evaluated in this article or claim that may be made by its manufacturer is not guaranteed or endorsed by the publisher.

frontiers | Frontiers in Environmental Science

ORIGINAL RESEARCH
published: 11 April 2022
doi: 10.3389/fenvs.2022.880113

# Distribution Characteristics and Formula Revision of Lightning Current Amplitude and Cumulative Probability in Zhejiang Province

*Li Xia*[1,2], *Song Nannan*[3]*, *Fan Yanfeng*[2], *Liu Yinping*[1], *Liu Qing*[4], *Guan Xiaolin*[1] *and Miao Pei*[1]

[1]Key Laboratory for Aerosol-Cloud-Precipitation of China Meteorological Administration, Collaborative Innovation Center on Forecast and Evaluation of Meteorological Disaster, Nanjing University of Information Science and Technology, Nanjing, China, [2]State Key Laboratory of Severe Weather, Chinese Academy of Meteorological Sciences, Beijing, China, [3]Tianjin Meteorological Disaster Defense Technology Centre, Tianjin, China, [4]Meteorological Bureau in Taizhou, Taizhou, China

The cumulative probability distribution of the lightning current amplitude can reflect the lightning activity and is important for the lightning protection engineering technology. Based on the lightning location data from 2009 to 2019, the distribution characteristics of the lightning current amplitude and cumulative probability are studied. The results show that a total of 8,634,858 lightning flashes occurred in Zhejiang province in last 11 years. Negative flashes are much more common than positive ones, accounting for 87.44% of the total. The percentage of the lightning current amplitude between 2 and 100 kA is 94.3%. The average amplitude of positive flashes is significantly higher than that of negative flashes. For the current amplitude of positive flashes, the peak occurs in March and gradually decreases with the increase of the month, reaching its lowest in December. But the monthly distribution of negative flashes is relatively concentrated, especially from February to October. When lightning current amplitude is higher than 25.5 kA, the cumulative probability of positive flashes is significantly higher than that of negative flashes and vice versa. The cumulative probability distribution of negative flashes is closer to that of total flashes and is significantly different from that of positive flashes. In order to get a more suitable cumulative probability formula of lightning current amplitude and corresponding parameters in Zhejiang province, the Levenberg–Marquardt method is used. By fitting the measured data with the formulas recommended by the Institute of Electrical and Electronics Engineers (IEEE) and Electric Power Industry Standard of China (Code for design of overvoltage protection and insulation coordination for AC electrical installations GB/T 50064-2014), respectively, the correlation coefficients of different polarities are obtained. By comparing the aforementioned two fitting results, it is found that the formula recommended by the IEEE can more objectively reflect the probability distribution characteristics in Zhejiang province, and the accuracy of the derived formula is verified by using the lightning current data in 2020. It shows that the curve based on the measured values is consistent with that fitted by the IEEE formula but quite different from that fitted by the GB/T 50064-2014 formula.

**Keywords: lightning current amplitude, cumulative probability, characteristics, median current, the Levenberg–Marquardt method**

OPEN ACCESS

***Edited by:***
*Xinyao Xie,*
*Institute of Mountain Hazards and Environment (CAS), China*

***Reviewed by:***
*Chunlong Zhang,*
*West Anhui University, China*
*Yi Yang,*
*Hebei Normal University, China*

***Correspondence:**
*Song Nannan*
*songnannan1216@126.com*

***Specialty section:***
*This article was submitted to Atmosphere and Climate, a section of the journal Frontiers in Environmental Science*

***Received:*** *21 February 2022*
***Accepted:*** *16 March 2022*
***Published:*** *11 April 2022*

***Citation:***
*Xia L, Nannan S, Yanfeng F, Yinping L, Qing L, Xiaolin G and Pei M (2022) Distribution Characteristics and Formula Revision of Lightning Current Amplitude and Cumulative Probability in Zhejiang Province. Front. Environ. Sci. 10:880113. doi: 10.3389/fenvs.2022.880113*

## INTRODUCTION

As lightning discharges often lead to lightning disasters (Paisios et al., 2007; Ma et al., 2008; Chemartin et al., 2012), the study of lightning physical characteristics has become more and more important (Finke and Hauf, 1996; Christian et al., 2003; Pinto et al., 2003; Soriano et al., 2005; Fleenor et al., 2009). Lightning's current amplitude of return stroke is one of its important parameters, closely responding to the lightning disaster. The cumulative probability of the lightning current amplitude has been widely used in the lightning protection engineering technology, which represents the distribution of lightning current amplitude (Yue et al., 2013; Zhao et al., 2017). The precise expression is useful for studying lightning activity, protecting the transmission line, and assessing the lightning disaster risk (Metwally t al. 2004; Zhang et al., 2011; He et al., 2017).

At present, more researchers have been studying about lightning current amplitude (Borghetti et al., 2004; Chowdhuri et al., 2005). As early as the 1880's, Kohlrausch had carried out the work of measuring the lightning current amplitude (Kohlrausch et al., 1888). Pobolansky (1977) proposed a formula for calculating the cumulative probability of lightning current amplitude based on data in Europe, Australia, and the United States (Shim et al., 2002). Thereafter, considerable progress has also been made on proposing different calculation formulas based on data in different regions (Grant et al., 1985; Orville and Huffines, 1999). The approximate expression of the cumulative probability of the lightning current amplitude was first given by Anderson based on the data of Berger, which was later recommended by the IEEE (Anderson et al., 1980). In China, the regulation method is mainly used to calculate the cumulative probability of lightning current amplitude in the lightning protection engineering technology (Du., 1996; Li, R.F et al., 2011). The corresponding logarithmic expression is recommended by GB/T 50064-2014. In the early days, lightning data were lacking, and the parameters of the formula were obtained by inversion using the data recorded by the Xinhang line from 1962 to 1987 (Li et al., 2019). It is still in use today.

Due to the vast territory and environmental differences in China, using the identical parameters in different regions shows great uncertainty. For example, the calculation results indicate that the most prominent manifestation is not wholly accurate, and thus, it perhaps cannot accurately reflect the cumulative probability of lightning current amplitude in the area, which affects its application in engineering. With the widespread application of lightning location systems, most of the systems have been running for more than 10 years. A large amount of lightning data has been accumulated, and so it provides the basis for research on parameters of temporal and spatial differences, such as lightning current amplitude and its cumulative probability (Wang et al., 2016; Zhao et al., 2018; Li et al., 2019). Li, J.Q et al. (2011) found that significant differences lay in the distribution characteristics of the cumulative probability of lightning current amplitude with the polarity in Chongqing, and the cumulative probability formulas recommended by the IEEE had better fitting effects than other formulas. Cheng et al. (2021) found that the cumulative probability curve of lightning current amplitude dropped faster in the interval of 20–50 kA and was consistent with the IEEE recommended formula in Liaoning. These research results provide the distribution characteristics of the lightning current amplitude and cumulative probability that are suitable for local use.

There is a subtropical monsoon climate with frequent lightning disasters in Zhejiang province, which lies in the central-eastern part of China. According to statistics, there were 9,728 recorded lightning disasters from 1998 to 2020, including 357 casualties, 282 injuries, and 307 deaths (Gu et al., 2021). The temporal and spatial characteristics of lightning activities have been mainly studied based on the lightning location system in Zhejiang province (Liu et al., 2009; Cui et al., 2021; Zhang et al., 2021). But the relevant research on lightning current amplitude and cumulative probability has not been carried out. Based on the lightning location system in Zhejiang province from 2009 to 2019, this article studies the characteristics of lightning current amplitude and localizes its parameters in the cumulative probability formula. The accuracy of the calculation results is helpful to the development of the lightning protection engineering technology.

## DATA AND METHODS

The data are collected by using the lightning location positioning system of the Meteorological Departments in Zhejiang province. The system is uniformly deployed by the China Meteorological Administration, and it has 11 substations in Zhejiang province, which are shown in **Figure 1**. Also, it has a monitoring accuracy of 300 m and a detection efficiency of over 85%. Based on the principle of magnetic field positioning and time difference positioning, the system can accurately determine the location and time of a lightning occurrence, using satellite positioning systems and geographic information systems. It is mainly used for the detection of cloud-to-ground flashes and provides basic data for the study of the physical characteristics of lightning current.

The cumulative probability formula for lightning current amplitude recommended by the IEEE is as follows:

$$p = \frac{1}{1 + (I/a)^b}. \tag{1}$$

The cumulative probability formula for lightning current amplitude recommended by GB/T 50064–2014 is as follows:

$$\lg P = -\frac{I}{c}, \tag{2}$$

where $I$ is lightning current amplitude (kA), $P$ is the cumulative probability that the lightning current amplitude is greater than $I$, $a$ is the median lightning current amplitude, and $b$ is the degree of change in the cumulative probability curve. In **Eq. 1**, IEEE

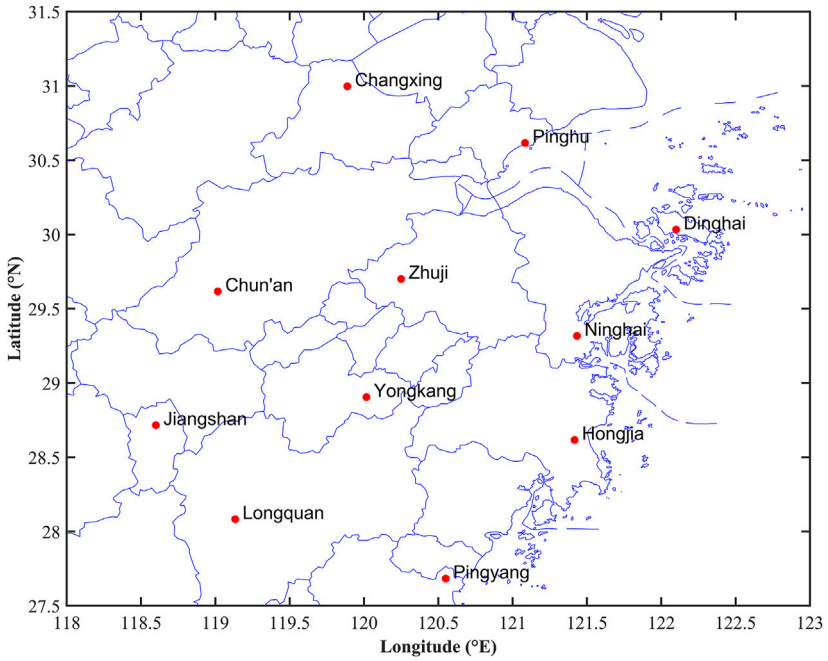


**FIGURE 1 |** Site distribution map for the lightning location system in Zhejiang province.

recommends $a = 31$, $b = 2.6$, and $I \in (2, 200]$, and in **Eq. 2**, GB/T 50064–2014 recommends $c = 88$.

The parameters recommended by the IEEE are the average results of global lightning current amplitude, and lightning activities vary greatly with time and space, so it is not appropriate to use the average results directly in Zhejiang province, and for **Eq. 2**, the parameters were obtained by inversion using the data recorded by the Xinhang line from 1962 to 1987. Therefore, the accuracy needs further verification according to the lightning observed data. In order to obtain a more suitable cumulative probability formula of lightning current amplitude and corresponding parameters in Zhejiang province, the least squares criterion is often used, and the Levenberg–Marquardt method is a commonly used method.

The study counts the observed data of the lightning location system in Zhejiang province from 2009 to 2019 and carries out quality control. According to IEEE regulations, the application range of the current is defined as 2–200 kA. Therefore, records with lightning current amplitudes of less than 2 kA and greater than 200 kA are excluded. The lightning number is counted according to the rule, which is that the current amplitude starts at 2 kA, then 5 kA, and increases by 5 kA until 200 kA. According to the results, the distribution characteristics of the lightning current amplitude are analyzed. According to the definition of the cumulative probability of lightning current amplitude, the percentages of positive flashes, negative flashes, and total flashes are calculated, respectively, based on the above intervals. Finally, the statistical points of the cumulative probability distribution of positive flashes, negative flashes, and total flashes are obtained.

In order to get a more suitable cumulative probability formula of the lightning current amplitude and corresponding parameters in Zhejiang province, the Levenberg–Marquardt method is used to fit the measured data with the formulas recommended by IEEE and GB/T 50064–2014, respectively, and the correlation coefficients of different polarities are obtained. The Levenberg–Marquardt method is a commonly used method that solves the non-linear least squares problem. In order to strengthen the robustness of the algorithm, it adds a damping factor on the basis of the Gauss-Newton method. The following is an example:

The vector $p$ is defined to consist of fitted parameters whose number is $M$, while the vector $X$ and $Y$ consists of horizontal and vertical coordinates of measured scatter points whose number is $N$, respectively. There is a corresponding residual between the measured value and the fitted function value at each observation point. The residual functions, which are $N$ form vector, are shown in **Eq. 3** and **Eq. 4**.

$$r_j(p) = Y_j - y\left(p, X_j\right), \tag{3}$$

$$r(p) = \left[r_1(p), r_2(p), \ldots, r_N(p)\right]^{\mathrm{T}}, \tag{4}$$

where $y(p, X_j)$ is the value substituted $p$ and $X_j$, $r_j(p)$ is the fitted residual function at the scatter point $j$, and $r(p)$ is the residual function vector.

The objective function $F(p)$ is defined as follows:

$$F(p) = \frac{1}{2} r^{\mathrm{T}}(p) r(p) = \frac{1}{2} \sum_{j=1}^{N} \left(Y_j - y\left(p, X_j\right)\right)^2. \tag{5}$$

**TABLE 1 |** Lightning Current Amplitude Statistics from 2009 to 2019.

| Year | Lightning polarity | Lightning current amplitude/kA | | | | | | | | | | |
|---|---|---|---|---|---|---|---|---|---|---|---|---|
| | | 2–20 | 20–40 | 40–60 | 60–80 | 80–100 | 100–120 | 120–140 | 140–160 | 160–180 | 180–200 | Total |
| 2009 | Positive | 1978 | 3,401 | 1854 | 1,453 | 1,126 | 852 | 639 | 479 | 353 | 281 | 12,416 |
| | Negative | 36,741 | 135,040 | 67,763 | 32,479 | 14,009 | 7,055 | 4,020 | 2,525 | 1,676 | 1,215 | 302,523 |
| 2010 | Positive | 3,408 | 9,984 | 9,065 | 6,672 | 4,642 | 2,870 | 1814 | 1,159 | 737 | 483 | 40,834 |
| | Negative | 85,010 | 413,549 | 218,787 | 84,831 | 35,673 | 17,547 | 9,025 | 4,723 | 2,770 | 1718 | 873,633 |
| 2011 | Positive | 5,085 | 8,705 | 5,432 | 3,664 | 2,459 | 1,526 | 974 | 634 | 383 | 262 | 29,124 |
| | Negative | 104,815 | 383,527 | 180,347 | 71,655 | 30,706 | 14,747 | 7,436 | 3,920 | 2,259 | 1,377 | 800,789 |
| 2012 | Positive | 4,041 | 8,664 | 6,874 | 5,302 | 3,542 | 2,294 | 1,513 | 1,022 | 718 | 499 | 34,469 |
| | Negative | 84,062 | 298,838 | 138,407 | 53,682 | 24,171 | 12,387 | 6,662 | 3,664 | 2,302 | 1,433 | 625,608 |
| 2013 | Positive | 3,005 | 6,346 | 5,567 | 4,043 | 2,574 | 1742 | 1,129 | 771 | 486 | 302 | 25,965 |
| | Negative | 84,423 | 257,990 | 111,096 | 40,089 | 17,627 | 9,022 | 4,945 | 2,779 | 1,731 | 1,101 | 530,803 |
| 2014 | Positive | 4,448 | 7,259 | 5,454 | 3,991 | 2,726 | 1,820 | 1,263 | 750 | 518 | 325 | 28,554 |
| | Negative | 113,638 | 287,108 | 124,881 | 50,420 | 23,583 | 12,756 | 7,688 | 4,983 | 3,276 | 2,204 | 630,537 |
| 2015 | Positive | 2,345 | 3,951 | 3,492 | 2,452 | 1,538 | 1,068 | 645 | 474 | 361 | 225 | 16,551 |
| | Negative | 51,038 | 89,793 | 39,004 | 16,530 | 9,073 | 5,760 | 3,564 | 2,511 | 1,745 | 1,282 | 220,300 |
| 2016 | Positive | 17,834 | 35,091 | 39,082 | 32,404 | 25,509 | 18,288 | 11,823 | 6,941 | 4,304 | 2,767 | 194,043 |
| | Negative | 133,069 | 343,428 | 166,380 | 63,990 | 29,171 | 15,985 | 9,828 | 6,341 | 4,134 | 2,703 | 775,029 |
| 2017 | Positive | 9,105 | 20,363 | 18,811 | 12,426 | 9,030 | 6,536 | 3,795 | 2,091 | 1,213 | 712 | 84,082 |
| | Negative | 96,739 | 294,593 | 140,968 | 52,229 | 22,166 | 11,518 | 6,761 | 4,061 | 2,403 | 1,501 | 632,939 |
| 2018 | Positive | 21,968 | 37,596 | 35,532 | 21,832 | 10,463 | 5,745 | 3,340 | 2,059 | 1,284 | 894 | 140,713 |
| | Negative | 134,246 | 455,124 | 227,914 | 84,956 | 35,452 | 17,659 | 10,043 | 6,180 | 3,825 | 2,430 | 977,829 |
| 2019 | Positive | 162,763 | 122,107 | 62,981 | 43,247 | 34,135 | 23,640 | 13,730 | 8,069 | 4,744 | 2,786 | 478,202 |
| | Negative | 280,119 | 466,658 | 236,105 | 95,354 | 44,804 | 24,873 | 14,297 | 8,739 | 5,548 | 3,327 | 1,179,824 |
| 合计 | Positive | 235,988 | 263,467 | 194,144 | 137,486 | 97,744 | 66,381 | 40,665 | 24,449 | 15,101 | 9,536 | 1,084,961 |
| | Negative | 1,203,900 | 3,425,648 | 1,651,652 | 646,215 | 286,435 | 149,309 | 84,269 | 50,426 | 31,669 | 20,374 | 7,549,897 |

Here $r^T(p)$ is the transposition of $r(p)$. It can be seen that $F(p)$ is exactly 1/2 of the sum of squares of the fitting residual $R$. Under the principle of least squares, the vector $p^*$ with the smallest value $F(p)$ is the optimal solution, and $R$ is also the smallest.

The partial derivatives of the residual vector $r(p)$ with respect to each variable in $p$ form the $N \times M$ order matrix. It is expressed as

$$J = \begin{bmatrix} \frac{\partial y_1}{\partial x_1} & \frac{\partial y_1}{\partial x_2} & \cdots & \frac{\partial y_1}{\partial x_M} \\ \frac{\partial y_2}{\partial x_1} & \frac{\partial y_2}{\partial x_2} & \cdots & \frac{\partial y_2}{\partial x_M} \\ \cdots & \cdots & \cdots & \cdots \\ \frac{\partial y_N}{\partial x_1} & \frac{\partial y_N}{\partial x_2} & \cdots & \frac{\partial y_N}{\partial x_M} \end{bmatrix}_{N \times M}. \quad (6)$$

In this study, based on **Eq. 1**, $p = [a, b]^{\mathrm{T}}$ and $M = 2$. Based on **Eq. 2**, $p = [c]^{\mathrm{T}}$ and $M = 1$.

On the basis of the initial value $p_0$, a suitable increment $\Delta p$ is found to make the objective function $F(p)$ change in the direction of the decreasing value, and $p = p + \Delta p$ is iterated until it approaches $p^*$; then, $F(p)$ reaches the minimum value. $\Delta p$ is obtained by **Eq. 7** and **Eq. 8**.

$$S(p) = J^{\mathrm{T}}(p)J(p) + \mu\, diag(J^{\mathrm{T}}(p)J(p)), \quad (7)$$

$$S(p)\Delta p = -J^{\mathrm{T}}(p)r(p). \quad (8)$$

where $\mu$ is the damping factor, $\mathrm{diag}(J^T(p)J(p))$ is the diagonal matrix consisting of main diagonal elements $J^T(p)J(p)$, $\Delta p$ is the iterative increment of $p$, and $S(p)$ is the intermediate variable.

In each iteration, the Levenberg–Marquardt method can have various indicators to measure the quality of this iteration, and the value of $\mu$ is adjusted accordingly. In this study, the method is to decide whether $\Delta p$ is acceptable or not by comparing the sizes of $F(p + \Delta p)$ and $F(p)$.

In order to verify the effect of fitting, the median current method is applied to test the results by the Levenberg–Marquardt method.

# RESULTS AND ANALYSIS

## Analysis of the Characteristics of Lightning Current Amplitude

**Table 1** indicates the counts of positive flashes, negative flashes, and total flashes from 2009 to 2019 in Zhejiang province. They are based on different intervals of 2, 5, 10, ... 195, and 200 kA. The total number of flashes is 8,634,858, with positive flashes of 1,084,961 and negative flashes of 7,549,897, accounting for 12.56 and 87.44%, respectively. Therefore, the number of negative flashes is far greater than that of positive flashes. For instance, the percentage of positive flashes is lower than what has been observed, in Belgium (Dieter 2014). For the average value of lightning current amplitude, it is 54.59 kA for positive flashes, and 41.39 kA for negative flashes. Lightning current amplitude is mainly concentrated in the range of 2–100 kA, with a total number of 8,142,671, accounting for 94.3%. In the range of 160–200 kA, the number becomes smaller, accounting for only 0.94%. Of the annual variations, the number of total flashes reached a maximum value of 1,658,026 in 2019, and a minimum value of 236,851 in 2015, and the average annual number of lightning strikes is 784,978, higher than that of Hubei province, which is 393,724 (Yu et al., 2021).

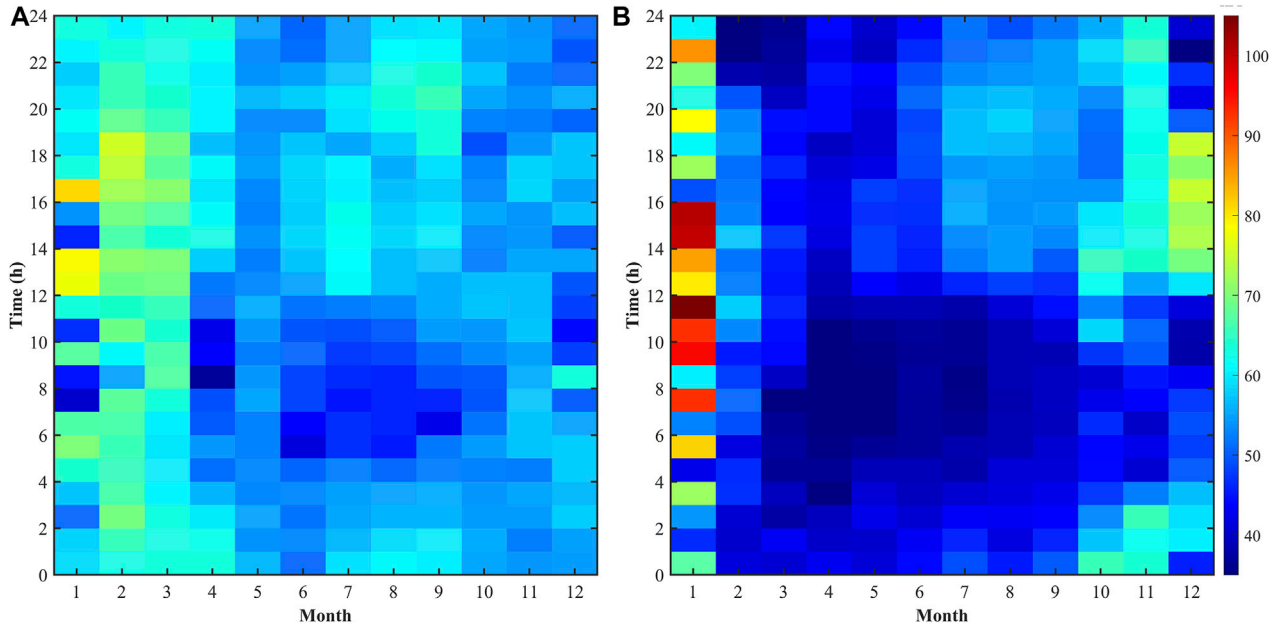


**FIGURE 2 |** Time distribution diagram of lightning current amplitude **(A)** Positive flashes and **(B)** Negative flashes.

The monthly and hourly distributions of lightning current amplitude are shown in **Figure 2**. It is found that positive flashes greater than 60 kA account for 53.96% of the total and negative flashes account for 38.68% of the total in Zhejiang province. The average current amplitude of positive flashes is significantly higher than that of negative flashes, and the monthly distribution presents a significant shape of a single peak. January is the first month with high current amplitude, and the peak value is reached in February. After that, the current amplitude gradually decreases. For negative flashes, the monthly distribution is relatively concentrated, especially from February to October, showing a significant shape of downward convexity, and the high currents mostly occur from November to January of the following year. In Zhejiang province, **Figure 2** shows that positive flashes are frequent in spring, followed by winter, while negative flashes are mainly concentrated in summer and autumn. In winter, there are fewer lightning activities, but the average current intensity is stronger than in other seasons. This is basically consistent with the observed results in Beijing (Gao et al., 2019). In an hourly distribution, the current amplitude variation of positive flashes is more significant than that of negative flashes, while in spring high values are mainly concentrated in 12–19, in summer mainly in 12–18, in autumn mainly in 19–23, and in winter mainly in 12–14. Otherwise, for negative flashes, the hourly variation is more significant in winter, mainly concentrated in 09–20, and changes little in other seasons.

## Characteristics of the Cumulative Probability Distribution of Lightning Current Amplitude

For different polarities, the cumulative probability distribution curves of lightning current amplitude are shown in **Figure 3**, which are quite different. The curve of negative flashes is steeper than that of positive flashes, that is, the cumulative probability distribution of negative flashes is more concentrated than that of positive flashes. When lightning current amplitude is higher than 25.5 kA, the cumulative probability of positive flashes is greater than that of negative flashes, and vice versa. The curve of negative flashes is closer to that of total flashes, especially due to the high proportion of negative flashes to total flashes (87.44%). Therefore, the cumulative probability distribution of lightning current amplitude of total flashes is mainly affected by negative flashes, which is consistent with the results of lightning current amplitude characteristics in Hubei province and Beijing (Wang et al., 2016; Gao et al., 2019).

When the cumulative probability of lightning current amplitude is 50%, the current of positive flashes, negative flashes, and total flashes is 44.4, 35.0, and 35.6 kA, respectively. It means that the median current of positive flashes, negative flashes, and total flashes in Zhejiang province is 44.4, 35.0, and 35.6 kA, respectively. The median current of total flashes (35.6 kA) is less than that in Guangzhou (36.7 kA) and greater than that in Liaoning (30.6 kA), which shows that the distribution in Zhejiang province is different from those in the southern and northern regions of China (Lu et al., 2009; Cheng et al., 2021). For the current amplitude of total flashes, which is higher than 80 and 100 kA, the corresponding cumulative probability is 10.15 and 5.7%, indicating that in Zhejiang province, less than 80 kA accounts for more than 89.85% and less than 100 kA accounts for more than 94.3%. It is similar to the result in Hubei province where lightning current amplitude is less than 100 kA, accounting for more than 98% (Wang et al., 2016). It is because the latitudes of Zhejiang and Hubei provinces are basically the same, and the water resources are relatively

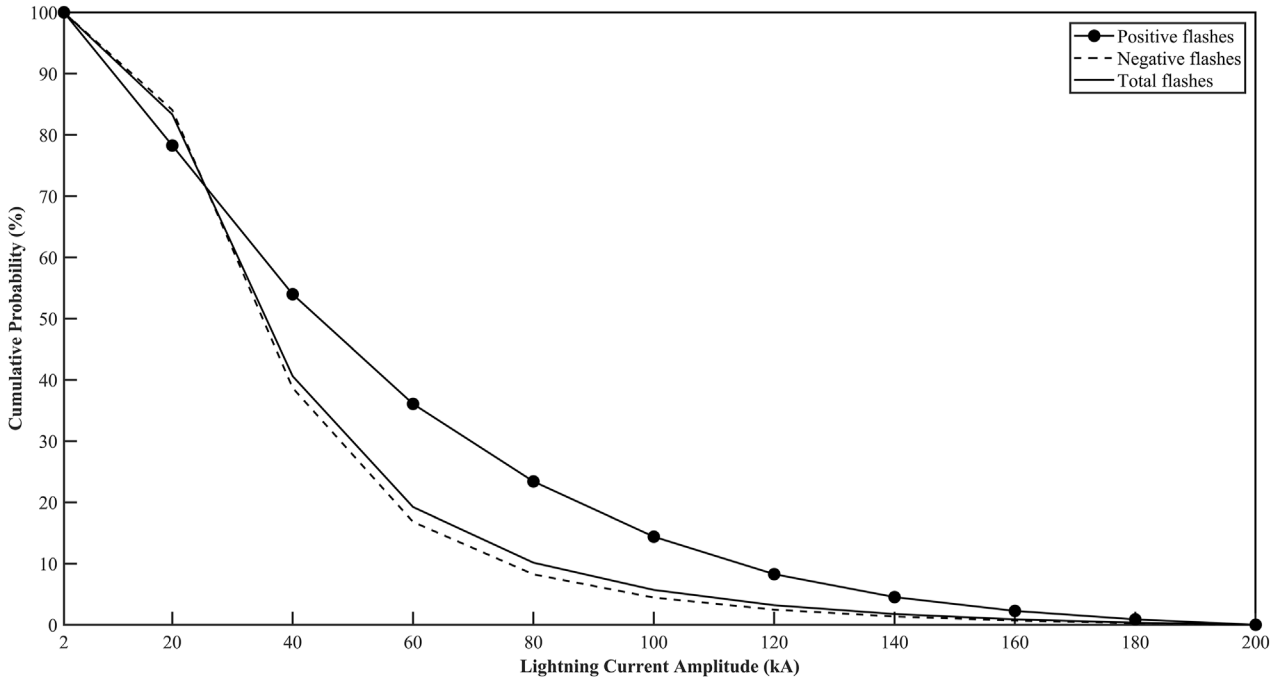


**FIGURE 3 |** Cumulative probability distribution curves of lightning current amplitude.

**TABLE 2 |** Fitting parameters recommended by the IEEE and GB/T 50064-2014.

| Polarity | IEEE | | GB/T 50064-2014 |
|---|---|---|---|
| | a | b | c |
| Positive flashes | 42.39 | 2.11 | 130.00 |
| Negative flashes | 34.60 | 2.97 | 97.20 |
| Total flashes | 35.30 | 2.77 | 100.88 |

**TABLE 3 |** Correlation coefficients between measured values and calculated values by the IEEE and GB/T 50064-2014.

| Polarity | PIEEE (%) | $P_{GB/T50064-2014}$ (%) |
|---|---|---|
| Positive flashes | 99.66 | 99.12 |
| Negative flashes | 99.99 | 98.41 |
| Total flashes | 99.98 | 98.72 |

abundant, which provides abundant water vapor for the breeding of lightning. Therefore, lightning activity occurs more frequently, and the distribution characteristics of lightning current amplitude are relatively similar.

## Formula Fitting

In order to calculate the exact parameters in the cumulative probability distribution formula of the lightning current amplitude for Zhejiang province, the Levenberg–Marquardt method is adopted. The data based on the lightning location system in Zhejiang province are fitted with the formula recommended by IEEE and GB/T 50064-2014, respectively. Then, the parameters and correlation coefficients of different current polarities for Zhejiang province are obtained, which are shown in **Tables 2** and **3**.

For positive flashes, negative flashes, and total flashes, the trends of the fitting curves are more consistent with those recommended by the IEEE and quite different from those recommended by GB/T 50064-2014, which is shown in **Figures 4** and **5**.

The correlation coefficients between the curves in **Figure 4** are greater than those between the curves in **Figure 5**. It shows that the correlation between the curves based on the measured values and the ones based on the IEEE formula is higher for Zhejiang province. Therefore, to calculate the cumulative probability of lightning current amplitude in Zhejiang province, it is more appropriate to use the IEEE formula. This conclusion is basically consistent with the results in other regions in China, such as Beijing, Yan'an, and Hubei province (Wang et al., 2016; Gao et al., 2019; Li et al., 2019).

Based on the aforementioned method, the formula for the cumulative probability distribution in Zhejiang province is shown in **Eq. 9**, which applies to the calculation of positive flashes.

$$P_{+} = \frac{1}{1 + (I/42.93)^{2.11}}. \tag{9}$$

The formula is shown in **Eq. 10**, which applies to the calculation of negative flashes.

$$P_{-} = \frac{1}{1 + (I/34.60)^{2.97}}. \tag{10}$$

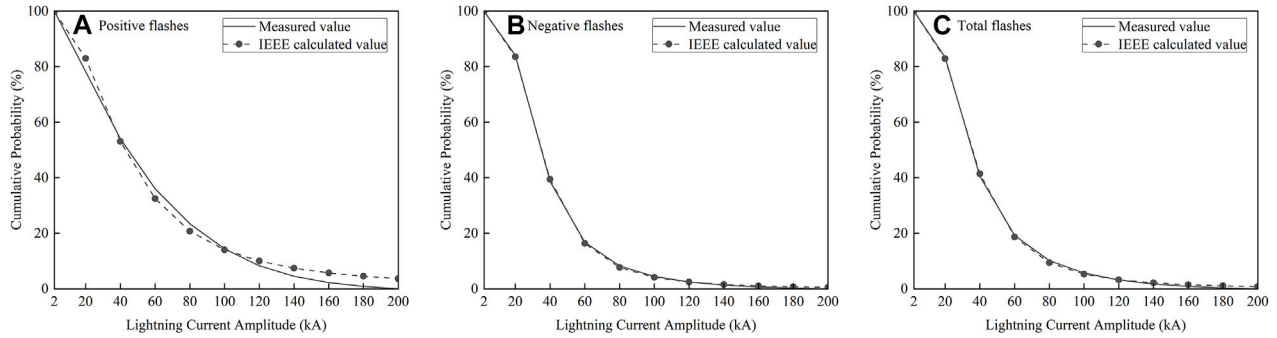


**FIGURE 4 |** Fitting curves based on measured values and calculated values by the IEEE **(A)** Positive flashes, **(B)** Negative flashes, and **(C)** Total flashes.

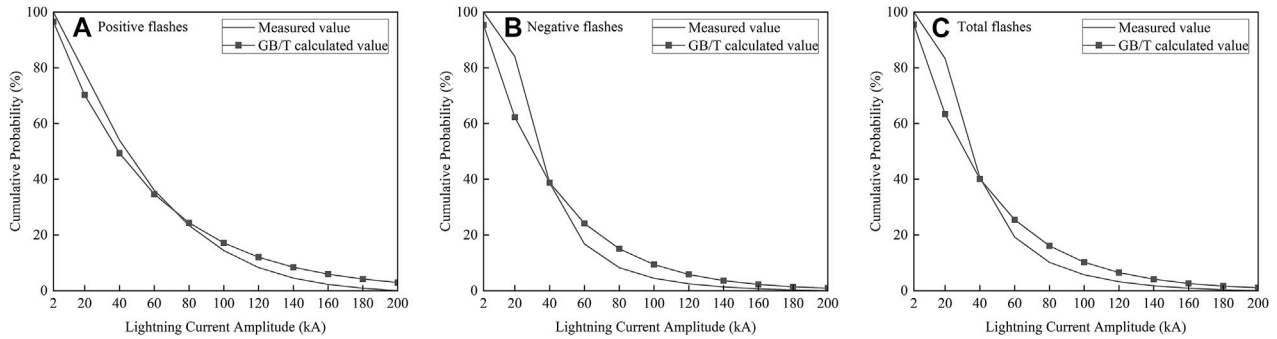


**FIGURE 5 |** Fitting curves based on measured values and calculated values by GB/T 50064-2014 **(A)** Positive flashes, **(B)** Negative flashes, and **(C)** Total flashes.

**TABLE 4 |** Comparison of fitting results between the Levenberg–Marquardt method and the median current method.

| Polarity | Levenberg–Marquardt method | | | Median current method | | |
|---|---|---|---|---|---|---|
| | a | b | $R^2$ | a | b | $R^2$ |
| Positive flashes | 51.19 | 2.28 | 0.9995 | 51.30 | 3.11 | 0.9989 |
| Negative flashes | 31.08 | 4.68 | 0.9997 | 30.54 | 4.28 | 0.9995 |
| Total flashes | 32.30 | 4.04 | 0.9993 | 31.57 | 3.78 | 0.9992 |

**Eq. 11** applies to the calculation of total flashes.

$$P = \frac{1}{1 + (I/35.30)^{2.77}}. \tag{11}$$

In order to test the accuracy of fitting results based on the Levenberg–Marquardt method, the median current method is used to test the fitting results. The test results are shown in **Table 4**. It is shown that the correlation coefficients ($R^2$) used by the Levenberg–Marquardt method are greater than those based on the Median Current method, so the reliability of fitting results used by the Levenberg–Marquardt method is higher.

## Verification

In order to verify the accuracy of **Eqs 9**, **10**, and **11**, the data of lightning current amplitude in 2020 are taken as an example, and the results are shown in **Figure 6**. It clearly shows that compared to the formula recommended by GB/T50064-2014, the curves based on **Eqs 9**, **10**, and **11** are closer to those of the measured lightning data in 2020. For the measured value curve and the IEEE fitted curve, **Figure 6A** shows that the two curves are closer when lightning current amplitude is around 80 kA, and the others are slightly divergent. However, the basic trend is the same. In **Figures 6B,C**, the two curves have the same trend of change. As observed data increase, the fit of the two curves will be higher. Therefore, the fitted formulas in this study are more suitable for describing the distribution characteristics of the cumulative probability of lightning current amplitude in Zhejiang province.

# SUMMARY AND DISCUSSION

In this work, a total of 8,634,767 flashes are used to analyze the characteristics of lightning current amplitude and cumulative probability, based on the lightning data from 2009 to 2019. In

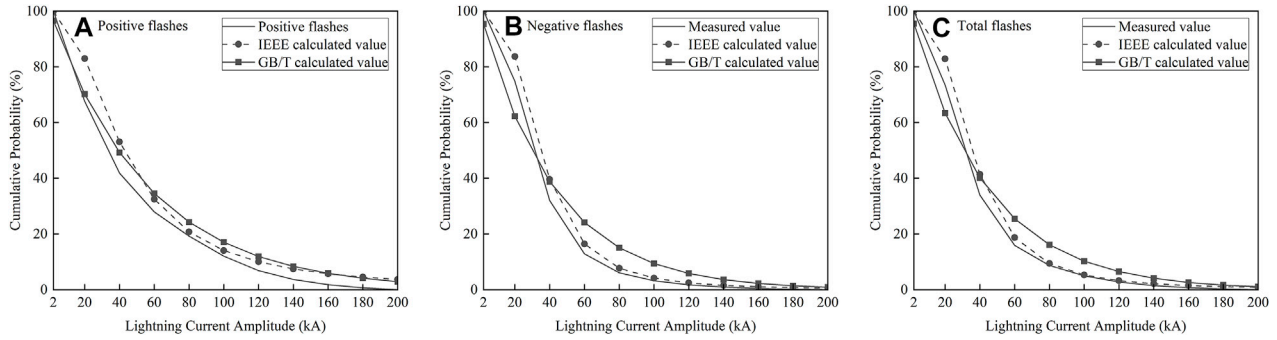


**FIGURE 6 |** Comparison of the cumulative probability distribution between measured values and calculated values in 2020 **(A)** Positive flashes, **(B)** Negative flashes, and **(C)** Total flashes.

addition, the parameters in the formulas recommended by the IEEE are corrected, which can more objectively reflect the cumulative probability distribution of lightning current amplitude in Zhejiang province.

It is found that the number of negative flashes is far more than that of positive flashes in Zhejiang province. But the average current amplitude of positive flashes is significantly higher than that of negative flashes. Lightning current amplitude is mainly concentrated in the range of 2–100 kA, accounting for 94.3%. In the range of 160–200 kA, the number becomes smaller, accounting for only 0.94%. The seasonal characteristics are significant, and the monthly distribution of the positive lightning current amplitude has a unimodal distribution, while that of negative flashes is relatively concentrated. Positive flashes are frequent in spring, but summer is the season of negative flashes. The cumulative probability distribution of the negative lightning current amplitude is closer to that of total flashes and is significantly different from that of positive flashes. The variation law of total flashes is mainly affected by negative flashes. Based on the Levenberg–Marquardt method, the measured data are fitted with the formulas recommended by the IEEE and GB/T 50064-2014, respectively, and the parameters of different polarities are obtained. By analysis, the cumulative probability distribution formula recommended by IEEE is more suitable for Zhejiang province, which is basically consistent with the results in other regions in China.

In **Figures 6B and C**, the changing trend of the two curves basically coincides. But there are two intersections between the two curves in **Figure 4A**, and when the value is higher than 100 kA, the fit of the two curves becomes lower. In other words, for describing the distribution characteristics of the cumulative probability of lightning current amplitude in Zhejiang province, the formulas applying to negative flashes and total flashes are more realistic than those for positive flashes. With more lightning observation data, a subsection refinement of the cumulative probability of the lightning current amplitude can be carried out in the following research, in order to obtain a more accurate cumulative probability formula.

## DATA AVAILABILITY STATEMENT

The original contributions presented in the study are included in the article/Supplementary Material, further inquiries can be directed to the corresponding author.

## AUTHOR CONTRIBUTIONS

Data acquisition; LQ. Methodology; LX, FY and SN. Software; SN and GX. Validation: LY, LQ and GX. Investigation; LX and LY. Writing—original draft preparation, LX. Writing—review and editing; LX, SN, MP and GX. All authors have read and agreed to the published version of the manuscript.

## FUNDING

This work was supported by the National Key Research and Development Program of China (No. 2017YFC1501502), the National Natural Science Foundation of China (No. 41975003), and the Open Grants of the State Key Laboratory of Severe Weather (No. 2020LASW-B08).

## ACKNOWLEDGMENTS

The authors are indebted to all members of the Department of Safety Engineering, especially Professor Shi Zheng, and the Zhejiang Meteorological Bureau. For further details, please contact LX (lixiasd74@163.com).

## REFERENCES


Anderson, R. B., and Eriksson, A. J. (1980). Lightning Parameters for Engineering Application. *Electra* 69, 65.

Borghetti, A., Nucci, C. A., and Paolone, M. (2004). Estimation of the Statistical Distributions of Lightning Current Parameters at Ground Level from the Data Recorded by Instrumented Towers. *IEEE Trans. Power Deliv.* 19 (3), 1400–1409. doi:10.1109/TPWRD.2004.829116

Chemartin, L., Lalande, P., Peyrou, B., Chazottes, A., Elias, P. Q., Delalondre, C., et al. (2012). Direct Effects of Lightning on Aircraft Structure: Analysis of the Thermal, Electrical and Mechanical Constraints. *Aerospace Lab.* 5, 1.

Cheng, P., Zeng, Y., Cheng, L., Pang, W. J., Xiao, G. L., and Rong, X. Y. (2021). Analysis of Characteristics of Lightning Current Amplitude in Liaoning Province from 2010 to 2018. *J. Meteorology Environ.* 37 (4), 107–113. doi:10.3969/j.issn.1673-503X.2021.04.015

Chowdhuri, P., Anderson, J. G., Chisholm, W. A., Field, T. E., Ishii, M., Martinez, J. A., et al. (2005). Parameters of Lightning Strokes: A Review. *IEEE Trans. Power Deliv.* 20 (1), 346–358. doi:10.1109/TPWRD.2004.835039

Christian, H. J., Blakeslee, R. J., Boccippio, D. J., Boeck, W. L., Buechler, D. E., Driscoll, K. T., et al. (2003). Global Frequency and Distribution of Lightning as Observed from Space by the Optical Transient Detector. *J. Geophys. Res.* 108 (D1), 4005. doi:10.1029/2002JD002347

Cui, X. D., Gu, Y., and Xu, Z. Y. (2021). Characteristic Analyses on Multi-Return Stroke of Lightning Parameters over Zhejiang Based on 3D Lightning Location System Data. *Sci. Tech. Eng.* 21 (23), 9706.

Du, S. C. (1996). Suggestion on Revising the Calculation Method and Some Parameters Used in Lightning Protection of Transmission Lines. *Power Syst. Tech.* 20 (12), 53–56. doi:10.13335/j.1000-3673.pst.1996.12.013

Finke, U., and Hauf, T. (1996). The Characteristics of Lightning Occurrence in Southern Germany. *Beitr. Phys. Atmosph.* 69 (3), 361.

Fleenor, S. A., Biagi, C. J., Cummins, K. L., Krider, E. P., and Shao, X.-M. (2009). Characteristics of Cloud-To-Ground Lightning in Warm-Season Thunderstorms in the Central Great Plains. *Atmos. Res.* 91, 333–352. doi:10.1016/j.atmosres.2008.08.011

Gao, J. G., Liu, Y., and Bu, W. (2019). Analysis on the Characteristics of Lightning Current Amplitude in Beijing Area Using ADTD Data. *Torrential Rain and Disasters* 38 (1), 92–96. doi:10.3969/j.issn.1004-9045.2019.01.012

Grant, I. S., Anderson, J. G., Hileman, A. R., Janischewskyj, W., Longo, V. J., Chisholm, W., et al. (1985). A Simplified Method for Estimating Lightning Performance of Transmission Lines. *IEEE Trans. Power Apparatus Syst.* 104 (4), 919.

Gu, Y., Xu, Z. Y., and Cui, X. D. (2021). Characteristics Analysis of Lightning Disasters in Zhejiang Province Province from 1998 to 2020. *Bull. Sci. Tech.* 37 (7), 38.

He, J. L., Yang, G., and Yu, Z. Q. (2017). A Study on Lightning Current Waveform Parameters for Lightning Protection. *Building Electricity* 36 (3), 3.

Kohlrausch, F. (1888). Ueber den electrischen leitungswiderstand des quecksilbers. *Ann. Phys. Chem.* 271 (12), 700–764. doi:10.1002/andp.18882711206

Li, J. Q., Wang, J. S., Shen, S. H., Li, B., Chen, H., and Lin, T. (2011). Analysis of the Cumulative Probability of Lightning Current Amplitudes Based on the Statistical Data Obtained from the ADTD System. *Meteorol. Monthly* 37 (2), 226–231.

Li, R. F., Wu, G. N., Cao, X. B., and Ma, Y. (2011). Formula for Probability of Lightning Current Amplitude. *Trans. China Electrotechnical Soc.* 26 (4), 161.

Li, T., Zhai, Y., Sun, Y., and Gao, H. (2019). Distribution Characteristics and Calculation Formula for Cumulative Probability of Lightning Current Amplitude in Yan'an Area. *J. Nanjing Univ. Inf. Sci. Technology(Natural Sci. Edition)* 11 (3), 360–366. doi:10.13878/j.cnki.jnuist.2019.03.01610.4236/jssm.2019.123024

Liu, Y., Wang, Z. H., Kang, F. Q., Zhang, H. L., Xiao, W. A., and Li, Z. R. (2009). Characteristics of Cloud-To-Ground Flashes in Zhejiang Province and Gansu Areas. *Plateau Meteorology* 28 (3), 669–674.

Lu, G. J., Xiong, J., Chen, J. H., Tong, X. F., and Gu, S. Q. (2009). Analysis of Ground Flash Density and Lightning Parameters of Guangzhou in 1999- 2008. *High Voltage Eng.* 34 (12), 2930–2936. doi:10.13336/j.1003-6520.hve.2009.12.015

Ma, M., Lv, W. T., Zhang, Y. J., Meng, Q., and Yang, J. (2008). Characteristics of Lightning Exposure in China from 1997 to 2006. *J. Appl. Meteorol. (Science Chinese)* 19 (4), 394.

Metwally, I. A., Heidler, F., and Zischank, W. (2004). Measurement of the Rear-Face Temperature of Metals Struck by Lightning Long-Duration Currents. *Euro. Trans. Electr. Power* 14 (4), 201–222. doi:10.1002/etep.16

Orville, R. E., and Huffines, G. R. (1999). Lightning Ground Flash Measurements over the Contiguous United States: 1995-97. *Mon. Wea. Rev.* 127 (11), 2693–2703. doi:10.1175/1520-0493(1999)127<2693:lgfmot>2.0.co;2

Paisios, M. P., Karagiannopoulos, C. G., and Bourkas, P. D. (2008). Estimation of the Temperature Rise in Cylindrical Conductors Subjected to Heavy 10/350μs Lightning Current Impulses. *Electric Power Syst. Res.* 78 (1), 80–87. doi:10.1016/j.epsr.2007.01.002

Pinto, O., Jr., Regina C.A. Pinto, I., H. Diniz, J., Cazetta Filho, A., C.L. Cherchiglia, L., and M. Carvalho, A. (2003). A Seven-Year Study about the Negative Cloud-To-Ground Lightning Flash Characteristics in Southeastern Brazil. *J. Atmos. Solar-Terrestrial Phys.* 65, 739–748. doi:10.1016/S1364-6826(03)00077-4

Poelman, D. R. (2014). A 10-Year Study on the Characteristics of Thunderstorms in Belgium Based on Cloud-To-Ground Lightning Data. *Monthly Weather Rev.* 142, 4839–4849. doi:10.1175/MWR-D-14-00202.1

Rivas Soriano, L., de Pablo, F., and Tomas, C. (2005). Ten-Year Study of Cloud-To-Ground Lightning Activity in the Iberian Peninsula. *J. Atmos. Solar-Terrestrial Phys.* 67, 1632–1639. doi:10.1016/j.jastp.2005.08.019

Shim, E. B., Woo, J. W., Han, S. O., and Moon, J. D. (2002). Lightning Characteristics in Korea and Lightning Performance of Power Systems. *Proc. IEEE/PES Transm. Distribution Conf. Exhibition*, 534–539.

Wang, X. L., Zhang, K. J., Yu, T. Y., and Wang, Z. H. (2016). Characteristics of Probability Distribution for Lightning Peak Current and Segment Revision for Cumulative Probability. *Meteorol. Sci. Tech.* 44 (6), 1037–1042. doi:10.19517/j.1671-6345.2016.06.028

Yu, T. Y., Wang, X. L., Zhang, K. J., Zhao, T., and Wang, X. F. (2021). The Distribution Characteristics of Ground Flash and Classification of Lightning Intensity in Hubei Province from 2007 to 2019. *J. Meteorology Environ.* 37 (6), 79.

Yue, P., Wu, M., Tan, J., Zhao, H. Y., Wang, C. C., Zhao, C., et al. (2013). Statistics and Application of Lightning Parameters Based on Tower Circle Method. *Insulators and Surge Arresters*. 35 (1), 107.

Zhang, Y., Bian, X. W., Wang, K. T., Zhang, W. B., and Wang, Z. H. (2021). Analysis of Lightning Characteristics and Their Relationship with Meteorological Parameters in Zhejiang Province and its Surrounding Areas Based on TRMM/LIS Data. *J. Trop. Meteorology* 37 (4), 602–610. doi:10.16032/j.issn.1004-4965.2021.057

Zhang, Y. J., Huang, H., Liu, H. Y., and Chen, Z. F. (2011). Lightning Strike Risk Evaluation of Power Grid with Distributed Hydropower. *J. South China Univ. Technology(Natural Sci. Edition)* 39 (10), 127.

Zhao, C., Lei, M. F., Chen, J. H., Gu, S. Q., Wang, P., and Zhao, J. J. (2017). Statistical Method of Lightning Current Amplitude Distribution along Transmission Line Corridor. *High Voltage Eng.* 43 (5), 1609–1614. doi:10.13336/j.1003-6520.hve.20170428029

Zhao, C., Lei, M. F., Wang, J., Jiang, W. D., Chen, J. H., and Wang, P. (2018). Curve Fitting Method of Cumulative Probability Distribution of Lightning Current Magnitude. *High Voltage Eng.* 44 (5), 1598–1604. doi:10.13336/j.1003-6520.hve.20180430027


**Conflict of Interest:** The authors declare that the research was conducted in the absence of any commercial or financial relationships that could be construed as a potential conflict of interest.

frontiers | Frontiers in Environmental Science

ORIGINAL RESEARCH
published: 26 April 2022
doi: 10.3389/fenvs.2022.890514

# Two Typical Patterns of Regional $PM_{2.5}$ Transport for Heavy Air Pollution Over Central China: Rapid Transit Transport and Stationary Accumulation Transport

*Ying Wang[1], Yongqing Bai[2]*, Xiefei Zhi[1]*, Kai Wu[3], Tianliang Zhao[1], Yue Zhou[2], Jie Xiong[2], Shoupeng Zhu[4], Wen Zhou[2], Weiyang Hu[1], Ling Zhang[1] and Kai Meng[5]*

*[1]Collaborative Innovation Center on Forecast and Evaluation of Meteorological Disasters/Key Laboratory of Meteorological Disasters, Ministry of Education, Nanjing University of Information Science and Technology, Nanjing, China, [2]Hubei Key Laboratory for Heavy Rain Monitoring and Warning Research, Institute of Heavy Rain, China Meteorological Administration, Wuhan, China, [3]Department of Land, Air, and Water Resources, University of California, Davis, CA, United States, [4]China Meteorological Administration Transportation Meteorology Key Laboratory, Nanjing Joint Institute for Atmospheric Sciences, Nanjing, China, [5]Key Laboratory of Meteorology and Ecological Environment of Hebei Province, Hebei Provincial Institute of Meteorological Sciences, Shijiazhuang, China*

OPEN ACCESS

**Edited by:**
*Xinyao Xie,*
*Institute of Mountain Hazards and Environment (CAS), China*

**Reviewed by:**
*Xiaolan Li,*
*CMA, China*
*Jinghui Ma,*
*SMB, China*

***Correspondence:**
*Yongqing Bai*
*2007byq@163.com*
*Xiefei Zhi*
*zhi@nuist.edu.cn*

**Specialty section:**
*This article was submitted to Atmosphere and Climate, a section of the journal Frontiers in Environmental Science*

**Received:** *06 March 2022*
**Accepted:** *25 March 2022*
**Published:** *26 April 2022*

**Citation:**
*Wang Y, Bai Y, Zhi X, Wu K, Zhao T, Zhou Y, Xiong J, Zhu S, Zhou W, Hu W, Zhang L and Meng K (2022) Two Typical Patterns of Regional $PM_{2.5}$ Transport for Heavy Air Pollution Over Central China: Rapid Transit Transport and Stationary Accumulation Transport. Front. Environ. Sci. 10:890514. doi: 10.3389/fenvs.2022.890514*

The regional transport of air pollutants has been identified as a critical factor that affects air quality over downwind receptor areas; however, the regional transport patterns for air pollution episodes remain poorly understood. In this study, we identified two distinct patterns of regional transport: rapid transit transport (RTT) and stationary accumulation transport (SAT), both of which induced severe $PM_{2.5}$ pollution episodes in central China during 2015–2020. The differences and similarities between the two regional transport patterns of air pollution were characterized by their influencing meteorological factors. Similar meteorological conditions trigger the RTT and SAT, with a high-$PM_{2.5}$ concentration air mass from the upstream regions transported to the Twain-Hu Basin (THB) by the strong northerly winds with a southward advance of cold air mass. The average rate of increase in the $PM_{2.5}$ concentration of the RTT (12.5 μg/$m^3$/h) is more than that of the SAT (5.7 μg/$m^3$/h). However, meteorological conditions evolved differently in RTT and SAT. For RTT with the fast passage of cold air, the THB is located behind the strong cold front during the later stage, and these events rapidly ended owing to the northerly winds and wet scavenging of precipitation. For SAT with the slow cold air accumulation, the THB is mainly occupied by a weak high-pressure system with low wind speeds, strong descending airflow, and a low atmospheric boundary layer height, trapping the air pollutants accumulated in the THB and resulting in persistent heavy pollution incidents. This study provides new insights into the meteorological mechanism underlying the formation of severe air pollution episodes over a receptor region owing to the regional transport patterns of air pollutants.

**Keywords: heavy air pollution, Twain-Hu Basin, regional $PM_{2.5}$ transport, meteorological drivers, atmospheric vertical structure**

## 1 INTRODUCTION

In China, air pollution, specifically elevated $PM_{2.5}$, due to rapid urbanization and industrial processes has become a serious public concern over the last few decades (Wu et al., 2013; Miao et al., 2017). Research on regional aerosol pollution over megacities and major city clusters has attracted considerable attention because of the detrimental effects of particulate matter on human health (Chan and Yao, 2008; Yan et al., 2019; Gu et al., 2021; Wu et al., 2021). Although strict anthropogenic emission regulation policies have been implemented since 2013, episodes with elevated $PM_{2.5}$ concentrations have been frequently observed, especially in winter (Wei et al., 2017; Wu et al., 2017).

Atmospheric circulation and weather systems have been widely reported to have significant effects on the occurrence of severe $PM_{2.5}$ episodes (Wu et al., 2016; Miao et al., 2017; Guo et al., 2019). The weakening of the near-surface East Asian winter monsoons and East Asian trough is a key reason for the frequent occurrence of haze in the North China Plain, which is generally linked to weak surface winds and high relative humidity and is conducive to the formation and accumulation of air pollutants (Niu et al., 2010; Cai et al., 2017). Weak cold air masses and stagnant weather conditions have also been considered the main reasons for the heavy haze in Eastern China in January 2013 (Zhang et al., 2014). The planetary boundary layer height (PBLH) plays a significant role in the formation and development of heavy haze (Quan et al., 2013; Zhao et al., 2013). A strong temperature inversion and downward airflow in the planetary boundary layer (PBL) can cause air pollutants to accumulate in shallow layers (Zhao et al., 2013), leading to heavy pollution events. The reduction in the PBLH and turbulent vertical mixing in the PBL are significantly related to an increase in primary pollutants in Europe (Fallmann, 2016). The $PM_{2.5}$ and the PBLH form a positive feedback loop for serious pollution events in megacities; the heat flux is significantly reduced because of the influence of haze, which inhibits the development of the PBL to some extent, and the restricted development of PBL further weakens the diffusion of air pollutants, eventually resulting in serious pollution incidents (Liu et al., 2019; Quan et al., 2013; Wenjie Zhang et al., 2019).

Regional transport plays a significant role in the formation and evolution of air pollution episodes, as well as the air quality over the receptor regions (Xiong et al., 2021; Bai et al., 2022; Shen et al., 2022). The measured concentrations of particulate matter in the metropolitan areas of South America have been caused predominantly by long-range transport (Diaz Resquin et al., 2018). Research on the Beijing–Tianjin–Hebei region found that in addition to the influence of the emission source intensity and chemical component formation, air quality is significantly affected by aerosol pollutants emitted from surrounding provinces (e.g., Shandong and Henan), which can be transported to the Beijing–Tianjin–Hebei region through transregional transport (Guo et al., 2013; Zhang et al., 2015). Ji et al. (2018) found that the transport of pollution from Hebei, Shandong, Anhui, and other regions to Hangzhou in Zhejiang Province could exceed 60% during the G20 period. Driven by regional transport, fine particulate matter in central Chile has increased by 13–15% on average (Lapere et al., 2021). The Pearl River Delta contributes an average of 56.5% of the $PM_{2.5}$ transported by northerly winds that contribute to increased $PM_{2.5}$ concentrations during a heavy haze event (Chen et al., 2019).

Studies have investigated the formation mechanism of severe $PM_{2.5}$ and explored effective regulations for mitigating $PM_{2.5}$ pollution in China, primarily focusing on the North China Plain (NCP), Yangtze River Delta (YRD), Pearl River Delta (PRD), and Sichuan Basin (SCB) (Cao et al., 2012; Wang et al., 2021; Wu et al., 2019; Yang et al., 2020; Lei Zhang et al., 2019). However, little attention has been paid to the middle reaches of the Yangtze River, especially the Twain-Hu Basin (THB) (**Figure 1A**). The dominant synoptic patterns have been classified as heavy $PM_{2.5}$ in the THB region of central China from 2013 to 2018 (Yan et al., 2021). Strong northerly winds influenced by the East Asian winter monsoons transport high concentrations of air pollutants downstream from the upper reaches of Hebei and Henan, resulting in heavy pollution incidents in the THB (Bai et al., 2021; Hu et al., 2021; Shen et al., 2021). Governed by non-stagnant conditions with strong near-surface winds, unstable atmospheric structures, and non-temperature inversions, severe $PM_{2.5}$ pollution episodes in the THB have been aggravated by regional transport (Yu et al., 2020; Zhou et al., 2022). Xiangyang (XY), Jingmen (JM), and Jingzhou (JZ) (**Figure 1B**), which are in the northwest of THB, are characterized by flat terrain adjoining the eastern slope of the Daba and Wushan Mountains, and the routes of the three cities have been identified as typical regional transport corridors in the THB (Huang et al., 2020). Under the influence of the East Asian winter monsoons, air pollutants in the upwind areas (such as the NCP and YRD) are transported to the THB (**Figure 1C**). This unique geographical location forms major corridors for the regional transport of air pollutants in China (Zhou et al., 2019; Hu et al., 2021), causing the THB to be a key receptor region of air pollutants (Yu et al., 2020; Bai et al., 2021; Shen et al., 2021). Although heavy $PM_{2.5}$ transport events in the THB have been analyzed, most studies have been limited to case studies that have not considered the differences and similarities among the transport pollution events and features of the influencing meteorological factors during different stages and patterns. Moreover, this information can be used to improve the understanding of the transport mechanisms during different patterns in the THB and provide a reference guide for governmental decision-making.

In this study, we used the ERA5 reanalysis dataset, ambient measurements of $PM_{2.5}$, and ground-level meteorological observations to identify two typical regional transport patterns of $PM_{2.5}$ and investigated the evolution processes for each typical $PM_{2.5}$ episode in the THB in central China. The remainder of this article is organized as follows. **Section 2** presents the data and the methods used in this study. The identified severe $PM_{2.5}$ episodes are investigated in **Section 3.1**. The impact of the meteorological mechanisms on the heavy $PM_{2.5}$ pollution process for RTT and SAT is discussed in **Section 3.2**.

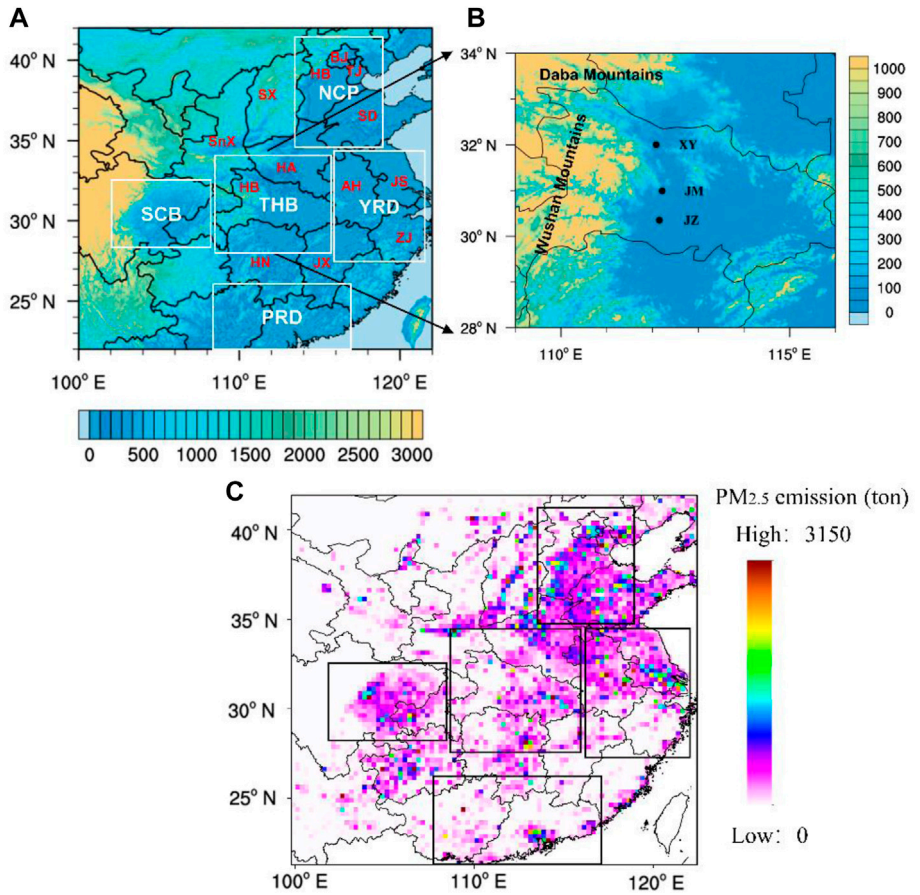


**FIGURE 1 | (A)** Terrain height (m) of central and eastern China with the locations of provinces. The regions of NCP, PRD, YRD, SCB, and THB are outlined approximately with a white frame. **(B)** Terrain height (m) of the THB and surrounding areas with the location of cities of XY, JM, and JZ (black dots). **(C)** Distribution of $PM_{2.5}$ emissions from anthropogenic sources in central and eastern China (2017 winter averaged).

## 2 DATA AND METHODS

### 2.1 Air Pollutants Monitoring Data

The hourly $PM_{2.5}$ concentrations over central–eastern China during winter (December to March of the following year) from 2015 to 2020 were obtained from the National Air Quality Monitoring Network operated by the Ministry of Ecology and Environment of China (http://www.mee.gov.cn). The ambient $PM_{2.5}$ concentrations were measured by using the tapered element oscillating microbalance method and the β absorption method by using a TEOM Series 1400a Ambient Particulate Monitor.

### 2.2 Meteorological Observations and Reanalysis Dataset

The ground-level observations of meteorological parameters, namely, air temperature, wind speed, wind direction, and precipitation, were obtained every hour from the China Meteorological Data Service Centre (http://data.cma.cn/).

In addition, the ERA5 global reanalysis dataset with a horizontal resolution of 0.25° × 0.25° was adopted to resolve the spatial limitations of the ground meteorological data. The key parameters of ERA5 used in this study were air temperature at 2 m, wind speed at 10 m, sea-level pressure, PBLH, vertical velocity, and potential pseudo-equivalent temperature. The ERA5 dataset is the fifth atmospheric reanalysis product of global climate developed by the European Centre for Medium-Range Weather Forecasts and has been widely used in weather and climate studies because of its fine spatial resolution (31-km grid spacing) and high temporal resolution (hourly analysis fields). The PBLH is a crucial meteorological parameter for air quality analysis. Compared with other reanalysis products, such as JRA-55 and MERRA-2, ERA5 has been recognized as the most promising product for PBLH measurements, with an estimated deviation of approximately 130 m, as compared to measurements using radiosondes released during daytime (Bao and Zhang, 2019; Guo et al., 2021; Huang et al., 2021).

### 2.3 Quantitative Measures of Atmospheric Conditions

#### 2.3.1 Pseudo-Equivalent Potential Temperature Difference ($\Delta\theta$ se)

Changes in the local meteorological conditions have an important relationship with the evolution of episodes of heavy pollution.

The atmospheric thermal factors related to temperature, humidity, and atmospheric stratification stability have a considerable impact on heavy pollution (Ning et al., 2018). We selected the pseudo-equivalent potential temperature difference ($\Delta\theta$ se) between 700 hPa and 1,000 hPa as a thermal factor, which can indicate the stratification instability of humid air in the lower troposphere and is indicative of the potential vertical mixing of air flows (Lin et al., 2016).

$$\Delta\theta se = \theta se_{700} - \theta se_{1000} \quad (1)$$

where $\theta se_{700}$ and $\theta se_{1000}$ are the pseudo-equivalent potential temperatures at 700 hPa and 1,000 hPa, respectively. A larger pseudo-equivalent potential temperature difference ($\Delta\theta se$) indicates a more stable atmospheric stratification in the middle and lower troposphere, and *vice versa*.

### 2.3.2 Ventilation Coefficient

Wind strength and boundary layer dynamics are critical meteorological factors that affect the horizontal and vertical diffusion of air pollutants, respectively (Zhang et al., 2014). We used the product of the PBLH and wind speed to determine the ventilation coefficient (*VC*) (Nair et al., 2007; Hou et al., 2018; Moreira et al., 2020), which is considered a robust indicator of the atmospheric transport and diffusion capability. The wind field data and PBLH were adopted from the ERA5 data. The *VC* was calculated as follows:

$$VC = \int_{P_1}^{P_2} \sqrt{u^2 + v^2}\, dp \cdot H \quad (2)$$

where $p$ is the pressure; $P_1$ and $P_2$ correspond to 1,000 hPa and 925 hPa, respectively; the height between the two atmospheric pressure layers is the main low-level pollution transport height; $u$ and $v$ are the zonal and meridional wind components between 925 and 1,000 hPa (m/s), respectively; and $H$ denotes the PBLH (m).

# 3 RESULTS AND DISCUSSION

## 3.1 Identified Heavy Pollution Features for RTT and SAT

When the THB regional transport corridor comprises XY, JM, and JZ (**Figure 1**), two or all three cities achieve severe $PM_{2.5}$, with the daily average concentration exceeding 150 μg/m$^3$; this situation can be defined as a heavy $PM_{2.5}$. Thus, we selected 46 heavy air pollution episodes that occurred in the winters of 2015–2020.

Additionally, when a severe $PM_{2.5}$ episode occurred accompanied by a north–south (28°N–34°N) pressure gradient (NSPG) larger than 2 hPa and a regional (28°N–34°N, 112°E–114°E) averaged northerly wind (NW) higher than 1.5 m/s, which favor the transport of $PM_{2.5}$ from upwind northern sources to downwind THB areas, this episode can be classified as a regional transport type. Accordingly, 27 severe $PM_{2.5}$ episodes were selected as the regional transport type, accounting for 58.7% of all severe episodes. The mean values of NSPG and NW are 3.8 hPa and 2.1 m/s, respectively, which are relatively higher than those of the remaining 19 heavy $PM_{2.5}$ episodes of 0.2 hPa and 1.1 m/s, respectively.

To understand the characteristics of regional $PM_{2.5}$, we defined the situation with short-term burst growth and rapid dissipation of heavy pollution accompanied by strong NWs as "rapid transit transport (RTT)." The situation of the triggering and growth stage is accompanied by a strong NW, while the $PM_{2.5}$ peak maintenance stage is accompanied by a decrease in wind speed, which is defined as "stationary accumulation transport (SAT)."

The RTT and SAT episodes had similar transport features during the early growth stage of $PM_{2.5}$, and the variation tendency of the meteorological parameters differed during the peak and maintenance stages. Thus, we identified RTTs by using the criteria of the peak maintenance stage accompanied by an NSPG larger than 3 hPa and NW exceeding 2.5 m/s. When the maintenance stage was characterized by an NSPG of less than 2 hPa and NW below 1.5 m/s, this episode was classified as SAT. Twelve RTT episodes and six SAT episodes were selected, accounting for 44.4 and 22.2% of the regional transport types, respectively. In **Figure 2A**, the NSPG and NW for RTT are significantly larger than those for SAT, with the mean NSPG and NW values reaching 6.4 hPa and 3.2 m/s, as opposed to −0.11 and 0.8 m/s for SAT. Therefore, investigating the features and meteorological parameters of the RTT and SAT on $PM_{2.5}$ has provided a profound understanding of the formation mechanism of heavy $PM_{2.5}$ pollution over the THB.

**Figure 2B** shows the rate of increase in the $PM_{2.5}$ during the early growth stage and the maintenance hours of the two patterns. The early growth stage is defined by the duration between the lowest $PM_{2.5}$ and the peak over the period of a sustained increase. The maintenance stage of each episode was defined as the duration during which the $PM_{2.5}$ concentrations continuously exceeded 150 μg/m$^3$. Notably, the increasing rate of $PM_{2.5}$, as shown in **Figure 2B** (**Supplementary Figure S1**), is defined by the peak $PM_{2.5}$ concentration minus the moderate pollution level of 115 μg/m$^3$ (light pollution level 75 μg/m$^3$), then divided by the duration of the sustained increase. We observed that the northern aerosol particles can be quickly advected to the THB by strong northern wind fields in the RTT, and the mean rate of increase reached 12.5 (7.5) μg/m$^3$/h, with the rate of increase greater than 5.7 (4.1) μg/m$^3$/h for SAT. Notably, the rate for moderate pollution is higher than that for light pollution. Additionally, although the rate of increase in the $PM_{2.5}$ concentration for the SAT is relatively slower than that of the RTT, the maintenance stage of the SAT is longer, and the mean duration could reach 72.8 h, which is significantly longer than the 27.5 h of RTT. Furthermore, several events had a SAT duration of over 80 h, usually resulting in long-lasting pollution over the THB.

## 3.2 Meteorological Mechanisms of RTT and SAT Affecting Heavy $PM_{2.5}$ Pollution Evolution Over Central China

### 3.2.1 Meteorological Conditions

Six typical RTT and SAT heavy pollution processes (**Supplementary Tables S1, S2**) were selected and used to

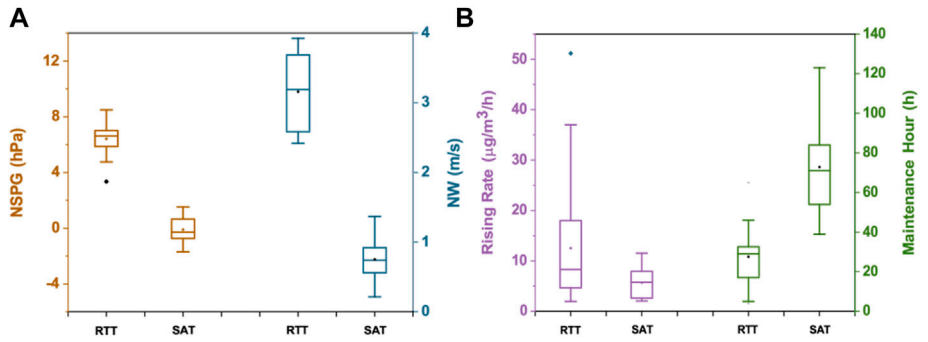


**FIGURE 2 | (A)** Boxplot of the NSPR (left) and NW (right) of six episodes for RTT and twelve episodes for SAT; **(B)** boxplot of the rising rate of $PM_{2.5}$ concentrations (left) and time duration (right) of severe $PM_{2.5}$ pollution maintenance stage of twelve episodes for RTT and six episodes for SAT in transport corridor cities: XY, JM, and JZ in the THB. The diamond beyond the box plot denotes the abnormal value.

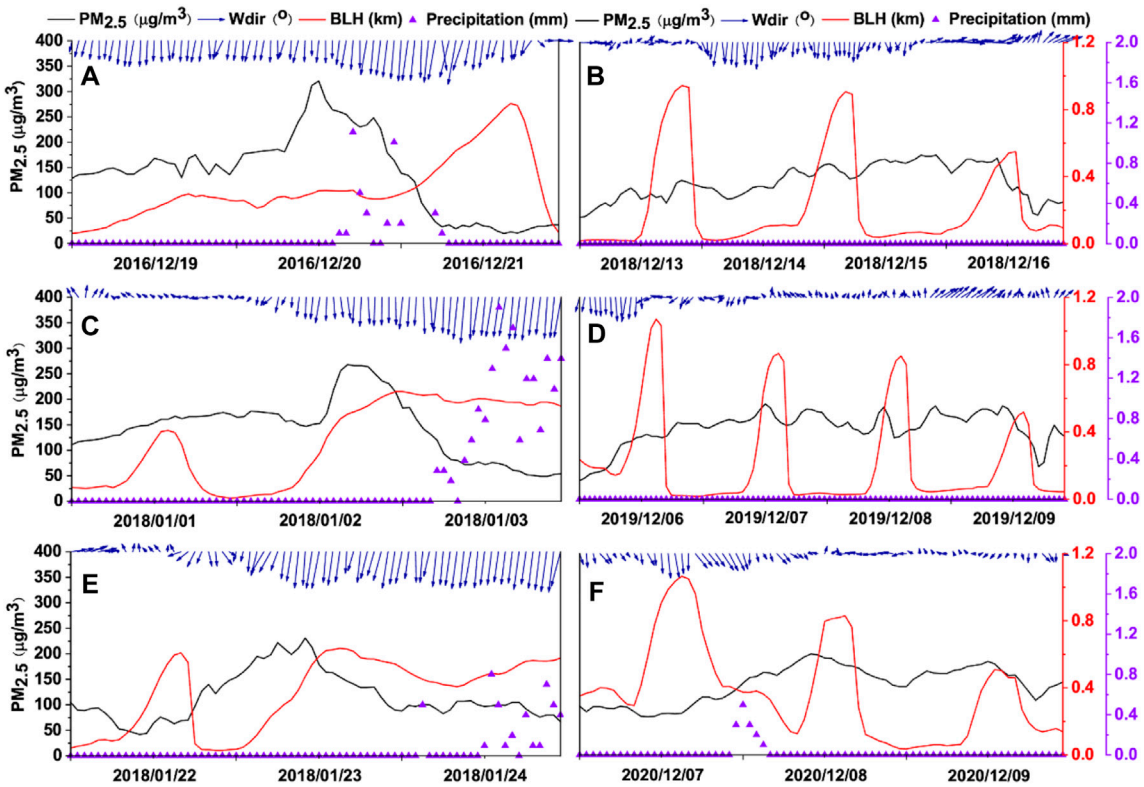


**FIGURE 3 |** Temporal changes in $PM_{2.5}$ concentration (black lines), PBLH (red lines), wind directions at 10 m (Wdir, vectors), and precipitation (purple triangles) were observed at JM in the THB. **(A,C,E)** Left column represents the three cases of RTT. **(B,D,F)** Right column represents the three cases of SAT.

analyze the influence of the boundary layer meteorological conditions at different stages of local $PM_{2.5}$, including the triggering, maintenance, and dissipation stages, in the THB. Three typical RTT heavy pollution processes are presented in **Figures 3A,C,E** (**Supplementary Figure S2A, C, E** are the other three processes of RTT), demonstrating that the early rapid growth stage of $PM_{2.5}$, corresponding to the strong NW, was favorable for the rapid horizontal transport of aerosol particles from the north (Li et al., 2013), resulting in the explosive growth of $PM_{2.5}$ pollutants in the THB. The peak $PM_{2.5}$ and heavy pollution maintenance stage are also followed by good transport conditions with strong NW fields. Specifically, during the first episodes (**Figure 2A**), the peak $PM_{2.5}$ concentrations reached 300 $\mu g/m^3$ within 6 h, indicating an explosive increase in $PM_{2.5}$ levels within a short period. Further strengthening of the NW and increased PBLH are

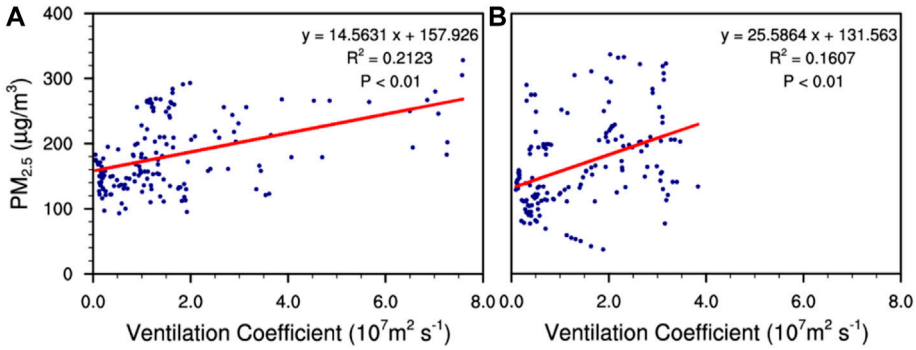


**FIGURE 4 |** Correlations of the surface $PM_{2.5}$ concentration to the ventilation coefficient ($10^7 m^2 s^{-1}$) over the region (112–114°E and 30.5–31°N) averaged in the early growth stage of six typical episodes for **(A)** RTT and **(B)** SAT in JM, respectively; the early growth stage of all patterns indicates the correlations are significant at 99%.

conducive to atmospheric diffusion conditions, especially the mean rainfall intensity (0.62 mm/h) and mean total rainfall (9.3 mm), which are responsible for the wet removal of $PM_{2.5}$ (Zhou et al., 2020). This typical transport pattern is RTT, which can be summarized as being affected predominantly by relatively strong cold air and NWs, corresponding to the rapid growth and spread of pollution in the THB. As the northerly winds further strengthen and wet scavenging occurs, the air pollution level can drop rapidly.

**Figures 3B,D, and F** present three typical SAT heavy pollution episodes (**Supplementary Figure S2B, D, and F** present the other three episodes of SAT), showing that the increase in the $PM_{2.5}$ level was generally accompanied by an increase in wind speed. During the $PM_{2.5}$ concentration peak and heavy pollution maintenance stage, the wind speed and PBLH significantly decreased, leading to meteorological conditions that were unfavorable for the horizontal transport and vertical mixing of aerosol particles in the boundary layer (Zhu et al., 2010). The $PM_{2.5}$ transported from upwind regions was trapped and gradually accumulated over the THB under stagnant weather conditions (Kang et al., 2019).

The typical features of SAT differ from those of RTT. Notably, at first, the prevalence of northerly winds deteriorates the air quality over the THB, and subsequently, THB experiences a relatively stable and stagnant stage accompanied by weak wind and low PBLH. The key features of the SAT are a long duration (**Supplementary Table S2**), low PBLH, and poor diffusion capacity, which are conducive to the accumulation of precursors and formation of secondary pollutants (Huang et al., 2014; Gao et al., 2015). The typical transport features in this pattern imply that the severe $PM_{2.5}$ episodes in the THB are affected not only by local emissions but also by the transboundary transport of $PM_{2.5}$ that originates from surrounding regions.

An increase in VC contributes to a decrease in $PM_{2.5}$, which leads to air quality improvement (Lu et al., 2012; Xu et al., 2015; Sujatha et al., 2016). However, it may not fit the transport pollution type, in which the occurrence of heavy pollution episodes is usually accompanied by good ventilation, bringing air pollutants from long-distance areas (Hou et al., 2018). As shown in **Figure 4**, $PM_{2.5}$ concentrations in the RTT (**Figure 4A**) and SAT (**Figure 4B**) were positively correlated with the VC during the early growth stage. The correlation coefficients between VC and $PM_{2.5}$ reach 0.46 and 0.40 for the RTT and SAT, respectively, and both pass the significance test of $\alpha = 0.01$. A larger VC is beneficial to the inflow of $PM_{2.5}$, indicating that transport is the trigger mechanism for RTT and SAT episodes.

### 3.2.2 Synoptic Circulation

Persistent heavy pollution events are influenced by synoptic circulation. Variations in the synoptic circulation play a primary role in modulating the day-to-day variations in air pollutants. The features in each evolution stage were determined by synthesizing $PM_{2.5}$ and the surface synoptic circulations of six typical RTT (**Supplementary Table S1**) cases and six typical SAT (**Supplementary Table S2**) cases on the day before transport (first day), the day of transport (second day), and the day after transport (third day) (**Figure 5**). The THB was controlled by the regional low-pressure equalization field on the first day of the RTT, which had the noticeable characteristic of static wind (**Figure 5A**). In the spatial distribution of VC, the first day of RTT in the THB indicated that the advection and diffusion conditions were relatively poor (**Supplementary Figure S3A**). The local pollution level was low because local pollution emissions in the THB were relatively low at that time. However, the $PM_{2.5}$ concentrations in the NCP were relatively high, and the local $PM_{2.5}$ concentrations exceeded 200 μg/m$^3$. As shown in **Figure 5B**, the atmospheric circulation was adjusted on the second day of regional transport. The atmospheric diffusion conditions improved significantly, especially in the XY–JM–JZ transport corridor in the THB, and its upwind areas appeared as high-value centers of the VC (**Supplementary Figure S3B**). The THB was located at the bottom rear of the ground high-pressure system such that there was an evident zonal pressure gradient, and the wind speed in the THB, including the upstream areas, increased significantly. The cold air dominated by NWs carried the upstream $PM_{2.5}$ southward rapidly, causing heavy pollution incidents in the THB; the $PM_{2.5}$ concentration decreased in the upstream area, demonstrating that the temporal and spatial changes in the $PM_{2.5}$ concentrations have a

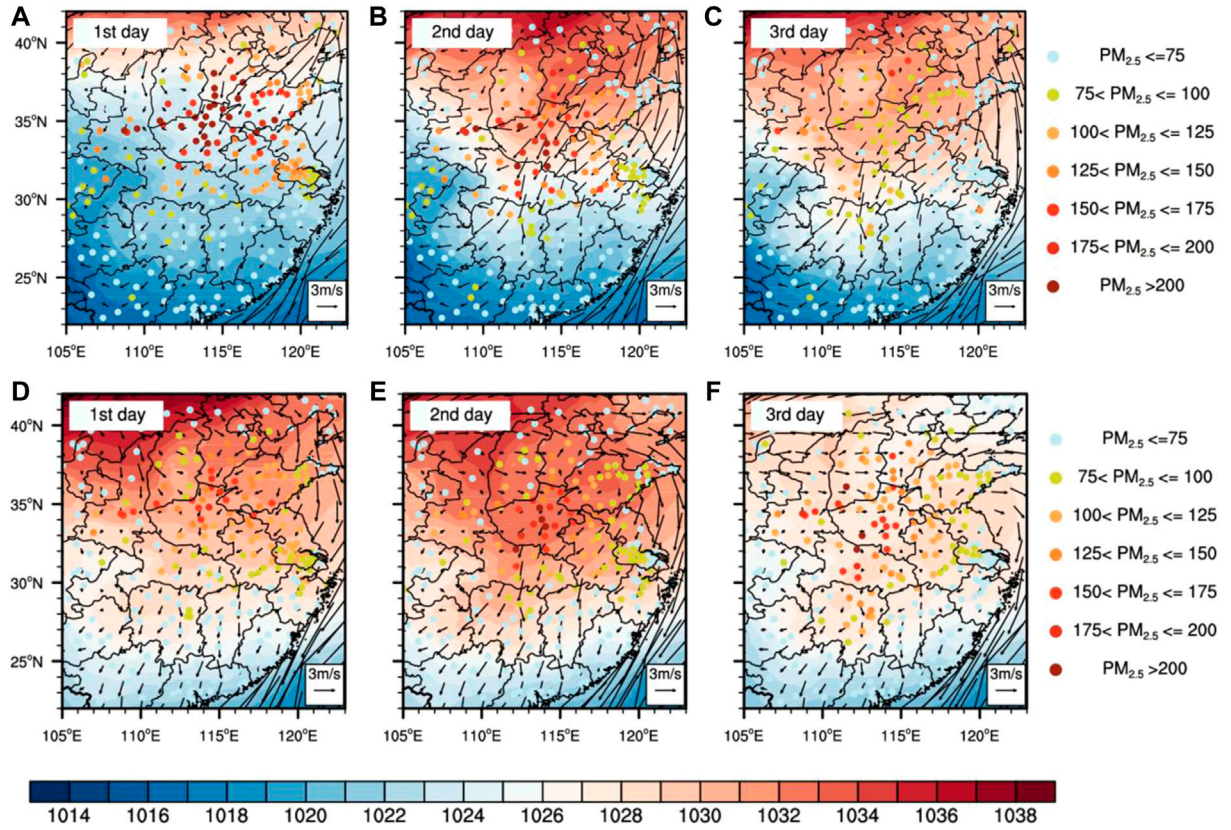


**FIGURE 5 |** Distributions of daily surface $PM_{2.5}$ concentrations (μg/m$^3$) observed at the sites (colored dots), daily sea-level air pressure (hPa, color contours), and daily 10 m horizontal wind vectors (arrow) of ERA5-Land during the heavy air pollution averaged over six severe $PM_{2.5}$ episodes of the top row **(A,B,C)** RTT and bottom row **(D,E,F)** SAT.

distinct cross-regional transport trend, and this transport is encouraged by NWs. On the third day of RTT, the influence of strong winds in the THB area continued, and the height of the PBL increased significantly (**Figure 2**). This caused atmospheric diffusion conditions to be sustained (**Supplementary Figure S3C**) and significantly affected the removal of $PM_{2.5}$.

The early stage of SAT was similar to that of RTT. The regional diffusion conditions during the early stage were poor, and heavy pollution was primarily concentrated in the NCP (**Supplementary Figure S3D**, **Figure 5D**). The advection and diffusion conditions were relatively good on the day of transport in the THB, and the upstream high-concentration pollutants were transported to the THB by the northerly wind of the East Asian winter monsoons (**Supplementary Figures S3E, 5E**). However, during the maintenance stage (**Figure 5F**), the circulation evolved into a static stability pattern controlled by high pressure, and the wind speed decreased. The pollutant diffusion capacity in the horizontal and vertical directions weakened in the THB (**Supplementary Figure S3F**); the air pollutants were not easily diluted and diffused, resulting in $PM_{2.5}$ remaining in the area, which aggravated the accumulation of local pollution. The $PM_{2.5}$ concentrations of SAT are the result of the combined effects of local and regional sources, and transport is the predominant reason for reaching the peak.

**Figure 6** depicts the evolution of the 925 hPa geopotential height and air temperature anomalies during the pollution processes. The results indicate that the 925 hPa synoptic circulation evolution is similar to that of the ground. In addition, on the first day of the RTT, positive air temperature anomalies appeared over the THB (**Figure 6A**). However, on the second day, the intensity of the southward cold air strengthened, and the air temperature anomalies in the THB reached −3°C to −2°C (**Figure 6B**); notably, the gradient of the geopotential strengthened, and the abnormal northeasterly wind carried upstream aerosol particles to the THB. The northern cold temperatures and high pressure were the greatest on the third day. Strong and deep cold air continued to sweep southward across the THB, and the air temperature anomalies reached −5°C to −3°C (**Figure 6C**). At this time, the intrusion of strong cold air could easily cause convective instability, and the local precipitation generated had a significant effect on the removal of $PM_{2.5}$.

The SAT was also affected by the southward cold air on the second day but was relatively weak; the air temperature anomalies in the THB were −2 to 0°C (**Figure 6E**), and the relatively strong northeast wind in front of the high-pressure circulation drove the transport of $PM_{2.5}$ from the north to the THB. On the third day, the cold air weakened and dissipated, the upstream cold high

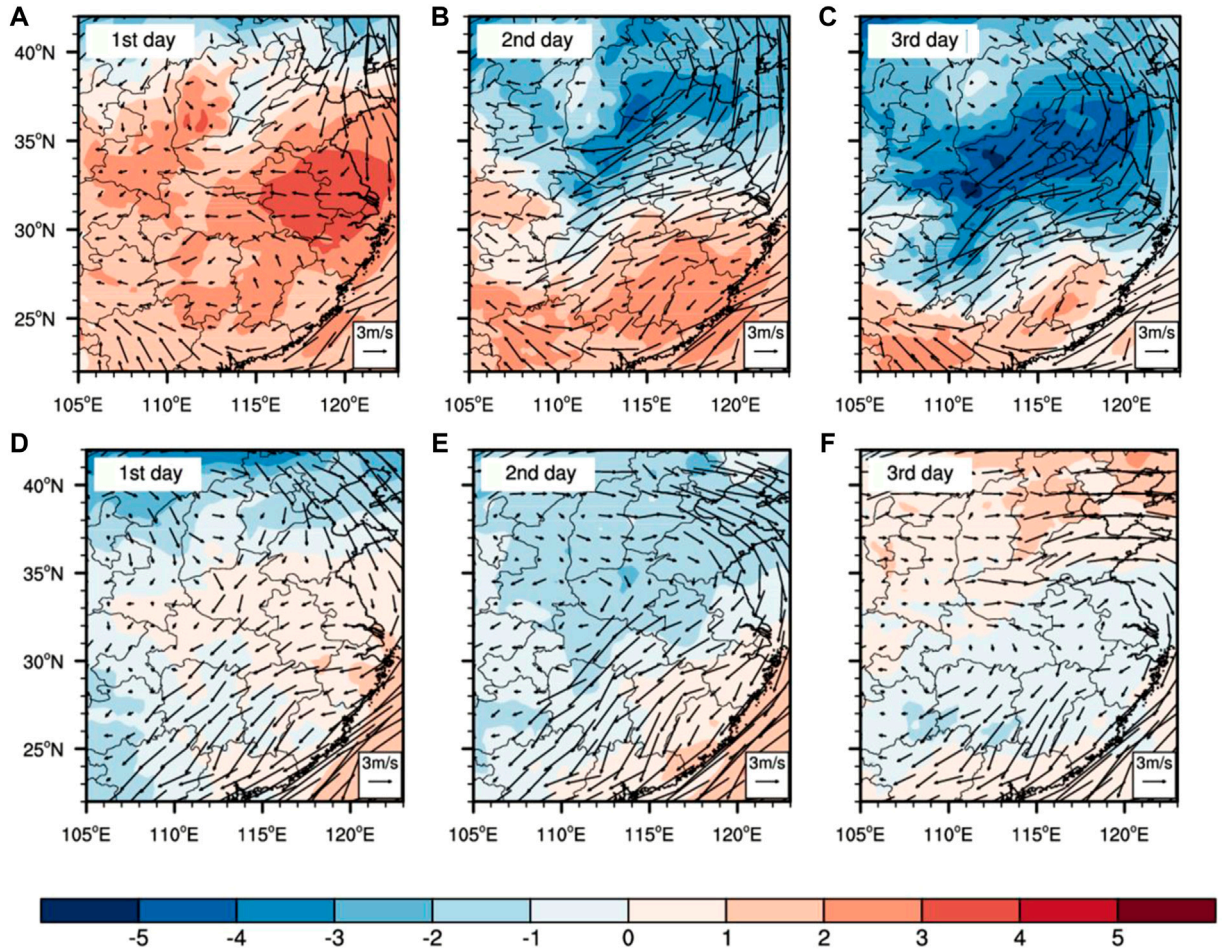


**FIGURE 6 |** Spatial distributions of 925 hPa air temperature anomalies (color contours; K) and mean wind vectors(arrow) during the heavy air pollution process averaged over six severe $PM_{2.5}$ episodes of the top row **(A,B,C)** RTT and bottom row **(D,E,F)** SAT.

pressure continued to move southward, and the THB was controlled by high-pressure circulation (**Figure 6F**). This high-pressure weather type is conducive to the retention of aerosol particles, such that they remain and accumulate over central China (Yan et al., 2021). Moreover, the influence of atmospheric diffusion conditions on the subsidence airflow induced by the weak northern high pressure requires attention (**Supplementary Figure S4A**). The descending motion in the low troposphere limited the development of the PBLH (**Supplementary Figure S4B**), which inhibited the vertical transport of $PM_{2.5}$.

### 3.2.3 Atmospheric Vertical Structures

To characterize the vertical structures of regional $PM_{2.5}$ transport during the two transport pollution patterns, **Figure 7** shows a vertical profile of the average air temperature anomalies and wind vectors along 112°E–114°E during the heavy air pollution process (synthesis of average images of six typical RTT and SAT cases).

The positive air temperature anomalies mainly covered the THB on the first day of the RTT (**Figure 7A**). On the second day, the cold-air mass within the PBL began to penetrate southward and was embedded at the bottom of the warm air mass, leading to a rapid decrease in the air temperature at the low level of the THB (**Figure 7B**). There was a distinct dense contoured area in the pseudo-equivalent potential temperature profile, which tilted toward the cold air with height, indicating a substantial cold front over the THB (**Supplementary Figure S5**). Because of the invasion of the cold front, the warm air mass was uplifted and maintained, and the stable stratification in the front zone in the vertical direction inhibited the diffusion of air pollutants (**Figure 7B**). The cold front invasion persisted on the third day, leading to a further decrease in the air temperature (**Figure 7C**). Additionally, the passage of the cold front was conducive to precipitation. Therefore, the heavy $PM_{2.5}$ pollution ended because of the lasting, strong northerly airflow diffusion and wet scavenging by the precipitation induced by the cold front.

To investigate the key factor for the decreasing $PM_{2.5}$ concentrations of RTT, we determined the correlation coefficient between the observed surface $PM_{2.5}$ concentrations and the VC and precipitation during the later stage (**Figure 8A**). **Figure 8A** indicates that the correlations between the VC and $PM_{2.5}$ concentrations were negative and passed the 99% significance test ($p < 0.01$), and the decrease in $PM_{2.5}$ was

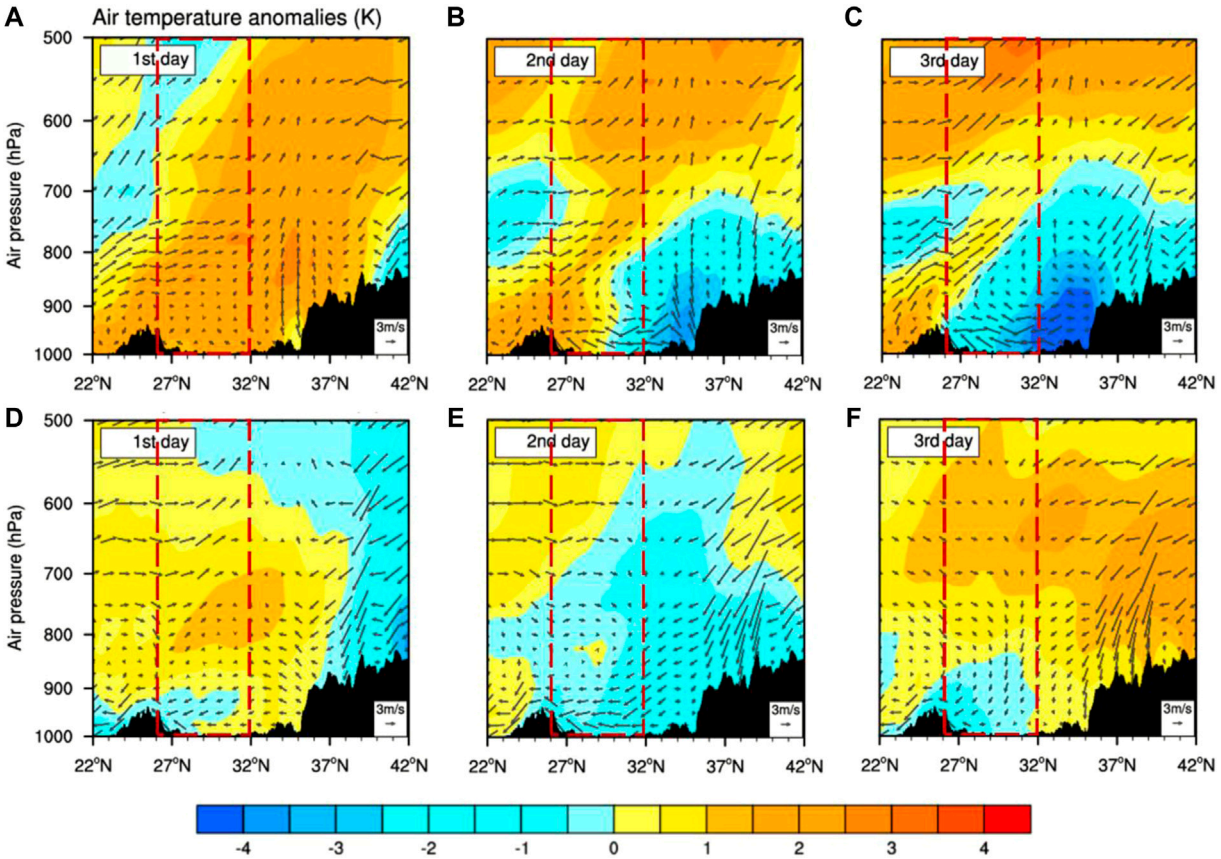


**FIGURE 7 |** Vertical (height-latitude) cross sections of air temperature anomalies (color contours; °C), wind vectors (arrow), and terrain (black shades) along the 112°E–114°E averaged during the heavy air pollution process averaged over six severe $PM_{2.5}$ episodes of the top row **(A,B,C)** RTT and bottom row **(D,E,F)** SAT. Red dotted frames denote the locations of the THB. Notably, the vertical speed of wind vectors is multiplied by -40 for the illustration of vertical circulation.

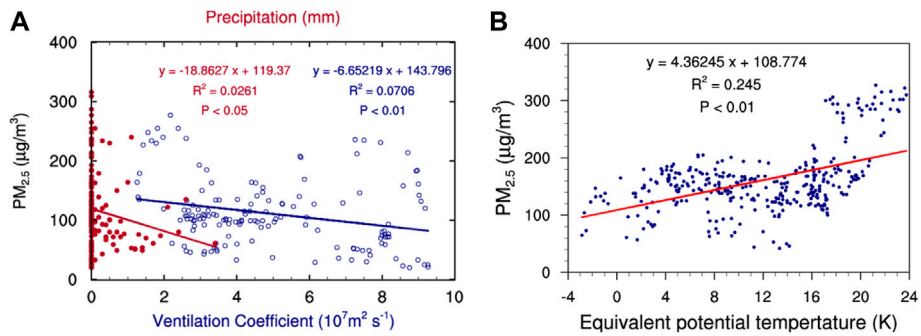


**FIGURE 8 |** Correlation of surface $PM_{2.5}$ concentration to precipitation (red solid circle) in JM in the later stage of **(A)** RTT, where the correlations are significant at 95%; correlations of surface $PM_{2.5}$ concentration to ventilation coefficient (blue hollow circle, $10^7 m^2 s^{-1}$) over the region (112–114°E and 30.5–31°N) averaged in the later stage of **(A)** RTT, where the correlations are significant at 99%; correlation of surface $PM_{2.5}$ concentration to the difference in pseudo-equivalent potential temperature between the 700 hPa and 1,000 hPa ($\Delta\theta$ se) over the region (112–114°E and 30.5–31°N) averaged in the later stage of **(B)** SAT, where the correlations are significant at 99%. The later stage denotes the duration between the peak to the lowest $PM_{2.5}$ value over the sustained decrease period.

primarily due to the outflow of air pollutants by the strong prevalence of the northeasterly wind, which is closely related to the dispersion of air pollutants. Additionally, the surface $PM_{2.5}$ concentrations and precipitation had negative correlations and passed the 95% significance test ($p < 0.05$), indicating that precipitation was a significant factor in the removal of $PM_{2.5}$. In conclusion, good ventilation conditions and wet scavenging led to a decrease in $PM_{2.5}$ during the RTT events.

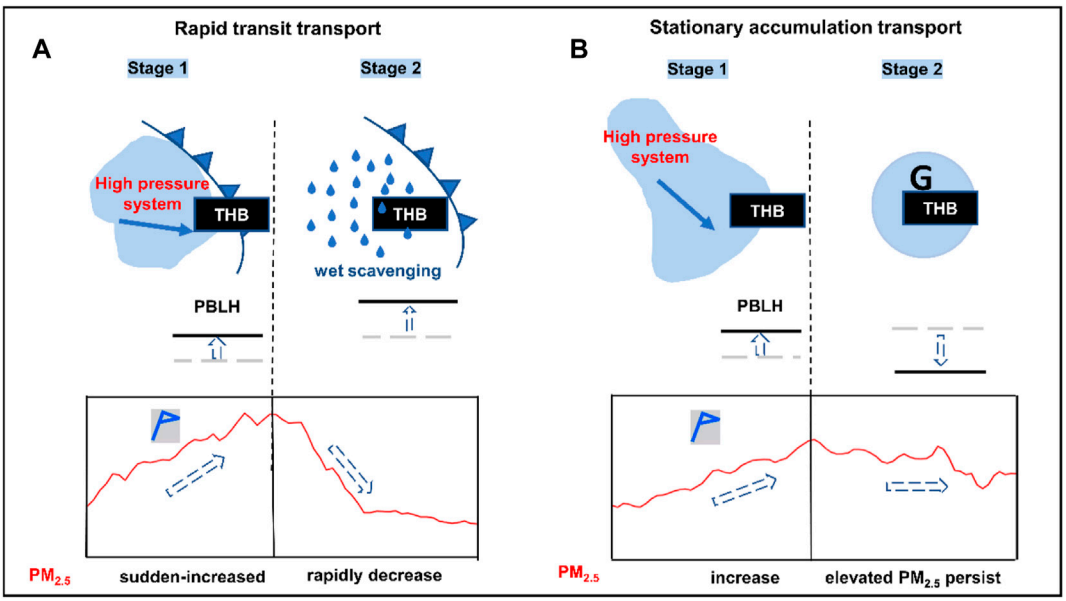


**FIGURE 9 |** Diagram of meteorological mechanism on regional $PM_{2.5}$ transport with the typical patterns of **(A)** RTT and **(B)** SAT driving the $PM_{2.5}$ concentration changes (bottom line graphs) for heavy air pollution over the THB revealed in this study.

**Figure 7E** indicates that on the second day of SAT, the northerly winds strengthened in the low troposphere over the THB and were controlled by a wide range of weak cold air. However, on the third day (**Figure 7F**), owing to the south-moving weak high-pressure control of the THB, the wind fields in the low troposphere gradually weakened, and the sinking airflow caused by the high pressure caused the troposphere to warm (Zhao et al., 2013; Wu et al., 2017). The atmospheric stratification of the middle and high levels was stable and often had air temperature inversions, inhibiting the vertical diffusion of air pollutants and aggravating the rapid accumulation of $PM_{2.5}$. In addition, the topography of the southern THB has a weakening effect on the diffusion of $PM_{2.5}$, resulting in persistent pollution over central China.

We selected the pseudo-equivalent potential temperature difference (700–1,000 hPa, $\Delta\theta$ se) as the thermal factor to analyze the relationship between the SAT pollution level and the thermal factor in the later stage. **Figure 8B** indicates that the greater the $\Delta\theta$ se, the higher the corresponding pollutant concentrations, and this positive correlation passed the 99% significance test ($p < 0.01$). Strong and stable atmospheric stratification contributed more to the aggravation of heavy pollutants ($PM_{2.5}$) in the later stage of SAT events.

Growing evidence has identified the dominant role of the regional transport of $PM_{2.5}$ and its precursors from upstream regions in the formation of severe $PM_{2.5}$ episodes over the THB (Lu et al., 2019; Hu et al., 2021; Shen et al., 2021; Bai et al., 2022). Thus, we identified two typical transport patterns, RTT and SAT, and analyzed the evolutionary features and meteorological mechanisms of the two patterns. The SAT in central China is similar to the heavy pollution in the NCP, which has instances of both the pollution transport stage (TS) and the cumulative stage (CS) during a heavy aerosol pollution episode (Liu et al., 2019; Zhong et al., 2018; Wenjie Zhang et al., 2019; Zhong et al., 2019). However, the formation and evolutionary mechanisms of the episodes in the two regions were different. For the NCP regions, the early stage of pollution already has unfavorable meteorological conditions, including a stable regional air mass and high condensation rate of water vapor (Zhong et al., 2018). The initial stage of SAT in central China emphasizes the dynamic driving function of cold air and strong NWs on the transport of $PM_{2.5}$. In addition, during the CS, the two-way feedback mechanism (turbulence weakening and decrease in PBLH) of aerosol accumulation and unfavorable meteorological conditions is emphasized in the NCP, resulting in the occurrence of the explosive growth of $PM_{2.5}$ during this period (Wenjie Zhang et al., 2019); the presence of heavy $PM_{2.5}$ pollution in central China emphasizes that local meteorological conditions tend to be stable and stagnant due to the evolution of the atmospheric circulation, especially the inhibition effect of the northern, weak, cold high-pressure downdraft on the PBLH and dynamic vertical diffusion conditions, which are conducive to the retention and accumulation of upwind area pollutants. Many pollution processes conducted in central China have the same feature of slow $PM_{2.5}$ accumulation during the CS, which differs substantially from the explosive growth of $PM_{2.5}$ in the NCP during the CS. The contribution of the two-way feedback mechanism of SAT during the CS in central China on the accumulation of local $PM_{2.5}$ concentration requires a quantitative evaluation in future research.

## 4 CONCLUSION

In this study, by integrating multiple observations and reanalysis data, two typical types of severe $PM_{2.5}$ episodes induced by the regional transport of $PM_{2.5}$ over central and eastern China were distinguished, with distinct patterns driven by changes in the synoptic patterns and meteorological conditions (**Figure 9**). This could provide a more comprehensive understanding of the meteorological formation of severe air pollution episodes over a receptor region in the regional transport of air pollutants.

The meteorological conditions triggering RTT and SAT episodes were similar to the invasion of cold air from strong northern winds, resulting in the rapid growth of $PM_{2.5}$ concentrations in the THB. Although the transport patterns were similar, their specific evolutionary patterns were different. The RTT episodes are characterized by explosive growth in $PM_{2.5}$, with the rate of the increase from moderate to severe pollution levels reaching 12.5 μg/$m^3$/h, and the duration of severe pollution is short, with an average time of approximately 27.5 h. By contrast, the rate of increase in $PM_{2.5}$ for the SAT episodes was lower than that of RTT, with a rate of 5.7 μg/$m^3$/h, and the duration of heavy pollution was much longer than that of RTT, with an average value of 72.8 h.

For the RTT pattern, the THB is affected by the invasion of a strong cold front during the early stage, creating favorable meteorological conditions for regional $PM_{2.5}$ pollution, with a rising boundary layer height and strong cold air owing to the north westerlies. Moreover, the stable vertical stratification in the free troposphere could prevent $PM_{2.5}$ from escaping outward, restricting the vertical diffusion of abundant aerosol particles within the PBL. Strong northerly winds and precipitation after the cold front have a considerable effect on the removal of $PM_{2.5}$.

In the SAT pattern, the THB is at the bottom of the northern weak cold high-pressure system during the early stage, and a wide range of weak cold air moves southward. During the later stage, the THB is mainly controlled by the southward advance of a weak high-pressure system, which generates a uniform pressure field, weak wind speed, and strong descending airflow in the lower troposphere, facilitating the accumulation of $PM_{2.5}$. Owing to the high-pressure downdraft, the troposphere is warmed significantly, and the PBLH is strongly reduced, restricting the high-concentration pollutants from upstream to the lower PBL. Strong stable stratifications contribute significantly to aggravating heavy air pollution during the later stage of SAT events.

Based on the investigation of the heavy $PM_{2.5}$ transport episodes over the THB area, this study reveals the synergetic mechanism of regional $PM_{2.5}$ concentrations, atmospheric circulation, atmospheric thermal conditions, and dynamic factors in two distinct transport patterns. Further exploration would focus on comprehensive modeling to assess the relative contributions of the physical and chemical processes of $PM_{2.5}$ for heavy-pollution episodes with different patterns of regional transport.

## DATA AVAILABILITY STATEMENT

Publicly available datasets were analyzed in this study. These data can be found at: https://www.ecmwf.int/en/forecasts/datasets/reanalysis-datasets/era5.

## AUTHOR CONTRIBUTIONS

YW: conceptualization, methodology, investigation, writing-original draft, and writing-review and editing. YB: conceptualization, methodology, funding acquisition, writing-review and editing, and supervision. XZ: conceptualization, writing-review and editing, and supervision. KW: conceptualization, data curation, and resources. TZ, YZ, JX, SZ, WZ, WH, LZ, and KM were involved in the scientific interpretation and discussion. All authors provided commentary on the study.

## FUNDING

This research has been supported by the National Natural Science Foundation of China (grant nos. 42075186 and 41830965) and the special project "The impact of weather conditions on the spread of pandemic influenza virus (2020xtzx004)" from the Collaborative Innovation Center on Forecast and Evaluation of Meteorological Disasters, Nanjing University of Information Science and Technology.

## ACKNOWLEDGMENTS

The authors thank the MEIC team from Tsinghua University for providing the multiscale emission inventory of China (MEIC).

## SUPPLEMENTARY MATERIAL

The Supplementary Material for this article can be found online at: https://www.frontiersin.org/articles/10.3389/fenvs.2022.890514/full#supplementary-material

**Supplementary Figure S1 |** Boxplot of the rising rate of PM2.5 concentrations from the light pollution (75 μg/m3) to heavy pollution (150 μg/m3) of 12 episodes for RTT and six episodes for SAT in transport corridor cities: XY, JM, and JZ in the THB.

**Supplementary Figure S2 |** Temporal changes in $PM_{2.5}$ concentration (black lines), PBLH (red lines), wind directions at 10 m (Wdir, vectors), and precipitation (purple triangles) were observed at JM in the THB. **(A,C,E)** The left column represents the other three cases of RTT, and **(B,D,F)** the right column represents the other three cases of SAT.

**Supplementary Figure S3 |** Spatial distributions of VC ($10^7$ $m^2s^{-1}$) during the heavy air pollution process averaged over six severe pollution episodes of (top row; **A,B,C)** RTT and (bottom row; **D,E,F)** SAT.

**Supplementary Figure S4 |** Spatial distributions of **(A)** 850 hPa vertical velocity (color contours; Pa/s); **(B)** PBLH anomalies (color contours; m) on the 3rd day of the heavy air pollution process averaged over six severe $PM_{2.5}$ episodes of SAT.

**Supplementary Figure S5 |** Vertical (height-latitude) cross-sections of pseudo-equivalent potential temperature (color lines; K) and terrain (black shades) along 112°E–114°E averaged on the 2nd day of the heavy air pollution process averaged over six severe $PM_{2.5}$ episodes of RTT. Red dotted frames denote the locations of the front zone.

**Supplementary Table S1 |** Overview of six heavy $PM_{2.5}$ episodes with the pattern RTT.

**Supplementary Table S2 |** Overview of six heavy $PM_{2.5}$ episodes with the pattern SAT.

## REFERENCES


Bai, Y.-Q., Wang, Y., Kong, S.-F., Zhao, T.-L., Zhi, X.-F., Zheng, H., et al. (2021). Modelling the Effect of Local and Regional Emissions on PM2.5 Concentrations in Wuhan, China during the COVID-19 Lockdown. *Adv. Clim. Change Res.* 12, 871–880. doi:10.1016/j.accre.2021.09.013

Bai, Y., Zhao, T., Hu, W., Zhou, Y., Xiong, J., Wang, Y., et al. (2022). Meteorological Mechanism of Regional PM2.5 Transport Building a Receptor Region for Heavy Air Pollution over Central China. *Sci. Total Environ.* 808, 151951. doi:10.1016/j.scitotenv.2021.151951

Bao, X., and Zhang, F. (2019). How Accurate Are Modern Atmospheric Reanalyses for the Data-Sparse Tibetan Plateau Region? *J. Clim.* 32, 7153–7172. doi:10.1175/JCLI-D-18-0705.1

Cai, W., Li, K., Liao, H., Wang, H., and Wu, L. (2017). Weather Conditions Conducive to Beijing Severe Haze More Frequent under Climate Change. *Nat. Clim Change* 7, 257–262. doi:10.1038/nclimate3249

Cao, J.-J., Shen, Z.-X., Chow, J. C., Watson, J. G., Lee, S.-C., Tie, X.-X., et al. (2012). Winter and Summer PM $_{2.5}$ Chemical Compositions in Fourteen Chinese Cities. *J. Air Waste Manage. Assoc.* 62, 1214–1226. doi:10.1080/10962247.2012.701193

Chan, C. K., and Yao, X. (2008). Air Pollution in Mega Cities in China. *Atmos. Environ.* 42, 1–42. doi:10.1016/j.atmosenv.2007.09.003

Chen, Q., Sheng, L., Gao, Y., Miao, Y., Hai, S., Gao, S., et al. (2019). The Effects of the Trans-regional Transport of PM2.5 on a Heavy Haze Event in the Pearl River Delta in January 2015. *Atmosphere* 10, 237. doi:10.3390/atmos10050237

Diaz Resquin, M., Santágata, D., Gallardo, L., Gómez, D., Rössler, C., and Dawidowski, L. (2018). Local and Remote Black Carbon Sources in the Metropolitan Area of Buenos Aires. *Atmos. Environ.* 182, 105–114. doi:10.1016/j.atmosenv.2018.03.018

Fallmann, J. (2016). Secondary Effects of Urban Heat Island Mitigation Measures on Air Quality. *Atmos. Environ.* 125, 199–211. doi:10.1016/j.atmosenv.2015.10.094

Gao, J., Tian, H., Cheng, K., Lu, L., Zheng, M., Wang, S., et al. (2015). The Variation of Chemical Characteristics of PM2.5 and PM10 and Formation Causes during Two Haze Pollution Events in Urban Beijing, China. *Atmos. Environ.* 107, 1–8. doi:10.1016/j.atmosenv.2015.02.022

Gu, S., Guenther, A., and Faiola, C. (2021). Effects of Anthropogenic and Biogenic Volatile Organic Compounds on Los Angeles Air Quality. *Environ. Sci. Technol.* 55, 12191–12201. doi:10.1021/acs.est.1c01481

Guo, J., Niu, T., Wang, F., Deng, M., and Wang, Y. (2013). Integration of Multi-Source Measurements to Monitor Sand-Dust Storms over North China: A Case Study. *Acta Meteorol. Sin* 27, 566–576. doi:10.1007/s13351-013-0409-z

Guo, J., Li, Y., Cohen, J. B., Li, J., Chen, D., Xu, H., et al. (2019). Shift in the Temporal Trend of Boundary Layer Height in China Using Long-Term (1979–2016) Radiosonde Data. *Geophys. Res. Lett.* 46, 6080–6089. doi:10.1029/2019GL082666

Guo, J., Zhang, J., Yang, K., Liao, H., Zhang, S., Huang, K., et al. (2021). Investigation of Near-Global Daytime Boundary Layer Height Using High-Resolution Radiosondes: First Results and Comparison with ERA5, MERRA-2, JRA-55, and NCEP-2 Reanalyses. *Atmos. Chem. Phys.* 21, 17079–17097. doi:10.5194/acp-21-17079-2021

Hou, X., Fei, D., Kang, H., Zhang, Y., and Gao, J. (2018). Seasonal Statistical Analysis of the Impact of Meteorological Factors on fine Particle Pollution in China in 2013-2017. *Nat. Hazards* 93, 677–698. doi:10.1007/s11069-018-3315-y

Hu, W., Zhao, T., Bai, Y., Kong, S., Xiong, J., Sun, X., et al. (2021). Importance of Regional PM2.5 Transport and Precipitation Washout in Heavy Air Pollution in the Twain-Hu Basin over Central China: Observational Analysis and WRF-Chem Simulation. *Sci. Total Environ.* 758, 143710. doi:10.1016/j.scitotenv.2020.143710

Huang, R.-J., Zhang, Y., Bozzetti, C., Ho, K.-F., Cao, J.-J., Han, Y., et al. (2014). High Secondary Aerosol Contribution to Particulate Pollution during Haze Events in China. *Nature* 514, 218–222. doi:10.1038/nature13774

Huang, Y., Ji, Y., Zhu, Z., Zhang, T., Gong, W., Xia, X., et al. (2020). Satellite-based Spatiotemporal Trends of Ambient PM2.5 Concentrations and Influential Factors in Hubei, Central China. *Atmos. Res.* 241, 104929. doi:10.1016/j.atmosres.2020.104929

Huang, J., Yin, J., Wang, M., He, Q., Guo, J., Zhang, J., et al. (2021). Evaluation of Five Reanalysis Products with Radiosonde Observations over the Central Taklimakan Desert during Summer. *Earth Space Sci.* 8. doi:10.1029/2021EA001707

Ji, Y., Qin, X., Wang, B., Xu, J., Shen, J., Chen, J., et al. (2018). Counteractive Effects of Regional Transport and Emission Control on the Formation of fine Particles: a Case Study during the Hangzhou G20 summit. *Atmos. Chem. Phys.* 18, 13581–13600. doi:10.5194/acp-18-13581-2018

Kang, H., Zhu, B., Gao, J., He, Y., Wang, H., Su, J., et al. (2019). Potential Impacts of Cold Frontal Passage on Air Quality over the Yangtze River Delta, China. *Atmos. Chem. Phys.* 19, 3673–3685. doi:10.5194/acp-19-3673-2019

Lapere, R., Menut, L., Mailler, S., and Huneeus, N. (2021). Seasonal Variation in Atmospheric Pollutants Transport in central Chile: Dynamics and Consequences. *Atmos. Chem. Phys.* 21, 6431–6454. doi:10.5194/acp-21-6431-2021

Li, J., Wang, Z., Huang, H., Hu, M., Meng, F., Sun, Y., et al. (2013). Assessing the Effects of Trans-boundary Aerosol Transport between Various City Clusters on Regional Haze Episodes in spring over East China. *Tellus B: Chem. Phys. Meteorol.* 65, 20052. doi:10.3402/tellusb.v65i0.20052

Lin, X., Wu, W., Han, M., Liu, T., Wu, X., and Liu, A. (2016). Cause Comparison Analysis of Different Fallen Area of Heavy Rain Caused by Typhoon landing in Northeast Fujian. *J. Nat. Disasters* 25, 48–55. doi:10.13577/j.jnd.2016.0406

Liu, L., Zhang, X., Zhong, J., Wang, J., and Yang, Y. (2019). The 'two-Way Feedback Mechanism' between Unfavorable Meteorological Conditions and Cumulative PM2.5 Mass Existing in Polluted Areas South of Beijing. *Atmos. Environ.* 208, 1–9. doi:10.1016/j.atmosenv.2019.02.050

Lu, C., Deng, Q.-h., Liu, W.-w., Huang, B.-l., and Shi, L.-z. (2012). Characteristics of Ventilation Coefficient and its Impact on Urban Air Pollution. *J. Cent. South. Univ. Technol.* 19, 615–622. doi:10.1007/s11771-012-1047-9

Lu, M., Tang, X., Wang, Z., Wu, L., Chen, X., Liang, S., et al. (2019). Investigating the Transport Mechanism of PM2.5 Pollution during January 2014 in Wuhan, Central China. *Adv. Atmos. Sci.* 36, 1217–1234. doi:10.1007/s00376-019-8260-5

Miao, Y., Guo, J., Liu, S., Liu, H., Zhang, G., Yan, Y., et al. (2017). Relay Transport of Aerosols to Beijing-Tianjin-Hebei Region by Multi-Scale Atmospheric Circulations. *Atmos. Environ.* 165, 35–45. doi:10.1016/j.atmosenv.2017.06.032

Moreira, G. d. A., Guerrero-Rascado, J. L., Bravo-Aranda, J. A., Foyo-Moreno, I., Cazorla, A., Alados, I., et al. (2020). Study of the Planetary Boundary Layer Height in an Urban Environment Using a Combination of Microwave Radiometer and Ceilometer. *Atmos. Res.* 240, 104932. doi:10.1016/j.atmosres.2020.104932

Nair, V. S., Moorthy, K. K., Alappattu, D. P., Kunhikrishnan, P. K., George, S., Nair, P. R., et al. (2007). Wintertime Aerosol Characteristics over the Indo-Gangetic Plain (IGP): Impacts of Local Boundary Layer Processes and Long-range Transport. *J. Geophys. Res.* 112, 2006JD008099. doi:10.1029/2006JD008099

Ning, G., Wang, S., Yim, S. H. L., Li, J., Hu, Y., Shang, Z., et al. (2018). Impact of Low-Pressure Systems on winter Heavy Air Pollution in the Northwest Sichuan Basin, China. *Atmos. Chem. Phys.* 18, 13601–13615. doi:10.5194/acp-18-13601-2018

Niu, F., Li, Z., Li, C., Lee, K.-H., and Wang, M. (2010). Increase of Wintertime Fog in China: Potential Impacts of Weakening of the Eastern Asian Monsoon Circulation and Increasing Aerosol Loading. *J. Geophys. Res.* 115, D00K20. doi:10.1029/2009JD013484

Quan, J., Gao, Y., Zhang, Q., Tie, X., Cao, J., Han, S., et al. (2013). Evolution of Planetary Boundary Layer under Different Weather Conditions, and its Impact on Aerosol Concentrations. *Particuology* 11, 34–40. doi:10.1016/j.partic.2012.04.005

RenHe, Z., Li, Q., and Zhang, R. (2014). Meteorological Conditions for the Persistent Severe Fog and Haze Event over Eastern China in January 2013. *Sci. China Earth Sci.* 57, 26–35. doi:10.1007/s11430-013-4774-3

Shen, L., Hu, W., Zhao, T., Bai, Y., Wang, H., Kong, S., et al. (2021). Changes in the Distribution Pattern of PM2.5 Pollution over Central China. *Remote Sens.* 13, 4855. doi:10.3390/rs13234855

Shen, L., Zhao, T., Liu, J., Wang, H., Bai, Y., Kong, S., et al. (2022). Regional Transport Patterns for Heavy $PM_{2.5}$ Pollution Driven by strong Cold Airflows in Twain-Hu Basin, Central China. *Atmos. Environ.* 269, 118847. doi:10.1016/j.atmosenv.2021.118847

Sujatha, P., Mahalakshmi, D. V., Ramiz, A., Rao, P. V. N., and Naidu, C. V. (2016). Ventilation Coefficient and Boundary Layer Height Impact on Urban Air Quality. *Cogent Environ. Sci.* 2, 1125284. doi:10.1080/23311843.2015.1125284

Wang, K., Tong, Y., Gao, J., Gao, C., Wu, K., Yue, T., et al. (2021). Impacts of LULC, FDDA, Topo-Wind and UCM Schemes on WRF-CMAQ over the Beijing-Tianjin-Hebei Region, China. *Atmos. Pollut. Res.* 12, 292–304. doi:10.1016/j.apr.2020.11.011

Wei, Y., Li, J., Wang, Z.-F., Chen, H.-S., Wu, Q.-Z., Li, J.-J., et al. (2017). Trends of Surface PM $_{2.5}$ over Beijing–Tianjin–Hebei in 2013–2015 and Their Causes: Emission Controls vs. Meteorological Conditions. *Atmos. Oceanic Sci. Lett.* 10, 276–283. doi:10.1080/16742834.2017.1315631

Zhang, W., Zhang, X., Zhong, J., Wang, Y., Wang, J., Zhao, Y., et al. (2019). The Effects of the "Two-Way Feedback Mechanism" on the Maintenance of Persistent Heavy Aerosol Pollution over Areas with Relatively Light Aerosol Pollution in Northwest China. *Sci. Total Environ.* 688, 642–652. doi:10.1016/j.scitotenv.2019.06.295

Wu, D., Fung, J. C. H., Yao, T., and Lau, A. K. H. (2013). A Study of Control Policy in the Pearl River Delta Region by Using the Particulate Matter Source Apportionment Method. *Atmos. Environ.* 76, 147–161. doi:10.1016/j.atmosenv.2012.11.069

Wu, G., Li, Z., Fu, C., Zhang, X., Zhang, R., Zhang, R., et al. (2016). Advances in Studying Interactions between Aerosols and Monsoon in China. *Sci. China Earth Sci.* 59, 1–16. doi:10.1007/s11430-015-5198-z

Wu, P., Ding, Y., and Liu, Y. (2017). Atmospheric Circulation and Dynamic Mechanism for Persistent Haze Events in the Beijing-Tianjin-Hebei Region. *Adv. Atmos. Sci.* 34, 429–440. doi:10.1007/s00376-016-6158-z

Wu, K., Kang, P., Tie, X., Gu, S., Zhang, X., Wen, X., et al. (2019). Evolution and Assessment of the Atmospheric Composition in Hangzhou and its Surrounding Areas during the G20 Summit. *Aerosol Air Qual. Res.* 9, 2757–2769. doi:10.4209/aaqr.2018.12.0481

Wu, K., Zhu, S., Liu, Y., Wang, H., Yang, X., Liu, L., et al. (2021). Modeling Ammonia and its Uptake by Secondary Organic Aerosol over China. *Geophys. Res. Atmos.* 126. doi:10.1029/2020JD034109

Xiong, J., Bai, Y., Zhao, T., Kong, S., and Hu, W. (2021). Impact of Inter-regional Transport in a Low-Emission Scenario on PM2.5 in Hubei Province, Central China. *Atmosphere* 12, 250. doi:10.3390/atmos12020250

Xu, J., Yan, F., Xie, Y., Wang, F., Wu, J., and Fu, Q. (2015). Impact of Meteorological Conditions on a Nine-Day Particulate Matter Pollution Event Observed in December 2013, Shanghai, China. *Particuology* 20, 69–79. doi:10.1016/j.partic.2014.09.001

Yan, S., Zhu, B., and Kang, H. (2019). Long-Term Fog Variation and its Impact Factors over Polluted Regions of East China. *J. Geophys. Res. Atmos.* 124, 1741–1754. doi:10.1029/2018JD029389

Yan, Y., Zhou, Y., Kong, S., Lin, J., Wu, J., Zheng, H., et al. (2021). Effectiveness of Emission Control in Reducing $PM_{2.5}$ Pollution in central China during winter Haze Episodes under Various Potential Synoptic Controls. *Atmos. Chem. Phys.* 21, 3143–3162. doi:10.5194/acp-21-3143-2021

Yang, X., Lu, Y., Zhu, X., He, J., Jiang, Q., Wu, K., et al. (2020). Formation and Evolution Mechanisms of Severe Haze Pollution in the Sichuan Basin, Southwest China. *Aerosol Air Qual. Res.* 20, 2557–2567. doi:10.4209/aaqr.2020.04.0173

Yu, C., Zhao, T., Bai, Y., Zhang, L., Kong, S., Yu, X., et al. (2020). Heavy Air Pollution with a Unique "Non-stagnant" Atmospheric Boundary Layer in the Yangtze River Middle basin Aggravated by Regional Transport of $PM_{2.5}$ over China. *Atmos. Chem. Phys.* 20, 7217–7230. doi:10.5194/acp-20-7217-2020

Zhang, R., Wang, G., Guo, S., Zamora, M. L., Ying, Q., Lin, Y., et al. (2015). Formation of Urban Fine Particulate Matter. *Chem. Rev.* 115, 3803–3855. doi:10.1021/acs.chemrev.5b00067

Zhang, L., Guo, X., Zhao, T., Gong, S., Xu, X., Li, Y., et al. (2019). A Modelling Study of the Terrain Effects on Haze Pollution in the Sichuan Basin. *Atmos. Environ.* 196, 77–85. doi:10.1016/j.atmosenv.2018.10.007

Zhao, X. J., Zhao, P. S., Xu, J., Meng, W., Pu, W. W., Dong, F., et al. (2013). Analysis of a winter Regional Haze Event and its Formation Mechanism in the North China Plain. *Atmos. Chem. Phys.* 13, 5685–5696. doi:10.5194/acp-13-5685-2013

Zhong, J., Zhang, X., Wang, Y., Liu, C., and Dong, Y. (2018). Heavy Aerosol Pollution Episodes in winter Beijing Enhanced by Radiative Cooling Effects of Aerosols. *Atmos. Res.* 209, 59–64. doi:10.1016/j.atmosres.2018.03.011

Zhong, J., Zhang, X., Wang, Y., Wang, J., Shen, X., Zhang, H., et al. (2019). The Two-Way Feedback Mechanism between Unfavorable Meteorological Conditions and Cumulative Aerosol Pollution in Various Haze Regions of China. *Atmos. Chem. Phys.* 19, 3287–3306. doi:10.5194/acp-19-3287-2019

Zhou, Y., Bai, Y., Yue, Y., Lü, J., Chen, S., and Xiao, H. (2019). Characteristics of the Factors Influencing Transportation and Accumulation Processes during a Persistent Pollution Event in the Middle Reaches of the Yangtze River, China. *Atmos. Pollut. Res.* 10, 1420–1434. doi:10.1016/j.apr.2019.03.014

Zhou, Y., Yue, Y., Bai, Y., and Zhang, L. (2020). Effects of Rainfall on $PM_{2.5}$ and $PM_{10}$ in the Middle Reaches of the Yangtze River. *Adv. Meteorol.* 2020, 1–10. doi:10.1155/2020/2398146

Zhou, Y., Guo, J., Zhao, T., Lv, J., Bai, Y., Wang, C., et al. (2022). Roles of Atmospheric Turbulence and Stratification in a Regional Pollution Transport Event in the Middle Reaches of the Yangtze River. *Earth Space Sci.* 9. doi:10.1029/2021EA002062

Zhu, B., Su, J.-f., Han, Z.-w., Cong, Y., Wang, T.-j., and Cai, Y. (2010). Analysis of a Serious Air Pollution Event Resulting from Crop Residue Burning over Nanjing and Surrounding Regions. *China Environ. Sci.* 30, 585–592. doi:10.1117/12.860353

**Conflict of Interest:** The authors declare that the research was conducted in the absence of any commercial or financial relationships that could be construed as a potential conflict of interest.

**Publisher's Note:** All claims expressed in this article are solely those of the authors and do not necessarily represent those of their affiliated organizations, or those of the publisher, the editors, and the reviewers. Any product that may be evaluated in this article, or claim that may be made by its manufacturer, is not guaranteed or endorsed by the publisher.

frontiers | Frontiers in Environmental Science

ORIGINAL RESEARCH
published: 12 May 2022
doi: 10.3389/fenvs.2022.908875

# Evaluating Cumulative Drought Effect on Global Vegetation Photosynthesis Using Numerous GPP Products

*Changlin Wu and Tengjun Wang**

*College of Geological Engineering and Geomatics, Chang'an University, Xi'an, China*

The increasing trend in drought events under the background of global warming makes it more important to understand the drought effect on vegetation photosynthesis. While diverse global gross primary production (GPP) datasets were adopted to investigate the drought impact on photosynthesis, few studies focused on the discrepancies of drought response among different GPP datasets, especially for the cumulative drought impact. Therefore, a total of twenty-six global GPP datasets based on process, machine learning (ML), and light-use efficiency (LUE) model schemes were obtained to appraise the cumulative impact of drought stress on photosynthesis from 2001 to 2010. Moreover, a relatively reliable global pattern of drought's cumulative effect on vegetation photosynthesis was acquired from these global GPP products through probability analysis. The results illustrated that the cumulative impact of drought existed in 52.11% of vegetation cover land with the cumulative time scales dominantly at a short term (1–4 months, 31.81%). Obvious heterogeneity of the drought cumulative effect in space and different vegetation functional types was observed, as the reliability of the drought effect decreased with latitude decreasing and a higher sensitivity to drought in herbaceous vegetation than woody plants. Our findings highlighted the importance of ways in characterizing moisture conditions across vegetation types among various GPP models and the necessity of GPP dataset selection in investigating drought effect on photosynthesis.

**Keywords: cumulative effect, drought, GPP dataset, photosynthesis, SPEI, reliability**

OPEN ACCESS

***Edited by:***
*Honglei Wang,*
*Nanjing University of Information Science and Technology, China*

***Reviewed by:***
*Shenxin Li,*
*Central South University, China*
*Lchihiro An,*
*Shandong Agricultural University, China*

***Correspondence:**
*Tengjun Wang*
*wangtj@chd.edu.cn*

***Specialty section:***
*This article was submitted to Atmosphere and Climate, a section of the journal Frontiers in Environmental Science*

***Received:*** *31 March 2022*
***Accepted:*** *12 April 2022*
***Published:*** *12 May 2022*

***Citation:***
*Wu C and Wang T (2022) Evaluating Cumulative Drought Effect on Global Vegetation Photosynthesis Using Numerous GPP Products. Front. Environ. Sci. 10:908875. doi: 10.3389/fenvs.2022.908875*

## 1 INTRODUCTION

Global climate change will cause significant effects on plant photosynthesis (Cramer et al., 2001; Richardson et al., 2013; Chen et al., 2014), especially with an increasing trend of infrequently severe drought events under the background of global warming (AghaKouchak et al., 2014; Naumann et al., 2018). In this way, it is essential to understand the various effects of drought on vegetation status and further investigate the terrestrial ecosystem carbon cycle (van der Molen et al., 2011; Barman et al., 2014; Anderegg et al., 2015).

Drought, as a complex and intermittent disturbance among climatic phenomena, can influence the traits of the terrestrial ecosystem and vegetation status (van der Molen et al., 2011; Reichstein et al., 2013; Anderegg et al., 2015), such as reducing the expansion of foliage and stomatal conductance (Passioura, 1991), inducing plant mortality (Huang et al., 2010; Rao et al., 2019), or even causing biotic disturbance and wildfire (Wendler et al., 2011; Huang et al., 2017). As the observable changes in plant status induced by drought are hard to be timely detected, it is difficult to

understand the reactions of the plant to drought (Zhao et al., 2020). Moreover, except for the current moisture conditions, early drought events may also control vegetation growth (Peng et al., 2019; Yuan et al., 2020). In this way, knowing the various time-scales of plant reactions to the drought effect is critical for understanding the interactions between climate and plants (Zhao et al., 2018; Peng et al., 2019; Wen et al., 2019). The drought effect on plants can be summarized in the cumulative and time-lag responses primarily (Zhao et al., 2020). Time-lag impacts illustrate the effect of early drought events at a specific time on the current plant status, and cumulative impacts are associated with lagged effects and climatic dynamics during a given period (Zhao et al., 2020). While there were an increasing number of studies that surveyed the time-lag impact of drought on the plant, it was found that it varies across species and ranges (Braswell et al., 1997; Huang et al., 2018; Peng et al., 2019). Some cumulative events (e.g., cumulative water deficits) could intensify drought effects on terrestrial ecosystems (Ivits et al., 2016). Therefore, it is necessary to assess the cumulative drought impact on global plant photosynthesis more robustly.

In general, the response sensitivity of vegetation photosynthesis (i.e., GPP) to dry conditions at the ecosystem scale was used to characterize drought effect on vegetation (Ciais et al., 2005; Sun et al., 2021). With the development of satellite remote sensing technology (Xiao et al., 2019; Chu et al., 2021; Pan et al., 2021; Guo et al., 2022), massive remotely sensed images provided unique opportunities for researching the ecosystem carbon cycle at multiple scales (e.g., regional, continental, or global). On this basis, many researchers have established a variety of models driven by remote sensing data to simulate GPP over the past few decades (Tan et al., 2012; Anav et al., 2015; Lees et al., 2018; Xie and Li, 2020b; a). Generally, all these remotely sensed data-driven GPP models could be divided into three parts based on different schemes, namely, process, machine learning (ML), and light-use efficiency (LUE) models. The process-oriented models always comprehensively considered the effects of several main biophysical and chemical processes on vegetation photosynthesis over the terrestrial ecosystem (Ito, 2010; Hayes et al., 2011; Tian et al., 2011; Zhu et al., 2014; Jiang and Ryu, 2016). In this way, GPP estimations obtained from them were more mechanistic and rigorous, while the ML models established complex nonlinear statistical relations between physiologically relevant input data and GPP, thus needing huge amounts of data for model training (Tramontana et al., 2016; Zheng et al., 2020). For LUE models, which simulated GPP through the theory of radiation conversion efficiency (Monteith, 1972), it is assumed that GPP had a direct relationship with the combination of absorbed photosynthetically active radiation and factual LUE (Xiao et al., 2004; Yuan et al., 2010; Guan et al., 2022) as the factual LUE was linked with the potential ceiling amount of LUE and various regulations of environmental factors on it (Hilker et al., 2008; Guan et al., 2021). Based on these various models and large amounts of remotely sensed and auxiliary data (e.g., meteorological reanalysis product), diverse GPP datasets have been generated and used to investigate the global climate change and carbon cycle (Campbell et al., 2017; Curasi et al., 2019). However, previous studies indicated that the model structures, model parameters, and input data among different models could bring uncertainties to final GPP simulations (Zhao et al., 2006; Xiao et al., 2011; Sanchez et al., 2015; Zhou et al., 2016; Zheng et al., 2018). In this way, the global pattern of drought effect on photosynthesis acquired from different GPP products might exist in unavoidable discrepancies.

As there were more and more global GPP datasets that could be accessed directly online (Zhang et al., 2017; Huntzinger et al., 2018; Zheng et al., 2020), they provided a feasible opportunity to derive a more reliable and robust global pattern of drought impact on vegetation photosynthesis. Considering these findings mentioned above, this study aimed to evaluate the cumulative impact of drought on plant photosynthesis quantitatively based on multiple global GPP products and a multiscale time-series global Standardized Precipitation Evapotranspiration Index (SPEI) dataset. Here, the major objectives of this work were as follows: 1) to explore the spatial pattern of cumulative drought impact on global photosynthesis, 2) to analyze the discrepancies of drought cumulative effect on photosynthesis across different vegetation types, and 3) to derive a global reliability pattern of drought cumulative effect on photosynthesis using the probability statistic based on numerous global GPP products.

# 2 DATA AND METHODS

## 2.1 Datasets

### 2.1.1 Global GPP Products

In this study, a total of twenty-six global GPP products were acquired to evaluate the cumulative drought impact on photosynthesis. These GPP products contain seventeen process-oriented models (i.e., BESS, BIOME-BGC, CLASS-CTEM-N+, CLM4, CLM4VIC, DLEM, GTEC, ISAM, JULES, LPJ-wsl, ORCHIDEE-LSCE, SIB3, SIBCASA, TEM6, TRIPLEX-GHG, VEGAS2.1, and VISIT), five LUE models (i.e., EC-LUE, MOD17, OPT-LUE, RC-LUE, and VPM), and four ML models (i.e., ANN, MARS, MTE, and RF). While these GPP datasets had different spatial and temporal resolutions, all GPP datasets were processed into a uniform format (i.e., 0.5° and monthly) based on the spatial average resampling and accumulated GPP within a month. In addition, the overlapped years of these GPP datasets (i.e., 2001–2010) were used as the study period in this work. More detailed information about these GPP datasets can be found in **Supplementary Material**.

### 2.1.2 Multiscale Global SPEI Data

In this work, monthly SPEI data at multiple time scales (1–12 months) from 2001 to 2010 were acquired from the SPEIbase v.2.5 datasets (Beguería et al., 2017) to identify the duration and intensity of drought. This product contained monthly SPEI data at 1–48 months' time-scales from 1901–2015 with a spatial resolution of 0.5°, while SPEI at i time-scale (i.e., i month SPEI) represented the cumulative climatic moisture cycling process for the earlier i months. In this way, SPEI data can be used to characterize different types of drought (e.g., short, middle, and long period drought) and

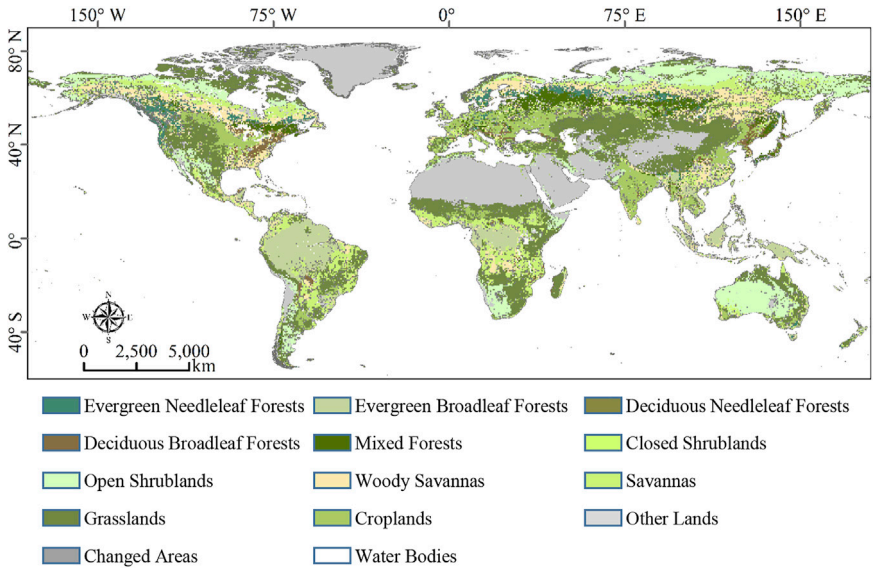


**FIGURE 1 |** Spatial distribution of unchanged IGBP land cover types obtained from MCD12C1 Version six during the study period.

various effects on vegetation status (Begueria et al., 2010; Vicente-Serrano et al., 2010; Peng et al., 2019). As for this product, the SPEI value at each grid was computed through the discrepancy among precipitation and reference evapotranspiration first, and then the final SPEI value was a standardized parameter related to the climatic moisture cycling process that obeys a log-logistic distribution (Vicente-Serrano et al., 2010). In addition, a more large positive SPEI value indicated surplus water supply after meeting the coincident moisture requirement, and a smaller negative value represented a more exigent water deficit (Begueria et al., 2014). In this way, SPEI was a reasonable parameter to characterize the degree of drought. Here, the 1–12 month SPEI data for 2001–2010 were adopted to explore the drought's cumulative impact on global photosynthesis according to previous studies (Kang et al., 2018; Peng et al., 2019).

### 2.1.3 Global Land Cover Data

In this work, moderate-resolution imaging spectroradiometer yearly global land cover types dataset Version 6 (MCD12C1 v006) was adopted to compare the cumulative effect on photosynthesis across vegetation types. The MCD12C1 dataset (Friedl and Sulla-Menashe., 2015) provided three land cover classification scheme layers at 0.05° spatial resolution yearly, and the International Geosphere–Biosphere Program (IGBP) layer was used in this work. Moreover, the 0.05° resolution land cover maps were resampled to the 0.5° resolution ones based on the assumption that the land cover of every 0.5- grid was the major stamp (i.e., with the maximal area percentage) among all the 0.05° subpixels. As for demonstrating the cumulative drought impact on global photosynthesis and reducing the uncertainties attracted by land cover alterations, merely the unchanged vegetation cover pixels (i.e., these pixels that remained the same vegetation type during 2001–2010) were selected as the study area. In this way, the unchanged vegetation cover map is based on the IGBP scheme as shown in **Figure 1**. A total of eleven vegetation types were selected from the unchanged vegetation cover map (the total amount of pixels was 77,930, accounting for 93.04% of all the land surface). All the used vegetation types, their total numbers of pixels, and area proportions to the land surface are shown below: deciduous broadleaf forests (DBFs, 941, 1.12%), deciduous needleleaf forests (DNFs, 120, 0.14%), evergreen broadleaf forests (EBFs, 4008, 4.79%), evergreen needleleaf forests (ENFs, 1144, 1.37%), mixed forests (MFs, 2204, 2.63%), closed shrublands (CSHs, 116, 0.14%), open shrublands (OSHs, 6638, 7.93%), savannas (SAVs, 6217, 7.42%), woody savannas (WSAs, 4412, 5.27%), croplands (CROs, 4717, 5.63%), and grasslands (GRAs, 12592, 15.03%).

## 2.2 Determining the Cumulative Drought Impact on Plant Photosynthesis

The cumulative drought effect on photosynthesis was concluded through correlation analysis in which time scale SPEI (i.e., any month in 1–12 months) had the maximum significant correlation with monthly GPP. For example, assuming that the i month SPEI data (i could be anyone in the range of 1–12) showed the largest correlation with monthly GPP at a pixel, the cumulative impact of drought on photosynthesis would be set as i months for this pixel, which indicated that the earlier i month climatic water balance was important to affect vegetation photosynthesis. The specific processes to determine the cumulative effect of drought for each GPP dataset could be summarized into three steps. At first, time series monthly GPP product and 1–12 months SPEI in the timeperiod of 2001–2010 were extracted. Second, the reaction of monthly GPP to 1–12 months SPEI was characterized through Pearson's correlation coefficient, while the significance level (i.e., $p$) was set to 0.05 for each pixel. Third, the accumulated months and intensity of drought cumulative impact on

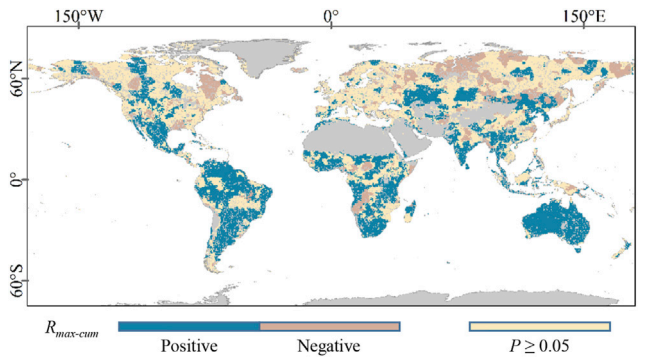


**FIGURE 2 |** Spatial distribution of $R_{max\text{-}cum}$ based on probability statistic.

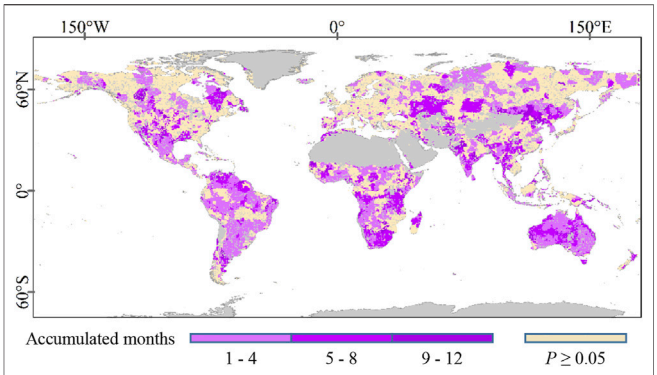


**FIGURE 3 |** Spatial distribution of accumulated months based on probability statistic.

photosynthesis was determined as i month and $R_{max\text{-}cum}$ ($R_{max\text{-}cum}$ with a range of −1 to 1), while the absolute largest significant Pearson's correlation coefficient (i.e., $|R_{max\text{-}cum}|$ when $p < 0.05$) happened between monthly GPP and i month SPEI.

## 2.3 Statistical Analyses

Based on Pearson's correlation coefficients between monthly GPP data and multiscale monthly SPEI, the $R_{max\text{-}cum}$ and accumulated mouth maps were obtained for each GPP dataset according to the method mentioned in **Section 2.2**. Furthermore, in order to compare the cumulative drought impacts on global photosynthesis which were acquired through different GPP datasets, the $R_{max\text{-}cum}$ were divided into three types, including a significant positive correlation (i.e., $R_{max\text{-}cum} > 0$ when $p < 0.05$), significant negative correlation (i.e., $R_{max\text{-}cum} < 0$ when $p < 0.05$), and no significant correlation (i.e., $p \geq 0.05$). Moreover, the accumulated months could be ranged likewise into three terms, namely, short term (1 ≤ months ≤4), medium term (5 ≤ months ≤8), and long term (9 ≤ months ≤12). In this way, there were both three possible results of $R_{max\text{-}cum}$ (i.e., positive, negative, and no significant correlation) and accumulated months (i.e., short, medium, and long term) for different GPP datasets at each pixel. Based on these results of $R_{max\text{-}cum}$ acquired from multiple GPP datasets, the final $R_{max\text{-}cum}$ outcome for each pixel was determined through probability statistics wherein one result had the highest proportion within all these GPP datasets. Moreover, the reliability (Re) of the final $R_{max\text{-}cum}$ for each pixel was determined as follows:

$$Re = \frac{N_{R_{\max\text{-}cum}}}{N_{GPP}}, \tag{1}$$

where $N_{Rmax\text{-}cum}$ represented the total number of final $R_{max\text{-}cum}$ from all GPP datasets and $N_{GPP}$ was the total amount of GPP products. At the same time, the final accumulated month outcome and its reliability for each pixel were also obtained using the same processes as the final $R_{max\text{-}cum}$.

As for comparing the cumulative drought impact on photosynthesis across vegetation types, the percentage (Pe) of different types of $R_{max\text{-}cum}$ for each vegetation cover was obtained as follows:

$$pe_j = \frac{M_j}{M_{all}}, \tag{2}$$

where $j$ was the types of $R_{max\text{-}cum}$ (i.e., positive, negative, and no significant correlation), $M$ was the number of pixels that showed $R_{max\text{-}cum}$, and $M_{all}$ was the total pixels for each vegetation type. Similar to the $R_{max\text{-}cum}$, the percentage of different types of accumulated months for each vegetation cover land was also acquired as follows:

$$pe_i = \frac{S_i}{S_{all}}, \tag{3}$$

where $i$ was the types of accumulated months (i.e., short, medium, and long term), $S$ was the number of pixels showing accumulated months, and $S_{all}$ was all the significant pixels for one vegetation type. In addition, the variation of mean reliability with latitudes can be obtained as follows:

$$Re_{Mean} = \frac{\sum_i P}{i}, \tag{4}$$

where $Re_{Mean}$ was the averaged reliability for each latitude, $P$ was the reliability of pixels at the same latitude, and $i$ was the number of pixels with reliability for the same latitude.

# 3 RESULTS

## 3.1 Spatial Pattern of Drought Cumulative Effect on Photosynthesis

The spatial distribution of $R_{max\text{-}cum}$ which is based on probability statistics is shown in **Figure 2**. The results indicated that 52.11% of vegetation cover lands have shown significant $R_{max\text{-}cum}$, and the positive correlations had a higher proportion (38.30%) than negative correlations (13.81%). Meanwhile, the positive $R_{max\text{-}cum}$ was primarily observed in North America, South America, South-central Africa, Central Asia, South Asia, Oceania, and some parts of East Asia. The negative $R_{max\text{-}cum}$ was mostly discovered at the medium and high latitudes of the Northern Hemisphere, such as eastern North America, Northern Asia, and

**TABLE 1 |** Percentages of different $R_{max\text{-}cum}$ (i.e., positive, negative, and no significant correlation) and accumulated months (i.e., short, medium, and long term) across vegetation types.

| Vegetation Types | Percentage (%) | | | | | |
|---|---|---|---|---|---|---|
| | $R_{max\text{-}cum}$ | | | Accumulated months | | |
| | Positive ($R_{cum\text{-}max} > 0$ when $p < 0.05$) | Negative ($R_{cum\text{-}max} < 0$ when $p < 0.05$) | No ($p \geq 0.05$) | Short (1–4) | Medium (5–8) | Long (9–12) |
| ENFs | 21.85 | 19.58 | 58.57 | 69.92 | 24.47 | 5.91 |
| EBFs | 58.28 | 4.17 | 37.55 | 68.80 | 27.29 | 3.92 |
| DNFs | 7.76 | 18.97 | 73.28 | 70.97 | 29.03 | 0 |
| DBFs | 28.80 | 17.64 | 53.56 | 48.28 | 50.11 | 1.60 |
| MFs | 8.89 | 28.95 | 62.16 | 69.42 | 26.38 | 4.20 |
| CSHs | 69.17 | 13.33 | 17.50 | 72.73 | 14.14 | 13.13 |
| OSHs | 42.54 | 19.77 | 37.69 | 64.65 | 27.90 | 7.45 |
| WSAs | 24.48 | 17.48 | 58.05 | 64.61 | 31.60 | 3.78 |
| SAVs | 37.30 | 13.64 | 49.06 | 64.35 | 32.81 | 2.84 |
| GRAs | 43.11 | 11.26 | 45.62 | 55.62 | 31.66 | 12.72 |
| CROs | 36.36 | 7.89 | 55.76 | 50.93 | 39.72 | 9.34 |
| ALL | 38.30 | 13.81 | 47.89 | 61.05 | 31.32 | 7.63 |

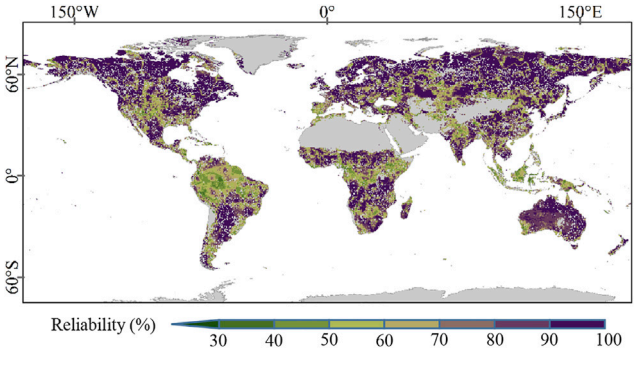


**FIGURE 4 |** Global reliability pattern of $R_{max\text{-}cum}$ obtained from probability statistic.

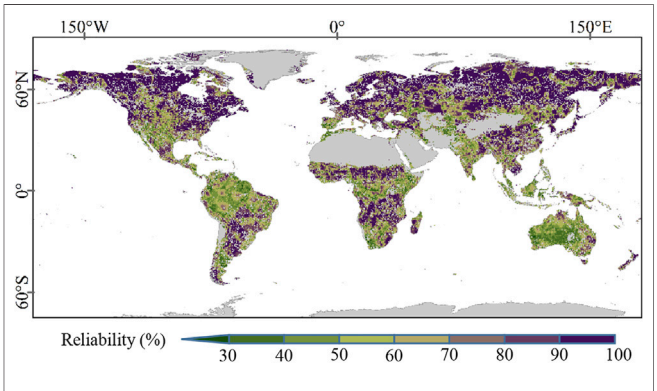


**FIGURE 5 |** Global reliability pattern of accumulated months obtained from probability statistic.

some parts of Eastern Europe. As shown in **Figure 3**, the spatial distribution of accumulated months was significantly different at the global scale, while the accumulated months were mainly concentrated in the short term (31.81%), followed by medium term (16.32%) and long term (3.98%). The accumulated months in the short term were mostly found in North America, South America, Central Africa, Northern Asia, and Oceania. The medium-term accumulated months were mainly observed among Central Asia, Southern Africa, and some parts of East Asia. Moreover, the long term accumulation mainly occurred in East and South Asia.

## 3.2 Cumulative Drought Impact on Photosynthesis Across Plant Types

As shown in **Table 1**, the area percentages among $R_{max\text{-}cum}$ and accumulated months changed obviously in different plant cover types. The area percentages of the vegetation cover land revealed positive $R_{max\text{-}cum}$ following the order: CSHs (69.17%) > EBFs (58.28%) > GRAs (43.11%) > OSHs (42.54%) > SAVs (37.30%) > CROs (36.36%) > DBFs (28.80%) > WSAs (24.48%) > ENFs (21.85%) > MFs (8.89%) > DNFs (7.76%), as the negative $R_{max\text{-}cum}$ with the order: MFs (28.95%) > OSHs (19.77%) > ENFs (19.58%) > DNFs (18.97%) > DBFs (17.64%) > WSAs (17.48%) > SAVs (13.64) > CSHs (13.33%) > GRAs (11.26%) > CROs (7.89%) > EBFs (4.17%). In addition, the accumulated months were primarily at the short term in most vegetation types, while DBFs was at the medium term (50.11%).

## 3.3 Global Reliability Pattern of Drought Cumulative Effect on Photosynthesis

The global reliability pattern of $R_{max\text{-}cum}$ thought probability analysis is shown in **Figure 4**. The $R_{max\text{-}cum}$ had relatively high reliability at the global scale (characterized by the averaged value of 80.37 ± 17.33%). Moreover, the $R_{max\text{-}cum}$ showed high reliability in high latitudes and low reliability around the equatorial regions. The reliability of accumulated

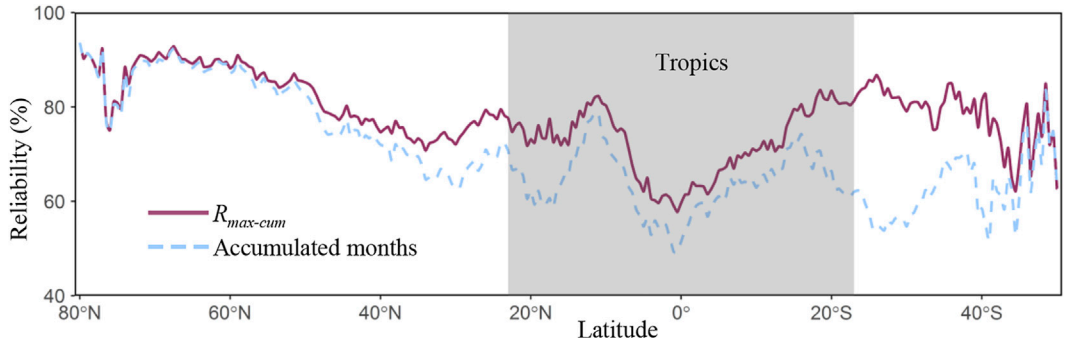


**FIGURE 6 |** Variability trend of reliability in $R_{max\text{-}cum}$ and accumulated months acquired from probability statistics across latitudes.

months displayed a similar global pattern with $R_{max\text{-}cum}$ (**Figure 5**), characterized by the mean value of 74.68 ± 20.79%. Notably, there were obvious discrepancies in the reliability of $R_{max\text{-}cum}$ and accumulated months around Oceania, South Asia, and South Africa, while the $R_{max\text{-}cum}$ presented high reliability and the accumulated months showed low reliability in these areas.

**Figure 6** showed the variability trend of reliability in $R_{max\text{-}cum}$ and accumulated months across latitudes. The reliability of $R_{max\text{-}cum}$ was decreased with the decreasing of latitude, while the reliability of accumulated months was undulated in the Southern Hemisphere. As for the reliabilities of both $R_{max\text{-}cum}$ and accumulated months, they were various across vegetation types (**Table 2**). The averaged reliabilities of $R_{max\text{-}cum}$ in diverse plant types followed the order: DNFs (90.02 ± 14.44%) > ENFs (89.88 ± 14.53%) > MFs (86.22 ± 15.97%) > OSHs (85.41 ± 14.63%) > WSAs (84.17 ± 17.17%) > DBFs (84.01 ± 15.68%) > SAVs (83.52 ± 16.57%) > GRAs (79.41 ± 16.60%) > CROs (77.27 ± 16.38%) > CSHs (74.58 ± 17.15%) > EBFs (62.74 ± 14.87%), while the averaged reliability of accumulated months showed a lower value than $R_{max\text{-}cum}$ among different species, characterized by the following order: DNFs (89.36 ± 15.24%) > ENFs (88.26 ± 16.12%) > MFs (85.28 ± 16.67%) > WSAs (81.88 ± 18.98%) > DBFs (81.39 ± 17.14%) > SAVs (79.34 ± 19.23%) > GRAs (73.93 ± 19.38%) > OSHs (72.74 ± 24.11%) > CROs (72.26 ± 18.68%) > EBFs (56.83 ± 15.81%) > CSHs (55.71 ± 16.61%).

## 4 DISCUSSION

This study evaluated the cumulative drought impact on global photosynthesis across vegetation types grounded on numerous GPP products and derived a global reliability pattern of drought cumulative effect through probability analysis. The results illustrated that the cumulative effects of drought occurred in 52.11% of the vegetation cover areas (**Figure 2**) and the dominant accumulated months were short term (1–4 months, 31.81%). Our study indicated the high spatial heterogeneity of drought effect at the global scale and the importance of the GPP dataset in evaluating the cumulative drought impact on photosynthesis.

In this study, the global reliability pattern of drought cumulative effect on photosynthesis was acquired through numerous GPP products, and both $R_{max\text{-}cum}$ and accumulated months exhibited spatially heterogenous distributions (**Figure 4** and **Figure 5**). Moreover, the reliability of cumulative effect in time scales was more undulated, especially in the southern hemisphere (**Figure 6**). These findings revealed that the water supply and availability could play a key role in GPP simulation. Generally, a total of twenty-six global GPP datasets generated from different model schemes (i.e., based on LUE, ML, and process) were used as indicators to represent the photosynthesis of vegetation. Among various models, these process-oriented models always considered many physiological or biogeochemical processes of photosynthesis mechanistically (Jiang and Ryu, 2016; Wagle et al., 2016; Xie et al., 2021), thus making the GPP estimation more rigorous. While these LUE models were developed through the theory of radiation conversion efficiency (Monteith, 1972; Yuan et al., 2014), the ML models estimated GPP based on the statistical relationship established between input data and outcome (Jiang and Ryu, 2016; Wolanin et al., 2019; Xie et al., 2022). In this way, different theoretical foundations among diverse models would bring unavoidable uncertainties in characterizing global photosynthesis (Zheng et al., 2020; Wang S. et al., 2021; Wang Z. et al., 2021). In addition, multiple GPP models have used various strategies to describe the water stress of vegetation. For example, the EC-LUE model used the rate between evapotranspiration and net radiation to consider the moisture regulations on LUE (Yuan et al., 2010), while the VPM model adopted a scaled Land Surface Water Index to characterize the moisture limitation for photosynthesis (Zhang et al., 2017). Moreover, the water limiting processes could be more complex in process-oriented models (Jiang and Ryu, 2016; Slevin et al., 2017). These different ways of regulating the moisture status of plants might also lead to a diverse response of photosynthesis to drought among different GPP datasets.

The cumulative drought impact on photosynthesis and its reliability showed obvious discrepancies among vegetation types

**TABLE 2 |** Averaged reliability and standard deviation of $R_{max\text{-}cum}$ and accumulated months across vegetation types.

| Reliability (%) | Vegetation types | | | | | | | | | | | |
|---|---|---|---|---|---|---|---|---|---|---|---|---|
| | ENFs | EBFs | DNFs | DBFs | MFs | CSHs | OSHs | WSAs | SAVs | GRAs | CROs | All |
| $R_{max\text{-}cum}$ | 89.88 ± 14.53 | 62.74 ± 14.87 | 90.02 ± 14.44 | 84.01 ± 15.68 | 86.22 ± 15.97 | 74.58 ± 17.15 | 85.41 ± 14.63 | 84.17 ± 17.17 | 83.52 ± 16.57 | 79.41 ± 16.60 | 77.27 ± 16.38 | 80.37 ± 17.33 |
| Accumulated months | 88.26 ± 16.12 | 56.83 ± 15.81 | 89.36 ± 15.24 | 81.39 ± 17.14 | 85.28 ± 16.67 | 55.71 ± 16.61 | 72.74 ± 24.11 | 81.88 ± 18.98 | 79.34 ± 19.23 | 73.93 ± 19.38 | 72.26 ± 18.68 | 74.68 ± 20.79 |

(**Table 1** and **Table 2**). The results showed that there were higher proportions of significant $R_{max\text{-}cum}$ pixels in CSHs, OSHs, and GRAs than those in DNFs, MFs, ENFs, and WSAs, confirming the importance of water supply and availability for grasslands and shrubs (Wu et al., 2015; Peng et al., 2019; Fan et al., 2020), while this might be attributed to the different structural and functional characteristics of rhizomes between herbs and woody plants (Chimento and Amaducci, 2015; Hudek et al., 2017; Lobmann et al., 2020), such as root diameter (Hudek et al., 2017), root depth (Seghieri, 1995), and stem specific gravity (McCoy-Sulentic et al., 2017). Herbaceous vegetations usually have abundant fine and shallow roots in the topsoil layer, making them respond more sensitively to drought due to the limitation in water availability through more deep layers of soil (Dodd et al., 1998; Wu et al., 2018; Lobmann et al., 2020). However, woody plants always have taproot structures with thick roots, and deeper roots facilitate the absorption of groundwater which causes them to be more resistant to drought (Dodd et al., 1998; Midwood et al., 1998; Bleby et al., 2010; Wang et al., 2020). Moreover, the roots of woody plants are further in evolution than herbaceous plants and are characterized by secondary growth (Ma et al., 2018; Wang et al., 2020), helping them withstand stress caused by drought. Different water storage modes may also result in diverse responses to drought across vegetations (Tian et al., 2018) because woody vegetations hold most plant water in their woody tissues and have more complex hydraulic strategies, while the moisture storage of herbs primarily depends on the amount of foliage (Sternberg and Shoshany, 2001; Morris et al., 2016).

## 5 CONCLUSION

In this work, a total of twenty-six global GPP products based on process, LUE, and ML models were obtained to evaluate and derive a global reliability pattern of drought's cumulative effect on photosynthesis. The results illustrated that the cumulative drought impact was observed in 52.11% of vegetation cover land primarily in the short term (31.81%). Obvious discrepancies of drought cumulative effect were observed in different plant functional types, while herbaceous vegetations were more sensitive to drought than woody plants. This could be attributed to the difference in root functional traits among vegetation functional types. Because the reliability pattern of drought depended on multiple GPP datasets, the results also showed marked heterogeneity in terms of space and vegetation type, while lower reliability was found in the tropics. Our findings highlighted the importance of water characterization strategies under different vegetation functional types in GPP models and the necessity of GPP dataset selection in assessing drought effect on vegetation.

## DATA AVAILABILITY STATEMENT

The raw data supporting the conclusions of this article will be made available by the authors, without undue reservation.

## AUTHOR CONTRIBUTIONS

CW: conceptualization, software, investigation, writing—original draft preparation, and writing—review and editing. TW: supervision, data curation, and funding acquisition.

## ACKNOWLEDGMENTS

All global GPP datasets used in this work are shown in **Supplementary Material**, and we sincerely thank all data providers. The fifteen process-oriented GPP products (BIOME-BGC, CLASS-CTEM-N+, CLM4, CLM4VIC, DLEM, GTEC, ISAM, LPJ-wsl, ORCHIDEE-LSCE, SiB3, SiBCASA, TEM6, TRIPLEX-GHG, VEGAS2.1, and VISIT) were acquired through "The North American Carbon Program (NACP) Multiscale Synthesis and Terrestrial Model Intercomparison Project (MsTMIP). (https://doi.org/10.3334/ORNLDAAC/1225)." The JULES GPP dataset was downloaded at "The University of Edinburgh. School of GeoSciences. (https://doi.org/10.7488/ds/1461)," while BESS data could be obtained at "Ecological Sensing AI Lab. Seoul National University. (https://www.environment.snu.ac.kr/)." EC-LUE data supported from "National Earth System Science Data Center. National Science & Technology Infrastructure of China. (http://www.geodata.cn)," and VPM data could be found at "(https://doi.org/10.6084/m9.figshare.c.3789814.v1)". Moreover, multiscale SPEI data could be accessed at "(https://spei.csic.es/database.html)." We would also like to thank the anonymous reviewers for their constructive comments.

## SUPPLEMENTARY MATERIAL

The Supplementary Material for this article can be found online at: https://www.frontiersin.org/articles/10.3389/fenvs.2022.908875/full#supplementary-material

## REFERENCES

AghaKouchak, A., Cheng, L., Mazdiyasni, O., and Farahmand, A. (2014). Global Warming and Changes in Risk of Concurrent Climate Extremes: Insights from the 2014 California Drought. *Geophys. Res. Lett.* 41 (24), 8847–8852. doi:10.1002/2014gl062308

Anav, A., Friedlingstein, P., Beer, C., Ciais, P., Harper, A., Jones, C., et al. (2015). Spatiotemporal Patterns of Terrestrial Gross Primary Production: A Review. *Rev. Geophys.* 53 (3), 785–818. doi:10.1002/2015rg000483

Anderegg, W. R. L., Schwalm, C., Biondi, F., Camarero, J. J., Koch, G., Litvak, M., et al. (2015). Pervasive Drought Legacies in forest Ecosystems and Their Implications for Carbon Cycle Models. *Science* 349 (6247), 528–532. doi:10.1126/science.aab1833

Barman, R., Jain, A. K., and Liang, M. (2014). Climate-driven Uncertainties in Modeling Terrestrial Gross Primary Production: a Site Level to Global-Scale Analysis. *Glob. Change Biol.* 20 (5), 1394–1411. doi:10.1111/gcb.12474

Beguería, S., Serrano, S. M. V., Reig-Gracia, F., and Garcés, B. L. (2017). *SPEIbase v.2.5*.

Beguería, S., Vicente-Serrano, S. M., and Angulo-Martínez, M. (2010). A Multiscalar Global Drought Dataset: The SPEIbase: A New Gridded Product for the Analysis of Drought Variability and Impacts. *Bull. Amer. Meteorol. Soc.* 91 (10), 1351–1356. doi:10.1175/2010bams2988.1

Beguería, S., Vicente-Serrano, S. M., Reig, F., and Latorre, B. (2014). Standardized Precipitation Evapotranspiration index (SPEI) Revisited: Parameter Fitting, Evapotranspiration Models, Tools, Datasets and Drought Monitoring. *Int. J. Climatol.* 34 (10), 3001–3023. doi:10.1002/joc.3887

Bleby, T. M., McElrone, A. J., and Jackson, R. B. (2010). Water Uptake and Hydraulic Redistribution across Large Woody Root Systems to 20 M Depth. *Plant Cel Environ.* 33 (12), 2132–2148. doi:10.1111/j.1365-3040.2010.02212.x

Braswell, B. H., Schimel, D. S., Linder, E., and Moore, B. (1997). The Response of Global Terrestrial Ecosystems to Interannual Temperature Variability. *Science* 278 (5339), 870–873. doi:10.1126/science.278.5339.870

Campbell, J. E., Berry, J. A., Seibt, U., Smith, S. J., Montzka, S. A., Launois, T., et al. (2017). Large Historical Growth in Global Terrestrial Gross Primary Production. *Nature* 544 (7648), 84–87. doi:10.1038/nature22030

Chen, B., Xu, G., Coops, N. C., Ciais, P., Innes, J. L., Wang, G., et al. (2014). Changes in Vegetation Photosynthetic Activity Trends across the Asia-Pacific Region over the Last Three Decades. *Remote Sensing Environ.* 144, 28–41. doi:10.1016/j.rse.2013.12.018

Chimento, C., and Amaducci, S. (2015). Characterization of fine Root System and Potential Contribution to Soil Organic Carbon of Six Perennial Bioenergy Crops. *Biomass and Bioenergy* 83, 116–122. doi:10.1016/j.biombioe.2015.09.008

Chu, D., Shen, H., Guan, X., Chen, J. M., Li, X., Li, J., et al. (2021). Long Time-Series NDVI Reconstruction in Cloud-Prone Regions via Spatio-Temporal Tensor Completion. *Remote Sensing Environ.* 264, 112632. doi:10.1016/j.rse.2021.112632

Ciais, P., Reichstein, M., Viovy, N., Granier, A., Ogée, J., Allard, V., et al. (2005). Europe-wide Reduction in Primary Productivity Caused by the Heat and Drought in 2003. *Nature* 437 (7058), 529–533. doi:10.1038/nature03972

Cramer, W., Bondeau, A., Woodward, F. I., Prentice, I. C., Betts, R. A., Brovkin, V., et al. (2001). Global Response of Terrestrial Ecosystem Structure and Function to CO2 and Climate Change: Results from Six Dynamic Global Vegetation Models. *Glob. Change Biol.* 7 (4), 357–373. doi:10.1046/j.1365-2486.2001.00383.x

Curasi, S. R., Parker, T. C., Rocha, A. V., Moody, M. L., Tang, J., and Fetcher, N. (2019). Differential Responses of Ecotypes to Climate in a Ubiquitous Arctic Sedge: Implications for Future Ecosystem C Cycling. *New Phytol.* 223 (1), 180–192. doi:10.1111/nph.15790

Dodd, M. B., Lauenroth, W. K., and Welker, J. M. (1998). Differential Water Resource Use by Herbaceous and Woody Plant Life-Forms in a Shortgrass Steppe Community. *Oecologia* 117 (4), 504–512. doi:10.1007/s004420050686

Fan, J., Xu, Y., Ge, H., and Yang, W. (2020). Vegetation Growth Variation in Relation to Topography in Horqin Sandy Land. *Ecol. Indicators* 113, 106215. doi:10.1016/j.ecolind.2020.106215

Friedl, M., and Sulla-Menashe, D. (2015). MCD12C1 MODIS/Terra+Aqua Land Cover Type Yearly L3 Global 0.05Deg CMG V006. *NASA EOSDIS Land Process. DAAC*. Accessed May 04, 2022. doi:10.5067/MODIS/MCD12C1.006

Guan, X., Chen, J. M., Shen, H., and Xie, X. (2021). A Modified Two-Leaf Light Use Efficiency Model for Improving the Simulation of GPP Using a Radiation Scalar. *Agric. For. Meteorology* 307, 108546. doi:10.1016/j.agrformet.2021.108546

Guan, X., Chen, J. M., Shen, H., Xie, X., and Tan, J. (2022). Comparison of Big-Leaf and Two-Leaf Light Use Efficiency Models for GPP Simulation after Considering a Radiation Scalar. *Agric. For. Meteorology* 313, 108761. doi:10.1016/j.agrformet.2021.108761

Guo, Y., Xia, H., Pan, L., Zhao, X., and Li, R. (2022). Mapping the Northern Limit of Double Cropping Using a Phenology-Based Algorithm and Google Earth Engine. *Remote Sensing* 14 (4), 1004. doi:10.3390/rs14041004

Hayes, D. J., McGuire, A. D., Kicklighter, D. W., Gurney, K. R., Burnside, T. J., and Melillo, J. M. (2011). Is the Northern High-Latitude Land-Based CO2sink Weakening? *Glob. Biogeochem. Cycles* 25, 1. doi:10.1029/2010gb003813

Hilker, T., Coops, N. C., Wulder, M. A., Black, T. A., and Guy, R. D. (2008). The Use of Remote Sensing in Light Use Efficiency Based Models of Gross Primary Production: A Review of Current Status and Future Requirements. *Sci. Total Environ.* 404 (2-3), 411–423. doi:10.1016/j.scitotenv.2007.11.007

Huang, C.-y., Asner, G. P., Barger, N. N., Neff, J. C., and Floyd, M. L. (2010). Regional Aboveground Live Carbon Losses Due to Drought-Induced Tree Dieback in Piñon-Juniper Ecosystems. *Remote Sensing Environ.* 114 (7), 1471–1479. doi:10.1016/j.rse.2010.02.003

Huang, L., He, B., Han, L., Liu, J., Wang, H., and Chen, Z. (2017). A Global Examination of the Response of Ecosystem Water-Use Efficiency to Drought Based on MODIS Data. *Sci. Total Environ.* 601-602, 1097–1107. doi:10.1016/j.scitotenv.2017.05.084

Huang, M., Wang, X., Keenan, T. F., and Piao, S. (2018). Drought Timing Influences the Legacy of Tree Growth Recovery. *Glob. Change Biol.* 24 (8), 3546–3559. doi:10.1111/gcb.14294

Hudek, C., Sturrock, C. J., Atkinson, B. S., Stanchi, S., and Freppaz, M. (2017). Root Morphology and Biomechanical Characteristics of High Altitude alpine Plant Species and Their Potential Application in Soil Stabilization. *Ecol. Eng.* 109, 228–239 . doi:10.1016/j.ecoleng.2017.05.048

Huntzinger, D. N., Schwalm, C. R., Wei, Y., Cook, R. B., Michalak, A. M., Schaefer, K., et al. (2018). *NACP MsTMIP: Global 0.5-degree Model Outputs in Standard Format, Version 1.0*. Oak Ridge, TN: ORNL Distributed Active Archive Center.

Ito, A. (2010). Changing Ecophysiological Processes and Carbon Budget in East Asian Ecosystems under Near-Future Changes in Climate: Implications for Long-Term Monitoring from a Process-Based Model. *J. Plant Res.* 123 (4), 577–588. doi:10.1007/s10265-009-0305-x

Ivits, E., Horion, S., Erhard, M., and Fensholt, R. (2016). Assessing European Ecosystem Stability to Drought in the Vegetation Growing Season. *Glob. Ecol. Biogeogr.* 25 (9), 1131–1143. doi:10.1111/geb.12472

Jiang, C., and Ryu, Y. (2016). Multi-scale Evaluation of Global Gross Primary Productivity and Evapotranspiration Products Derived from Breathing Earth System Simulator (BESS). *Remote Sensing Environ.* 186, 528–547. doi:10.1016/j.rse.2016.08.030

Kang, W., Wang, T., and Liu, S. (2018). The Response of Vegetation Phenology and Productivity to Drought in Semi-arid Regions of Northern China. *Remote Sensing* 10 (5), 727. doi:10.3390/rs10050727

Lees, K. J., Quaife, T., Artz, R. R. E., Khomik, M., and Clark, J. M. (2018). Potential for Using Remote Sensing to Estimate Carbon Fluxes across Northern Peatlands - A Review. *Sci. Total Environ.* 615, 857–874. doi:10.1016/j.scitotenv.2017.09.103

Löbmann, M. T., Geitner, C., Wellstein, C., and Zerbe, S. (2020). The Influence of Herbaceous Vegetation on Slope Stability - A Review. *Earth-Science Rev.* 209, 103328. doi:10.1016/j.earscirev.2020.103328

Ma, Z., Guo, D., Xu, X., Lu, M., Bardgett, R. D., Eissenstat, D. M., et al. (2018). Evolutionary History Resolves Global Organization of Root Functional Traits. *Nature* 555 (7694), 94–97. doi:10.1038/nature25783

McCoy-Sulentic, M. E., Kolb, T. E., Merritt, D. M., Palmquist, E. C., Ralston, B. E., and Sarr, D. A. (2017). Variation in Species-level Plant Functional Traits over Wetland Indicator Status Categories. *Ecol. Evol.* 7 (11), 3732–3744. doi:10.1002/ece3.2975

Midwood, A. J., Boutton, T. W., Archer, S. R., and Watts, S. E. (1998). Water Use by Woody Plants on Contrasting Soils in a savanna Parkland: Assessment with delta H-2 and delta O-18. *Plant and Soil* 205 (1), 13–24. doi:10.1023/a:1004355423241

Monteith, J. L. (1972). Solar Radiation and Productivity in Tropical Ecosystems. *J. Appl. Ecol.* 9 (3), 747–766. doi:10.2307/2401901

Morris, H., Plavcová, L., Cvecko, P., Fichtler, E., Gillingham, M. A. F., Martínez-Cabrera, H. I., et al. (2016). A Global Analysis of Parenchyma Tissue Fractions in Secondary Xylem of Seed Plants. *New Phytol.* 209 (4), 1553–1565. doi:10.1111/nph.13737

Naumann, G., Alfieri, L., Wyser, K., Mentaschi, L., Betts, R. A., Carrao, H., et al. (2018). Global Changes in Drought Conditions under Different Levels of Warming. *Geophys. Res. Lett.* 45 (7), 3285–3296. doi:10.1002/2017gl076521

Pan, L., Xia, H., Zhao, X., Guo, Y., and Qin, Y. (2021). Mapping Winter Crops Using a Phenology Algorithm, Time-Series Sentinel-2 and Landsat-7/8 Images, and Google Earth Engine. *Remote Sensing* 13 (13), 2510. doi:10.3390/rs13132510

Passioura, J. B. (1991). "The Yield of Crops in Relation to Drought," in *International Symposium on Physiology and Determination of Crop Yield*. Editors K. J. Boote, J. M. Bennett, T. R. Sinclair, and G. M. Paulsen (MADISON: Soil Science Soc Amer), 343–359.

Peng, J., Wu, C., Zhang, X., Wang, X., and Gonsamo, A. (2019). Satellite Detection of Cumulative and Lagged Effects of Drought on Autumn Leaf Senescence over the Northern Hemisphere. *Glob. Change Biol.* 25 (6), 2174–2188. doi:10.1111/gcb.14627

Rao, K., Anderegg, W. R. L., Sala, A., Martínez-Vilalta, J., and Konings, A. G. (2019). Satellite-based Vegetation Optical Depth as an Indicator of Drought-Driven Tree Mortality. *Remote Sensing Environ.* 227, 125–136. doi:10.1016/j.rse.2019.03.026

Reichstein, M., Bahn, M., Ciais, P., Frank, D., Mahecha, M. D., Seneviratne, S. I., et al. (2013). Climate Extremes and the Carbon Cycle. *Nature* 500 (7462), 287–295. doi:10.1038/nature12350

Richardson, A. D., Keenan, T. F., Migliavacca, M., Ryu, Y., Sonnentag, O., and Toomey, M. (2013). Climate Change, Phenology, and Phenological Control of Vegetation Feedbacks to the Climate System. *Agric. For. Meteorology* 169, 156–173. doi:10.1016/j.agrformet.2012.09.012

Sánchez, M. L., Pardo, N., Pérez, I. A., and García, M. A. (2015). GPP and Maximum Light Use Efficiency Estimates Using Different Approaches over a Rotating Biodiesel Crop. *Agric. For. Meteorology* 214-215, 444–455. doi:10.1016/j.agrformet.2015.09.012

Seghieri, J. (1995). The Rooting Patterns of Woody and Herbaceous Plants in a savanna; Are They Complementary or in Competition? *Afr. J Ecol* 33 (4), 358–365. doi:10.1111/j.1365-2028.1995.tb01045.x

Slevin, D., Tett, S. F. B., Exbrayat, J.-F., Bloom, A. A., and Williams, M. (2017). Global Evaluation of Gross Primary Productivity in the JULES Land Surface Model v3.4.1. *Geosci. Model. Dev.* 10 (7), 2651–2670. doi:10.5194/gmd-10-2651-2017

Sternberg, M., and Shoshany, M. (2001). Aboveground Biomass Allocation and Water Content Relationships in Mediterranean Trees and Shrubs in Two Climatological Regions in Israel. *Plant Ecol.* 157 (2), 173–181. doi:10.1023/a:1013916422201

Sun, S., Du, W., Song, Z., Zhang, D., Wu, X., Chen, B., et al. (2021). Response of Gross Primary Productivity to Drought Time-Scales across China. *J. Geophys. Res. Biogeosci* 126 (4), 19. doi:10.1029/2020jg005953

Tan, K. P., Kanniah, K. D., and Cracknell, A. P. (2012). A Review of Remote Sensing Based Productivity Models and Their Suitability for Studying Oil palm Productivity in Tropical Regions. *Prog. Phys. Geogr. Earth Environ.* 36 (5), 655–679. doi:10.1177/0309133312452187

Tian, F., Wigneron, J.-P., Ciais, P., Chave, J., Ogée, J., Peñuelas, J., et al. (2018). Coupling of Ecosystem-Scale Plant Water Storage and Leaf Phenology Observed by Satellite. *Nat. Ecol. Evol.* 2 (9), 1428–1435. doi:10.1038/s41559-018-0630-3

Tian, H., Xu, X., Lu, C., Liu, M., Ren, W., Chen, G., et al. (2011). Net Exchanges of CO2, CH4, and N2O between China's Terrestrial Ecosystems and the Atmosphere and Their Contributions to Global Climate Warming. *J. Geophys. Res.* 116, 13. doi:10.1029/2010jg001393

Tramontana, G., Jung, M., Schwalm, C. R., Ichii, K., Camps-Valls, G., Ráduly, B., et al. (2016). Predicting Carbon Dioxide and Energy Fluxes across Global FLUXNET Sites with Regression Algorithms. *Biogeosciences* 13 (14), 4291–4313. doi:10.5194/bg-13-4291-2016

van der Molen, M. K., Dolman, A. J., Ciais, P., Eglin, T., Gobron, N., Law, B. E., et al. (2011). Drought and Ecosystem Carbon Cycling. *Agric. For. Meteorology* 151 (7), 765–773. doi:10.1016/j.agrformet.2011.01.018

Vicente-Serrano, S. M., Beguería, S., and López-Moreno, J. I. (2010). A Multiscalar Drought Index Sensitive to Global Warming: The Standardized Precipitation Evapotranspiration Index. *J. Clim.* 23 (7), 1696–1718. doi:10.1175/2009jcli2909.1

Wagle, P., Zhang, Y., Jin, C., and Xiao, X. (2016). Comparison of Solar-induced Chlorophyll Fluorescence, Light-use Efficiency, and Process-based GPP Models in maize. *Ecol. Appl.* 26 (4), 1211–1222. doi:10.1890/15-1434

Wang, P., Huang, K., and Hu, S. (2020). Distinct fine-root Responses to Precipitation Changes in Herbaceous and Woody Plants: a Meta-analysis. *New Phytol.* 225 (4), 1491–1499. doi:10.1111/nph.16266

Wang, S., Zhang, Y., Ju, W., Qiu, B., and Zhang, Z. (2021a). Tracking the Seasonal and Inter-annual Variations of Global Gross Primary Production during Last Four Decades Using Satellite Near-Infrared Reflectance Data. *Sci. Total Environ.* 755, 142569. doi:10.1016/j.scitotenv.2020.142569

Wang, Z., Liu, S., Wang, Y.-P., Valbuena, R., Wu, Y., Kutia, M., et al. (2021b). Tighten the Bolts and Nuts on GPP Estimations from Sites to the Globe: An

Assessment of Remote Sensing Based LUE Models and Supporting Data Fields. *Remote Sensing* 13 (2), 168. doi:10.3390/rs13020168

Wen, Y., Liu, X., Xin, Q., Wu, J., Xu, X., Pei, F., et al. (2019). Cumulative Effects of Climatic Factors on Terrestrial Vegetation Growth. *J. Geophys. Res. Biogeosci.* 124 (4), 789–806. doi:10.1029/2018jg004751

Wendler, G., Conner, J., Moore, B., Shulski, M., and Stuefer, M. (2011). Climatology of Alaskan Wildfires with Special Emphasis on the Extreme Year of 2004. *Theor. Appl. Climatol* 104 (3-4), 459–472. doi:10.1007/s00704-010-0357-9

Wolanin, A., Camps-Valls, G., Gómez-Chova, L., Mateo-García, G., van der Tol, C., Zhang, Y., et al. (2019). Estimating Crop Primary Productivity with Sentinel-2 and Landsat 8 Using Machine Learning Methods Trained with Radiative Transfer Simulations. *Remote Sensing Environ.* 225, 441–457. doi:10.1016/j.rse.2019.03.002

Wu, D., Zhao, X., Liang, S., Zhou, T., Huang, K., Tang, B., et al. (2015). Time-lag Effects of Global Vegetation Responses to Climate Change. *Glob. Change Biol.* 21 (9), 3520–3531. doi:10.1111/gcb.12945

Wu, X., Liu, H., Li, X., Ciais, P., Babst, F., Guo, W., et al. (2018). Differentiating Drought Legacy Effects on Vegetation Growth over the Temperate Northern Hemisphere. *Glob. Change Biol.* 24 (1), 504–516. doi:10.1111/gcb.13920

Xiao, J., Chevallier, F., Gomez, C., Guanter, L., Hicke, J. A., Huete, A. R., et al. (2019). Remote Sensing of the Terrestrial Carbon Cycle: A Review of Advances over 50 Years. *Remote Sensing Environ.* 233, 111383. doi:10.1016/j.rse.2019.111383

Xiao, J., Davis, K. J., Urban, N. M., Keller, K., and Saliendra, N. Z. (2011). Upscaling Carbon Fluxes from Towers to the Regional Scale: Influence of Parameter Variability and Land Cover Representation on Regional Flux Estimates. *J. Geophys. Res.* 116, 15. doi:10.1029/2010jg001568

Xiao, X., Zhang, Q. Y., Braswell, B., Urbanski, S., Boles, S., Wofsy, S., et al. (2004). Modeling Gross Primary Production of Temperate Deciduous Broadleaf forest Using Satellite Images and Climate Data. *Remote Sensing Environ.* 91 (2), 256–270. doi:10.1016/j.rse.2004.03.010

Xie, X., Chen, J. M., Gong, P., and Li, A. (2021). Spatial Scaling of Gross Primary Productivity over Sixteen Mountainous Watersheds Using Vegetation Heterogeneity and Surface Topography. *J. Geophys. Res. Biogeosci* 126 (5), 21. doi:10.1029/2020jg005848

Xie, X., and Li, A. (2020a). An Adjusted Two-Leaf Light Use Efficiency Model for Improving GPP Simulations over Mountainous Areas. *J. Geophys. Res. Atmos.* 125 (13), 19. doi:10.1029/2019jd031702

Xie, X., and Li, A. (2020b). Development of a Topographic-Corrected Temperature and Greenness Model (TG) for Improving GPP Estimation over Mountainous Areas. *Agric. For. Meteorology* 295, 108193. doi:10.1016/j.agrformet.2020.108193

Xie, X., Tian, J., Wu, C., Li, A., Jin, H., Bian, J., et al. (2022). Long-term Topographic Effect on Remotely Sensed Vegetation index-based Gross Primary Productivity (GPP) Estimation at the Watershed Scale. *Int. J. Appl. Earth Observation Geoinformation* 108, 102755. doi:10.1016/j.jag.2022.102755

Yuan, M., Zhao, L., Lin, A., Wang, L., Li, Q., She, D., et al. (2020). Impacts of Preseason Drought on Vegetation spring Phenology across the Northeast China Transect. *Sci. Total Environ.* 738, 140297. doi:10.1016/j.scitotenv.2020.140297

Yuan, W., Cai, W., Xia, J., Chen, J., Liu, S., Dong, W., et al. (2014). Global Comparison of Light Use Efficiency Models for Simulating Terrestrial Vegetation Gross Primary Production Based on the LaThuile Database. *Agric. For. Meteorology* 192-193, 108–120. doi:10.1016/j.agrformet.2014.03.007

Yuan, W., Liu, S., Yu, G., Bonnefond, J.-M., Chen, J., Davis, K., et al. (2010). Global Estimates of Evapotranspiration and Gross Primary Production Based on MODIS and Global Meteorology Data. *Remote Sensing Environ.* 114 (7), 1416–1431. doi:10.1016/j.rse.2010.01.022

Zhang, Y., Xiao, X., Wu, X., Zhou, S., Zhang, G., Qin, Y., et al. (2017). A Global Moderate Resolution Dataset of Gross Primary Production of Vegetation for 2000-2016. *Sci. Data* 4, 13. doi:10.1038/sdata.2017.165

Zhao, A., Yu, Q., Feng, L., Zhang, A., and Pei, T. (2020). Evaluating the Cumulative and Time-Lag Effects of Drought on Grassland Vegetation: A Case Study in the Chinese Loess Plateau. *J. Environ. Manage.* 261, 110214. doi:10.1016/j.jenvman.2020.110214

Zhao, A., Zhang, A., Cao, S., Liu, X., Liu, J., and Cheng, D. (2018). Responses of Vegetation Productivity to Multi-Scale Drought in Loess Plateau, China. *Catena* 163, 165–171. doi:10.1016/j.catena.2017.12.016

Zhao, M., Running, S. W., and Nemani, R. R. (2006). Sensitivity of Moderate Resolution Imaging Spectroradiometer (MODIS) Terrestrial Primary Production to the Accuracy of Meteorological Reanalyses. *J. Geophys. Res.* 111 (G1), 13. doi:10.1029/2004jg000004

Zheng, Y., Shen, R., Wang, Y., Li, X., Liu, S., Liang, S., et al. (2020). Improved Estimate of Global Gross Primary Production for Reproducing its Long-Term Variation, 1982-2017. *Earth Syst. Sci. Data* 12 (4), 2725–2746. doi:10.5194/essd-12-2725-2020

Zheng, Y., Zhang, L., Xiao, J., Yuan, W., Yan, M., Li, T., et al. (2018). Sources of Uncertainty in Gross Primary Productivity Simulated by Light Use Efficiency Models: Model Structure, Parameters, Input Data, and Spatial Resolution. *Agric. For. Meteorology* 263, 242–257. doi:10.1016/j.agrformet.2018.08.003

Zhou, Y., Wu, X., Ju, W., Chen, J. M., Wang, S., Wang, H., et al. (2016). Global Parameterization and Validation of a Two-leaf Light Use Efficiency Model for Predicting Gross Primary Production across FLUXNET Sites. *J. Geophys. Res. Biogeosci.* 121 (4), 1045–1072. doi:10.1002/2014jg002876

Zhu, Q., Liu, J., Peng, C., Chen, H., Fang, X., Jiang, H., et al. (2014). Modelling Methane Emissions from Natural Wetlands by Development and Application of the TRIPLEX-GHG Model. *Geosci. Model. Dev.* 7 (3), 981–999. doi:10.5194/gmd-7-981-2014

**Conflict of Interest:** The authors declare that the research was conducted in the absence of any commercial or financial relationships that could be construed as a potential conflict of interest.

**Publisher's Note:** All claims expressed in this article are solely those of the authors and do not necessarily represent those of their affiliated organizations, or those of the publisher, the editors, and the reviewers. Any product that may be evaluated in this article, or claim that may be made by its manufacturer, is not guaranteed or endorsed by the publisher.

frontiers | Frontiers in Environmental Science

ORIGINAL RESEARCH
published: 31 May 2022
doi: 10.3389/fenvs.2022.910579

# Impacts of Winter and Summer COVID-19 Lockdowns on Urban Air Quality in Urumqi, Northwest China

*Ali Mamtimin[1,2,3,4], Yu Wang[1,2,3,4], Tianliang Zhao[5]*, Hajigul Sayit[6], Fan Yang[1,2,3,4], Wen Huo[1,2,3,4], Chenglong Zhou[1,2,3,4] and Jiacheng Gao[1,2,3,4]*

[1]*Institute of Desert Meteorology, China Meteorological Administration, Urumqi, China,* [2]*Taklimakan Desert Meteorology Field Experiment Station of CMA, Urumqi, China,* [3]*National Observation and Research Station of Desert Meteorology, Taklimakan Desert of Xinjiang/Xinjiang Key Laboratory of Desert Meteorology and Sandstorm, Urumqi, China,* [4]*Key Laboratory of Tree-Ring Physical and Chemical Research, China Meteorological Administration, Urumqi, China,* [5]*Key Laboratory for Aerosol-Cloud-Precipitation of China Meteorological Administration, Nanjing University of Information Science and Technology, Nanjing, China,* [6]*Newsroom of Xinjiang Meteorological Bureau, Urumqi, China*

After the COVID-19 pandemic began in 2020, Urumqi, a remote area in northwest China, experienced two lockdowns, in January and July 2020. Based on ground and satellite observations, this study assessed the impacts of these lockdowns on the air quality in Urumqi and the seasonal differences between them. The results showed that, during the wintertime lockdown, $PM_{10}$, $PM_{2.5}$, $NO_2$, CO, and $SO_2$ levels decreased by 38, 40, 45, 27, 8%, respectively, whereas $O_3$ concentrations increased by 113%. During the summer lockdown, $PM_{10}$, $PM_{2.5}$, $NO_2$, CO, and $SO_2$ levels decreased by 39, 24, 59, 2, and 13%, respectively, and the $O_3$ concentrations increased by 21%. During the lockdowns, the $NO_2$ concentrations decreased by 53% in winter and 13% in summer in the urban areas, whereas they increased by 23% in winter and 9% in summer in the suburbs. Moreover, large seasonal differences were observed between winter and summer $SO_2$, CO, and $O_3$. The lockdown played a vital role in the rapid decline of primary air pollutant concentrations, along with fewer meteorological impacts on air pollution changes in this area. The increase in $O_3$ concentrations during the COVID-19 lockdowns reflects the complexity of air quality changes during reductions in air pollutant emissions.

**Keywords: COVID-19, city lockdown, air pollutants, urumqi, satellite remote sensing**

OPEN ACCESS

***Edited by:***
*Xinyao Xie,*
*Institute of Mountain Hazards and Environment (CAS), China*

***Reviewed by:***
*Hui Xiao,*
*Guangzhou Institute of Tropical and Marine Meteorology (GITMM), China*
*Liang Yuan,*
*Chengdu University of Information Technology, China*

****Correspondence:***
*Tianliang Zhao*
*tlzhao@nuist.edu.cn*

***Specialty section:***
*This article was submitted to Atmosphere and Climate, a section of the journal Frontiers in Environmental Science*

***Received:*** *01 April 2022*
***Accepted:*** *11 May 2022*
***Published:*** *31 May 2022*

***Citation:***
*Mamtimin A, Wang Y, Zhao T, Sayit H, Yang F, Huo W, Zhou C and Gao J (2022) Impacts of Winter and Summer COVID-19 Lockdowns on Urban Air Quality in Urumqi, Northwest China. Front. Environ. Sci. 10:910579. doi: 10.3389/fenvs.2022.910579*

## INTRODUCTION

In response to the COVID-19 pandemic, most countries adopted anti-epidemic measures, such as lockdowns, home isolation, and travel restrictions, to reduce the spread of the virus (Maier and Brockmann, 2020). In addition, the lockdowns provided air quality benefits (He et al., 2020). Owing to reductions in urban traffic during lockdowns, levels of $NO_2$, CO, $CO_2$, and particulate matter (PM) were greatly reduced, resulting in improved urban air quality (Beckerman et al., 2008; Guo et al., 2020). By using ground-based and satellite observation data, the impacts of epidemic lockdown on air quality are studied. For example, Daniel et al. (Goldberg et al., 2020) used Sentinel 5P data and found that atmospheric $NO_2$ concentrations in the United States and Canada decreased significantly. Liu et al. (2019), Zhang et al. (2021), and Huang and Sun (2020) analyzed satellite remote sensing data during lockdowns and found that $NO_2$ levels in China decreased significantly during the COVID-19 pandemic, similar to those reported in India (ESA, 2020a) and Italy (ESA, 2020b).

Nevertheless, analyzing ground-based measurements are the most direct method for quantifying local air quality changes. Studies using ground-based monitoring data in India, Barcelona, Madrid, Morocco, South America, and North America found that the varying levels of pandemic prevention and control measures in each location resulted in significant differences in air quality (Baldasano, 2020; Berman and Ebisu, 2020; Dantas et al., 2020; Otmani et al., 2020; Sharma et al., 2020; Tobías et al., 2020). Most studies on air quality during COVID-19 lockdowns in China have focused on cities in central and eastern China (Chang et al., 2020; Shi and Brasseur, 2020; Yuan et al., 2021; Zhang et al., 2022). Wang et al. (2020) found that $PM_{2.5}$, $NO_2$, and CO decreased by 9.9–64.0% during a lockdown in winter. However, few studies have reported on the arid region of northwest China.

Urumqi, a major city in northwest China, and its surrounding areas have been affected by COVID-19, with two lockdowns in 2020. The first lockdown was during winter (NHC (National Health Center), 2022a), from January 23 to 8 March 2020, and the second was during summer, from July 16 to 29 August 2020 (NHC (National Health Center), 2022b). During the two epidemics, the city implemented a full lockdown for all communities and restricted access to parks to prevent transmission of the virus. As targets were achieved for each phase of the epidemic prevention and control measures, the city gradually resumed industrial production and social activities in an orderly manner. These lockdown measures provided an unexpected opportunity to study the impact of human activities on air quality. This study analyzed the changes in air pollutant concentrations, specifically $PM_{2.5}$, $PM_{10}$, $SO_2$, $NO_2$, and $O_3$, during the lockdowns in Urumqi using comparisons with air quality during the same periods in 2015 and 2019. These results could improve our scientific understanding of the effects of emission reduction on air quality.

# MATERIALS AND METHODS

## Study Area

Urumqi is located at the northern foot of the central Tianshan Mountains and the southern edge of the Junggar Basin in northwest China with a semi-arid continental climate. The total area of Urumqi is 13,800 $km^2$ with a permanent population of 3.552 million. It is the largest and the most prosperous city in Central Asia (UG (Urumqi Government), 2022). In 2020, Urumqi suffered two COVID-19 epidemics in winter with the lockdowns from February 7 to 8 March 2020 and in summer from July 16 to 7 September 2020.

## Measurement Data

This study used 24 h averages of air quality monitoring data from 2015 to 2020 for the periods of January 11 to March 31 and July 1 to September 8 from five monitoring stations in Urumqi. The data were downloaded from the National Environmental Quality Monitoring Center (www.cnemc.cn/en).

In this study, the method used by Berman (Berman and Ebisu, 2020) was applied to average these measurement data to obtain daily average air quality data for the city. Data from January 23 to March 7 and July 17 to August 29 of 2015–2019 were regarded as 'historical' data, whereas data from the periods of January 23 to March 7 and July 17 to August 29 during 2020 were considered 'current' data. Data from January 11 to January 26 and July 1 to 16 July 2020, were used as 'control' data. All monitoring instruments in the Urumqi Air Quality Automatic Monitoring System operated automatically to continuously measure aerosol particles ($PM_{2.5}$, $PM_{10}$) and gaseous pollutants ($NO_2$, $SO_2$, CO, $O_3$) in the air. $PM_{2.5}$ and $PM_{10}$ levels were monitored using a tapered element oscillating microbalance (TEOM; Thermo Fisher Scientific, Waltham, MA, United States ) and a BAM 1020 on-line particulate matter monitor (Met One Instruments, Grants Pass, OR, United States ). The gaseous pollutants were monitored using TEI-43i, TEI-42i, TEI-48i, and TEI-49i gas analyzers (Thermo Fisher Scientific).

We also used data from the Sentinel-5P $NO_2$ satellite because the wide coverage of the satellite data complements the surface site observations. Owing to serious concerns about air quality, the Copernican Sentinel-5P (https://scihub.copernicus.eu/) was launched in October 2017 to observe air pollutants worldwide. This satellite carries one of the most advanced sensors to date, TROPO spheric Monitoring Instrument (TROPOMI). This instrument detects the unique fingerprints of atmospheric gases to accurately image atmospheric pollutants with a high spatial resolution.

In this study, the $NO_2$ data from the Sentinel-5P satellite from January 11 to January 26 and July 1 to 16 July 2020, were used to represent the concentrations of $NO_2$ in Urumqi before the lockdown. The $NO_2$ data from January 23 to March 7 and July 17 to 29 August 2020, were used to represent the concentrations during the lockdown, and the 14-days moving average was used for the average $NO_2$ concentrations in the urban area. The concentrations of short-term pollutants, such as $NO_2$, are indicators of economic slowdown, which can be connected to emission changes. Using the 14-days average eliminates the effects of short-term meteorological changes and better reflects the effects of air pollutant emission changes.

# RESULTS

The comparisons between the weather conditions during the lockdowns and those during the corresponding historical periods showed minimal differences, indicating that the changes in air pollutant concentrations during the lockdowns were primarily due to local anthropogenic emissions. Therefore, this study focused on the seasonal impacts of the lockdowns on the urban air quality in Urumqi.

The winter and summer lockdowns impacted air pollutants differently. After the winter lockdown measures were implemented, the impacts on gaseous pollutants ($NO_2$, $SO_2$, CO, and $O_3$) were significant (**Figure 1**). During both winter and summer, the concentrations of $NO_2$, $SO_2$, and CO dropped rapidly after the implementation of strict lockdown measures and subsequently varied over time. $O_3$ was the only air pollutant whose concentration increased during the lockdowns.

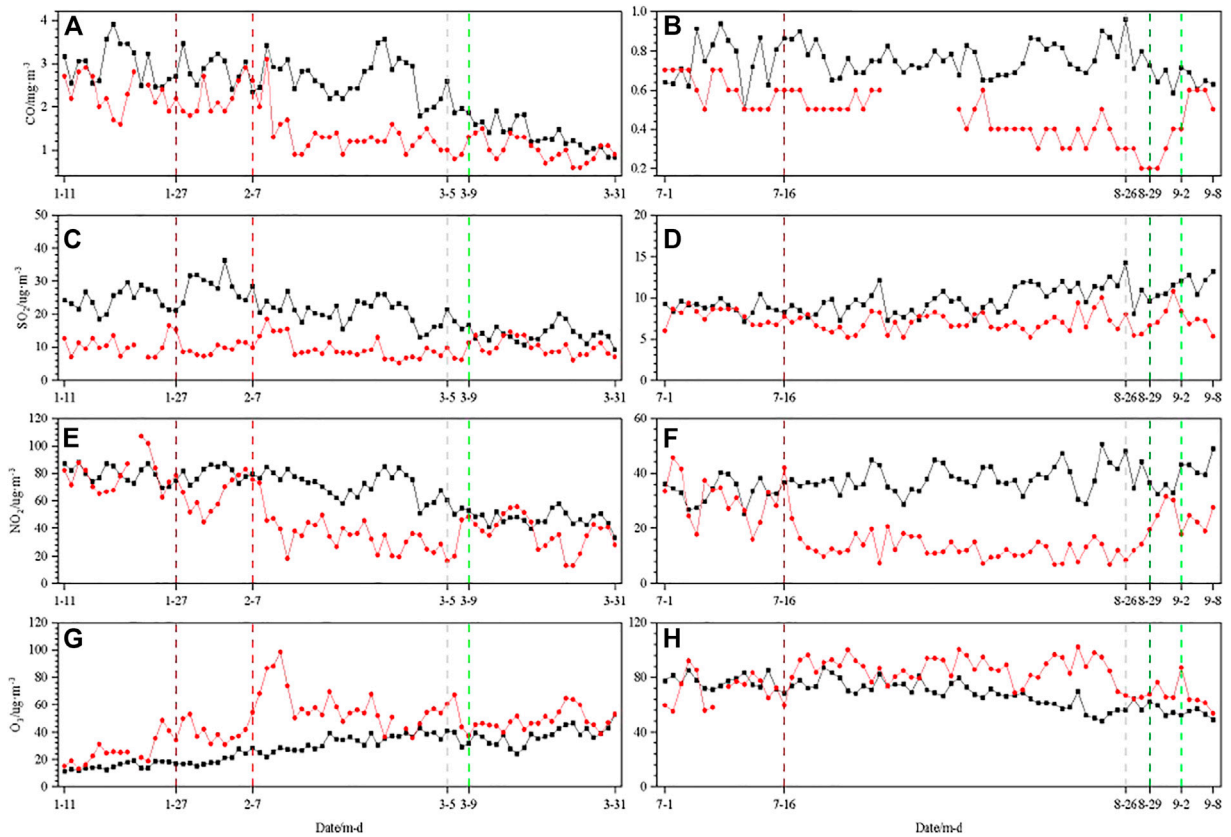


**FIGURE 1 |** Daily average CO, $SO_2$, $NO_2$, and $O_3$ concentrations during the **(A–D)** winter and **(E–H)** summer lockdowns in Urumqi. The black dots represent the 2015–2019 historical data and the red dots represent the 2020 data. The dark red vertical line indicates the beginning of the winter lockdown. The red vertical lines indicate the beginning of strict lockdown measures, and the gray vertical lines indicate the initial lifting of lockdown measures. The dark green line indicates the lifting of vehicle restrictions during the summer lockdown, and the green lines indicate the complete lifting of lockdown measures.

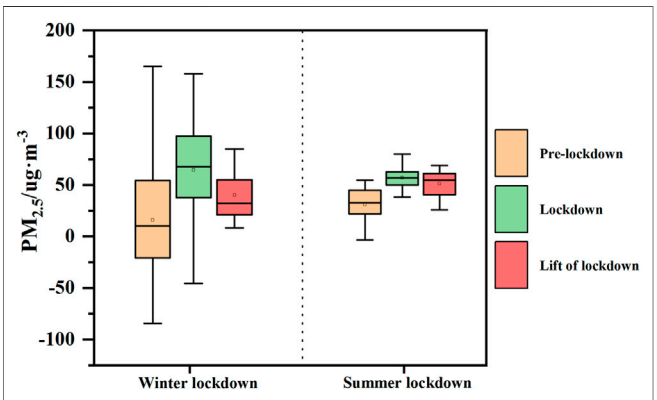


**FIGURE 2 |** Deviation between historical and lockdown periods for $PM_{2.5}$ concentrations during the winter and summer lockdowns in Urumqi.

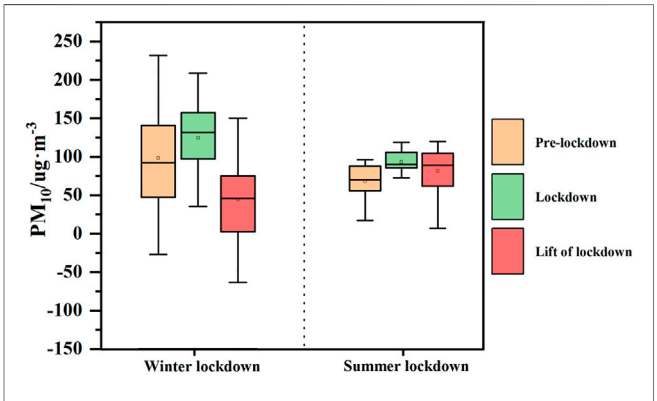


**FIGURE 3 |** Deviation between historical and lockdown periods for $PM_{10}$ concentrations during the winter and summer lockdowns in Urumqi.

Before the winter and summer lockdowns, the CO concentrations were 2.21 and 0.58 mg $m^{-3}$, respectively (**Table 1**). During the winter lockdown, the CO concentration dropped to 1.62 mg $m^{-3}$, which was a decrease of 1.06 mg $m^{-3}$ (39.54% decrease) compared to the corresponding historical period and 0.59 mg $m^{-3}$ (27.0%) compared to the period before the lockdown. During the summer lockdown, the CO concentrations decreased by 0.17 mg $m^{-3}$ (22.6%) compared with the corresponding historical period and by 0.01 mg $m^{-3}$ (2.4%)

**TABLE 1 |** Mean concentrations of air pollutants in Urumqi during the winter (I) and summer (II) lockdowns.

| | Air Pollutant | Historical Levels | Levels before Lockdown (Control) | Levels during Lockdown (Current) | Difference Between Historical and Current Levels [% Change] | Difference Between Control and Current Levels [% Change] |
|---|---|---|---|---|---|---|
| I | $NO_2$ (μg $m^{-3}$) | 76.92 | 80.01 | 44.36 | 30.13 [-40.45%] | 35.65 [-44.6%] |
| | $PM_{10}$ (μg $m^{-3}$) | 223.03 | 147.92 | 91.34 | 122.30 [-57.25%] | 56.58 [-38.3%] |
| | $PM_{2.5}$ (μg $m^{-3}$) | 171.17 | 168.81 | 101.23 | 60.46 [-37.39%] | 67.57 [-40.0%] |
| | CO (mg $m^{-3}$) | 2.82 | 2.21 | 1.62 | 1.06 [-39.54%] | 0.59 [-27.0%] |
| | $SO_2$ (μg $m^{-3}$) | 25.32 | 11.41 | 10.45 | 14.36 [-57.88%] | 0.96 [-8.4%] |
| | $O_3$ (μg $m^{-3}$) | 23.84 | 25.70 | 54.63 | −22.97 [+72.55%] | −28.92 [+112.5%] |
| | Main pollutants | $PM_{10}$ | $PM_{2.5}$ | $PM_{2.5}$ | | |
| II | $NO_2$ (μg $m^{-3}$) | 35.86 | 30.96 | 12.72 | 25.44 [-66.66%] | 18.23 [-58.9%] |
| | $PM_{10}$ (μg $m^{-3}$) | 78.35 | 55.91 | 34.28 | 49.56 [-59.12%] | 21.64 [-38.7%] |
| | $PM_{2.5}$ (μg $m^{-3}$) | 24.65 | 20.00 | 15.28 | 12.13 [-44.26%] | 4.72 [-23.6%] |
| | CO (mg $m^{-3}$) | 0.71 | 0.58 | 0.57 | 0.17 [-22.60%] | 0.01 [-2.4%] |
| | $SO_2$ (μg $m^{-3}$) | 9.61 | 7.76 | 6.74 | 3.44 [-33.81%] | 1.03 [-13.2%] |
| | $O_3$ (μg $m^{-3}$) | 75.81 | 73.76 | 89.40 | −18.03 [+25.27%] | −15.64 [+21.2%] |
| | Main pollutants | $PM_{10}$ | $PM_{10}$ | $O_3$ | | |

compared with the period before the lockdown. These seasonal differences in CO reductions indicate the importance of local anthropogenic emissions to regional air quality.

Variations in the $SO_2$ concentrations during the lockdowns differed slightly from those in CO (**Figure 1**). During the winter lockdown, the variations in $SO_2$ concentration markedly differed compared to those during the corresponding historical period. After strict home isolation measures were adopted on February 7, the $SO_2$ concentration declined by a maximum of 57.88%; however, this decrease was not as rapid as those observed in other pollutants. After the lockdown was lifted, $SO_2$ concentration increased rapidly. During the summer lockdown, the $SO_2$ concentration decreased compared to that during the corresponding historical and control periods, but the rate of the decrease (a decline of 33.81%) was lower than that during the winter lockdown.

After the most stringent measures began, the $NO_2$ concentrations decreased rapidly. They gradually recovered by March 5, and the $NO_2$ concentration did not increase substantially after commercial and industrial production fully resumed on March 8. As the summer lockdown began, the $NO_2$ concentration decreased rapidly on July 17. $NO_2$ concentrations decreased the most during the strict home isolation measures (**Figure 1**). During the winter lockdown, the $NO_2$ concentration decreased by 40.45 and 44.6% compared to that during the historical and control periods, respectively. During the summer lockdown, the $NO_2$ concentration decreased by 66.66 and 58.9% compared to that during the historical and control periods.

In the early stages of the winter lockdown, the $O_3$ concentrations were generally higher than those during the corresponding historical period (**Figure 1**). However, during the summer lockdown, $O_3$ concentrations differed from those observed during the winter lockdown and were higher than those during the corresponding historical and control periods. During the winter lockdown, the $O_3$ concentrations reached 54.6 μg $m^{-3}$, which was an increase of 23.0 μg $m^{-3}$ (72.55%) and 28.92 μg $m^{-3}$ (112.5%) compared to the historical and control periods, respectively. During the summer lockdown, the $O_3$ concentration was 89.4 μg $m^{-3}$, which was an increase of 18.03 μg $m^{-3}$ (25.27%) and 15.64 μg $m^{-3}$ (21.2%) compared to the historical and control periods, respectively.

The lockdown and home isolation measures had similar effects on aerosol particles ($PM_{2.5}$ and $PM_{10}$). After strict home isolation measures were adopted and traffic and industrial production were restricted, their concentrations dropped rapidly. With the resumption of work and industrial production, the $PM_{10}$ and $PM_{2.5}$ concentrations slowly increased (**Figures 2**,**3**). The effects of the summer lockdown occurred more rapidly than those during the winter; $PM_{10}$ and $PM_{2.5}$ concentrations dropped rapidly and remained constant. The $PM_{10}$ and $PM_{2.5}$ concentrations were 139.95 μg $m^{-3}$ and 157.36 μg $m^{-3}$, respectively, during the winter lockdown, and 55.65 μg $m^{-3}$ and 19.5 μg $m^{-3}$, respectively, during the summer lockdown.

The ground observation is limited for the site, which is insufficient for spatial distribution of air pollutants in an area. Therefore, this study by combining the $NO_2$ data of satellite remote sensing with the surface site observations to explore the variations of air pollutant concentrations affected by the lockdown in Urumqi.

Before the lockdown (**Figure 4**), the densely populated Tianshan district (TS), Toutunhe district (TTH) and Shayibake district (SYBK) had the highest tropospheric $NO_2$ values, ranging from 100 to 201 μmol $m^{-2}$ in winter and 80–99 μmol $m^{-2}$ in summer, which may have been related to significant motor vehicle emissions in these areas. The $NO_2$ concentration in winter to be greater than that in summer, which could be connected with the higher oxidability in the atmosphere with summertime strong solar radiation and high air temperature in this region. Comparing with the urban region, Urumqi County (WLMQ) and Dabancheng district (DBC), in the suburban areas, had lower tropospheric $NO_2$ concentrations, which ranged from 32 to 100 μmol $m^{-2}$ in winter and from 56 to 80 μmol $m^{-2}$ in summer; this reflects the impact of urban transportation on air

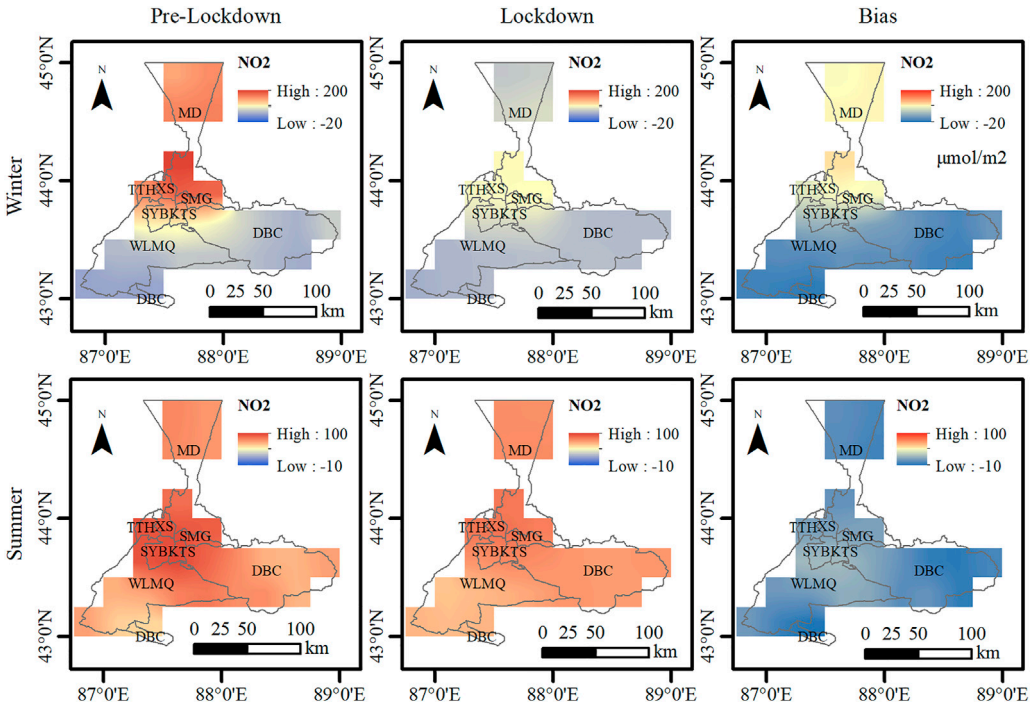


**FIGURE 4 |** The changes in tropospheric $NO_2$ (μmol $m^{-2}$) in the study region before and during the winter and summer lockdowns, showing the bias before the lockdown minus the lockdown.

pollutant emissions. During the lockdown, the tropospheric $NO_2$ vertical column content during the lockdown in 90% of the high value areas was $-13{\sim}10^7$ μmol $m^{-2}$ lower than that before the lockdown in winter, and the tropospheric $NO_2$ vertical column content was reduced −9~21 μmol $m^{-2}$ in summer.

## DISCUSSION

The lockdowns in Urumqi had the significant impacts on $NO_2$, $PM_{10}$, $PM_{2.5}$, and $O_3$ levels. The $NO_2$ concentrations decreased by 44.6% during the winter lockdown and 58.9% during the summer lockdown. During the winter lockdown, $PM_{10}$ and $PM_{2.5}$ concentrations decreased by 38.0 and 40%, respectively. During the summer lockdown, the $PM_{10}$ concentration decreased by 38.7%. However, compared with the historical and control periods, the $O_3$ concentration tended to increase. During the winter lockdown, the $O_3$ concentration increased by 112.5% compared with the control period. Similar positive anomalies in $O_3$ concentrations were observed in the Wuhan and Yangtze River Deltas during their lockdowns (Yuan et al., 2021; Zhang et al., 2022). The increased $O_3$ concentrations in Urumqi and other cities in China during lockdowns reflect the complexity of improving urban air quality by reducing anthropogenic air pollutant emissions (Ju et al., 2021; Peng, 2022). Additionally, the decline in $SO_2$ concentration reflected a reduction in industrial activities under the lockdown measures and was similar in magnitude to the $SO_2$ decline in Hangzhou (Yuan et al., 2021). However, the fluctuations in $SO_2$ concentrations in Urumqi during the lockdown mainly resulted from the many factories in the Midong area, which was northeast of the city.

During the winter lockdown, the $NO_2$ and $PM_{10}$ concentrations decreased less than those during the summer lockdown. This was mainly due to the higher $NO_2$ and $PM_{10}$ concentrations in Urumqi during winter from artificial heat sources. Additionally, turbulence in the atmospheric boundary layer is far less intense in winter than that in summer; moreover, the boundary layer height is lower in winter than that in summer (Zhang et al., 2021). Hence, atmospheric pollutant transport was limited, thereby increasing their concentrations. The decline in $SO_2$ and CO concentrations during the two lockdowns differed from that in $NO_2$. During the winter lockdown, $SO_2$ and CO concentrations declined relatively sharply and rapidly. Additionally, $O_3$ concentrations responded at a similar speed but increased instead. The increase in $O_3$ concentrations during the winter lockdown exceeded that during the summer.

However, avoiding the influence of weather systems or external factors on urban air pollution is often impossible, as was the case during the lockdowns. For example, during the summer lockdown, $PM_{10}$ and $PM_{2.5}$ concentrations in Urumqi spiked on August 25. The $PM_{10}$ concentration rose from 40 μg $m^{-3}$ during the previous day to 144 27 μg $m^{-3}$; 1 day later, it decreased to 48 μg $m^{-3}$. The $PM_{2.5}$ concentration increased from 16 μg $m^{-3}$ during the previous day to 27 μg $m^{-3}$; it decreased to 18 μg $m^{-3}$ the next day. A precipitation event occurred in Urumqi on 25 August, and sand blew into the city at 20:00 (Beijing time). Thus, the air

over Urumqi became more turbid and the PM concentration increased, causing the atmospheric visibility to fall to 2.6 km. Precipitation began at approximately 7:00 on the morning of August 26 and lasted until 8:00 on the morning of August 27. The 24-h precipitation was 19.1 mm. Nevertheless, in this study, we did not eliminate the impacts of precipitation on air quality change, considering the low precipitation in Urumqi. In a future work, we will consider the complex influences of precipitation on air pollutant changes in this arid region of Northwest China.

## CONCLUSION

Owing to the COVID-19 lochdowns in Urumqi, the $PM_{10}$, $PM_{2.5}$, $NO_2$, $SO_2$ and CO concentrations in the city decreased, and the $O_3$ concentration increased. This effect was notable in the changes in the $NO_2$, $PM_{10}$, $PM_{2.5,}$ and $O_3$ concentrations. During the lockdown, the $NO_2$ concentrations decreased by 53% in winter and 13% in summer in the main urban areas, whereas they increased by 23% in winter and 9% in summer in the suburbs. These changes reflect the decline in total aerosols and the increase in some short-term air pollutants during lockdowns. Additionally, the various seasons and lockdown levels also had differing effects on the concentrations of urban air pollutants. Changes in pollutant concentrations during the gradual resumption of work and industrial production can provide a reference for the government to balance industrial production and air quality.

Nevertheless, seasonal impacts on $SO_2$, CO, and $O_3$ concentrations and the primary pollutant types exceeded those of the lockdown measures. However, strict city lockdown measures played a vital role in the rapid decline of most air pollutant concentrations. In addition to lockdown measures, external factors and weather conditions influenced the pollution. Therefore, atmospheric pollutant concentrations can be improved by adopting certain government interventions or guidance measures. Notably, the $O_3$ concentration did not decrease during the lockdown. Thus, during the development of future pollution reduction policies, targeted measures should be formulated to reduce $O_3$ concentrations, thereby reducing the pollution and harm caused by $O_3$. Understanding the impacts of urban lockdowns and the subsequent restoration of activities on air quality will aid urban emissions control and further improve urban air pollution strategies.

## DATA AVAILABILITY STATEMENT

Publicly available datasets were analyzed in this study. This data can be found from www.cnemc.cn/en https://scihub.copernicus.eu.

## AUTHOR CONTRIBUTIONS

Conceptualization, AM and TZ; methodology, YW and JG; data curation, HS and YW; writing—original draft preparation, AM and YW; writing—review and editing, YW and FY; visualization, WH; supervision, CZ; project administration, JG; funding, YW and AM All authors have read and agreed to the published version of the manuscript.

## FUNDING

This research was funded by the National Natural Science Foundation of China (41875023), Central Scientific Research Institute of the Public Basic Scientific Research Business Professional (IDM2021005, IDM2021001, IDM2017001), Innovative and Development Project of China Meteorological Administration (CXFZ2021J044), the Central Asia Atmospheric Research Foundation (CASS202009), Flexible Talents Introducing Project of Xinjiang (2018).

## REFERENCES

Baldasano, J. M. (2020). COVID-19 Lockdown Effects on Air Quality by NO2 in the Cities of Barcelona and Madrid (Spain). *Sci. Total Environ.* 741, 140353. doi:10.1016/j.scitotenv.2020.140353

Beckerman, B., Jerrett, M., Brook, J. R., Verma, D. K., Arain, M. A., and Finkelstein, M. M. (2008). Correlation of Nitrogen Dioxide with Other Traffic Pollutants Near a Major Expressway. *Atmos. Environ.* 42, 275–290. doi:10.1016/j.atmosenv.2007.09.042

Berman, J. D., and Ebisu, K. (2020). Changes in U.S. Air Pollution during the COVID-19 Pandemic. *Sci. Total Environ.* 739, 139864. doi:10.1016/j.scitotenv.2020.139864

Chang, Y., Huang, R. J., Ge, X., Huang, X., Hu, J., Duan, Y., et al. (2020). Puzzling Haze Events in China during the Coronavirus (COVID-19) Shutdown. *Geophys. Res. Lett.* 47, 88533. doi:10.1029/2020GL088533

Dantas, G., Siciliano, B., França, B. B., da Silva, C. M., and Arbilla, G. (2020). The impact of COVID-19 partial lockdown on the air quality of the city of Rio de Janeiro, Brazil. *Sci. Total Environ.* 729, 139085. doi:10.1016/j.scitotenv.2020.139085

ESA (2020a). *Air Pollution Drops in India Following Lockdown*. Retrieved from: http://www.esa.int/Applications/Observing_the_Earth/Copernicus/Sentinel-5P/Air_pollution_drops_in_India_following_lockdown January 26, 2022).

ESA (2020b). *Coronavirus: Nitrogen Dioxide Emissions Drop over Italy*. Retrieved from: http://www.esa.int/ESA_Multimedia/Videos/2022/01/Coronavirus_nitrogen_dioxide_emissions_drop_over_Italy January 26, 2022).

Goldberg, D. L., Anenberg, S. C., Griffin, D., McLinden, C. A., Lu, Z., and Streets, D. G. (2020). Disentangling the Impact of the COVID-19 Lockdowns on Urban NO 2 from Natural Variability. *Geophys. Res. Lett.* 47, 17. doi:10.1029/2020GL089269

Guo, S., Hu, M., Peng, J., Wu, Z., Zamora, M. L., Shang, D., et al. (2020). Remarkable Nucleation and Growth of Ultrafine Particles from Vehicular Exhaust. *Proc. Natl. Acad. Sci. U.S.A.* 117, 3427–3432. doi:10.1073/pnas.1916366117

He, G., Pan, Y., and Tanaka, T. (2020). COVID-19, City Lockdowns, and Air Pollution: Evidence from China. *Med. Rxiv* 3, 29. doi:10.1101/2020.03.29.20046649

Huang, G., and Sun, K. (2020). Non-negligible Impacts of Clean Air Regulations on the Reduction of Tropospheric NO2 over East China during the COVID-19 Pandemic Observed by OMI and TROPOMI. *Sci. Total Environ.* 745, 141023. doi:10.1016/j.scitotenv.2020.141023

Ju, M. J., Oh, J., and Choi, Y.-H. (2021). Changes in Air Pollution Levels after COVID-19 Outbreak in Korea. *Sci. Total Environ.* 750, 141521. doi:10.1016/j.scitotenv.2020.141521

Liu, M., Lin, J., Boersma, K. F., Pinardi, G., Wang, Y., Chimot, J., et al. (2019). Improved Aerosol Correction for OMI Tropospheric NO<sub>2</

sub> Retrieval over East Asia: Constraint from CALIOP Aerosol Vertical Profile. *Atmos. Meas. Tech.* 12 (1), 1–21. doi:10.5194/amt-12-1-2019

Maier, B. F., and Brockmann, D. (2020). Effective Containment Explains Subexponential Growth in Recent Confirmed COVID-19 Cases in China. *Science* 368, 742–746. 6492. doi:10.1126/science.abb4557

NHC (National Health Center) (2022a). URL: http://www.nhc.gov.cn/xcs/yqtb/202201/c5da49c4c5bf4bcfb320ec2036480627.shtml (accessed January 26, 2022).

NHC (National Health Center) (2022b). URL: http://www.nhc.gov.cn/xcs/yqtb/202201/376d479871e04f19b8e9a444baa9a677.shtml (accessed January 26, 2022).

Otmani, A., Benchrif, A., Tahri, M., Bounakhla, M., Chakir, E. M., El Bouch, M., et al. (2020). Impact of Covid-19 Lockdown on PM10, SO2 and NO2 Concentrations in Salé City (Morocco). *Sci. Total Environ.* 735, 139541. doi:10.1016/j.scitotenv.2020.139541

Peng, D. (2022). *Pollution under the Blue Sky: Ozone Strikes*. Available from: http://www.inewsweek.cn/viewpoint (accessed January 26, 2022).

Sharma, S., Zhang, M., AnshikaGao, J., Gao, J., Zhang, H., and Kota, S. H. (2020). Effect of Restricted Emissions during COVID-19 on Air Quality in India. *Sci. Total Environ.* 728, 138878. doi:10.1016/j.scitotenv.2020.138878

Shi, X., and Brasseur, G. P. (2020). The Response in Air Quality to the Reduction of Chinese Economic Activities during the COVID-19 Outbreak. *Geophys. Res. Lett.* 47, 88070. doi:10.1029/2020GL088070

Tobías, A., Carnerero, C., Reche, C., Massagué, J., Via, M., Minguillón, M. C., et al. (2020). Changes in Air Quality during the Lockdown in Barcelona (Spain) One Month into the SARS-CoV-2 Epidemic. *Sci. Total Environ.* 726 (15), 138540. doi:10.1016/j.scitotenv.2020.138540

UG (Urumqi Government) (2022). URL: http://www.urumqi.gov.cn/wlmjgk/447021.htm (accessed January 26, 2022).

Wang, P., Chen, K., Zhu, S., Wang, P., and Zhang, H. (2020). Severe Air Pollution Events Not Avoided by Reduced Anthropogenic Activities during COVID-19 Outbreak. *Resour. Conservation Recycl.* 158, 104814. doi:10.1016/j.resconrec.2020.104814

Yuan, Q., Qi, B., Hu, D., Wang, J., Zhang, J., Yang, H., et al. (2021). Spatiotemporal Variations and Reduction of Air Pollutants during the COVID-19 Pandemic in a Megacity of Yangtze River Delta in China. *Sci. Total Environ.* 751, 141820. doi:10.1016/j.scitotenv.2020.141820

Zhang, Q., Pan, Y., He, Y., Walters, W. W., Ni, Q., Liu, X., et al. (2021). Substantial Nitrogen Oxides Emission Reduction from China Due to COVID-19 and its Impact on Surface Ozone and Aerosol Pollution. *Sci. Total Environ.* 753 (4), 142238–142433. doi:10.3390/atmos1104043310.1016/j.scitotenv.2020.142238

Zhang, X., Zhang, Z., Xiao, Z., Tang, G., Li, H., Gao, R., et al. (2022). Heavy Haze Pollution during the COVID-19 Lockdown in the Beijing-Tianjin-Hebei Region, China. *J. Environ. Sci.* 114, 170–178. doi:10.1016/j.jes.2021.08.030

**Conflict of Interest:** The authors declare that the research was conducted in the absence of any commercial or financial relationships that could be construed as a potential conflict of interest.

**Publisher's Note:** All claims expressed in this article are solely those of the authors and do not necessarily represent those of their affiliated organizations, or those of the publisher, the editors and the reviewers. Any product that may be evaluated in this article, or claim that may be made by its manufacturer, is not guaranteed or endorsed by the publisher.

frontiers | Frontiers in Environmental Science

ORIGINAL RESEARCH
published: 23 June 2022
doi: 10.3389/fenvs.2022.946551

# Influences of Soil Water Content and Porosity on Lightning Electromagnetic Fields and Lightning-Induced Voltages on Overhead Lines

*Yinping Liu[1]*, Yuhui Jiang[1], Qisen Gao[1], Xia Li[1,2], Gan Yang[3], Qilin Zhang[1] and Bo Tang[1]*

[1]Key Laboratory of Meteorological Disaster, Ministry of Education (KLME)/Joint International Research Laboratory of Climate and Environment Change (ILCEC)/Collaborative Innovation Center on Forecast and Evaluation of Meteorological Disasters (CIC-FEMD)/Key Laboratory for Aerosol-Cloud-Precipitation of China Meteorological Administration, Nanjing University of Information Science and Technology, Nanjing, China, [2]State Key Laboratory of Severe Weather, Chinese Academy of Meteorological Sciences, Beijing, China, [3]Guangdong Technical Support Center of Meteorological Public Security, Guangzhou, China

This study is performed to analyze the effects of both soil water content and porosity, two of the influencing factors of the finite conductivity, on the propagation of lightning electromagnetic fields (LEMFs) and lightning-induced voltages (LIVs) on overhead lines. A two-dimensional finite difference time domain (FDTD) model together with an improved Archie's soil model is adopted for the field calculation at close distances from the lightning channel. The obtained results confirm that the soil water content and porosity have notable impacts on the peak values of LEMFs, especially the horizontal electric field. Moreover, the soil water content and porosity are correlated when acting together. The peak values of the horizontal electric field are found to be markedly influenced by the porosity changes at high water content or the water content changes at low porosity. The LIVs on overhead lines in these two cases are also studied. There appear to be greater differences in the induced voltages as the water content changes at low porosity.

**Keywords: lightning electromagnetic fields, lightning-induced voltages, finite difference time domain method, soil water content, soil porosity**

OPEN ACCESS

***Edited by:***
*Xinyao Xie,*
*Institute of Mountain Hazards and Environment (CAS), China*

***Reviewed by:***
*Guoqing Ma,*
*Jilin University, China*
*Fuyu Jiang,*
*Hohai University, China*

****Correspondence:***
*Yinping Liu*
*yuan8503@163.com*

***Specialty section:***
*This article was submitted to Atmosphere and Climate, a section of the journal Frontiers in Environmental Science*

***Received:*** *17 May 2022*
***Accepted:*** *06 June 2022*
***Published:*** *23 June 2022*

***Citation:***
*Liu Y, Jiang Y, Gao Q, Li X, Yang G, Zhang Q and Tang B (2022) Influences of Soil Water Content and Porosity on Lightning Electromagnetic Fields and Lightning-Induced Voltages on Overhead Lines. Front. Environ. Sci. 10:946551. doi: 10.3389/fenvs.2022.946551*

## 1 INTRODUCTION

The finitely conducting ground is widely recognized to possibly influence the propagation of lightning electromagnetic fields (LEMFs) with advances in the knowledge of it. This effect will cause a great difference from the value estimated for perfectly conducting ground, thereby affecting the results of lightning location and lightning-induced voltage (LIV) computation. Thus, a comprehensive study on the finite conductivity and its influencing factors, such as the soil water content and porosity, could deepen the research of LEMFs, which is also a contributing factor to lightning detection technology, lightning disaster assessment, and lightning protection.

The studies on LEMFs have primarily involved development of algorithms, the earliest one of which is Sommerfeld's integrals (Sommerfeld, 1909). Later, many approximation methods derived from it were proposed (Rubinstein, 1996; Wait, 1997). The application of the above classical analytical methods is sometimes subject to the complexity of the actual situation to some extent. In this aspect, the results of numerical methods are more accurate than analytical results. Based on the finite difference time domain (FDTD) method (Kane Yee, 1966), a numerical method of popularity, considerable efforts have been dedicated to examining the characteristics of LEMFs along different

propagation paths, including rough surfaces (Shoory et al., 2005; Li et al., 2014), stratified paths (Zhang et al., 2012; Zhang et al., 2015), irregular terrains (Soto et al., 2014a; Li D. et al., 2019; Arzag et al., 2019; He et al., 2019), and tall objects (Baba and Rakov, 2008; Araki et al., 2018).

In the existing studies on the propagation of LEMFs, many articles mentioned the lack of consideration of the soil medium. Recently, through the SHAndong Triggering Lightning Experiment, Li et al. found that the soil medium may lead to amplitude attenuation of the magnetic field generated by lightning discharge radiation (Li X. et al., 2019). In the calculation of LEMFs, the soil medium is always represented by soil electrical parameters, mainly referring to soil permittivity and conductivity. The influence of permittivity on the horizontal electric field has been found to be ignorable compared with soil conductivity (Yu et al., 2017). The attenuation effect of soil conductivity on electromagnetic field propagation is indispensable. Additionally, the water content may affect the soil conductivity particularly, among many factors.

Some of the studies assumed conductivities influenced by the water content to be constant parameters. For example, Liu et al. set up different conductivities of wetland, dry land, and sand to numerically simulate the propagation characteristics of LEMFs (Liu et al., 2012). As to whether making soil electrical parameters constant is reasonable when studying the LEMFs in air and underground, Delfino et al. (2009) concluded in their study that the assumption seems reasonable for soil with a water content of 2%–10%. However, for soil with very low or very high water content, the electromagnetic field appears to be significantly affected by the frequency dependence of ground electrical parameters. From the same point of view of frequency-dependent soil, a natural rough surface (Ouyang et al., 2012) and stratified ground (Li et al., 2020) were also studied. It was also considered in studies on LIVs on overhead lines (Akbari et al., 2013; Schroeder et al., 2018; Rizk et al., 2021) and grounding systems (Visacro and Alipio, 2012; Nazari et al., 2021). In addition, an expression between soil water content and conductivity obtained from engineering surveys was applied by Yang et al. (2021) to the simulation of LEMFs. They found that the water content affects the propagation characteristics of lightning electromagnetic pulses along the surface to a certain extent.

However, soil is a typical porous medium composed of soil particles, air voids between particles and liquid water (Hallikainen et al., 1985). The breakdown inside the air voids is what initiates the soil ionization (Ghania, 2019). Meanwhile, the porosity may determine the proportion of air and water in the soil. Therefore, analyzing the influence of water content on LEMF propagation without considering the impact of the soil porosity does not seem comprehensive.

This study is performed to analyze the influences of both soil water content and porosity on the propagation of LEMFs at close distances. A two-dimensional (2-D) FDTD model and a generalized Archie's model are used. To the best of our knowledge, few previous studies have taken porosity into account in the analysis of LEMFs. Our model could help in further understanding the relationship between soil physical properties and LEMF propagation. Moreover, the following computation of the LIVs on overhead lines under different water contents and porosities can contribute a sound theoretical basis for lightning protection of overhead transmission lines.

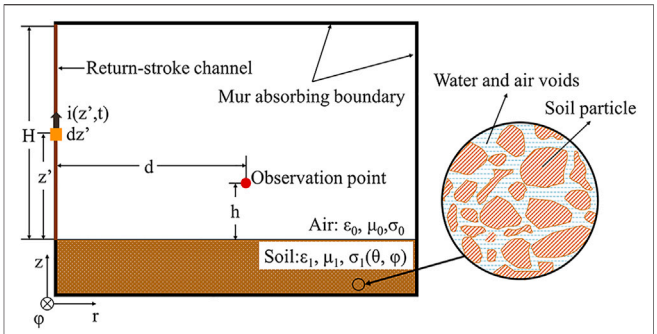


**FIGURE 1 |** Geometry: 2-D FDTD simulation model of LEMFs for the soil considering both soil water content and porosity.

## 2 METHODOLOGY

### 2.1 Lightning Electromagnetic Field Calculation

**Figure 1** illustrates the configuration of the 2-D FDTD model for calculating the LEMFs employed in this study. The working space is set to $5km \times 5km$ and is divided into $1m \times 1m$. The time increment is $1.67 \times 10^{-9}s$, which meets the Courant stability condition to ensure the stability of the iterative solution in the time domain. Assuming that the ground is homogeneous and lossy, the soil electrical conductivity $\sigma_1$ will vary with different settings of the water content $\theta$ and porosity $\varphi$. $\varepsilon_1$ and $\mu_1$ denote the soil permittivity and magnetic permeability, which are set to 10 and 1, respectively. The soil zone thickness is 300 m. The upper space is characterized by $\sigma_0$, $\varepsilon_0$, and $\mu_0$, representing the electrical conductivity, permittivity, and magnetic permeability of air. The permittivity $\varepsilon_0$ is $8.85 \times 10^{-12}F/m$ and the magnetic permeability $\mu_0$ is $4\pi \times 10^{-7}H/m$ in this model. These parameters are used to fill the spatial grid. To truncate the scattered waves at the boundaries since the simulation domain is limited, a first-order Mur absorbing boundary condition is utilized (Mur, 1981).

In this model, the simplified lightning model corresponds to an antenna perpendicular to the ground. The observation point is located at distance $d$ from the lightning channel and height $h$ from the surface. The modified transmission-line model with linear current decay (MTLL) is employed to represent the lightning return stroke. The current distribution at height $z'$ and time $t$ in the channel is given in **Eq. 1**.

$$i(z',t) = \left(1 - z'/H\right) i\left(0, t - z'/v\right), \; t \geq z'/v \tag{1}$$

where the channel height $H = 7500m$ and the speed of the return stroke $v = c/2 = 1.5 \times 10^{8}m/s$. As shown in **Eq. 2**, the channel-

**TABLE 1 |** Typical current parameters of subsequent return stroke.

| $i_{01}$/kA | $\tau_{11}$/μs | $\tau_{21}$/μs | $i_{02}$/kA | $\tau_{12}$/μs | $\tau_{22}$/μs |
|---|---|---|---|---|---|
| 10.7 | 0.25 | 2.5 | 6.5 | 2 | 230 |

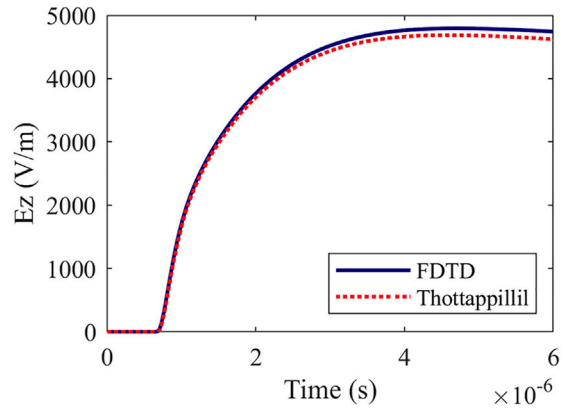


**FIGURE 2 |** Examination of the FDTD model by comparing it to the result of Thottappillil formula.

base current $i(0,t)$ is expressed by Heidler's functions (Heidler, 1985). **Table 1** shows the typical subsequent return stroke current parameters (Rachidi et al., 2001).

$$i(0,t) = \frac{i_{01}}{\eta_1} \frac{\left(\frac{t}{\tau_{11}}\right)^2}{\left(\frac{t}{\tau_{11}}\right)^2 + 1} e^{-t/\tau_{12}} + \frac{i_{02}}{\eta_2} \frac{\left(\frac{t}{\tau_{21}}\right)^2}{\left(\frac{t}{\tau_{21}}\right)^2 + 1} e^{-t/\tau_{22}} \quad (2)$$

with $\eta_1 = exp[-(\frac{\tau_{11}}{\tau_{12}})(\frac{2\tau_{12}}{\tau_{11}})^{1/2}]$, and $\eta_2 = exp[-(\frac{\tau_{21}}{\tau_{22}})(\frac{2\tau_{22}}{\tau_{21}})^{1/2}]$.

Note that different from most other FDTD models for calculating the lightning-generated electromagnetic field, we focus on the changes in soil conductivity caused by the soil water content and porosity. The specific soil microstructure is highlighted in **Figure 1**. Additionally, as we only study the changes in LEMFs in a close range, the influence of earth curvature is not considered.

## 2.2 Soil Model

Archie's model is an empirical formula for simulating the formation resistivity of saturated cohesionless soil through experiments (Archie, 1942). Archie's second law was then developed in applications to unsaturated porous media. In addition, many improved models of Archie's model have been proposed (Ewing and Hunt, 2006; Ghanbarian et al., 2014; Glover, 2017).

A generalized Archie's model developed by Fu et al. (2021) which is verified to be simpler and easier than the previous models is chosen in this research. This model takes surface conduction into account, which may be important in porous media containing many clay particles. As expressed in **Eq. 3**, the soil conductivity $\sigma_1$ can be directly estimated based on the soil

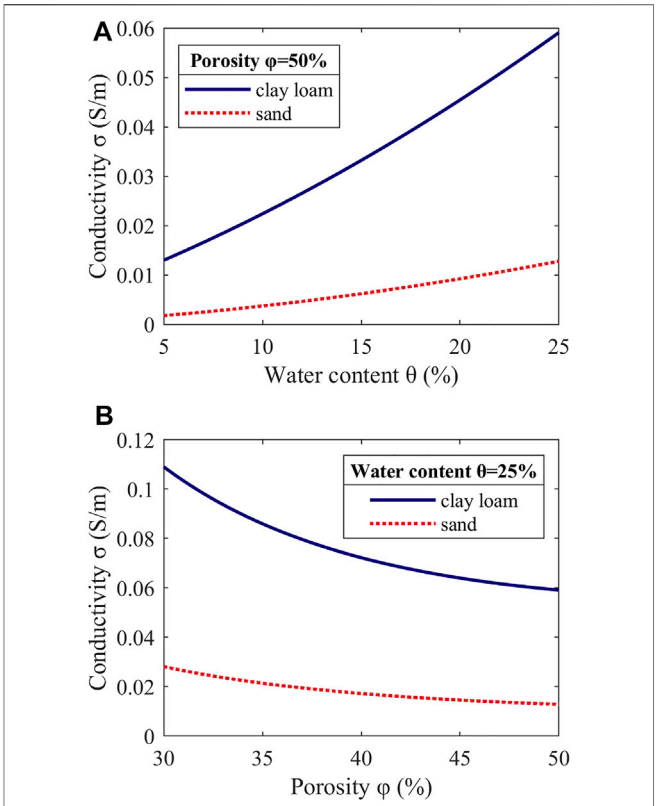


**FIGURE 3 | (A)** Relationship between water content and electrical conductivity in clay loam and sand. The porosity is set to φ = 50%. **(B)** Relationship between porosity and electrical conductivity in clay loam and sand. The water content is set to $\theta$ = 25%.

water content $\theta$, porosity $\varphi$, and several other soil properties that are easy to measure.

$$\sigma_1 = \sigma_{dry} + \left(\frac{\sigma_{sat} - \sigma_{dry}}{\varphi^2} - \left(0.654\frac{f_{clay}}{f_{sand} + f_{silt}} + 0.018\right)\right)\theta^2 + \left(0.654\frac{f_{clay}}{f_{sand} + f_{silt}} + 0.018\right)\varphi\theta \quad (3)$$

where $\sigma_{sat}$ and $\sigma_{dry}$ are the soil conductivity under saturated and dry conditions, which can be obtained from soil electrical conductivity measurements. $f_{clay}$, $f_{sand}$ and $f_{silt}$ represent the fractions of sand, silt, and clay in the bulk soil.

## 2.3 Model Validation

The continuity equation calculation method proposed by Thottappillil is used here to verify our FDTD simulation model (Thottappillil et al., 1997). The parameters chosen in both methods are completely consistent in the following calculation. The results obtained from the two methods can be compared in **Figure 2**. It is apparent that our result of the vertical electric field (Ez) is in close agreement with Thottappillil's. As a result, the simulation model used in this paper is deemed to be reasonable and effective.

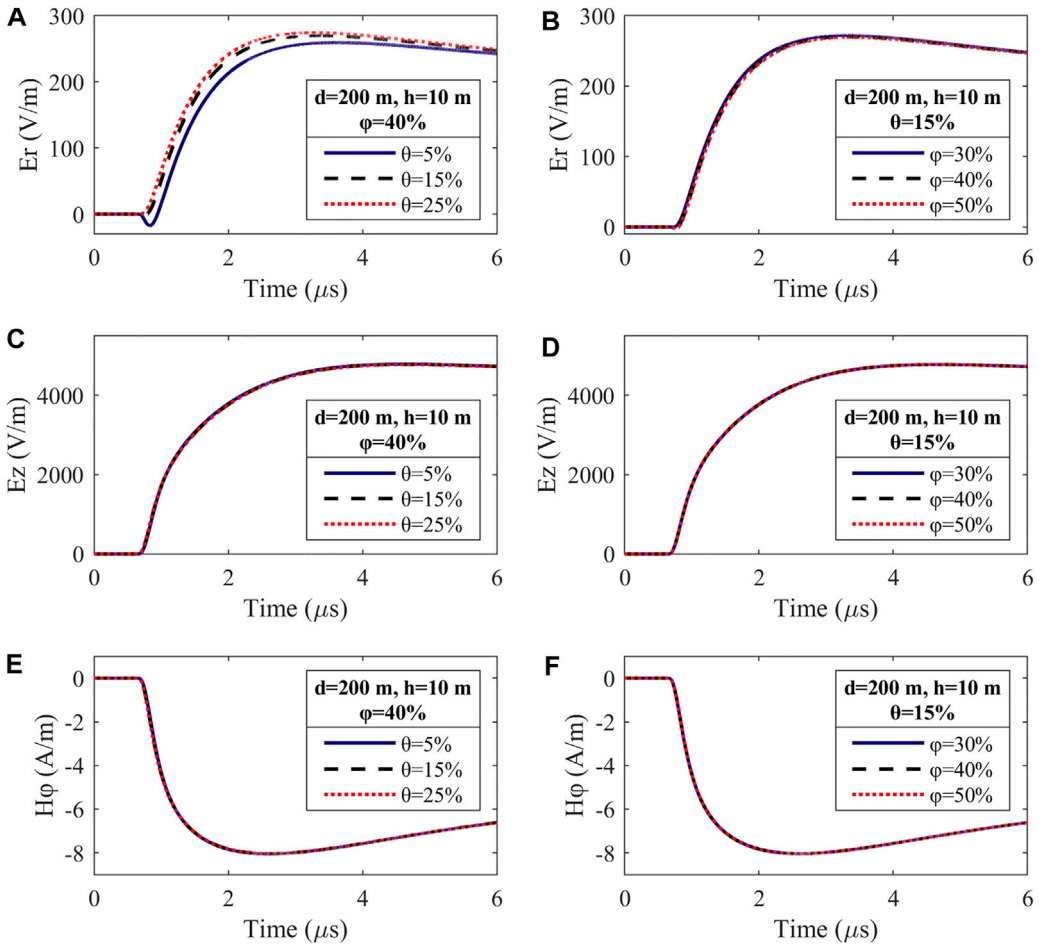


**FIGURE 4 |** FDTD-computed subsequent return stroke waveforms of the **(A,B)** horizontal electric field (Er), **(C,D)** vertical electric field (Ez), and **(E,F)** azimuthal magnetic field (Hφ) (d = 200m, h = 10m). **(A,C,E)** Different water contents $\theta$ = 5%, 15%, and 25% when the porosity $\varphi$ = 40%. **(B,D,F)** Different porosities $\varphi$ = 30%, 40%, and 50% when the water content $\theta$ = 15%.

## 3 INFLUENCES ON LIGHTNING ELECTROMAGNETIC FIELDS

**Figure 3A** depicts the changes in electrical conductivity caused by different water contents in clay loam ($f_{clay}$: $f_{sand}$: $f_{silt}$ = **30**: **40**: **30**, $\sigma_{sat}$ = **0.15**, $\sigma_{dry}$ = **0.005**) and sand ($f_{clay}$: $f_{sand}$: $f_{silt}$ = **5**: **90**: **5**, $\sigma_{sat}$ = **0.04**, $\sigma_{dry}$ = **0.0004**) (Fu et al., 2021). **Figure 3B** shows the changes in electrical conductivity caused by different porosities for the same cases. According to the figures, the conductivity of clay loam is obviously more susceptible to changes in the soil water content and porosity than the conductivity of sand. A possible explanation for this might be that clay loam can more easily form conductive paths, as the water retention capacity of clay loam is better than that of sand. Additionally, there are fewer minerals with high electrical resistivity in clay loam.

Therefore, clay loam is selected as the main research object in this paper. After referring to the actual range of the parameters of clay loam (Zhou, 2003), the water content $\theta$ is set from 5% to 25%, and the porosity $\varphi$ is set from 30% to 50%.

The electromagnetic field for various water contents when the porosity is fixed at 40% and the influence of soil porosity for a water content of 15% can be seen in **Figure 4**. In this figure, the calculated electromagnetic field components waveforms due to the lightning subsequent stroke include (A-B) horizontal electric field (Er), (C-D) vertical electric field (Ez), and (E-F) azimuthal magnetic field (Hφ). The observation point is located at distance d = 200 m from the lightning channel and the height $h$ is set to 10 m from the ground surface.

**Tables 2**, **3** list the peak values and rise times of LEMFs with changing water content and porosity, respectively. In light of **Figure 4** together with **Tables 2**, **3**, the following conclusions can be drawn:

1) Both the water content and the porosity exert the greatest influence on the horizontal electric field. It is found that the vertical electric field and the azimuthal magnetic field are almost unaffected by the change in the water content or porosity except for some small changes. The same cases are also studied at three other horizontal distances from the

**TABLE 2 |** Peak values and rise times of the horizontal electric field (Er), vertical electric field (Ez), and azimuthal magnetic field (H$\varphi$) for different water contents $\theta$ when the porosity $\varphi$ = 40%; $d$ = 200m, $h$ = 10m.

| $\theta$(%) | Er | | Ez | | H$\varphi$ | |
|---|---|---|---|---|---|---|
| | **Positive peak (V/m)** | **Rise time (μs)** | **Positive peak (V/m)** | **Rise time (μs)** | **Positive peak (A/m)** | **Rise time (μs)** |
| 5 | 259.431 | 1.262 | 4816.193 | 1.828 | 8.050 | 0.793 |
| 10 | 265.957 | 1.233 | 4814.532 | 1.848 | 8.045 | 0.800 |
| 15 | 269.937 | 1.222 | 4813.534 | 1.860 | 8.041 | 0.803 |
| 20 | 272.617 | 1.213 | 4812.870 | 1.867 | 8.039 | 0.805 |
| 25 | 274.540 | 1.207 | 4812.396 | 1.872 | 8.038 | 0.808 |

**TABLE 3 |** Same as **Table 2** but for different porosities $\varphi$ when the water content $\theta$ = 15%.

| $\theta$(%) | Er | | Ez | | H$\varphi$ | |
|---|---|---|---|---|---|---|
| | **Positive peak (V/m)** | **Rise time (μs)** | **Positive peak (V/m)** | **Rise time (μs)** | **Positive peak (A/m)** | **Rise time (μs)** |
| 30 | 271.950 | 1.215 | 4813.034 | 1.865 | 8.039 | 0.805 |
| 35 | 270.738 | 1.218 | 4813.334 | 1.862 | 8.040 | 0.805 |
| 40 | 269.937 | 1.221 | 4813.534 | 1.860 | 8.041 | 0.803 |
| 45 | 269.473 | 1.221 | 4813.650 | 1.858 | 8.042 | 0.803 |
| 50 | 269.267 | 1.223 | 4813.702 | 1.858 | 8.042 | 0.803 |

lightning channel (50 m, 1 km, and 3 km), and the same conclusion is obtained. As expected, this result is consistent with previous studies. Aoki et al. found that there is little change in the vertical electric field and azimuthal magnetic field with the ground conductivity within 5 km (Aoki et al., 2015). Therefore, the change in soil conductivity caused by the soil water content or porosity studied in this paper would also not cause great changes in the two fields.

2) Referring to **Figures 4A,B**, different soil water contents or porosities can result in a noticeable difference in the peaks of the horizontal electric field, while the rise time and steepness of the waveforms change little. Note that the peak values acutely vary at different soil water contents or porosities, especially around the peak. As the water content increases, the positive peak of horizontal electric field increases under the settings shown in **Figure 4A**. In contrast, under the settings shown in **Figure 4B**, when the porosity increases, the positive peak of the horizontal electric field decreases.
3) With decreasing soil water content or porosity, the effect of its change on the peak values is more intense. This can be attributed to the ion movement in clay loam that originally has a at low water content, which is more likely to form conductive pathways, even if the water content increases slightly. When the porosity increases, the connectivity of the conductive paths becomes stronger for the clay loam that originally has low porosity. However, clay loam has a certain saturation. When the water in the soil voids forms a conductive path, changes in the water content have no obvious effect on the horizontal electric field.

As illustrated in **Figure 5**, to further analyze the specific effects of the soil water content and porosity on the peak values of the horizontal electric field, we study the waveforms of the horizontal electric field at different distances: (A-B) 50 m, (C-D) 200 m, (E-F) 1 km and (G-H) 3 km. The observation point is set to 10 m above the ground. The porosity in **Figures 5A,C,E,G** is set to 40%, and the water content changes. The water content in **Figures 5B,D,F,H** is set to 15% with the porosity changes.

**Figure 5** shows that as the horizontal distance increases, the positive peak of the horizontal electric field significantly decreases. This can be explained by the fact that the high-frequency component will experience rapid attenuation in the propagation of LEMF. Simultaneously, the waveforms are found to present positive polarity at very close distances. They also exhibit a zero-crossing at low water content or high porosity at 200 m. Moreover, the waveform of the horizontal electric field tends to be more bipolar with increasing distance.

**Tables 4**, **5** list the positive and negative peaks of the horizontal electric field for the case at different distances and a height of 10 m with changing water content. The porosity is set to 40%. Consider the same case with changing porosity at the water content of 15%, the positive and negative peaks of the horizontal electric field are listed in **Tables 6**, **7**. The change rate of the values at different water contents (porosities) relative to that at the water content of 5% (porosity of 30%) is marked in parentheses.

It is shown in **Table 4** that when the porosity is 40%, a stronger influence is exerted by the soil water content on the positive peak of the horizontal electric field at 200 m than on that at 50 and 500 m. **Table 5** shows that the water content has the biggest effect on the negative peaks of the horizontal electric field at 200 m. The increase in the water content from 5% to 20% results in a 99.85% reduction in the negative peak at 200 m.

**Table 6** reveals that the influence of the soil porosity on the positive peaks of the horizontal electric field at 200 m is more

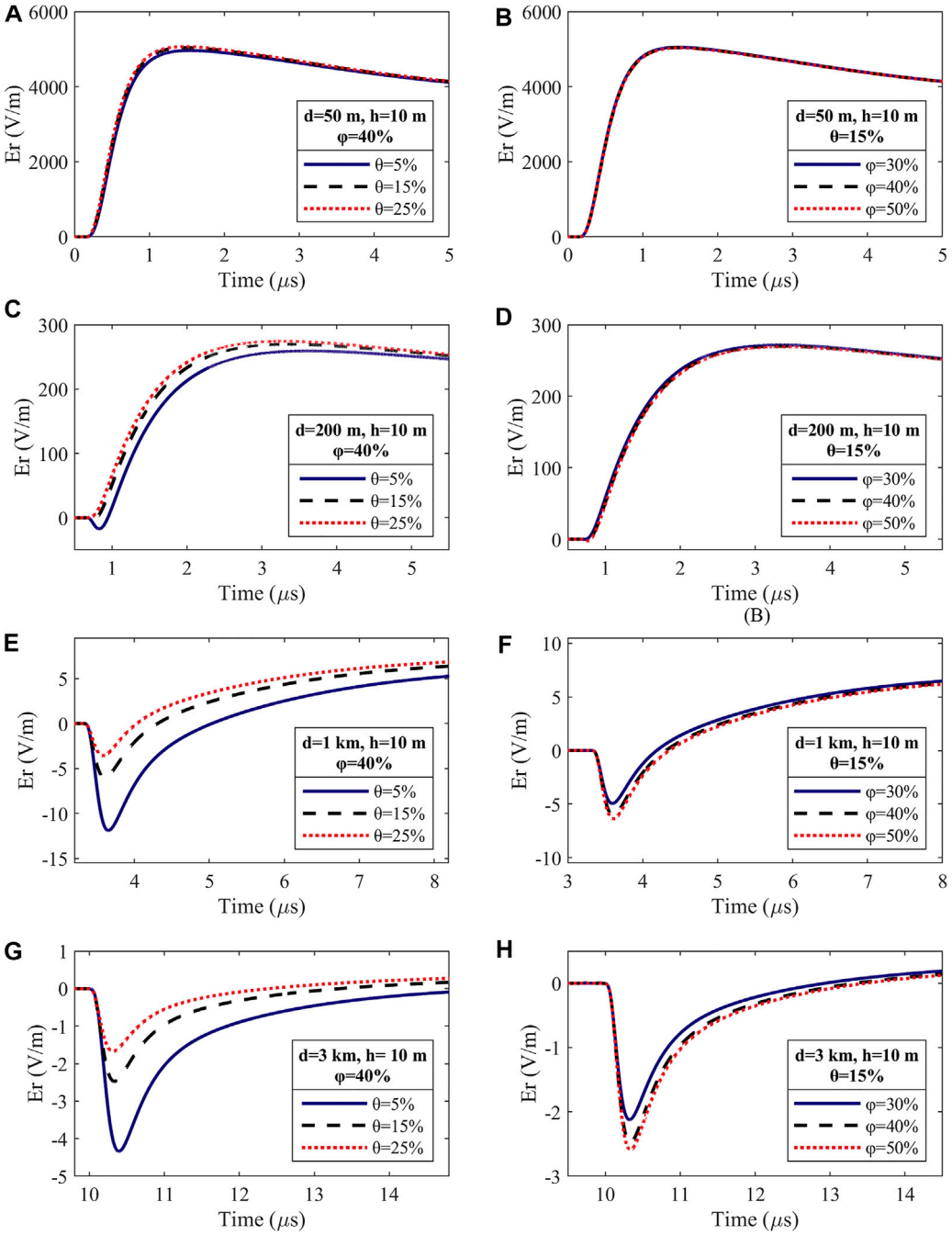


**FIGURE 5 |** FDTD-computed subsequent return stroke waveforms of the horizontal electric field (Er). **(A,C,E,G)** Different water contents $\theta$ = 5%, 15%, and 25% when the porosity $\varphi$ = 40%. **(B,D,F,H)** Different porosities $\varphi$ = 30%, 40%, and 50% when the water content $\theta$ = 15%. The observation point is set at different distances **(A,B)** d = 50 m, **(C,D)** d = 200 m, **(E,F)** d = 1 km, and **(G,H)** d = 3 km from the lightning channel and height h = 10 m from the ground surface.

prominent when the porosity is 45% and 50% for a water content of 15%. However, in **Table 7**, the porosity has a very strong influence on the negative peak values at 200 m. When the porosity increases from 30% to 50%, the negative peak value at 200 m increases by 672.55%.

**Figure 6** shows line charts of the positive peak value changes of the horizontal electric field when the soil water content and porosity change simultaneously. **Figure 6A** presents the influence of the water content at different porosities. The effect of the porosity at different water contents is shown in **Figure 6B**. To focus on the changes in the positive peak values, the horizontal distance in **Figure 6** is set to 200 m. It should be noted that the negative peaks at 1 km are also studied but not shown in this paper. The results show that the overall rules in the change of the positive

**TABLE 4 |** Positive peak values of the horizontal electric field (Er) for different water contents $\theta$ at different distances $d$ = 50m, 200m, 500m, and 1km from the lightning channel; $\varphi$ = 40%; $h$ = 10m; The change rate of the values at different water contents relative to that at the water content of 5% is marked in parentheses.

| Water content $\theta$(%) | Positive peak (V/m) | | | |
|---|---|---|---|---|
| | 50 m | 200 m | 500 m | 1 km |
| 5 | 4964.57 | 259.43 | 34.37 | 7.05 |
| 10 | 5010.92 (+0.93%) | 265.96 (+2.52%) | 35.06 (+2.01%) | 7.42 (+5.28%) |
| 15 | 5037.81 (+1.48%) | 269.94 (+4.05%) | 35.46 (+3.18%) | 7.63 (+8.35%) |
| 20 | 5055.34 (+1.83%) | 272.62 (+5.08%) | 35.88 (+4.39%) | 7.77 (+10.36%) |
| 25 | 5067.67 (+2.08%) | 274.54 (+5.82%) | 36.30 (+5.64%) | 7.88 (+11.78%) |

**TABLE 5 |** Same as **Table 4** but for negative peak values of the horizontal electric field (Er) for different water contents $\theta$ at different distances $d$ = 200m, 500m, 1km, and 3km from the lightning channel.

| Water content $\theta$(%) | Negative peak (V/m) | | | |
|---|---|---|---|---|
| | 200 m | 500 m | 1 km | 3 km |
| 5 | 17.37 | 19.23 | 11.88 | 4.34 |
| 10 | 6.30 (–69.74%) | 11.98 (–37.68%) | 8.18 (–31.13%) | 3.18 (–26.80%) |
| 15 | 1.72 (–90.09%) | 7.88 (–59.04%) | 6.02 (–49.35%) | 2.47 (–42.96%) |
| 20 | 0.03 (–99.85%) | 5.26 (–72.66%) | 4.59 (–61.34%) | 2.01 (–53.76%) |
| 25 | — | 3.46 (–82.01%) | 3.58 (–69.87%) | 1.67 (–61.51%) |

**TABLE 6 |** Positive peak values of the horizontal electric field (Er) for different porosities $\varphi$ at different distances d = 50m, 200m, 500m, and 1 km from the lightning channel; $\theta$ = 15%; $h$ = 10m; the change rate of the values at different porosities relative to that at the porosity of 30% is marked in parentheses.

| Porosity $\varphi$(%) | Positive peak (V/m) | | | |
|---|---|---|---|---|
| | 50 m | 200 m | 500 m | 1 km |
| 30 | 5051.00 | 271.95 | 35.73 | 7.74 |
| 35 | 5043.12 (–0.16%) | 270.74 (–0.45%) | 35.54 (–0.52%) | 7.68 (–0.82%) |
| 40 | 5037.81 (–0.26%) | 269.94 (–0.74%) | 35.46 (–0.75%) | 7.63 (–1.38%) |
| 45 | 5031.70 (–0.32%) | 269.47 (–0.91%) | 35.41 (–0.88%) | 7.61 (–1.70%) |
| 50 | 5033.31 (–0.35%) | 269.27 (–0.99%) | 35.39 (–0.93%) | 7.60 (–1.84%) |

**TABLE 7 |** Same as **Table 6** but for negative peak values of the horizontal electric field for different porosities $\varphi$ at different distances $d$ = 200m, 500m, 1km, and 3km from the lightning channel.

| Porosity $\varphi$(%) | Negative peak (V/m) | | | |
|---|---|---|---|---|
| | 200 m | 500 m | 1 km | 3 km |
| 30 | 0.30 | 5.90 | 4.95 | 2.12 |
| 35 | 1.06 (+250.27%) | 7.08 (+19.96%) | 5.59 (+12.96%) | 2.33 (+9.96%) |
| 40 | 1.72 (+466.44%) | 7.88 (+33.49%) | 6.02 (+21.64%) | 2.47 (+16.57%) |
| 45 | 2.15 (+607.07%) | 8.34 (+41.43%) | 6.27 (+26.71%) | 2.56 (+20.43%) |
| 50 | 2.35 (+672.55%) | 8.55 (+44.96%) | 6.38 (+28.96%) | 2.59 (+22.14%) |

or negative peaks are almost identical except for the opposite trends. Thus, the concrete analysis is only made on the changes in positive peak values.

According to **Figure 6A**, on the one hand, porosity has little impact on the peak values at low water content. With increasing water content, the porosity plays an increasingly important role. This is because as the volume of air voids in clay loam increases, so does the water and air capacity. Therefore, conductive pathways more easily form. On the other hand, a low porosity will increase the sensitivity of horizontal electric field to changes in the water content. At high porosity, taking 40% and 50% as examples, the change in water content hardly makes effect on the peaks of the horizontal electric field at high water content. This can be explained by the fact that the soil conductivity mainly depends on the water conductivity at low porosity. When the porosity is high, the influence of the water content beyond a certain value on the conductivity is weakened.

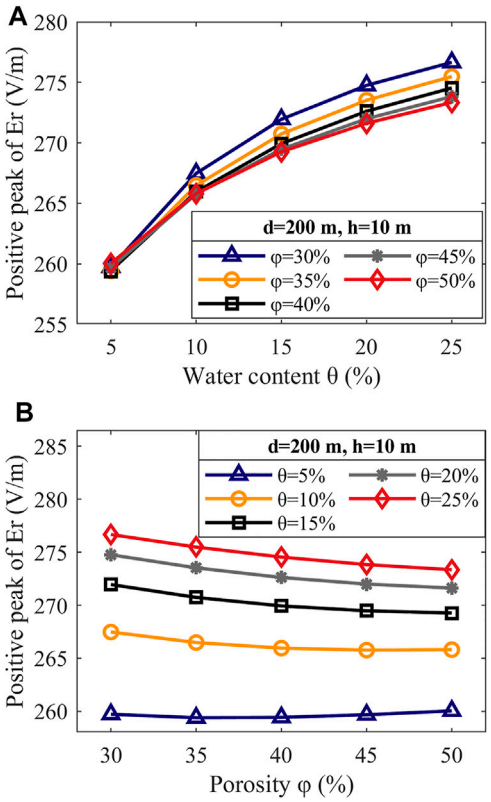


**FIGURE 6 | (A)** Influence of water content on FDTD-computed subsequent return stroke waveforms of the horizontal electric field (Er) at different porosities $\varphi$ = 30%, 35%, 40%, 45%, and 50%. The water content $\theta$ is set to 5%, 10%, 15%, 20%, and 25% (d = 200 m, h = 10 m). **(B)** Influence of porosity on FDTD-computed subsequent return stroke waveforms of the horizontal electric field at different water contents $\theta$ = 5%, 10%, 15%, 20%, and 25%. The porosity φ is set to 30%, 35%, 40%, 45%, and 50% (d = 200 m, h = 10 m).

Note that the conclusions obtained above, specifically that the change in porosity is inversely proportional (proportional) to the change in the positive peak (negative peak) of the horizontal electric field, are not applicable when the water content is set to 5% and 10% as shown in **Figure 6B**. However, consistent with the previous conclusions, first, the sensitivity of the horizontal electric field peak values to the water content decreases as the porosity increases. Second, if the water content decreases, its impact on the horizontal electric field increases.

Overall, it is evident that the soil water content and porosity affect each other when they act together on the horizontal electric field. The effect of the soil water content on the peaks of the horizontal electric field is more distinct than the effect of soil porosity. The reason may be that the fluid in clay voids is mainly composed of air and water, and the conductivity of air is far less than that of water. However, the effect of the porosity cannot be ignored, especially at high water contents. In addition, when the porosity is low, changes in the soil water content will also have a great influence on the peak values of the horizontal electric field. In fact, thunderstorms are often accompanied by rainfall, which increases the water content in clay loam. Hence, more attention should be given to differentiated lightning protection in areas with low-porosity clay loam.

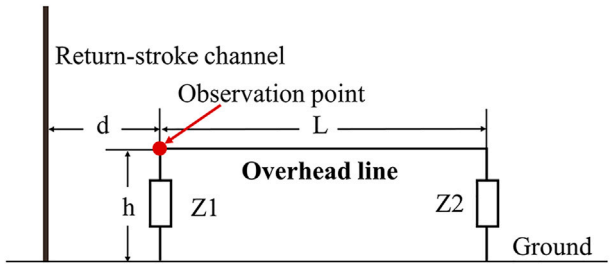


**FIGURE 7 |** The sketch map of the locations of the lightning channel and the overhead line.

## 4 INFLUENCES ON LIGHTNING-INDUCED VOLTAGES ON OVERHEAD LINES

The induced voltages coupled on overhead lines will seriously endanger the stable operation of power systems when lightning strikes near transmission lines. The Agrawal model is a commonly used transmission line model to analyze induced voltages of LEMFs on overhead lines (Agrawal et al., 1980). In this model, the horizontal electric field plays an important role as the excitation source of induced voltages. We analyzed the influences of the soil water content and porosity on LEMFs in **Section 3**, especially the horizontal electric field. On this basis, we further analyze the effect of the water content and porosity on LIVs on overhead lines.

In this paper, the Agrawal method is adopted. The FDTD method is employed to discretely solve the Agrawal model of a single-conductor transmission line. The total induced voltages of overhead lines consist of the incident voltage and the scattered voltage. As given in **Eq. 4**, the incident voltage $U_i(x)$ is calculated by integrating the electric field component perpendicular to the overhead line over height $h$.

$$\boldsymbol{U_i(x) = -\int_0^h E_p(x,h)dh} \tag{4}$$

As expressed in **Eqs 5**, **6**, the scattered voltage $U_s(x,t)$ is calculated by the Agrawal coupling formula in the time domain.

$$\frac{\partial \boldsymbol{U_s(x,t)}}{\partial \boldsymbol{x}} + \boldsymbol{L'}\frac{\partial \boldsymbol{i(x,t)}}{\partial \boldsymbol{t}} = \boldsymbol{E_t(x,h,t)} \tag{5}$$

$$\frac{\partial \boldsymbol{i(x,t)}}{\partial \boldsymbol{x}} + \boldsymbol{C'}\frac{\partial \boldsymbol{U_s(x,t)}}{\partial \boldsymbol{t}} = \boldsymbol{0} \tag{6}$$

where $E_t$ is the tangential component of the electric field along the overhead line, and $i$ is the incident current. $L'$ and $C'$ are the distributed inductance and distributed capacitance per unit length of the ideal transmission line, respectively.

**Figure 7** is a sketch map of the locations of the overhead line and the lightning strike point. The distance $d$ between the near end of the line and the lightning channel is set to 200 m. The line

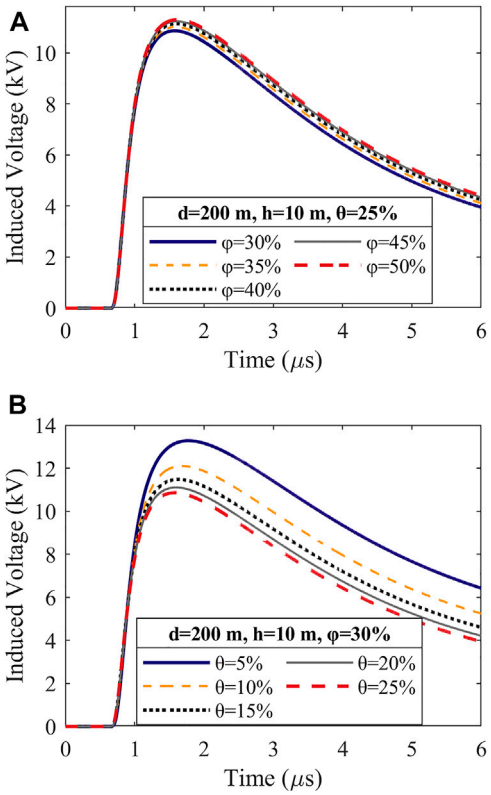


**FIGURE 8 | (A)** Influence of the porosity on LIVs at the near end of the overhead line for high water content θ = 25%. **(B)** Influence of the water content on LIVs at the near end of the overhead line for low porosity φ = 30%.

length $L$ is 1 km, and the height $h$ is set to 10 m. The radius a of the line is 5 mm. The grounding impedance at both ends of the line is set to 498 Ω, and impedance matching is maintained (Soto et al., 2014b).

The conclusion has been drawn from **Section 3** that two situations require attention when considering the influences of soil water content and porosity on the horizontal electric field simultaneously. One is changes in soil porosity at high water content and the other is changes in water content at low porosity. **Figure 8** shows the results of analyzing the influences of the soil water content and porosity on the LIVs on the overhead lines from these two perspectives.

The effect of the soil porosity on LIVs at the near end point of the overhead line at a high water content of 25% is shown in **Figure 8A**. The results show that the LIV amplitude increases with increasing porosity. However, the increasing extent decreases with the increase of soil porosity. At the same point, the variation in LIVs with changing water content at a low porosity of 30% is depicted in **Figure 8B**. Contrary to the influence of the porosity, the change in the soil water content is negatively correlated with the induced voltage; that is, the amplitude of the induced voltage increases with decreasing water content. The increasing extent decreases with decreasing water content. Comparing **Figures 8A,B**, the change in soil water content at low porosity has a more severe impact on LIVs on overhead lines than the change in porosity at high water content.

## 5 SUMMARY AND DISCUSSION

Changes in soil water content and porosity can affect soil conductivity, which in turn affect the propagation of LEMFs. To explore the specific laws, the 2-D FDTD algorithm and a generalized Archie's model are used to study the influences of the water content and the porosity on the LEMFs propagation and LIVs on overhead lines in this paper. The results obtained are as follows:

When the change in a single factor is discussed, the soil water content and the porosity are found to have the most significant impact on the peaks of the horizontal electric field of lightning and hardly affect the vertical electric field and magnetic field. The water content and porosity have prominent effects on the positive and negative peaks of the horizontal electric field at a horizontal distance of 200 m from the lightning channel. Specifically, an increase in the water content leads to an increase in the positive peak values and a decrease in the negative peak values. In contrast, the positive peak values decrease, and the negative peak values increase as the porosity increases, except in the cases where the water content is set to 5% and 10%.

The results show that the water content and porosity affect each other when they act together on the peaks of the horizontal electric field. In general, the influence of the soil water content on the peaks of the horizontal electric field is more obvious. Changes in the porosity at high water content and changes in the water content at low porosity have the greatest influence on the peaks of the horizontal electric field.

Additionally, we also analyzed the influences of water content and porosity on LIVs on overhead lines. We found that the effect of the soil water content at low porosity on the induced voltages was more severe, which can provide a reference for the design of lightning protection projects for overhead transmission lines under soil conditions with different water contents and porosities.

Due to the limitation of the observation experiments and calculation models, only two factors that affect soil conductivity, namely, water content and porosity, can be analyzed in this paper, and the relationship between them cannot be covered. Establishing a more comprehensive and scientific soil model to further analyze the propagation law of LEMFs under different soil conditions could be the direction of our follow-up improvement and exploration.

## DATA AVAILABILITY STATEMENT

The original contributions presented in the study are included in the article/Supplementary Material, further inquiries can be directed to the corresponding author.

## AUTHOR CONTRIBUTIONS

YL and YJ contributed to conception and design of the study. YL and YJ performed the analysis and wrote the first draft of the manuscript. QG, XL, GY, and QZ contributed to manuscript revision. QG and BT contributed to coding. All authors contributed to manuscript revision approved the submitted version.

## FUNDING

This work was supported by the Natural Science Foundation of China (41575004), the Jiangsu Provincial Natural Science Foundation of China (BK20150903), and the NUIST Students' Platform for Innovation and Entrepreneurship Training Program (XJDC202110300024 and XJDC202110300020).

## REFERENCES

Agrawal, A., Price, H., and Gurbaxani, S. (1980). "Transient Response of Multiconductor transmission Lines Excited by a Nonuniform Electromagnetic Field," in 1980 Antennas and Propagation Society International Symposium, Quebec, Canada, June 2–6, 1980 Institute of Electrical and Electronics Engineers, 432–435. doi:10.1109/APS.1980.1148283

Akbari, M., Sheshyekani, K., Pirayesh, A., Rachidi, F., Paolone, M., Borghetti, A., et al. (2013). Evaluation of Lightning Electromagnetic Fields and Their Induced Voltages on Overhead Lines Considering the Frequency Dependence of Soil Electrical Parameters. *IEEE Trans. Electromagn. Compat.* 55, 1210–1219. doi:10.1109/TEMC.2013.2258674

Aoki, M., Baba, Y., and Rakov, V. A. (2015). FDTD Simulation of LEMP Propagation over Lossy Ground: Influence of Distance, Ground Conductivity, and Source Parameters. *J. Geophys. Res. Atmos.* 120, 8043–8051. doi:10.1002/2015JD023245

Araki, S., Nasu, Y., Baba, Y., Rakov, V. A., Saito, M., and Miki, T. (2018). 3-D Finite Difference Time Domain Simulation of Lightning Strikes to the 634-m Tokyo Skytree. *Geophys. Res. Lett.* 45, 9267–9274. doi:10.1029/2018GL078214

Archie, G. E. (1942). The Electrical Resistivity Log as an Aid in Determining Some Reservoir Characteristics. *Trans. AIME* 146, 54–62. doi:10.2118/942054-G

Arzag, K., Azzouz, Z.-E., Baba, Y., and Ghemri, B. (2019). 3-D FDTD Computation of Electromagnetic Fields Associated with Lightning Strikes to a Tower Climbed on a Trapezoidal Mountain. *IEEE Trans. Electromagn. Compat.* 61, 606–616. doi:10.1109/TEMC.2019.2895689

Baba, Y., and Rakov, V. A. (2008). Influence of Strike Object Grounding on Close Lightning Electric Fields. *J. Geophys. Res.* 113, D12109. doi:10.1029/2008JD009811

Delfino, F., Procopio, R., Rossi, M., and Rachidi, F. (2009). Influence of Frequency-dependent Soil Electrical Parameters on the Evaluation of Lightning Electromagnetic Fields in Air and Underground. *J. Geophys. Res.* 114, D11113. doi:10.1029/2008JD011127

Ewing, R. P., and Hunt, A. G. (2006). Dependence of the Electrical Conductivity on Saturation in Real Porous Media. *Vadose Zone J.* 5, 731–741. doi:10.2136/vzj2005.0107

Fu, Y., Horton, R., Ren, T., and Heitman, J. L. (2021). A General Form of Archie's Model for Estimating Bulk Soil Electrical Conductivity. *J. Hydrol.* 597, 126160. doi:10.1016/j.jhydrol.2021.126160

Ghanbarian, B., Hunt, A. G., Ewing, R. P., and Skinner, T. E. (2014). Universal Scaling of the Formation Factor in Porous Media Derived by Combining Percolation and Effective Medium theories. *Geophys. Res. Lett.* 41, 3884–3890. doi:10.1002/2014GL060180

Ghania, S. M. (2019). Grounding Systems under Lightning Surges with Soil Ionization for High Voltage Substations by Using two Layer Capacitors (TLC) Model. *Electr. Power Syst. Res.* 174, 105871. doi:10.1016/j.epsr.2019.105871

Glover, P. W. J. (2017). A New theoretical Interpretation of Archie's Saturation Exponent. *Solid earth.* 8, 805–816. doi:10.5194/se-8-805-2017

Hallikainen, M., Ulaby, F., Dobson, M., El-rayes, M., and Wu, L.-k. (1985). Microwave Dielectric Behavior of Wet Soil-Part 1: Empirical Models and Experimental Observations. *IEEE Trans. Geosci. Remote Sens.* GE-23, 25–34. doi:10.1109/TGRS.1985.289497

He, L., Rachidi, F., Azadifar, M., Rubinstein, M., Rakov, V. A., Cooray, V., et al. (2019). Electromagnetic Fields Associated with the M-Component Mode of Charge Transfer. *J. Geophys. Res. Atmos.* 124, 6791–6809. doi:10.1029/2018JD029998

Heidler, F. (1985). *Travelling Current Source Model for LEMP Calculations*. Zurich Switzerland.

Kane Yee, Yee. (1966). Numerical Solution of Initial Boundary Value Problems Involving Maxwell's Equations in Isotropic Media. *IEEE Trans. Antennas Propagat.* 14, 302–307. doi:10.1109/TAP.1966.1138693

Li, D., Zhang, Q., Wang, Z., and Liu, T. (2014). Computation of Lightning Horizontal Field over the Two-Dimensional Rough Ground by Using the Three-Dimensional FDTD. *IEEE Trans. Electromagn. Compat.* 56, 143–148. doi:10.1109/TEMC.2013.2266479

Li, D., Luque, A., Rachidi, F., Rubinstein, M., Azadifar, M., Diendorfer, G., et al. (2019a). The Propagation Effects of Lightning Electromagnetic Fields over Mountainous Terrain in the Earth-Ionosphere Waveguide. *J. Geophys. Res. Atmos.* 124, 14198–14219. doi:10.1029/2018JD030014

Li, X., Lu, G., Fan, Y., Jiang, R., Zhang, H., Li, D., et al. (2019b). Underground Measurement of Magnetic Field Pulses during the Early Stage of Rocket-Triggered Lightning. *J. Geophys. Res. Atmos.* 124, 3168–3179. doi:10.1029/2018JD029682

Li, Q., Rubinstein, M., Wang, J., Cai, L., Zhou, M., Fan, Y., et al. (2020). On the Influence of the Soil Stratification and Frequency-dependent Parameters on Lightning Electromagnetic Fields. *Electr. Power Syst. Res.* 178, 106047. doi:10.1016/j.epsr.2019.106047

Liu, X., Zhang, Q., and Feng, X. (2012). Effect of Finite Conductivity on Rise Time and Field Strength Amplitude of Return Stroke Radiation Field of Cloud-Ground Flash. *High. Volt. Eng.* 38, 457–463. doi:10.3969/j.issn.1003-6520.2012.02.029

Mur, G. (1981). Absorbing Boundary Conditions for the Finite-Difference Approximation of the Time-Domain Electromagnetic-Field Equations. *IEEE Trans. Electromagn. Compat.* EMC-23, 377–382. doi:10.1109/TEMC.1981.303970

Nazari, M., Moini, R., Fortin, S., Dawalibi, F. P., and Rachidi, F. (2021). Impact of Frequency-Dependent Soil Models on Grounding System Performance for Direct and Indirect Lightning Strikes. *IEEE Trans. Electromagn. Compat.* 63, 134–144. doi:10.1109/TEMC.2020.2986646

Ouyang, S., Zhang, Q., Li, Y., Li, D., and Zhang, Y. (2012). Impact on Lightning Electromagnetic Field Propagation of Soil Electrical Parameter Variation Induced by Varying Surface Soil Moisture. *Meteorol. Sci. Technol.* 40, 1018–1024. doi:10.3969/j.issn.1671-6345.2012.06.025

Rachidi, F., Janischewskyj, W., Hussein, A. M., Nucci, C. A., Guerrieri, S., Kordi, B., et al. (2001). Current and Electromagnetic Field Associated with Lightning-Return Strokes to tall towers. *IEEE Trans. Electromagn. Compat.* 43, 356–367. doi:10.1109/15.942607

Rizk, M. E. M., Abulanwar, S. M., Ghanem, A. T. M., and Lehtonen, M. (2021). Computation of Lightning-Induced Voltages Considering Ground Impedance of Multi-Conductor Line for Lossy Dispersive Soil. *IEEE Trans. Power Deliv.*, 1. doi:10.1109/TPWRD.2021.3111149

Rubinstein, M. (1996). An Approximate Formula for the Calculation of the Horizontal Electric Field from Lightning at Close, Intermediate, and Long Range. *IEEE Trans. Electromagn. Compat.* 38, 531–535. doi:10.1109/15.536087

Schroeder, M. A. O., de Barros, M. T. C., Lima, A. C. S., Afonso, M. M., and Moura, R. A. R. (2018). Evaluation of the Impact of Different Frequency Dependent Soil Models on Lightning Overvoltages. *Electr. Power Syst. Res.* 159, 40–49. doi:10.1016/j.epsr.2017.09.020

Shoory, A., Moini, R., Sadeghi, S. H. H., and Rakov, V. A. (2005). Analysis of Lightning-Radiated Electromagnetic Fields in the Vicinity of Lossy Ground. *IEEE Trans. Electromagn. Compat.* 47, 131–145. doi:10.1109/TEMC.2004.842104

Sommerfeld, A. (1909). Über die Ausbreitung der Wellen in der drahtlosen Telegraphie. *Ann. Phys.* 333, 665–736. doi:10.1002/andp.19093330402

Soto, E., Perez, E., and Herrera, J. (2014a). Electromagnetic Field Due to Lightning Striking on Top of a Cone-Shaped Mountain Using the FDTD. *IEEE Trans. Electromagn. Compat.* 56, 1112–1120. doi:10.1109/TEMC.2014.2301138

Soto, E., Perez, E., and Younes, C. (2014b). Influence of Non-flat terrain on Lightning Induced Voltages on Distribution Networks. *Electr. Power Syst. Res.* 113, 115–120. doi:10.1016/j.epsr.2014.02.034

Thottappillil, R., Rakov, V. A., and Uman, M. A. (1997). Distribution of Charge along the Lightning Channel: Relation to Remote Electric and Magnetic Fields and to Return-Stroke Models. *J. Geophys. Res.* 102, 6987–7006. doi:10.1029/96JD03344

Visacro, S., and Alipio, R. (2012). Frequency Dependence of Soil Parameters: Experimental Results, Predicting Formula and Influence on the Lightning Response of Grounding Electrodes. *IEEE Trans. Power Deliv.* 27, 927–935. doi:10.1109/TPWRD.2011.2179070

Wait, J. R. (1997). Concerning the Horizontal Electric Field of Lightning. *IEEE Trans. Electromagn. Compat.* 39, 186. doi:10.1109/15.584943

Yang, Y., Liu, Y., Liu, F., Zhang, N., Liu, G., and Zhai, H. (2021). Research on Influence of Different Soil Types and Moisture on Lightning Electromagnetic Field Based on FDTD. *J. Trop. Meteorol.* 37, 348–357. doi:10.16032/j.issn.1004-4965.2021.03410.1016/j.celrep.2021.110097

Yu, J. L., Fan, Y. D., Wang, J. G., Qi, R. H., Zhou, M., Cai, L., et al. (2017). Characteristics of the Horizontal Electric Field Associated with Nearby Lightning Return Strokes. *J. Atmos. Solar-Terr. Phys.* 154, 207–216. doi:10.1016/j.jastp.2016.02.017

Zhang, Q., Li, D., Fan, Y., Zhang, Y., and Gao, J. (2012). Examination of the Cooray-Rubinstein (C-R) Formula for a Mixed Propagation Path by using FDTD: TECHNIQUES FOR A MIXED GROUND. *J. Geophys. Res.* 117, 117–D15309. doi:10.1029/2011JD017331

Zhang, Q., Tang, X., Hou, W., and Zhang, L. (2015). 3-D FDTD Simulation of the Lightning-Induced Waves on Overhead Lines Considering the Vertically Stratified Ground. *IEEE Trans. Electromagn. Compat.* 57, 1112–1122. doi:10.1109/TEMC.2015.2420653

Zhou, W. (2003). *A Study on Avaliable Water Capacity of Main Soil Types in China Based on Geographic Information System*. M.S. Thesis. Nanjing, China: Nanjing Agricultural University.

**Conflict of Interest:** The authors declare that the research was conducted in the absence of any commercial or financial relationships that could be construed as a potential conflict of interest.

**Publisher's Note:** All claims expressed in this article are solely those of the authors and do not necessarily represent those of their affiliated organizations, or those of the publisher, the editors and the reviewers. Any product that may be evaluated in this article, or claim that may be made by its manufacturer, is not guaranteed or endorsed by the publisher.

frontiers | Frontiers in Environmental Science

ORIGINAL RESEARCH
published: 27 June 2022
doi: 10.3389/fenvs.2022.948318

# Effects of Relative Humidity on the Diurnal Variation of Raindrop Size Distribution in Southwest China

*Jing Sun*[1,2], *Rong Wan*[1]* *and Yue Zhou*[1]

[1]Hubei Key Laboratory for Heavy Rain Monitoring and Warning Research, Institute of Heavy Rain, China Meteorological Administration, Wuhan, China, [2]State Key Laboratory of Severe Weather, Chinese Academy of Meteorological Sciences, Beijing, China

This study examined the effects of relative humidity (RH) on the diurnal variation of raindrop size distribution (RSD) over valley topography (Zigui region) of China from 2019 to 2020 based on a two-dimensional video disdrometer (2DVD), auto-weather station (AWS) and ERA5. The RSD structure of daytime shows a triple peaks when the RH is lower than 60% and it shows a single peak in other RH conditions, for the RSD of nighttime, the RSD structure shows a single peak when the RH is greater than 60%, and the RSD shape shows a bimodal structure with RH ≤ 60%. Significant day-night difference was found in RSDs between short-duration precipitation Amount (SPA) and long-duration precipitation Amount (LPA) under the different RH conditions. The daytime RSDs of SPA showed broader distributions than the nighttime RSDs, whereas the nighttime RSDs of LPA exhibited the opposite to that of SPA. Higher ground RH modified the RSD shape through raindrop sorting, collision-coalescence and breakup resulting with the formation of large size raindrops. Under the effect of same RH, the melting and collision-coalescence of large raindrops in the daytime of SPA are obviously stronger than those of LPA. This difference may be related to the near-surface wind filed and the intensity of convection.

**Keywords: raindrop size distribution (RSD), precipitation, relative humidity, Southwest of China, diurnal variation**

OPEN ACCESS

***Edited by:***
*Honglei Wang,*
*Nanjing University of Information Science and Technology, China*

***Reviewed by:***
*Jingjing Lv,*
*Nanjing University, China*
*Yi Yang,*
*Hebei Normal University, China*

***Correspondence:**
*Rong Wan*
*wanrong@whihr.com.cn*

***Specialty section:***
*This article was submitted to Atmosphere and Climate, a section of the journal Frontiers in Environmental Science*

***Received:*** *19 May 2022*
***Accepted:*** *06 June 2022*
***Published:*** *27 June 2022*

***Citation:***
*Sun J, Wan R and Zhou Y (2022) Effects of Relative Humidity on the Diurnal Variation of Raindrop Size Distribution in Southwest China. Front. Environ. Sci. 10:948318. doi: 10.3389/fenvs.2022.948318*

## 1 INTRODUCTION

Rain microphysical structure is basic to cloud physics of rain formation, and the raindrop size distribution (RSD) is an important microphysical characteristic of precipitation. The importance of RSD mainly is reflected in the three aspects: estimation or retrieval of DSD parameters and rainfall rates (Bringi et al., 2003; Chen et al., 2017; Adirosi et al., 2014), attenuation correction at C-and X-bands (Gorgucci et al., 2001; Thurai et al., 2017), and evaluating propagation effects in rain (Ryzhkov et al., 2005). Moreover, the information of range, coverage, resolution, precision and continuity with precipitation is obtained, which gives a great opportunity to improve microphysical scheme, climate models and rainfall prediction (Abel and Boutle, 2012; Thurai et al., 2017).

Previous studies have reported the changes of RSD in different climatic region and rain types from diurnal to seasonal scales by using the disdrometer data (Bringi et al., 2003; Rao, 2005; Thurai et al., 2010; Kumar and Reddy, 2013; Dolan et al., 2018; Seela et al., 2018; Suh et al., 2021). For example, Kozu et al. (2005) studied the diurnal and seasonal variations of RSD in the Asian monsoon region (Gadanki, Singapore and Kototabang), and the diurnal convective cycles and seasonal variations of precipitation have significant influences on the characteristic of RSD. Suh et al. (2016) found that the

frequency of Dm is higher at nighttime than during the daytime when $D_m > 0.65$ mm. For $N_w$, which tends to be inversely related to $D_m$, its frequency is higher at nighttime than during the daytime when $\log_{10}(N_w) > 3.9\ m^{-3}\ mm^{-1}$. Chen et al. (2017) revealed that little difference was found in stratiform DSDs between day and night, and daytime convective DSDs had a higher mass-weighted mean diameters (Dm) and lower generalized intercepts (NW) than the nighttime DSDs.

The middle and lower reaches of the Yangtze River basin is one of the regions where heavy rainfall is frequent. Especially, when the East Asian summer monsoon breaks out and advances northward to this region, the extremely frequent convective activities often cause strong precipitation and bring serious flood disasters (Ding and Chan, 2005; Yu and Li, 2012; Yu et al., 2021). Previous studies have revealed the fact that there is diurnal variation in precipitation in the middle and lower reaches of the Yangtze River, and pointed out that the convective burst from afternoon to night caused by the difference in surface radiative heating is the main period for the formation of heavy rainfall (Held and Soden, 2006; Tang et al., 2022). Zhou et al. (2008) revealed that the two peaks of the diurnal variation of precipitation in the middle and lower reaches of the Yangtze River occurred in the afternoon and early morning, respectively. Yu et al. (2007a) and Yu et al. (2007b) found that the afternoon precipitation peaks are often caused by convective activities with a short time (<3 h), while the night-to-morning precipitation peaks are related to convective activities with a long time in the central and eastern china (>6 h). These research results have enriched the understanding of the diurnal variation of precipitation in the Yangtze River Basin and its formation mechanism. However, what are the characteristics of the RSD corresponding to the diurnal variation of precipitation, and what are the microphysical processes that cause the diurnal variation of the RSD are still unclear.

Due to the formation of diurnal variation of precipitation is often related to various diurnal variation in the atmosphere, some studies revealed that relative humidity also has obvious diurnal variation (Zhang et al., 2008) and linked with convective initiation (Sobel and Bretherton, 2000), and the variation of relative humidity have an impact on the coalescence of small drops (Ochs III et al., 1995). Therefore, the relative humidity may be a key factor to affect convective cloud dynamics and microphysical processes, and the relative humidity also changes the RSD structure. Coupled with the effect of valley topography, the valley effect causes a pronounced difference between the daytime and nighttime RSD characteristics (Suh et al., 2016; Chen et al., 2017; Zagrodnik et al., 2018).

In addition to the observational analysis, the diurnal variation of RSD with different relative humidity, the day-night RSD difference between short-duration precipitation amount (SPA) and long-duration precipitation amount (LPA) and the day-night RSD difference between the convective and stratiform rainfall in SPA and LPA were studied. A brief description of observation data and rain integral parameters are provided in **Section 2**. Observational analysis is given in **Section 3**. The conclusions are summarized in the last section along with a discussion on future research.

# 2 DATA SOURCE AND METHODOLOGY

## 2.1 Data Source

The data sets used in this study were collected at Zigui national weather station (ZG: 30.83°N, 110.96°E, and elevation is 295.5 m) from September 2019 to August 2020. The topography of ZG belongs to the mountainous landform of the Three Gorges of the Yangtze River in China, and the region strongly influenced by the southwest vortex. The southwest vortex generated in the southeast of Qinghai-Tibet Plateau and it is a low-value vortex system with cyclonic circulation in the lower troposphere. Its development and eastward movement can bring heavy rainfall to the adjacent areas of the plateau (Jiang et al., 2015; Wang et al., 2020; You et al., 2021). The geographic location of the ZG site is shown in **Figure 1A**.

The 2DVD used was the current third-generation version manufactured by Joanneum Research at the Institute for Applied Systems Technology in Graz, Austria (2DVD, sn116) (Schönhuber et al., 1994). The core element of 2DVD has two orthogonally placed line scan cameras and illumination sources, and produces a horizontal measuring area of 10 cm × 10 cm. The horizontal imaging resolution of the unit is approximately 0.2 mm. The temporal resolution for the 2DVD data is 1 min in this study. The reanalysis wind field and relative humidity at 850 hpa from the ERA5 reanalysis data (0.25° × 0.25°, hourly) from 2019 to 2020 are used to elucidate the climatological background and the diurnal variation of relative humidity (RH) and ground temperature (T).

It has been frequently noticed that during heavy rain, there are a number of particle velocity outliers measured by the 2DVD due to raindrops that are wrongly matched by two cameras of 2DVD, and the mismatch will lead to incorrect estimates of drops shape and velocity (Yuter et al., 2006). Based on a recommended falling speeds deviating more than ±40% from the falling speed versus diameter relationship (Atlas and Ulbrich, 2000), the total number of raindrops is less than 10 or those that correspond to rain rates that are less than 0.1 mm $h^{-1}$ are also eliminated from dataset for each 1 min data (Tokay et al., 2013). The scatter plots of rainfall show a higher correlation coefficients between 2DVD and AWS measurements (**Figure 1B**). This clearly indicates that the rain integral parameters derived from 2DVD can be used to understand the RSD characteristics in ZG site. Additionally, due to the wind tower and 2DVD are on the same horizontal plane, we believe that the observation period is affected by the same horizontal winds. Lin et al. (2021) indicated the optical disdrometer may underestimate the rain rate in strong-wind environments during tropical cyclones, so we choose the DSD data corresponding to horizontal wind speed less than 14 m $s^{-1}$.

## 2.2 Methodology

The integral rainfall parameters are derived by the RSD moments, including the mass-weighted mean diameter ($D_m$: mm), normalized intercept parameter ($N_w$: $mm^{-1}m^{-3}$), rain rate ($R$: mm $h^{-1}$), liquid water content ($LWC$: g $m^{-3}$), radar reflectivity ($Z$: dBZ). The normalized intercept parameter $N_w$ represents $N(D)$

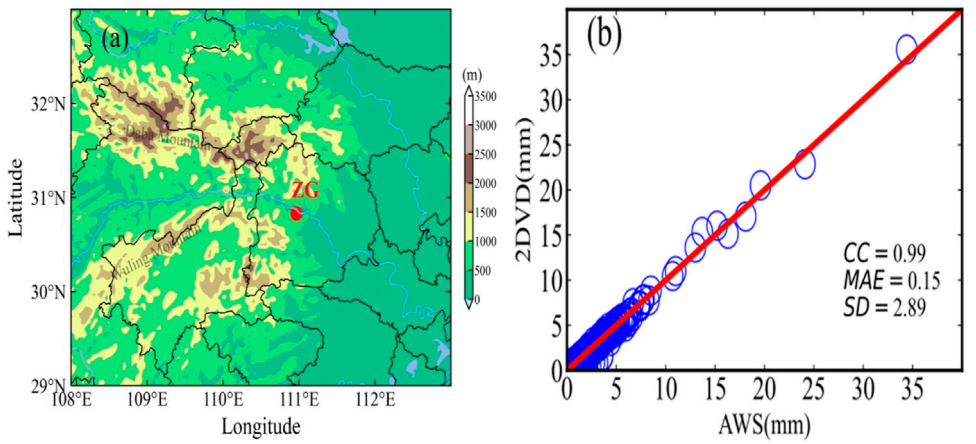


**FIGURE 1 |** Location of the observation site at Zigui site **(A)** and the comparison of hourly precipitation between 2DVD and AWS **(B)**.

when raindrops diameter approaches to its minimum value. The slope parameter ($\Lambda$) designates the truncation of RSD tail with drop diameter. The shape ($\mu$) parameter represents the breadth of the RSD shape.

The well-known gamma function is used to obtain the distribution of RSD(Ulbrich, 1983), and the gamma size distribution is given as follows:

$$\mathrm{N}(D) = N_0 D^{\mu} \exp(-\Lambda D) \tag{1}$$

where $N(D)$ is the RSD($\mathrm{m^{-3}mm^{-1}}$), $D$ is the raindrop diameter (mm), $N_0$ is the intercept parameter ($\mathrm{mm^{-1-\mu}m^{-3}}$), $\mu$ (dimensionless) and $\Lambda$ ($\mathrm{mm^{-1}}$) are the shape and slope parameters, respectively.

$$M_n = \int_0^{\infty} D^n N(D) dD \tag{2}$$

where $M_n$ is the nth-order moment of the RSD for the gamma RSD model.

$$\mu = \frac{(11Q - 7) \pm \sqrt{1 + 14Q + Q^2}}{2(1 - Q)} \tag{3}$$

where

$$\mathrm{Q} = \frac{M_4^3}{M_6 M_3^2} \tag{4}$$

$$\Lambda = \sqrt{(4 + \mu)(3 + \mu)} \sqrt{\frac{(\mathrm{D}^2)}{(\mathrm{D}^4)}} \tag{5}$$

Parameters $D_m$ and $\mathrm{N_W}$ are reprehensive parameters for a RSD and the distribution of $D_m$ and $N_W$ can directly express the nature of precipitation and the microphysical characteristics of precipitation.

$$\mathrm{D_m} = \frac{\mathrm{M_4}}{\mathrm{M_3}} \tag{6}$$

$$N_w = \frac{4^4}{\pi \rho_w} \left( \frac{10^3 LWC}{D_m^4} \right) \tag{7}$$

Where $\rho_w$ is the water density (the value is assumed to 1.0 g $\mathrm{cm^{-3}}$), and the above equation was derived from Bringi et al. (2003).

$$\mathrm{R} = \frac{6\pi}{10^4} \sum_{i=1}^{41} D_i^3 V_i N(D_i) \Delta D_i \tag{8}$$

$$\mathrm{LWC} = \frac{\pi}{6000} \sum_{i=1}^{41} D_i^3 N(D_i) \Delta D_i \tag{9}$$

$$\mathrm{Z} = \sum_{\mathrm{i=1}}^{41} \mathrm{D_i^6 N(D_i)} \Delta \mathrm{D_i} \tag{10}$$

$$\mathrm{N_t} = \sum_{\mathrm{i=1}}^{41} \mathrm{N(D_i)} \Delta \mathrm{D_i} \tag{11}$$

Based on the quality-controlled datasets, the definition of persistent rainfall as followed: the precipitation intensity has been greater than 0.1 mm $\mathrm{h^{-1}}$ and the duration is greater than 1 h at the beginning of precipitation. Therefore, 59 persistent rainfall events(between 9 September in 2019 and 26 August in 2020 are used to analyze the diurnal variation of precipitation and RSD.

The hourly precipitation data from September 2019 to August 2020 are analyzed and the number of total precipitation and total precipitation hours are calculated for each hour in every day. For a certain hour of the day, the total number of hours is 304 h. Based on the statistical results, the hourly climate averaged precipitation frequency (PF), and precipitation intensity (PI) for each hour of the day are further calculated as follows:

$$\mathrm{PF} = \left( \frac{Total\ precipitation\ hours}{304} \right) * 100\% \tag{12}$$

$$\mathrm{PI} = \frac{Total\ precipitation}{PF} \tag{13}$$

Since different property of precipitation corresponds to different durations, and has an important effect on the diurnal variation of precipitation(Yu et al., 2007a; Chen et al., 2010; Han et al., 2017), and Moreover, the dominant microphysical processes corresponding to precipitation with different durations are also different. In order to investigate the differences of RSD between different precipitation, we will focus the discussion on the RSD

**TABLE 1 |** Mean (standard deviation) of several integral RSD parameters for rainfall.

| Rain types | Samples | $D_m$ | | $\log_{10}Nw$ | | LWC | | Z(dBZ) | | μ | | Λ | |
|---|---|---|---|---|---|---|---|---|---|---|---|---|---|
| | | Mean | Std | Mean | Std | Mean | Std | Mean | Std | Mean | Std | Mean | Std |
| All | 15,169 | 1.07 | 0.4 | 3.71 | 0.55 | 0.14 | 0.25 | 22.3 | 8.6 | 7.9 | 10.2 | 14.0 | 16.1 |
| Daytime | 9,284 | 1.03 | 0.33 | 3.73 | 0.52 | 0.13 | 0.24 | 21.7 | 8.2 | 8.1 | 10.5 | 14.0 | 17.8 |
| Nighttime | 5,885 | 1.12 | 0.4 | 3.69 | 0.59 | 0.15 | 0.26 | 23.2 | 9.2 | 7.6 | 10.3 | 13.9 | 16.1 |

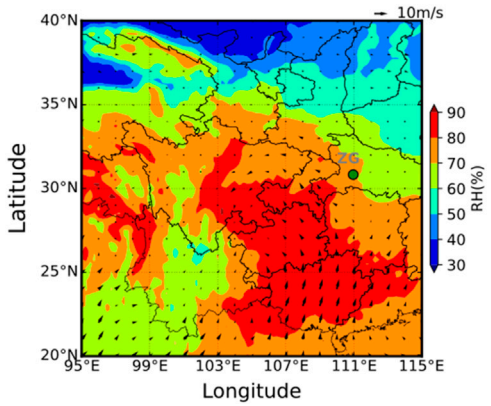


**FIGURE 2 |** Mean wind field and relative humidity (%) at 850 hPa based on the ERA5 data. The scale of the wind vector (10 m $s^{-1}$) is marked by wind arrows at the top of panels, while relative humidity is revealed by the color bar.

differences between SPA (Short-duration Precipitation Amount, duration of precipitation is less than 3 h, and referenced from Yu et al. (2007b) and LPA (Long-duration Precipitation Amount, duration of precipitation is longer than 6 h) based on the different HR, and the differences of convective and stratiform rainfall between SPA and LPA. Mean and standard deviation values of $D_m$, $\log_{10}N_w$, LWC, Z, μ and Λ in daytime and nighttime are given in **Table1**.

# 3 RESULTS

## 3.1 Synoptic Environment and Precipitation Daily Variation

**Figure 2** shows the seasonal mean of the ERA5 reanalysis wind field and relative humidity at 850 hPa from the year 2019–2020. As can be seen, the warm and moist air is transported from the Indian Ocean and South China Sea to the continent by the dominant southwesterly winds, and the mean relative humidity is around 70%–80% in ZG region. In the context of terrain obstruction (**Figure 1**), the southwest warm and humid airflow formed a vortex around the mountain range nearby ZG region, and the average relative humidity of this vortex was maintained above 80%. If there is a low-pressure trough or shortwave moving eastward on the Tibetan Plateau, the heavy rainfall or extreme precipitation will easily occur at ZG region under the combined effect of topography and thermal conditions in the mountains (Wang et al., 2020).

Based on the synoptic environments described above, the hourly precipitation frequency (PF) and precipitation intensity (PI) were calculated by using the hour precipitation data of auto weather station (AWS), it can be found that the occurrence and development of precipitation had obvious the characteristic of daily variation in **Figure 3**. The peak of PF occurs mainly at 0900 BJT during the daytime (DT), and the secondary peak occurs at 2300 BJT during the night-time (NT) (**Figures 3A,B**). The PI peaks occur at 1800 BJT and 2200 BJT, and this is consistent with the results of Yu et al. (2007b). From the diurnal variation of hourly precipitation, it can be inferred that the precipitation can be triggered in the early morning over valley terrain. The surface temperature increases during the DT by the influences of solar shortwave radiation, atmospheric instability and convective weather activity are also increased, which results in the increasing of short time heavy precipitation (Yu et al., 2007a). Although the $PF_{\_NT}$ and $PI_{\_NT}$ peaks are slightly smaller than that of DT precipitation, the PI value of NT is significantly greater than that of DT, suggesting that the NT precipitation is mainly caused by persistent precipitation, and this is closely related to large-scale circulation and stratiform precipitation (Chen et al., 2010). Because of the weakening of the atmospheric thermal effect at NT and the weakening of the thermal convective precipitation, which leads to the gradually weaken of the precipitation system, so that the PF has a valley value at 0700 in the early morning (**Figure 3A**). In addition, the ground temperature reduced by 5°C at the time of PF minimum, and the RH decreased from 93% at the beginning of precipitation to about 86% in **Figures 3C,D**. Precipitation was found to enhance with decreasing temperature and humidity under high temperature and high humidity conditions, which Utsumi et al. (2011) suggested was mainly caused by the long duration of precipitation.

## 3.2 Diurnal Variations of RSDs With Respect to Different Relative Humidity

Past studies have suggested that the variation of precipitation with temperature is mainly related to water vapor conditions (Fan et al., 2007; Qian et al., 2010), and the above studies have also shown that the diurnal variation of precipitation is related to the RH. Considering that RSD is the main microphysical parameter to characterize precipitation, it is necessary to analyze the diurnal variations of RSD and the difference of diurnal variation of RSD under different RH conditions.

**Figure 5** illustrates the distributions of $D_m$, $\log_{10}N_w$, μ, liquid water content (LWC) and RH. There were large variations of $D_m$ with time. The $D_m$ values varied from 0.37 to 3.93 mm, and the

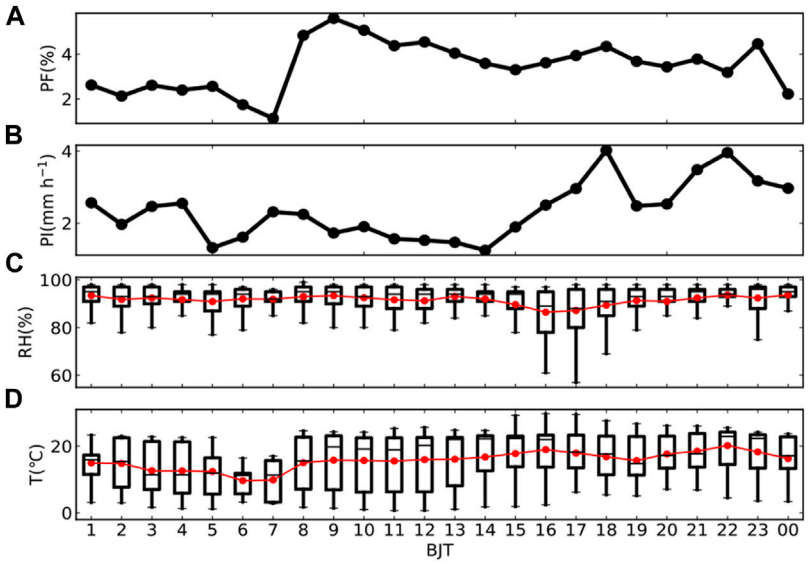


**FIGURE 3 |** Diurnal variations of PF(Precipitation Frequency, unit:%) **(A)**, PI (Precipitation Intensity, unit: mm $h^{-1}$) **(B)**, RH (Relative Humidity, unit:%) and the red line is mean value of RH **(C)**, and T (Temperature, unit:°C) and the red line is mean value of T **(D)** averaged over the ZG region.

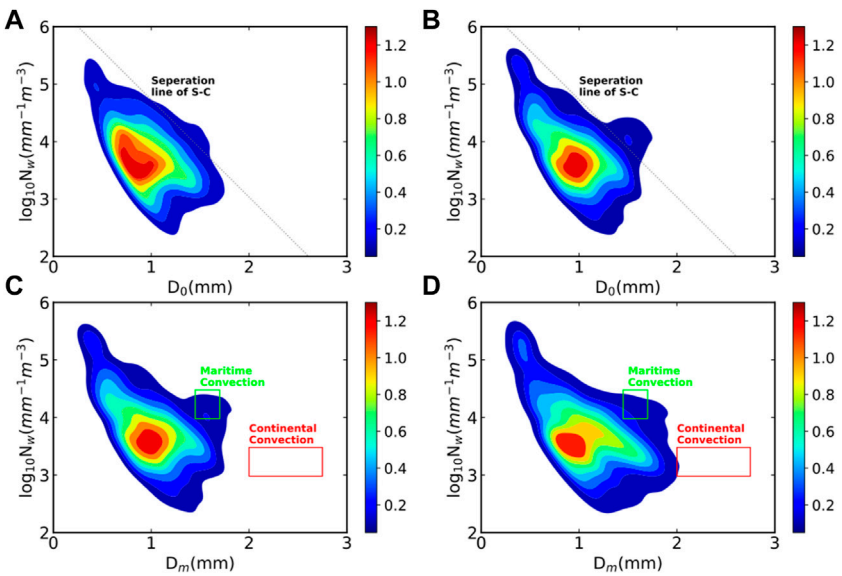


**FIGURE 4 |** Probability density distribution of $D_0$-$\log_{10}N_w$ for DT **(A)** and NT **(B)** with stratiform and convective separation line(inclined black dashed line) of Bingi et al. (2003). Distribution of Dm and $\log_{10}N_w$ over period of DT **(C)** and NT **(D)**. Green and red rectangular boxes represent continental-like and maritime-like convection, respectively.

minimum and maximum $D_m$ values occurred at 05:00 and 0400 BJT, respectively (**Figure 5A**). The $D_m$ larger than 1.0 mm dominated from 00:00 to 09:00 BJT (before PF1_peak), and then the mean Dm decreasing remarkably between 09:00 to 14: 00 BJT. The maximum $D_m$ at 14:00 BJT is significantly smaller than the other times, but the RH is close to 95% at this time. Moreover, the RH gradually decreases before PI1_peak, and the maximum $D_m$ shows an increasing trend at the moment. The $N_w$ distribution showed inversely to $D_m$; however, no inverse relationship was identified between $D_m$ and $N_w$ after the PI1_peak (**Figure 5B**).

For the distribution of μ and LWC, there was an increasing trend from 17:00 to 23:00 BJT followed by a remarkably decreasing trend from 00:00 to 08:00 BJT (**Figure 5C**). Note that the time of the sharp decline for RH between 14:00 and 17:00 BJT is simultaneous with the mean of μ value increasing. Then, the LWC shows a valley at 14:00 BJT, corresponding to RH being

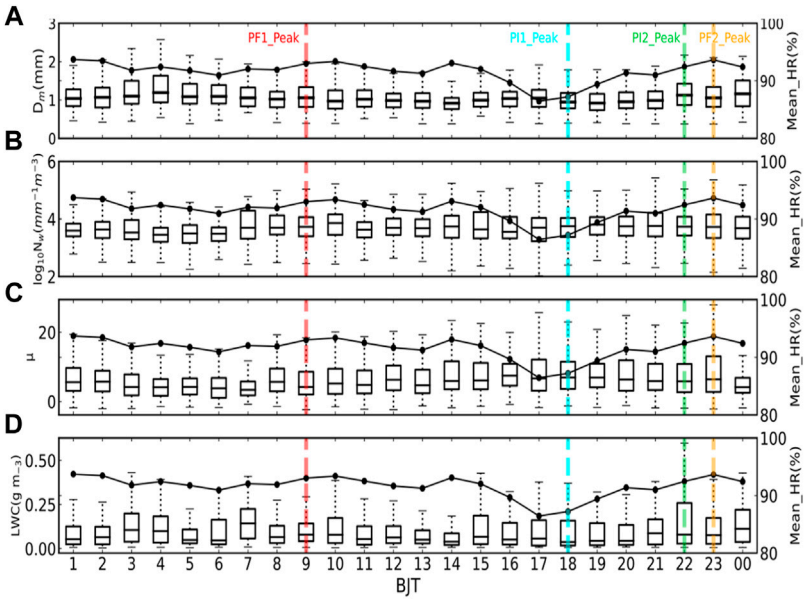


**FIGURE 5 |** Time series of **(A)** Dm, **(B)** $\log_{10}N_w$,**(C)** μ, and **(D)** LWC with mean humidity for the total period. Solid lines are the mean relative humidity for each time. Red dashed line is the PF peak, orange dashed line is the second peak of PF, blue dashed line is the PI peak, and green dashed line is the second peak of PF.

close to saturation state. Moreover, the LWC trend shows a gradually increases when RH decreases sharply (**Figure 5D**). In order to compare the RSDs differences between different RH conditions the RH is classified as relative dry (RH<60%), semi-moist (60%~70%), moist (80%~90%) and very moist(>90%). The mean values of $D_m$, $\log_{10}N_w$, LWC, Z, μ, Λ and R corresponding to different RH conditions are given in **Table 1**, respectively. We can see that relative large $D_m$ and small $\log_{10}N_w$ are displayed during the relative dry (RH<60%), and the mean of μ decreases with the increase of RH. It is inferred from the lower RH condition will benefit to the formation of large raindrops. Moreover, the mean of $\log_{10}N_w$ (μ) increases (decreases) with the increase of RH (**Table 1**).

t r o F

## 3.3 RSD Differences of SPA and LPA

Since different property of precipitation corresponds to different durations, and has an important effect on the diurnal variation of precipitation(Yu et al., 2007a; Chen et al., 2010; Han et al., 2017). Using the definitions in **Section 2.2**, the RSDs differences of precipitation during the SPA (Short-duration precipitation Amount) and LPA(Long-duration precipitation Amount) are analyzed.

**Figure 6A** shows a peak of SPA and LPA at 09:00 BJT (black line) and 12:00 BJT (blue line), and the PF value of LPA is always lager than that of SPA. The peak of PI for SPA coincide with the LPA at 19:00 BJT, the time series of LPA_PI displays considerably larger values than that of SPA between 18:00 and 09:00 BJT, but the PI of SPA is significantly greater than that of LPA between 12:00 and 16:00 BJT (**Figure 6B**). Compared with the RH and ground temperature of SPA and LPA, the RH is mainly distributed between 80% and 90% for SPA, and the minimum of mean RH is about 75% at 16:00 BJT(**Figure 6C**). For LPA, it is obvious that the average RH of LPA basically to sustain around 93% near saturation, and only the average RH decreases to below 90% when the precipitation reaches the peak (**Figure 6D**). The positive △T occurs mainly from 07:00 to 17:00 BJT in LPA, and the △T are below 0°C from 18:00 to 22:00 BJT, which is exactly to coincide with the two peaks of PI in the NT of LPA (**Figures 6E,F**). This temperature gradient formed by the difference between DT warming and NT cooling is easy to excite topographic thermal circulation for valley topography, which often facilitates the triggering and development of convective systems by superimposing topographic effects.

According to previous studies(e.g., Porcù et al., 2014; Wen et al., 2016; Krishna et al., 2016; Ma et al., 2019), the time evolution of RSDs show a regular behavior with respect to rain intensity, and the RSD is a key feature for describing liquid precipitation. **Figure 7** shows the diurnal variations of RSD in the different RH conditions between SPA and LPA. For the RSDs of SPA, the RSDs of DT show a structure of single, double and triple peaks at different RH conditions, and the RSDs shape of SPA_DT is generally concave upward, especially, a significant increase in the number concentration of raindrops with a diameter of 3–4 mm is observed (**Figure 7A**). Compared to RSDs of SPA_DT, the RSDs of SPA-NT have nearly exponential distribution with less tendency toward concavity, and raindrop concentration of NT is higher than that of DT when the RH is above 90%. However, the width of RSDs shape in SPA-NT is significantly smaller than that of SPA_DT, and this characteristic is similar with the diurnal variation of RSDs in Tibetan Plateau (Chen et al., 2017). The day-night difference in the RSDs of SPA and LPA most likely indicate that the microphysical processes that dominate SPA and LPA are significantly different. For the

**TABLE 2 |** Mean values of $D_m$, $log_{10}N_w$, LWC, Z_dbz, μ, Λ and R for different relative humidity.

| RH Class | $D_m$ (mm) | $log_{10}N_w$ ($mm^{-1}m^{-3}$) | LWC (g $m^{-3}$) | Z_dbz (dBZ) | μ | Λ(mm−1) | R (mm $h^{-1}$) |
|---|---|---|---|---|---|---|---|
| ~60% | 1.29 | 2.87 | 0.03 | 19.1 | 9.24 | 12.3 | 0.62 |
| 60~80% | 1.08 | 3.41 | 0.07 | 19.5 | 8.95 | 13.9 | 1.32 |
| 80~90% | 1.03 | 3.61 | 0.08 | 20.5 | 8.15 | 14.2 | 1.3 |
| 90%~ | 1.08 | 3.78 | 0.03 | 23.2 | 7.75 | 13.9 | 2.82 |

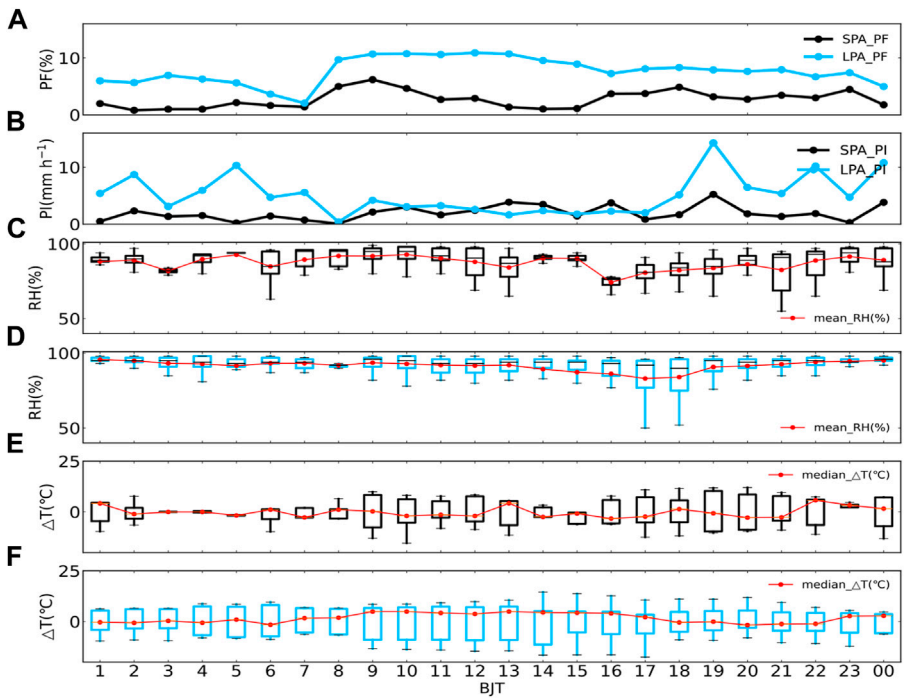


**FIGURE 6 |** Diurnal variations of PF(Precipitation Frequency, unit:%), PI(Precipitation Intensity, unit: mm $h^{-1}$), RH(Relative Humidity, unit:%) and △T(Temperature deviation, unit:°C) for SPA and LPA. The blue line and boxplot represent the LPA, the black line and boxplot represent the SPA, and the red lines are mean value of RH and T, respectively.

SPA, the collision-coalescence is more effective at day than night, due to the coalescence produces a decrease of small drops and an increase of large drops (Rosenfeld & Ulbrich, 2003).

In **Figures 7C,D**, the RSD shapes of the 2.4–3 mm and 1.6 mm diameters are concave-shaped and inverted-triangular in the SPA_DT and LPA_DT in the case of low relative humidity, respectively. This characteristic shows that both the RSDs of SPA_DT and LPA_DT have an evaporation spectrum when the ambient humidity is relatively dry, the main feature is that the number concentration of small drops decreases rapidly with the increase of diameter, the slope of the curve is large, and the curve of larger drops concentration is small and the curve is relatively flat. The RSD shape is similar to the simulated result of Hu and Sivastava. (1995) with obvious evaporation process, which illustrates the melting and collision-coalescence of large raindrops in SPA_DT are obviously stronger than those of LPA_DT. Compared with the night difference in the RSDs of SPA, the RSDs of LPA_NT shows a broader distribution than that of DT, which is opposite to the day-night RSD difference of SPA. The RSDs shape of LPA is generally concave downward, which is similar to the results of other studies (Porcù et al., 2014; Huang et al., 2021).

## 3.4 RSDs Between Convective and Stratiform Rainfall in SPA and LPA

To find out the RSDs differences in convective and stratiform regimes of SPA and LPA, the probability distribution functions (PDFs) of the integral parameters $log_{10}R$, $D_m$, $log_{10}LWC$, $log_{10}N_w$, Z, and μ) for SPA are calculated and are given in **Figure 8**. The precipitation is classified into stratiform and convective type by adopting the Bringi et al. (2003). That is, if the standard deviation of rain rate over five consecutive DSD samples is > 1.5 mm $h^{-1}$ and rain rate is > 5 mm $h^{-1}$, then it is classified as convective. Otherwise, it is assumed to be stratiform if the standard deviation of rain rate is ≤1.5 mm $h^{-1}$.

The PDF distribution of rain rate shows that the peak frequency is higher for convective distribution than for the

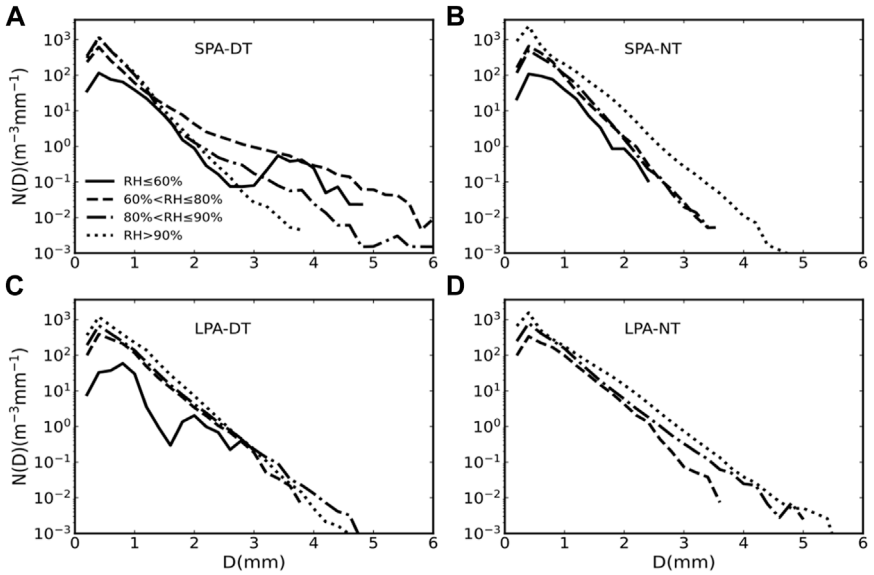


**FIGURE 7 |** Mean raindrop concentration in the DT and NT of SPA **(A,B)** and LPA **(C,D)** under different RH condition.

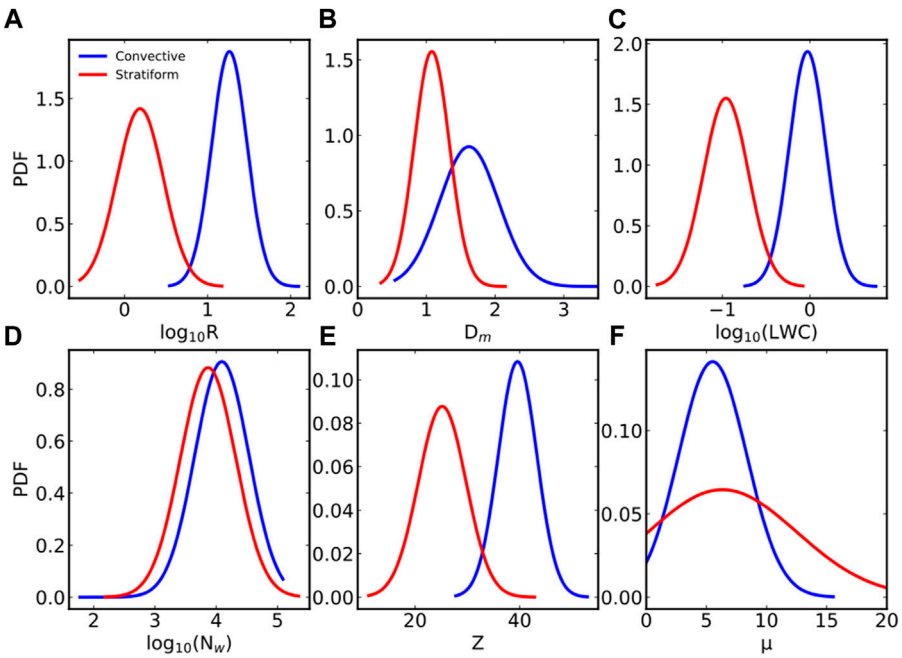


**FIGURE 8 |** The probability distribution functions (PDFs) of **(A)** rain rate, $\log_{10}$R(mm h$^{-1}$), **(B)** mass-weighted mean diameter, Dm(mm), **(C)** liquid water content, $\log_{10}$LWC(g m$^{-3}$), **(D)** normalized intercept parameter, $\log_{10}N_w$ (m$^{-3}$mm$^{-1}$), **(E)** radar reflective, Z,**(F)** shape parameter, μ for convective and stratiform rainfall in SPA.

stratifrom distribution in SPA when $\log_{10}R > 0.8$ dB (**Figure 8A**). The $D_m$ distribution curve in convective is distinctly different from stratiform, and the Dm distribution shows peak PDF values around 1.4–1.8 mm in convective rainfall and around 0.7–1.2 mm in stratiform rainfall(**Figure 8B**). The PDF of liquid water content ($\log_{10}$LWC) shows a similar distribution curves with log10R and a comparatively more frequency in convective compared to stratiform for $\log_{10}LWC > -0.6$ dB(**Figure 8C**). The probability distribution of normalized intercept parameter ($\log_{10}N_w$) shows a higher percentage at lower $\log_{10}N_w$ values in stratiform and a higher percentage at higher $\log_{10}N_w$ values in convective rainfall(**Figure 9D**). The radar reflectivity (Z) distribution shows peak PDF values at 40 dBZ is higher in convective

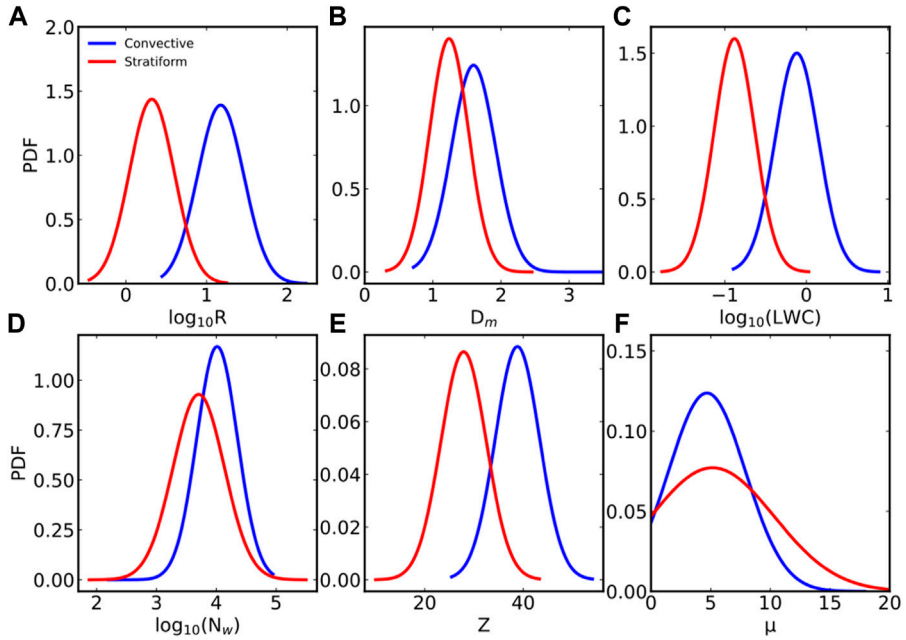


**FIGURE 9 |** The probability distribution functions (PDFs) of **(A)** rain rate, $\log_{10}$R(mm $h^{-1}$), **(B)** mass-weighted mean diameter, Dm(mm), **(C)** liquid water content, $\log_{10}$LWC(g $m^{-3}$), **(D)** normalized intercept parameter, $\log_{10}$Nw ($m^{-3}mm^{-1}$)), **(E)** radar reflective, Z, **(F)** shape parameter, μ for convective and stratiform rainfall in LPA. The blue and red lines represent the PDF of convective and stratiform precipitation, respectively.

rainfall than that of stratiform rainfall (23dBZ, **Figure 8E**). The distribution of μ is higher in stratiform than convective rainfall for μ>10(**Figure 8F**), which suggests a narrower RSDs shape in stratifrom than convective rainfall.

Comparing with the probability distribution functions (PDFs) of the integral parameters in SPA, overall, there are some differences between probability distributions of RSDs in SPA and LPA (**Figure 9**). The PDF peaks of rain rate and LWC in stratiform rainfall for LPA are higher than that of convective rainfall, and these characteristics are exactly the opposite of SPA. The distribution of rain rate, $D_m$, and the shape parameter highlights the dominance of light, small-moderated drop rainfall with narrow size spectra in the stratiform than the convective rainfall. To further confirm the contribution of different size raindrops to the formation of SPA and LPA, the frequency distributions of different raindrop sizes in convective and stratiform regimes for SPA and LPA are given in **Figure 10**. For ease of description, the raindrops sizes are divided into very small (the diameter is smaller than 0.7 mm), small size (0.7–1.4 mm), medium size (1.4–2.44 mm) and large size (greater than 2.4 mm) (Hopper et al., 2019; Huang et al., 2021). We found that the stratiform precipitation in DT and NT for SPA is dominated by 0.7–1.44 mm, the convective precipitation of DT for this type was dominated by large sized raindrops, and NT convection is dominated by 1.4–2.44 mm. For LPA, the raindrops diameter distribution is relatively uniform, with small size raindrops accounting for 78.5% and 62% of DT and NT in stratiform precipitation, respectively, while convection rainfall is dominated by medium size raindrops (the frequencies of DT and NT are 67% and 86%, respectively).

## 4 DISCUSSION AND CONCLUSION

The diurnal variations of RSD characteristics in different precipitation system and different duration of precipitation by the influences of relative humidity have been investigated based on the RSD spectra from 2DVD deployed at ZG. Along with the 2DVD, hourly rainfall, temperature (T) and relative humidity(RH) values from the *in situ* AWS, as well as ERA-Interim data are used

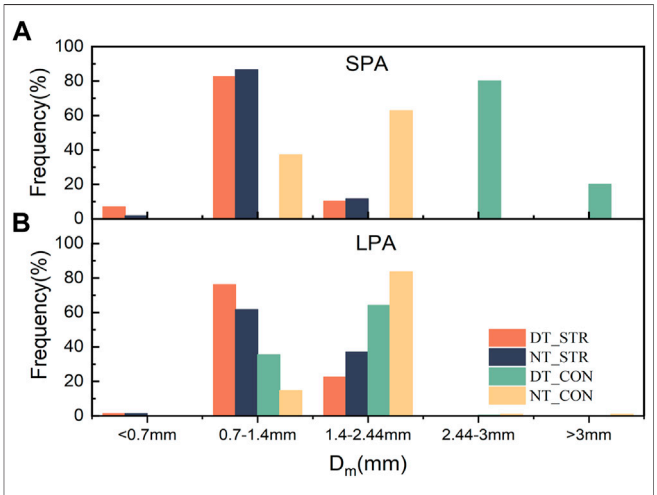


**FIGURE 10 |** The Dm frequency of convective and stratifrom during DT and NT for SPA **(A)** and LPA **(B)**.

to illustrate the effect of relative humidity on the diurnal variations and its connections to the microphysical mechanism.

The synoptic background of the ZG region are different from those of the plain and plateau of China(Volker et al., 2008; Zhou et al., 2008), the southwest warm and humid airflow formed a vortex around the mountain range nearby ZG region, and the average relative humidity of this vortex was maintained above 80%. In the context of the climatic condition, the frequency and intensity of precipitation show a bimodal structure, namely, a peak of precipitation frequency mainly appeared at 09:00 BJT and 23:00 BJT, and the peak of precipitation intensity mainly appeared at 18:00 BJT and 22:00 BJT.

The diurnal variation of precipitation has a relation with the RSD characteristics, we found that the $D_m$-$N_w$ distributions of daytime (DT) and nighttime (NT) is close to the "maritime-like" cluster. Overall, the relative large $D_m$ and small $\log_{10}N_w$ are displayed during the relative dry (RH<60%). Based on the classification of the SPA (Short-duration precipitation Amount) and LPA(Long-duration precipitation Amount), the RSDs shape of SPA_DT and LPA_DT show a triple peaks when the RH is less than 60%, and the RSDs structure in other RH conditions are single peak. A remarkable difference in the RSDs of DT between SPA and LPA is that the RSDs shape of SPA_DT is generally concave upward, and the RSDs shape of LPA_DT is generally concave downward. It indicates that the RSDs of LPA is mainly controlled by the collision-coalescence and breakup in warm clouds. In the case of lower RH condition, the melting and collision-coalescence of large raindrops in SPA_DT are obviously stronger than those of LPA_DT. Compared with the night difference in the RSDs of SPA, the RSDs of LPA_NT shows a broader distribution than that of DT, which is opposite to the day-night RSD difference of SPA.

In addition, statistical analysis is performed for the contribution of different scale particles to different types of precipitation in SPA and LPA. The results show that the stratiform precipitation in SPA is dominated by the raindrop diameter of 0.7–1.44 mm, the convective precipitation of DT for this type is dominated by large sized raindrops, and NT convection is dominated by medium size raindrops (1.4–2.44 mm). For the stratiform of LPA, the raindrops with small size raindrops accounting for 78.5% and 62% in the DT and NT, respectively. But for convection rainfall is dominated by medium size raindrops (the frequencies of DT and NT are 67% and 86%, respectively).

This study has provided some new insights into the diurnal variation of RSDs and the associated the ground meteorological condition for the different types and durations, which was utilized to address the diurnal variations of precipitation and RSDs, the RSDs differences of SPA and LPA and the effect of relative humidity on RSDs in different precipitation. Effects of other factors on the diurnal variation of RSD, for example, horizontal and vertical winds, and its impact on the diurnal variation of RSDs will been quantitatively studied in the future study. Of course, it is necessary to extract more information about the evolution of RSD from other observations, including polarimetric radars, micro rain radar, and microwave radiometers. The understanding would greatly benefit from additional information, such as the hydrometer types, hydrometer spatial distributions, raindrops fall velocity, the evolution of RSD with height and liquid water mass. For the follow-up studies, the above information and wind tower data will be analyzed to improve the conclusions.

## DATA AVAILABILITY STATEMENT

The datasets presented in this study can be found in online repositories. The names of the repository/repositories and accession number(s) can be found below: https://cds.climate.copernicus.eu/.

## AUTHOR CONTRIBUTIONS

JS: Conceptualization, methodology, writing-original draft, visualization. RW: Validation, supervision, funding acquisition. YZ: Conceptualization, writing- review and Editing.

## FUNDING

This research was funded by the National key R&D Program of China (Grant No. 2018YFC1507201), and the National Natural Science Foundation of China (Grant No. 41875170) and The Open Grants of the State Key Laboratory of Severe Weather (Grant No.2021LASW-A03).

## REFERENCES

Abel, S. J., and Boutle, I. A. (2012). An Improved Representation of the Raindrop Size Distribution for Single-Moment Microphysics Schemes. *Q.J.R. Meteorol. Soc.* 138, 2151–2162. doi:10.1002/qj.1949

Adirosi, E., Gorgucci, E., Baldini, L., and Tokay, A. (2014). Evaluation of Gamma Raindrop Size Distribution Assumption through Comparison of Rain Rates of Measured and Radar-Equivalent Gamma DSD. *J. Appl. Meteor. Climatol.* 53, 1618–1635. doi:10.1175/JAMC-D-13-0150.1

Atlas, D., and Ulbrich, C. W. (2000). An Observationally Based Conceptual Model of Warm Oceanic Convective Rain in the Tropics. *J. Appl. Meteor.* 39, 2165–2181. doi:10.1175/1520-0450(2001)040<2165:AOBCMO>2.0.CO;2

Bringi, V. N., Chandrasekar, V., Hubbert, J., Gorgucci, E., Randeu, W. L., and Schoenhuber, M. (2003). Raindrop Size Distribution in Different Climatic Regimes from Disdrometer and Dual-Polarized Radar Analysis. *J. Atmos. Sci.* 60 (2), 3542–4365. doi:10.1175/1520-0469(2003)0602.0.CO10.1175/1520-0469(2003)060<0354:rsdidc>2.0.co;2

Chen, B., Hu, Z., Liu, L., and Zhang, G. (2017). Raindrop Size Distribution Measurements at 4,500 M on the Tibetan Plateau during TIPEX-III. *J. Geophys. Res. Atmos.* 122, 092–111. doi:10.1002/2017JD027233

Chen, H., Yu, R., Li, J., Yuan, W., and Zhou, T. (2010). Why Nocturnal Long-Duration Rainfall Presents an Eastward-Delayed Diurnal Phase of Rainfall Down the Yangtze River Valley. *J. Clim.* 23 (4), 905–917. doi:10.1175/2009JCLI3187.1

Dolan, B., Fuchs, B., Rutledge, S. A., Barnes, E. A., and Thompson, E. J. (2018). Primary Modes of Global Drop Size Distributions. *J. Atmos. Sci.* 75, 1453–1476. doi:10.1175/JAS-D-17-0242.1

Fan, J., Zhang, R., Li, G., and Tao, W.-K. (2007). Effects of Aerosols and Relative Humidity on Cumulus Clouds. *J. Geophys. Res.* 112 (D14), D14204. doi:10.1029/2006JD008136

Gorgucci, E., Scarchilli, G., Chandrasekar, V., and Bringi, V. N. (2001). Rainfall Estimation from Polarimetric Radar Measurements: Composite Algorithms Immune to Variability in Raindrop Shape-Size Relation. *J. Atmos. Ocean. Technol.* 18, 1773–1786. doi:10.1175/1520-0426(2001)018%3C1773:REFPRM%3E2.0.CO;210.1175/1520-0426(2001)018<1773:refprm>2.0.co;2

Han, H., Wu, H. M., and Huang, A. N. (2017). Temporal and Spatial Distributions of the Diurnal Cycle of Summer Precipitation over North China. *Chin. J. Atmos. Sci. (in Chinese)* 41 (2), 263–274. doi:10.3878/j.issn.1006-9895.1610.15312

Held, I. M., and Soden, B. J. (2006). Robust Responses of the Hydrological Cycle to Global Warming. *J. Climate* 19, 5686–5699. doi:10.1175/JCLI3990.1

Hopper, L. J., Schumacher, C., Humes, K., and Funk, A. (2019). Drop-Size Distribution Variations Associated with Different Storm Types in Southeast Texas. *Atmosphere* 11, 8. doi:10.3390/atmos11010008

Hu, Z., and Srivastava, R. C. (1995). Evolution of Raindrop Size Distribution by Coalescence, Breakup, and Evaporation: Theory and Observations. *J. Atmos. Sci.* 52 (10), 1761–1783. doi:10.1175/1520-0469(1995)052<1761:eorsdb>2.0.co;2

Huang, C., Chen, S., Zhang, A., and Pang, Y. (2021). Statistical Characteristics of Raindrop Size Distribution in Monsoon Season over South China Sea. *Remote Sensing* 13, 2878. doi:10.3390/rs13152878

Jiang, L., Li, G., and Wang, X. (2015). Comparative Study Based on TRMM Data of the Heavy Rainfall Caused by the Tibetan Plateau Vortex and the Southwest Vortex. *Chinese. J. Atmos. Sci.* 39 (2), 249–259. doi:10.3878/j.issn.1006-9895.1407.13260

Kozu, T., Shimomai, T., Akramin, Z., MarzukiShibagaki, Y., Shibagaki, Y., and Hashiguchi, H. (2005). Intraseasonal Variation of Raindrop Size Distribution at Koto Tabang, West Sumatra, Indonesia. *Geophys. Res. Lett.* 32, a–n. doi:10.1029/2004GL022340

Krishna, U. V. M., Reddy, K. K., Seela, B. K., Shirooka, R., Lin, P.-L., and Pan, C.-J. (2016). Raindrop Size Distribution of Easterly and Westerly Monsoon Precipitation Observed over Palau Islands in the Western Pacific Ocean. *Atmospheric Research* 174-175, 41–51. doi:10.1016/j.atmosres.2016.01.013

Kumar, S., and Reddy, K. (2013). Rain Drop Size Distribution Characteristics Of Cyclonic And North East Monsoon Thunderstorm Precipitating Clouds Observed Over Kadapa (14°4′N, 78°82′E), Tropical Semi-Arid Region of India. *MAUSAM* 64 (1), 35–48. doi:10.54302/mausam.v64i1.653

Ma, Y., Ni, G., Chandra, C. V., Tian, F., and Chen, H. (2019). Statistical Characteristics of Raindrop Size Distribution during Rainy Seasons in the Beijing Urban Area and Implications for Radar Rainfall Estimation. *Hydrol. Earth Syst. Sci.* 23 (10), 4153–4170. doi:10.1155/2021/666778610.5194/hess-23-4153-2019

Ochs, H. T., Beard, K. V., Laird, N. F., Holdridge, D. J., and Schaufelberger, D. E. (1995). Effects of Relative Humidity on the Coalescence of Small Precipitation Drops in Free Fall. *J. Atmos. Sci.* 52 (21), 3673–3680. doi:10.1175/1520-0469(1995)052%3C3673:EORHOT%3E2.0.CO;210.1175/1520-0469(1995)052<3673:eorhot>2.0.co;2

Porcù, F., D'Adderio, L. P., Prodi, F., and Caracciolo, C. (2014). Rain Drop Size Distribution over the Tibetan Plateau. *Atmospheric Research* 150, 21–30. doi:10.1016/j.atmosres.2014.07.005

Qian, J.-H., Robertson, A. W., and Moron, V. (2010). Interactions Among ENSO, the Monsoon, and Diurnal Cycle in Rainfall Variability over Java, Indonesia. *J.Atmos.Sci.* 67 (11), 3509–3524. doi:10.1175/2010JAS3348.1

Rao, G. H. (2005). Orographic Precipitation. *Annu. Rev. Earth Planet. Sci.* 33, 645–671. doi:10.1146/annurev.earth.33.092203.122541

Rosenfeld, D., and Ulbrich, C. W. (2003). Cloud Microphysical Properties, Processes, and Rainfall Estimation Opportunities. *Meteorological Monographs* 30 (52), 237. doi:10.1175/0065-9401(2003)030<0237:cmppar>2.0.co;2

Ryzhkov, A. V., Giangrande, S. E., Melnikov, V. M., and Schuur, T. J. (2005). Calibration Issues of Dual-Polarization Radar Measurements. *J Atmos Ocean Technol* 22, 1138–1155. doi:10.1175/JTECH1772.1

Schönhuber, M., Urban, H., Baptista, J. P., Randeu, W., and Riedler, W.(1994). Measurements of Precipitation Characteristics by a New Distrometer Preprints, Proceedings of Atmospheric Physics and Dynamics in the Analysis and Prognosis of Precipitation Fields, La Sapienza, Rome, Italy. Universita degli studi di Roma. 15–18.

Seela, B. K., Janapati, J., Lin, P.-L., Wang, P. K., and Lee, M.-T. (2018). Raindrop Size Distribution Characteristics of Summer and Winter Season Rainfall over North Taiwan. *J. Geophys. Res. Atmos.* 123, 602–611. doi:10.1029/2018JD028307

Sobel, A. H., and Bretherton, C. S. (2000). Modeling Tropical Precipitation in a Single Column. *J. Climate* 13, 43782–44392. doi:10.1175/1520-0442(2000)0132.0.CO10.1175/1520-0442(2000)013<4378:mtpias>2.0.co;2

Suh, S.-H., Kim, H.-J., Lee, D.-I., and Kim, T.-H. (2021). Geographical Characteristics of Raindrop Size Distribution in the Southern Parts of South Korea. *J. Climate. Appl. Meteor.* 60, 157–169. doi:10.1175/JAMC-D-20-0102.1

Suh, S.-H., You, C.-H., and Lee, D.-I. (2016). Climatological Characteristics of Raindrop Size Distributions in Busan, Republic of Korea. *Hydrol. Earth Syst. Sci.* 20, 193–207. doi:10.5194/hess-20-193-2016

Tang, Y. L., Xu, G. R., and Wan, R. (2022). Temporal and Spatial Distribution Characteristics of Short-Duration Heavy Rainfall in the Yangtze River Basin during the Main Flood Season of 2020. *Transactions of Atmospheric Sciences* 45 (2), 212–224. doi:10.13878/j.cnki.dqkxxb.20211124002

Thurai, M., Bringi, V. N., and May, P. T. (2010). CPOL Radar-Derived Drop Size Distribution Statistics of Stratiform and Convective Rain for Two Regimes in Darwin, Australia. *J. Atmos. Ocean. Technol.* 27 (5), 932–942. doi:10.1175/JAMC-D-20-0102.110.1175/2010jtecha1349.1

Thurai, M., Gatlin, P., Bringi, V. N., Petersen, W., Kennedy, P., Notaroš, B., et al. (2017). Toward Completing the Raindrop Size Spectrum: Case Studies Involving 2D-Video Disdrometer, Droplet Spectrometer, and Polarimetric Radar Measurements. *J.Appl.Meteorol.Climatic.* 56, 877–896. doi:10.1175/JAMC-D-16-0304.1

Tokay, A., Petersen, W. A., Gatlin, P., and Wingo, M. (2013). Comparison of Raindrop Size Distribution Measurements by Collocated Disdrometers. *J. Atmos. Ocean. Technol.* 30 (8), 1672–1690. doi:10.1175/JTECH-D-12-00163.1

Utsumi, N., Seto, S., Kanae, S., Maeda, E. E., and Oki, T. (2011). Does Higher Surface Temperature Intensify Extreme Precipitation? *Geophys. Res. Lett.* 38 (16), 239–255. doi:10.1029/2011GL048426

Volker, W., Andreas, B., Bauer, H. S., Kottmeier, C., Corsmier, U., Blyth, A. M., et al. (2008). The Convective and Orographically Induced Precipitation Study: A Research and Development Project of the World Weather Program for Improving Quantitative Precipitation Forecasting in Low-Mountain Regions. *Bull.Amer.Meteor.Soc* 89, 1477–1486. doi:10.1175/2008BAMS2367.1

Wang, X., Li, C., Yang, H., Wang, J., Fu, S., Wang, M., et al. (2020). Research Progress on East- Moving Cloud Clusters from the Qinghai-Tibet Plateau. *Torrential Rain and Disasters* 39 (5), 433–441. (in Chinese). doi:10.3969/j.issn.1004-9045.2020.05.001

Wen, L., Zhao, K., Zhang, G., Xue, M., Zhou, B., Liu, S., et al. (2016). Statistical Characteristics of Raindrop Size Distributions Observed in East China during the Asian Summer Monsoon Season Using 2-D Video Disdrometer and Micro Rain Radar Data. *J. Geophys. Res. Atmos.* 121, 2265–2282. doi:10.1002/2015JD024160

Xiaobing, Y., Chenliang, L., Tongzhao, H., and Zhonghui, J. (2021). Information Diffusion Theory-Based Approach for the Risk Assessment of Meteorological Disasters in the Yangtze River Basin. *Nat Hazards* 107 (3), 2337–2362. doi:10.1007/s11069-020-04418-6

Yihui, D., and Chan, J. C. L. (2005). The East Asian Summer Monsoon: An Overview. *Meteorol. Atmos. Phys.* 89 (1–4), 117–142. doi:10.1007/s00703-005-0125-z

You, Y., Ting, M., and Camargo, S. J. (2021). Heavy Rain-Producing Terrestrial Low-Pressure Systems Over East Asian Summer Monsoon Region: Evolution, Energetics, and Trend. *J.Climate.* 34, 1–40. doi:10.1175/JCLI-D-20-0667.1

Yu, R., and Li, J. (2012). Hourly Rainfall Changes in Response to Surface Air Temperature over Eastern Contiguous China. *J. Climate.* 25 (19), 6851–6861. doi:10.1175/JCLI-D-11-00656.1

Yu, R., Xu, Y., Zhou, T., and Li, J. (2007b). Relation between Rainfall Duration and Diurnal Variation in the Warm Season Precipitation over Central Eastern China. *Geophys. Res. Lett.* 34 (13), 1–4. doi:10.1029/2007GL030315

Yu, R., Zhou, T., Xiong, A., Zhu, Y., and Li, J. (2007a). Diurnal Variations of Summer Precipitation over Contiguous China. *Geophys. Res. Lett.* 34 (1), 223–234. doi:10.1029/2006GL028129

Yuter, S. E., Kingsmill, D. E., Nance, L. B., and Löffler-Mang, M. (2006). Observations of Precipitation Size and Fall Speed Characteristics within Coexisting Rain and Wet Snow. *J. Appl. Meteor. Climatol.* 45, 1450–1464. doi:10.1175/JAM2406.1

Zagrodnik, J. P., McMurdie, L. A., and Houze, R. A. (2018). Stratiform Precipitation Processes in Cyclones Passing over a Coastal Mountain Range. *J. Atmos. Sci.* 75, 983–1004. doi:10.1175/JAS-D-17-0168.1

Zhang, Y., Klein, S. A., Liu, C., Tian, B., Marchand, R. T., Haynes, J. M., et al. (2008). On the Diurnal Cycle of Deep Convection, High-Level Cloud, and Upper Troposphere Water Vapor in the Multiscale Modeling Framework. *J. Geophys. Res.* 113 (1-19), D16105. doi:10.1029/2008jd009905

Zhou, T., Yu, R., Chen, H., Dai, A., and Pan, Y. (2008). Summer Precipitation Frequency, Intensity, and Diurnal Cycle over China: A Comparison of Satellite Data with Rain Gauge Observations. *J.Climate.* 21 (16), 3997–4010. doi:10.1175/2008JCLI2028.1

**Conflict of Interest:** The authors declare that the research was conducted in the absence of any commercial or financial relationships that could be construed as a potential conflict of interest.

**Publisher's Note:** All claims expressed in this article are solely those of the authors and do not necessarily represent those of their affiliated organizations, or those of the publisher, the editors and the reviewers. Any product that may be evaluated in this article, or claim that may be made by its manufacturer, is not guaranteed or endorsed by the publisher.

frontiers | Frontiers in Environmental Science

ORIGINAL RESEARCH
published: 05 July 2022
doi: 10.3389/fenvs.2022.946020

# 3D Corona Discharge Model and Its Use in the Presence of Wind During a Thunderstorm

*Xiufeng Guo*[1,2,3]*, *Ziyu Ji*[3], *Yue Gao*[3], *Jie Ding*[3] and *Ling Zhang*[3]

[1]College of Atmosphere and Remote Sensing, Wuxi University, Wuxi, China, [2]State Key Laboratory of Severe Weather, Chinese Academy of Meteorological Sciences, Beijing, China, [3]College of Electronic and Information Engineering, Nanjing University of Information Science and Technology, Nanjing, China

In this study, the authors developed a three-dimensional (3D) numerical model for the diffusion of positive corona charges based on a 2D model with a uniform grid to explore the characteristics of corona discharge at a building tip during a thunderstorm in the presence of wind. The variable-grid meshing method is used to solve the problems of implementing a large simulation domain for thunder clouds (kilometer-scale) and the minute calculations of corona discharge at the tip (centimeter scale) in the 3D numerical simulation. The proposed model has advantages in terms of the acquisition of the parameters of corona charges and the spatial distribution of the electric field (E-field) in the environment. We used positive corona discharge at the tip of a building under a negative thunderstorm, along with three wind fields (horizontal wind, updraft, and downdraft with wind speeds of 10 m/s) as an example. The presence of the wind increased the density of corona charges at the tip, where the horizontal wind was the most beneficial for its occurrence. Moreover, the characteristics of distortion of the electric field around the tip were significantly different, owing to the different directions of the wind. Downdraft led to the maximum enhancement in the E-field above the tip, and updraft prompted the minimum increase in it, by only 1.19 times. However, the opposite results were obtained for the enhancement in the spatial range of the charges: The updraft led to the greatest increase in it, and the downdraft caused the smallest. Corona charges had an apparent shielding effect on the E-field below the tip and can even change the polarity of the E-field in a small area close to it. The strongest shielding effect on the ground E-field occurred in the case of the downdraft, which decreased the E-field to 0.36 times compared with that without the corona charges. On the contrary, corona discharge had the weakest shielding ability on the ground when it met the updraft. The horizontal wind had the largest range of shielding on the ground, of up to 14,699.36 $m^2$, while the updraft had the lowest, at only 6,170.91 $m^2$.

**Keywords: corona discharge, wind direction, 3D numerical simulation, charge distribution, electric field distribution, shielding effect**

OPEN ACCESS

***Edited by:***
*Lijuan Shen,*
*University of Toronto, Canada*

***Reviewed by:***
*Jinbo Zhang,*
*Jiangsu University of Science and Technology, China*
*Yi Yang,*
*Hebei Normal University, China*

***Correspondence:**
*Xiufeng Guo*
*guoxf_88@163.com*

***Specialty section:***
*This article was submitted to Atmosphere and Climate, a section of the journal Frontiers in Environmental Science*

***Received:*** *17 May 2022*
***Accepted:*** *26 May 2022*
***Published:*** *05 July 2022*

***Citation:***
*Guo X, Ji Z, Gao Y, Ding J and Zhang L (2022) 3D Corona Discharge Model and Its Use in the Presence of Wind During a Thunderstorm. Front. Environ. Sci. 10:946020. doi: 10.3389/fenvs.2022.946020*

## INTRODUCTION

Corona discharge is the phenomenon whereby the local electric field (E-field) at the tip of the building exceeds the breakdown threshold of air. Large-scale laboratory simulations and field observations have shown that the initial E-field of corona discharge (Peek, 1929) and the relationship between the corona-induced current and the environmental E-field (Zhou et al., 1965; Lu et al., 2010; Yanhui et al., 2021) are influenced by many factors, such as the shape and material of the tip, the terrain, and characteristics of the thunderstorm E-field (Golde, 1977; Standler and Winn, 1979; Chauzy and Raizonville, 1982; Qie et al., 1994; Soula, 1994). Zhang et al. (2016) measured corona charges in the air in the range from several hundred to thousands of meters above the ground, with an average magnitude of about 1 nC/m$^3$. The observations verified the 1D characteristics of the distribution of the average values of the corona charge, but it is difficult to obtain its 3D spatial distribution and the characteristics of its evolution over time.

The numerical simulation of corona discharge can compensate for the insufficiency of observational data, from which the distribution of corona charges is difficult to obtain. Aleksandrov et al. (2001) and Aleksandrov et al. (2002) established a 1D model for the initialization and diffusion of corona ions and discussed the effects of the characteristics of the tip on corona discharge and its use in the design of lightning rods in subsequent studies (Aleksandrov et al., 2005a; Aleksandrov et al., 2005b). Becerra (2013) extended the 1D model to a 2D symmetric model to clarify the characteristics of the distribution of corona ions around the lightning rod. However, neither model can be used to simulate tips with asymmetric structures. Guo et al. (2017) established a time-dependent model of corona discharge with a uniform grid meshing in a 2D Cartesian coordinate system by using Peek's formula to calculate the thresholds of corona discharge at the tips of different structures. The model overcomes the shortcomings of the existing 1D and 2D axisymmetric models. Simulations of corona discharge under different wind conditions and on multiple tips were achieved. Chen (2018) established a model of corona discharge for 2D high-voltage transmission lines and discussed the spatiotemporal evolution of corona ions around the line of the E-field during a thunderstorm. However, the limitations to the 2D model, such as the inability to obtain the characteristics of the spatiotemporal evolution of corona charges in 3D space and the underestimation of the E-field and the effects of its distortion (lack of a horizontal component), highlight the need to carry out high-resolution 3D simulations of this phenomenon.

To sum up, methods of observation are inadequate for research on corona discharge at the tip of buildings during a thunderstorm, and 3D numerical simulations can be used as a supplement. At the same time, a balance needs to be struck between the large simulation domain required to represent thunder clouds (the kilometer scale) and the minute calculations involved in discharges (the centimeter scale). This study develops a 3D numerical model of the diffusion of positive corona charges with variable-grid meshing based on a 2D uniform model and considers the presence of the E-field of the thunderstorm and the wind field. The model is applied to examine the influence of wind on corona discharge in buildings and to identify the characteristics of variations in each corona-related parameter with the wind field. The aim was to reveal the influence of wind on various aspects of corona discharge.

## MATERIALS AND METHODS

### Introduction to the Model

The authors used the 2D model developed by Guo et al. (2017) and their discussion of the corona current and the E-field in the presence of wind to establish a corresponding 3D model. We used three steps similar to those used in Guo et al.'s model: Peek's formula, Kaptzov assumption, and diffusion–convection equations.

The environmental E-field gradually increases in the upward direction under an approaching thunderstorm cloud with a negative polarity. Due to its distortion by the shape of the tip, the E-field on the surface of the tip exceeds the threshold E-field, called $E_{cor}$, and a positive corona discharge is initiated at the tip of the building. $E_{cor}$ is defined in Peek's law as a constant for a certain building and a given relative atmospheric density.

Over time, the surface of the tip generates corona ions, and the number of ions can be determined by using the Kaptzov assumption such that the value of the E-field at the tip should be maintained at $E_{cor}$. To calculate the number of small positive ions created on the surface of the lightning rod according to the Kaptzov assumption, the E-field on the surface should be maintained within the range of $E_{cor}$ ±2% in this model.

We referred to the diffusion–convection continuity equation coupled with the wind field, proposed by Guo and Zhang (2017), for the newly generated ions. We considered only small positive ions $n_+$, large positive ions $N_+$, and aerosol neutrals $N_a$ and calculated the diffusion, convection, and transformation as follows, respectively:

$$\frac{\partial n_+}{\partial t} = D\nabla^2 n_+ - \nabla\left[n_+\left(\mu_{n_+}\boldsymbol{E} + \boldsymbol{\nu}\right)\right] - k_{nN} n_+ N_a,$$

$$\frac{\partial N_+}{\partial t} = D\nabla^2 N_+ - \nabla\left[N_+\left(\mu_{N_+}\boldsymbol{E} + \boldsymbol{\nu}\right)\right] + k_{nN} n_+ N_a,$$

$$\frac{\partial N_a}{\partial t} = D\nabla^2 N_a - \nabla\left(N_a\boldsymbol{\nu}\right) - k_{nN} n_+ N_a,$$

where $t$ represents time, $D$ is the coefficient of turbulent diffusion, $\mu_{n+}$ is the mobility of small positive ions, $\mu_{N+}$ is the mobility of large positive ions, and $k_{nN}$ is the rate of adsorption of aerosol particles to small ions. The reference values (Qie et al., 1994; Qie, 1996; Becerra et al., 2007; Becerra, 2013) of $D$, $\mu_{n+}$, $\mu_{N+}$, and $k_{nN}$, are 1 m$^2$/s, 1.5 × 10$^{-4}$ m$^2$/(V·s), 1.5 × 10$^{-6}$ m$^2$/(V·s), and 2.9 × 10$^{-12}$ m$^3$/s, respectively. $\boldsymbol{\nu}$ is the wind field, $\boldsymbol{E}$ is the electric field, and both are vectors. The E-field $\boldsymbol{E}$ is calculated by the negative gradient of the electric potential $\varphi$:

$$\boldsymbol{E} = -\nabla\varphi.$$

The electric potential can be solved by transforming the Poisson equation of the electrostatic field into an over-relaxed iteration (SOR) form as follows:

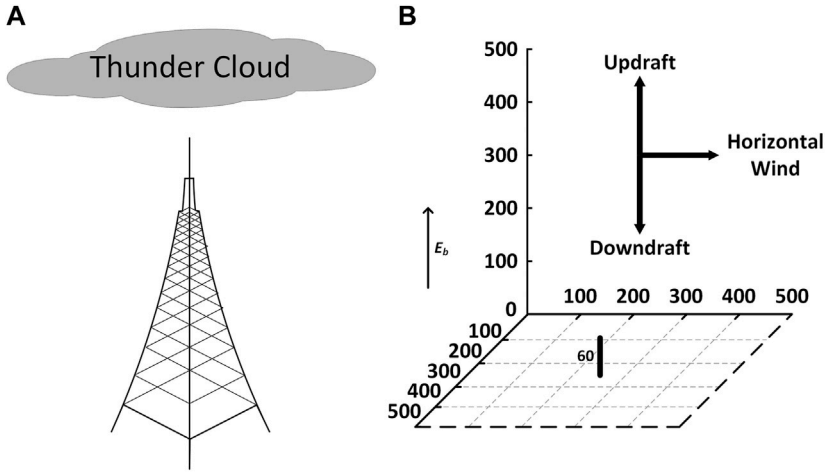


**FIGURE 1 |** Signal tower **(A)** and model settings **(B)**. All units of distance in **(B)** are meters.

$$\nabla^2\varphi = -\frac{e_0\,(n_+ + N_+)}{\varepsilon_0},$$

where $e_0$ is the charge of the electron, and $\varepsilon_0$ is the permittivity of the vacuum.

The boundary conditions for the continuous equations are defined as follows: for all outside boundaries, the corona charges are set to absorption, and all differential terms are reduced to zero. The boundaries of the building are divided into two types. The first consists of points of the corona discharge, which are regarded as forming a fixed boundary. They do not participate in previous continuity equations except in the case of the wind field, and the number of small ions depends only on the Kaptzov assumption. The second boundary is obtained when the number of small ions is approximated by using the forward difference method.

## Model Settings

During the formation of a negatively charged thundercloud, the thunderstorm background E-field ($E_b$) changes relatively slowly and can be regarded as an electrostatic field. Since the thunderstorm cloud has a large range and a high distance from the ground, the E-field near the ground can be approximated as a uniform E-field with its direction perpendicular to the ground. Thus, according to Becerra (2013) and Guo et al. (2017), it is assumed that $E_b$ increases linearly up to 20 kV/m in 10 s and then remains constant. The simulation domain was a 500 m × 500 m × 500 m region above the ground with a signal tower in the center. We did not consider the shape of the building and other complex characteristics in the simulation but were concerned only with the characteristics of discharge at the tip because they make a major contribution to the corona discharge. The building was represented as a cube, with a length and width of 10 cm and a height of 60 m, at the center of the simulation domain. **Figure 1** shows a schematic diagram of the model.

The uniform 2D grid mesh struggles to simulate small tips in a large simulation domain for the 3D simulation of corona discharge. If the uniform mesh generation method is used on 3D simulation, it is hard to complete under the existing personal computer storage conditions. The proposed model uses variable-grid meshing to deal with this problem, where which has two advantages over the previous model. First, the 3D model can obtain specific data on the spatial parameters and compensate for the shortcomings of the 2D model, especially the values on the ground. Second, the variable-grid meshing technology can expand the simulation domain to a greater extent while simulating small tips, which makes the model more flexible and accurate than the one that uses uniform grids. The computation time required for such a large amount of data should not be ignored. We parallelized the calculation of the E-field to speed up the computation.

It is necessary to verify the calculation of the E-field of the model. We compared its result with that of the commercial software COMSOL based on a finite element simulation. To ensure the consistency of comparison, the minimum grid needed to be set to the same size for both as this mostly affects the E-field of the tip. The minimum grid in both models was 10 cm while the maximum grid in the variable-grid meshing-based model was 27.1 m. COMSOL used tetrahedrons to discretize the space, with a maximum mesh size of 20 m. A comparison of the variations in the E-field with the height above the tip is shown in **Figure 2**. When the environmental E-field was set to −10 kV/m, the results of COMSOL were consistent with those of the proposed model. This verifies the reliability of the 3D variable-grid meshing-based calculation of the E-field by the model.

Given that the minimum grid at the tip was 10 cm, the temporal resolution needed to be less than 1,343 μs to match this spatial resolution and ensure the stability of the results of the differential form. We used a temporal resolution of 500 μs

## Model Validation

We compared the proposed model with Becerra's 2D symmetric model for corona discharge and Guo et al.'s 2D

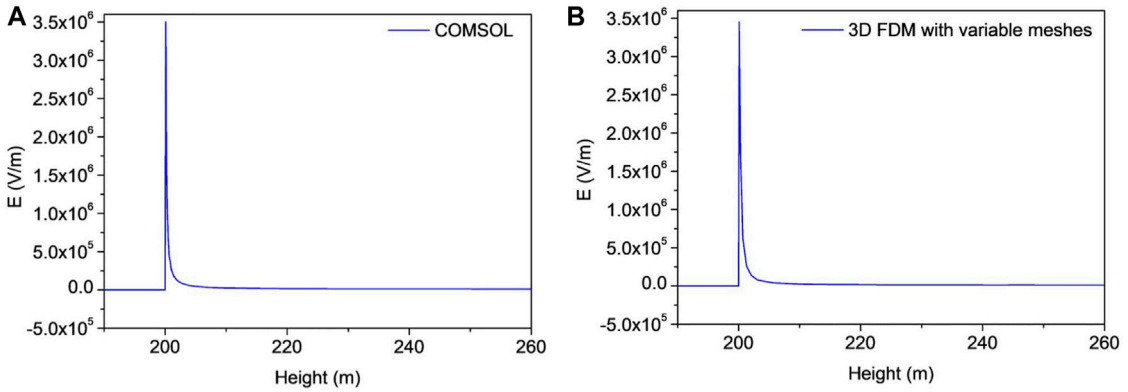


**FIGURE 2 |** Variation in the E-field above the tip when the background E-field was −10 kV/m. **(A)** Result of calculation by COMSOL. **(B)** Result of calculation by the proposed model.

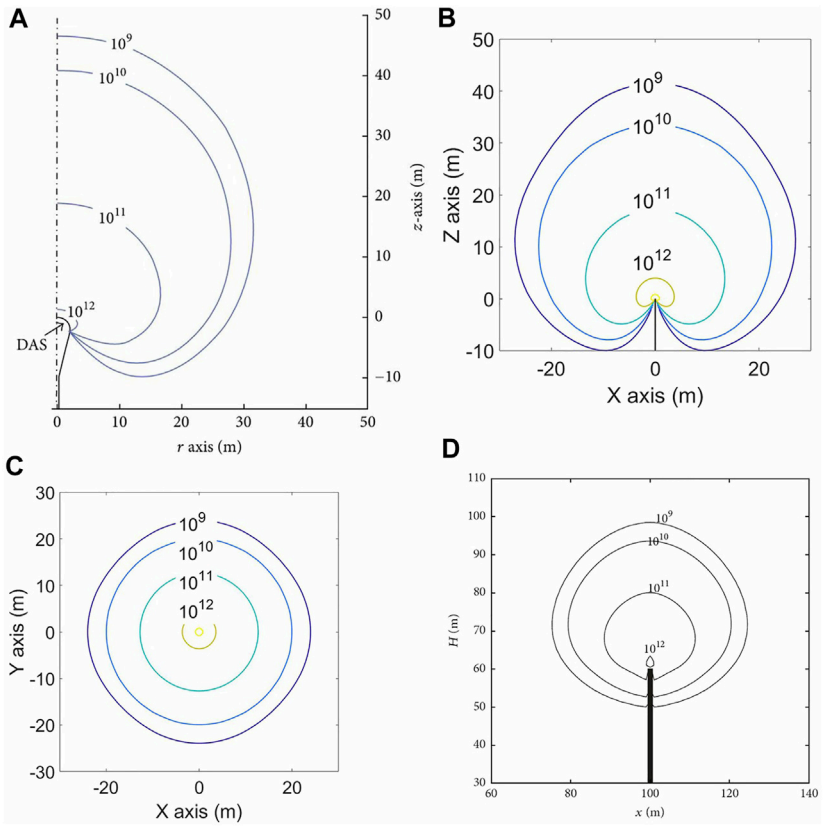


**FIGURE 3 |** Comparison of the range of diffusion of small ions when the environmental E-field reached its peak. **(A)** shows the result of Becerra's model, **(B)** and **(C)** show results of the proposed model, where directions are divided into the side view and the top view. **(D)** shows the result of Guo et al.'s model.

asymmetric model along two dimensions: the range of diffusion of small ions and the corona current. **Figure 3** shows the distribution of small ions as calculated by the three models when the environmental E-field reached its peak value. **Figures 3A,B** show that the number of small ions at the tip and their range of diffusion calculated by the 3D model matched well with those of Becerra's model. **Figure 3C** shows the top view of the distribution due to the advantage of the 3D simulation. **Figure 3D** shows the result of the 2D model. It encountered such problems as an overestimation of small ions below the tip and a smaller range of diffusion than the proposed method.

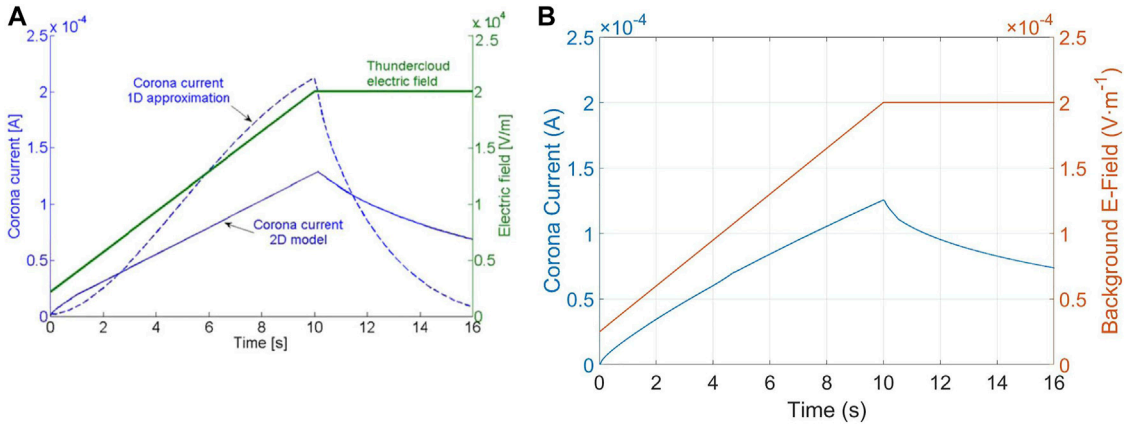


**FIGURE 4 |** Comparison of corona currents at the tip under a certain environmental E-field obtained by using two models. **(A)** is the result of Becerra's model, and **(B)** is the result of the proposed model.

**Figure 4** shows a comparison of the relationship between the corona current and time according to the proposed model and Becerra's model. The two models exhibited the same trend whereby the corona current and environmental E-field increased to their maximum values, after which the corona current slowly decreased while the environmental E-field remained constant. This comparison also verifies the correctness of the proposed 3D model.

# RESULTS

## Effects of Wind on the Diffusion of Corona Charges

Due to the presence of the wind, the convective force for corona charges not only come from the E-field, but the wind also plays an important role here. Different wind conditions lead to different corona charge spatial distributions and then lead to different E-field spatial distributions. The authors discussed cases without any wind and those involving the presence of horizontal wind, updraft, and downdraft at a speed of 10 m/s. Of note is the fact that the speed of wind is one of the important factors in corona discharges which have been discussed via 2D numerical simulation shown in Guo et al. (2017). However, the aim of this study was to show the 3D numerical model has more preponderance than the 2D model in obtaining characteristics of corona charges and E-field distribution. Different wind directions lead to different sharpness of the corona charge distribution, while different speeds only lead to the different sizes of the sharpness. Therefore, the effects of wind on corona discharge were mostly focused on its direction in this study. **Figure 5** shows the range of diffusion and density of the corona charges under different conditions when the E-field reached its maximum value. Because this is a 3D model, the side and top views are both provided to better represent the physical process.

The first considered the maximum magnitude of corona charges at the tip, where this is also directly related to the corona current. The top charge reached its highest value of $1.59 \times 10^5$ nC/m$^3$ in the presence of horizontal wind, followed by $1.20 \times 10^5$ nC/m$^3$ in the case of the updraft, $1.19 \times 10^5$ nC/m$^3$ in case of the downdraft, and $1.18 \times 10^5$ nC/m$^3$ in the absence of wind. The horizontal wind had a greater effect on the diffusion of ions than the other conditions, and their corona currents might have increased accordingly.

We combined the side and the top views and took the range of corona charge density greater than 0.1 nC/m$^3$ as an example. The results showed that in the absence of wind, the distribution of corona charge was symmetrical and was mainly concentrated in the range of 60 m from the tip. With the occurrence of wind, the corona charges had a strong tendency to follow its direction. The presence of wind thus changed the direction of motion of the corona charges by adding a new dynamic. The presence of the downdraft constituted a special case. The corona charges accumulated above the ground and below the tip in this case. Moreover, in the case of horizontal wind conditions, the corona charge diffusion range in the horizontal direction was larger than the others; it reached 120 m away from the tip along the horizontal wind direction (from west to east) while 60 m in the normal direction (from south to north) in this case. Therefore, the effects of wind on the diffusion of corona charges were significant. The range of diffusion could be achieved by the 3D numerical model developed in this study but could not be represented by the 2D models.

## Characteristics of the E-Field Around a Building During Corona Discharges in Different Wind Conditions

The E-field around the building tip or at the ground nearby the building could be distorted by the corona charges released into the air during a thunderstorm. However, the degree and range of the E-field distortion would be affected by corona charges with different distribution characteristics in different wind conditions. Furthermore, the lightning monitoring results forecasted by using the ground E-field data in atmospheric electric field measurement

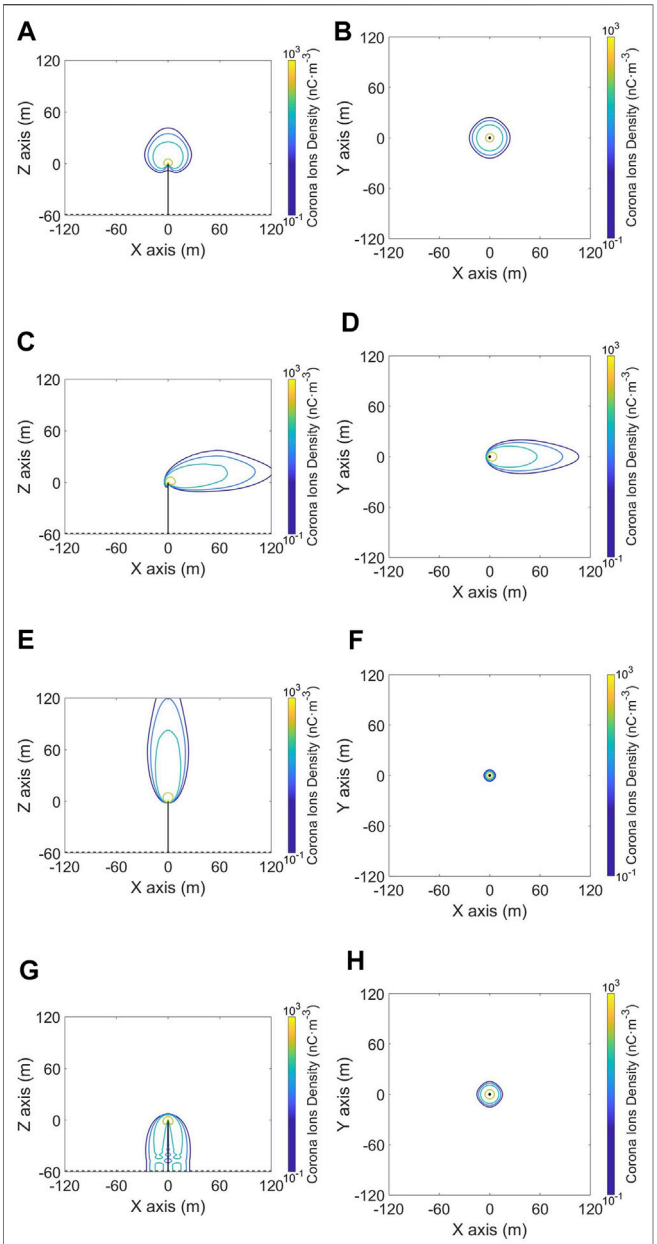


**FIGURE 5 |** Contours of the density of corona charges produced at the tip of a 60-m rod when the thunderstorm background E-field reached its maximum value (20 kV/m). The results are given in the case of no wind **(A,B)**, horizontal wind **(C,D)**, updraft **(E,F)**, and downdraft **(G,H)**. The side views are given to the left and the top views to the right.

early warning system would be affected. This E-field distortion around the building even affects the lightning stroking process on it. Therefore, this section will focus on analyzing the distortion characteristics of the corona charges to the environmental E-field under different wind conditions.

**Figure 6** shows the distribution of the vertical component of the E-field around the tip in different conditions. The distortion of the E-field only brought by the building is also given (**Figure 6A**) for comparing with the corona conditions (**Figures 6B–E**). We found that no matter what kind of wind condition, the influence of corona charges on the environmental E-field cannot be ignored. During a thunderstorm and after the corona discharge occurred at the tip, the distortion of the building tip on the surrounding E-field was magnified by corona charges released to the air from the tip, whether it is the enhancement of the E-field above the tip or the shielding effect below the tip.

Comparing the enhancement of corona charges on the E-field above the tip under different wind fields, it is found that in the absence of wind (shown in **Figure 6B**), the enhanced E-field above the tip spread roughly in a conical shape with a radius of 30 m. In the presence of horizontal wind (shown in **Figure 6C**), the E-field was enhanced in the upper-right direction, and its height remained constant at 30 m, but its horizontal range expanded to 60 m along the wind direction. The updraft extended the range of the enhanced E-field to 90 m above the tip (shown in **Figure 6D**), but the enhancement degree on the E-field was not much significant. Contrary to the case of the updraft, the range of the enhanced E-field above the tip is minimum in the downdraft (shown in **Figure 6E**), but the enhancement degree on the E-field was the greatest.

Comparing the shielding effect of corona charges on the E-field below the tip in different wind conditions, we found that the corona charges had a prominent shielding effect on the E-field below the tip and could even change its polarity in a small area close to the tip. Further study on the shielding effect of corona charges on the E-field below the building tip will be detailed in the following section.

## E-Field Distortion Caused by Corona Charges in Different Wind Conditions

As mentioned earlier, the influence of the tip on the E-field needed to be eliminated to clarify the enhancement or shielding effect of the corona charge on it. We thus defined the coefficient of electric field distortion $N$ as follows:

$$N = \frac{E_{corona}}{E_{original}},$$

where $E_{corona}$ is the environmental E-field obtained by considering the corona corresponding to **Figures 6B–E**, and $E_{original}$ is the environmental E-field without the corona charge, as shown in **Figure 6A**. If $N > 1$, this means that the E-field was enhanced by corona discharges; if $0 < N < 1$, it means that the E-field was shielded, and if $N < 0$, it means that the corona charges were too strong such that they prompted a negative enhancement in the E-field.

The aforementioned formula was used to draw **Figure 7**, which shows the distribution of the coefficient of distortion of the E-field, owing to different wind conditions. **Table 1** also provides the relevant specific values. Red in the graphs below indicates an enhancement in the E-field ($N > 1$). The darker the color, the greater is the enhancement. Blue indicates the shielding of the E-field ($N < 1$); the darker the color, the weaker is the E-field. Gray means no distortion ($N = 1$), where the original environmental E-field persisted. It should be noted

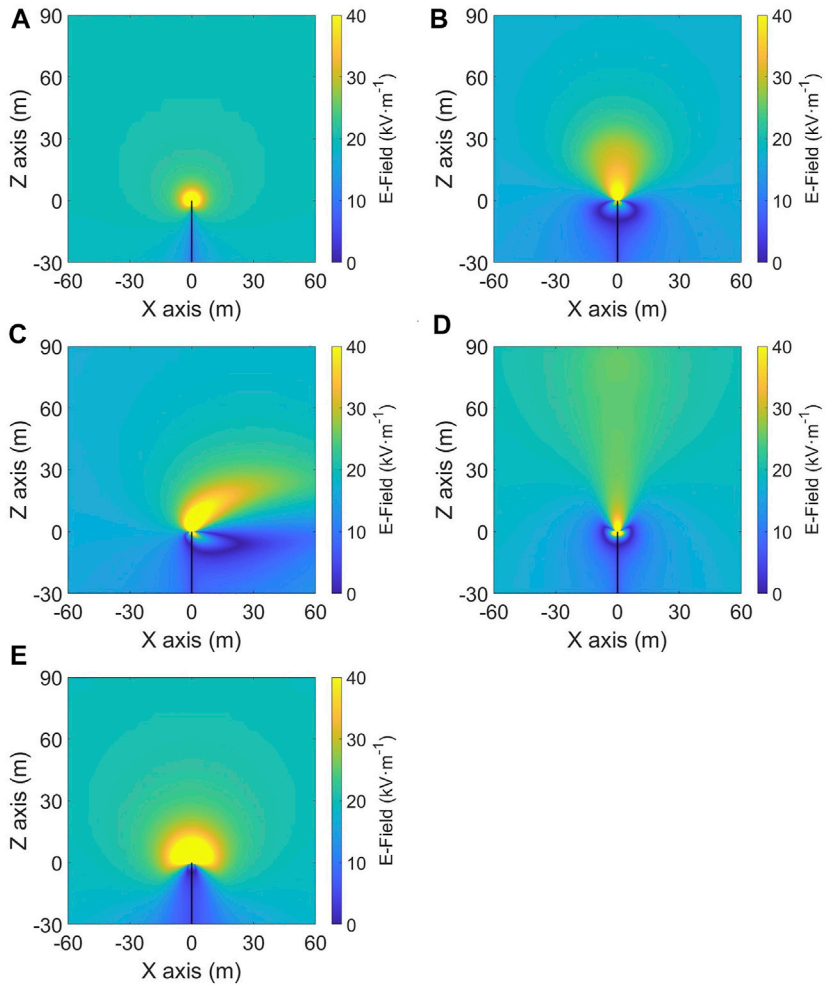


**FIGURE 6 |** Contours of the vertical component of E-field when the thunderstorm background E-field reached its maximum value (20 kV/m). No corona discharge **(A)**. No wind **(B)**. Horizontal wind **(C)**. Updraft **(D)**. Downdraft **(E)**.

that the top view could not be obtained by the 2D model. It was, however, obtained by the proposed model and can provide content for supplementary discussions of the impact of distortion in the E-field on the ground.

**Figure 7** and **Table 1** both show that the enhanced E-field above the tip and shielded it below, but the degrees and ranges of these enhancements and shielding effects were different. In side views, downdraft has the greatest enhancement on the environmental E-field, updraft is the smallest, and the reverse E-field (Minimum *N*) below the tip caused by different wind conditions kept the opposite trend. Regarding the enhancement range, updraft has the largest range that reaches to 4,213 $m^2$, while downdraft was the smallest only, reaching about 2042 $m^2$.

As for the shielding effect on the environmental E-field at the ground level, we can see these shielding degrees were quite different in different wind conditions. Corona charges have the greatest shielding effect at the ground level in $N = 0.36$ near the bottom of the building in the downdraft, while having a weak shielding effect in other wind conditions relatively. About the shielding range on the ground level, in a horizontal wind condition, it was the largest about 14,699 $m^2$ and nearly twice the size of others, while in the updraft condition, it was the smallest about 6,171 $m^2$.

Consequently, the E-field around the building tip or at the ground nearby the building was distorted in different degrees and ranges by corona charges from the tip with different distribution characteristics in different wind conditions, especially in a downdraft and in the horizontal wind during thunderstorms. This might be one of the reasons why for a certain building with the same lightning current, the strike distances were often different in observations (Rakov et al., 2018; Qi et al., 2019; Jiang et al., 2020). Therefore, in the process of leader initiation simulations, the influence of the corona discharge should not be ignored, while the existing leader initiation simulations (Becerra and Cooray, 2006; Cooray et al., 2014; Tan et al., 2016; Guo et al., 2019) ignored their effects mostly. In addition, when correcting the measurement results of the ground atmospheric E-field

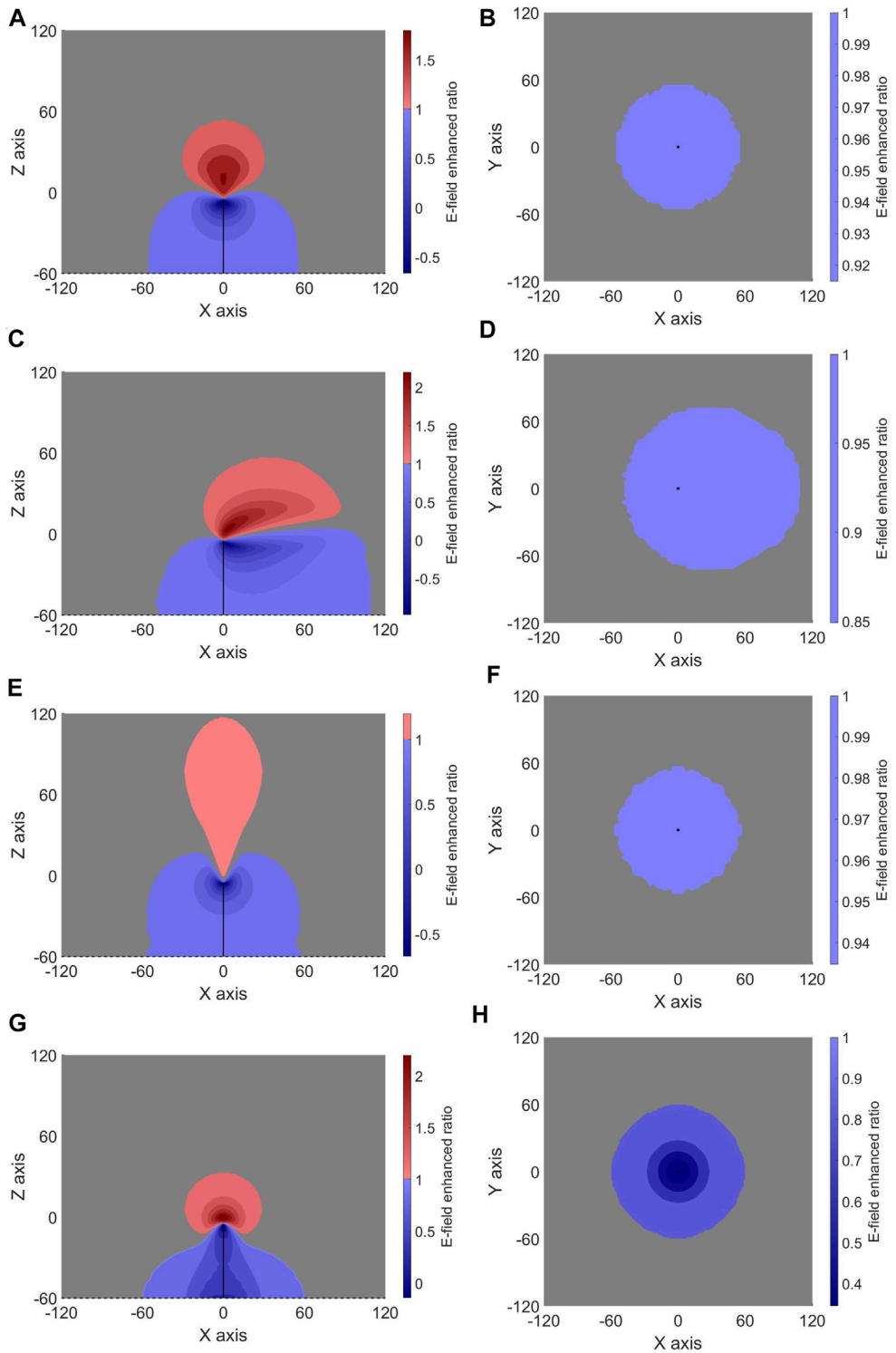


**FIGURE 7 |** Contours of distortion caused by corona charges in the E-field (N) around the building tip when the thunderstorm background E-field reached its maximum value (20 kV/m). No wind **(A,B)**. Horizontal wind **(C,D)**. Updraft **(E,F)**. Downdraft **(G,H)**. The left side shows the side views, and the right side shows the top view.

**TABLE 1 |** Properties of distortion caused by corona charges in the E-field (N and the range of influence) under different wind conditions when the background E-field reached its maximum value.

| Wind condition | Side view | | | On the ground | | |
|---|---|---|---|---|---|---|
| | Minimum *N* | Maximum *N* | Enhancement range ($m^2$) | Minimum *N* | Maximum *N* | Shielding range ($m^2$) |
| No wind | −0.53 | 1.74 | 2,610.84 | 0.92 | 1 | 7,788.15 |
| Horizontal wind | −0.58 | 1.98 | 3,831.67 | 0.85 | 1 | 14,699.36 |
| Updraft | −0.67 | 1.19 | 4,212.93 | 0.94 | 1 | 6,170.91 |
| Downdraft | −0.14 | 2.19 | 2041.62 | 0.36 | 1 | 6,956.03 |

and using its data as lightning warning studies (D'Alessandro, 2003; Aranguren et al., 2009; Ferro et al., 2012), we not only consider the influence of the building itself to the atmospheric E-field but also take the shielding effect of the corona charges and different wind fields to the ground E-field into consideration.

## CONCLUSIONS AND DISCUSSION

The influence of corona charges generated at the tip of a building on the grounded E-field during corona discharge and the effects of this on the subsequent lightning strike have long been a subject of interest in research. The influence of wind on corona discharge has been discussed numerically, but few studies have considered the influence of the direction of the wind in this context by using a 3D model. This study examined the influence of a specific wind field on corona discharge in the presence of thunderstorm clouds. The authors considered the density of the corona charges, the environmental E-field, and the distortion in it by establishing a 3D numerical model. The following conclusions can be drawn as follows:

1) The 3D model established here has advantages over the 2D model in terms of the acquisition of the relevant parameters, such as the spatial distribution characteristics of corona charges and the environmental E-field.
2) The presence of the wind field (horizontal wind, updraft, and downdraft with 10 m/s) increased the density of corona charges at the tip. The horizontal wind had the greatest effect, followed by the downdraft and updraft.
3) The corona charges distorted the E-field around the tip. The maximum enhancement in the E-field above the tip was in the case of a downdraft and was 2.19 times its normal value in the case of no corona, followed by that owing to the horizontal wind. The minimum enhancement was obtained by the updraft, that of only 1.19 times. On the contrary, the spatial range of the enhancement was the largest in the case of the updraft and the smallest in the case of the downdraft. Moreover, the corona charges had a prominent shielding effect on the spatial E-field below the tip and could even change its polarity in a small area close to the tip.
4) The corona discharge had a non-negligible shielding effect on the E-field on the ground. The shielding effect was the strongest in the case of a downdraft, which reduced the E-field to only 0.36 times its value without the corona. In the case of an updraft, the corona discharge had the weakest ability to shield the E-field on the ground. The range of shielding on the ground was the largest in the case of horizontal wind, up to 14,699.36 $m^2$, followed by the cases without wind, a downdraft, and an updraft (6,170.91 $m^2$).

The authors here developed a 3D model of corona discharge that provided some useful results for certain wind conditions. However, the subsequent lightning process also needs to be discussed in depth. Furthermore, we will examine corona discharges over multiple buildings and buildings with complex shapes in our future work in the area.

## DATA AVAILABILITY STATEMENT

The original contributions presented in the study are included in the article/Supplementary Material; further inquiries can be directed to the corresponding author.

## AUTHOR CONTRIBUTIONS

Original ideas and overall planning, XG. Model establishment and coding, ZJ. The original draft, XG and ZJ. All authors contributed to revising the manuscript and have agreed to its publication.

## FUNDING

Natural Science Foundation of Jiangsu Province (BK20190147), Natural Science Fundamental Research Project of Jiangsu Colleges and Universities (19KJB170025), the Open Grants of the State Key Laboratory of Severe Weather (2021LASW-B04), and the Postgraduate Practice Innovation Project of Wuxi Graduate School of NUIST (WXCX202102).

## REFERENCES


Aleksandrov, N. L., Bazelyan, E. M., Carpenter, R. B., Drabkin, M. M., and Raizer, Y. P. (2001). The Effect of Coronae on Leader Initiation and Development under Thunderstorm Conditions and in Long Air Gaps. *J. Phys. D. Appl. Phys.* 34 (22), 3256–3266. doi:10.1088/0022-3727/34/22/309

Aleksandrov, N. L., Bazelyan, E. M., Drabkin, M. M., Carpenter, R. B., and Raizer, Y. P. (2002). Corona Discharge at the Tip of a Tall Object in the Electric Field of a Thundercloud. *Plasma Phys. Rep.* 28 (11), 953–964. doi:10.1134/1.1520289

Aleksandrov, N. L., Bazelyan, E. M., and Raizer, Y. P. (2005b). Initiation and Development of First Lightning Leader: The Effects of Coronae and Position of Lightning Origin. *Atmos. Res.* 76 (1-4), 307–329. doi:10.1016/j.atmosres.2004.11.007

Aleksandrov, N. L., Bazelyan, E. M., and Raizer, Y. P. (2005a). The Effect of a Corona Discharge on a Lightning Attachment. *Plasma Phys. Rep.* 31 (1), 75–91. doi:10.1134/1.1856709

Aranguren, D., Montanya, J., Solá, G., March, V., Romero, D., and Torres, H. (2009). On the Lightning Hazard Warning Using Electrostatic Field: Analysis of Summer Thunderstorms in Spain. *J. Electrost.* 67 (2-3), 507–512. doi:10.1016/j.elstat.2009.01.023

Becerra, M., and Cooray, V. (2006). A Simplified Physical Model to Determine the Lightning Upward Connecting Leader Inception. *IEEE Trans. Power Deliv.* 21 (2), 897–908. doi:10.1109/TPWRD.2005.859290

Becerra, M., Cooray, V., Soula, S., and Chauzy, S. (2007). Effect of the Space Charge Layer Created by Corona at Ground Level on the Inception of Upward Lightning Leaders from Tall Towers. *J. Geophys. Res.* 112 (D12), 1103–1118. doi:10.1029/2006JD008308

Becerra, M. (2013). Glow Corona Generation and Streamer Inception at the Tip of Grounded Objects during Thunderstorms: Revisited. *J. Phys. D. Appl. Phys.* 46 (13), 135205. doi:10.1088/0022-3727/46/13/135205

Chauzy, S., and Raizonville, P. (1982). Space Charge Layers Created by Coronae at Ground Level below Thunderclouds: Measurements and Modeling. *J. Geophys. Res. Oceans* 87 (C4), 3143–3148. doi:10.1029/JC087iC04p03143

Chen, S. S. (2018). Distribution of Corona Space Charge Generated from the UHVDC Overhead Transmission Line during a Thunderstorm. Master Degree Thesis. Wuhan: Huazhong University of Science & Technology.

Cooray, V., Kumar, U., Rachidi, F., and Nucci, C. A. (2014). On the Possible Variation of the Lightning Striking Distance as Assumed in the IEC Lightning Protection Standard as a Function of Structure Height. *Electr. Power Syst. Res.* 113, 79–87. doi:10.1109/ICLP.2012.634430510.1016/j.epsr.2014.03.017

D'Alessandro, F. (2003). The Use of 'Field Intensification Factors' in Calculations for Lightning Protection of Structures. *J. Electrost.* 58 (1-2), 17–43. doi:10.1016/s0304-3886(02)00178-x

Ferro, M. A. D. S., Yamasaki, J., Pimentel, D. R. D. M., NaccaratoSaba, K. P., and Saba, M. M. F. (2012). Lightning Risk Warnings Based on Atmospheric Electric Field Measurements in Brazil. *J. Aerosp. Technol. Manag.* 3 (3), 301–310. doi:10.5028/jatm.2011.03032511

Golde, R. H. (1977). *Physics of Lightning*. Florida: Academic Press.

Guo, X., and Zhang, Q. (2017). Effects of Geometrical Parameters of Two Height-Unequal Adjacent Objects on Corona Discharges from Their Tips during a Thunderstorm. *Atmos. Res.* 190, 113–120. doi:10.1016/j.atmosres.2017.02.010

Guo, X., Zhang, Q., and Zhang, J. (2017). Improvement of Corona Discharge Model and its Application on Simulating Corona Discharge in the Presence of Wind. *Math. Probl. Eng.* 2017, 1–10. doi:10.1155/2017/9853439

Guo, Z., Li, Q., Bretas, A., and Rakov, V. A. (2019). A Simplified Physical Model of Negative Leader in Long Sparks. *Electr. Power Syst. Res.* 176, 105955. doi:10.1016/j.epsr.2019.105955

Jiang, R., Lyu, W., Wu, B., Qi, Q., Ma, Y., Su, Z., et al. (2020). Simulation of Cloud-To-Ground Lightning Strikes to Structures Based on an Improved Stochastic Lightning Model. *J. Atmos. Solar-Terrestrial Phys.* 203 (2), 105274. doi:10.1016/j.jastp.2020.105274

Lu, X., Zhang, Y. J., Lu, W. T., and Wang, D. H. (2010). Networking Observation and Data Analysis of Corona Current Near Ground. *Meteorol. Sci. Technol.* 38, 746–751. doi:10.19517/j.1671-6345.2010.06.017

Peek, F. W. (1929). *Dielectric Phenomena in High-Voltage Engineering*. New York: McGraw-Hill, 63.

Qi, Q., Wu, S., Su, Z., Lyu, W., Chen, L., and Zhang, Y. (2019). Shielding Effect of Surrounding Buildings on the Lightning-Generated Vertical Electric Field at the Top of a Tall Building. *IEEE Trans. Electromagn. Compat.* 61, 174–182. doi:10.1109/TEMC.2018.2790346

Qie, X. S. (1996). Numerical Calculation of Evolution of Corona Ions Produced from the Ground under Thunderstorm. *Acta Geophys. Sin.* 39 (s1), 43–51.

Qie, X., Soula, S., and Chauzy, S. (1994). Influence of Ion Attachment on the Vertical Distribution of the Electric Field and Charge Density below a Thunderstorm. *Ann. Geophys.* 12 (12), 1218–1228. doi:10.1007/s00585-994-1218-6

Rakov, V. A., Mareev, E. A., Tran, M. D., Zhu, Y., Bogatov, N. A., Kostinskiy, A. Y., et al. (2018). High-Speed Optical Imaging of Lightning and Sparks: Some Recent Results. *IEEJ Trans. PE* 138, 321–326. doi:10.1541/ieejpes.138.321

Soula, S. (1994). Transfer of Electrical Space Charge from Corona between Ground and Thundercloud: Measurements and Modeling. *J. Geophys. Res. Atmos.* 99 (D5), 10759–10765. doi:10.1029/93JD02596

Standler, R. B., and Winn, W. P. (1979). Effects of Coronae on Electric Fields beneath Thunderstorms. *Q. J. Roy. Meteor. Soc.* 105, 285–302. doi:10.1002/qj.49710544319

Tan, Y. B., Chen, C., Zhou, J. C., Zhou, B. W., Zhang, D. D., and Guo, X. F. (2016). A Parameterization Scheme for Upward Lightning in the Cloud Model and a Discussion of the Initial Favorable Environmental Characteristics in the Cloud. *Sci. China Earth Sci.* 59 (7), 1440–1453. doi:10.1007/s11430-016-5309-5

Yanhui, W., Xiangpeng, F., Tuo, W., Yingchang, M., Yali, L., and Guo, Z. (2021). Characteristics of Regular Pulse Bursts Generated from Lightning Discharges. *Front. Environ. Sci.* 9, 799115. doi:10.3389/fenvs.2021.799115

Zhang, Y. J., Lu, W. T., Chen, S. D., Zheng, D., Zhang, Y., Yan, X., et al. (2016). A Review of Lightning Observation Experiments during the Last Ten Years in Guangdong. *Acta Geophys. Sin.* 74 (5), 655–671. doi:10.11676/qxxb2016.051

Zhou, S. J., Ren, L. X., and Chen, L. X. (1965). An Experimental Investigation on the Point-Inductor Used for the Strong Field-Radiosonde. *Acta Geophys. Sin.* 14, 20–32.


**Conflict of Interest:** The authors declare that the research was conducted in the absence of any commercial or financial relationships that could be construed as a potential conflict of interest.

frontiers | Frontiers in Environmental Science

ORIGINAL RESEARCH
published: 06 July 2022
doi: 10.3389/fenvs.2022.934281

# Uncertainty Analysis of Premature Death Estimation Under Various Open $PM_{2.5}$ Datasets

*Jing Liu[1], Shenxin Li[1]*, Ying Xiong[2], Ning Liu[1], Bin Zou[1] and Liwei Xiong[3]*

*[1]School of Geosciences and Info-physics, Central South University, Changsha, China, [2]School of Architecture, Changsha University of Science and Technology, Changsha, China, [3]School of Municipal and Surveying Engineering, Hunan City University, Yiyang, China*

Assessments of premature deaths caused by $PM_{2.5}$ exposure have important scientific significance and provide valuable information for future human health–oriented air pollution prevention. $PM_{2.5}$ concentration data are particularly vital and may cause great uncertainty in premature death assessments. This study constructed an index of deviation frequency to compare differences in premature deaths assessed by five sets of extensively used $PM_{2.5}$ concentration remote sensing datasets. Then, a preferred combination project of the $PM_{2.5}$ dataset was proposed by selecting relatively high-accuracy $PM_{2.5}$ concentration datasets in areas with significant differences. Based on this project, an index of uncertainty was constructed to quantify the effects of using different $PM_{2.5}$ datasets on premature death assessments. The results showed that there were significant differences in $PM_{2.5}$ attributable to premature deaths assessed by different datasets from 2000 to 2016, and the differences were most obvious in 2004. Spatially, differences were most significant in Jilin, Fujian, Liaoning, Hebei, Shanxi, Hubei, Sichuan, and Yunnan. The differences were caused by $PM_{2.5}$ concentration; therefore, in order to reduce uncertainty in subsequent premature death assessments because of using different $PM_{2.5}$ concentration data, the CGS3 dataset was recommended for Jilin, Sichuan, Yunnan, and Fujian, and the CHAP dataset was recommended for Liaoning, Hebei, Shanxi, and Hubei, and for other regions, CGS3, CHAP, or PHD datasets were more applicable. The CHAP dataset was the best selection for premature death assessments in the whole area. Based on the preferred combination project of the $PM_{2.5}$ dataset, uncertainty in annual premature death assessments could be reduced by 31 and 159% in the whole and local area, respectively. The research results will provide a scientific basis for a reasonable selection of $PM_{2.5}$ concentration remote sensing datasets in air pollution premature death assessments in China.

**Keywords: PM2.5, premature deaths, spatial–temporal analysis, uncertainty, remote sensing**

OPEN ACCESS

***Edited by:***
*Honglei Wang,*
*Nanjing University of Information Science and Technology, China*

***Reviewed by:***
*Jing Wei,*
*University of Maryland, United States*
*Qingqing He,*
*Wuhan University of Technology, China*

****Correspondence:***
*Shenxin Li*
*shenxin823@csu.edu.cn*

***Specialty section:***
*This article was submitted to Atmosphere and Climate, a section of the journal Frontiers in Environmental Science*

***Received:*** *02 May 2022*
***Accepted:*** *18 May 2022*
***Published:*** *06 July 2022*

***Citation:***
*Liu J, Li S, Xiong Y, Liu N, Zou B and Xiong L (2022) Uncertainty Analysis of Premature Death Estimation Under Various Open $PM_{2.5}$ Datasets. Front. Environ. Sci. 10:934281. doi: 10.3389/fenvs.2022.934281*

## 1 INTRODUCTION

$PM_{2.5}$ is the primary air pollutant in China, and long-term exposure to high $PM_{2.5}$ pollution levels will increase the risk of cardiovascular disease, respiratory disease, etc. (Laden et al., 2006; Cohen et al., 2018; Maji et al., 2020; Shen M. et al., 2021). Accurate assessments of health risks caused by $PM_{2.5}$ pollution are important for the Chinese government to carry out environmental measures for

improving people's health. Air pollution concentration data are critical for assessing the health risks of $PM_{2.5}$ (Ma et al., 2022).

Traditionally, ground monitoring networks have been the basic method to provide $PM_{2.5}$ concentration, which were established in late 2012 in China (Wang H. et al., 2021). Although ground monitoring of $PM_{2.5}$ data is accurate, it is difficult to reveal the spatial distribution of regional-scale $PM_{2.5}$ concentration due to the limited spatial representation (Gupta et al., 2006; Van Donkelaar et al., 2010). In addition, the lack of historical data has limited the acquisition of longitudinal data on $PM_{2.5}$ concentration. Health risk assessments deeply depend on large-scale and long-term $PM_{2.5}$ concentration data. However, the limitation mentioned above has affected the development of the studies on large-scale and long-term health risk assessments.

Fortunately, satellite remote sensing has the advantage of wide spatial-temporal coverage, which can effectively fill the spatial–temporal $PM_{2.5}$ gaps left by ground monitoring networks (Hu et al., 2014; Hoogh et al., 2018; Stafoggia et al., 2019; He et al., 2021). Hence, it has been widely used to estimate $PM_{2.5}$ spatial–temporal continuous data in recent years. Also it further provides technical support for large-scale and long-term health risk assessments (Liu et al., 2017; Wang L. et al., 2021). For example, Zou et al. (2019) estimated premature deaths in China were 1.05 million based on $PM_{2.5}$ concentration refined by a hybrid remote sensing-geostatistical approach. Li et al. (2021) estimated that premature deaths in China were 1.1 million based on $PM_{2.5}$ concentration simulated by the WRF-Chem. Liang et al. (2020) concluded that premature deaths in China were 2.2 million assessed by $PM_{2.5}$ concentration simulated by high-performance machine learning models based on satellite data, meteorological conditions, land cover information, and so on. Although the disadvantages of spatial–temporal coverage were remedied by the satellite remote sensing technique, there were differences in $PM_{2.5}$ concentration and premature death assessments due to differences in parameters and model algorithm of $PM_{2.5}$ estimation.

In order to reduce differences in premature deaths assessed by different $PM_{2.5}$ concentration remote sensing data, a large number of researchers focus on proposing a set of standard datasets with large scale and long term assessment. At present, the extensively used datasets in China include three sets of "Geophysical Satellite-Based $PM_{2.5}$ datasets" (1 km, 5 km, 10 km) with different spatial resolutions released by the Atmospheric Composition Analysis Group (Van Donkelaar et al., 2015; Van Donkelaar et al., 2016; Van Donkelaar et al., 2019; Hammer et al., 2020). The "$PM_{2.5}$ Hindcast database" (10 km) was released by Xue et al. (2019) as well as the "ChinaHigh$PM_{2.5}$" dataset (1 km) was published by Wei et al. (2020), Wei et al. (2021). However, there are no relevant studies that compare systematically the differences in health risks assessed by these five sets of $PM_{2.5}$ concentration remote sensing datasets.

In view of this, how to take full advantage of these five sets of $PM_{2.5}$ concentration remote sensing datasets and reduce the uncertainty in health risk assessments in China is an urgent problem in the cross-research field of remote sensing and health risks. In this study, an index of deviation frequency was constructed to evaluate the differences in $PM_{2.5}$ attributable premature deaths when choosing various $PM_{2.5}$ data. Then, in order to reduce uncertainty in premature death assessments caused by various $PM_{2.5}$ concentration data, the preferred combination project of the $PM_{2.5}$ dataset was proposed in the areas with significant differences. The preferred combination project of the $PM_{2.5}$ dataset was proposed for different regions to provide data support for accurately estimating the effects of air pollution in health risk research. Also, it also put forward new ideas for the focus of air quality data simulation in the future. Findings from this study will provide new knowledge for policy-making of "China's 14th Five-Year Plan" air pollution intervention and health risk prevention.

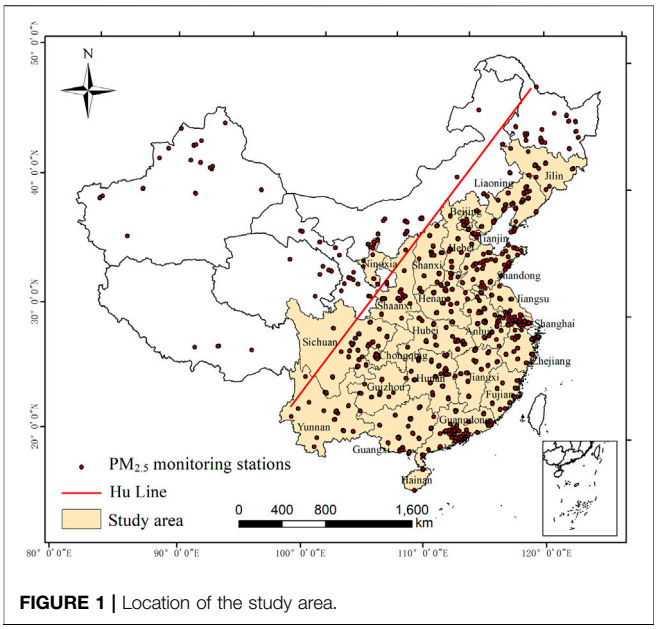


**FIGURE 1 |** Location of the study area.

## 2 DATA AND METHODS

As an important east–west boundary, cities on each side of the Hu line showed obvious differences both in $PM_{2.5}$ concentration and population density (Li et al., 2020). The Yangtze River Delta Urban Agglomerations, the urban agglomeration in the middle reaches of the Yangtze River, and other regions, which were located in the east of the Hu Line, were agglomeration areas of cities with high levels of $PM_{2.5}$ pollution (Shen L. et al., 2021). As an important agglomeration area of population and economy in China, the population in this area reaches 1.2 billion, accounting for 94% of the country (Wang et al., 2019). Therefore, the study area is defined as the mainland of eastern China below the Hu line (excluding Heilongjiang Province, Hong Kong, Macao, and including Ningxia Hui Autonomous Region) and includes 19 provinces, four central government–controlled municipalities, and two autonomous regions, all referred to here as provinces (**Figure 1**).

The technical flowchart of this study is shown in **Figure 2**. There were three main steps. The first step was to analyze spatial–temporal differences of $PM_{2.5}$ attributable to premature deaths based on the index of deviation frequency. The second step was to propose a preferred combination project of the $PM_{2.5}$ dataset based on the

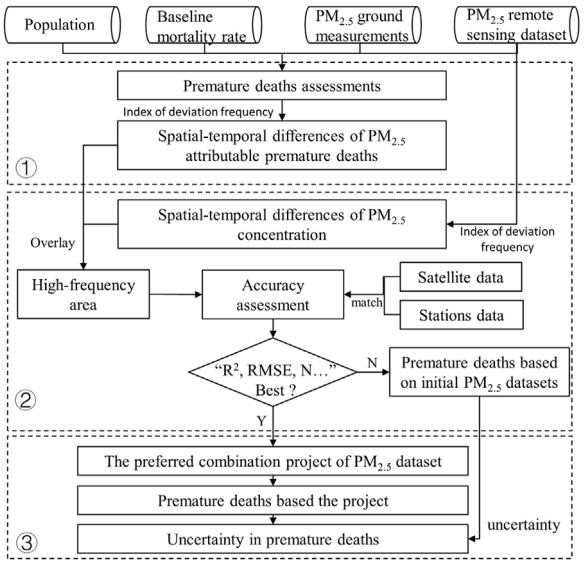


**FIGURE 2 |** Technical flowchart of this study.

accuracy assessment in the areas with significant differences. The third step focuses on identifying uncertainty in health risk assessments by comparing assessments of the preferred combination project of the $PM_{2.5}$ dataset with assessments of five sets of initial datasets.

## 2.1 Data

### 2.1.1 $PM_{2.5}$ Concentration Remote Sensing Datasets

$PM_{2.5}$ concentration remote sensing datasets used in the study mainly include 1) $PM_{2.5}$ concentration retrieved by the atmospheric chemical transport model, including three sets of datasets: China Geophysical Satellite–Based $PM_{2.5}$-V4.CH.03 (CGS3), Global Geophysical Satellite–Based $PM_{2.5}$-V4.GL.03 (GGS3), and China Geophysical Satellite–Based $PM_{2.5}$-V4.GL.02 (CGS2), with $R^2$ between 0.81–0.92. 2) Using the STET machine learning method to retrieve the ChinaHigh$PM_{2.5}$ (CHAP) dataset, $R^2$ is 0.94. 3) Using the HD-expansion machine learning method to retrieve the $PM_{2.5}$ Hindcast Database (PHD) with $R^2$ of 0.77. The details of the datasets are shown in **Table 1**.

### 2.1.2 $PM_{2.5}$ Ground Measurements

The station-based annually averaged $PM_{2.5}$ concentration (μg/$m^3$) data were calculated. Hourly $PM_{2.5}$ concentration from January 2013 to December 2016 was obtained from the China National Environmental Monitoring Center website (http://106.37.208.233:20035/). According to the Chinese National Ambient Air Quality Standards (CNAAQS), the following preprocessing was performed on data: all missing or invalid data were removed from original observations. Values of observations at stations with fewer than 20 h in a day, fewer than 27 days in a month (25 in February), or fewer than 324 days in a year were eliminated when calculating the annually averaged $PM_{2.5}$ concentration.

### 2.1.3 Populations and Baseline Mortality Rate Data

Populations and baseline mortality rates are fundamental parameters for premature death assessments. Population data at 1 km resolution across mainland China were downloaded from Worldpop (https://www.worldpop.org/). The population of adults (aged ≥25 years) was obtained by subtracting the population aged under 25 years old from the total population at 1 km resolution in China. Baseline mortality rate data were derived from Global Burden of Disease (GBD) (http://ghdx.healthdata.org/), including lower respiratory infection and non-communicable diseases.

## 2.2 Methods

### 2.2.1 Premature Death Assessments

This study used the Global Exposure Mortality Model (GEMM) to estimate $PM_{2.5}$ attributable premature deaths. The GEMM is an improved and optimized health risk estimation model based on the Integrated Exposure Response (IER) (Burnett et al., 2014). Compared with IER, the GEMM covers a large number of population samples and $PM_{2.5}$ concentration data and optimizes the accuracy of $PM_{2.5}$ health risk assessments at low concentrations (Burnett et al., 2018; Li et al., 2021). Using the

**TABLE 1 |** Five sets of $PM_{2.5}$ datasets in China.

| Dataset | Short name | Spatial coverage | Spatial resolution | Temporal coverage | Temporal resolution | Data source | | | Method |
|---|---|---|---|---|---|---|---|---|---|
| | | | | | | AOD | Model | *In situ* | |
| China Geophysical Satellite Based $PM_{2.5}$ -V4.CH.03 | CGS3 | China | 0.01 ° × 0.01 ° | 2000–2018 | Annual | MODIS, MISR, SeaWIFS | GEOS-Chem | US EPA AQS | Scale factor& GWR |
| Global Geophysical Satellite-Based $PM_{2.5}$-V4.GL.03 | GGS3 | Global | 0.05 ° × 0.05 ° | 1998–2018 | Annual | MODIS, MISR, SeaWIFS | GEOS-Chem | US EPA AQS | Scale factor& GWR |
| China Geophysical Satellite-Based $PM_{2.5}$-V4.GL.02 | CGS2 | China | 0.1 ° × 0.1 ° | 1998–2016 | Annual | MODIS, MISR, SeaWIFS | GEOS-Chem | CNEMC | Scale factor& GWR |
| ChinaHigh$PM_{2.5}$ | CHAP | China | 0.01 ° × 0.01 ° | 2000–2020 | Annual | MODIS | — | CNEMC | Machine learning (STET) |
| $PM_{2.5}$ Hindcast Database | PHD | China | 0.1 ° × 0.1 ° | 2000–2016 | Annual | MODIS | MEIC-CMAQ | CNEMC | Machine learning (HD-expansion) |

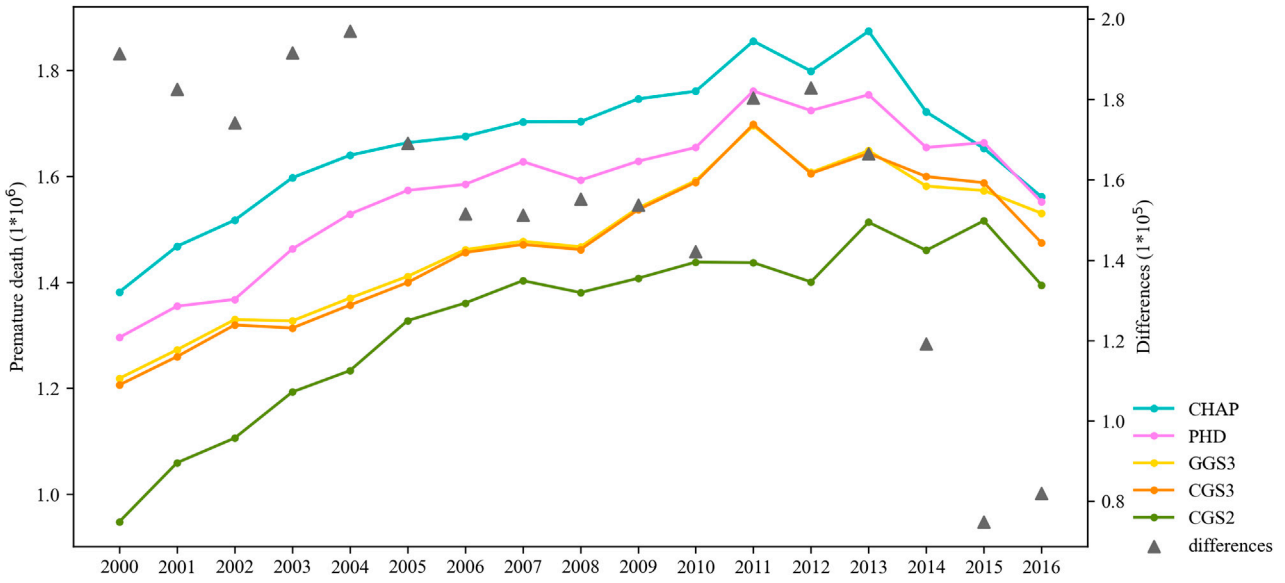


**FIGURE 3 |** Annual premature deaths were assessed by five sets of $PM_{2.5}$ datasets from 2000 to 2016.

GEMM to estimate premature deaths in adults due to long-term exposure to $PM_{2.5}$, the equation is as follows:

$$Mortality_{ij} = \frac{HR(C_{ij}) - 1}{HR(C_{ij})} \times Pop_{ij} \times I_{ij}, \quad (1)$$

where $Mortality_{ij}$ is $PM_{2.5}$ attributable premature deaths in the grid $i$ at year $j$. $HR(C_{ij})$ is the estimated hazard ratio in the grid $i$ at year $j$. $Pop_{ij}$ is the adult population exposed to $PM_{2.5}$ in the grid $i$ at year $j$. $I_{ij}$ is the baseline mortality rate of adults in the grid $i$ at year $j$.

The main difference between the IER and GEMM model is the calculation of $HR(C_{ij})$. Compared with IER, the GEMM was estimated as a common hazard ratio model among the 41 cohorts by pooling predictions of the hazard ratio among cohorts over their range of exposure. $HR(C_{ij})$ in the GEMM is calculated by the following equation:

$$HR(C_{ij}) = \exp\left\{\frac{\theta \log\left(\frac{z}{\alpha}+1\right)}{1+\exp\left(-\frac{z-\mu}{\nu}\right)}\right\}, z = \max(0, C - 2.4\mu g/m^3), \quad (2)$$

where $HR(C)$ is the hazard ratio of non-accident mortality under $PM_{2.5}$ concentration. In this model, 2.4 μg/m$^3$ is used as a counterfactual concentration, below which the hazard ratio of mortality associated with $PM_{2.5}$ exposure is assumed to be constant 1. C is the annual $PM_{2.5}$ concentration. $\theta$, $\alpha$, $\mu$, and $\upsilon$ are the modeled age-specific parameters.

### 2.2.2 Differences Quantitative Indicator Construction

Deviation frequency was constructed to evaluate the degree of differences in $PM_{2.5}$ concentration and premature deaths between five sets of datasets. The index of deviation frequency refers to the frequency of occurrence of high deviation between any two datasets. The calculation processing was as follows: $PM_{2.5}$ concentration data and premature death data were resampled to a resolution of 1 × 1 km from 2000 to 2016 and then the absolute value of relative differences between any two datasets was taken as deviation. The third quartile of all deviation values was the threshold, and values above the threshold were defined as high deviation. The equation is as follows:

$$count_{ij} = I\left(R_{ij,a} > R_t\right)^T I\left(R_{ij,a} > R_t\right), \quad (3)$$

where $count_{ij}$ is an index of deviation frequency of the dataset $i$, $j$. $R_{ij,a}$ is the deviation of $PM_{2.5}$ concentration or premature deaths between dataset $i$ and dataset $j$. $R_t$ is the threshold. $I(R_{ij,a} > R_t)$ is the indicator function, which is 1 when $R_{ij,a} > R_t$, while is 0 when $R_{ij,a} < R_t$.

The deviation equation of $PM_{2.5}$ concentration or premature deaths between dataset $i$ and dataset $j$ at the year a is as follows:

$$R_{ij,a} = \left|\frac{\left(x_{i,a} - x_{j,a}\right)}{\overline{x_{ij,a}}}\right|, \quad (4)$$

where $x_{i,a}$, $x_{j,a}$, is $PM_{2.5}$ concentration or premature deaths of dataset $i$, $j$ at year a.

### 2.2.3 Uncertainty Quantitative Indicator Construction

Uncertainty was used to estimate differences in premature deaths between the preferred combination project of the $PM_{2.5}$ dataset and five sets of initial datasets. The preferred combination project of the $PM_{2.5}$ dataset was obtained by assessing the $PM_{2.5}$ concentration accuracy and selecting the dataset with higher accuracies. Through matching of ground monitoring stations and satellite data, satellite data with the same spatial–temporal coverage as station data were screened out. Then, statistical values ($R^2$,

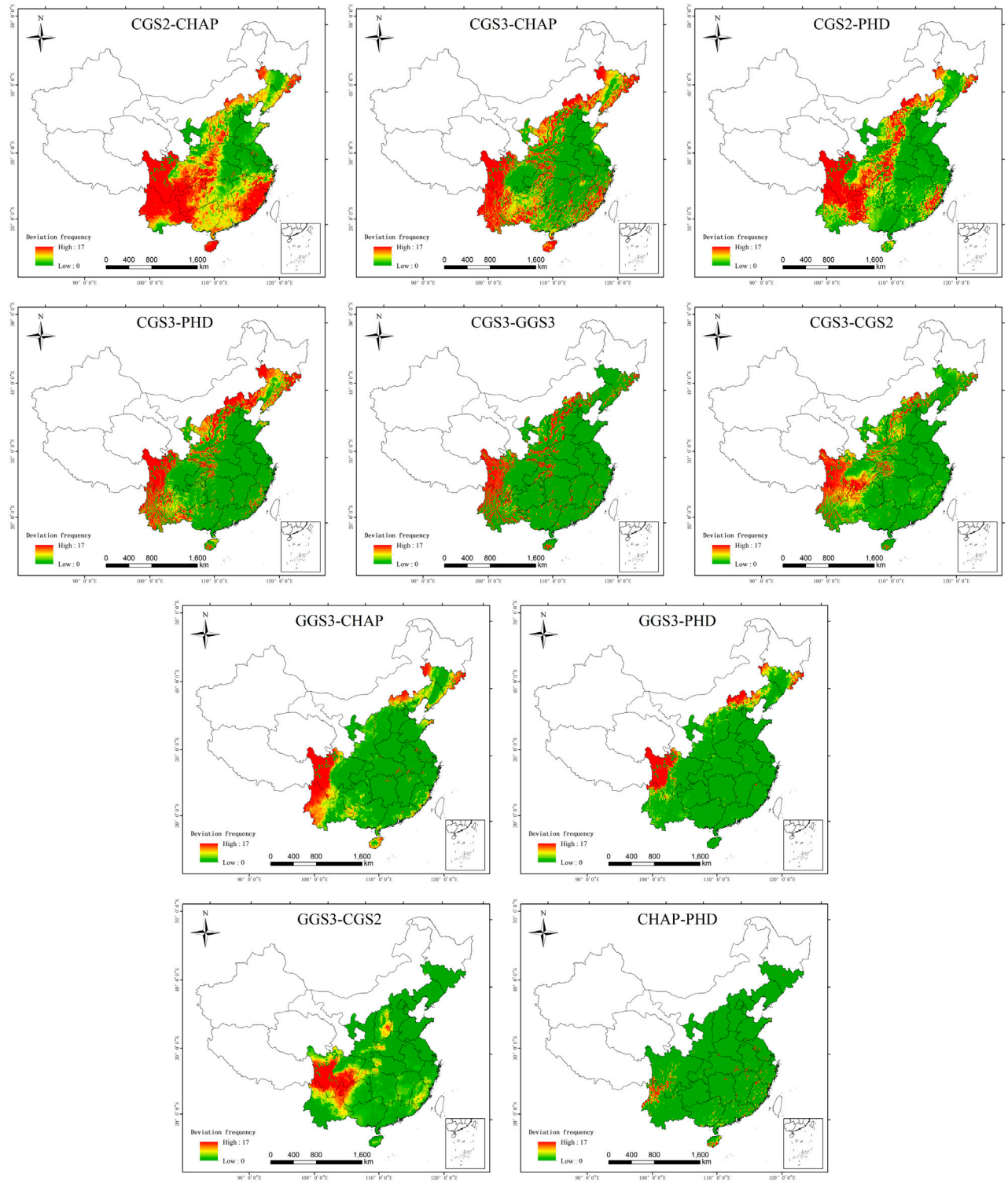


**FIGURE 4 |** Spatial distribution of deviation frequency in premature deaths assessed by any two $PM_{2.5}$ datasets.

RMSE, MAE, Slope, N, etc.) were selected as the quantitative evaluation indicators to evaluate the accuracy of satellite data. Taking the number of premature deaths assessed by the preferred combination project of the $PM_{2.5}$ dataset as a benchmark, uncertainty was the percentage of differences between the number of premature deaths assessed by five sets of initial $PM_{2.5}$ datasets and the benchmark data. The equation is as follows:

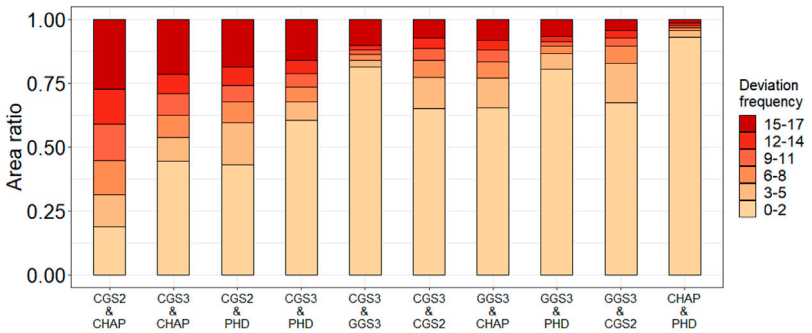


**FIGURE 5 |** Area ratio of deviation frequency in premature deaths was assessed by any two $PM_{2.5}$ datasets.

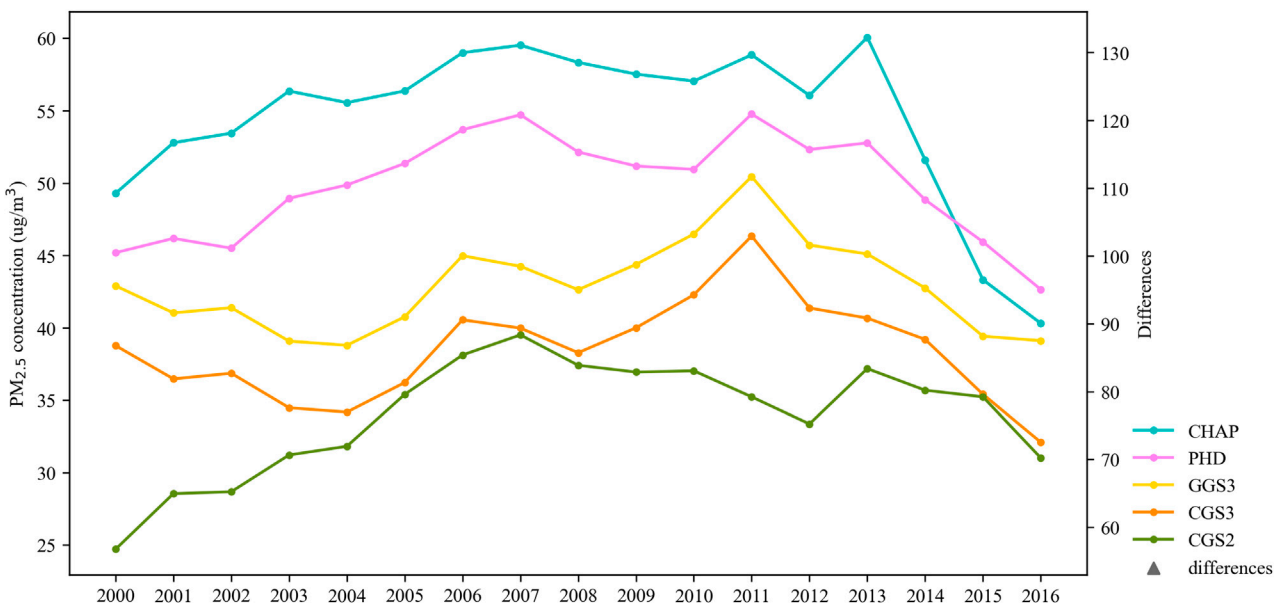


**FIGURE 6 |** Annual $PM_{2.5}$ concentration of five sets of $PM_{2.5}$ datasets from 2000 to 2016.

$$\delta_{i,j_0} = \frac{\left(x_i - x_{j_0}\right)}{x_{j_0}} \times 100\%, \tag{5}$$

where $\delta_{i,j_0}$ is the uncertainty in premature deaths assessed by the $PM_{2.5}$ dataset $i$ and dataset $j_0$. $x_{j_0}$ denotes premature deaths assessed by the preferred combination project of the $PM_{2.5}$ dataset. $x_i$ denotes premature deaths assessed by five sets of initial $PM_{2.5}$ datasets.

# 3 RESULTS

## 3.1 Spatial–Temporal Differences of $PM_{2.5}$ Attributable Premature Deaths

**Figure 3** shows the temporal trend of annual premature deaths based on five sets of $PM_{2.5}$ concentration remote sensing datasets. Generally, the temporal trend of premature deaths assessed by five sets of datasets was consistent, and the number of premature deaths first increased and then decreased. For the number, premature deaths assessed by five sets of $PM_{2.5}$ datasets were in order of CHAP > PHD > GGS3 > CGS3 > CGS2. Premature death assessed by the CHAP dataset was the largest, ranging from 1.38 million (in 2000) to 1.87 million (in 2013). Premature death assessed by the CGS2 dataset was the lowest, ranging between 0.94 million (in 2000) and 1.51 million (in 2015). On the aspect of growth rate, premature death assessed by the CGS2 dataset was most pronounced at 47%, whereas the CHAP was lowest at 13%. In terms of temporal variation, premature deaths assessed by the CHAP, PHD, GGS3, and CGS3 datasets showed an increasing trend from 2000 to 2011, fluctuated from 2011 to 2013, and decreased from 2013 to 2016. The peak value of premature deaths assessed by the PHD, GGS3, and CGS3 datasets appeared in 2011, while the peak value of CHAP appeared in 2013. However, premature

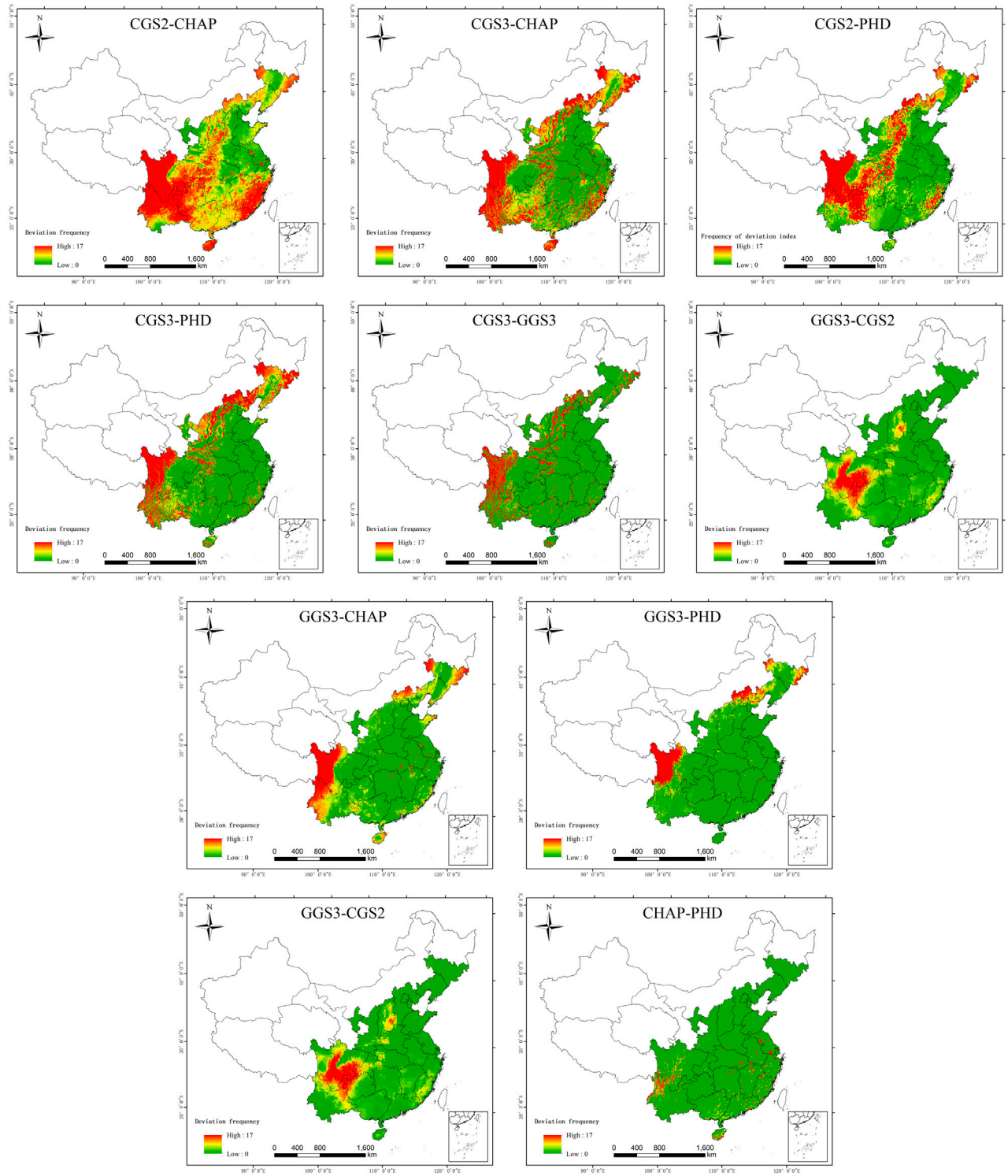


**FIGURE 7 |** Spatial distribution of deviation frequency in $PM_{2.5}$ concentration between any two $PM_{2.5}$ datasets.

deaths assessed by the CGS2 dataset had decreased since 2011, fluctuated from 2013 to 2015, and peaked in 2015. In addition, differences in premature deaths assessed by five sets of $PM_{2.5}$ datasets were obvious in 2000–2004 and 2011–2013 and sharply decreased since 2013, which may be related to the improvement in accuracy of $PM_{2.5}$ concentration data after 2013.

**Figure 4** shows the spatial distribution of deviation frequency in premature deaths assessed by different $PM_{2.5}$ datasets. The

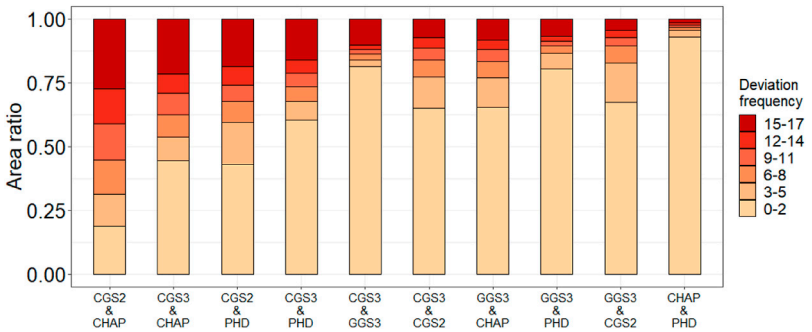


**FIGURE 8 |** Area ratio of deviation frequency in $PM_{2.5}$ concentration between any two $PM_{2.5}$ datasets.

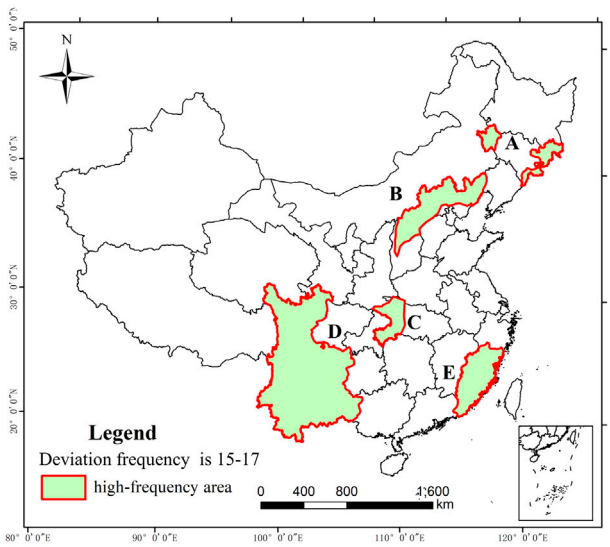


**FIGURE 9 |** Areas with significant differences both in $PM_{2.5}$ concentration and premature deaths.

obvious differences were in western Sichuan, with deviation frequency in premature deaths assessed by all datasets of 15–17. There were great differences in premature deaths in western and eastern Jilin, northern Hebei, and southwestern Yunnan, with deviation frequency of 15–17 between CHAP and CGS2, CHAP and CGS3, CHAP and GGS3, PHD and CGS2, and PHD and CGS3 datasets. Regions with little differences were mainly concentrated in Shandong, Henan, Anhui, and Jiangsu.

**Figure 5** shows the area ratio of the deviation frequency index between different datasets. Differences in premature deaths assessed by the CGS2 and CHAP datasets were the largest, and the area ratio of deviation frequency of 15–17 was 26%. Differences in premature deaths assessed by the CHAP and PHD datasets were minimal, and the area ratio of deviation frequency of 15–17 was less than 1%, while the area ratio of deviation frequency of 0–2 was as high as 94%.

## 3.2 Spatial–Temporal Differences of $PM_{2.5}$ Concentration

**Figure 6** shows the temporal trend of annual $PM_{2.5}$ concentration of five sets of datasets from 2000 to 2016. In general, the temporal trend of $PM_{2.5}$ concentration of all datasets was the same except for the CGS2 dataset, which first increased and then decreased. For annual $PM_{2.5}$ concentration, the order of five sets of datasets was CHAP > PHD > GGS3>CGS3>CGS2. $PM_{2.5}$ concentration of the CGS2 dataset was the lowest, ranging from 25 $\mu g/m^3$ (in 2000) to 40 $\mu g/m^3$ (in 2007), with an average $PM_{2.5}$ concentration of 34 $\mu g/m^3$. $PM_{2.5}$ concentration of the CHAP dataset was the highest, ranging from 40 $\mu g/m^3$ (in 2016) to 60 $\mu g/m^3$ (in 2013), with an average of 54 $\mu g/m^3$. From the perspective of temporal variation, the $PM_{2.5}$ concentration of the CHAP and PHD datasets showed an upward trend from 2000 to 2007, fluctuated from 2007 to 2013, and decreased from 2013 to 2016, and the peak values of $PM_{2.5}$ concentration appeared in the year of 2011 and 2013. Different from the CHAP and PHD datasets, the $PM_{2.5}$ concentration of the GGS3 and CGS3 datasets showed a downward trend from 2000 to 2004, fluctuated upward from 2004 to 2011, and then decreased rapidly, peaking in 2011. There were significant differences in $PM_{2.5}$ concentration temporal variation between the CGS2 dataset and other datasets as its $PM_{2.5}$ concentration showed a downward trend from 2010 to 2012, and the peak value appeared in 2007.

**Figure 7** shows the spatial distribution of deviation frequency in the $PM_{2.5}$ concentration. Generally, differences in $PM_{2.5}$ concentration of five sets of datasets were few. However, in local areas, similar to the spatial distribution of differences in premature deaths, the significant differences in $PM_{2.5}$ concentration were found in western Sichuan, with a deviation frequency of 15–17. Then, differences were followed by those in western and eastern Jilin, northern Hebei, and southwestern Yunnan, and few differences were found in Shandong, Henan, Anhui, and Jiangsu.

**Figure 8** shows the area ratio of deviation frequency in different $PM_{2.5}$ concentrations. $PM_{2.5}$ concentration of the CGS2 and CHAP datasets experienced the largest differences, and the area ratio of deviation frequency of 15–17 accounted for 27%. The CHAP and PHD datasets had little differences in $PM_{2.5}$ concentration, and the area ratio of deviation frequency of 0–2

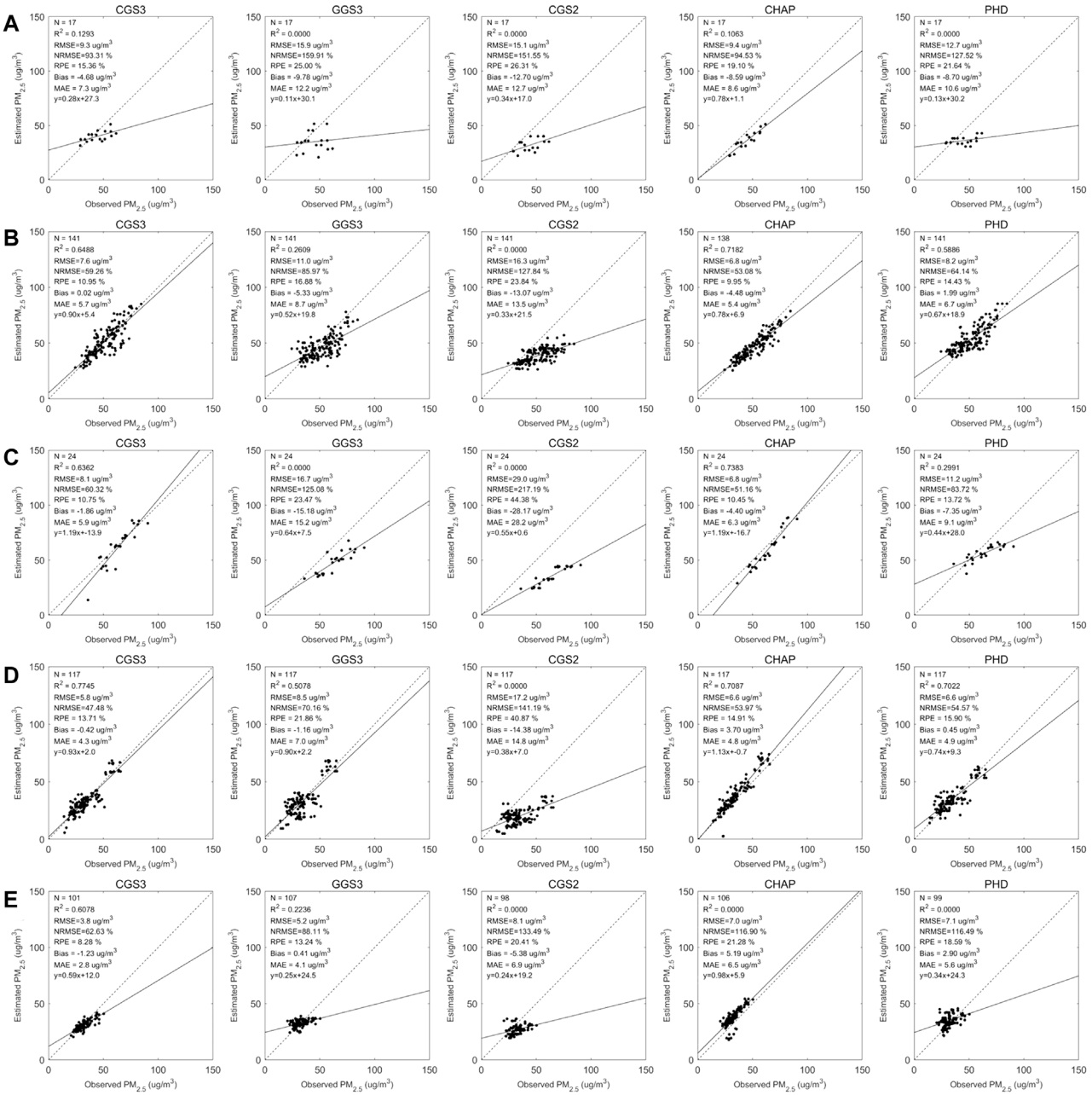


**FIGURE 10 |** Scatterplots of fitting and cross-validating results in the areas with significant differences. P.S. **(A–E)** are areas with significant differences in **Figure 9**.

accounted for as high as 93%. Comparing the differences in premature deaths with differences in $PM_{2.5}$ concentration, it could be seen that these were highly consistent in spatial distribution. This result indicated that differences in $PM_{2.5}$ concentrations may be the important factor leading to differences in premature deaths. Screening and using the higher precision $PM_{2.5}$ concentration remote sensing data are the key to accurately assessing the $PM_{2.5}$ attributable premature deaths.

## 3.3 Accuracy Assessment of $PM_{2.5}$ Concentration Remote Sensing Datasets

In order to evaluate the applicability of $PM_{2.5}$ datasets in assessments of premature deaths, this study compared the accuracy of $PM_{2.5}$ concentration remote sensing datasets in the areas with significant differences. To overlay analysis of high-frequency areas of $PM_{2.5}$ concentration differences (i. e. deviation frequency is 15–17) and high-frequency areas of premature death differences, the areas with significant

**TABLE 2 |** Selection suggestion of the $PM_{2.5}$ dataset for premature deaths.

| Area | CGS3 | GGS3 | CGS2 | CHAP | PHD |
|---|---|---|---|---|---|
| Jilin | III | NR | NR | NR | NR |
| Liaoning | NR | NR | NR | III | NR |
| Hebei | NR | NR | NR | III | NR |
| Shanxi | NR | NR | NR | III | NR |
| Hubei | NR | NR | NR | III | NR |
| Sichuan | III | NR | NR | II | I |
| Yunnan | III | NR | NR | II | I |
| Fujian | III | NR | NR | NR | NR |
| else | III | III | III | III | III |
| Study area | II | NR | NR | III | I |

*P.S. NR, means "Not Recommended". I mean "Carefully Used". II, means "Moderate Recommended". III, means "Most Recommended".*

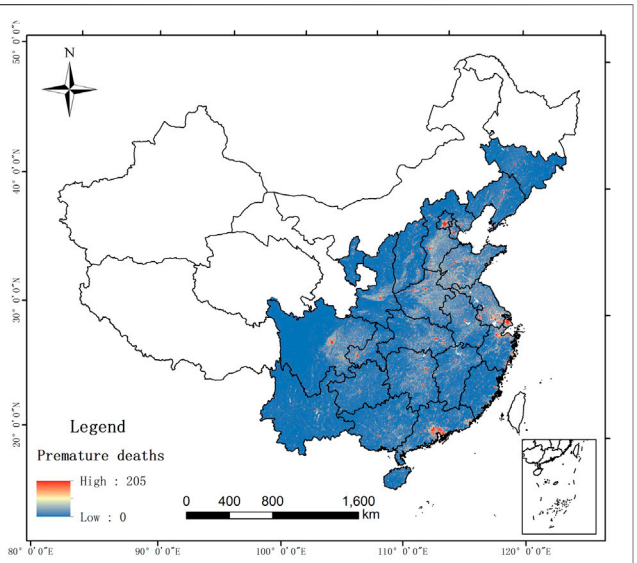


**FIGURE 11 |** Spatial distribution of premature deaths assessed by the preferred combination project of $PM_{2.5}$ dataset.

differences were screened out (**Figure 9**). Among them, region A mainly includes the northwestern and eastern parts of Jilin, region B mainly includes southwestern Liaoning, northern Hebei, and northern Shanxi, region C mainly includes western Hubei, region D mainly includes Sichuan and western Yunnan, and region E mainly includes Fujian.

The accuracy assessment results of different $PM_{2.5}$ concentration remote sensing datasets are shown in **Figure 10**. Five sets of $PM_{2.5}$ concentration remote sensing datasets in the northwest and eastern Jilin (region A) were inconsistent with ground-based $PM_{2.5}$ measurements, with the highest $R^2$ of 0.13 (the CGS3 dataset), while the slope of the CHAP dataset was best. In region B, the CHAP dataset worked well, and the cross-validation result was 0.72, while the cross-validation result of the CGS2 dataset was the worst. The CHAP dataset in region C had the best cross-validation result, with an $R^2$ of 0.74. In region D, $PM_{2.5}$ concentration of the CGS3, CHAP, and PHD datasets agreed well with ground-based $PM_{2.5}$ measurements, with $R^2$ of 0.77, 0.71, and 0.70, respectively. The CGS3 dataset had the best fitting result in region E, with an $R^2$ of 0.61. In summary, among currently representative $PM_{2.5}$ concentration remote sensing datasets in China, the model fitting results of the CHAP datasets were better than those of the other datasets by comparing the indicator of $R^2$, MAE, slope, and so on.

## 3.4 Uncertainty Analysis of $PM_{2.5}$ Attributable Premature Deaths

By comparing the accuracy assessment results in $PM_{2.5}$ concentration of five sets of $PM_{2.5}$ datasets, the selection suggestions of the $PM_{2.5}$ dataset for premature deaths were obtained (**Table 2**). According to the selection suggestions, the preferred combination project of the $PM_{2.5}$ dataset is as follows: the CGS3 dataset was recommended for Jilin, Sichuan, Yunnan, and Fujian; the CHAP dataset was recommended for Liaoning, Hebei, Shanxi, and Hubei; and for other regions, CGS3, CHAP, or PHD datasets were more applicable. The results showed that, on the one hand, five sets of $PM_{2.5}$ concentration datasets in Jilin, Liaoning, Fujian, and other regions need to be selected and used carefully due to significant differences in accuracy, and the premature deaths assessed by any single $PM_{2.5}$ concentration remote sensing dataset in the total area will enlarge the uncertainty of assessment results. On the other hand, the CHAP dataset was the best selection for premature death assessments in the whole area.

Based on the preferred combination project of the $PM_{2.5}$ dataset, this study evaluated the spatial distribution of the annual $PM_{2.5}$ attributable premature deaths from 2000 to 2016 (**Figure 11**). Over the past 17 years, $PM_{2.5}$ attributable premature deaths in the mainland of eastern China below the Hu line showed that the eastern coastal areas were higher in

**TABLE 3 |** Uncertainty of the average premature deaths in 17 years in different areas.

| Area | Premature deaths assessed by $PM_{2.5}$ datasets ($1*10^3$) | | | | | | Uncertainty (%) |
|---|---|---|---|---|---|---|---|
| | Preferred combination project | CGS3 | GGS3 | CGS2 | CHAP | PHD | |
| Study area | 1,641 | 1,479 | 1,486 | 1,332 | 1,674 | 1,585 | (−19, 2) |
| A | 4.268 | 4.268 | 4.291 | 3.980 | 5.903 | 5.409 | (−7, 38) |
| B | 36.562 | 30.261 | 30.781 | 27.849 | 36.562 | 37.156 | (−24, 2) |
| C | 13.527 | 12.123 | 11.925 | 9.541 | 13.527 | 13.228 | (−29, −2) |
| D | 63.997 | 63.997 | 68.076 | 50.271 | 82.401 | 73.695 | (−21, 29) |
| E | 51.536 | 51.536 | 50.888 | 42.264 | 65.609 | 56.013 | (−18, 27) |

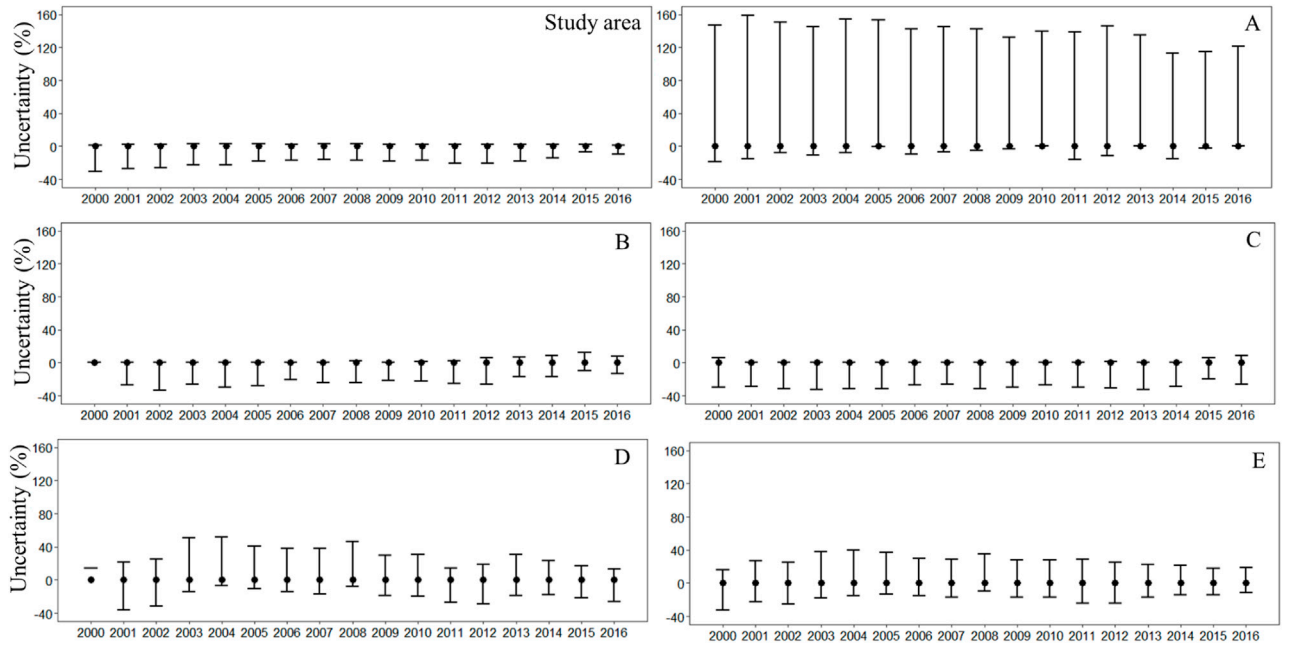


**FIGURE 12 |** Uncertainty of annual premature deaths in different areas. Areas with significant differences both in PM2.5 concentration and premature deaths.

concentration than the other areas of China, and provincial capital cities were high-risk centers, with spreading to the surrounding cities. High-risk areas were mainly concentrated in Beijing–Tianjin–Hebei, Yangtze River Delta, Pearl River Delta, and Chengdu–Chongqing urban agglomerations. These areas were densely populated and had high levels of urbanization and industrialization (Ye et al., 2018), which has led to severe health risks of air pollution.

**Table 3** showed the 17-year average of premature deaths and uncertainty in the study area based on the preferred combination project of the $PM_{2.5}$ dataset and five sets of initial $PM_{2.5}$ datasets. In general, compared with the 17-year average premature deaths (1.64 million) assessed by the preferred combination project of the $PM_{2.5}$ dataset, the assessment result of other arbitrary datasets had a bias, ranging between 1.33 and 1.67 million, with the uncertainty of 19%. For local areas, the uncertainty in premature death assessments was more pronounced. In region A, the degree of overestimation of premature deaths was the largest, with an uncertainty of 38%, while in region C, the degree of underestimation of premature deaths was the largest, with an uncertainty of 29%. There was also more or less uncertainty of premature deaths in regions B, D, and E, ranging from 24 to 29%.

**Figure 12** showed the uncertainty in annual premature deaths assessed by different $PM_{2.5}$ datasets. It can be seen that in the whole study area, annual premature death assessments based on five sets of initial $PM_{2.5}$ datasets were significantly underestimated, with an uncertainty of 31% in 2000. For local areas, the uncertainty in the annual premature deaths based on initial $PM_{2.5}$ datasets was larger than the uncertainty of 17-year average premature deaths. For region A, the 17-year average uncertainty ranged from -7 to 38%, while the annual uncertainty was as high as 159% in 2001. The uncertainty in annual premature deaths ranged from -42 to 52% and reached the highest in 2004 in region D. The uncertainty interval in regions B, C, and E was (−41% and 40%), reaching the highest in 2000, 2003, and 2004, respectively. Therefore, the selection of $PM_{2.5}$ datasets should be carried out cautiously when assessing premature deaths in local areas during these periods.

## 4 DISCUSSION AND CONCLUSION

This study estimated spatial–temporal differences in health risk assessments and $PM_{2.5}$ concentration from 2000 to 2016 in eastern China with five sets of $PM_{2.5}$ datasets. The preferred combination project of the $PM_{2.5}$ dataset was proposed to quantitatively analyze spatial–temporal uncertainty in health risk assessments caused by selecting different $PM_{2.5}$ datasets. To the best of our knowledge, this is the first effort to quantify the effects of concentration data on health risk assessments due to $PM_{2.5}$ selection in China by using five $PM_{2.5}$ concentration remote sensing datasets. These results contribute to accurately assessing health risks of air pollution which may be a benefit to formulate policies for preventing and controlling regional-scale health risks by governments.

The results of this study are comparable to those of previous studies. The results show that there were significant differences in premature death assessments using different $PM_{2.5}$ concentration remote sensing datasets from 2000–2016. $PM_{2.5}$ attributable premature deaths varied from 0.94 to 1.38 million in 2000 among the five sets of datasets in eastern China and varied from 1.39 to 1.56 million in 2016. A similar finding is observed when comparing those previously reported research

studies on premature deaths in China (Rohde and Muller, 2015; Fang et al., 2016). For example, the premature deaths reported were estimated to be 1.38 to 1.47 million in 2014 using the different concentration data in China (Wang C. et al., 2021).

The study shows that differences both in the number and trends of $PM_{2.5}$ concentration and premature deaths and were significant. The five sets of datasets adopted various algorithms, data sources, and input parameters (**Table 1**); therefore, there were differences in concentration values and trends. For example, the CGS3 dataset was estimated using advances in satellite observations, chemical transport modeling, and ground-based monitoring (Hammer et al., 2020), while the CHAP dataset was stimulated by the STET model which was improved by using corrected AODs, adding pollutant emissions, updating the feature selection, and improving the determination of spatiotemporal information (Wei et al., 2021). For the difference in premature deaths, because input parameters, methods, and data sources except for $PM_{2.5}$ concentration data were the same in the process of premature death assessments, the reason causing it was differences in the concentration of five sets of $PM_{2.5}$ datasets.

The study shows that differences in premature deaths and $PM_{2.5}$ concentration have decreased rapidly since 2013. The $PM_{2.5}$ concentration retrieved by satellite remote sensing data takes ground monitoring data as a truth value. To pollution control, the government of China established its $PM_{2.5}$ ground monitoring networks in late 2012, and data before 2013 have been lacking (Ma et al., 2016; Ma et al., 2019). Therefore, differences in premature deaths and $PM_{2.5}$ concentration were significant before 2013, which indicated that cities should continue to densify ground measurement networks to enhance accuracy and reduce uncertainty in data.

Spatially, differences in premature deaths and $PM_{2.5}$ concentration were most obvious in Jilin, Fujian, Liaoning, Hebei, Shanxi, Hubei, Sichuan, and Yunnan. The reason why differences were significant in these areas may lie in the missingness of AOD. The satellite AOD has been used to retrieve air pollution data in five sets of $PM_{2.5}$ concentration remote sensing datasets. Previous studies indicated that due to cloud/snow cover, high surface reflectance, and extremely high aerosol loading, satellite AOD can be misclassified as a cloud (Van Donkelaar et al., 2011; Tao et al., 2012). The non-random missingness in AOD retrievals may lead to bias in exposure assessment due to potential systematic differences in $PM_{2.5}$ concentrations when AOD is missing or retrieved (Xiao et al., 2017; He et al., 2019; Liu et al., 2019). Therefore, the selection of $PM_{2.5}$ concentration data must be carried out cautiously when conducting $PM_{2.5}$ health risks studies, especially in regions such as Jilin, Liaoning, Hebei, Shanxi, Hubei, Sichuan, Yunnan, and Fujian, with significant differences in premature death assessments.

Many studies have been focused on the impact of resolution in concentration and health risk assessments in recent years (Pugh et al., 2013; Pepe et al., 2016; Korhonen et al., 2019; Liu et al., 2020). Zou et al. found that compared to those research studies at resolutions of approximately 110 km, 45, and 10 km (Lelieveld et al., 2015; Liu et al., 2017; Wang et al., 2018), the accuracy of premature deaths estimated could be theoretically enhanced by combining the air quality data and population data at 1 km resolution (Zou et al., 2019). This study confirmed this theory to some extent, in which the CHAP and CGS3 datasets at 1 km resolution worked well than the GGS3 dataset at 5 km resolution and CGS2 and PHD datasets at 10 km resolution. The high resolution with 1 km could better reflect the spatial–temporal distributions of $PM_{2.5}$ concentration and health risks. In addition, the CHAP and CGS2 datasets were estimated by two categories of approaches, that is, the statistical approach and scaling approach, which performed well in different areas, so they can be complementary in assessing concentration and health risks.

While this study reduced the uncertainty in health risk assessments by the preferred combination project of the $PM_{2.5}$ dataset, several limitations remain. First, the baseline mortality rates of different age and sex population are various. The negative health effects of air pollution increase with age as the reduction in physiological processes leads to more age-related diseases (Pope, 2007; Yin et al., 2021). Thus, there was uncertainty in health risk assessments due to the consideration of only baseline mortality rates of adults (aged ≥25 years). To enhance accuracy and reduce uncertainty in health risk assessments because of age and sex structure, future studies should pay attention to assessing premature deaths of different age and sex structure population. Second, health risks of air pollution are not only correlated to air quality and concentration–response relationship considered in the GEMM functions (Xie et al., 2018; Ding et al., 2019; Wang et al., 2020; Li et al., 2021), but it is also a process related to human activity pattern. Spatially different human activity patterns may trigger various exposure scenarios (e.g., respiratory rates) (Zou et al., 2019), and it will theoretically bias the air quality and the GEMM-based premature death assessments. Therefore, the effects of human activity patterns on health risks should be considered in future studies.

## DATA AVAILABILITY STATEMENT

The datasets presented in this study can be found in online repositories. The names of the repository/repositories and accession number(s) can be found in the article/ Supplementary Material.

## AUTHOR CONTRIBUTIONS

All authors participated in the field survey and data collection. JL analyzed the data and drafted the manuscript. SL and YX designed the study. NL and LX revised the manuscript. All authors participated in the field survey and data collection, critically revised the manuscript, and gave final approval to the version submitted for publication.

## FUNDING

This research was funded by the National Natural Science Foundation of China (Grant No. 41871317).

## REFERENCES


Burnett, R. T., Pope, C. A., III, Ezzati, M., Olives, C., Lim, S. S., Mehta, S., et al. (2014). An Integrated Risk Function for Estimating the Global Burden of Disease Attributable to Ambient Fine Particulate Matter Exposure. *Environ. Health Perspect.* 122, 397–403. doi:10.1289/ehp.1307049

Burnett, R., Chen, H., Szyszkowicz, M., Fann, N., Hubbell, B., Pope, C. A., et al. (2018). Global Estimates of Mortality Associated with Long-Term Exposure to Outdoor Fine Particulate Matter. *Proc. Natl. Acad. Sci. U.S.A.* 115, 9592–9597. doi:10.1073/pnas.1803222115

Cohen, A. J., Brauer, M., and Burnett, R. (2018). Estimates and 25-Year Trends of the Global Burden of Disease Attributable to Ambient air Pollution: An Analysis of Data from the Global Burden of Diseases Study 2015 (vol 389, pg 1907, 2017). *Lancet* 391, 1576. doi:10.1016/S0140-6736(18)30900-0

Ding, D., Xing, J., Wang, S., Liu, K., and Hao, J. (2019). Estimated Contributions of Emissions Controls, Meteorological Factors, Population Growth, and Changes in Baseline Mortality to Reductions in Ambient [Formula: See Text] and [Formula: See Text]-Related Mortality in China, 2013-2017. *Environ. Health Perspect.* 127, 067009. doi:10.1289/EHP4157

Fang, D., Wang, Q. G., Li, H., Yu, Y., Lu, Y., and Qian, X. (2016). Mortality Effects Assessment of Ambient PM2.5 Pollution in the 74 Leading Cities of China. *Sci. Total Environ.* 569-570, 1545–1552. doi:10.1016/j.scitotenv.2016.06.248

Gupta, P., Christopher, S. A., Wang, J., Gehrig, R., Lee, Y., and Kumar, N. (2006). Satellite Remote Sensing of Particulate Matter and Air Quality Assessment over Global Cities. *Atmos. Environ.* 40, 5880–5892. doi:10.1016/j.atmosenv.2006.03.016

Hammer, M. S., van Donkelaar, A., Li, C., Lyapustin, A., Sayer, A. M., Hsu, N. C., et al. (2020). Global Estimates and Long-Term Trends of Fine Particulate Matter Concentrations (1998-2018). *Environ. Sci. Technol.* 54, 7879–7890. doi:10.1021/acs.est.0c01764

He, Q., Gu, Y., and Zhang, M. (2019). Spatiotemporal Patterns of Aerosol Optical Depth throughout China from 2003 to 2016. *Sci. Total Environ.* 653, 23–35. doi:10.1016/j.scitotenv.2018.10.307

He, Q., Gao, K., Zhang, L., Song, Y., and Zhang, M. (2021). Satellite-Derived 1-km Estimates and Long-Term Trends of PM2.5 Concentrations in China from 2000 to 2018. *Environ. Int.* 156, 106726. doi:10.1016/j.envint.2021.106726

Hoogh, K. D., Héritier, H., Stafoggia, M., Künzli, N., and Kloog, I. (2018). Modelling Daily PM2.5 Concentrations at High Spatio-Temporal Resolution across Switzerland. *Environ. Pollut.* 233, 1147–1154. doi:10.1016/j.envpol.2017.10.025

Hu, X., Waller, L. A., Lyapustin, A., Wang, Y., Al-Hamdan, M. Z., Crosson, W. L., et al. (2014). Estimating Ground-Level PM2.5 Concentrations in the Southeastern United States Using MAIAC AOD Retrievals and a Two-Stage Model. *Remote Sens. Environ.* 140, 220–232. doi:10.1016/j.rse.2013.08.032

Korhonen, A., Lehtomäki, H., Rumrich, I., Karvosenoja, N., Paunu, V.-V., Kupiainen, K., et al. (2019). Influence of Spatial Resolution on Population PM2.5 Exposure and Health Impacts. *Air Qual. Atmos. Health* 12, 705–718. doi:10.1007/s11869-019-00690-z

Laden, F., Schwartz, J., Speizer, F. E., and Dockery, D. W. (2006). Reduction in Fine Particulate Air Pollution and Mortality. *Am. J. Respir. Crit. Care Med.* 173, 667–672. doi:10.1164/rccm.200503-443OC

Lelieveld, J., Evans, J. S., Fnais, M., Giannadaki, D., and Pozzer, A. (2015). The Contribution of Outdoor Air Pollution Sources to Premature Mortality on a Global Scale. *Nature* 525, 367–371. doi:10.1038/nature15371

Li, S., Zou, B., Fang, X., and Lin, Y. (2020). Time Series Modeling of PM2.5 Concentrations with Residual Variance Constraint in Eastern Mainland China during 2013-2017. *Sci. Total Environ.* 710, 135755. doi:10.1016/j.scitotenv.2019.135755

Li, Y., Liao, Q., Zhao, X., Tao, Y., Bai, Y., and Peng, L. (2021). Premature Mortality Attributable to PM2.5 Pollution in China during 2008-2016: Underlying Causes and Responses to Emission Reductions. *Chemosphere* 263, 127925. doi:10.1016/j.chemosphere.2020.127925

Liang, F., Xiao, Q., Huang, K., Yang, X., Liu, F., Li, J., et al. (2020). The 17-y Spatiotemporal Trend of PM 2.5 and its Mortality Burden in China. *Proc. Natl. Acad. Sci. U.S.A.* 117, 25601–25608. doi:10.1073/pnas.1919641117

Liu, M., Huang, Y., Ma, Z., Jin, Z., Liu, X., Wang, H., et al. (2017). Spatial and Temporal Trends in the Mortality Burden of Air Pollution in China: 2004-2012. *Environ. Int.* 98, 75–81. doi:10.1016/j.envint.2016.10.003

Liu, N., Zou, B., Feng, H., Wang, W., Tang, Y., and Liang, Y. (2019). Evaluation and Comparison of Multiangle Implementation of the Atmospheric Correction Algorithm, Dark Target, and Deep Blue Aerosol Products Over China. *Atmos. Chem. Phys.* 19, 8243–8268. doi:10.5194/acp-19-8243-2019

Liu, T., Wang, C., Wang, Y., Huang, L., Li, J., Xie, F., et al. (2020). Impacts of Model Resolution on Predictions of Air Quality and Associated Health Exposure in Nanjing, China. *Chemosphere* 249, 126515. doi:10.1016/j.chemosphere.2020.126515

Ma, Z., Hu, X., Sayer, A. M., Levy, R., Zhang, Q., Xue, Y., et al. (2016). Satellite-Based Spatiotemporal Trends in PM 2.5 Concentrations: China, 2004-2013. *Environ. Health Perspect.* 124, 184–192. doi:10.1289/ehp.1409481

Ma, Z., Liu, R., Liu, Y., and Bi, J. (2019). Effects of air Pollution Control Policies on PM2.5 Pollution Improvement in China from 2005 to 2017: A Satellite-Based Perspective. *Atmos. Chem. Phys.* 19, 6861–6877. doi:10.5194/acp-19-6861-2019

Ma, Z., Dey, S., Christopher, S., Liu, R., Bi, J., Balyan, P., et al. (2022). A Review of Statistical Methods Used for Developing Large-Scale and Long-Term PM2.5 Models from Satellite Data. *Remote Sens. Environ.* 269, 112827. doi:10.1016/j.rse.2021.112827

Maji, K. J., Li, V. O., and Lam, J. C. (2020). Effects of China's Current Air Pollution Prevention and Control Action Plan on Air Pollution Patterns, Health Risks and Mortalities in Beijing 2014-2018. *Chemosphere* 260, 127572. doi:10.1016/j.chemosphere.2020.127572

Pepe, N., Pirovano, G., Lonati, G., Balzarini, A., Toppetti, A., Riva, G. M., et al. (2016). Development and Application of a High Resolution Hybrid Modelling System for the Evaluation of Urban Air Quality. *Atmos. Environ.* 141, 297–311. doi:10.1016/j.atmosenv.2016.06.071

Pope, C. A. (2007). Mortality Effects of Longer Term Exposures to Fine Particulate Air Pollution: Review of Recent Epidemiological Evidence. *Inhal. Toxicol.* 19, 33–38. doi:10.1080/08958370701492961

Pugh, T. A. M., Ashworth, K., Wild, O., and Hewitt, C. N. (2013). Effects of the Spatial Resolution of Climate Data on Estimates of Biogenic Isoprene Emissions. *Atmos. Environ.* 70, 1–6. doi:10.1016/j.atmosenv.2013.01.001

Rohde, R. A., and Muller, R. A. (2015). Air Pollution in China: Mapping of Concentrations and Sources. *PLoS One* 10, e0135749. doi:10.1371/journal.pone.0135749

Shen, L., Wang, H., Kong, X., Zhang, C., Shi, S., and Zhu, B. (2021a). Characterization of Black Carbon Aerosol in the Yangtze River Delta, China: Seasonal Variation and Source Apportionment. *Atmos. Pollut. Res.* 12, 195–209. doi:10.1016/j.apr.2020.08.035

Shen, M., Gu, X., Li, S., Yu, Y., Zou, B., and Chen, X. (2021b). Exposure to Black Carbon is Associated with Symptoms of Depression: A Retrospective Cohort Study in College Students. *Environ. Int.* 157, 106870. doi:10.1016/j.envint.2021.106870

Stafoggia, M., Bellander, T., Bucci, S., Davoli, M., de Hoogh, K., de' Donato, F., et al. (2019). Estimation of Daily PM10 and PM2.5 Concentrations in Italy, 2013-2015, Using a Spatiotemporal Land-Use Random-Forest Model. *Environ. Int.* 124, 170–179. doi:10.1016/j.envint.2019.01.016

Tao, M., Chen, L., Su, L., and Tao, J. (2012). Satellite Observation of Regional Haze Pollution Over the North China Plain. *J. Geophys. Res.* 117, D12203. doi:10.1029/2012JD017915

Van Donkelaar, A., Martin, R. V., Brauer, M., Kahn, R., Levy, R., Verduzco, C., et al. (2010). Global Estimates of Ambient Fine Particulate Matter Concentrations from Satellite-Based Aerosol Optical Depth: Development and Application. *Environ. Health Perspect.* 118, 847–855. doi:10.1289/ehp.0901623

Van Donkelaar, A., Martin, R. V., Levy, R. C., da Silva, A. M., Krzyzanowski, M., Chubarova, N. E., et al. (2011). Satellite-Based Estimates of Ground-Level Fine Particulate Matter during Extreme Events: A Case Study of the Moscow Fires in 2010. *Atmos. Environ.* 45, 6225–6232. doi:10.1016/j.atmosenv.2011.07.068

Van Donkelaar, A., Martin, R. V., Brauer, M., and Boys, B. L. (2015). Use of Satellite Observations for Long-Term Exposure Assessment of Global Concentrations of Fine Particulate Matter. *Environ. Health Perspect.* 123, 135–143. doi:10.1289/ehp.1408646

Van Donkelaar, A., Martin, R. V., Brauer, M., Hsu, N. C., Kahn, R. A., Levy, R. C., et al. (2016). Global Estimates of Fine Particulate Matter Using a Combined Geophysical-Statistical Method with Information from Satellites, Models, and Monitors. *Environ. Sci. Technol.* 50, 3762–3772. doi:10.1021/acs.est.5b05833

Van Donkelaar, A., Martin, R. V., Li, C., and Burnett, R. T. (2019). Regional Estimates of Chemical Composition of Fine Particulate Matter Using a Combined

Geoscience-Statistical Method with Information from Satellites, Models, and Monitors. *Environ. Sci. Technol.* 53, 2595–2611. doi:10.1021/acs.est.8b06392

Wang, Q., Wang, J., He, M. Z., Kinney, P. L., and Li, T. (2018). A County-Level Estimate of PM 2.5 Related Chronic Mortality Risk in China Based on Multi-Model Exposure Data. *Environ. Int.* 110, 105–112. doi:10.1016/j.envint.2017.10.015

Wang, F., Liu, C., and Xu, Y. (2019). Analyzing Population Density Disparity in China with GIS-Automated Regionalization: The Hu Line Revisited. *Chin. Geogr. Sci.* 29, 541–552. doi:10.1007/s11769-019-1054-y

Wang, Y., Wild, O., Chen, X., Wu, Q., Gao, M., Chen, H., et al. (2020). Health Impacts of Long-Term Ozone Exposure in China over 2013-2017. *Environ. Int.* 144, 106030. doi:10.1016/j.envint.2020.106030

Wang, C., Wang, Y., Shi, Z., Sun, J., Gong, K., Li, J., et al. (2021a). Effects of Using Different Exposure Data to Estimate Changes in Premature Mortality Attributable to PM2.5 and O3 in China. *Environ. Pollut.* 285, 117242. doi:10.1016/j.envpol.2021.117242

Wang, H., Miao, Q., Shen, L., Yang, Q., Wu, Y., and Wei, H. (2021b). Air Pollutant Variations in Suzhou during the 2019 Novel Coronavirus (COVID-19) Lockdown of 2020: High Time-Resolution Measurements of Aerosol Chemical Compositions and Source Apportionment. *Environ. Pollut.* 271, 116298. doi:10.1016/j.envpol.2020.116298

Wang, L., Chen, G., Pan, Y., Xia, J., Chen, L., Zhang, X., et al. (2021c). Association of Long-Term Exposure to Ambient Air Pollutants with Blood Lipids in Chinese Adults: The China Multi-Ethnic Cohort Study. *Environ. Res.* 197, 111174. doi:10.1016/j.envres.2021.111174

Wei, J., Li, Z., Cribb, M., Huang, W., Xue, W., Sun, L., et al. (2020). Improved 1 km Resolution PM2.5 Estimates Across China using Enhanced Space-Time Extremely Randomized Trees. *Atmos. Chem. Phys.* 20, 3273–3289. doi:10.5194/acp-20-3273-2020

Wei, J., Li, Z., Lyapustin, A., Sun, L., Peng, Y., Xue, W., et al. (2021). Reconstructing 1-Km-Resolution High-Quality PM2.5 Data Records from 2000 to 2018 in China: Spatiotemporal Variations and Policy Implications. *Remote Sens. Environ.* 252, 112136. doi:10.1016/j.rse.2020.112136

Xiao, Q., Wang, Y., Chang, H. H., Meng, X., Geng, G., Lyapustin, A., et al. (2017). Full-Coverage High-Resolution Daily PM2.5 Estimation Using MAIAC AOD in the Yangtze River Delta of China. *Remote Sens. Environ.* 199, 437–446. doi:10.1016/j.rse.2017.07.023

Xie, Z., Qin, Y., Zhang, L., and Zhang, R. (2018). Death Effects Assessment of PM2.5 Pollution in China. *Pol. J. Environ. Stud.* 27, 1813–1821. doi:10.15244/pjoes/77077

Xue, T., Zheng, Y., Tong, D., Zheng, B., Li, X., Zhu, T., et al. (2019). Spatiotemporal Continuous Estimates of PM2.5 Concentrations in China, 2000-2016: A Machine Learning Method with Inputs from Satellites, Chemical Transport Model, and Ground Observations. *Environ. Int.* 123, 345–357. doi:10.1016/j.envint.2018.11.075

Ye, W.-F., Ma, Z.-Y., and Ha, X.-Z. (2018). Spatial-Temporal Patterns of PM2.5 Concentrations for 338 Chinese Cities. *Sci. Total Environ.* 631-632, 524–533. doi:10.1016/j.scitotenv.2018.03.057

Yin, H., Brauer, M., Zhang, J. F., Cai, W. J., Navrud, S., Burnett, R., et al. (2021). Population Ageing and Deaths Attributable to Ambient PM2.5 Polluyion: A Global of Economic Cost. *Lancet* 5, E356–E367. doi:10.1016/S2542-5196(21)00131-5

Zou, B., You, J., Lin, Y., Duan, X., Zhao, X., Fang, X., et al. (2019). Air Pollution Intervention and Life-Saving Effect in China. *Environ. Int.* 125, 529–541. doi:10.1016/j.envint.2018.10.045

**Conflict of Interest:** The authors declare that the research was conducted in the absence of any commercial or financial relationships that could be construed as a potential conflict of interest.

**Publisher's Note:** All claims expressed in this article are solely those of the authors and do not necessarily represent those of their affiliated organizations, or those of the publisher, the editors, and the reviewers. Any product that may be evaluated in this article, or claim that may be made by its manufacturer, is not guaranteed or endorsed by the publisher.

frontiers | Frontiers in Environmental Science

ORIGINAL RESEARCH
published: 11 July 2022
doi: 10.3389/fenvs.2022.947894

# Impacts on Meteorological Parameters and Pollutants by Aerosol Direct Radiative Effect Over Tianjin, China

*Jian Hao*[1,2], *Ziying Cai*[3,4]*, *Suqin Han*[3,4], *Gengxue Ma*[5], *Min Zhang*[3,4] and *Xiaobin Qiu*[1,2]

[1]Tianjin Institute of Meteorological Science, Tianjin, China, [2]Tianjin Key Laboratory for Oceanic Meteorology, Tianjin, China, [3]Tianjin Environmental Meteorological Center, Tianjin, China, [4]CMA-NKU Cooperative Laboratory for Atmospheric Environment-Health Research, Tianjin, China, [5]Beichen Meteorological Bureau, Tianjin, China

The direct radiative effect (DRE) of anthropogenic aerosols on meteorological elements and pollutants over Tianjin, China, was investigated using a fully coupled meteorology-chemistry model [Weather Research and Forecasting (WRF) model coupled with Chemistry (WRF-Chem)] for the entire year of 2021. The results showed that the ground solar radiation decreased from 208.84 W m$^{-2}$ to 194.52 W m$^{-2}$ due to DRE in Tianjin, and the percentage of the reduction was 6.86%. The reduction of ground solar radiation resulted in a 0.90% decrease in temperature, 1.13% decrease in boundary layer height, and 6.01% decrease in visibility, respectively, and a 0.80% increase in relative humidity. Changes in meteorological parameters changed the diffuse conditions of pollutants, leading to an increase of $PM_{2.5}$. Higher concentration of pollutants leads to stronger DRE, and the percentages of changes caused by DRE on polluted days are higher than those on clean days. The DRE influence on pollutants can be summarized as a weather → aerosol → weather → air quality circulation mechanism. The DRE had more severe influence on meteorological elements and pollutants on foggy days. With the emission reduction of pollutants, the influence of the DRE has declined.

**Keywords: direct radiative effect, anthropogenic aerosol, WRF-Chem simulation, west coast of the Bohai Sea, foggy days, emission reduction**

OPEN ACCESS

***Edited by:***
*Honglei Wang,*
*Nanjing University of Information Science and Technology Nanjing, China*

***Reviewed by:***
*Yue Peng,*
*Chinese Academy of Meteorological Sciences, China*
*Dongdong Wang,*
*China Meteorological Administration, China*

***Correspondence:**
*Ziying Cai*
*120078030@163.com*

***Specialty section:***
*This article was submitted to Atmosphere and Climate, a section of the journal Frontiers in Environmental Science*

***Received:*** *19 May 2022*
***Accepted:*** *06 June 2022*
***Published:*** *11 July 2022*

***Citation:***
*Hao J, Cai Z, Han S, Ma G, Zhang M and Qiu X (2022) Impacts on Meteorological Parameters and Pollutants by Aerosol Direct Radiative Effect Over Tianjin, China. Front. Environ. Sci. 10:947894. doi: 10.3389/fenvs.2022.947894*

## INTRODUCTION

The aerosol particles are suspended in the atmosphere. They can reduce atmospheric visibility, impede air quality, and harm human health (Cao et al., 2013; Liu et al., 2014; Gupta et al., 2016; Liang et al., 2016; Syu et al., 2016; Khaefi et al., 2017); they can also affect the earth's climate directly by scattering and absorbing solar and terrestrial radiation and indirectly by serving as cloud condensation nuclei (CCN) and ice nuclei (IN), whereby influencing the microphysical and radiative properties of clouds (Mccormick and Ludwig, 1967; Twomey, 1974; Twomey, 1977; Albrecht, 1989; Charlson et al., 1992; Ramanathan et al., 2001; IPCC, 2013). The IPCC Fifth Assessment Report AR5 (Myhre et al., 2013) shows that the total (all aerosol types) global aerosol radiative forcing is −0.35 Wm$^{-2}$ (uncertainty range between −0.85 and +0.15 Wm$^{-2}$). Compared to the previous AR4, there is a decrease in the negative radiative forcing and an increase in the range, which even includes a positive radiative. This indicates that the effects of aerosols on solar radiation are still not well understood and further research is needed.

The aerosol radiative effect can reduce the occurrence of precipitation, affect the East Asian monsoon, and enhance the fog range (Wu and Han., 2011; Wu and Zhou, 2013; Li et al., 2015). Studies in Eastern China show that due to the large number of pollution emission generated by human activities, a vicious cycle between weather and aerosol is formed under adverse weather conditions (Zhang et al., 2013). That is, when adverse meteorological conditions occur, there are larger amounts of small particles in the air, which reduces the solar radiation reaching the surface through scattering and absorption, thus weakening the atmospheric turbulence and reducing the height of the boundary layer, making the atmosphere more stable and meteorological conditions more unfavorable to the diffusion of pollutants (Liu et al., 2011). In addition, under high-humidity conditions, the presence of a large number of fog condensation nuclei (FCN) in the air on heavily polluted days will prolong the life time and enhance the intensity of fog. A long-time maintenance of the inversion in fog top and light wind weather in the fog area further aggravate the degree of heavy pollution, thus leading to frequent and long-term maintenance of heavy pollution (Deng et al., 2011; Zhang et al., 2011; Zhang et al., 2012).

A lot of studies have been conducted to research the influence of aerosol direct radiative effect through observations (Patadia et al., 2008; Li et al., 2017; Zhang et al., 2019; Kumar et al., 2020; Nojarov et al., 2021) and model simulations (Wang et al., 2015; Das et al., 2016; Sekiguchi et al., 2018; Nguyen et al., 2019). In recent years, with the emergence of online coupled bidirectional feedback weather chemical models, quantitative description of mesoscale weather models has become an option. The Weather Research and Forecasting (WRF) model coupled with Chemistry (WRF-Chem) is a mesoscale online coupled meteorology-chemistry model developed by NCAR, universities, and research institutes. The WRF-Chem model considers the chemical processes of air pollution, advective transport, and turbulent diffusion and wet and dry deposition processes, which is widely used in global air quality forecasts and simulations (Forkel et al., 2012; Forkel et al., 2013; Crippa et al., 2016; Kedia et al., 2016). Liao et al. (2015), Yang et al. (2015), and Cai et al. (2017) used the WRF-Chem model to study the influence of aerosol direct radiative effect on temperature, fog-haze, and pollutants.

Tianjin is the largest open coastal city in north China, west of Beijing. It is located on the west coast of the Pacific Ocean, north of the North China Plain, east of the Bohai Sea, and north of the Yanshan Mountains. With the rapid development of the economy and industrialization process in Tianjin, environmental pollution is still not well controlled, and the aerosol direct radiative effect in Tianjin is not well understood. In this article, the WRF-Chem model was used to simulate the influence of aerosol direct radiative effect on the meteorological parameters and pollutants in Tianjin to provide better conclusions to control air pollution.

# MODEL AND DATA DESCRIPTION

## Monitoring Data

The meteorological data were collected from 13 regional meteorological stations, Tianjin, China, during 01-01-2021 to 31-12-2021, including hourly data of temperature, relative humidity, atmospheric pressure, and precipitation. The pollutant data such as $PM_{2.5}$, $PM_{10}$, $SO_2$, CO, and $O_3$ were collected from the Tianjin environmental monitoring center with a time resolution of 5 min during 01-01-2021 to 31-12-2021. The pollutant data were from 20 environmental monitoring stations belonging to the Tianjin environmental monitoring center. The incorrect data were culled, and the pollutant data were calculated into an hourly average.

## Model Configurations

The Weather Research and Forecasting (WRF) model coupled with Chemistry (WRF-Chem) version 3.8.1, a fully coupled, online meteorology-chemistry model (Grell et al., 2005), was used to investigate the DRE of anthropogenic aerosol in Tianjin, China. The Carbon Bond Mechanism, version Z (CBMZ), gas-phase chemistry mechanism, and the Model for Simulating Aerosol Interactions and Chemistry (MOSAIC) scheme for aerosol simulation were selected (Fast et al., 2006). Aerosol radiative feedback was coupled with the radiative transfer model (RRTMG) for both shortwave and longwave radiation. The simulations were performed at a 15 km horizontal resolution, covering China and its surrounding areas with 121 × 121 grid cells, the central latitude and longitude being 39N° and 116E°. The 41 vertical layers from the ground level to the top pressure of 50 hPa were used for all grids. The boundary layer parameter scheme used the Yonsei University (YSU) scheme. The land surface parameter scheme used the Noah scheme. The microphysical parameter schemes used the single-moment 5-class microphysics (WSM5) scheme.

## Experimental Design

Three cases were designed to study the influence of the DRE on meteorological parameters and pollutants. The DRE was considered in case 1. The Tsinghua University MEIC 2020 anthropogenic emission source inventory was used for the simulation of the entire year of 2021, covering the simulation area except Tianjin, with a resolution of 0.25° × 0.25°. The emission source used over Tianjin was the data from the Tianjin emission census in 2021. In order to discuss the DRE influence, case 2 did not consider the DRE. The emission source was the same as in case 1. Case 3 considered the DRE; the emission was from the Tsinghua University MEIC 2015 anthropogenic emission source inventory. The simulation was also conducted for the entire year of 2021. The emission reduction was conducted since 2015, and the aim of case 3 was to study the influence of emission reduction of pollutants. The initial meteorological fields and boundary conditions were from the 6 h National Centers for Environmental Prediction (NCEP) Final Analysis (FNL) with 1° × 1° spatial resolution. The FNL meteorological initial field was reused every 24 h, and the outputs from previous runs were used as the pollution field initial conditions for the next run.

# RESULTS AND DISCUSSIONS

## Model Evaluation

Before the discussion of the DRE influence, whether the simulation results can be used should be ensured. As case 1 was more similar to reality, the observation data and simulation

**TABLE 1 |** The statistical correlation between observation data and simulation results of WRF-Chem.

| Parameters | Simulation average value | Observation average value | Correlation coefficient | Relative error (%) |
|---|---|---|---|---|
| $PM_{2.5}$/μg $m^{-3}$ | 43.18 | 41.40 | 0.76 | 35.90 |
| T/°C | 13.37 | 13.54 | 0.99 | 6.85 |
| RH/% | 54.80 | 61.36 | 0.92 | 11.94 |

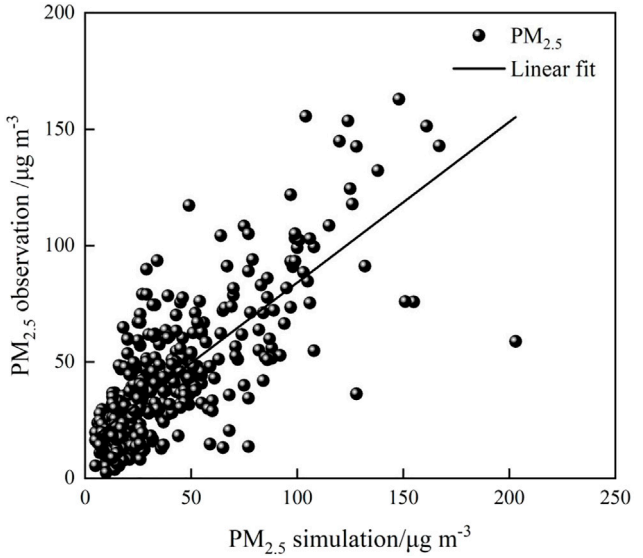


**FIGURE 1 |** Linear relationship between the $PM_{2.5}$ observation data and $PM_{2.5}$ simulation result.

results of case 1 are listed in **Table 1**, including $PM_{2.5}$, temperature (T), and relative humidity (RH). Their correlation coefficient and the annual mean relative error were calculated. The simulated $PM_{2.5}$ was at a height of 2–5 m, and the simulated temperature and RH were at a height of 2 m. The simulation result was averaged from 13 regional stations' simulation results.

The simulated $PM_{2.5}$ in 2021 was 43.18 μg $m^{-3}$, and the $PM_{2.5}$ observation was 41.20 μg $m^{-3}$. The bias of the simulated $PM_{2.5}$ was just 1.78 μg $m^{-3}$, and the relative error was 35.90%. The correlation coefficient between simulated $PM_{2.5}$ and $PM_{2.5}$ observation was 0.76. They were in a positive linear correlation (**Figure 1**). The bias value of simulated $PM_{2.5}$ less than 10 μg $m^{-3}$, 15 μg $m^{-3}$, 20 μg $m^{-3}$, and 25 μg $m^{-3}$ accounted for 44.93%, 65.48%, 75.34%, and 82.19%, respectively, in total samples. Therefore, the $PM_{2.5}$ simulation results of WRF-Chem were close to the observation data, and the simulation performance was good. The biases of T and RH were 0.17°C and 6.56%, and the correlation coefficients were 0.99 and 0.92. WRF-Chem was more accurate in the simulation of meteorological elements. Overall, the simulation results were reliable, which can prove the performance of WRF-Chem was good.

## The Direct Radiative Effect on Ground Solar Radiation

The DRE is the effect of aerosols affecting the earth's climate directly by scattering and absorbing solar and terrestrial radiation. The simulation results showed that ground solar radiation (GSR) was reduced due to the DRE in Tianjin, China. The simulated GSR was 194.52 W $m^{-2}$ in case 1 and 208.84 W $m^{-2}$ in case 2. The simulated GSR was reduced by 14.32 W $m^{-2}$ in 2021 in Tianjin due to the DRE, and the percentage of reduction was 6.86%. The reduction and reduction percentage in each month are shown in **Figure 2**. In March, the decline was most pronounced; the GSR was reduced

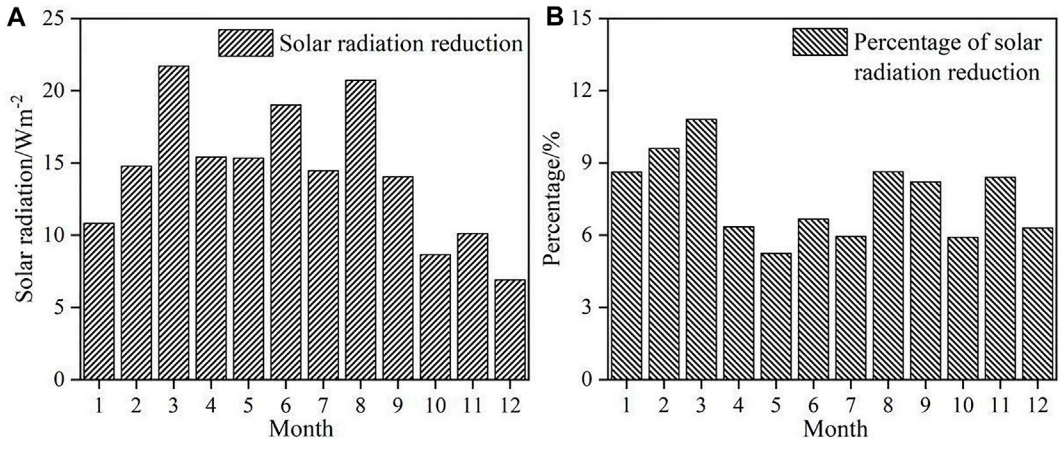


**FIGURE 2 |** Reduction **(A)** and percentage of reduction **(B)** of simulated ground solar radiation caused by the DRE in 2021.

**TABLE 2 |** The DRE on simulated meteorological elements.

| Case | T/°C | RH/% | PBLH/m | Visibility/km |
|---|---|---|---|---|
| Case 1 | 13.37 | 56.15 | 483.37 | 26.78 |
| Case 2 | 13.49 | 55.70 | 498.36 | 28.39 |
| Case 1 minus case 2 | −0.12 | 0.45 | −14.99 | −1.61 |

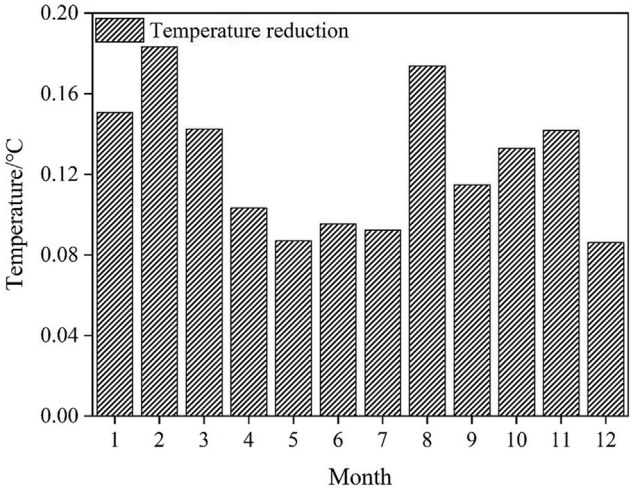


**FIGURE 3 |** Reduction of simulated temperature caused by the DRE in each month of 2021.

by 21.72 W $m^{-2}$ with a percentage of 10.81%. The declines in June and August were also evident, with values of 20.73 W $m^{-2}$ and 19.03 W $m^{-2}$, while the reductions in October and December were the most inapparent, with a value of less than 10 W $m^{-2}$. The GSR decreased most in summer, then spring, and autumn and least in winter. The reduction percentage value was in the range of 5.24%–10.81%. The order of reduction percentage from high to low was winter, autumn, spring, and summer. Although the GSR and its reduction were most in summer and least in winter, the DRE had the most severe influence in winter.

## The Direct Radiative Effect on Meteorological Parameters

The scattering of aerosol can reduce the incoming solar radiation and lead to a reduction of GSR, and then, the temperature decreases. The black carbon can absorb the incoming radiation and heat the atmosphere. The DRE broke the original thermal and dynamic structure of the boundary layer, further affected the transport of water vapor, turbulence, sensible heat, and latent heat, and then, changed the meteorological elements. As **Table 2** shows, the annual temperature decreased by 0.12°C, RH increased by 0.45%, planetary boundary layer height (PBLH) decreased by 14.99 m, and the visibility decreased by 1.61 km. The DRE decreased the temperature firstly, then the evaporation process was weakened, and the RH increased.

The reduction of temperature caused by the DRE in all months is shown in **Figure 3**. The temperature decreased 0.18°C in February,

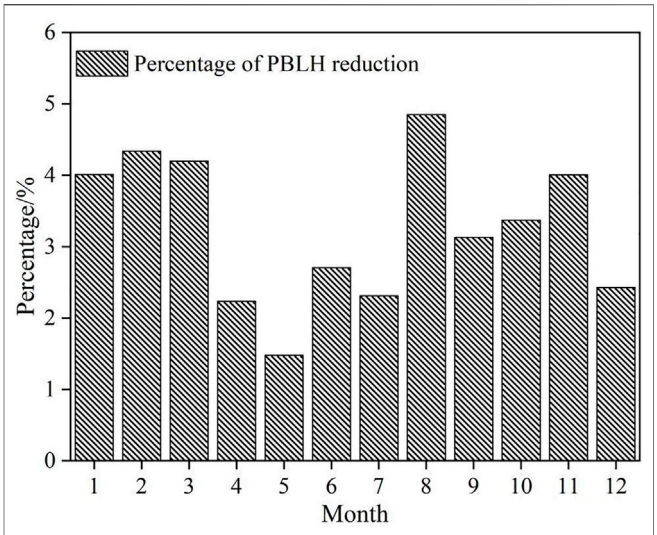


**FIGURE 4 |** Simulated PBLH reduction percentage caused by the DRE in 2021.

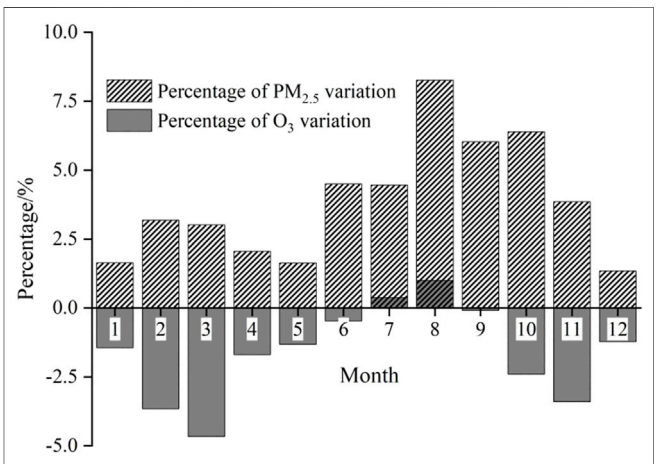


**FIGURE 5 |** Percentage of simulated $PM_{2.5}$ and $O_3$ variation caused by the DRE in 2021.

the highest decrement in the whole year. The reduction in August and January followed February with 0.17°C and 0.15°C, and the temperature decreased less than 0.15°C in all other months. The simulated temperature decreased most in winter, then autumn, and summer and least in spring. The seasonal variation trend of simulated temperature reduction and percentage of GSR reduction was the same. Winter and autumn were more influenced by the DRE than spring and summer. Furthermore, the linear correlation coefficient between these two parameters was 0.69. It means that the effect of DRE on temperature is most direct and significant.

PBLH is determined by the solar radiation, weather system, and local terrain. With the variation of GSR, the PBLH also varied. The decrease in simulated PBLH was in the range of 7.98–22.60 m. The reduction percentage of the simulated PBLH was the highest in August with 4.85%, followed by February and March with 4.33% and

**TABLE 3 |** The DRE on meteorological elements and pollutants on polluted days and clean days.

| Elements | Air quality | Case 1 | Case 2 | Case 1 minus case 2 | Percentage of difference |
|---|---|---|---|---|---|
| GSR/W $m^{-2}$ | Polluted | 140.38 | 165.00 | −24.62 | −17.54% |
| | Clean | 197.18 | 211.21 | −14.03 | −7.15% |
| T/°C | Polluted | 9.66 | 9.99 | −0.33 | −3.42% |
| | Clean | 13.55 | 13.67 | −0.12 | −0.89% |
| RH/% | Polluted | 60.97 | 59.72 | 1.25 | 2.05% |
| | Clean | 55.82 | 55.38 | 0.44 | 0.79% |
| PBLH/m | Polluted | 312.06 | 348.01 | −35.95 | −11.52% |
| | Clean | 492.08 | 506.14 | −14.06 | −2.86% |
| $PM_{2.5}$/μg $m^{-3}$ | Polluted | 114.63 | 106.34 | 8.29 | 7.23% |
| | Clean | 40.45 | 39.09 | 1.36 | 3.36% |
| $O_3$/ppb | Polluted | 18.16 | 19.91 | −1.75 | −9.64% |
| | Clean | 28.75 | 28.96 | −0.21 | −0.73% |

**TABLE 4 |** The DRE on meteorological elements and pollutants on foggy days and non-foggy days.

| Elements | Weather | Case 1 | Case 2 | Case 1 minus case 2 | Percentage of difference |
|---|---|---|---|---|---|
| T/°C | Foggy | 11.14 | 11.36 | −0.22 | −1.97% |
| | Non-foggy | 13.58 | 13.70 | −0.12 | −0.88% |
| RH/% | Foggy | 64.15 | 63.19 | 0.96 | 1.50% |
| | Non-foggy | 55.38 | 54.96 | 0.42 | 0.76% |
| GSR/W $m^{-2}$ | Foggy | 149.64 | 165.50 | −15.86 | −10.60% |
| | Non-foggy | 198.83 | 213.01 | −14.18 | −7.13% |
| PBLH/m | Foggy | 405.23 | 428.56 | −23.33 | −5.76% |
| | Non-foggy | 490.88 | 504.85 | −13.97 | −2.85% |
| Vapor/g $kg^{-1}$ | Foggy | 5.79 | 5.78 | 0.01 | 0.17% |
| | Non-foggy | 6.75 | 6.74 | 0.01 | 0.15% |
| FWC/μg $kg^{-1}$ | Foggy | 6.28 | 4.89 | 1.39 | 22.13% |
| $PM_{2.5}$/μg $m^{-3}$ | Foggy | 72.87 | 68.31 | 4.56 | 6.26% |
| | Non-foggy | 40.32 | 38.98 | 1.34 | 3.32% |
| $O_3$/ppb | Foggy | 20.47 | 21.11 | −0.64 | −3.13% |
| | Non-foggy | 28.92 | 29.16 | −0.24 | −0.83% |

**TABLE 5 |** Pollutant emission in Tianjin in 2015 and 2021.

| Elements | 2015 | 2021 | Reduction percentage (%) |
|---|---|---|---|
| $PM_{2.5}$/10 kt | 7.50 | 4.55 | 39.33 |
| $SO_2$/10 kt | 15.70 | 9.34 | 40.51 |
| $NO_2$/10 kt | 34.20 | 14.76 | 56.82 |

4.20% (**Figure 4**). The seasonal variation trend of simulated PBLH reduction percentage was the same as the reduction of simulated temperature and reduction percentage of GSR. The DRE caused a worse diffusion condition for the pollutants.

## Relation Between the Direct Radiative Effect and Pollutants

Simulated $PM_{2.5}$ caused by the DRE increased by 1.62 μg $m^{-3}$, and the percentage was 3.75%, while the simulated $O_3$ decreased by 0.97%. As shown in **Figure 5**, the simulated $PM_{2.5}$ increased throughout the year. The increment percentage in August was 8.26%, which was the highest in the whole year, and the value in December was the lowest, which was 1.35%. The increase in summer and autumn was higher than in spring and winter. According to the statistics of 365 daily samples throughout the year, the maximum increment was 23.35 μg $m^{-3}$. The increment in 0.27% of the total simulated days was larger than 20 μg $m^{-3}$, and the values larger than 10 μg $m^{-3}$ and 5 μg $m^{-3}$ accounted for 1.64% and 7.95% of the total simulated days. While on 59.45% of the total days, the feedback of the DRE was not obvious, the increment was less than 1 μg $m^{-3}$. The DRE changed the atmospheric stability and meteorological diffusion conditions by breaking the radiation balance, thus increasing the aerosol number concentration. The increase in $PM_{2.5}$ further enhanced DRE and formed a positive feedback, resulting in poor air quality. The DRE affected meteorological elements such as temperature, RH, and PBLH and then changed the diffusion conditions of pollutants, which can be expressed as a cyclic feedback effect of weather → aerosol → weather → air quality.

The DRE of anthropogenic aerosols mainly inhibited the generation of $O_3$ in the Tianjin area. Except for July and August, the simulated $O_3$ decreased in all other months, with the reduction percentage ranging from 0.09% to 4.66%. The increment percentage in July and August was 0.38% and 1.00%. The reduction percentage was the highest in March

**TABLE 6 |** Effects of emission reduction on meteorological elements and pollutants.

| Case | T/°C | RH% | GSR/W $m^{-2}$ | PBLH/km | $PM_{2.5}$/μg $m^{-3}$ | $O_3$/ppb |
|---|---|---|---|---|---|---|
| Case 1 | 13.37 | 56.15 | 194.52 | 483.37 | 43.18 | 28.18 |
| Case 3 | 13.32 | 56.38 | 184.80 | 472.95 | 69.34 | 25.76 |
| Case 1 minus case 3 | 0.05 | -0.23 | 9.72 | 10.42 | -26.16 | 2.42 |

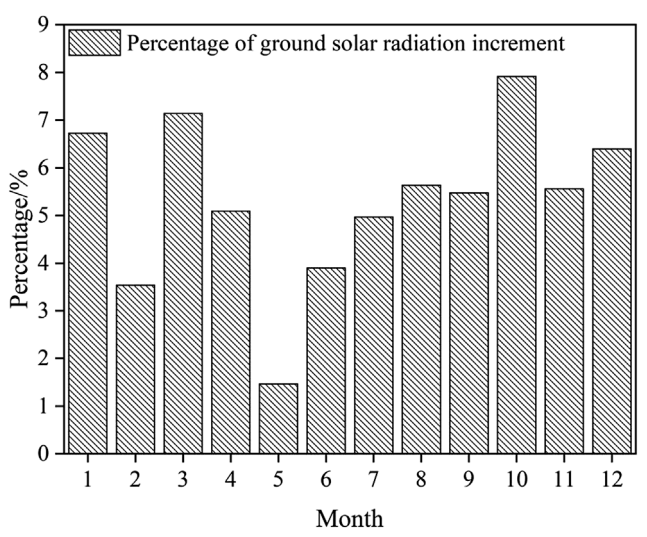


**FIGURE 6 |** Percentage of simulated ground solar radiation increment caused by emission reduction from 2015 to 2021.

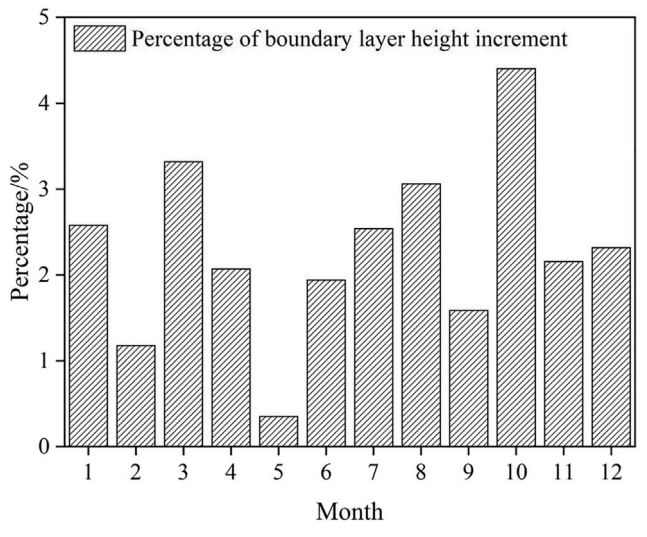


**FIGURE 7 |** Percentage of simulated planetary boundary layer height increment caused by emission reduction from 2015 to 2021.

and the lowest in September. As a photochemical pollutant, $O_3$ was more sensitive to radiation than diffusion (Gao et al., 2020). As the GSR decreased, the photochemical intensity decreased, resulting in the decrease of $O_3$ concentration.

The days with a daily average observed $PM_{2.5}$ > 115 μg $m^{-3}$ were defined as polluted days, and the other days were clean days (Chen et al., 2016); there were 15 polluted days in 2021. **Table 3** shows the DRE on meteorological elements and pollutants on polluted days and clean days. As shown in **Table 3**, the GSR of polluted days was weaker than that of clean days. This is because the pollution cases almost occurred in autumn and winter with weak basic solar radiation. Meanwhile, polluted days were also characterized by low temperature, high RH, and low PBLH (Han et al., 2018a; Han et al., 2018b).

**Table 3** shows that the meteorological parameters and pollutants were influenced strongly on polluted days than on clean days. The GSR decreased by 17.54% due to the DRE on polluted days, 10% higher than on clean days. As the aerosol concentration on polluted days was higher than on clean days, more solar radiation was scattered by aerosol particles at high altitude, leading to more reduction of the GSR, and the DRE was enhanced. The decrement of T was 0.33°C on polluted days and 0.12°C on clean days, the percentage of decrement was 3.42% and 0.89%, and the reduction percentage of T on polluted days was about four times that of clean days. The RH increased 2.05% and 0.79% on polluted and clean days, respectively; the PBLH decreased by 35.95 m on polluted days and 14.06 m on clean days. Due to the DRE, the variation of T, RH, and PBLH was significantly higher on polluted days. $PM_{2.5}$ increased to 8.29 μg $m^{-3}$ with a percentage of 7.23% on polluted days and 1.36 μg $m^{-3}$ with a percentage of 3.36%, which was half of that on polluted days. The DRE decreased $O_3$ by 1.71 and 0.20 ppb on polluted and clean days, respectively, and $O_3$ was almost not affected by the DRE on clean days.

The formation and maintenance of fog are affected by solar radiation and the boundary layer. The DRE can aggravate air pollution, and its influence on foggy days was studied in the following. The definition of foggy days should meet the following three conditions: 1) RH > 90%; 2) visibility < 1 km; and 3) foggy weather had been recorded in more than 50% regional meteorological stations. From the statistics, there were 33 foggy days in 2021.

**Table 4** shows the DRE on meteorological elements and pollutants on foggy days and non-foggy days. On foggy days, the temperature was low, RH was high, GSR was weak, and the PBLH was low. The DRE led to a more severe change on foggy days in both the meteorological parameters and the pollutants. T decreased more than two times on foggy days than on non-foggy days, RH and $PM_{2.5}$ increased two times on non-foggy days, and PBLH and $O_3$ decreased two times and about four times on non-foggy days. On foggy days, the DRE can play a stronger role on the meteorological elements and pollutants which lead to external conditions that are not conductive to fog dissipation. The fog

**TABLE 7 |** Simulated meteorological parameters and pollutants on foggy and non-foggy days caused by emission reduction from 2015 to 2021.

| Elements | Weather | Case 1 | Case 3 | Case 1 minus case 3 | Percentage of difference |
|---|---|---|---|---|---|
| T/°C | Foggy | 11.14 | 11.04 | 0.10 | 0.90% |
| | Non-foggy | 13.58 | 13.53 | 0.05 | 0.37% |
| RH/% | Foggy | 64.15 | 64.50 | −0.35 | −0.55% |
| | Non-foggy | 55.38 | 56.00 | −0.62 | −1.12% |
| GSR/$Wm^{-2}$ | Foggy | 149.64 | 139.38 | 10.26 | 6.86% |
| | Non-foggy | 198.83 | 189.16 | 9.67 | 4.86% |
| PBLH/m | Foggy | 405.23 | 390.20 | 15.03 | 3.71% |
| | Non-foggy | 490.88 | 480.90 | 9.98 | 2.03% |
| $PM_{2.5}$/μg $m^{-3}$ | Foggy | 72.87 | 112.15 | −39.28 | −53.90% |
| | Non-foggy | 40.32 | 65.23 | −24.91 | −61.78% |

water content (FWC) increased to 1.39 μg $kg^{-1}$ by a percentage of 22.13% due to the DRE, meaning the concentration of fog droplets increased. The DRE strengthened the intensity of fog by influencing the meteorological conditions and increasing the aerosol concentrations in the atmosphere, and higher concentration of fog condensation nuclei, lower temperature, lower boundary layer height, and higher RH were made for the maintenance and strengthening of fog.

## Influence of Pollution Abatement on the Direct Radiative Effect

The influence of emission reduction is studied through simulation of case 3. In case 3, the emission source is from the year of 2015, and the rest of the parameters were set as in case 1.

The pollutant emission in Tianjin from MEIC 2015 and the Tianjin emission census in 2021 listed in **Table 5** was the sum of the whole year. It can be seen that from 2015 to 2021, the emission of all pollutants decreased obviously. The primary emission of $PM_{2.5}$ in 2015 was 1.65 times that of 2021. Due to the effective control of air pollution in recent years, the simulated $PM_{2.5}$ decreased from 69.34 μg $m^{-3}$ in 2015 to 43.18 μg $m^{-3}$ in 2021 (**Table 6**), the value in 2015 was 1.61 times that in 2021, and the emission reduction effectively reduced $PM_{2.5}$ pollution. As a significant emission reduction effect of pollutants, the GSR increased from 184.80 W $m^{-2}$ in 2015 to 194.52 W $m^{-2}$ in 2021, with an increment of 9.72 W $m^{-2}$. Meanwhile, the temperature and PBLH increased 0.05°C and 10.42 m, respectively, while the RH decreased 0.23% influenced by the emission reduction. Overall, the control of air pollution has been very effective.

The percentage of the GSR and PBLH increment in each month is shown in **Figures 6**, **7**. In October, the percentages of the GSR and PBLH increment were both the highest of the whole year, and the lowest value of the percentage was shown in May. The emission reduction was most significant in autumn and least significant in spring.

On foggy days, the effect of emission reduction on meteorological parameters and pollutants was more significant than on non-foggy days except for the RH and $PM_{2.5}$ (**Table 7**). That means the improvement of air quality plays a certain role in reducing the occurrence and development of fog.

# CONCLUSION

Based on the simulation of three cases by WRF-Chem, the direct radiative effect of anthropogenic aerosols on meteorological parameters and pollutants was studied. The direct radiative effect on polluted days and foggy days was analyzed, and the results of emission reduction from 2015 to 2021 were also shown. The results showed the following:

1) Affected by the direct radiative effect, the simulated ground solar radiation in Tianjin decreased to 14.32 W $m^{-2}$ with a percentage of 6.86% in 2021. The other simulated meteorological parameters such as temperature, boundary layer height, and visibility decreased by 0.12°C, 5.48 m, and 1.61 km, respectively, and the relative humidity increased by 0.45%, which caused a worse diffusion condition for the pollutants. The direct radiative effect was more pronounced in winter and autumn than in summer and spring.
2) A worse diffusion condition caused by the direct radiative effect concentrated the aerosol particles in the boundary layer, leading to an increment of $PM_{2.5}$. On the opposite, weaker solar radiation was not conducive to photochemical reactions and reduced $O_3$ content. A more polluted environment strengthened the direct radiative effect; all the meteorological parameters and pollutants had greater magnitude of change caused by the direct radiative effect on polluted days. A cyclic feedback effect of weather → aerosol → weather → air quality can be described on polluted days.
3) The emission reduction conducted during 2015–2021 was effective with a reduction percentage of 39.33% in $PM_{2.5}$. Improvement in air quality increased the temperature by 0.05°C, ground solar radiation by 9.72 W $m^{-2}$, and boundary layer height by 10.42 m and decreased the relative humidity by 0.23%. The meteorological parameters were beneficial to the diffusion of pollutants, reduction of pollution, and suppression of occurrence and development of fog.

# DATA AVAILABILITY STATEMENT

The original contributions presented in the study are included in the article/Supplementary Material; further inquiries can be directed to the corresponding author.

## AUTHOR CONTRIBUTIONS

JH is responsible for full manuscript writing, ZC is responsible for the simulation, SH polished the manuscript, GM and MZ looked for the observation data, and XQ ensured the normal operation of the mode.

## FUNDING

This study was jointly sponsored by the National Natural Science Foundation of China (Grant No. 42130513) and the Bohai Rim Meteorological Science Collaborative Innovation Fund (QYXM202014).

## REFERENCES

Albrecht, B. A. (1989). Aerosols, Cloud Microphysics, and Fractional Cloudiness. *Science* 245, 1227. doi:10.1126/science.245.4923.1227

Cai, Z. Y., Yao, Q., Han, S. Q., and Liu, J. L. (2017). The Influence of the Air Quality and Meteorological Field about Aerosol Direct Climate Effect on Tianjin. *Chin. Environ. Sci.* 37 (3), 908–914. (in Chinese).

Cao, J., Chow, J. C., Lee, F. S. C., and Watson, J. G. (2013). Evolution of PM2.5 Measurements and Standards in the U.S. And Future Perspectives for China. *Aerosol Air Qual. Res.* 13, 1197–1211. doi:10.4209/aaqr.2012.11.0302

Charlson, R. J., Schwartz, S. E., Hales, J. M., Cess, R. D., Coakley, J. A., Hansen, J. E., et al. (1992). Climate Forcing by Anthropogenic Aerosols. *Science* 255, 423–430. doi:10.1126/science.255.5043.423

Chen, W., Tang, H., and Zhao, H. (2016). Urban Air Quality Evaluations under Two Versions of the National Ambient Air Quality Standards of China. *Atmos. Pollut. Res.* 7 (1), 49–57. doi:10.1016/j.apr.2015.07.004

Crippa, P., Sullivan, R. C., Thota, A., and Pryor, S. C. (2016). Evaluating the Skill of High-Resolution WRF-Chem Simulations in Describing Drivers of Aerosol Direct Climate Forcing on the Regional Scale. *Atmos. Chem. Phys.* 16 (1), 397–416. doi:10.5194/acp-16-397-2016

Das, S., Dey, S., and Dash, S. K. (2016). Direct Radiative Effects of Anthropogenic Aerosols on Indian Summer Monsoon Circulation. *Theor. Appl. Climatol.* 124, 629–639. doi:10.1007/s00704-015-1444-8

Deng, Z. Z., Zhao, C. S., Ma, N., Liu, P. F., Ran, L., Xu, W. Y., et al. (2011). Size-resolved and Bulk Activation Properties of Aerosols in the North China Plain. *Atmos. Chem. Phys.* 11 (8), 3835–3846. doi:10.5194/acp-11-3835-2011

Fast, J. D., Gustafson, W. I., Easter, R. C., Zaveri, R. A., and Peckham, S. E. (2006). Evolution of Ozone, Particulates, and Aerosol Direct Radiative Forcing in the Vicinity of Houston Using a Fully Coupled Meteorology-Chemistry-Aerosol Model. *J. Geophys. Res. Atmos.* 111, D21. doi:10.1029/2005jd006721

Forkel, R., Werhahn, J., Hansen, A. B., Mckeen, S., Peckham, S., Grell, G., et al. (2012). Effect of Aerosol-Radiation Feedback on Regional Air Quality - A Case Study with WRF/Chem. *Atmos. Environ.* 53, 202–211. doi:10.1016/j.atmosenv.2011.10.009

Forkel, R., Werhahn, J., and Suppan, P. (2013). *Case Studies on Aerosol Feedback for Europe with WRF-Chem.* EGU General Assembly Conference Abstracts.

Gao, J., Li, Y., Zhu, B., Hu, B., Wang, L., and Bao, F. (2020). What Have We Missed when Studying the Impact of Aerosols on Surface Ozone via Changing Photolysis Rates? *Atmos. Chem. Phys.* 20, 10831–10844. doi:10.5194/acp-20-10831-2020

Grell, G. A., Peckham, S. E., Schmitz, R., Mckeen, S. A., Frost, G., Skamarock, W. C., et al. (2005). Fully Coupled "Online" Chemistry within the WRF Model. *Atmos. Environ.* 39, 6957–6975. doi:10.1016/j.atmosenv.2005.04.027

Gupta, G. P., Kumar, B., Singh, S., and Kulshrestha, U. C. (2016). Deposition and Impact of Urban Atmospheric Dust on Two Medicinal Plants during Different Seasons in NCR Delhi. *Aerosol Air Qual. Res.* 16, 2920–2932. doi:10.4209/aaqr.2015.04.0272

Han, S.-q., Hao, T.-y., Zhang, Y.-f., Liu, J.-l., Li, P.-y., Cai, Z.-y., et al. (2018a). Vertical Observation and Analysis on Rapid Formation and Evolutionary Mechanisms of a Prolonged Haze Episode over Central-Eastern China. *Sci. Total Environ.* 616-617, 135–146. doi:10.1016/j.scitotenv.2017.10.278

Han, S., Liu, J., Hao, T., Zhang, Y., Li, P., Yang, J., et al. (2018b). Boundary Layer Structure and Scavenging Effect during a Typical Winter Haze-Fog Episode in a Core City of BTH Region, China. *Atmos. Environ.* 179, 187–200. doi:10.1016/j.atmosenv.2018.02.023

Intergovernmental Panel on Climate Change (IPCC) (2013). "Climate Change 2013: The Physical Science Basis," in *Contribution of Working Group I to the Fifth Assessment Report of the Intergovernmental Panel on Climate Change* (Cambridge, United Kingdom and New York, NY, USA: Cambridge University Press).

Kedia, S., Cherian, R., Islam, S., Das, S. K., and Kaginalkar, A. (2016). Regional Simulation of Aerosol Radiative Effects and Their Influence on Rainfall over India Using WRFChem Model. *Atmos. Res.* 182, 232–242. doi:10.1016/j.atmosres.2016.07.008

Khaefi, M., Geravandi, S., Hassani, G., Yari, A. R., Soltani, F., Dobaradaran, S., et al. (2017). Association of Particulate Matter Impact on Prevalence of Chronic Obstructive Pulmonary Disease in Ahvaz, Southwest Iran during 2009-2013. *Aerosol Air Qual. Res.* 17, 230–237. doi:10.4209/aaqr.2015.11.0628

Kumar, K. R., Devi, N. L., Khan, R., Kang, N., and Griffith, D. (2020). Multi-year Analysis of Aerosol Optical Properties and Implications to Radiative Forcing over Urban Pretoria, South Africa. *Theor. Appl. Climatol.* 141 (1-2), 1–15. doi:10.1007/s00704-020-03183-7

Li, Y., Song, J., and Sun, L. (2015). A Numerical Study of Sulfate Aerosol Direct Effect and its Impact on the East Asia Climate. *J. Meteorol. Res. Appl.* 36 (3), 13–21. (in Chinese). doi:10.3969/j.issn.1673-8411.2015.03.003

Li, J., Jiang, Y., Xia, X., and Hu, Y. (2017). Increase of Surface Solar Irradiance across East China Related to Changes in Aerosol Properties during the Past Decade. *Environ. Res. Lett.* 13, 034006. doi:10.1088/1748-9326/aaa35a

Liang, D., Wang, Y. Q., Ma, C., and Wang, Y. J. (2016). Variability in Transport Pathways and Source Areas of $PM_{10}$ in Beijing during 2009–2012. *Aerosol Air Qual. Res.* 16, 3130–3141. doi:10.4209/aaqr.2015.01.0057

Liao, L., Lou, S. J., Fu, Y., Chang, W. Y., and Liao, H. (2015). Radiative Forcing of Aerosols and its Impact on Surface Air Temperature on the Synoptic Scale in Eastern China. *Chin. J. Atmos. Sci.* 39 (1), 68–82. (in Chinese). doi:10.3878/j.issn.1006-9895.1402.13302

Liu, X., Xie, X., Yin, Z., Liu, C., and Gettelman, A. (2011). A Modeling Study of the Effects of Aerosols on Clouds and Precipitation over East Asia. *Theor. Appl. Climatol.* 106 (3), 343–354. doi:10.1007/s00704-011-0436-6

Liu, Y.-J., Zhang, T.-T., Liu, Q.-Y., Zhang, R.-J., Sun, Z.-Q., and Zhang, M.-G. (2014). Seasonal Variation of Physical and Chemical Properties in TSP, PM10 and PM2.5 at a Roadside Site in Beijing and Their Influence on Atmospheric Visibility. *Aerosol Air Qual. Res.* 14, 954–969. doi:10.4209/aaqr.2013.01.0023

Mccormick, R. A., and Ludwig, J. H. (1967). Climate Modification by Atmospheric Aerosols. *Science* 156, 1358–1359. doi:10.1126/science.156.3780.1358

Myhre, G., Shindell, D., Br´eon, F.-M., Collins, W., Fuglestvedt, J., Huang, J., et al. (2013). "Anthropogenic and Natural Radiative Forcing," in *Climate Change 2013: The Physical Science Basis. Contribution of Working Group I to the Fifth Assessment Report of the Intergovernmental Panel on Climate Change*. Editors T. F. Stocker, D. Qin, G.-K. Plattner, M. Tignor, S. K. Allen, J. Boschung, et al. (Cambridge, United Kingdom and New York, NY, USA: Cambridge University Press).

Nguyen, G. T. H., Shimadera, H., Sekiguchi, A., Matsuo, T., and Kondo, A. (2019). Investigation of Aerosol Direct Effects on Meteorology and Air Quality in East Asia by Using an Online Coupled Modeling System. *Atmos. Environ.* 207, 182–196. doi:10.1016/j.atmosenv.2019.03.017

Nojarov, P., Arsov, T., Kalapov, I., and Angelov, H. (2021). Aerosol Direct Effects on Global Solar Shortwave Irradiance at High Mountainous Station Musala, Bulgaria. *Atmos. Environ.* 244, 117944. doi:10.1016/j.atmosenv.2020.117944

Patadia, F., Gupta, P., and Christopher, S. A. (2008). First Observational Estimates of Global Clear Sky Shortwave Aerosol Direct Radiative Effect over Land. *Geophys. Res. Lett.* 35, L04810. doi:10.1029/2007GL032314

Ramanathan, V., Crutzen, P. J., Kiehl, J. T., and Rosenfeld, D. (2001). Aerosols, Climate, and the Hydrological Cycle. *Science* 294, 2119–2124. doi:10.1126/science.1064034

Sekiguchi, A., Shimadera, H., and Kondo, A. (2018). Impact of Aerosol Direct Effect on Wintertime PM2.5 Simulated by an Online Coupled Meteorology-Air Quality Model over East Asia. *Aerosol Air Qual. Res.* 18 (4), 1068–1079. doi:10.4209/aaqr.2016.06.0282

Syu, J.Y., Cheng, Y.C., Kao, Y.Y., Liang, C. S., Yan, Y. L., and Lai, C. Y. (2016). The Horizontal and Vertical Characteristics of Aeolian Dust From Riverbed. *Aerosol Air Qual. Res.* 16, 3026–3036. doi:10.4209/aaqr.2016.08.0347

Twomey, S. (1977). The Influence of Pollution on the Shortwave Albedo of Clouds. *J. Atmos. Sci.* 34, 1149–1152.

Twomey, S. (1974). Pollution and the Planetary Albedo. *Atmos. Environ. (1967)* 8, 1251–1256. doi:10.1016/0004-6981(74)90004-3

Wang, J., Allen, D. J., Pickering, K. E., Li, Z., and He, H. (2015). Impact of Aerosol Direct Effect on East Asian Air Quality during the EAST-AIRE Campaign. *J. Geophys. Res. Atmos.* 121, 6534–6554. doi:10.1002/2016jd025108

Wu, P. P., and Han, Z. W. (2011). A Modeling Study of Indirect Radiative and Climatic Effects of Sulfate over East Asia. *Chin. J. Atmos. Sci.* 35 (3), 547–559. (in Chinese). doi:10.3878/j.issn.1006-9895.2011.03.14

Wu, P. P., and Zhou, C. C. (2013). A Review of Indirect Anthropogenic Aerosol Effect (In Chinese). *Plate. Mt. Meteorol. Res.* 33 (2), 84–92. (in Chinese). doi:10.3969/j.issn.1674-2184.2013.02.015

Yang, Y. L., Tan, J. H., Sun, J. R., Wang, L. L., Wang, X. Y., Zhang, Y. X., et al. (2015). Synoptic Effect of a Heavy Haze Episode over North China (In Chinese). *Clim. Environ. Res.* 20 (5), 555–570. (in Chinese). doi:10.3878/j.issn.1006-9585.2015.15018

Zhang, Q., Quan, J., Tie, X., Huang, M., and Ma, X. (2011). Impact of Aerosol Particles on Cloud Formation: Aircraft Measurements in China. *Atmos. Environ.* 45, 665–672. doi:10.1016/j.atmosenv.2010.10.025

Zhang, Q., Meng, J., and Quan, J. (2012). Impact of Aerosol Composition on Cloud Condensation Nuclei Activity. *Atmos. Chem. Phys.* 12, 3783–3790. doi:10.5194/acp-12-3783-2012

Zhang, X. Y., Sun, J. Y., Wang, Y. Q., Li, W. J., Zhang, Q., Wang, W., G., et al. (2013). Factors Contributing to Haze and Fog in China (In Chinese). *Chin. Sci. Bull. Chin. Ver.* 58 (13), 1178–1187. doi:10.1007/s11434-012-5460-0

Zhang, J., Xia, X., Zong, X., Fan, X., Chen, H., and Li, J. (2019). Dust Properties and Radiative Impacts at a Suburban Site during 2004-2017 in the North China Plain. *Remote Sens.* 11 (16), 1842. doi:10.3390/rs11161842

**Conflict of Interest:** The authors declare that the research was conducted in the absence of any commercial or financial relationships that could be construed as a potential conflict of interest.

**Publisher's Note:** All claims expressed in this article are solely those of the authors and do not necessarily represent those of their affiliated organizations, or those of the publisher, the editors, and the reviewers. Any product that may be evaluated in this article, or claim that may be made by its manufacturer, is not guaranteed or endorsed by the publisher.

frontiers | Frontiers in Environmental Science

ORIGINAL RESEARCH
published: 13 July 2022
doi: 10.3389/fenvs.2022.943000

# Lightning Disaster Risk Zoning in Jiangsu Province of China Based on the Analytic Hierarchy Process and Entropy Weight Method

*Chenlu Jin, Yu Shu*, Zhaoquan Han, Qu Chen, Jing He and Song Wang*

*Nanjing Meteorology Bureau, Nanjing, China*

Jiangsu Province is located in the middle coastal area of East China, and has a relatively developed economy and a large population density. Severe convection often occurs in Jiangsu Province, and the lightning activities may cause great economic losses and social impact in this region. Based on the theory of natural disaster risk assessment, this study investigates the risk of hazard factors, the sensitivity of hazard-pregnant environment, and the frangibility of a hazard-bearing body in Jiangsu Province. Then, we select thunderstorm days, cloud-to-ground (CG) lightning density, CG lightning current intensity, altitude, topographic relief, soil-electric conductivity, drainage density, population density, gross domestic product (GDP) per land area, and soil utilization type as the influencing factors, and then we use the analytic hierarchy process and entropy weight method to calculate the weights of the influencing factors. Furthermore, all the factors are weighted stacked in ArcGIS, and finally the lightning disaster risk zoning map (1 × 1 km of Jiangsu Province is presented. The results show that the risk of lightning disaster in Jiangsu is low in the north and high in the south. The area of different risk level increases with the decrease in risk level. High-risk areas are mainly in the middle of Nanjing, eastern Changzhou, eastern Wuxi, and the middle of Suzhou. Medium-risk areas are mainly in northern Nanjing, eastern Changzhou, eastern Suzhou, the Tongshan District of Xuzhou City, the Chongchuan District of Nantong City, Lianyun District of Lianyungang City, and the Xiangshui County, Sheyang County, and Dafeng District of Yancheng City. The sub–low-risk areas are mainly in Xuzhou, Suqian, Huai'an, and the middle of Yangzhou City. The low-risk areas are mainly in Lianyungang, Yancheng, northern Nantong, Taizhou, Zhenjiang, southern Nanjing, western Changzhou, western Wuxi, and western Suzhou. We hope this study could provide some references for the lightning disaster prevention and mitigation in Jiangsu Province and East China.

**Keywords: lightning disaster, risk zoning, analytic hierarchy process, entropy weight method, cloud-to-ground lightning**

OPEN ACCESS

***Edited by:***
*Honglei Wang,*
*Nanjing University of Information Science and Technology, China*

***Reviewed by:***
*Xiufeng Guo,*
*Wuxi University, China*
*Zheng Shi,*
*Nanjing University of Information Science and Technology, China*

****Correspondence:***
*Yu Shu*
*njushuyu@sina.com*

***Specialty section:***
*This article was submitted to Atmosphere and Climate, a section of the journal Frontiers in Environmental Science*

***Received:*** *13 May 2022*
***Accepted:*** *23 May 2022*
***Published:*** *13 July 2022*

***Citation:***
*Jin C, Shu Y, Han Z, Chen Q, He J and Wang S (2022) Lightning Disaster Risk Zoning in Jiangsu Province of China Based on the Analytic Hierarchy Process and Entropy Weight Method. Front. Environ. Sci. 10:943000. doi: 10.3389/fenvs.2022.943000*

## 1 INTRODUCTION

Lightning often occurs during a strong atmospheric convection. The physical effects of lightning, such as high current, high voltage, and strong electromagnetic radiation, have a serious impact on transportation, electric power, broadcasting, communication, petroleum, chemical industry, aviation, and aerospace industries (Christian et al., 2003; Zhang et al., 2006; Qie et al., 2013). Therefore, it is called "a major public hazard in the electronic age" by the International Electrotechnical Commission (Xu, 2004; Li et al., 2009). Lightning not only greatly affects mobile communication, but also seriously threatens people's lives and property Zhang et al. (2011). As one of the important means of risk management, risk zoning can effectively avoid and prevent risks (Zhang, 2014). Therefore, carrying out a regional lightning disaster risk assessment and zoning is of great significance in disaster prevention and reduction.

In recent years, some scholars have conducted in-depth research on lightning disaster risk in different regions and have achieved some meaningful results (Black et al., 2015; Miller et al., 2018; Mahdariza, 2018; Zhang K. et al., 2021). The risk assessment of lightning disaster mainly has two technical problems. The first one is to determine the influencing factors of lightning disaster risk and establish the lightning disaster risk assessment model. The other is to calculate the weights of influencing factors. In the early years, people mainly considered the risk of lightning disaster from the risk of hazard factors and the frangibility of a hazard-bearing body. Most of them selected thunderstorm days, CG lightning density, lightning current intensity, lightning disaster frequency, economic loss, casualty, population density, GDP per capita (or per land area) as the influencing factors (Yin et al., 2009; Guo and Xiong, 2008; Yuan et al., 2017). With the deepening of lightning research, people began to realize that the spatial difference of lightning disaster risk is also closely related to climate, terrain, landform, air composition, and local thermal and dynamic conditions (Carey and Buffalo, 2007; Kar et al., 2009; Kar and Liou, 2014; Xia et al., 2015; Rathindra et al., 2020; Nicora et al., 2021; Yu et al., 2021). Therefore, in the recent research on lightning disaster risk assessment and zoning, more lightning disaster influencing factors are selected. Some sensitivity factors of hazard-pregnant environment are included, such as altitude, drainage density, topographic relief, soil utilization type, defense capacity, and soil electric conductivity (Cheng and Wang, 2017; Chen et al., 2019; Li et al., 2021; Wu and Xu, 2021).

Moreover, a large number of studies have adopted analytic hierarchy process to calculate the weights of influencing factors (Wang et al., 2007; Tian et al., 2012; Li et al., 2017; Liu et al., 2021). Combining qualitative and quantitative methods, AHP can deal with many practical problems that cannot be solved by traditional optimization technology. However, the construction of judgment matrix is subjective. In general, the AHP is a subjective weighting method, and the results may be unacceptable for some decision makers. Some studies tried other methods to assess the weights of lightning disaster risk indexes. Chen et al. (2021) used entropy weight comprehensive evaluation model to evaluate the regional lightning disasters in 68 counties and cities in Fujian Province. The entropy weight method (EWM) is an objective method to determine the weight, which is more accurate than subjective methods such as AHP. By using the support vector machine, Sheng et al. (2021) explored a way to combine artificial intelligence algorithms with lightning disaster risk assessment. Zhang and Han (2021) solved the problem of imbalanced lightning disaster data in geographic grid samples based on

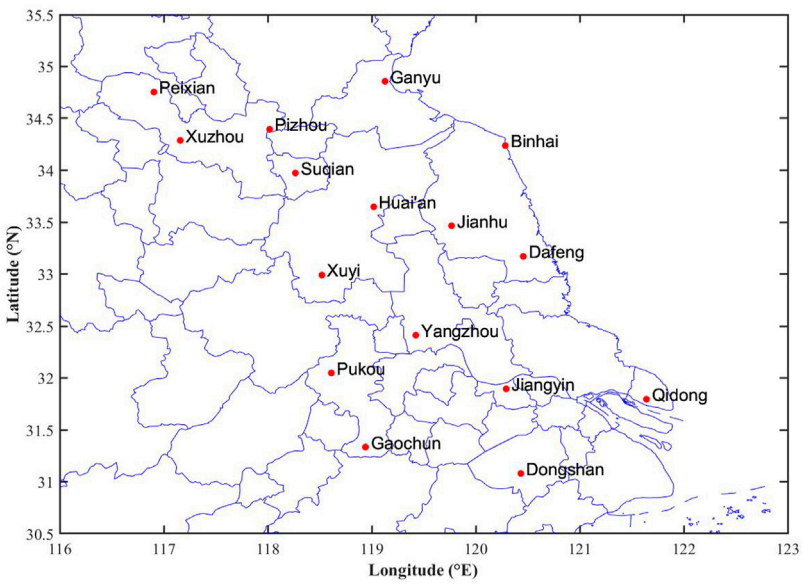


**FIGURE 1 |** Site distribution of ADTD-II lightning positioning system.

**TABLE 1 |** Scaling method for element $a_{ij}$ of judgment matrix.

| Factor *i* compared with factor *j* | Quantized value |
|---|---|
| Equally important | 1 |
| Slightly more important | 3 |
| More important | 5 |
| Much more important | 7 |
| Extremely more important | 9 |
| Intermediate value of two adjacent judgments | 2, 4, 6, 8 |

the K-means clustering algorithm, which calculates the feature of lightning disaster in each small field with the help of neural network structure.

Jiangsu Province is in the middle coastal area of East China (30°45′N–35°08′N, 116°21′E–121°56′E). It is of humid or semi-humid monsoon climate. With the advance and retreat of the western Pacific subtropical high, cold, and warm air frequently converge in Jiangsu Province from spring to autumn, making it the sub–high-value area of lightning density in China (Wang and Chen, 2015). Some studies on the risk and vulnerability of lightning disasters in Jiangsu have been carried out (Zhang et al., 2007; Chen et al., 2017), but some of them have not considered the natural environment and socio-economic development. Moreover, the assignment methods for factor weights in their studies are somewhat subjective, and the research results take city as the basic unit, resulting in a low spatial accuracy in zoning results. Therefore, based on the previous research and the actual situation of Jiangsu, this study selects the evaluation indexes from the risk of hazard factors, the sensitivity of hazard-pregnant environment and the frangibility of a hazard-bearing body. Then, the subjective and objective weight-assignment methods are combined, and the AHP and EWM are used to quantitatively calculate the weight of each index. Afterward, each index is weighted-stacked in the geographic information system (GIS) to draw the lightning disaster risk zoning map (1 × 1 km grid) of Jiangsu. We hope this study could provide a scientific basis for lightning disaster prevention and reduction in Jiangsu.

The remainder of this article is organized as follows. Section 2 shows the data and methods used in this study. Section 3 introduces the establishment of lightning disaster risk zoning model. The lightning disaster risk zoning is given in Section 4. Finally, the summary and conclusions are presented in section 5.

# 2 DATA AND METHODS

## 2.1 Data Introduction

The research data in this study include three categories, that is, the lightning location data, the geographic information data and the socio-economic data. The lightning location data are obtained from the CG lightning data detected by the Jiangsu ADTD-II lightning positioning system from 2016 to 2020. The system is composed of 16 stations (**Figure 1**), and can accurately detect the arriving time of the electromagnetic pulse generated in the discharging of thunderstorms. Therefore, it can obtain the occurrence time, position, height, polarity, intensity, steepness, and other parameters of lightning in real time (Feng et al., 2015), and achieve the 3-dimensional lightning positioning. Meng et al. (2022) found that the horizontal and vertical location errors of the Jiangsu ADTD-II lightning positioning system are less than 300 and 500 m, respectively.

**TABLE 2 |** Average random consistency index value.

| Matrix order | 1 | 2 | 3 | 4 | 5 | 6 | 7 |
|---|---|---|---|---|---|---|---|
| *R.I.* | 0.00 | 0.00 | 0.52 | 0.90 | 1.12 | 1.26 | 1.36 |

If there is lightning record in 1 day, then this day is counted as a thunderstorm day. The lightning density denotes the average frequency of lightning per area. The lightning intensity denotes the average current intensity per area. The thunderstorm days, lightning density, and lightning intensity are counted in the 1 × 1 km grids. According to the quality control method specified in the industrial group document of the Institute of Electrical and Electronics Engineers, the lightning data with the absolute value of lightning current being 0–2 kA and greater than 200 kA are eliminated (IEEES Std., 1997). The elevation data come from the Shuttle Radar Topography Mission, with an accuracy of 90 m, and it can be obtained from the geospatial data cloud (http://srtm.csi.cgiar.org/). The drainage density data are from the National Basic Geographic Information Center (https://www.ngcc.cn). The soil electric conductivity is from the Harmonized World Soil Database (http://www.ncdc.ac.cn). The soil utilization type is from the Resource and Environment Science and Data Center (https://www.resdc.cn). The population and GDP data are from the Resource and Environment Science and Data Center (https://www.resdc.cn). The geographic information and social economy data are from 2016 to 2020 with a resolution of 1 × 1 km.

## 2.2 Methods

### 2.2.1 Data Normalization

To eliminate the differences in physical dimension among the indexes, each index that is involved in grid calculation is normalized. The calculation formula is as follows.

$$a_{ij} = \frac{\left(x_{ij} - x_{\min}\right)}{\left(x_{\max} - x_{\min}\right)}, \tag{1}$$

where $a_{ij}$ is the normalized value of the $j$th sample of the $i$th index, $x_{ij}$ is the actual value of the index, and $x_{\min}$ and $x_{\max}$ are the minimum and maximum values of the index, respectively.

### 2.2.2 Analytic Hierarchy Process

The AHP is a multicriteria decision-making method that combines qualitative and quantitative analysis. It was first proposed by the well-known American operational research scientist Saaty (1980). The operation steps of AHP include judgment matrix construction, consistency test, and weight ranking. Each index is compared in pairs by using the 1–9 scale method in judgment matrix construction (**Table 1**). By solving the maximum eigenvalue $\lambda_{\max}$ of judgment matrix **A** and the eigenvector **W** corresponding to $\lambda_{\max}$, the relative weight coefficient of each index at the same level is obtained. When the order of the judgment matrix is not less than 3, a consistency test

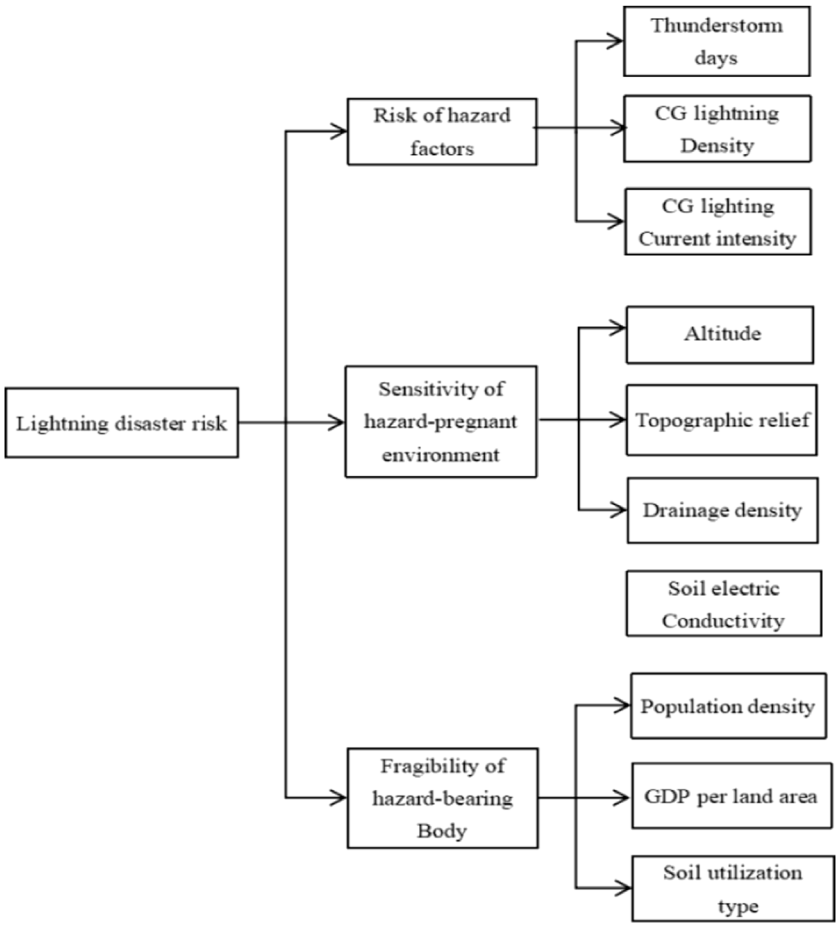


**FIGURE 2 |** Lightning disaster risk evaluation index system.

is required. The calculation of the inspection index, *C.I.*, is shown in **Eq. 2**.

$$C.I. = \frac{\lambda_{\max} - n}{n - 1}, \tag{2}$$

According to the order of the judgment matrix, the average random consistency index value *R.I.* in **Table 2** is checked, and the consistency test coefficient *C.R.* is calculated according to **Eq. 3**.

$$C.R. = \frac{C.I.}{R.I.}. \tag{3}$$

If $C.R. \leq 0.1$, the judgment matrix meets the consistency requirement, otherwise the judgment matrix should be rebuilt.

### 2.2.3 Entropy-Weight Method

The EWM is an objective assignment method. According to the characteristics of entropy, the randomness and disorder degree of an event can be judged by calculating the entropy, and the dispersion degree of an index can also be judged by the entropy. The greater the dispersion degree of the index is, the greater the weight of the index to the comprehensive evaluation is. Entropy weight can be calculated by **Eqs. 4–6**.

$$p_{ij} = \frac{a_{ij}}{\sum_{j-1}^{n} a_{ij}}, \tag{4}$$

$$h_i = -k\sum_{j=1}^{n} p_{ij}\, ln\, p\left(k_{ij}\frac{1}{ln\,\mathrm{n}}\right), \tag{5}$$

$$w_i = \frac{1 - h_i}{m - \sum_{i=1}^{m} h_i}. \tag{6}$$

$w_\mathrm{i}$ is the entropy weight of the *i*th evaluation index, $h_\mathrm{i}$ is the entropy of the *i*th evaluation index, n is the number of evaluation indexes, $m$ is the number of samples, and $p_\mathrm{ij}$ is the proportion of the *j*th sample value to *i*th index.

## 3 ESTABLISHMENT OF LIGHTNING DISASTER RISK ZONING MODEL

### 3.1 Construction of Lightning Disaster Risk Evaluation Index System

Lightning disaster risk refers to the possibility of lightning disaster and its possible losses. Based on the theory of natural disaster risk assessment and zoning, this study constructs the

lightning disaster risk assessment index system of "target layer-criterion layer-index layer" (**Figure 2**). It can be seen that the risk of lightning disaster is the target layer; the risk of hazard factors, the sensitivity of hazard-pregnant environment, and the frangibility of hazard-bearing body form the criterion layer; the thunderstorm days, CG lightning density, CG lightning current intensity, altitude, topographic relief, drainage density, soil electric conductivity, population density, average GDP per land area, and soil utilization type form the index layer.

## 3.2 Calculation of Lightning Disaster Risk Index

The lightning disaster risk index is composed of the risk of hazard factors, the sensitivity of hazard-pregnant environment, and the frangibility of hazard-bearing body. The corresponding relationships among each index and disaster risk are shown in **Eqs. 7–10**:

$$L_{\mathrm{DRI}} = (R_{\mathrm{h}} w_{\mathrm{r}}) + (R_{\mathrm{e}} w_{\mathrm{e}}) + (R_{\mathrm{f}} w_{\mathrm{f}}), \tag{7}$$

$$R_{\mathrm{h}} = \sum_{\mathrm{i}=1}^{n} W_{\mathrm{hi}} Q_{\mathrm{hi}} = W_{\mathrm{h1}} Q_{\mathrm{h1}} + W_{\mathrm{h2}} Q_{\mathrm{h2}} + W_{\mathrm{h3}} Q_{\mathrm{h3}}, \tag{8}$$

$$R_{\mathrm{e}} = \sum_{\mathrm{i}=1}^{n} W_{\mathrm{ei}} Q_{\mathrm{ei}} = W_{\mathrm{e1}} Q_{\mathrm{e1}} + W_{\mathrm{e2}} Q_{\mathrm{e2}} + W_{\mathrm{e3}} Q_{\mathrm{e3}} + W_{\mathrm{e4}} Q_{\mathrm{e4}}, \tag{9}$$

$$R_{\mathrm{f}} = \sum_{\mathrm{i}=1}^{n} W_{\mathrm{fi}} Q_{\mathrm{fi}} = W_{\mathrm{f1}} Q_{\mathrm{f1}} + W_{\mathrm{f2}} Q_{\mathrm{f2}} + W_{\mathrm{f3}} Q_{\mathrm{f3}}. \tag{10}$$

In **Equation 8**, the greater the lightning disaster risk evaluation index is $L_{\mathrm{DRI}}$, the greater the risk degree is, $R_{\mathrm{h}}$, $R_{\mathrm{e}}$, and $R_{\mathrm{f}}$ are evaluation indexes of the risk of hazard factors, the sensitivity of hazard-pregnant environment, and the frangibility of hazard-bearing body, respectively; $w_{\mathrm{r}}$, $w_{\mathrm{e}}$, and $w_{\mathrm{f}}$ are the weights corresponding to each influencing factor of the criterion layer. In **Eqs. 9, 10**, $W_{\mathrm{i}}$ is the weight of each index in the index layer; $Q_{\mathrm{h1}}$, $Q_{\mathrm{h2}}$, and $Q_{\mathrm{h3}}$ are the normalized values of thunderstorm days, CG lightning density, and CG lightning current intensity, respectively; $Q_{\mathrm{e1}}$, $Q_{\mathrm{e2}}$, $Q_{\mathrm{e3}}$, and $Q_{\mathrm{e4}}$ are the normalized values of altitude, topographic relief, soil electric conductivity, and drainage density, respectively; and $Q_{\mathrm{f1}}$, $Q_{\mathrm{f2}}$, and $Q_{\mathrm{f3}}$ are the normalized values of population density, average GDP per land area, and soil utilization type, respectively. The normalized values of each index in the index layer are multiplied by the corresponding weights to obtain the evaluation index of the factors in the criterion layer of the lightning disaster risk evaluation model. Then, the weighted stack analysis is carried out level by level to obtain the comprehensive evaluation index value of lightning disaster risk in the target layer.

## 3.3 Determining Weights of the Index

The AHP-EWM model, using a combinative weighting approach, considers both subjective and objective weighted procedures and is adopted to yield more accurate criteria weight results as recommended by some researchers (Jahan et al., 2012; Alemi et al., 2016; Ding et al., 2018; Dehdasht et al., 2020). According to the Technical Guidelines for Lightning Disaster Risk Zoning (QX/T 405-2017), the weights of the indexes in the criterion level are determined by the AHP, and the weights of the indexes in the index level are determined by the EWM. According to past studies (Li et al., 2018; Long et al., 2019; Shi et al., 2019; Ren et al., 2020; Cui et al., 2021), it is clear that the hazard-bearing body is the object of hazard factors, and the interaction between the two contributes greatly to the formation of lightning disasters. The order of the indexes in the criterion level is determined as the risk of hazard factors, the frangibility of the hazard-bearing body, and the sensitivity of the hazard-pregnant environment. By constructing the priority judgment matrix and giving the relative scores of various indexes, the AHP is carried out based on the scoring results. The weight coefficients of the risk of hazard factors, the sensitivity of the hazard-pregnant environment, and the frangibility of the hazard-bearing body are 0.41, 0.24, and 0.35, respectively. The consistency test coefficient $C.R.= 0.002 < 0.10$, showing that the judgment matrix is acceptable. The weights of indexes in the index layer are determined by the EWM. We use GIS to generate 5,000 random points within the study area, extract the normalized factor values of 10 indexes in the index layer to the random points, derive the attribute table, and calculate the weights of each index according to **Eqs. 4–6**. Finally, the weights of the index layer and the criterion layer are weighted to obtain the comprehensive weight of each index, as shown in **Table 3**.

# 4 LIGHTNING DISASTER RISK ZONING

## 4.1 Risk of Hazard Factors

**Figure 3A** shows the spatial distribution of thunderstorm days in Jiangsu. As can be seen, the number of thunderstorm days in Jiangsu is generally large in the south and small in the north, which is consistent with the spatial distribution of convective activities in Jiangsu (Shu et al., 2022). The areas with thunderstorm days greater than 60 days per year (d/a) are mainly in Suzhou, Wuxi, Changzhou, Nanjing, and northwestern Xuzhou. The average thunderstorm days in most parts of northern-middle Jiangsu are 30–50 d/a, and the areas with thunderstorm days less than 30 d/a are mainly in Yancheng of eastern Jiangsu. **Figure 3B** shows the spatial distribution of CG lightning density in Jiangsu. It can be seen that the annual average CG lightning density in Jiangsu is 2.35 times/($km^2$·a). Few areas are with CG lightning density greater than 6 times/($km^2$·a), such as eastern Suzhou, northern Changzhou, northern Nanjing, and southern Huai'an. The areas with lightning density less than 3 times/($km^2$·a) are the eastern coastal cities and Taizhou. **Figure 3C** shows the spatial distribution of CG lightning current intensity in Jiangsu. It can be seen that the CG lightning current intensity is generally low in Jiangsu, with an average value of 9.9 kA, indicating that the lightning in Jiangsu is mainly negative CG lightning with low energy. The high-value areas of CG lightning current intensity are mainly in central Nanjing, eastern Changzhou, southeastern Nantong City, Yangzhou City, western Zhenjiang City, and southern Yangzhou, where the CG lightning current intensity is 50–70 kA, indicating that the proportion of positive CG lightning in these areas is higher than that in other areas. The

**TABLE 3 |** Weights of lightning disaster risk assessment indexes in Jiangsu.

| Target layer | Criterion layer | | Index layer | | Comprehensive weight |
|---|---|---|---|---|---|
| | Content | Weight | Content | Weight | |
| Lightning disaster Risk | Risk of hazard factors | 0.41 | CG lightning density | 0.1103 | 0.0452 |
| | | | CG lightning current density | 0.8764 | 0.3593 |
| | | | Thunderstorm days | 0.0133 | 0.0055 |
| | Sensitivity of hazard-pregnant environment | 0.24 | Altitude | 0.0894 | 0.0215 |
| | | | Topographic relief | 0.4473 | 0.1074 |
| | | | Drainage density | 0.0401 | 0.0096 |
| | | | Soil electric conductivity | 0.4232 | 0.1016 |
| | Frangibility of hazard-bearing body | 0.35 | GDP per land area | 0.5636 | 0.1973 |
| | | | Population density | 0.3843 | 0.1345 |
| | | | soil utilization type | 0.0521 | 0.0182 |

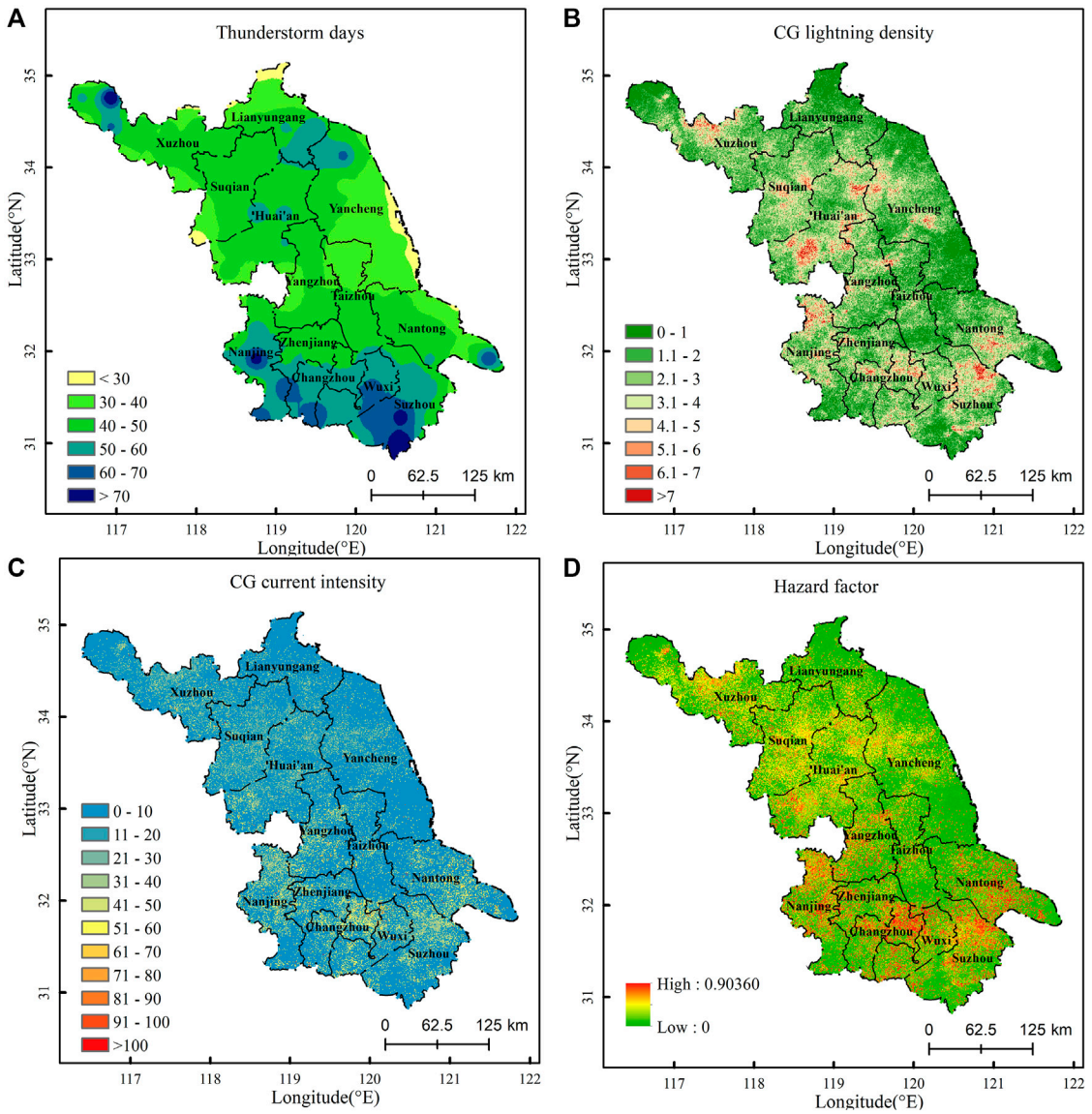


**FIGURE 3 |** Distribution of the risk of lightning hazard factors in Jiangsu. **(A)** Thunderstorm days, unit: days/year; **(B)** CG lightning density, unit: km$^2$/year; **(C)** CG current intensity, unit: KA; **(D)** hazard factor.

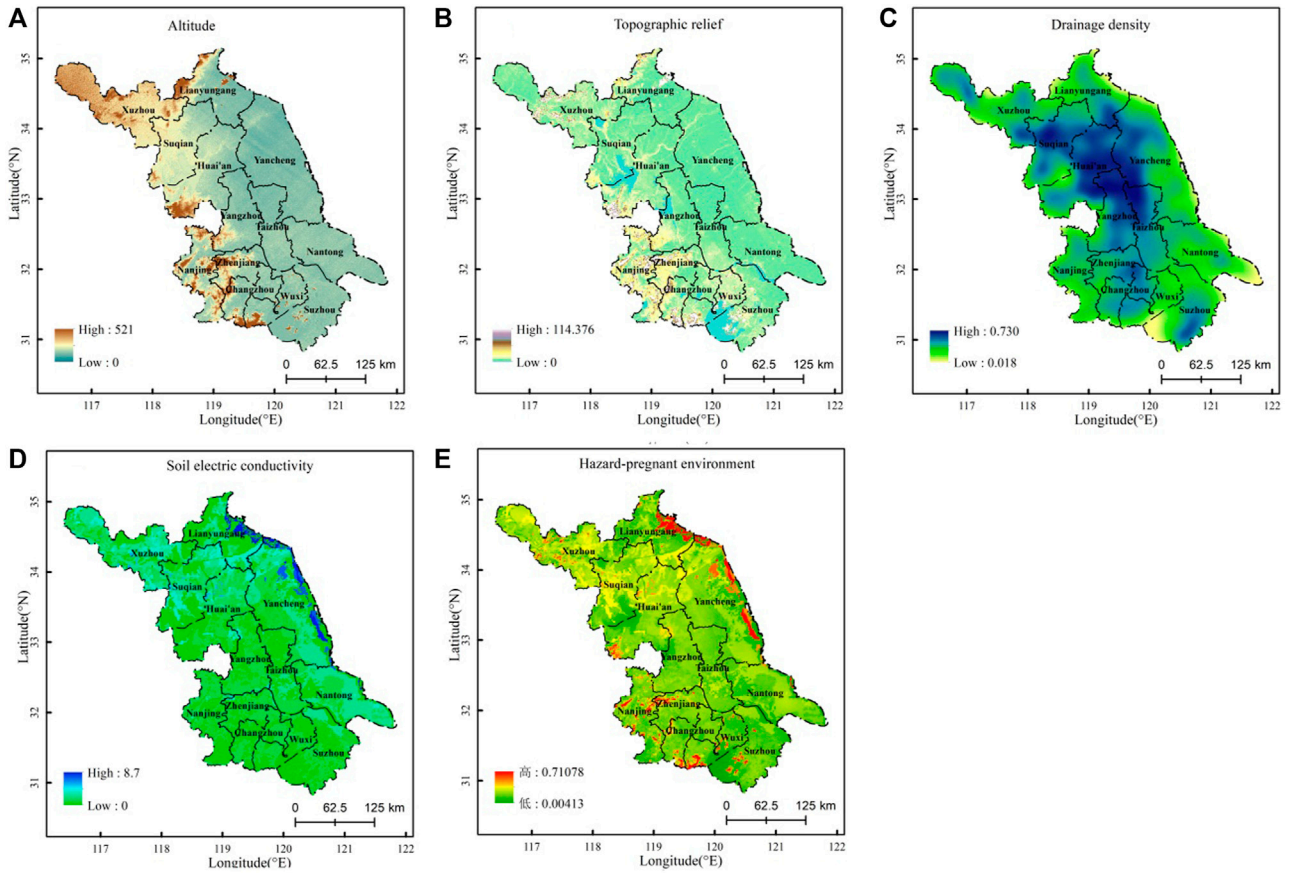


**FIGURE 4 |** Distribution of the sensitivity of hazard-pregnant environment in Jiangsu. **(A)** Altitude, unit: m; **(B)** Topographic relief, unit: m; **(C)** Drainage density, unit: km/km$^2$. **(D)** Soil electric conductivity, unit: ds/m; **(E)** Hazard-pregnant environment.

CG lightning current intensity in northern Jiangsu is relatively low. Specifically, it is within 20–40 kA in Xuzhou, Suqian, Huai'an, and central-northern Yancheng; while it is below 20 kA in Lianyungang, southern Yancheng, Taizhou, and southern Nanjing. It is indicated that the lightning activities are weak in the above areas.

Lightning disaster hazard factors are natural and uncontrollable. The risk of hazard factors reflects the activity degree of lightning in the study area. The higher the risk of hazard factors, the greater the risk of lightning disaster. The risk of lightning hazard factors in Jiangsu is calculated with **Eq. 8**, as shown in **Figure 3D**. The risk of lightning hazard factors in Jiangsu is generally high in the south and low in the north, which is consistent with the distribution of thunderstorm days. The high-risk areas of hazard factors are mainly in northern Nanjing, the junction area between Nanjing and Zhenjiang, eastern Changzhou, and eastern Suzhou. There are also some scattered distributions in central Nantong, northwestern Yangzhou, and eastern Wuxi. The CG lightning density and current intensity in these areas are high, resulting in the high risk of hazard factors. The sub–high-risk areas of hazard factors are mainly distributed in Xuzhou, Suqian, Huai'an, and parts of Funing County of Yancheng City. The low-risk areas are concentrated in Lianyungang, southern Yancheng, Taizhou, and central Zhenjiang, southern Nanjing, western Suzhou. The low-risk area is dominant in Jiangsu, accounting for about 70.56%.

## 4.2 Analysis of the Sensitivity of the Hazard-Pregnant Environment

**Figure 4A** shows the altitude distribution of Jiangsu Province. It can be seen that the main landform of Jiangsu is plain with generally low altitude, and the average altitude is only about 13 m. 80% of the areas are less than 15 m above sea level. Most relatively, high-altitude areas are in the southwest. There are few areas with an altitude over 100 m, mainly distributed in the Xuyi hills in southwestern Huai'an, western Zhenjiang, the hills extending from Zhenjiang to Nanjing, Laoshan Mountain in Pukou District of northern Nanjing, Maoshan Mountain in the junction area of Changzhou and Zhenjiang, hilly areas in Wuxi and southern Changzhou, and the Yuntai Mountain range in eastern Lianyungang. **Figure 4B** shows the topographic relief of Jiangsu. Topographic relief can reflect the local relief of landform. In ArcGIS, the neighborhood analysis tool is used to count the standard deviation of maximum elevation and minimum elevation at 1 km resolution, which is taken as the

topographic relief of the study area. The overall terrain of Jiangsu is flat, with 90% of the topographic relief less than 10 m. The areas with topographic relief of 15–45 m are mainly in the middle of Xuzhou, western Suqian, Nanjing, and parts of Zhenjiang. The areas with topographic relief over 45 m are mainly in western Wuxi. **Figure 4C** shows the distribution of drainage density in Jiangsu. It can be seen that there are many water systems in Jiangsu, showing the characteristics of high in the middle and low in the surrounding areas. The areas with a density over 0.5 km/km$^2$ are mainly in eastern Huai'an, the middle of Suqian, western Yancheng, northern Yangzhou, and northern Taizhou. The soil electric conductivity indicates the strength of soil conductivity. The greater the soil electric conductivity is, the stronger the ability to discharge lightning current is, and the larger the possibility to form lightning disasters is. **Figure 4D** shows the distribution of soil electric conductivity in Jiangsu. As can be seen, the overall distribution of soil electric conductivity in Jiangsu is uniform, which is high in the north and east, and low in the south and west. The high-value areas are mainly in a narrow strip along the coastline of Lianyungang and Yancheng. These areas have high soil humidity, high salt content, and low resistance, which are conducive to conducting electricity. Most sub–high-value areas are in Xuzhou, Suqian, northern Huai'an, and eastern Nantong. Low-value areas are mainly in central and southern Jiangsu.

The sensitivity of the hazard-pregnant environment is calculated by using **Eq. 9**, as shown in **Figure 4E**. It can be seen that the sensitivity of lightning hazard-pregnant environment in Jiangsu is generally low. Areas with high sensitivity are scattered, such as northern-central Nanjing, northern Zhenjiang, southwestern Wuxi, southwestern Huai'an, and western Suzhou. These areas are in the low mountains or hills in southwestern Jiangsu, and the altitude is relatively high. The comparison of altitude and topographic relief with the distribution of thunderstorm days shows that most high-value areas of thunderstorm days in Jiangsu are in the hilly and low mountain areas with topographic relief greater than 15 m and altitude more than 100 m, indicating that the hilly terrain may be one of the important conditions for frequent lightning in Jiangsu. The low-value areas of thunderstorm days are mainly in the plain areas in northern Jiangsu, which may be related to its flat terrain. Meanwhile, the salt ions dissolved in the water vapor in the sea breeze of coastal cities can prevent the ionization in the lightning channel from bringing clean atmosphere, which is not conducive to the generation of lightning. The specific reasons need to be further analyzed. Another area with high sensitivity of the hazard-pregnant environment is in Guanyun County of Lianyungang City, Xiangshui County, and Sheyang County of Yancheng City, and a narrow strip along the coastline of Dafeng District of Yancheng City. These areas have high soil electric conductivity. Large areas in central-eastern Xuzhou, Suqian, and Huai'an have high drainage density and high soil electric conductivity, so the sensitivity of hazard-pregnant environment is also high. The comparison of the distribution of drainage density and CG lightning density shows that there is a circle of high-value area of CG lightning density around the high-value area of drainage density, indicating that the difference of the underlying surface between land and water body in Jiangsu may also be one of the important conditions for lightning. The areas with low sensitivity of the hazard-pregnant environment are widely distributed in Lianyungang, Yancheng, Taizhou, Nantong, and Yangzhou, and the low sensitivity of hazard-pregnant environment is dominant in Jiangsu.

## 4.3 Frangibility of Hazard-Bearing Body

Population density and GDP per land area directly affect the magnitude of disaster losses. **Figure 5A** and **Figure 5B** show the spatial distribution of population density and GDP per land area in Jiangsu, respectively. Population density and GDP per land area both belong to socio-economic data, and as seen from **Figure 5**, their distributions are basically the same, showing the characteristics of high in the south and low in the north. High-value areas are mainly in Nanjing, Wuxi, Changzhou, Suzhou, Tongshan District of Xuzhou, and Chongchuan District of Nantong. Other regions are of small population and low GDP, and the distribution is relatively uniform. Soil utilization type can reflect the protection ability of a hazard-bearing body against lightning disaster to a certain extent. According to the *Land Use Status Classification* (GB/T 21010-2017), there are three soil utilization types: construction land, agricultural land, and unused land. Agricultural land includes cultivated land, forest land, garden land, etc. Studies have shown that strong lightning activities with high average lightning intensity mainly occur in forest land, followed by cultivated land (Yu and Liu, 2020). The agricultural land is usually in an open area without an effective lightning protection device, so strong lightning activity can cause serious casualties there. Construction land includes the land for urban and rural housing and public facilities. Heat island effect is likely to occur in construction land which is densely populated, and aerosol may promote CG lightning activities on construction land by changing the cloud microphysical process (Steiger and Orville, 2003). Fortunately, construction land is generally equipped with lightning protection devices, which can effectively resist the risk of lightning disasters. Unused land refers to wasteland, sandy land, swamp, etc. Although lightning protection devices are not installed, the cumulative losses of life and property are small due to the low population density there.

The risk assignment shows that the risk of agricultural land is 1.0, followed by construction land (0.6) and unused land (0.4), and the land use risk distribution map of Jiangsu is shown in **Figure 5C**. Due to the wide distribution and the high risk of cultivated land, high-risk values are widely distributed. The frangibility of lightning hazard-bearing body in Jiangsu is calculated with **Eq. 10**, as shown in **Figure 5D**. The frangibility of a hazard-bearing body in Jiangsu is highly consistent with the distribution of population density and GDP, which is high in the south and low in the north. High-vulnerability areas account for a relatively small proportion, mainly in Nanjing, Changzhou, Wuxi, Suzhou, Xuzhou, the center of Nantong, and economically developed county-level city Kunshan governed by Suzhou. The aforementioned areas have high population density and high GDP per land area. Around the high-vulnerability areas, there are some sub–high-vulnerability areas, mainly in the suburbs or county-level cities of economically developed cities in southern Jiangsu.

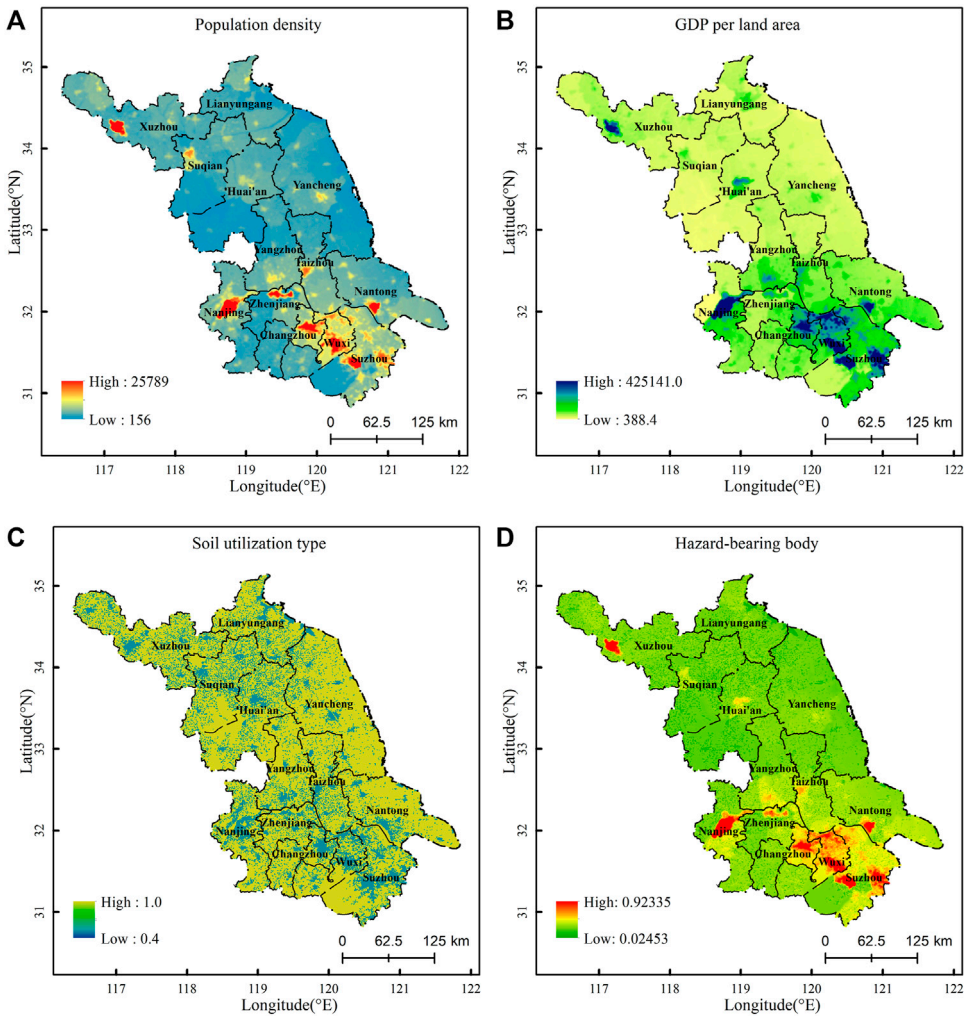


**FIGURE 5 |** Frangibility of lightning hazard-bearing body in Jiangsu. **(A)** Population density, unit: person/km$^2$; **(B)** GDP value of the region, unit: ten thousand Yuan/km$^2$. **(C)** Soil utilization type. **(D)** Hazard-bearing body.

## 4.4 Analysis of Lightning Disaster Risk Zoning in Jiangsu

The comprehensive evaluation index of lightning disaster risk in the target layer is obtained by weighting the indexes of hazard factors, hazard-pregnant environment, and hazard-bearing body. The risk levels are divided by using the natural breakpoint method in GIS, and the lightning disaster risk zoning in Jiangsu is shown in **Figure 6**. The risk of lightning disaster in Jiangsu is high in the south and low in the north. The area of high risk is the smallest (1,338.22 km$^2$, accounting for 1.25%), and it increases with the decrease of risk level. The high-risk areas are mainly distributed in central Nanjing, eastern Changzhou, eastern Wuxi, and central Suzhou. These areas are all downtown, with a large population density and developed economy. The risk of human life loss and economic loss caused by lightning is higher. At the same time, there are plenty of construction land and electric equipment in these areas, and the electric equipment should be protected from being damaged by induced lightning. The medium-risk area covers an area of 14,272.88 km$^2$, accounting for 13.31% of the total area. It is mainly in northern Nanjing, eastern Changzhou, eastern Suzhou, Tongshan District of Xuzhou, Chongchuan District of Nantong, Lianyun District of Lianyungang, and Xiangshui County, Sheyang County, and Dafeng District of Yancheng. These areas have high CG lightning density, high-risk hazard factors, high soil electric conductivity, and high sensitivity of a hazard-pregnant environment. The sub–low-risk area covers an area of 22,648.44 km$^2$, accounting for 21.13% of the total area, mainly in Xuzhou, Suqian, Huai'an, and the middle of Yangzhou. The drainage density in these areas is high, and there is a high risk for the people near the water area to suffer direct lightning attack. Therefore, the protection of people from direct lightning strike in these areas should be strengthened. The low-risk area covers an area of 68,940.47 km$^2$, accounting for 64.31% of the total area, and it is the main type of lightning disaster risk in Jiangsu. It is distributed in Lianyungang, southern Yancheng, northern

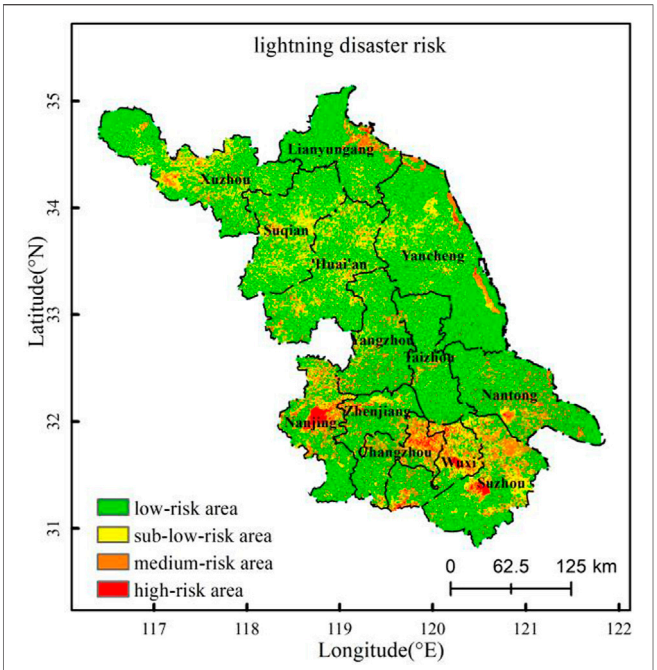


**FIGURE 6 |** Lightning disaster risk zoning in Jiangsu.

Nantong, Taizhou, central Zhenjiang, southern Nanjing, western Changzhou, western Wuxi, and western Suzhou. These areas are mainly plain areas, and have a low value of CG lightning density and current intensity, low population density, and low GDP. However, the aforementioned areas are mostly agricultural land which lacks effective lightning protection measures. A lightning disaster can easily cause casualties. It is necessary to strengthen the publicity of lightning protection knowledge.

## 5 CONCLUSION AND DISCUSSIONS

Focused on the lightning disaster and based on the theory of natural disaster risk assessment, this study investigates the risk of hazard factors, the sensitivity of hazard-pregnant environment, and the frangibility of a hazard-bearing body in Jiangsu Province. Then, we select thunderstorm days, CG lightning density, CG lightning current intensity, altitude, topographic relief, soil electric conductivity, drainage density, population density, GDP per area, and soil utilization type as the evaluation indexes, and establish the quantitative relationship and calculation program between the impact indexes and lightning disaster risk.

The correlations among hazard factors, hazard-pregnant environment, and hazard-bearing body have been analyzed. It is found that the high-value areas of thunderstorm days in Jiangsu are mainly in the hilly and low mountain areas with topographic relief greater than 15 m and altitude over 100 m. The low-value areas of thunderstorm days are mainly in the plain areas of northern Jiangsu. The hilly terrain in Jiangsu may be one of the important conditions for frequent lightning. A circle of high-value area of CG lightning density is wrapped around the high-value area of drainage density, indicating that the difference of underlying surface between land and water body in Jiangsu may also be one of the important conditions for lightning.

We use the AHP and EWM to determine the comprehensive weight of indexes, calculate the risk value of lightning disaster, divide the risk level, and draw the lightning disaster risk zoning map. The results show that the risk of lightning disaster in Jiangsu is high in the south and low in the north, and the risk area is inversely proportional to the risk level. The areas in Jiangsu are mainly with low risk of lightning disaster. High-risk areas are mainly in the middle of Nanjing, eastern Changzhou, eastern Wuxi, and the middle of Suzhou. Medium-risk areas are mainly in northern Nanjing, eastern Changzhou, eastern Suzhou, Tongshan District of Xuzhou, Chongchuan District of Nantong, Lianyun District of Lianyungang, and Xiangshui County, Sheyang County, and Dafeng District of Yancheng. The sub–low-risk areas are mainly in Xuzhou, Suqian, Huai'an, and the middle of Yangzhou. The low-risk areas are in Lianyungang, southern Yancheng, northern Nantong, Taizhou, central Zhenjiang, southern Nanjing, western Changzhou, western Wuxi, and western Suzhou.

Although this study only focuses on the Jiangsu Province of China, the results obtained in this study are robust and of great significance. We hope this study can provide some references for lightning disaster prevention and mitigation in Jiangsu Province and East China.

## DATA AVAILABILITY STATEMENT

The original contributions presented in the study are included in the article/Supplementary Material; further inquiries can be directed to the corresponding author.

## AUTHOR CONTRIBUTIONS

Conceptualization, YS; methodology, YS; software, ZH; validation, CJ; formal analysis, YS; investigation, JH; resources, CJ; data curation, QC; writing original draft preparation, CJ; writing review and editing, YS; visualization, SW; supervision, YS; project administration, YS; and funding acquisition, CJ.

## FUNDING

This research was funded by the Jiangsu Province "333" project (BRA2020429), and the National Natural Science Foundation of China (41305051).

## ACKNOWLEDGMENTS

We thank Nanjing Hurricane Translation for reviewing the English language quality of this article.

## REFERENCES


Alemi-Ardakani, M., Milani, A. S., Yannacopoulos, S., and Shokouhi, G. (2016). On the Effect of Subjective, Objective and Combinative Weighting in Multiple Criteria Decision Making: A Case Study on Impact Optimization of Composites. *Expert Syst. Appl.* 46, 426–438. doi:10.1016/j.eswa.2015.11.003

Black, A. W., and Mote, T. L. (2015). Effects of Winter Precipitation on Automobile Collisions, Injuries, and Fatalities in the United States. *J. Transp. Geogr.* 48, 165–175. doi:10.1016/j.jtrangeo.2015.09.007

Carey, L. D., and Buffalo, K. M. (2007). Environmental Control of Cloud-To-Ground Lightning Polarity in Severe Storms. *J.Monthly Weather Rev.* 135 (4), 1327–1353. doi:10.1175/mwr3361.1

Chen, G. C., Cui, X., and Tian, X. R. (2017). Quantitative Assessment and Zoning of Lightning Hazard in Jiangsu Province. *J. Catastrophology* 32 (1), 32–35. doi:10.3969/j.issn.1000-811X2017.01.007

Chen, L., Chen, C. Z., Hu, Y. J., Yang, X. M., and Zhu, Y. F. (2021). Thunder Disaster Risk Division in Fujian Province Based on Entropy Weight Comprehensive Evaluation Mode. *J. Meteorological Res. Appl.* 42 (1), 46–52. doi:10.19849/j.cnki.CN45-1356/P.2021.2.09

Chen, L. T., Long, S., Yu, H. Y., Li, H. Y., and Wang, Y. (2019). Research on Risk Zoning of Lightning Disaste in Hebei Province. *J.Journal Catastrophology* 34 (3), 189–195. doi:10.3969/j.issn.1000-811X.2019.03.035

Cheng, M., and Wang, X. L. (2017). Risk Vulnerability Zoning of Lightning Disaster in Southwest Shandong Based on the Data of Lightning Orientation. *J.Meteoro-logical Environ. Sci.* 40 (4), 126–131. doi:10.16765/j.cnki.1673-7148.2017.04.018

Christian, H. J., Blakeslee, R. J., Boccippio, D. J., Boeck, W. L., Buechler, D. E., Driscoll, K. T., et al. (2003). Global Frequency and Distribution of Lightning as Observed from Space by the Optical Transient Detector. *J.Geophysical Res. Atmos.* 108 (D1), 4–15. doi:10.1029/2002jd002347

Cui, X. Q., Fu, J., Dai, J., Liu, Y., Hu, Z. H., and Tang, J. (2021). Lightning Disaster Risk Zoning on the High-Speed Railway (City Railway) Lines in Hubei Province Based on Arcgis and AHP. *J. Catastrophology*. 36 (02), 79–83. doi:10.3969/j.issn.1000-811X.2021.02.014

Dehdasht, G., Ferwati, M. S., Zin, R. M., and Abidin, N. Z. (2020). A Hybrid Approach Using Entropy and TOPSIS to Select Key Drivers for a Successful and Sustainable Lean Construction Implementation. *PLoS One* 15 (2), e0228746. doi:10.1371/journal.pone.0228746

Ding, Z., Zhu, M., Wu, Z., Fu, Y., and Liu, X. (2018). Combining AHP-Entropy Approach with GIS for Construction Waste Landfill Selection-A Case Study of Shenzhen. *Ijerph* 15 (10), 2254. doi:10.3390/ijerph15102254

Feng, M. X., Zhou, Y., Yu, M., and Zhang, Y. H. (2015). Evaluation of Jiangsu ADTD Lightning Location System Data in 2013. *J. Sci. Technol. Eng.* 15 (7), 79–84.

Guo, H., and Xion, Y. J. (2008). Vulnerability Analysis, Evaluation and Vulnerability Zoning of Lightning Disaster in Beijing. *J. Appl. Meteorological Sci.* 19 (1), 35–40.

IEEES Std (1997). *IEEE Guide for Improving the Lightning Performance of Transmission Lines*. NewYork: IEEE, 1243–1997.

Jahan, A., Mustapha, F., Sapuan, S. M., Ismail, M. Y., and Bahraminasab, M. (2012). A Framework for Weighting of Criteria in Ranking Stage of Material Selection Process. *Int. J. Adv. Manuf. Technol.* 58, 411–420. doi:10.1007/s00170-011-3366-7

Kar, S. K., Liou, Y.-A., and Ha, K.-J. (2009). Aerosol Effects on the Enhancement of Cloud-To-Ground Lightning over Major Urban Areas of South Korea. *Atmos. Res.* 92 (1), 80–87. doi:10.1016/j.atmosres.2008.09.004

Kar, S. K., and Liou, Y. A. (2014). Enhancement of Cloud-To-Ground Lightning Activity over Taipei, Taiwan in Relation to Urbanization. *Atmos. Res.* 147-148, 111–120. doi:10.1016/j.atmosres.2014.05.017

Li, W. H., Liu, X., Wu, R., Zhong, Y., Mai, Y., Wang, J., et al. (2021). Comprehensive Risk Regionalization of Lightning Disaster over Qinghai Province from 2010 to 2019. *J. Arid. Meteorol.* 39 (6), 1017–1024. doi:10.11755/j.issn.1006-7639(2021)-06-1017

Li, X. L., Chen, J. H., Gu, S. Q., and Tong, X. (2009). Statistics and Analysis of Lightning Flashovers of Transmission Lines during 2000–2007. *J. High. Volt. Eng.* 35 (3), 705–710. doi:10.1109/ICHVE.2008.4773871

Li, Y. C., Wu, L. F., Yu, C. H., Lin, W. H., and Wang, T. T. (2017). Lightning Characteristics and Lightning Disaster Vulnerability Zoning in Sanming of Fujian Province. *J. Nanjing Univ. Inf. Science&Technology Nat. Sci. Ed.* 9 (1), 220–226. doi:10.13878/j.cnki.jnuist.2017.02.016

Li, Y. C., Shen, Y. S., Chen, A. Z., Zhang, Z. F., Cai, H. Z., and Sun, C. L. (2018). Vulnerability Zoning Model of Fine Lightning Disasters Based on GIS Overlay Method. *Meteorological Sci. Technol.* 46 (1), 182–188. doi:10.19517/j.1671-6345.20170136

Liu, P. Y., Zhang, T. F., Yin, L. Y., Zhou, Q. Q., and Yang, X. P. (2021). Comprehensive Evaluation and Zoning of Lightning Disaster Risks in Yunnan Province Based on Multi-Source Data Fusion. *J. Meteorological Sci. Technol.* 49 (2), 269–277. doi:10.19517/j.1671-6345.20200034

Long, S., Yu, H. Y., Li, T., Li, Q., Zou, Z. X., and Wang, Y. (2019). Research on Lightning Disaster Risk Zoning in the Rural Areas of Hebei Province. *J. Chin. J. Agric. Resour. Regional Plan.* 40(11),174–179.

Mahdariza, F. (2018). The Determination of Lightning Disaster Hazard Index Using Analytical Hierarchy Process. *J. Islamic Sci. Technol.* 3 (2), 233–238. doi:10.22373/ekw.v3i2.1630

Meng, X. Y., Wang, J. Q., Ma, Q. M., Yuan, S. B., Song, Y. J., and Zhou, X. (2022). A Dataset of Lightning in China Based on VLF/LF Lightning Location Monitoring System. *J. China Sci. Data* 7 (1). doi:10.11922/11-6035.csd.2021.0059

Miller, P. W., and Mote, T. L. (2018). Characterizing Severe Weather Potential in Synoptically Weakly Forced Thunderstorm Environments. *J. Nat. Hazards &Earth Syst. Sci.* 18 (4), 1–39. doi:10.5194/nhess-18-1261-2018

Nicora, M., Mestriner, D., Brignone, M., Bernardi, M., Procopio, R., and Fiori, E. (2021). A 10-year Study on the Lightning Activity in Italy Using Data from the SIRF Network. *Atmos. Res.* 256 (2021), 105552. doi:10.1016/j.atmosres.2021.105552

Qie, X. S., Zhang, Q. L., Yuan, T., and Zhang, T. L. (2013). *Lightning Physics*. Beijing: Science Press.

Rathindra, N. B., Islam, Md. N., Mia, Md. J., and Islam, M. N. (2020). Modeling on the Spatial Vulnerability of Lightning Disaster in Bangladesh Using GIS and IDW Techniques. *J. Spatial Inf. Res.* 28 (5), 507–521. doi:10.1007/s41324-019-00311-y

Ren, Z. H., Xu, W., Yu, S. Y., and Luo, F. (2020). The Lightning Disaster Regionalization in Chongqing. *J.Chinese J. Agric. Resour. Regional Plan.* 41 (04), 317–324. doi:10.7621/cjarrp.1005-9121.20200437

Saaty, T. (1980). *The Analytical Hierarchy Process*. New York: McGraw-Hill.

Sheng, J., Xu, M., Han, J., and Deng, X. (2021). A Lightning Disaster Risk Assessment Model Based on SVM. *J. Big Data.* 3 (4), 183–190. doi:10.32604/jbd.2021.024892

Shi, J. M., Xu, W. J., Xu, L., Jin, X., and Zhu, Y. J. (2019). Risk Assessment of Lightning Disaster Events in the Agricultural Areas of Eastern Qinghai Province. *J. Glaciol. Geocryol.* 41 (06), 1359–1366. doi:10.7522/j.issn.1000-0240.2019.0079

Shu, Y., Sun, J., and Chenlu, J. (2022). A 10-Year Climatology of Midlevel Mesoscale Vortices in China. *J. Appl. Meteorology Climatol.* 61, 309–328. doi:10.1175/JAMC-D-21-0095.1

Steiger, S. M., and Orville, R. E. (2003). Cloud-to-ground Lightning Enhancement over Southern Louisiana. *Geophys. Res. Lett.* 30 (19), 1975. doi:10.1029/2003GL017923

Tian, Y. T., Wu, M. H., Shi, F. Q., and Wei, X. M. (2012). Evaluation and Regionalization of Lightning Disaster Vulnerability over Hebei. *J. Meteorological Sci. Technol.* 40 (3), 507–512. doi:10.19517/j.1671-6345.2012.03.032

Wang, H., Deng, Y., Yin, L. Y., Xu, Y. J., and Jing, Y. S. (2007). Vulnerability Analysis and Zoning of Lightning Disaster in Yunnan Province. *J. Meteorol.* 12, 83–87. doi:10.7519/j.issn.1000-0526.2007.12.012

Wang, J., and Chen, Y. (2015). Analysis of the 2009-2012 Lightning Distribution Characteristics inChina. *J. Meteorol. Mon.* 41 (2), 160–170. doi:10.7519/j.issn.1000-0526.2015.02.004

Wu, B., and Xu, X. F. (2021). Risk Assessment and Zoning of Lightning Disasters of Neijiang City. *J.Plateau Mt. Meteorology Res.* 41 (3), 115–120. doi:10.3969/j.issn.1674-184.2021.03.016

Xia, R. D., Zhang, D. L., and Wang, B. L. (2015). A 6-yr Cloud-To-Ground Lightning Climatologyand its Relationship to Rainfall over Central and Eastern China. *J. Appl. Meteorology Climatol.* 540 (12), 2443–2460. doi:10.1175/JAMC-D-15-0029.1

Xu, X. F. (2004). Lightning Induced Disasters and its Detecting and Forecasting. *J. Meteorol.* 30 (12), 17–21. doi:10.7519/j.issn.1000-0526.2004.12.004

Yin, X., Xiao, W. A., Feng, M. X., Jiao, X., Wang, Z. H., and Li, X. (2009). Regional Distribution and Vulnerability Regionalization of Lightning Disaster. *J. Meteorological Sci. Technol.* 37 (2), 216–222. doi:10.19517/j.1671-6345.2009.02.021

Yu, J. H., and Liu, H. B. (2020). Extreme Lightning Activity and its Correlation to Topography and Land Use Type. *J. Meteorological Sci. Technol.* 48 (6), 898–902. doi:10.19517/j.1671-6345.20190443

Yu, R., Zhang, X. L., Du, M. Y., Ma, H. Z., Yuan, H. F., and Zhu, C. L. (2021). Analysis of Characteristics of Cloud-To-Groundlightning: Activity of Thunderstorms over Different Topography in Central China. *J. Trop. Meteorol.* 37 (3), 329–340. doi:10.16032/j.issn.1004-4965.2021.031

Yuan, X. L., Zhou, Q., and Wang, Z. H. (2017). A Study on the Lightning Disaster Risk Gradimethods. *J. Catastrophology.* 32 (1), 26–31. doi:10.3969/j.issn.1000-811X.2017.01.006

Zhang, G. C. (2014). *Theory and Methods in Natural Disaster Risk Assessment and Zoning*. Beijing: China Meteorological Press.

Zhang, K., Yu, H. R., and Pu, J. W. (2021a). Study on Risk Assessment of Lightning Disaster in Sichuan Province. *J. Agric. Catastrophology* 11 (4), 130–131.

Zhang, W., Meng, Q., Ma, M., and Zhang, Y. (2011). Lightning Casualties and Damages in China from 1997 to 2009. *Nat. Hazards* 57 (2), 465–476. doi:10.1007/s11069-010-9628-0

Zhang, X. H., Wu, H. Y., Xu, X., Li, Y. C., and Jiao, S. M. (2007). An Analysis on Thunder Storm Vulnerability in Jiangsu Province. *J. Sci. Meteorol. Sin.* 27 (5), 536–542.

Zhang, Y., Han, J., Yuan, C. S., Yang, S., Li, C. L., and Sun, X. M. (2021b). A Rasterized Lightning Disaster Risk Method for Imbalanced Sets Using Neural Network. *J. Comput. Mater. Continua* 66 (1), 563–574. doi:10.32604/cmc.2020.012502

Zhang, Y. J., Meng, Q., Ma, M., Dong, W. S., and Lu, W. D. (2006). Development of Lightning Detection Technique with Application of Lightning Data. *J. Appl. Meteorological Sci.* 17 (5), 611–620. doi:10.3969/j.issn.1001-7313.2006.05.011

**Conflict of Interest:** The authors declare that the research was conducted in the absence of any commercial or financial relationships that could be construed as a potential conflict of interest.

frontiers | Frontiers in Environmental Science

TYPE Original Research
PUBLISHED 18 July 2022
DOI 10.3389/fenvs.2022.949271



OPEN ACCESS

EDITED BY
Xinyao Xie,
Institute of Mountain Hazards and Environment (CAS), China

REVIEWED BY
Chunlong Zhang,
West Anhui University, China
Fengxia Gao,
Chinese Academy of Geological Sciences (CAGS), China

*CORRESPONDENCE
Yinping Liu,
yuan8503@163.com

SPECIALTY SECTION
This article was submitted to Atmosphere and Climate, a section of the journal Frontiers in Environmental Science

RECEIVED 20 May 2022
ACCEPTED 28 June 2022
PUBLISHED 18 July 2022

CITATION
Liu Y, Jiang Y, Gao Q, Shi Z, Jiang Z and Hu J (2022), Characteristic analysis of lightning activities on the Yungui Plateau using ground-based remote sensing. *Front. Environ. Sci.* 10:949271. doi: 10.3389/fenvs.2022.949271



# Characteristic analysis of lightning activities on the Yungui Plateau using ground-based remote sensing

Yinping Liu[1,2]*, Yuhui Jiang[1], Qisen Gao[1], Zheng Shi[1], Zhuyi Jiang[1] and Jiarui Hu[1]

[1]Key Laboratory of Meteorological Disaster, Ministry of Education (KLME)/Joint International Research Laboratory of Climate and Environment Change (ILCEC)/Collaborative Innovation Center on Forecast and Evaluation of Meteorological Disasters (CIC-FEMD)/Key Laboratory for Aerosol-Cloud-Precipitation of China Meteorological Administration, Nanjing University of Information Science and Technology, Nanjing, China, [2]Nanjing Xinda Institute of Safety and Emergency Management, Nanjing, China

The spatiotemporal distribution of cloud-to-ground (CG) lightning activities on the Yungui Plateau is investigated in this study by using a 5-year dataset (2016–2020) from the ground-based National Lightning Detection Network (CNLDN). The correlations between the lightning activities and different meteorological factors in the region are also analyzed. The results show that there is an obvious difference in the spatial distribution of lightning activities on the Yungui Plateau during the 5 years, with high lightning density in the east and low lightning density in the west. The lightning activities shift and gather more towards the eastern plateau especially after 2019. Affected by the quasi-stationary front in Kunming, the spatial distributions of lightning flashes in cold and warm seasons are different. On the other hand, the frequency of the lightning activities varies from year to year, such as the surge in 2019. But in general, 62% of the lightning activities are produced in summer and the lightning flashes occur more often in the afternoon and evening on the Yungui Plateau. Additionally, it is found that lightning activities in the 5 years are closely related to precipitation and temperature, while there is a weak correlation with relative humidity and almost no correlation with sensible heat flux. The analysis also indicates that the CAPE×P (convective available potential energy times precipitation rate) proxy can be effectively used to describe and predict lightning activities on the Yungui Plateau as the lightning flashes corresponds well to CAPE×P, especially of the spatial distribution.

KEYWORDS

**cloud-to-ground lightning, spatiotemporal characteristics, Yungui Plateau, ground-based remote sensing, ADTD, CAPE times precipitation rate**

# 1 Introduction

As an important part of thunderstorm activities, the cloud-to-ground (CG) lightning flash is considered a highly destructive meteorological disaster. It may lead to power system faults, cause wildfires, and even threaten life safety (Krause et al., 2014; Veraverbeke et al., 2017). In order to reduce the harm of lightning activities and further understand them for lightning monitoring and forecasting, the characteristics of lightning activities under different climatic factors are studied, such as temperature (Price and Asfur, 2006), precipitation (Zheng et al., 2016), aerosol (Tan et al., 2016; Shi et al., 2020), convective available potential energy (CAPE) (Qie et al., 2003; Pawar et al., 2012), and sensible heat flux (Qie et al., 2004; Li et al., 2020). Because the lightning activity occurs with complex physical mechanisms that are closely related to these meteorological factors. In addition, the topography and geomorphology will also affect the occurrence of lightning flashes by changing the convective motion in the atmosphere (Ramesh Kumar and Kamra, 2012), so it is of great significance to study the temporal and spatial distribution characteristics of lightning activities in different regions.

In recent years, many researchers have studied lightning activities in China (Yang et al., 2015; Xu et al., 2022). In general, there are more lightning activities in the south than in the north of China and more in the east than in the west (Xu et al., 2022). The lightning density in the high-altitude and arid areas of western China is lower than that in the low-altitude and coastal areas of southeastern China. The distribution of lightning flashes in the plateau areas of China can be affected by the complex terrain (Yang et al., 2015). The Tibetan Plateau, the highest and largest plateau in the world, has unique circulation and climatic conditions. The lightning activities produced there is closely related to the plateau thermodynamics (Qie et al., 2004). The charge structure of the thunderstorm cloud and the characteristics of lightning activities are also distinct from others (Li et al., 2020). Possibly affected by the Tibetan Plateau (Yu et al., 2007; Zhang et al., 2014), the Sichuan Basin on the east of it is the only high lightning density center in western China (Yang et al., 2015). It is also a famous nocturnal precipitation basin, as lightning activities mostly occur at night (Xu and Zipser, 2011).

The Yungui Plateau is the transitional zone from the Tibetan Plateau to eastern hilly regions (Li and Yu, 2014). It is well known as a typical karst landform with unique topographic characteristics. There is a gradual decline of the terrain from the west to the southeast (Ge, 2021). Due to the uneven vertical distribution of heat caused by altitude, the climate patterns in the east and west of the Yungui Plateau are different. Lightning density on the Yungui plateau is also influenced by the topography (Yang et al., 2015). Based on satellite data, it is found that the lightning density in southern China and the Yungui Plateau is high (Ma et al., 2007). In addition, Ma et al. analyzed the lightning activities in China from December 2010 to February 2020, and concluded that the southwestern and southeastern sides of the Yungui Plateau are lightning-prone areas in winter (Ma et al., 2022). In recent years, there has been a warming trend on the Yungui Plateau (Shi and Chen, 2018; Ma et al., 2019). However, to the best of our knowledge, the specific analysis of lightning activities of this region remains in 2015 (Wu et al., 2017).

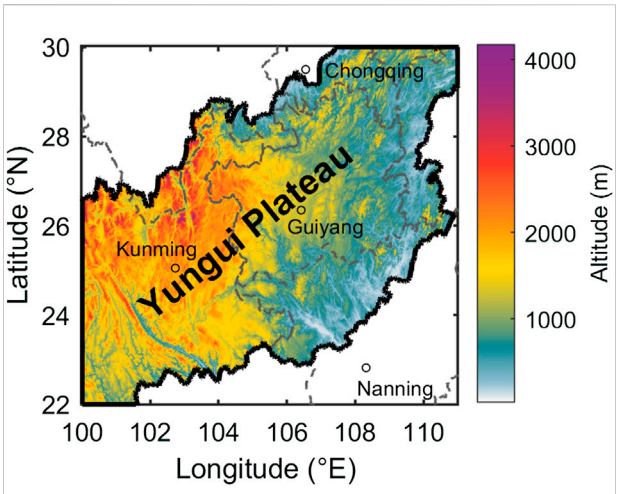


FIGURE 1
The region of interest (marked by the black line) selected in the study: Yungui Plateau (100°–111° E, 22°–30° N). The provincial boundaries are marked by a dotted gray line and the capitals of the provinces are marked.

Is the lightning activity on the Yungui Plateau affected by the Tibetan Plateau? What is the relationship between lightning activities on the Yungui Plateau and its special topography and climate? Will the climate change on the Yungui Plateau affect the characteristics of lightning activities? In order to answer the above questions, in this paper, we focus on analyzing the spatiotemporal characteristics of CG lighting activities on the Yungui Plateau and the correlation with the meteorological factors. The results of this paper can provide a basic reference for lightning risk assessment and lightning protection in the Yungui Plateau and its surrounding areas.

# 2 Data and methods

## 2.1 Region of interest

The region of interest in this study, namely the Yungui Plateau (100°–111° E, 22°–30°N), is shown in Figure 1. The Yungui Plateau is located on the southeast of the Tibetan Plateau (Ge, 2021). It runs from the Hengduan mountains in

the west to the Xuefeng Mountain in Hunan in the east and the Sichuan Basin lies on the north of it. Specifically, Yungui Plateau includes the eastern parts of Yunnan Province, whole area of Guizhou Province, northwestern parts of Guangxi Province and the borders of Sichuan, Hubei, Hunan, and other provinces. The terrain of the Yungui Plateau is rugged, with high in the northwest and low in the southeast. The climate of the Yungui Plateau is characterized by seasonal heavy rainfall and drought as a result of the control of the westerlies and summer monsoons of the southwest monsoon from Bay of Bengal and the East Asian monsoon from South China Sea (Wu et al., 2022).

## 2.2 Data source

The lightning dataset used in this paper is derived from the advanced time of arrival and direction (ADTD) detection system of the National Lightning Detection Network (CNLDN), which was established by the China Meteorological Administration in late 2000 (Zhang et al., 2022). It is said that the efficiency of this system can reach about 90%, and the locating accuracy error is around 300–500 m (Xu et al., 2022). The total number of the lightning activities happened on the Yungui Plateau between 2016 and 2020 obtained from the dataset is $9.42 \times 10^6$, including the information of time, latitude, longitude, intensity, and location.

Based on the ERA5 dataset of the European Centre for Medium-Range Weather Forecasts (ECMWF) (Pérez-Invernón et al., 2021), the surface temperature, precipitation, surface sensible heat flux, relative humidity (850 hPa), CAPE and precipitation rate are collected to analyze the meteorological conditions of the Yungui Plateau from 2016 to 2020. The spatial resolution of the obtained data is 0.25° × 0.25°, and the temporal resolution is 1 month.

## 2.3 Data processing

In order to ensure the reliability and accuracy of the analysis, the lightning data is preprocessed. The data outside the Yungui Plateau are cut, and then the results of three and below lightning detection sensors are deleted. As the cloud lightning flashes less than 10 kA and the CG lightning flashes cannot be reliably distinguished, the positive CG (PCG) lightning flashes with current less than 10 kA is deleted from the dataset (Zheng et al., 2016; Zhang et al., 2017). In addition, we group return strokes with time intervals less than 500 ms and horizontal distances less than 10 km as the same set of a lightning flash (Xie et al., 2013). Finally, the CG lightning data are resampled to grid data with spatial resolution of 0.25° × 0.25°.

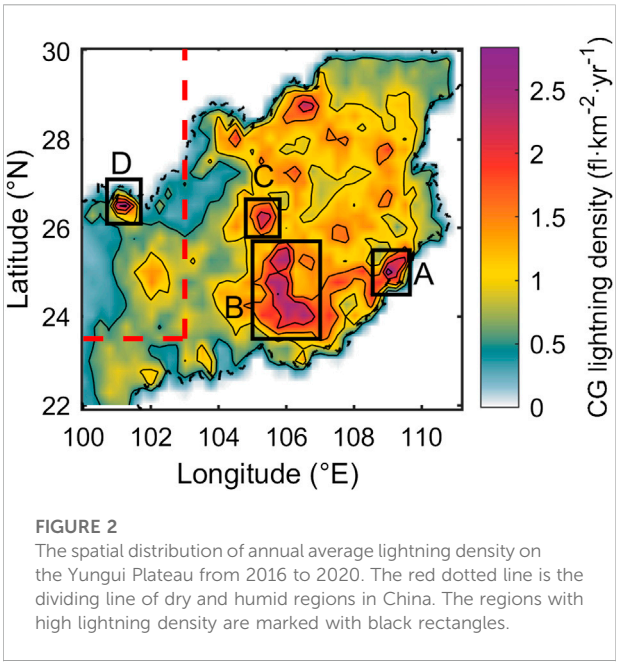


FIGURE 2
The spatial distribution of annual average lightning density on the Yungui Plateau from 2016 to 2020. The red dotted line is the dividing line of dry and humid regions in China. The regions with high lightning density are marked with black rectangles.

# 3 Distribution characteristics of lightning activities

## 3.1 Spatial distribution

Figure 2 shows the spatial distribution of annual average lightning density on the Yungui Plateau from 2016 to 2020. It is obvious that there are significant spatial differences in lightning activities on the Yungui Plateau. Specifically, the lightning density is high in the eastern plateau and low in the western plateau. This may be explained by the fact that the eastern plateau (east of the red dotted line in Figure 2) is classified in the eastern coastal humid and semi-humid region of China in Climatology (Ma et al., 2005). In addition, Guizhou, in the east of the plateau, is an area of typical karst landform and the tridimensional climate characteristics formed by the influence of topography are obvious, resulting in complex and changeable CG lightning activities in this region.

In Figure 2, the highest value of CG lightning density appears in region A (109°E, 25°N), located in the southeast of the Yungui Plateau, reaching 2.83 fl $km^{-2}$·$yr^{-1}$. The reason why the lightning activity is active here may be due to the influence of the sea position. This area is close to the South China Sea, rich in water vapor and sufficient rainfall. Figure 2 also shows three regions with high lightning density over the 5 years on the Yungui Plateau. Region B lies in the eastern part of Yunnan Province, where the warm and humid airflow uplifted by the terrain in summer is conducive to the development of thunderstorms (Li et al., 2008). The reason for high lightning density in region C, namely the west side of Guizhou, may be that it is blocked by Wumeng Mountain and located on the southeast monsoon

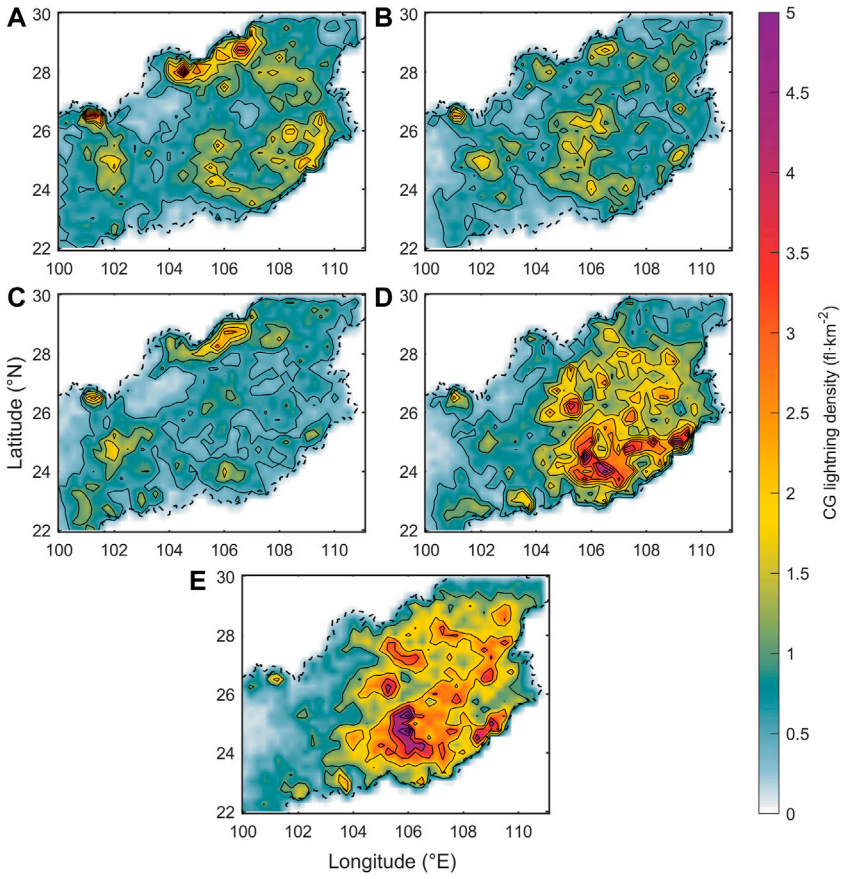


FIGURE 3
The inter-annual variation of the spatial distribution of the lightning density on the Yungui Plateau from 2016 to 2020: **(A)** 2016, **(B)** 2017, **(C)** 2018, **(D)** 2019, and **(E)** 2020.

windward slope with abundant precipitation. Region D, on the north side of Yunnan region, is located at the junction of Lijiang and Panzhihua. It belongs to the south-central part of the Panxi rift valley, where the maximum altitude difference is more than 3,000 m. The center of the lightning density appears in the area of the valley, where is appropriate to the occurrence of lightning activities (Li et al., 2020). Also, the Hengduan Mountain near it belongs to the southeast corner of the Tibetan Plateau. The influence of lightning activities produced on the Tibetan Plateau makes the average annual lightning density in the area of the Hengduan Mountain larger.

Figure 3 shows that the inter-annual variation of the spatial distribution of the lightning density on the Yungui Plateau is obvious from 2016 to 2020. In general, there is no significant difference in the distribution of the high lightning density area in each year. However, the lightning activities in the first 3 years are uniformly distributed. Since 2019, lightning activities have remarkably shifted to the central and eastern parts of the Yungui Plateau. By 2020, lightning activity had been more concentrated in the middle and eastern plateau.

Figure 4 shows the seasonal distribution of average lightning density on the Yungui Plateau between 2016 and 2020. It can be seen that the distribution in spring and winter are highly consistent, with lightning flashes are mainly concentrated in the eastern side of the Yungui Plateau. The consistency of summer and autumn is also strong, as the lightning events mainly occur on the central and western Yungui Plateau. This may be related to the Kunming quasi-stationary front. In winter, during the southward movement of cold air from northern China, blocked by the terrain of Yungui Plateau, the cold air keeps still here and forms a quasi-stationary front. The specific position is about 103.5°E ~ 104°E. It is characterized by significant differences in cloud and rainfall (Qian and Fu, 2010; Du et al., 2007). Therefore, there is more rainfall in the east of Kunming stationary front in winter, which may be the cause of dense lightning flashes. In addition, in summer and autumn, lightning activities is active near 102°E, 26°N, while there is almost no lightning activity in spring and winter in this region. This may be due to the unique climate model of Yungui Plateau. The west-wind drift in the southern margin of the Tibetan Plateau sinks on

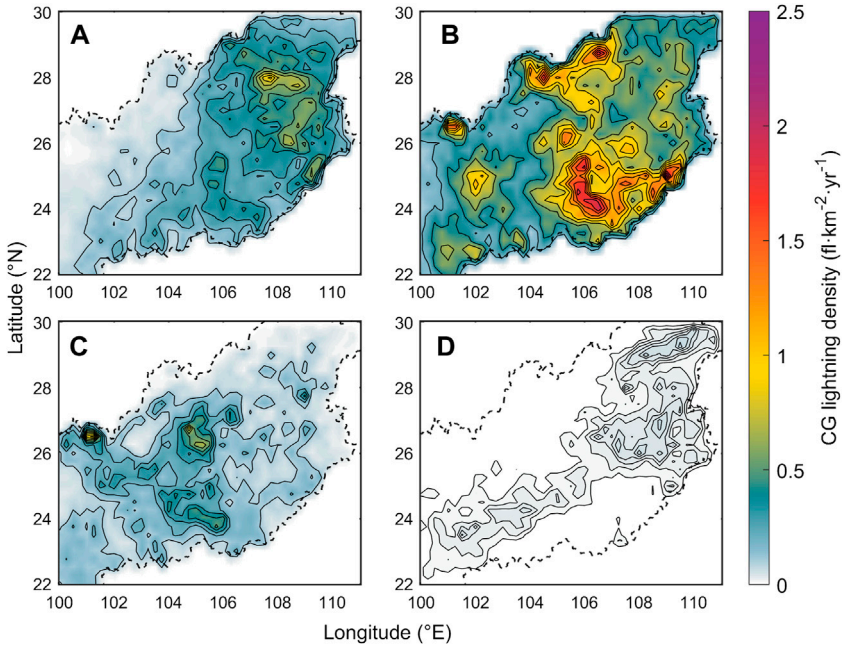


FIGURE 4
The seasonal distribution of average lightning density on the Yungui Plateau between 2016 and 2020: **(A)** Spring, **(B)** Summer, **(C)** Autumn, and **(D)** Winter.

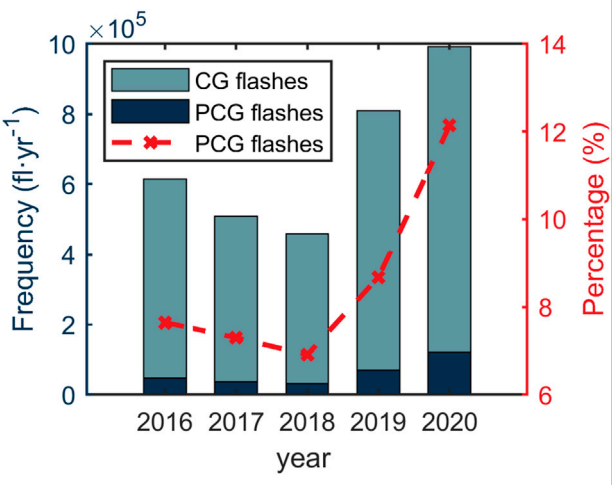


FIGURE 5
The distribution of CG and PCG lightning frequency (y-axis on the left) and the proportion of PCG lightning flashes (y-axis on the right) on the Yungui Plateau from 2016 to 2020.

the leeward side of the high ridge in the western Hengduan Mountains, inhibiting precipitation and increasing surface temperature. Therefore, the area west of 104°E can be divided into obvious drought (from November to April) and rainy season (from May to October) (Li and Yu, 2014). Most rainfall and its frequency are concentrated in the rainy season, controlled by the southwest summer monsoon.

## 3.2 Temporal distribution

The distribution of lightning frequency and the proportion of PCG lightning flashes on the Yungui Plateau from 2016 to 2020 is shown in Figure 5. It is found that Yungui Plateau is a lightning-prone area, with the total frequency of lightning flashes during the 5 years reaches $3.4\times10^6$ and the annual average frequency reaches $6.8 \times 10^5$. Secondly, there is an obvious inter-annual variation of the lightning frequency. From 2016 to 2018, the total frequency of CG lightning flashes decreased slowly, from $6.1 \times 10^5$ to $4.5 \times 10^5$. However, there was a surge to $8.1 \times 10^5$ in 2019, and next year it increased to nearly one million.

By comparing the frequency of PCG and negative CG lightning activities in Figure 5, it can also be found that the negative CG lightning flashes has the dominant role on the Yungui Plateau, with only 9.1% of the flashes are PCG lightning flashes. The frequency of negative CG lightning flashes is far greater than that of positive ones. This may be closely related to the distribution structure of the charge in the cloud. The charge generally presents a dipole distribution. Therefore, under the action of the atmospheric electric field,

the negative charge is closer to the ground and discharges to the ground. The positive charge is far from the ground, so its probability of discharge to the ground is smaller than that of the negative charge. However, especially after 2018, there was a substantial growth in the proportion of PCG lightning flashes, which may be the result from the changes in cloud depth, environmental conditions, and topography (Yang et al., 2015).

Figure 6 is the line chart of the average current intensity of positive and negative CG lightning flashes from 2016 to 2020. It can be found that in these 5 years, the average intensity of PCG lightning flashes is always greater than that of negative ones. This is mainly because the occurrence opportunity of positive flashes is less than that of negative flashes. The charge in the thunderstorm cloud needs to be conserved, so the intensity of the PCG lightning flashes will be correspondingly greater than that of the negative CG lightning flashes. To be specific, the average intensity of PCG lightning flashes in the 5 years is 64 kA, which is about 1.3 times of the average intensity of negative CG lightning flashes.

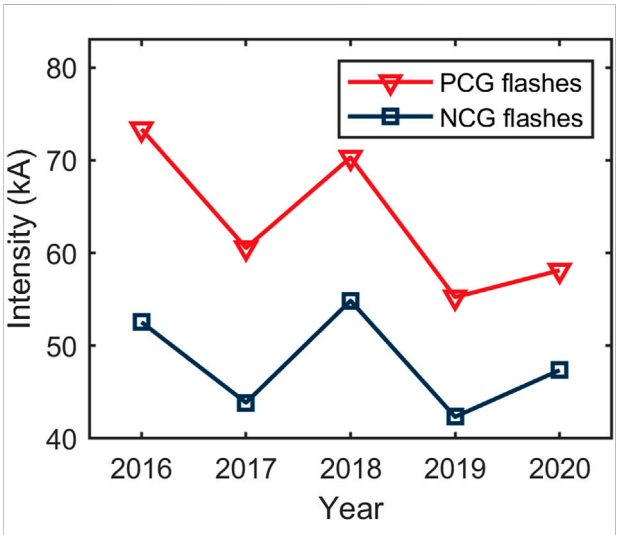


FIGURE 6
The line chart of the average current intensity of positive and negative CG lightning flashes from 2016 to 2020.

Figure 7A shows the monthly distribution of the lightning frequency on the Yungui Plateau from 2016 to 2020. In general, most of the lightning activities happen in summer (June ~ August), accounting for around 62% of the lightning flashes. While the flashes in winter (December ~ February) are only about 1%. This is consistent with previous results, that CG lightning activities mainly occurs in the warm season (Xie et al., 2013), as a result of prevailed convection in this season. In addition, it can also be found that, except for 2020, the monthly distribution of lightning frequency in other years presents double peaks, that is, lightning activities also peaks in the spring. This may be due to the intense heating and convective precipitation during the pre-monsoon season (Chandra et al., 2021).

The monthly distribution of the frequency and percentage of PCG lightning activities can be seen from Figure 7B. The percentage of PCG lightning flashes in cold season is much higher than that in warm season. This is consistent with previous research results (Xie et al., 2013). In November, the percentage of PCG lightning flashes even reaches nearly 50%. There is a negative correlation between the number of lightning activities and the proportion of PCG lightning flashes in this region.

Figure 8 shows the 24-h variation of lightning frequency on the Yungui Plateau, including the frequency of CG lightning activities and the percentage of PCG lightning flashes. Overall, lightning activities occur more frequently in the afternoon and evening, especially between 16 and 18 p.m., with a maximum at 17 p.m. There are fewer lightning activities produced in the morning, with a valley at 10 a.m.

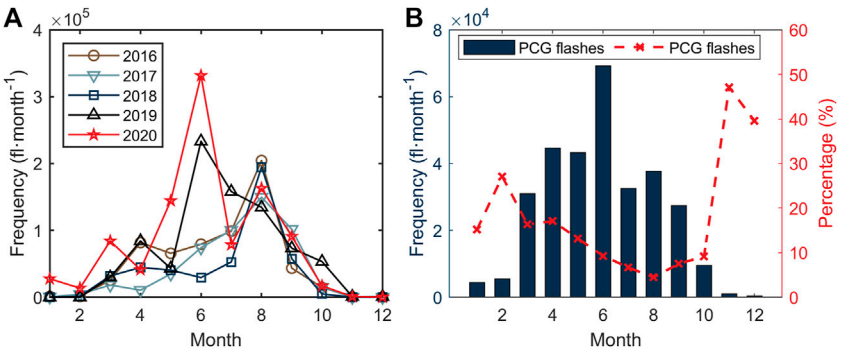


FIGURE 7
**(A)** The monthly distribution of the lightning frequency on the Yungui Plateau from 2016 to 2020. **(B)** The monthly distribution of the frequency and percentage of PCG lightning activities.

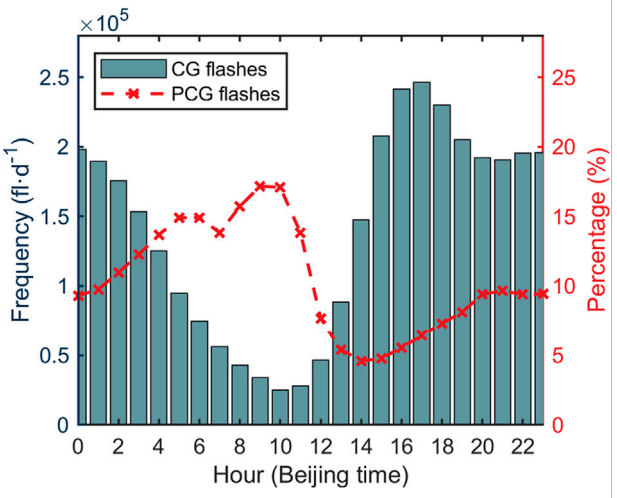


FIGURE 8
The 24-h variation of lightning frequency on the Yungui Plateau, including the frequency of CG lightning activities (y-axis on the left) and the percentage of PCG lightning flashes (y-axis on the right).

This may be because the strengthening of solar radiation in the afternoon, which radiates through the atmosphere to the ground and changes the temperature of the underlying surface. The atmosphere near the ground absorbs more heat, resulting in the atmospheric convergence and uplift of the ground. The convection forms, which will promote the formation of convective clouds and further strengthen the lightning activities. The proportion of PCG lightning flashes is inversely proportional to the total frequency of CG lightning flashes, peaking in the morning and reaching the valley value in the afternoon.

## 4 Analysis of influencing factors

Lightning activities are affected by many meteorological factors at the same time. In order to further explore the possible effects of various meteorological factors on the temporal and spatial distribution of lightning activities on the Yungui Plateau, the Pearson linear correlation coefficients between the lightning frequency and various influencing factors are calculated and analyzed. Figure 9 shows the correlations

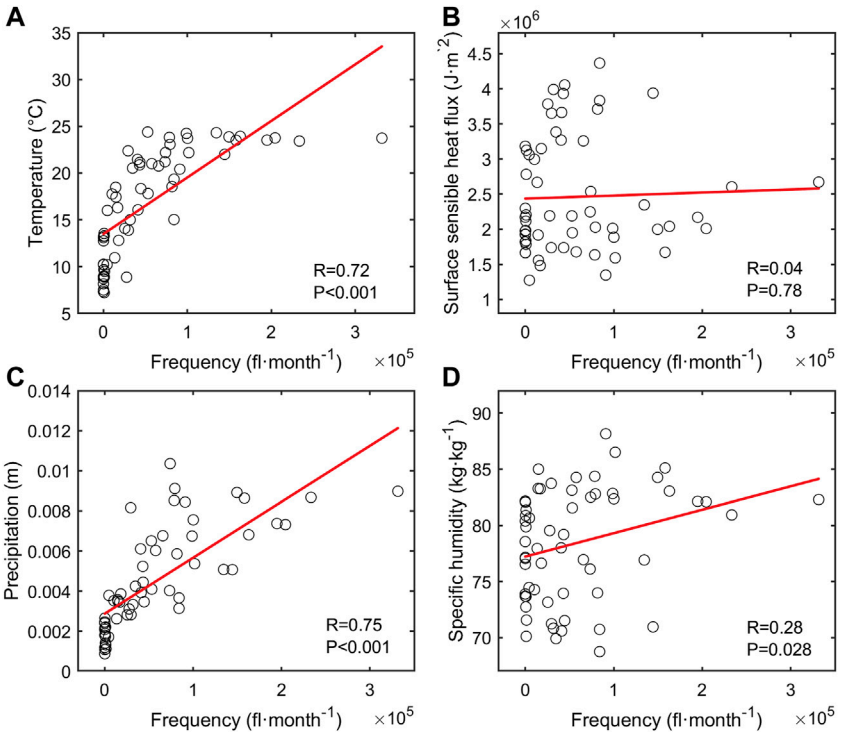


FIGURE 9
The correlations between monthly lightning frequency in the 5 years from 2016 to 2020 and the meteorological factors selected in the corresponding time and region: **(A)** Temperature, **(B)** Surface sensible heat flux, **(C)** Precipitation, and **(D)** Specific humidity (850 hPa). R represents the value of correlation coefficient and *p* shows the significance level.

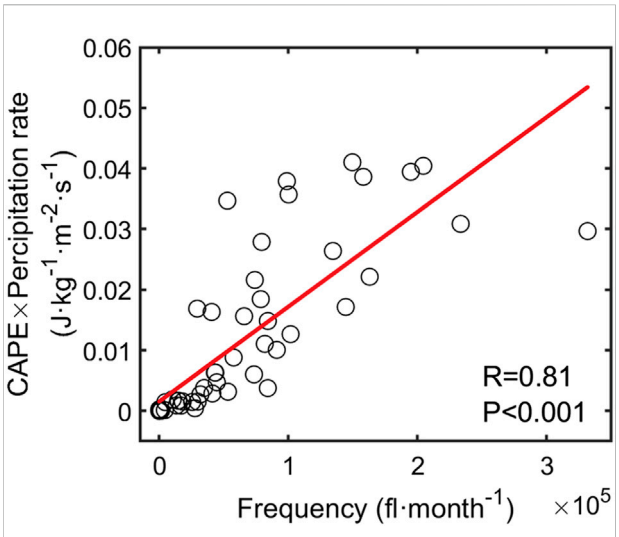


FIGURE 10
The scatter plot of the correlation between monthly lightning frequency and CAPE×P on the Yungui Plateau from 2016 to 2020.

between monthly lightning frequency in the 5 years from 2016 to 2020 and the meteorological factors selected in the corresponding time and region. It can be found that among the four selected meteorological factors, the lightning activity on the Yungui Plateau has a high correlation with precipitation and temperature, reaching 0.75 and 0.72, respectively. The correlation between lightning activities and relative humidity is weak, and it is almost irrelevant to sensible heat flux. In other words, the precipitation in Yungui Plateau, including the difference in rainfall distribution caused by the Kunming quasi-stationary front mentioned above, can indeed have a significant indigenous impact on lightning activities in the region.

Due to the complexity of the lightning event, it is widely recognized that it is difficult to describe the generation and development of the lightning activity through specific physical processes. Romps et al. explained 77% of the temporal and spatial distribution of CG lightning activities in the United States and predicted the lightning density by using CAPE×P (convective available potential energy times precipitation rate) proxy (Romps et al., 2014). After being validating and evaluating (Romps et al., 2018; Tippett et al., 2019; Zhao et al., 2022), it turns out that CAPE×P can indirectly describe and quantify lightning-related atmospheric processes under certain conditions.

Figure 10 is the scatter plot of the correlation between monthly lightning frequency and CAPE×P on the Yungui Plateau from 2016 to 2020. It can be seen that there is a strong correlation between CAPE×P and the lightning activity, reaching 0.81.

The specific temporal and spatial distribution relationships between CAPE×P and lightning activities on the Yungui Plateau are shown in Figures 11, 12. It can be seen from Figure 11 that in the 5 years from 2016 to 2020, the trend of monthly change of CAPE×P is consistent with the corresponding frequency of lightning flashes, especially the time when the annual peak appears. In terms of the extent of change, the change of CAPE×P and lightning frequency is very similar in the cold seasons each year. In the warm seasons, especially in summer, the change of CAPE×P is much higher than that of lightning frequency except in 2020. This indicates that there may be other factors that affect CG lightning activities on the Yungui Plateau in summer.

Figure 12C shows the corresponding relationship between the spatial distribution of monthly density of lightning flashes (Figure 12A) and the spatial distribution of monthly CAPE×P (Figure 12B) in the 5 years. It can be clearly seen that except for the northeastern margin of the Yungui Plateau, the spatial distribution correlation of the region is above 0.5, which proves that the density of the lightning activities in the region is correlated with the spatial distribution of CAPE×P. This also indicates that CAPE×P could be effectively used to describe and predict lightning activities on the Yungui Plateau.

## 5 Summary and discussion

Based on the ADTD ground-based lightning location data on the Yungui Plateau from 2016 to 2020, the temporal and spatial distribution characteristics of lightning activities were obtained. Combined with the reanalysis meteorological data of ERA5, the correlations between lightning activities and different meteorological factors during this period were analyzed. Finally, the relationship between CAPE×P and the frequency of lightning activities in this area was studied. The main conclusions of this paper are as follows:

1) There is a significant difference in the spatial distribution of the lightning activities on the Yungui Plateau, showing high lightning density in the east and low lightning density in the west. During the years from 2016 to 2020, the spatial distribution of lightning activities on the Yungui Plateau presents obvious interannual variations. There is an eastward migration and accumulation of lightning flashes after 2019. Due to the influence of Kunming quasi-stationary front, the spatial distribution of lightning activities in cold and warm seasons of Yungui Plateau is significantly different.
2) The CG lightning activities on the Yungui Plateau is mainly dominated by negative flashes, and the difference in the temporal distribution of the lightning activities is also significant. There has been an obvious surge in the lightning frequency since 2019. Most CG lightning flash occurs in summer, but the percentage of PCG lightning flashes is the lowest during this period. In addition, lightning activities occur more frequently in the afternoon and evening.

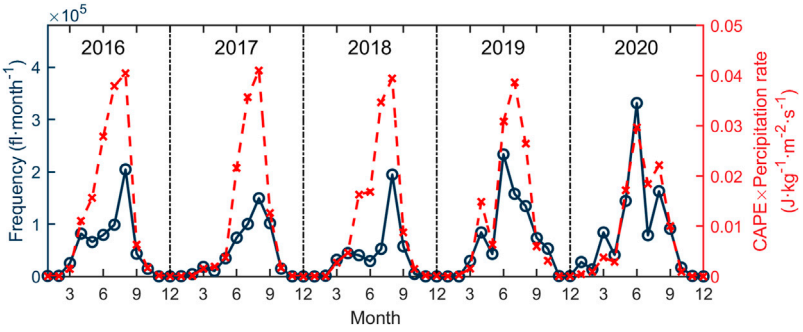


FIGURE 11
The monthly temporal distribution of the lightning frequency (y-axis on the left) and CAPE×P (y-axis on the right) on the Yungui Plateau from 2016 to 2020.

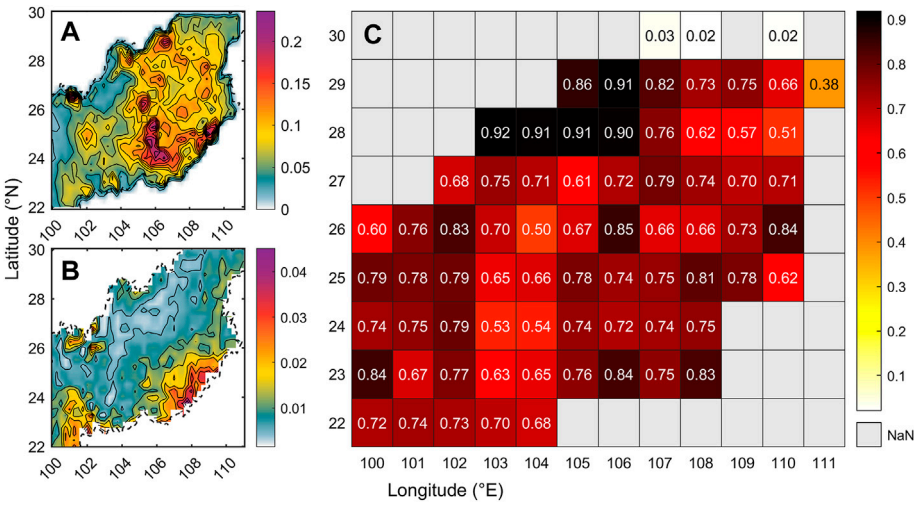


FIGURE 12
**(A)** The monthly spatial distribution of the lightning density (fl·km$^{-2}$·month$^{-1}$) on the Yungui Plateau from 2016 to 2020. **(B)** Same as **(A)** but for CAPE×P (J·kg$^{-1}$·m$^{-1}$·s$^{-1}$). **(C)** The spatial distribution of correlation coefficients between the spatial distribution of monthly density of lightning flashes and the spatial distribution of monthly CAPE×P in the 5 years. The spatial resolution is 1° × 1°.

3) Lightning activities on the Yungui Plateau are mainly affected by precipitation and temperature. The correlation between lightning activities and relative humidity is weak, and it is almost irrelevant to sensible heat flux. In addition, the CAPE×P proxy is closely related to the lightning activity, especially spatial distribution. This indicates that CAPE×P proxy can be effectively used to describe and predict lightning activities on the Yungui Plateau.

It is undeniable that the above analysis of lightning activities on the Yungui Plateau could be affected by the efficiency and accuracy of lightning location system. In the future, we will try to use longer-term observation data to further explore the corresponding relationship between lightning activities and its topography and climate in the region.

## Data availability statement

The original contributions presented in the study are included in the article/supplementary material, further inquiries can be directed to the corresponding author.

## Author contributions

YL and YJ contributed to conception and design of the study. ZS and JH contributed to data collection. YL, YJ, QG, and ZJ wrote the first draft of the manuscript. All authors contributed to manuscript revision approved the submitted version.

## Funding

This work was supported by the Natural Science Foundation of China (41575004) and the Jiangsu Provincial Natural Science Foundation of China (BK20150903).

## Conflict of interest

The authors declare that the research was conducted in the absence of any commercial or financial relationships that could be construed as a potential conflict of interest.

## Publisher's note



## References

Chandra, S., Siingh, D., Jeni Victor, N., and Kamra, A. K. (2021). Lightning activity over South/Southeast Asia: Modulation by thermodynamics of lower atmosphere. *Atmos. Res.* 250, 105378. doi:10.1016/j.atmosres.2020.105378

Du, Z., Ding, Z., and Zhang, S. (2007). Analysis of atmospheric circulation and structure of Yunnan-Guizhou quasi-stationary front during its evolution. *J. Trop. Meteor.* 23, 284–292. doi:10.3969/j.issn.1004-4965.2007.03.011

Ge, W., Han, J., Zhang, D., and Wang, F. (2021). Divergent impacts of droughts on vegetation phenology and productivity in the Yungui Plateau, southwest China. *Ecol. Indic.* 11, 107743. doi:10.1016/j.ecolind.2021.107743

Krause, A., Kloster, S., Wilkenskjeld, S., and Paeth, H. (2014). The sensitivity of global wildfires to simulated past, present, and future lightning frequency. *J. Geophys. Res. Biogeosci.* 119, 312–322. doi:10.1002/2013JG002502

Li, J., Wu, X., Yang, J., Jiang, R., Yuan, T., Lu, J., et al. (2020). Lightning activity and its association with surface thermodynamics over the Tibetan Plateau. *Atmos. Res.* 245, 105118. doi:10.1016/j.atmosres.2020.105118

Li, J., and Yu, R. (2014). Characteristics of cold season rainfall over the Yungui plateau. *J. Appl. Meteorol. Climatol.* 53, 1750–1759. doi:10.1175/JAMC-D-13-0285.1

Li, Y., Wei, N., Niu, S., Luo, N., Wen, J., and Huang, H. (2008). "Spatial and temporal characteristics of cloud to ground lightning in Guizhou province," in 2008 Fifth International Conference on Fuzzy Systems and Knowledge Discovery, Jinan Shandong, China, 18-20 October 2008 (IEEE), 660–664. doi:10.1109/FSKD.2008.491

Ma, J., Weng, B., Bi, W., Xu, D., Xu, T., Yan, D., et al. (2019). Impact of climate change on the growth of typical crops in karst areas: A case study of Guizhou province. *Adv. Meteorology* 2019, 1–16. doi:10.1155/2019/1401402

Ma, M., Huang, X., Fei, J., Zhang, C., Li, C., Cheng, X., et al. (2022). Analysis of the winter cloud-to-ground lightning activity and its synoptic background in China during 2010–20. *Adv. Atmos. Sci.* 39, 985–998. doi:10.1007/s00376-021-1260-2

Ma, M., Lyu, W., Zhang, Y., and Meng, Q. (2007). Analysis of lightning activity in China. *METEOROLOGICAL Sci. Technol.* 35, 1–7. doi:10.3390/atmos10060298

Ma, M., Tao, S., Zhu, B., and Lü, W. (2005). Climatological distribution of lightning density observed by satellites in China and its circumjacent regions. *Sci. China Ser. D-Earth. Sci.* 48, 219–229. doi:10.1360/03yd0204

Pawar, S. D., Lal, D. M., and Murugavel, P. (2012). Lightning characteristics over central India during Indian summer monsoon. *Atmos. Res.* 106, 44–49. doi:10.1016/j.atmosres.2011.11.007

Pérez-Invernón, F. J., Huntrieser, H., Gordillo-Vázquez, F. J., and Soler, S. (2021). Influence of the COVID-19 lockdown on lightning activity in the Po Valley. *Atmos. Res.* 263, 105808. doi:10.1016/j.atmosres.2021.105808

Price, C., and Asfur, M. (2006). Inferred long term trends in lightning activity over Africa. *Earth Planets Space* 58, 1197–1201. doi:10.1186/BF03352010

Qian, W., and Fu, J. (2010). Frontal Genesis of moisture atmosphere during the early 2008 persistent freezing-rain event in southern China. *Sci. China Earth Sci.* 53, 454–464. doi:10.1007/s11430-009-0101-4

Qie, X. S., Yuan, T., Xie, Y. R., and Ma, Y. M. (2004). Spatial and temporal distribution of lightning activities on the Tibetan plateau. *Chin. J. Geophys.* 47, 1122–1127. doi:10.1002/cjg2.596

Qie, X., Toumi, R., and Zhou, Y. (2003). Lightning activity on the central Tibetan Plateau and its response to convective available potential energy. *Chin. Sci. Bull.* 48, 296–299. doi:10.1007/BF03183302

Ramesh Kumar, P., and Kamra, A. K. (2012). The spatiotemporal variability of lightning activity in the Himalayan foothills: Lightning in the Himalayan Foothills. *J. Geophys. Res.* 117, n/a. doi:10.1029/2012jd018246

Romps, D. M., Charn, A. B., Holzworth, R. H., Lawrence, W. E., Molinari, J., Vollaro, D., et al. (2018). CAPE times P explains lightning over land but not the land-ocean contrast. *Geophys. Res. Lett.* 45, 630–712. doi:10.1029/2018GL080267

Romps, D. M., Seeley, J. T., Vollaro, D., and Molinari, J. (2014). Projected increase in lightning strikes in the United States due to global warming. *Science* 346, 851–854. doi:10.1126/science.1259100

Shi, H., and Chen, J. (2018). Characteristics of climate change and its relationship with land use/cover change in yunnan province, China: Climate change and its relationship with land use/cover change. *Int. J. Climatol.* 38, 2520–2537. doi:10.1002/joc.5404

Shi, Z., Wang, H., Tan, Y., Li, L., and Li, C. (2020). Influence of aerosols on lightning activities in central eastern parts of China. *Atmos. Sci. Lett.* 21, e957. doi:10.1002/asl.957

Tan, Y. B., Peng, T., and Chen, H. R. (2016). Lightning flash density in relation to aerosol over Nanjing (China). *Atmos. Res.* 174–175, 1–8. doi:10.1016/j.atmosres.2016.01.009

Tippett, M. K., Lepore, C., Koshak, W. J., Chronis, T., and Vant-Hull, B. (2019). Performance of a simple reanalysis proxy for U.S. cloud-to-ground lightning. *Int. J. Climatol.* 39, 3932–3946. doi:10.1002/joc.6049

Veraverbeke, S., Rogers, B. M., Goulden, M. L., Jandt, R. R., Miller, C. E., Wiggins, E. B., et al. (2017). Lightning as a major driver of recent large fire years in North American boreal forests. *Nat. Clim. Chang.* 7, 529–534. doi:10.1038/nclimate3329

Wu, A., Wu, S., Zeng, Y., and Zhang, S. (2017). Analysis of the characteristics of lightning activities in Yunnan Guizhou Plateau. *Insulators Surge Arresters*. 02, 74–79,84. doi:10.16188/j.isa.1003-8337.2017.02.015

Wu, H., Fu, C., Zhang, C., Zhang, J., Wei, Z., and Zhang, X. (2022). Temporal variations of stable isotopes in precipitation from Yungui plateau: Insights from moisture source and rainout effect. *J. Hydrometeorol.* 23, 39–51. doi:10.1175/JHM-D-21-0098.1

Xie, Y., Xu, K., Zhang, T., and Liu, X. (2013). Five-year study of cloud-to-ground lightning activity in Yunnan province, China. *Atmos. Res.* 129–130, 49–57. doi:10.1016/j.atmosres.2012.12.012

Xu, M., Qie, X., Pang, W., Shi, G., Liang, L., Sun, Z., et al. (2022). Lightning climatology across the Chinese continent from 2010 to 2020. *Atmos. Res.* 275, 106251. doi:10.1016/j.atmosres.2022.106251

Xu, W., and Zipser, E. J. (2011). Diurnal variations of precipitation, deep convection, and lightning over and east of the eastern Tibetan plateau. *J. Clim.* 24, 448–465. doi:10.1175/2010JCLI3719.1

Yang, X., Sun, J., and Li, W. (2015). An analysis of cloud-to-ground lightning in China during 2010–13. *WEATHER Forecast.* 30, 1537–1550. doi:10.1175/waf-d-14-00132.1

Yu, R., Zhou, T., Xiong, A., Zhu, Y., and Li, J. (2007). Diurnal variations of summer precipitation over contiguous China. *Geophys. Res. Lett.* 34, L01704. doi:10.1029/2006GL028129

Zhang, C., Lu, W., Chen, L., Qi, Q., Ma, Y., Yao, W., et al. (2017). Influence of the Canton Tower on the cloud-to-ground lightning in its vicinity. *J. Geophys. Res. Atmos.* 122, 5943–5954. doi:10.1002/2016JD026229

Zhang, Y., Sun, J., and Fu, S. (2014). Impacts of diurnal variation of mountain-plain solenoid circulations on precipitation and vortices east of the Tibetan Plateau during the mei-yu season. *Adv. Atmos. Sci.* 31, 139–153. doi:10.1007/s00376-013-2052-0

Zhang, Y., Zhang, Y., Zou, M., Wang, J., Li, Y., Tan, Y., et al. (2022). Advances in lightning monitoring and location technology research in China. *Remote Sens.* 14, 1293. doi:10.3390/rs14051293

Zhao, P., Xiao, H., Liu, C., Zhou, Y., Xu, X., Hao, K., et al. (2022). Evaluating a simple proxy for climatic cloud-to-ground lightning in Sichuan Province with complex terrain, Southwest China. *Int. J. Climatol.* 42, 3909–3927. doi:10.1002/joc.7451

Zheng, D., Zhang, Y., Meng, Q., Chen, L., and Dan, J. (2016). Climatology of lightning activity in South China and its relationships to precipitation and convective available potential energy. *Adv. Atmos. Sci.* 33, 365–376. doi:10.1007/s00376-015-5124-5

frontiers | Frontiers in Environmental Science

ORIGINAL RESEARCH
published: 22 July 2022
doi: 10.3389/fenvs.2022.949564

# Spatiotemporal Variations of Vegetation Net Primary Productivity and Its Response to Meteorological Factors Across the Yellow River Basin During the Period 1981–2020

*Hongwei Tian*[1,2], *Xingjie Ji*[1,3]* *and Fangmin Zhang*[4]*

[1]Key Laboratory of Agrometeorological Safeguard and Applied Technique, CMA, Zhengzhou, China, [2]Institute of Meteorological Sciences of Henan Province, Zhengzhou, China, [3]Henan Provincial Climate Centre, Zhengzhou, China, [4]Collaborative Innovation Center on Forecast and Evaluation of Meteorological Disasters, Jiangsu Key Laboratory of Agricultural Meteorology, College of Applied Meteorology, Nanjing University of Information Science and Technology, Nanjing, China

Based on trend analysis, partial correlation analysis, and Mann–Kendall test, we analyzed the spatiotemporal variations of net primary productivity (NPP) in the Yellow River Basin and their responses to meteorological factors during the period 1981–2020. The results revealed that NPP had high values in the mid-south part but low values in the northwestern part of the Yellow River Basin. The average NPP was 195.3 g C·m$^{-2}$·a$^{-1}$ from 1981 to 2020, and the inter-annual fluctuation of NPP showed a significant increasing trend with an increasing rate of 2.35 g C·m$^{-2}$·a$^{-2}$ ($p < 0.01$). The annual mean temperature showed a positive correlation with NPP in 99.6% of the basin, and 91.4% of which passed the 0.01 significant test. NPP and annual precipitation positively correlated in 87.1% of the basin, and 41.7% of which passed the 0.01 significant test. In 75.2% of the basin, NPP was related negatively with annual sunshine hours, and 17.6% of which of which passed the 0.01 significant test.

**Keywords: net primary productivity, climate change, Yellow River Basin, meteorological factors, spatiotemporal analysis**

OPEN ACCESS

***Edited by:***
*Xinyao Xie,*
*Institute of Mountain Hazards and Environment (CAS), China*

***Reviewed by:***
*Yang Hu,*
*Ningxia University, China*
*Luo Liu,*
*South China Agricultural University, China*

***Correspondence:**
*Xingjie Ji*
*jixingjie2004@ aliyun.com*
*Fangmin Zhang*
*fmin.zhang@nuist.edu.cn*

***Specialty section:***
*This article was submitted to Atmosphere and Climate, a section of the journal Frontiers in Environmental Science*

***Received:*** *21 May 2022*
***Accepted:*** *06 June 2022*
***Published:*** *22 July 2022*

***Citation:***
*Tian H, Ji X and Zhang F (2022) Spatiotemporal Variations of Vegetation Net Primary Productivity and Its Response to Meteorological Factors Across the Yellow River Basin During the Period 1981–2020. Front. Environ. Sci. 10:949564. doi: 10.3389/fenvs.2022.949564*

## 1 INTRODUCTION

According to the Intergovernmental Panel on Climate Change's (IPCC) sixth assessment report, the last 4 decades have been successively warmer than any decade that preceded them since 1850 (IPCC, 2021). The acceleration of climate warming has increased the frequency and intensity of meteorological disasters, severely impacting global food security and the environment (Zhou et al., 2019a; Zhou et al., 2019b; Guo et al., 2022; Zhao et al., 2022). Vegetation, which can be an indicator of global or regional climate change, plays an important role in terrestrial ecosystems (Piao et al., 2006). Climate warming can strongly impact vegetation phenology and may also cause dramatic changes in the distribution of terrestrial vegetation and environmental quality (Kong et al., 2017; Pan et al., 2021a; Pan et al., 2021b), and global warming has positive effects in boreal and arctic biomes but negative effects in the tropics (Piao et al., 2020). Climate change and human activities are considered the main drivers of regional vegetation variation. Studies showed that the temperature and precipitation exhibited high heterogeneity with changes in vegetation (Park et al., 2015; Fang et al., 2018). Net primary productivity (NPP), which refers to the amount of carbon fixed through

photosynthesis by green plants per unit of time and area, is not only an important indicator of vegetation growth status and ecosystem health, but also plays a crucial role in the terrestrial carbon cycle (Potter et al., 2012; Chen et al., 2015). It revealed that the climate change influenced NPP by affecting the distribution of radiation, heat, and water in the process of plant growth (Zhu et al., 2007a; Piao et al., 2011). Climate change had the most dominant-negative impact on the accumulated carbon sink in 14.2% of the total vegetated area of the globe (Chen et al., 2019), and soil drying caused by precipitation change contributes to 19% of global GPP change (Chen et al., 2021). The influence of climatic factors on vegetation NPP also showed strong spatiotemporal variations (Zhu et al., 2007b), and NPP of different vegetation types reacted differently to climatic factors (Khalifa et al., 2018).

The NPP estimation models can be divided into four categories based on their different operating mechanisms: climate, ecological process, light energy utilization, and ecological remote sensing coupled models. Ecological process models, which simulate vegetation growth, are well suited for simulating NPP as well as the impact and mechanisms of global climate change on vegetation NPP. As an ecological process model, the Boreal Ecosystem Productivity Simulator (BEPS) model separates the canopy into sunlit leaves and shaded leaves and uses the Farquhar photochemical model to simulate carbon–water processes (Liu et al., 1997; Chen et al., 1999; Liu et al., 2002). The BEPS model has been widely used to estimate the terrestrial ecosystem productivity globally (Amthor et al., 2001; Zhang F. M. et al., 2012; Chen et al., 2019; Zhao et al., 2021a).

As an important ecological barrier, the Yellow River Basin contains several fragile ecological regions and is confronted by environmental problems such as soil erosion and ecological function degradation. In the past decades, several environmental projects (e.g., soil and water conservation, forest and grassland rehabilitation from agriculture, and afforestation) have been carried out by the government of China and have resulted in increases in regional vegetation cover (Sun et al., 1998; Yuan et al., 2013). Fractional vegetation cover in the Yellow River Basin showed a positive increase in the past 2 decades, and increase in temperature, precipitation, and $CO_2$ concentration presented positive contributions to vegetation increase (Sun et al., 2021; Zhang et al., 2021). On the other hand, the MODIS MOD17A3 NPP product showed that NPP in the Yellow River Basin exhibited a slightly increasing trend between 2000 and 2015 (Tian et al., 2019). However, the influence of climate change on NPP across the Yellow River Basin needs a longer time span than that available through the MODIS data, which is of great importance for the studies of global changes and ecosystem changes. Therefore, in this study, NPP estimated from the BEPS from 1981 to 2020 was used to explore the spatiotemporal variation and its response to climate change over a 40-year time span, which will strengthen our understanding of the relationship between carbon cycle and climate change.

# 2 MATERIALS AND METHODS

## 2.1 Research Area and Meteorological Data

The Yellow River Basin is located between 95°53′E to 119°12′E and 32°9′N to 41°50′N, with a total area of 79 thousand km$^2$, covering 9 provinces of China (Zhao et al., 2021b). The Yellow River originates from the Qinghai Province and flows into the Bohai Sea in Shandong Province. The terrain of this basin decreases from west to east (**Figure 1**). High mountain areas with an average elevation of more than 4,000 m are mainly located in the western part, the Loess Plateau with an elevation of 1,000–2,000 m is located in the middle part, and the North China Plain with elevation lower than 100 m is located in the eastern part. The whole basin is divided into 11 secondary water resource areas (**Figure 1**). Land cover types in the western and northern parts of the basin are mainly shrub lands and savannas, while the middle and eastern parts are mainly covered by forests, wetlands, and croplands.

The required BEPS input data include land cover, leaf area index (LAI), available soil water capacity (AWC), and daily meteorological data. Land cover data came from the Institute of Geography and Resources, Chinese Academy of Sciences (http://www.resdc.cn/). Time series of LAI were from GLOBMAP LAI V3, which was generated every 8 days by the team of Liu in the Institute of Geography and Resources, Chinese Academy of Sciences (Liu et al., 2012). Available soil water capacity (AWC) came from the International Geosphere-Biosphere Program, Data and Information System (IGBP-DIS; http://www.daac.ornl.gov). Meteorological data at 318 weather stations were used from the daily meteorological datasets (V3.0) at the National Meteorological Science Data Center of China (http://data.cma.cn). Data including daily precipitation, mean temperature, and sunshine hours were averaged or summed to the annual precipitation (AP), annual mean temperature (AMT), and annual sunshine hours (ASH) year by year, then all data were interpolated into 0.01 ° × 0.01 ° grid data with the Kriging method to drive the BEPS model and analyze their influence on NPP in the Yellow River Basin.

## 2.2 Research Methods

### 2.2.1 The Boreal Ecosystems Productivity Simulator

In this study, we used the process-based ecological model BEPS to simulate NPP. The BEPS model was originally built using the biological principles of forest biogeochemical cycles (FOREST-BGC) (Hunt and Running, 1992; Kimball et al., 1997) with some modifications. The model has been refined by incorporating an advanced photosynthesis model, the Farquhar model, to the canopy using a sunlit and shaded leaf stratification approach (Farquhar et al., 1980). The instantaneous model at the leaf level is scaled to the whole canopy at a daily timescale using a temporal and spatial integration scheme (Liu et al., 1997), and the detailed steps of calculation of NPP can be referred to in Chen et al. (1999). The results of BEPS model had been widely verified in East Asia by comparing flux site data with different terrestrial ecosystems from China and AsiaFlux network (Zhang F. et al., 2012; Zhang et al., 2014; Liu et al., 2015; Zhao et al., 2021a). Thus,

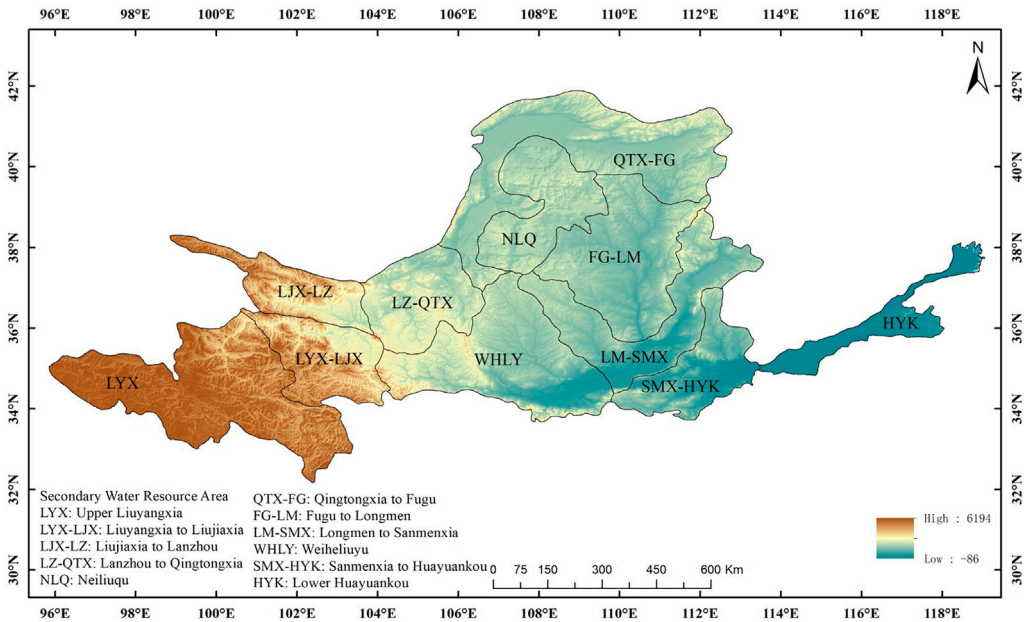


**FIGURE 1 |** Terrain and secondary water resource areas of the Yellow River Basin.

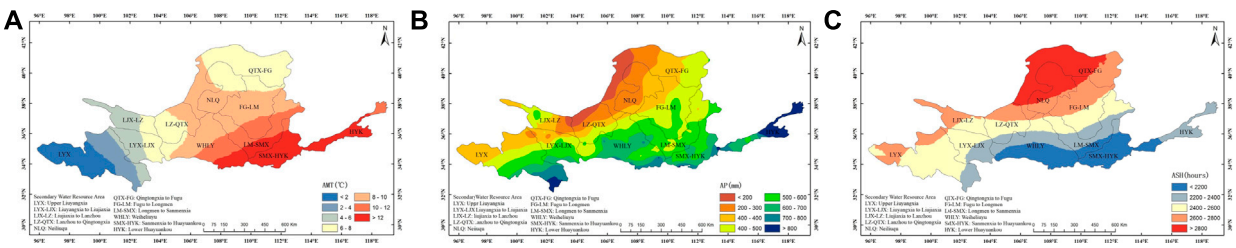


**FIGURE 2 |** Spatial distribution of average AMT **(A)**, AP **(B)**, and ASH **(C)** in the last 4 decades.

the BEPS model is considered credible and its NPP results can be used to the Yellow River Basin.

### 2.2.2 Trend Analysis of NPP

The ordinary least-squares method was used to calculate a linear regression of NPP for the period 1981 to 2020 to study the annual change trend of NPP (Gang et al., 2014; Yan et al., 2019).

$$slope = \frac{n \times \sum_{i=1}^{n} i \times NPP_i - \left(\sum_{i=1}^{n} i\right) \times \left(\sum_{i=1}^{n} NPP_i\right)}{n \times \sum_{i=1}^{n} i^2 - \left(\sum_{i=1}^{n} i\right)^2} \quad (1)$$

where *slope* is the inter-annual rate of NPP change; $n$ is 40 for years from 1981 to 2020; $i$ is 1 for year 1981, 2 for year 1982, and so on; and $NPP_i$ is the value of annual NPP at year $i$.

### 2.2.3 Partial Correlation Analysis

Light, heat, and water, represented as sunshine hours, mean temperature, and precipitation, respectively, are dominant factors affecting the vegetation growth. A statistical partial correlation analysis was used to study the effects of a single climatic factor on NPP and exclude the interference from others. When two other climatic factors are used as dependent variables, the partial correlation coefficients of NPP and individual climatic factors can be calculated by **Eq. 5** (Beer et al., 2010; Wu et al., 2015; Wen et al., 2018):

$$R_{xy,z} = \frac{R_{xy} - R_{xz} \times R_{yz}}{\sqrt{\left(1 - R_{xz}^2\right) \times \left(1 - R_{yz}^2\right)}} \quad (2)$$

where $R_{xy,\ z}$ is the partial correlation coefficient between $x$ and $y$ when excluding the impact of variable $z$; $x$ and $y$ are the dependent variables, and $z$ is the control variable. $R_{xy}$, $R_{xz}$, and $R_{yz}$ are the simple correlation coefficients between $x$, $y$, and $z$. $R_{xy}$ was taken as an example to calculate the correlation coefficients between NPP and climatic factor (**Eq. 3**):

$$R_{xy} = \frac{\sum_{i=1}^{n} \left(x_i - \bar{x}\right) \times \left(y_i - \bar{y}\right)}{\sqrt{\sum_{i=1}^{n} \left(x_i - \bar{x}\right)^2} \times \sqrt{\sum_{i=1}^{n} \left(y_i - \bar{y}\right)^2}} \quad (3)$$

where $x_i$ and $y_i$ are the annual NPP and climatic factor, respectively; $x$ and $y$ are the average NPP and mean climatic factor from 1981 to

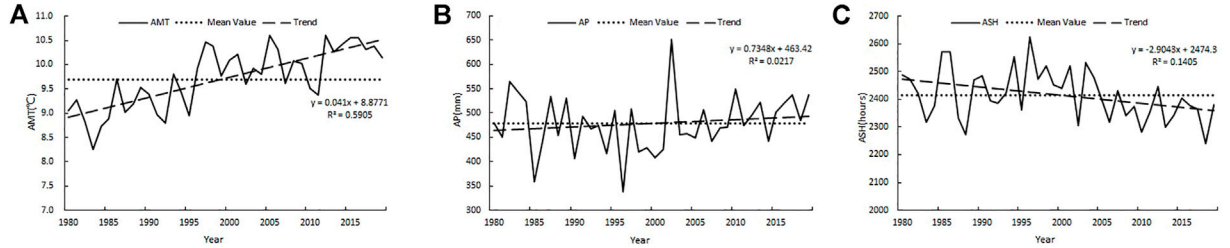


**FIGURE 3 |** Inter-annual variation of the AMT **(A)**, AP **(B)**, and ASH **(C)** in the Yellow River Basin.

2020. Finally, a bilateral t-test was implemented to assess the significance of the partial correlation coefficients.

### 2.2.4 Mann–Kendall Test

The Mann–Kendall test was used in the trend analysis of the climatic factors, including the annual mean temperature (AMT), annual sunshine hours (ASH), and annual precipitation (AP) during the period 1981–2000. The Mann–Kendall statistic Z-value for a time series $x_1, x_2, x_3, \ldots x_n$ was calculated as:

$$Z = \begin{cases} \dfrac{S-1}{\sqrt{var\,(S)}}, & S > 0 \\ 0, & S = 0 \\ \dfrac{S+1}{\sqrt{var\,(S)}}, & S < 0 \end{cases} \tag{4}$$

$$S = \sum_{i=1}^{n=1} \sum_{j=i+1}^{n} sign\left(x_j - x_i\right) \tag{5}$$

$$var\,(S) = \frac{n\,(n-1)\,(2n+5)}{18} \tag{6}$$

$$sign\left(x_j - x_i\right) = \begin{cases} 1, & x_j - x_i > 0 \\ 0, & x_j - x_i = 0 \\ -1, & x_j - x_i < 0 \end{cases} \tag{7}$$

In this study, $n$ refers to the number of time series, sign is a sign function, and $x_i$ and $x_j$ are elements of the time series. When the absolute value of Z is greater than 1.96 and 2.58, the trend analysis is at the significance level of 0.05 and 0.01.

Based on the trend analysis and Mann–Kendall test, the change slope was classified into six classes (Liu et al., 2019): 1) extremely significant decrease, slope < 0, $p \leq 0.01$; 2) significant decrease, slope < 0, $0.01 < p \leq 0.05$; 3) nonsignificant decrease, slope < 0, $p > 0.05$; 4) non-significant increase, slope > 0, $p > 0.05$; 5) significant increase, slope > 0, $0.01 < p \leq 0.05$; and 6) extremely significant increase, slope > 0, $p \leq 0.01$.

# 3 RESULTS

## 3.1 Climate Change in the Yellow River Basin

The spatial distribution of AMT, AP, and ASH from 1981 to 2020 are shown in **Figure 2**. The distribution of AMT, AP, and ASH show similar patterns in the Yellow River Basin, with similar values along with the belts extending from the northeast to the southwest. Regions with high AMT and AP are distributed in the southeast, while the high ASH is distributed in the northwestern part of the research region. The western part of the Yellow River Basin with the lowest AMT lies in the Tibetan Plateau with an elevation higher than 3,000 m. The eastern part of the Yellow River Basin had the highest AP in the Shandong Peninsula, which belongs to the coastal area.

Inter-annual variations of AMT, AP, and ASH are shown in **Figure 3**. AMT shows a strong increasing trend in the past 40 years, with the lowest value in 1983 (8.3°C) and the highest value in 2006 (10.6°C). AMT shows a stable, increasing trend between 1981 and 1997, while there is no trend after 1997. AP shows a slight increasing trend in the past 4 decades, with the highest value in 2002 (651.4 mm) and the lowest value in 1996 (338.0 mm); the fluctuation after 2003 seems not as drastic as before 2003. ASH shows a decreasing trend in the past 4 decades, with the highest value in 1996 (2,624.2 h) and the lowest value in 2019 (2,239.7 h); there were only 2 years with higher ASH than the average after 2005.

The average value, change slope, and Z-value of the Mann–Kendall test of AMT, AP, and ASH in the past 40 years are shown in **Table 1**. The AMT of the study area from 1981 to 2020 was 9.7°C, with a change slope of 0.0410°C·a$^{-1}$ in the extremely significant level. The secondary water resource areas with the top three lowest AMT were LYX (2.2°C), LJX-LZ (5.5°C), and LYX-LJX (5.8°C), but they show the top three highest warming trends, with change rates of 0.0506°C·a$^{-1}$, 0.0453°C·a$^{-1}$, and 0.0446°C·a$^{-1}$, respectively. AMT in all 11 secondary water resource areas shows a significant warming trend. The average AP of the study area is 478.5 mm, with a change slope of 0.7348 mm·a$^{-1}$ at the nonsignificant level. A total of ten secondary water resources show an increasing trend; only SMX-HYK shows a decreasing trend, but the change slope in all of the 11 secondary water resource areas were at the nonsignificant level. Average ASH in the study area was 2,414.7 h, with a decreasing rate of −2.9043 h·a$^{-1}$ in the nonsignificant level. ASH in all of the 11 secondary water resource areas showed a decreasing trend; three of them were extremely significant and three were significant. HYK and SMX-HYK were areas with the top two decreasing rates, both at the extremely significant level.

## 3.2 Spatiotemporal Variation of NPP in the Last 40 years

The spatial distribution of 40 years' and each decade average NPP are shown in **Figures 4**, **5**. As a whole, NPP in the Yellow River

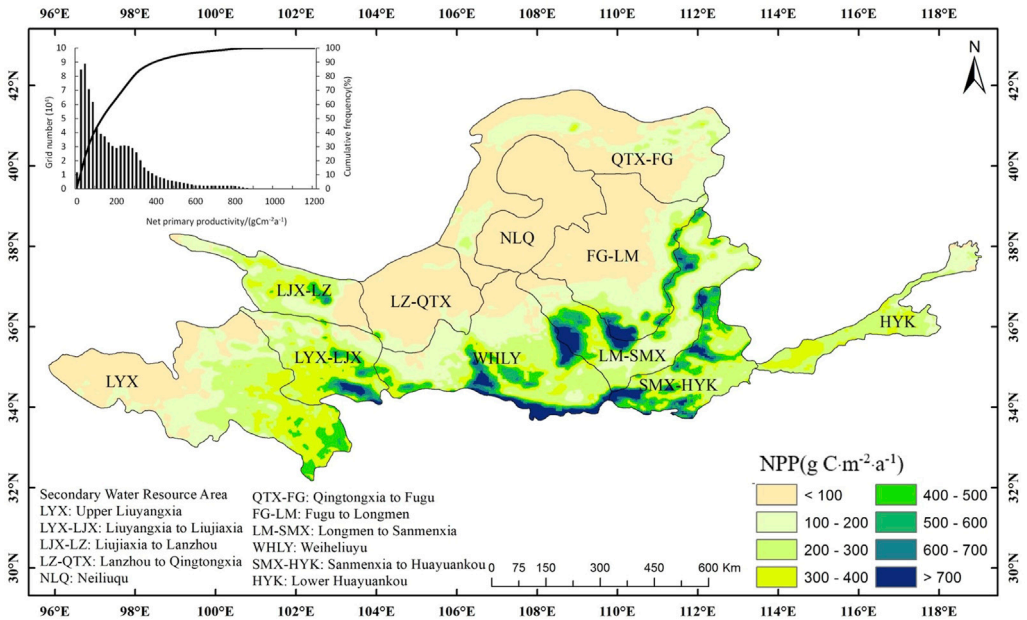


**FIGURE 4 |** Spatial distribution of net primary productivity (NPP) during 1981 and 2020.

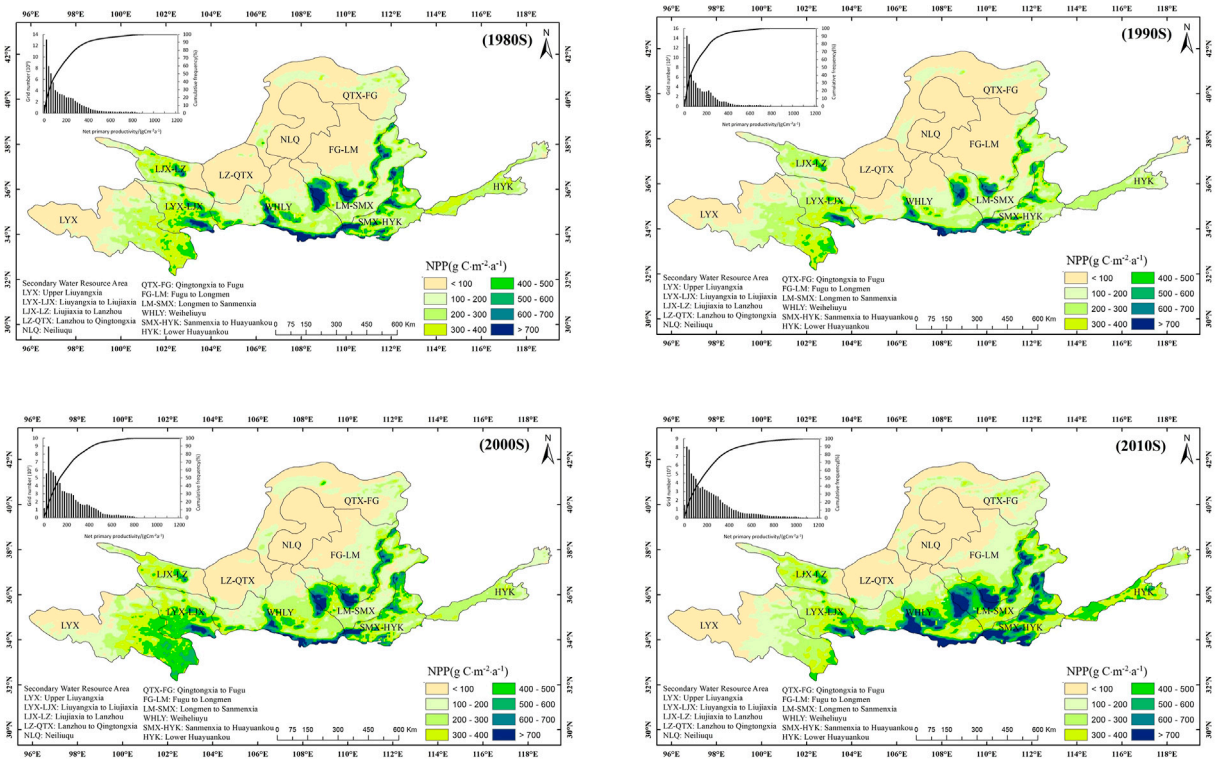


**FIGURE 5 |** Spatial distribution of 10-year average NPP from 1981 to 2020.

**TABLE 1 |** Statistical values of climatic factors in secondary water resource areas.

| Region | AMT | | | AP | | | ASH | | |
|---|---|---|---|---|---|---|---|---|---|
| | 40a average (°C) | Slope ($°C a^{-1}$) | Z-value of MK Test | 40a average (mm) | Slope ($mm·a^{-1}$) | Z-value of MK test | 40a average (hours) | Slope ($hours·a^{-1}$) | Z-value of MK Test |
| QTX-FG | 7.6 | 0.0411 | 4.11** | 309.1 | 0.9836 | 0.91 | 2859.3 | −3.9384 | −2.85** |
| NLQ | 8.4 | 0.0398 | 4.09** | 280.4 | 1.7460 | 1.42 | 2851.3 | −1.5410 | −0.97 |
| FG-LM | 9.3 | 0.0367 | 4.06** | 449.1 | 2.0957 | 1.39 | 2594.8 | −3.0138 | −2.13* |
| LM-SMX | 10.9 | 0.0387 | 4.58** | 514.0 | 0.6258 | 0.39 | 2362.5 | −3.0303 | −1.98* |
| HYK | 12.6 | 0.0382 | 4.98** | 792.8 | 1.1883 | 0.38 | 2244.7 | −6.4193 | −3.38** |
| LJX-LZ | 5.5 | 0.0453 | 5.34** | 362.8 | 1.0687 | 1.11 | 2603.6 | −4.1558 | −2.15* |
| LZ-QTX | 8.1 | 0.0431 | 4.87** | 311.0 | 0.8786 | 0.86 | 2556.5 | −2.5211 | −1.46 |
| NLQ | 10.1 | 0.0426 | 4.91** | 585.2 | 0.6397 | 0.51 | 2223.2 | −0.2580 | −0.59 |
| SMX-HYK | 13.0 | 0.0393 | 4.92** | 617.9 | −0.4341 | −0.28 | 2089.5 | −5.2767 | −2.80** |
| LYX-LJX | 5.8 | 0.0446 | 5.46** | 478.7 | 1.1801 | 0.95 | 2427.7 | −3.9468 | −1.85 |
| LYX | 2.2 | 0.0506 | 5.77** | 494.8 | 1.7794 | 1.70 | 2526.4 | −4.2883 | −1.89 |
| Whole basin | 9.7 | 0.0410 | 4.79** | 478.5 | 0.7348 | 0.95 | 2414.7 | −2.9043 | −1.93 |

** Significant level, ** extremely significant level.*

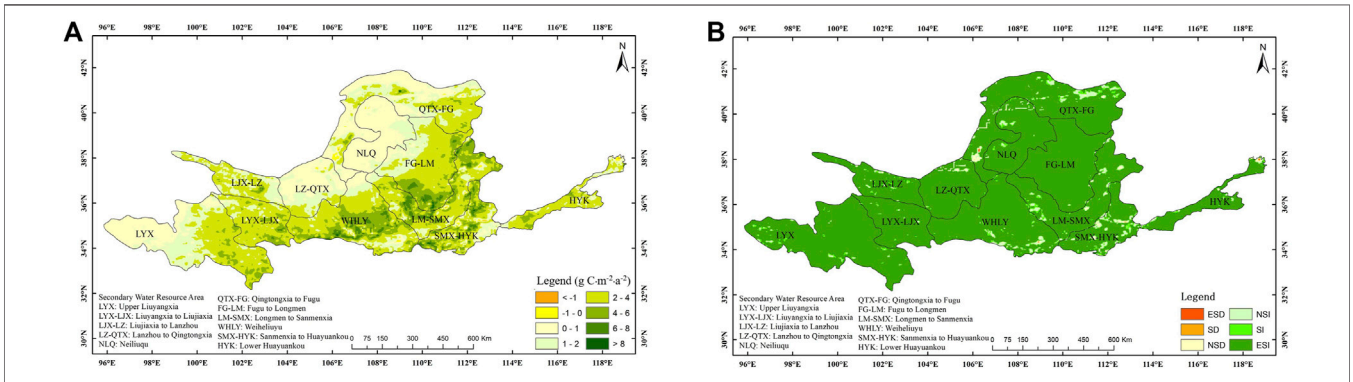


**FIGURE 6 |** Spatial distribution of the NPP change slope **(A)** in the last 40 years and its significance level **(B)** (ESD, extremely significant decrease; SD, significant decrease; NSD, nonsignificant decrease; NSI, nonsignificant increase; SI, significant increase; and ESI, extremely significant increase).

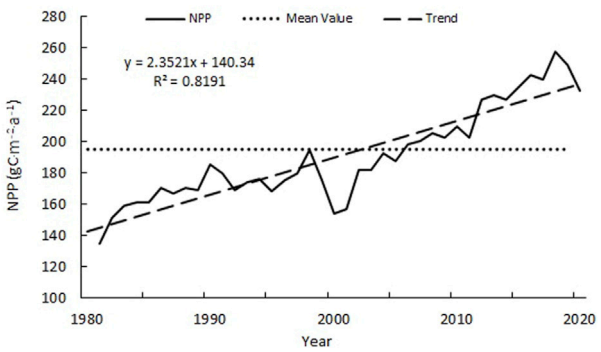


**FIGURE 7 |** Inter-annual variation of the NPP in the Yellow River Basin from 1981 to 2020.

Basin shows the highest value in the mid-south area, and decreases in the other parts, while the northwest region shows the lowest values. The average NPP in the entire research region is 195.3 g $C·m^{-2}·a^{-1}$, with 82% of the pixels with values less than 300 g $C·m^{-2}·a^{-1}$, and less than 10% of the pixels with values higher than 400 g $C·m^{-2}·a^{-1}$. The spatial distribution of 10-year average NPP in the last 4 decades is shown in **Figure 6** and listed in **Table 2**. As a whole, the distribution of NPP decreased from the southeast to the northwest.

## 3.3 Inter-Annual Variation of NPP

The inter-annual variation of NPP in the Yellow River Basin from 1981 to 2020 is shown in **Figure 7**. A slightly increasing trend was observed, ranging from 134.5 g $C·m^{-2}·a^{-1}$ in 1981 to 257.5 g $C·m^{-2}·a^{-1}$ in 2018, with an increasing rate of 2.35 g $C·m^{-2}·a^{-2}$ across the whole basin, at the extremely significant level with an MK test Z-value of 5.19. There were two short time decreases, from 194.9 g $C·m^{-2}·a^{-1}$ in 1998 to 153.9 g $C·m^{-2}·a^{-1}$ in 2000, and from 257.5 g $C·m^{-2}·a^{-1}$ in 2018 to 232.3 g $C·m^{-2}·a^{-1}$ in 2020.

The trend analysis and the Mann–Kendall test show that all the secondary water resource areas had increasing trends at

**TABLE 2 |** Statistical values of NPP in secondary water resource areas.

| Region | 1980s (g C·m$^{-2}$·a$^{-1}$) | 1990s (g C·m$^{-2}$·a$^{-1}$) | 2000s (g C·m$^{-2}$·a$^{-1}$) | 2010s (g C·m$^{-2}$·a$^{-1}$) | 40a (g C·m$^{-2}$·a$^{-1}$) | Slope (g C·m$^{-2}$·a$^{-2}$) | Z-value of MK test |
|---|---|---|---|---|---|---|---|
| QTX-FG | 83.3 | 71.0 | 94.7 | 102.6 | 87.9 | 1.46 | 5.44 |
| NLQ | 35.8 | 34.4 | 44.7 | 44.1 | 39.8 | 0.56 | 6.02 |
| FG-LM | 135.7 | 96.3 | 171.8 | 205.6 | 152.3 | 3.03 | 5.85 |
| LM-SMX | 283.1 | 217.9 | 294.9 | 392.0 | 297.0 | 3.51 | 4.81 |
| HYK | 247.8 | 196.6 | 225.1 | 345.7 | 263.4 | 2.53 | 4.50 |
| LJX-LZ | 216.8 | 178.9 | 230.4 | 221.5 | 211.9 | 2.16 | 5.04 |
| LZ-QTX | 56.9 | 47.6 | 67.9 | 78.6 | 62.7 | 1.07 | 5.97 |
| NLQ | 271.8 | 210.3 | 285.3 | 395.1 | 290.6 | 3.38 | 4.91 |
| SMX-HYK | 371.1 | 320.5 | 370.9 | 529.9 | 398.1 | 3.31 | 4.13 |
| LYX-LJX | 311.1 | 248.4 | 351.9 | 298.1 | 302.4 | 3.06 | 5.12 |
| LYX | 168.5 | 180.0 | 241.2 | 140.2 | 180.2 | 1.94 | 4.86 |
| Whole basin | 185.1 | 153.5 | 209.1 | 232.3 | 195.3 | 2.35 | 5.19 |

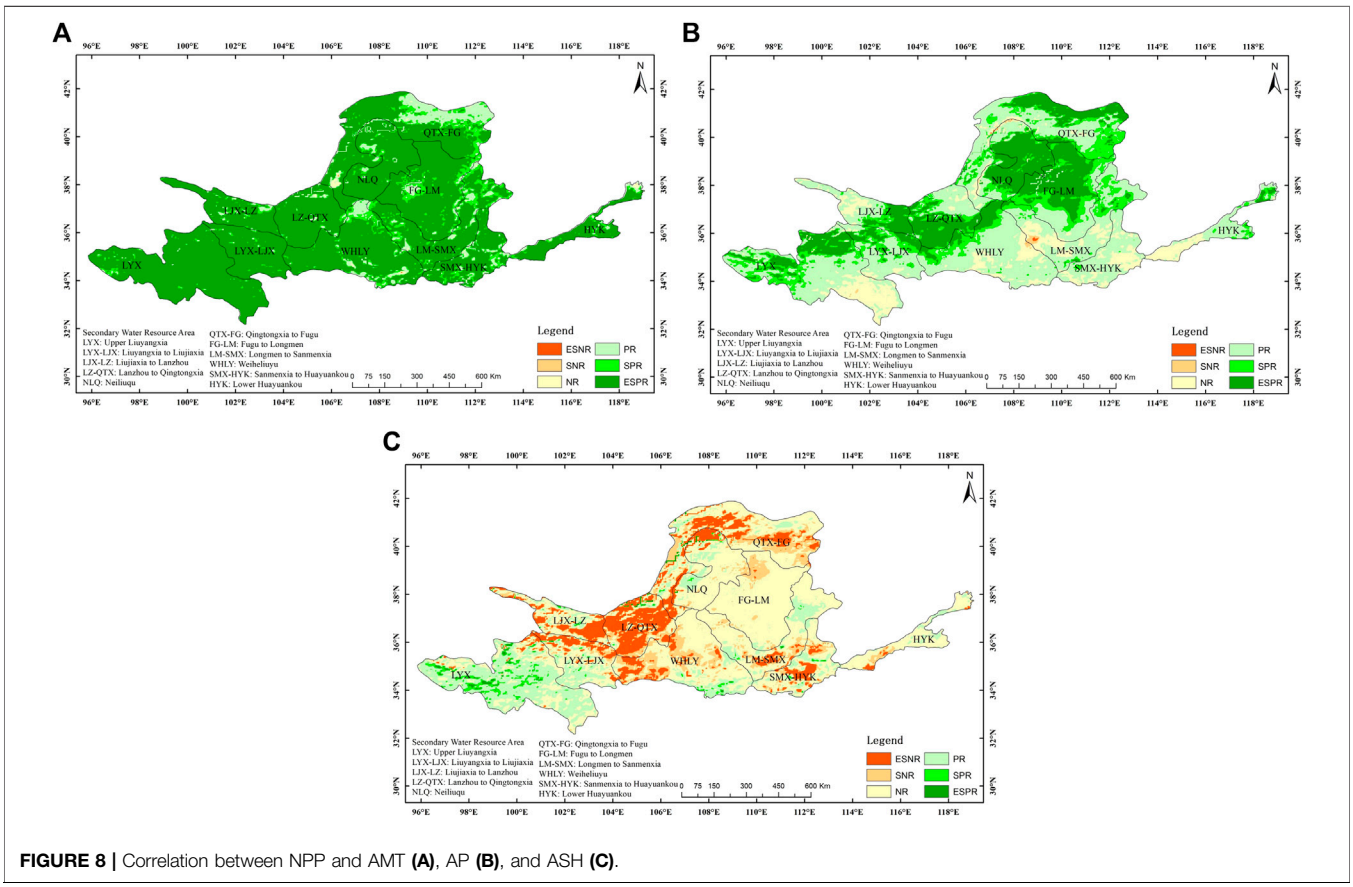


**FIGURE 8 |** Correlation between NPP and AMT **(A)**, AP **(B)**, and ASH **(C)**.

extremely significant levels (**Table 2**). The LM-SMX had the highest increasing rate. The change slopes in 5 of 11 secondary water resource areas were higher than 3.0 g C·m$^{-2}$·a$^{-2}$. The NLQ had the lowest increasing slope but the highest MK test z-value.

The spatial distribution of the vegetation NPP variation trend in the Yellow River Basin and its significance test are shown in **Figure 6**. During the last 40 years, about 99.6% of the study area showed increasing trends, including 94.3% at the extremely significant level and 2.5% percent at the significant level. Some areas showed increasing rates of more than 6 g C·m$^{-2}$·a$^{-2}$, mainly distributed in WHLY, LM-SMX, SMX-HYK, and the southern part of FG-LM. There were only small decreasing regions sporadically distributed. Regarding the secondary water resource areas, FG-LM, LYX-LJX, LYX, LZ-QTX, NLQ, and LJX-LZ showed at least 95% area increase at the extremely significant level. SMX-HYK showed 83.0% of the area increased at the extremely significant level.

### 3.4 Correlation Between NPP and Climatic Factors

The spatial distribution of the partial coefficients between NPP and climatic factors at a different significance level are presented in **Figure 8**. The regions where AMT exhibited a positive correlation with NPP occupy 99.6% of the entire research region, and the region that correlated at the extremely significant level occupies 83.1%, while the significant level occupies 8.3%. The areas of negative correlation only occupy 0.4% of the whole basin and are mainly distributed in NLQ, WHLY, and HYK.

The spatial distribution of the partial coefficients between NPP and AP shows that positive relation areas account for 87.1% of the whole study area, of which 25.4% at the extremely significant level and 16.3% at the significant level. Negative correlation areas account for 12.9%, only 0.3% at the significant level. Negative correlations are mainly distributed in the southeast LYX, northwest of LJX-LZ, and part of the areas in WHLY, LM-SMX, SMX-HYK and HYK.

The spatial distribution of partial coefficients between NPP and ASH shows that NPP is positively correlated in 24.8% of the study area. Only 0.8% at the extremely significant level and 2.0% at the significant level. The negative correlation occupies 75.2% of the study area, 2.7% at the extremely significant level, and 14.9% at the significant level.

## 4 DISCUSSION

### 4.1 Vegetation Dynamics in the Yellow River Basin

Previous studies have shown that the normalized difference vegetation index (NDVI) and vegetation cover have increased in the Yellow River Basin in the past decades. Vegetation cover in the forest showed a decreasing trend, while alpine shrubs, meadow, typical steppe, desert steppe, and forest (meadow) steppe vegetation all showed a marked increasing trend (Nie et al., 2012). During 1982 and 2013, areas that showed a trend toward improvement accounted for 59.49% of the Yellow River Basin area, while the area that showed no change accounted for about 33.96% (Niu et al., 2021). The average NDVI in the Yellow River Basin showed large fluctuations from 2000 to 2004, but showed a rapid upward trend since 2005, while 62.9% of the total area showed increasing trend during 2000 and 2010 (Yuan et al., 2013). From 1982 to 2019, the NDVI of the Yellow River Basin showed a significant increasing trend with a change trend of 0.0024 $a^{-1}$ (Liu et al., 2021). The fractional vegetation cover of the Yellow River Basin also showed a strong rising tendency during 2000–2019, with a growth rate of 0.6,030 $a^{-1}$ (Zhang et al., 2021), and the vegetation cover in the middle part of the Yellow River Basin improved significantly.

### 4.2 NPP Variations

Previous studies have shown that climate constraints on the vegetation growth relaxed with increasing temperature and solar radiation, allowing an upward trend in NPP in the past decades. The global NPP in grasslands experienced a significant increase from 1982 to 2008, with an increasing annual rate of 0.03 Pg C·$a^{-1}$ (Liu et al., 2019). NPP has shown an upward trend at the century scale, with an average trend coefficient reaching 0.88 between 1901 and 2005 in China (Gao et al., 2020). The GPP in the Yangtze River Basin showed an increasing trend but not a significant trend, with a linear change rate of 2.39 g C·$m^{-2}$·$a^{-1}$ from 2000 to 2015 (Ye et al., 2021). The grassland NPP in Inner Mongolia has experienced an increment of 0.89 g C·$m^{-2}$·$a^{-1}$ from 2001 to 2018 (Guo et al., 2021). The MODIS NPP product (MOD17A3) showed that from 2000 to 2015, the average annual NPP was 228.2 g C·$m^{-2}$·$a^{-1}$ with a slightly volatile increase (Tian et al., 2019). The NPP retrieved by the random forest algorithm showed an increasing trend of 2.37 g C·$m^{-2}$·$a^{-1}$ ($p$ = 0.09) in the Hexi Corridor of China between 2002 and 2018 (Li et al., 2021). The NPP showed an increasing rate of 2.35 g C·$m^{-2}$·$a^{-2}$ across the Yellow River Basin, which is slightly lower than in the Yangtze River Basin and Hexi Corridor, but the MK test in this research conformed to the change at an extremely significant level.

### 4.3 Response of NPP to Climatic Factors

Climate change influences vegetation ecosystems mostly through changes in temperature, precipitation, and solar radiation, by altering soil moisture, soil microbes, and additionally affecting the photosynthesis and plant respiration, which are further regulated by vegetation growth and ecosystem productivity (Horion et al., 2013; He et al., 2015; Ma et al., 2019). Temperature is the primary climatic factor that controls the inter-annual variation in NPP over most ecosystems, while precipitation may play a different role in different ecosystems (Liang et al., 2015). According to this research, temperature, precipitation, and sunshine hours positively correlate with NPP over 99.6, 87.1, and 24.8% of the research region, respectively. Areas where precipitation shows a positive correlation and sunshine hours show a negative correlation with NPP are mainly located in the western and northern parts of the Yellow River Basin, with an arid climate and covered by vast shrubland, grassland, and desert areas. In arid areas, plant growth is mainly restricted by soil moisture, and lower soil moisture reduces the photosynthetic rate and thus reduces the accumulation of photosynthetic products. In contrast, the correlation between precipitation and NPP rarely reaches a significant level in the eastern and southern parts of the Yellow River Basin, where precipitation is above 600 mm·$a^{-1}$.

### 4.4 Limitations and Next Work

This study analyzed the annual response of NPP to climatic factors during the period 1981–2020. The annual values of temperature, precipitation, and sunshine hours included the occurrence of meteorological disasters. According to the previous research, drought dominates the inter-annual variability in the global terrestrial NPP by controlling semi-arid ecosystems. Soil moisture variability drive 90 percent of inter-annual variability in the global land carbon uptake (Vincent et al., 2021). Drought may have reduced global NPP by 0.55 Pg C from 2000 to 2009. A drying trend decreased NPP in the southern hemisphere (Zhao and Running, 2010), which can explain 29% of the inter-annual variation in the global NPP in semi-arid ecosystems (Huang et al., 2016). Extremely severe meteorological disasters have become more frequent due to climate change. Our study will include the impact of severe flood and drought on the terrestrial ecosystem in future research.

## 5 CONCLUSION

This article analyzed the NPP simulated by the BEPS model and corresponding meteorological data to help understand the spatiotemporal variation of vegetation NPP and its response to climate change. The NPP in the Yellow River Basin showed high values in the mid-south part, while the lowest values were recorded in the northwestern part. The average NPP in the 40 years was 195.3 g $C{\cdot}m^{-2}{\cdot}a^{-1}$ with an extremely significant increasing trend and with an increasing rate of 2.35 g $C{\cdot}m^{-2}{\cdot}a^{-2}$. All of the 11 secondary water resource areas showed increasing trends at an extremely significant level. The spatial distribution of AMT, AP, and ASH showed similar patterns in the Yellow River Basin, with similar values along belts extending from the northeast to the southwest. AMT showed a change slope of 0.0410°C·$a^{-1}$ in the extremely significant level. AP showed a change slope of 0.7348 mm·$a^{-1}$, while ASH showed a decreasing rate of −2.9043 h·$a^{-1}$, both in the nonsignificant level. NPP is mainly positively related with AMT and AP, and negatively related with ASH. The regions where NPP exhibited a positive correlation with AMT, AP, and ASH occupy 99.6, 87.1, and 24.8% of the entire research region, respectively.

## DATA AVAILABILITY STATEMENT

The raw data supporting the conclusions of this article will be made available by the authors, without undue reservation.

## AUTHOR CONTRIBUTIONS

HT analyzed the spatiotemporal distribution of NPP and meteorological factors and their relationship. XJ calculated yearly values of meteorological factors, and FZ calculated NPP.

## FUNDING

This work was supported by the foundation of Key Laboratory of Agro-meteorological Safeguard and Applied Technique China Meteorological Administration (KZ202005).

## REFERENCES

Amthor, J. S., Chen, J. M., Clein, J. S., Frolking, S., Goulden, M. L., Carvalhais, N., et al. (2001). Boreal Forest $CO_2$ Exchange and Evapotransporation Predicted by Nine Ecosystems Process Models: Intermodel Comparisons and Relationships to Field Measurements. *J. Geophys. Res. Atmos.* 106 (D24), 33623–33648. doi:10.1029/2000JD900850

Beer, C., Reichstein, M., Tomelleri, E., Ciais, P., Jung, M., Carvalhais, N., et al. (2010). Terrestrial Gross Carbon Dioxide Uptake: Global Distribution and Covariation with Climate. *Science* 329, 834–838. doi:10.1126/science.1184984

Chen, H., Bai, X., Li, Y., Li, Q., Wu, L., Chen, F., et al. (2021). Soil Drying Weakens the Positive Effect of Climate Factors on Global Gross Primary Production. *Ecol. Indic.* 129, 107953. doi:10.1016/j.ecolind.2021.107953

Chen, J. M., Ju, W., Ciais, P., Viovy, N., Liu, R., Liu, Y., et al. (2019). Vegetation Structural Change since 1981 Significantly Enhanced the Terrestrial Carbon Sink. *Nat. Commun.* 10, 4259. doi:10.1038/s41467-019-12257-8

Chen, J. M., Liu, J., Cihlar, J., and Goulden, M. L. (1999). Daily Canopy Photosynthesis Model through Temporal and Spatial Scaling for Remote Sensing Applications. *Ecol. Model.* 124, 99–119. doi:10.1016/s0304-3800(99)00156-8

Chen, L., Li, H., Zhang, P., Zhao, X., Zhou, L., Liu, T., et al. (2015). Climate and Native Grassland Vegetation as Drivers of the Community Structures of Shrub-Encroached Grasslands in Inner Mongolia, China. *Landsc. Ecol.* 30 (9), 1627–1641. doi:10.1007/s10980-014-0044-9

Fang, J., Yu, G., Liu, L., Hu, S., and Chapin, F. S. (2018). Climate Change, Human Impacts, and Carbon Sequestration in China. *Proc. Natl. Acad. Sci. U. S. A.* 115 (15), 4015–4020. doi:10.1073/pnas.1700304115

Farquhar, G. D., von Caemmerer, S., and Berry, J. A. (1980). A Biochemical Model of Photosynthetic CO2 Assimilation in Leaves of C3 Species. *Planta* 149, 78–90. doi:10.1007/bf00386231

Gang, C., Zhou, W., Chen, Y., Wang, Z., Sun, Z., Li, J., et al. (2014). Quantitative Assessment of the Contributions of Climate Change and Human Activities on Global Grassland Degradation. *Environ. Earth Sci.* 72, 4273–4282. doi:10.1007/s12665-014-3322-6

Gao, D., Dan, L., Fan, G., Tian, H., Peng, J., Yang, X., et al. (2020). Spatiotemporal Variations of Carbon Flux and Nitrogen Deposition Flux Linked with Climate Change at the Centennial Scale in China. *Sci. China Earth Sci.* 63, 731–748. doi:10.1007/s11430-018-9548-3

Guo, D., Song, X., Hu, R., Cai, S., Zhu, X., and Hao, Y. (2021). Grassland Type-dependent Spatiotemporal Characteristics of Productivity in Inner Mongolia and its Response to Climate Factors. *Sci. Total Environ.* 775, 145644. doi:10.1016/j.scitotenv.2021.145644

Guo, Y., Xia, H., Pan, L., Zhao, X., and Li, R. (2022). Mapping the Northern Limit of Double Cropping Using a Phenology-Based Algorithm and Google Earth Engine. *Remote Sens.* 14 (4), 1004.

He, Y., Wang, F., MuZhao, X. Y., Yan, H., and Zhao, G. (2015). An Assessment of Human versus Climatic Impacts on Jing River Basin, Loess Plateau, China. *Adv. Meteorology* 2015, 1–13. doi:10.1155/2015/478739

Horion, S., Cornet, Y., Erpicum, M., and Tychon, B. (2013). Studying Interactions between Climate Variability and Vegetation Dynamic; Using a Phenology Based Approach. *Remote Sens.* 14, 20–32. doi:10.3390/rs14041004

Huang, L., He, B., Chen, A., Wang, H., Liu, J., Lǚ, A., et al. (2016). Corrigendum: Drought Dominates the Interannual Variability in Global Terrestrial Net Primary Production by Controlling Semi-arid Ecosystems. *Sci. Rep.* 6, 35126. doi:10.1038/srep35126

Hunt, E. R., Jr, and Running, S. W. (1992). Simulated Dry Matter Yields for Aspen and Spruce Stands in the North American Boreal Forest. *Can. J. Remote Sens.* 18, 126–133. doi:10.1080/07038992.1992.10855315

Khalifa, M., Elagib, N. A., Ribbe, L., and Schneider, K. (2018). Spatio-temporal Variations in Climate, Primary Productivity and Efficiency of Water and Carbon Use of the Land Cover Types in Sudan and Ethiopia. *Sci. Total Environ.* 624, 790–806. doi:10.1016/j.scitotenv.2017.12.090

Kimball, J. S., Thornton, P. E., White, M. A., and Running, S. W. (1997). Simulating Forest Productivity and Surface-Atmosphere Carbon Exchange in the BOREAS Study Region. *Tree Physiol.* 17, 589–599. doi:10.1093/treephys/17.8-9.589

Kong, D., Zhang, Q., Huang, W., and Gu, X. (2017). Vegetation Phenology Change in Tibetan Plateau from 1982 to 2013 and its Related Meteorological Factors. *Acta Geogr. Sin.* 72 (1), 39–52. (Chinese).

Li, C., Zhu, T., Zhou, M., Yin, H., Wang, Y., Sun, H., et al. (2021). Temporal and Spatial Change of Net Primary Productivity of Vegetation and its Determinants in Hexi Corridor. *Acta Ecol. Sin.* 41 (5), 1931–1943. (Chinese). doi:10.5846/stxb202001130105

Liang, W., Yang, Y., Fan, D., Guan, H., Zhang, T., Long, D., et al. (2015). Analysis of Spatial and Temporal Patterns of Net Primary Production and Their Climate Controls in China from 1982 to 2010. *Agric. For. Meteorology* 204, 22–36. doi:10.1016/j.agrformet.2015.01.015

Liu, H., Liu, F., and Zheng, L. (2021). Effects of Climate Change and Human Activities on Vegetation Cover Change in the Yellow River Basin. *J. Soil Water Conservation* 35 (4), 143–151. (Chinese).

Liu, J., Chen, J., Cihlar, J., and Park, W. M. (1997). A Process-Based Boreal Ecosystem Productivity Simulator Using Remote Sensing Inputs. *Remote Sens. Environ.* 62, 158–175. doi:10.1016/s0034-4257(97)00089-8

Liu, J., Chen, J. M., Cihlar, J., and Chen, W. (2002). Net Primary Productivity Mapped for Canada at 1-km Resolution. *Glob. Ecol.* 11, 115–129. doi:10.1046/j.1466-822x.2002.00278.x

Liu, Y., Liu, R., and Chen, J. (2012). Retrospective Retrieval of Long-Term Consistent Global Leaf Area Index (1981-2011) from Combined AVHRR and MODIS Data. *J. Geophys. Res.* 117 (G4). doi:10.1029/2012jg002084

Liu, Y., Xiao, J., Ju, W., Zhou, Y., Wang, S., and Wu, X. (2015). Water use Efficiency of China's Terrestrial Ecosystems and Responses to Drought. *Sci. Rep.* 5. doi:10.1038/srep13799

Liu, Y., Yang, Y., Wang, Q., Khalifa, M., Zhang, Z., Tong, L., et al. (2019). Assessing the Dynamics of Grassland Net Primary Productivity in Response to Climate Change at the Global Scale. *Chin. Geogr. Sci.* 29 (5), 725–740. doi:10.1007/s11769-019-1063-x

Ma, L., Xia, H., and Meng, Q. (2019). Spatiotemporal Variability of Asymmetric Daytime and Night-Time Warming and its Effects on Vegetation in the Yellow River Basin from 1982 to 2015. *Sensors* 19, 1832. doi:10.3390/s19081832

IPCC (2021). "Summary for Policymakers," in *Climate Change 2021: The Physical Science Basis. Contribution of Working Group I to the Sixth Assessment Report of the Intergovernmental Panel on Climate Change*. Editors V. Masson-Delmotte, P. Zhai, A. Pirani, S. L. Connors, C. Péan, S. Berger, et al. (Cambridge University Press). In Press.

Nie, Q., Xu, J., Li, Z., and Hong, Y. (2012). Spatial-temporal Variation of Vegetation Cover in Yellow River Basin of China during 1998-2008. *Sci. Cold Arid Regions* 4 (3), 0211–0221. doi:10.3724/SP.J.1226.2012.00211

Niu, W., Xia, H., Wang, R., Pan, L., Meng, Q., Qin, Y., et al. (2021). Research on Large-Scale Urban Shrinkage and Expansion in the Yellow River Affected Area Using Night Light Data. *ISPRS Int. J. Geo-Information.* 10 (1), 5. doi:10.3390/ijgi10010005

Pan, L., Xia, H., Yang, J., Niu, W., Wang, R., Song, H., et al. (2021a). Mapping Cropping Intensity in Huaihe Basin Using Phenology Algorithm, All Sentinel-2 and Landsat Images in Google Earth Engine. *Int. J. Appl. Earth Observation Geoinformation* 102, 102376. doi:10.1016/j.jag.2021.102376

Pan, L., Xia, H., Zhao, X., Guo, Y., and Qin, Y. (2021b). Mapping Winter Crops Using a Phenology Algorithm, Time-Series Sentinel-2 and Landsat-7/8 Images, and Google Earth Engine. *Remote Sens.* 13 (13), 2510. doi:10.3390/rs13132510

Park, H., Jeong, S.-J., Ho, C.-H., Kim, J., Brown, M. E., and Schaepman, M. E. (2015). Nonlinear Response of Vegetation Green-Up to Local Temperature Variations in Temperate and Boreal Forests in the Northern Hemisphere. *Remote Sens. Environ.* 165 (165), 100–108. doi:10.1016/j.rse.2015.04.030

Piao, S., Ciais, P., Lomas, M., Beerd, C., Liu, H., Fang, J., et al. (2011). Contribution of Climate Change and Rising $CO_2$ to Terrestrial Carbon Balance in East Asia: a Multi-Model Analysis. *Glob. Planet. Change* 75 (3/4), 133–142. doi:10.1016/j.gloplacha.2010.10.014

Piao, S., Fang, J., Zhou, L., Ciais, P., and Zhu, B. (2006). Variations in Satellite-Derived Phenology in China's Temperate Vegetation. *Glob. Change Biol.* 12 (4), 672–685. doi:10.1111/j.1365-2486.2006.01123.x

Piao, S., Wang, X., Park, T., Chen, C., Lian, X., He, Y., et al. (2020). Characteristics, Drivers and Feedbacks of Global Greening. *Nat. Rev. Earth Environ.* 1, 14–27. doi:10.1038/s43017-019-0001-x

Potter, C., Klooster, S., and Genovese, V. (2012). Net Primary Production of Terrestrial Ecosystems from 2000 to 2009. *Clim. Change* 115 (2), 365–378. doi:10.1007/s10584-012-0460-2

Sun, G., Liu, X., Wang, X., and Li, S. (2021). Changes in Vegetation Cover and its Influencing Factors across the Yellow River Basin during 2001-2020. *J. Desert Res.* 41 (4), 205–212. (Chinese).

Sun, H., Wang, C., Niu, Z., Bukhosorand Li, B. (1998). Analysis of Vegetation Cover Change and the Relationship between NDVI and Environmental Factors by Using NOAA Time Series Data. *Jounal Remote Sens.* 2 (3), 204–210. (Chinese).

Tian, Z., Zhang, D., He, X., Guo, H., and Wei, H. (2019). Spatiotemporal Variations in Vegetation Net Primary Productivity and Their Driving Factors in Yellow River Basin from 2000 to 2015. *Res. Soil Water Conservation* 26 (2), 255–262. (Chinese).

Wen, Y., Liu, X., Pei, F., Li, X., and Du, G. (2018). Non-uniform Time-Lag Effects of Terrestrial Vegetation Responses to Asymmetric Warming. *Agric. For. Meteorology* 252, 130–143. doi:10.1016/j.agrformet.2018.01.016

Wu, D., Zhao, X., Liang, S., Zhou, T., Huang, K., Tang, B., et al. (2015). Time-lag Effects of Global Vegetation Responses to Climate Change. *Glob. Change Biol.* 21, 3520–3531. doi:10.1111/gcb.12945

Yan, Y., Liu, X., Wen, Y., and Ou, J. (2019). Quantitative Analysis of the Contributions of Climatic and Human Factors to Grassland Productivity in Northern China. *Ecol. Indic.* 103, 542–553. doi:10.1016/j.ecolind.2019.04.020

Ye, X., Yang, X., Liu, F., Wu, J., and Liu, J. (2021). Spatio-temporal Variations of Land Vegetation Gross Primary Production in the Yangtze River Basin and Correlation with Meteorological Factors. *Acta Ecol. Sin.* 41 (17), 3–11. (Chinese).

Yuan, L., Jiang, W., Shen, W., Liu, Y., Wang, W., Tao, L., et al. (2013). The Spatio-Temporal Variations of Vegetation Cover in the Yellow River Basin from 2000 to 2010. *Acta Ecol. Sin.* 339 (24), 7798–7806. (Chinese). doi:10.5846/stxb201305281212

Zhang, F., Ju, W., Shen, S., Wang, S., Yu, G., and Han, S. (2012). Variations of Terrestrial Net Primary Productivity in East Asia. *Terr. Atmos. Ocean. Sci.* 23 (4), 425–437. doi:10.3319/tao.2012.03.28.01(a)

Zhang, F., Ju, W., Shen, S., Wang, S., Yu, G., and Han, S. (2014). How Recent Climate Change Influences Water Use Efficiency in East Asia. *Theor. Appl. Climatol.* 116, 359–370. doi:10.1007/s00704-013-0949-2

Zhang, F. M., Ju, W. M., Chen, J. M., Wang, S. Q., Yu, G. R., and Han, S. J. (2012). Characteristics of Terrestrial Ecosystem Primary Productivity in East Asia Based on Remote Sensing and Process-Based Model. *Ying Yong Sheng Tai Xue Bao* 23 (2), 307–318. (Chinese).

Zhang, Z., Liu, H., Zuo, Q., Yu, J., and Li, Y. (2021). Spatiotemporal Change of Fractional Vegetation Cover in the Yellow River Basin during 2000-2019. *Resour. Sci.* 43 (4), 849–858. (Chinese). doi:10.18402/resci.2021.04.18

Zhao, M., and Running., S. W. (2010). Drought-Induced Reduction in Global Terrestrial Net Primary Production from 2000 through 2009. *Science* 329, 940–943. doi:10.1126/science.1192666

Zhao, X., Xia, H., Liu, B., and Jiao, W. (2022). Spatiotemporal Comparison of Drought in Shaanxi-Gansu-Ningxia from 2003 to 2020 Using Various Drought Indices in Google Earth Engine. *Remote Sens.* 14 (7), 1570. doi:10.3390/rs14071570

Zhao, X., Xia, H., Pan, L., Song, H., Niu, W., Wang, R., et al. (2021a). Drought Monitoring over Yellow River Basin from 2003-2019 Using Reconstructed MODIS Land Surface Temperature in Google Earth Engine. *Remote Sens.* 13 (18), 3748. doi:10.3390/rs13183748

Zhao, X., Zhang, F., Su, R., Gao, C., and Xing, K. (2021b). Response of Carbon and Water Fluxes to Dryness/wetness in China. *Terr. Atmos. Ocean. Sci.* 32, 53–67. doi:10.3319/tao.2020.08.25.01

Zhou, S., Zhang, Y., Park Williams, A., and Gentine, P. (2019b). Projected Increases in Intensity, Frequency, and Terrestrial Carbon Costs of Compound Drought and Aridity Events. *Sci. Adv.* 5 (1), eaau5740. doi:10.1126/sciadv.aau5740

Zhou, S., Williams, A. P., Berg, A. M., Cook, B. I., Zhang, Y., Hagemann, S., et al. (2019a). Land-atmosphere Feedbacks Exacerbate Concurrent Soil Drought and Atmospheric Aridity. *Proc. Natl. Acad. Sci. U.S.A.* 116 (38), 18848–18853. doi:10.1073/pnas.1904955116

Zhu, W., Pan, Y., Yang, X., and Song, G. (2007a). Comprehensive Analysis of the Impact of Climatic Changes on Chinese Terrestrial Net Primary Productivity. *Chin. Sci. Bull.* 52 (21), 3250–3260. (Chinese). doi:10.1007/s11434-007-0521-5

Zhu, W., Pan, Y., and Zhang, J. (2007b). Estimation of Net Primary Productivity of Chinese Terrestrial Vegetation Based on Remote Sensing. *J. plant Ecol.* 31 (3), 413–424.

**Conflict of Interest:** The authors declare that the research was conducted in the absence of any commercial or financial relationships that could be construed as a potential conflict of interest.

**Publisher's Note:** All claims expressed in this article are solely those of the authors and do not necessarily represent those of their affiliated organizations, or those of the publisher, the editors, and the reviewers. Any product that may be evaluated in this article, or claim that may be made by its manufacturer, is not guaranteed or endorsed by the publisher.

frontiers | Frontiers in Environmental Science

ORIGINAL RESEARCH
published: 01 August 2022
doi: 10.3389/fenvs.2022.945100

# Potential Relationship Between Aerosols and Positive Cloud-to-Ground Lightning During the Warm Season in Sichuan, Southwest China

*Pengguo Zhao*[1,2], *Yuanyang Zhang*[3]*, *Chang Liu*[3], *Peiwen Zhang*[2], *Hui Xiao*[4] and *Yunjun Zhou*[1]

[1]Plateau Atmosphere and Environment Key Laboratory of Sichuan Province, College of Atmospheric Science, Chengdu University of Information Technology, Chengdu, China, [2]Institute of Plateau Meteorology, China Meteorological Administration, Chengdu, China, [3]Sichuan Lightning Protection Center, Chengdu, China, [4]Guangzhou Institute of Tropical and Marine Meteorology, China Meteorological Administration, Guangzhou, China

OPEN ACCESS

**Edited by:**
Honglei Wang,
Nanjing University of Information Science and Technology, China

**Reviewed by:**
Zheng Shi,
Nanjing University of Information Science and Technology, China
Yue Zhou,
China Meteorological Administration, China

***Correspondence:**
Yuanyang Zhang
zyysgtc@yeah.net

**Specialty section:**
This article was submitted to Atmosphere and Climate, a section of the journal Frontiers in Environmental Science

**Received:** 16 May 2022
**Accepted:** 23 June 2022
**Published:** 01 August 2022

**Citation:**
Zhao P, Zhang Y, Liu C, Zhang P, Xiao H and Zhou Y (2022) Potential Relationship Between Aerosols and Positive Cloud-to-Ground Lightning During the Warm Season in Sichuan, Southwest China. Front. Environ. Sci. 10:945100. doi: 10.3389/fenvs.2022.945100

This study discussed the influence of aerosols on the relative frequency of positive cloud-to-ground (CG) lightning and its dependence on thermodynamic and cloud-related factors in Sichuan during the warm season from 2005 to 2017. The relative frequency of positive CG lightning is defined as the proportion of positive CG lightning flashes to total CG lightning flashes. Although the total CG lightning density in the Western Sichuan Plateau is significantly lower than that in the Sichuan Basin, the relative frequency of positive CG lightning is higher than that in the basin. Convective available potential energy (CAPE) and vertical wind shear in the low-to-mid level of the troposphere (SHEAR-5 km) are the controlling factors of positive CG lightning frequency. A small CAPE and a large SHEAR-5 km represent weak convection, which is more conducive to the generation of positive CG lightning. The upper main positive charge region in a thriving thunderstorm is higher from the ground, which is not conducive to the transport of positive charge to the ground, so it is not conducive to the generation of positive CG lightning. In the basin, the relationship between aerosols and positive lightning is not significant, which may be due to the strong total CG lightning and the low proportion of positive CG lightning. In the plateau, both sulfate aerosol and black carbon (BC) aerosol have a significant inhibition effect on the positive CG lightning relative frequency. Sulfate aerosol stimulates the ice-phase process through a microphysical effect and promotes the development of convection. The distribution of the main positive charge center is higher, which is not conducive to the transport of positive charge to the ground and the generation of positive CG lightning. The significant heating effect of BC aerosol on the lower troposphere makes the convective development more vigorous and is not conducive to the occurrence of positive CG lightning.

**Keywords: sulfate aerosol, black carbon aerosol, positive lightning, thermodynamic factors, Sichuan**

## INTRODUCTION

Observational evidence and numerical simulation studies indicated that aerosol has an outstanding effect on lightning activity. One view holds that aerosols could stimulate lightning activity through a microphysical effect (Wang et al., 2011; Mansell and Ziegler, 2013; Yang and Li, 2014; Liu et al., 2020), more aerosols serve as cloud condensation nuclei to reduce the radius of cloud droplets and then reduce the collision–coalescence efficiency, thus inhibiting the warm rain process. The small cloud droplets are transported above the freezing level to participate in the ice-phase microphysical processes, forming more ice particles and releasing a large amount of latent heat to further stimulate convection. Stronger convection and more ice particles are involved in the non-inductive electrification process, making lightning more vigorous. Another view suggests that aerosols inhibit lightning activity through a radiative effect (Yang et al., 2013; Tan et al., 2016; Altaratz et al., 2017), the scattered aerosols reduce the solar radiation reaching the ground, which weakens the thermal conditions in the lower troposphere, and the relatively stable atmospheric conditions are not conducive to the development of convection, thus inhibiting lightning activity. The radiative forcing effect of BC aerosol affects the structure of atmospheric thermal stability and convective development, which is closely related to its vertical distribution and heating rate (Lu et al., 2020). Sulfate aerosols have different effects on lightning activity through the microphysical effect and radiation effect. Sulfate aerosols could stimulate lightning activity through microphysical effect, and could inhibit lightning activity through radiation effect (Yang et al., 2013; Yang and Li, 2014; Zhao et al., 2020).

There were also two different views on the effect of aerosols on positive CG lightning. On the one hand, previous studies suggested that anthropogenic aerosols in the urban increase the percentage of positive CG lightning (Steiger et al., 2002; Naccarato et al., 2003). According to their urban aerosol hypothesis, urban aerosols influence the polarity of lightning by influencing the charge separation process in thunderstorms. Atmospheric pollutants in super cooled cloud droplets would cause graupel particles to be charged negatively in a warmer temperature region, and a wider negative charge region is conducive to the generation of negative CG lightning, thus reducing the percentage of positive CG lightning. On the other hand, the effect of smoke aerosol from fires on the percentage of positive CG lightning is opposite to that of urban aerosols (Lyons, 1998; Murray et al., 2000; Lang and Rutledge, 2006). The smoke aerosol hypothesis considers that smoke aerosol would narrow the droplet spectrum, and the narrow droplet spectrum leads to the graupel particles charging positively between −10°C and −20°C in the thunderstorm, which would lead to a wider distribution of lower positive charge region, which is conducive to the generation of positive CG lightning.

Previous studies (Eddy, 2018; MacGorman et al., 2018) have suggested that thermodynamic and moisture factors, such as thermal stability, vertical wind shear, and moisture in the low- to the mid-level troposphere, are crucial to the generation of positive CG lightning. Weaker thermal instability conditions mean weaker thunderclouds, while the distribution of the main positive charge region is relatively low, which is conducive to the triggering of positive CG lightning from there (Orville and Huffines, 1999; Rakov, 2003; Wang et al., 2018). Stronger vertical wind shear causes the cloud body to tilt, so that positively charged ice particles in the upper part of the cloud are repositioned and are no longer blocked by the negative charged region below, making it easier to transport positive charge to the ground and generate positive CG lightning (Brook et al., 1982; Zhao et al., 2021). Dry low-to mid-level troposphere also has an excitation effect on positive CG lightning (Carey and Buffalo, 2007).

The west of Sichuan is the West Sichuan Plateau, and the east is the Sichuan Basin. On the one hand, the special terrain and thermal dynamic conditions lead to the obvious spatial difference in lightning activity in this region (Xia et al., 2015; Zhao et al., 2022b). On the other hand, the topographic conditions unfavorable to the diffusion of atmospheric pollutants and the prominent anthropogenic emissions result in the aerosol concentration in the basin area being significantly higher than that in the plateau area (Ning et al., 2018). The influence of aerosols on CG lightning density in Sichuan has obvious spatial differences (Zhao et al., 2020), so, what is the relationship between aerosols and positive CG lightning activity? In this study, we focus on this interesting issue, analyzing the possible influence of black carbon aerosols and sulfate aerosols on the relative frequency of positive CG lightning and the role of environmental conditions in this effect.

## DATA AND METHODOLOGY

### CG Lightning

The CG lightning data were obtained from the Sichuan Lightning Detection Network (SCLDN) of the Sichuan Province Lightning protection center, including the flash number of CG lightning, CG lightning polarity, and peak current. SCLDN consists of 25 Advanced Time of Arrival and Direction (ADTD) ground-based sensors with an average detection efficiency of more than 90% [CMA (China Meteorological Administration), 2009; Yang et al., 2015]. The CG lightning data employed in this study was processed with quality control, which was based on previous studies (Cummins et al., 1998; Yang et al., 2015; Zhao et al., 2020; Zhao et al., 2021). Lightning data during the warm season (May to October) from 2005 to 2017 were applied. To match environmental factors data, lightning data were processed to a temporal of 1 month and spatial resolution of 0.25 × 0.25. The positive CG lightning relative frequency is defined as the percentage of positive CG lightning flashes in total CG lightning flashes.

$$PRF = \frac{N_{positive}}{N_{total}} \times 100\%, \quad (1)$$

where $PRF$ is the relative frequency of positive CG lightning, $N_{positive}$ is the positive CG lightning flashes, $N_{total}$ is the total CG lightning flashes.

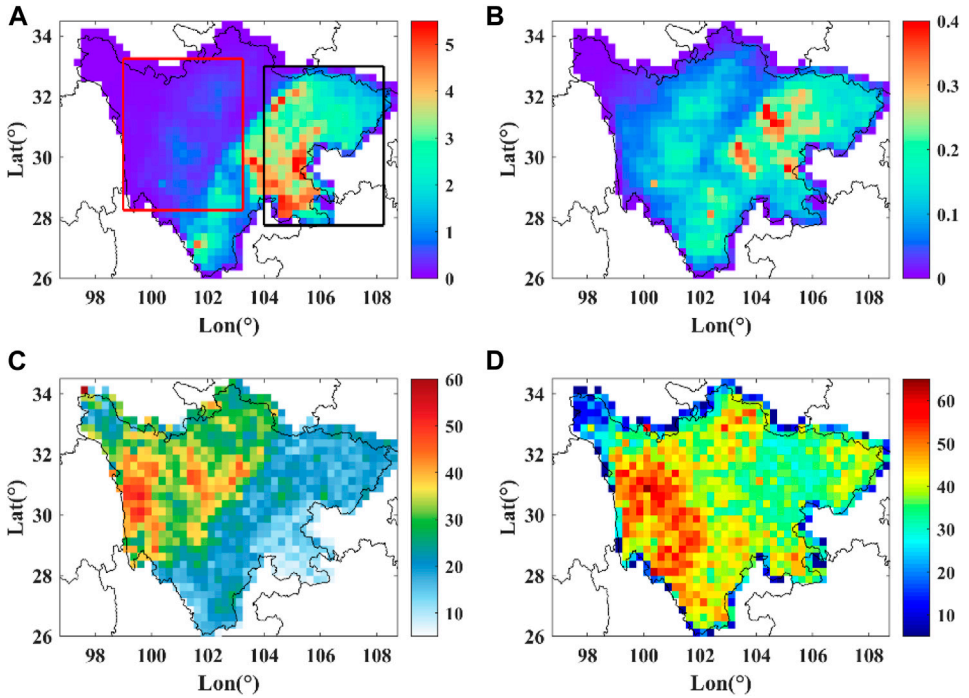


**FIGURE 1 |** Spatial distribution of **(A)** total CG lightning density (in flashes km$^{-2}$ year$^{-1}$), **(B)** positive CG lightning density (in flashes km$^{-2}$ year$^{-1}$), **(C)** positive CG lightning peak current (in kA), and **(D)** positive CG lightning relative frequency (in %) in Sichuan during the warm season. The red rectangle represents the plateau region, and the black rectangle represents the basin region.

## Aerosol Optical Depth

AODs data sets were derived from MERRA-2 (Modern-Era Retrospective analysis for Research and Applications, version 2) and include the optical thickness of various aerosols, such as total aerosol, sulfate, black carbon (BC), organic carbon, sea salt, and dust (Buchard et al., 2017; Randles et al., 2017). Our previous study (Zhao et al., 2020) compared AOD products of MISR (Multi-angle Imaging SpectroRadiometer) with AOD products of MERRA-2 over Sichuan, showing good consistency. Sulfate AOD and BC AOD with a spatial resolution of 0.25 × 0.25 interpolated from the original spatial resolution of 0.5 × 0.625 were selected in this study to discuss the relationship between aerosol and positive CG lightning.

## Thermodynamic and Cloud-Related Factors

Convective available potential energy (CAPE), vertical wind shear in the low-to middle troposphere (SHEAR-5 km), liquid water path (LWP), and ice water path (IWP) with a spatial resolution of 0.25 × 0.25 from ERA5 were selected as thermodynamic and cloud-related factors. These environmental factors are more representative to control positive CG lightning (Zhao et al., 2021; Zhao et al., 2022a). SHEAR-5 km is defined as vertical wind shear from the ground to 5 km level above the ground, the specific calculation method referred to in our previous studies (Zhao et al., 2020; Zhao et al., 2021).

$$SHEAR-5km=\sqrt{(u_{5km}-u_{0km})^2+(v_{5km}-v_{0km})^2}, \quad (2)$$

where $u_{5km}$, $u_{5km}$, $v_{0km}$, and $v_{0km}$ are zonal and meridional wind speeds interpolated to 5 km level above ground and the ground level from isobaric layers, respectively.

# RESULTS AND DISCUSSIONS

## Positive CG Lightning and Aerosols in Sichuan

Due to the special terrain difference, the thermal dynamic conditions of the western Plateau and the eastern basin of Sichuan are different, which leads to the obvious difference in lightning activity characteristics in the two regions. **Figure 1** illustrates the spatial distribution characteristics of total CG lightning density, positive CG lightning density, the peak current of positive CG lightning, and the relative frequency of positive CG lightning in Sichuan during the warm season. Influenced by the high topography of the Qinghai-Tibet Plateau, the Sichuan Basin has become a region with a high concurrence of cyclonic circulation (such as the southwest vortex and plateau vortex), the abundant thermal and water vapor conditions make the convective systems and heavy precipitation in this region very vigorous (Yu et al., 2007; Zhang et al., 2014). As can be seen in **Figure 1A**, the Sichuan Basin is an area with exuberant lightning activity, and the total CG lightning density is significantly higher than that of the Western Sichuan Plateau, the maximum lightning density is more than 5 flashes km$^{-2}$ year$^{-1}$ in the southeastern part of

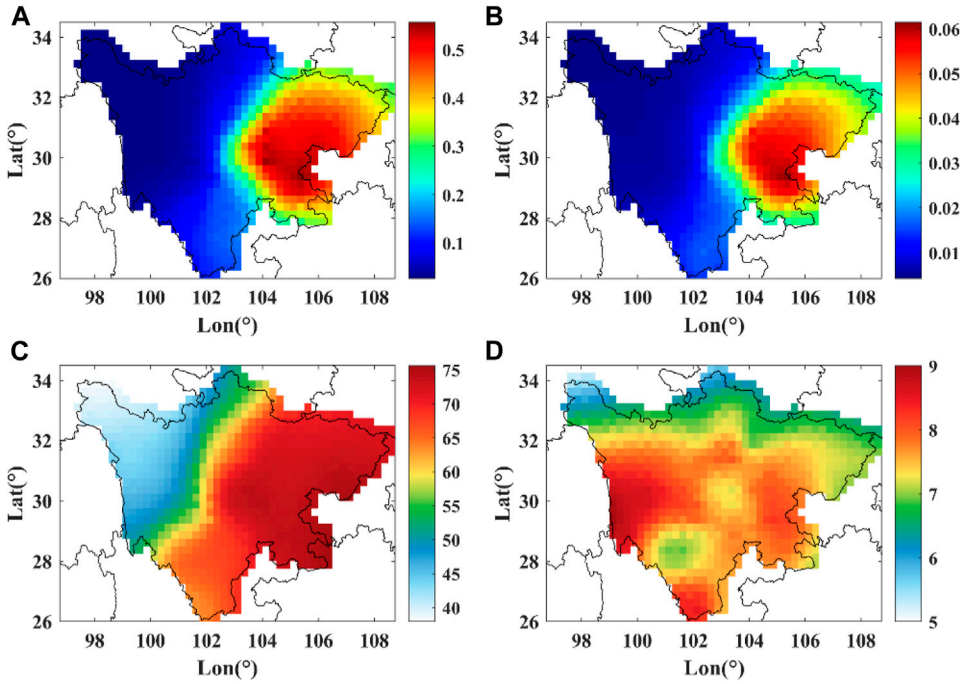


**FIGURE 2 |** Spatial distribution of **(A)** sulfate AOD, **(B)** BC AOD, **(C)** sulfate AOD ratio (in %), and **(D)** BC AOD ratio (in %) in Sichuan during warm season.

the Basin, the southern part of Sichuan is an area with secondary lightning activity, and the maximum lightning density in the Western Sichuan Plateau is about 1 flash $km^{-2}$ $year^{-1}$. As a whole, in the Sichuan region, the positive CG lightning density is about one-tenth of the total CG lightning density. The difference in positive CG lightning density between the basin region and plateau region is not as obvious as the difference in total CG lightning density (**Figure 1B**). The maximum positive CG lightning density is approximately 0.4 flashes $km^{-2}year^{-1}$ in the central part of the basin, and the maximum positive CG lightning density is approximately 0.1–0.2 flashes $km^{-2}$ $year^{-1}$ in the plateau.

Although the occurrence probability of positive CG lightning is much lower than that of negative CG lightning, it has become the focus of many studies because of the large current generated by it (Nag and Rakov, 2012). Although the positive CG lightning activity in the plateau region is not as strong as that in the basin region, the positive CG lightning producing a large peak current is concentrated in the plateau region (**Figure 1C**). In the main plateau region, the peak current of positive CG lightning is over 30 kA, and the maximum is about 60 kA, while in the basin region, the peak current of positive lightning is below 25 kA. The relative frequency of positive CG lightning in the plateau region is also significantly higher than that in the basin region (**Figure 1D**). The relative frequency of positive CG lightning in the main plateau region is more than 40%, and the maximum value is approximately 65%, while the relative frequency of positive CG lightning in the main basin region is approximately 30%.

Although the positive CG lightning density in the plateau is lower than that in the basin region, the peak current and relative frequency are higher than that in the basin region. Aerosols have an outstanding influence on the total CG lightning density in Sichuan (Zhao et al., 2020). Is there a potential connection between aerosols and positive lightning activities? To probe this interesting issue, we discuss the relationship between the relative frequency of positive CG lightning and aerosols in the following sections.

Sichuan Basin is one of the most densely populated areas in Southwest China, which is one of the most prominent air pollution areas in China due to many anthropogenic emissions and special terrain that is not conducive to the diffusion of air pollutants (Zhang et al., 2012; Ning et al., 2018). **Figure 2** shows the sulfate AOD, BC AOD, sulfate AOD ratio in total AOD, and BC AOD ratio in total AOD in Sichuan during the warm season. The aerosol loading in the basin region is significantly higher than that in the Plateau region (**Figures 2A,B**), and the sulfate AOD and BC AOD in the basin region are over 0.4 and 0.04, respectively, while the sulfate AOD and BC AOD in the Plateau area are approximately 0.1 and 0.01, respectively. The sulfate ratio in the basin is larger than 70%, while in the main part of the plateau is approximately 40%–65%. The difference in BC AOD between basin and plateau is not obvious, and the ratio is approximately 8%. Although the ratio of BC aerosols in total aerosols is not prominent, the influence of BC aerosols on atmospheric thermal structure through heating cannot be ignored (Jacobson, 2001; Nenes et al., 2002), so the influence of sulfate aerosols and BC aerosols on positive lightning is considered simultaneously in our study.

**Figure 3** shows the annual variation of total CG lightning density, the relative frequency of CG positive lightning (PRF),

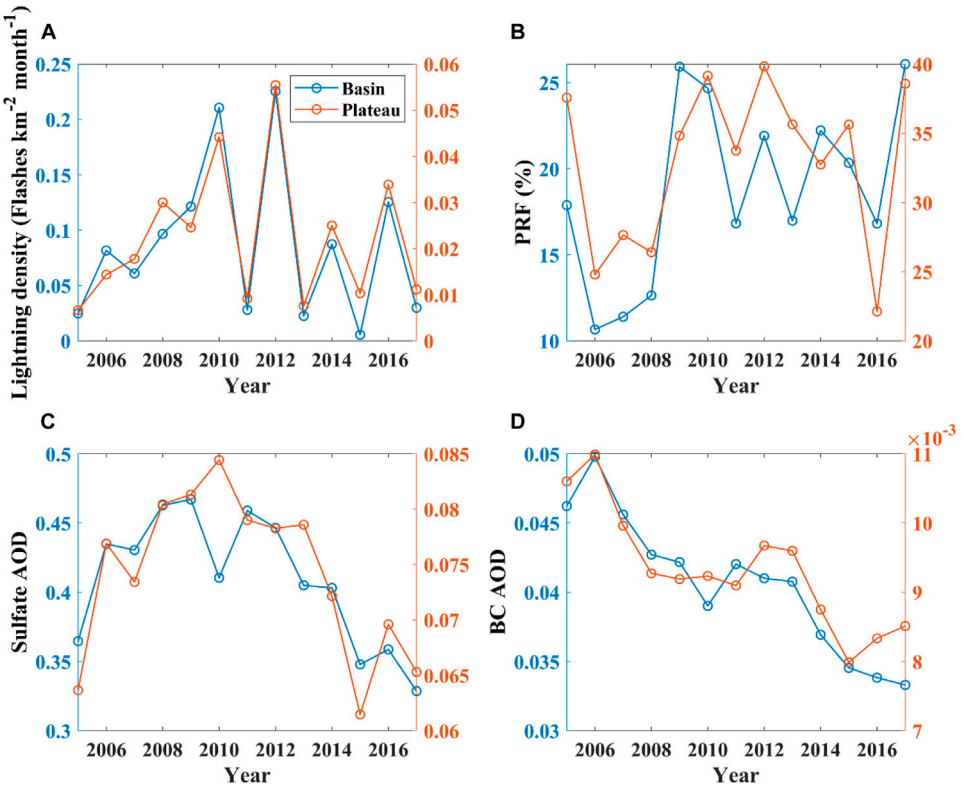


**FIGURE 3 |** Annual variations of **(A)** total CG lightning density, **(B)** relative frequency of positive CG lightning (PRF), **(C)** sulfate AOD, and **(D)** BC AOD in the basin and plateau regions during the warm season.

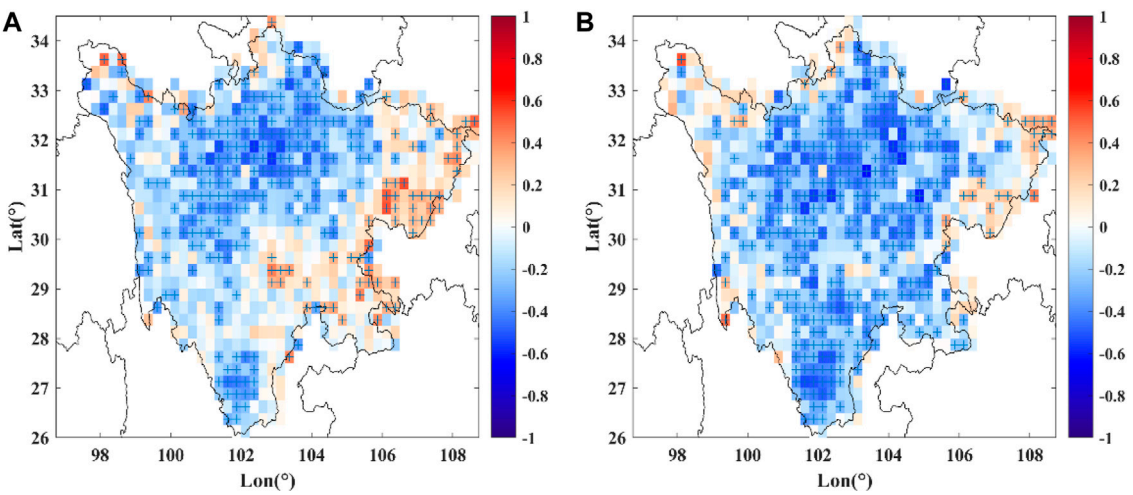


**FIGURE 4 |** Pearson correlation coefficients between **(A)** the sulfate aerosol and positive CG lightning relative frequency, and correlation coefficients between **(B)** the BC aerosol and positive CG lightning relative frequency in Sichuan during the warm season. The cross symbol indicates that the grid has passed the 95% significance test.

sulfate AOD and BC in the basin and plateau during the warm season from 2005 to 2017. From 2005 to 2010, the total CG lightning density in the basin and plateau showed an obvious upward trend and fluctuated after that. The relative frequency of CG positive lightning showed a significant upward trend from 2006 to 2010 and remained at a high value after that. The annual

change trend of sulfate AOD increased firstly and then decreased, it increased significantly from 2005 to 2010, and then decreased significantly. In both plateau and basin, BC AOD showed a monotonically decreasing annual trend, and the decreasing range was relatively prominent.

## Relationship Between Aerosols and Positive CG Lightning

**Figure 4** shows the Pearson correlation coefficients between sulfate aerosol and positive CG lightning relative frequency and between BC aerosol and positive CG lightning relative frequency in Sichuan. As shown in **Figure 4A**, the correlation between sulfate aerosol and positive CG lightning is spatially different in Sichuan, in the Western Sichuan Plateau region, sulfate aerosol shows a significant negative correlation with positive CG lightning relative frequency suggesting that increases in sulfate aerosol loading would reduce the proportion of positive CG lightning in total CG lightning, and in the basin region of eastern Sichuan, the correlation between sulfate aerosol and positive CG lightning is not significant, but a few areas show a positive correlation. In **Figure 4B**, there is a significant negative correlation between BC aerosol and positive CG lightning in the Western Sichuan Plateau, suggesting that the increase in BC aerosol would lead to a decrease in the relative frequency of positive CG lightning. In the basin, there is a negative correlation between BC aerosol and positive CG lightning relative frequency, but the correlation is weak.

Previous studies have indicated that less developed thunderstorms are more likely to produce positive CG lightning because the upper main positive charge region of the cloud is closer to the ground, which is easier for transporting positive charge to the ground (Rakov, 2003; Wang et al., 2018). Zhao et al. (2020) suggested that in the Western Sichuan Plateau with low aerosol loading, sulfate aerosol stimulated the ice-phase microphysical processes through microphysical effect, making the lightning activity more vigorous; while in the Sichuan Basin, with high aerosol loading, sulfate aerosol reduced the solar radiation reaching the ground through radiation effect, inhibiting lightning activity. In the Western Sichuan Plateau, the negative correlation between sulfate aerosol and positive CG lightning relative frequency is mainly since sulfate aerosols stimulate thunderstorms, and strong thunderclouds are not conducive to positive lightning. In the Sichuan Basin, the correlation between sulfate aerosol and positive CG lightning is not significant, which may be related to the low relative frequency of positive CG lightning in this area, the relationship between sulfate aerosol and positive CG lightning relative frequency is covered by other potentially influencing factors. Black carbon aerosol and positive CG lightning ratio showed a consistent negative correlation over the Sichuan region, suggesting that excitation effects of black carbon aerosol for lightning activities, thereby inhibiting the positive CG lightning, this may be due to the heating effects of black carbon aerosol for the lower atmosphere, the heating effect is beneficial to convection development. Liang et al. (2021) also indicated that the heating effect of black carbon aerosol on the lower atmosphere stimulated the convective intensity.

Previous observational evidence suggested that urban atmospheric particulate pollutants lead to a decline in the proportion of positive lightning (Steiger et al., 2022; Naccarato et al., 2003). They speculated that many anthropogenic atmospheric pollutants in super cooled water make graupel particles charging negatively have a wider area, and the main negative charge region extends to the ground, so more negative lightning is formed, and positive lightning activities are suppressed. These results explained the decrease in the proportion of positive lightning caused by aerosols from the perspective of the electrification process of thunderstorms, and further illustrate the important contribution of aerosols to the polarity of lightning. However, in our study, we tend to consider that aerosols change the development intensity of thunderstorms by influencing microphysical and radiation processes, thus affecting CG lightning polarity.

## Dependence of the Relation Between Aerosol and Positive CG Lightning on Environmental Factors

To further analyze the dependence of aerosol influence on the relative frequency of positive CG lightning relative frequency on environmental factors, thermodynamic factors, and cloud factors were selected. **Figure 5** shows the effects of CAPE, SHEAR-5km, LPW, and IWP on positive CG lightning relative frequency in the basin and plateau regions (**Figure 1A**). CAPE in the plateau region is smaller than that in the basin region, and CAPE has a significant inhibition effect on positive CG lightning in both regions. CAPE explains 40% and 44% of positive CG lightning relative frequency variances in the basin and plateau regions, respectively. SHEAR-5 km in the plateau region is higher than that in the basin region, and the larger vertical wind shear is favorable to the occurrence of positive CG lightning. SHEAR-5 km explains 51% of positive lightning relative frequency variance in the basin region and 60% of positive CG lightning relative frequency variance in the plateau region. In the basin, higher LWP is favorable to positive lightning, LWP explains 31% of positive CG lightning relative frequency variance, while in the plateau, the relationship between LWP and positive CG lightning is not significant. This may be since the topography of the plateau compresses the clouds, making the warm clouds thinner. In the basin, the higher LWP means the liquid-phase process is more vigorous than the ice-phase process, and the convective activity is weaker. The correlation between LWP and positive CG lightning is obviously different between the plateau and basin, which may be related to two aspects. On the one hand, due to the compression effect of the plateau terrain on a cloud, the warm cloud in the plateau is relatively thin, and LWP is relatively low. On the other hand, a thermal condition in the plateau area is weaker than that in the basin, resulting in relatively weak lightning activity. As a result, the correlation between LWP and positive CG lightning

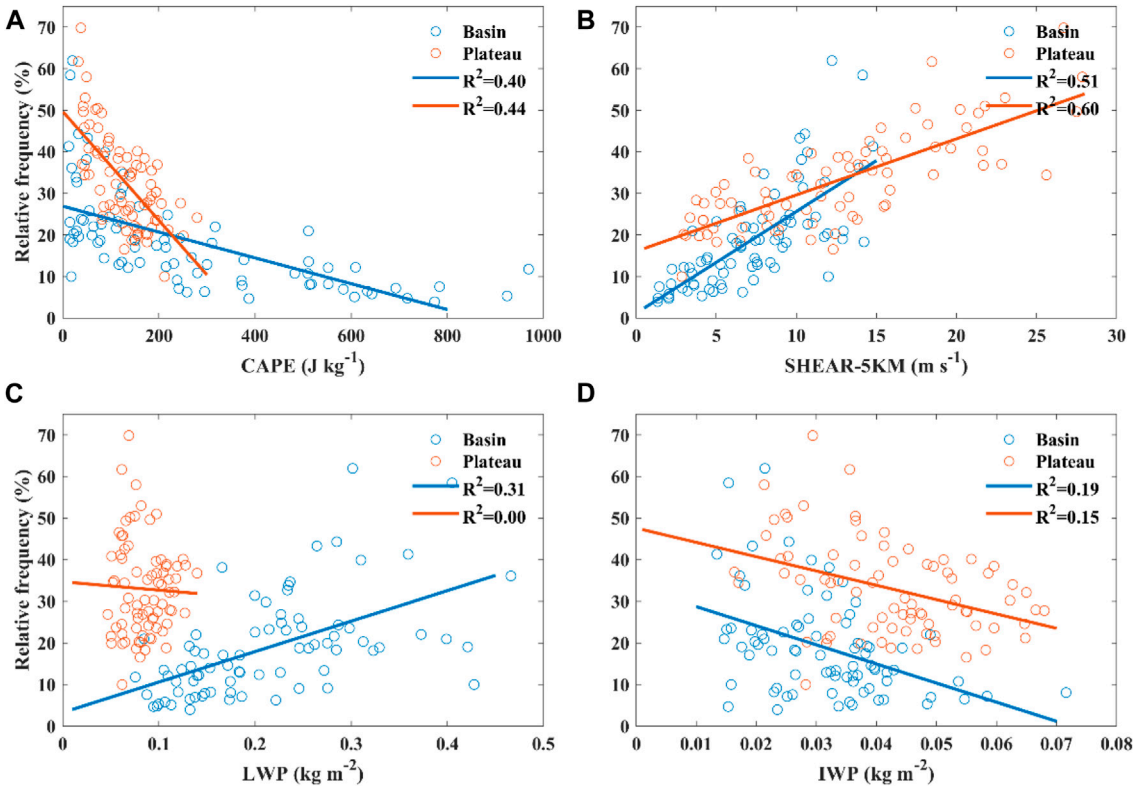


**FIGURE 5 |** The function of CAPE **(A)**, SHEAR-5 km **(B)**, LWP **(C)**, and IWP **(D)** with the relative frequency of positive CG lightning in the basin and plateau regions during the warm season.

is weak over the plateau. There is a negative correlation between IWP and positive CG lightning relative frequency. IWP explains 19% and 15% of positive CG lightning relative frequency variances in basin and plateau regions, respectively. Higher ice water content indicates stronger convection, while strong convection is not conducive to positive CG lightning because a higher upper main positive charge region is not conducive to the transfer of positive charge to the ground.

In general, CAPE and SHEAR-5 km are the most prominent factors affecting positive CG lightning, weak convection is more likely to form positive lightning, and the environmental factors conducive to the development of convection have a certain inhibitory effect on positive CG lightning. Previous studies have (Wang et al., 2018; Zhao et al., 2021) also indicated that the main positive charge region at the upper part of the thunderstorm with weak development is closer to the ground, which is conducive to the transport of positive charge to the ground, meanwhile, the positive charge area of the thunderstorm which is affected by large vertical wind shear is no longer blocked by the main negative charge area at the lower part, which is more conducive to the occurrence of positive CG lightning (Brook et al., 1982; Zhao et al., 2021).

Although aerosols may have a potential relationship with positive lightning, it is still the atmospheric thermodynamic conditions that play a major role in controlling positive CG lightning. In plateau and basin areas, the relative frequency of positive CG lightning is strongly dependent on CAPE, SHEAR-5km, and IWP. **Figure 6** shows the dependence of the correlation between positive CG lightning relative frequency and aerosols on CAPE, SHEAR-5 km, and IWP in the basin region. Overall, the proportion of positive CG lightning in the basin region is more dependent on environmental factors than on aerosols. When CAPE is greater than 200 J $kg^{-1}$, the relative frequency of positive CG lightning is about 5%–20%, while when CAPE is less than 200 J $kg^{-1}$, the relative frequency of positive CG lightning increases significantly, about 25%–65%. When SHEAR-5 km is between 5 and 15 m $s^{-1}$, the relative frequency of positive CG lightning is significantly higher, about 20%, while when SHEAR-5 km is less than 5 m $s^{-1}$, the relative frequency of positive CG lightning is about 10%. Compared with the thermodynamic factors, the positive lightning is less dependent on ice water content, the average relative frequency of positive CG lightning is about 20% when IPW is greater than 0.03 kg $m^{-2}$, and about 30% when IWP is less than 0.03 kg $m^{-2}$. For sulfate AOD, the probability of forming more positive lightning increases when AOD is greater than 0.5. For BC aerosol, the proportion of positive lightning is not significantly dependent on it. In the basin area, the lightning activity is more vigorous than that in the plateau area, but the relative frequency of positive lightning is lower than that in

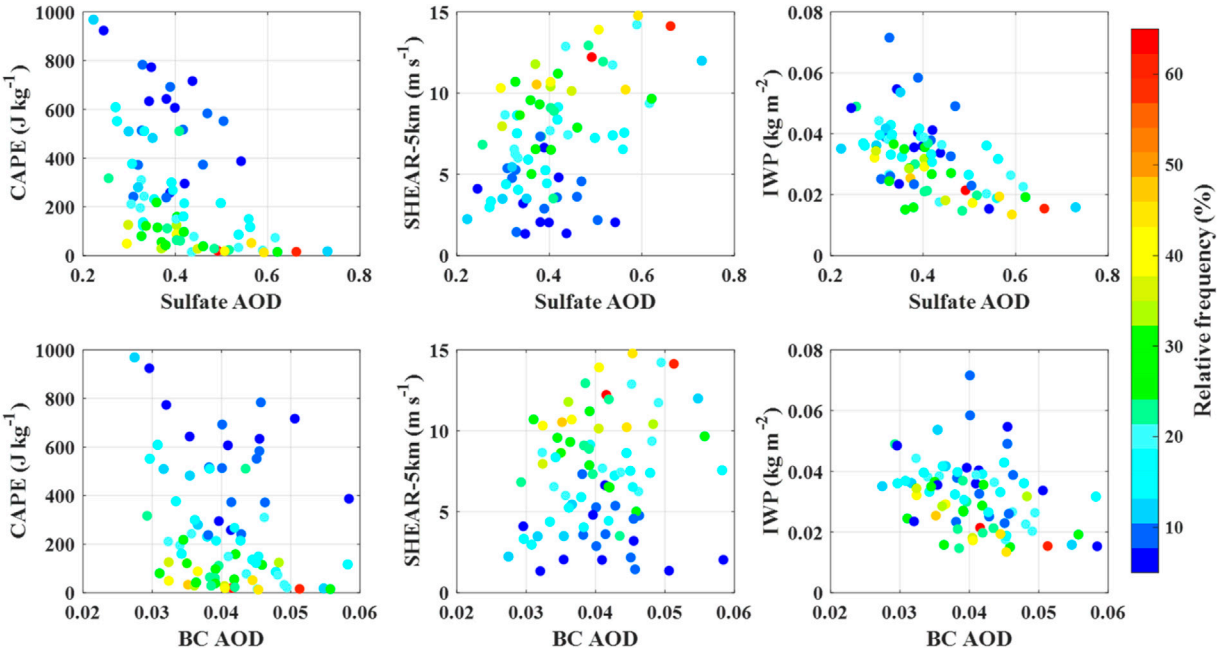


**FIGURE 6 |** Function of positive CG lightning relative frequency with sulfate AOD, BC AOD, CAPE, SHEAR-5 km, and IWP in the basin region.

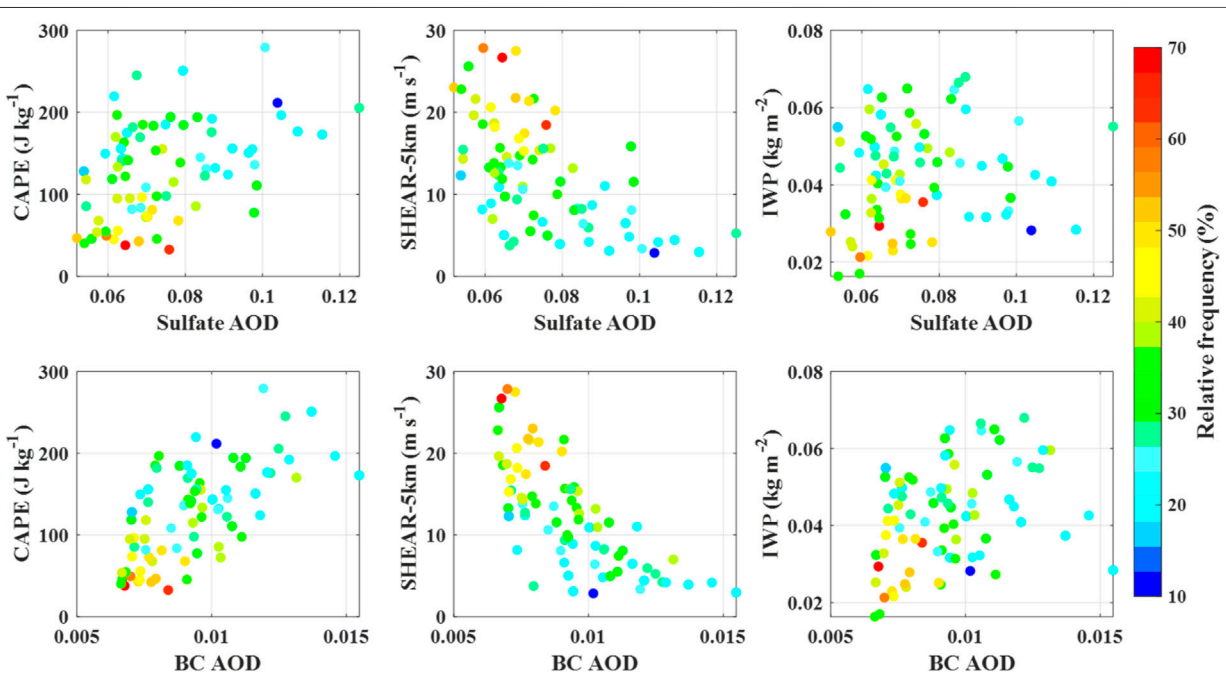


**FIGURE 7 |** Function of positive CG lightning relative frequency with sulfate AOD, BC AOD, CAPE, SHEAR-5km, and IWP in the plateau region.

the plateau area. Although Zhao et al. (2020) indicated that sulfate aerosol could inhibit the lightning activity in the Sichuan Basin area through aerosol radiation interaction, for the region with a low frequency of positive lightning. The effect of aerosols on positive lightning relative frequency may be overridden by the effect of thermodynamic factors controlling lightning activities.

**Figure 7** displays the dependence of aerosols effects on the relative frequency of positive CG lightning on CAPE, SHEAR-5 km, and IWP over the plateau. Low sulfate aerosol loading is

favorable for positive lightning in the plateau region. When the sulfate AOD is less than 0.08, the average relative frequency of positive CG lightning is approximately 40%. When the sulfate AOD is less than 0.08 and CAPE is less than 100 J $kg^{-1}$, the relative frequency of positive CG lightning is approximately 40%–70%. When SHEAR-5 km exceeds 10 m $s^{-1}$, IWP is less than 0.04 kg $m^{-2}$, and sulfate AOD is less than 0.08, the relative frequency of positive CG lightning is higher, with an average of more than 50%. A similar phenomenon exists for BC aerosols. Under small CAPE and IWP and large SHEAR-5 km conditions, low BC aerosol loading is more conducive to the occurrence of positive lightning.

From another perspective, aerosols may have a potential influence on thermodynamic and cloud-related factors, and thus on lightning polarity. Over the plateau, sulfate aerosols may act as cloud condensation nuclei, regulating cloud thermodynamic structures by influencing microphysical processes. More sulfate aerosols make the cloud droplet radius reduced, and the number concentration increases, the cloud droplet's collision-coalescence efficiency decreases, thus inhibiting the warm rain process. Smaller cloud droplets to be delivered to the ice-phase region form more ice particles, The release of a large latent heat of freezing process further stimulates convection development. Strong convective motion means higher positive charge distribution is not conducive for positive lightning. BC aerosols may influence the thermodynamic and microphysical processes of a thunderstorm by heating the lower atmosphere and then influencing the lightning activity. By heating the lower atmosphere, BC aerosol increases the convective energy of the local environment and then reduces the vertical wind shear, making the convective development more vigorous, promoting the formation of ice particles, and stimulating the lightning activity, while the proportion of positive lightning decreases.

## CONCLUSION

Data on CG lightning, AOD, and environmental factors during the warm season from 2005 to 2017 in Sichuan, Southwest China, were employed to investigate the possible influence of aerosols on the relative frequency of positive CG lightning, and the dependence of this effect on thermodynamic and cloud-related factors.

In the Sichuan region, the spatial difference in thermal and water vapor conditions caused by the special terrain leads to the obvious spatial difference in lightning activity characteristics (Xia et al., 2015; Yang et al., 2015). The total CG lightning and positive CG lightning density in Sichuan Basin are significantly higher than that in the Western Sichuan Plateau, while the relative frequency and peak current of positive CG lightning in the plateau are significantly higher than that in the basin, that is, although the lightning activity is relatively weak in higher area, there are more severe positive CG lightning. The relatively high positive CG lightning relative frequency in the plateau region is dominated by multiple thermal and cloud-related factors, and relatively frequent weak convection produces more positive CG lightning (Qie et al., 2003; Qie et al., 2005; Qie et al., 2014; Zhao et al., 2021). The Sichuan Basin is one of the areas with serious air pollution in China because of the prominent anthropogenic emissions and the special terrain that is not conducive to the diffusion of atmospheric pollutants (Zhang et al., 2012; Ning et al., 2018). The sulfate aerosol and BC aerosol loads in the basin are significantly higher than those in the plateau. The ratio of sulfate AOD in total AOD is higher in the basin, while the spatial difference of BC AOD ratio in Sichuan is not significant. Observational evidence suggested that aerosols are associated with lightning activity in Sichuan, and aerosols affect the intensity of lightning activity through microphysical and radiation effects (Zhao et al., 2020). In this study, we focus on the potential impact of sulfate aerosols and BC aerosols on the relative frequency of positive CG lightning.

In the plateau region, both sulfate aerosols and BC aerosols have a significant inhibition effect on the relative frequency of CG positive lightning, while in the basin region, the correlation between aerosols and relative frequency of positive CG lightning is not significant. Due to abundant thermodynamic and water vapor conditions, convective cloud and lightning activities are vigorous in the basin, while the relative frequency of positive CG lightning is low. The influence of aerosol on positive lightning may be covered by the strong total CG lightning and the complex relationship between aerosol and convection systems. Previous studies (Lyons, 1998; Murray et al., 2000; Steiger et al., 2002; Naccarato et al., 2003; Lang and Rutledge, 2006) have found that urban anthropogenic aerosols and smoke from forest fires have significant effects on positive lightning, and it is believed that aerosols affect positive lightning by affecting the electrification process of cloud particles. In our study, we tend to consider that aerosols affect charge structure and thus positive lightning by influencing convective intensity. In the plateau region, sulfate aerosols could act as cloud condensation nuclei and stimulate thunderclouds through a microphysical effect (Zhao et al., 2020). In the highly developed thunderclouds, the distribution of the main positive charge is higher, and the positive charge is more difficult to transport to the ground, which is not conducive to the generation of positive CG lightning. BC aerosols have a prominent heating effect on the lower atmosphere, which would promote the further development of convection (Liang et al., 2021), which is not conducive to positive CG lightning. Therefore, BC aerosols are negatively correlated with the relative frequency of positive CG lightning over the Plateau. Thermodynamic and cloud-related factors play an important role in the influence of aerosols on positive lightning, and smaller CAPE and larger vertical wind shear are more conducive to the generation of positive lightning. In other words, aerosols may influence the generation of

positive lightning by influencing thermodynamics and cloud structure.

## DATA AVAILABILITY STATEMENT

The MERRA-2 AODs data can be found in online repositories. The names of the repository/repositories and accession number(s) can be found at: https://disc.gsfc.nasa.gov/datasets/M2TMNXAER_5.12.4/summary, and the ERA5 dataset can be found at https://cds.climate.copernicus.eu/cdsapp#!/dataset/10.24381/cds.f17050d7?tab=overview; the CG lightning dataset can be obtained by contacting the first author (zpg@cuit.edu.cn).

## AUTHOR CONTRIBUTIONS

PZ and YZ contributed to the conception and design of this study. CL and YJZ contributed to data analysis and visualization. PZ, PWZ, and HX wrote the manuscript.

## FUNDING

This research was jointly supported by the Second Tibetan Plateau Scientific Expedition and Research (STEP) program (2019QZKK0104), the Sichuan Science and Technology Program (2021YJ0393), and the National Natural Science Foundation of China (41905126 and 42075086).

## REFERENCES

Altaratz, O., Kucienska, B., Kostinski, A., Raga, G. B., and Koren, I. (2017). Global Association of Aerosol with Flash Density of Intense Lightning. *Environ. Res. Lett.* 12, 114037. doi:10.1088/1748-9326/aa922b

Brook, M., Nakano, M., Krehbiel, P., and Takeuti, T. (1982). The Electrical Structure of the Hokuriku Winter Thunderstorms. *J. Geophys. Res.* 87 (C2), 1207–1215. doi:10.1029/jc087ic02p01207

Buchard, V., Randles, C. A., Da Silva, A. M., Darmenov, A., Colarco, P. R., Govindaraju, R., et al. (2017). The MERRA-2 Aerosol Reanalysis, 1980 Onward. Part II: Evaluation and Case Studies. *J. Clim.* 30, 6851–6872. doi:10.1175/jcli-d-16-0613.1

Carey, L. D., and Buffalo, K. M. (2007). Environmental Control of Cloud-To-Ground Lightning Polarity in Severe Storms. *Mon. Wea. Rev.* 135, 1327–1353. doi:10.1175/mwr3361.1

CMA (China Meteorological Administration) (2009). *China Lightning Monitoring Reports*. Beijing, China: China Meteorological Press, 142.

Cummins, K. L., Murphy, M. J., Bardo, E. A., Hiscox, W. L., Pyle, R. B., and Pifer, A. E. (1998). A Combined TOA/MDF Technology Upgrade of the U.S. National Lightning Detection Network. *J. Geophys. Res.* 103, 9035–9044. doi:10.1029/98jd00153

Eddy, A. (2018). Environmental Conditions Producing Thunderstorms with Anomalous Vertical Polarity of Charge Structure. Master dissertation. Norman, OK: University of Oklahoma.

Jacobson, M. Z. (2001). Strong Radiative Heating Due to the Mixing State of Black Carbon in Atmospheric Aerosols. *Nature* 409, 695–697. doi:10.1038/35055518

Lang, T. J., and Rutledge, S. A. (2006). Cloud-to-ground Lightning Downwind of the 2002 Hayman Forest Fire in Colorado. *Geophys. Res. Lett.* 33 (3), L03804. doi:10.1029/2005gl024608

Liang, Z., Ding, J., Fei, J., Cheng, X., and Huang, X. (2021). Direct/indirect Effects of Aerosols and Their Separate Contributions to Typhoon Lupit (2009): Eyewall versus Peripheral Rainbands. *Sci. China Earth Sci.* 64 (12), 2113–2128. doi:10.1007/s11430-020-9816-7

Liu, Y., Guha, A., Said, R., Williams, E., Lapierre, J., Stock, M., et al. (2020). Aerosol Effects on Lightning Characteristics: A Comparison of Polluted and Clean Regimes. *Geophys. Res. Lett.* 47, e2019GL086825. doi:10.1029/2019gl086825

Lu, Q., Liu, C., Zhao, D., Zeng, C., Li, J., Lu, C., et al. (2020). Atmospheric Heating Rate Due to Black Carbon Aerosols: Uncertainties and Impact Factors. *Atmos. Res.* 240, 104891. doi:10.1016/j.atmosres.2020.104891

Lyons, W. A., Nelson, T. E., Williams, E. R., Cramer, J. A., and Turner, T. R. (1998). Enhanced Positive Cloud-To-Ground Lightning in Thunderstorms Ingesting Smoke from Fires. *Science* 282 (5386), 77–80. doi:10.1126/science.282.5386.77

MacGorman, D. R., Eddy, A. J., Homeyer, C. R., and Williams, E. (2018). "Environmental Conditions Producing Thunderstorms with Anomalous Vertical Polarity of Charge Structure," in 25th International Lightning Detection Conference & 7th International Lightning Meteorology Conference, Florida, USA, March 12–15.

Mansell, E. R., and Ziegler, C. L. (2013). Aerosol Effects on Simulated Storm Electrification and Precipitation in a Two-Moment Bulk Microphysics Model. *J. Atmos. Sci.* 70 (7), 2032–2050. doi:10.1175/jas-d-12-0264.1

Murray, N. D., Orville, R. E., and Huffines, G. R. (2000). Effect of Pollution from Central American Fires on Cloud-To-Ground Lightning in May 1998. *Geophys. Res. Lett.* 27 (15), 2249–2252. doi:10.1029/2000gl011656

Naccarato, K. P., Pinto, O., Jr, and Pinto, I. R. C. A. (2003). Evidence of Thermal and Aerosol Effects on the Cloud-to-Ground Lightning Density and Polarity Over Large Urban Areas of Southeastern Brazil. *Geophys. Res. Lett.* 30, 13–1674. doi:10.1029/2003GL017496

Nag, A., and Rakov, V. A. (2012). Positive Lightning: An Overview, New Observations, and Inferences. *J. Geophys. Res.* 117, D08109. doi:10.1029/2012jd017545

Nenes, A., Conant, W. C., and Seinfeld, J. H. (2002). Black Carbon Radiative Heating Effects on Cloud Microphysics and Implications for the Aerosol Indirect Effect, 2, Cloud Microphysics. *J. Geophys. Res.* 107 (D21), 4605. doi:10.1029/2002jd002101

Ning, G., Wang, S., Ma, M., Ni, C., Shang, Z., Wang, J., et al. (2018). Characteristics of Air Pollution in Different Zones of Sichuan Basin, China. *Sci. Total Environ.* 612, 975–984. doi:10.1016/j.scitotenv.2017.08.205

Orville, R. E., and Huffines, G. R. (1999). Lightning Ground Flash Measurements over the Contiguous United States: 1995-97. *Mon. Wea. Rev.* 127, 2693–2703.

Qie, X., Kong, X., Zhang, G., Zhang, T., Yuan, T., Zhou, Y., et al. (2005). The Possible Charge Structure of Thunderstorm and Lightning Discharges in Northeastern Verge of Qinghai-Tibetan Plateau. *Atmos. Res.* 76 (1–4), 231–246. doi:10.1016/j.atmosres.2004.11.034

Qie, X., Liu, D., and Sun, Z. (2014). Recent Advances in Research of Lightning Meteorology. *J. Meteorol. Res.* 28 (5), 983–1002. doi:10.1007/s13351-014-3295-0

Qie, X., Toumi, R., and Zhou, Y. (2003). Lightning Activity on the Central Tibetan Plateau and its Response to Convective Available Potential Energy. *Chin. Sci. Bull.* 48 (3), 296–299. doi:10.1007/bf03183302

Rakov, V. A. (2003). A Review of Positive and Bipolar Lightning Discharges. *Bull. Amer. Meteor. Soc.* 84 (6), 767–776. doi:10.1175/BAMS-84-6-767

Randles, C. A., Da Silva, A. M., Buchard, V., Colarco, P. R., Darmenov, A., Govindaraju, R., et al. (2017). The MERRA-2 Aerosol Reanalysis, 1980 Onward. Part I: System Description and Data Assimilation Evaluation. *J. Clim.* 30, 6823–6850. doi:10.1175/jcli-d-16-0609.1

Steiger, S. M., Orville, R. E., and Huffines, G. R. (2002). Cloud-to-ground Lightning Characteristics over Houston, Texas: 1989–2000. *J. Geophys. Res.* 107 (D11), 4117. doi:10.1029/2001jd001142

Tan, Y., Peng, L., Shi, Z., and Chen, H. (2016). Lightning Flash Density in Relation to Aerosol over Nanjing (China). *Atmos. Res.* 174, 1–8.

Wang, D., Wu, T., and Takagi, N. (2018). Charge Structure of Winter Thunderstorm in Japan: A Review and an Update. *IEEJ Trans. PE* 138 (5), 310–314. doi:10.1541/ieejpes.138.310

Wang, Y., Wan, Q., Meng, W., Liao, F., Tan, H., and Zhang, R. (2011). Long-term Impacts of Aerosols on Precipitation and Lightning over the Pearl River Delta Megacity Area in China. *Atmos. Chem. Phys.* 11, 12421–12436. doi:10.5194/acp-11-12421-2011

Xia, R., Zhang, D.-L., and Wang, B. (2015). A 6-yr Cloud-To-Ground Lightning Climatology and its Relationship to Rainfall over Central and Eastern China. *J. Appl. Meteorol. Clim.* 54, 2443–2460. doi:10.1175/jamc-d-15-0029.1

Yang, X., and Li, Z. (2014). Increases in Thunderstorm Activity and Relationships with Air Pollution in Southeast China. *J. Geophys. Res.* 119, 1835–1844. doi:10.1002/2013jd021224

Yang, X., Sun, J., and Li, W. (2015). An Analysis of Cloud-To-Ground Lightning in China during 2010–13. *Weather Forecast* 30 (6), 1537–1550. doi:10.1175/WAF-D-14-00132.1

Yang, X., Yao, Z., Li, Z., and Fan, T. (2013). Heavy Air Pollution Suppresses Summer Thunderstorms in Central China. *J. Atmos. Solar-Terrestrial Phys.* 95-96, 28–40. doi:10.1016/j.jastp.2012.12.023

Yu, R., Xu, Y., Zhou, T., and Li, J. (2007). Relation between Rainfall Duration and Diurnal Variation in the Warm Season Precipitation over Central Eastern China. *Geophys. Res. Lett.* 34, L13703. doi:10.1029/2007gl030315

Zhang, X. Y., Wang, Y. Q., Niu, T., Zhang, X. C., Gong, S. L., Zhang, Y. M., et al. (2012). Atmospheric Aerosol Compositions in China: Spatial/temporal Variability, Chemical Signature, Regional Haze Distribution and Comparisons with Global Aerosols. *Atmos. Chem. Phys.* 12, 779–799. doi:10.5194/acp-12-779-2012

Zhang, Y., Sun, J., and Fu, S. (2014). Impacts of Diurnal Variation of Mountain-Plain Solenoid Circulations on Precipitation and Vortices East of the Tibetan Plateau during the Mei-Yu Season. *Adv. Atmos. Sci.* 31, 139–153. doi:10.1007/s00376-013-2052-0

Zhao, P., Li, Z., Xiao, H., Wu, F., Zheng, Y., Cribb, M. C., et al. (2020). Distinct Aerosol Effects on Cloud-To-Ground Lightning in the Plateau and Basin Regions of Sichuan, Southwest China. *Atmos. Chem. Phys.* 20, 13379–13397. doi:10.5194/acp-20-13379-2020

Zhao, P., Xiao, H., Liu, C., and Zhou, Y. (2021). Dependence of Warm Season Cloud-To-Ground Lightning Polarity on Environmental Conditions over Sichuan, Southwest China. *Adv. Meteorology* 2021, 1–12. doi:10.1155/2021/1500470

Zhao, P., Xiao, H., Liu, C., Zhou, Y., Xu, X., and Hao, K. (2022a). Evaluating a Simple Proxy for Climatic Cloud-to-ground Lightning in Sichuan Province with Complex Terrain, Southwest China. *Intl J. Climatol.* 42 (7), 3909–3927. doi:10.1002/joc.7451

Zhao, P., Xiao, H., Liu, J., and Zhou, Y. (2022b). Precipitation Efficiency of Cloud and its Influencing Factors over the Tibetan Plateau. *Intl J. Climatol.* 42 (1), 416–434. doi:10.1002/joc.7251

**Conflict of Interest:** The authors declare that the research was conducted in the absence of any commercial or financial relationships that could be construed as a potential conflict of interest.

**Publisher's Note:** All claims expressed in this article are solely those of the authors and do not necessarily represent those of their affiliated organizations, or those of the publisher, the editors, and the reviewers. Any product that may be evaluated in this article, or claim that may be made by its manufacturer, is not guaranteed or endorsed by the publisher.

frontiers | Frontiers in Environmental Science

TYPE Original Research
PUBLISHED 16 August 2022
DOI 10.3389/fenvs.2022.878341



OPEN ACCESS

EDITED BY
Honglei Wang,
Nanjing University of Information Science and Technology, China

REVIEWED BY
Lisette Klok,
Amsterdam University of Applied Sciences, Netherlands
Hideki Takebayashi,
Kobe University, Japan

*CORRESPONDENCE
Jan Urban,
urban.j@czechglobe.cz

SPECIALTY SECTION
This article was submitted to Atmosphere and Climate, a section of the journal Frontiers in Environmental Science

RECEIVED 17 February 2022
ACCEPTED 05 July 2022
PUBLISHED 16 August 2022

CITATION
Urban J, Pikl M, Zemek F and Novotný J (2022), Using Google Street View photographs to assess long-term outdoor thermal perception and thermal comfort in the urban environment during heatwaves. *Front. Environ. Sci.* 10:878341. doi: 10.3389/fenvs.2022.878341



# Using Google Street View photographs to assess long-term outdoor thermal perception and thermal comfort in the urban environment during heatwaves

Jan Urban[1]*, Miroslav Pikl[1], František Zemek[1,2] and Jan Novotný[1]

[1]Global Change Research Institute, Czech Academy of Sciences, Brno, Czechia, [2]Department of Landscape Management, University of South Bohemia in České Budějovice, České Budějovice, Czechia

The outdoor thermal comfort of urban residents is negatively affected by heatwaves that are becoming more frequent and severe with the ongoing climate crisis. As such, the assessment of outdoor perception and comfort during heatwaves has become an important ingredient of successful urban adaptation strategies. However, systematic assessment of long-term thermal perception across a large number of places and large populations of people is difficult. In this study, we consider an approach to the assessment of long-term thermal perception that combines features of currently used approaches (i.e., use of rating scales of thermal perception, use of surveys, and the use of photographs representing places) and we provide some preliminary validation of this approach. Specifically, across three studies conducted in two Czech cities, we show that long-term thermal perceptions for a large sample of 1,856 urban places can be elicited in a large sample of city residents (total $N$ = 1,812) using rating scales in off-site surveys complemented with visual representations of the target locations. In Studies 1 and 2, we partially validate this approach by showing that such long-term thermal perceptions can be traced back to average surface temperature, sky-view factor, and the presence of blue and green infrastructure, all factors that the literature relates to thermal perception. Moreover, we show evidence that observers can reliably glean these properties from the visual representation of places. In Study 3, we provide additional evidence of the predictive validity of such long-term thermal perceptions by showing that they predict place-related activities (waiting and walking) and the place preference of other people more than one year later. Thus, this approach to the measurement of long-term thermal perception related to heatwaves can be a useful addition to currently used approaches.

KEYWORDS

**long-term thermal perception, expected thermal comfort, heatwave, climate adaptation, urban planning–social aspects, urban greenery, remote sensing**

# 1 Introduction

The climate crisis will increase the frequency and severity of heatwave impacts in urban areas resulting in many detrimental effects on residents, including negative impacts on their thermal comfort (Shukla et al., 2019; Aram et al., 2020). For urban adaptations to be effective and efficient, adaptation measures should prioritize those urban areas where the impacts on residents' thermal comfort are potentially the largest (Aram et al., 2020).

One of the aspects of outdoor thermal comfort that is particularly relevant for policymakers is the long-term (subjective) thermal perception (Lenzholzer, 2010). Long-term thermal perception is essentially a thermal expectation that people associate with a certain place they know but also places that have not yet visited. Long-term thermal perceptions are based on people's experience with the environment and with similar environments (Nikolopoulou et al., 2001; Lenzholzer, 2010; Eysenck and Brysbaert, 2018). Such long-term thermal expectations are important because they influence how people adapt to thermal conditions by, for instance, adjusting their clothing style or changing their commuting patterns (Langevin et al., 2015; Sun et al., 2018).

In this study, we present an approach to the assessment of long-term thermal perception that combines features of currently used approaches (i.e., use of rating scales of thermal perception, use of surveys, and the use of photographs representing places) and we provide some preliminary validation of this approach. We believe that this approach might be useful for theoretical as well as practical purposes as it offers some methodological benefits, namely that it can cover large representative samples of spatial points and participants and thus allow for valid generalizations.

# 2 Outdoor thermal perceptions

Early research in thermal perception focused almost exclusively on the physiological aspects of thermal perception. Researchers have developed complex indices to characterize indoor perception such as the *Standard Effective Temperature* and *Predicted Mean Vote* (Fanger, 1970) to characterize expected thermal comfort based on micro-climatic characteristics such as air temperature, air movement, relative humidity, radiant temperature, and a host of personal characteristics such as clothing and metabolic level. Similarly, complex indices, such as the *Physiological Equivalent Temperature* (Mayer and Höppe, 1987) and *Outdoor Standard Effective Temperature* (Pickup and de Dear, 2000) were later developed to characterize the physiological aspects of outdoor thermal perception based on micro-climatic and personal variables.

Although the physiological aspects of thermal perception are important, some literature points to the limitations of physiological models of thermal perception (Auliciems, 1981) and the importance of psychological aspects of thermal perception and thermal comfort (Nikolopoulou et al., 2001; Thorsson et al., 2004). The literature also shows that subjective thermal perception is important because it is predictive of the use of public spaces (Eliasson et al., 2007; Walton et al., 2007) and outdoor activities (Thorsson et al., 2007).

## 2.1 Long-term thermal perception

Especially of interest to policymakers is long-term thermal perception, sometimes referred to as thermal expectation (Lenzholzer, 2010). Long-term thermal perception is based on people's experience with the environment and with similar environments (Nikolopoulou et al., 2001; Lenzholzer, 2010; Eysenck and Brysbaert, 2018). People plan their outdoor activities based on their thermal expectations; long-term thermal expectations also influence how people adapt to thermal conditions by, for instance, adjusting their clothing style or changing their commuting patterns (Langevin et al., 2015; Sun et al., 2018). The long-term thermal perception of places is based on repetitive experiences with these and similar places; these repeated experiences become ingrained in people's memory (Klemm et al., 2015a).

Some scholars have suggested that people use visual cues available in the environment to infer their thermal perception of that environment (Lenzholzer and van der Wulp, 2010). Such attribution is probably driven by a well-known psychological mechanism whereby people use distal cues to infer probabilistically properties of objects that they cannot directly observe (Brunswik, 1956). For instance, squares that are very wide, open, or decorated with materials considered "cold" (e.g., stone and concrete) are perceived as uncomfortable (Lenzholzer and van der Wulp, 2010). On the other hand, the presence of green infrastructure improves perceived thermal comfort (Klemm et al., 2015b), as we will discuss in some detail later.

# 3 Approaches to assessment of outdoor thermal perception

## 3.1 Subjective thermal perception votes

One of the approaches to thermal perception assessment is based on the use of subjective thermal perception scales. For instance, Ahmed (2003) conducted a survey in six locations in the city of Dhaka, Bangladesh, which represented six local climate zones (e.g., street canyons). He then related the personal thermal sensation votes of interviewees with the micro-climatic characteristics of the climate zones to identify which zones

were perceived as more ambient and under what conditions. Another study by Katzschner (2004) explored momentary thermal perception in two squares in the city of Kassel, Germany using a five-point Likert scale of thermal perception. The study resulted in maps of perceived thermal comfort of selected localities but did not result in a comparison of subjective thermal perception and objective thermal data. However, the correspondence between the micro-climatic conditions (sky clearness index, wind speed, and air temperature) and subjective thermal perception in four places (square, courtyard, park, waterfront) in the city of Gothenburg, Sweden, was clearly found in a study by Eliasson et al. (2007). A more dynamic and continuous picture of thermal perception can be obtained with the relatively new method of thermal walks whereby micro-climatic data together with subjective data from participant questionnaires can be gathered over the course of a pedestrian route (Vasilikou and Nikolopoulou, 2020). One of the limitations of existing studies using subjective thermal perception scales is that these typically evaluate perceptions related to a very limited number of specific places or spatial points.

## 3.2 Cognitive maps

As an alternative approach to thermal perception assessment, some researchers have used cognitive thermal perception maps (e.g., Lenzholzer, 2010; Lenzholzer and Koh, 2010; Lehnert et al., 2021) that can potentially cover large areas. In cognitive mapping, participants are typically asked to indicate, using maps, spatial areas where they think they would have certain thermal perceptions (such as feeling too cold or too hot). Such information can be then aggregated across all participants, resulting in a map that displays where most people would have certain thermal perceptions. Such cognitive mapping can be done for selected urban areas (Lenzholzer, 2010; e.g., Lenzholzer and Koh, 2010) or it can span a whole city (Lehnert et al., 2021).

Even though cognitive maps generally match other thermal perception data, they have been often found to overrepresent extreme thermal perceptions (Lenzholzer and Koh, 2010; Lehnert et al., 2021). In other words, participants tend to better recollect areas where they experienced extreme thermal perceptions, such as feeling too windy, too cold, or too hot. This is in line with psychological theorizing that highly negative phenomena (e.g., experiencing an extremely uncomfortable environment) affect human perception more than relatively positive phenomena (e.g., experiencing only a mildly uncomfortable environment; Rozin and Royzman, 2001). Another limitation of studies using cognitive maps (but also most studies using subjective rating scales) is that they are conducted on convenience samples of participants that do not represent any known population.

## 3.3 Photograph-assisted thermal perception assessment

Yet another but rather rare approach to the assessment of long-term thermal perceptions is based on the use of photographs to assist thermal perception measurement. Photographs can be used as stimuli in landscape analyses, particularly in studies of people's preferences related to certain features of the landscape (Rodiek and Fried, 2005). Visual representation of places was also used by economists in choice experiments to represent any visually accessible attributes of places before people make decisions related to these places (Patterson et al., 2017). Some scholars have suggested that visual appraisal of photographs could help to get a better understanding of how observable features of the environment affect people's perception of the microclimate (Lenzholzer and Koh, 2010). As such, photographs could potentially convey visual information upon which people base their long-term thermal perception.

Despite their potential usefulness in assisting the measurement of long-term thermal perception, photographs of places have been rarely used in the assessment of thermal perception in specific places. As far as we are aware, only the study by Cortesão et al. (2020) used photographs to assist thermal perception assessment. These authors used photographs of three different places in Porto, Portugal, and asked their participants to select the most comfortable and most uncomfortable environments among them. They found that these choices matched data from *in situ* measurements of thermal perceptions and suggested that the decision tasks using visual representations of places can complement conventional *in situ* assessment of thermal perception.

# 4 Effect of blue and green infrastructure on thermal perception

Perceived thermal comfort is linked to psychological, physical, psychological factors, and behavioral factors (Chen and Ng, 2012). Among these, naturalness and aesthetics of the place, and experience with the place play an important role as factors of perceived outdoor thermal comfort (Nikolopoulou and Steemers, 2003; Eliasson et al., 2007; Nikolopoulou, 2011).

Given these patterns of perceived thermal comfort, it is not surprising that the presence of green infrastructure improves thermal comfort in outdoor places (Höppe, 2002; Nikolopoulou and Steemers, 2003; Knez and Thorsson, 2006; Lin, 2009; Lenzholzer and van der Wulp, 2010; Klemm et al., 2015a, 2015a; Aram et al., 2019, 2020). There is also some evidence that the presence of blue (i.e., water) infrastructure improves thermal comfort in outdoor places, particularly in places that are exposed to high temperatures (Völker and Kistemann, 2011; Gao et al., 2018). This is, again, not surprising given that the

presence of water infrastructure reduces heat load in outdoor spaces (Broadbent et al., 2018).

# 5 Current study

In this study, we propose an approach to long-term thermal perception assessment that combines previously used methods, namely the use of subjective rating scales of thermal perception, the use of photographs that assist thermal perception assessment, and survey-based elicitation of thermal perceptions. The approach that we propose can be easily scaled up across large samples of spatial points and a large number of participants. There are two potential benefits of this approach: 1) it can be used on a representative and large sample of spatial points representing a certain area (rather than on a set of arbitrarily selected spatial points), and 2) it can be administered to a large sample of participants representing a certain population (rather than convenience samples of participants).

We aim to partially validate this approach by showing that thermal perception ratings thus obtained are related to objective micro-climatic properties of places (average surface temperature) and that these ratings take into account place properties that are known to positively affect perceived thermal comfort (the presence of blue and green infrastructure). In addition, we also examine the predictive validity of long-term thermal perception ratings. Specifically, we are interested in whether average ratings of long-term thermal perceptions associated with places can predict outdoor activities (waiting and walking) in these places and preference for these places one year later.

## 5.1 Overview of studies

In Study 1, we conducted a survey of long-term thermal perception during summer heatwaves in the Czech city of České Budějovice and we looked at whether such thermal perception can be traced back to surface temperature, the presence of green and blue infrastructure, and the sky-view factor, as they should. Study 2 replicated the methodology in the Czech city of Brno. Finally, in Study 3, we looked at whether the long-term thermal perception measured in Study 2 was predictive of decision making regarding outdoor activities and place preference in the city of Brno one year later.

The case studies have been intentionally conducted in two typologically different cities. These differences concern climate, orography, and land cover. The city of Brno is located at the edge of the Pannonian biogeographical region. Summers are rather dry, with a sum of monthly precipitation of 60–80 mm, and hot, with the daily average temperature ranging between 21–23°C. The territory displays a significant orographic variability (190–385 m asl) and this–together with extended impervious surfaces–causes most of the water from precipitations to be drained away without being absorbed and could potentially impact microclimate by latent heat. The city of České Budějovice has a continental climate, the sum of monthly summer precipitation is 90–100 mm, the summer daily average temperature ranges between 19–21°C. The orography is smooth, with an average altitude of 405 m asl. The most typical features of the city and the whole region are open water bodies, both rivers, and manufactured ponds. Because of extended areas of grasslands, precipitation water can be absorbed and impact the local microclimate. The differences in the land cover of the two experimental sites can be recognized in Figure 1.

# 6 Study 1: Thermal perception and comfort in the city of České Budějovice

In Study 1 we look at whether a survey-based approach that uses rating scales to measure long-term thermal perception and perceived thermal comfort in combination with photographs of selected localities in the city of České Budějovice can provide measurements of long-term thermal perception and perceived thermal comfort. More specifically, we are interested in whether such measurements can be traced back to surface temperature, the presence of blue and green infrastructure, and the sky-view factor, which should theoretically affect long-term thermal perception and thermal comfort. In addition, we also wanted to know how well city residents can glean information about the presence of blue and green infrastructure from photographs of the places.

## 6.1 Method and procedure

### 6.1.1 Participants

A sample of participants with permanent residentship in the city of České Budějovice, recruited from a database of a marketing agency, was invited to participate in an online study; 483 participants entered the study and 336 (69.6%) completed it in July and August 2019. We have removed observations from two participants who received visual stimuli that we could not fully match with remote sensing data on the sampled locations (these 30 m buffers were not fully covered by remote sensing data). The final sample of participants ($N$ = 334) was fairly variable in terms of gender (74.5% were women), age (M = 37, $SD$ = 12.8), and education (4.2% were people with primary education; 21.6% were people with secondary education without a high school diploma; 42.8% were people with a high school diploma; 31.4% were people with a university degree).

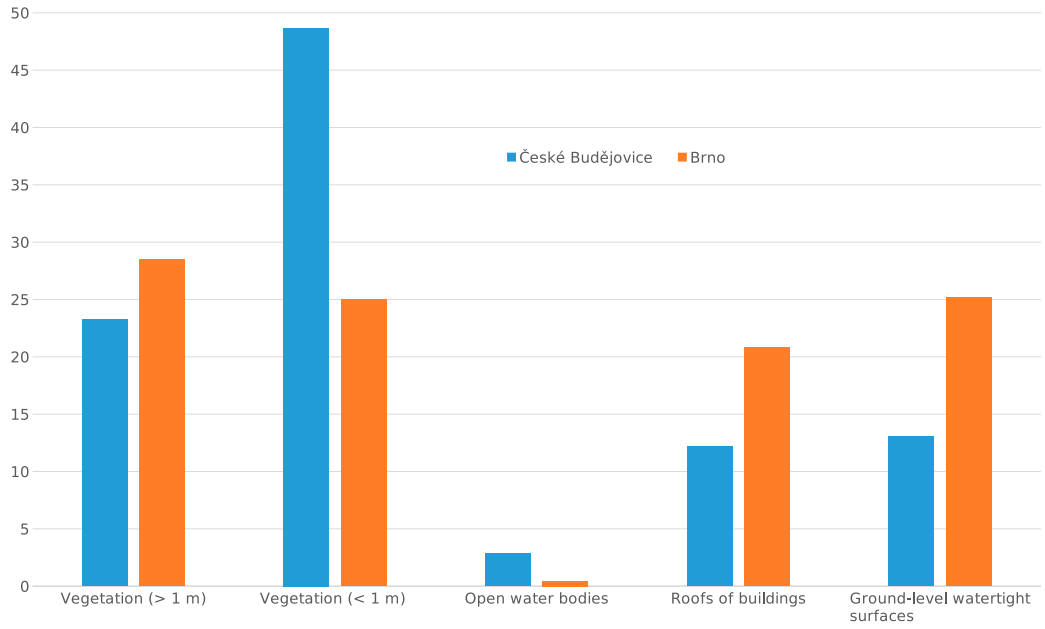


FIGURE 1
Proportion [%] of land cover and land use classes in the two experimental sites. *Note. Vegetation (> 1 m)* and *vegetation (< 1 m)* denote vegetation taller and smaller than 1 m. Source: based on remote sensing data from Study 1 and Study 2 (see respective Method sections for details).

## 6.1.2 Materials

### 6.1.2.1 Development of visual stimuli

In České Budějovice, we defined a square encompassing a major part of the city; this square was defined by the coordinates E14.4255-14.5352, N48.940-49.0116 (see Figure 2). Note that we chose the square, rather than the administrative boundaries of the city because the square-shaped area was technically easier to sample spatial points from. Given that our aim here was to demonstrate a proof of the concept, rather than to generalize our results to administrative spatial units, this choice did not affect our conclusions.

Within this square, we randomly selected 2000 spatial points based on uniform distribution along the x- and y-axes. Using Google Street View Static API (Google Map, 2019b). Next, we searched the database of Google Street View to find the closest location within 20 m distance represented in the database. We found 799 locations that fulfilled these criteria (see Figure 2). For each of these locations, we downloaded, using Google API, four pictures from the Google Street View database showing northward, eastward, southward, and westward views from each location and we collated these pictures into one visual stimulus representing each location (see Figure 3 for an example of the stimuli). We then manually screened the photographs and excluded 58 pictures that depicted interiors of buildings, roads, highways, and overpasses where pedestrians cannot walk or stand nearby. The remaining set of 741 images was selected to be used in data collection. In reality, 739 images were drawn randomly at least once during the survey process by the web-based questionnaire. However, we had to exclude another 13 visual stimuli that could not be correctly matched against the remotely sensed data because the remotely sensed data did not fully cover the 30 m buffer for these locations. The visual stimuli thus represented a fairly representative sample of publicly accessible outdoor places within the selected sub-section of the city of České Budějovice.

### 6.1.2.2 Remotely sensed independent variables

#### 6.1.2.2.1 Land cover classes

Two normalized differential vegetation indices (*VI*) were calculated from reflectance images as inputs to classification:

$$VI = \frac{(R_{B1} - R_{B2})}{(R_{B1} + R_{B2})}$$

Where $R_{Bx}$ represents reflectance at wavelength *B*x. The first *VI* used *B*1 = 800 nm and *B*2 = 670 nm and therefore corresponds to *NDVI* [23], commonly used to distinguish photosynthetically active vegetation. The second *VI* used *B*1 = 1,287 nm and *B*2 = 1,512 nm and enhanced differences in vegetation water content.

We classified the city's surface from *VI*s and normalized Digital Surface Model data into the following five classes: 1) roofs of buildings, 2) vegetation >1 m, 3) vegetation ≤1 m, 4) other impervious surfaces (e.g., roads), and 5) open water bodies. The

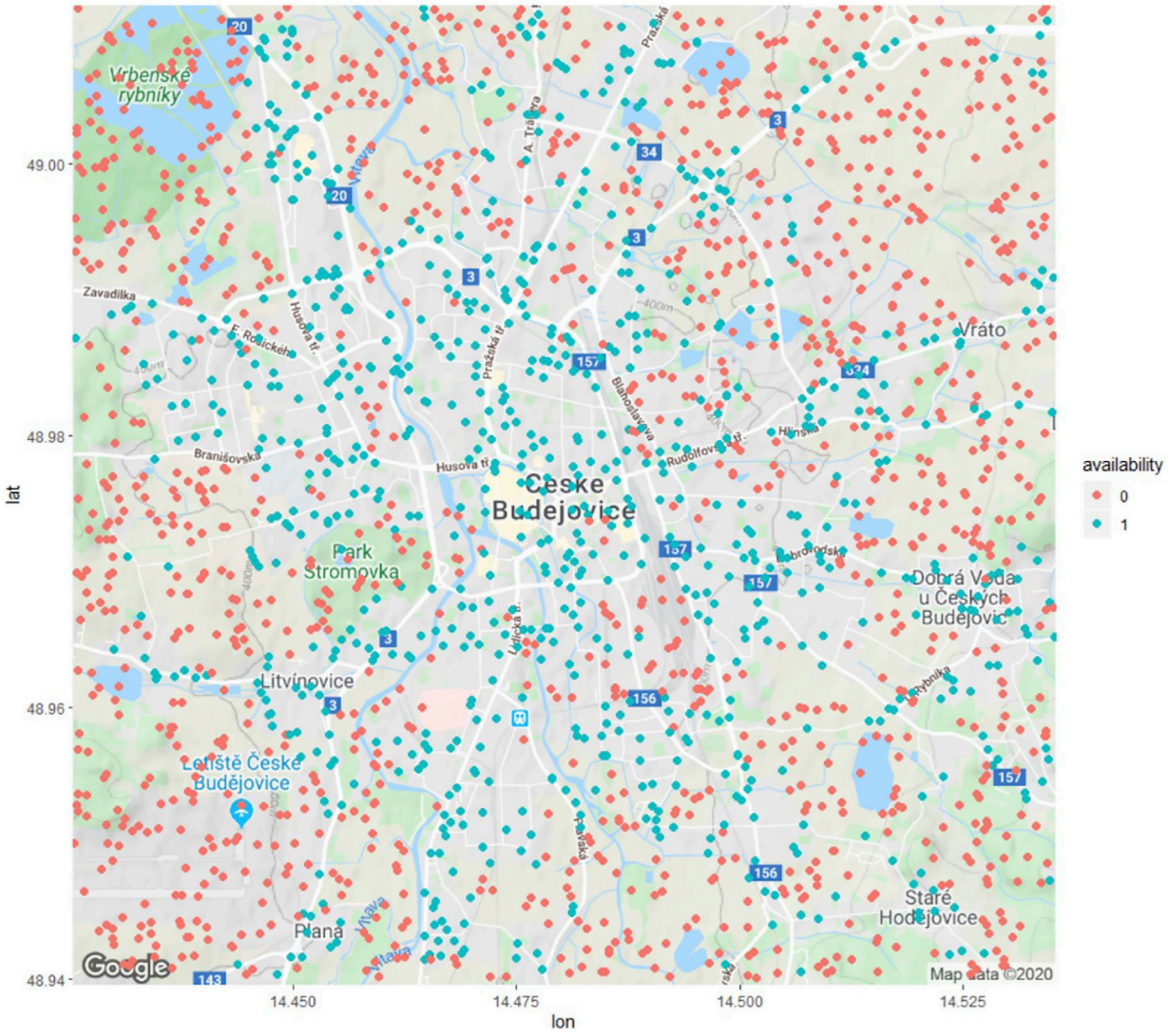


FIGURE 2
Availability of randomly selected locations in the Google Street View database (city of České Budějovice, Study 1). *Note.* Red and blue dots denote spatial points that were randomly selected within the square. Red dots denote locations that were not available in the database of Google Street View photographs, whereas blue dots denote locations that were available as Google Street View photographs and were used to develop visual stimuli for the current study.

classification was performed in the eCognition software (Trimble, Inc.) that uses an "object-oriented approach" to analyze images. The process comprises two steps. Firstly, the image is segmented into objects with a defined degree of homogeneity of input parameters. Secondly, the objects are categorized into classes following a programmed decision tree.

Our decision tree used normalized Digital Surface Model to separate high objects (trees, buildings) from objects with low height (low vegetation, roads), then the two vegetation indices enabled distinction between vegetation and other surfaces. The classification accuracy was evaluated on 800 randomly selected points, which were visually validated. Overall classification accuracy reached 84%.

In the current analysis, we used three land cover classes, namely classes of low and high vegetation (capturing presence of green infrastructure), and the open water body class (capturing presence of blue infrastructure). These indicators were computed as the proportion of pixels of respective class within a 30 m buffer. These indicators were standardized prior to analyses. However, we could not match 13 of the selected locations with remotely sensed data due to incomplete coverage of the 30 m buffers at these locations. Unmatched observations (57 out of the total of 5,010 observations given by the combination of 15 trials over 334 participants) were not used in the analysis.

FIGURE 3
Example of visual stimuli (city of České Budějovice, Study 1). *Note.* The four pictures (from top left to bottom right) capture, respectively, northward, eastward, southward, and westward views from the selected location.

#### 6.1.2.2.2 Land surface temperature

Land surfaces temperature image was obtained from the hyperspectral scanner TASI (8,000–11,000 nm). Data were acquired simultaneously with reflectance HS and LiDAR data. The radiometric and geometric preprocessing of thermal TASI data is identical to that of reflectance HS data. The calculation of land surface temperature (LST) is based on the Temperature and Emissivity Separation algorithm (TES, Pivovarnik et al., 2017). The measured radiance at sensor level (Lm) mainly consists of radiance emitted from the land surface, downwelling atmospheric radiance reflected by the surface ($L_{atm}^{\downarrow}$), and the atmospheric upwelling radiance ($L_{atm}^{\uparrow}$). The sum of all these components is expressed by a radiative transfer equation (RTE) as follows:

$$L_m = \tau\varepsilon B(T_s) + \tau(1-\varepsilon)L_{atm}^{\downarrow} + L_{atm}^{\uparrow} \quad (1)$$

where B (Ts) is the radiance of the surface at temperature Ts according to Planck's law, ε is the surface's emissivity, and τ is the atmospheric transmittance. The atmospheric parameters, $L_{atm}^{\downarrow}$, $L_{atm}^{\uparrow}$, and τ are modeled using the MODTRAN 5.3 radiation transfer model. The TES is based on the similarity between brightness temperature spectral features and emissivity spectral features. It uses an iterative process in estimating spectral emissivity and the respective temperatures. The calculus minimizes a difference between the black body radiance curve and the curve of spectral radiance obtained for given emissivity and temperature.

#### 6.1.2.2.3 The sky-view factor

The sky-view factor was computed as a percentage of hemisphere representing the sky in SAGA GIS software (Conrad et al., 2015) from the digital surface model interpolated from the LiDAR data with a very high spatial resolution (0.25 m).

We used zonal statistics to calculate the number of pixels of each land cover class within a buffer zone of diameter 30 m around the target position, the average surface temperature of a

zone, and the sky-view factor as the mean value of the sky-view factor from ground pixels (pixels classified as vegetation <1 m, impervious surfaces and water bodies). The sky-view factor was standardized before analyses.

#### 6.1.2.3 Dependent variables based on survey responses

##### 6.1.2.3.1 Rating of thermal perception

Participants assessed sequentially their long-term thermal perception at 15 randomly selected locations shown on visual stimuli. Specifically, participants indicated how they would describe the temperature that they would feel at each location "during a heatwave" using a seven point scale with seven labelled points (*cool, slightly cool, neutral, slightly warm, warm, hot, extremely hot*). Our scale was derived from the ASHRAE scale of thermal perception. The only difference was that in our scale, we added one point (extremely hot), and we removed one point (cold) from the original scale to allow for better differentiation in the higher thermal perception levels that we expected given that participants estimated their thermal perception during a heatwave. Note that this methodological decision was vindicate by the fact that the lowest category on our scale (*cool*) was used extremely rarely (0.9% of ratings), whereas the two highest categories were used frequently (*hot* in 27.0% of cases and *extremely hot* in 16.4% of cases).

##### 6.1.2.3.2 Rating of thermal comfort

Participants used the same 15 randomly selected stimuli as in the thermal comfort measure but this time they sequentially rated how they would feel overall at the location shown in the stimulus during a heatwave using a seven-point scale (*extremely uncomfortable, very uncomfortable, uncomfortable, neutral, pleasant, very pleasant, extremely pleasant*).

#### 6.1.2.4 Perceived properties of sampled locations

For the set of photographs of target points from České Budějovice, we performed manual coding of their content. Three coders evaluated six attributes of the photographs (whether the sky in the image is cloudy, whether there are bodies of water in the image, whether there are trees within 30 m distance, whether there are trees within 5 m, whether there is grass or shrubs within 5 m, and whether the location is shaded during the day by an artificial structure). Each attribute was independently rated by two coders, and if they disagreed, we used a third coder's rating for that photograph. Inter-rater variability (i.e., inter-rater correlation of ratings) was moderate or reduced for all attributes: cloud cover rating, $irr$ = 0.83; presence of water bodies, $irr$ = 0.80; presence of trees, $irr$ = 0.64; presence of nearby trees, $irr$ = 0.63; presence of shrubs, $irr$ = 0.62; presence of artificial shading, $irr$ = 0.25. These results suggest that different people can identify blue and green infrastructure, and shading structures in the pictures rather similarly.

### 6.1.3 Procedure

After giving informed consent, each participant browsed a set of 15 randomly selected images of sampled locations in České Budějovice taken from Google Street View and indicated for each location whether they had ever been to that location. Subsequently, for the same 15-point images, participants rated the perceived heat they would feel at that location during a heatwave. Subsequently, participants rated, for the same 15 locations, how they would feel overall at that location during a heatwave. At the end of the questionnaire, participants answered two questions assessing subjective attention and concentration and three demographic questions (gender, age, education). Upon completion of the study, participants were directed to the web page of the opinion poll company, and they received a small reward for their participation in the study (20 CZK; equivalent to $0.85).

### 6.1.4 Analyses

We used correlational analysis to check the match between perceived properties and remotely sensed properties of sampled locations. This analysis shows whether people can glean information about the presence of blue and green infrastructure and exposure to the Sun from our visual stimuli. Further, we used a mixed ordinal logit model to analyze whether subjective ratings of long-term thermal perception and thermal comfort can be related to surface temperature, the presence of blue and green infrastructure, and the sky-view factor, as they theoretically should.

## 6.2 Results

### 6.2.1 Relationship between remotely sensed and perceived place attributes

Perceived attributes of each point determined by independent coders from pictures correlated with attributes of those points derived through methods of remote sensing regarding the presence of trees, $r_{pb}$ = 0.46 (point biserial correlation), presence of bush and shrub, $r_{pb}$ = 0.48, presence of water bodies, $r_{pb}$ = 0.70, and presence of obstacles that shade the area (i.e., with remotely-sensed sky-view factor), $r_{pb}$ = −0.50, all $p$s < 0.001. Expectedly, there was no relationship between sky cloudiness observed by coders on the visual stimuli and the mean direct irradiation recorded for each location by remote sensing, as the two sets of observations were made on different days. $r_{pb}$ = 0.03, $p$ = 0.380. This was the reason why we did not include remotely sensed indicator of cloudiness (i.e., proxied by inverse of the direct irradiation) in our main models reported in the next two sections.

TABLE 1 Models of thermal perception and thermal comfort (mixed ordinal logit Model, city of České Budějovice, Study 1).

| | Thermal perception | | | | Thermal comfort | | | |
|---|---|---|---|---|---|---|---|---|
| | Reduced model | | Full model | | Reduced model | | Full model | |
| | β | *p* | β | *p* | β | *p* | β | *p* |
| *Effects of remotely sensed variables* | | | | | | | | |
| Surface temp | 0.08 | <0.001 | 0.03 | 0.166 | −0.11 | <0.001 | −0.04 | 0.045 |
| Trees | | | −0.22 | 0.001 | | | 0.26 | <0.001 |
| Bushes | | | −0.16 | 0.009 | | | 0.16 | 0.007 |
| Water | | | −0.04 | 0.410 | | | 0.09 | 0.037 |
| Sky-view factor | | | 0.14 | 0.008 | | | −0.21 | <0.001 |
| *Model properties* | | | | | | | | |
| Nobs | 4,953 | | 4,953 | | 4,953 | | 4,953 | |
| Log likelihood | −7,703 | | −7,671 | | −7,532 | | −7,477 | |
| Conditional R2 | 0.367 | | 0.373 | | 0.366 | | 0.375 | |
| Marginal R2 | 0.021 | | 0.034 | | 0.035 | | 0.056 | |

Note. *DV*s, are thermal perception (higher scores indicate higher level of perceived heat) and thermal comfort (higher scores indicate a higher level of thermal comfort) at the place during a hot day. *Surface temp*. Is the average land surface temperature (deg C) inside a 30 m buffer. The following independent variables were measured as the proportion of pixels within a 30 m buffer around the sampled locations that were classified into the following land cover types: *trees* (vegetation higher than 1 m), *bushes* (vegetation smaller than 1 m), water (any water elements such as rivers, streams, ponds). To avoid singularity of the model, we have not included watertight surfaces (including building roofs) in the model. *Sky-view factor* is the estimated sky-view factor at each sampled location. *Nobs* is the number of observations across participants and trials (334 × 15), minus 57 observations that cannot be matched against complete remotely sensed data. Log *likelihood* is the log-likelihood value of the model. *Conditional R2* is the variance explained by fixed and random effects, *marginal R2* is the variance explained by the fixed effects. Six ordinal thresholds and two random intercepts were omitted.

### 6.2.2 Thermal perception

As theoretically expected, the mixed ordinal logit model revealed that people's subjective rating of long-term thermal perception at the sampled location was positively affected by land surface temperature based on remote sensing (see estimates of the reduced model in Table 1 for details). Importantly, the effect of surface temperature on long-term thermal perception was completely mediated by the presence of green and blue infrastructure and presence of shading elements (captured by the sky-view factor) as indicated by the fact that when these attributes were introduced in the model, the effect of surface temperature on thermal perception dropped significantly and became statistically insignificant (see estimates of the full model in Table 1 for details). This result suggests that survey participants used the presence of blue and green infrastructure and the presence of shading elements as cues that help them to determine their long-term thermal perception in each of the places. This interpretation is further supported by the fact that the presence of trees and bushes had the expected negative effect on thermal perception, whereas the sky-view factor had a positive effect on thermal perception. The presence of water did not have a statistically significant effect on thermal perception, probably due to the relative scarcity of blue infrastructure in sampled locations (see Supplementary Table SA1 in the Appendix for descriptives of independent variables).

Importantly, we were able to partly corroborate the main results on a sub-sample of observations from participants who had little or no prior experience with the sampled locations and who had not visited them in the last year (79.1% of observations). Specifically, even these participants reported long-term thermal perception that matched remotely sensed surface temperature (see the reduced model in Supplementary Table SA2 for details). However, this relationship disappeared once we added remotely sensed indicators of the presence of the green and blue infrastructure and the sky-view factor in the model (see the reduced model in Supplementary Table SA2 for details). Again, this result suggests that people tend to estimate their long-term thermal perception using available visual cues, such as the presence of green and blue infrastructure and the presence of shading elements (inversely related to the sky-view factor). Indeed, the presence of trees had the expected negative effect whereas the sky-view factor had the expected positive effect on long-term thermal perception. The presence of bushes and water elements had no statistically significant effect on long-term thermal perception possibly due to the smaller size of the sub-sample which might have reduced the statistical power of the study.

#### 6.2.3 Thermal comfort

The mixed ordinal logit model also revealed the theoretically expected negative effect of surface temperature (based on remote sensing) on the rating of expected thermal comfort (based on survey data; for details, see the reduced model in Table 1). This effect was partially mediated by the presence of blue and green infrastructure and the presence of shading elements (inversely related to the sky-view factor), suggesting, again, that participants estimated their expected thermal comfort based on visual cues available in the visual stimuli (i.e., presence of blue and green infrastructure and presence of shading elements). This conclusion is further supported by the fact that the presence of trees, bushes, and water and the sky-view factor are all statistically significantly related to the expected thermal comfort expressed by participants (see the full model in Table 1). Note that all these substantial results hold when the model is estimated on a sub-sample of observations from participants who have not visited these locations (for details, see Supplementary Table SA2).

### 6.3 Discussion of study 1

We corroborated in Study 1 that people use visual cues present in photographs of locations, such as the presence of blue and green infrastructure and the presence of shading elements to determine their long-term thermal perception and expected thermal comfort at each location during a hot day. These subjective judgments match objective properties of these locations (based on remote sensing data) that are known to affect thermal perception and comfort, such as land surface temperature, the presence of blue and green infrastructure, and shading of locations.

## 7 Study 2: Thermal perception in the city of Brno

Study 1 used a relatively small number of sampled locations and individual participants, potentially decreasing the statistical power of the study. In Study 2 we aimed to replicate the results from Study 1 using data from a larger sample of locations from the city of Brno and a larger sample of participants (Brno residents).

### 7.1 Method and procedure

#### 7.1.1 Participants

A sample of participants with permanent residentship in the city of Brno, recruited from a database of a marketing agency, was invited to participate in an online study; 925 participants entered the study and 615 (66.5%) completed it in July and August 2019. The final sample of participants was fairly variable in terms of age ($M$ = 37.2; $SD$ = 12.5), gender (71.6% were women), and education (4.1% were people with primary education; 17.3% were people with secondary education without a high school diploma; 47.5% were people with a high school diploma; 31.1% were people with a university degree).

#### 7.1.2 Materials

##### 7.1.2.1 Development of visual stimuli

Similar to Study 1, we defined a square encompassing the wider city center of Brno; this square was defined by the coordinates E 16.552-16.66175, N 49.1592–49.2308 (see Figure 4). Within this square, we randomly selected (without replacement) 2000 spatial points; the uniform distribution of point selection probabilities along the x- and y-axes resulted in each point in the square having the same selection probability. Using Google Street View Static API (Google Map, 2019a), we searched the database of Google Street View pictures to find a picture that would represent this point or a nearest point within 20 m distance. Google Street View was available for 1,272 points. We manually screened the photographs and excluded 142 pictures that depicted interiors of buildings, roads, highways and overpasses where pedestrians cannot walk or stand nearby. The remaining set of 1,130 pictures was used as stimuli in data collection. The stimuli were processed as in Study 1 by collating the four views from each location (see Figure 5 for an example of the stimuli).

##### 7.1.2.2 Measures

We used the same measures as in Study 1.

#### 7.1.3 Procedure and analyses

We used the same procedure and analyses as in Study 1.

### 7.2 Results

#### 7.2.1 Relationship between remotely sensed and perceived place attributes

Perceived attributes of each point determined by independent coders from pictures correlated with attributes of those points derived through methods of remote sensing regarding the presence of trees, $r_{pb}$ = 0.47 (point biserial correlation), presence of bush and shrub, $r_{pb}$ = 0.40, presence of water, $r_{pb}$ = 0.46, and presence of obstacles that shade the area (i.e., with remotely-sensed sky-view factor), $r_{pb}$ = −0.52 all $p$s < 0.001. Expectedly, there was a relatively small match between mean direct irradiation at the moment of taking the remotely sensed data and rating of cloudiness on pictures of locations by raters, $r_{pb}$ = −0.12, $p$ < 0.001, due to the fact that the two measurements capture different moments with different cloudiness. This was the reason why we did not include the remotely sensed

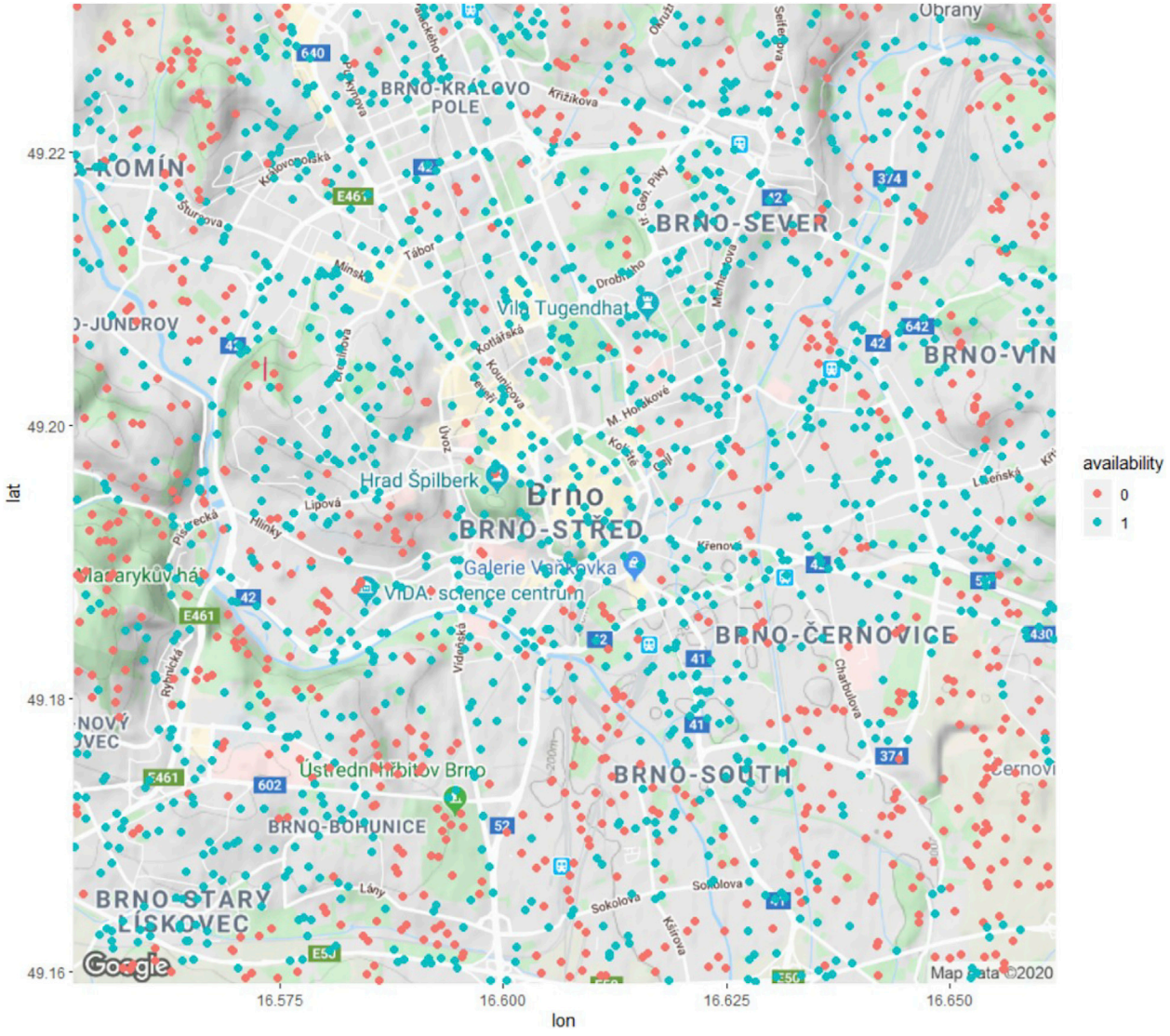


FIGURE 4
Availability of randomly selected locations in Google Street View database (city of Brno, Study 2). *Note.* Red and blue dots denote spatial points that were randomly selected within the square. Red dots denote locations that were not available in the database of Google Street View photographs, whereas blue dots denote locations that were available as Google Street View photographs and were used to develop visual stimuli for the current study.

indicator of cloudiness (i.e., proportional to the inverse of the direct irradiation) in our main model, similarly to Study 1.

### 7.2.2 Thermal perception

The results of Study 2 fully corroborated the results of Study 1. Specifically, we observed the theoretically expected positive relationship between (remotely sensed) surface temperature and (subjective survey-based) long-term thermal perception (for details, see the reduced model in Table 2). However, a large part of this relationship was mediated by the presence of blue and green infrastructure and the sky-view factor, suggesting that people used these attributes as visual cues when inspecting the visual stimuli and determining their long-term perceived thermal comfort at each location (for details, see the full model in Table 2). This conclusion is supported also by the fact that all remotely sensed characteristics of locations included in the model (i.e., presence of trees and bushes, presence of water, and sky-view factor) had theoretically expected effects on the subjective long-term thermal perception.

Importantly, the model estimated on the sub-sample of participants who had little or no experience with respective

FIGURE 5
Example of visual stimuli (city of Brno, Study 2). *Note.* The four pictures (from top left to bottom right) capture, respectively, northward, eastward, southward, and westward views from the selected location.

locations and did not visit them in the last year (85.5% of observations) revealed essentially the same results (for details, see Supplementary Table SA4). This means that people were able to infer from pictures of locations rather than from their personal experience information that they used to estimate their long-term thermal perception.

Taken together, these results suggest, once again, that visual cues available in photographs of locations allow people to estimate their long-term thermal perception at each sampled location that matches thermal patterns (surface temperature) that we objectively observe at these locations (through remote sensing).

### 7.2.3 Thermal comfort

We were also able to corroborate the results of Study 1 concerning thermal comfort. Again, we found that the (remotely sensed) surface temperature was negatively related to (subjective survey-based) perceived thermal comfort (for details, see the reduced model in Table 2). This relationship was considerably reduced when (remotely-sensed) indicators capturing the presence of green and blue infrastructure and the sky-view factor were introduced in the model (for details, see the full model in Table 2). This observation suggests that participants based their judgment of perceived thermal comfort on visual cues available in the pictures, namely the presence of blue and green infrastructure and the presence of shading elements. This conjecture is further supported by the fact that (remotely sensed) presence of bushes, trees and water as well as the sky-view factor all had the theoretically expected effect on (subjective survey-based) thermal comfort. Additionally, this conclusion is also supported by the fact that the same substantial results were obtained on a sub-sample of observations from participants who had little or no direct experience with respective locations (for details, see Supplementary Table SA4).

Taken together, these results suggest, once again, that people base their subjective rating of expected perceived thermal comfort on visual cues that are available in photographs of target locations. More importantly, we found that these subjective expectations match objective thermal properties (surface temperature) across the locations.

TABLE 2 Models of thermal perception and thermal comfort (mixed ordinal logit Model, city of Brno, Study 2).

| | Thermal perception | | | | Thermal comfort | | | |
|---|---|---|---|---|---|---|---|---|
| | Reduced model | | Full model | | Reduced model | | Full model | |
| | β | *p* | β | *p* | β | *p* | β | *p* |
| *Effects of remotely sensed variables* | | | | | | | | |
| Surface temp | 0.10 | <0.001 | 0.02 | 0.032 | −0.18 | <0.001 | −0.03 | 0.013 |
| Trees | | | −0.37 | <0.001 | | | 0.38 | <0.001 |
| Bushes | | | −0.16 | <0.001 | | | 0.25 | <0.001 |
| Water | | | −0.09 | 0.004 | | | 0.18 | <0.001 |
| Sky-view factor | | | 0.45 | <0.001 | | | −0.60 | <0.001 |
| *Model properties* | | | | | | | | |
| Nobs | 9,225 | | 9,225 | | 9,225 | | 9,225 | |
| Log likelihood | −13641 | | −13429 | | −13628 | | −13431 | |
| Conditional R2 | 0.477 | | 0.488 | | 0.584 | | 0.541 | |
| Marginal R2 | 0.021 | | 0.086 | | 0.049 | | 0.113 | |

Note. *DV*s, are thermal perception (higher scores indicate higher level of perceived heat) and thermal comfort (higher scores indicate a higher level of thermal comfort) at the place during a hot day. *Surface temp*. Is the average land surface temperature (deg C) inside a 30 m buffer. The following independent variables were measured as the number of pixels within a 30 m buffer around the sampled locations that were classified into the following land cover types: *trees* (vegetation higher than 1 m), *bushes* (vegetation smaller than 1 m), water (any water elements such as rivers, streams, ponds). *Sky-view factor* is the estimated sky-view factor at each sampled location. *Nobs* is the number of observations (615 participants x 15 trials). Log *likelihood* is the log-likelihood value of the model. *Conditional R2* is the variance explained by fixed and random effects, *marginal R2* is the variance explained by the fixed effects. Six ordinal thresholds and two random intercepts were omitted.

## 7.3 Discussion of study 2

In Study 2, we corroborated results from Study 1 using a large dataset of target location and participants from the city of Brno. Specifically, we found, as in Study 1, that people can very well glean from photographs information about the properties of those locations that should theoretically affect their thermal perception and comfort such as exposure to the Sun and the presence of blue and green infrastructure. We also corroborated that people's subjective rating of long-term thermal perception and comfort at the sampled locations reflects the objective thermal properties of these places (remotely sensed surface temperature).

# 8 Study 3: Thermal perception and decision making in the city of Brno

In Study 3 we look at whether long-term thermal perceptions associated with certain locations are useful for the prediction of pedestrians' behavior in those locations. Specifically, we are interested in whether the average long-term thermal perceptions associated with specific spatial points collected in Study 2 can be used to predict the choice of a walking route, choice of a waiting place, and the preference of a place in a new sample of participants more than one year later.

## 8.1 Method

### 8.1.1 Participants

The participants of the study were all residents of Brno. Participants were recruited in November and December 2020 based on quota characteristics from a participant panel of an opinion poll company. The study recruited 1,099 participants, of whom 865 completed the study (78.7% completion rate). We excluded 2 participants for whom the data was incomplete due to technical error, resulting in a sample size of $N$ = 863 participants. The sample of participants was fairly variable in terms of age ($M$ = 40.4; $SD$ = 13.4), gender (56.2% were women), and education (6.0% were people with primary education; 22.0% were people with secondary education without a high school diploma; 42.5% were people with a high school diploma; 29.5% were people with a university degree).

### 8.1.2 Materials

#### 8.1.2.1 Independent variable

Average long-term thermal perception. Based on participants' rating of their thermal perception in Study 2, we computed the average thermal perception rating of each of the 1,130 spatial points in the city of Brno featured in Study 2.


FIGURE 6
Example of the stimuli used in a trial of the choice experiment (place preference for walking in the city of Brno, Study 3)

#### 8.1.2.1 Dependent variables

Place preference for walking. We measured place preference for walking with a choice experiment. The choice experiment had 15 trials. Each trial of the choice experiment consisted of pairs of photographs depicting two randomly selected locations (northward view) from the database of 1,130 locations in the city of Brno used in Study 2. The photographs were arranged side by side (see Figure 6 for an example of the stimuli). In each trial, participants selected one place from the pair where they would "prefer to walk on a very hot day."

Place preference for waiting. We measured place preference for waiting with a similar choice experiment (using the same set of randomly chosen photograph pairs) as place preference for walking, except that participants selected in each trial a place where they would "prefer to wait for somebody on a very hot day."

Thermal comfort preference. We measured the thermal comfort preference using a choice experiment, similar to walking and waiting place preference. The only difference was that participants selected in each trial a place where they would "feel better on a very hot day."

### 8.1.3 Procedure

Study participants received a personalized invitation to enter an online study. Before entering the study, prospective participants indicated whether they lived in the Brno district or elsewhere. Only those who indicated the Brno-City district as their place of residence were allowed to enter the study. After providing informed consent, a set of 15 stimuli for the choice experiment was randomly generated for each participant for use in the three choice experiment tasks. Subsequently, participants went through 15 trials of the walking preference task, 15 trials of the place preference task, and 15 trials of the thermal comfort preference task. At the conclusion of the study, participants provided basic demographic information (gender, age, and education), identified their area of residence via zip code, and answered two self-assessment questions (attention to instructions and accuracy of responses). Upon completion of the study, participants were directed to the web page of the opinion poll company and they received a small reward for their participation in the study (20 CZK; equivalent to $0.85).

### 8.1.4 Analyses

We used mixed binary logit models to analyze each of the three choice experiment tasks. These models had the place preferences as dependent variables and average thermal comfort ratings from Study 2, associated with each location, as their independent variable. The model also included random intercepts that captured idiosyncratic effects of each choice set. Besides estimating the effects of the thermal preference ratings on place preference, we also estimated how well one can predict people's behavior based on such a model.

## 8.2 Results

### 8.2.1 Place preference for walking

Using the mixed logit model, we found that the average thermal perception from Study 2, associated with each place,

TABLE 3 Model of the preference of walking route, waiting place, and choice of the place where one would feel better (mixed binary logit models, city of Brno, Study 3).

| | Walking | | Waiting | | Feeling | |
|---|---|---|---|---|---|---|
| | β | *p* | β | *p* | β | *p* |
| *Model estimates* | | | | | | |
| Intercept | 3.57 | <0.001 | 3.15 | <0.001 | 3.42 | <0.001 |
| Average thermal comfort | −0.70 | <0.001 | -0.62 | <0.001 | −0.67 | <0.001 |
| *Model properties* | | | | | | |
| Nobs | 25,890 | | 25,890 | | 25,890 | |
| Log likelihood | −16230 | | −16429 | | −16342 | |
| *Explained variance* | | | | | | |
| Conditional R2 | 0.24 | | 0.22 | | 0.23 | |
| Marginal R2 | 0.07 | | 0.06 | | 0.07 | |
| *Outcome prediction* | | | | | | |
| Accuracy | 0.69 | | 0.69 | | 0.69 | |

*Note.* DVs, are: choice of walking route, choice of waiting place, and choice of place where one would feel better. *Average thermal comfort* is the average thermal comfort associated with each of the target places based on participants' ratings in Study 2. *Nobs* is the number of observations (863 participants x 15 trials x 2 possible place preferences). Log *likelihood* is the log-likelihood value of the model. Conditional R2 is the variance explained by fixed and random effects, marginal R2 is the variance explained by the fixed effects. *Accuracy* is the overall rate of successful predictions of participants' choices based on the model.

had the expected negative effect on the choice of the walking route (see Table 3 for details). In other words, the average long-term thermal perceptions associated with each place and captured in Study 2 predicted how different people one year later preferred these places for walking. Importantly, such a model has 69% accuracy. This means that the model can correctly predict 69% of behavioral choices regarding the choice of walking route.

### 8.2.2 Place preference for waiting

Using a similar model as for walking preference, we found that the average thermal perception also had the expected negative effect on waiting place preference (see Table 3 for details). In other words, the hotter the place was perceived by participants in Study 2, the less likely were participants in Study 3 to choose it as a waiting place. Again, the model correctly predicted about 69% of behavioral choices regarding the choice of waiting place.

### 8.2.3 Thermal comfort preference

Finally, using a similar model as we used for the waiting and walking tasks, we found that average thermal perception also has the expected negative effect on where people think they would feel better (see Table 3 for details). Again, this means that average long-term perceptions associated with each place were predictive of where people would feel better. The accuracy of such a prediction was 69%.

## 8.3 Discussion of study 3

In Study 3, we found that long-term thermal perceptions associated with specific places in the city of Brno and estimated on one sample of participants during a heatwave predicted how a different group of people preferred these places one year later for activities such as walking and waiting, and where they would feel better on an extremely hot day. These results suggest that subjective ratings of expected thermal perception are valid predictors of human behavior, as we would theoretically expect them to be.

# 9 General discussion

This study aimed to present and partially validate an approach to assessment of outdoor long-term thermal perception and comfort in urban environments. This approach combines some techniques previously used in thermal perception assessment, namely subjective rating scales, off-site survey administration, and representation of specific urban locations with photographs.

Across three studies conducted in two Czech cities, we found some preliminary evidence that long-term thermal perception and comfort elicited through a combination of these techniques is theoretically valid and practically useful. Specifically, in two of the studies, we were able to corroborate that photographs of

urban locations are sufficient to convey information about the properties of urban locations, such as the sky-view factor and the presence of blue and green infrastructures, upon which people based their long-term thermal perception. More importantly, we saw that long-term thermal perception elicited through this approach is related in a theoretically expected way to objective thermal properties of these places (remotely sensed surface temperature) and to properties of these places that affect local micro-climate (sky-view factor, and the presence of blue and green infrastructure).

Finally, and perhaps most importantly, we also demonstrated that long-term thermal perception is useful practically as it can predict mundane outdoor behavior such as choice of waiting place or preference for a walking route. Specifically, we showed that thermal perception associated with specific places and derived using one sample of participants can be used to predict mundane outdoor activities in the very sample places of a different group of people more than one year later.

## 9.1 Validity of thermal perception

Obviously, our study could only provide limited evidence of the validity of what we can call a photographic method of long-term thermal perception assessment. It is rather obvious that the task that our participants were accomplishing by trying to rate their thermal expectations associated with specific urban locations "during a heatwave" or "on a very hot day" is cognitively demanding. However, the literature shows that people are skilled in inferring thermal properties from subtle cues that visual inspection of environments can provide (Lenzholzer, 2010). This is not so surprising if we consider that the human ability to predict how one would feel in different environments under different conditions was key to the human ability to adapt to and survive in harsh environments.

We can hypothesize that it is this cognitive ability to predict one's thermal perceptions that makes long-term thermal expectations so useful in the prediction of human outdoor behavior. As a result, average thermal expectations associated with some locations in one group of people can explain the outdoor behavior of a different group of people more than one year later, as we have seen in one of our studies.

We think that the photographic approach to thermal perception assessment can be used to complement other methods of thermal perception assessment. This can be particularly useful in situations where we want to know how certain (and potentially large) populations of people perceive thermal comfort in a large number of locations. Such tasks are typically addressed with cognitive mapping approaches but these are known to be biassed and tend to oversample locations associated with extreme thermal perceptions (Lehnert et al., 2021).

## 9.2 Practical implications

Long-term thermal perception is recognized as an important factor that determines people's outdoor behavior (e.g., Lenzholzer, 2010). One of our studies supports this conclusion by showing that long-term thermal perception predicts how people prefer specific urban locations for walking and waiting. Obviously, these are just two of many examples of outdoor activities that are potentially affected by people's thermal expectations. As such, knowing long-term thermal expectations regarding different locations under different conditions (e.g., time of the year, occurrence of extreme weather events) can be useful for understanding and predicting human outdoor behavior in urban settings. As such, long-term thermal expectations can provide important input for urban planners.

## 9.3 Limitations and avenues for future research

One of the challenges for any study that tries to elicit people's long-term thermal perceptions and thermal comfort associated with specific places is that such studies must ask people to imagine specific conditions that apply to these thermal perceptions and thermal comfort. For instance, in our study, we asked participants to imagine how they would feel at each location on "a very hot summer day". Arguably, each person has a slightly different idea of what "a very hot day" means. Such idiosyncratic inter-personal differences undoubtedly introduce random error in persons' responses. However, as our studies show, the ratio of this error to the measured quantity (i.e., rating of thermal perception and rating of thermal comfort) has to be relatively low because we were still able to reveal the theoretically expected relationship between people's subjective perceptions and objective thermal properties of these places (i.e., remotely sensed surface temperature on a hot day) and the presence of (remotely sensed) blue and green infrastructure and sky-view factor. Thus, even with the measurement error that is necessarily associated with the elicitation of subjective thermal perceptions, such have enough precision to be useful to meaningfully compare specific urban locations.

Given that the present study could only provide limited evidence of the validity of the photographic approach to thermal perception assessment, future studies should seek to provide additional validity checks of this method. For instance, the results from the current approach can be cross-checked with results from *in-situ* measurements of thermal perception and with cognitive mapping. Further, the temporal stability of long-term thermal perception in persons should be studied.

Another limitation of our study is that we did not explore the mechanism through which people arrive at the thermal perception assessments when observing visual stimuli. While we know that people infer their thermal expectations from visual cues available in locations, experiments that would manipulate

these properties can shed more light on how people arrive at their long-term thermal perceptions.

Another limitation of the current study is that it only focused on three behavioral outcomes affected by long-term thermal perception, namely preference of place for walking, waiting, and overall place preference. Future studies may focus on other types of outdoor behavior and use methods, such as experience sampling (Bolger and Laurenceau, 2013) that allow for a study of human behavior in realistic and dynamic settings.

Finally, the current study is also limited in that it covers only two Czech cities. Future studies may explore the generalizability of our approach in different urban, climatic, and cultural contexts. For instance, cultural differences are known to play a significant role in thermal perception (Chen and Ng, 2012). Thus, using the current photographic method in varied cultural contexts can help us to understand the limits of its generalizability.

## 10 Conclusion

We presented and partially validated a photographic approach to assessment of long-term outdoor thermal perception and comfort related to heatwaves in urban environments. This approach combines subjective rating scales, off-site survey administration, and representation of specific urban locations with photographs. As such, this approach is suitable for the assessment of how a large group of people perceives thermal comfort in a large number of places during heatwaves. Measurements of the long-term thermal perception and comfort based on this approach are related to theoretically known predictors of thermal perception and thermal comfort. Moreover, such measures are also predictive of outdoor activities. This approach to thermal perception and assessment can complement similar existing methods such as cognitive mapping.

## Data availability statement

The datasets and analytical scripts used for analyses presented in this study can be found in an online repository at: https://osf.io/qw9fg/.

## Ethics statement

Ethical review and approval was not required for the study on human participants in accordance with the local legislation and institutional requirements. The participants provided their implicit informed consent to participate in this study.

## Author contributions

JU: Conceptualization, data curation, formal analysis, investigation; methodology, writing–original draft; MP: Data curation, formal analysis, investigation, writing–review and editing. FZ: Funding acquisition, project administration, investigation, formal analysis, writing–review and editing. JN: Investigation, formal analysis, writing–review and editing.

## Acknowledgments

We would like to thank the Technology Agency of the Czech Republic (project "Thermal comfort in urban areas: human perception, physics based reality, role of greenery", grant no. TL02000322) and the Ministry of Education, Youth and Sports of the Czech Republic (CzeCOS program, grant no. LM2018123) for their financial support. We would also like to thank Cliff McLenehan and Siri Jodha Singh Khalsa for their language support and the reviewers for their insightful comments.

## Conflict of interest

The authors declare that the research was conducted in the absence of any commercial or financial relationships that could be construed as a potential conflict of interest.

## Publisher's note



## Supplementary material

The Supplementary Material for this article can be found online at: https://www.frontiersin.org/articles/10.3389/fenvs.2022.878341/full#supplementary-material

# References


Ahmed, K. S. (2003). Comfort in urban spaces: Defining the boundaries of outdoor thermal comfort for the tropical urban environments. *Energy Build.* 35, 103–110. doi:10.1016/S0378-7788(02)00085-3

Aram, F., Solgi, E., Garcia, E. H., and Mosavi, A. (2020). Urban heat resilience at the time of global warming: Evaluating the impact of the urban parks on outdoor thermal comfort. *Environ. Sci. Eur.* 32, 117. doi:10.1186/s12302-020-00393-8

Aram, F., Solgi, E., Higueras García, E., Mosavi, A., and Várkonyi-Kóczy, R. A. (2019). The cooling effect of large-scale urban parks on surrounding area thermal comfort. *Energies* 12, 3904. doi:10.3390/en12203904

Auliciems, A. (1981). Towards a psycho-physiological model of thermal perception. *Int. J. Biometeorol.* 25, 109–122. doi:10.1007/BF02184458

Bolger, N., and Laurenceau, J.-P. (2013). *Intensive longitudinal methods: An introduction to diary and experience sampling research*. New York, NY: Guilford Press.

Broadbent, A. M., Coutts, A. M., Tapper, N. J., Demuzere, M., and Beringer, J. (2018). The microscale cooling effects of water sensitive urban design and irrigation in a suburban environment. *Theor. Appl. Climatol.* 134, 1–23. doi:10.1007/s00704-017-2241-3

Brunswik, E. (1956). *Perception and the representative design of psychological experiments*. 2nd ed. Berkeley, CA, US: University of California Press.

Chen, L., and Ng, E. (2012). Outdoor thermal comfort and outdoor activities: A review of research in the past decade. *Cities* 29, 118–125. doi:10.1016/j.cities.2011.08.006

Conrad, O., Bechtel, B., Bock, M., Dietrich, H., Fischer, E., Gerlitz, L., et al. (2015). System for automated geoscientific analyses (SAGA) v. 2.1.4. *Geosci. Model Dev.* 8, 1991–2007. doi:10.5194/gmd-8-1991-2015

Cortesão, J., Brandão Alves, F., and Raaphorst, K. (2020). Photographic comparison: A method for qualitative outdoor thermal perception surveys. *Int. J. Biometeorol.* 64, 173–185. doi:10.1007/s00484-018-1575-6

Eliasson, I., Knez, I., Westerberg, U., Thorsson, S., and Lindberg, F. (2007). Climate and behaviour in a Nordic city. *Landsc. Urban Plan.* 82, 72–84. doi:10.1016/j.landurbplan.2007.01.020

Eysenck, M. W., and Brysbaert, M. (2018). *Fundamentals of cognition*. Third Edition. New York: Routledge.

Fanger, P. O. (1970). Thermal comfort. Analysis and applications in environmental engineering. Available at: http://www.cabdirect.org/abstracts/19722700268.html (Accessed November 15, 2012).

Gao, Y., Church, S. P., Peel, S., and Prokopy, L. S. (2018). Public perception towards river and water conservation practices: Opportunities for implementing urban stormwater management practices. *J. Environ. Manag.* 223, 478–488. doi:10.1016/j.jenvman.2018.06.059

Google Map (2019a). *Street view static API*. City of Brno: Google.

Google Map (2019b). *Street view static API*. City of České Budějovice: Google.

Höppe, P. (2002). Different aspects of assessing indoor and outdoor thermal comfort. *Energy Build.* 34, 661–665. doi:10.1016/S0378-7788(02)00017-8

Katzschner, L. (2004). "Open space design strategies based on thermal comfort analysis," in Proceedings PLEA *(Eindhoven)*, 47–52. Available at: https://citeseerx.ist.psu.edu/viewdoc/download?doi=10.1.1.548.2341&rep=rep1&type=pdf (Accessed July 2, 2022).

Klemm, W., Heusinkveld, B. G., Lenzholzer, S., Jacobs, M. H., and Van Hove, B. (2015a). Psychological and physical impact of urban green spaces on outdoor thermal comfort during summertime in The Netherlands. *Build. Environ.* 83, 120–128. doi:10.1016/j.buildenv.2014.05.013

Klemm, W., Heusinkveld, B. G., Lenzholzer, S., and van Hove, B. (2015b). Street greenery and its physical and psychological impact on thermal comfort. *Landsc. Urban Plan.* 138, 87–98. doi:10.1016/j.landurbplan.2015.02.009

Knez, I., and Thorsson, S. (2006). Influences of culture and environmental attitude on thermal, emotional and perceptual evaluations of a public square. *Int. J. Biometeorol.* 50, 258–268. doi:10.1007/s00484-006-0024-0

Langevin, J., Gurian, P. L., and Wen, J. (2015). Tracking the human-building interaction: A longitudinal field study of occupant behavior in air-conditioned offices. *J. Environ. Psychol.* 42, 94–115. doi:10.1016/j.jenvp.2015.01.007

Lehnert, M., Geletič, J., Kopp, J., Brabec, M., Jurek, M., Pánek, J., et al. (2021). Comparison between mental mapping and land surface temperature in two Czech cities: A new perspective on indication of locations prone to heat stress. *Build. Environ.* 203, 108090. doi:10.1016/j.buildenv.2021.108090

Lenzholzer, S. (2010). Engrained experience—A comparison of microclimate perception schemata and microclimate measurements in Dutch urban squares. *Int. J. Biometeorol.* 54, 141–150. doi:10.1007/s00484-009-0262-z

Lenzholzer, S., and Koh, J. (2010). Immersed in microclimatic space: Microclimate experience and perception of spatial configurations in Dutch squares. *Landsc. Urban Plan.* 95, 1–15. doi:10.1016/j.landurbplan.2009.10.013

Lenzholzer, S., and van der Wulp, N. Y. (2010). Thermal experience and perception of the built environment in Dutch urban squares. *J. Urban Des.* 15, 375–401. doi:10.1080/13574809.2010.488030

Lin, T.-P. (2009). Thermal perception, adaptation and attendance in a public square in hot and humid regions. *Build. Environ.* 44, 2017–2026. doi:10.1016/j.buildenv.2009.02.004

Mayer, H., and Höppe, P. (1987). Thermal comfort of man in different urban environments. *Theor. Appl. Climatol.* 38, 43–49. doi:10.1007/BF00866252

Nikolopoulou, M., Baker, N., and Steemers, K. (2001). Thermal comfort in outdoor urban spaces: Understanding the human parameter. *Sol. Energy* 70, 227–235. doi:10.1016/S0038-092X(00)00093-1

Nikolopoulou, M. (2011). Outdoor thermal comfort. *Front. Biosci.*, 1552. doi:10.2741/245

Nikolopoulou, M., and Steemers, K. (2003). Thermal comfort and psychological adaptation as a guide for designing urban spaces. *Energy Build.* 35, 95–101. doi:10.1016/S0378-7788(02)00084-1

Patterson, Z., Darbani, J. M., Rezaei, A., Zacharias, J., and Yazdizadeh, A. (2017). Comparing text-only and virtual reality discrete choice experiments of neighbourhood choice. *Landsc. Urban Plan.* 157, 63–74. doi:10.1016/j.landurbplan.2016.05.024

Pickup, J., and de Dear, R. (2000). "An Outdoor Thermal Comfort Index (OUT_SET*) - Part I - the model and its assumptions," in *Selected papers from the conference ICB-ICUC*. Editors R. de Dear, J. Kalma, and A. Auliciems (Geneva, Switzerland: World Meteorological Organization in association with the United Nations Environment Programme and Macquarie University), 279–283.

Pivovarnik, M., Khalsa, S. J. S., Jimenez-Munoz, J. C., and Zemek, F. (2017). Improved temperature and emissivity separation algorithm for multispectral and hyperspectral sensors. *IEEE Trans. Geosci. Remote Sens.* 55, 1944–1953. doi:10.1109/TGRS.2016.2631508

Rodiek, S. D., and Fried, J. T. (2005). Access to the outdoors: Using photographic comparison to assess preferences of assisted living residents. *Landsc. Urban Plan.* 73, 184–199. doi:10.1016/j.landurbplan.2004.11.006

Rozin, P., and Royzman, E. B. (2001). Negativity bias, negativity dominance, and contagion. *Pers. Soc. Psychol. Rev.* 5, 296–320. doi:10.1207/S15327957PSPR0504_2

Shukla, P. R., Skea, J., Calvo Buendia, E., Masson-Delmotte, V., Pörtner, H.-O., Roberts, D. C., et al. (2019). *Climate change and land: An IPCC special 659 report on climate change, desertification, land degradation, sustainable land management, food security, and greenhouse gas fluxes in terrestrial ecosystems*. Summary for policymakers. Geneva, Switzerland: Intergovernmental Panel on Climate Change.

Sun, C., Zhang, R., Sharples, S., Han, Y., and Zhang, H. (2018). A longitudinal study of summertime occupant behaviour and thermal comfort in office buildings in northern China. *Build. Environ.* 143, 404–420. doi:10.1016/j.buildenv.2018.07.004

Thorsson, S., Honjo, T., Lindberg, F., Eliasson, I., and Lim, E.-M. (2007). Thermal comfort and outdoor activity in Japanese urban public places. *Environ. Behav.* 39, 660–684. doi:10.1177/0013916506294937

Thorsson, S., Lindqvist, M., and Lindqvist, S. (2004). Thermal bioclimatic conditions and patterns of behaviour in an urban park in Göteborg, Sweden. *Int. J. Biometeorology* 48, 149–156. doi:10.1007/s00484-003-0189-8

Vasilikou, C., and Nikolopoulou, M. (2020). Outdoor thermal comfort for pedestrians in movement: Thermal walks in complex urban morphology. *Int. J. Biometeorol.* 64, 277–291. doi:10.1007/s00484-019-01782-2

Völker, S., and Kistemann, T. (2011). The impact of blue space on human health and well-being – salutogenetic health effects of inland surface waters: A review. *Int. J. Hyg. Environ. Health* 214, 449–460. doi:10.1016/j.ijheh.2011.05.001

Walton, D., Dravitzki, V., and Donn, M. (2007). The relative influence of wind, sunlight and temperature on user comfort in urban outdoor spaces. *Build. Environ.* 42, 3166–3175. doi:10.1016/j.buildenv.2006.08.004

frontiers | Frontiers in Environmental Science

TYPE Original Research
PUBLISHED 31 August 2022
DOI 10.3389/fenvs.2022.893437



OPEN ACCESS

EDITED BY
Junke Zhang,
Southwest Jiaotong University, China

REVIEWED BY
Ana Cristina Russo,
University of Lisbon, Portugal
Dipesh Rupakheti,
Nanjing University of Information Science and Technology, China

*CORRESPONDENCE
Dongwei Liu,
liudw@imu.edu.cn

SPECIALTY SECTION
This article was submitted to Atmosphere and Climate, a section of the journal Frontiers in Environmental Science

RECEIVED 10 March 2022
ACCEPTED 05 August 2022
PUBLISHED 31 August 2022

CITATION
Wang J, Liu D, Xu X, Ma J and Han L (2022), Analysis of the temporal and spatial pattern of air pollution and the heterogeneity of its influencing factors in central Inner Mongolia from 2016 to 2018.
*Front. Environ. Sci.* 10:893437.
doi: 10.3389/fenvs.2022.893437



# Analysis of the temporal and spatial pattern of air pollution and the heterogeneity of its influencing factors in central Inner Mongolia from 2016 to 2018

Jie Wang[1,2], Dongwei Liu[1,3,4]*, Xijie Xu[5], Jiali Ma[1] and Lijing Han[1]

[1]School of Ecology and Environment, Inner Mongolia University, Hohhot, China, [2]School of Life Sciences, Technical University of Munich, München, Germany, [3]Inner Mongolia Key Laboratory of River and Lake Ecology, Hohhot, China, [4]Key Laboratory of Ecology and Resource Use of the Mongolian Plateau, Ministry of Education of China, Hohhot, China, [5]IoT2US Laboratory, School of Electronic Engineering and Computer Science, Queen Mary University of London, London, United Kingdom

The central region of Inner Mongolia is the northern ecological safety barrier of Beijing and even the whole country. It is one of the main sources of dust in North China, and air pollution control is the top priority in this region. In this study, the central region of Inner Mongolia was selected as the study area, multiple auxiliary variables were used to estimate the spatial distribution of PM2.5 concentration from 2016 to 2018 by geographically weighted regression, and the socioeconomic determinants of PM2.5 concentration were analyzed by geographic detectors. The results show that: 1) the established model can better estimate the spatial distribution of PM2.5 concentration in the study area, and the monthly mean correlation coefficient R of the verification parameters is stable, ranging from 0.58 to 0.66. 2) PM2.5 concentration in central Inner Mongolia showed significant temporal and spatial variation. The mean annual PM2.5 concentration along the Yellow River basin is the highest in the study area. PM2.5 concentration first increased and then decreased from 2016 to 2018. 3) Urban built-up area, permanent population and per capita GDP are the key factors affecting the spatial and temporal distribution of PM2.5 concentration in the study area. The results of this study provide theoretical basis and technical support for air pollution monitoring, management and prevention in central Inner Mongolia.

KEYWORDS

**central inner Mongolia, PM2.5 concentrations, geographically weighted regression, geographic detector, pollution prevention and control**

# 1 Introduction

With the rapid development of global economy, the progress of urbanization and industrialization has accelerated, people's living standards have improved. The consumption of coal and electricity have increased (Xiao et al., 2015), and the demand for sand, steel, etc. Required in the process of urban construction has increased (Wu et al., 2015). The extensive development of industry and the substantial increase in pollutant emissions have directly or indirectly brought about an important impact on atmospheric pollution (Miao Zhang et al., 2021). At the same time, air pollution has a greater impact on the ecological environment (Yan, 2012), climate change (Sui, 2019) and human health (Guan et al., 2016), and it has become a global focus of attention.

Air pollution refers to the phenomenon that the concentration of pollutants in the atmosphere reaches a harmful level, even destroying the conditions for the normal survival and development of the ecosystem and human beings, and causing harm to people and objects (Bai et al., 2018). Suspended Particulate Matter is an important source of air pollution (Meng et al., 2019; Kong et al., 2020). Fine Particulate Matter (PM2.5, Particulate Matter, PM) is the Particulate with aerodynamic equivalent diameter less than or equal to 2.5 microns in ambient air (Vo et al., 2020), and is also an important component of suspended Particulate Matter (Yang and Jiang, 2020). From the perspective of research methods, scholars from various countries made a thorough analysis of air pollution, which has laid a relatively solid theoretical foundation. In 1969, Ken Whitby, an American scientist, conducted the first study on PM2.5 (Whitby et al., 1972). In 1970, the United States enacted and implemented the Clean Air Act, establishing an air pollution control system (Domenici, 1979). In 1984, the European Community established the EMEP (European Monitoring and Evaluation Program) (Tørseth et al., 2012), and in 1987, the European Union issued an air pollution restriction order to control the discharge of relevant pollutants (McNaughton, 2018). In 1997, The US National Environmental Protection Agency proposed a relatively accurate concentration standard value based on particulate matter, and a higher standard was proposed in 2013 (Esworthy, 2014). Juliette et al. (2008) mainly explored the connection between PM10 and meteorological factors, and studied the relationship between the concentration of PM10, $O_3$, NOX and $SO_2$ and the spatial change by using the environmental data detected by the weather station for a trade port. For the study of air pollution in typical regions, scholars from various countries have conducted research and analysis to different degrees for regions with different geographical and social environments. Liu et al. (2020) studied on the environmental air quality of 366 cities in China showed that China's air pollution is mainly PM10 and PM2.5. The high value of PM10 is mainly concentrated in Xinjiang and greatly influenced by natural factors. The high value of PM2.5 is mainly distributed in central China, North China and northern Jiangsu and is more influenced by human activities. Wang et al. (2019) studied the change characteristics of PM2.5 in the Beijing-Tianjin-Hebei region from 2013 to 2018. They found that PM2.5 pollution in the Beijing-Tianjin-Hebei plain showed a more significant change than that in the mountainous region. PM2.5 mass concentration was the highest in winter and the lowest in summer, and its spatial distribution was high in the south and low in the north. Zhou et al. (2019) found that air quality is closely related to the synoptic circulation and local wind field affecting a specific area, and conducted a validation analysis in Shanghai, China. They found that the Shanghai area is most prone to severe haze under specific circulation patterns (CT1, CT2, and CT4), mainly related to cold air activity and the displacement of the high pressure system relative to Shanghai (Zhao et al., 2019). At present, there are few studies in arid and semi-arid regions dominated by dust pollution, and in China it is mainly concentrated in the northwest regions (Haijun et al., 2020; Rupakheti et al., 2021). Understanding the characteristics of air pollution is the basis for scientific decision-making and comprehensive management of air pollution control.

Scientific identification of spatial heterogeneity and driving factors of PM2.5 concentration is of great significance to regional air linkage governance and has become the focus of various disciplines. Current research methods can be divided into the following six categories: 1) Using the statistical yearbook data of a certain region, combined with the data of the meteorological department and the environmental protection department, the results are obtained by integrated analysis. 2) Through a combination of questionnaires and interviews, the awareness and specific opinions of residents on urban air pollution are obtained. 3) Specific models are used to obtain information on major urban pollution sources, such as AOD (Aerosol optical thickness) remote sensing model, super-efficiency DEA (Data envelopment analysis) model, DOAS (Differential Optical Absorption Spectroscopy) technology, TDLAS (Tunable Diode Laser Absorption Spectroscopy) technology, ground-based multi-axis differential absorption spectrometer (MAX-DOAS), weather research and prediction model chemical module WRF-Chem (Zhang and Li, 2020). 4) the specific relationship between urbanization level and air pollution in multiple cities is comparatively analyzed by selecting urbanization indicators and specific pollutant information of multiple cities. 5) Comparing and analyzing the differences and contents of pollutants in different economic zones by selecting specific locations and monitoring them at fixed points. 6) Through the magnetic and heavy metal monitoring of the samples, the specific association between the samples and air pollutants is found. The most common used model of these is remote sensing model, which uses Aerosol Optical Depth (AOD) data from satellite remote sensing to evaluate the PM2.5 concentration in a wide range. In remote sensing models, commonly used inversion models include semi-empirical Model (Yuan Wei et al., 2021), Artificial Neural Network (ANN) Model

(Casallas et al., 2021), Machine Learning Algorithm Model (Jain et al., 2021), Generalized Additive Model (GAM) (Analitis et al., 2020), General Linear Regression Model (Xin Zhang et al., 2021), Geographically Weighted Regression (GWR) model (Song et al., 2014), remote sensing formula (Lin et al., 2015), statistical downscaling method (Qian Yang et al., 2020), Geographically and Temporally Weighted Regression (GTWR) model (Wei et al., 2019), etc. In recent years, the GTWR model has become increasingly popular in environmental research because the model can incorporate temporal information into spatial variability (He and Huang, 2018a; Mirzaei et al., 2019; Liu et al., 2021). However, when GTWR lacks sample points in time and region, the accuracy of the model needs to be optimized (He and Huang, 2018b). GWR is a technique to test spatial variability and non-stationarity by generating local regression results, which is suitable for PM2.5 prediction at regional scale (Hu et al., 2013). Therefore, the GWR model was selected for PM2.5 estimation in this study.

The central region of Inner Mongolia includes Ordos, Hohhot, Bayannur, Ulanqab and Baotou. They are located in the traffic arteries of China's western development. Their terrain is flat, and the land resources are relatively rich. In addition, the region has a strong economic foundation, certain technological innovation capabilities and good development potential (Liu, 2002). However, the central region of Inner Mongolia is one of the largest coal chemical bases in China, and its air quality has been greatly affected. Therefore, how to better improve the air quality of Inner Mongolia's central cities while ensuring the supply of energy in the Beijing-Tianjin-Hebei region has become the primary problem to be solved in the protection of atmospheric environment in this region (Qiu et al., 2017; Gao et al., 2021). And it is also the key problem of air pollution prevention and control in the region in the future.

In this paper, the central region of Inner Mongolia was selected as the study area, and the factor with the greatest monthly correlation with PM2.5 from 2016 to 2018 was selected from multiple factors to establish a GWR model and invert the spatial distribution data of PM2.5 from 2016 to 2018. In this study, the spatial and temporal distribution characteristics of PM2.5 in central cities of Inner Mongolia were analyzed from different time scales, such as space, year, season and month, and the impact of economic development, urbanization, industrialization and energy on PM2.5 was analyzed. The results of this paper provide a theoretical basis for air pollution monitoring, management and prevention in central Inner Mongolia.

# 2 Data and methods

## 2.1 Study area

The central region of Inner Mongolia belongs to the Yin Mountains, located on the northern slope of Daqing Mountain in Inner Mongolia, 105°12′–114°49′E, 37°37′–43°23′N, including Ordos, Hohhot, Bayannur, Ulanqab and Baotou. (Figure 1A). The Inner Mongolia Autonomous Region is the northern ecological security barrier for Beijing and even the whole country. The central part of Inner Mongolia is 804–2345 m above sea level, the terrain is low in the middle part and high in the north and south (Figure 1B). The south is dominated by low mountains, the middle is dominated by low hills and tidal wetlands, and the north is dominated by grasslands (Figure 1C). The study area belongs to a continental monsoon arid climate with large temperature changes. The highest temperature in the past 20 years reaches 39°C, the lowest temperature in the past 20 years is −41°C, and the wind is mostly above six levels. The maximum annual temperature difference can reach 70–80°C, and the annual mean temperature is about 4°C. Since 1999, the annual precipitation has been 200–360 mm, and the evaporation has been 7–8 times of the precipitation. Sand and deserts are distributed in the study area, which is one of the main sources of sand and dust in North China and one of the chief culprits of sand and dust weather in the surrounding areas of Beijing (Yang et al., 2021).

The central region of Inner Mongolia is the region with the highest regional economy in the Inner Mongolia Autonomous Region. Among them, the economic development speed of Ordos has ranked first in the Inner Mongolia Autonomous Region (Guo and Wu, 2011). The central part of Inner Mongolia is one of the largest coal chemical industrial bases in China. In the region, the heating fuel is mainly coal, and the transportation fuel is mainly gasoline. Combustion of these two fuels produces a large amount of air pollution emissions. The heating period in central Inner Mongolia is mainly in winter and spring (Bai et al., 2010). Coal-fired heating has greatly increased the frequency of use of coal-fired power plants and thermal power plants, resulting in more air pollutants (Khuzestani et al., 2017). In addition, the number of private motor vehicles in central Inner Mongolia is higher than that in other areas of Inner Mongolia, and air pollution caused by vehicle exhaust is also worthy of attention (Liu et al., 2022). The air pollutant considered in this study is the PM2.5.

In 2013, the State Council of China issued the Air Pollution Prevention and Control Action Plan, focusing on strengthening the prevention and control of air pollution with a focus on fine particulate matter (PM2.5). In 2018, the air pollution prevention and control plan was successfully concluded by the Inner Mongolia Autonomous Region, and the Inner Mongolia Autonomous Region successfully completed various national goals and tasks. Therefore, the research time interval of this paper is in the 2016–2018 years of the completion plan.

## 2.2 Data

### 2.2.1 PM2.5 station data

The air pollutants considered in this study are mainly PM2.5. The PM2.5 monitoring station data comes from the China

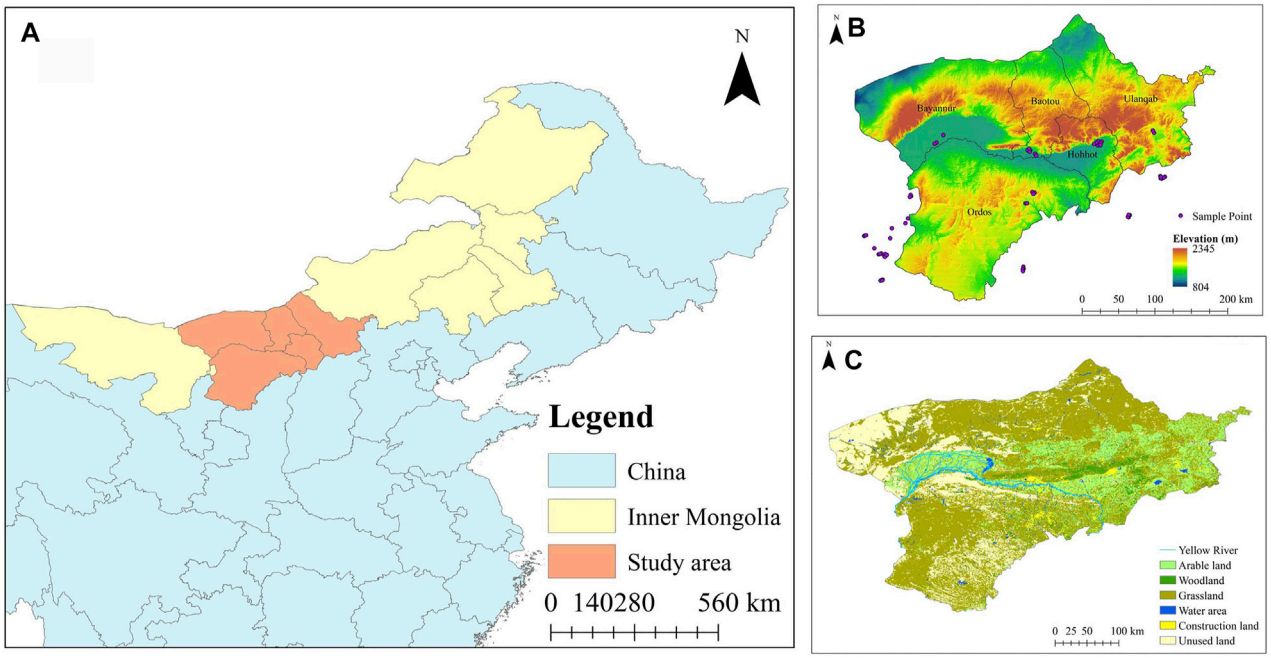


FIGURE 1
**(A)** Geographical location of the study area; **(B)** Surface elevation and PM2.5 monitoring stations in the study area; **(C)** Land use types in the study area.

National Environmental Monitoring Center (http://www.cnemc.cn). The data format is the mean daily PM2.5 concentration value, the concentration unit is μg/m$^3$, and the selected time range is 1 January 2016 to 31 December 2018. PM2.5 concentration data quality in line with China ambient air quality standards (Wang et al., 2010).

There are a total of 75 monitoring stations around the selected study area, and the distribution of the stations is shown in Figure 1B. In this study, the PM2.5 concentration value was used as the model dependent variable. In order to reduce the model error, the value of PM2.5 less than 2 μg/m$^3$ was discarded, and the stations with measurement days less than 10 days were also excluded. The monthly mean PM2.5 concentration value is calculated by calculating the monthly mean value from the daily mean PM2.5 concentration value of each station. Since the distribution of stations is too concentrated, 50 stations are randomly selected to build the PM2.5 estimation model, and the remaining 25 points are used for model accuracy verification.

### 2.2.2 MODIS AOD data

MODIS AOD data is a level 2 aerosol product released by NASA, which can be used to obtain atmospheric aerosol optical properties (such as optical thickness and size distribution) and mass concentration in the global ocean and terrestrial environment. In order to obtain higher spatial resolution PM2.5 pollution inversion results, we use MODIS Collection 061 3 km (cross-border time 10:30 and 13:30 Beijing time) aerosol data (https://ladsweb.modaps. eosdis. nasa.gov/), select daily AOD data with a resolution of 3 km from January 2016 to December 2018, and use the layer name: Optical_Depth_Land_And_Ocean (AOT at 0.55 micron for both ocean (Mean) (Quality Flag) = 1, 2, 3) and land (corrected) (Quality Flag = 3)).

In this study, ENVI 5.3 was used to organize and calculate the monthly mean AOD data of MODIS AOD.

### 2.2.3 Meteorological data

We used the ERA-Interim (ECMWF Re-Analysis) reanalysis data (http://apps.ecmwf.int/datasets/) of the European Center for Medium-Range Weather Forecast (ECMWF) as the meteorological data. Its spatial resolution is 0.125° and its temporal resolution is Monthly Means of Daily Means. We selected a total of five meteorological factors in the Surface variable and Pressure levels variable: relative humidity (RH, %) under 1000 h Pa, temperature of 2 m (T2m, K), wind speed of 10 m (WS10, m/s), surface pressure (SP, Pa), boundary layer height (BLH, m).

### 2.2.4 Socioeconomic data

Due to the inconsistency of statistical indicators in various cities and incomplete data in some cities, the acquisition of data is subject to certain restrictions. Based on the overall integrity and

TABLE 1 Description of all data used in this study.

| Variable | Full name | Unit | Spatial resolution | Time resolution |
|---|---|---|---|---|
| PM2.5 | Particulate matter with aerodynamic equivalent diameter less than or equal to 2.5 microns | μg/m$^3$ | Station | Month |
| AOD | Aerosol Optical Depth, MODIS Collection 061 | | 3 km | Day |
| NDVI | Normalized Difference Vegetation Index | | 1 km | Month |
| DEM | Digital elevation model | m | 30 m | Year |
| RH | Relative humidity under RH 1000 h Pa | % | 0.125° | Month |
| T2m | 2 m temperature | K | 0.125° | Month |
| WS10 | 10 m wind speed | m/s | 0.125° | Month |
| SP | Surface pressure | Pa | 0.125° | Month |
| BLH | Boundary layer height | m | 0.125° | Month |
| UBA | Urban built-up area | km$^2$ | City | Year |
| PP | Permanent population | 10$^4$ people | City | Year |
| SIP | Secondary industry as a percentage of regional GDP | % | City | Year |
| PGDP | GDP per capita | yuan | City | Year |
| NIE | Number of industrial enterprises above designated size | units | City | Year |
| AGS | Annual gas supply | 10$^4$m$^3$ | City | Year |
| HS | heat supply (water) | 10$^4$J | City | Year |

availability of data, considering economic development, urbanization, industrialization, etc., the urban built-up area (km2), permanent population (10,000 people), and the proportion of the secondary industry in the regional GDP (%), GDP per capita (yuan), number of industrial enterprises above designated size (unit), annual gas supply (natural gas, 104m3) and heat supply (water, 104 GJ) are selected as independent variables to make the spatial relationship model between PM2.5 and socioeconomic factors. Influencing factor index data comes from the "2017–2019 Inner Mongolia Statistical Yearbook" published by the Inner Mongolia Bureau of Statistics (http://tj.nmg.gov.cn/tjyw/jpsj/). The 2017 Statistical Yearbook is actually an overview of 2016 in 2017. Similarly, the 2018 and 2019 Statistical Yearbooks represent the values of Inner Mongolia statistical data in 2017 and 2018, respectively.

### 2.2.5 Geographical data

In order to improve the accuracy of PM2.5 estimation, NDVI (Normalized Difference Vegetation Index) and DEM (Digital elevation model) are selected to provide reference for the research. The NDVI data comes from MODIS 3 level 1 km monthly NDVI data (https://ladsweb.modaps.eosdis.nasa.gov/). DEM data is selected from ASTGTM: ASTER Global Digital Elevation Model V002, with a resolution of 30 m (https://search.earthdata.nasa.gov/). All the above data can be sorted into Table 1.

### 2.2.6 Data preprocessing

In order to estimate the monthly PM2.5 data with a spatial resolution of 3 × 3 km, the data of different spatial sizes and time scales need to be processed uniformly, data integration, and uniform resolution. The IDL software is used to resample the meteorological factors with reference to the pixel size of the fused MODIS 3 km AOD data. The DEM data first uses the Arc GIS "mosaic" and "mask" tools to make the DEM coincide with the study area, and then uses ArcGIS 10.3 to downscale the DEM and NDVI data to 3 km.

## 2.3 Method

### 2.3.1 Geographically weighted regression model

Previous studies have shown that the relationship between PM2.5 and AOD will change differently with the change of geographical space, and there is spatial dependence and spatial non-stationary between PM2.5 and AOD. For this local variation GWR model, local variable parameters can be more accurately used to reflect the spatial variation and difference, and a continuous parameter value surface is generated (Engel-Cox et al., 2004; Hu et al., 2013). GWR is a regression model for testing continuous surface spatial variation and non-stationary problems of regression parameter values on a regional scale (Wang et al., 2020). Although AOD is the most significant indicator of PM2.5 concentration, PM2.5 concentration is also significantly affected by temperature, precipitation and other climatic factors (Lv and Li, 2018). AOD, RH, T2m, WS10, BLH, SP, DEM, and NDVI were used as auxiliary variables to estimate the spatial distribution of PM2.5 concentration.

Based on the significant spatial difference between PM2.5 and auxiliary variables, GWR was selected to test the

variation and non-stationarity of continuous surface of parameter values. Due to the serious loss of AOD daily data, in order to reduce the model error and improve the accuracy, this paper constructed the model on the monthly scale. The basic form of the model is shown in Eq. 1:

$$PM2.5_{im} = \beta_{0,im} + \beta_{1,im}AOD_{im} + \beta_{2,im}RH_{im} + \beta_{3,im}T2m_{im} + \beta_{4,im}WS10_{im} + \beta_{5,im}SP_{im} + \beta_{6,im}BLH_{im} + \beta_{7,im}DEM_{im} + \beta_{8,im}NDVI_{im} + \varepsilon_{im} \quad (1)$$

Where, $PM2.5_{im}$ (μg/m$^3$) is the PM2.5 concentration value of the i grid cell in the m month; $AOD_{im}$ (without unit) is the i grid cell of AOD in the m month, $T2m_{im}$, $WS10_{im}$, $RH_{im}$, $BLH_{im}$, $SP_{im}$ are the values of the i grid cell in the m month corresponding to other auxiliary variables; $\beta_{0,im}$ represents the intercept of the i grid cell in the m-month, $\beta_{1,im}$, $\beta_{2,im}$, $\beta_{3,im}$, $\beta_{4,im}$, $\beta_{5,im}$, $\beta_{6,im}$, $\beta_{7,im}$, and $\beta_{8,im}$ are the regression coefficients of the corresponding variable of the i grid cell in the m month, $\varepsilon_{im}$ is the random error of the I grid cell in the m month. The model is a local model, and the coefficients of the model will vary with the time and geographic location of the sample point.

Regarding the temporal heterogeneity relationship between PM2.5 and auxiliary variables, the auxiliary variables of the model are selected according to the following criteria: 1) the selected auxiliary variables are significantly related to PM2.5; 2) the selected auxiliary variables improve the model's inversion of PM2.5 spatiotemporal variation. In other words, under the influence of the temporal and spatial heterogeneity of PM2.5, the auxiliary variables used in the monthly GWR model are different, and the models constructed are also different.

In the process of model construction, the self-adaptive Gauss function is used to create the core surface according to the density of the relevant element distribution (Utari et al., 2019), and the cross-validation method proposed by Cleveland in 1979 is used (Zhai et al., 2018).

### 2.3.2 Accuracy evaluation index

In order to test the accuracy of PM2.5 estimation, the error between the actual observation value and the estimated value of the effective PM2.5 stations used for verification is used to judge the pros and cons of the model. The test indicators used are correlation coefficient (R), residuals (RD) and root mean square error (RMSE). R is used to measure the degree of agreement between the measured value and the estimated value, and the calculation method is shown in Eq. 2 (Machin et al., 2018). The closer the statistic is to 1, the higher the accuracy of the model result and the better the agreement between the measured value and the estimated value. RMSE is used to measure the deviation between the observed value and the true value, reflecting the estimation sensitivity and extreme value of sample data (Joseph and Agustí, 2021). The smaller the value of RMSE, the higher the accuracy of PM2.5 estimation. The calculation method is shown in Eq. 4.

$$R = \frac{\sum_i^n \left(Y_{oi} - \overline{Y_o}\right)\left(Y_{si} - \overline{Y_s}\right)}{\sqrt{\sum_i^n \left(Y_{oi} - \overline{Y_o}\right)^2}\sqrt{\sum_i^n \left(Y_{si} - \overline{Y_s}\right)^2}} \quad (2)$$

$$RD = Y_{oi} - Y_{si} \quad (3)$$

$$RMSE = \sqrt{\frac{\sum_{i=1}^n \left(Y_{oi} - \overline{Y_o}\right)^2}{n}} \quad (4)$$

Where, $Y_{si}$ is the i of PM2.5 estimated value, $Y_{oi}$ is the i of PM2.5 measured value; $\overline{Y_s}$ is the mean value of estimated PM2.5, $\overline{Y_o}$ is the mean value of measured PM2.5, n is number of samples.

### 2.3.3 Geographic detector

Geographic detector is a new statistical method for detecting spatial differentiation and revealing the driving factors behind it (Wang and Xu, 2017). The basic idea is: assuming that the study area is divided into several sub-regions, if the sum of the variances of the sub-regions is less than the total area variance, there is spatial differentiation; if the spatial distribution of the two variables tends to be the same, there is a statistical correlation between the two. There are four sub-detectors in the geographic detector. This article analyzes the results of factor detectors. Factor detector explore the spatial differentiation of Y, and detect the degree of interpretation of the factor X to the spatial differentiation of Y (Wang and Xu, 2017). Measured by the q value, the expression is:

$$q = 1 - \frac{\sum_{h=1}^L N_h \sigma_h^2}{N\sigma^2} \quad (5)$$

Where, h = 1, 2, 3. . . L is the stratification of variable Y or factor X. There are seven types of variables in this article; $N_h$ and N are the number of units in the whole domain and a certain layer, respectively. In this article, they represent central Inner Mongolia total number of units and the number of units in each type of prefecture-level city; and are the variances of the Y values of layer h and the whole region, respectively.

In order to analyze the seasonal effects of socioeconomic factors on PM2.5, a year was divided into four seasons. The classification criteria are: spring from March to 359 May, summer from June to August, autumn from September to November, and winter from December 360 to January and February of the following year.

## 3 Results and analysis

### 3.1 Analysis of model results

#### 3.1.1 Model construction results

The correlation matrix between different explanatory variables and PM2.5 from January to December in central

TABLE 2 Unsigned correlation matrix between different explanatory variables and PM2.5 from January to December.

| Month | AOD | RH | T2m | WS10 | BLH | SP | DEM | NDVI |
|---|---|---|---|---|---|---|---|---|
| 1 | 0.122 | 0.588** | 0.507* | 0.382* | 0.216* | 0.100 | 0.178 | 0.235* |
| 2 | 0.271 | 0.121 | 0.474* | 0.297* | 0.149 | 0.161 | 0.136 | 0.258* |
| 3 | 0.584** | 0.632 | 0.508 | 0.203 | 0.305 | 0.223 | 0.370 | 0.148 |
| 4 | 0.406* | 0.443* | 0.212 | 0.462* | 0.492* | 0.350* | 0.138 | 0.111 |
| 5 | 0.196 | 0.211 | 0.258* | 0.109 | 0.330* | 0.152 | 0.261* | 0.188 |
| 6 | 0.155 | 0.510* | 0.287 | 0.457* | 0.565** | 0.255 | 0.273 | 0.120 |
| 7 | 0.172 | 0.331* | 0.254* | 0.325* | 0.401* | 0.260 | 0.216 | 0.118 |
| 8 | 0.655** | 0.366 | 0.324 | 0.726** | 0.455* | 0.261 | 0.337 | 0.117 |
| 9 | 0.284 | 0.413* | 0.648** | 0.655* | 0.687* | 0.629* | 0.303 | 0.331 |
| 10 | 0.347 | 0.285 | 0.404* | 0.527* | 0.297 | 0.324 | 0.482* | 0.214 |
| 11 | 0.570** | 0.620** | 0.594* | 0.137 | 0.574* | 0.324 | 0.465* | 0.151 |
| 12 | 0.141 | 0.410* | 0.540* | 0.368* | 0.169 | 0.191 | 0.118 | 0.188 |
| Mean | 0.325* | 0.411* | 0.417* | 0.387* | 0.387* | 0.269 | 0.273 | 0.181 |

Note: * is sig <0.05, ** is sig <0.01.

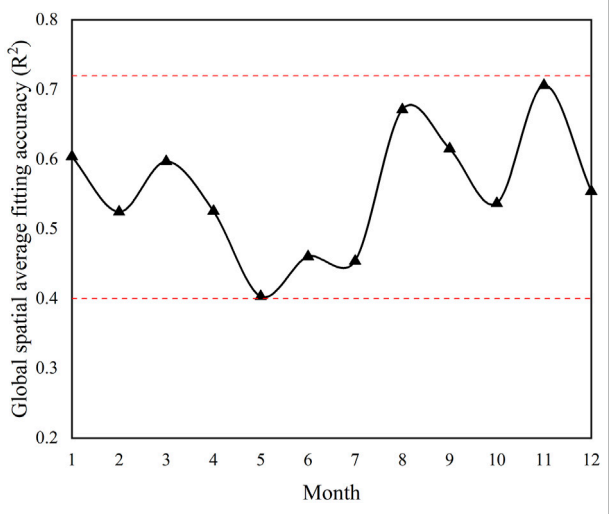


FIGURE 2
The average fitting accuracy of the models in the study area from 2016 to 2018.

Inner Mongolia from 2016 to 2018 is shown in Table 2. It can be observed that the variable with the highest correlation coefficient with PM2.5 is T2m, followed by RH, and NDVI has the lowest correlation coefficient. In addition, we found that although the monthly mean correlations of AOD, WS10 and BLH with PM2.5 were not high; in some months, their correlations also had significant advantages over other variables. For example, in August, the correlation coefficient of AOD reached 0.655, and that of WS10 reached 0.726, which was significantly higher than other variables in the same month; in June and October, the correlation coefficient of BLH reached 0.565 and 0.574, respectively. Therefore, for the explanatory variables of the GWR model in central Inner Mongolia, we choose T2m, RH, AOD, WS10, and BLH.

The global mean fit ($R^2$) of the 12 GWRs in central Inner Mongolia from January to December 2016–2020 constructed in this study is shown in Figure 2. It can be found from the figure that 1) throughout the study period, the global mean build $R^2$ of GWR was higher than 0.40, with the highest value reaching 0.71. In other words, the GWR model constructed in this study has a high degree of fit. 2) The fit of the model from May to July was generally inferior to other models, indicating that the explanatory variables of PM2.5 concentration in these months were complex and affected by multiple factors. The model fitting $R^2$ of August, September, and November is higher than that of other months, indicating that the model has fully considered the main explanatory variables of PM2.5 concentration in that month, so the fitting degree is higher, which makes the results more believable.

### 3.1.2 Model verification results

The verification data is used to verify the accuracy of the PM2.5 inversion results in the study area. The verification diagram is shown in Figure 3. From the figure, we can find: 1) The change of the monthly mean correlation coefficient R in the verification parameters in 2016–2018 is relatively stable, between 0.58–0.66; 2) The monthly mean correlation coefficients R from August to December and January to March in the 3 years are extremely stable, and fluctuate greatly from April to July. Therefore, it is predicted that the spatial heterogeneity of the simulation results from April to July is relatively large. 3) The monthly mean RMSE of the verification parameters fluctuated greatly from 2016 to 2018, from 4.0 to 15.0; 4) The RMSE of September to December and January of the

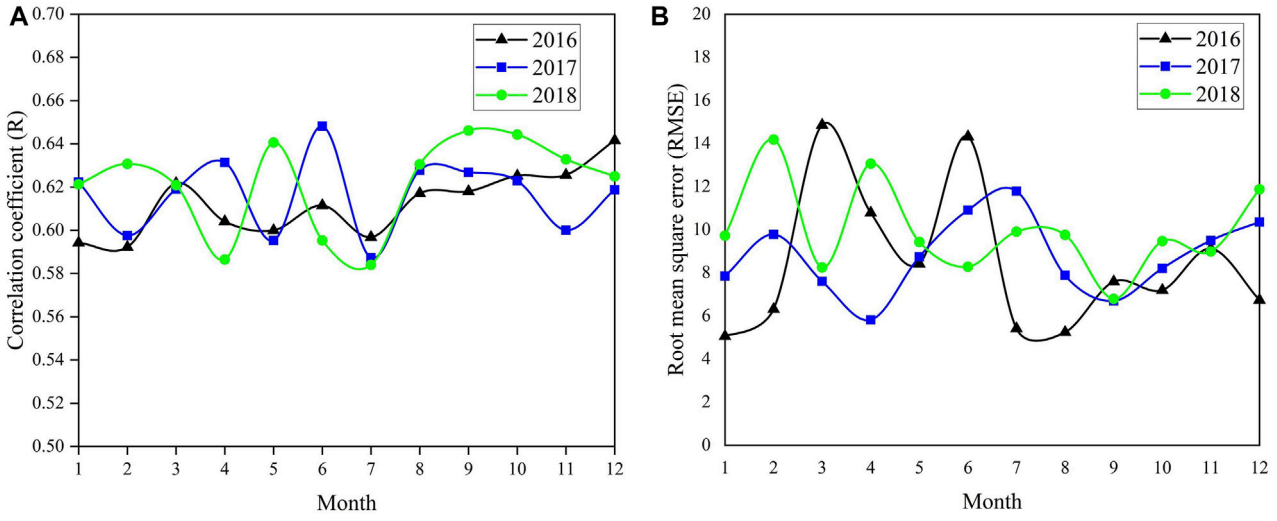


FIGURE 3
Model accuracy verification results in the study area: **(A)** Monthly average correlation coefficient between measured data and inverted data; **(B)** Monthly average root mean square error of measured data and inverted data (μg/m$^3$).

following year fluctuated little in the 3 years, and the RMSE from February to July fluctuates greatly, which is similar to the rule of (2). Therefore, it is guessed that the spatial heterogeneity of the PM2.5 concentration simulation results from February to July is relatively large.

The comparison between the measured value and the predicted value of the verification point is shown in Supplementary Appendix Figure S1. From the figure we can find that all verification points are evenly distributed on both sides of the dotted axis ($y = x$). Our model validation results are good. Supplementary Appendix Figure S2 shows the residual probability distribution. The validation residuals for all months were normally distributed. The constructed model conforms to statistical laws. In addition, the residual probability distribution in July-October is more compact. Combining Supplementary Appendix Figure S1 and Figure 3B, we find that the comprehensive RMSE of July-October is also smaller, and the verification points are more concentrated. It shows that the model adaptability from July to October is better.

## 3.2 Analysis of the temporal and spatial changes of PM2.5 concentration

### 3.2.1 The spatial variation of PM2.5 concentration

The distribution of monthly PM2.5 patterns estimated by the GWR model is presented in a later chapter. We superimposed the PM2.5 data in different months from 2016 to 2018 to calculate the annual mean, and obtained the spatial distribution pattern of the annual mean PM2.5 concentration in the study area from 2016 to 2018 (Figure 4). The annual mean PM2.5 distribution map can more directly observe the spatial distribution law. It can be found from Figure 4 that the spatial distribution pattern of the annual mean concentration of PM2.5 from 2016 to 2018 is basically the same, with obvious spatial differentiation. The 3-years mean PM2.5 concentration in the study area fluctuated between 5 and 30 μg/m$^3$. Comparing the ground elevation and land use in the study area (Figures 1B,C), the spatial distribution of PM2.5 concentration in the study area is similar to the distribution of ground elevation and land use. Combining the land use and ground elevation of the study area, we found that: 1) Ground elevation was negatively correlated with the annual mean PM2.5 concentration. The higher the ground elevation, the lower the PM2.5 concentration. 2) The distribution of annual mean PM2.5 concentration also has a certain correlation with the distribution of land use types. The area above the lake is the place with the lowest PM2.5 concentration in the entire study area; secondly, the annual mean PM2 above the cultivated land far away from the tributaries of the Yellow River. The concentration of PM2.5 is also low; the annual mean PM2.5 concentration over the unused land is the highest.

In addition, we can observe from Figure 4: 1) From 2016 to 2018, the central and southern parts of Ulanqab, the northeastern end of Hohhot, and the southeastern end of Baotou were the lowest in the study area (central Inner Mongolia). 2) The annual mean PM2.5 concentration along the Yellow River Basin in Bayannur is the highest in the study area. 3) The mean annual PM2.5 along the Yellow River Basin in the northern section of Ordos is also high. 4) On the whole, the mean annual

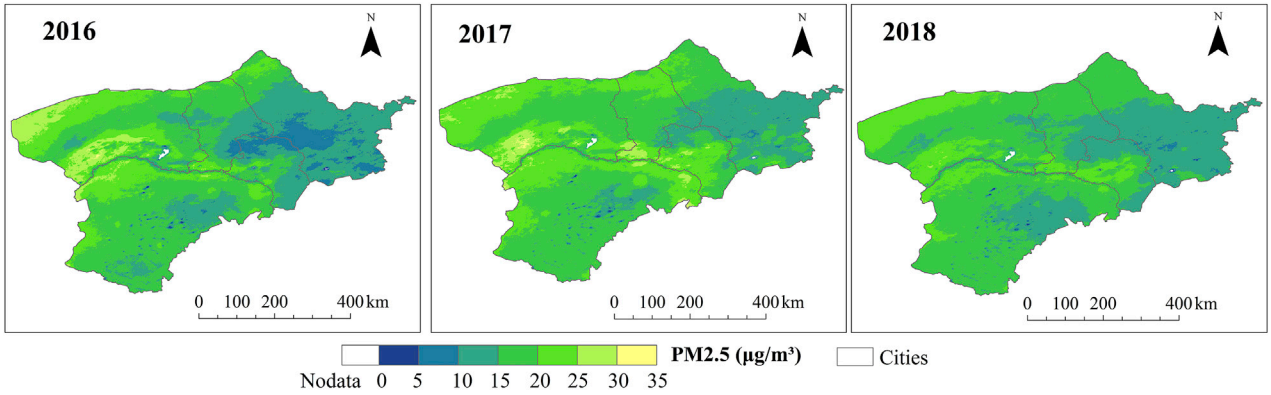


FIGURE 4
The spatial distribution of the average annual PM2.5 concentration in the study area from 2016 to 2018.

TABLE 3 Description of the statistical characteristics of the annual mean PM2.5 concentration (μg/m³) of cities in central Inner Mongolia from 2016 to 2018.

| Year | Bayannur | Baotou | Ordos | Ulanqab | Hohhot | Mean |
|---|---|---|---|---|---|---|
| 2016 | 21.24 | 16.67 | 17.82 | 14.51 | 14.90 | 17.03 |
| 2017 | 21.06 | 18.71 | 18.53 | 15.00 | 18.79 | 18.42 |
| 2018 | 18.77 | 16.07 | 16.65 | 13.80 | 16.18 | 16.30 |
| Annual mean | 20.36 | 17.15 | 17.66 | 14.44 | 16.63 | 17.25 |

PM2.5 concentration of central Inner Mongolia from 2016 to 2018 was the lowest in the east, increasing in order to the west, lower in the south, and gradually increasing to the northwest.

## 3.2.2 Analysis of PM2.5 concentration time change

### 3.2.2.1 Annual change

Table 3 describes the statistical characteristics of the annual mean PM2.5 concentration in the study area from 2016 to 2018. It can be directly observed from the table that 1) Bayannur is the city with the highest annual mean concentration of PM2.5 in central Inner Mongolia, followed by Ordos and Baotou. Hohhot has a lower annual PM2.5 concentration, and Ulanqab has the lowest annual PM2.5 concentration. Most cities exceed the China national mean PM2.5 level 1 standard [(GB3095-2012) "Ambient Air Quality Standard" (Wang et al., 2010), the annual mean PM2.5 concentration limit is 15 μg/m³ at level 1 and 35 μg/m³ at level 2]. The mean annual PM2.5 concentration in all cities is greater than the health standard recommended by the World Health Organization (WHO Air Quality Guidelines), that is, the mean annual PM2.5 concentration is 5 μg/m³ (Ouyang et al., 2022). 2) The mean annual concentration of PM2.5 in the study area in 2016 was 17.03 μg/m³, the mean annual concentration of PM2.5 in the study area in 2017 was 18.42 μg/m³, and the mean annual concentration of PM2.5 in the study area in 2018 was 16.30 μg/m³. In the 3 years from 2016 to 2018, the overall concentration value in 2017 was also the highest. 3) From

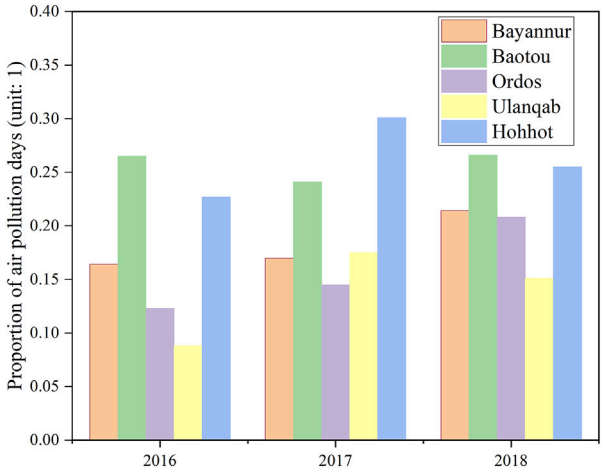


FIGURE 5
Percentage of air pollution days in central Inner Mongolia cities from 2016 to 2018.

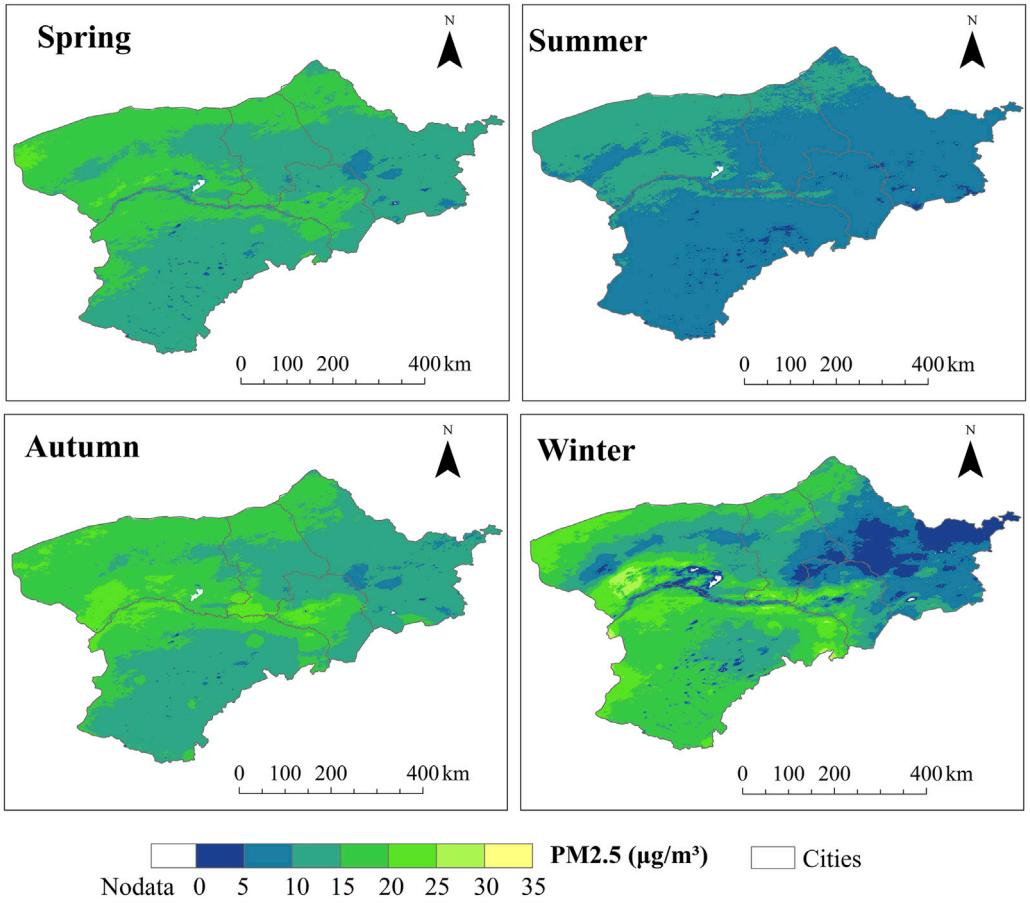


FIGURE 6
Spatial distribution of seasonal average PM2.5 concentration from 2016 to 2018.

2016 to 2018, it generally increased first and then decreased. Except for Bayannur, which has been declining, other cities also increased first and then decreased.

At the same time, we calculated the percentage of air pollution days in central Inner Mongolia cities from 2016 to 2018 to the number of days in the whole year, as shown in Figure 5. From the figure, we can find that the proportion of air pollution days in Baotou and Hohhot in the past 3 years is higher than 0.20, especially in 2017, the proportion of Hohhot is higher than 0.3. Compared with the other four cities, Ulanqab has a lower proportion of polluted days, but it is also higher than 0.1. As a result, cities in central Inner Mongolia are plagued by air pollution.

### 3.2.2.2 Seasonal change

The central part of Inner Mongolia has a continental monsoon arid climate with four distinct seasons. In addition, the region's economic development is faster than other regions in Inner Mongolia, and has obvious seasonal characteristics, which has an important impact on the seasonal distribution of PM2.5, so it is necessary to study and analyze the seasonal changes of PM2.5 concentration. According to the monthly mean PM2.5 concentration data in the study area from 2016 to 2018, the mean PM2.5 concentration values of the corresponding seasons are calculated for many years. Figure 6 shows the spatial distribution of seasonal mean PM2.5 from 2016 to 2018. It can be seen from the figure that the highest seasonal mean PM2.5 concentration value for many years occurs in winter, and the spatial variation of the seasonal mean PM2.5 concentration value in winter is also the largest. The PM2.5 concentration value is the smallest in summer, and is at the intermediate level in spring and autumn. The seasonal mean concentration of PM2.5 has high value areas, which are concentrated in the Yellow River Basin in the northern part of Bayannur and along the banks of the Yellow River Basin in other cities, especially in autumn and winter.

Figure 7 shows the change of the seasonal mean concentration of PM2.5 in the cities of central Inner Mongolia from 2016 to 2018. It can be found from the figure that the seasonal variation of PM2.5 concentration in

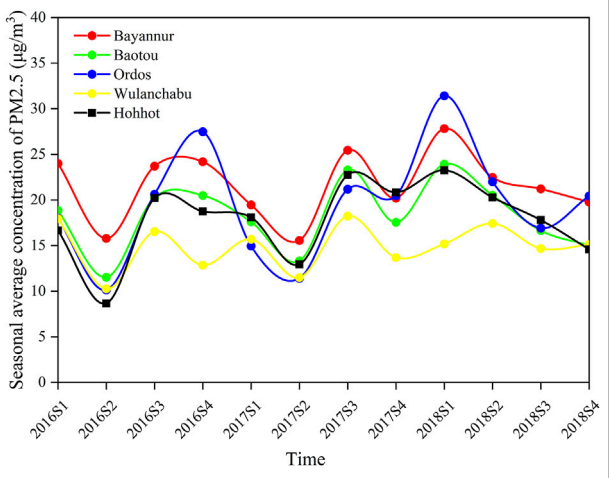


FIGURE 7
The seasonal variation of PM2.5 concentration of cities in central Inner Mongolia.

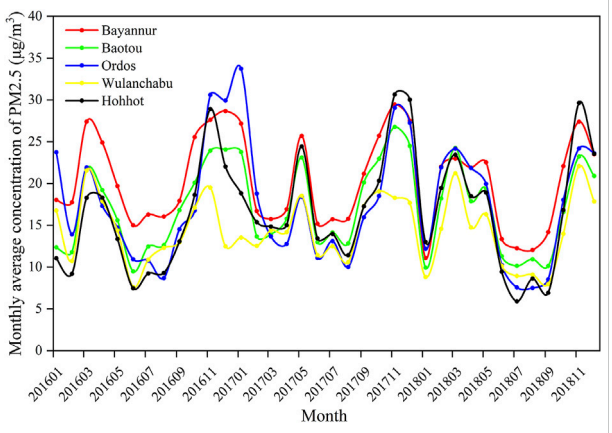


FIGURE 8
The monthly average change of PM2.5 concentration in cities from 2016 to 2018.

the five cities is basically the same. The mean PM2.5 concentration in the three seasons of spring, autumn and winter in each city is higher, and the lowest in summer. However, starting from the summer of 2018, the seasonal mean concentration of PM2.5 in all cities began to decline. The mean PM2.5 of Bayannur in each season is mostly higher than that of other cities, except for Ordos in the winter of 2016 and spring of 2018. In the summer of 2016, all cities had the lowest mean PM2.5. In the fall of 2017 and the spring of 2018, the seasonal mean PM2.5 concentration of all cities was the highest in 3 years, especially in the spring of 2018.

#### 2.3.3.3 Monthly change

The spatial distribution pattern of the monthly mean concentration of PM2.5 in the study area from 2016 to 2018 from January to December can be found in the Supplementary Appendix Figures S3–S5. The monthly changes of PM2.5 concentration in the cities of central Inner Mongolia from 2016 to 2018 are shown in Figure 8. It can be seen from Figure 8 that the overall change patterns of the five cities are basically the same. November is the month with the most severe PM2.5 concentration in the urban agglomeration of central Inner Mongolia, followed by January, March, and May. In addition, June and September are months with lower PM2.5 concentrations.

The monthly mean concentration of PM2.5 in most areas of central Inner Mongolia from June to September was lower than 20 μg/m$^3$, and the pollution was relatively small. In January, the concentration of PM2.5 was highest in southwestern Bayannur, southern Baotou, and northeastern Ordos; starting from February, the overall PM2.5 concentration value slowed down and drifted laterally along the main stream of the Yellow River; until October, the PM2.5 concentration value began to increase significantly, and continued to decay around the main stream of the Yellow River, reaching the highest month of the overall PM2.5 concentration distribution in the study area in November and December. In addition, other spatial distribution laws are consistent with the above-mentioned characteristics of annual and seasonal changes of PM2.5.

## 3.3 Analysis of driving factors

Using factor detectors to determine the influence degree of each influencing factor on the seasonal variation of PM2.5, the results are shown in Table 4. It can be seen from Table 4 that, overall, the single factor that has the greatest impact on the seasonal concentration of PM2.5 is the urban built-up area (UBA, $q = 0.386$), followed by the permanent population (PP, $q = 0.340$), the least impact is the number of industrial enterprises above designated size (NIE, $q = 0.016$). In addition, the concentration of PM2.5 varies in different seasons, and the impact factors are naturally also inconsistent. In spring, the most explanatory factor is the permanent population, followed by the urban built-up area and heat supply. In summer, the most explanatory factor is GDP per capita (PGDP), followed by the area of urban built-up areas and the number of industrial enterprises above designated size. In autumn, the most explanatory factor is the area of urban built-up areas (UBA). In winter, except for per capita GDP (PGDP) and the number of industrial enterprises above designated size (NIE), other factors have a high degree of explanation. The most explanatory factor in winter and spring is the permanent population (PP, $q = 0.728$), followed by heat supply (HS, $q = 0.562$) and urban built-up area (UBA, $q = 0.536$).

TABLE 4 Explanation degree of different social factors to PM2.5 concentration changes.

| Factor | UBA | PP | SIP | PGDP | NIE | AGS | HS |
|---|---|---|---|---|---|---|---|
| spring | 0.613** | 0.679* | 0.208 | 0.057 | 0.141 | 0.413* | 0.564** |
| summer | 0.328* | 0.158 | 0.110 | 0.461** | 0.259* | 0.023 | 0.202 |
| autumn | 0.369* | 0.138 | 0.058 | 0.260* | 0.072 | 0.001 | 0.019 |
| winter | 0.386* | 0.626** | 0.599* | 0.087 | 0.083 | 0.438* | 0.457** |
| spring + winter | 0.536** | 0.728** | 0.496* | 0.084 | 0.008 | 0.481* | 0.562** |
| Overall | 0.386* | 0.340* | 0.151 | 0.334* | 0.016 | 0.125 | 0.292** |

Note: * is sig <0.05, ** is sig <0.01.

TABLE 5 Explanation Degree of Different Social Factors to PM2.5 Concentration Changes in different cities.

| Factor | UBA | PP | SIP | PGDP | NIE | AGS | HS |
|---|---|---|---|---|---|---|---|
| Bayannur | 0.998** | 0.985** | 0.636* | 0.045 | 0.654** | 0.955** | 0.763* |
| Baotou | 0.533** | 0.051 | 0.299 | 0.951* | 0.354* | 0.101 | 0.283 |
| Ordos | 0.927** | 0.540* | 0.244 | 0.456* | 0.341 | 0.182 | 0.603* |
| Ulanqab | 0.128 | 0.520 | 0.899** | 0.586** | 0.108 | 0.249 | 0.795** |
| Hohhot | 0.808** | 0.683** | 0.024 | 0.014 | 0.829** | 0.503 | 0.370 |

Note: * is sig <0.05, ** is sig <0.01.

We calculated the influence degree of each impact factor on the annual PM2.5 of different cities, and the results are shown in Table 5. From the table, we can find that the main social factors affecting PM2.5 are different for different cities. Among them, for Bayannur, except for per capita GDP (PGDP, $q = 0.045$), other factors have a very high degree of explanation. However, in Baotou, the per capita GDP (PGDP) is highly explanatory, followed by the urban built-up area. In Ordos, the most explanatory factors are the urban built-up area (UBA), heat supply (HS), and permanent population (PP). In Ulanqab, the most explanatory factors are the proportion of secondary industry (SIP), heat supply (HS), per capita GDP (PGDP), and permanent population (PP). In Hohhot, the most explanatory factors are the number of units of industrial enterprises (NIE), urban built-up area (UBA), permanent population (PP), and annual gas supply (AGS). This is related to the development of different cities and pillar industries.

## 4 Discussion

We choose this time period and build the model month by month. Although there are only three distinct years for a month, we have 50 data for modeling for each year, for a total of 150 modeling data for each month. Increasing the year can make the model generalize better, but at the same time too many variables and data can lead to degraded computing performance and data redundancy. So we chose this typical time period. On the other hand, 2016–2018 is the final stage to complete the action plan for air pollution prevention and control.

The central area of Inner Mongolia is cold and dry in winter, consumes a large amount of coal (Zheng et al., 2018), and increases the number of car trips, which increases the concentration of PM2.5 in the air, so the PM2.5 in winter is extremely high. In summer, there is more rain, which has a certain purification effect on pollutants in the air. The vegetation coverage in summer also reaches the highest level, so the concentration of PM2.5 in summer is low (Junyan Yang et al., 2020). In spring and autumn, it is windy and there is more sand and dust in the air (Gao et al., 2018). Especially in spring, when sandstorms are reported, PM2.5 is also high. This is basically consistent with our previous results.

The surface of the alluvial plain of the Yellow River is flat and the terrain is open. Except that the roughness of the surface affects the atmospheric turbulence near the ground, the air flow does not have much interference (Zhuorui Wei et al., 2021). Under normal circumstances, pollutants will diffuse according to the Gaussian diffusion model (Tee et al., 2020). As the Yin Mountains, which run east-west and have an altitude of more than 1000 m along the Yellow Plain, are distributed to the north of the Yellow River, which prevents the diffusion of pollutants from strong winds. Therefore, the concentration of air pollutants in the northern part of Ordos and the southern part of Bayannur is slightly higher.

The most important factor affecting PM2.5 concentration in central Inner Mongolia from 2016 to 2018 was the urban built-up

areas. In other words, urbanization was the main factor affecting PM2.5 pollution in central Inner Mongolia during this period. There are a certain number of industrial parks in the urban areas of central Inner Mongolia, and the growth rate of green area is not enough to offset the growth rate affected by urban development. In addition, car ownership is high in this area, and car emissions can also cause pollution (Khuzestani et al., 2017). Therefore, in the process of urbanization, we must pay attention to the prevention and control of air pollution, and plan the urban layout according to the different economic and natural conditions of each city. The number of permanent residents and per capita GDP are also important influencing factors of PM2.5 pollution. In the process of economic development, we must pay attention to pollution prevention and control, appropriately adjust the industrial structure, and develop public transportation.

Heat supply is an extremely important factor influencing PM2.5 pollution in winter and spring in central Inner Mongolia. The peak heating period in this area is from October of the current year to the beginning of May of the following year, and the heating period is as long as 6 months. Air pollution is mainly concentrated in spring and winter. At the turn of spring and summer, the pollution will continue to reduce. When the autumn and winter alternate, the pollution will increase again. The burning of a large amount of coal during the heating process in winter is the main reason for the increase of air pollution in winter (Khuzestani et al., 2017; Khuzestani et al., 2018). Therefore, the government should actively and orderly promote new energy, rationally and effectively use clean energy, reduce the use of coal, and look for alternatives such as electricity and natural gas.

## 5 Conclusion

In this paper, the central region of Inner Mongolia was selected as the study area, and the factor with the greatest correlation with monthly PM2.5 concentration from 2016 to 2018 was selected from multiple factors to establish a GWR model and invert the spatial distribution data of PM2.5 concentration from 2016 to 2018. In this study, the spatial and temporal (annual, seasonal, and monthly) spatial distribution characteristics of PM2.5 concentration in cities of central Inner Mongolia were analyzed, and the impact on PM2.5 concentration was analyzed from the aspects of economic development, urbanization, industrialization and energy. The results of this paper provide a theoretical basis for air pollution monitoring, management and prevention in central Inner Mongolia.

This study investigated the temporal and spatial distribution characteristics of PM2.5 concentration in central Inner Mongolia from 2016 to 2018 and the impact of social and economic factors on it. First, a geographically weighted regression model considering the heterogeneity of time and space was established to describe the time and space pattern of PM2.5 concentration in the study area. Then we used geographic detectors to determine the impact of socio-economic factors on PM2.5. The main conclusions of this study include:

1. There is significant temporal and spatial heterogeneity between PM2.5 concentration and the selected auxiliary variables. The established model can better estimate the spatial distribution of PM2.5 concentration in the study area. The variation of the monthly mean correlation coefficient R in the verification parameters is relatively stable, between 0.58–0.66.
2. PM2.5 concentration in central Inner Mongolia showed significant temporal and spatial changes. The annual mean PM2.5 concentration along the Yellow River Basin is the highest in the study area. Although the PM2.5 concentration increased first and then decreased, it was still higher than the China national quality standard. Therefore, further reducing the PM2.5 concentration is still a huge challenge.
3. Urban built-up area, permanent population and per capita GDP are the key factors affecting the temporal and spatial distribution of PM2.5 concentration in the study area. In addition, the influencing factors of PM2.5 concentration changes in different seasons are inconsistent. In winter and spring, heat supply is also an extremely important factor.

## Data availability statement

The raw data supporting the conclusion of this article will be made available by the authors, without undue reservation.

## Author contributions

JW: Model construction, sub-analysis of results; investigation; validation; writing-original draft; writing-review and editing. DL: Conceptualization; Methods; writing-review and editing. XX: Conceptualization; data management; results analysis; investigation; Software. JM: Writing-review and editing; LH: Writing-review and editing.

## Funding

This research is funded by the National Natural Science Foundation of China (No. 42067013), the Program for Young Talents of Science and Technology in Universities of Inner Mongolia Autonomous Region (No. NJYT-19-A18), and the China Scholarship Council Study Abroad Program.

## Acknowledgments

Authors would like to thank the China Environmental Monitoring Station for the daily mean PM2.5 concentration

value stations data set, the MODIS AOD/NDVI data released by NASA, and the ERA-Interim climate data released by the European Center for Mid-range Weather Forecast. Authors are grateful for the funding support of the Youth Science and Technology Leading Talents Project of Higher Education Institutions in Inner Mongolia Autonomous Region. Authors sincerely thank the reviewers and journal editors for their pertinent comments and valuable suggestions.

## Conflict of interest

The authors declare that the research was conducted in the absence of any commercial or financial relationships that could be construed as a potential conflict of interest.

## Publisher's note



## Supplementary material

The Supplementary Material for this article can be found online at: https://www.frontiersin.org/articles/10.3389/fenvs.2022.893437/full#supplementary-material

## References

Analitis, A., Barratt, B., Green, D., Beddows, A., Samoli, E., Schwartz, J., et al. (2020). Prediction of PM2.5 concentrations at the locations of monitoring sites measuring PM10 and NOx, using generalized additive models and machine learning methods: A case study in london. *Atmos. Environ.* 240 (6), 117757. doi:10.1016/j.atmosenv.2020.117757

Bai, M., Hao, R., Li, X., Di, R., Yang, J., and Liu, H. (2010). Variation characteristics and prediction methods of heating period in Inner Mongolia. *Meteorol. Sci. Technol.*, 38 (06), 709–714. doi:10.19517/j.1671-6345.2010.06.009

Bai, L., Wang, J., Ma, X., and Lu, H. (2018). Air pollution forecasts: An overview. *Int. J. Environ. Res. Public Health* 15 (4), 780. doi:10.3390/ijerph15040780

Casallas, A., Ferro, C., Celis, N., Guevara-Luna, M. A., Mogollon-Sotelo, C., Guevara-Luna, F. A., et al. (2021). Long short-term memory artificial neural network approach to forecast meteorology and PM2.5 local variables in Bogota, Colombia. *Model. Earth Syst. Environ* 09, 1–14. doi:10.1007/s40808-021-01274-6

Domenici (1979). Clean air Act amendments of 1977. *Nat. Resour. J.* 19.

Engel-Cox, J., Holloman, C., Coutant, B., and Hoff, R. (2004). Qualitative and quantitative evaluation of MODIS satellite sensor data for regional and urban scale air quality. *Atmos. Environ.* 38, 2495–2509. doi:10.1016/j.atmosenv.2004.01.039

Esworthy, R. (2014). *Air quality: EPA'S 2013 changes to the particulate matter (PM) standard*, 157–208.

Gao, J., Wang, K., Wang, Y., Liu, S., Zhu, C., Hao, J., et al. (2018). Temporal-spatial characteristics and source apportionment of PM2.5 as well as its associated chemical species in the Beijing-Tianjin-Hebei region of China. *Environ. Pollut.* 233, 714–724. doi:10.1016/j.envpol.2017.10.123

Gao, W., Zhu, L., Ma, Z., Gao, Q., Yu, X., Wu, S., et al. (2021). Particulate matter trends and quantification of the spring sand-dust contribution in Hohhot, Inner Mongolia, from 2013 to 2017. *Atmos. Ocean. Sci. Lett.* 14 (2), 100036. doi:10.1016/j.aosl.2021.100036

Guan, W.-J., Zheng, X.-Y., Chung, K. F., and Zhong, N.-S. (2016). Impact of air pollution on the burden of chronic respiratory diseases in China: Time for urgent action. *Lancet* 388 (10054), 1939–1951. doi:10.1016/S0140-6736(16)31597-5

Guo, Y., and Wu, T. (2011). Analysis on the economic development of Hubao'e urban agglomeration and its intergovernmental relations. *J. Finance Econ. Theory* 17 (03), 98–103. doi:10.3969/j.issn.1004-5295.2011.03.021

Haijun, Z., Xiu, W., Tao, L., Xingjun, Z., and Feng, H. (2020). Air pollution characteristics of xilinhot in 2019. *J. Inn. Mong. Normal Univ. Sci. Ed.* 49 (06), 475–482. doi:10.3969/j.issn.1001-8735.2020.06.002

He, Q. Q., and Huang, B. (2018a). Satellite-based high-resolution PM2.5 estimation over the Beijing-Tianjin-Hebei region of China using an improved geographically and temporally weighted regression model. *Environ. Pollut.* 236, 1027–1037. doi:10.1016/j.envpol.2018.01.053

He, Q. Q., and Huang, B. (2018b). Satellite-based mapping of daily high-resolution ground PM2.5 in China via space-time regression modeling. *Remote Sens. Environ.* 206, 72–83. doi:10.1016/j.rse.2017.12.018

Hu, X., Waller, L. A., Al-Hamdan, M. Z., Crosson, W. L., Estes, M. G., Jr., Estes, S. M., et al. (2013). Estimating ground-level PM2.5 concentrations in the southeastern US using geographically weighted regression. *Environ. Res.* 121, 1–10. doi:10.1016/j.envres.2012.11.003

Jain, S., Presto, A. A., and Zimmerman, N. (2021). Spatial modeling of daily PM2.5, NO2, and CO concentrations measured by a low-cost sensor network: Comparison of linear, machine learning, and hybrid land use models. *Environ. Sci. Technol.* 55 (13), 8631–8641. doi:10.1021/acs.est.1c02653

Joseph, S., and Agustí, P. (2021). Compositional spatio-temporal PM2.5 modelling in wildfires. *Atmosphere* 12, 1309. doi:10.3390/atmos12101309

Juliette, R.-P., Perdrix, E., Sobanska, S., and Bremard, C. (2008). PM10 air quality variations in an urbanized and industrialized harbor. *Atmos. Environ.* 42 (31), 7274–7283. doi:10.1016/j.atmosenv.2008.07.005

Junyan Yang, J., Shi, B., Shi, Y., Marvin, S., Zheng, Y., and Xia, G. (2020). Air pollution dispersal in high density urban areas: Research on the triadic relation of wind, air pollution, and urban form. *Sustain. Cities Soc.* 54, 101941. doi:10.1016/j.scs.2019.101941

Khuzestani, R. B., Schauer, J. J., Wei, Y., Zhang, L., Cai, T., Zhang, Y., et al. (2017). Quantification of the sources of long-range transport of PM2.5 pollution in the Ordos region, Inner Mongolia, China. *Environ. Pollut.* 229, 1019–1031. doi:10.1016/j.envpol.2017.07.093

Khuzestani, R. B., Schauer, J. J., Shang, J., Cai, T., Fang, D., Wei, Y., et al. (2018). Source apportionments of PM2.5 organic carbon during the elevated pollution episodes in the Ordos region, Inner Mongolia, China. *Environ. Sci. Pollut. Res.* 25 (13), 13159–13172. doi:10.1007/s11356-018-1514-4

Kong, L., Tan, Q., Feng, M., Qu, Y., An, J., Liu, X., et al. (2020). Investigating the characteristics and source analyses of PM2.5 seasonal variations in Chengdu, Southwest China. *Chemosphere* 243, 125267. doi:10.1016/j.chemosphere.2019.125267

Lin, C., Li, Y., Yuan, Z., Lau, A. K. H., Li, C., and Fung, J. C. H. (2015). Using satellite remote sensing data to estimate the high-resolution distribution of ground-level PM2.5. *Remote Sens. Environ.* 156, 117–128. doi:10.1016/j.rse.2014.09.015

Liu, J. (2002). Integrate into "great beijing" and develop inner Mongolia. *North. Econ.* 01 (06), 10–11.

Liu, Q., Yang, Y., and Liu, H. (2020). Spatiotemporal evolution characteristics of air pollution degree of in 366 cities of China. *Arid. Land Geogr.* 43 (03), 820–830. doi:10.12118/j.issn.1000-6060.2020.03.28

Liu, N., Zou, B., Li, S. X., Zhang, H. H., and Qin, K. (2021). Prediction of PM2.5 concentrations at unsampled points using multiscale geographically and temporally weighted regression. *Environ. Pollut.* 284, 117116. doi:10.1016/j.envpol.2021.117116

Liu, G., Sun, S., Zou, C., Wang, B., Wu, L., and Mao, H. (2022). Air pollutant emissions from on-road vehicles and their control in Inner Mongolia, China. *Energy* 238, 121724. doi:10.1016/j.energy.2021.121724

Lv, W., and Li, L. (2018). PM2.5 pollution characteristics in main observation stations in hubei and the impact analysis of meteorological factors. *Ecol. Environ. Sci.* 27 (11), 2073–2080. doi:10.16258/j.cnki.1674-5906.2018.11.013

Machin, D., Campbell, M., Tan, S., and Tan, S. (2018). *The correlation coefficient*, 305–315.

McNaughton, N. (2018). *European Union issues*.

Meng, X., Wu, Y., Pan, Z., Wang, H., Yin, G., and Zhao, H. (2019). Seasonal characteristics and particle-size distributions of particulate air pollutants in Urumqi. *Int. J. Environ. Res. Public Health* 16 (3), 396. doi:10.3390/ijerph16030396

Miao Zhang, M., Shi, L., Ma, X., Zhao, Y., and Gao, L. (2021). Study on comprehensive assessment of environmental impact of air pollution. *Sustainability* 13 (2), 476. doi:10.3390/su13020476

Mirzaei, M., Amanollahi, J., and Tzanis, C. G. (2019). Evaluation of linear, nonlinear, and hybrid models for predicting PM2.5 based on a GTWR model and MODIS AOD data. *Air Qual. Atmos. Health* 12 (10), 1215–1224. doi:10.1007/s11869-019-00739-z

Ouyang, H., Tang, X., Kumar, R., Zhang, R., Brasseur, G., Churchill, B., et al. (2022). Toward better and healthier air quality: Implementation of WHO 2021 global air quality Guidelines in asia. *Bull. Am. Meteorol. Soc.* 103, E1696–E1703. doi:10.1175/bams-d-22-0040.1

Qian Yang, Q., Yuan, Q., Li, T., and Yue, L. (2020). Mapping PM2.5 concentration at high resolution using a cascade random forest based downscaling model: Evaluation and application. *J. Clean. Prod.* 277, 123887. doi:10.1016/j.jclepro.2020.123887

Qiu, X., Duan, L., Cai, S., Yu, Q., Wang, S., Chai, F., et al. (2017). Effect of current emission abatement strategies on air quality improvement in China: A case study of Baotou, a typical industrial city in inner Mongolia. *J. Environ. Sci.* 57, 383–390. doi:10.1016/j.jes.2016.12.014

Rupakheti, D., Yin, X., Rupakheti, M., Zhang, Q., Li, P., Rai, M., et al. (2021). Spatio-temporal characteristics of air pollutants over Xinjiang, northwestern China. *Environ. Pollut.* 268, 115907. doi:10.1016/j.envpol.2020.115907

Song, W., Jia, H., Huang, J., and Zhang, Y. (2014). A satellite-based geographically weighted regression model for regional PM2.5 estimation over the Pearl River Delta region in China. *Remote Sens. Environ.* 154, 1–7. doi:10.1016/j.rse.2014.08.008

Sui, M. (2019). Impact and feedback of air pollution on climate change. *Resour. Econ. Environ. Prot.* 01 (07), 43. doi:10.3969/j.issn.1673-2251.2019.07.051

Tee, C., Ng, E. Y. K., and Xu, G. (2020). Analysis of transport methodologies for pollutant dispersion modelling in urban environments. *J. Environ. Chem. Eng.* 8 (4), 103937. doi:10.1016/j.jece.2020.103937

Tørseth, K., Aas, W., Breivik, K., Fjaeraa, A., Fiebig, M., Hjellbrekke, A., et al. (2012). Introduction to the European Monitoring and Evaluation Programme (EMEP) and observed atmospheric composition change during 1972–2009. *Atmos. Chem. Phys.* 12, 5447–5481. doi:10.5194/acp-12-5447-2012

Utari, N. I., Srinadi, I. G. A., and Susilawati, M. (2019). Model geographically weighted regression (GWR) faktor-faktor yang memengaruhi kecelakaan lalu lintas di provinsi bali. *E-Jurnal Mat.* 8, 140. doi:10.24843/MTK.2019.v08.i02.p245

Vo, T. T. T., Wu, C.-Z., and Lee, I.-T. (2020). Potential effects of noxious chemical-containing fine particulate matter on oral health through reactive oxygen species-mediated oxidative stress: Promising clues. *Biochem. Pharmacol.* 182 (2), 114286. doi:10.1016/j.bcp.2020.114286

Wang, J., and Xu, C. (2017). *Geodetector: Principle and prospective*, 72, 116–134. doi:10.11821/dlxb201701010

Wang, Z., Wu, T., Che, F., Wang, S., Zhou, Y., Qian, X., et al. (2010). Comparison between domestic and international ambient air quality standards. *Res. Environ. Sci.* 23 (03), 253–260. doi:10.13198/j.res.2010.03.7.wangzsh.001

Wang, L., Xiong, Q., Wu, G., Gautam, A., Jiang, J., Liu, S., et al. (2019). Spatio-temporal variation characteristics of PM2.5 in the beijing-tianjin-hebei region, China, from 2013 to 2018. *Int. J. Environ. Res. Public Health* 16 (21), 4276–76. doi:10.3390/ijerph16214276

Wang, W., Zhang, L., Zhao, J., Qi, M., and Chen, F. (2020). The effect of socioeconomic factors on spatiotemporal patterns of PM2.5 concentration in beijing–tianjin–hebei region and surrounding areas. *Int. J. Environ. Res. Public Health* 17, 3014. doi:10.3390/ijerph17093014

Wei, Q., Zhang, L., Duan, W., and Zhen, Z. (2019). Global and geographically and temporally weighted regression models for modeling PM2.5 in heilongjiang, China from 2015 to 2018. *Int. J. Environ. Res. Public Health* 16 (24), 5107. doi:10.3390/ijerph16245107

Whitby, K. T., Husar, R., and Liu, B. Y. H. (1972). The aerosol size distribution of los angeles smog. *J. Colloid Interface Sci.* 39, 177–204. doi:10.1016/0021-9797(72)90153-1

Wu, Z., Zhang, X., and Wu, M. (2015). Mitigating construction dust pollution: State of the art and the way forward. *J. Clean. Prod.* 112 (01), 1658–1666. doi:10.1016/j.jclepro.2015.01.015

Xiao, Q., Ma, Z., Li, S., and Liu, Y. (2015). The impact of winter heating on air pollution in China. *PloS one* 10, e0117311. doi:10.1371/journal.pone.0117311

Xin Zhang, X., Fan, Y., Wei, S., Wang, H., and Zhang, J. (2021). Spatiotemporal distribution of $PM_{2.5}$ and ItsCorrelation with other air pollutants in WinterDuring 2016~2018 in xi'an, China. *Pol. J. Environ. Stud.* 30 (2), 1457–1464. doi:10.15244/pjoes/124755

Yan, H. (2012). Research on the influence of air pollution on ecological environment and countermeasures. *Mod. Agric.* 01 (03), 95–96. doi:10.3969/j.issn.1008-0708.2012.03.087

Yang, J., Zhao, T., Cheng, X., Ren, Z., Meng, L., He, Q., et al. (2021). Temporal and spatial variations of sandstorm and the related meteorological influences over northern China from 2000 to 2019. *Acta Sci. Circumstantiae* 41 (08), 2966–2975. doi:10.13671/j.hjkxxb.2021.0234

Yang, W., and Jiang, X. (2020). Interannual characteristics of fine particulate matter in North China and its relationship with land use and land cover change. *Environ. Sci.* 41 (07), 2995–3003. doi:10.13227/j.hjkx.201911079

Yuan Wei, Y., Li, Z., Zhang, Y., Chen, C., Xie, Y., Lv, Y., et al. (2021). Derivation of PM10 mass concentration from advanced satellite retrieval products based on a semi-empirical physical approach. *Remote Sens. Environ.* 256 (16), 112319. doi:10.1016/j.rse.2021.112319

Zhai, L., Li, S., Zou, B., Sang, H., Fang, X., and Xu, S. (2018). An improved geographically weighted regression model for PM 2.5 concentration estimation in large areas. *Atmos. Environ.* 181 (03), 145–154. doi:10.1016/j.atmosenv.2018.03.017

Zhang, D., and Li, W. (2020). Analysis on the progress of urban air pollution research. *Technol. Innovation Appl.* 01 (19), 79–80+83.

Zhao, Z., Xi, H., Russo, A., Du, H., Gong, Y., Xiang, J., et al. (2019). The influence of multi-scale Atmospheric circulation on severe haze events in autumn and winter in Shanghai, China. *Sustainability* 11 (21), 5979. doi:10.3390/su11215979

Zheng, C., Zhao, C., Li, Y., Wu, X., Zhang, K., Gao, J., et al. (2018). Spatial and temporal distribution of NO2 and SO2 in Inner Mongolia urban agglomeration obtained from satellite remote sensing and ground observations. *Atmos. Environ.* 188, 50–59. doi:10.1016/j.atmosenv.2018.06.029

Zhou, C., Wei, G., Zheng, H., Russo, A., Li, C., Du, H., et al. (2019). Effects of potential recirculation on air quality in coastal cities in the Yangtze River Delta. *Sci. Total Environ.* 651, 12–23. doi:10.1016/j.scitotenv.2018.08.423

Zhuorui Wei, Z., Zhang, L., Ren, Y., Wei, W., Zhang, H., Cai, X., et al. (2021). Characteristics of the turbulence intermittency and its influence on the turbulent transport in the semi-arid region of the Loess Plateau. *Atmos. Res.* 249, 105312. doi:10.1016/j.atmosres.2020.105312

# Advantages of publishing in Frontiers

**OPEN ACCESS**
Articles are free to read for greatest visibility and readership

**FAST PUBLICATION**
Around 90 days from submission to decision

**HIGH QUALITY PEER-REVIEW**
Rigorous, collaborative, and constructive peer-review

**TRANSPARENT PEER-REVIEW**
Editors and reviewers acknowledged by name on published articles

**Frontiers**
Avenue du Tribunal-Fédéral 34
1005 Lausanne | Switzerland

**Visit us:** www.frontiersin.org
**Contact us:** frontiersin.org/about/contact

**REPRODUCIBILITY OF RESEARCH**
Support open data and methods to enhance research reproducibility

**DIGITAL PUBLISHING**
Articles designed for optimal readership across devices

**FOLLOW US**
@frontiersin

**IMPACT METRICS**
Advanced article metrics track visibility across digital media

**EXTENSIVE PROMOTION**
Marketing and promotion of impactful research

**LOOP RESEARCH NETWORK**
Our network increases your article's readership